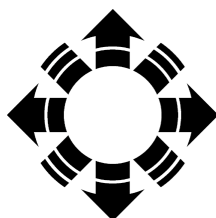


Proceedings of the 2000 U.S. DOE Hydrogen Program Review

Sponsored by the Office of Power Delivery
Systems, Office of Power Technologies,
U.S. Department of Energy

*Presented at the 2000 U.S. DOE
Hydrogen Program Review
San Ramon, California
May 9–11, 2000*



NREL

National Renewable Energy Laboratory

1617 Cole Boulevard
Golden, Colorado 80401-3393

NREL is a U.S. Department of Energy Laboratory
Operated by Midwest Research Institute • Battelle • Bechtel

Contract No. DE-AC36-99-GO10337

NOTICE

This report was prepared as an account of work sponsored by an agency of the United States government. Neither the United States government nor any agency thereof, nor any of their employees, makes any warranty, express or implied, or assumes any legal liability or responsibility for the accuracy, completeness, or usefulness of any information, apparatus, product, or process disclosed, or represents that its use would not infringe privately owned rights. Reference herein to any specific commercial product, process, or service by trade name, trademark, manufacturer, or otherwise does not necessarily constitute or imply its endorsement, recommendation, or favoring by the United States government or any agency thereof. The views and opinions of authors expressed herein do not necessarily state or reflect those of the United States government or any agency thereof.

Proceedings of the 2000 U.S. DOE Hydrogen Program Review

Sponsored by the Office of Power Delivery Systems,
Office of Power Technologies, U.S. Department of Energy

Table of Contents

Overview Presentations

| | | |
|--|----------|--------|
| DOE Hydrogen Program Overview | Overview | 1- 32 |
| Sig Gronich | | |
| Validation Projects | Overview | 33- 38 |
| Jay Keller | | |
| Analysis Coordinations | Overview | 39- 43 |
| Margaret Mann | | |
| Production Projects | Overview | 44- 55 |
| Catherine Grégoire Padró | | |
| Storage Projects | Overview | 56- 69 |
| George Thomas | | |

Volume I

| | | |
|---|--|--------|
| Liquid Fuel Reformer Development: Autothermal Reforming of Diesel Fuel | | 1- 11 |
| C. Pereira, J-M Bae, S. Ahmed and M. Krumpelt, Argonne National Laboratory | | |
| Thermal Dissociation of Methane Using a Solar Coupled Aerosol Flow Reactor | | 12- 34 |
| A.W. Weimer, J. Dahl, and J. Tamburini, University of Colorado; A. Lewandowski, R. Pitts, and C. Bingham, National Renewable Energy Laboratory; G.C. Glatzmaier, Peak Design | | |
| Defect-Free Thin Film Membranes for H₂ Separation and Isolation | | 35- 40 |
| T.M. Nenoff, Sandia National Laboratories | | |
| Separation Membrane Development (presentation) | | 41- 56 |
| L.K. Heung, Savannah River Technology Center | | |
| Integrated Ceramic Membrane System for Hydrogen Production | | 57- 62 |
| M. Shah, R.F. Drnevich, Praxair, Inc.; U. Balachandran, Argonne National Laboratory | | |
| Hydrogen Production by Superadiabatic Decomposition of Hydrogen Sulfide | | 63- 69 |
| R. Slimane, F. Lau, and J. Abbasian, Gas Technology Institute (GTI) | | |

| | |
|---|---------|
| Thermocatalytic CO₂-Free Production of Hydrogen from Hydrocarbon Fuels | 70- 97 |
| N. Muradov, Florida Solar Energy Center | |
| Sorption Enhanced Reaction Process (SERP) for Production of Hydrogen | 98-109 |
| J. Hufton, W. Waldron, S. Weigel, M. Rao, S. Nataraj, S. Sircar, Air Products and Chemicals, Inc. | |
| Engineering Development of Ceramic Membrane Reactor Systems for Converting Natural Gas to Hydrogen and Synthesis Gas for Liquid Transportation Fuels | 110-120 |
| P.N. Dyer, C.M. Chen, Air Products and Chemicals, Inc. | |
| Novel Catalytic Reforming Using Microtechnology with Advanced Separations Technology | 121-129 |
| P.M. Irving, W.L. Allen, and T. Henley, InnovaTek, Inc.; W.J. Thomsen, Washington State University | |
| Production of Hydrogen from Biomass-Derived Liquids | 130-140 |
| S. Czernik, R. French, C. Feik and E. Chornet, National Renewable Energy Laboratory | |
| Modeling of Dense Gas-Solid Reactive Mixtures Applied to Biomass Pyrolysis in a Fluidized Bed | 141-203 |
| D. Lathouwers and J. Bellan. California Institute of Technology | |
| Solar Photocatalytic Hydrogen Production from Water Using a Dual Bed Photosystem | 204-216 |
| C.A. Linkous, D.K. Slattery, Florida Solar Energy Center | |
| Photoelectrochemical Hydrogen Production | 217-230 |
| E. Miller and R. Rocheleau, University of Hawaii | |
| Photoelectrochemical System Studies | 231-247 |
| A. Bansel, O. Khaselev, and J.A. Turner, National Renewable Energy Laboratory | |
| Biological H₂ from Fuel Gases and from H₂O | 248-261 |
| P-C. Maness and P.F. Weaver, National Renewable Energy Laboratory | |
| Bioreactor Development for Biological Hydrogen Production | 262-271 |
| E.J. Wolfrum and P.F. Weaver, National Renewable Energy Laboratory | |
| Development of an Efficient Algal H₂-Producing System | 272-281 |
| M.L. Ghirardi, Z. Huang, M. Forestier, S. Smolinski, M. Posewitz and M. Seibert, National Renewable Energy Laboratory | |
| Two-Phase Photobiological Algal H₂-Production System | 282-294 |
| M.L. Ghirardi, S. Kosourov, A. Tsygankov and M. Seibert, National Renewable Energy Laboratory | |
| Discovery of an Alternative Oxygen Sensitivity in Algal Photosynthetic H₂ Production | 295-299 |
| J.W. Lee and E. Greenbaum, Oak Ridge National Laboratory | |

| | |
|--|---------|
| Photosynthetic Solar Conversion Efficiency in Wild Type and Truncated Chl Antenna Transformant (Chl <i>b</i>-less Mutant) of the Green Alga, <i>Chlamydomonas reinhardtii</i> | 300-319 |
| J.E.W. Polle, J.R. Benemann, A. Tanaka, A. Melis, University of California, Berkeley | |
| Efficient Production of Hydrogen from Glucose-6-Phosphate | 320-328 |
| J. Woodward, M. Orr, K. Cordray, and E. Greenbaum, Oak Ridge National Laboratory | |
| Integrated Renewable Hydrogen Utility System | 329-334 |
| R.J. Friedland, Proton Energy Systems, Inc. | |
| High Efficiency Steam Electrolyzer | 335-344 |
| A-Q. Pham, Lawrence Livermore National Laboratory | |
| Filling Up with Hydrogen 2000 | 345-353 |
| M.J. Fairlie, P.B. Scott, Stuart Energy USA | |
| Technology Development & Validation of Industrial Fuel Cell Vehicles—Phases II/III | 354-359 |
| J.M. Morrison, Southeastern Technology Center | |
| Hydrogen-Enriched Natural Gas Bus Demonstration | 360-374 |
| R. Roser, NRG Technologies, Inc. | |
| Progress on Improvements to a Hydrogen/Electric Hybrid Bus | 375-387 |
| Y. Baghzouz, J. Fiene, J. Van Dam, L. Shi, E. Wilkinson, R. Boehm, University of Nevada; T. Kell, Kell's Automotive | |
| H₂ Reformer, Fuel Cell Power Plant & Vehicle Refueling System (presentation) .. | 388-401 |
| V.Raman, Air Products and Chemicals, Inc. | |
| The Remote Area Power Program (RAPP) | 402-407 |
| D. Witmer, R. Johnson, T. Johnson, University of Alaska; J. Keller, A. Lutz, Sandia National Laboratories. | |
| Fuel-Cell Mine Vehicle—Development and Testing | 408-420 |
| A.R. Miller, Fuelcell Propulsion Institute | |

Volume II

| | |
|---|---------|
| Carbon Nanotube Materials for Hydrogen Storage | 421-440 |
| A.C. Dillon, T. Gennett, J.L. Alleman, K.M. Jones, P.A. Parilla, M.J. Heben, National Renewable Energy Laboratory | |
| Hydrogen Transmission/Storage with a Metal Hydride-Organic Slurry and Advanced Chemical Hydride/Hydrogen for PEMFC Vehicles | 441-454 |
| A.W. McClaine, R.W. Breault, C. Larsen, R. Konduri, J. Rolfe, F. Becker, and G. Miskolczy, Thermo Technologies | |
| An Integrated PV—Electrolysis Metal Hydride Hydrogen Generation and Storage System | 455-462 |
| K. Sapru, S. Ramachandran, Z. Tan, Energy Conversion Devices, Inc. | |
| High-Pressure Conformable Hydrogen Storage for Fuel Cell Vehicles | 463-469 |
| A. Haaland, Thiokol Propulsion | |
| Vehicular Hydrogen Storage Using Lightweight Tanks | 470-551 |
| F. Mitlitsky, A.H. Weisberg, and B. Myers, Lawrence Livermore National Laboratory | |
| Low Temperature and High Pressure Evaluation of Insulated Pressure Vessels for Cryogenic Hydrogen Storage | 552-565 |
| S. Aceves, Lawrence Livermore National Laboratory; J. Martinez-Frias, Centro de Ingenieria y Desarrollo Industrial; O. Garcia-Villazana, FINEE, Universidad de Guanajuato | |
| Hydride Development for Hydrogen Storage | 566-581 |
| K.J. Gross, G.J. Thomas and G. Sandrock, Sandia National Laboratories | |
| Hydride Bed/Fuelcell Project | 582-587 |
| G. Cook Story, Sandia National Laboratories | |
| Catalytically Enhanced Systems for Hydrogen Storage | 588-593 |
| C.M. Jensen, S. Takara, University of Hawaii | |
| The Corrosion of Metallic Components in Fuel Cells | 594-596 |
| J.A. Turner, National Renewable Energy Laboratory | |
| Small Battery—Fuel Cell Alternative Technology Development | 597-605 |
| M.S. Wilson, E.B. Brown, C. Zawodzinski., Los Alamos National Laboratory; M. Daugherty, Enable Fuel Cell Corp. | |
| PEMFC Stacks for Power Generation | 606-617 |
| M.S. Wilson, C. Zawodzinski, G. Bender, T.A. Zawodzinski, and D.N. Busick, Los Alamos National Laboratory | |
| Low Cost Reversible Fuel Cell System | 618-626 |
| R.C. Ruhl, Technology Management, Inc. | |
| Gallium Nitride Integrated Gas/Temperature Sensors for Fuel Cell System Monitoring for Hydrogen and Carbon Monoxide | 627-638 |
| S.C. Pyke, Peterson Ridge, LLC; J-H. Chern, R.J. Hwu, L.P. Sadwick, University of Utah | |

| | |
|--|---------|
| Advanced Internal Combustion Engine Research | 639-657 |
| P. Van Blarigan, Sandia National Laboratories | |
| Development of Low Cost Hydrogen Sensors | 658-667 |
| R.J. Lauf, Oak Ridge National Laboratory, C. Salter, R.D. Smith II, DCH Technology | |
| Interfacial Stability of Thin Film Hydrogen Sensors | 668-683 |
| J.R. Pitts, P. Liu, S.-H. Lee, and C.E. Tracy, National Renewable Energy Laboratory; R.D. Smith and C. Salter, DCH Technology | |
| Hydrogen Pressure Vessel Testing Program | 684-688 |
| B.C. Odegard Jr., G.J. Thomas, Sandia National Laboratories | |
| Dispersion of Hydrogen Clouds | 689-719 |
| M.R. Swain, E.S. Grilliot, M.N. Swain, University of Miami | |
| Advanced Thermal Hydrogen Compression | 720-727 |
| D. DaCosta, Ergenics, Inc. | |
| Microhotplate Based H₂ Gas Sensors | 728-736 |
| F. DiMeo Jr., B. Chen, ATMI, Inc. | |
| Process Analysis Work for the DOE Hydrogen Program—1999 | 737-747 |
| M.K. Mann, P.L. Spath, W.A. Amos, and J.M. Lane, National Renewable Energy Laboratory | |
| An Investigation of the Integration of Hydrogen Technologies into Maritime Applications | 748-755 |
| R.W. Foster, DCH Technology Inc. | |
| Analysis of Residential Fuel Cell Systems & PNGV Fuel Cell Vehicles | 756-784 |
| C.E. (Sandy) Thomas, B.D. James and F.D. Lomax, Jr., Directed Technologies, Inc. | |
| Assessment of Hydrogen-Fueled Proton Exchange Membrane Fuel Cells for Distributed Generation and Cogeneration | 785-827 |
| T.G. Kreutz and J.M. Ogden, Princeton University | |
| Integrated Hydrogen Fuel Infrastructure Research and Technology Development | 828-834 |
| J. Ohi, B. Farhar, C. Hammel, R. Hewett, and P. Norton, National Renewable Energy Laboratory | |
| Opportunities for Hydrogen: An Analysis of the Application of Biomass Gasification to Farming Operations Using Microturbines and Fuel Cells | 835-846 |
| D.D. Schmidt, J.R. Gunderson, University of North Dakota | |
| Commercial Applications of Fuel Cells at Billings | 847-855 |
| T. Galloway, J. Waidl, Intellery Corp.; C. Heath, Center for Applied Economic Research; L. Ratcliff, Big Sky Economic Development Authority | |
| Technical Assessment and Analysis of Hydrogen R&D Projects | 856-859 |
| E.G. Skolnik, Energetics, Incorporated | |

| | |
|--|---------|
| Analysis of the Sodium Hydride-Based Hydrogen Storage System Being Developed by PowerBall Technologies, LLC | 860-888 |
| E.G. Skolnik, Energetics, Incorporated | |
| NHA DOE Cost Shared Activities | 889-896 |
| R.L. Mauro and K.L. Miller, National Hydrogen Association | |
| Education Outreach | 897-909 |
| M. Szoka-Valladares, M.R.S. Enterprises | |
| Creating an Informed Public through a Video on Hydrogen Safety (presentation)..... | 910-918 |
| G. Holland, Hydrogen 2000 | |



Hydrogen Program Goals and Outcomes

Presented at:

2000 Hydrogen Program Annual Review Meeting

Presented by:

Sig Gronich, Hydrogen Team Leader



Legislative Mandates



Pursuant to Hydrogen Futures Act of 1996 and the Matsunaga Hydrogen RD&D Act of 1990:

- DOE shall conduct a research, development, and demonstration program leading to the production, storage, transport, and use of hydrogen for industrial, residential, transportation, and utility applications.
- DOE shall conduct a program to accelerate wider application of hydrogen technologies available in the near term as a result of aerospace experience and other research progress.



Hydrogen Program Vision



In the next twenty years, concerns about global climate change and energy security will create the platform for the penetration of hydrogen into several niche markets. Ultimately, hydrogen and electricity will come from sustainable renewable energy resources, but fossil fuels will be a significant transitional resource during this period. The growth of fuel cell technology will provide a basis for the establishment of the hydrogen option into both transportation and electricity supply markets.



Strategic Goals



Mid-Term

Support technologies that enable early introduction of distributed electric-generation fuel cell systems, and hydrogen fuel-cell vehicles for transportation applications.

Long-Term

Support development of hydrogen technologies that enhance intermittent renewable systems and offer society the promise of clean, abundant fuels.



Current Forces



- **SIGNIFICANT FUEL CELL DEVELOPMENTS AND PARTNERSHIPS**
 - Daimler-Chrysler, Ford and Ballard have formed partnerships, and pledged \$1.5 Billion for commercialization of automotive Fuel Cells
 - Edison Development Company, G.E., SoCal Gas, Plug Power have agreement to commercialize residential fuel cells (other companies are also pursuing residential systems)
 - I.F.C. has developed high performance fuel cell for automotive and electrical generation systems
- **CALIFORNIA ZERO EMISSIONS VEHICLE REQUIREMENTS FAVOR EARLY INTRODUCTION OF EITHER ELECTRIC OR HYDROGEN VEHICLES**
- **CALIFORNIA FUEL CELL PARTNERSHIP WAS FORMED**
 - Demonstrate 50 Hydrogen Fuel Cell cars and 20 Buses by 2003
- **SIGNIFICANT INDUSTRY INTEREST IN PARTNERSHIP TO BRING FUEL CELLS INTO MINES**



Strategic Approach



Hydrogen Industry: → **Smaller reformers and electrolyzer systems**

- Improve efficiency, lower emissions, and lower the cost of H₂ production

Fuel Cell/Hydrogen Integration: → **Industry deployment of fuel cells**

- Enhance the introduction and production of distributed systems that enhance refueling and generation system missions

Fuel Choice/Infrastructure: → **Zero Emission Vehicles**

- Demonstrate safe and cost-effective systems for hydrogen vehicles in urban non-attainment areas, and to provide on-board hydrogen storage systems

Long-term Research and Development:

- Lower the cost of technologies that produce hydrogen directly from sunlight and water



Hydrogen Program Funding



FY 1999-FY 2001 Budgets:

| Hydrogen Program Funding Summary | FY 1999 Appropriated | FY 2000 Appropriated | FY 2001 Request |
|--|-----------------------------|-----------------------------|------------------------|
| Core Research and Development Production Storage Utilization | 8,951 | 13,353 | 13,020 |
| Technology Validation Renewable/ H₂ Systems H₂ Infrastructure Distributed/ Remote Power Systems | 10,856 | 8,754 | 7,500 |
| Analysis and Outreach | 2,169 | 2,480 | 2,480 |
| Total | 21,976 | 24,587 | 23,000 |



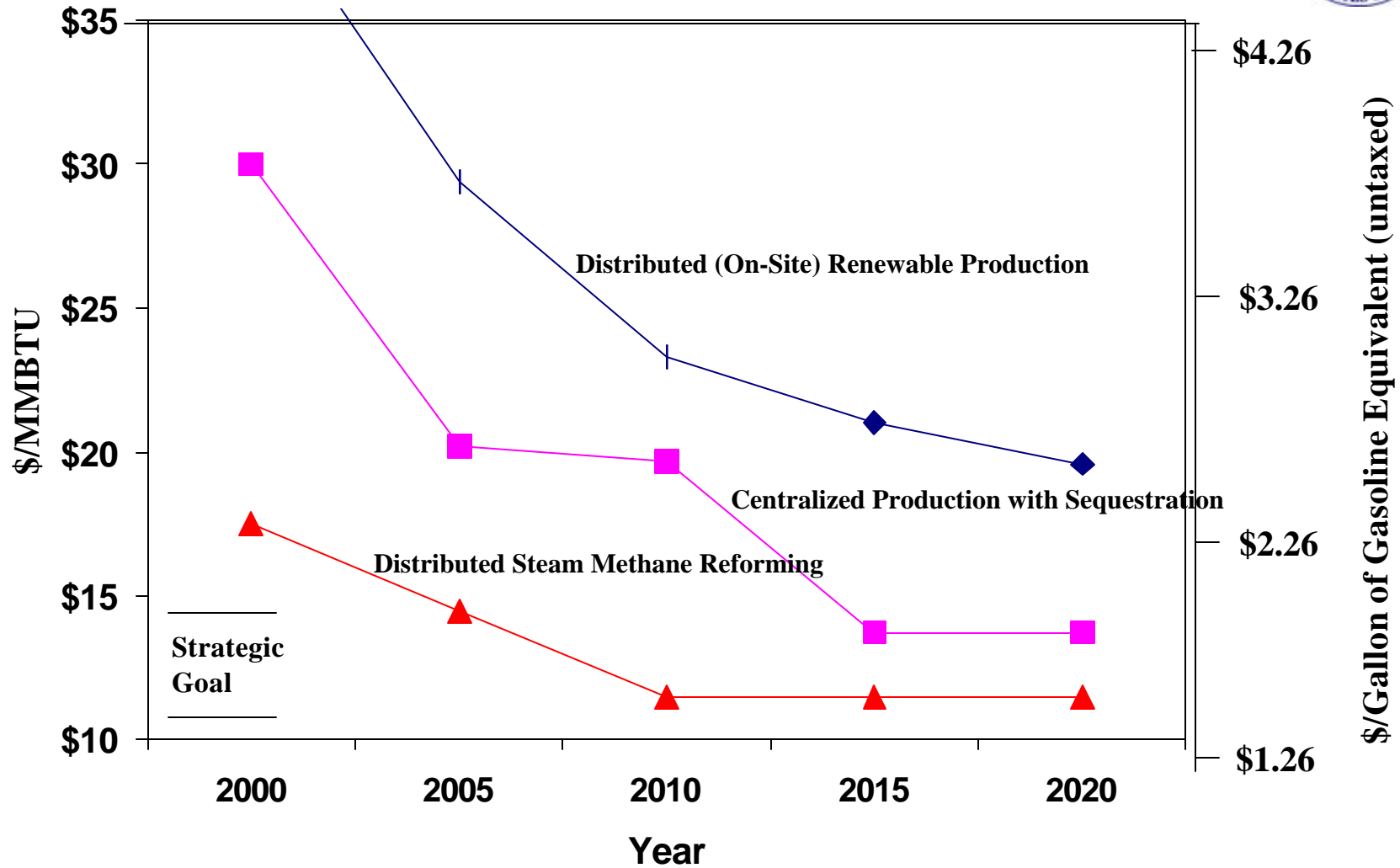
Production Goals



- Improve the efficiency and lower the cost of fossil-based and biomass-based hydrogen production processes to achieve \$12 - \$15/MMBtu for pressurized hydrogen when reformers are mass produced
- Advance emission-free and renewable-based hydrogen production technologies towards commercial viability, with a target cost of \$10 - \$15/MMBtu



Cost of Delivered Hydrogen



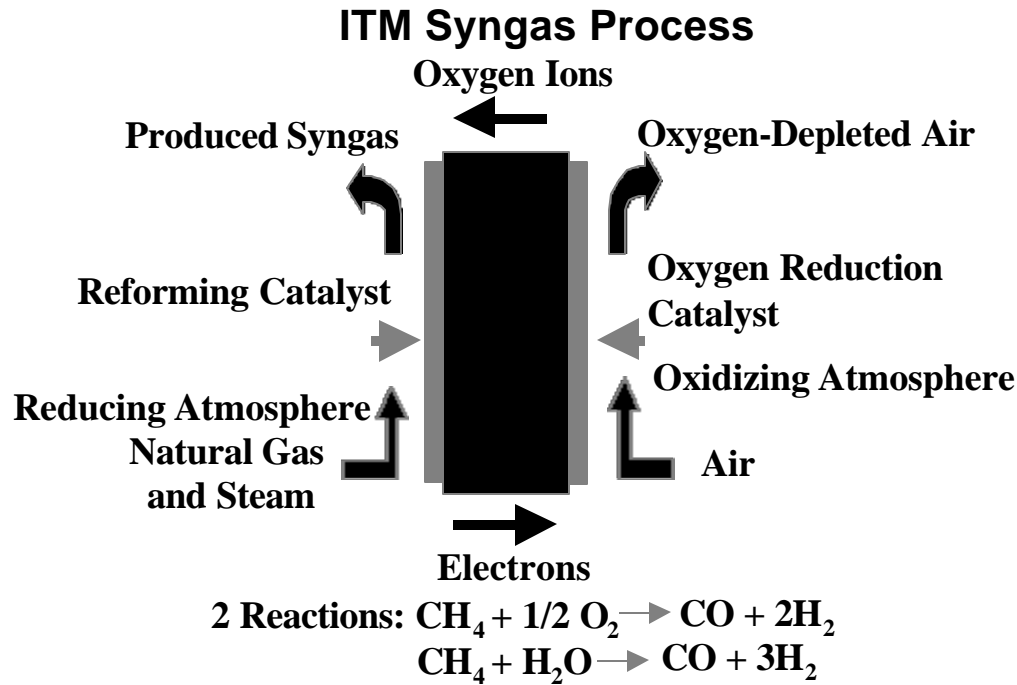


Fossil-based Production

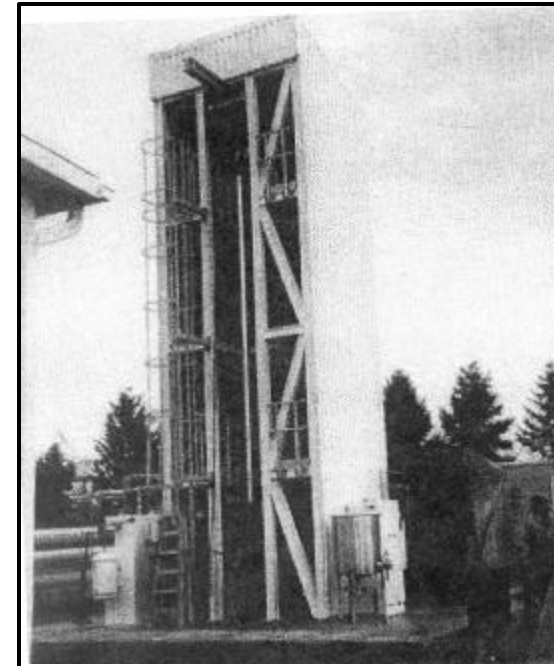


| Fossil-based Hydrogen Production | | |
|----------------------------------|--|----------------------------------|
| | ITM Syngas Process | Air Products |
| | Sorption Enhanced Reaction Process for Production of H2 | Air Products |
| | Liquid Fuel-Reformer Development | Argonne National Laboratory |
| NEW | Integrated Ceramic Membrane System for H2 Production | Praxair |
| NEW | Novel Catalytic Fuel Reforming | InnovaTek |
| NEW | Production of H2 by Superadiabatic Decomposition of Hydrogen Sulfide | Institute of Gas Technology |
| NEW | Thermo-catalytic CO2-Free Production of Hydrogen using Hydrocarbon Fuels | Florida Solar Energy Center |
| NEW | Thermal Dissociation of Methane using a Solar Coupled Aerosol Flow Reactor | University of Colorado/NREL |
| NEW | Hydrogen Membrane Separation | Sandia National Laboratories |
| | Separation Membrane Development | Savannah River Technology Center |

ITM Syngas and SER Processes



SER Process



- Advance reformer technology that can reduce the cost of hydrogen production by > 25%



Biomass-based Production



| Biomass-based Production | | |
|---------------------------------|---|--------------------------------------|
| | Biomass to Hydrogen via Fast Pyrolysis and Catalytic Steam Reforming | National Renewable Energy Laboratory |
| | Biomass Pyrolysis for Hydrogen Production | Jet Propulsion |
| NEW | Integrated H2 Production for Agricultural Residues for Urban Transportation | Clark Atlanta University |
| NEW | Supercritical Water; Partial Oxidation | General Atomics |
| NEW | Biohydrogen Production from Renewable Organic Wastes | Iowa State University |



Photoelectrochemical/Biological Production



| Photoelectrochemical /Biological Hydrogen Production | | |
|--|--|--------------------------------------|
| NEW | Photoelectrochemical Hydrogen Production | University of Hawaii |
| | Photoelectrochemical based Direct Conversion Systems for Hydrogen Production | National Renewable Energy Laboratory |
| NEW | Solar Photocatalytic H ₂ Production from Water using a Dual bed Photosystem | Florida Solar Energy Center |
| | Development of an Efficient Algal H ₂ Producing System | National Renewable Energy Laboratory |
| | Two Phase Photobiological Algal H ₂ Production System | National Renewable Energy Laboratory |
| | Hydrogen Production by Photosynthetic Water Splitting | Oak Ridge National Laboratory |
| NEW | Maximizing Photosynthetic efficiencies and Hydrogen Production by Microalgal Cultures | University of California, Berkeley |
| | Photoproduction of Hydrogen from Glucose | Oak Ridge National Laboratory |
| | Biological H ₂ from Fuel Gases and Water | National Renewable Energy Laboratory |
| | Bioreactor Development for Biological H ₂ Production | National Renewable Energy Laboratory |



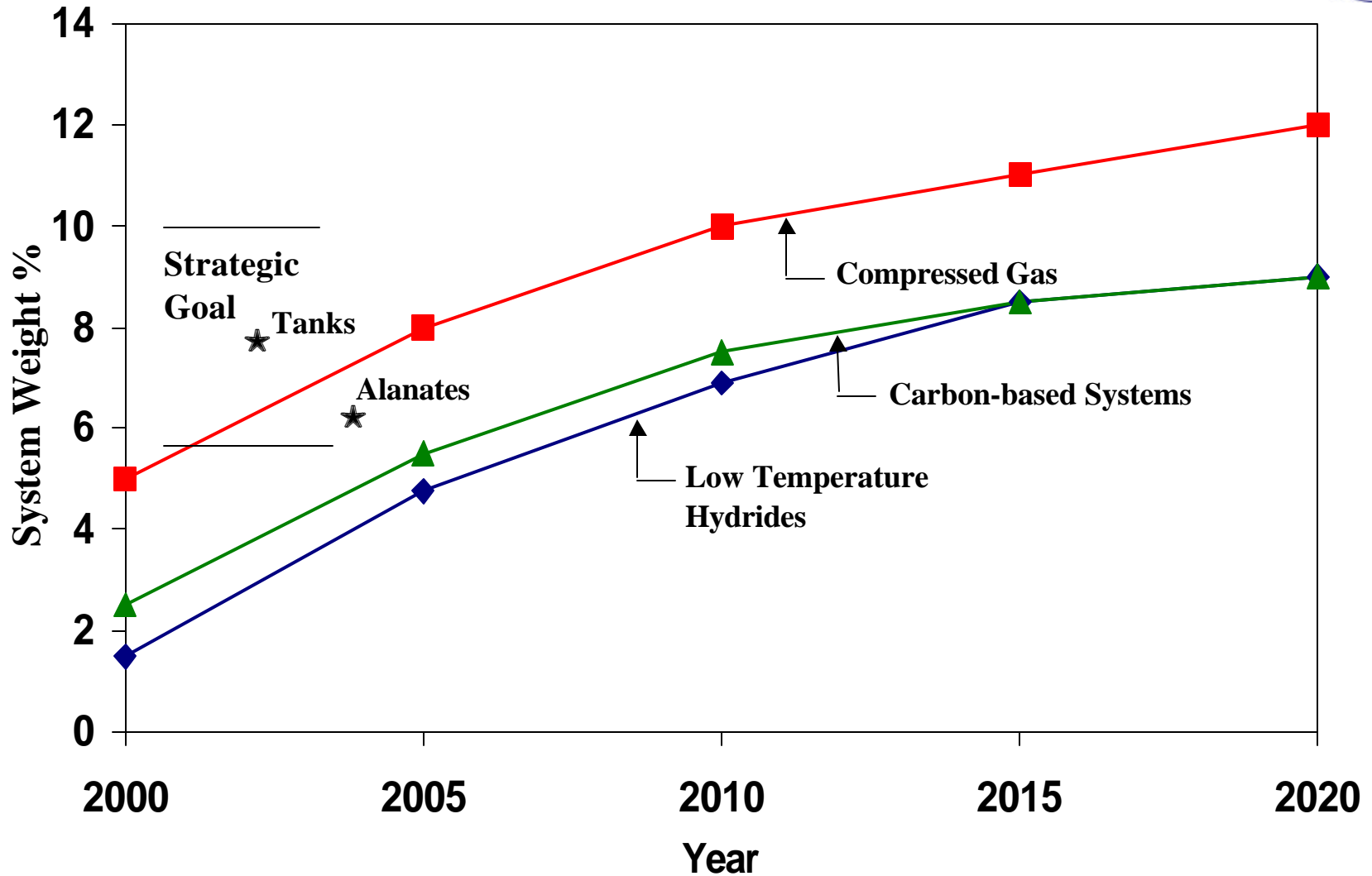
Storage and Utilization Goals



- Demonstrate safe and cost-effective storage systems for use in on-board and stationary distributed electricity generation applications
- Demonstrate safe and cost-effective storage systems for on-board applications in urban nonattainment areas
 - > 5.5% by weight at low temperature 100°C
 - > 20 kg/m³ for pressurized hydrogen; > 50kg/m³ for hydrides and carbon-based systems
- Develop fuel cell and reversible fuel cell technologies as an efficient low-cost means of converting hydrogen into electric power



Lightweight and Safe Storage Systems



Car Drop Test



Conformable Tank





Storage



| Hydrogen Storage | | |
|------------------|---|--|
| | Vehicular Hydrogen Storage using Cryogenic Hydrogen | Lawrence Livermore National Laboratory |
| NEW | Composite Tank Testing | Sandia National Laboratories |
| | Hydride Development for Hydrogen Storage | Sandia National Laboratories |
| NEW | Catalytically Enhanced Hydrogen Storage Systems | University of Hawaii |
| NEW | Alamate Hydrides | University of Hawaii |
| | Carbon Nanotube Materials for H2 Storage | National Renewable Energy Laboratory |
| NEW | Feasibility of Fullerene Hydride as High Capacity H2 Storage System | MER Corporation |
| NEW | Hydrogen Storage in Polymer Dispersed Metal Hydrides | United Technologies |
| | Advanced Chemical Hydride/H2 for PEMFC Vehicles | Thermo Power |



Stuart Electrolyser





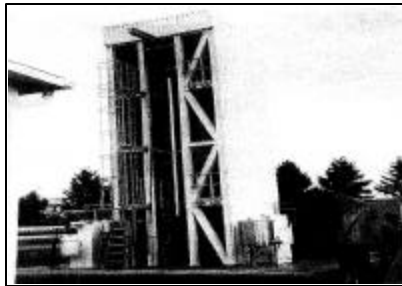
Utilization



| Utilization | | |
|-------------|--|--|
| | Corrosion of Metallic Components in Fuel Cells | National Renewable Energy Laboratory |
| | Small Battery-Fuel Cell Alternative Technology Development | Los Alamos National Laboratory |
| | PEMFC Stacks for Power Generation | Los Alamos National Laboratory |
| NEW | Low Cost Reversible Fuel Cell System | Technology Management, Inc. |
| NEW | Hydrogen Delivery Systems to PEMFC | New Jersey Dept. of Transportation |
| NEW | Gallium Nitride Integrated Gas/ Temperature Sensors for FC System Monitoring H2 and CO | Fluence |
| | Thick Film Hydrogen Sensor Detector | Oak Ridge National Laboratory |
| | Interfacial Stability of Thin Film Hydrogen Sensors | National Renewable Energy Laboratory |
| | High Efficiency Steam Electrolyzer | Lawrence Livermore National Laboratory |



Technology Summary



Production



Storage

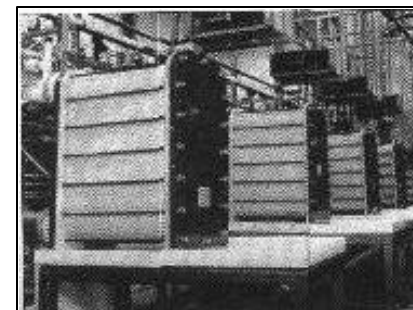


Electrolyzer

The Hydrogen R&D Program is concentrating on a set of “hydrogen appliances” that can be used at any point along the electric transmission or natural gas pipeline systems for distributed electric generation and transportation applications.



Distributed Generation



Reversible Fuel Cell



Technology Validation Criteria



Demonstrate Mid-Term Economically Viable Options

Demonstration of Integrated Systems to Verify Market Performance and Systems Economics, and Codes and Standards Development



Technology Validation Programmatic Factors and Lessons Learned



Renewable/ Hydrogen Systems

Electrolyzers and reversible fuel cells are being developed

Solar economics and development lag

Wind Powering America and Bioenergy are significant DOE initiatives

Hydrogen Infrastructure

Zero Emission Vehicles

California Fuel Cell Partnership

Production and Storage Systems Demonstrations

Distributed/ Remote Power Systems

Collaborate Fuel Cell Strategy with Buildings and Transportation Sectors

Understand Diesel Reformation Better



Technology Validation Projects

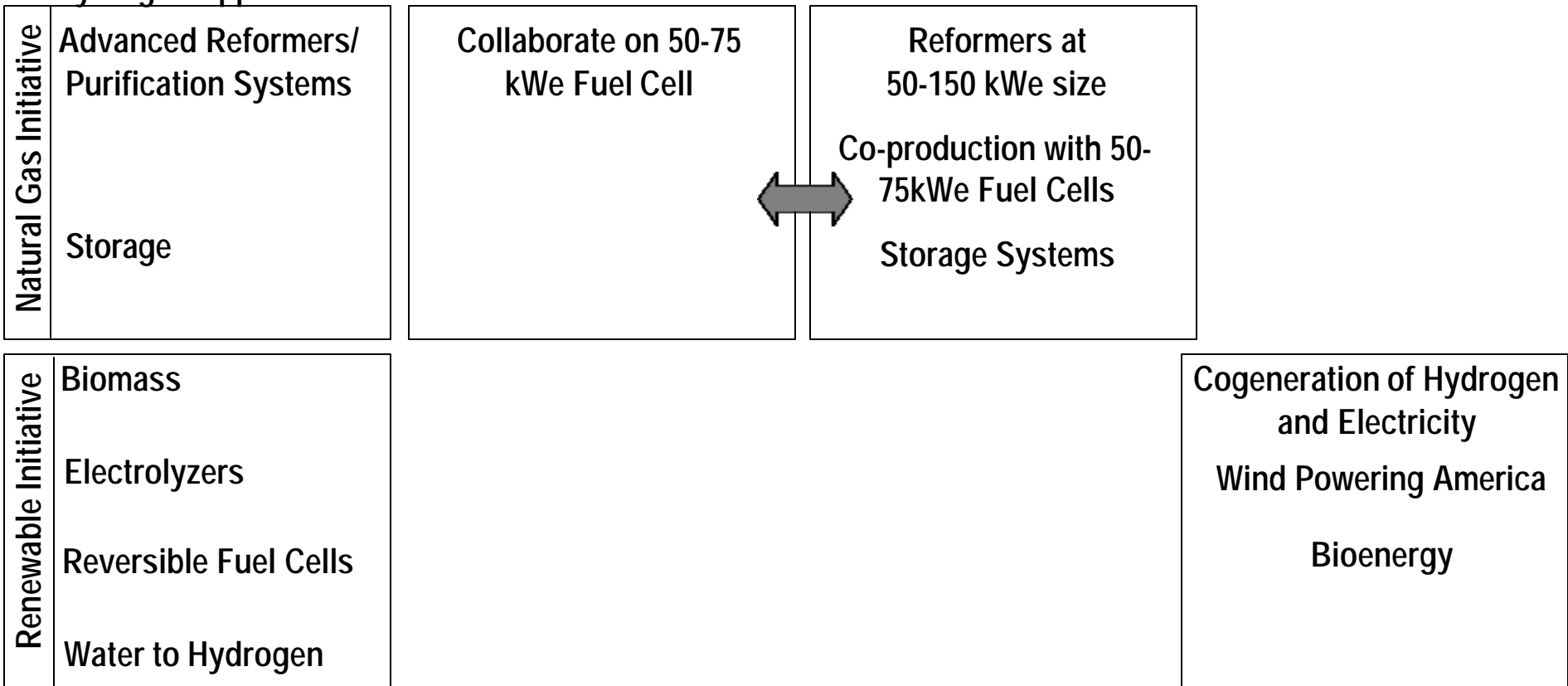


Core Research and Development
"Hydrogen Appliances"

Distributed Generation
OBT/OPT

H₂ Infrastructure
OTT

Renewable H₂ Systems
OPT





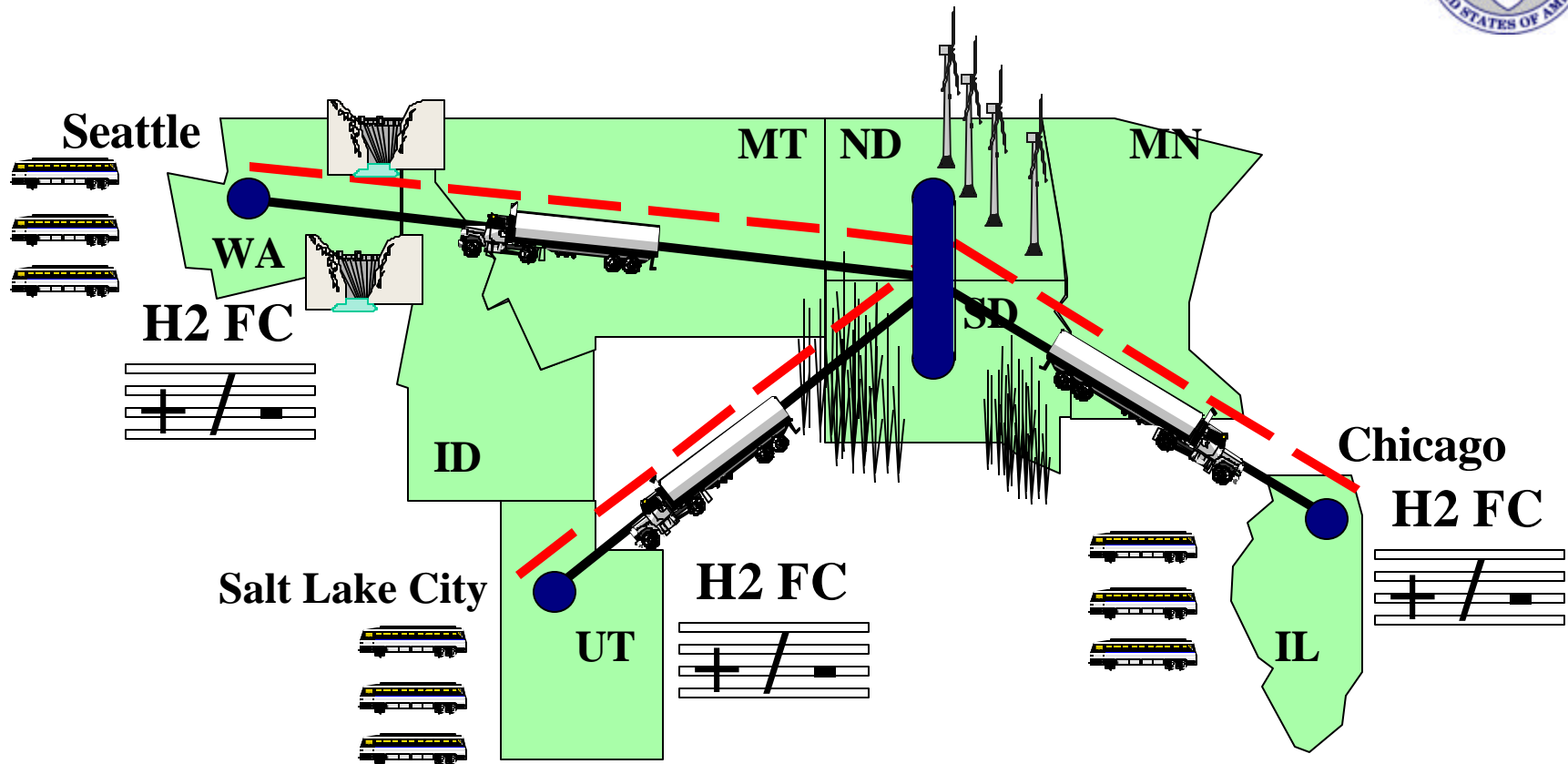
Technology Validation



| Technology Validation | | |
|--------------------------------|--|--|
| Renewable/Hydrogen | | |
| | Production of Hydrogen through Electrolysis | Proton Energy Systems |
| | Integrated PV Electrolysis Metal Hydride Storage System Assessment | Energy Conversion Devices |
| | Hydrogen Based Utility Energy Storage | Solar Reactor Technology Group; National Power |
| Hydrogen Infrastructure | | |
| | Hydrogen Reformer Fuel Cell Power Generator and Vehicle | Air Products and Chemicals |
| NEW | Hydrogen Generation Field Valadaation System | TBD |
| | Hybrid Hydrogen Electric Bus Development | University of Nevada Las Vegas |
| | Hydrogen Enriched Natural Gas Heavy Duty Engine Development | NRG Technologies |
| | Filling up with Hydrogen-2000 | Stuart Energy Systems |
| | High Pressure Conformable Hydrogen Storage of FC Vehicles | Thiokol Propulsion Company |
| | Vehicular Hydrogen Storage using Lightweight Tanks | Lawrence Livermore National Laboratory |
| NEW | High-Pressure Lightweight Tanks | TBD |
| | Fabrication of Hydride Bed for Technology Validation Project | Sandia National Laboratories |
| | Fuel Cell Mine Vehicle Development and Testing | Fuel Cell Propulsion Institute |
| | Industrial Fuel Cell Vehicle | Southeastern Technoogy Center |
| Remote Power Fuel Cells | | |
| | PEM Fuel Cell Alaskan RAPP | Northwest Power |
| NEW | Fuel Cell Technology Phase III Alaska | Dias Analytical Power |
| | Remote Power Fuel Cells Development | University of Alaska |
| | Big Sky-Analysis of State Resources for Fuel Cell Potential | Montana Trade Authority |



Hydrogen Technology Can Carry Farm Power to the Cities



———— Bio-crude and electricity are delivered to market centers for thermal and electrolytic conversion to H₂ (respectively)

- - - - Direct hydrogen delivery via pipelines to market centers



Reversible Fuel Cell for Wind Integration



- Time-of-day tariff for Chicago (ComEd)
 - Peak (9 a.m. - 10 p.m.) energy charge $\text{¢}5.5/\text{kWh}$, off-peak is $\text{¢}2.3/\text{kWh}$
 - Summer (June - September) demand charge of $\$14.24/\text{kW}$, winter is $\$11.13$
- Wind power is assumed to substitute for off-peak energy at $\text{¢}4/\text{kWh}$
- Reversible Fuel Cell (RFC) assumed at $\$1000/\text{kW}$
- Annual savings of $\$130/\text{kW}$, RFC pays for itself in 7.72 years
- Time-of-day tariff for New York (ConEd), “supplementary service”
 - Peak (8 a.m. - 10 p.m.) composite energy charge of $\text{¢}4/\text{kWh}$, off-peak composite of $\text{¢}3/\text{kWh}$ (rate is adjusted during summer)
 - Year-round demand charge of $\$2.70/\text{kW}$, summer-only, add $\$43.58$
- Same wind & RFC assumptions as Chicago
- Annual savings of $\$205/\text{kW}$, RFC pays for itself in 4.87 years



Title II—*Transition to a Hydrogen Based Economy*



- **Reauthorization of Hydrogen Future Act in 2002**
- **Title II Opportunities**
 - **Demonstration of Low-cost Hydrogen Production Systems in the Market Place**
 - **Development of Hydrogen Infrastructure to Support Zero Emission Vehicles**
 - **Demonstration and Cost Reduction of Distributed Power Generation Fuel-Cell Systems**
 - **Increasing Field Experience with these Integrated Systems**



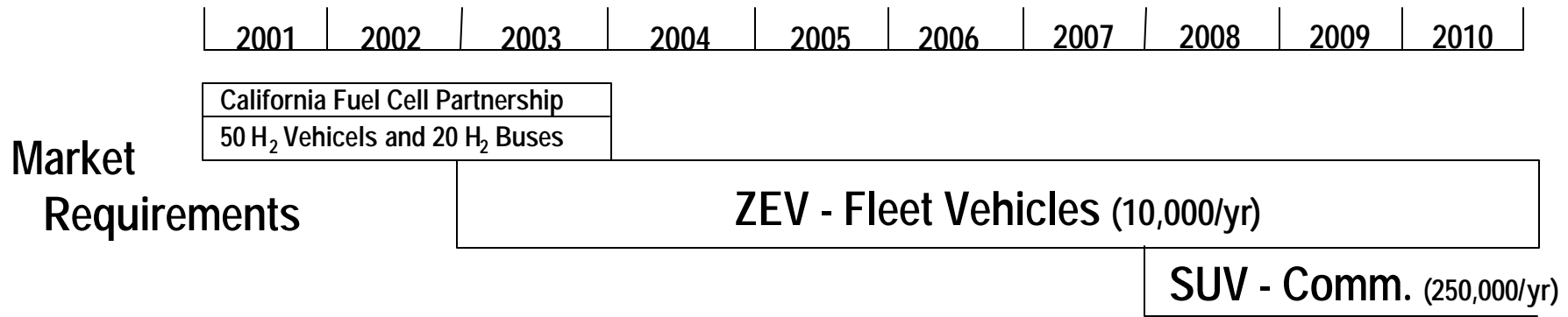
Filling ZEV Vehicle Requirements



| Vehicle Type (Must meet all PZEV requirements) | Primary Energy Source | Secondary Energy Source | Zero Emission Range (miles) | PZEV Baseline Allowance | Zero- Emission VMT Allowance | Low Fuel Cycle Emissions Allowance | Total ZEV Allowance |
|---|---|-------------------------------|--------------------------------------|-------------------------------|--|---|------------------------|
| Pure ZEV | | | | | | | |
| Battery EV | Grid Electricity | | Any | | | | ZEV |
| Stored Hydrogen FCV | Hydrogen | | Any | | | | ZEV |
| Direct Methanol FCV | Methanol | Electricity | Any | | | | ZEV |
| Fully Meets ZEV Allowance | | | | | | | |
| LFCE ICE HEV, 73 mile ZE range | Grid Electricity | CNG, Methanol, etc. | 73 | .2 | .5+.1 (max off- vehicle charging) | .2 | 1.0 |
| Gasoline HEV, 100 mile ZE range | Grid Electricity | Gasoline | 100 | .2 | .6 | .2 | 1.0 |
| Hydrogen ICE HEV, 20 mile ZE range | Grid Electricity or H2 with FC APU | Hydrogen | 20 | .2 | .3+.3 (0 NMOG) | .2 | 1.0 |



Technology Pathways



Continued R & D on Fuel Cells to Improve Performance and Lower Cost of High Volume Fabrication of Components

Early Utilization of Fuel Cells in Federal Buildings and Vehicles

Provide Low-cost H₂ Production Infrastructure

Off-board Reforming of Natural Gas (100-300 Vehicles)

Electrolysers (10-30 Vehicles)

Small Multi-Residential Fuel Appliances (3-5 Vehicles)

Introduction of Hybrid Electric Vehicles



Safety, Analysis, and Outreach



| Safety, Analysis, and Outreach | | |
|--------------------------------|---|-------------------------------|
| Hydrogen Safety | | |
| | Dispersion of Hydrogen Clouds | University of Miami |
| | Integrated Micromachined H2 Gas Sensors | Advanced Technology Materials |
| Analysis | | |
| | Analysis of Hydrogen Vehicle Pathways | Directed Technologies |
| | Process Analysis of Hydrogen Research Activities | NREL |
| | Hydrogen Energy System Studies | Princeton University |
| | Integrated Hydrogen Fuel Infrastructure Research and Technology Development | NREL |
| | Technical and Systems Assessments and IEA Support | Energetics |
| NEW | Analysis of Hydrogen Production using Biofarming for Microturbine Power | University of North Dakota |
| NEW | Analysis of Fuel Cells for Maritime Applications | DCH Technologies |
| Outreach | | |
| | Outreach: Education, Information Exchange, Joint International Working Groups | NHA |
| | Education Outreach | MRS Enterprises |
| NEW | H2000 Project Safety Film | H2000 |



Carbon Displacement (MMTCE/Year)



| | <u>2010</u> | <u>2020</u> |
|--|-------------|-------------|
| Wind | 10.8 | 22.2 |
| Biomass | 11.7 | 17.4 |
| Hydrogen | 1.9 | 13.5 |
| High Temperature Super Conductivity | 1.6 | 6.2 |
| Transmission Reliability | 2.8 | 5.5 |
| Geothermal | 1.7 | 5.5 |
| Solar Buildings | 0.9 | 2.5 |
| Photovoltaics | 0.4 | 1.8 |
| Concentrating Solar Power | 0.1 | 0.2 |

Prepared GPRA Report of the Office of Power Technologies

Utilization and Technology Validation Highlights



Jay Keller
Sandia National Laboratories
Combustion Research Facility

**Hydrogen Program Annual
Technical Review**

May 9-11, 2000



End-Use Components



◆ Reversible Fuel Cells - Renewable Energy Storage

- ◇ Low Cost Reversible Fuel Cell - Technology Management Inc

◆ Engines - End-Use

- ◇ Natural Gas / Hydrogen blends - NRG Technologies
- ◇ Free piston - Sandia National Laboratory

◆ Sensors - Safety

- ◇ Gallium Nitride Integrated Gas/Temperature Sensors for FC System Monitoring H_2 and CO - Fluence
- ◇ Thick Film Hydrogen Sensor Detector - Oak Ridge National Laboratory
- ◇ Interfacial Stability of Thin Film H_2 Sensors - National Renewable Laboratory

◆ Electrolyzers - Infrastructure

- ◇ Home Refueling - Stuart Energy
- ◇ High Efficiency Steam Electrolyzer - Lawrence Livermore National Laboratory





Stuart Electrolyser



Hydrogen Infrastructure



◆ Las Vegas

- ◇ Co-production of hydrogen and electrical power
- ◇ Systems integration of hydrogen components
- ◇ Create and support local hydrogen fleet
 - Pure Hydrogen Hybrid Bus
 - Hydrogen/Natural Gas Blends



NRG's Crown Vic

◆ Sunline Transit Agency

- ◇ Support of the California Fuel Cell Partnership
 - H₂ Production
 - HBT Autothermal Reforming of Natural Gas

◆ H₂ source - the chicken and the egg

- ◇ Electrolyzers - Stuart Energy, Proton
 - Active discussion with major automobile manufacturers



Hydrogen Infrastructure



◆ Mining Vehicles

- ◇ Natural fit for PEMFC and Hydride technologies
- ◇ A market pull

◆ High Pressure Composite Tanks

- ◇ On board storage solution today - TBD

◆ Storage Safety Comparison

- ◇ Different technologies and fuels - SNL
 - Safety perception / certification

◆ Distributed Power

- ◇ Development of stationary fuel cells and hydrogen systems for stationary applications



Conformable Tanks



Northwest Power Systems Distributed Power Unit



Analysis in the Hydrogen Program

Margaret K. Mann
National Renewable Energy Laboratory

DOE Hydrogen Program Annual Review
May 9-11, 2000
Livermore, CA

Role of Analysis in the DOE Hydrogen Program:

- Ensure that Federal R&D investments in hydrogen production, storage, distribution, and end-use technologies will provide the *maximum value added to national strategic goals including global greenhouse gas mitigation.*
- *Identify and evaluate key market segments and market entry conditions* for hydrogen utilization in transportation and in electricity generation at distributed and remote locations.
- Develop and apply metrics to *measure the Program's contribution* to attaining national strategic energy goals and market share in key market segments.

-From: Strategic Plan for DOE Hydrogen Program, January 1998

Strategic Objectives of Hydrogen Analysis

From: Strategic Plan for DOE Hydrogen Program, January 1998

Portfolio analysis to define market criteria to guide R&D investments

- Hydrogen as a competitive fuel in transportation
- Enhance global competitive leadership in hydrogen technology development

Characterize key market segments and define pathways

- Market size
- End-use patterns
- Cost/performance
- Consumer requirements/preferences
- Return on investment (private and public)
- Regulations

Perform technical and economic analyses

- Guide research
- Identify opportunities for hydrogen technologies

Develop programmatic database

- Metrics
- Cost/performance/reliability of hydrogen technologies

Enhanced Analysis Planning

Analysis coordinator will hold two parallel types of workshops

Expert committee

Industry representatives, HTAP, NHA, DOE, other H2 activities coordinators

Review analysis plan, make recommendations to DOE and analysis coordinator

Analysts

Present new ideas

Peer review

Integrate efforts

Study of previous analyses conducted for H2 Program

Will provide institutional knowledge

Will give a better understanding of the gaps in analysis

Used in analysis workshops

Periodic reports on analysis activities will be prepared

Current Analysis Solicitation

Applications received by March 31, 2000

Five Areas:

- 1: Technical analysis of currently funded projects
- 2: Technical analysis of hydrogen production systems not currently funded by DOE
3. Dissemination of information
4. Codes and standards analysis
5. Technical analysis on matters being considered by the International Energy Agency



Hydrogen Production

Now and Then, and Then Some

Strategic Goals

The use of hydrogen as a fuel and energy carrier can provide options toward achieving our national strategic goals

- Energy security
- Environmental security
- International competitiveness

Technology Development Goals

Hydrogen production projects

- Improve efficiency and lower the cost of fossil-based and biomass-based hydrogen production processes
- Advance emission-free and renewable-based hydrogen production technologies toward commercial viability

Fossil-Based Production Processes

In addition to ITM and SER mentioned by Sig

- Thermal dissociation of methane using concentrated solar power
- Thermocatalytic production without CO₂ emissions
- Plus a number of other exciting projects that will be presented Tuesday afternoon and Wednesday morning in Group A

Thermal Dissociation of Methane

Using a Solar-Coupled Aerosol Flow Reactor

- University of Colorado at Boulder and NREL
- Use of the High Flux Solar Furnace with concentrations up to 2000 suns
- Preliminary results indicate extremely high conversion efficiencies
- Excellent teaching tool (2 Senior Design project teams and a number of graduate students)

Thermocatalytic Production

CO₂-free from Fossil Fuels

- Florida Solar Energy Center
- One-step thermocatalytic decomposition of hydrocarbons in the absence of air and/or water
- Produces hydrogen and solid carbon, no CO or CO₂
- Fuel flexible - investigating methane, propane, and liquid hydrocarbons

Electrolytic Hydrogen Production

- High efficiency steam electrolysis
- PEM electrolysis
- Electrolytic refueling appliance (Sig showed photo)
- Projects will be presented on Thursday morning

Biomass-Based Hydrogen Production

- Biomass pyrolysis for hydrogen production
- Integrated hydrogen production from agricultural residues for urban transportation
- Supercritical water gasification with partial oxidation
- Hydrogen production from renewable organic waste
- Projects will be presented on Wednesday morning in Group A

Integrated Production

Agricultural residues for hydrogen production
with co-product carbon

- Clark Atlanta University and Scientific Carbons
- Improvements to existing activated carbon process using peanut shells in a pyrolysis reactor
- Pyrolysis vapors can be processed to produce hydrogen for use in urban bus fleet
- Other valuable co-products are also possible, and fit well with the local industrial makeup

Photolytic Production of Hydrogen

Biological and Electrochemical Approaches

- Bacterial water-gas shift
- Algal hydrogen production
- Photoproduction of hydrogen from glucose
- Photoelectrochemical hydrogen production
- Photocatalytic hydrogen production using a dual bed system
- Projects will be presented Wednesday morning and afternoon in Group A

Algal Hydrogen Production

2-phase system making lots of hydrogen

- NREL, ORNL, University of CA Berkeley
- Innovative system discovered in FY1999
- Temporal separation of hydrogen and oxygen production
- Deprive the algae of sulfur, and they will do anything - even produce hydrogen
- Highly successful team effort that has attracted significant interest in the general and scientific press

Hydrogen Production

Now and Then, and Then Some

- 27 projects will be critically reviewed
- Near-term fossil-based and electrolytic processes can provide hydrogen for end-use applications at competitive prices
- Mid-term biomass- and improved fossil-based processes have excellent economic potential, AND can contribute to reductions in greenhouse gases
- Long-term renewable-based systems will provide water-based production systems with no emissions

Overview of Storage Development DOE Hydrogen Program

***Safe, efficient and cost-effective storage
is a key element in the development of
hydrogen as an energy carrier***

George Thomas
Sandia National Laboratories
Livermore, CA

Hydrogen Program Review
San Ramon, CA
May 9-11, 2000



Hydrogen storage requires something more than a can or a bucket

Hydrogen has the highest mass energy density of any fuel:

120 MJ/kg (LHV) 144 MJ/kg (HHV)

however

At ambient conditions (300 K, 1 atm.):

the energy content of 1 liter of H₂ is only 10.7 kJ,

three orders of magnitude too low for practical applications.


Issues:

1. What are the options available for storage?
2. What are the theoretical limits to storage density and how close can we come?
3. How do we organize a development program to achieve adequate stored energy in an efficient, safe and cost-effective manner?



Mass energy densities for various fuels

Increasing molecular wt.



| Fuel | Hydrogen weight fraction | Ambient state | Mass energy density (MJ/kg) |
|----------|--------------------------|---------------------------|-----------------------------|
| Hydrogen | 1 | Gas | 120 |
| Methane | 0.25 | Gas | 50 (43) ² |
| Ethane | 0.2 | Gas | 47.5 |
| Propane | 0.18 | Gas (liquid) ¹ | 46.4 |
| Gasoline | 0.16 | Liquid | 44.4 |
| Ethanol | 0.13 | Liquid | 26.8 |
| Methanol | 0.12 | Liquid | 19.9 |

(1) A gas at room temperature, but normally stored as a liquid at moderate pressure.

(2) The larger values are for pure methane. The values in parantheses are for a “typical” Natural Gas.



Maximum energy density is achieved in liquid state

| Fuel | Hydrogen weight fraction | Ambient state | Liquid volumetric energy density (MJ/liter) | Hydrogen volumetric energy density in liquid (MJ/liter) |
|-----------------|---------------------------------|---------------------------------|--|--|
| Hydrogen | 1 | Gas | 8.4 – 10.4³ | 8.4 – 10.4³ |
| Methane | 0.25 | Gas | 21 (17.8)² | 12.6 (10.8)² |
| Ethane | 0.2 | Gas | 23.7 | 12 |
| Propane | 0.18 | Gas (liquid)¹ | 22.8 | 10.6 |
| Gasoline | 0.16 | Liquid | 31.1 | 13.2 |
| Ethanol | 0.13 | Liquid | 21.2 | 12.3 |
| Methanol | 0.12 | Liquid | 15.8 | 11.9 |

(1) A gas at room temperature, but normally stored as a liquid at moderate pressure.

(2) The larger values are for pure methane. The values in parentheses are for a “typical” Natural Gas.

(3) The higher value refers to hydrogen density at the triple point.



Hydrogen energy content in liquid fuels

| Fuel | Hydrogen weight fraction | Ambient state | Liquid volumetric energy density (MJ/liter) | Hydrogen volumetric energy density in liquid (MJ/liter) |
|----------|--------------------------|---------------------------|---|---|
| Hydrogen | 1 | Gas | 8.4 – 10.4 ³ | 8.4 – 10.4 ³ |
| Methane | 0.25 | Gas | 21 (17.8) ² | 12.6 (10.8) ² |
| Ethane | 0.2 | Gas | 23.7 | 12 |
| Propane | 0.18 | Gas (liquid) ¹ | 22.8 | 10.6 |
| Gasoline | 0.16 | Liquid | 31.1 | 13.2 |
| Ethanol | 0.13 | Liquid | 21.2 | 12.3 |
| Methanol | 0.12 | Liquid | 15.8 | 11.9 |

Hydrogen density is nearly the same in all fuels.
This narrow range suggests a natural benchmark for comparison of storage performance.



Maximum storage densities (w/o system)

Energy Density MJ/liter

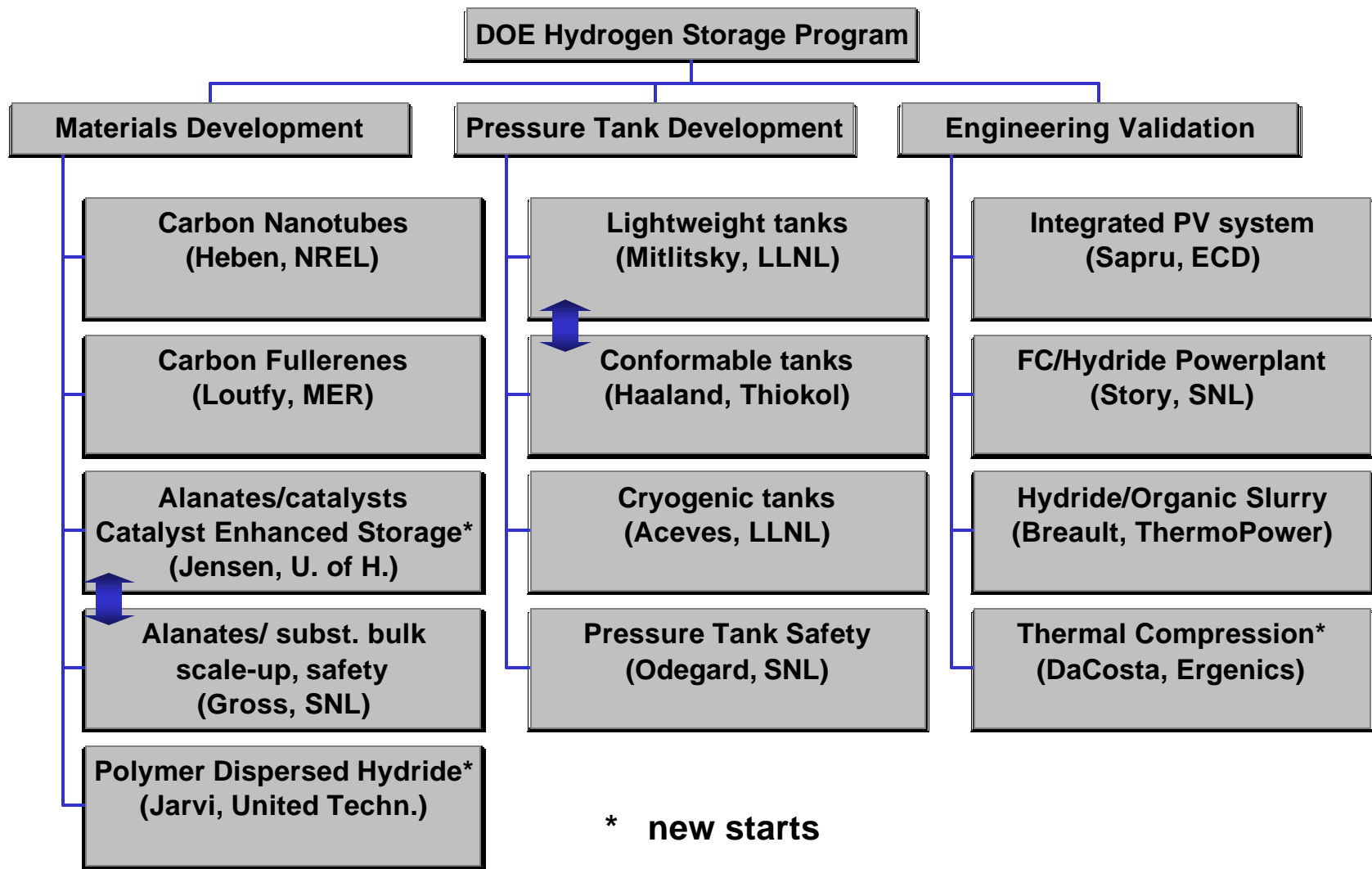
| | | | |
|----------------------------|-------------|--------------------|-----------------------|
| • High pressure gas | | | |
| – ambient temperature | 3600 psi: | 2.0 | 5000 psi: 2.75 |
| – cryogenic system | 150 K: | 3.5 | 20 K: 8.4 |
| • Liquid hydrogen | | 8.4 | |
| • Reversible storage media | | | |
| – carbon structures | | | |
| • nanotubes | | ? | |
| • fullerenes | | ? | |
| – hydrides | | | |
| • intermetallics | | 10.8 - 12.0 | |
| • alanates | | 8.25 | |
| – composite materials | | ? | |
| • Chemical methods | <u>Eff.</u> | <u>gasoline</u> | <u>methanol</u> |
| – liquid fuel + reformer | 50%: | 6.6 | 5.9 |
| | 75%: | 9.9 | 8.9 |
| – off-board reprocessing | | ? | |



Programmatic guidelines

- A balanced program between scientific discovery and engineering validation is needed.
 - Portion of program invested in high risk approaches.
 - Collaboration with industry at all levels.
 - International partnerships beneficial.
 - Leverage off other programs.
- Program should not downselect technologies too early
 - Options should be fully explored.
 - Different technologies suited for different applications.
- Realistic goals should be set as metrics for progress.
 - Evaluate goals on a continuing basis
 - continue to refine roadmap





Materials Development

- Carbon nanotubes M. Heben, NREL
 - near-term goal: ~6 wt.%
 - synthesis, processing, hydrogen absorption/desorption
- Carbon fullerenes R. Loutfy, MER
 - feasibility of fullerene-based storage
- Alanate hydrides C. Jensen, Univ. of Hawaii
 - NaAlH₄ : 5.5 wt.% hydrogen capacity
 - catalysts, properties
- Hydride development K. Gross, SNL
 - near-term goal: 5.5 wt.% at <100 C (NaAlH₄)
 - bulk synthesis, scaled-up beds, characterization, safety studies
- Catalytically enhanced storage C. Jensen, Univ. of Hawaii
 - new start
- Polymer dispersed metal hydrides T. Jarvi, United Technologies
 - new start



Pressure Tank Development

- Lightweight tanks F. Mitlitisky, LLNL
 - goal: >10 wt.% 5000 psi
- Conformable tanks R. Golde, Thiokol Propulsion Co.
 - high pressure tanks with improved packing efficiency
- cryogenic hydrogen vessels S. Aceves, LLNL
 - design and testing for improved volume density
- Composite tank testing B. Odegard, SNL
 - comparison of high pressure hydrogen tank failure to other fuels. CNG, gasoline, methanol.



Engineering Validation

- PV/electrolysis/metal hydride K. Sapru, ECD
 - modeling and integration of storage with renewable energy sources
- Metal hydride/ organic slurry R. Breault, Thermo Power
 - chemical hydride for PEMFC vehicles
 - hydrogen transmission and storage
- Fuelcell/hydride powerplant G. C. Story, SNL
 - for underground mine and tunneling locomotive
- Thermal hydrogen compression D. DaCosta, Ergenics, Inc.
 - new start



Other hydrogen storage programs (US)

- DOE/OTT
 - Fuels for Fuel Cells Program (P. Devlin)
Parallel development of fuel processor and onboard H storage.
- DOE/OIT
 - Low cost hydrides for mine vehicles (SRTC)
Part of Mining Industry of the Future initiative.
- IEA
 - Task 12 will be completed Oct. 2000
 - New task being formed: Advanced Solid and Liquid State Hydrogen Storage Materials (G. Sandrock)
- Industry Projects



Other hydrogen storage programs (non US)

- Canadian Projects
 - Alanates (A. Zaluska, McGill Univ.)
 - Nanocrystalline Mg-based hydrides (Hydro-Quebec)
 - Carbon adsorption (IRH)
- European Projects
 - liquid hydrogen storage (BMW)
 - refueling station (BMW)
- WENET (Japan)
 - Metal-H complex ions (S. Suda, Kogakuin Univ.)
 - others



Some highlights from this year

- Continuing progress in nanotubes
 - high purity synthesis and processing methods.
 - > 6 wt.% appears feasible.
- Important progress achieved on alanates
 - 5.5 wt.% at low temperatures appears feasible.
- Continued improvement in lightweight and conformable tanks
 - more efficient packing of high pressure tanks
- integration of storage with applications
 - PV system
 - mine vehicle
- Three new starts
 - catalyst enhanced storage
 - polymer dispersed hydride
 - thermal hydrogen compression



**Liquid Fuel Reformer Development:
Autothermal Reforming of Diesel Fuel[†]**

**C. Pereira, J-M Bae, S. Ahmed,
and M. Krumpelt**

Electrochemical Technology Program
Chemical Technology Division
Argonne National Laboratory
9700 S. Cass Avenue
Argonne, Illinois 60439

Presented at the
U.S. Department of Energy
2000 Hydrogen Program Technical Review
San Ramon, California

May 9, 2000

The submitted manuscript has been created by the University of Chicago as Operator of Argonne National Laboratory ("Argonne") under Contract No. W-31-109-ENG-38 with the U.S. Department of Energy. The U.S. Government retains to itself, and others acting on its behalf, a paid-up, nonexclusive, irrevocable worldwide license in said article to reproduce, prepare derivative works, distribute copies to the public, and perform publicly and display publicly, by or on behalf of the Government.

[†] Work supported by the U.S. Department of Energy and Office of Hydrogen Technology, under Contract W-31-109-ENG-38.

LIQUID FUEL REFORMER DEVELOPMENT: AUTOTHERMAL REFORMING OF DIESEL FUEL

**C. Pereira , J-M. Bae, S. Ahmed, and M. Krumpelt
Argonne National Laboratory
Chemical Technology Division
Argonne, IL 60439**

Abstract

Argonne National Laboratory is developing a process to convert hydrocarbon fuels to clean hydrogen feeds for a polymer electrolyte fuel cell. The process incorporates an autothermal reforming catalyst that can process hydrocarbon feeds at lower temperatures than existing commercial catalysts. We have tested the catalyst with three diesel-type fuels: hexadecane, certified low-sulfur grade 1 diesel, and a standard grade 2 diesel. Hexadecane yielded products containing 60% hydrogen on a dry, nitrogen-free basis at 850°C, while maximum hydrogen product yields for the two diesel fuels were near 50%. Residual products in all cases included CO, CO₂, ethane, and methane. Further studies with grade 1 diesel showed improved conversion as the water:fuel ratio was increased from 1 to 2 at 850°C. Soot formation was reduced when the oxygen:carbon ratio was maintained at 1 at 850°C. There were no significant changes in hydrogen yield as the space velocity and the oxygen:fuel ratio were varied. Tests with a microchannel monolithic catalyst yielded similar or improved hydrogen levels at higher space velocities than with extruded pellets in a packed bed.

Introduction

The Department of Energy's Hydrogen Program is sponsoring the development of remote power generation in the Arctic circle. Because the fuel available is diesel, the traditional means of power generation in these remote locations has been internal combustion engines. Recent developments in fuel cell power systems, which are more efficient and produce cleaner emissions, suggest that these systems, if adapted to operate with diesel fuels, can be used in the Arctic. Since fuel cells operate on hydrogen, the operation of fuel cells with a diesel feed requires that the fuel be efficiently converted into a hydrogen-rich, sulfur-free gas.

In the chemical process industries, hydrogen is produced in large quantity by the steam reforming process – where the hydrocarbon fuel, typically methane, is reacted with steam. Because this reaction is endothermic, an efficient heat exchanger is required to transfer heat from another source, such as a fuel burner, to the reformer. Consequently, steam reforming is best suited for large chemical plants, which normally have excess heat available from other processes. At a smaller scale, an attractive alternative is autothermal reforming, where the hydrocarbon fuel is reacted with both air and steam to produce hydrogen. The heat generated by this reaction can be controlled directly by adjusting the proportions of fuel, air, and steam in the feed. With an appropriate feed, external heat is not required, making autothermal reformers simpler, smaller, and lighter than steam reformers. Autothermal reforming in the petrochemical industry is typically done in a two-step process – a high-temperature (1200°C) step where the complex hydrocarbons are broken down into simpler molecules (methane and oxides of carbon), followed by (catalytic) steam reforming of methane.

At Argonne National Laboratory, we are developing a process to convert hydrocarbon fuels to clean hydrogen feeds for polymer electrolyte fuel cells (PEFC). The process incorporates an autothermal reforming catalyst that can process hydrocarbon feeds at lower temperatures than existing commercial catalysts. We have developed an autothermal reforming catalyst that converts gasoline to hydrogen, carbon monoxide, and carbon dioxide at temperatures as low as 650-900°C. We have also demonstrated complete conversion of these feeds, producing enough hydrogen to power a 5-kW fuel cell stack (Ahmed, 1998).

The effluent from the reformer requires further treatment before it can be fed to a PEFC stack. Carbon monoxide and sulfur poison the fuel cell electrodes when present above a few parts per million. To address this problem Argonne National Laboratory is optimizing sulfur scrubbers for compact systems like autothermal reformers, developing more robust water-gas shift catalysts that will work better under transient operating conditions than current catalysts (Kumar, 1999), and testing catalysts for preferential oxidation of CO and CO sorbents to treat the product stream.

Reforming diesel fuel requires that several problems be overcome. These problems are related to degradation of catalysts over time because of the nature of the fuel. Causes of degradation include poisoning of catalysts by sulfur; diesel typically has a higher fraction of sulfur than other fuels. Thermal cycling, particularly on startup and shutdown, leads to thermal shock. Because of the low H:C ratio and high molecular weight of diesel, extensive coke formation deactivates catalysts. High temperatures improve conversion, resulting in better system efficiency, but reduce material stability.

In a previous paper (Pereira, 1999) we reported preliminary results on autothermal reforming of three fuels: hexadecane, grade 1 diesel, and grade 2 diesel. This paper reports the effect of operating conditions on the performance of the catalyst and on reforming of the diesel fuel. Results of diesel reforming over a new monolithic microchannel catalyst show improved conversion at higher fuel throughputs. Finally, results of fuel tests run with reformer in tandem with water-gas shift reactors show

reduction of carbon monoxide to less than 2%. These results show that autothermal reforming appears promising as an alternative to steam reforming for remote applications, and that Argonne's autothermal reforming catalyst shows superior performance.

Experimental

Certified low-sulfur diesel fuel, grade no. 1, was obtained from Phillips Petroleum Co. Standard diesel fuel, grade no. 2, was obtained from a local service station (nomenclature according to ASTM D975-97). The fuels were not treated further; fuel properties are provided in the previous report (Pereira, 1999). The autothermal catalyst was prepared in-house as extrudates and in a monolithic form. The catalyst was placed in a 0.41 cm ID tubular reactor within a tube furnace. The bed height was approximately 2.5 cm for the extrudates, and either 1 or 2 cm for the monolith. The temperatures at the top and bottom of the bed were monitored with thermocouples. Water-gas shift catalysts were fabricated as extrudates. Commercial zinc oxide and iron-chromium oxide catalysts were obtained from United Catalysts, Inc., for sulfur removal and high temperature shift, respectively.

The fuel and water were fed at the top of the reactor, where they were vaporized and mixed with the incoming oxygen and nitrogen; the nitrogen was used as an internal standard. The liquid feed rates were controlled with high pressure liquid chromatography (HPLC) pumps; the gas flow rates were maintained with mass flow controllers. The reactant stream was passed over the catalyst, and the products analyzed with a gas chromatograph. Pure oxygen was used in the reactant stream to improve detection of any hydrocarbons that may be present in the product. The gas chromatograph (GC) could not be used to quantify water and heavy hydrocarbons. Therefore, we used the hydrogen-to-carbon (H/C) ratio to obtain an atom balance and approximate a mass balance. In addition to the GC, an infrared detector was used to continuously measure the CO concentration in the effluent from the water-gas shift beds.

Results and Discussion

Compositional Analysis

In previous feasibility studies, hexadecane ($C_{16}H_{34}$) was used as a surrogate for diesel fuel (Pereira, 1999). The initial operating conditions used for diesel fuel were set based on the results obtained for hexadecane. In this study, we have refined our operating conditions based on a more detailed analysis of the composition of diesel fuel in order to determine suitable operating conditions for the ANL catalyst. We examined more closely the composition of the two diesel fuels that were used in our tests with the autothermal reforming catalyst. The two fuels were a certified low-sulfur grade 1 fuel and a standard grade 2 fuel obtained from the ANL motor-pool. The two fuels were analyzed by two analytical methods. The analysis of the certified diesel used in the microreactor tests described in this report is discussed below.

Because of the complex nature of diesel fuel (several hundred separate components have been identified), a complete chemical breakdown of the fuel was not feasible. However, we have obtained elemental and compositional data based on chemical structure. Using

this breakdown and assigning a reference compound for each grouping, we obtained an "average" chemical composition to further refine the operating parameters for the fuels. This analysis is shown in Table 3 for the certified fuel. The elemental composition derived from this analysis matches the measured elemental composition well. These results were used to set the ranges of oxygen and water feed rates.

Table 3: Compositional analysis of certified grade 1 diesel fuel

| Compound Type | Wt.% | Avg. or Ref. Compd. | Avg. Mol. Wt. | Wt% C | Wt% H | Est. mol % |
|------------------------|-------------|---------------------|---------------|--------------|--------------|--------------|
| Saturates | 83.7 | $C_{14.2}H_{29.4}$ | 199.6 | 0.853 | 0.147 | 0.726 |
| Paraffins | 38.7 | $C_{16}H_{34}$ | 226 | 0.850 | 0.150 | 0.2965 |
| Cycloparaffins | 29.6 | $C_{10}H_{21}$ | 141 | 0.851 | 0.149 | 0.3635 |
| 2-ring cycloparaffins | 11.5 | $C_{16}H_{32}$ | 224 | 0.857 | 0.143 | 0.0889 |
| 3-ring cycloparaffins | 4 | $C_{22}H_{38}$ | 302 | 0.874 | 0.126 | 0.0229 |
| Aromatics | 16.3 | $C_{9.5}H_{11}$ | 125.6 | 0.912 | 0.088 | 0.2248 |
| <u>Mono-aromatics</u> | 10.5 | $C_{9.2}H_{10.4}$ | 121.1 | 0.914 | 0.086 | 0.1502 |
| Benzenes | 7.3 | C_8H_8 | 104 | 0.923 | 0.077 | 0.1215 |
| Naphthene benzenes | 3.2 | $C_{12}H_{16}$ | 160 | 0.900 | 0.100 | 0.0346 |
| Dinaphthene benzenes | 0 | NA | NA | NA | NA | NA |
| <u>Di-aromatics</u> | 5.7 | $C_{10.3}H_{12.3}$ | 136.1 | 0.910 | 0.090 | 0.0725 |
| Naphthalenes | 1.8 | $C_{13}H_{14}$ | 170 | 0.918 | 0.082 | 0.0183 |
| Acenaphthenes | 3.5 | C_9H_{12} | 120 | 0.900 | 0.100 | 0.0505 |
| Fluorenes | 0.3 | $C_{13}H_{10}$ | 166 | 0.940 | 0.060 | 0.0031 |
| <u>Tri-aromatics</u> | 0 | NA | NA | NA | NA | NA |
| <u>Tetra-aromatics</u> | 0 | NA | NA | NA | NA | NA |
| Total | 100 | $C_{13.4}H_{26.3}$ | 187.5 | 0.859 | 0.141 | 1.000 |

NA = not available, i.e. concentration of compound type is below detection limits.

Based on the results of the analyses, grade 1 diesel was determined to be significantly richer in alkanes than the grade 2 diesel. Grade 2 is significantly richer in aromatic compounds, particularly naphthalenes and naphthene benzenes. These differences in composition lead to differences in the hydrogen yield obtained with the reforming catalyst. Grade 2, although having a lower H:C and thus being relatively hydrogen poor, yielded a greater fraction of hydrogen in the product. This finding indicates that aromatics may be more easily reformed than cyclic aliphatics.

Effect of Operating Conditions on Hydrogen Yield

The reference compounds used to determine an "average" composition for the diesel fuel were used to calculate the equilibrium composition versus temperature, as shown in Figure 1. An $H_2O:C$ ratio of 1.25 and an $O:C$ of 1 were used for most tests and in this

calculation. The curves in Figure 1 show that at thermodynamic equilibrium hydrogen formation is maximized near 700°C. These results are very similar to those obtained for hexadecane. The hydrogen fraction in the product at this temperature is 57% on a dry, nitrogen-free basis. As the temperature is reduced, the methane fraction increases, and the hydrogen yield decreases commensurately.

Figure 2 shows the product composition as a function of temperature for reforming a certified low-sulfur diesel fuel at a water:fuel ratio of 20 and oxygen:fuel ratio of 8. In Figure 2, hydrogen production is maximized at 875°C. This temperature is higher than obtained with hexadecane, where, with similar oxygen- and water-to-fuel ratios, hydrogen production was maximized at 800°C with a hydrogen fraction (on a dry, nitrogen-free basis) of 60% in the products. For the certified fuel, the average hydrogen fraction in the product at 840°C is 46%, while at 880°C it is 50%. These values are somewhat higher than previous data with this same fuel (Pereira, 1999), but still somewhat lower than the results obtained for grade 2 diesel, where 52% hydrogen was obtained in the product at 850°C.

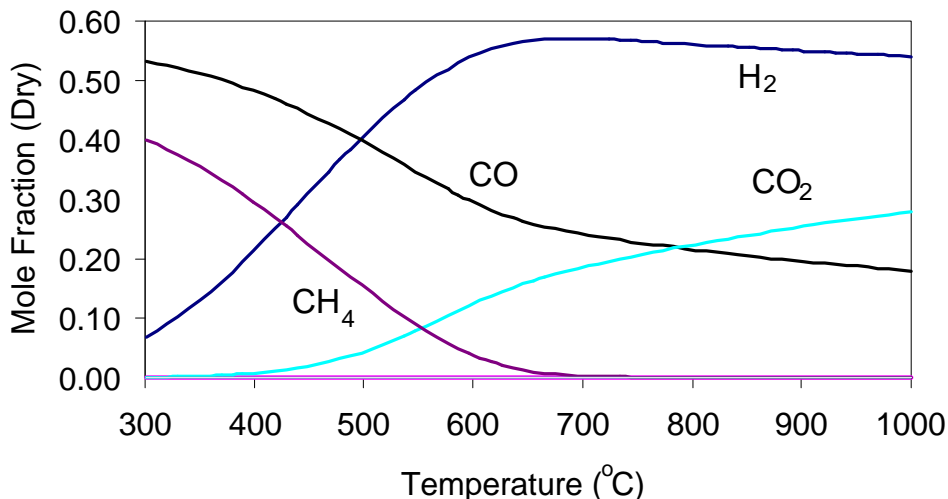
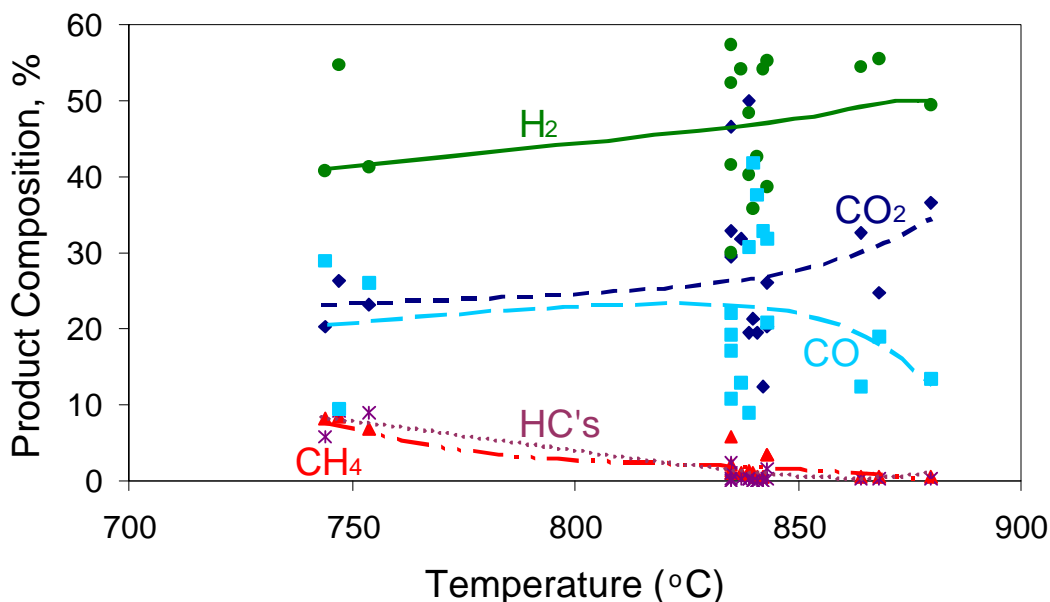


Figure 1: Equilibrium composition vs. temperature for diesel. Oxygen:fuel = 8; water:fuel = 20.

There was a large amount of scatter in all of the data obtained with diesel fuel. The scatter was related to liquid injection of the fuel and water. We also examined the effect on hydrogen production of direct injection of steam into the reactor in place of water. This change reduced the amount of scatter somewhat, but separating the fuel and water streams led to increased soot formation above the bed. A reduction in scatter should be achieved with improvements to the design of the liquid injectors.

The product composition from diesel reforming was examined as a function of gas hourly space velocity (GHSV), oxygen:fuel ratio, and water:fuel ratio. Although apparent trends were present for some variables, the large scatter precluded any firm conclusions on their effect on hydrogen production. Some qualitative conclusions, however, can be made. Reducing the oxygen feed rate from 8 to 6 O₂ per mole of fuel, with a water:fuel ratio of

20, resulted in a much greater variety and larger fraction of hydrocarbons in the product stream; aromatics, especially, were much more prevalent. Apparently, a greater fraction of the fuel components, notably the aromatics, was not being cracked or oxidized effectively with less oxygen in the feed. There was also an increase in pressure drop across the reactor, as would be expected with an increase in coke or soot formation. At an oxygen:fuel ratio of 8 and a water:fuel ratio of 20, methane was the predominant hydrocarbon present at 840°C, and no increase in pressure drop was observed.



**Figure 2: Composition vs. temperature for Grade 1 diesel.
Oxygen:fuel = 8; water:fuel = 20.**

The GHSV was varied from 2000 to 10,000 h⁻¹ at 840°C and from 2000 to 4000 h⁻¹ at 880°C. The curves obtained were flat, with no trends evident. No significant changes were detected in the product distribution over the range of space velocities tested; no effect of GHSV on hydrogen production could be measured. Therefore, the reformer hydrogen yield in the product gas should be relatively uniform over a range of diesel fuel feed rates.

Figure 3 shows the results for the effect of water:carbon ratio, which does show an upward trend in hydrogen yield with excess water. As the water:carbon ratio was increased from 1 to 2, at a constant O₂:C ratio of 1 (oxygen:fuel ratio = 8), hydrogen yield steadily increased. As was observed with oxygen, low water:fuel ratios, resulted in increased coke or soot formation, evidenced by an increase in the pressure drop across the reactor. Soot deposits were observed in the reactor above the catalyst bed, though the catalyst did not show evidence of coke formation. As observed for low oxygen:fuel ratios, gas chromatograms showed a greater fraction and variety of hydrocarbon products at lower reaction temperatures; however, simple aromatics were not as prevalent.

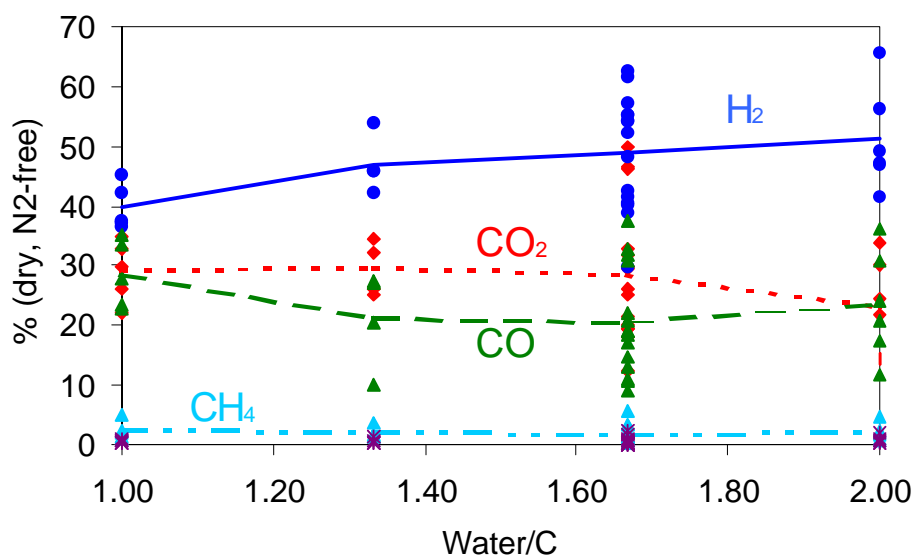


**Figure 3: Product composition as a function of water:carbon ratio.
Oxygen:fuel = 8 Temperature = 850°C**

We have recently developed a monolithic catalyst of a composition similar to the extruded form, but with a microchannel form. The channel diameters range in size from 30 to 300 μm . The product yield for a diesel feed over the monolithic catalyst is shown as a function of space velocity in Figure 4. Included also are average values for the extrudates. As can be seen in the figure, there is no change in yield as the space velocity is increased from 10,000 to 20,000 h^{-1} in going from extrudates to monoliths, there is no reduction in hydrogen yield. Furthermore, when the temperature was increased from 850 to 900°C at 10,000 h^{-1} , the hydrogen yield increased from 50 to 55% with the monoliths. These results show that the microchannel monolith can maintain or improve the hydrogen yield over a packed bed while reducing the size of the diesel reformer.

Diesel Fuel Processing

As part of the fuel processor development, we are tying the catalytic reforming of diesel fuel with the processing of the product gas. At the large scale, this will be done with the 5 kW(e) processor discussed later. However, because microreactor tests are much more rapid and allow us to better determine operating conditions for a large-scale unit, we are examining the entire diesel fuel process by connecting the reformer microreactor with a series of sulfur and carbon monoxide scrubbers. The scrubbers consist of a sulfur removal bed, high- and low-temperature shift beds, and a preferential oxidizer. This process train is nearly identical in configuration with the 5 kW(e) unit. However, it is much more flexible, allowing changes to materials, reactor configuration, or feeds to be made quickly.

As a test of the processing of diesel we sent a portion of the effluent from the reformer microreactor through a sulfur scrubber and the high- and low-temperature shift beds.

Because the conditions were not yet optimized for operation with a reformate produced by diesel, only a portion of the effluent was passed through the process train.

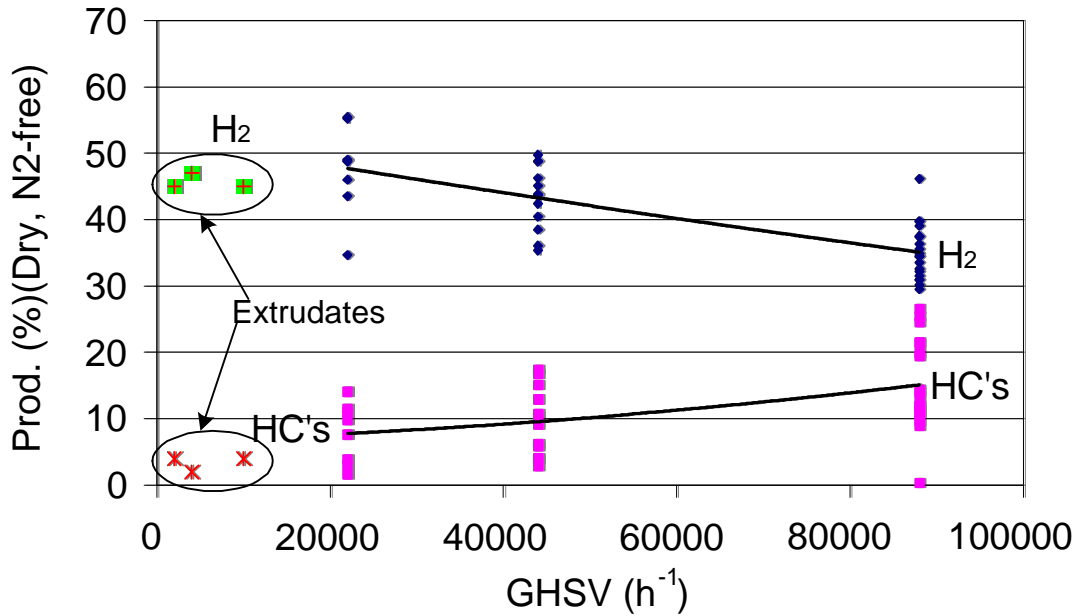


Figure 4: Results of test with monolithic microchannel catalyst. Temperature = 850°C; water:fuel ratio = 20; oxygen:fuel ratio = 8

With this process we were able to reduce the carbon monoxide content of the reformate from 20% to less than 2% on a dry basis with the two water-gas shift reactors. Figure 5 shows the carbon monoxide level of the effluent, as a function of time, after it had dropped below 2%. There is a slight upward trend in the middle segment of data shown. However, the variation in reformer effluent composition observed above suggests that a constant CO level should not be expected for this test. Indeed the system may be reacting to a CO concentration spike. In the final segment of data, the upward trend stops, and the CO concentration drops closer to the initial level. Sulfur, as H₂S could not be measured with the on-line instruments.

Fabrication of 5 kW(e) Fuel Processor

As mentioned earlier, Argonne National Laboratory has developed an autothermal reforming catalyst that can convert diesel fuel to a hydrogen-rich stream. The reformate must be further processed to remove carbon monoxide and sulfur. To demonstrate this process, a large-scale unit is being fabricated by Dais Analytic Inc. This unit will incorporate the autothermal reforming catalyst with sulfur removal, water-gas shift, and preferential oxidization reactors.

Fabrication and assembly of the 5 kW(e) fuel processor are underway at Dais Analytic. All of the major components of the fuel processor have been procured or fabricated. The processor is being readied for final assembly. Recently, 5 kg of the reforming catalyst

(approximately 5 L total volume) was shipped to Dais Analytic for inclusion in this processor. After assembly, a series of tests will be run on the unit to assure successful operation.

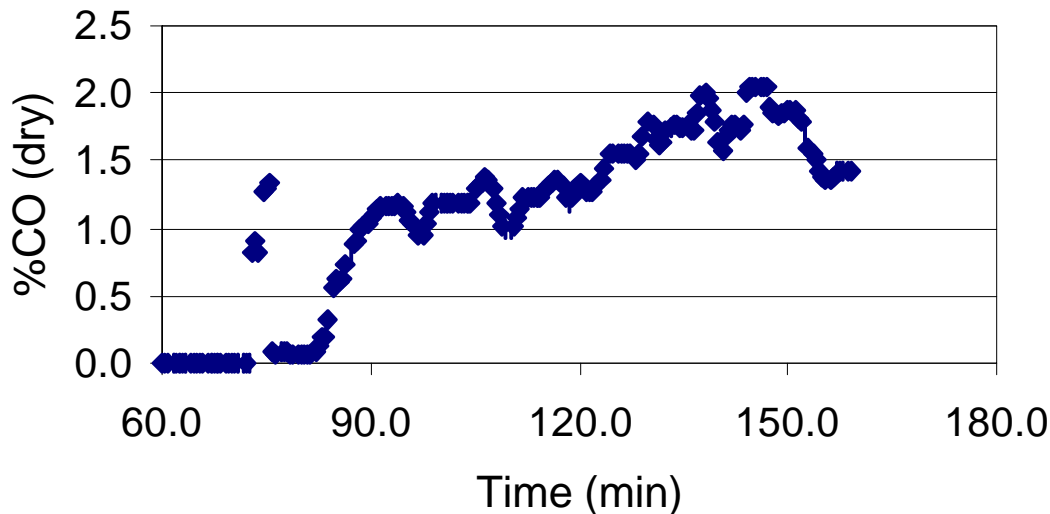


Figure 5: Carbon monoxide vs. time

Conclusions

Experiments were conducted to study the effects of temperature, water:fuel, oxygen:fuel, steam injection, and space velocity on the product composition for a certified diesel. We demonstrated improved hydrogen production from the certified diesel than was obtained previously; however, hydrogen production was still somewhat less than was obtained for grade 2 diesel. There was no clear effect due to $O_2:C$ ratio or space velocity on the hydrogen yield. Steam injection appeared to reduce scatter but increase soot formation over liquid water injection. Increasing the $H_2O:C$ ratio increased hydrogen yield. A five-fold increase in GHSV did not affect the hydrogen yield. Microchannel monolithic catalysts produced hydrogen yields comparable to extrudates at low space velocities for a diesel feed. There was a reduction in hydrogen yield at very high space velocities. As the temperature was raised, yields were well above those obtained for the extrudates.

The diesel reformat was further processed to remove carbon monoxide and sulfur using a train of reactors consisting of a sulfur scrubber and two water-gas shift beds. The carbon monoxide content of the process gas was reduced from approximately 20% to 2% on a dry basis using this process train. The process train is similar to the arrangement of reactors in the 5kW(e) diesel fuel processor.

All of the tests performed to date have been of less than 40 hours duration. We are preparing to run longer-term tests with diesel fuel. Such longer-term tests will allow us to better evaluate the effect of sulfur on catalyst activity, the long-term effects of coke formation, and the thermal stability of the catalyst to thermal cycling. Once fabrication of the 5 kW(e) diesel fuel processor is complete, it will be tested by Dais Analytic under the guidance of Argonne using the operating conditions established by the microreactor tests with diesel fuel.

Acknowledgments

This work was funded by the U.S. Department of Energy Hydrogen Program under Contract W-31-109-ENG-38. Chemical analysis of diesel was done by Lillian Ruscic, Chemistry Division, Argonne National Laboratory.

References

Ahmed, S., M. Krumpelt, R. Kumar, S.H.D. Lee, J.D. Carter, R. Wilkenhoener, and C. Marshall, "Catalytic Partial Oxidation Reforming of Hydrocarbon Fuels," 1998 Fuel Cell Seminar Abstracts, Courtesy Associates, Inc., Washington, D.C., 1998, 242-245.

Kumar, R., D. Myers, C. Kinsinger, and M. Krumpelt, "Alternative Water-Gas Shift Catalysts," Annual National Laboratory R&D Meeting of the DOE Fuel Cells for Transportation Program, June 23-25, 1999, Argonne National Laboratory, Argonne, IL.

"Standard Specification for Diesel Fuel Oils," American Society of Testing Materials, Philadelphia, PA, ASTM Designation D 975-97, 1997.

Pereira, C., R. Wilkenhoener, S. Ahmed, and M. Krumpelt, "Liquid Fuel Reformer Development," DOE Hydrogen Program Annual Review, May 5-9, 1999, Lakewood, CO.

THERMAL DISSOCIATION OF METHANE USING A SOLAR COUPLED AEROSOL FLOW REACTOR

Alan W. Weimer, Jaimee Dahl, and Joseph Tamburini
University of Colorado, Department of Chemical Engineering
Boulder, CO 80309-0424

Allan Lewandowski, Roland Pitts, and Carl Bingham
National Renewable Energy Laboratory
Golden, CO 80401-3393

Gregory C. Glatzmaier
Peak Design
Evergreen, CO 80439

Abstract

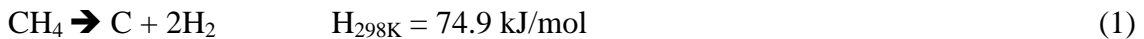
A solar-thermal aerosol flow reactor has been constructed, installed and tested at the High-Flux Solar Furnace (HFSF) at the National Renewable Energy Laboratory (NREL). “Proof-of-concept” experiments were successfully carried out for the dissociation of methane to produce hydrogen and carbon black. Approximately 90% dissociation of methane was achieved in a 25-mm diameter quartz reaction tube illuminated with a solar flux of 2400 kW/m² (or suns). Preliminary economics for a 1,000,000 kg/yr solar-thermal hydrogen plant were evaluated using a discount cash flow analysis that required a 15% Internal Rate of Return (IRR). If either product is the sole source of revenue, the required selling price for hydrogen was \$27/MBtu (\$0.092/kWhr or \$25.6/GJ) and for carbon black it was \$0.55/lb (\$1.21/kg). If both products are sold, and carbon black is sold for \$0.35/lb (\$0.77/kg), the required selling price for hydrogen was \$10/MBtu (\$9.47/GJ or \$0.034/kWhr). Both the experimental and economic results are very encouraging and support further work to address the technical issues and to develop the process.

Introduction

The primary driver for the development of renewable energy strategies is current concern over the potential, irreversible environmental damage that may occur with the continued or accelerated use of fossil fuels. Movement toward a hydrogen (H₂) based economy is an essential component of an international program to address that concern and will, in addition, address concerns over pollution in cities and associated health costs. However, current methods for producing H₂ incur a large environmental liability because fossil fuels are burned to supply the energy to reform methane (CH₄). We propose an alternate strategy using highly concentrated sunlight as the energy source that does not result in an increase of environmental liability. Indeed, it represents a route for utilizing current natural gas reserves that fixes carbon as well as increasing the energy content of the fuel. The research presented here is oriented at developing a cost-effective, solar-thermal method of deriving H₂ from natural gas.

Background

Steinberg [1986, 1987, 1994, 1995, 1998, 1999] and Steinberg and co-workers [Steinberg and Cheng, 1989] have been major proponents of the thermal decomposition of CH₄ process for H₂ production. Methane (CH₄) is dissociated to carbon (C) black and H₂ according to:



Methane (CH₄) is a preferred choice for the production of H₂ from a hydrocarbon because of its high H to C ratio (H/C = 4), availability, and low cost. Furthermore, the C produced can be sold as a co-product into the carbon black market (inks, paints, tires, batteries, etc.) or sequestered, stored, and used as a clean fuel for electrical power generation. The sequestering or storing of solid C requires much less development than sequestering gaseous CO₂.

Gibbs free energy minimization calculations have been carried out (P = 0.1 MPa; 873 K ≤ T ≤ 2273 K) for the CH₄ dissociation system (i.e. CH₄ + heat → equilibrium products) to determine equilibrium products. The concentrations of chemical species reaching a state of chemical equilibrium from reaction or partial reaction at atmospheric pressure for various reaction temperatures have been calculated using the F*A*C*T equilibrium code EQUILIB (Thompson et al., 1985). Thermodynamically favored products (Figure 1) indicate dissociation above 600 K and that temperatures T > 1600 K are required to achieve nearly complete dissociation. Although not shown, trace products at 1600 K include C₂H₂, C₂H₄, C₄H₈, C₃H₆, C₂H₆, and other species at concentrations < 40 ppm.

There are several alternatives to supply the energy required to drive reaction (1). In the commercial “Thermal Black Process” [Donnet, 1976], the energy is provided by burning CH₄ with air to heat a fire brick furnace to temperatures as high as 1673 K. Once hot, the air is shut off and the CH₄ decomposes according to reaction (1) until the wall temperature drops to below 1073 K. The system is operated semi-continuously with CH₄ burned in one sequence of the cycle to supply the heat necessary to carry out the decomposition in the second sequence. This process has been practiced for many years for the production of carbon black. The H₂ produced is used as a fuel to heat the furnace and the CH₄ feedstock.

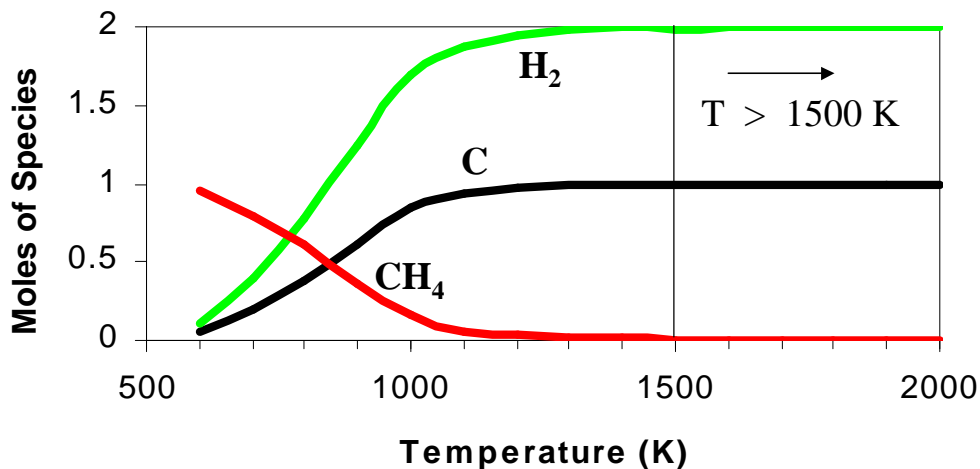


Figure 1. Primary Methane Decomposition Equilibrium Products $P = 0.1$ MPa

Pohleny and Scott (1962) used a fluidized bed/riser thermal decomposition reactor process that uses iron oxide for heat transfer and as a catalyst. Carbon collected on the iron oxide particles in the fluidized bed is burned off in the riser reactor for reheating the iron oxide particles that are recirculated to the endothermic fluidized bed reactor. Hydrogen is produced continuously by the decomposition occurring in the fluidized bed.

Gaudermack and Lynum (1996) and Bromberg et al. (1998) used a plasma torch to supply the necessary energy to decompose CH_4 and produce a continuous stream of H_2 . The plasma gas is H_2 that is recirculated from the process. Although no CO_2 is liberated from the process reactor itself, electricity is required to produce the plasma. When the electrical power is produced from natural gas fuel combustion, even in an efficient combined cycle plant, the overall thermal efficiency is significantly reduced and the CO_2 emission per unit energy is significantly increased.

In another process [Steinberg, 1995a], a molten metal bath reactor (such as tin or copper) is used to transfer heat to CH_4 that is bubbled through the molten metal. The reactor is heated by combustion products (CH_4 or H_2 burned with air) that flow through an internal heat exchanger. In this process, it is proposed to capture carbon in the liquid metal and to separate it from the metal by density difference, skimming the carbon off from the surface much as slag is skimmed off the surface of molten iron in a conventional blast furnace.

Although thermodynamics can predict when a reaction will not occur, it cannot predict whether a reaction will indeed occur in practice. Activation energies, transport processes (e.g. heating rate), and other reaction kinetic considerations are needed in order to determine if a reaction can be completed for a given amount of time in a chemical reactor design. Such kinetic data have been reported for reaction (1) using electrically heated pilot-scale aerosol flow reactors [Matovich, 1977].

Matovich (1977) showed that the decomposition of CH_4 could be carried to completion in a short residence time aerosol reaction tube at temperatures $T > 2088 \text{ K}$. The reactor consisted of a 0.0762-m diameter x 0.914-m long (3 inch ID x 3 ft long) graphite aerosol reaction tube heated indirectly by radiation from external electrodes heated directly by electrical resistance. Later studies included work carried out in 0.305-m ID x 3.66-m long (1 ft ID x 12 ft long) reaction tubes [Lee et al., 1984]. A small amount of carbon black was introduced in the CH_4 feed stream to serve as a radiation-absorbing target to initiate the pyrolytic reaction. Due to the high temperatures involved and the difficulty in heating a gas to those temperatures (by convection from the reactor walls), the carbon particles are the key to this process.

Reactions were carried out in the temperature range of $1533 < T < 2144 \text{ K}$ with residence times between approximately 0.1 and 1.5 seconds. The fraction of CH_4 dissociated was determined by measuring the thermal conductivity of the effluent gas after filtering the carbon black particles from the sample. Hydrogen (H_2) flowed radially through a porous reaction tube, providing a fluid-wall to prevent carbon black from depositing on the wall. The residence time in the reactor was controlled by the inlet flow of CH_4 , the radial flow of H_2 , and the reactor temperature. Some reported results [Matovich, 1977] where data were available for both a minimum residence time ($t_{r(\text{min})}$) of 0.2 s and a maximum residence time ($t_{r(\text{max})}$) of 1 s are summarized in Figure 2. It is clear from these results that residence time has little effect on dissociation for temperatures $T > 1900 \text{ K}$ and that complete dissociation can be achieved in aerosol flow reactors for temperatures greater than approximately 2100 K for reaction times of $t = 0.2 \text{ s}$.

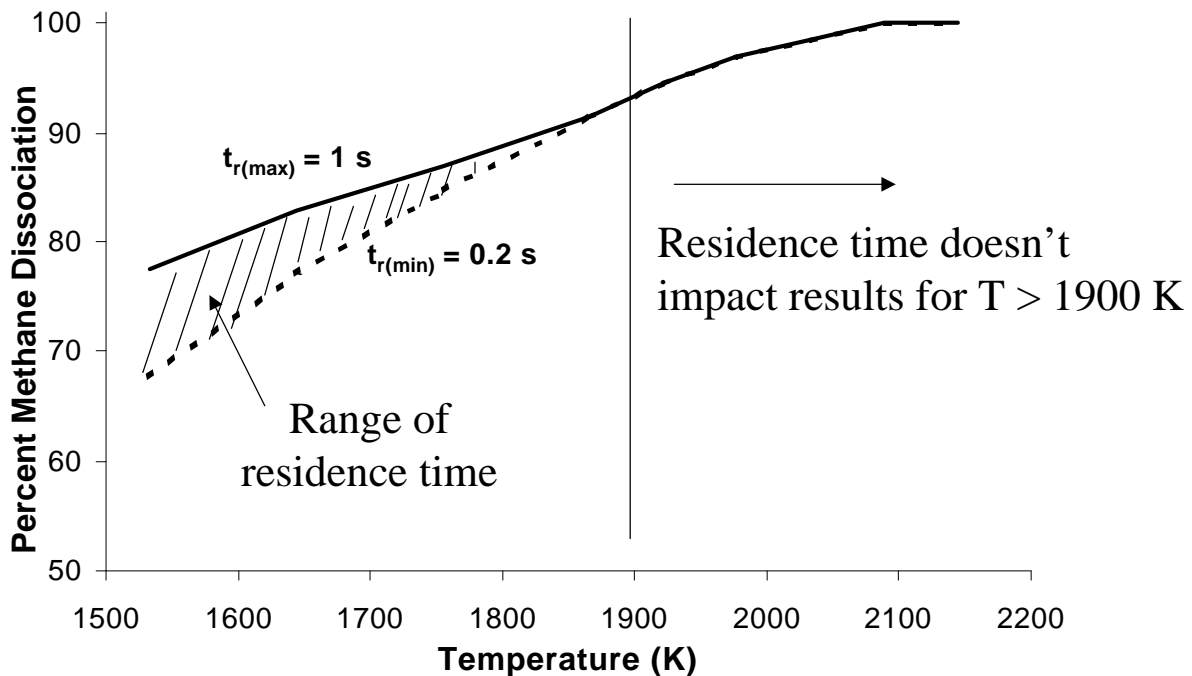


Figure 2. Effect of Residence Time & Temperature

The process investigated here is the high-temperature thermal dissociation of CH_4 using a solar-thermal aerosol flow reactor. The energy required to drive reaction (1) is supplied by concentrated sunlight. An experimental reactor apparatus was constructed and interfaced to NREL's HFSF [Jenkins et al., 1996; Lewandowski, 1993; Lewandowski et al., 1991; and Pitts et al., 1993]. There is no need for auxiliary cooling at the optical source. The reactor is operated as a cold wall process, because the beam is delivered directly on target. In addition, the control of solar radiation (on/off) is almost instantaneous. Absorbing surfaces exposed to concentrated solar radiation can reach temperatures of between 1000 K and 3000 K in fractions of a second. The process produces H_2 using high efficiency direct solar-thermal heating with no associated CO_2 generation.

Experimental Work

High-Flux Solar Furnace

The HFSF facility (Figure 3) at NREL in Golden, CO was used for this research. NREL is the primary national laboratory in the United States for renewable energy research. The HFSF uses a series of mirrors that concentrate sunlight to a focused beam at maximum power levels of 10 kW into an approximate diameter of 10 cm. The solar furnace's long focal length and its off-axis design give researchers flexibility and control over the delivered flux. It operates with a heliostat that has an area of 31.8 m^2 and a 92% solar-weighted reflectivity. The heliostat reflects sunlight to a primary concentrator consisting of 25 hexagonal facets that are spherical mirrors ground to a 14.6-m radius of curvature. The total surface area of the primary concentrator is 12.5 m^2 and it reflects radiation from the entire solar spectrum (300 nm to 2500 nm). Under optimal conditions, the primary concentrator can achieve maximum flux intensities of 2,500 suns. Secondary concentrators that achieve intensities of more than 20,000 suns and refractive designs approaching 50,000 suns can be installed at the primary concentrator's focal point to increase the intensity further. The furnace is easily capable of delivering flux densities on the order of $100\text{-}1000 \text{ W/cm}^2$. No secondary solar concentration was used in these studies.

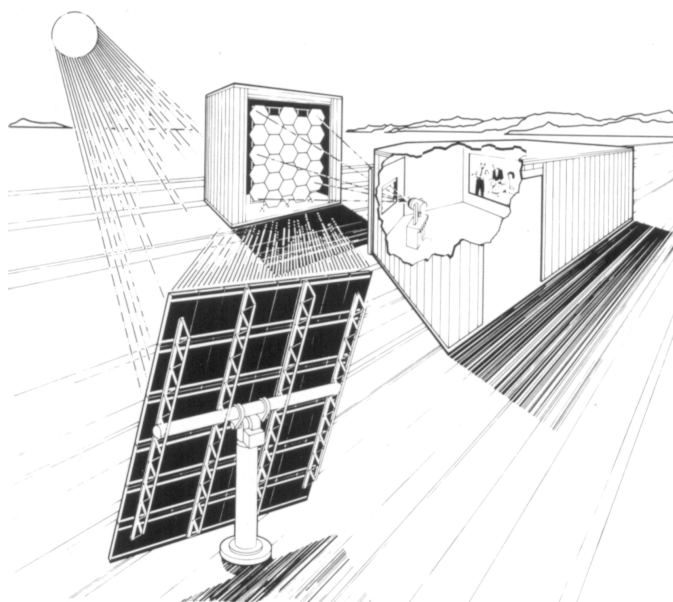


Figure 3. High-Flux Solar Furnace Schematic

Reactor System

Proof-of-concept experiments were carried out using a modified reactor system originally built for previous experiments in fullerene production [Mischler et al., 1997]. The reactor consists of a particle and gas feed mechanism, quartz reactor tube, an internal graphite “target” feed tube, and a filter housing. The reactor operates at atmospheric pressure with gas flow driven and controlled through a series of mass flow controllers. An in-line Horiba model TCA-300 H₂ detector was inserted downstream of the particle filter. This detector is based on thermal conductivity measurements and was calibrated for 5 % H₂ in argon (Ar). Gas samples were also taken and analyzed using an off-line gas chromatograph (GC). CH₄ and produced H₂ were kept outside flammability limits by operating with a dilute 5% CH₄ in Ar feed gas mixture and a pure Ar purge stream. The temperature inside the quartz tube reactor is exceedingly difficult to determine. However, the temperature of the quartz tube is carefully monitored using an infrared camera positioned on the side of the reactor. The quartz temperature is monitored to avoid warping or even melting the reactor wall with concentrated sunlight. A schematic of the reactor system is shown in Figure 4.

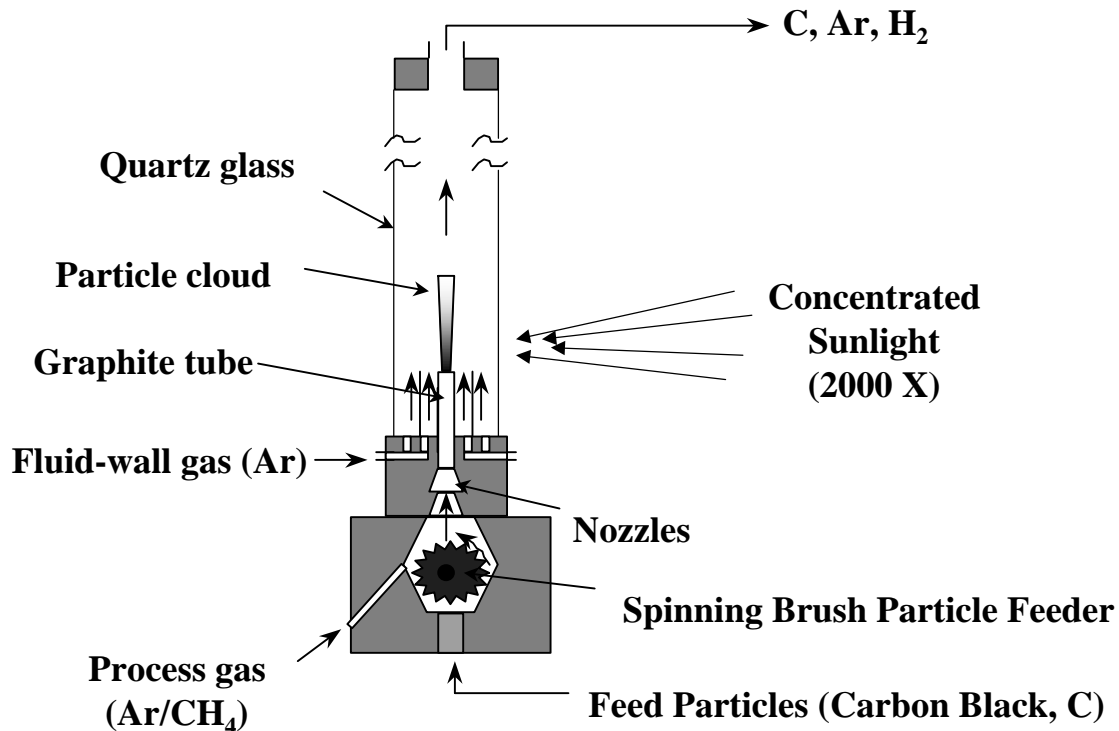


Figure 4. Schematic of Solar-thermal Aerosol Flow Reactor

A key aspect of the reactor operation is the heating means for the feed CH₄. The reactor has been designed for three alternative heating methods: (1) heating a 6 mm OD x 3 mm thick “target” graphite tube with concentrated sunlight, the heated target then heating the CH₄-containing feed gas by conduction; (2) heating the “target” graphite tube, but with radiation absorbing fine carbon black particles suspended in the CH₄-containing feed gas stream so the inside wall of the

“target” radiates to the flowing particles that subsequently heat the flowing feed gas by particle surface conduction in addition to the wall conduction; and (3) heating the suspended carbon black particles directly with concentrated sunlight, the sunlight directed above the top of the graphite tube. Alternatives (2) and (3) involve volumetric absorption of light by a gas-solid suspension. The graphite tube can be seen contained within the quartz tube reactor assembly as shown in Figure 5. The quartz tube extends beyond the limits of the concentrated solar flux provided by the HFSF. The quartz tube was positioned at the nominal focus along the optical axis of the HFSF with its axis “vertical”.

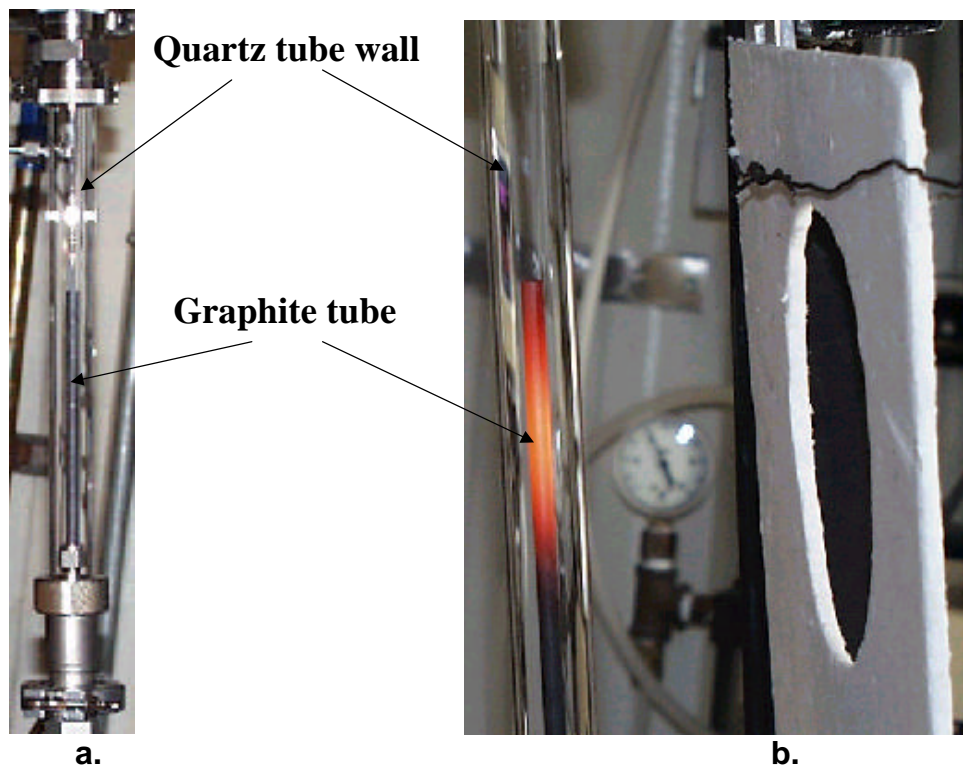


Figure 5. Reactor Tube Assembly: a. before heating, b. immediately after heating (shutter closed)

The particle suspension is generated in a feed mechanism located below the quartz tube (see Figure 6). Lightly compacted carbon black particles (“ShawiniganTM,” acetylene carbon black; product of Chevron Chemical Co., Houston, TX) are fed against a rotating steel brush that conveys the particles to a space where they are mixed with the 5% CH₄/Ar feed gas. The suspension then flows through a set of nozzles that destroy any particle agglomerates. The nozzle size varies between 0.33 mm and 0.64 mm. Before the particle cloud passes through the focal area, two streams of “sweep” Ar gas are “wrapped” around the gas-solid suspension. This “fluid-wall” is designed to prevent particles from reaching the quartz glass in locations where heating by the highly concentrated sunlight might soften or melt the tube. The gas and particles are fed from bottom to top of the quartz reactor. With the ratio of “sweep” Ar to feed 5% CH₄/Ar on the order of 10:1, the overall percentage of CH₄ or H₂ was relatively low for these proof-of-concept experiments. These low concentrations are used as a safety precaution for initial studies. A side view of the reactor assembly above the particle feeding system is shown in Figure 7.



Figure 6. Particle Feeding System (below reactor assembly)

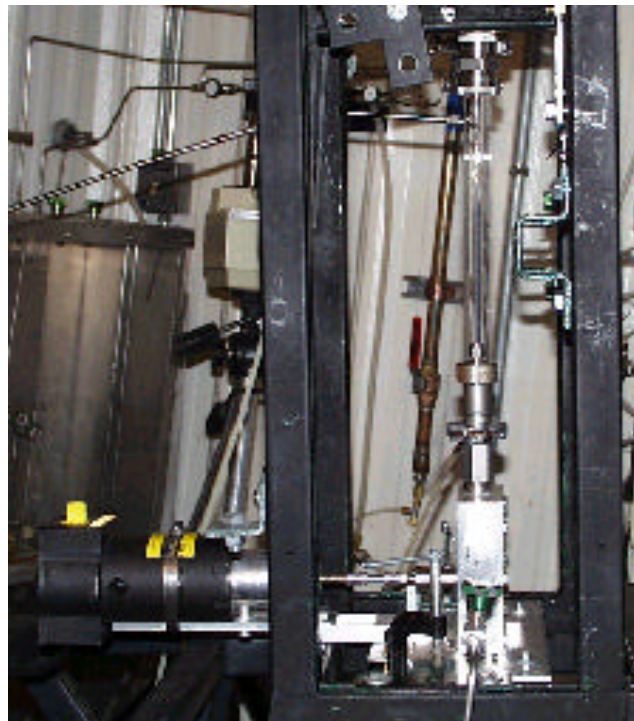


Figure 7. Reactor Assembly (above particle feeding system)

Proof-of-concept Results and Discussion

The signal response for a typical experiment is shown in Figure 8. This was a very clear day with direct normal irradiance at approximately 1000 W/m^2 . The estimated flux on the target (reactor) was about 2400 kW/m^2 or 2400 suns. The gas temperature was monitored by a thermocouple downstream of the reactor and the quartz temperature was monitored with an infrared video camera (IR in Figure 8). First the flow of sweep argon gas was initiated at 2 slpm (standard liters per minute), then the particle feed and 5 mol % CH_4/Ar (at a flow of 0.1 slpm) were started at about 4 minutes (0.22 mol % CH_4/Ar total). The particles and CH_4/Ar feed gas mixture entered the reaction tube through a 0.15-m long internal graphite tube as described earlier. A change in the H_2 % can be seen since the thermal conductivity of CH_4 is higher than argon (there is a time delay for the flow to reach the H_2 detector of about 20 to 30 seconds). This signal was allowed to steady, then the concentrated sunlight was introduced by opening a fast-acting shutter. A nearly immediate increase in the H_2 signal can be seen in the dashed trace. The shutter was closed at about 11 minutes and a corresponding decrease in the H_2 signal can be seen. At 16 minutes the flow of CH_4/Ar feed gas was stopped, then restarted, stopped again and restarted at 0.2 slpm at 18 minutes (0.45 mol % CH_4/Ar total). The changes in the H_2 signal clearly indicate that the H_2 production is following these flow manipulations. A sample bag was filled for subsequent analysis from about 20 to 25 minutes. The shutter was closed at about 27 minutes. The subsequent off-line GC analysis (0.8 mol % H_2 , 180 ppm CH_4 , 180 ppm C_2H_2 , 520 ppm C_2H_4 , 0.06 mol % CO , 0.05 mol % CO_2 , 1.5 mol % air, balance Ar) of the collected gas sample indicated an 88 % dissociation of methane. The air was introduced when the sample bag was detached from the collection valve and possibly also when attaching it to the GC system. The CO and CO_2 indicate that there is some air in the system. The ethylene and acetylene are incomplete reaction products. At the flows of CH_4 and Ar in this experiment, complete dissociation of CH_4 to H_2 would have yielded 0.91 mol % H_2 . These results indicate that, with constant solar flux, an increase in the CH_4 feed rate results in an increase in the H_2 synthesis rate.

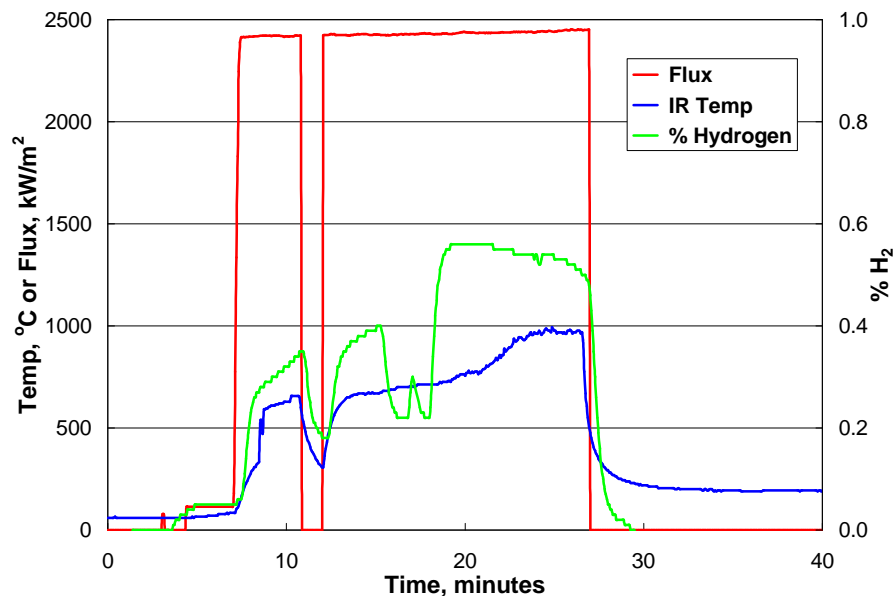


Figure 8. Signal Response to Solar Flux (with particle feed)

Successful experiments were also carried out (Figure 9) without carbon particle co-feed and with a higher concentration of CH₄ in the gas stream (1.7 mol% CH₄/Ar total). When the amount of solar flux striking the reactor increased, the signal from the H₂ detector increased accordingly. In Figure 9, the initial solar flux was 1160 kW/m², resulting in little dissociation of CH₄. When the flux was raised to 1760 kW/m² the % H₂ signal quickly jumped to over 1 mol % H₂ (about 32% dissociation). As the solar flux continued to increase to 2060 kW/m² and 2360 kW/m², the H₂ signal increased accordingly to values of 1.4 and 1.5 mol %, respectively. These results indicate that, for a constant CH₄ feed rate, an increase in solar flux results in an increase in the H₂ synthesis rate. The effect of solar flux on dissociation is more apparent from the results presented in Figure 10 for a 1 mol % CH₄ in argon total feed composition. Clearly, a flux of at least approximately 1200 kW/m² is necessary to dissociate CH₄.

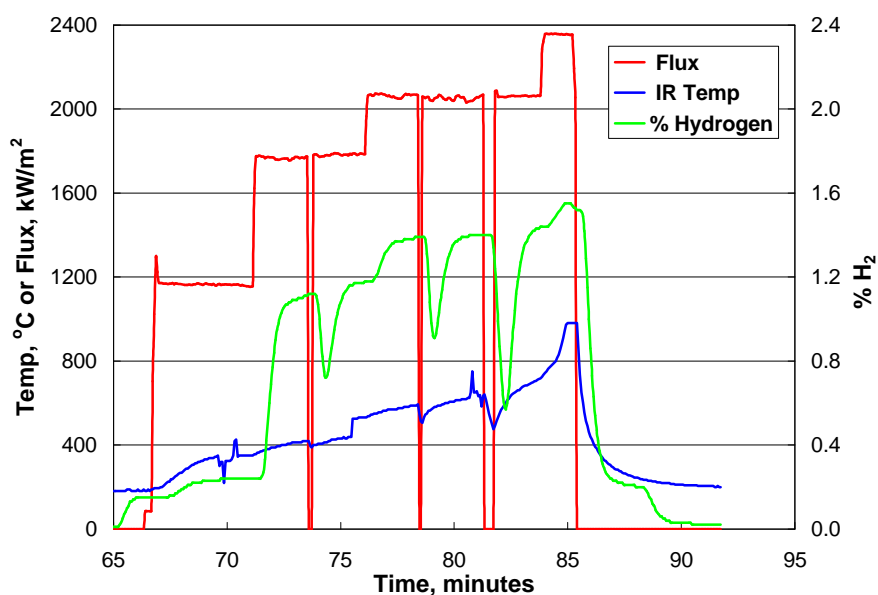


Figure 9. Signal Response to Solar Flux (no particle feed)

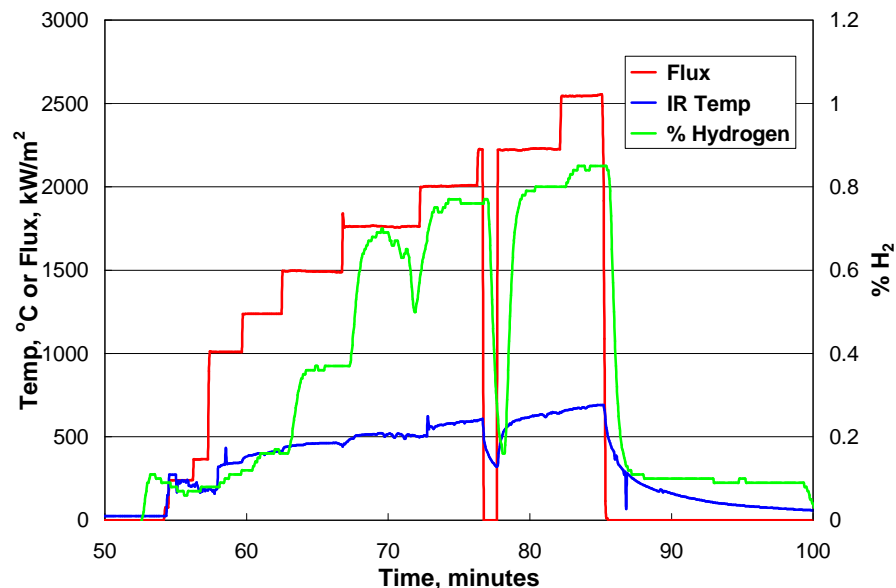


Figure 10. Signal Response to Solar Flux (1 mol % CH₄ in total argon feed)

Process Design and Cost Analysis

A preliminary plant design was developed for a solar-coupled process for the thermal decomposition of methane to hydrogen and carbon black. The process economics were evaluated using discount cash flow analysis. Cash flow analysis determines the required selling prices of the hydrogen and carbon black products. The sales price of these products must generate sufficient revenue to pay for annual operating expenses and the initial capital investment, and provide an acceptable internal rate of return over the lifetime of the process.

Since some of the specific design factors and process costs were not known exactly, these factors and costs were treated as parameters in the analysis. This approach provides insight into how the process economics depends on the values of these factors and costs and determines which factors and costs are most important in determining the overall process economics.

A preliminary evaluation of the current carbon black commercial market was also performed to determine current market sizes for the various grades of carbon black products and their corresponding selling prices. Results from the process design, economic analysis, and market evaluation were used to draw conclusions and make recommendations for future research and process development.

Process Plant Design

The solar-coupled plant is envisioned to have many of the same unit operations as those of a current commercial carbon black plant [Wang, 1993]. A schematic of the plant is shown in Fig. 11. The reactor is mounted on top of the tower which receives concentrated solar from a field of tracking mirrors or heliostats. The concentrated solar energy provides the energy needs for the process and eliminates the need for partial combustion of the feed. The feed for this process is natural gas, which is preheated in the heat exchanger by the product stream. Natural gas, recycled hydrogen and carbon particles enter the top of the reactor and flow downward where they are heated directly with solar flux. Decomposition of the natural gas results in a product stream consisting of carbon black and hydrogen.

A water quench is not used in this design to maintain a pure stream of carbon black and hydrogen. The product stream flows through the tube side of the heat exchanger and is cooled to about 200°C (473 K) before entering the bag houses. The carbon black is separated in the bag houses and transferred to the storage tanks in the same manner as that of the commercial carbon black process. Hydrogen gas exits the top of the bag houses at near ambient temperature and pressure. A portion of the hydrogen gas is recycled back to the reactor and fed separately to flow past the reactor window and prevent deposition of carbon black. This process design and analysis does not include unit operations for the compression and storage of the hydrogen gas product.

Operation of a solar-coupled plant will be continuous but will only operate when sufficient solar irradiance is available. This fraction of time is referred to as the solar capacity factor and varies with geographic location. Capacity factors for locations that are favorable for solar processes, such as the desert southwest portion of the United States, have been measured to be as high as 0.41. For this work, the capacity factor was varied from 0.28 to 0.41. Limited operation of the

solar-coupled plant results in higher capital costs as compared to a continuous operation plant with the same annual production capacity.

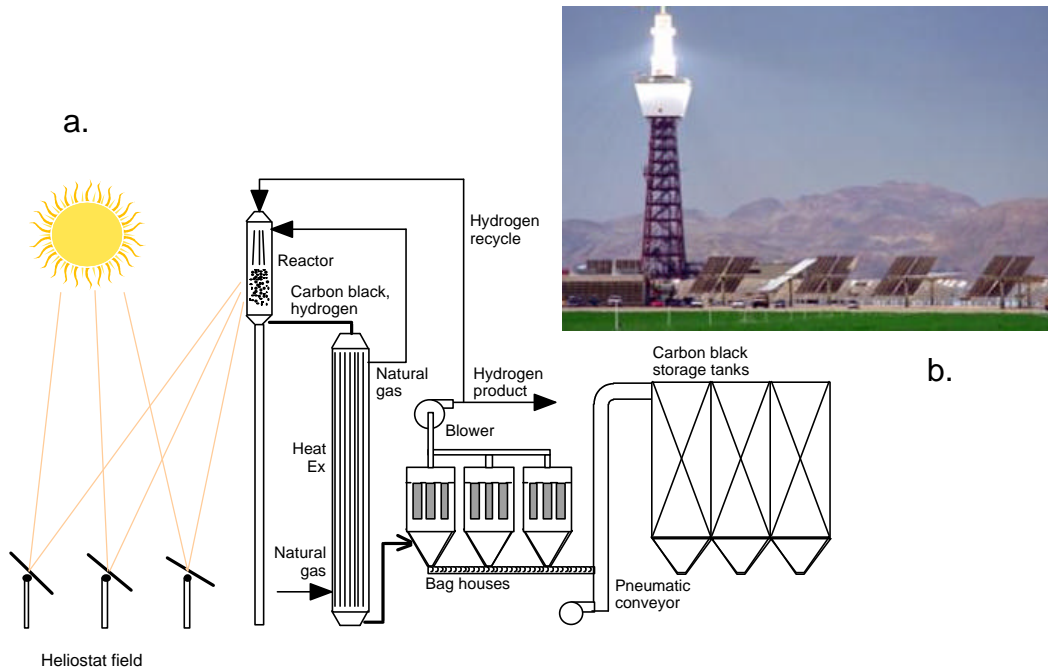


Figure 11. Solar-thermal Processing: a. schematic of aerosol CH_4 dissociation process, b. photograph of 10 MW Barstow, CA facility

Cash Flow Analysis

Cash flow analysis was performed to determine process economics for the solar-coupled process. The analysis consisted of determining the fixed capital and annual operating costs for the process as a function of key design and cost parameters. These parameters included 1) heliostat cost, 2) annual production rate, 3) reaction temperature, 4) reaction residence time, 5) hydrogen fraction recycled, 6) reactor thermal efficiency, and 7) solar capacity factor. The methods for determining these costs are described below.

After fixed capital and annual operating costs for each case were determined, cash flow analysis was performed to determine the required selling prices for hydrogen and carbon black. The cash flow analysis had the following assumptions:

1. Project lifetime: 21 years
2. Construction period: 1 year
3. Working capital: 10% of total capital
4. Capital depreciated, 10% per year
5. Tax rate: 28%
6. Internal rate of return (IRR): 15%

Cash flow analysis determined the required selling prices of hydrogen and carbon black to achieve a net present value of zero at the end of the lifetime of the process. This approach is consistent with the method used by the Hydrogen Program to assess the economics of hydrogen production processes [Mann, 1995]. For all cases, the hydrogen that was produced was assumed to have an energy content of 39.4 kWhr/kg (0.0611 MBtu/lb), which corresponds to its higher heating value (HHV). The final hydrogen product was at ambient temperature and pressure.

Capital Cost Estimation

The capital equipment items for the process included the land, heliostats and tower, reactor, heat exchanger, bag houses, pneumatic conveyor, blower, and storage tanks. For each item, a purchase cost was determined. Methods for calculating purchase costs for each item are described below. The purchase cost included shipping and sales taxes. The fixed capital cost for each item was determined by multiplying the purchase cost by an inflation factor, a set of direct and indirect cost factors, and a contingency and fee. These factors varied with equipment item and values and are summarized in Table 1. For each item, the fixed capital cost was determined by the formula:

$$\text{Fixed Capital Cost} = \text{Purchase cost} * F^{\text{Inflation}} * (1 + F^{\text{Direct}} + F^{\text{Indirect}}) * (1 + F^{\text{Contingency \& Fee}}) \quad (2)$$

Each item had an inflation factor based on the year from which purchase costs were obtained. All inflation factors were based on cost indices taken from Chemical Engineering (2000). The heliostat, tower, and reactor purchase costs were based on current (2000) cost estimates so the factor for those items was 1. The bag house costs were determined from an estimation procedure based on 1987 costs [Turner et al., 1987a,b]. Purchase costs for the remainder of the equipment items were based on cost tables for January 1990 taken from Peters & Timmerhaus (1991).

The purchase price of land was assumed to be current (Year 2000) at \$500/1000m². Since the cost of land improvement was factored into the cost of equipment, all of the direct and indirect cost factors were taken to be 0 for land. For this item, the fixed capital and purchase costs were equal. The quantity of land required for the process was determined from the required heliostat area. The ratio of required land area to heliostat area was 6 to account for reasonable spacing between heliostats.

Table 1. Capital Cost Factors for Purchased Capital Equipment

| Factors | Heliostats & Tower | Reactor | Bag Houses | Heat EX, etc |
|---------------------|-------------------------------|----------------|-------------------|---------------------|
| Inflation | 1 (2000) | 1 (2000) | 1.56 (1987) | 1.41 (1990) |
| Direct | | | | |
| Foundation prep. | 0 | 0 | 0.1 | 0.1 |
| Support housing | 0 | 0.08 | 0 | 0 |
| Installation | 0 | 0.39 | 0.39 | 0.39 |
| Electrical & piping | 0 | 0.41 | 0.41 | 0.41 |
| Instrum & controls | 0 | 0.15 | 0.15 | 0.15 |
| Service facilities | 0.1 | 0.55 | 0.55 | 0.55 |

| Factors | Heliostats & Tower | Reactor | Bag Houses | Heat EX, etc |
|-------------------|-------------------------------|----------------|-------------------|---------------------|
| Indirect | | | | |
| Engineering | 0.1 | 0.32 | 0.32 | 0.32 |
| Construction | 0.1 | 0.34 | 0.34 | 0.34 |
| Contingency & fee | 0.1 | 0.15 | 0.15 | 0.15 |

The purchase cost for heliostats and tower were assumed to include most of the direct cost factors listed in Table 1. A cost factor was included for the cost of service facilities. Because the capital expense for these items is much greater than that of the process equipment, the indirect cost factors and contingency & fee were assumed to be less for these items. The tower was assumed to cost \$7,500/m of height. This cost is based on estimates from Epstein et al. (1996). The estimated cost for heliostats varies widely depending on the size of the plant and state of maturity of the solar industry. For this reason, heliostat cost was made a parameter in this analysis. Values from \$50/m² to \$1000/m² were evaluated. Epstein et al. (1996) reported a vendor heliostat quotation of \$150/m² (for 60,800 m² of heliostat) installed, but not including the foundation, wiring, or site development.

The tower height was determined from the heliostat area according to the formula [Precision Glassblowing, 2000]:

$$\text{Height} = 10 * (\text{heliostat area} / 1000)^{0.5} \quad (3)$$

This formula accounts for the need to increase the tower height as the heliostat area increases. This is done to prevent shading between heliostats. The heliostat area was determined from the required reactor power, the available solar resource, and several efficiency factors, which account for energy losses as the power is delivered to the reactor. Heliostat area was determined using the expression:

$$\text{Heliostat area} = \text{Power}^{\text{reactor}} / \text{Efficiency}^{\text{reactor}} / \text{Efficiency}^{\text{heliostat}} / \text{Resource} \quad (4)$$

In this formula, $\text{Power}^{\text{reactor}}$ is the required reactor power in kW. $\text{Efficiency}^{\text{reactor}}$ is the thermal efficiency of the reactor. It accounts for thermal energy losses through the reactor walls and window. Most of the loss results from radiation losses through the window. This efficiency was evaluated as a parameter with values of 0.3, 0.5, and 0.7. $\text{Efficiency}^{\text{heliostat}}$ is the efficiency of the heliostats. It accounts for reflectivity losses (about 5%), projected area losses due to the angle between the incident sunlight and the target reactor and soiling due to dust and dirt. Values for this efficiency vary depending on the location of the heliostat and tower relative to the position of the sun in the sky. An average value for all of the heliostats was assumed to be 0.69. Resource is the average solar resource that is available when the plant is operating. For this analysis, the solar resource was assumed to be 0.75 kW/m². Once reactor power is known, values for heliostat area and tower height, along with their corresponding fixed capital costs can be determined from the above formulas.

The reactor was assumed to be a vertical, cylindrical design with some portion or all of the reactor length consisting of a quartz wall that is supported inside a steel housing. A portion of the length would not have the steel housing and would function as the window. A cost factor was included for the steel housing and insulation. There was no cost factor for foundation preparation since the reactor is mounted on top of the tower. The purchase cost was based on cost estimates obtained from a local vender [Precision Glassblowing, 2000] for quartz tubing having diameters of 1, 2, 2.5, 3, and 3.5 ft (i.e. 0.305, 0.61, 0.762, 0.914, and 1.07 m). For all sizes, the cost of the quartz tubing, on a volume basis, varied from \$900/ft³ to \$1,200/ft³ (\$31,780 to \$42,373/m³). The purchase cost of the reactor was chosen to be \$1,100/ft³ or \$38,870/m³. The purchase cost of the reactor was assumed to be linear with reactor volume.

The key factors for determining the reactor volume were the volumetric flow rate and reactor residence time. Since the molar and volumetric flow rates increase as the decomposition of methane proceeds, these flow rates were based on product flow rates. Direct heating of the reactants in the reactor is expected to allow for very short residence times. The residence time was evaluated as a parameter with conservative values from 1 to 4 seconds, although fractions of a second have been shown to be sufficient (Figure 2). The total volumetric flow rate depends on the instantaneous molar flow rate of methane, the fraction of recycled hydrogen, and the reactor temperature and pressure. The instantaneous molar flow rate of methane was determined from the annual production of hydrogen, using the solar capacity factor to account for the actual operating time. The total molar flow rate through the reactor assumed that all methane is converted to hydrogen and accounts for the additional molar flow due to recycled hydrogen. The total volumetric flow rate was determined from the total molar flow rate, reactor temperature and pressure, using the ideal gas law as the state function. Reactor pressure was atmospheric for all cases. Reactor temperature was varied as a parameter from 1,600 to 1,900°C (1873 to 2173 K).

To determine heliostat area, total reactor power was also determined. This was based on the instantaneous molar flow rate of methane, the molar heat of reaction, and the energy required to heat methane to the reaction temperature. Values for the heat of reaction and enthalpy for methane as a function of temperature were obtained from Roine (1997). A portion of the sensible energy in the products is recovered in the heat exchanger. This recovered power is accounted for as a credit in the total reactor power calculation.

A summary of the equipment size and equipment fixed capital cost according to equation (2) for each piece of equipment is included in Table 2 for the base case of 1,000,000 kg H₂/yr. The total equipment fixed capital investment is \$7,941,000.

Table 2. Summary of Fixed Capital Equipment Cost (Base Case)

| Equipment | Size | Fixed Capital Cost |
|------------------|--------------------------------|---------------------------|
| Land: | 72,608 m ² | \$36,300 |
| Heliostat: | 12,101 m ² | \$4,360,000 |
| Tower: | 35 m | \$376,000 |
| Reactor: | 3.13 MWth, 10.4 m ³ | \$1,513,000 |
| Heat Exchanger: | 795 m ² | \$620,000 |

| Equipment | Size | Fixed Capital Cost |
|---------------------|-------------------------------------|---------------------------|
| Baghouse Filter: | 117 m ² | \$137,000 |
| Other Equipment | | Other Equipment Total: |
| Pneumatic Conveyer: | 1000 kg/hr | \$936,000 |
| Storage Tanks: | 115 m ³ | |
| & Blower: | 2.36 m ³ /s (5,000 acfm) | |
| Total Equipment: | | \$7,941,000 |

The operating and maintenance (O&M) costs for the process were determined for each major equipment item. The annual cost of natural gas (\$594,000/yr @ \$3.00/1000 scf) was also determined. For each item, the number of labor hours per day or per some measure of equipment size or production capacity was estimated. This yielded a 7.5 operator/labor force with a fully-burdened labor rate of \$40/hour/operator. Supervision labor was estimated at 15% of the total O&M labor.

Base Case

A base case for the process was developed in which the most likely values for the parameters were used. The parameter values for the base case are given in Table 3.

Table 3. Parameter Values for the Base Case

| Parameter | Value |
|-------------------------------|----------------------|
| Annual hydrogen production | 1,000,000 kg/yr |
| Heliostat cost | \$250/m ² |
| Fraction of hydrogen recycled | 0.2 |
| Reactor temperature | 1,600°C (1873 K) |
| Reactor residence time | 1 second |
| Reactor thermal efficiency | 0.5 |
| Solar capacity factor | 0.28 |

Cash flow analysis determined the required selling prices of hydrogen and carbon black to achieve a net present value of zero at the end of the lifetime of the plant. A graph of the annual and cumulative discount cash flow over the lifetime of the process is shown in Fig. 12.

Various price combinations for hydrogen and carbon black were determined. The extreme cases are hydrogen sales only where the price of carbon black is \$0/kg and carbon black sales only where the hydrogen price is \$0/kWhr. Intermediate cases set the price for carbon black and the required price for hydrogen was determined. A summary of these results is presented in Table 4.

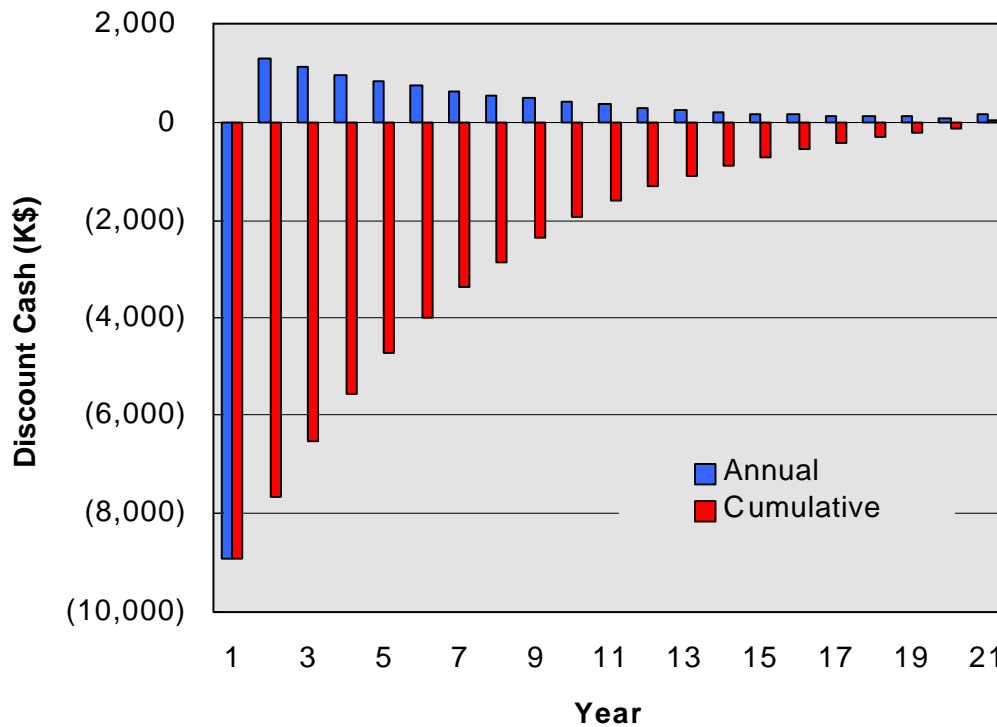


Figure 12. Annual and Cumulative Discount Cash Flow (Base Case)

Table 4. Required Sales Prices for Hydrogen and Carbon Black for Base Case.

| Case | Hydrogen Selling Price | | | Carbon Black Selling Price | |
|------|------------------------|-----------|---------|----------------------------|---------|
| | (\$/MBtu) | (\$/kWhr) | (\$/GJ) | (\$/lb) | (\$/kg) |
| 1 | 27 | 0.0922 | 26.2 | 0.00 | 0.00 |
| 2 | 20 | 0.0683 | 19.0 | 0.15 | 0.33 |
| 3 | 15 | 0.0512 | 14.2 | 0.25 | 0.55 |
| 4 | 10 | 0.0341 | 9.5 | 0.35 | 0.77 |
| 5 | 5 | 0.0171 | 4.8 | 0.45 | 0.99 |
| 6 | 0 | 0 | 0 | 0.55 | 1.21 |

Results show that if only hydrogen is sold, the price must be \$27/MBtu (\$0.0922/kWhr or \$26.2/GJ). If only carbon black is sold, the price must be \$0.55/lb (\$1.21/kg).

Another scenario was considered in which the solar capital and operating costs were set to 0 and the hydrogen product was assumed to provide the thermal energy requirements for the process. The hydrogen byproduct in the conventional process is often used in this manner. For this scenario, the hydrogen price would be \$0.0/kWhr. Since the process is not solar-coupled, the capacity factor can be increased from 0.28 to 0.95, indicating the plant would operate 95% of the time. The selling price of carbon black was determined using several values for reactor residence

time. In the commercial process, the reactor residence time is typically greater than 1 second. Results are presented in Table 5.

Table 5. Selling Price for Carbon Black vs. Residence Time (conventional plant).

| Reactor Residence Time (seconds) | Carbon Black Price | |
|-------------------------------------|--------------------|---------|
| | (\$/lb) | (\$/kg) |
| 1 | 0.22 | 0.49 |
| 2 | 0.25 | 0.55 |
| 3 | 0.27 | 0.60 |
| 4 | 0.33 | 0.73 |

These costs are consistent with the current selling price of commercial carbon black that sells for \$0.30/lb to \$0.35/lb (\$.66/kg to \$0.77/kg) [Chemical Marketing Reporter, 2000] and indicate that the economic analysis for the conventional portions of this plant are reasonable.

Parametric Analysis

The selling prices for hydrogen and carbon black were determined for variations of the base case in which the parameter values, which are listed in Table 3, were varied one at a time. The cost of heliostats is uncertain because the technology and the market are still developing. This cost was varied from \$50/m² to \$1000/m². Results are presented in Table 6 with prices assuming only one product is sold.

Table 6. Selling Prices for Hydrogen and Carbon Black vs. Heliostat Cost

| Heliostat Cost (\$/m ²) | Hydrogen Selling Price | | | Carbon Black Selling Price | |
|--|------------------------|-----------|---------|----------------------------|---------|
| | (\$/MBtu) | (\$/kWhr) | (\$/GJ) | (\$/lb) | (\$/kg) |
| 50 | 22 | 0.0751 | 20.9 | 0.44 | 0.97 |
| 100 | 23 | 0.0785 | 21.8 | 0.47 | 1.04 |
| 250 | 27 | 0.0922 | 25.6 | 0.55 | 1.21 |
| 500 | 34 | 0.1161 | 32.3 | 0.70 | 1.54 |
| 750 | 41 | 0.1400 | 38.9 | 0.84 | 1.85 |
| 1000 | 48 | 0.1639 | 45.5 | 0.98 | 2.16 |

Other parameter values in Table 3 were also varied to determine the variation of selling prices with the values of these parameters. Each of the following parameter variations assumes that only one product is sold. As with the other cost studies in this paper, the required selling price of hydrogen will be reduced if the carbon black can be sold, and vice versa. When the size of the plant was decreased from 1,000,000 kg/yr to 100,000 kg/yr, the required sales price of hydrogen increased to \$32/MBtu (\$0.1092/kWhr or \$30.3/GJ) and the price of carbon black increased to \$0.65/lb (\$1.43/kg).

A portion of the hydrogen product must be recycled back to the reactor in order to keep the window clean and cool. Increasing the recycled fraction increases the total gas volumetric flow through the reactor and therefore, reactor size and cost. When the fraction of recycled hydrogen increased from 0.2 to 0.5, the sales price of hydrogen increased to \$29/MBtu (\$0.099/kWhr or \$27.5/GJ) and the sales price of carbon black increased to \$0.59/lb (\$1.30/kg). Increasing the reactor temperature may improve the carbon black product quality. Increasing the reactor temperature also increases total gas volumetric flow through the reactor. When the reactor temperature is increased to 1,900°C (2173 K) the hydrogen price increased to \$29/MBtu (\$0.099/kWhr or \$27.5/GJ) and the carbon black price to \$0.58/lb (\$1.28/kg). Increasing the reactor residence time may allow for lower operating temperatures but also increases reactor size. Increasing the residence time to 2 seconds increased the hydrogen sales price to \$32/MBtu (\$0.1092/kWhr or \$30.3/GJ) and the carbon black sales price to \$0.65/lb (\$1.43/kg).

Decreasing the reactor thermal efficiency increases the thermal energy requirement for the reaction, and therefore, the size of the heliostat field. Decreasing this efficiency from 0.5 to 0.25 increased the sales price of hydrogen to \$39/MBtu (\$0.133/kWhr or \$36.9/GJ) and the sales price of carbon black to \$0.79/lb (\$1.74/kg).

The solar capacity factor will also impact the economics of the process. Values for this factor have been measured to be as high as 0.41 in areas of very high solar irradiance. Increasing the capacity factor from 0.28 to 0.41 decreases the price of hydrogen to \$22/MBtu (\$0.075/kWhr or \$20.8/GJ) and the price of carbon black to \$0.44/lb (0.97/kg).

The profitability analysis is summarized in Figure 13. The effect of heliostat cost and reactor efficiency on required hydrogen selling price is shown at arbitrary, fixed values of carbon black selling price.

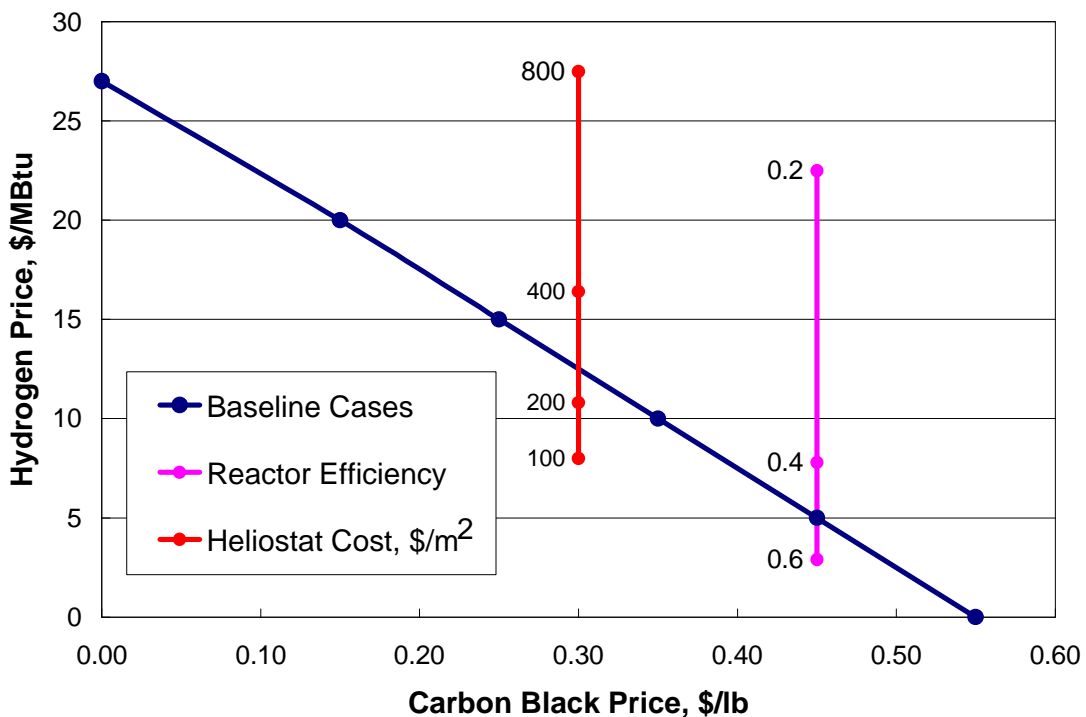


Figure 13. Profitability Analysis Summary

Market Analysis for Carbon Black

A preliminary evaluation of the current carbon black commercial market was also performed to determine current market sizes for the various grades of carbon black products and their corresponding selling prices. Applications for carbon black include the reinforcement of rubber, use as black pigment, and as a conductive additive to rubber and plastic products [Kirk-Othmer, 1991]. World production of carbon black in 1989 was greater than 6 million metric tons. United States production was about 1.6 million metric tons. About 70% of the carbon black that is produced is used in the reinforcement of rubber for tires, 20% is used in other rubber products, and the remaining 10% in non-rubber products. Carbon black used for rubber reinforcement sells for about \$0.30/lb to \$0.35/lb (\$0.66/kg to \$0.77/kg) [Chemical Marketing Reporter, 2000].

The non-rubber applications include additives to plastics, printing inks, paint, and paper. A special electrically conductive grade of carbon black sells for prices that are considerably higher than those that are used in rubber reinforcement. Electrically conductive grades are used to produce conductive and antistatic polymer composites. Applications include antistatic carpeting, floor tile, heating elements, videotapes and disks, and electrical shielding. Markets for these applications are increasing faster, on a percentage basis, than those for conventional uses. The current price for a higher grade of carbon black (Thermax) is \$0.78/lb [Canadian Carbon Company, 2000]. An even higher grade of carbon black produced from acetylene sells for \$1.40/lb [Chevron Chemical Company, 2000].

In 1989, the total market for specialty grade carbon blacks was 126,000 metric tons or 126,000,000 kg. A solar-coupled hydrogen production plant, which produces 1,000,000 kg/yr of hydrogen, will produce 3,000,000 kg/yr of carbon black. This represents about 2.4% of the current United States market for higher-grade carbon blacks. The addition of this production capacity to the current market would not have a significant impact on the price of higher-grade carbon blacks and since this market is increasing faster than other carbon black markets, demand for the additional production capacity should be easy to identify.

Summary and Conclusions

The objectives of this work were to carry out “proof-of-concept” experiments at the NREL HFSF, develop a preliminary design for a solar-coupled process for the thermal decomposition of methane to hydrogen and carbon black, and to evaluate the process economics using discount cash flow analysis. The initial results are encouraging and have demonstrated that the process works in principle. High conversions have been achieved using a solar-thermal reactor not designed for the specific process using only modest solar concentration levels.

The conceptualized plant design includes the same major equipment components as current commercial carbon black production plants. These components include a high temperature reactor, heat exchanger, bag house filters, pneumatic conveyor, blower, and storage tanks. In addition, the process includes a solar heliostat field and tower to provide the thermal energy needs of the process. The process design and economic analysis contain enough refinement to determine how the price of hydrogen and carbon black vary with the values of several key

process parameters and costs. Parametric analysis provides insight into how the process economics depends on the values of these factors and costs and determines which factors and costs are most important in determining the overall process economics.

Results of the discount cash flow analysis show that the required single product selling price for hydrogen for the base case 1,000,000 kg/yr hydrogen plant is \$27/MBtu (\$0.0922/kWhr or \$25.6/GJ) and for carbon black is \$0.55/lb (\$1.21/kg). These prices assume that only one product is sold. If both products are sold, then the selling price for each decreases. For example, selling prices of \$10/MBtu (\$0.0341/kWhr or \$9.5/GJ) for hydrogen and \$0.35/lb (\$0.77/kg) for carbon black meet the discounted cash flow requirements. An analysis of the price of carbon black when the solar costs are set to 0 and the hydrogen is used to provide the thermal energy needs of the process indicates that the selling price for carbon black needs to be in the range of \$0.22/lb to \$0.33/lb (\$0.49/kg to \$0.73/kg). These results are consistent with the current prices for commercial carbon black.

The selling prices were determined as a function of heliostat costs because the cost of heliostats is uncertain due to a developing technology and market. The heliostat cost was varied from \$50/m² to \$1000/m². The hydrogen price varied from \$22/MBtu (\$0.075/kWhr or \$20.8/GJ) to \$48/MBtu (\$0.164/kWhr or \$45.6/GJ) while the carbon black price varied from \$0.44/lb (\$0.97/kg) to \$0.98/lb (\$2.16/kg). Variation of the prices with other process parameters showed that the prices did not vary dramatically with changes in plant size, hydrogen fraction recycled, reactor temperature and residence time. The prices did increase significantly when the thermal efficiency of the reactor was decreased. This is due to the need for a larger heliostat field as the reactor efficiency decreases.

A preliminary evaluation of the current carbon black commercial market was also performed to determine current market sizes for the various grades of carbon black products and their corresponding selling prices. About 90% of the carbon black that is produced worldwide is used for rubber reinforcement. About 10% is considered specialty grade carbon black and is used as additives in plastics, printing inks, paint, and paper. The current price for a higher grade of carbon blacks is about \$0.78/lb (\$1.72/kg). A solar-coupled hydrogen production plant, which produces 1,000,000 kg/yr of hydrogen, will produce about 2.4% of the current United States market for higher-grade carbon blacks. Since this market is increasing faster than other carbon black markets, demand for the additional production capacity should be easy to identify.

The encouraging experimental results and attractive economic analysis indicate that this process warrants further investigation. The sensitivity of the hydrogen selling price to reactor efficiency points out the need to focus on reactor design and performance in the next stages of the project.

Acknowledgement

The authors want to thank the DOE Hydrogen Program and The University of Colorado for financially supporting this work under Grants DE-FC36-99GO10454 and DE-PS36-99GO10383.

References

- Bromberg, L., D. Cohn, and A. Rabinovich. 1998. "Plasma Reforming of Methane," *Energy & Fuels*, 12, 11-18.
- Canadian Carbon Company. 2000. Personal Communication. Cancarb Limited, 1702 Brier Park Crescent NW, Medicine Hat, Alberta, Canada T1A 7G1 (www.CanCarb.com).
- Chemical Engineering*. 2000. McGraw-Hill Publishing Co. (New York).
- Chemical Marketing Reporter*. 2000.
- Chevron Chemical Company. 2000, Personal Communication, Houston, TX
- Donnet, J.B. 1976. Carbon Black, 16-18, Marcel Dekker, New York.
- Epstein, M., A. Yogev, I. Hodara, and A. Segal. 1996. "Results of a Feasibility Study on the Possible Use of The Solar Tower Technology at the Dead Sea Works," in *Solar Thermal Concentrating Technologies (Proceedings of the 8th International Symposium, October, 6-11, Koln, Germany (M. Becker and M. Bohmer, editors))*.
- Gaudermack, B. and S. Lynum. 1996. "Hydrogen Production from Natural Gas Without Release of CO₂ to the Atmosphere," *Proceedings of the 11th World Hydrogen Energy Conference*, 511-523, Coco Beach, Florida (June, 1996).
- Jenkins, D., R. Winston, J. O'Gallagher, C. Bingham, A. Lewandowski, R. Pitts, and K. Scholl. 1996. "Recent Testing of Secondary Concentrators at NREL's High-Flux Solar Furnace," *ASME J. of Solar Energy Engineering*, 29-33.
- Kirk-Othmer Encyclopedia of Chemical Technologies. 1991. 4th ed., 4, 1037-1072, John Wiley & Sons.
- Lee, K.W., W.R. Schofield, and D. Scott Lewis. 1984. "Mobile Reactor Destroys Toxic Wastes" *Chemical Engineering*, 46 – 47, April 2, 1984.
- Lewandowski, A. 1993. "Deposition of Diamond-Like Carbon Films and Other Materials Processes Using a Solar Furnace," *Mat. Tech.*, 8, 237-249.
- Lewandowski, A., C. Bingham, J. O'Gallagher, R. Winston, and D. Sagie. 1991. "Performance Characteristics of the SERI High-Flux Solar Furnace," *Solar Energy Materials*, 24, 550-563.
- Mann, M.K. 1995. "Technical and Economic Assessment of Producing Hydrogen by Reforming Syngas from the Battelle Indirectly Heated Biomass Gasifier," *NREL/TP-431-8143*, 10-13.
- Matovich, E. 1977. "High Temperature Chemical Reaction Processes Utilizing Fluid-Wall" *U.S. Patent 4056602* (Nov. 1, 1977).

- Mischler, D., R. Pitts, C. Fields, C. Bingham, M. Heben, and A. Lewandowski. 1997. "Solar Production of Fullerenes from a Powdered Graphite Source," *presented at the International Symposium on Solar Chemistry*, Villigen, Switzerland, October 6-7.
- Peters, M.S. and K.D. Timmerhaus. 1991. Plant Design & Economics for Chemical Engineers, 4th ed. McGraw-Hill, Inc. (New York).
- Pohleny, J.B. and N.H. Scott. 1962. "Method of Hydrogen Production by Catalytic Decomposition of a Gaseous Hydrogen Stream," Chemical Engineering, 69, 90-91.
- Pitts, J.R., E. Tracy, Y. Shinton, and C.L. Fields. 1993. "Application of Solar Energy to Surface Modification Processes," *Critical Reviews in Surface Chemistry*, 2 (4), 247.
- Roine, A. 1997. *Outokumpu HSC Chemistry for Windows Version 3.0*.
- Steinberg, M. 1986. "The Direct Use of Natural Gas for Conversion of Carbonaceous Raw Materials to Fuels and Chemical Feedstocks," *Int. J. Hydrogen Energy*, 11, 715-720.
- Steinberg, M. 1987. "A Low Cost High Energy Density Carbon Black Fuel Mix for Heat Energy Sources," 9, 161-171.
- Steinberg, M. 1994. "Fossil Fuel and Greenhouse Gas Mitigation Technologies," *Int. J. Hydrogen Energy*, 19, 659-665.
- Steinberg, M. 1995a. "The Carnol Process for CO₂ Mitigation from Power Plants and the Transportation Sector," *Brookhaven National Laboratory Report BNL 62835*, Upton, NY.
- Steinberg, M. 1995b. "The Hy-C Process (Thermal Decomposition of Natural Gas) Potentially the Lowest Cost source of Hydrogen with the Least CO₂ Emission," *Energy Convers. Mgmt.*, 36 (6-9), 791-796.
- Steinberg, M. 1998. "Production of Hydrogen and Methanol from Natural Gas with Reduced CO₂ Emission," *Int. J. Hydrogen Energy*, 23, 419-425.
- Steinberg, M. 1999. "Fossil Fuel Decarbonization Technology for Mitigating Global Warming," *Int. J. Hydrogen Energy*, 24, 771-777.
- Steinberg, M. and H.C. Cheng. 1989. "Modern and Prospective Technologies for Hydrogen Production from Fossil Fuels," *Int. J. Hydrogen Energy*, 14, 797-820.
- Turner, J.H., A.S. Viner, J.D. McKenna, R.E. Jenkins, and W.M. Vatauvuk. 1987a. "Sizing and Costing of Fabric Filters, Part 1: Sizing Considerations," *JAPCA*, 37 (6), 749-759.
- Turner, J.H., A.S. Viner, J.D. McKenna, R.E. Jenkins, and W.M. Vatauvuk. 1987b. "Sizing and Costing of Fabric Filters, Part 1: Costing Considerations," *JAPCA*, 37 (9), 1105-1112.
- Wang, J. 1993. Carbon Black (2nd ed.), Marcel Dekker.

T. M. Nenoff, Sandia National Labs, "Membranes for H₂ Separations...", FY00 Annual Report.

DEFECT-FREE THIN FILM MEMBRANES FOR H₂ SEPARATION AND ISOLATION

Tina M. Nenoff
Sandia National Laboratories
PO Box 5800, MS 0710
Albuquerque, NM 87185-0710

Abstract

Our long-term goal is to synthesize defect-free thin film membranes with crystalline inorganic molecular sieves (zeolites) for use in hydrogen production technologies. Current hydrogen separation membranes are based on Pd alloys or on chemically and mechanically unstable organic polymer membranes. The use of molecular sieves brings a stable inorganic matrix to the membrane. The crystalline frameworks have "tunable" pores that are capable of size exclusion separations. The frameworks are made of inorganic oxides (e.g., Zinc Oxide, Gallium Oxide, Alumino Silicates) and result in materials with thermal stability over 600°C. The pore sizes and shapes are defined crystallographically (<1Å deviation) which allows for size exclusion of very similarly sized molecules. In comparison, organic polymer membranes are successful based on diffusion separations, not size exclusion.

Introduction

This is a new project, begun in December 1999, and is focused on the research and development of crystalline, inorganic, molecular sieve (zeolite) thin film membranes for light gas molecule separations. In particular, we are interested in separating and isolating H₂ from CH₄, CO and N₂ gases. Current hydrogen separation membranes are based on Pd alloys or on chemically and mechanically unstable organic polymer membranes. The use of molecular sieves brings a stable (chemically and mechanically stable) inorganic matrix to the membrane. The crystalline frameworks have "tunable" pores that are capable of size exclusion separations. We envision impact of positive results from this program in the near term with Hydrocarbon fuels, and long term with Biomass fuels.

During this reporting period, we focused our research on to the synthesis of microporous phosphate-based phases, both as bulk and thin film materials. Within this

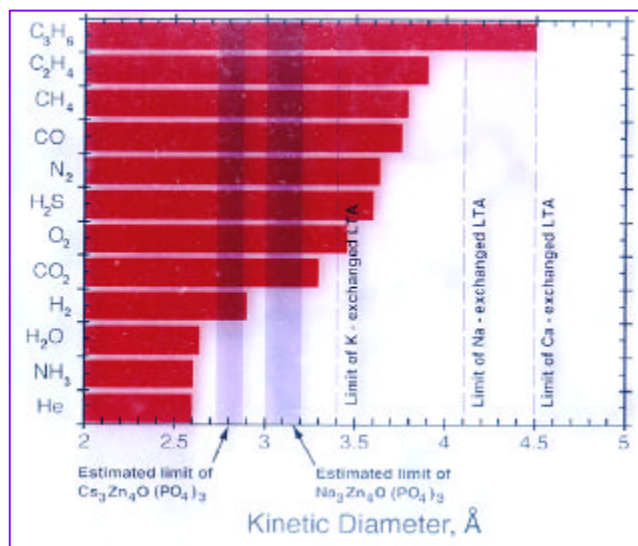
arena, we have begun to explore the gallium/phosphate phase space; five new phases have been synthesized. We have also updated our unique permeation unit to accommodate novel membrane disks for pure and mixed gas studies. Also, we have exciting new results and computational validation (collaboration with New Mexico State University) by molecular dynamics modeling, transition state theory and simulations of light gas molecules diffusing through commercially available molecular sieves and our novel materials.

Discussion

This year, we are building the proper equipment modifications to our *unique* permeation equipment for testing in this project. Furthermore, we are focusing on ZnPO phases that have internal porosity accessible to certain light gases and are easily synthesized as thin film membranes.

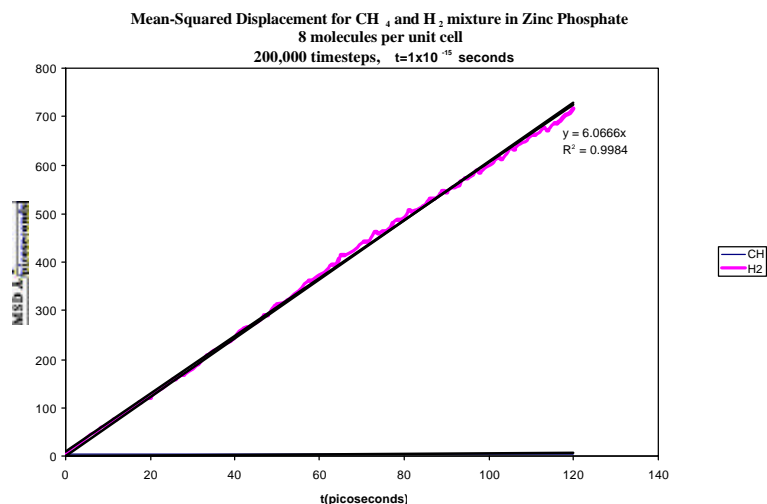
Known, commercially available zeolites that have pore sizes in the range of light gas molecules are Zeolite LTA. Changing the cation in the pores effectively changes the kinetic diameter of the opening of the pore. K/LTA has an effective pore diameter of 3.4Å. (See figure 1) However, to get into the range of H₂ separation and isolation, smaller pored zeolites are necessary.

Figure 1: Zeolite kinetic diameters versus molecule kinetic diameters (Å)



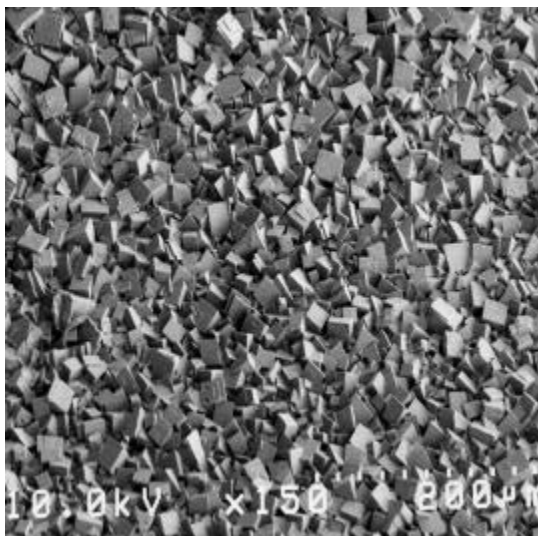
We have combined bulk and thin film synthesis with modeling and simulation to make small pored zeolite films specifically for H₂ separations. Na₃Zn₄O(PO₄)₃ and CsZn₂OPO₄ were synthesized, characterized and studied.¹ Through permeation modeling and simulations, we determined that Na₃Zn₄O(PO₄)₃ should accommodate H₂, but not CO₂; while CsZn₂OPO₄ should allow H₂, but still be impermeable to H₂O and NH₃. An example of the calculated output is in figure 2, which shows the mean-squared displacement vs. time for a mixture of four H₂ and four CH₄ per unit cell (this also mimics the pure gas studies). The hydrogen moves through the system but the methane is essentially stationary.²

Figure 2: Mean-Square displacement (movement) H₂ molecules through Zn/P cages (pink line overlaying black calculated slope) versus CH₄ molecules (horizontal black line).



We have been able to synthesize and characterize the cesium phase as a thin film membrane. (See figures 3 and 4) To date, we have been able to synthesize the sodium phase as a bulk crystalline powder, but not as a defect-free thin film..

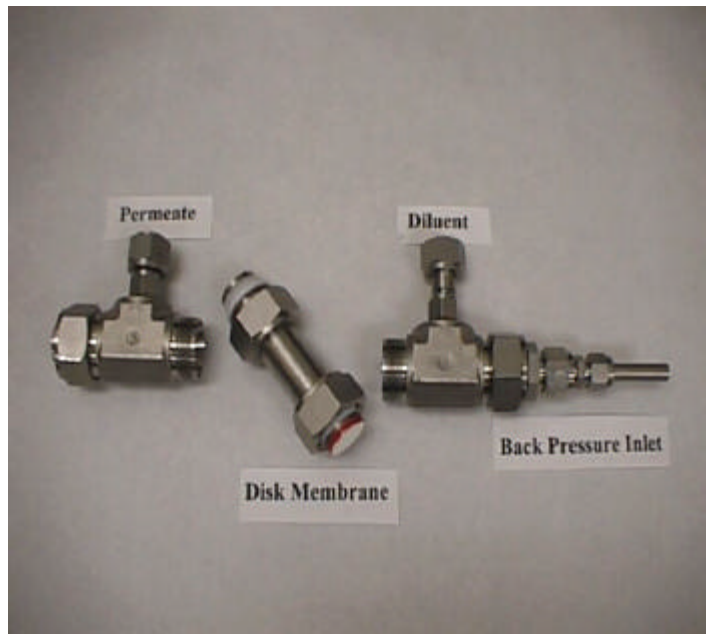
Figure 3: Scanning Electron Micrograph (SEM) of CsZn₂OPO₄



Permeation data has shown that at room temperature studies, single gas testing, there is good crystal coverage on the membranes. These films show significant permeabilities only to H₂ and He. *This is consistent with molecular sieving.* While the films can be made leak-free, they are still fairly thick (ca. 20 µm), and thus do not yield high gas flow rates yet. This is shown in the low flux ratios of H₂/SF₆ = 6.05 and H₂/N₂ = 5.42. Close inspection by SEM shows that a crystalline layer of zeolite has been

synthesized but that a densified layer is forming between the crystals and the substrate, inhibiting molecular sieving. We continue to work on the elimination of this problem.

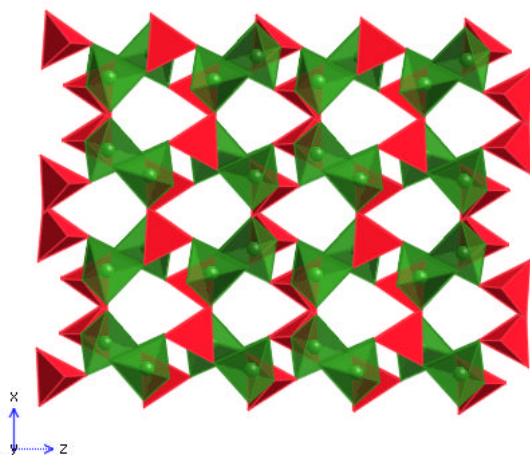
Figure 4: Thin Film Membrane sealed into permeation holder for testing



Because of initial successes, we are also focusing on the synthesis of bulk and thin films of novel microporous phases (such as gallophosphate based molecular sieves) and known aluminosilicate zeolites. We have been able to synthesize five new bulk crystalline phases with characterization studies underway. One of the phases is a microporous GaPO₄ phase, with pores of 3.9 x 3.2Å.^{3,4} Attempts are underway to synthesize this and the other phases as thin film membranes.

Preliminary economic calculations as to the importance of membranes in current industry were also performed this year. The first commercialization of a membrane gas separation was in 1979, and currently there are 10,000 commercial membrane systems in various gas separations applications. Industry experts (including Air Products) estimated in 1996 that the gas separation business was valued at \$85M in the US and was growing at a rate of approximately 8%/year. They estimated that by 2000, the membrane gas separation business would grow to about \$500M.⁵

Figure 5: Novel GaPO₄ phase



Conclusion

This new program (started in December 1999) is focused on the synthesis, modeling, validation and testing of defect-free thin film membranes for the separation and isolation of H₂ gas. These robust thin films are made of chemically and mechanically stable crystalline inorganic molecular sieves (zeolites). Successes from this program will have direct effects on national concerns such as hydrocarbon fuels and biomass energy. The membranes are molecular sieve/zeolite crystalline phases that are capable of molecular sieving small gas molecules, thereby allowing for H₂ purification.

This year we have accomplished our milestones. We have updated our unique permeation testing unit to fit thin film disk membranes. We have formed a collaboration with NMSU for modeling and simulation; initial studies indicate Zincphosphate crystalline phases capable of the sieving. We have synthesized one of the phases as a thin film membrane, tested for permeation and separations, and are making further improvements on the material. We have also expanded the synthesis research to gallium phosphate (Ga/P) phases; we have synthesized 5 new bulk phases, 2 of which contain microporous phases. Work continues on synthesizing the Ga/P as thin films.

Future Work

Future work plans for next year include the continuation of our work on synthesis, modeling and thin film growth of novel microporous phases for light gas separations, including novel gallophosphates and silicotitanate phases. Furthermore, we plan to explore the thin film growth of aluminosilicates zeolites doped with other elements for maximized adsorption and selectivity of H₂ over other light gases of interest. The permeation work will focus on the study of pure and mixed gas systems, both at room temperature and 80°C. Again we plan to tie this research with the modeling and

simulation efforts of this past year, with collaborators at New Mexico State University (Dr. Martha Mitchell, Dept. of Chemical Engineering, NMSU).

We will also begin to build interactions and collaborations with outside industries for potential future collaborations and commercialization partnerships.

References

1. Harrison, W. T. A, Broach, R. W., Bedard, R. A., Gier, T. E., Bu, X., Stucky, G. D., *Chem. Mater.*, **1996**, 8, 691.
2. M. Mitchell, J. Autry, T. M. Nenoff, "Molecular Dynamics Simulations of Binary Mixtures of Methane and Hydrogen in Zeolite A and a novel Zinc Phosphate", *Molecular Simulations*, 2000, in preparation.
3. F. Bonhomme, T. M. Nenoff, "A Novel Crystalline GaPO₄ phase", *J. Solid State Chem.*, 2000, submitted.
4. F. Bonhomme, T. M. Nenoff, "A new microporous phase, organic gallophosphate Phase", *Micro. & Mesoporous Mater.* 2000, in preparation.
5. P. S. Puri, Chemical Industry Digest, 4th Quarter, 1996.

Acknowledgement

This work was supported by the United States Department of Energy under contract DE-AC04-94AL85000. Sandia is a multi-program laboratory operated by Sandia Corporation, a Lockheed Martin Company, for the United States Department of Energy.

I would like to thank my co-workers who also participated in this program: Dr. Francois Bonhomme and Mr. Daniel Trudell of SNL, and Dr. Martha Mitchell (NMSU).



Separation Membrane Development

U. S. DOE Hydrogen Program Annual Review
May, 2000

L. Kit Heung

Savannah River Technology Center

for

Myung W. Lee (1937-1999)

Contributors: J. M. Duffey, W. A. Summers, T. Motyka

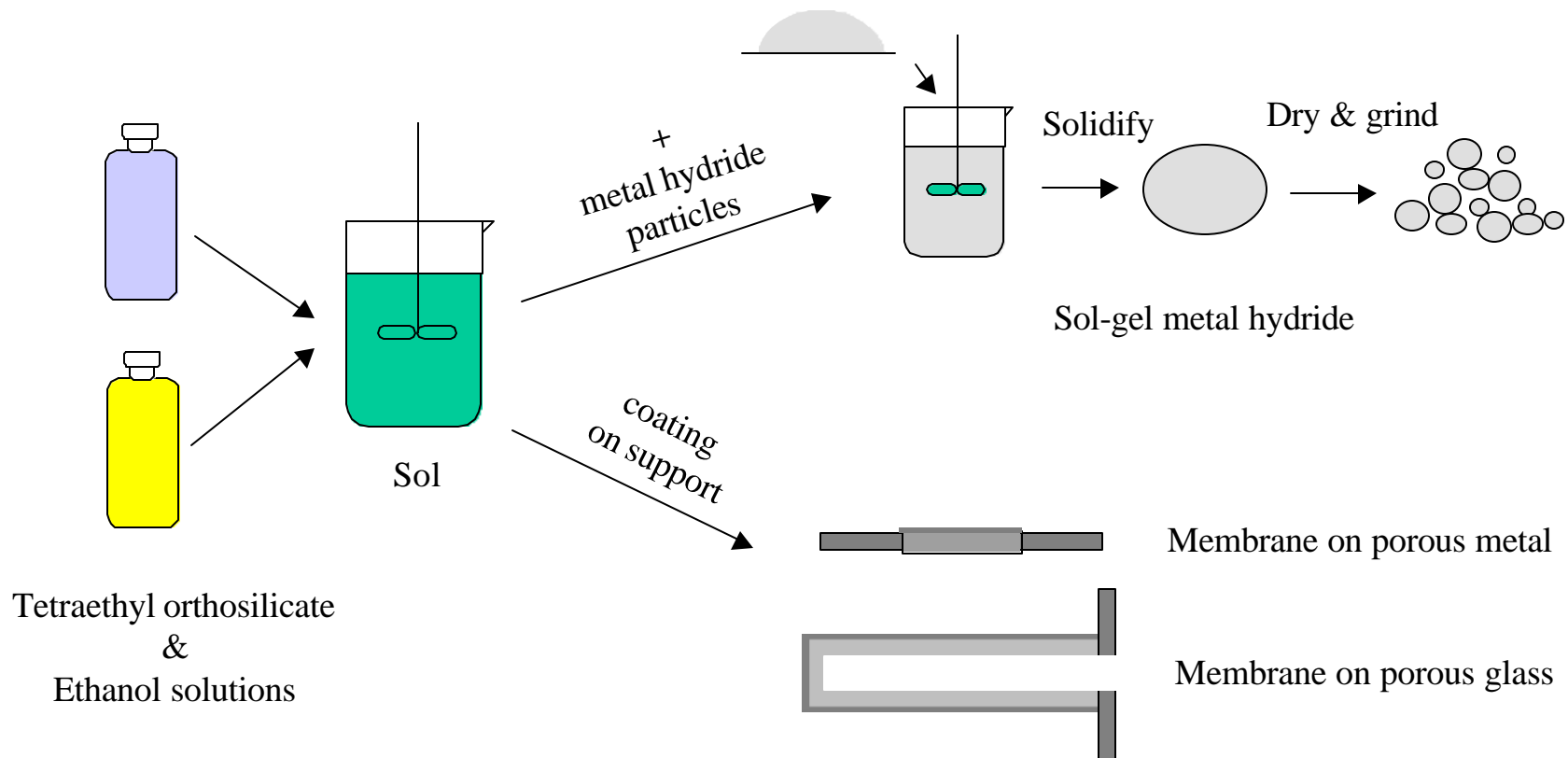
Long-Term Goals

- Develop efficient hydrogen separation process that will resist the adverse effects of reactive impurities (O₂, CO....)
- Demonstrate hydrogen absorption material based on sol-gel membrane encapsulated metal hydrides
- Investigate the feasibility of using sol-gel method to fabricate effective hydrogen separation membrane

Background

- New class of composite material has been developed using a sol-gel process
- Material found to selectively absorb H₂ from gas mixtures and to resist poison impurities
- Commercially attractive in hydrogen recovery and removal from industrial gas streams
- Potential applications include chemical, refinery, transportation and consumer products

Schematic of Sol-gel Metal Hydride & Sol-gel Membrane Process



FY-00 Objective and Rationale

- Extend the sol-gel encapsulation method to hydrides beyond LaNiAl (to develop process parameters that can encapsulate high hydrogen content metal hydrides)
- Produce defect-free membrane for permeation evaluation (to define rate and selectivity potentials)

FY-00 Tasks

- Fabricate silica based membrane using porous glass as support
- Fabricate silica based membrane using sintered porous metal as support
- Test membrane samples for hydrogen and nitrogen permeation properties
- Develop procedure for making silica encapsulated metal hydride with improved H₂ capacity.
- Test and compare hydrogen absorption property of encapsulated, improved metal hydride with LaNiAl.

FY-00 Progress

- Tested porous glass as the support for sol-gel coating
- Tested sintered porous stainless steel as support for sol-gel coating
- Produced silica encapsulated ZrCo samples
- Tested oxygen (air) exposure effect on encapsulated ZrCo, in comparison with that of encapsulated LaNiAl
- Patent and publication:
 - Patent issued: “Composition for absorbing hydrogen from gas mixtures”, U.S. patent 5965482
 - Paper published: “Silica embedded metal hydrides”, J. of Alloys and Compounds, 293-295 (1999) 446-451
 - Patent pending: “Container and method for absorbing and reducing hydrogen concentration”.

Sample of Sol-Gel Encapsulated Metal Hydride



Metal hydride as received



Metal hydride after H₂ abs.& des,



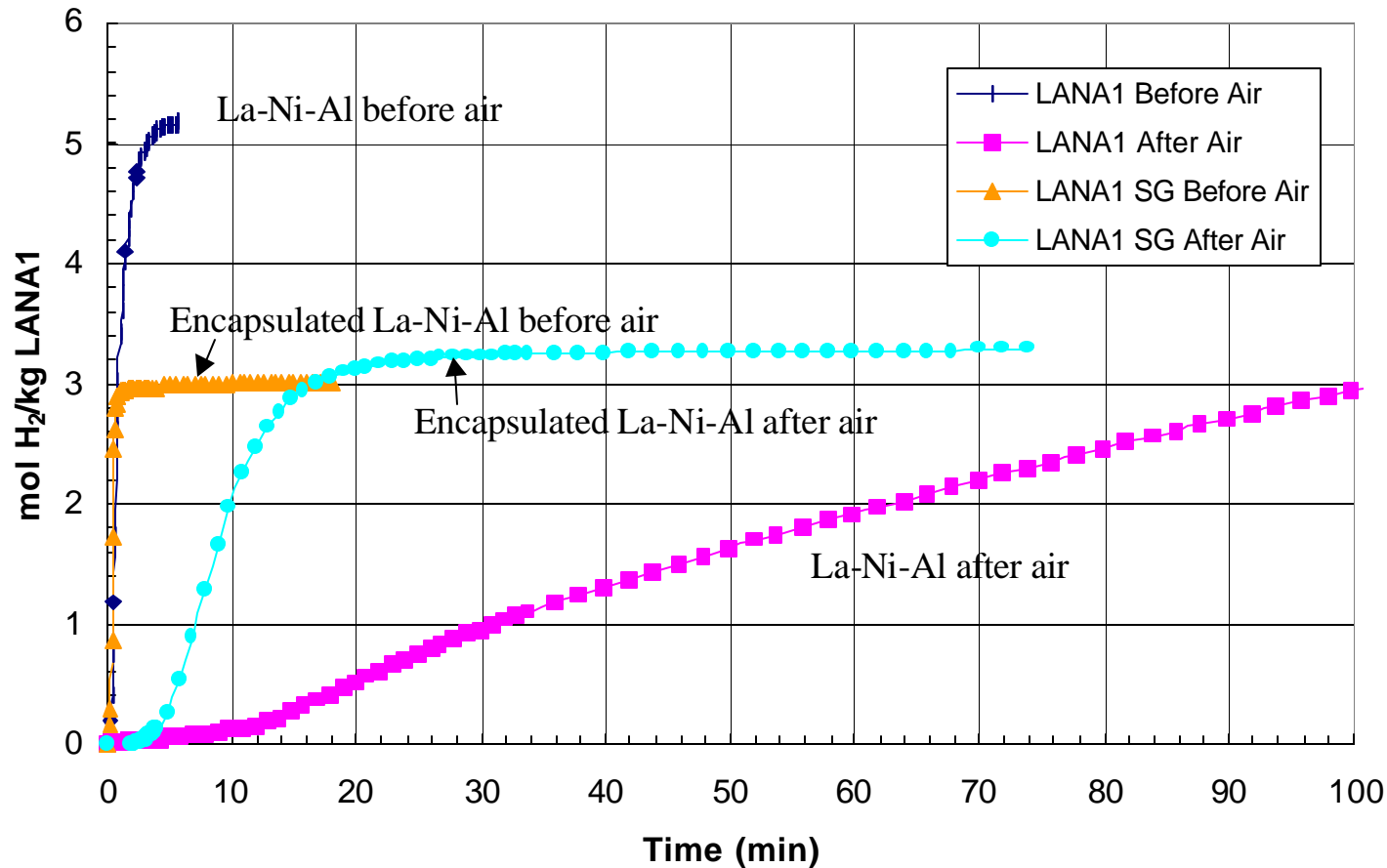
Sol-gel encapsulated Metal hydride
after H₂ abs. & des.

LKH 5/2000

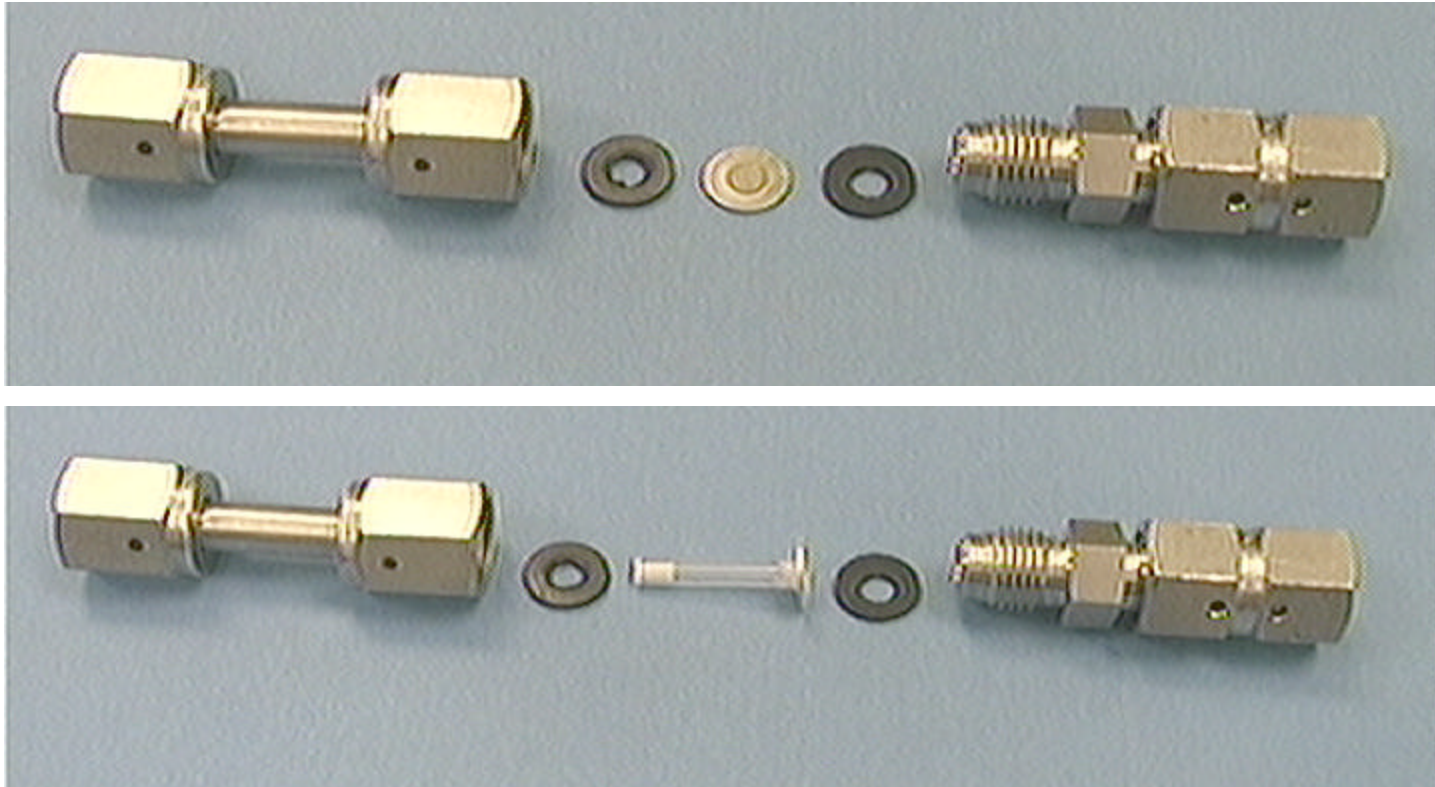
Encapsulated Metal Hydride Resists Poisons

| Feed gas | H ₂ absorption capacity (H/M) | |
|------------------------------|---|--------------------------|
| | Pure La-Ni-Al | Encapsulated La-Ni-Al |
| Pure H ₂ feed | 0.7 | 0.5 |
| 10 mol% CO in H ₂ | 0 | 0.5 |

H₂ Absorption Of Encapsulated Metal Hydride Before & After Air Exposure



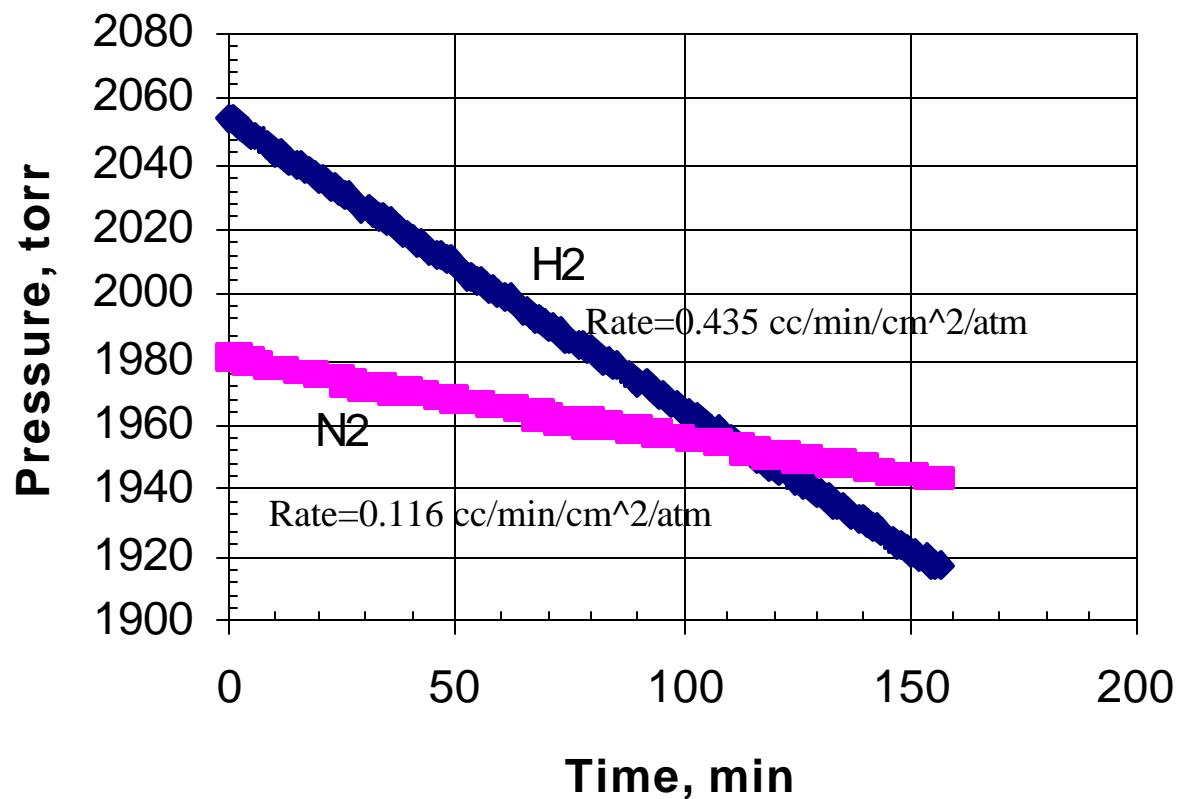
Permeation Test Apparatus



LKH 5/2000

Porous Glass Support Membrane Results

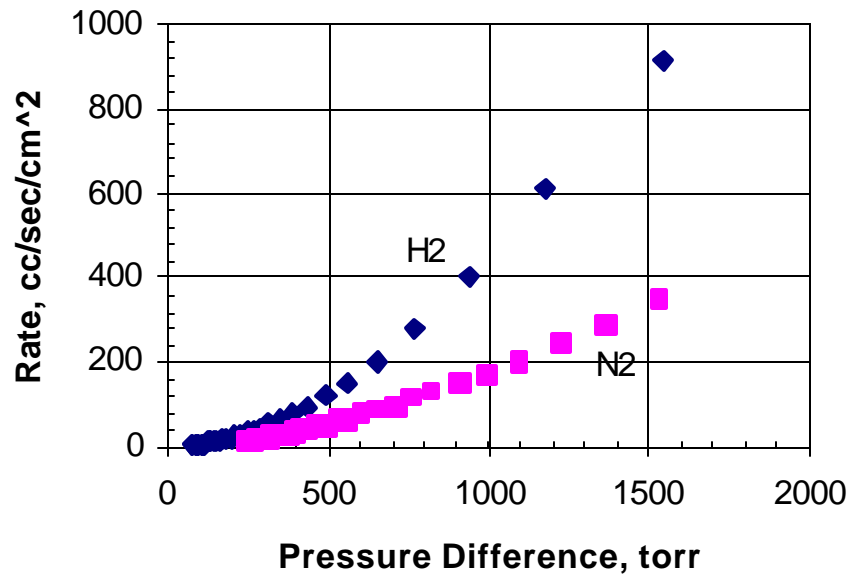
Porous Glass Blank



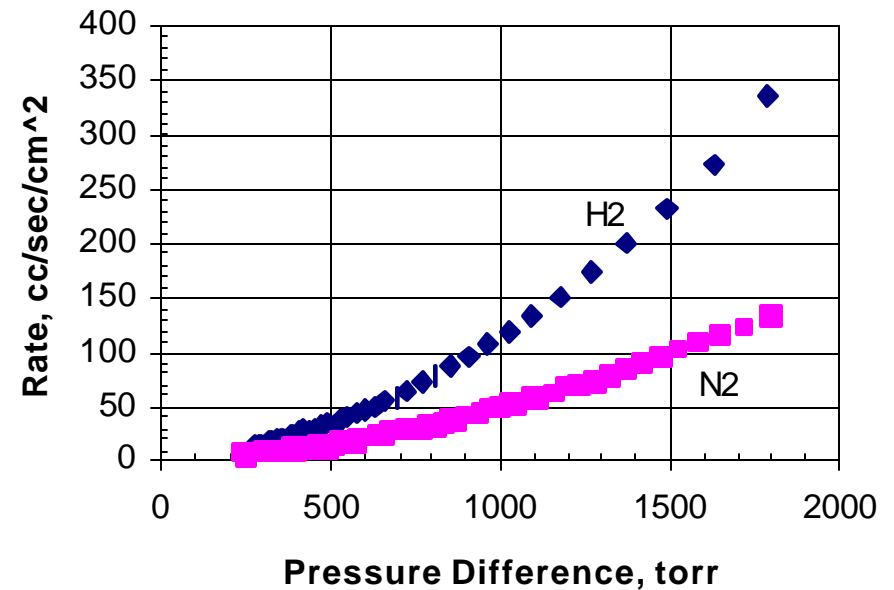
Selectivity H₂/N₂=3.747 vs 3.742 for Knudsen diffusion
Rate for 4 mil Pd/25Ag=18 cc/min/cm²/atm (Rubin 1966)

Porous Stainless Steel Support Membrane Results

Uncoated 2-micron filter



Coated 2-micron filter



Status of Economic and Systems Analysis



- **Completed a Market Study and Commercialization Assessment**
 - Study by Foresight Science and Technology (separately funded)
 - Identified market applications and entry strategies
 - Concluded there is very significant market potential

- **Contacts with Potential Users and Development Partners**
 - Previous CRADA with major oil company
 - Discussions and conceptual design for major chemical company
 - Discussions and conceptual design for automotive company

- **Target Market Applications**
 - Hydrogen Gettering (with encapsulated metal hydrides)
 - Opportunity for early niche market
 - Automotive batteries: Total market = \$3 Billion; Getter cost goal < \$5 per battery
 - Nuclear waste containers: High value application
 - Stationary Hydrogen Separation
 - Refineries, chemical plants, H2 refueling stations, gas processing for fuel cell plants
 - H2 recovery cost with SGMH = approx. \$0.75/lb, depending on gas conditions, waste heat cost, etc.
 - Onboard Fuel Processing Systems for FCVs
 - Gas purification in conjunction with POX
 - Goals for 50 kW system: 40 kg, 60 liters, \$500 per vehicle

Plan For FY-01

- Continue development of sol-gel encapsulated metal hydrides for hydrogen separation and hydrogen gettering applications
- Demonstrate hydrogen separation process in laboratory scale with encapsulated metal hydrides
- Close-out development of sol-gel membrane
- Continue to identify commercial applications in conjunction with industrial partners.

Objectives For FY-01

- Make hundred-gram quantity of sol-gel encapsulated LaNiAl and new hydrides with higher hydrogen capacity
- Design & construct life-cycle test apparatus
- Modify laboratory scale equipment to permit continuous hydrogen separation test
- Perform life-cycle test of encapsulated hydrides
- Test material resistance to CO & other impurities
- Test hydrogen separation performance in a continuous process under simulated industrial conditions.

INTEGRATED CERAMIC MEMBRANE SYSTEM FOR HYDROGEN PRODUCTION

Minish M. Shah and Raymond F. Drnevich
Praxair, Inc.
Tonawanda, NY 14150

U. Balachandran
Argonne National Laboratory
Argonne, IL 60439

Abstract

This paper describes a new technology development program launched by Praxair with Argonne National Laboratory (ANL) as a subcontractor. The proposed program will lead to commercialization of cost-effective and environmentally-friendly hydrogen production systems for use in the transportation sector for fuel-cell vehicle refueling stations and in the industrial sector as a small, on-site hydrogen supply. The proposed system will integrate ceramic membrane based syngas production and hydrogen separation technologies. The Phase 1 activities in the current year will focus on techno-economic feasibility evaluation and hydrogen separation membrane testing to validate the concept and define the critical development program for subsequent years.

Introduction

Hydrogen is expected to play a vital role in the transportation sector for fuel cell vehicles and in the distributed power generation market for stationary fuel cells. One of the crucial factors for successful introduction of fuel cell vehicles on US roadways is a low-cost supply of hydrogen for refueling. Steam methane reforming (SMR) is a process of choice for large-scale hydrogen

production. This process requires several processing steps including reforming, heat recovery/steam generation, shift conversion, further heat recovery and hydrogen purification. The cost of hydrogen from a plant producing 40 - 100 MMscfd H₂ is \$6 to \$8/MMBtu, of which fuel costs account for 52 - 68 % (Padro 1999). Due to costs of liquefaction, distribution and storage, the cost of liquid hydrogen at the refueling station is estimated to be in the range of \$16 to \$20/MMBtu (Thomas 1998). A small on-site plant can eliminate the costs associated with liquefaction and distribution. However, when a multi-step process like SMR is scaled down to 3000 scfh capacity, typically anticipated for vehicle fueling stations, capital related charges represent almost 90% of the total product cost which is ~\$75/MMBtu (Thomas 1998).

Praxair's vision to lower hydrogen cost is based on reducing the number of processing steps required to produce hydrogen. The reduction in number of pieces of equipment and resulting simplicity of plant layout would significantly reduce the capital cost. Praxair has defined and is in the process of obtaining patent coverage on the concept that involves integration of syngas generation, shift reaction and hydrogen separation into a single membrane-reactor separator. The key elements required to make this possible are an oxygen transport membrane (OTM) and a hydrogen transport membrane (HTM). Both of these membranes are based on ceramic mixed conducting materials and both operate at similar temperatures (800 - 1000 C). The OTM conducts oxygen ions and electrons and has infinite selectivity for oxygen over other gases. Similarly, the HTM conducts only protons and electrons and therefore infinitely selective for hydrogen.

Integrated-Membrane Reactor Concept

A schematic diagram of the integrated-membrane reactor separator is shown in Figure 1. The reactor is divided in three compartments by integrating both OTM and HTM into a single unit.

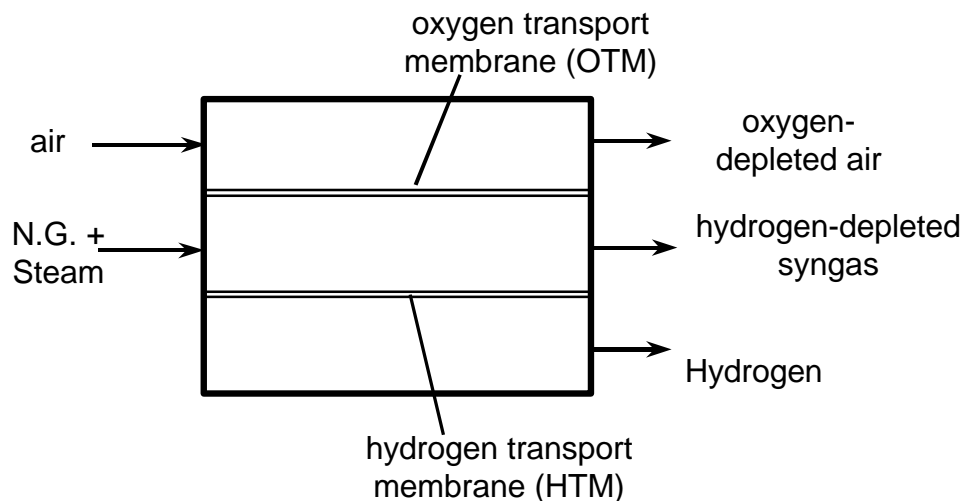
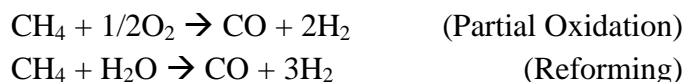


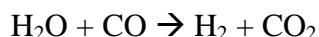
Figure 1. Integrated-Membrane Reactor Separator

Air at low pressure (~25 psia) is passed to the cathode side of the OTM and compressed natural gas (200 - 300 psia) and water/steam are passed to the anode side of OTM. Oxygen is transported

across OTM to the anode side, where it reacts with natural gas to form syngas. A portion of natural gas also reacts with steam to form syngas. Catalyst is incorporated in the reactor to promote reforming reaction.



The syngas side is also exposed to feed side of HTM. Hydrogen is transported through HTM to the permeate side driven by partial pressure difference. Due to removal of hydrogen from the reaction zone, more hydrogen is formed by the shift reaction:



As much hydrogen as possible is recovered from the reaction zone by its transport through HTM to the permeate side. Eventually, a pinch partial pressure difference between reaction zone and permeate side is reached and no more hydrogen can be recovered.

Technology Status

Praxair, Inc. is a member of the Oxygen Transport Membrane (OTM) Syngas Alliance, whose other members are BP Amoco, Sasol (South Africa) and Statoil (Norway). The alliance was formed in 1997 to develop a low-cost environmentally friendly technology for the manufacture of syngas. The OTM Syngas Alliance entered Phase II, the pilot demonstration phase, in 2000. The alliance completed Phase I of its program in December 1999. Phase I focused on ceramic membrane materials development, manufacturing technology and bench scale testing of syngas production reactions.

The HTM development is at much earlier stage compared to the OTM technology and significant development efforts will be required to take this technology to commercial scale. Argonne

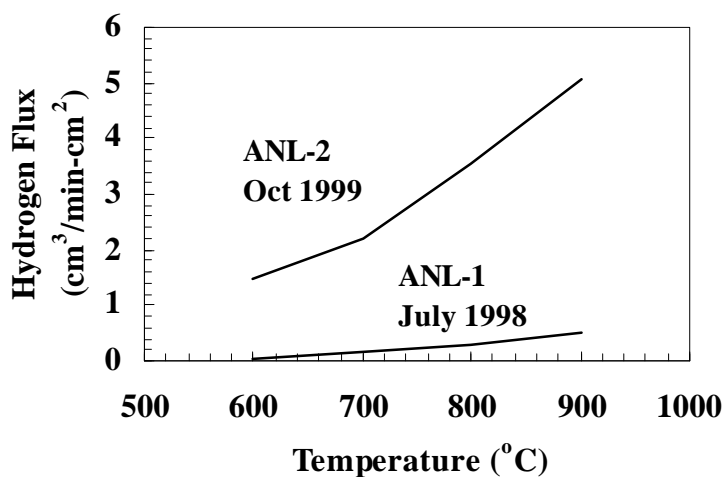


Figure 2. Progress in HTM Materials Development

National Laboratory (ANL) is developing materials for HTM. The proof-of-concept experiments at coupon-scale have demonstrated the feasibility of separating pure hydrogen from hydrogen containing gas mixtures. ANL has developed improved HTM materials with an order of magnitude higher hydrogen flux in last couple of years (Figure 2).

Program Overview

The long-term goal of the program is to commercialize a small-scale cost effective hydrogen production system with the hydrogen cost target of \$6-\$8/MMBtu. The program will be completed in three phases. Phase 1 spanning one year will focus on technical and economic feasibility studies to validate the concept and screen process schemes, performing experiments to obtain basic information for technoeconomic evaluation and defining a development program that will lead to commercialization. A multi-year Phase 2 program will focus on HTM material development and characterization, lab-scale testing of key components, marketing/business studies, economic analysis and development of a commercialization plan. In Phase 3, a pilot-scale unit will be built, a manufacturing process will be developed and detailed engineering design and cost estimation will be carried out.

Phase 1 Tasks

Technoeconomic feasibility analysis of the proposed concepts and critical experimental tests to support this activity will be the focus of Phase 1. Economic feasibility analysis will be used to compare product costs of the proposed concept with the competitive systems. Business model will be developed to perform profitability analysis.

Initial testing will study the effect of various operating parameters (hydrogen partial pressure, temperature, and membrane thickness) on flux. The data generated from the flux experiments and reaction kinetics for reforming and shift reaction will be used to design an integrated reactor separator.

Endurance and viability tests will be performed for the membrane in the presence of various components (CH₄, CO, CO₂, H₂O, N₂, sulfur compounds) expected to be present in the reactor. This test will identify any problem components for the membrane and will be useful to define future efforts on materials development. Flux studies in the presence of simulated reaction mixtures will also be performed. This study will test viability of membrane in the presence of actual mixtures and generate meaningful data for better reactor-separator design. This information will be recycled to revise the membrane-reactor separator design. Flux and cost targets necessary for both OTM and HTM will be identified to produce hydrogen at a cost of \$6-\$8/MMBtu.

Technical risks related to the membrane reactor will be evaluated. If OTM-HTM reactor is found to be a viable option then the rest of activities will focus only on this option. If technical risk analysis suggests that the difficulties with an integrated reactor are insurmountable then other alternative concepts will be explored. These options will also go through the same technical risk analysis.

A marketing study will identify potential opportunities for small hydrogen plants in the transportation sector, in the distributed power generation market and in the industrial sector. Assessment will also be made for competing options such as liquid hydrogen and electrolysis. The potential market share that the proposed technology could capture will be estimated based on its competitive position vs. other alternatives. The results of marketing study and the key financial parameters will form the basis for business analysis. Preliminary estimate of future development costs will be made. Financial analysis models will be used to determine viability of the proposed program. If a commercially viable hydrogen production system is unattainable, the program will be terminated.

Assuming that the business is viable and consistent with Praxair's business strategies, the project team (Praxair-ANL) will prepare a detailed plan and proposal for Phase 2 and provide an overview of Phase 3 activities.

Future Plans

Phase 2 efforts will ultimately lead to bench-scale testing units of key subsystems such as HTM separator, and integrated HTM-shift conversion reactor. Praxair's experience in development of OTM syngas reactor will be very useful in expediting the development work for this program. Some of the technical goals for the HTM will be to achieve specific flux targets and desirable operating characteristic with respect to tolerance for various components. Bench scale testing unit will be useful in generating flux data under actual operating conditions. If the performance targets for membrane matches Praxair's expectation and if business profitability analysis is still favorable then we will proceed to Phase 3.

The primary goal of Phase 3 will be to build a pilot-scale unit. This will be useful to generate key technical data necessary for engineering design and economic analysis for a commercial unit. It is anticipated that present development of cost-effective manufacturing of OTM elements will be also applicable to HTM elements.

Acknowledgement

The authors would like to acknowledge DOE's support for this program.

References

Padro, C.E.G. and Putsche, V. September 1999. *Survey of the Economics of Hydrogen Technologies*, Technical Report NREL/TP-570-27079. National Renewable Energy Laboratory.

Thomas, C. E., Kuhn, I. F. Jr., James, B. D., Lomax, F. D. Jr. and Baum G. N. 1998. "Affordable Hydrogen Supply Pathways for Fuel Cell Vehicles." *Int. J. of Hydrogen Energy*, 23(6):507-516.

List of Figures

Figure 1. Integrated-Membrane Reactor Separator

Figure 2. Progress in HTM Materials Development

HYDROGEN PRODUCTION BY SUPERADIABATIC COMBUSTION OF HYDROGEN SULFIDE

Rachid B. Slimane, Francis S. Lau, and Javad Abbasian
Gas Technology Institute (GTI)
1700 S. Mt. Prospect Rd
Des Plaines, IL 60018

Abstract

In a two-phase program, the Gas Technology Institute (GTI), UOP and BP Amoco in an advisory role, and the University of Illinois at Chicago (UIC) are developing a process for the thermal decomposition of H_2S in H_2S -rich waste streams to high-purity hydrogen and elemental sulfur. The novel feature of this process is the superadiabatic combustion (SAC) of part of the H_2S in the waste stream to provide the thermal energy required for the decomposition reaction. The SAC process being developed will offer a more economical alternative to conventional technology (i.e., Claus Process) which, although it recovers elemental sulfur, wastes the more valuable hydrogen component as water.

In Phase 1, a one-dimensional numerical model has been developed for rich and ultra-rich filtration combustion of H_2S /air mixtures over a range of equivalence ratios, flow rates, and other packed bed parameters. Particular consideration is given to the optimization of hydrogen production via ultra-rich superadiabatic combustion of hydrogen sulfide. Model predictions have offered valuable guidelines for the preparation of a design and cost estimate of a suitable bench-scale reactor testing system to be assembled and tested in Phase 2 of the program. Modeling efforts also made possible the identification of key SAC process parameters and the preparation of a detailed parametric testing plan for Phase 2. The chemical kinetic mechanisms used in the formulation of this preliminary model will be updated based on direct comparison with the experimental data that will be obtained in Phase 2, further enhancing the reliability of the model.

Introduction

Hydrogen sulfide (H₂S) is present in the industrial world chiefly as an undesirable byproduct of fossil fuel processing, including natural gas, petroleum, and coal. These produce unwanted combustion products and so must be removed either from the fuel or from the combustion products. In natural gas, H₂S is the primary sulfur component, along with lower levels of hydrocarbon sulfides (mercaptans). In petroleum, H₂S appears at various stages in the refining process, and it must be removed to facilitate the production of low-sulfur liquid fuels. H₂S also appears in coal gasification and is generally removed prior to fuel gas utilization.

The conventional technologies in use to decompose H₂S (Claus, Superclaus, and variations thereof) produce elemental sulfur as a byproduct, which sells for about \$30/ton. The hydrogen present in the original H₂S leaves the process as water. At the same time, hydrogen is in demand at petroleum refineries and other facilities such as ammonia synthesis plants. The value of hydrogen in these applications exceeds its fuel value, and so it may be worthwhile to recover the hydrogen as H₂ from the H₂S, if an economical and reliable process can be found to do so.

In this project, GTI, UOP and BP Amoco in an advisory role, and the University of Illinois at Chicago (UIC) are developing a process for the thermal decomposition of H₂S in H₂S-rich waste streams to high-purity hydrogen and elemental sulfur. The original conceptual layout of the SAC process is shown in Figure 1. The novel feature of this process is the superadiabatic combustion (SAC) of part of the H₂S in the waste stream to provide the thermal energy required for the decomposition reaction, as indicated by the following two reactions:



Each molecule of H₂S reacting with oxygen can provide enough energy to dissociate up to 10 additional molecules of H₂S. While this chemistry offers an attractive way to decompose H₂S, it cannot be done using conventional burners because the adiabatic temperature is not sufficient to support the reaction kinetics. However, the SAC reactor can support this reaction because the temperature obtained at rich conditions is much higher with SAC than with conventional combustion.

Superadiabatic combustion (SAC), also known as filtration combustion, consists of combustion of a fuel gas-oxidant mixture in a porous ceramic medium with a high thermal capacity.¹ The intense heat exchange between burning gas mixture and the porous medium permits the accumulation of combustion energy in the solid matrix. As a result, the flame temperatures developed can be much higher than the adiabatic temperature for the mixture in free air. Using an H₂S-rich stream as both the fuel and hydrogen source, the high SAC flame temperature promotes rapid thermal decomposition of most of the H₂S to hydrogen and elemental sulfur.

Successful development of SAC technology for acid gas treatment in refining, natural gas sweetening, and IGCC power generation applications can result in the recovery of significant quantities of hydrogen from acid gas waste streams that would otherwise be lost as water vapor in conventional sulfur recovery processes. Recovery of hydrogen as a byproduct of sulfur

recovery offers the potential for hydrogen production at very low or even negative cost, with no additional carbon dioxide emissions to the environment. Further benefits include the elimination of sulfur recovery catalyst and chemical costs, and the cost and environmental liability of spent catalyst and chemical disposal.

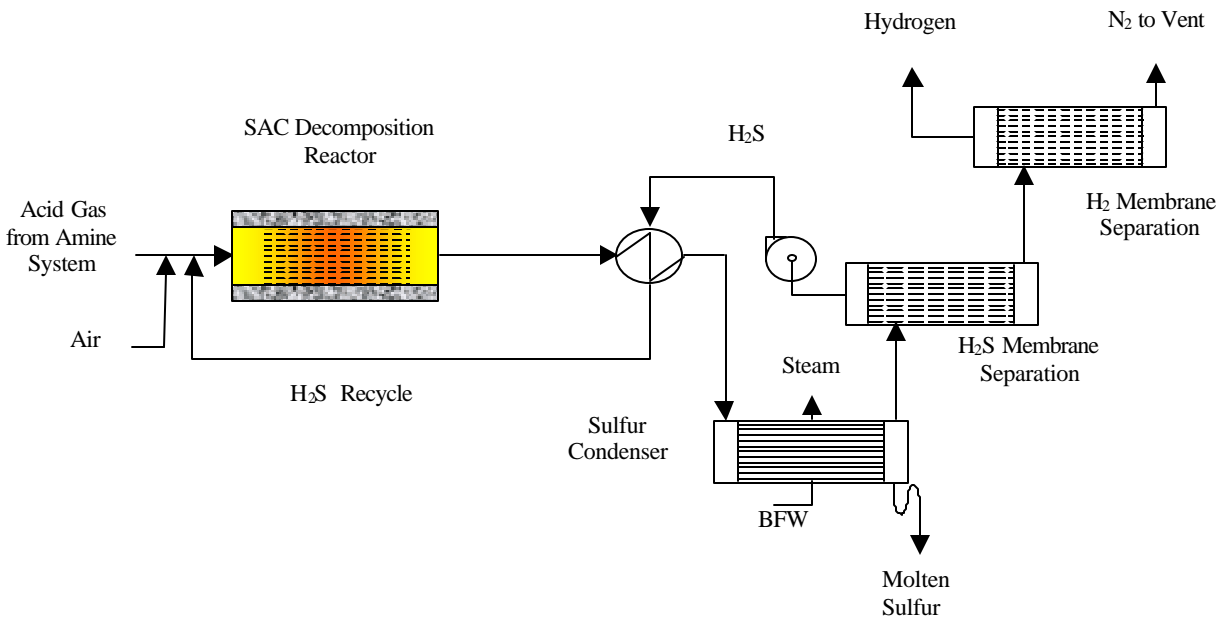


Figure 1. Conceptual Process Design for SAC-Based H₂S Decomposition/Hydrogen Recovery System

This research program is divided into two phases. In Phase 1, a one-dimensional numerical model has been developed for rich and ultra-rich filtration combustion of H₂S/air mixtures over a range of equivalence ratios, flow rates, and other packed bed parameters. Particular consideration is given to the optimization of hydrogen production via ultra-rich superadiabatic combustion of hydrogen sulfide. Model predictions have offered valuable guidelines for the preparation of a design and cost estimate of a suitable bench-scale reactor testing system to be assembled and tested in Phase 2 of the program. Modeling efforts also made possible the identification of key SAC process parameters and the preparation of a detailed parametric testing plan for Phase 2. The chemical kinetic mechanisms used in the formulation of this preliminary model will be updated based on direct comparison with the experimental data that will be obtained in Phase 2, further enhancing the reliability of the model.

Reactor Modeling

In this work filtration combustion waves in hydrogen sulfide (H₂S)/air mixtures are modeled within the one-dimensional approach, taking into account multi-step chemistry and separate energy equations for the gas and solid phases. The superadiabatic wave propagation is a complex phenomenon, and many factors that influence wave properties, in particular the heat loss rate and the interfacial heat exchange or effective heat conductivity of the porous medium, must be accurately specified. A numerical model was developed to describe combustion wave

characteristics in a coordinate system moving together with the wave front. Two chemical kinetic mechanisms have been used. The first mechanism was developed by Frenklach's group² and is applicable under combustion conditions (i.e., moderately high equivalence ratios); the second kinetic mechanism has been developed at UIC to describe more accurately the partial oxidation of H₂S (i.e., ultra-high equivalence ratios).³ The products of partial H₂S oxidation, hydrogen (H₂) and elemental sulfur (S₂), are dominant for ultra-rich superadiabatic combustion, which is essentially a fuel reforming reaction. The chemistry in the combustion wave is modeled and species and temperature profiles are predicted.

Preliminary numerical modeling of the SAC reactor has been performed. The parameters considered in the modeling effort included fuel gas composition (i.e., H₂S-rich and H₂S-lean), oxidant composition (air/enriched air), equivalence ratio, superficial gas velocity, feed gas temperature (pre-heating effect), and product gas quenching. The major conclusions from the modeling predictions obtained are:

In oxygen-enriched air (i.e., 30% O₂-N₂ gas mixture), conversions of H₂S to hydrogen and elemental sulfur are better than when pure oxygen is used as the oxidant.

Product gas quenching can substantially increase the selectivity of H₂S conversion to H₂; however, the selectivity of H₂S conversion to elemental sulfur decreases. For example, at typical filtration velocities ranging from 20 to 30 cm/s, equivalence ratios of about 2-3, and oxygen-enriched air containing about 20-40% O₂, H₂S conversion to hydrogen is about 20% and H₂S conversion to elemental sulfur is about 60%. With quenching of product gas, H₂S conversion to hydrogen and elemental sulfur is about 35% and 25%, respectively.

Water addition to the initial mixture does not improve the reactor performance with respect to hydrogen and elemental sulfur production.

When air is used as the oxidant, conversion of H₂S to H₂ decreases as filtration velocity increases. In contrast, when pure oxygen is used as the oxidant, increasing the filtration velocity plays a positive role.

SAC reactor performance can be significantly improved by separating and recirculating unreacted H₂S in the product gas.

Based on the developed numerical model, optimization studies of hydrogen production were conducted by varying the characteristics of the ultra-rich superadiabatic waves. The major findings appear to indicate that by optimizing the porous body reactor configuration, equivalence ratio, and filtration velocity, the overall H₂S decomposition in a single pass can be as high as 30-50%, with a conversion of H₂S to the desirable product hydrogen (H₂) reaching a level of 30%. This reactor performance can be obtained using equivalence ratios in the range of 10 to 15, while maintaining a filtration velocity greater than 100 cm/s. For these high values of equivalence ratio and filtration velocity, the combustion temperature is considerably higher than the adiabatic temperature, which is in fact too low for combustion to take place in the gas phase. Such high temperature promotes the decomposition of H₂S, the hydrogen (H₂)/water (H₂O) selectivity, and the elemental sulfur (S₂)/sulfur dioxide (SO₂) selectivity. Given that in a single pass the H₂S

decomposition can reach 30-50%, the overall process performance can be substantially improved, with respect to hydrogen production, by membrane separation of product gases and recirculation of unreacted H_2S . It can be shown that in 4 to 5 passes nearly total hydrogen sulfide decomposition into sulfur can be realized, with recovery of 30-40% of the hydrogen component.

The most optimum scenario in the results of the computer modeling to-date indicate that, with feed gases entering the reactor at ambient temperature, a maximum temperature of 1631 K (1394°C or 2541°F) can be achieved in the SAC reactor, resulting in an overall H_2S conversion of 50%, with a hydrogen (H_2)/water (H_2O) selectivity of 57/43 and an elemental sulfur (S_2)/sulfur dioxide (SO_2) selectivity of 99/1.

These predictions have offered valuable guidelines for the preparation of a design and cost estimate of a suitable bench-scale reactor testing system to be assembled and tested in Phase 2 of the program. Modeling efforts also made possible the identification of key SAC process parameters and the preparation of a parametric testing plan for Phase 2. The chemical kinetic mechanisms used in the formulation of this preliminary model will be updated based on direct comparison with the experimental data that will be obtained in Phase 2, further enhancing the reliability of the model.

Lab-Scale Testing System Design

To develop the necessary experimental data to demonstrate the technical and economical viability of the SAC reactor unit, a bench-scale testing system has been designed for H_2 production from thermal decomposition of up to 1,400 standard cubic feet per hour (SCFH) of H_2S -oxidant gas mixture. Schematic diagrams of the P&ID for this system are shown in Figure 2. In the proposed testing system, predetermined amounts of feed gas components are mixed and delivered to a packed-bed reactor where H_2S is converted to H_2 and S at high temperatures. Hot off-gas leaving the reactor is cooled with a cooling medium in a condenser where sulfur vapor ($\text{S}(\text{g})$) is condensed and collected. Cooled gas is then scrubbed with a caustic solution where H_2S and sulfur dioxide (SO_2) are removed and the cleaned gas is discharged to the atmosphere.

The bench-scale SAC reactor system consists of a fuel gas/oxidant conditioning system to generate appropriate inlet gas mixtures, a packed-bed reactor, a sulfur condenser and recovery subsystem, an exit gas scrubbing subsystem, and equipment for sampling and analysis of H_2S decomposition products. The major equipment for the proposed lab-scale testing system includes: a gas mixing chamber, a reactor, a thermal fluid cooler, a thermal fluid pump, a sulfur condenser, a gas scrubber, a caustic tank, a recirculating caustic pump, and a makeup caustic pump. The information required for design, engineering, procurement and installation of this system including the system description, equipment design, and equipment specifications has been prepared in a design package.

Important features of the designed bench-scale SAC reactor system include:

A reactor diameter of 6 inches (15 cm) is used so that the data generated from the bench-scale testing can be used for future scale-up design.

A minimum gas residence time of 2 seconds in the packed-bed of the reactor (based on the maximum superficial gas velocity) is used to ensure complete conversion of the H₂S decomposition reaction.

The designed reactor is capable of processing up to 1,400 SCFH of total feed gas mixture containing H₂S and oxidant.

The estimated pressure drop across the packed-bed at maximum gas throughput ranges from 0.7 to 1.6 psi at average gas temperatures ranging from 1000 to 2500°F (538 to 1371°C).

The reactor consists of a vertical, cylindrical carbon steel shell (21-inch ID x 21.5-inch OD x 72-inch H) lined with 6-inch thick rigid fibrous ceramic insulation. An impervious ceramic tube (6-inch ID x 7-inch OD x 72-inch H) containing 99+% alumina is used as the inner reactor tube to contain the inert pellets and reactor gases.

A 30 kW 3-zone, silicon carbide or molybdenum disilicide electric heater is located in the space between the ceramic tube and the insulation to provide auxiliary heat for cold startup and temperature control.

Support and hold-down plates are used to support and contain the inert pellets and ceramic insulation.

High-temperature gaskets are used in the ceramic-metal joints and the flanged connections to prevent any leakage of reactor gases.

During Phase 2 of this program, GTI, UIC, and industry advisors UOP and BP Amoco will construct the bench-scale unit and conduct parametric testing to validate the SAC concept. The computer model developed in Phase 1 will be updated with the experimental data and used in future scale-up efforts. The process design will be refined and the cost estimate updated. Market survey and assessment will continue so that a commercial demonstration project can be identified.

References

1. Kennedy, L. A., Fridman, A. A., and Saveliev, A.V., "Superadiabatic Combustion in Porous Media: Wave Propagation, Instabilities, New Type of Chemical Reactor", *Fluid Mechanics Research* 22:2, 1-25 (1995).
2. Kennedy, L.A., Bingue, J.P., Drayton, M.K., Saveliev, A.V. submitted to *The 27th Symposium (International) on Combustion*, The Combustion Institute, Pittsburgh, 1998.
3. Frenklach, M., Wang, H., Yu, C.-L., Goldenberg, M., Bowman, C.T., Hanson, R.K., Davidson, D.F., Chang, E.J., Smith, G.P., Golden, D.M., Gardiner, W.C., and Lissianski, V., http://www.me.berkeley.edu/gri_mech/; and Gas Research Institute Topical Report: Frenklach, M., Wang, H., Goldenberg, M., Smith, G.P., Golden, D.M., Bowman, C.T., Hanson, R.K., Gardiner, W.C., and Lissianski, V., "GRI-Mech---An Optimized Detailed Chemical Reaction Mechanism for Methane Combustion", Report No. GRI-95/0058, November 1, 1995.

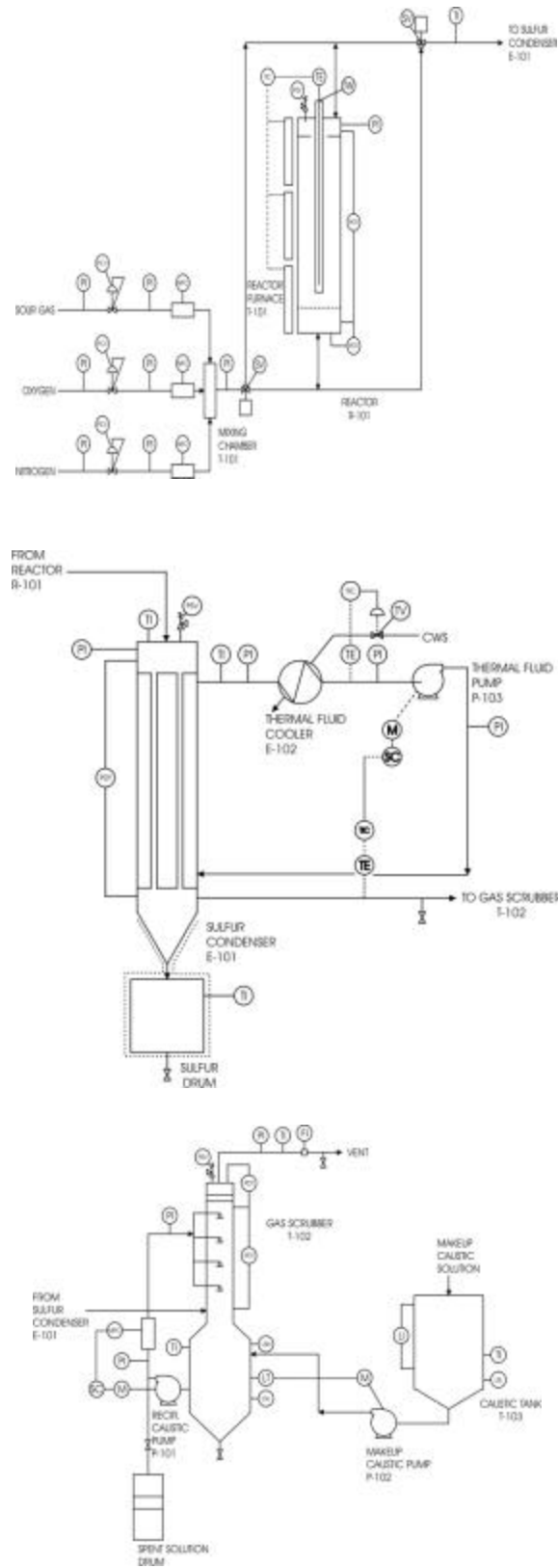


Figure 2. P&ID for the Bench-Scale SAC Reactor Testing System

THERMOCATALYTIC CO₂-FREE PRODUCTION OF HYDROGEN FROM HYDROCARBON FUELS

Nazim Muradov
Florida Solar Energy Center,
1679 Clearlake Road, Cocoa, FL 32922

Abstract

Conventional processes of hydrogen production are among major producers of CO₂ emissions. It has been proposed recently that CO₂ produced in steam reforming (or partial oxidation) processes could be captured and sequestered under the ocean or underground. However CO₂ sequestration is an energy intensive and costly process associated with ecological uncertainties. CO₂-free production of hydrogen via thermocatalytic decomposition of hydrocarbon fuels as a viable alternative to the conventional processes is discussed in this paper. The technical approach is based on a single-step decomposition (pyrolysis) of hydrocarbons over carbon catalysts in air/water free environment. This approach eliminates the need for water-gas shift reactor, CO₂ removal, and the catalyst regeneration, which significantly simplifies the process. Clean carbon is also produced as a valuable byproduct of the process. Over 30 different samples of carbon were screened for the catalytic activity in methane decomposition reaction and several of them were selected for the further evaluation. The factors affecting carbon catalyst activity and long term stability in hydrocarbon decomposition reactions were studied. It was found that the crystallographic structure and the surface area of carbon species mostly determine the catalytic activity of carbon catalysts. Carbon species produced in the process were characterized by XRD and SEM methods. A kinetic model of methane decomposition over carbon catalysts was developed, and major kinetic parameters of methane decomposition reaction (rate constants, activation energies, etc.) over selected catalysts were determined. Various conceptual designs for the hydrocarbon decomposition reactor, including packed bed, tubular, free volume, fluid wall and fluidized bed reactors, were evaluated. A bench-scale thermocatalytic fluidized bed reactor was designed, fabricated and tested. The reactor was tested using methane, propane, methane-

propane mixture, and gasoline, and CO/CO₂-free production of hydrogen-rich gas and carbon was demonstrated. Preliminary techno-economic assessment of the process indicated that the hydrogen could be produced at a cost of \$5.0/MMBTU (if carbon sold at \$100/t), which is less than that for steam reforming process coupled with CO₂ sequestration. Comparative assessment of CO₂ emissions from different hydrogen production processes clearly demonstrated the significant ecological advantages of the thermocatalytic decomposition of natural gas.

Background

Given the advantages inherent in fossil fuels, such as their availability, cost-competitiveness, convenience of storage and transportation, they are likely to play a major role in global energy supply for the 21st century. On the other hand, fossil fuels are major source of anthropogenic CO₂ emissions into the atmosphere. There are several possible ways to mitigate CO₂ emission problem. Among them are traditional (e.g. more efficient use of fossil fuel energy resources, increase the use of non-fossil fuels, etc.) as well as novel approaches which include:

- hydrogen production by conventional processes (steam reforming, partial oxidation, etc.) coupled with CO₂ sequestration
- hydrogen production via decomposition (pyrolysis) of hydrocarbons with co-production of carbon

Steam reforming (SR) of natural gas (NG) is the most efficient and widely used process for the production of hydrogen. The theoretical energy requirement per mole of hydrogen produced for the overall process is equal to 40.75 kJ/mole H₂. There is no by-product credit for the process and, in the final analysis, it does not look environmentally benign due to large CO₂ emissions. The total CO₂ emissions (including stack gases) from SR process reach up to 0.3-0.4 m³ CO₂ per each m³ of hydrogen produced. In partial oxidation (PO) and autothermal reforming (AR) processes a fuel, oxygen and steam are combined in proportions such that a fuel is converted into a mixture of H₂ and CO. PO process can be carried out catalytically or non-catalytically. The maximum theoretical concentration of hydrogen in the effluent gas using pure oxygen is 66.7 v.%, however, the concentration drops to 40.9 v.% if air is used as an oxidizer. Amount of CO₂ produced by PO process depends on the composition of the feedstock used and could reach up to 0.5 m³ CO₂ per each m³ of hydrogen produced.

CO₂ Sequestration

The perspectives of CO₂ capture and sequestration is actively discussed in the literature (Nakicenovic 1993, Block et al. 1997, Audus et al. 1996). The commercially available processes for CO₂ capture include: physical and chemical absorption, physical and chemical adsorption, low temperature distillation and gas-separation membranes. It should be noted that the capture, transportation and sequestration of CO₂ are energy intensive processes. The total electric energy consumption to capture CO₂ from both concentrated and diluted (stack) gases, pressurize, transport 100-500 km and inject it to the underground disposal site was estimated at approximately 5000 kJ/kg CO₂ (Muradov 2000). World average for CO₂ emission associated with the electricity production is 0.153 kg of CO₂ per each kWh produced (Block et al. 1997). In

consequence, the total CO₂ emissions from CO₂ sequestration could potentially reach 0.25 kg CO₂ per kg of sequestered CO₂.

There have been some estimates reported in the literature on the economics of CO₂ sequestration associated with hydrogen production from fossil fuels. Thus, according to Audus et al. (1996), the capture and disposal of CO₂ (80-85% of CO₂ captured from the concentrated streams of SR process) add about 25-30% to the cost of hydrogen produced by the SR of NG. The capture and disposal of CO₂ from diluted stack gases is even more costly. For example, it was estimated that the cost of eliminating CO₂ emissions from stack gases of advanced power generation plants range from \$35 to 264 per ton of CO₂ (IEA 1998). Thus, CO₂ sequestration is an energy intensive and expensive process and, in the final analysis, does not completely eliminate CO₂ emission. In addition to this problem, some uncertainties remain regarding the duration and extent of CO₂ retention (underground or under the ocean) and its possible environmental effect.

Methane Decomposition

One alternative to the conventional hydrogen production processes is decomposition of hydrocarbon fuels (e.g. NG) into hydrogen and carbon, e.g.



Methane decomposition reaction is moderately endothermic process. The energy requirement per mole of hydrogen produced (8.9 kcal/mole H₂) is somewhat less than that for the SR process. Due to a relatively low endothermicity of the process, less than 10% of the heat of methane combustion is needed to drive the process. In addition to hydrogen as a major product, the process produces a very important byproduct: clean carbon. Unlike SR and PO processes, NG decomposition process does not include water-gas shift (WGS) reaction and energy intensive gas separation stages.

There has been attempts to use catalysts in order to reduce the maximum temperature of methane thermal decomposition (Calahan 1974, Muradov 1993). It was found that the majority of transition metals (d-metals) to some extent exhibited catalytic activity toward methane decomposition. Some of them, for example Ni, Fe, Co and others, demonstrated a remarkable activity in methane dissociation reaction. However, there is a catalyst deactivation problem associated with the carbon build up on the catalyst surface. Carbon is produced as a byproduct of the process and over period of time it accumulates on the catalyst surface affecting its activity and in some cases causing the reactor clogging. Thus, in the vast majority of related publications and patents (e.g. Pourier 1997) carbon produced was burned off the catalyst surface in order to remove it from the reactor and regenerate the original catalytic activity. Since all the carbon produced from hydrocarbon is burned, the amount of CO₂ produced is comparable to that of the conventional processes (SR and PO), and no byproduct carbon is produced in this process. All these factors impose serious limitations to overcome before the process becomes commercial.

Technical Approach

Our technical approach is based on thermocatalytic decomposition of hydrocarbons over carbon-based catalysts in air/water-free environment. The use of carbon-based catalysts offers the following advantages over metal catalysts:

- no need for the separation of carbon from the catalyst
- no need for the regeneration of the catalyst by burning carbon off the catalyst surface
- no CO/CO₂ production due to the combustion of carbon
- no contamination of hydrogen with carbon oxides and, consequently, no need for the additional gas purification (e.g. via methanation)
- the process could be arranged in a continuous mode similar to the industrial processes of fluid coking or fluid catalytic cracking.

Current Year Objectives:

- To demonstrate the technical feasibility of CO₂-free production of hydrogen and carbon via catalytic decomposition of hydrocarbons
- To determine efficient carbon catalysts and conditions for sustainable production of hydrogen-rich gases from different hydrocarbons (methane, propane, gasoline)
- To determine factors affecting catalyst activity and long-term stability
- To evaluate different conceptual designs for the thermocatalytic reactor suitable for simultaneous production of hydrogen and carbon
- To preliminarily estimate economic benefits of producing hydrogen and carbon in comparison with steam reforming coupled with CO₂ sequestration

Results and Discussion

Methane Decomposition over Carbon Catalysts

We determined the catalytic activity of the variety of carbon-based materials of different structure and origin toward methane decomposition. Table 1 summarizes the experimental results of methane decomposition reaction in the presence of different modifications of elemental carbon including wide range of activated carbons (AC), carbon blacks (CB), carbon fiber, glassy carbon, and crystalline graphites, and others, at 850°C and residence time of approximately 1 s. Each carbon sample was characterized by two important parameters: initial activity presented as an initial methane conversion rate, in mmole/min-g (K_m^0) and sustainability displayed in the Table 1 as the ratio of methane conversion rate after one hour to the initial methane conversion rate (K_m^1/K_m^0). The available data on the surface area (SA) of carbon samples tested are also presented in the Table 1.

It is understood that higher are both K_m^0 and K_m^1/K_m^0 parameters, better is the carbon catalyst. The experiments indicated that, in general, activated carbons exhibited highest initial activity (per unit of catalyst weight), but relatively low sustainability (K_m^1/K_m^0). It is noteworthy that AC

samples of different origin and surface area displayed relatively close initial activity (K_m^0) in the range of 1.6-2.0 mmole/min-g.

Table 1. Comparative Assessment of Different Carbon Catalysts in Methane Decomposition Reaction

| Carbon Catalyst | SA, m ² /g | K_m^0 , mmole/min-g | K_m^1/K_m^0 | Carbon Catalyst | SA, m ² /g | K_m^0 , mmole/min-g | K_m^1/K_m^0 |
|--------------------|-----------------------|-----------------------|---------------|-------------------------------|-----------------------|-----------------------|---------------|
| AC, Coconut KE | 1150 | 1.76 | 0.05 | Acetylene Black | 80 | 0.22 | 0.98 |
| AC, Coconut CL | 1650 | 1.67 | 0.18 | CB, Black Pearls | 25 | 0.22 | 0.48 |
| AC, Coconut GI | 1300 | 1.90 | 0.07 | CB, Regal 330 | 94 | 0.42 | 0.40 |
| AC, Hardwood | 1500 | 2.04 | 0.32 | CB, Vulcan XC72 | 254 | 0.48 | 0.41 |
| AC, G-60 | 900 | 1.63 | 0.28 | CB, Black Pearls | 1500 | 1.15 | 0.60 |
| AC, Lignite | 650 | 1.77 | 0.31 | Glassy Carbon | - | 0.95 | 0.06 |
| AC, Peat RO | 900 | 1.63 | 0.19 | Diamond Powder | - | 0.16 | 0.48 |
| AC, petrol. coke | - | 1.29 | 0.47 | Carbon FibersPAN | - | 0.05 | 0.50 |
| Graphite, natural | 4-6 | 0.02 | 2.87 | Carbon Nanotubes | - | 0.08 | 0.92 |
| Graphite, crystal. | 3-10 | 0.10 | 0.63 | Soot (Fullerene) | - | 1.90 | 0.63 |
| Graphite, crystal. | 10-12 | 0.07 | 0.82 | Fullerenes C _{60/70} | - | 1.34 | 0.11 |

Carbon black catalysts (including acetylene black) exhibited somewhat lower initial activity than AC, but better sustainability. Carbons with the ordered structure (graphite, diamond, carbon fiber) demonstrated the lowest initial activity toward methane decomposition reaction. Fullerenes C_{60/70} and fullerene soot displayed relatively high initial activity, whereas, multi-walled carbon nanotubes showed very low catalytic activity in methane decomposition.

It was found that besides the nature of carbon material, its relative catalytic activity in methane decomposition reaction was proportional to the surface area of carbon. Figure 1 depicts the methane conversion rate (in mmole/min-g) as a linear function of the surface area of carbon catalysts in semi-log coordinates. The plot includes data for all the modifications of carbon tested, including AC, CB, graphites and others. It should be noted that only limited number of carbon catalysts could be compared based on the unit of surface area. For example, activated carbon (KBB) produced from hardwood (with SA=1500 m²/g) demonstrated the initial methane conversion rate of 1.36 mole/min-m², comparing to 0.77 mole/min-m² for carbon black (BP-2000) with the same surface area.

Figure 2 (a) demonstrates the kinetic curves of methane decomposition over different types of AC, CB and graphite at 850°C and different residence times. It can be seen that at comparable

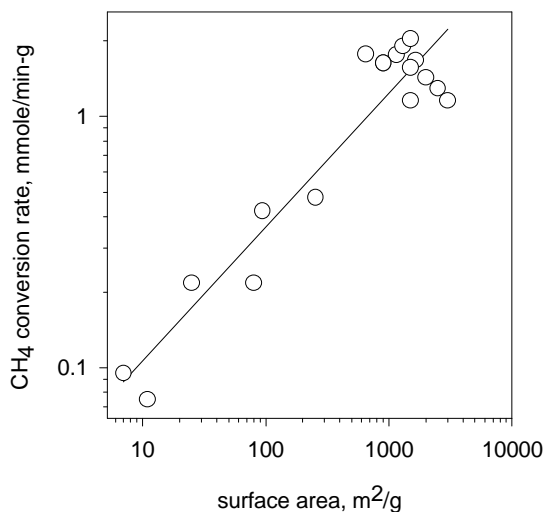


Figure 1 - Methane Conversion Rate as a Function of Catalyst Surface Area

conditions AC catalysts have higher initial activity than CB catalysts, although, CB-catalyzed decomposition of methane is more sustainable than AC-catalyzed. At relatively high residence times AC catalysts produced H_2/CH_4 mixtures with the initial hydrogen concentrations reaching up to 90 v.% and higher, which is an indication of the high catalytic activity. This, however, was followed by the rapid drop in the catalytic activity and the decrease in methane decomposition rate. CB-catalyzed methane decomposition reached quasi-steady state rate over 20-30 min and remained practically stable for several hours, followed by the gradual decline in the reaction rate.

The initial rate of methane decomposition over amorphous carbons (e.g. acetylene black and others) was relatively low, but the process demonstrated good sustainability over long period of time. Figure 3 demonstrates the kinetic curves of methane decomposition over acetylene black which was conducted at $850^\circ C$ and residence time of 12 s for almost 24 hours.

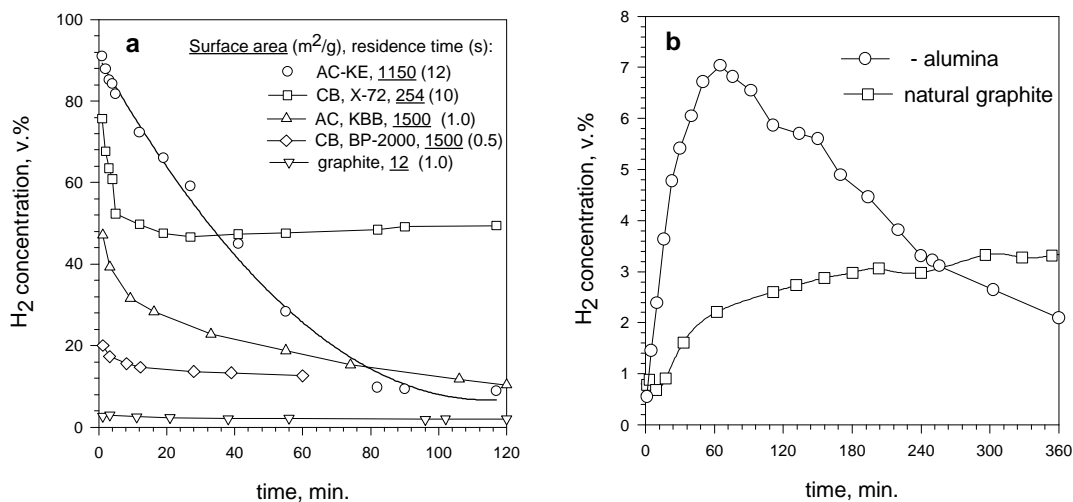


Figure 2 - Methane Decomposition over Different Carbon Catalysts at $850^\circ C$

Over period of 6 hours the process reached quasi-state regime which lasted for 9 hours, after which the methane decomposition rate slowly declined. No methane decomposition products other than hydrogen and carbon and small amounts of C_2 hydrocarbons ($C_2H_4 + C_2H_6 < 0.3$ v.%) were detected in the effluent gas during the entire process. The amount of carbon produced

corresponded to the volume of H₂ within the experimental margin of error (5%).

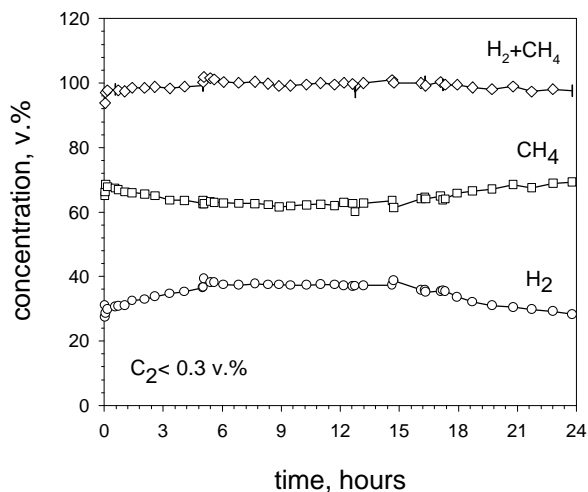


Figure 3 - Methane Decomposition over Acetylene Black at 850°C

It was found that the initial methane conversion rates in the presence of synthetic and natural graphites (with SA from 3 to 12 m²/g) and three different modifications of Al₂O₃ (including - and -forms) with the surface area from 6 to 275 m²/g were in the same range of 0.2-1.0 mmol/min-g (at the same temperature and residence time). This experiment indicates that methane decomposition over graphites is most likely due to the thermal rather than catalytic processes. Inertness of graphite toward methane decomposition was earlier reported by Diefendorf (1960), who demonstrated that at 800°C no methane conversion was observed over graphite surface for 2 weeks.

It is noteworthy that the sustainability factor (K_m^1/K_m^0) for natural graphite is more than unity, which indicates that the catalytic activity of carbon produced from methane is higher than that of the graphite. The same kinetic behavior was observed with both - and - modifications of alumina. Figure 2 (b) depicts the kinetic curves of hydrogen production over natural graphite (SA=4-6 m²/g) and -alumina (SA= 275 m²/g) at 850°C and residence time of approximately 1 s. These experiments clearly point toward certain catalytic properties of carbon produced from methane. However the catalytic activity of this form of carbon is quite low and, obviously, much less than that of AC and CB-type catalysts.

These experimental results can be explained as follows. It is known that the initial rate of hydrocarbon decomposition depends on the nature of a support (substrate). As the substrate surface is covered with carbon species, the rate of methane decomposition may increase or decrease, depending on the relative catalytic activity of the substrate and the carbon produced. The total rate of the methane decomposition process is the sum of the rates of carbon nuclei formation and carbon crystallites growth. It was determined that the activation energy of the carbon nuclei formation during methane decomposition (75.6 kcal/mole) is much higher than the

According to the Table 1 and Figure 2 graphites have the lowest initial catalytic activity (per unit of weight) in methane decomposition reaction. Among other factors, this could be attributed to the low surface area of graphites. However, the following experimental observation proves that graphites are indeed catalytically inert toward methane decomposition. In this experiment the catalytic activity of carbon materials with different chemical composition and surface area toward methane decomposition was compared.

activation energy of the carbon crystallites growth (54.2 kcal/mole) (Tesner 1987). Thus, in general, the rate of carbon crystallites growth tends to be higher than the rate of carbon nuclei production. The carbon particles produced during methane decomposition over AC catalysts, most likely, tend to have an ordered graphite-like structure and the rate of carbon crystallite growth exceeds that of nuclei formation. The catalyst surface is rapidly covered with relatively large graphite-like crystallites, which occupy active sites and result in inhibition of the catalytic activity toward methane decomposition. In the case of CB-type catalysts, the rates of crystallites growth and nuclei formation become comparable, resulting in the quasi-steady state methane decomposition. Low initial hydrogen production rate over alumina and natural graphite surface is due to high activation energy of nuclei formation over these materials. The increase in hydrogen production rate after the short induction period can be explained by the increase in the concentration of carbon nuclei on the surface and the methane decomposition rate over relatively small carbon crystallites. This is followed by the growth of the existing carbon crystallites and, as a result, the reduction of the active surface area and gradual decrease in methane decomposition rate. In case of graphite, methane decomposition rate slowly reached the steady state conversion rate controlled by the catalytic activity of carbon produced from methane. The nature of active sites responsible for the efficient decomposition of methane over the fresh surface of AC and CB catalysts is yet to be understood.

Effect of Temperature and Space Velocity on Methane Decomposition Yield

We studied the effect of temperature and methane space velocity on the yield of methane decomposition using different carbon catalysts. Figure 4 (a) depicts the temperature dependence of the initial H_2 concentration in the effluent gas in the presence of carbon black and activated carbon catalysts at different residence times (). It is clear that the initial activity of AC catalysts is higher than that of CB catalysts over the entire range of temperatures 600-1000°C.

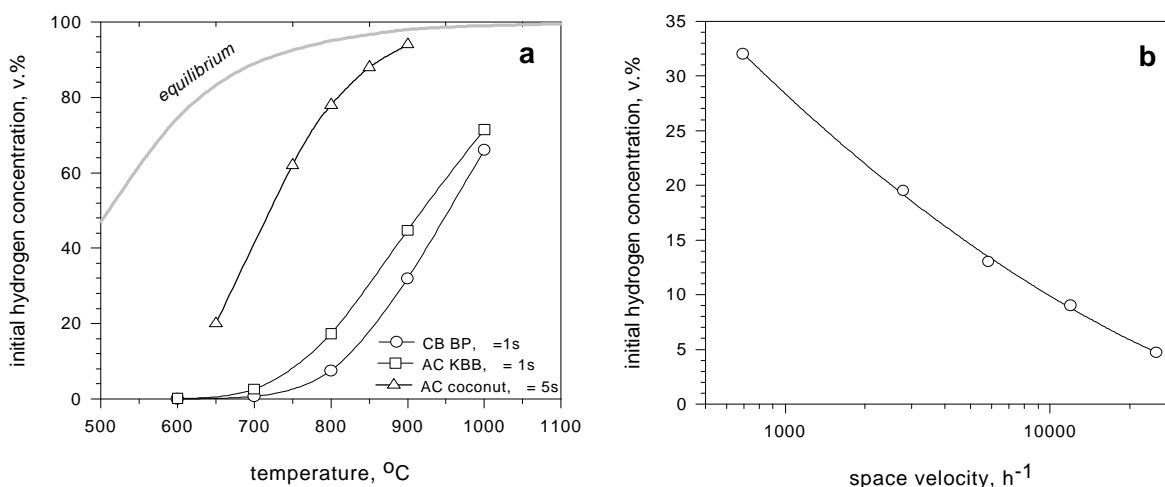


Figure 4 - Effect of Temperature (a) and Methane Space Velocity (b) on Methane Decomposition Yield.

At sufficiently high temperatures (e.g. 900°C and higher) and residence times (e.g. 5 s and higher) the initial concentration of hydrogen in the effluent gas approaches the thermodynamic equilibrium concentration, which is an indication of high catalytic activity at these conditions. At 650°C and below the methane conversion rate was negligible.

Figure 4 (b) demonstrates the effect of methane space velocity on the initial concentration of hydrogen in the effluent gas produced by methane decomposition over carbon black (BP-2000) at 850°C, presented in semi-log coordinates. Ten fold increase in space velocity of methane results in 3-4 fold decrease in methane decomposition yield. It should be noted that in this paper, for the sake of comparability, both the residence time and the space velocity relate to the volume of the carbon catalyst within the reactor.

Kinetic Model and Major Kinetic Parameters of CH₄ Decomposition

We developed a kinetic model of the methane decomposition reaction over carbon catalysts. It was assumed that CH₄ decomposition over the surface of carbon catalyst is controlled by two simultaneous processes:

1. decrease in methane decomposition rate due to the blocking of catalytic active sites by the carbon species produced via methane decomposition:

$$\frac{d[CH_4]}{dt} = k_1 S_1 (1 - q) [CH_4]$$

where, k_1 - rate constant, S_1 - catalyst surface area, q - the fraction of catalyst surface covered by carbon produced from methane; q is a function of time

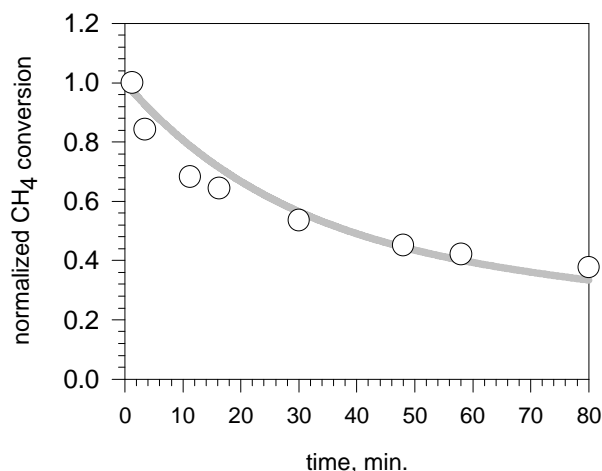
2. increase in methane decomposition rate due to the formation of catalytically active carbon species produced from methane

The sum of two components results in the following kinetic equation for the methane conversion:

$$c_{CH_4} = e^{-k_1 S_1 (1 - q)t} + \frac{[CH_4]_e}{[CH_4]_o} (1 - e^{-k_2 S_2 t})$$

where, c_{CH_4} is methane conversion, $[CH_4]_o$ and $[CH_4]_e$ are the initial and quasi-steady state methane concentrations in the effluent gas, respectively, S_2 and k_2 , are catalyst surface area and rate constant, respectively, for methane decomposition over carbon particles produced from methane; S_2 is a function of time

The first component of the equation describes the decrease in methane conversion by the exponential decay law, whereas, the second component represents exponential rise to maximum, i.e. to the quasi-steady state value of methane conversion.



The kinetic equation obtained satisfactorily describes the experimental data during the initial stage of the methane decomposition process (1-1.5 hour). For example, Figure 5 compares the experimental results for methane decomposition over carbon black (BP-2000) catalyst at 850°C (circles) with the curve produced by fitting the data to the above kinetic model (gray line). The model can explain the peculiarities of the kinetic curves for methane decomposition over different types of carbon catalysts.

Figure 5 - Experimental Data (circles) and Curve Fit Using Kinetic Model (gray line)

The initial catalytic activity of AC is much higher than that of carbon produced from methane, therefore, the second component of the kinetic equation could be neglected, which results in a typical exponential drop shape of the kinetic curve. In contrast to AC, graphite catalysts (particularly, natural graphite) have very low initial catalytic activity toward methane decomposition reaction, therefore the first component of the kinetic equation is negligible, and the resulting kinetic curve is either flat, or is described by the exponential rise to maximum law (see also Figure 2, b). The same is true for the methane decomposition over alumina surface.

We determined the kinetic parameters of methane decomposition reaction over different carbon catalysts. Table 2 summarizes the major kinetic parameters (apparent reaction rate constants, frequency factors and activation energies) for CB and AC catalysts at the range of temperatures 700-900°C.

Table 2. Apparent Reaction Rate Constants and Activation Energies for CH₄ Decomposition over CB and AC Catalysts

| Catalyst | T°C | k, s ⁻¹ | E _a , kCal/mol | , s ⁻¹ |
|--|-----|--------------------|---------------------------|-----------------------|
| Carbon black, BP-2000 SA= 1500 m ² /g | 750 | 0.035 | 56.3 | 4.3 · 10 ⁹ |
| | 850 | 0.480 | | |
| | 950 | 2.125 | | |
| Activated carbon, KBB SA= 1500 m ² /g | 600 | 0.0015 | 47.9 | 4.9 · 10 ⁸ |
| | 700 | 0.026 | | |
| | 800 | 0.178 | | |
| | 900 | 0.602 | | |

Thus, the apparent rate constants for methane decomposition in the presence of carbon black BP-2000 (k_{CB}) and activated carbon KBB (k_{AC}) catalysts could be expressed as follows:

$$k_{CB} = 4.3 \cdot 10^9 \exp(-56.3/RT) \quad 750-950^\circ\text{C}$$

$$k_{AC} = 4.9 \cdot 10^8 \exp(-47.9/RT) \quad 600-900^\circ\text{C}$$

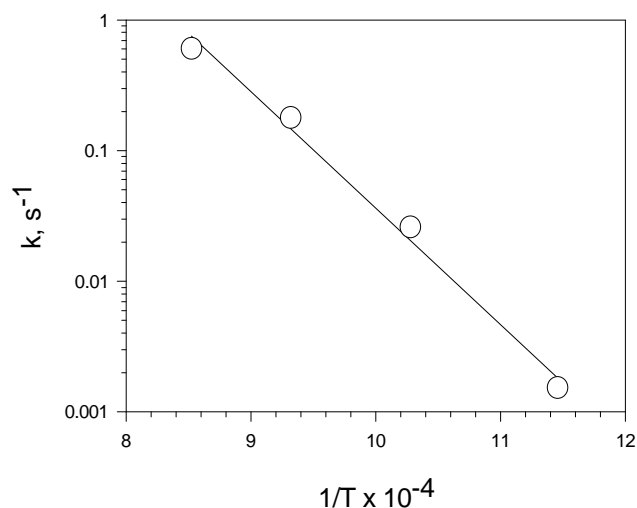


Figure 6 depicts the Arrhenius plot for methane decomposition over AC (KBB) catalyst. The activation energies of methane decomposition reactions over carbon catalysts are characteristic of surface reaction rate controlled processes.

Figure 6 - Arrhenius Plot for CH₄ Decomposition

Propane Pyrolysis over Carbon Catalysts

Due to a relatively weak C – H bond in propane molecule (96 kcal/mol) it is somewhat easier to split propane than methane molecule (methane C – H bond energy is 105 kcal/mol). 6.2 kcal is required to produce one mole H₂ from propane, comparing that to 8.9 kcal for methane:



However thermal cracking of propane at high temperatures proceeds via a thermodynamically more favorable formation of methane and ethylene:



Therefore, during pyrolysis of propane, in most cases, we observed the production of gaseous mixture containing hydrogen, methane, ethylene and small amounts of ethane and propylene. Figure 7 depicts the experimental results of propane catalytic pyrolysis over CB (a) and AC (b) type catalysts at 800°C in a packed bed reactor. Similar to methane decomposition, activated carbon demonstrated high initial activity followed by the rapid drop in catalytic activity. At the onset of the process hydrogen and methane were the only products of propane pyrolysis. Practically no C₂⁺ byproducts were found in the effluent gas during first 10 min.

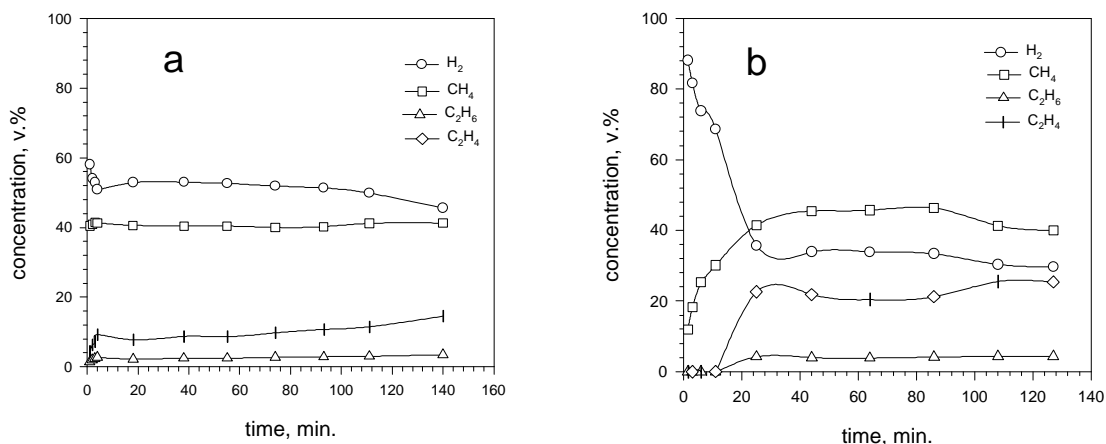


Figure 7 - Propane Pyrolysis over CB (XC-72) (a) and AC (KE) (b) at 800°C

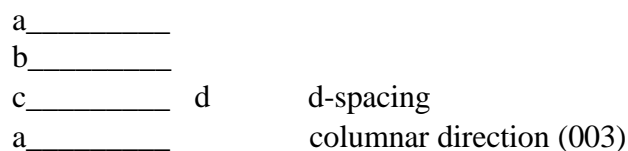
Quasi-steady state pyrolysis of propane was established after 30-40 min with methane being the major product of pyrolysis and significant concentration of ethylene in the effluent gas. The composition of the effluent gas of propane pyrolysis over AC catalyst approximately corresponded to the following chemical equation:



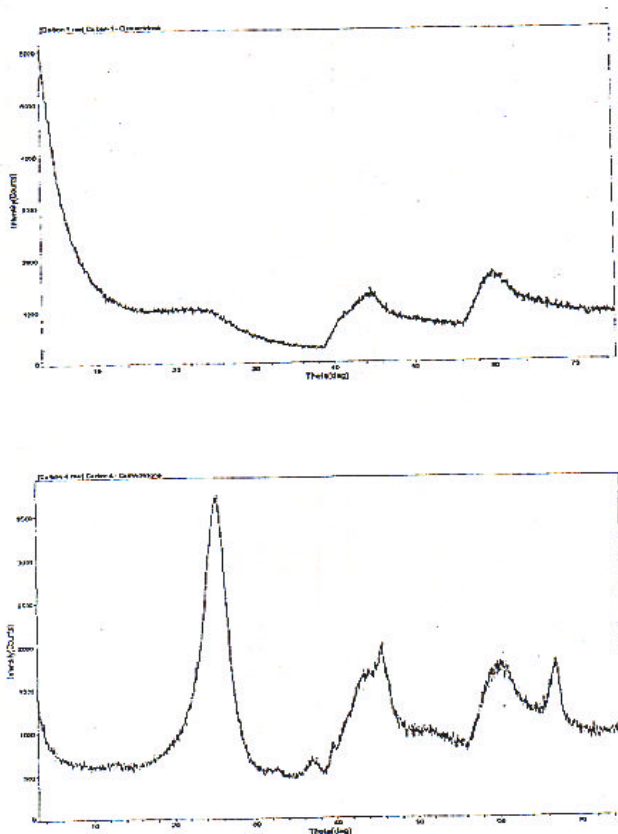
Propane pyrolysis over carbon black was characterized by lower initial rate, but was more sustainable comparing to AC catalyst, as shown on Figure 7 (a). Quasi-steady state rate of propane pyrolysis was reached in approximately 5 min and the process remained stable for approximately 2 hours. Hydrogen was a major component of the effluent gas during CB-catalyzed pyrolysis of propane.

XRD Studies of Carbon Catalysts

We conducted X-ray diffraction (XRD) studies of the original carbon catalysts and carbon samples produced during hydrocarbon (methane or propane) decomposition. Carbon black BP-2000 with the surface area of 1500 m²/g and activated carbon Darco KBB (produced from hardwood) with the same surface area were used in these studies. Figure 8 depicts XRD spectra of the original carbon black (BP-2000) sample (top) and the carbon produced by propane pyrolysis at 850°C (bottom). It was found that the original sample had one- or, possibly, some two-dimensional ordering, whereas, sample produced from propane had ordering in the “columnar” or stacking (003) direction. The following diagram illustrates this concept:



where, a, b, and c are alternating arrangements of carbon ring plates. The d-spacing (lattice spacing) or spacing between plates is practically uniform, so that the (003) columnar reflection is clearly present. Thus, carbon produced during propane pyrolysis clearly has a typical graphite a-b-c-a type stacking of the carbon ring plates.



The actual d-spacing ($d = 3.4948 \text{ \AA}$) of this (003) peak is larger than that of the standard graphite structure ($d = 3.3480 \text{ \AA}$), which indicates that the plates are slightly further apart in the columnar stacking direction. This reflection is almost absent in the original carbon black sample which indicates that the plates are not stacked in a columnar arrangement, but, instead, are randomly oriented with respect to each other. The other two crystalline diffraction peaks in carbon sample produced by propane decomposition (43.5 and $46.2^\circ 2\theta$) also result from the three dimensional ordering, and result from the regular arrangement of spacings in various directions with respect to the columnar direction. The peaks 62.2 and $67.2^\circ 2\theta$ are due to scattering rather than to crystalline diffraction.

Figure 8 - XRD Spectra of Carbon Samples

The peak at 62.2 is due to C – C atomic distance for atoms which are out-of-plane, and the peak at 67.2 results from the C – C atomic distance for the in-plane carbon atoms. The size of graphite crystallite produced by propane decomposition was estimated at 23 Angstrom. XRD spectrum of the sample of activated carbon (Darco KBB) also indicated the lack of clear three dimensional ordering.

Thus, XRD studies confirmed that carbon species produced by decomposition of alkanes (methane and propane) at 850°C predominantly have an ordered (graphite-like) structure. This fact explains the gradual drop in the activity of AC and other carbon catalysts during methane and propane pyrolysis.

SEM Studies of Carbon Catalysts

We conducted Scanning Electron Microscope (SEM) studies of the surface of carbon catalysts. Average particle size of powdered activated carbons was 40-100 μm . Carbon black particles were significantly smaller in size and varied in the range of 0.1 – 1 μm . Figure 9 depicts SEM micrographs of CB (BP-2000) catalyst before (left) and after exposure to propane at 850°C for 3.5 h (right).

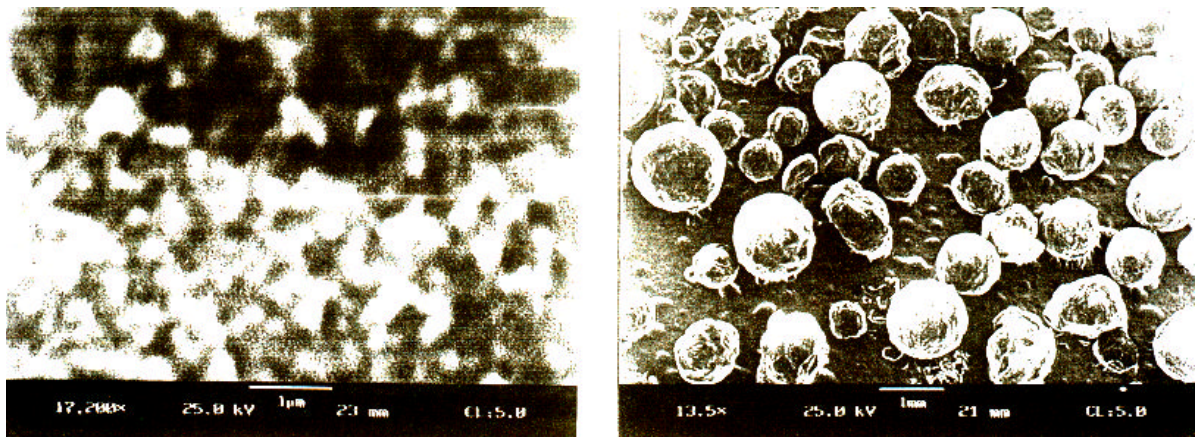


Figure 9 - SEM Micrographs of Carbon Black (BP-2000) Sample Before (left, 1 μm scale) and After Exposure to Propane at 850°C for 3.5 h (right, 1 μm scale)

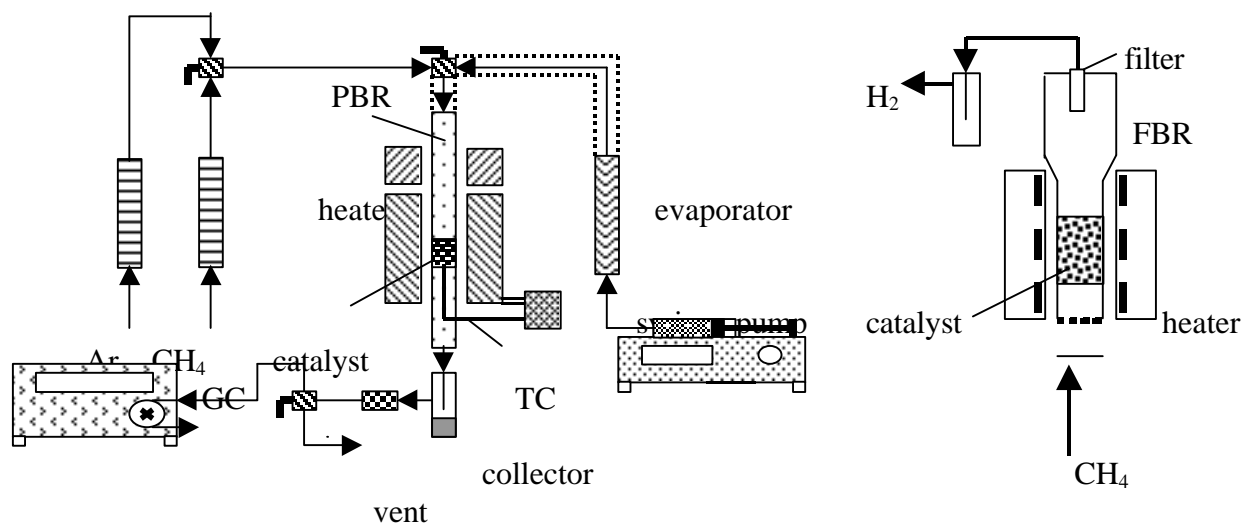
It can be seen that the average diameter of carbon particles increased from 0.1-0.3 μm (for the original carbon sample) to approximately 0.1-1 μm due to carbon deposition during propane pyrolysis, which corresponded to more than thousand fold increase in particles mean diameter. On the other hand, the amount (weight) of carbon in the reactor increased only 6 times as a result of propane pyrolysis. This implies that a great deal of the agglomeration of carbon particles occurred during the process. Surface area calculations indicate that propane pyrolysis over CB catalyst would result in the reduction of the total geometrical surface of carbon particles by two orders of magnitude. This would have led to a drastic decrease in propane pyrolysis rate due to a significant reduction in the catalytic surface, which did not happen. The reason for that is that the actual surface area of each particle was much higher than its geometrical surface due to the presence of clusters of carbon particles about 3-10 μm in diameter on the surface of the larger carbon particles (not shown on the micrograph).

Thermocatalytic Reactors for Hydrocarbon Decomposition

The objective was to conduct studies on various conceptual designs for the thermocatalytic reactor for hydrocarbon decomposition. The reactors were designed, fabricated and tested for the simultaneous production of hydrogen and carbon using methane, propane and gasoline as feedstocks.

5 different types of reactors for hydrocarbon decomposition were considered:

- packed bed reactor (PBR)
- tubular reactor (TR)
- free volume reactor (FVR)
- fluid wall reactor (FWR)
- fluidized bed reactor (FBR)



GC- gas chromatograph, TC- thermocouple

Figure 10 - Schematic Diagram of the Experimental Set-up with PBR (left) and FBR (right) Reactors

Figure 10 demonstrates the experimental set-up with a packed bed reactor (left) used for the decomposition of methane, propane and gasoline. It should be noted that the same experimental set-up was also used for testing of the fluidized bed (right) and other reactors.

Packed Bed Reactor

PBR was mainly used for carbon catalysts screening, and studies on the effect of operational parameters (temperature, space velocity) on hydrogen yield, and kinetic measurements. Several examples of PBR test runs are presented in the Table 3. In some cases, it was difficult to conduct long run experiments with PBR due to carbon build up within the reactor and potential reactor clogging. It is apparent that the continuous removal of carbon from PBR would be a daunting technical problem, therefore, this type of the reactor is unlikely to be used in large scale hydrogen production units.

Tubular Reactor

We conducted a series of experiments on methane decomposition using tubular reactors. The objective was to thermally decompose methane into hydrogen and carbon in a continuous process. Tubular reactors with the internal diameters of 3-6 mm and a small reaction zone enabling to achieve the residence times in the range of 1-20 milliseconds, were used in these experiments. Preheated (400°C) methane stream entered the reaction zone where it was subjected to decomposition (pyrolysis) at the temperatures of 1000-1300°C. At these conditions the conversion of methane was a function of the residence time. For example, at the residence time of 1.0, 2.0 and 6.2 ms, methane conversions were (mol.%): 0.1, 2.0 and 16.1, respectively. Hydrogen, carbon and unconverted methane accounted for more than 80-90 m.% of the products. Unsaturated (mostly, C₂H₄) and aromatic (including polynuclear) hydrocarbons were also produced in significant quantities as byproducts of methane decomposition. For example, at the residence time of 6.2 ms the yields of gaseous and liquid products were as follows (mol.%): C₂H₆- 0.9, C₂H₄- 3.3, C₂H₂- 5.8, C₃-C₆- 1.5, polynuclear aromatics (mostly, naphthalene)- 2.0. Unidentified liquid products of pyrolysis accounted for approximately 5 w.% of methane pyrolysis products. Carbon (coke) was mostly deposited on the reactor wall down-stream of the reaction zone, which indicated that methane decomposition reaction occurred predominantly homogeneously in gas phase. At higher residence times (tens of seconds), the yields of C₂⁺ and polyaromatic hydrocarbons dramatically dropped. These experiments demonstrated that TR could potentially be scaled up for the use in full scale methane decomposition process, although, it would require the elevated temperatures (above 1000°C) and special surface-treated tubes to prevent carbon deposition in the reaction zone.

Free Volume Reactor

Free volume reactor is designed to carry out high temperature reactions by contacting a reagent gas with a stream of preheated carrier gas. FVR could be advantageous for the conducting of different dissociation reactions with formation of solid phase products, including methane decomposition reaction. For example, Shpilrain et al. (1999) reported on testing of a regenerative type FVR in a cyclic methane decomposition process. In our work we designed and tested FVR for a continuous production of hydrogen and carbon via methane decomposition. Methane decomposition occurred homogeneously by contacting a hot carrier gas such that carbon was produced in a free volume of the reactor and carried away by the gaseous stream, thus preventing carbon from deposition on the reactor wall. Two options for introducing thermal energy into the reaction zone were considered: by the stream of inert gas (Ar) or hydrogen. Figure 11 shows the schematic diagram of FVR used for decomposition of methane and propane.

Methane was introduced into the reactor through the inner ceramic tube, and the heat carrier gas entered the space between the inner and outer (quartz) tubes of FVR. We used Ar or hydrogen as heat carrier gases in a ratio 4:1 (by volume) to methane. The heat carrier gas was heated by the electric heater to 1200-1300°C and entered the reaction zone where it contacted the preheated

stream of methane. The results of the FWR testing using hydrogen as a carrier gas are presented in the Table 3.

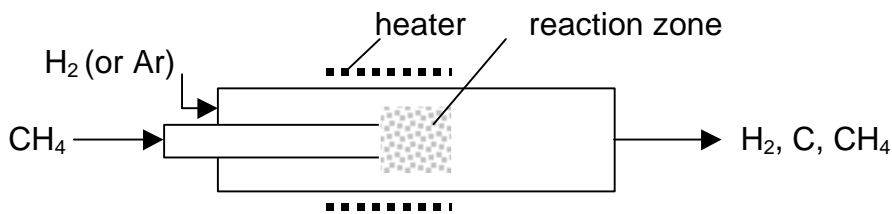


Figure 11 - Schematic Diagram of Free Volume Reactor

There were some carbon deposits around and, especially, downstream of the reaction zone, which indicated that some portion of methane contacted the hot surface of the outer wall due to a mixing of gases in the reaction zone. This could be prevented if the temperature of a heat carrier gas was higher than that of the wall in the reaction zone. The use of an inert gas as a heat carrier requires a subsequent gas separation stage, which would add to the cost of hydrogen. On the other hand, the use of hydrogen would somewhat reduce the net hydrogen yield.

Fluid Wall Reactor

The objective of FWR is to carry out the high temperature hydrocarbon decomposition reactions in the layer of a carrier gas heated to the required temperature, thus preventing carbon from deposition on the reactor wall. This can be done by passing a preheated inert gas (or hydrogen) through the porous tubing (which acts as an internal reactor wall) such that it thermally decomposes methane in the reaction zone and carries away produced carbon. Simplified schematic diagram of the FWR is shown on Figure 12.

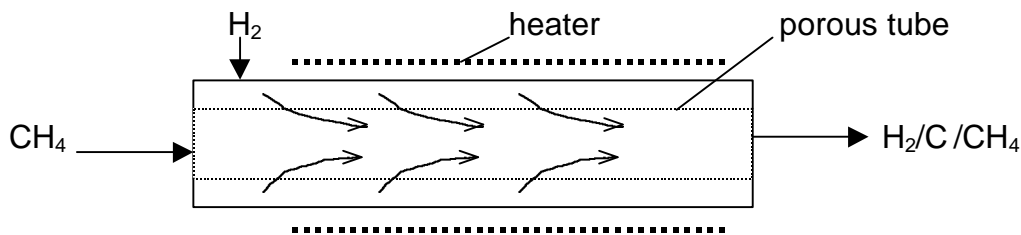


Figure 12 - Schematic Diagram of Fluid Wall Reactor

We conducted methane decomposition test runs using small size FWR. A flow of hydrogen at positive pressure was introduced into annulus between outer tube (quartz) and the internal porous ceramic tube, and a flow of methane at the atmospheric pressure was introduced into the inner ceramic tube at H_2/CH_4 ratio of 1:3. The outer wall of the reactor was heated by the electric heater to 1100-1300°C. A stream of heated hydrogen permeated through the porous ceramic tube and entered the reaction zone where it contacted a preheated stream of methane. A mixture of hydrogen and unconverted methane after the reactor was metered and analyzed by GC method.

Methane conversion was about 10-15%. Carbon was collected in the down stream trap. More experiments will be conducted to optimize the yield of products. These proof-of-concept experiments demonstrated that FWR could potentially be suitable for medium and large scale units for the simultaneous production of hydrogen and carbon from NG and other hydrocarbons.

Fluidized Bed Reactor

Fluidized bed reactors are widely used in chemical, metallurgical and petroleum industries. FBR could be particularly suitable for hydrocarbon decomposition process since it allows to continuously remove carbon from the reactor, similar to fluid catalytic cracking processes. A schematic diagram of FBR used in our experiments is shown on Figure 3 (right). It was found that an adequate fluidization of carbon (particularly, CB) particles could be achieved at space velocities of 300-600 h⁻¹. Preheated to 400-500°C a hydrocarbon stream entered the FBR from the bottom, and contacted with the fluidized bed of carbon particles heated to 850-950°C in the reaction zone, where decomposition (pyrolysis) of hydrocarbons occurred. A hydrogen-rich gas exited from the top of the reactor through a ceramic wool filter. FBR reactor was tested using methane, propane, methane-propane mixtures, gasoline vapor and gasoline-methane mixture as feedstocks. Because of relatively short residence times (1-3 s) in the reaction zone methane decomposition yields were relatively low, whereas, propane and gasoline were almost quantitatively converted into hydrogen-rich gas using FBR. Figure 13 depicts the experimental results of propane and gasoline vapor pyrolysis over CB (BP-2000) catalyst at 850°C using FBR.

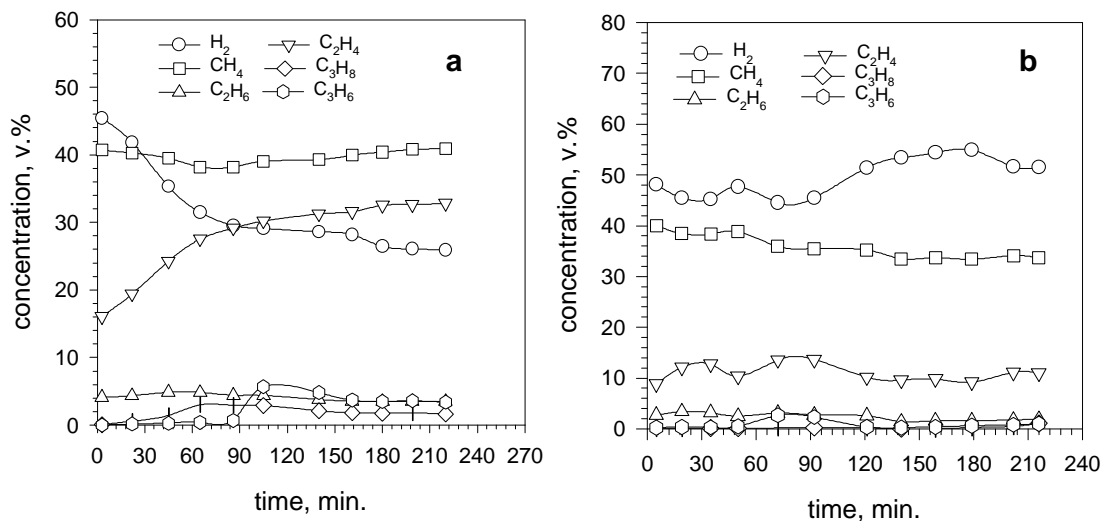


Figure 13 - Thermocatalytic Pyrolysis of Propane (a) and Gasoline (b) over CB (BP-2000) at 850°C Using FBR

It is noteworthy that pyrolysis of propane and gasoline in FBR produce more C₂⁺ byproducts comparing to PBR. Thermocatalytic pyrolysis of gasoline over CB catalyst lasted more than 3.5

hours during which the gaseous mixture with the average hydrogen concentration of 50 v.% was produced.

Comparative Assessment of Different Reactors for Hydrocarbon Decomposition

The results of testing of different thermocatalytic reactors for decomposition/pyrolysis of methane, propane and gasoline using carbon catalysts are presented in Table 3. Note that the data on the hydrocarbon conversion and the effluent gas composition relate to the average quasi-steady state values.

Table 3. Thermocatalytic Reactor Test Results

| Hydrocarbon | Catalyst | Reac-tor | T°C | Conver-sion, % | Gaseous Products, v.% | | | | | |
|---|-----------------|----------|------|----------------|-----------------------|-----------------|-------------------------------|---|----------------|-----------------------------|
| | | | | | H ₂ | CH ₄ | C ₂ H ₆ | C ₂ H ₄ (C ₂ H ₂) | C ₃ | C ₄ ⁺ |
| Methane | CB, BP-2000 | PBR | 950 | 30.9 | 47.2 | 52.7 | 0 | 0.1 | 0 | 0 |
| Methane | Acetylene Black | PBR | 850 | 23.3 | 37.8 | 61.9 | 0.1 | 0.2 | 0 | 0 |
| Methane | CB, XC-72 | PBR | 850 | 28.0 | 43.7 | 56.2 | 0 | 0.1 | 0 | 0 |
| Methane | CB, BP-2000 | FBR | 850 | 9.1 | 16.7 | 83.1 | 0 | 0.2 | 0 | 0 |
| Methane | - | TR | 1200 | 53.8 | 63.8 | 27.4 | 0.1 | 1.2 (7.5) | 0 | 0 |
| CH ₄ /H ₂ (4:1) | - | FVR | 1200 | | 89.3 | 10.7 | 0 | 0 | 0 | 0 |
| CH ₄ /C ₃ H ₈ (3:1) | CB, BP-2000 | FBR | 850 | 38.2 | 50.1 | 2.1 | 9.0 | 0.6 | 0 | |
| CH ₄ /C ₂ H ₄ (3:1) | CB, BP-2000 | FBR | 850 | | 36.2 | 53.9 | 2.0 | 7.9 | 0 | 0 |
| Propane | AC, KE | PBR | 800 | 100.0 | 88.3 | 11.7 | 0 | 0 | 0 | 0 |
| Propane | Acetylene Black | PBR | 850 | 100.0 | 62.1 | 37.9 | 0 | 0 | 0 | 0 |
| Propane | CB, BP-2000 | FBR | 850 | 98.0 | 27.0 | 39.5 | 1.5 | 29.4 | 2.6 | 0 |
| Gasoline | AC, KE | PBR | 800 | 100.0 | 49.4 | 37.6 | 2.1 | 9.8 | 0.6 | 0.5 |
| Gasoline | CB, BP-2000 | FBR | 850 | 100.0 | 52.0 | 33.2 | 2.1 | 11.1 | 0.7 | 0.9 |
| CH ₄ /gasoline | CB, BP-2000 | FBR | 850 | | 40.0 | 55.5 | 0.3 | 3.0 | 0.5 | 0.7 |

Economic Analysis

We conducted a preliminary economic analysis of the thermocatalytic decomposition (TCD) process for production of hydrogen and carbon from natural gas. Figure 14 depicts the simplified flow diagram of the thermocatalytic process employing a fluidized bed reactor (FBR).

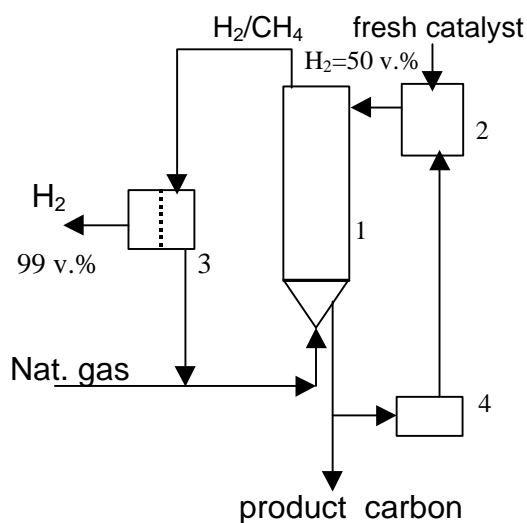


Figure 14 - Simplified Flow Diagram of TCD Process for Production of Hydrogen and Carbon. 1- FBR, 2- heater, 3- membrane, 4- grinder

According to this flow diagram hydrogen concentration in the reactor effluent gas is 50 v.%, with balance being methane and small amounts of C₂⁺ hydrocarbons. Thus, the employment of the membrane gas separation unit is required to produce 99 v.% hydrogen.

Non-permeate is recycled back to the reactor. Product carbon is removed from FBR and some portion of it is ground and recycled to maintain the average particle size in the range suitable for fluidization (100 – 500 μm). The catalyst is heated in the heater to the required temperature 800-900°C. Thus, the technological scheme of the process is very close to that of fluid coking (FC) process, except, in case of FC process the temperature is lower (510-550°C), and the hydrocarbon feedstock is heavier.

Therefore, for the preliminary estimate, the capital cost of the FC plant (including grinder) and its annual operational costs were taken as a basis for the hydrogen cost estimate for TCD process (it was assumed that FC and TCD have the same capacity on a feedstock BTU basis) (Garrett 1989).

It was estimated that the usage of 17% of the non-permeate gas as a process fuel would cover thermal requirements of the TCD process. Carbon is a valuable byproduct of the process, with prices from several hundreds to several thousands of dollars per ton depending on its quality. Thus, the credit for byproduct carbon could significantly reduce the cost of hydrogen. For the purpose of our estimate we used a conservative sale price of carbon at \$100/ton, which is the average cost of carbon (in the form of petroleum coke) used in metallurgical industry (Kirk-Othmer 1978). The following Table demonstrates the results of the economic evaluation of TCD plant with the capacity of 10⁶ m³/day (which is close to that of a typical steam reforming plant).

Cost of hydrogen production from natural gas by thermocatalytic decomposition process was compared to that of steam reforming process. Figure 15 depicts the comparative assessment of TCD of NG (with and without carbon credit) and SR of NG (with and without CO₂ sequestration) processes.

Table 4. Cost of Hydrogen Production by TCD Process

Capacity: 10⁶ m³ H₂/day
H₂ purity: 99.0 v.%
Natural gas: \$2.5/MMBTU

| | \$10 ⁶ | \$10 ⁶ /Year | \$/MMBTU |
|--|-------------------|-------------------------|----------|
| <u>Capital Cost:</u> | | | |
| Reactor/ Heater/ Grinder (from FC plant) | 18.0 | | |
| Membrane Hydrogen Separator | 2.0 | | |
| Total Capital Cost | 20.0 | | |
| <u>Annual Operating Cost:</u> | | | |
| Feedstock (Natural Gas) | | 33.9 | |
| Catalyst/reagents/desulfurization | | 1.0 | |
| Power | | 0.3 | |
| Labor | | 0.1 | |
| Depreciation (10%) | | 2.0 | |
| | | | 7.1 |
| Total Hydrogen Production Cost | | 10.7 | |
| Carbon Credit (\$100/t) | | | 5.0 |
| Net Hydrogen Production Cost | | | |

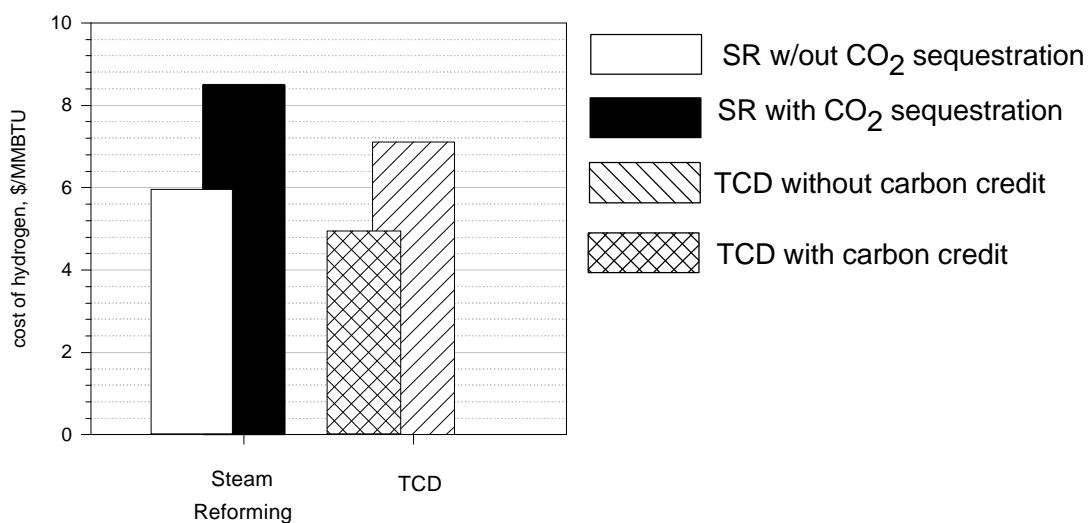


Figure 15 - Comparative Assessment of Hydrogen Production Cost by SR and TCD Processes

For the purpose of the comparative economic evaluation we used the cost of hydrogen produced by modern methane steam reforming plant (Ogden 1997). As mentioned in the Background section, capture of CO₂ from concentrated streams of SR plant and its disposal adds 25-30% to the cost of hydrogen production by SR process. One should also add to it the cost of eliminating CO₂ emissions from the diluted (stack) gases of SR process.

The results of the comparative economic assessment of different options for hydrogen production from NG are as follows. TCD with carbon credit is the most cost effective process followed by SR without CO₂ sequestration. Note that the cost of hydrogen produced by the TCD without carbon credit (that is, carbon is not sold, but stored for the future use) is still lower than that of SR coupled with CO₂ sequestration (assuming that the cost of carbon storage is negligible compared to that of CO₂ sequestration). This is a preliminary economic assessment of TCD process, and more detailed cost analysis will be conducted upon testing pilot scale unit.

Current and Future Markets for Carbon

Currently, the total world production of carbon black is close to 6 mln tons per year, with prices varying in the range of hundreds to thousands dollars per ton, depending on the carbon quality (Fulcheri 1995). For example, prices for the good quality carbon black could reach \$1000-4000 per ton. The carbon black has a great market potential both in traditional (rubber industry, plastics, inks, etc.) and new areas. For example, Gaudernack et al. (1996) identified the metallurgical industry as a very promising market for carbon black. Carbon black is particularly valuable as a reducing reagent for the production of SiC and other carbides, and as a carbon additive (carburizer) in steel industry. The carbon black market for these applications in Europe currently approaches 0.5 mln ton/year with the prices for the high quality materials reaching \$615 per ton. Carbon-based composite and construction materials potentially can absorb a tremendous amount of produced carbon. Besides the traditional markets for carbon, some novel applications for the carbon produced via methane decomposition are discussed in the literature. For example,

Kvaerner has initiated R&D program to investigate the potential of novel grades of carbon black as a storage medium for hydrogen, and as a feedstock for the production of solar grade silicone (Linum 1998).

A market for carbon-based materials is continuously growing, however, it is unlikely that all the carbon produced via NG decomposition for mitigating the global warming will be absorbed by the traditional and perspective application areas. In this case, carbon can be stored for the future use, as discussed by Muradov 1993, and Steinberg 1999). No significant energy consumption would be expected with regard to the storage of solid carbon (comparing to CO₂ sequestration).

Comparison of CO₂ Emissions from Different Hydrogen Production Processes

A comparative assessment of CO₂ emissions produced by different hydrogen production processes is shown on Figure 16. The following NG-based processes were compared:

- SR (without and with CO₂ sequestration),
- partial oxidation (without and with CO₂ sequestration),
- plasma-assisted decomposition (PAD), and
- TCD (with CH₄ and H₂ as a process fuel options).

PAD of methane is a well developed technology for the production of hydrogen and carbon black via high temperature decomposition of natural gas (Linum 1998). However, it consumes up to 1.9 kWh of electric energy to produce one normal cubic meter of hydrogen. Due to relatively low endothermicity of the methane decomposition process, the thermal energy requirements of the TCD process could be covered either by 10% of methane feedstock, or 14% of hydrogen produced in the process.

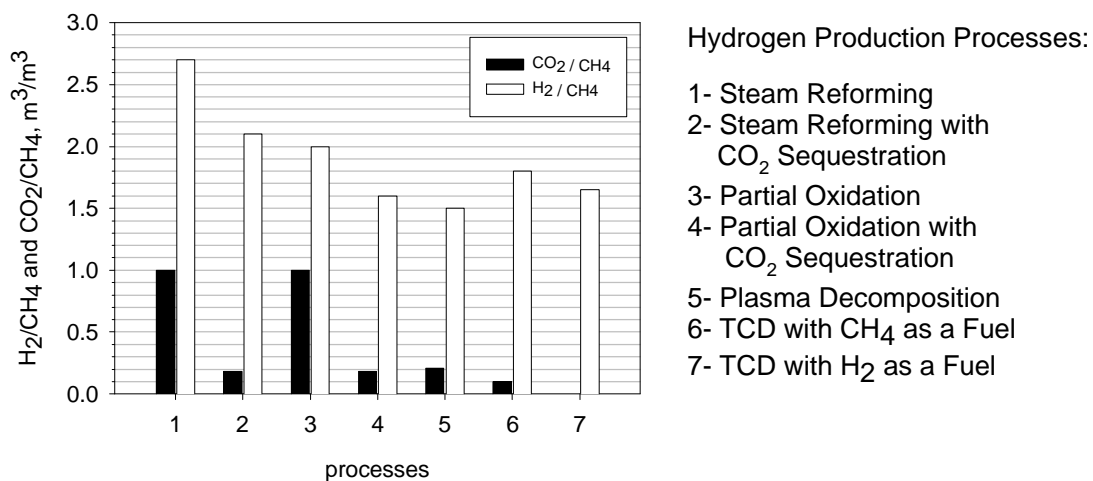


Figure 16 – Comparison of CO₂ Emissions from Different Hydrogen Production Processes

The comparison is based on two parameters, which reflect the energetic and ecological features of

the processes. The E_1 -parameter is equal to the volume of H_2 produced from the unit volume of NG consumed as a feedstock and a process fuel ($E_1 = H_2/NG, m^3/m^3$). The E_2 -parameter is equal to the total volume of CO_2 (from the process and stack gases) produced from a unit volume of NG ($E_2 = CO_2/H_2, m^3/m^3$). Evidently, the higher is E_1 and lower is E_2 parameter, the better is the hydrogen production process.

For the sake of simplicity and comparability, it was assumed that NG was the primary fuel for the supply of both thermal and electric energy for all the processes, including PAD of NG, and for CO_2 sequestration. Almost 80% of the total world energy supply is based on fossil fuels, and NG average share is 19% (Nakicenovic 1993). Since NG produces 1.9 and 1.7 times less CO_2 (per kWh produced) than oil and coal, respectively, this assumption would result in somewhat more conservative values for CO_2 emissions.

The following conclusions can be extracted from Figure 16.

Plasma decomposition of NG has lowest hydrogen yield and highest CO_2 emissions because of large consumption of electric energy (note that this estimate is based on the world average energy production scenario, therefore, in countries with a large non-fossil fuel energy sector, e.g. hydroelectric, nuclear energy, both E_1 and E_2 parameters could be higher and lower, respectively).

PO produces less hydrogen than SR process per unit of NG, although, both processes have comparable CO_2 emission levels.

TCD of NG (with NG as a fuel option) produces almost half of the CO_2 emissions produced by SR with CO_2 sequestration.

TCD of NG (with H_2 as a fuel option) produces hydrogen in quantities comparable with that of PO and SR (with CO_2 sequestration), however, it does not produce any CO_2 .

Thus, it is the only fossil fuel based process which shows a real potential to be a completely CO_2 -free hydrogen production process.

Experimental

Reagents. Methane (99.99%v.) (Air Products and Chemicals, Inc.) was used without further purification. Samples of activated carbons, graphites, glassy carbon, synthetic diamond powder, fullerenes, carbon nanotubes and acetylene black were obtained from Alfa Aesar and used without further purification. Barneby Sutcliffe Corp. and Cabot Corp. supplied different CB and AC (coconut) samples, respectively. All carbon samples were used in the form of fine powder (<100 m). Activated alumina samples (Fisher Scientific and Alfa Aesar) were used without further purification.

Apparatus. The experimental set-up depicted on Figure 3- was used for the screening of carbon catalysts, kinetic measurements and testing of different thermocatalytic reactors. The set-up consisted of 3 main subsystems: (1) a thermocatalytic reactor (with temperature-controlled electric heater and pre-heater), (2) a feedstock metering and delivery sub-system for gaseous and liquid hydrocarbons, and (3) analytical sub-system. The catalytic reactors were made out of a fused quartz or ceramic (alumina) in order to reduce the effect of the reactor material on the rate

of hydrocarbon decomposition. The reactor temperature was maintained at a constant temperature via a type K thermocouple and Love Controls microprocessor. Amount of carbon catalyst used in the experiments varied in the range of 0.03-5.0 g. Gaseous hydrocarbons flow rates varied from 5 ml/min to 2 l/min.

Gaseous hydrocarbons (methane, propane) were metered by flow meters, and liquid hydrocarbons were metered and delivered to the reactor by a syringe pump via a temperature-controlled evaporator. Gaseous products of hydrocarbon decomposition passed through a condenser (for separation of liquid byproducts), a filter (for separation of airborne carbon particles and aerosols) and were analyzed gas-chromatographically).

Analysis. The analysis of the products of methane decomposition was performed gas chromatographically: SRI- 8610A (a thermal conductivity detector, Ar carrier gas, a silicagel column, temperature programming from 27 to 180°C) and Varian-3400, FID, He-carrier gas, Hysep D_b. SEM studies were performed using Amray 1810 scanning electron microscope. XRD studies were conducted using Rigaku diffractometer with D/MAX 2200T/PC ULTIMA accessory. Polynuclear aromatic byproducts were analyzed spectrophotometrically (Shimadzu UV-2401PC).

Summary

The technical feasibility of CO₂-free production of hydrogen via one-step thermocatalytic decomposition of hydrocarbons was demonstrated. Methane, propane and gasoline were efficiently converted into hydrogen and carbon using carbon catalysts.

The catalytic activity and stability of more than 30 different forms and modifications of carbon were examined, and several of them were selected for further evaluation.

The effect of operational parameters on the H₂ yield was determined. H₂ concentration in the effluent gas varied in the range of 30-90 v.%, the balance being CH₄ and small amount of C₂⁺ hydrocarbons. CO or CO₂ were not detected among the products. Intermediate and byproducts of methane and propane decomposition reactions were identified and quantified.

The factors affecting carbon catalyst activity and long term stability in hydrocarbon decomposition reactions were studied. It was found that the surface area and crystallographic structure of carbon species mostly determine the catalytic activity of carbon catalysts. This was confirmed by XRD and SEM studies of carbon catalysts.

A kinetic model for methane decomposition over carbon catalysts was developed. Major kinetic parameters of methane decomposition reaction (rate constants, activation energies, etc.) over selected catalysts were determined.

Various conceptual designs for the thermocatalytic reactors suitable for simultaneous production of hydrogen and carbon were evaluated. The following reactors were built and tested: packed bed, tubular, fluidized bed, free volume and fluid wall reactors.

A bench-scale thermocatalytic fluidized bed reactor was designed and fabricated. The reactor was successfully tested using methane, propane, methane-propane mixture, and gasoline as feedstocks. Simultaneous production of hydrogen-rich gas (free of carbon oxides) and carbon was demonstrated.

Preliminary techno-economic assessment of the TCD process indicated that the thermocatalytic unit with the capacity of an average steam reforming plant would yield hydrogen at a cost of \$5.0/MMBTU (if carbon sold at \$100/t), which is less than that from steam reforming process coupled with CO₂ sequestration.

Comparative assessment of CO₂ emissions from different hydrogen production processes was conducted. It was shown that the TCD is the only fossil fuel based process which shows a real potential to be completely free of CO₂ emissions.

If cost effective processes of hydrogen production via decomposition of NG will be developed and implemented, there would be practically no environmental constraints on using fossil fuels on a large scale.

Current Year Publications:

1. "Hydrogen from Fossil Fuels without CO₂ Emissions", N. Muradov, in *Advances in Hydrogen Energy*, Kluwer Academic/Plenum Publishers, 2000, p.1-16
2. "On Perspectives of CO₂-free Production of Hydrogen from Hydrocarbon Fuels for Small Scale Applications", N. Muradov, *Symposium on Hydrogen Production, Storage and Utilization, 1999 ACS Meeting*, New Orleans
3. "Hydrocarbon-based Systems for CO₂-free Production of Hydrogen", N. Muradov, *13th World Hydrogen Energy Conference, Beijing, China, 2000*
4. "Compact Fuel Reformer for Mobile/Stationary Applications", N. Muradov, *Summit on Miniaturization of Energy, Chemical and Biomedical Systems*, Orlando, 1999
5. "Thermocatalytic Process for CO₂-free Production of Hydrogen and Carbon from Hydrocarbon Fuels", N. Muradov, U.S. Patent Application No. 60/194828, filed 04/05/2000, assignee: University of Central Florida

Acknowledgements

This work was supported by the U.S. Department of Energy and the Florida Solar Energy Center.

References

- Audus, H., O. Kaarstad, and M. Kowal. 1996. "Decarbonization of Fossil Fuels: Hydrogen as an Energy Carrier." In *Proceedings of 11th World Hydrogen Energy Conference*, 525. Stuttgart, Germany
- Blok, K., R. Williams, R. Katofsky, and C. Hendriks. 1997. "Hydrogen Production from Natural Gas, Sequestration of Recovered CO₂ in Depleted Gas Wells and Enhanced Natural Gas Recovery." *Energy*, 22: 161
- Calahan, M. 1974. "Catalytic Pyrolysis of Methane and Other Hydrocarbons." In *Proceedings of Conference on Power Sources*. 26: 181
- Diefendorf, R. 1960. *J. Chem. Physics*, 57, 3, 815
- Fulcheri, L., and Y. Schwob 1995. "From Methane to Hydrogen, Carbon Black and Water." *Int. J. Hydrogen Energy*, 20: 197
- Garrett, D. 1989. *Chemical Engineering Economics*. New York: Van Nostrand Reinhold

- Gaudernack, B., and S. Lynum. 1996. "Hydrogen from Natural Gas without Release of CO₂ to the Atmosphere." In *Proceedings of 11th World Hydrogen Energy Conference*, Stuttgart, Germany, 511-523.
- International Energy Agency. 1998. *Carbon Dioxide Capture from Power Stations*. IEA
- Kirk-Othmer Encyclopedia of Chemical Technology*. 1978. V. 4. New York: John Wiley & Sons
- Nakicenovic, N. 1993. "Energy Gases: The Methane Age and Beyond." *IIASA, Working Paper-93-033*, Laxenburg, Austria, 1-13
- Lynum, S., R. Hildrum, K. Hox, and J. Hugdabl. "Kvarner Based Technologies for Environmentally Friendly Energy and Hydrogen Production." In *Proceedings of 12th World Hydrogen Energy Conference, 697*. Buenos Aires, Argentina
- Muradov, N. 1993. "How to Produce Hydrogen from Fossil Fuels without CO₂ Emission." *Intern. J. Hydrogen Energy*, 18: 211
- Muradov, N. 1998. "CO₂-free Production of Hydrogen by Catalytic Pyrolysis of Hydrocarbon Fuel." *Energy & Fuels*, 12:41
- Muradov, N. 2000. "Hydrogen from Fossil Fuels without CO₂ Emissions." In *Advances in Hydrogen Energy*. New York: Kluwer Academic/Plenum Publishers
- Ogden, J., M. Steinbugler, and T. Kreutz. 1997. "Hydrogen as a Fuel for Fuel Cell Vehicles: a Technical and Economic Comparison." In *Proceedings of the *th Annual U.S. Hydrogen Meeting*, 469. Alexandria, VA: NHA
- Pourier, M., and C. Sapundzhiev. 1997. "Catalytic Decomposition of Natural Gas to Hydrogen for Fuel Cell Applications." *Intern. J. Hydrogen Energy*, 22:429
- Shpilrain, E., V. Shterenberg, and V. Zaichenko. 1999. "Comparative Analysis of Different Natural Gas Pyrolysis Methods." *Intern. J. Hydrogen Energy*, 24: 613
- Steinberg, M. 1999. "Fossil Fuel Decarbonization Technology for Mitigating Global Warming." *Intern. J. Hydrogen Energy*, 24: 771
- Tesner, A. 1987. *The Kinetics of Carbon Black Production*. VINITI: Moscow

List of Figures

Figure 1 - Methane Conversion Rate as a Function of Catalyst Surface Area

Figure 2 - Methane Decomposition over Different Carbon Catalysts at 850°C

Figure 3 - Methane Decomposition over Acetylene Black at 850°C

Figure 4 - Effect of Temperature (a) and Methane Space Velocity (b) on Methane Decomposition Yield.

Figure 5 - Experimental Data (circles) and Curve Fit Using the Kinetic Model (gray line)

Figure 6 - Arrhenius Plot for CH₄ Decomposition

Figure 7 - Propane Pyrolysis over CB (XC-72) (a) and AC (KE) (b) at 800°C

Figure 8 - XRD Spectra of Carbon Samples

Figure 9 - SEM Micrographs of Carbon Black (BP-2000) Sample Before (left, 1 μm scale) and After Exposure to Propane at 850°C for 3.5 h (right, 1 mm scale)

Figure 10 - Schematic Diagram of the Experimental Set-up with PBR (left) and FBR (right)

Figure 11 - Schematic Diagram of Free Volume Reactor

Figure 12 - Schematic Diagram of Fluid Wall Reactor

Figure 13 - Thermocatalytic Pyrolysis of Propane (a) and Gasoline (b) over CB (BP-2000) at 850°C Using FBR

Figure 14 - Simplified Flow Diagram of TCD Process for Production of Hydrogen and Carbon
1- FBR, 2- heater, 3- membrane, 4- grinder

Figure 15 - Comparative Assessment of Hydrogen Production Cost by SR and TCD Processes

Figure 16 – Comparison of CO₂ Emissions from Different Hydrogen Production Processes

SORPTION ENHANCED REACTION PROCESS (SERP) FOR THE PRODUCTION OF HYDROGEN

J. Hufton, W. Waldron, S. Weigel, M. Rao, S. Nataraj, S. Sircar
Air Products and Chemicals, Inc.
Allentown, PA 18195

Abstract

This paper summarizes recent progress in developing the Sorption Enhanced reaction Process for hydrogen production. Details of single-step reaction experiments and fully cyclic process experiments are described. It is demonstrated that enhanced H₂ product (higher purity, conversion) can be continuously produced during cyclic operation of the reactors. The reactor performance is improved by increasing the reactor temperature, steam/methane ratio, or purge amount, or by decreasing the reactor pressure. The data generated by the cyclic process unit is currently being used to generate an H₂-SER process design for fuel cell applications.

Introduction

The goal of this work is to develop a novel, more cost-effective steam-methane reforming (SMR) process for the production of hydrogen. The overall SMR reaction is given by:



The novel concept is called the Sorption Enhanced Reaction Process (SERP). The reactants, steam and methane, are fed at 450-550°C and 10-50 psig into a tubular reactor containing an admixture of reforming catalyst and an adsorbent for removing carbon dioxide from the reaction zone. A reactor effluent consisting of enriched hydrogen (~90%) is directly produced during this step. The primary impurity is methane with relatively low levels (ppm) of carbon oxides. Once the adsorbent is saturated with CO₂, it is regenerated in situ by using the principles of pressure swing adsorption (PSA) at the reaction temperature.

The potential benefits of producing H₂ by the SERP concept are:

1. reforming at a significantly lower temperature (400-500°C) than a conventional SMR process (800-1000°C), while achieving high conversion of methane to hydrogen
2. production of hydrogen at feed gas pressure (10-50 psig) and at relatively high purity directly from the reactor (e.g., 90% H₂, 10% CH₄, < 0.5% CO₂, < 50 ppm CO on a dry basis)
3. significant reduction or even elimination of downstream hydrogen purification steps
4. reduction of CO in the SER reactor effluent to ppm levels - elimination of shift reactors
5. minimization of side reactions, e.g., coking
6. reduction of the excess steam used in conventional SMR.

Key program objectives for the cooperative APCI/DOE SER Project during the current year are listed below:

1. Demonstrate the H₂-SER process under cyclic operation and characterize performance with respect to important operation parameters
2. Refine H₂-SER designs and evaluate process economics
3. Scale-up production of the proprietary high temperature adsorbent with an external vendor

Experimental Systems

Most of the experimental equipment used to characterize the performance of various CO₂ adsorbents and for investigating the H₂-SER process steps has been described by Hufton et al. (1997; 1998; 1999) and Mayorga et al. (1997). Adsorbent screening is performed with a thermal gravimetric adsorption unit (for measurement of dry CO₂ working capacity), a binary desorption unit (to determine CO₂ capacity in steam environments), and a hydrothermal stability unit (to

assess physical and chemical stability of adsorbents in steam/CO₂ mixtures at elevated temperatures). Single-step reaction experiments and adsorption breakthrough experiments have been carried out in an electrically-heated fixed bed tubular reactor (SER#1) system. This unit can be used to investigate individual steps of the process, rather than the fully cyclic operation of an industrial SER process unit.

This year we built and operated three new pieces of equipment. A major investment of both time and (APCI) capital was focussed on construction of a process test unit (SER#2) required to demonstrate the H₂-SER process under cyclic operation conditions. A schematic and photograph of this unit was given by Hufton et al. (1999), along with a detailed description of the system. Unlike the current SER#1 lab unit, the SER#2 system permits study of the full sequence of SER process steps, performed in repetitive fashion, in a pair of industrial-scale tubular reactors at relatively high feed/purge flow rates (feed G-rates up to 30 lbmole/hr-ft²). These steps include high pressure reaction, countercurrent depressurization, countercurrent subatmospheric purge with steam or steam/H₂, and repressurization with steam or steam/H₂. Analytical equipment permits evaluation of effluent gas compositions, temperature, pressure, and flow rates, which ultimately can be used to evaluate the CH₄ conversion, H₂ product purity, and H₂ productivity with respect to important process variables.

The Cyclic Lifetime Unit (CLU) was built in the lab to enable evaluation of the long-term stability of the CO₂ adsorbent during repetitive cyclic exposure to SER reaction and regeneration conditions (i.e., 250 psig steam/N₂ followed by depressurization and purge with 10 psig N₂, all at 400-550C). The unit was automated and routinely operated 24 hours a day. The experimental approach was to place a sample of adsorbent into the unit, expose it to a sequence of reaction/regeneration steps (e.g., 1000 steps), remove the sample and compare its adsorption properties with fresh material.

The last piece of equipment was used to characterize the heat of adsorption of CO₂ on the CO₂ adsorbent at 400-500C. It consisted of an isolated vessel submerged in a temperature-controlled fluidized sand bath. Adsorbent was placed within the vessel, regenerated at 500C with N₂, evacuated, and then dosed with a known amount of CO₂. By isolating the CO₂-containing vessel and changing the temperature, one could monitor the change in CO₂ pressure via a pressure transducer. These P-T data were then analyzed to evaluate the heat of adsorption associated with the experimental CO₂ adsorption capacity.

Results and Discussion

H₂-SER Process Experiments

The process steps utilized in the H₂-SER process are listed in Table 1. An industrial system would utilize two or more reactors in parallel, each subjected to the process steps, but staggered in time so constant feed and product streams would be produced.

Table 1. H₂-SER Process Steps.

- 1. Sorption-Reaction Step:** The reactor is initially presaturated with a mixture of steam and H₂ at the desired reaction temperature and pressure. Steam and methane at a prescribed ratio (e.g., 6:1) are fed to the reactor and an enriched H₂ product (~90% purity) is collected as the reactor effluent. The reaction step is continued up to the point when the H₂ purity in the product decreases to a preset level. The feed is then diverted to a second identical reactor.
- 2. Depressurization Step:** The reactor is countercurrently depressurized. The effluent gas can be recycled as feed to another reactor or used as fuel.
- 3. Purge Step:** The reactor is countercurrently purged with a mixture of 5-10% H₂ in steam to desorb the CO₂. The desorption pressure may range between 0.2 and 1.1 atmospheres. The desorbed gas consists of CH₄, CO₂, H₂ and H₂O and is used as fuel after removing H₂O via condensation.
- 4. Pressurization:** The reactor is countercurrently pressurized to the reaction pressure with the steam / H₂ mixture. At this point, the regeneration of the reactor is complete and it is ready to undergo a new cycle.

Experiments with Ni-based catalyst

Hufton et al. (1999) presented experimental results which demonstrated the concept of H₂-SER in the single-step SER#1 test unit. These experiments were not cyclic, rather they focused on the reaction step of the process. The laboratory reactor was packed with a 1:1 (wgt) mixture of CO₂ adsorbent and Ni-based catalyst and heated to 450C. After reducing the catalyst with H₂, the reactor was saturated with a mixture of 20% H₂ / 80% steam, and then fed a feed gas of 14% methane in steam. Reactor performance was evaluated by measuring the effluent gas composition and flow rate during the experiment and using these data to calculate the CH₄ conversion and amount of H₂ produced. The reactor produced 0.8 mmole of H₂ product per g of solid at an average purity of 96% H₂, 4% CH₄, and less than 50 ppm CO + CO₂. The methane conversion to H₂ product reached 82%. The conversion and product purity were substantially higher than the thermodynamic limits for a catalyst-only reactor at these same conditions (28% conversion, 53% H₂, 34% CH₄, 13% CO/CO₂).

The next major task for development of the H₂-SER technology was to demonstrate the continuous production of H₂ under completely cyclic operating conditions. These tests were carried out this year with the SER#2 test unit. A 2:1 mixture of CO₂ adsorbent / Ni-based catalyst was packed into both reactors and subjected to the process steps of Table 1. The reaction feed gas was 6:1 steam/methane (S/C) and the reaction was carried out at 450C, 50 psig. At the specific conditions of the experiments, a product gas consisting of 71-75% H₂ was produced at a methane conversion of 33-37%. The amount of H₂ produced per unit mass of solid (adsorbent and catalyst) was only ~0.15 mmole/g. Although the H₂ production was enhanced in these experiments (equilibrium H₂ mole fraction is 53% and CH₄ conversion is 28% at these

conditions), it was clear that the results were not nearly as good as expected from the single-step experiments.

Further investigation of the Ni-based catalyst in the non-cyclic laboratory unit (SER#1) showed that the fully reduced nickel catalyst can remove significant quantities of CO₂ from the reaction gas in addition to the CO₂ adsorbent. Therefore, the nickel catalyst contributes to the SER effect during the reaction experiments. Although the form of CO₂ on the catalyst was not determined, it cannot be effectively removed by purging with N₂. Hydrogen is required to remove the CO₂ as CH₄. Since this is not acceptable for the H₂-SER process, efforts were directed towards identification of an alternative catalyst material.

Single-step experiments with alternative catalyst

An alternative catalyst was found and tested in the SER#1 test unit. Catalyst-only experiments clearly revealed that it did not adsorb CO₂, nor did it induce an SER effect when exposed to steam and methane. Since the material appeared promising, an extensive series of experiments, with both the single step and cyclic test units, was initiated. The rest of the experiments described in this report will deal with mixtures of CO₂ adsorbent and the alternative catalyst.

Mixtures of CO₂ adsorbent and alternative catalyst, in weight ratios of 1:2, 1:1, and 2:1, were sequentially tested in the single-step SER#1 unit. The influence of reaction temperature, pressure, and feed gas S/C ratio were evaluated, and the results are presented in Table 2. The base case experiment was conducted at 450C, 55 psig, and with a 6:1 steam/methane feed gas. Effluent gas was collected until the average H₂ composition dropped to 85%. At that point, a total of 0.56 mmoles of H₂ / g of solid had been collected (referred to as the H₂ productivity), and the effective CH₄ conversion to H₂ product (defined as moles H₂ produced / 4 / moles CH₄ fed) was 54%. Both the CH₄ conversion and H₂ productivity declined sharply when the reaction pressure was increased to 155 psig or the feed gas S/C ratio was decreased to 3:1. Conversely, the CH₄ conversion and H₂ productivity both increased significantly when the temperature was raised to 500C. Thus, one can conclude that the reaction step performance is favored by higher temperature, higher S/C ratio, and lower pressure. These are the same effects which tend to increase the conversion of the overall reforming reaction.

Table 2. Results of Single-Step Reaction Experiments with 2:1 adsorbent / alternative catalyst.

| Conditions | H ₂ Purity (%) | CH ₄ Conversion (%) | H ₂ Productivity (mmole H ₂ /g solid) |
|---------------------------------|---------------------------|--------------------------------|---|
| 6:1 S/C, 55 psig, 450C | 85 | 54 | 0.56 |
| 6:1 S/C, 155 psig , 450C | 85 | 24 | 0.08 |
| 3:1 S/C , 55 psig, 450C | 85 | 20 | 0.05 |
| 6:1 S/C, 55 psig, 500C | 85 | 59 | 0.78 |

The next set of single-step reaction experiments was designed to investigate the effect of adsorbent / catalyst ratio on reaction step performance. The data in Table 3 show that the amount of 80% H₂ product is consistent between all of the experiments if the productivity is normalized by the amount of adsorbent in the reactor. This indicates that the amount of adsorbent in the reactor is largely responsible for determine how much H₂ will be generated. It will therefore be beneficial to use a high adsorbent / catalyst ratio in the SER reactors (up to the point where catalytic limitations become important).

Table 3. Results of Single-Step Reaction Experiments with 1:2, 1:1, and 2:1 adsorbent / alternative catalyst.

| Reactor Mixture | H ₂ Purity (%) | H ₂ Productivity (mmole H ₂ / g solid) | H ₂ Productivity (mmole H ₂ / g adsorbent) |
|-----------------|---------------------------|--|--|
| 1 ads : 2 cat | 80 | 0.33 | 1.0 |
| 1 ads : 1 cat | 80 | 0.44 | 0.9 |
| 2 ads : 1 cat | 80 | 0.75 | 1.1 |

Cyclic experiments with alternative catalyst

Thirty six cyclic H₂-SER process experiments were conducted in the SER#2 test unit using a reactor packed with 2:1 adsorbent / alternative catalyst mixture. The cycle steps of Table 1 were used except H₂ was omitted from steps 3 and 4. A typical experiment was carried out at 490C with 6:1 S/C feed gas at 50 psig, followed by regeneration with steam at 5 psia. In all of the runs, the average H₂ product purity was maintained at ~88% by adjusting the reaction and purge times. The effect of reaction pressure, temperature, feed S/C ratio, and purge amount on the cyclic steady-state H₂ productivity (defined at 88% H₂ for the rest of this report) was evaluated.

In all of the cyclic experiments, more H₂ is produced from the feed methane than would be by a catalyst-alone reactor (predicted by reaction thermodynamics), and it is of higher purity. The major contaminant in the SER H₂ product is CH₄, with typically less than 0.5% CO₂ (and very often nondetectable, or less than 50 ppm) and typically non-detectable (< 50 ppm) levels of CO. For reference, a catalyst-only system would yield 67.5% H₂, 16.0% CO₂, 12,000 ppm CO, balance CH₄ for operation at 490C, 6:1 S/C, 10 psig.

The effects of reaction pressure and temperature on the normalized H₂ productivity (for ~88% average H₂ product) are illustrated in Figures 1 and 2 for 6:1 S/C feed gas. A fixed amount of purge gas was used. Decreasing the feed gas pressure and increasing the reactor temperature increases the cyclic steady-state H₂ productivity. These trends are consistent with the results obtained from single-step experiments. They are opposite the trends normally observed for conventional pressure swing adsorption (PSA) systems used for bulk separations, where generally decreasing the feed gas pressure and increasing the temperature yields lower adsorption capacity and bed productivity. The difference is believed to be due to the influence of the reforming reaction - lower pressure / higher temperature increase the amount of CO₂ formed in the

equilibrium zone of the reactor, making it easier to remove a larger fraction of that CO₂ and hence drive the reforming reactions towards completion. Higher temperatures can also improve the efficiency of desorbing CO₂ from the adsorbent, which may also have a role in increasing the H₂ productivities in Figure 2.

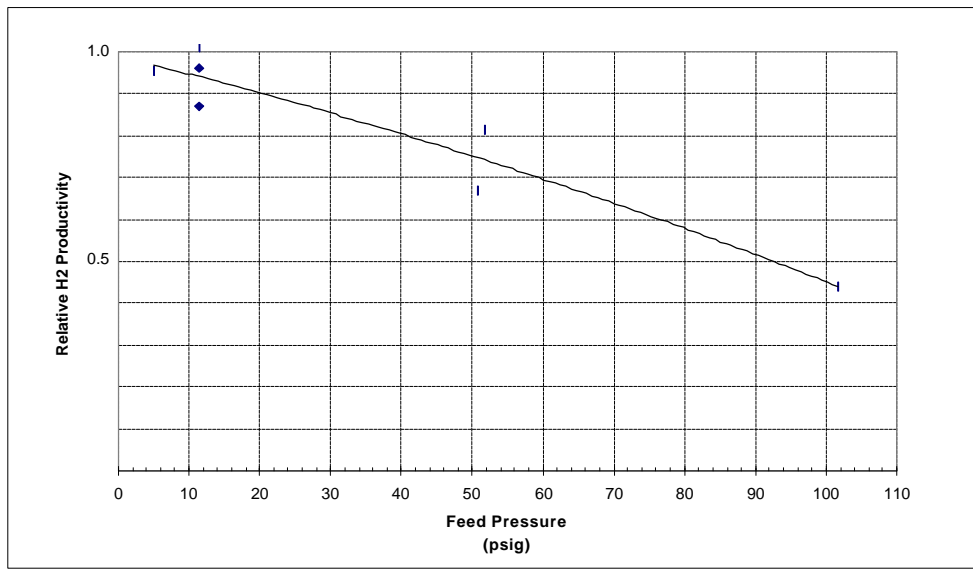


Figure 1. Effect of Feed Pressure on Cyclic H₂ Productivity for H₂ Product of 88% average Purity; 2:1 adsorbent / catalyst, 490C, 6:1 S/C feed.

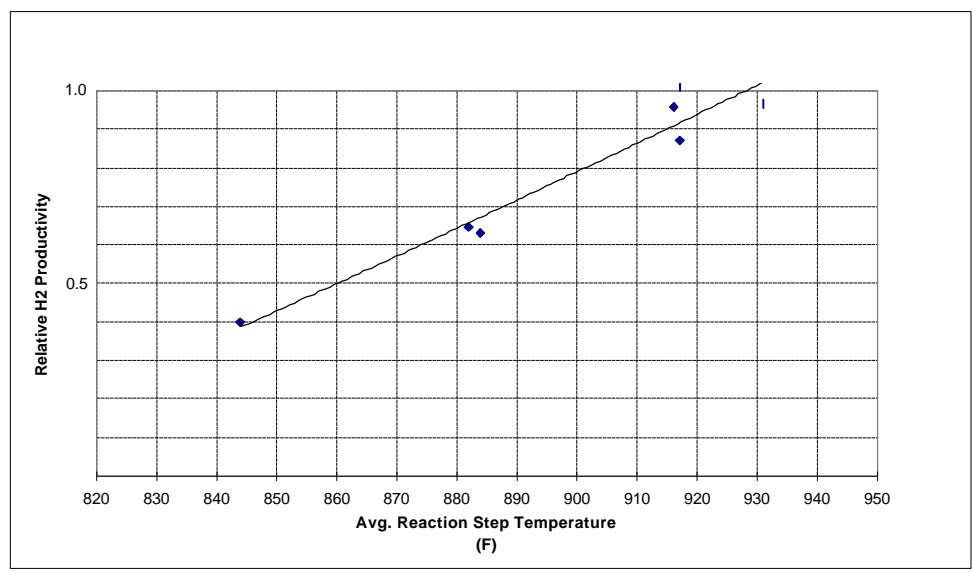


Figure 2. Effect of Feed Temperature on Cyclic H₂ Productivity for H₂ Product of 88% average Purity; 2:1 adsorbent / catalyst, 6:1 S/C feed, 10 psig.

Increasing the S/C ratio of the reaction step feed gas improves the H₂ productivity, as evidenced by the 4:1 and 6:1 S/C data in Figure 3 (plotted on a relative basis). This is also consistent with the results of the SER#1 single-step reaction experiments (Figure 1).

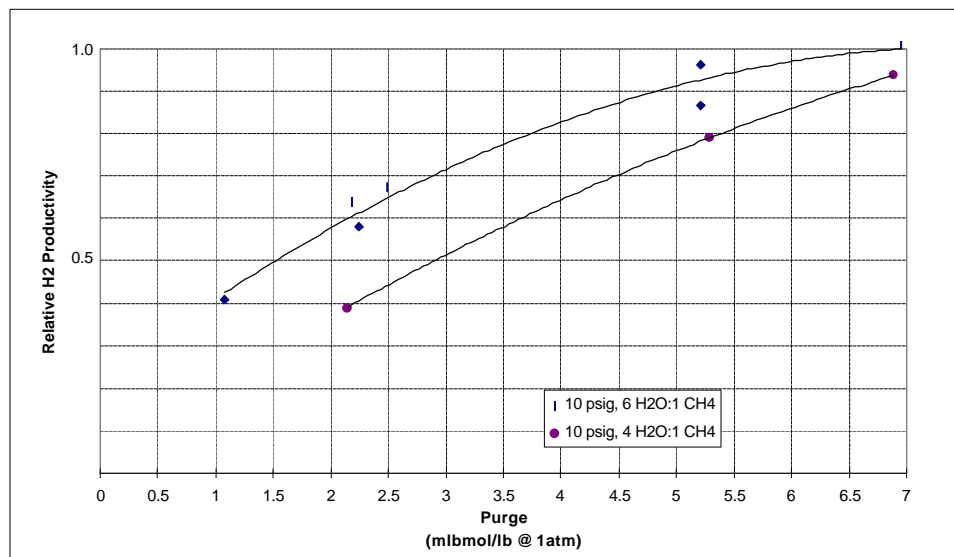


Figure 3. Effect of Purge Amount on Cyclic H₂ Productivity for H₂ Product of 88% average Purity; 2:1 adsorbent / catalyst, 10 psig, 490C.

Figure 3 also shows that increasing the amount of purge gas can substantially increase the H₂ productivity for a given S/C ratio. Increasing the amount of purge removes more CO₂ from the adsorbent and cleans the product-end of the reactor more thoroughly, so it is not surprising that this improves reactor performance. The benefit of increasing the purge amount declines as higher purge amounts are approached.

In summary, the above data shows that the H₂-SER process concept works under cyclic conditions to yield relatively high purity (~88%) H₂ product containing very low CO₂ and CO levels. The H₂ productivity of the SER reactor can be increased by increasing the reaction temperature, S/C feed ratio or purge amount, or by decreasing the reaction pressure. These trends are consistent with the results of single step reaction experiments carried out in the SER#1 unit.

Process Design and Economic Evaluation

Hufton et al. (1999) compared the economics of a conventional H₂ production process with first pass H₂-SER process designs and noted that product cost savings of 15-30% were possible depending on plant size and H₂ purity requirements. The SER design was based on previous single-step reaction experiments and a number of engineering assumptions. The H₂ purity, conversion, and H₂ productivity used to generate the process design were 95%, 72%, and 1.1 mmole H₂/g solid, respectively. Cyclic performance parameters were not available, and the SER#2 test unit was built primarily to test these assumptions.

Now that cyclic process data are available, it is logical to revise the old process designs with the new input parameters. Although the cyclic data show that the SER concept is working, the performance is not nearly as good as assumed in the earlier designs. Typical H₂ purity, conversion, and H₂ productivity values obtained from the SER#2 tests are 88%, ~55-65%, and ~0.2 - 0.3 mmole/g solid.

The impact of these new parameters on the SER process was determined by generating H₂-SER process designs for the production of high purity (99.5%), high pressure (200-800 psig) H₂ product. Production levels of 0.2 and 22 MM SCFD H₂ were investigated. Since high purity H₂ was desired (and therefore a PSA separation unit was needed), it was assumed that the H₂-SER reaction step was carried out at 250 psig, with a 3:1 S:C feed gas. The economics of the first-pass, revised process design were found to be noncompetitive with conventional technology.

The major difficulty in developing a cost effective H₂-SER process for high pressure, high purity applications is due to some of the inherent characteristics of the SER process. Although the H₂-SER unit can directly produce higher purity H₂ than a conventional catalyst-only reactor, it is not high enough to satisfy high purity customers (99.9+%). Thus, a PSA unit is required to purify the SER effluent gas. The PSA adds a ~15% recovery loss to the process, and also requires that the feed gas be at an elevated pressure. More importantly, the requirement for high pressure product gas requires either operation of the SER unit at high pressure (where performance is poor) or use of a relatively expensive compressor to pressurize SER effluent gas produced at low pressure. Either approach adds cost to the system. It is also possible to improve the SER performance by increasing the S/C ratio of the feed gas and increasing the amount of purge gas (steam) during regeneration. Both of these require the use of more steam, which increases the operating cost for the process (especially large plants) and decreases the thermodynamic efficiency.

Thus, the best application for SER would be one where the SER effluent gas could be used directly (i.e., ~90% H₂ purity is acceptable), the product pressure can be low (~10 psig), and steam costs are not necessarily a major cost item (smaller scale production units). These characteristics are consistent with fuel cell applications. In this case, the H₂ product gas is used at relatively low pressure, impure H₂ (50-90%) is acceptable as long as the CO level is kept low (<10 ppm), and the applications are typically small capacity (~0.1-0.2 MM SCFD)). Our future development efforts will be focused on this application.

CO₂ Adsorbent Development

Long range supply of the promoted K₂CO₃/hydrotalcite CO₂ adsorbent relies on the manufacture

of the activated adsorbent by an external vendor. We have been working with two separate vendors of the HTC support to help develop an approach for producing an acceptable adsorbent. We interacted closely with our primary vendor to help solve a number of problems associated with extruding the promoted adsorbent. Eventually they were able to produce 160 lbs of the promoted extrudate using a 4" pilot extruder. This material showed a lower CO₂ capacity than the lab-generated material, although the steam stability, crush strength, and aging profile were acceptable. The vendor is not concerned with scaling the production up to a 6" commercial extruder, which would be capable of supplying projected commercial volumes.

We have also engaged a second vendor in case the first fails to deliver [commercially or technically]. This vendor produced formed adsorbent in the lab in both extrudate and tablet forms. The lab tablets have similar crush strength and steam stability as benchmark extrudates and adequate CO₂ adsorption capacity. The pilot sample was not as successful, however, and was deficient in CO₂ capacity & crush strength after steaming. The second vendor now believes it was due to a change in the recipe where the hydrotalcite tablets were exposed to K₂CO₃ for an extended period of time, affecting the products more than expected. Two new samples have been recently received and are being evaluated in our lab (one of which has > 2X the targeted CO₂ capacity).

A critical requirement for the CO₂ adsorbent is that it remain stable over many adsorption-desorption cycles. Adsorbent stability was tested by repetitively exposing the adsorbent in the CLU to 34:1 steam:CO₂ at 250 psig for 20 mins followed by 5 mins of N₂ purge at atmospheric pressure. The testing was done at 450C. The adsorbent was periodically removed from the test apparatus and the equilibrium CO₂ capacity was determined at 450C and 0.7 atm CO₂. The results, illustrated in Figure 4, show that the adsorbent was indeed stable, and maintained an equilibrium CO₂ capacity of 0.3-0.45 mmol/g over nearly 6000 cycles.

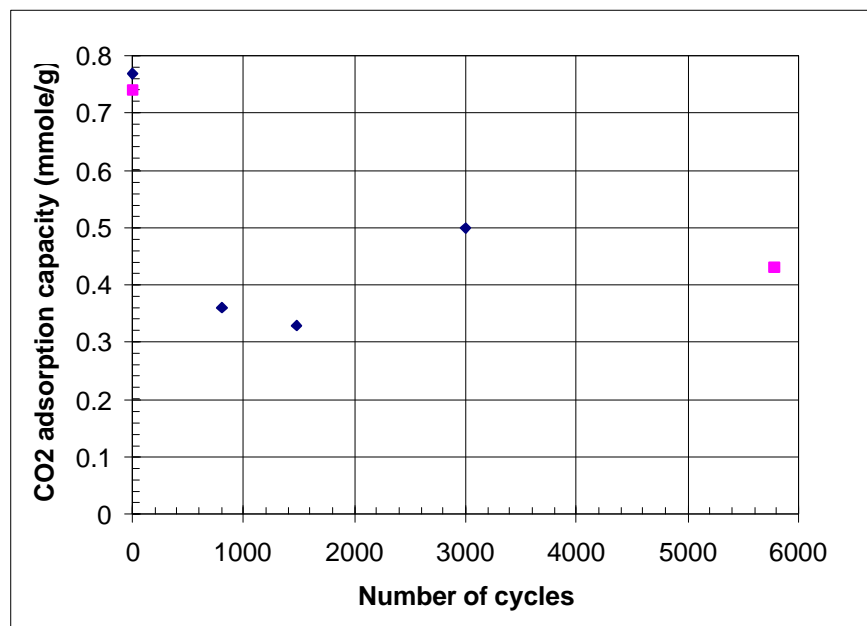


Figure 4. CO₂ Adsorption Capacity Measured after Repetitive Cycling in Steam.

Future Work

Future efforts will be directed towards the development of an H₂-SER process to satisfy the requirements of fuel cell applications. Process designs will be generated based on the cyclic process data from SER#₂ and evaluated against conventional technologies.

We are also planning some experiments to gain more fundamental knowledge regarding the interplay of adsorption and reaction in the SER process. We would like to determine the root cause of the immediate appearance of methane in the H₂ product gas (even though reaction kinetics and mass transfer kinetics have been determined to be very fast). Greater insight may lead to modifications which could potentially improve the SER process performance.

Acknowledgments

The authors wish to thank J. Zenon, R. Meyers, and J. Brzozowski for performing most of the experiments described in this report. Thanks are also due to R. Tsao for carrying out the economic analysis, P. Tsui and M. Rodgers for assisting with adsorbent development efforts, and B. Casas, T. Gosling, and K. Fabregas for SER#₂ construction efforts.

References / Publications / Patents

- Anand, M., J. Hufton, S. Mayorga, S. Nataraj, S. Sircar, T. Gaffney, "Sorption Enhanced Reaction Process (SERP) for Production of Hydrogen", *Proceedings of the 1996 U.S. DOE Hydrogen Program Review*, **1**, 537 (1996).
- Anand, M., Sircar, S., and Carvill, B.T., "Processes for Operating Equilibrium Controlled Reactions," 271PUS04904, U.S. Patent Pending (1995).
- Carvill, B.T., Hufton, J.R., Anand, M., and Sircar, S., "Sorption Enhanced Reaction Process," *AICHE J.*, **42**, 2765 (1996)
- Hufton, J.R., Mayorga, S.G., and Sircar, S., "Sorption Enhanced Reaction Process for Hydrogen Production," *AICHE J.*, **45**, 248 (1999).
- Hufton, J.R., S. Mayorga, T. Gaffney, S. Nataraj, and S. Sircar, 'Sorption Enhanced Reaction Process for Production of Hydrogen,' Proceedings of the 1997 U.S. DOE Hydrogen Program Review, 179 (1997).
- Hufton, J.R., S. Mayorga, T. Gaffney, S. Nataraj, M. Rao, and S. Sircar, 'Sorption Enhanced Reaction Process for Production of Hydrogen,' Proceedings of the 1998 U.S. DOE Hydrogen Program Review, 693 (1998).
- Hufton, J.R., S. Weigel, W. Waldron, S. Nataraj, M. Rao, and S. Sircar, 'Sorption Enhanced Reaction Process for Production of Hydrogen,' Proceedings of the 1999 U.S. DOE Hydrogen Program Review (1999).
- Mayorga, S. G., Golden, T. C., Gaffney, T. R., Brzozowski, J. R., and Taylor, F. W., "Carbon Dioxide Pressure Swing Adsorption Process Using Modified Alumina Adsorbents," U. S. Patent Pending (1996).
- Mayorga, S.G., J. R. Hufton, S. Sircar and T.R. Gaffney, 'Sorption Enhanced Reaction Process for Production of Hydrogen', Phase 1 Final Report, U.S. Department of Energy, July 1997.
- Nataraj, S.N., Carvill, B.T., Hufton, J.R., Mayorga, S.M., Gaffney, T.R., and Brzozowski, J.R., "Process for Operating Equilibrium Controlled Reactions," 271PUS05548, U.S. Patent Pending (1996).
- Sircar, S., Anand, M., Carvill, B.T., Hufton, J.R., Mayorga, S.G., and Miller, R.N., "Sorption Enhanced Reaction Process for Production of Hydrogen," *Proceedings of the 1995 U.S. DOE Hydrogen Program Review*, **1**, 815 (1995).
- Sircar, S., Hufton, J.R. and Nataraj, S., "Process and Apparatus for the Production of Hydrogen by Steam Reforming of Hydrocarbon", 271PUS05829, U.S. Patent allowed (1999).

ITM SYNGAS AND ITM H2

ENGINEERING DEVELOPMENT OF CERAMIC MEMBRANE REACTOR SYSTEMS FOR CONVERTING NATURAL GAS TO HYDROGEN AND SYNTHESIS GAS FOR LIQUID TRANSPORTATION FUELS: DE-FC26-97FT96052

**Paul N. Dyer and Christopher M. Chen
Air Products and Chemicals Inc.
7210 Hamilton Boulevard
Allentown, PA 18195 - 1501**

Abstract

Air Products, in collaboration with the United States Department of Energy (U.S. DOE) and other members of the ITM Syngas Team, is developing ceramic membrane technology for the generation of hydrogen and synthesis gas. These membranes are non-porous, multi-component metallic oxides that operate at high temperatures and have exceptionally high oxygen flux and selectivity. Such membranes are known as Ion Transport Membranes (ITMs).

The ITM H2 process is a potential break-through technology that could have a major impact on the cost of distributed hydrogen, especially in the range of 0.1 to 1 MMSCFD. Initial estimates indicate the potential for a significant reduction in the cost of high pressure hydrogen produced by this new route, compared with the cost of trucked-in liquid hydrogen. A successful development of the ITM

technology could be important to emerging hydrogen markets such as hydrogen-based fuel cells for transportation.

Synthesis gas is an important intermediate product required for the production of liquid transportation fuels from natural gas. Preliminary cost estimates indicate that ceramic membrane reactors could decrease the capital cost for syngas by more than one third. This reduction would have a very significant impact on the costs of liquid transportation fuels derived from natural gas.

The major goals of the ITM Syngas and ITM H₂ development program are summarized in this paper, and the progress of the ITM Syngas Team in successfully meeting those goals and objectives is described.

Introduction

Hydrogen is an important industrial gas with many existing and future applications. Current production technology is typically through the steam reforming of natural gas or, for lower requirements, the purification of off-gas from, for example, refineries. Purified hydrogen can be liquefied and transported to the point of use and vaporized. This is currently the most economic source for hydrogen when the requirement is modest. For larger supply requirements, for example greater than 1 to 10 MMSCFD, on-site steam reforming is typically more cost effective.

Air Products and Chemicals in collaboration with the United States Department of Energy (US DOE) and others is developing a potential break-through technology that could have a significant impact on the cost of hydrogen, especially in the range of 0.1 to 1 MMSCFD. If successful, this technology could be important to emerging hydrogen markets such as hydrogen-based fuel cells for transportation [1].

The new technology utilizes non-porous ceramic membranes that are fabricated from multi-component metallic oxides that conduct both electrons and oxygen ions at high temperatures (greater than approximately 700 °C). These types of membranes are known as ITMs, and are of special interest because the oxygen ions permeate at a very high flux rate and with infinite selectivity. The oxygen can be separated from air fed to one side of the membrane at ambient or moderate pressure, and reacted on the other surface with natural gas at a higher total pressure to form a mixture of H₂ and CO.

A schematic of the membrane is illustrated in Figure 1. The membrane structure is complex incorporating both the non-porous ITM and oxygen reduction and syngas reforming catalyst layers.

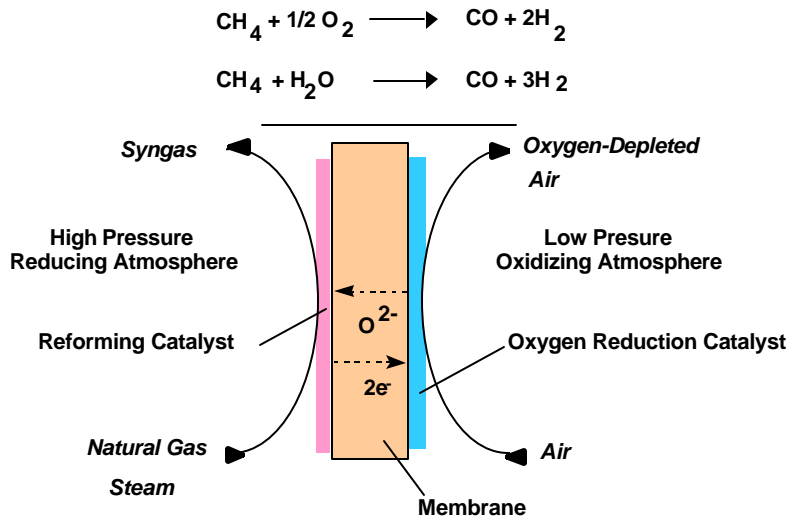


Figure 1 - Functions of the ITM Syngas/ITM H2 membrane

Oxygen from a hot air stream is reduced to oxygen ions which flow through the membrane where, in combination with a reforming catalyst, they partially oxidize a pre-reformed mixture of hot natural gas and steam, thereby forming syngas, a combination of carbon monoxide and hydrogen. The ratio of hydrogen to carbon monoxide is in part dependent upon the amount of steam. The membrane material must show long-term stability in reducing and oxidizing atmospheres, and long-term compatibility with the oxygen reduction and reforming catalysts.

ITM Syngas and ITM H2 Development Program

The ITM H2 and ITM Syngas technology is being developed in an eight year, \$86 MM development program supported by the US DOE. The objective of the program is to research, develop and demonstrate a novel ceramic membrane reactor system for the low-cost conversion of natural gas to synthesis gas and hydrogen for liquid transportation fuels: the ITM Syngas and ITM H2 processes [2 - 6].

ITM Syngas / ITM H2 is a complex new technology whose successful progress toward a commercial process requires a mix of closely integrated, unique technical and commercial capabilities. Air Products has assembled a highly qualified team from industry, national laboratories, and universities. The ITM Syngas team comprises leading ionic ceramic material scientists, experienced ceramic fabrication technologists, process, design, structural and reaction modeling engineers, and commercial experts. Our team includes;

Air Products and Chemicals, Inc., Ceramatec Inc., Chevron, Eltron Research Inc., McDermott Technology Incorporated, Norsk Hydro, Pacific Northwest National Laboratory, Pennsylvania State University, the University of Alaska, and the University of Pennsylvania.

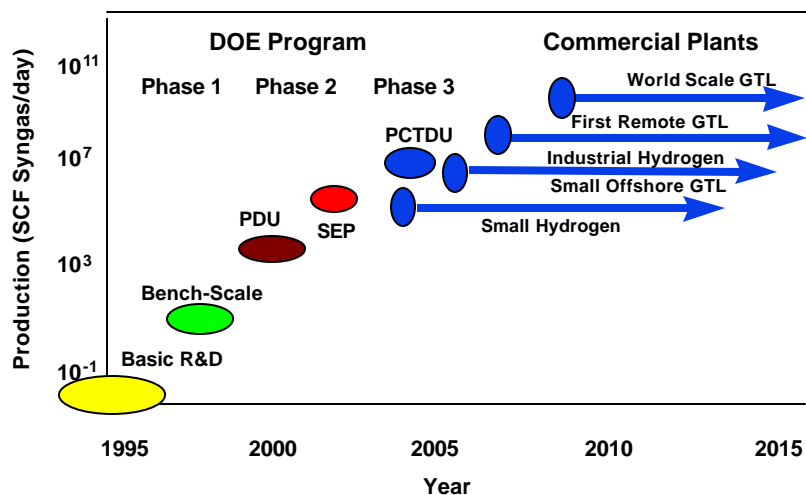


Figure 2 - The Development Schedule for ITM Syngas / ITM H2

The overall development schedule, from laboratory feasibility studies to commercialization, is aggressive and is illustrated in Figure 2. The program has completed Phase 1 and is now beginning Phase 2 with the design and construction of a nominal 24 MSCFD Process Development Unit (PDU).

Phase 1 - ITM Materials and Process R&D

Phase 1 (2.5 years) was divided into three tasks, and studied engineering fundamentals and evaluated materials, ceramic membrane and process concepts at the bench-scale level.

Task 1.1 Process Engineering and Economics

In this task, Air Products, Chevron, Norsk Hydro, and McDermott developed specific process designs and evaluated process economics. The University of Alaska gave input on operations specific to the Alaskan environment. The results were used to set objectives for the development of ITM Syngas and ITM H₂ materials.

Task 1.2 Materials and Seals Development

Air Products, Ceramatec, Eltron Research and Penn State jointly performed the materials development to achieve the required performance and stability at process conditions. Ceramatec produced ITM powder and laboratory test samples for the materials development tasks. Air Products, Ceramatec and PNNL developed high-temperature seals. Eltron Research and Air Products tested the performance of

various ITM materials and seals at pressure in laboratory-scale reactors. Penn State University evaluated mechanical properties, and the University of Pennsylvania provided input on materials.

Task 1.3 ITM Syngas Reactor Design and Engineering

McDermott, Ceramatec and Air Products designed the conceptual ITM membrane and reactor. Ceramatec developed the membrane fabrication process, and produced sub-scale thin film membrane samples. Air Products and McDermott designed and engineered a reactor vessel for a nominal 24 MSCFD PDU which will utilize sub-scale membrane modules.

At the end of Phase 1, a selection was made for further development of the ITM material/catalyst combinations, the membrane seals, and the membrane reactor design. Process economic and performance data were evaluated, and the decision was made to proceed with the scale-up in Phase 2.

Phase 2 - Engineering and Development of an ITM Syngas / ITM H2 PDU and SEP

Phase 2 (3.5 years) will validate process concepts in two stages of scale-up, and create an engineering, operating and economic database.

Task 2.1 Commercial Plant Economic Evaluation

An advanced ITM Syngas and ITM H2 process will be developed, and the economics of operation at the commercial plant scale will be evaluated by Air Products, Chevron, McDermott and Norsk Hydro, based on the results of the Phase 2 program.

Task 2.2 Materials and Seals Development and Evaluation

The combined ITM Syngas testing facilities of Air Products and Eltron Research will be utilized to obtain statistical performance and lifetime data under process conditions for the ITM Syngas materials and seals, fabricated by Ceramatec.

Task 2.3 ITM Syngas Membrane and Module Design and Fabrication

Air Products, McDermott and Ceramatec will carry out the detailed design of the membrane, modules and manifolding for the ITM Syngas reactor. Ceramatec will scale up the fabrication of the ceramic membrane reactor modules in a Processing Development Facility (PDF) to supply the requirements of the SEP.

Task 2.4 Nominal 24 MSCFD ITM Syngas PDU

The components of the ITM Syngas and H2 technology will be demonstrated in a laboratory PDU. The PDU will operate at up to an equivalent of 24 MSCFD of syngas capacity, and will be used to performance test sub-scale membranes under process operating conditions for the H2 production and syngas /GTL applications.

Task 2.5 Nominal 500 MSCFD ITM Syngas SEP

A Sub-scale Engineering Prototype (SEP) Unit will be built to demonstrate the ITM Syngas and H₂ technology using full-size membranes in sub-scale modules. The SEP will demonstrate the operation of the ITM Syngas and ITM H₂ processes at up to an equivalent of 500 MSCFD of syngas capacity.

Phase 3

Phase 3 (2 years) will demonstrate the production of syngas from an approximately 15 MMSCFD Pre-Commercial Technology Demonstration Unit (PCTDU) using the ITM Syngas process.

Current Year Tasks

The tasks for the fiscal year 2000 included the completion of Phase 1 and the initiation of Phase 2. Specific objectives for the current year can be summarized as follows:

- Complete the Phase 1 process designs and economic evaluations for ITM Syngas and ITM H₂ processes (Air Products, Chevron, McDermott, Norsk Hydro, University of Alaska).
- Develop and demonstrate, under process conditions at the laboratory scale, stable ITM material and seals for syngas and hydrogen production (Air Products, Ceramatec, Eltron Research, Penn State University and University of Pennsylvania)
- Demonstrate sub-scale thin membranes in reducing conditions (Air Products, Ceramatec, Eltron Research)
- Select and develop the ITM membrane and reactor vessel design for scale-up in Phase 2 (McDermott, Ceramatec and Air Products)
- Develop and specify the PDU membrane and module design (Air Products, Ceramatec, McDermott)
- Fabricate the specified PDU membrane design (Ceramatec)
- Design the PDU reactor vessel and initiate construction of the PDU (Air Products, McDermott)
- Deliver the PDU reactor vessel to the Air Products site (McDermott)

Results

All the objectives of Phase 1 have been successfully met by the ITM Syngas Team, and work has been initiated on Phase 2, which is on schedule.

Process Engineering and Economic Evaluation

Air Products, Chevron, and McDermott Technology have developed ITM Syngas processes to produce syngas with H₂/CO ratio of 2, suitable for Fischer-Tropsch Gas-to-Liquids (GTL) applications. Preliminary process designs and cost estimates were completed in Phase 1. For an offshore GTL plant processing 50 MMSCFD of associated gas and producing approximately 6000 BPD of syncrude, capital cost savings of greater than 33% were predicted for ITM Syngas when

compared to conventional O₂-blown Autothermal Reforming (ATR) with a cryogenic Air Separation Unit (ASU) for syngas production.

Air Products and Norsk Hydro have developed ITM H₂ processes to produce H₂ at various scales. ITM H₂ processes are being studied for large-scale H₂ applications, where oxidative reforming using the ITM membrane reactor offers opportunities to sequester CO₂ while producing fuel-grade H₂. This application is attractive in light of the Kyoto Protocol and incentives for reducing CO₂ emissions.

Preliminary process designs and cost estimates were completed for “distributed-scale” H₂ processes which produce 0.1 to 1.0 MMSCFD of PSA-grade H₂. A conceptual design for the ITM H₂ process is illustrated in Figure 3 [7]. Applications at this scale include H₂ for distributed refueling stations for Fuel Cell Vehicles (FCVs) and H₂ for industrial use (e.g. H₂ generators). At these scales, oxidative reforming processes offer attractive economics compared to steam reforming.

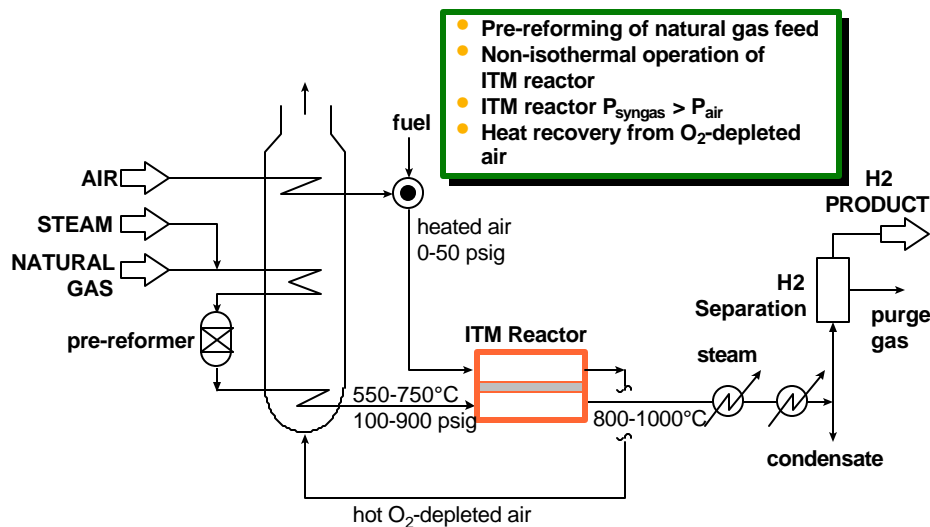


Figure 3 - Conceptual ITM H₂ Process Design

The process was evaluated for the production of distributed hydrogen at 5000 psia delivery pressure suitable for fuelling fuel cell powered vehicles, and a design strategy was chosen to minimize process and equipment capital costs. A nominal capacity of 0.5 MMSCFD H₂ was selected, and the basis for the evaluation followed the “Hydrogen Infrastructure Report” produced by Directed Technologies and Ford for the DOE [1]. The costs of hydrogen compression, storage and dispensing were included. Up to 27% savings in high pressure hydrogen production costs were predicted for the ITM H₂ process compared with trucked-in liquid hydrogen.

Materials and Seals Development and Evaluation

Air Products, Ceramtec and Eltron developed suitable ITM materials and seals with the characteristics and stability required for the ITM Syngas and ITM H₂ processes.

High pressure, laboratory scale, test reactors were designed by Air Products, and constructed and installed at Eltron Research and Air Products. These are illustrated diagrammatically in Figure 4. The test samples are tubular membranes fabricated by Ceramtec and sealed into Haynes 230 alloy tubes using proprietary high temperature ceramic/metal seals. Pre-reformed natural gas mixtures at elevated process pressure are passed over the outer surface of the tubular membrane, while air at atmospheric pressure is fed to the inner surface of the tube. The whole assembly is contained in a heated pressure vessel. The reaction is monitored by GC analysis of the high pressure oxidation products and by measuring the oxygen depletion of the exhaust air stream.

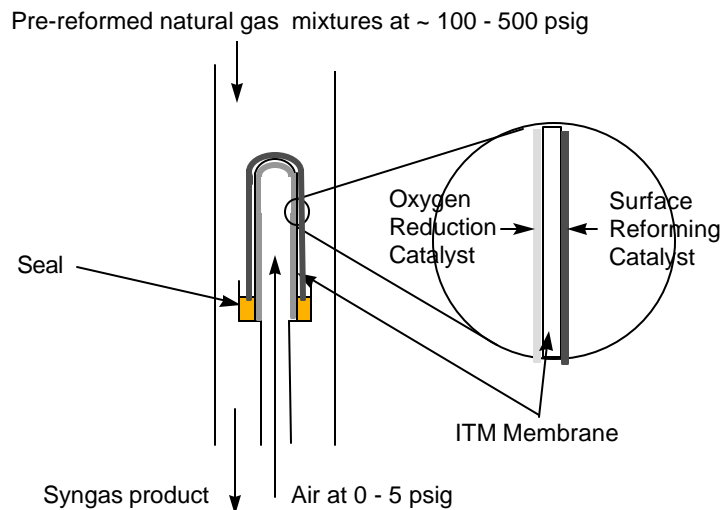


Figure 4 - Laboratory-scale, high pressure test reactor

Using the laboratory scale high pressure reactors, oxidation of gas mixtures simulating the large scale reactor has been carried out at high pressure and temperature at both Eltron Research and Air Products, using ceramic membrane and seal assemblies fabricated from ITM materials by Ceramtec. For example, a membrane and seal assembly was tested, using a feed S/C ratio typical for the ITM H₂ process, with oxidation by air at atmospheric pressure under the following conditions and without any leakage:

> 2400 hours at 825°C and 250 psig.

Other assemblies have been tested with continuous atmospheric air oxidation of a high pressure pre-reformed natural gas mixture under the following conditions:

- > 1000 hours at 250 psia and 900°C, and
- > 160 hours at 400 psia and 825°C.

These tests also evaluated the performance of the seals at high pressure and high temperature. In addition, a seal assembly was thermally cycled eight times from room temperature to 825°C under 250 psig pressure without leakage.

ITM Syngas Reactor Design and Engineering

Initial membrane and membrane reactor designs were developed McDermott, with input from Ceramtec and Air Products. Illustrations of the ITM membrane reactor geometries that were considered are shown in Figure 5.

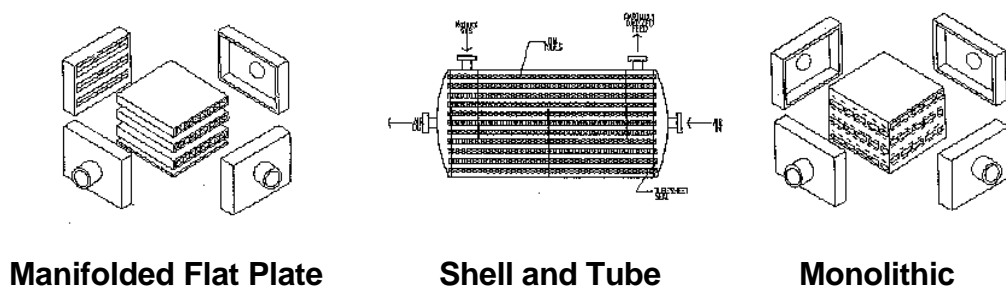


Figure 5 - ITM membrane reactor configurations

After extensive thermo-mechanical analysis, a planar membrane reactor configuration was selected for further development and scale-up. The advantages of this design, compared to the alternative shell-and-tube configuration, include a reduction in the number of ceramic/metal seals per unit active surface area of membrane.

ITM Syngas Membrane and Module Design and Fabrication

Following selection of the planar membrane reactor configuration, Ceramtec developed the membrane fabrication process, and produced sub-scale test samples of supported thin film planar membranes. Initial tests of the performance of these thin film membranes at Eltron Research under low pressure syngas process conditions has demonstrated the achievement of the design oxygen flux.

Nominal 24 MSCFD ITM Syngas PDU

A process development unit (PDU) with a nominal capacity of 24 MSCFD of H₂ and CO has been designed by Air Products, Ceramtec and McDermott. The initial hazards review was completed and the design and construction of the pressure vessel was begun by McDermott

The PDU will integrate the various components of the ITM reactor design, and will be used to confirm the performance of the planar membrane modules and seals under commercial process conditions. The

PDU will be able to access the full range of ITM Syngas and ITM H₂ process conditions, and will simulate sections of the full-scale non-isothermal ITM Syngas reactor.

Initial Objectives for Phase 2

The Phase 2 objectives for the ITM Syngas / ITM H₂ program in the near term are aggressive and include the following:

- Initial scale-up of the ITM membrane fabrication process
- Design and fabrication of membranes, modules and manifolds for the PDU
- Construction and commissioning of the nominal 24 MSCFD PDU
- Demonstration in the PDU of the commercial ITM Syngas and ITM H₂ processes.

Conclusions

The objectives of Phase 1 have been achieved, but substantial technical hurdles remain to be overcome in the scale-up and technology demonstrations planned for Phase 2. The ITM Syngas Team, however, has extensive experience in ITM membrane development and fabrication, and has a broad base of additional skills and commercial incentives. Technical success is likely to lead to, among other advantages, a step-change in the costs of distributed hydrogen and syngas required to produce low cost liquid transportation fuels from natural gas. Both of these goals, lower cost distributed hydrogen and lower cost liquid transportation fuels from natural gas are important to the United States economy and environmental quality. The collaboration between industry, academia, and the government present in the ITM Syngas / ITM H₂ program is critical for the aggressive development of ITM membranes for these important applications.

References

1. DE-AC02-94CE50389 (April 1997 draft), "Hydrogen Infrastructure Report" by Directed Technologies Inc. for Ford and US DOE.
2. P.N.Dyer, R.E.Richards and S.L.Russek, American Ceramic Soc. Ann. Meeting, Indianapolis, April 1999, "ITM Technology for Oxygen Separation and Syngas Production".
3. P.N.Dyer and C.M.Chen, US DOE H₂ R&D Program Review, Denver, May 1999, "Engineering Development of Ceramic Membrane reactor Systems for Converting Natural Gas to H₂ and Syngas for Liquid Transportation Fuels".
4. C.M.Chen and P.N.Dyer, US DOE Alaska GTL Review, Anchorage, May 1999, "Engineering Development of Ceramic Membrane reactor Systems for Converting Natural Gas to H₂ and Syngas for Liquid Transportation Fuels".
5. P.N.Dyer, R.E.Richards and S.L.Russek, Materials for Electrochemical Energy Conversion/Storage, Festschrift for Prof. Brian Steele, Imperial College, June 1999, "ITM Technology for Oxygen Separation and Syngas Production" (Invited Paper).

6. C.M.Chen and P.N.Dyer, US DOE Fossil Energy Fuels Program Review, Cincinnati, September 1999, "Engineering Development of Ceramic Membrane Reactor Systems for Converting Natural Gas to Hydrogen and Synthesis Gas for Liquid Transportation Fuels."
7. S. Nataraj, R.B. Moore and S.L.Russeck, Air Products and Chemicals, US Patent 6048472, April 2000, "Production of Synthesis Gas by Mixed Conducting Membranes"

Novel Catalytic Reforming Using Microtechnology with Advanced Separations Technology

Patricia M. Irving, W. Lloyd Allen, Todd Healey

InnovaTek, Inc.
350 Hills Street
Richland, WA 99352

William J. Thomson

Department of Chemical Engineering
Washington State University
Pullman, WA 99164

Abstract

InnovaTek is combining microreactor technology with advanced catalysts and separations technology to create a portable-sized hydrogen generator. The ultimate goal of this 4-year cooperative project is the development of a microchannel catalytic reactor for the production of clean hydrogen by the catalytic reforming of methanol. Advanced membrane technology will be incorporated to remove carbon dioxide and water from the output stream. Our technology will provide a pure output stream of hydrogen that can be used in a compatibly sized PEM fuel cell for electrical generation. Work accomplished during the first year of the program is summarized. Achievements include catalyst testing, computational model development, micro reactor design, fabrication and testing, and preliminary membrane evaluation.

Introduction

InnovaTek is applying the advantages of microtechnology in the development of catalytic fuel reforming. The specific problem being addressed is a chemical conversion and separation process to provide clean hydrogen from methanol that is produced from renewable biomass energy sources. This approach to fuel processing provides a revolutionary breakthrough in terms of system size, weight, and dynamic response when compared to more conventional processing carried out in standard packed bed reactors.

This year's objectives and rationale were the following.

1. On the basis of catalyst testing, design and construct a computational model for the basic thermal and chemical component systems required for integration into a multi-component catalytic micro-reaction process unit for methanol reforming. The results of this analysis and modeling will provide a sound basis for proceeding with reactor design, fabrication and testing.

2. Based on results of catalyst testing and systems modeling, design, fabricate and test an integrated microreactor system for methanol reforming and hydrogen separation. The process feasibility of each individual system component will be tested evaluated and demonstrated.

Experimental

Laboratory Catalyst Testing

Several sets of experiments were conducted during the project to assess catalyst performance. One set of tests consisted of longer-term experiments in a fixed bed, plug flow reactor (PFR) while other work involved reduction and reforming experiments carried out in in-situ DXRD apparatus. Ultimately the catalysts were tested in micro channel reactor configurations.

In the tests, a liquid mixture of methanol and water was vaporized in pre-heated tubing and entered the reactor at near atmospheric pressure. The exit stream cooled and separated into liquid and gaseous phases which were both analyzed by gas chromatography. The reactor was a 4 mm diameter quartz tube with a catalyst loading of typically 50-200 mg of 40 μm catalyst particles. These were mixed with 100 mg of powdered quartz wool to produce an active bed volume of about 0.34 cm^3 . The catalyst was a Cu/Zn/Al methanol reforming catalyst supplied in the oxide form by United Catalyst and with a nominal composition of 50-60 % copper oxide and 25-35% zinc oxide.

The Dynamic X-ray Diffraction (DXRD) experiments were carried out, using 100 mg of catalyst while a gaseous methanol-water feed mixture flowed over the catalyst. The feed was diluted 50% with ultra high purity helium in order to avoid condensation within the DXRD hot stage. The gases exiting the hot stage were analyzed via gas chromatography. Simultaneous x-ray diffraction spectra were recorded as a function of time. In this mode, experiment measurements were taken during catalyst reduction as well as during actual reforming. Because of the helium dilution, the flow rates of the methanol-water feed were adjusted to approximate the conversions observed in the PFR experiments.

Tests were also performed in several micro-channel reactor configurations to determine optimal channel geometry. Figure 1 is a photo of one of our micro-channel reactors. Catalyst particle size was based on the width of the micro channels and ranged from 100-300 μm . The reactors were operated at temperatures between 240°C and 285°C and space velocities between 12-24 g feed per hour per gram catalyst. Conversion efficiency was determined using gas chromatography analysis of the reactor output stream.

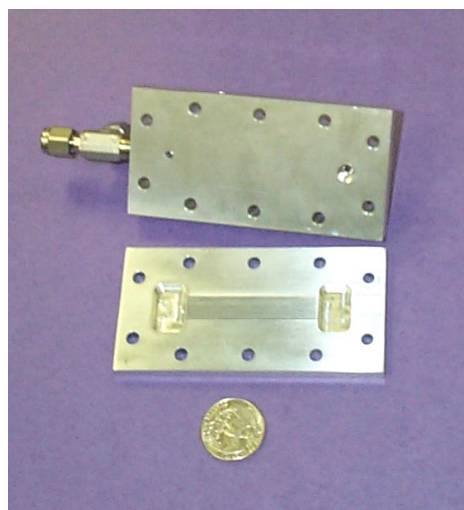


Figure 1. InnovaTek's Micro Channel Reactor for Methanol Reforming.

Results and Discussion

System Modeling

An initial set of process flow models for the microreactor system has been completed for reforming of methanol fuel using HYSYS simulation (Figure 2). The flow model incorporates chemical and thermal equilibrium equations for each major chemical reactor and heat exchanger in the system. It will help project input and output budgets for thermal and chemical reactions, providing information that will aid in system design, such as reactor geometry, flow rate requirements, materials needs, catalyst choices, etc.

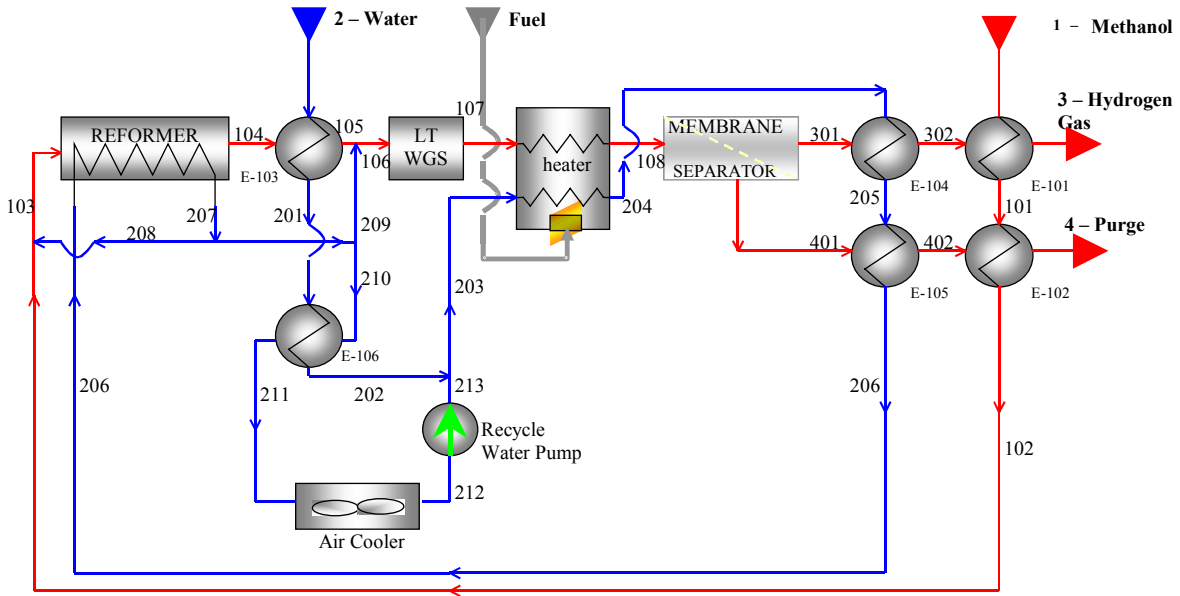


Figure 2. Simulation of Methanol Reforming Using Membrane Separation for CO Cleanup.

HYSYS simulation of a methanol reformer with membrane purification (Figure 2) shows the anticipated output of both a pure hydrogen product and the reject purge gas from the operation (Table 1). From this projection, a feed rate of 1.176 moles of methanol and 1.710 moles of water will produce a pure hydrogen stream at 1201 sccm. Similar simulations were accomplished to project output using water gas shift reactions to clean up CO from the system. These analyses are used to compare approaches for CO removal.

Table 1. HYSYS Projections for Methanol Reforming Using Membrane Separation

| | 1-methanol | 2-water | 3-hydrogen gas | 4-purge |
|----------------|------------|---------|----------------|---------|
| Vapor Fraction | 0.0 | 0.0 | 1.0 | 1.0 |
| Temp, °C | 25 | 25 | 50 | 123 |
| Pressure, bar | 4 | 4 | 1.5 | 4 |
| mole/hr | 1.176 | 1.710 | 3.214 | 2.021 |
| g/hr | 37.69 | 30.81 | 6.48 | 62.01 |
| ppm CO | 0 | 0 | 0 | 20313 |
| sccm H2 | 0 | 0 | 1201 | 100 |

Catalyst Evaluation

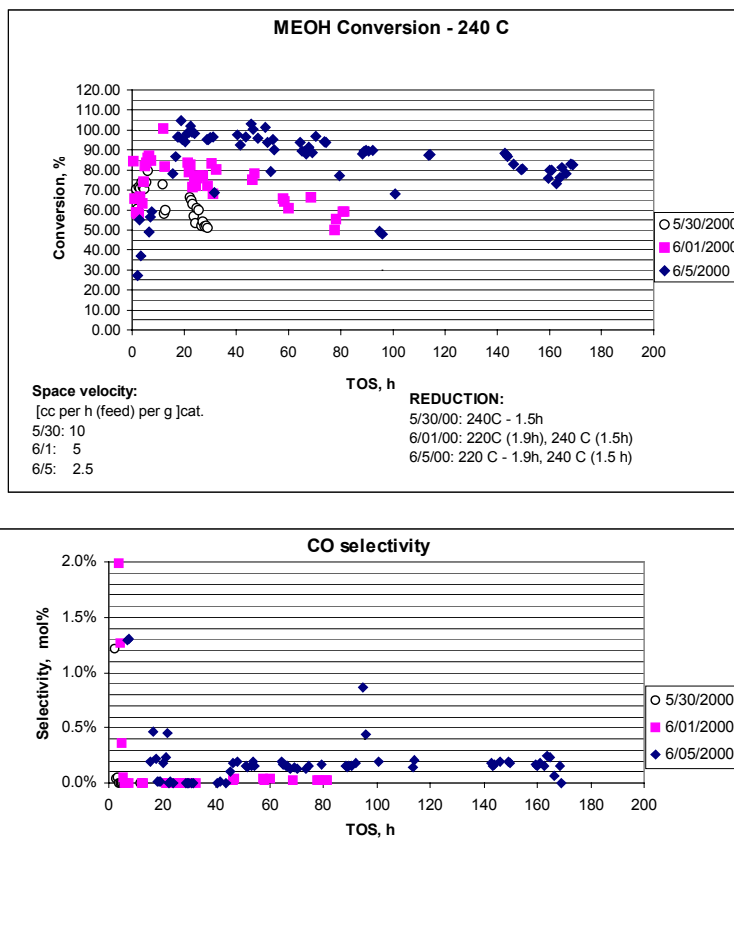
The parameters affecting reaction efficiency include the reaction temperature, the space velocity and the H₂O/MEOH feed ratio. The presentation of the results is divided into two parts: a section dealing with the results obtained in the PFR, followed by the results of in-situ DXRD experiments.

Plug Flow Reactor (PFR) Experiments

In the PFR experiments, temperatures were varied between 240 C and 300 C, space velocities were varied between 40 and 2.5 ml/h-g, and the H₂O/MEOH feed ratio was varied between 1.0 and 1.5.

Figure 3 shows the effect of space velocity (defined as the liquid mixture feed rate (mass/h) divided by the catalyst loading (in grams), at a reaction temperature of 240 C. As can be seen, there is an "induction time" for these runs that is a direct function of the space velocity, with shorter induction times at higher space velocities. This induction period appears to be the result

**Figure 3. Effect of Space Velocity on Methanol Conversion
240° C; H₂O/MEHO = 1.3**



further catalyst reduction caused by the methanol feed. Nevertheless, high conversions were obtained and, in the run with the lowest space velocity, conversions in excess of 90% were achieved for up to 100 hours on stream time. In all cases, deactivation occurred, and the onset of deactivation was an inverse function of space velocity. As shown in Figure 3, CO concentrations were high very early in each experiment, where methanol conversions were also high. After this initial period, the CO concentrations were below the detectable limit (~ 1500 ppm), even though conversions were still in excess of 90%.

The effect of temperature of reaction at constant space velocity of 40 ml/h-g. is shown in Figure 4. Interestingly, the initial conversion in both experiments is very high. Note also that the highest CO concentrations are about the same as those in Figure 3. Figure 5 shows the results when the H₂O/MEOH feed ratio was varied between 1.5 and 1.0 at a reaction temperature of 240 and the lowest space velocity of 2.5 ml/h-g. As can be seen, a ratio of 1.3 appears to be optimum, producing methanol conversions which are significantly higher than those observed at either higher or lower ratios.

*In-Situ
Reduction/Reforming*

Although high methanol conversions were obtained and could be maintained for time on streams in excess of 100 hours, deactivation was observed in all of the PFR experiments. This, and the fact that there was a considerable induction time before high conversions were reached, are indications that the catalyst undergoes chemical changes during exposure to the methanol-water mixture. Consequently, a number of DXRD experiments were conducted in order to observe changes in crystallinity during reduction and reaction. Simultaneous measurements of XRD spectra and exit gas concentrations provide a correlation of catalyst activity with crystalline changes in the bulk catalyst.

As a result of the DXRD studies, we conclude that:

- the active catalyst is a mixture of amorphous Cu₂O and crystalline copper
- deactivation takes place when the amorphous Cu₂O crystallizes
- it is necessary to maintain the proper ratio of amorphous Cu₂O:Cu.

Figure 4. Effect of Temperature on Methanol Conversion (Space Velocity = 40 ml/hr per g catalyst, H₂O/MEHO = 1.3

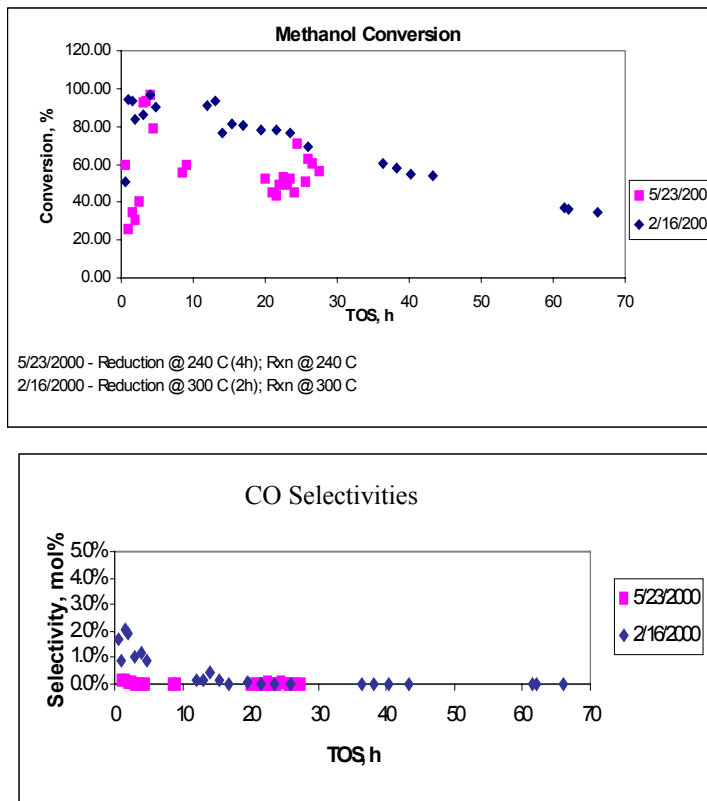
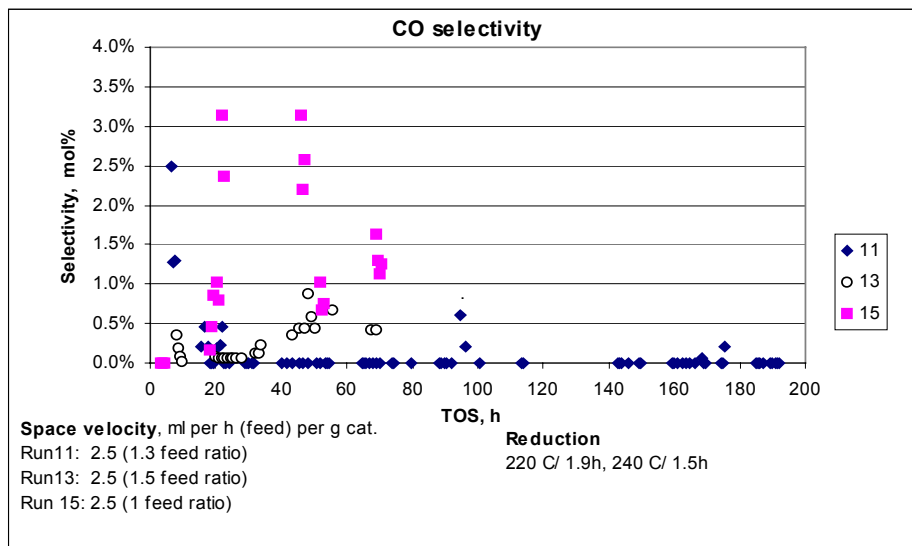
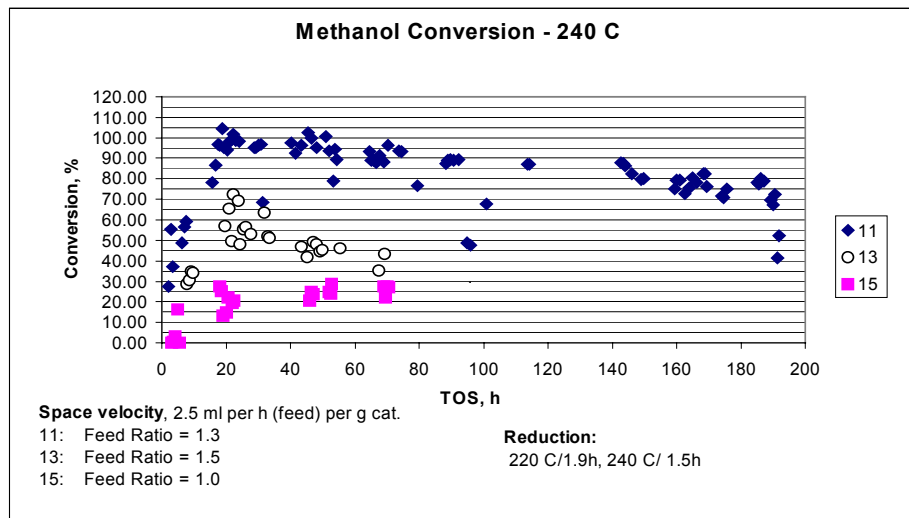
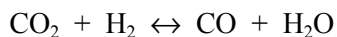


FIGURE 5 - Effect of Feed Ratio on Methanol Conversion
 [240 C, Sp. Vel. = 2.5 ml/h-g]



CO Production

One of the advantages of methanol reforming is that the product gas has minimal CO. Of course, any CO concentration greater than about 50 ppm, is still too high for a fuel cell. The CO produced during methanol reforming is generally higher, the higher the conversion and the higher the temperature. This is generally attributed to the reverse water gas shift reaction

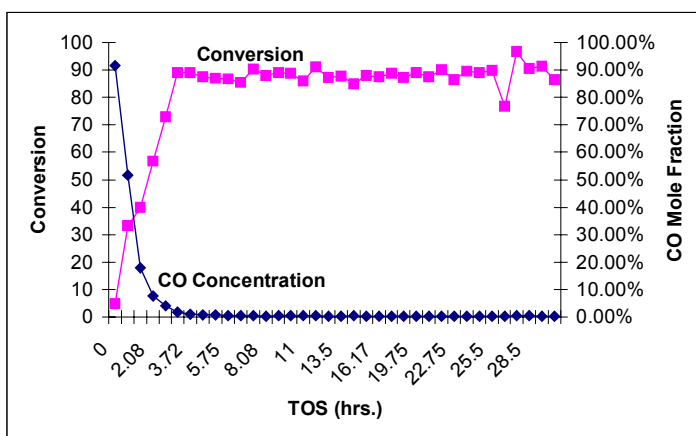


which would tend to occur at high CO₂ concentrations (high conversions) and high temperatures (thermodynamically favored). However, our results indicate that the high CO concentrations observed early in the runs, are more likely due to other factors.

Figure 6 is the result from an in-situ experiment showing CO concentration along with methanol conversion once the mildly reduced catalyst (5% H₂, 240 C, 1.5h) was exposed to the 1.3:1 water/methanol mixture. The initial CO concentration is very high, even at very low methanol conversions. However, once the catalyst becomes fully reduced, the methanol conversion reaches 90% but the CO concentration drops below the detectable limit of 1500 ppm.

Figure 6. Methanol Conversion vs CO Concentration

[Reduction: 5% H₂, 240C, 1.5h; Reaction: 300C, at TOS=0, H₂O/MeOH=1.3]



Micro Channel Reactor Testing

An initial set of experiments to evaluate the effects of space velocity and catalyst longevity was conducted using a micro-channel reactor. The results showing the effects of space velocity are presented in Figure 7. The use of micro channels improves performance with respect to space velocity. High conversions (> 80 percent) are maintained with space velocities up to 24 g feed/h per gram catalyst. The initial test for longevity shows a rapid decrease in activity at about 100 hours, which is consistent with earlier lab results (Fig. 8). These tests were performed with a micro-channel reactor with channels 500 microns wide and loaded with 0.5 grams of catalyst with a size distribution of 150-300 microns. This reactor was operated at 285° C.

The stability and longevity of the catalyst has been examined more thoroughly through additional duration runs. Using the 500 micrometer reactor loaded with 0.5 grams of 150-300 micron sized catalyst, 285° C, and a space velocity of 12 g feed/h per gram catalyst, 100

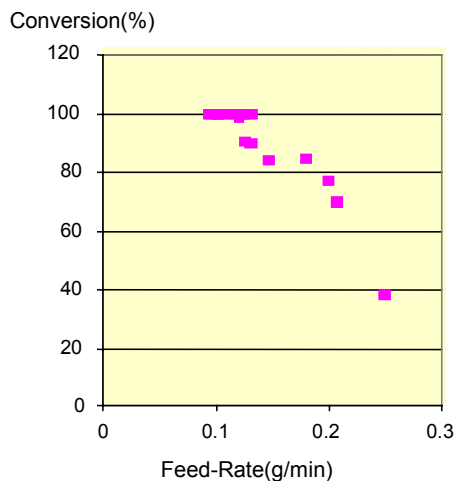


Figure 7. Effects of Space Velocity on Methanol Conversion

percent conversion was maintained for over 200 hours (Figure 9). Deactivation occurred quickly at about 200 hours and the conversion had dropped to below 20 percent at 300 hours.

It has not been possible up to this point to regenerate the catalyst after deactivation. The observed physical condition of the deactivated catalyst has shown great diversity. In some instances the catalyst's appearance is that of being in an extremely reduced condition (metal copper obvious) while in other instances it has an overly oxidized appearance (green copper oxide). The explanation for this may be that the catalyst deactivates similarly in each case, however, the prevailing conditions within the reactor after the catalyst deactivated affected the final physical appearance.

A number of experiments were conducted with the following variables to examine their effect of catalyst activity: feed compositions, operating temperatures, reduction times and temperatures, regeneration with air, regeneration with H₂O, regeneration with varying concentrations of H₂, and reduced vs. oxidized catalyst. The result of all these experiments is that no noticeable improvement in catalyst lifetime has been observed.

Preliminary XRD results performed on spent (deactivated) catalyst indicated possible sintering of the catalyst. This would explain the inability to regenerate the catalyst. The sample that was examined however, had been tested under more extreme conditions than normal. Operating temperatures were 300 C for extended periods, reductions were extreme (pure H₂ at >285 C) and multiple attempts made to regenerate and test this particular sample. Catalyst that had not been as severely utilized i.e. operating temperatures under 250 C and mild reduction of 2 hours in 20 percent hydrogen have not exhibited any better tendency towards regeneration.

The issues of catalyst longevity and reactivation will be studied further during Year 2.

Membrane Testing

A commercially available membrane unit was tested as a possible hydrogen purifier. The unit was rated at 750 sccm at 450° C and 120 psi. The specifications described it as a noble metal coated over a porous stainless steel tube. This unit was attached to the microchannel catalytic

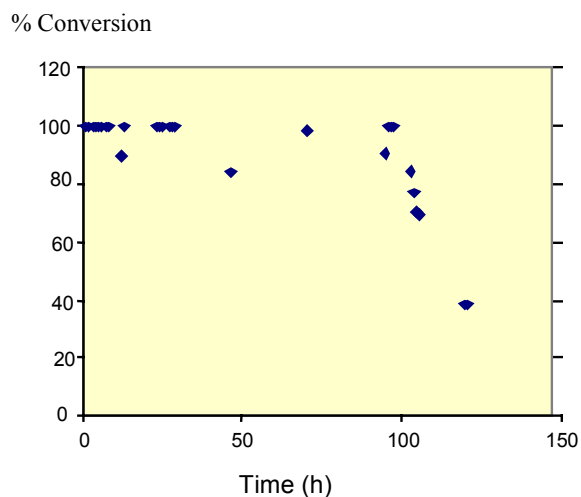


Figure 8. Methanol Conversion vs Time

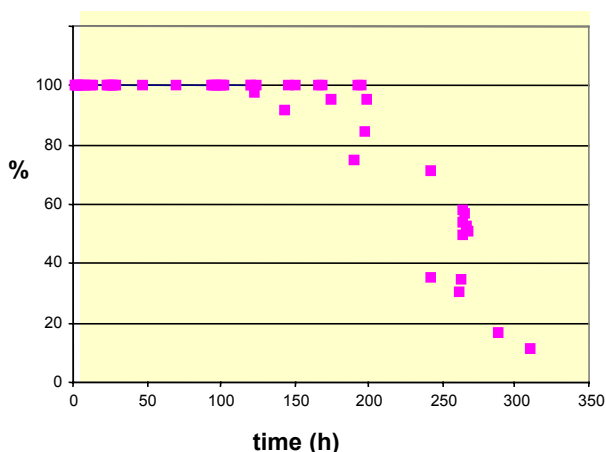


Fig. 9 Conversion vs time (500 micrometer aluminum reactor with 0.5g catalyst)

reactor. Because our system did not achieve the high pressure requirement for separation the flow rate was quite low. However, hydrogen output was 100% pure. Further work is needed in Year 2 to match the reformer with a suitable membrane, possibly one with lower pressure requirements.

Conclusions

- A thermal and process system model that was developed as a system simulator can be used to optimize the design of a micro channel reactor. The active length and inlet cross section of catalytic methanol reforming is optimized through temperature control and throughput rate for a specific catalyst. With iterative testing and further refinement, the base model will be used to provide a sound basis for improved reactor and process engineering.
- Hydrogen production is maximized and CO production is minimized by proper selection of 1) temperature-dependent reaction equilibria, 2) ratio of methanol to steam, and 3) catalyst activity. Through the innovative use of sensors and controls, the reformer operating system can be controlled to respond to different load requirements while maintaining optimum performance. Such a control system can be used to control volume of active catalyst bed, methanol to steam ratio, and catalyst reactivation (through hydrogen flushing).
- Long term, detailed steam reforming tests using a copper-zinc-oxide catalyst revealed fundamental information on the catalytic process, including method of deactivation. As a result, we have formulated a possible mechanism for catalyst action in the process. We will use this mechanism to design catalyst forms for appropriate action in the process.
- The combination of a burner to heat fluid in the heat exchangers with layers of co-current and counter-current flow against the reaction components will yield temperature zones in the reactor to achieve optimum performance.
- As a result of reactor and burner assembly and testing, a laminar sealing and gasketing process was discovered that provides ease of assembly, temperature and feed stream compatibility, and strong sealing capability.

References

W. Lloyd Allen, Patricia M. Irving and William J. Thomson, "MICROREACTOR SYSTEMS FOR HYDROGEN GENERATION AND OXIDATIVE COUPLING OF METHANE", in Proceedings of the 4th International Conference on Micro Reaction Technology, AIChE Spring National Meeting, March 2000, Atlanta, GA, USA.

Patricia M. Irving and W. Lloyd Allen, "MICRO FUEL PROCESSOR FOR HYDROGEN PRODUCTION" in Proceedings of the 2000 Conference on Small Fuel Cells, April 2000, sponsored by The Knowledge Foundation, Brookline MA.

Acknowledgements

This work was funded by the U.S. Department of Energy Hydrogen Program under Contract DE-FC36-99GO.

Production of Hydrogen from Biomass-Derived Liquids

Stefan Czernik, Richard French, Calvin Feik, and Esteban Chornet

Chemistry for BioEnergy Systems Center

National Renewable Energy Laboratory, Golden, Colorado, USA 80401

Abstract

Biomass as a product of photosynthesis is a renewable resource that can be used for sustainable production of hydrogen. However, direct production of hydrogen from biomass by gasification/water-gas shift technology is unfavorable economically, except for very low cost feedstocks and very large plants. Our approach proposes an alternative strategy with potentially better economics resulting from the combined production of hydrogen with valuable co-products. The concept is based on a two-stage process: fast pyrolysis of biomass to generate bio-oil; and catalytic steam reforming of the oil or its fractions to produce hydrogen. Fast pyrolysis, a technology near commercial scale, could be carried out in a regional network of plants that would supply bio-oil to a central reforming facility. The preferred option is to separate bio-oil into a lignin-derived fraction, which could be used for producing phenolic resins or fuel additives, and a carbohydrate-derived material that would be steam reformed to produce hydrogen. The key research issue for this concept is to demonstrate that bio-oil can be efficiently steam reformed. The co-product strategy can also be applied to residual fractions derived from pulping operations and from ethanol production. Effluents from other biomass processing technologies such as transesterification of vegetable oils can also be attractive feedstocks for the production of hydrogen. This year, we focused on catalytic steam reforming of different biomass-derived liquids. We employed a fluidized bed reactor configuration with commercial nickel catalysts developed for processing natural gas and naphtha. The hydrogen yields approached or exceeded 90% of the values possible for stoichiometric conversion.

Introduction

At present, hydrogen is produced almost entirely from fossil fuels such as natural gas, naphtha, and inexpensive coal. In such a case, the same amount of CO₂ as that formed from combustion of those fuels is released during hydrogen production stage. Renewable biomass is an attractive alternative to fossil feedstocks because of the essentially zero net CO₂ impact. Unfortunately, hydrogen content in biomass is only 6-6.5%, compared to almost 25% in natural gas. For this reason, on a cost basis, producing hydrogen by a direct conversion process such as the biomass gasification/water-gas shift cannot compete with the well-developed technology for steam reforming of natural gas. Vegetable oils have a better potential for producing hydrogen than lignocellulosic materials but their high costs make the process economics unfavorable. Only an integrated process, in which biomass is used to produce valuable materials or chemicals with the residual fractions utilized for generation of hydrogen, can be an economically viable option. The concept of our approach to producing hydrogen from biomass is shown in Figure 1. In earlier papers¹⁻³ we proposed a method which combines two stages: fast pyrolysis of biomass to generate bio-oil; and catalytic steam reforming of the bio-oil to hydrogen and carbon dioxide. This concept has several advantages over the traditional gasification technology. First, bio-oil is much easier to transport than solid biomass and therefore, pyrolysis and reforming can be carried out at different locations to improve the economics. For instance, a series of small-size pyrolysis units could be constructed at the sites where low cost feedstock is available. Then the oil could be transported to a central reforming plant located at a site with existing hydrogen storage and distribution infrastructure. The second advantage is the potential for production and recovery of higher-value co-products from bio-oil that could significantly impact the economics of the entire process. The lignin-derived fraction can be separated from bio-oil and used as a phenol substitute in phenol-formaldehyde adhesives⁴ or converted to cyclohexyl ethers (fuel additives⁵) while the carbohydrate-derived fraction is catalytically steam reformed to produce hydrogen.

In previous years we demonstrated, initially through micro-scale tests¹ then in bench-scale fixed-bed reactor experiments^{2,3} that bio-oil model compounds as well as bio-oil carbohydrate-derived fraction can be efficiently converted to hydrogen. Using commercial nickel catalysts, the

hydrogen yields obtained approached or exceeded 90% of the yield possible for stoichiometric conversion.

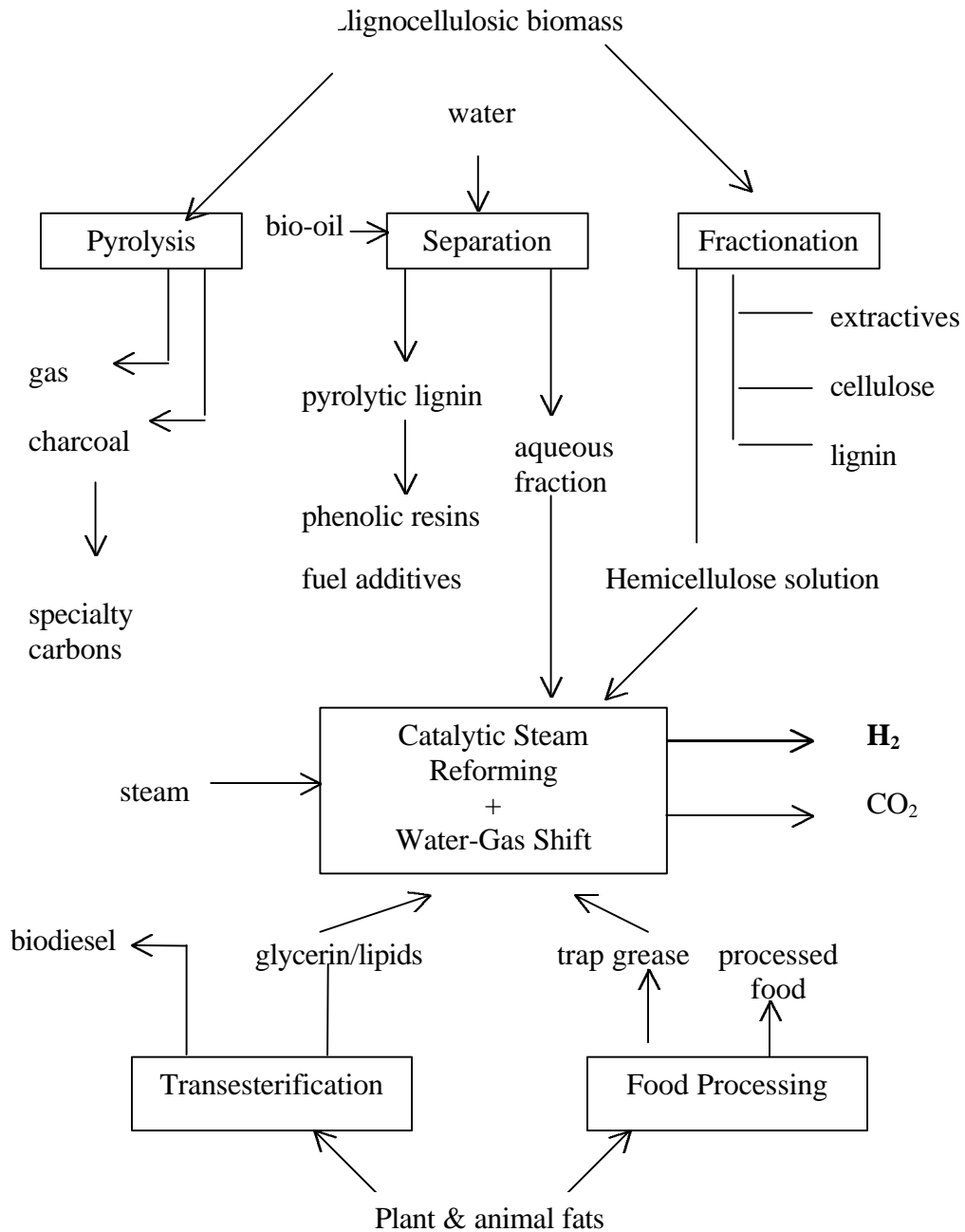


Figure 1. Biomass to hydrogen – Process concept

The carbohydrate-derived bio-oil fraction contains substantial amounts of non-volatile compounds (sugars, oligomers) which tend to decompose thermally and carbonize before contacting the steam reforming catalyst. Even with the large excess of steam used, the carbonaceous deposits on the catalyst and in the reactor freeboard limited the fixed-bed reforming time to 3-4 hours. For this reason we decided to employ a fluidized bed reactor configuration that can overcome some limitations of the fixed-bed unit for this application. Though carbonization cannot be completely avoided, the bulk of the fluidizing catalyst remains in contact with the liquid droplets fed to the reactor. Catalyst regeneration can be done by steam or carbon dioxide gasification of carbonaceous residues in a second fluidized bed reactor providing additional amounts of hydrogen.

Experimental

1. Materials

Bio-oil used for this study was generated from pine sawdust using the NREL fast pyrolysis vortex reactor system⁶. The oil composition was 47.7% carbon, 7.4% hydrogen, and 44.8% oxygen with water content of 26.7%. It was separated into aqueous (carbohydrate-derived) and organic (lignin-derived) fractions by adding water to the oil in a weight ratio of 2:1. The aqueous fraction (75% of the whole oil) contained 21.8% organics ($\text{CH}_{1.25}\text{O}_{0.55}$) and 78.2% water.

“Crude glycerin” samples were obtained from West Central Co-op bio-diesel plant in Ralston, Iowa. Transesterification of vegetable oils with methanol produces a mixture of bio-diesel (methyl esters of fatty acids) and glycerin. Glycerin settles down at the bottom of a separation tank while bio-diesel forms the top layer. “Crude glycerin” is a very viscous liquid, only partially miscible with water. Its elemental composition includes 54.7% carbon, 9.9% hydrogen, and 35.5% oxygen, which suggests that the phase separation in the tank was not very clean and the liquid is a mixture of glycerin (55%) with methyl esters of fatty acids (45%).

Methane (C.P. grade was supplied by Scott Specialty Gases).

C11-NK, a commercial nickel-based catalyst used for steam reforming of natural gas and naphtha, was obtained from United Catalysts and ground to the particle size of 300-500 μ .

2. Fluidized bed reformer

The bench-scale fluidized bed reactor is shown in Figure 2.

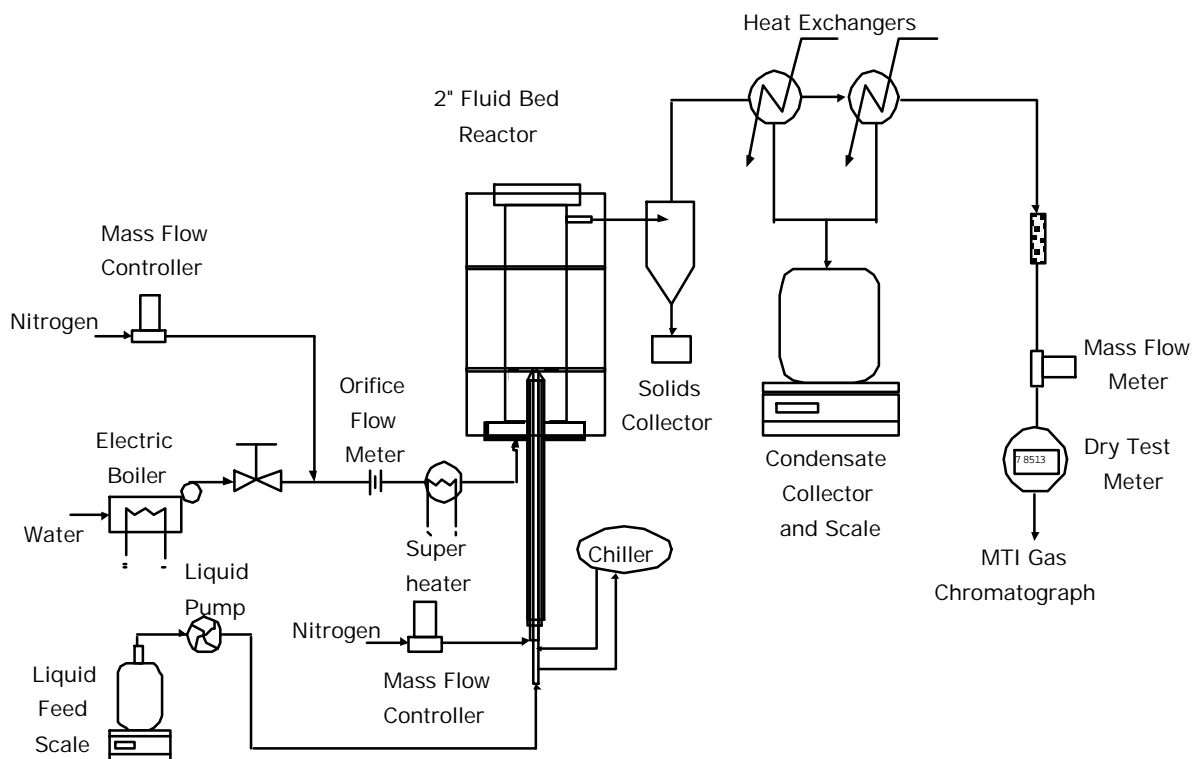


Figure 2. Fluidized bed reformer system

The two-inch-diameter inonel reactor with a porous metal distribution plate was placed inside a three-zone electric furnace. The reactor contained 150-200g of commercial nickel-based catalyst ground to the particle size of 300-500 μ . The catalyst was fluidized using superheated steam, which is also a reactant in the reforming process. Steam was generated in a boiler and superheated to 750 C before entering the reactor at a flow rate of 2-4 g/min. Methane, used in separate experiments to compare the performances of the fluidized bed with the fixed-bed commercial reactors, was fed to the reactor mixed with steam. Liquids were fed at a rate of 4-5 g/min using a diaphragm pump. A specially designed injection nozzle supplied with a cooling

jacket was used to spray liquids into the catalyst bed. The temperature in the injector was controlled by coolant flow and maintained below the feed boiling point to prevent evaporation of volatile and deposition of nonvolatile components. The product gas passed through a cyclone that captured fine catalyst particles and any char generated in the reactor, and then through two heat exchangers to remove excess steam. The condensate was collected in a vessel whose weight was continuously monitored. The outlet gas flow rate was measured by a mass flow meter and by a dry test meter. The concentrations of CO₂, CO, and CH₄ in the reforming gas composition were monitored by a non-dispersive infra-red analyzer (NDIR Model 300 from California Analytical Instruments) and that of hydrogen by a thermal conductivity monitor TCM4 manufactured by Gerhard Wagner. In addition, the gas was analyzed every 5 minutes by an on-line MTI gas chromatograph, which provided concentrations of hydrogen, carbon monoxide, carbon dioxide, methane, ethylene, and nitrogen as a function of time of the test. The temperatures in the system as well as the flows were recorded and controlled by the OPTO data acquisition and control system. Total and elemental balances were calculated as well as the yield of hydrogen generated from the feed.

Results and Discussion

Reforming of methane.

We measured performances of the fluidized bed reactor for steam reforming of methane in order to compare its performance to that of fixed beds and to verify that fluidized beds could be successfully applied for co-processing biomass-derived liquids or vapors with volatile hydrocarbon feedstocks. We carried out a series of reforming tests at 800°C varying the steam-to-carbon ratio (S/C) and space velocity (WHSV). The reactor operated very smoothly with only minimal fluctuations. Gas composition as a function of the run time is shown in Figure 3.

At the S/C=3.85 and WHSV of 1500 h⁻¹ the yield of hydrogen was 81% of that possible for stoichiometric conversion to CO₂ and H₂ and the methane conversion was 97.5%. In industrial processes at the same S/C and WHSV and the temperature of 870-950°C the methane conversion is usually 92-94%. As expected, at a higher steam-to-carbon ratio and lower space velocity, methane conversion to carbon dioxide and hydrogen was even greater. At S/C=4.2 and WHSV

of 500 h^{-1} methane conversion was greater than 99%. At $S/C=7.1$ and $WHSV=300 \text{ h}^{-1}$ only traces of methane ($<20 \text{ ppm}$) were detected in the product gas.

Reforming of carbohydrate-derived bio-oil fraction

The steam reforming experiments on aqueous extract of the pine bio-oil were carried out at the temperature of 800°C and 850°C . The steam to carbon ratio was in the range of 7-9 while methane-equivalent gas hourly space velocity $G_{C_1}HSV$ was $1200\text{-}1500 \text{ h}^{-1}$. During the experiments at 800°C a slow decrease in the concentration of hydrogen and carbon dioxide and an increase of carbon monoxide and methane was observed. These changes resulted from a gradual loss of the catalyst activity, probably due to coke deposits. As a consequence of that, the yield of hydrogen produced from the oil fraction decreased from the initial value of 85% of stoichiometric (3.24 g of hydrogen from 100 g of feed) to 77% after 12 hours on stream. If a water-gas shift reactor followed the reformer, the hydrogen yields would have been 94% initially, falling to 84% of stoichiometric.

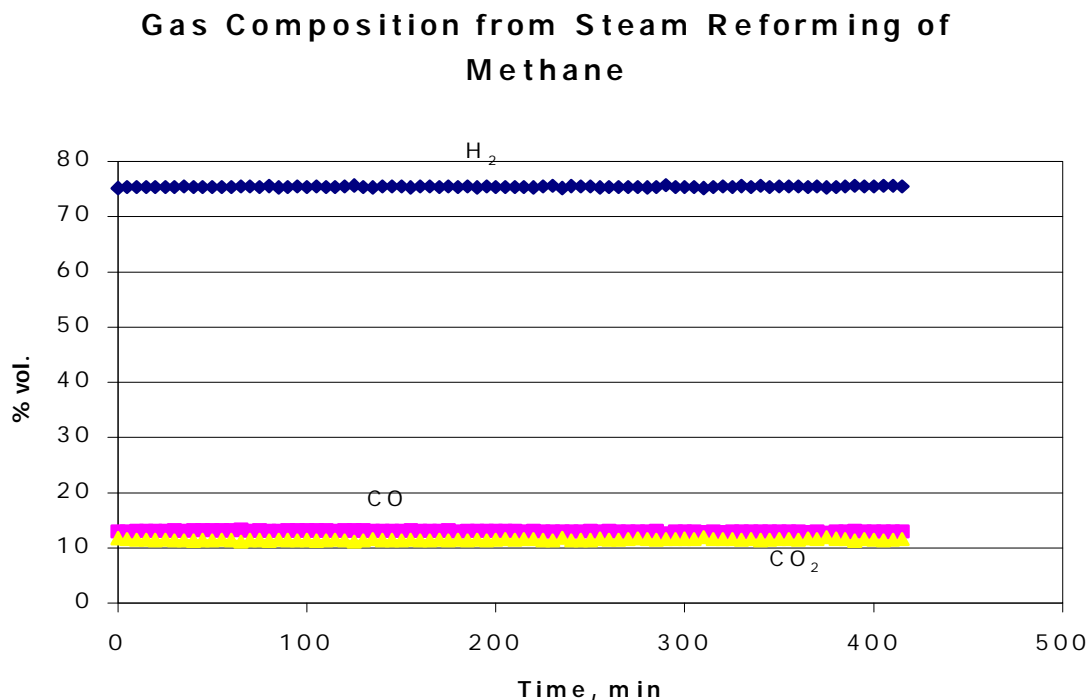


Figure 3. Reforming gas composition as a function of run time

At 850°C, the formation of char and coke was much lower because their gasification by steam was more efficient than that at 800°C. During over 90 hours of uninterrupted reforming of the bio-oil carbohydrate-derived fraction, the product gas composition remained nearly constant and only a small decrease in the concentration of hydrogen was observed, as presented in Figure 4.

Over the run time, the concentration of methane increased and then stabilized at the 2.5% level. This indicates that the catalyst deactivation proceeded very slowly. The yield of hydrogen produced from the bio-oil fraction oscillated around 80% of that possible for stoichiometric conversion (Figure 5). It would be greater than 90% if carbon monoxide underwent the complete shift reaction with steam. Only small amounts of feed were collected as char in the cyclone and condensers, and little or no coke was deposited on the catalyst.

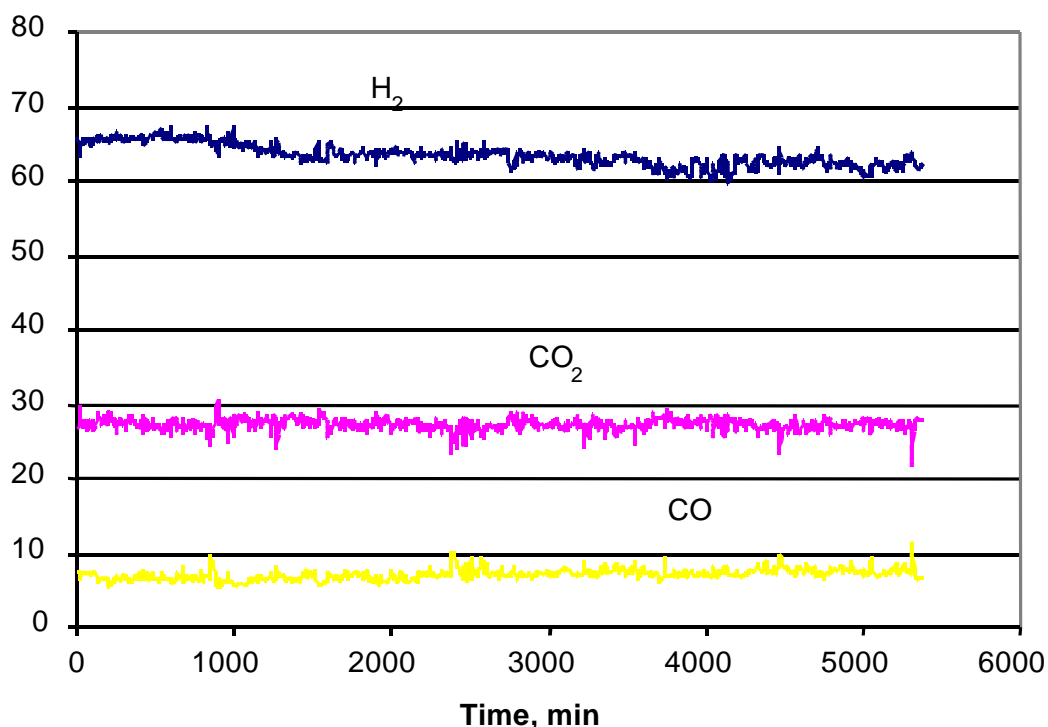


Figure 4. Reforming of bio-oil aqueous extract. Gas composition (vol %) as a function of process time

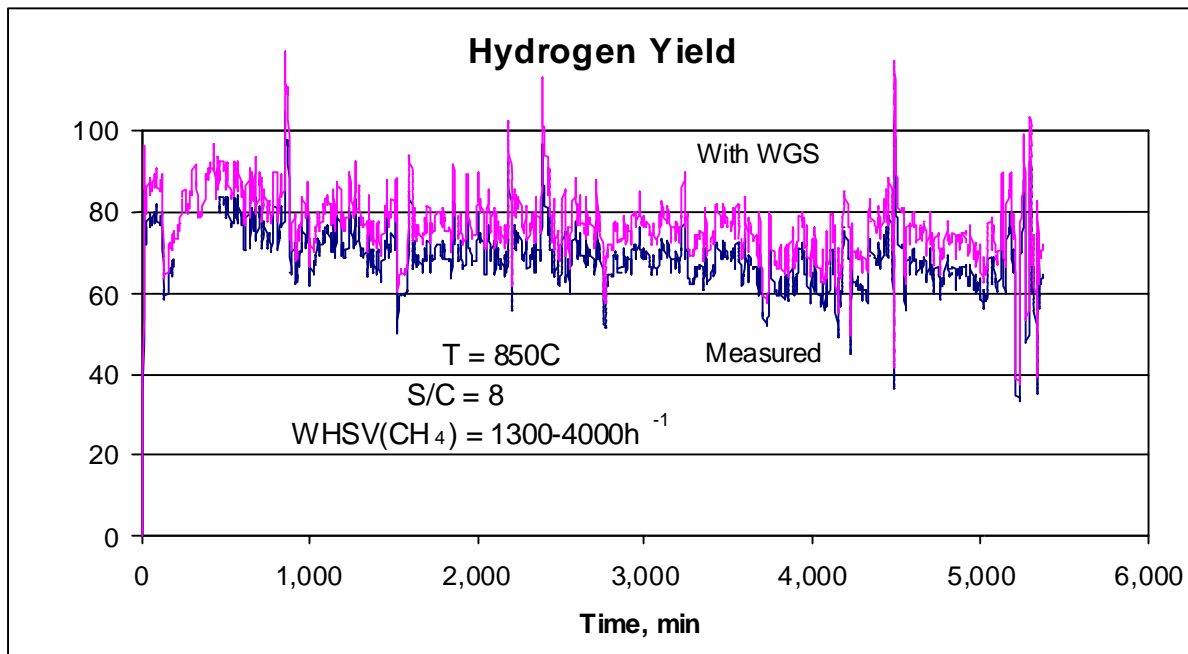


Figure 5. Reforming bio-oil aqueous fraction. % stoichiometric yield of hydrogen as a function of time.

Reforming of “crude glycerin”

“Crude glycerin” is a high viscosity liquid and, therefore, it had to be preheated to facilitate pumping and atomizing (the whole feeding line was maintained at 60-80°C). The liquid was fed at a rate of 78 g/h ($G_{Cl}VHSV = 1600 h^{-1}$) and steam at a rate of 145 g/h, which corresponds to the molar steam to carbon ratio of 2.3. The experiments proceeded very smoothly with only occasional fluctuations in the liquid feed rate resulting from a non-complete homogeneity of the feed. The concentration of the major gas products was constant during the run time but a gradual increase in methane production was noticed (Figure 6). The process performance measured as the yield of hydrogen did not decrease significantly during several hours on stream. The overall mass balance closure was close to 100% at the beginning of the tests then decreased to 95-96% after four hours on stream. Similar closure was also observed for elemental balances of carbon, hydrogen and oxygen. The hydrogen yield oscillated around 77% of the stoichiometric potential, which was 23.6 g per 100 g of feed. It could be significantly higher if more steam were used in the reaction. Conversion of CO in the gas through water-gas shift to CO₂ and H₂ would increase

the hydrogen yield to 95% of that theoretically possible. These promising results suggest that a low-value by-product from bio-diesel production could become a viable renewable raw material for producing hydrogen. An integration of these two technologies could significantly improve the economics of both processes.

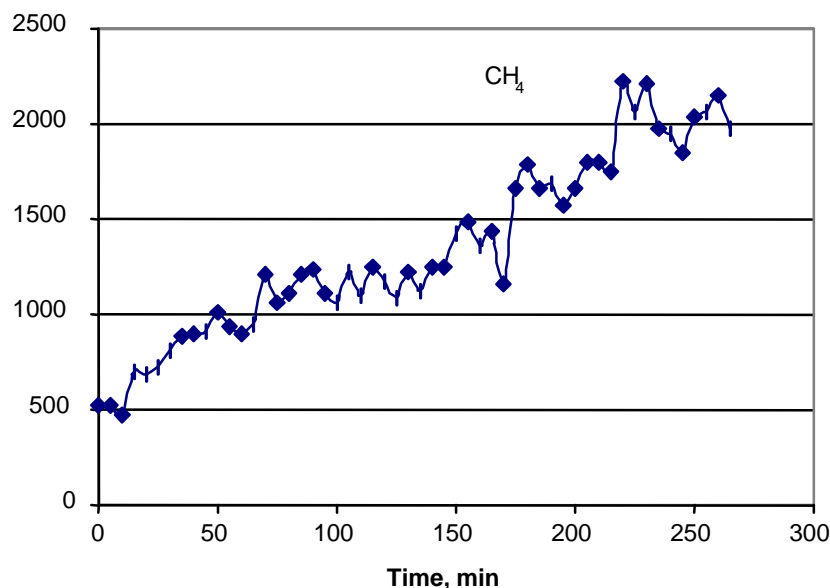


Figure 6. Methane concentration (ppm volume) during steam reforming of “crude glycerin”

SUMMARY AND CONCLUSIONS

Biomass can be a valuable resource for producing hydrogen if done as an integrated process that also generates higher value co-products. Following this strategy we have presented two process options: fast pyrolysis/steam reforming and transesterification of vegetable oils/steam reforming.

Bio-oil from pyrolysis or its aqueous, carbohydrate-derived fraction and glycerin from bio-diesel production can be catalytically steam reformed to generate hydrogen using commercial nickel-based catalysts.

The hydrogen yield obtained in a fluidized bed reactor from the aqueous fraction of bio-oil was about 85% of the stoichiometric value, which corresponds to almost 6 kg of hydrogen from 100 kg of wood.

The hydrogen yield from “crude glycerin” was 18 g per 100 g of the feedstock, which corresponds to 76% of the stoichiometric potential. If the steam reforming were followed by a water-gas shift process or a higher amount of steam were used in the reforming stage, the hydrogen yield could increase above 90%.

Fluidized bed reactor configuration proved to be efficient for reforming both methane and biomass-derived liquids. It can be used for producing hydrogen by co-processing bio-oils with natural gas or liquid hydrocarbons.

The process needs to be optimized to determine conditions that allow for maximum yields of hydrogen and minimum coke formation.

REFERENCES

1. Wang, D., Czernik, S., Montané, D., Mann, M., and Chornet, E. (1997) Biomass to hydrogen via pyrolysis and catalytic steam reforming of the pyrolysis oil and its fractions. *I&EC Research*, **36**, 1507-1518.
2. Wang, D.; Czernik, S., and Chornet, E. (1998) Production of hydrogen from biomass by catalytic steam reforming of fast pyrolysis oils. *Energy & Fuels*, **12**, 19-24.
3. Czernik, S., French, R., Feik, C, and Chornet, E. (1999) Fluidized bed catalytic reforming of pyrolysis oils for production of hydrogen. In: *Proceedings of the Fourth Biomass Conference of the Americas*, (Ed. by R.P. Overend and E. Chornet), pp. 827-832. Elsevier Science Ltd., Oxford.
4. Kelley, S. S., Wang, X.-M., Myers, M. D., Johnson, D. K., Scahill, J. W. (1997) Use of biomass pyrolysis oils for preparation of modified phenol formaldehyde resins. In: *Development in Thermochemical Biomass Conversion*, (Ed. By Bridgwater, A.V. and Boocock, D.G.B.), pp. 557-572. Blackie Academic & Professional, London.
5. Shabtai, J.S., Zmierczak, W., and Chornet, E. (1997) Conversion of lignin to reformulated gasoline compositions. In: *Proceedings of the Third Biomass Conference of the Americas*, (Ed. by Overend, R.P. and Chornet, E.), pp. 1037-1040. Elsevier Science Ltd., Oxford.
6. Diebold, J.; Scahill, J. (1988) Production of primary pyrolysis oils in a vortex reactor. In: *Pyrolysis Oils from Biomass: Producing, Analyzing and Upgrading*; (Ed. by Soltes, E. J. and Milne, T. A.), pp. 31-40. American Chemical Society, Washington, D.C.

Modeling of dense gas-solid reactive mixtures applied to biomass pyrolysis in a fluidized bed

D. Lathouwers and J. Bellan
Jet Propulsion Laboratory
California Institute of Technology
Pasadena, CA 91109

Abstract

A model is presented for mathematically describing the thermo fluid dynamics of dense, reactive, gas-solid mixtures. The model distinguishes among multiple particle classes, either on the basis of their physical properties (diameter, density) or through their thermo-chemistry (reactive vs. inert particles). A multifluid approach is followed where macroscopic equations are derived from the kinetic theory of granular flows using inelastic rigid-sphere models, thereby accounting for collisional transfer in high-density regions. Separate transport equations are constructed for each of the particle classes, allowing for the description of the independent acceleration of the particles in each class and the interaction between size classes, as well as for the equilibration processes whereby momentum and energy are exchanged between the respective classes and the carrier gas. Aimed at high density suspensions, such as fluidized beds, the relations obtained for the stress tensor are augmented by a model for frictional transfer, suitably extended to multiple-class systems. Although applicable to general gas-solid combustion systems, the model is combined here with a detailed, separately validated, chemistry model describing the pyrolysis of biomass particles. The noteworthy novelties of the model include: (i) a systematic and consistent derivation of the solids transport equations and transport properties within the multifluid concept, allowing for non-equilibrium effects between the respective particle classes, (ii) the ability to explicitly account for the possibility of porous solid fuel particles, and (iii) the modeling of multiple chemical reactions in both gas and solid phases and the associated effects of heat and mass transfer. The model is applied to high-temperature biomass particle pyrolysis in a lab-scale fluidized bed reactor and is evaluated on comparing yield of reaction products. The results indicate that the gas temperature is the foremost parameter influencing tar yield. The biomass feed temperature, the nature of the feedstock, and the fluidization velocity, all have minor impact on the yield. It is also shown that the gas temperature can be optimized for maximizing the tar yield.

Contents

| | | |
|----------|---|----------|
| 1 | Introduction | 2 |
| 2 | Mathematical model | 3 |
| 2.1 | Single particle biomass pyrolysis model | 4 |
| 2.2 | Gas phase transport equations | 4 |
| 2.3 | Particle phase transport equations | 6 |

| | | |
|----------|---|-----------|
| 2.3.1 | Collision dynamics | 8 |
| 2.3.2 | Particle dynamics | 9 |
| 2.3.3 | The moment equations | 11 |
| 2.4 | Closure | 13 |
| 2.4.1 | Collisional and kinetic contributions | 13 |
| 2.4.2 | Exchange terms | 15 |
| 2.4.3 | In-phase transport fluxes and evaluation of transport properties | 17 |
| 2.4.4 | Transport equations for the mean particle mass and solidity | 18 |
| 2.5 | Frictional transfer | 18 |
| 3 | Solution procedure | 19 |
| 4 | Results | 19 |
| 4.1 | Homogeneously sheared mixture | 19 |
| 4.2 | Particle pressure along the wall of a bubbling fluidized bed | 20 |
| 4.3 | Behavior of homogeneously fluidized beds | 21 |
| 4.4 | Biomass particle pyrolysis in a fluidized bed reactor | 21 |
| 4.4.1 | Detailed physico-chemical parameters of biomass pyrolysis | 22 |
| 4.4.2 | Simulation details | 22 |
| 4.4.3 | Results | 23 |
| 5 | Conclusions | 25 |
| 6 | Acknowledgments | 26 |
| 7 | Appendix A: Estimate of the ratio of heat transfer through direct particle contact to gas-particle heat transfer | 26 |
| 8 | Appendix B: Calculation of collision integrals | 28 |
| 9 | Appendix C: Derivation of the self-diffusion coefficient | 29 |

1 Introduction

Many practical multiphase flow systems involve the flow of a dense, reactive, gas-particle mixture. Examples include coal combustion, catalyst regeneration and pyrolysis applications, among others. Because of the lack of fundamental knowledge of both the fluid-mechanical and thermal behavior of these systems, the design of these processes has been necessarily based on empirical correlations and experiments performed in laboratory or pilot scale units. However, models and simulations of these systems would allow the optimization of the processes and their scaling, without the need for expensive and time consuming testing. This work is the first step towards providing such a model.

One of the distinctive characteristics of these dense flows is that momentum and energy are primarily exchanged through collisions between particles rather than through the gaseous phase (Savage and Sayed, 1984). The particles then interact similarly to the molecules of a dense gas. Jenkins and Savage (1983) first exploited this analogy and used a kinetic theory approach, based on Gaussian velocity distributions, to derive macroscopic equations of the mixture. Since then, this concept has been expanded and improved by considering more general velocity distributions (Lun et al., 1984; Jenkins and Richman, 1985), important for more dilute regions, and by including

effects of the interstitial gas (e.g. Balzer et al., 1993), which may be important for small particles. A crucial role in these theories is played by the ‘granular temperature’, the mean kinetic energy associated with the velocity fluctuations of the particles. Reviews on granular flows are given by Campbell (1990) and Goldhirsch (1999).

Most of the modeling work performed so far has focussed on isothermal, monodisperse mixtures. The majority of industrial interest, however, lies in systems that include multiple particle types and reactive flows, with their associated effects of mixing, segregation and heat transfer (see the recent review of Ottino and Khakhar, 2000 for segregation phenomena). Analyses of binary (or multicomponent) dry granular mixtures are available (Farell et al., 1986; Jenkins and Mancini, 1987; Jenkins and Mancini, 1989; Zamankhan, 1995), and are based on extensions of standard kinetic theory of dense gases (e.g. Tham and Gubbins, 1971), appropriately modified to include the effect of dissipation due to inelasticity. In all of the aforementioned references, equipartition of granular energy of the respective particle classes is assumed. However, this assumption holds for molecular systems where dissipative effects are absent, and when the mass ratio of the respective particles is moderate. For granular flows, this assumption is inappropriate due to the dissipation associated with the inelasticity of particle collisions. Furthermore, all aforementioned studies assume the drift velocity between the respective particle classes to be small compared to a representative velocity of particle fluctuation, an assumption that is inappropriate for more dilute granular systems subject to body forces, causing appreciable drift (Gourdel et al., 2000).

The theoretical investigation of heat transfer in granular systems has been initiated only recently. Louge et al. (1993) investigated the thermal behavior of a dilute suspension whereas Hsiau (2000) has given a detailed analysis of the heat transfer coefficient for a wide region of particle fractions, both for monodisperse and for binary mixtures. Theoretical foundations on dense, reactive multicomponent, mixtures, where all of the above processes play a role, are virtually absent in literature.

In the present study, we derive a comprehensive model for the flow of a multicomponent, dense, reactive, particle mixture. To this end, separate dynamic equations are derived for each particle class describing the evolution of its mean velocity, temperature, etc. These transport equations are coupled through source terms that describe the various non-equilibrium processes, such as mass, momentum and energy transfer, both between particles and the gas, and between the respective particle classes. The kinetic theory is based on a Gaussian approximation for the velocity distribution, assuming the spatial gradients of the mean variables to be small and the particles to be nearly elastic. Detailed analysis of the heat transfer during a collision between particles indicates that this constitutes a negligible contribution, and consequently the conduction in the particle phases is treated as a self-diffusion phenomenon, based on the recent analysis given by Hsiau (2000). Other diffusive contributions, resulting from the random motion of the particles are modeled in a similar way. The source terms expressing the transfer mechanisms are obtained by averaging the appropriate transfer correlations for a single particle.

As an application of the present work, the hydrodynamic equations are combined with a validated chemistry model for the description of biomass particle pyrolysis, consisting of 7 solid species and 2 gaseous components. The complete model is then applied to the pyrolysis in a pilot-scale fluidized bed and compared to appropriate experimental data of specific product yields.

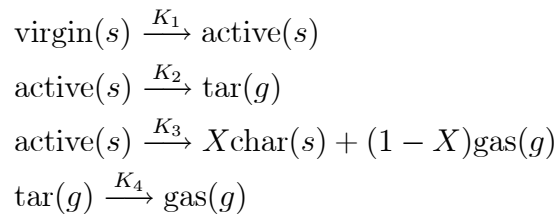
2 Mathematical model

A continuum model is derived by applying separate averaging procedures for both the carrier gas and solid phases. A phase ensemble average is used for the carrier phase, combined with a particle

ensemble average where particle properties, such as velocity, are directly averaged. This is attractive when resolution of the detailed degrees of freedom of the particles (e.g. internal temperature profiles or profiles of the internal chemical composition) is undesirable or unnecessary.

2.1 Single particle biomass pyrolysis model

The particle pyrolysis model employed here is that of the detailed kinetics derived by Miller and Bellan (1997), based on superimposed cellulose, hemicellulose, and lignin reactions. This enables the simulation of different biomass feedstock through knowledge of the initial mass composition with respect to these three primary components; biomass impurities are lumped with the hemicellulose as this model correlated best with the experimental data. Each of the virgin components undergoes the same generic competitive reaction scheme:



As indicated in the above kinetics scheme, the virgin components, the active intermediates and the char are solid phase species, while tar and gas are vapor products; these species are not pure chemical species but represent groups of compounds. All reactions are modelled with first order Arrhenius kinetics; $K_i = A_i \exp(-E_i/RT)$, where the rate constants, A_i , activation energies, E_i for reactions K_1, K_2, K_3 and the mass ratio X are dependent on the particular component, whereas all heats of reaction and secondary tar decomposition parameters (K_4) are independent of the source component.

This kinetics model combined with a porous particle flow dynamics model yielded validated predictions on tar/char yields ranging from the kinetically controlled region (micro particles) to the diffusion controlled limit (macro particles), cf. Miller and Bellan (1997). In the present paper, for simplicity, the biomass pyrolysis is assumed kinetically controlled. This assumption may be justified in the dense particulate regime where contact between particles may induce fragmentation (see Miller and Bellan, 1998, for a fragmentation model) and reduce the size of the particles to the point where the internal temperature equilibrates rapidly. Thus, the particle temperature, its mass and composition (global solid mass fractions) completely describe the state of the particle.

The sand and biomass particles are both solid and hence thermodynamically belong to the same phase. They, however, have different physical properties and different temperatures, etc. In particular, the biomass particles are porous whereas the sand particles are not. Therefore these particle classes are handled separately.

2.2 Gas phase transport equations

As the procedure for phase ensemble averaging is well-known (Drew, 1983), we will restrict the present discussion to the necessary results. The general ensemble average of a field quantity $\Psi(\mathbf{x}, t)$, (\mathbf{x}, t denoting space and time coordinates) is

$$\langle \Psi(\mathbf{x}, t) \rangle = \int \Psi(\mathbf{x}, t) P(\omega) d\omega \quad (1)$$

where $P(\omega)$ is the probability that a specific realization ω is encountered in the ensemble. The gas-phase ensemble average and its density-weighted counterpart are defined Drew (1983) as $\bar{\Psi} \equiv \langle \chi_g \Psi(\mathbf{x}, t) \rangle / \alpha_g$ and $\tilde{\Psi} \equiv \langle \chi_g \rho_g \Psi(\mathbf{x}, t) \rangle / \alpha_g \bar{\rho}_g$, where ρ_g is the gas density, χ_g denotes the phase indicator of the gas phase which is unity in the gas phase and zero otherwise, and the gas phase fraction, α_g , is defined as the ensemble average of the indicator function, i.e. $\alpha_g = \langle \chi_g \rangle$. The average transport equations for the gas phase now follow by multiplying the local instantaneous equations (the Navier Stokes set supplemented with energy and species equations) by the phase indicator and ensemble averaging:

$$\frac{\partial(\alpha\bar{\rho})_g}{\partial t} + \nabla \cdot (\alpha\bar{\rho}\tilde{\mathbf{u}})_g = \Gamma_g \quad (2)$$

$$\frac{\partial(\alpha\bar{\rho}\mathbf{u})_g}{\partial t} + \nabla \cdot (\alpha\bar{\rho}\tilde{\mathbf{u}}\tilde{\mathbf{u}})_g = \nabla \cdot \alpha[-\bar{p} + \bar{\boldsymbol{\tau}} + \boldsymbol{\Sigma}_g^{\text{Re}}]_g + \alpha_g \bar{\rho}_g \mathbf{f}_g + \mathbf{M}_g + \Gamma_g \mathbf{u}_g^i \quad (3)$$

$$\frac{\partial(\alpha\bar{\rho}h)_g}{\partial t} + \nabla \cdot (\alpha\bar{\rho}\tilde{\mathbf{u}}\tilde{h})_g = -\nabla \cdot \alpha[\bar{\mathbf{q}} + \mathbf{q}^{\text{Re}}]_g + F_g + \Gamma_g h_g^i \quad (4)$$

$$\frac{\partial(\alpha\bar{\rho}\tilde{Y}_\xi)_g}{\partial t} + \nabla \cdot (\alpha\bar{\rho}\tilde{\mathbf{u}}\tilde{Y}_\xi)_g = -\nabla \cdot \alpha[\bar{\mathbf{j}}_{g\xi} + \mathbf{j}_\xi^{\text{Re}}]_g + \alpha_g \bar{\rho}_g \tilde{R}_{g\xi} + H_{g\xi} + \Gamma_g Y_{g\xi}^i. \quad (5)$$

Here, the main variables are the gas velocity \mathbf{u} , the specific enthalpy h , the gas pressure p , and the mass fractions of specie ξ , Y_ξ . $\boldsymbol{\tau}$, \mathbf{q} , and $\mathbf{j}_{g\xi}$ denote the molecular viscous stress, the molecular heat flux vector and the species diffusion flux vector, respectively. The gravitational acceleration is given by \mathbf{f}_g , and $R_{g\xi}$ is the reaction rate for specie ξ . The terms \mathbf{M}_g , F_g , and $H_{g\xi}$ denote the diffusive interfacial transfer of momentum, enthalpy and species mass, respectively, and are defined as

$$\mathbf{M}_g \equiv - \langle (-p + \boldsymbol{\tau}) \cdot \nabla \chi_g \rangle; H_{g\xi} \equiv \langle \mathbf{j}_{g\xi} \cdot \nabla \chi_g \rangle; F_g \equiv \langle \mathbf{q}_g \cdot \nabla \chi_g \rangle. \quad (6)$$

The terms Γ_g , $\Gamma_g \mathbf{u}_g^i$, $\Gamma_g Y_{g\xi}^i$, and $\Gamma_g h_g^i$ are the convective interfacial transfer fluxes of mass, momentum, enthalpy and species mass, and are expressed in terms of the gas velocity at the interface between the phases, \mathbf{u}_{gi}

$$\Gamma_g \equiv \langle \rho_g (\mathbf{u}_g - \mathbf{u}_{gi}) \cdot \nabla \chi_g \rangle \quad (7)$$

$$\Gamma_g \mathbf{u}_g^i \equiv \langle \rho_g \mathbf{u}_g (\mathbf{u}_g - \mathbf{u}_{gi}) \cdot \nabla \chi_g \rangle \quad (8)$$

$$\Gamma_g Y_{g\xi}^i \equiv \langle \rho_g Y_{g\xi} (\mathbf{u}_g - \mathbf{u}_{gi}) \cdot \nabla \chi_g \rangle \quad (9)$$

$$\Gamma_g h_g^i \equiv \langle \rho_g h_g (\mathbf{u}_g - \mathbf{u}_{gi}) \cdot \nabla \chi_g \rangle. \quad (10)$$

Finally, the equations contain ‘turbulent’ fluxes, $\boldsymbol{\Sigma}_g^{\text{Re}}$, $\mathbf{j}_{g\xi}^{\text{Re}}$, \mathbf{q}_g^{Re} expressing the flux of momentum, enthalpy and species mass given by the following expressions

$$\boldsymbol{\Sigma}_g^{\text{Re}} \equiv - \frac{\langle \chi_g \rho_g \mathbf{u}'_g \mathbf{u}'_g \rangle}{\alpha_g}; \mathbf{j}_{g\xi}^{\text{Re}} \equiv \frac{\langle \chi_g \rho_g \mathbf{u}'_g Y'_{g\xi} \rangle}{\alpha_g}; \mathbf{q}_g^{\text{Re}} \equiv \frac{\langle \chi_g \rho_g \mathbf{u}'_g h'_g \rangle}{\alpha_g}, \quad (11)$$

where the fluctuations result from a decomposition of each of the instantaneous variables into its mean and a fluctuation, e.g. $\mathbf{u}_g = \tilde{\mathbf{u}}_g + \mathbf{u}'_g$. A detailed turbulence model derivation for the general reactive case can be found in Lathouwers and Bellan (1999b). Owing to the usage of appropriate density-weighted variables, the general form of these transport equations is comparable to their local instantaneous form. In the above enthalpy equation, we have neglected the effect of pressure work and viscous dissipation.

Neglecting correlations between the gas temperature and mass fractions gives the averaged equations of state

$$\bar{p}_g = R^0 \bar{\rho}_g \sum_{\xi} \frac{\tilde{Y}_{\xi}}{W_{\xi}} \tilde{T}_g \quad (12)$$

where R^0 denotes the universal gas constant, W_{ξ} is the molecular weight of specie ξ , and T_g is the gas temperature.

The average viscous stress tensor is approximated by a form similar to its microscopic counterpart $\bar{\boldsymbol{\tau}}_g = 2\mu_g \mathbf{S}_g$, where \mathbf{S}_g denotes the strain rate tensor: $\mathbf{S}_g = (\nabla \tilde{\mathbf{u}}_g + \nabla \tilde{\mathbf{u}}_g^T)/2 - (\nabla \cdot \tilde{\mathbf{u}}_g)/3$ and μ_g is the gas viscosity. The average specie flux $\bar{\mathbf{j}}_{\xi}$ is written as a simple gradient diffusion (Fickian) relation, neglecting multicomponent aspects:

$$\bar{\mathbf{j}}_{\xi} = -\bar{\rho}_g D_{\xi} \nabla \tilde{Y}_{\xi}, \quad (13)$$

where D_{ξ} is the mass diffusion coefficient. Similarly, the average molecular heat flux $\bar{\mathbf{q}}_g$ is modeled in analogy with its molecular counterpart (Bird, 1960)

$$\bar{\mathbf{q}}_g = -\lambda_g \nabla \tilde{T}_g - \sum_{\xi} h_{\xi} \bar{\mathbf{j}}_{\xi} \quad (14)$$

with λ_g denoting the heat conductivity coefficient, and where the second term represents the effect of species interdiffusion. Following Drew (1983), the momentum transfer term may be decomposed into two contributions:

$$\mathbf{M}_g = -p_g^i \nabla \alpha_g + \mathbf{M}'_g \quad (15)$$

where we have introduced the average interfacial gas pressure, p_g^i . The first term in eq. 15 accounts for the buoyant force while the second incorporates such forces as gas-particle drag, etc. The momentum equation is then

$$\frac{\partial \alpha_g \bar{\rho}_g \tilde{\mathbf{u}}_g}{\partial t} + \nabla \cdot \alpha_g \bar{\rho}_g \tilde{\mathbf{u}}_g \tilde{\mathbf{u}}_g = -\alpha_g \nabla \bar{p}_g + \nabla \cdot [\alpha_g \bar{\boldsymbol{\tau}}_g + \boldsymbol{\Sigma}_g^{Re}] + \alpha_g \bar{\rho}_g \mathbf{f}_g + \mathbf{M}'_g + \Gamma_g \mathbf{u}_g^i \quad (16)$$

where the difference between the interfacial and the average gas pressure has been neglected, i.e. $p_g^i = \bar{p}_g$. Closure of the average transfer of mass, momentum and energy between the phases is derived below.

2.3 Particle phase transport equations

The transport equations are derived similarly to those for dense gases, using kinetic theory concepts. Important differences from classical kinetic theory are the inelasticity of collisions between macroscopic particles leading to dissipation, and the presence of an interstitial gas exerting drag on the particles, which leads to interaction terms in the averaged transport equations.

While a considerable literature exists on the development of equations of motion for multicomponent mixtures, most of it is restricted to the case where the temperatures and velocities of the species are nearly equal and evolve according to the dynamic equations of the mixture. This classical mixture theory (Chapman and Cowling, 1970) requires that $\Delta u / \Theta_c \ll 1$ (Δu being a characteristic relative velocity of the particle classes and Θ_c a characteristic rms velocity, related to a temperature in the molecular context). Furthermore, granular energy is assumed to be partitioned among the various particle classes according to their mass ratios (equipartition). The latter assumption is specifically inappropriate for granular flows due to the inelasticity of collisions. Therefore, here we

derive separate dynamic equations for each of the particle classes, similar to that of Goldman and Sirovich (1967) for a dilute mixture of interacting species.

Let $f_i^{(1)}(\mathbf{x}, \mathbf{c}, Y_\xi, T, m, t)$ denote the single particle distribution function of particle class i such that $f_i^{(1)}$ is the probable number of particles of class i having their center of mass in the region $[\mathbf{x}, \mathbf{x} + d\mathbf{x}]$, a velocity in the region $[\mathbf{c}, \mathbf{c} + d\mathbf{c}]$, mass in the region $[m, m + dm]$, mass fractions in $[Y_\xi, Y_\xi + dY_\xi]$, and temperature in $[T, T + dT]$. The evolution of each of these distribution functions is governed by a set of Boltzmann equations (Simonin, 1996)

$$\frac{\partial f_i^{(1)}}{\partial t} + \frac{\partial}{\partial \mathbf{x}}[\mathbf{c}_i f_i^{(1)}] + \frac{\partial}{\partial \mathbf{c}_i} \left[\frac{\mathbf{F}_i}{m_i} f_i^{(1)} \right] + \frac{\partial}{\partial m_i} \left[\frac{dm_i}{dt} f_i^{(1)} \right] + \frac{\partial}{\partial T_i} \left[\frac{dT_i}{dt} f_i^{(1)} \right] + \sum_{\xi} \frac{\partial}{\partial Y_{i,\xi}} \left[\frac{dY_{i,\xi}}{dt} f_i^{(1)} \right] = \sum_j J_{ij} \quad (17)$$

where \mathbf{F}_i is the external force on the particle (gravity and particle drag). The right hand side represents the effect of collisions with particles of all classes.

The number density, n_i , of particle phase i follows by integration of the single-particle distribution function f_i over all of phase space

$$n_i(\mathbf{x}, t) = \int f_i d\mathbf{c} dY_\xi dT dm. \quad (18)$$

With the previously derived single-particle distribution, a particle average may be introduced as follows

$$\bar{\Psi}_i(\mathbf{x}, t) = \frac{1}{n_i} \int \Psi_i f_i d\mathcal{Z} \quad (19)$$

where $d\mathcal{Z}$ denotes the set of integration variables. The mass of the particles need not be a constant, therefore mass weighted averages are also introduced:

$$\tilde{\Psi}_i(\mathbf{x}, t) = \frac{1}{\alpha_i \bar{\rho}_i} \int m_i \Psi_i f_i d\mathcal{Z} \quad (20)$$

where

$$\alpha_i \bar{\rho}_i = n_i \bar{m}_i = \int m_i f_i d\mathcal{Z}. \quad (21)$$

This definition of the mass-weighted particle average is completely comparable to that used for the carrier phase and leads to more convenient forms of the moment equations derived later. In the above expression, α_i denotes the local phase fraction of class i (where pores are excluded) and $\bar{\rho}_i$ its corresponding average particle density. We also introduce equivalent definitions for $\hat{\alpha}_i$ and $\hat{\rho}_i$ where the pores of the particles are counted as volume belonging to the particle. Note that $\alpha_i \bar{\rho}_i = \hat{\alpha}_i \hat{\rho}_i$. Mass weighted averages will also be denoted by brackets, i.e. $\langle \Psi \rangle_i = \tilde{\Psi}_i$ in the derivation below. Using the above definitions we define the average velocity $\mathbf{u}_i = \langle \mathbf{c}_i \rangle$, the fluctuation velocity component, $\mathbf{C}_i = \mathbf{c}_i - \mathbf{u}_i$, and the granular temperature, $\Theta_i = \frac{1}{3} \langle C^2 \rangle$. The solidity, $\eta = 1 - \epsilon$, where ϵ is the porosity of a particle, is defined as the ratio of the volume displaced by the particle and the volume displaced by the particle if its pores had been closed. The solidity is then easily shown to equal

$$\eta_i = \frac{m_i}{V_i} \sum \frac{Y_\xi}{\rho_\xi}. \quad (22)$$

In the present case of biomass pyrolysis, we assume that the particle diameter stays constant throughout the pyrolysis, and that the porosity of the particle simply increases in time (Miller and Bellan, 1997). This assumption is correct when the particle does not break or erodes.

The moment equations are derived by multiplying the Boltzmann equation by a variable $m\Psi$ and integrating over phase space. The general transport equation obtained is

$$\begin{aligned} \frac{\partial \alpha_i \bar{\rho}_i \tilde{\Psi}_i}{\partial t} + \nabla \cdot (\alpha_i \bar{\rho}_i \langle \mathbf{c}_i \Psi_i \rangle) &= \sum_{k=A,B} C_{ik}(m_i \Psi_i) + \\ \alpha_i \bar{\rho}_i \langle \frac{\mathbf{F}_i}{m_i} \frac{\partial \Psi_i}{\partial \mathbf{c}_i} \rangle + \alpha_i \bar{\rho}_i \langle \frac{dT_i}{dt} \frac{\partial \Psi_i}{\partial T_i} \rangle + & \\ \alpha_i \bar{\rho}_i \sum_{\xi} \langle \frac{dy_{i\xi}}{dt} \frac{\partial \Psi_i}{\partial y_{i\xi}} \rangle + \alpha_i \bar{\rho}_i \langle \frac{dm_i}{dt} [\frac{\partial \Psi_i}{\partial m_i} + \frac{\Psi_i}{m_i}] \rangle & \end{aligned} \quad (23)$$

where $C_i(m_i \Psi_i)$ is the mean collisional rate of change of particle property Ψ_i . It represents an integral over all possible (binary) collisions of the change in $m_i \Psi_i$ multiplied by the probability that such a collision occurs. Jenkins and Mancini (1987, 1989) show that this integral can be written as the sum of a source-like contribution and a flux term, representing transport by collisions:

$$C_{ik}(m_i \Psi_i) = \chi_{ik}(m_i \Psi_i) - \nabla \cdot \theta_{ik}(m_i \Psi_i) \quad (24)$$

The precise forms of these integrals is given in Appendix A where an outline is given on a method for calculating these collision integrals.

2.3.1 Collision dynamics

As in kinetic theory, it is assumed that only binary collisions occur, i.e. collisions among multiple particles are neglected. Although at high solids concentrations this assumption is questionable (especially when the particle size ratio is large), it is the only mathematically tractable approach (even in the simpler, molecular theory; see Chapman and Cowling, 1970).

As in Jenkins and Mancini (1987), we consider two particle classes, A and B, although more classes may be added without changing the formalism. These particles are assumed perfectly smooth and spherical. Their respective masses and diameters are m_A , m_B , σ_A , and σ_B . Consider a collision between particle 1 of class i and particle 2 of class k where i and k may be A or B. Furthermore, when considering collisions, primes will be used to denote a variable right after collision, a variable without a prime denoting a variable right before collision. Below we consider the conservation of momentum and energy (mass and species are trivial) during a collision between particle 1 and 2.

Momentum Assuming exclusively binary collisions and perfectly spherical and smooth particles, the relation between the velocities of the particles right before and after a collision of particle 1 of class i and particle 2 of class k is determined from the conservation of momentum and energy; see Chapman and Cowling (1970). Defining \mathbf{g} as the relative velocity, $\mathbf{c}_1 - \mathbf{c}_2$, we assume \mathbf{g} before and after collision to be related as $(\mathbf{g}' \cdot \mathbf{k}) = -e_{ik}(\mathbf{g} \cdot \mathbf{k})$, where e_{ik} is the restitution coefficient, incorporating the effect of inelasticity on the collisions ($e_{ik} = 1$ for perfectly elastic encounters). Further define the sum of the particle's masses $m_{ik} = m_i + m_k$ and the reduced mass $M_i = m_i/m_{ik}$. The center of mass velocity, \mathbf{c}_m , is constant during a collision and is found from

$$\mathbf{c}_m = M_k \mathbf{c}_2 + M_i \mathbf{c}_1 = M_k \mathbf{c}'_2 + M_i \mathbf{c}'_1. \quad (25)$$

From these relations we derive,

$$\mathbf{c}'_1 - \mathbf{c}_1 = -M_k(1 + e_{ik})(\mathbf{g} \cdot \mathbf{k})\mathbf{k}. \quad (26)$$

In general, for any particle property $\Psi = \Psi(\mathbf{c})$, these relations may be used to calculate its rate of change $\Psi' - \Psi$ in a collision. In the above we have assumed that the collision is not abrasive, i.e. the mass the particles does not change during a contact.

Energy Sun and Chen (1988) presented a detailed analysis of the heat transfer between two colliding particles. Their theory is based on the analysis of the elastic deformation of the spheres as they contact, and the resulting heat conduction. Since detailed information may be found in the aforementioned reference, only the pertinent essentials are emphasized here. The spheres are termed with indices 1 and 2. If one defines the average radius, R , the average mass, m and the average elastic modulus, E as follows

$$R = \frac{R_1 R_2}{R_1 + R_2}; \quad m = \frac{m_1 m_2}{m_1 + m_2}; \quad E = \frac{4/3}{\frac{1-\nu_1^2}{E_1} + \frac{1-\nu_2^2}{E_2}} \quad (27)$$

where ν_i and E_i denotes the Poisson ratios and the Young moduli of the respective materials. The contact time is usually very small which implies that the temperature of the particle remains uniform except in a very small region around the contact area. For small Fourier numbers for both spheres, based on the total contact time, t_c and the contact area, A_c ($Fo = \pi a t_c / A_c$, with a the thermal diffusivity of the particle), the problem may be approximated by 2 contacting infinite plates. The heat exchange between the two particles in this simplified case is given by

$$\Delta E = \frac{5.36(m/E)^{3/5}(Rg)^{7/10}(T_1 - T_2)}{(\rho c_p \lambda)_1^{-1/2} + (\rho c_p \lambda)_2^{-1/2}} \quad (28)$$

where g denotes the magnitude of \mathbf{g} and the numerical constant is obtained from numerical integration. Sun and Chen (1988) further note that the small Fourier number approximation is valid if the velocity at which the particles collide is not too small ($\simeq 1$ cm/s for sand).

2.3.2 Particle dynamics

The second component needed for the derivation of the moment equations is the rate of change of the particle properties along their trajectory.

Species mass fractions As outlined earlier, the mass conversion rates are linear in the mass of the particle itself. In general we may write

$$\frac{dm_{i,\xi}}{dt} = \frac{dmY_{i,\xi}}{dt} = mR_{i,\xi} \quad (29)$$

where $R_{i,\xi}$ represents the total rate, and may be the sum of several reactions involving the same component. The rate is linear in the mass fractions and exponential in the particle temperature (Arrhenius kinetics). From the previous equation one obtains the rate of change of $Y_{i,\xi}$

$$\frac{dY_{i,\xi}}{dt} = R_{i,\xi} - \frac{Y_{i,\xi}}{m_i} \frac{dm_i}{dt}. \quad (30)$$

Particle mass The rate of change of the particle mass is obtained by summing the individual species rates

$$\frac{dm_i}{dt} = \sum_{\xi} \frac{dm_{i,\xi}}{dt} = m_i \sum_{\xi} R_{i,\xi}. \quad (31)$$

In practice, only some reactions contribute to phase change.

Momentum The momentum equation of a single particle can be approximated as

$$m_i \frac{d\mathbf{c}_i}{dt} = \mathbf{F}_i = m_i \mathbf{f}_g - V_i \nabla \overleftarrow{p}_g + \frac{m_i}{\tau_{i,12}} (\overleftarrow{\mathbf{u}}_g - \mathbf{c}_i) \quad (32)$$

where the total force on the particle is due to the gravitational acceleration, \mathbf{f}_g , gas pressure gradient and gas-particle drag. V_i is the volume of the particle including the pores (i.e. $\pi d_i^3/6$) and $\tau_{i,12}$ represents the relaxation time scale of the particle. The $\overleftarrow{(\)}$ on the gas-phase variables denotes the evaluation of the variable at the location of the particle, as if the surrounding flow was undisturbed by its presence (Balzer et al., 1993). The gas-particle interaction time scale depends strongly on the flow regime; in the dilute regime it is derived from the drag coefficient, C_d , of a single particle in an infinite medium, empirically corrected for the presence of other surrounding particles by a function $f(\alpha_g) = \hat{\alpha}_g^{-1.7}$ (e.g. Gidaspow, 1986) whereas in the dense regime the classical Ergun relation is used. To avoid discontinuous behavior, a weighted average of the two time scales is introduced

$$\frac{1}{\tau_{i,12}} = W \frac{3\rho_g C_d(Re_i)}{4\rho_i d_i} |\mathbf{c}_i - \overleftarrow{\mathbf{u}}_g| f(\hat{\alpha}_g) + (1 - W) \frac{\rho_g}{\rho_i} \left[(1 - \hat{\alpha}_g) \frac{150}{Re_i} + 1.75 \right] \frac{|\mathbf{c}_i - \overleftarrow{\mathbf{u}}_g|}{d_i} \quad (33)$$

where the present switch function, $W(\hat{\alpha}_g) = \arctan(150(\hat{\alpha}_g - 0.8))/\pi + 1/2$, gives a rapid transition from one regime to the other. d_i is the diameter of the particle and Re_i the Reynolds number based on the relative velocity with the gas, $Re_i = \hat{\alpha}_g \rho_g |\mathbf{c}_i - \overleftarrow{\mathbf{u}}_g| d_i / \mu_g$. In the above expressions we have introduced $\hat{\alpha}_g$ which represents the volume fraction of the gas-phase, not counting the pores of the particles. The single particle drag coefficient C_d is determined from the well-known correlation (Schiller and Nauman, 1935)

$$C_d = \frac{24}{Re_p} (1 + 0.15 Re^{0.687}). \quad (34)$$

Although not attempted in the present work due to the different range in Re_p , this correlation may be further improved by adding a correction which results from the effect of mass transfer, as done in the validated model of Miller et al. (1999).

Energy The rate of change of the particle's internal energy is due to heat exchange with the surrounding gas resulting from convection and diffusion, loss of vapor components to the gaseous phase carrying a specific enthalpy, h_v , and expansion work performed against the gas phase

$$m_i \frac{dh_i}{dt} = Q_{r,i} + \frac{dm_i}{dt} (h_v - h_i) + \frac{m_i}{\rho_i} \frac{dp_g}{dt}. \quad (35)$$

Here, the particle's specific enthalpy, h_i , is defined as $h_i = \sum Y_{i,\xi} h_{i,\xi}$ and the average density of the particle is related to the 'true' densities of the individual solid species by $1/\rho_i = \sum Y_{i,\xi} / \rho_{i,\xi}$. The above equation, in fact defines the heat flux $Q_{r,i}$ (Young, 1995). It can also be written in terms of the particle temperature, T_i by using the thermodynamic differential for the specific enthalpy of a component:

$$dh_{i,\xi} = C_{p,i,\xi} dT_i + \frac{dp_g}{\rho_{i,\xi}} \quad (36)$$

where the pressure inside the particle has been equated to the gas pressure outside the particle. Using this relation in (35) leads to the expected result

$$(mC_p)_i \frac{dT_i}{dt} = Q_{r,i} + \sum \frac{dm_{i,\xi}}{dt} (h_v - h_\xi) \quad (37)$$

where the effect of pressure has cancelled, as it should. The second term on the right hand side is exactly equal to the total heat of reaction for the particle.

The combined effect of convective and conductive heat transfer can be written in terms of an appropriate Nusselt relation

$$Q_{r,i} = -\lambda_g \pi d_i Nu_i (T_i - \overleftarrow{T}_g) \quad (38)$$

where Nu_i depends on the Reynolds number of the particle and on the Prandtl number, Pr_g , of the carrier gas. In obtaining relevant Nusselt relations for this situation, it is assumed that the particle temperature is uniform, i.e. the resistance to heat transfer is mainly in the gas-phase. This assumption is consistent with those used to actually derive the continuum theory, as the state variables of the particles include their mean temperature only, i.e. no information on the internal temperature distribution is available. Implicitly, the Biot numbers are assumed small ($Bi = hd_i/\lambda_i$, where h is the gas-particle heat transfer coefficient). In the present case, the Nusselt number is taken as the single particle Nusselt relation, Nu_i^0 , multiplied by a correction factor, F_b , accounting for the effect of mass transfer on the heat transfer rate, i.e.

$$Nu = Nu^0 F_b(Re, Pr_g). \quad (39)$$

The formulation used here for the blowing factor is that taken from Miller et al. (1999) and was also given by Gyarmathy (1982) where the factor depends on the ‘blowing Reynolds number’, $Re_b = \dot{m} / \pi d_i \mu_g$,

$$\begin{aligned} F_b &= \frac{X}{e^X - 1}; \\ X &= \frac{Pr_g Re_b}{2}. \end{aligned} \quad (40)$$

For Nu^0 , we use the standard Ranz correlation

$$Nu^0 = 2 + 0.66 Re^{1/2} Pr^{1/3}. \quad (41)$$

There does not appear to be much information on the dependence of Nu^0 on α_g for cases where the particle number density is high, such as in the packed region. A correlation, based on experimental observations, proposed by Gunn (1978) for the porosity range of 0.35 to 1 is

$$Nu^0 = (5\alpha_g^2 - 10\alpha_g + 7)(1 + 0.7 Re^{0.2} Pr^{1/3}) + (1.2\alpha_g^2 - 2.4\alpha_g + 1.33) Re^{0.7} Pr^{1/3} \quad (42)$$

In the limit of $\alpha_g \rightarrow 1$, this relation reduces to

$$Nu^0 = (2 + 1.4 Re^{0.2} Pr^{1/3}) + 0.13 Re^{0.7} Pr^{1/3} \quad (43)$$

which clearly illustrates its discrepancy with the commonly accepted Ranz relation. Furthermore, the values of the coefficients in the Gunn relation are not strong functions of the volume fraction: for α_g between 0.4 and 1, $5\alpha_g^2 - 10\alpha_g + 7$ varies between 3.8 and 2 while $1.2\alpha_g^2 - 2.4\alpha_g + 1.33$ varies between 0.56 and 0.13. For these reasons, the single-sphere relation is adopted here. Heat transfer through radiation is neglected since the gas is considered transparent.

2.3.3 The moment equations

By making specific choices for the general variable Ψ in the transport theorem, specific moment equations are recovered.

Mass The mass conservation equations are recovered by taking $\Psi = 1$:

$$\frac{\partial(\alpha_i \bar{\rho}_i)}{\partial t} + \nabla \cdot (\alpha_i \bar{\rho}_i \mathbf{u}_i) = \Gamma_i \quad (44)$$

where the mass transfer $\Gamma_i = \alpha_i \bar{\rho}_i \langle \frac{1}{m_i} \frac{dm_i}{dt} \rangle = \alpha_i \bar{\rho}_i \sum_{\xi} \langle R_{i,\xi} \rangle$ can be coupled to the conversion rate of solid- to gas-phase reactions. For inert particles, this term is absent.

Momentum The momentum equations are generated using $\Psi = \mathbf{c}$

$$\begin{aligned} \frac{\partial(\alpha_i \bar{\rho}_i \mathbf{u}_i)}{\partial t} + \nabla \cdot (\alpha_i \bar{\rho}_i \mathbf{u}_i \mathbf{u}_i) &= \alpha_i \bar{\rho}_i \langle \frac{\mathbf{F}_i}{m_i} \rangle + \alpha_i \bar{\rho}_i \langle \frac{dm_i}{dt} \frac{\mathbf{c}_i}{m_i} \rangle \\ &\quad - \nabla \cdot \boldsymbol{\Sigma}_i + \sum_{k=A,B} \chi_{ik}(m_i \mathbf{C}_i) \end{aligned} \quad (45)$$

where $\boldsymbol{\Sigma}_i = \alpha_i \bar{\rho}_i \langle \mathbf{C}_i \mathbf{C}_i \rangle + \sum_{k=A,B} \theta_{ik}(m_i \mathbf{C}_i)$. The first term on the right hand side of eq. ?? is the average force exerted on the particle by the surrounding gas; the second represents the effect of mass transfer. The effective stress tensor $\boldsymbol{\Sigma}_i$ consists of a kinetic part and a collisional part which incorporates both effects from collisions between particles of the same class and between unlike particles. The final term in the transport equation is a source term which is also composed of collisional contributions between like and unlike particles. However, as the total momentum of phase i is conserved in a collision between two particles of that phase, only unlike particle collisions contribute to this term. Note that an equivalent term does not appear in single-class formulations.

Species mass fractions Taking $\Psi = Y_{i\xi}$ gives

$$\frac{\partial(\alpha_i \bar{\rho}_i \tilde{Y}_{i\xi})}{\partial t} + \nabla \cdot (\alpha_i \bar{\rho}_i \mathbf{u}_i \tilde{Y}_{i\xi}) = -\nabla \cdot (\alpha_i \bar{\rho}_i \langle \mathbf{C}_i Y'_{i\xi} \rangle) + \Gamma_{i\xi}. \quad (46)$$

The first term on the right hand side denotes the turbulent transport of the mass fraction. The second term, $\Gamma_{i\xi} = \alpha_i \bar{\rho}_i \langle R_{i,\xi} \rangle$ is the average mass source arising from reaction. Note that no collisional terms are present, as the mass fractions do not change during a collision.

Granular temperature Choosing $\Psi = 1/2C^2$

$$\begin{aligned} \frac{3}{2} \left[\frac{\partial(\alpha_i \bar{\rho}_i \Theta_i)}{\partial t} + \nabla \cdot (\alpha_i \bar{\rho}_i \mathbf{u}_i \Theta_i) \right] &= -\boldsymbol{\Sigma}_i : \nabla \mathbf{u}_i - \nabla \cdot \mathbf{q}_i \\ &\quad + \gamma_i + \alpha_i \bar{\rho}_i \langle \frac{dm_i}{dt} \frac{1/2C_i^2}{m_i} \rangle + \alpha_i \bar{\rho}_i \langle \frac{\mathbf{F}_i}{m_i} \cdot \mathbf{C}_i \rangle, \end{aligned} \quad (47)$$

where $\Theta_i = 1/3 \langle C_i^2 \rangle$ is the ‘granular temperature’. The first term on the right hand side of eq. 47 is the production of fluctuation kinetic energy due to shearing of the solid phase. $\mathbf{q}_i = \alpha_i \bar{\rho}_i \langle 1/2C_i^2 \mathbf{C} \rangle + \sum_{k=A,B} \theta_{ik}(1/2m_i C_i^2)$ is the average ‘heat flux’ both due to velocity fluctuations and through collisions. The source term, $\gamma_i = \sum_k \chi_{ik}(\frac{1}{2}m_i C_i^2)$, represents the effects of energy redistribution among particle classes and the dissipative effect of inelastic collisions. Similar to the momentum equation, the source term is composed of a sum over both particle classes. Here, however, due to the inelasticity of collisions, all collision types contribute. The effect of mass transfer is contained in the next to the last term of eq. 47. The final term, which may be either a source or sink, represents the coupling with the surrounding gas phase.

Energy Choosing $\Psi = h$, one obtains

$$\begin{aligned} \frac{\partial(\alpha_i \bar{\rho}_i \tilde{h}_i)}{\partial t} + \nabla \cdot (\alpha_i \bar{\rho}_i \mathbf{u}_i \tilde{h}_i) &= \alpha_i \bar{\rho}_i \left\langle \frac{Q_{r,i}}{m_i} \right\rangle + \alpha_i \bar{\rho}_i \left\langle \frac{1}{\rho_i} \frac{dp_g}{dt} \right\rangle + \alpha_i \bar{\rho}_i \left\langle \frac{dm_i}{dt} \frac{h_v}{m_i} \right\rangle \\ &\quad - \nabla \cdot \alpha_i \bar{\rho}_i \left\langle \mathbf{C}_i h'_i \right\rangle \end{aligned} \quad (48)$$

Here, the terms on the right hand side denote the mean heat transfer with the surrounding gas, the effect of mean enthalpy carried by the vapors exiting the porous particle, and the ‘turbulent’ flux. The collision terms are negligible, as shown by the analysis given in Appendix B.

2.4 Closure

The above model describes a particle mixture in a gaseous carrier using conservation equations for mass, momentum energy and granular temperature of each solid class. These multiple-class equations describe the independent accelerations of the species, as well as momentum and energy exchange between solids classes. Moreover, these transport equations are valid even when Δu is of the same order as Θ_c , and when the granular temperatures do not obey the equipartition law. The above system of equations contains several correlations, and is therefore unclosed. These correlations are of several types: (i) collisional contributions to both transport and source terms, (ii) exchange terms between gas and solid, (iii) in-phase transport terms and transport properties.

In principle, the single particle distribution functions are solutions of the Boltzmann equations (17), however, they are difficult to obtain in situations when the phase space includes many variables (mass fractions, temperature, etc.). Therefore, it is assumed that the velocity distribution function for solution of the hydrodynamic problem can be obtained without incorporating the explicit effect of the thermochemistry. The hydrodynamic problem is then basically decoupled from the thermochemistry as far as the velocity distribution is concerned, and the velocity distributions may be obtained by similar techniques as are used in non-reactive flow, taking into account the mean evolution of, for instance, the particle mass. The single particle distribution function is then considered to be

$$f_i^{(1)}(\mathbf{x}, \mathbf{c}_i, Y_{\xi,i}, m_i, T_i, t) = f_i^{(1)*}(\mathbf{x}, \mathbf{c}_i, t) \delta(m_i - \bar{m}_i) \delta(T_i - \tilde{T}_i) \sum_{\xi} \delta(Y_{\xi,i} - \tilde{Y}_{\xi,i}) \quad (49)$$

where $f_i^{(1)*}$ is commonly called the velocity distribution, excluding the effect of particle mass, particle temperature, and species concentrations. For convenience, the asterisk is omitted on subsequent use of the velocity distribution.

2.4.1 Collisional and kinetic contributions

Additional to decoupling thermochemistry from hydrodynamics, a further simplification is made herein. Instead of using a distribution computed from the Boltzmann equations (excluding the effects of the thermochemistry), a Maxwellian distribution is assumed, i.e. the lowest order approximation to the Boltzmann equation in the absence of dissipative effects

$$f_i^{(1)}(\mathbf{x}, \mathbf{c}_i, t) = \frac{n_i}{(2\pi\Theta_i)^{3/2}} \exp\left[-\frac{(\mathbf{c}_i - \mathbf{u}_i)^2}{2\Theta_i}\right]. \quad (50)$$

This is a good approximation when the flow has small spatial gradients, the collisions are nearly elastic and the particles are sufficiently heavy (i.e. the time between collisions is much smaller

than the particle relaxation time; the particle-fluid correlation is small). The integrals require specification of the radial distribution function at contact, $h_{ik}(\mathbf{r})$ (see Appendix A), accounting for the effects of excluded area and particle shielding on the spatial distribution of colliding pairs. The form of the radial distribution function is taken from Jenkins and Mancini (1987), slightly adjusted to prevent overpacking of the solids

$$h_{ik} = \frac{1}{1 - \hat{\alpha}/\alpha_0} + 6 \frac{\sigma_i \sigma_k}{\sigma_i + \sigma_k} \frac{\xi}{(1 - \hat{\alpha}/\alpha_0)^2} + 8 \left(\frac{\sigma_i \sigma_k}{\sigma_i + \sigma_k} \right)^2 \frac{\xi}{(1 - \hat{\alpha}/\alpha_0)^2}. \quad (51)$$

Here $\hat{\alpha}$ denotes the total particle volume fraction, accounting for the porosity inside the particles, and $\xi = 2\pi/3 \sum n_i \sigma_i^2$ where σ_i denotes the radius of a particle of class i . The present paper is targeted towards dense systems where the drift between particle classes is small. In our context, using distributions where each particle class has its own mean velocity introduces unnecessary complexity (also see Appendix A). Therefore, the collision integrals are approximated by assuming that the relative velocity $\Delta \mathbf{u}_{ik} = \mathbf{u}_i - \mathbf{u}_k$, is small compared to the square root of the sum of the granular temperatures, $(\Theta_i + \Theta_k)^{1/2}$. This significantly simplifies the calculation of the required integrals, and furthermore should not affect the applicability of the equations for our purposes; this assumption is also the basis of the classic Enskog expansion where in addition the granular temperatures are assumed equilibrated. Here, the effects of having different granular temperatures for each particle class is, however, fully retained, which is important in these dissipative systems, leading to deviations from equipartition.

Manger (1996), assumed a distribution identical to ours in order to obtain closure for a binary mixture. In the work of Kumaran and Koch (1993a,b) the authors considered a slightly more general velocity distribution, i.e. an anisotropic Gaussian, where a distinction is made between the direction of gravity and the direction perpendicular to it. Although slightly more general, their work was restricted to homogeneous flows and is algebraically difficult to extend to inhomogeneous flows. Recently, Gourdel et al. (2000), also used Gaussians but they allowed for large drift between particle classes, leading to a theory suitable for the complete range of particle densities, i.e. from dilute to densely packed. Their work, however, was also restricted to homogeneous flows.

Using the above distributions and neglecting products of the spatial gradients, products of $(1 - e_{ik})$ with spatial gradients, and products of $\Delta \mathbf{u}_{ik}$ with the spatial gradients, yields the following constitutive equations for ϕ_i , Σ_i , \mathbf{q}_i , and γ_i . Some details on the computation of the integrals leading to the final result are listed in Appendix A

$$\phi_i = \sum_k F_{ik} \left\{ \frac{4}{3} \sqrt{2\pi} (\Theta_i + \Theta_k)^{1/2} (\mathbf{u}_k - \mathbf{u}_i) + \frac{\pi}{3} \sigma_{ik} (\Theta_i + \Theta_k) \nabla \ln \frac{n_i}{n_k} \right\} \quad (52)$$

$$\Sigma_i = n_i m_i \Theta_i + \sum_k \left\{ p_{ik} \mathbf{I} - \mu_i^{ik} [2\mathbf{S}_i + \frac{5}{3} \nabla \cdot \mathbf{u}_i] - \mu_i^{kk} [2\mathbf{S}_k + \frac{5}{3} \nabla \cdot \mathbf{u}_k] \right\} \quad (53)$$

$$\mathbf{q}_i = \sum_k \left\{ \kappa_i^{ik} \nabla \Theta_i + \kappa_i^{kk} \nabla \Theta_k \right\} \quad (54)$$

$$\gamma_i = \sum_k -2\sqrt{2\pi} F_{ik} (\Theta_i + \Theta_k)^{1/2} \left\{ 2(M_i \Theta_i - M_k \Theta_k) + M_k (1 - e_{ik}) (\Theta_i + \Theta_k) \right\} \quad (55)$$

where $F_{ik} = n_i n_k m_i M_k (1 + e_{ik}) h_{ik} \sigma_{ik}^2$. The indices on the viscosities and conductivities are arranged as follows, the subscript i indicates the relevance for class i , the first superscript labels the pertinent velocity gradient, and the k superscript denotes the dependence of the expressions on k . The

pressure and transport coefficients are

$$p_{ik} = \frac{1}{3}\pi n_i n_k m_i M_k (1 + e_{ik}) h_{ik} \sigma_{ik}^3 (\Theta_i + \Theta_k) \quad (56)$$

$$\mu_i^{ik} = \frac{1}{15}\sqrt{2\pi} n_i n_k m_i M_k^2 (1 + e_{ik}) h_{ik} \sigma_{ik}^4 (\Theta_i + \Theta_k)^{3/2} / \Theta_i \quad (57)$$

$$\mu_i^{kk} = \frac{1}{15}\sqrt{2\pi} n_i n_k m_k M_i^2 (1 + e_{ik}) h_{ik} \sigma_{ik}^4 (\Theta_i + \Theta_k)^{3/2} / \Theta_k \quad (58)$$

$$\kappa_i^{ik} = \frac{1}{3}\sqrt{2\pi} n_i n_k m_i M_k (1 + e_{ik}) h_{ik} \sigma_{ik}^4 (\Theta_i + \Theta_k)^{1/2} (M_k \Theta_k / \Theta_i) \quad (59)$$

$$\kappa_i^{kk} = \frac{1}{3}\sqrt{2\pi} n_i n_k m_i M_k (1 + e_{ik}) h_{ik} \sigma_{ik}^4 (\Theta_i + \Theta_k)^{1/2} (M_i \Theta_i / \Theta_k). \quad (60)$$

The terms in ϕ_i represent solid-solid drag and ordinary diffusion, respectively (thermal diffusion has been neglected). The stress tensor depends on the shear rates of all solid classes where the shear viscosities arise entirely from collisions, not from streaming; this is a result of the Gaussian approximation. Similar remarks hold for the heat flux vector. Manger (1996) has presented similar closure relations for binary mixtures. For coding purposes, the shear rates of both phases are assumed equal (small drift) so that the actually used viscosity equals the sum of several contributions: $\mu_i = \sum_k \mu_i^{ik} + \mu_i^{kk}$. The source terms in the granular energy equations contain two terms: a temperature equilibrating and a dissipative term.

2.4.2 Exchange terms

A prerequisite for closing the formulation is the evaluation of exchange terms between each particle class and the carrier gas.

Mass and species The mass exchange terms in the mass and species equations are evaluated at the average temperature and mass fractions, i.e.

$$\Gamma_i = \alpha_i \bar{\rho}_i \sum_{\xi} \tilde{R}_{i,\xi}^{s \rightarrow g} = \alpha_i \bar{\rho}_i \sum_{\xi} R_{i,\xi}(\{\tilde{Y}\}, \tilde{T}_i) \quad (61)$$

where $\{\tilde{Y}\}$ denotes any combination of the set of species mass fractions and where only solid to gas reactions need to be considered. Although this procedure neglects correlations between particle temperature and the mass fractions, these approximations are not too strict since the reaction rates are first order with respect to the species, and therefore do not exhibit the stronger nonlinearity normally associated with second or higher order reaction rates. For consistency between the solids and gas phase we require

$$\Gamma_g = - \sum_i \Gamma_i. \quad (62)$$

A similar approach is followed for the reactive source terms in the individual species mass fraction equations for both carrier gas and the solid classes. Thus, these are evaluated at the mean temperature and mass fractions

$$\alpha \bar{\rho} \tilde{R}_{\xi} = \alpha \bar{\rho} R_{\xi}(\{\tilde{Y}\}, \tilde{T}). \quad (63)$$

Interfacial species transfer occurs only for the tar and gas species. The combined terms $H_{g\xi} + \Gamma_g Y_{g\xi}^i$ form a mass source for the species equations originating from the appropriate solid to gas phase

reactions (see section 2.1 for the kinetics) which is calculated from the mean particle temperature and mean solid phase mass fractions

$$H_{g\xi} + \Gamma_g Y_{g\xi}^i = \sum_i \alpha_i \bar{\rho}_i R_{i,\xi}(\{\tilde{Y}\}, \tilde{T}_i). \quad (64)$$

Enthalpy We first remark that the enthalpy equations of the gas and solid phases may be rewritten in non-conservative form:

$$(\alpha \bar{\rho} C_p)_g \frac{D\tilde{T}_g}{Dt} = -\nabla \cdot (\alpha \bar{\mathbf{q}})_g + F_g + \Gamma_g (h_g^i - \tilde{h}_g) \quad (65)$$

$$(\alpha_i \bar{\rho} C_p)_i \frac{D\tilde{T}_i}{Dt} = \alpha_i \bar{\rho}_i \langle \frac{Q_{r,i}}{m_i} \rangle + \alpha_i \bar{\rho}_i \langle \frac{dm_i}{dt} \frac{(h_v - \tilde{h}_i)}{m_i} \rangle - \nabla \cdot \alpha_i \bar{\rho}_i \langle \mathbf{C}_i h'_i \rangle \quad (66)$$

where the gas pressure derivative in the solid equations has vanished; alternatively, one may start with the particle equation in terms of the particle temperature, eq. 37. The last term in the solids equation is the average reaction heat of all particle reactions (including solid to gas conversions). The energy equation contains the interaction term $\alpha_i \bar{\rho}_i \langle Q_{r,i} \rangle$ that accounts for the gas-particle heat transfer. The following closure is provided for this term

$$\alpha_i \bar{\rho}_i \langle \frac{Q_{r,i}}{m_i} \rangle = -\frac{6\hat{\alpha}_i \lambda_g}{d_i^2} \langle Nu_i \rangle (\tilde{T}_i - \tilde{T}_g), \quad (67)$$

where the average Nusselt number is calculated from the mean slip velocity, etc. For low turbulence intensity of the gas and solids (compared to the average slip velocity), this is an accurate approximation. Although Louge et al. (1993) have incorporated the effect of particle velocity fluctuations on the Nusselt number, considering the complexity of the present problem including porous particles, heat transfer and chemical reactions, such an approach has not been pursued here. The enthalpy flux associated with the vapor exiting the particle (tar and gas), $\sum_i \alpha_i \bar{\rho}_i \langle \frac{dm_i}{dt} \frac{h_v}{m_i} \rangle$, requires knowledge of the specific enthalpies of the respective components. Such detailed properties are unknown in the present case where many components are lumped together into pseudo-components referred to as gas and tar. This enthalpy flux is only needed for the gas-phase, as the vapor enthalpy term is part of the total heat of reaction for the solids. To obtain closure, the differences in the formation enthalpies between the gas and the exiting vapors are neglected. We then obtain final closure of the gas-phase equation

$$F_g + \Gamma_g (h_g^i - \tilde{h}_g) = \sum_i \frac{6\hat{\alpha}_i \lambda_g}{d_i^2} \langle Nu \rangle_i (\tilde{T}_i - \tilde{T}_g) + \sum_i \Gamma_{tar}^{s \rightarrow g} (C_p^{tar} \tilde{T}_b - C_{p,g} \tilde{T}_g) + \Gamma_{gas}^{s \rightarrow g} (C_p^{gas} \tilde{T}_i - C_{p,g} \tilde{T}_g), \quad (68)$$

where we have further assumed that the vapor products are leaving the particle at its mean temperature, and where $\Gamma_{tar}^{s \rightarrow g}$, and $\Gamma_{gas}^{s \rightarrow g}$ denote the averaged mass transfer rates of respectively, tar and gas.

Momentum The mass transfer related term is modeled using a mean value approximation, i.e.

$$\Gamma_g \mathbf{u}_g^i = \sum_i \langle \frac{dm_i}{dt} \frac{\mathbf{c}_i}{m_i} \rangle = \sum_i \Gamma_i \tilde{\mathbf{u}}_i. \quad (69)$$

Hence, the average interfacial gas velocity is approximated by the mean velocity of the particle class responsible for the mass transfer. The interaction term in the momentum equation may be expanded to

$$\alpha_i \bar{\rho}_i \langle \frac{\mathbf{F}_i}{m_i} \rangle = \alpha_i \bar{\rho}_i [\mathbf{f}_g - \langle \frac{V_p}{m_i} \nabla \overleftarrow{p}_g \rangle - \langle \frac{1}{\tau_{12}} (\mathbf{w}_i - \overleftarrow{\mathbf{u}}_g) \rangle]. \quad (70)$$

The pressure gradient term is closed in terms of the mean gas pressure gradient:

$$-\alpha_i \bar{\rho}_i \langle \frac{V_p}{m_i} \nabla \overleftarrow{p}_g \rangle \approx -\hat{\alpha}_i \nabla \bar{p}_g. \quad (71)$$

Similarly, for the drag force related term:

$$-\alpha_i \bar{\rho}_i \langle \frac{1}{\tau_{12}} (\mathbf{c}_i - \overleftarrow{\mathbf{u}}_g) \rangle \approx -\frac{\alpha_i \bar{\rho}_i}{\tau_{12}} (\mathbf{u}_i - \langle \overleftarrow{\mathbf{u}}_g \rangle_i), \quad (72)$$

where fluctuations in the particle relaxation time are neglected. The particle average of the locally undisturbed velocity is set equal to the phase averaged velocity: $\langle \overleftarrow{\mathbf{u}}_g \rangle \approx \tilde{\mathbf{u}}_g$. For consistency between the gas and solids equations, $\mathbf{M}'_g = \sum_i \frac{\alpha_i \rho_i}{\tau_{i,12}} (\mathbf{u}_i - \tilde{\mathbf{u}}_g)$.

Granular energy Two terms require closure, the mass transfer related correlation and the term related to the presence of an interstitial gas. The transfer term is closed assuming that fluctuations in the granular temperature are negligible, i.e.

$$\langle \frac{dm_i}{dt} \frac{1/2 C_i^2}{m_i} \rangle = \Gamma_i \Theta_i. \quad (73)$$

The interaction term with the gas phase can be expanded as

$$\alpha_i \bar{\rho}_i \langle \frac{\mathbf{F}_i}{m_i} \cdot \mathbf{C}'_i \rangle = \frac{\alpha_i \bar{\rho}_i}{\tau_{12}} (\langle \mathbf{C}'_i \cdot \mathbf{u}''_g \rangle_i - \langle \mathbf{C}'_i \cdot \mathbf{C}'_i \rangle_i) \quad (74)$$

where gas pressure gradient fluctuations have been neglected and we have decomposed the undisturbed gas velocity in a mean value at the particle location and a fluctuation $\overleftarrow{\mathbf{u}}_g = \langle \overleftarrow{\mathbf{u}}_g \rangle_i + \mathbf{u}''_g$. For fairly large particles, having large particle fluid interaction time compared to the time between collisions, the term in (74) may be neglected (dry granular mixture).

2.4.3 In-phase transport fluxes and evaluation of transport properties

Many of the transport closure used for the gas-phase have already been outlined in the section on gas-phase averaging. Here we focus on the solid-phase closure. The in-phase transport fluxes for the solids classes comprise the correlations between the velocity of the respective class and a variable, not explicitly considered in the distribution function, i.e. the species mass fractions, $Y_{i\xi}$, the particle mass, m or the temperature T . These transport fluxes arise from the self-diffusive transport of the respective property, carried by the particles. In analogy with the work of Louge et al. (1993), these ‘turbulent’ fluxes are modeled using a self-diffusive coefficient, D_{ii} , derived from the Gaussian velocity distribution

$$-\nabla \cdot (\alpha_i \bar{\rho}_i \langle \mathbf{C}_i Y'_{i\xi} \rangle) = \nabla \cdot (\alpha_i \bar{\rho}_i D_{ii} \nabla \tilde{Y}_{i\xi}) \quad (75)$$

$$-\nabla \cdot (\alpha_i \bar{\rho}_i \langle \mathbf{C}_i h'_{i\xi} \rangle) = \nabla \cdot (\alpha_i \bar{\rho}_i C_{p,i} D_{ii} \nabla \tilde{T}_i) \quad (76)$$

$$-\nabla \cdot (\alpha_i \bar{\rho}_i \langle \mathbf{C}_i m'_i \rangle) = \nabla \cdot (\alpha_i \bar{\rho}_i D_{ii} \nabla \bar{m}_i) \quad (77)$$

The derivation of D_{ii} is detailed in Appendix C and follows the recent work of Hsiau (2000).

Transport properties are required for such parameters as the specific heats (both gas and solids) and thermal conductivities (gas only). These are calculated from a mass-weighted average of the individual species properties. Considering ϕ to be one such general property, its average is then computed from $\bar{\phi} = \sum_{\xi} Y_{\xi} \phi_{\xi}$. An exception to this procedure is in the calculation of the average particle density, $1/\bar{\rho}_i = \sum_{\xi} Y_{i,\xi} \rho_{\xi}$.

2.4.4 Transport equations for the mean particle mass and solidity

The transport theorem, used for the particle mass, gives a transport equations for \tilde{m}_i , not \bar{m}_i . The approach used here is to equate the mass-weighted average to the non-weighted result; a procedure commonly practiced in work related to compressible single phase turbulence. The following transport equation then follows

$$\frac{\partial(\alpha \rho \bar{m})_i}{\partial t} + \nabla \cdot (\alpha \rho \mathbf{u} \bar{m})_i = \nabla \cdot \alpha_i \bar{\rho}_i D_{ii} \nabla \bar{m}_i - 2\Gamma_i \bar{m}_i \quad (78)$$

where turbulent diffusion has been included in a similar manner as in the energy and species equations and the factor 2 arises from the conservative form of the equation (both \bar{m}_i and $(\alpha \rho)_i$ decrease due to mass transfer to the gas phase). The average solidity is then derived from the average particle mass as

$$\bar{\eta}_i = \frac{\bar{m}_i}{V_p} \sum_{\xi} \frac{\tilde{Y}_{\xi}}{\rho_{\xi}}. \quad (79)$$

2.5 Frictional transfer

The constitutive equations derived above are restricted to the region where particles interact exclusively through slightly inelastic, short duration, collisions. However, as the volumetric fraction approaches the maximum packing volume fraction, α_0 , particles will, increasingly, be in simultaneous contact with several neighbors and stresses will be transmitted at points of sustained sliding or rolling contact. This situation is very difficult to model at the microscopic level, leading to its neglect in many bubbling fluidized bed models. However, in certain regions where shear rates are very small, the granular temperature may be too small to support the solids phase. Hence, codes based on models neglecting friction require a ‘numerical fix’, generally restricting the value of the computed granular temperature (e.g. Boemer and Renz, 1997; Ma et al., 1993). To avoid this situation, we explicitly model the frictional regime, particularly since it was shown by Anderson and Jackson (1992) and Lathouwers and Bellan (2000a) that inclusion of the frictional regime is necessary for obtaining qualitatively correct results. The approach followed is similar to that used in Syamlal (1993), extended here for the case of multiple particle classes. The model proposed attains a simple relation between stresses and strains: $\Sigma_i^f = -p_i^f \mathbf{I} + 2\mu_i^f \mathbf{S}_i$ for $\alpha > \alpha_{min}$ where α_{min} is the minimum solids fraction at which frictional transfer becomes influential. Experimental observations indicate that the frictional normal stress increases rapidly with bulk density and diverges as the maximum packing fraction, α_0 , is approached (Savage and Sayed, 1984). A simple algebraic representation of this behavior is (cf. Anderson and Jackson, 1992)

$$p_i^f = \frac{\alpha_i \rho_i}{\sum \alpha_i \rho_i} Fr \frac{(\hat{\alpha} - \alpha_{min})^p}{(\alpha_0 - \hat{\alpha})^n} \quad (80)$$

where Fr is a material constant. The frictional viscosity, μ_i^f , is related to the frictional pressure and the angle of internal friction, ϕ , as $\mu_i^f = p_i^f \sin(\phi) / 2\sqrt{I_2}$ where I_2 denotes the second invariant

of the strain rate tensor. The following values for the parameters have been used in the present work: $p = 2$, $n = 5$, $Fr = 0.005$, $\alpha_{min} = 0.6$, $\alpha_0 = 0.64$, and $\phi = 25$ degrees, which are in general agreement with those of Anderson and Jackson (1992) and Johnson and Jackson (1987).

Following Johnson and Jackson (1987), the total stress is taken as the sum of the contributions from the separate mechanisms, each evaluated as though it acted alone: $\Sigma^{tot} = \Sigma^f + \Sigma^c$. Here the superscript c indicates both collisional and kinetic contributions. However, in the production term of Eq. (47), the frictional terms are deleted, inherently assuming that the frictional work is directly converted to thermal internal energy.

3 Solution procedure

Spatial discretization of the governing equations is based on a finite volume technique using a staggered grid. All convective fluxes are approximated with a second-order accurate bounded TVD-scheme avoiding the excessive numerical diffusion associated with the first-order accurate upwind scheme which is still used today in many multiphase flow research codes (e.g. Mathiesen et al., 2000). The time discretization is based on a backward Euler scheme in combination with a pressure-correction technique. The momentum equations of all phases are solved in a coupled manner, though separately for each velocity direction. Compared with the well-known Partial Elimination Algorithm (PEA) the present approach is more general (see Lathouwers, 1999 for more details on full-field coupling and multiphase pressure correction algorithms). The species and energy equations constitute a strongly coupled, stiff system of equations. To avoid very large linear systems arising from (the necessarily) implicit discretization, a time splitting is used (Strang, 1968) for the combined species and energy system consisting of three steps: (i) performance of a half convection-diffusion timestep, (ii) time integration of the equations over a full timestep with only the reactive terms present, (iii) performance of another half convection-diffusion timestep. The advantage of this split scheme is that during steps (i) and (iii), the equations are decoupled into standard convection-diffusion systems which are easily handled, whereas in step (ii) there is no spatial coupling. The stiff integration in step (ii) is performed by using the well-known stiff integrator VODE (Hindmarsh et al., 1989). All sparse linear systems arising from the discretization of convection-diffusion systems are solved with preconditioned Krylov methods (CG for the pressure Poisson equation and GMRES for the other transport equations; see e.g. Barrett et al., 1994).

4 Results

The model has been applied to a variety of testcases in order to quantify its predictive capabilities. These are (i) the shearing of a homogeneous mixture, (ii) comparison of the particle pressure generated along the wall of a bubbling fluidized bed, (iii) the characteristic behavior of homogeneously fluidized beds, and (iv) biomass particle pyrolysis calculations for a fluidized bed reactor and comparison of obtained yield to experimental data. The first three sets of calculations do not involve reacting biomass; the temperature of the gas and particles is fixed at the same value ($T = 300K$) and is uniform in the reactor.

4.1 Homogeneously sheared mixture

Savage and Sayed (1984) have measured the normal and shear stresses developed by granular materials in a shear flow cell. The binary mixture consists of polystyrene beads (specific gravity 1.095)

where $d_A = 0.55$ and $d_B = 1.68mm$, respectively with a restitution coefficient of 0.8. The solids fractions for the small and large particles constitute 30 and 70 percent of the total bulk solids volume fraction.

For the case of simple shear, the model presented above becomes a set of ODE's which have to be supplemented with boundary conditions on the solid surfaces of the shear cell. However, as the distribution of solids in the shear cell is unknown and the boundary conditions uncertain, we assume the velocity gradient to be uniform and equal for both particle classes. The system simplifies to two coupled algebraic equations for Θ_A and Θ_B , stating that production equals dissipation for each size class: $-\Sigma_{i,xy} \frac{du}{dy} + \gamma_i = 0$. Frictional transfer has been excluded from the present model. The present analysis differs from that in Farrell et al. (1986), since unequal granular temperatures are used here and a different radial distribution function is employed. Fig. 1 shows the comparisons of the present numerical solution of the set of equations and the experimental results for the mixture shear stress and the normal stress as function of the shear rate du/dy and of the bulk volume fraction. Also shown are predictions with a single particle model using a mean particle diameter of $1.34mm$. Generally, for the lower solids fractions, both theories somewhat overpredict the stresses. At the highest bulk solids fraction, all stress components are, however, strongly underestimated which most likely indicates that the transfer of momentum becomes affected by friction, which was neglected in this specific case. The present, more general, binary model predictions are higher than the corresponding predictions in Farrell et al. (1986), owing to the separate granular temperatures for each class. At these diameter ratios (≈ 3), the temperatures do not equilibrate completely, leading to higher stress levels. The differences with the experimental data at lower solids bulk fraction are attributed to the assumption of Gaussian distributions and to the form of the radial distribution function to which the results are highly sensitive.

4.2 Particle pressure along the wall of a bubbling fluidized bed

To validate the solids pressure model, a comparison was made with the experimental data of Campbell and Wang (1991) reporting measurements of the solids pressure magnitude in a bubbling bed consisting of a square channel ($1.22 \times 0.127 \times 0.127m^3$), homogeneously fluidized with air. The bed is initially filled with glass beads ($d_p = 0.5mm$; $\rho = 2500kg/m^3$), to a depth of 43 cm. As three dimensional calculations are very computationally intensive, the square channel was approximated by a flat two-dimensional geometry having a width equal to the size of the channel. Calculations were performed at three conditions, i.e. at superficial gas-velocities of 0.4, 0.6 and 0.8 m/s. The grid consists of 40×96 points. Fig. 2 shows vertical profiles of the computed time-averaged (over left and right wall) solids pressure (kinetic plus frictional) along the wall, together with the experimental data of Campbell and Wang (1991). Considering the geometric approximation, the agreement is reasonable, demonstrating an increase of solids pressure with height caused by fluctuating particle motion as induced by bubble growth, and a decrease to zero at greater heights where the solids fraction vanishes. Furthermore, the calculated profiles exhibit an increase in solids pressure as the superficial gas velocity is increased. Most of the solids pressure originates from the kinetic part, not from the frictional regime. The remaining discrepancies with the experimental data are attributed to (i) an insufficient period of averaging causing scatter, and (ii) the geometric approximations made by simulating a two dimensional geometry which may change the bubble dynamics. A similar comparison was presented recently in Boemer and Renz (1997), using a kinetic theory model, but excluding frictional stresses. Although the period of averaging was similar (9 sec), their results exhibit rather spiky profiles.

4.3 Behavior of homogeneously fluidized beds

The present study focuses on the global behavior of homogeneously fluidized beds, as these are to be used for the biomass pyrolysis. The fluidized bed studied is $0.68m$ wide, initially filled up to $0.4m$ with sand ($\rho_s = 2600kg/m^3, d_p = 0.5mm$) or with a sand-biomass mixture (2/3 sand 1/3 biomass volumetrically; biomass properties: $\rho_b = 700kg/m^3, d_p = 0.5mm$). All computations were performed on a 40×128 grid. To trigger bubbling, a disturbance was introduced in the initial volume fraction distribution.

The obtained fields are transient owing to hydrodynamic instabilities giving rise to spatial inhomogeneity. Fig. 3 shows a snapshot of the solids volume fraction and phase velocities at $t = 3$ s. Bubbles can be identified which form at the bottom of the bed and rise, growing through coalescence, in accordance with visual observations in the bubbly flow regime. Typical bubble shapes consist of spheres with an excluded wake at the bottom; also in accordance with experimental data (cf. Balzer et al., 1993). Time-averaged results (not shown) lead to a flow pattern with two symmetric circulation loops and a solid fraction distribution showing a reasonably uniform dense lower bed and a gradually more diluted upper region. The solids fraction is not homogeneous over the width of the bed, exhibiting higher values at the lower near-wall region, induced by the large scale circulation.

Fig. 4 shows the time-averaged solids volume fraction (computed from data along the centerline) in the lower part of the bed as function of the superficial gas velocity, compared to an experimental correlation from Johnsson et al. (1991). Also shown is an equilibrium solution obtained from a balance between gravity, gas-pressure gradient and gas-solid drag. The computed solids fraction agrees quite well with the experimental correlation although some scatter is present in the simulated data due to the restricted period of time averaging. It is also concluded that the average lower-bed solids concentration is well predicted by the assumption of steady homogeneous flow.

To investigate the differences between a binary and a monodisperse mixture, 2 computations are compared: i) using the present binary flow model with sand and biomass properties for the separate solids classes, and ii) using a monodisperse model with volume fraction weighted particle properties. Qualitatively, the simulations exhibit very similar behavior. One important difference is however the predicted solids distribution. The different properties of the particles cause the particle mixture to segregate. A quantitative measure of segregation may be defined as $S = (0.2\alpha_s - 0.4\alpha_b)/(0.2\alpha_s + 0.4\alpha_b)$, being zero if no segregation is present and 1 or -1 for complete segregation.

Fig 5. shows instantaneous distributions of the solids fractions and of the segregation parameter in the bed at $t = 6$ sec. Though initially the solids are perfectly mixed, already at this short time scale, segregation of the mixture is significant on a local scale, S mostly ranging between -0.2 and 0.2 (negative inside bubbles, carrying biomass to the top of the bed). The segregation can also be quantified by the y-coordinate of the centers of mass of the sand and biomass, which are shown in Fig 6 as a function of time. It is shown that already one or two seconds after startup, segregation is significant and tends to increase with time. Segregation was found to increase when the size of the biomass particles was decreased, due to a greater difference in terminal velocity. The monodisperse simulation is clearly unable to predict any of these features.

4.4 Biomass particle pyrolysis in a fluidized bed reactor

Among the pyrolysis reactor designs investigated for commercial production of condensable tars from biomass, the fluidized bed reactor is potentially efficient due to the high particle heating rates that can be achieved (Scott et al., 1999) and its excellent mixing properties, assuring a reasonably uniform product quality. A further interesting feature of this type of reactor is that char does not

accumulate in the bed, but is rapidly elutriated with the gas flow instead, after which it may be filtered out, making the reactor very suitable for continuous operation.

The fluidized bed reactor contains a large amount of sand that is used as inert bed material which acts as heat capacitor for the biomass that is injected into the bed. Fluidization of the sand-biomass mixture is generally achieved by using either hot steam or nitrogen, some of which is also injected with the biomass, therefore preheating it. Once the particles enter the reactor, the temperature of the biomass rises rapidly and pyrolysis rates increase causing solid biomass species to be converted into tar and gas which are subsequently ejected from the particle, while char which is also formed in the process maintains the particle matrix. Biomass particle pyrolysis is an endothermic process and heat has to be supplied continuously by the surrounding gas, which in turn gets heated by the sand. The gaseous reaction products are convected out of the reactor together with the fluidization gas to locations where it is subsequently cooled (quenched) to prevent product degradation.

Although the process has received considerable attention experimentally (Scott and Piskorz, 1982, 1984), currently there are no thorough theoretical analyses available, addressing simultaneously all physico-chemical processes in the reactor. Most of the work to date has focused on single-particle pyrolysis in a gas stream which requires *a priori* knowledge of ambient gas flow parameters, its temperature in particular (Di Felice et al., 1999).

Below, we present quantitative results from numerical simulations based on a detailed mathematical model, including a realistic chemistry model that is able to differentiate between various feedstock.

4.4.1 Detailed physico-chemical parameters of biomass pyrolysis

The kinetics scheme of the present biomass pyrolysis model was already given in section 2. The main advantage of the present kinetics scheme is the ability to differentiate between feedstock through knowledge of the initial mass composition with respect to the primary components, cellulose, hemicellulose and lignin. All of the reaction rates in the model, K_j , are considered irreversible, first order Arrhenius

$$K_j = A_j \exp(-E_j/R^0T), \quad (81)$$

with A denoting the rate constant, and E the reaction's activation energy, are tabulated in Table 1 (cf. Miller and Bellan, 1997) and are dependent of the source component. Due to a lack of more detailed knowledge, the heats of reaction are taken as independent of the source component. The polymerization reaction K_1 has $\Delta h_1 = 0 \text{ kJ/kg}$, reaction K_2 is endothermic with $\Delta h_2 = 255 \text{ kJ/kg}$, and both the char formation and the secondary tar reactions are exothermic with $\Delta h_2 = -20 \text{ kJ/kg}$ and $\Delta h_2 = -42 \text{ kJ/kg}$. All other properties of gaseous and solid species are listed in Tables 2 and 3, respectively.

4.4.2 Simulation details

A sketch of the simulated geometry and the boundary conditions employed is given in Figure 7. The geometry has been chosen to resemble that used in experiments by Scott and Piskorz (1982, 1984), among others. Although the real fluidized bed is a cylindrical vessel, for computational simplicity, the present computational domain is approximated to be rectangular. Some care must therefore be taken in translating/comparing experimental data to simulations. The biomass is fed through an inlet section in one of the side walls, together with an amount of gas, which preheats the biomass during the feeding process. The center of feedpoint 1 is located 4.6 cm from the bottom of the bed and has a height (area) of 1.86 cm; feeder no 2 has the same height (area) and is located 12.1

cm from the bottom. In the present simulations, the temperature of the gas used for fluidization is equal to that fed through the biomass feed section (T_g); the inlet temperature of the biomass, however is assumed to vary (T_b) to investigate the effect of preheating. Note that, regardless of the biomass feed temperature, the biomass compositions used at the inlet correspond to those of biomass that has not pyrolyzed, i.e. it is assumed that the residence time in the feeder is short (no appreciable biomass conversion) while the effective heating of the particles is as efficient as required (by specifying the required temperature). To vary the cellulose/hemicellulose/lignin proportions of the feedstock, bagasse, olive husk, maple, and oak are used in the simulations. The initial biomass composition of these biomass types are given in Table 4. The diameter of the sand and biomass particles is assumed 0.5 mm, which is a common value in practical operation. The biomass particles are assumed to have an initial porosity of 0.7 (cf. Miller and Bellan, 1997). The biomass feed flux is ramped from 0 at $t=0$ to a value of $0.5 \text{ kg/m}^2\text{s}$ at $t=0.5$ s, after which it is kept constant (when two feedpoints are used, the flow is equally split between feedpoints). A constant value of $1 \text{ kg/m}^2\text{s}$ is specified for the gas flux through the feeder. The gas flow used for fluidization of the mixture is varied from 0.3 to $0.4 \text{ kg/m}^2\text{s}$ and is uniform over the bottom of the domain. A summary of all simulations performed is listed in Table 5. Initial conditions correspond to a bed filled with sand only up to a height of 0.163 m at a volume fraction of 0.6 which corresponds to dense packing. To initiate bubbling of the bed, several disturbances in the volume fraction are inserted. The initial temperature of the sand and the gas in the domain is set equal to the inlet temperature of the fluidization gas. Hence, it is assumed that the fluidization gas has preheated the sand, even though initially the sand bed is stationary. This does not affect the calculation of product yield, as we are interested in the asymptotic (i.e. long time) behavior of the reactor; that is long after which a statistically steady flowfield has emerged. All computations have been performed on a 40×148 grid (x and z directions respectively). No-slip and free slip conditions are used at walls for the gas and solid, respectively. At the outlet, the pressure is prescribed as atmospheric while solids are inhibited to exit the domain (simulating a fine solids-filtering grid).

4.4.3 Results

Regardless of the local phenomena in the reactor, the true measure of the reactor efficiency for the tar production can be quantitatively determined by comparing the actual mass of tar exiting the reactor (Ω_{tar}) and the amount still present in its interior (M_{tar}) to the biomass feed flow (M_{feed}):

$$\Omega_{tar} = \int_0^t \int_{outlet} (\alpha_g \rho_g \mathbf{u}_g Y_{tar}) \cdot \mathbf{dA} dt' \quad (82)$$

$$M_{tar} = \int_{reactor} (\alpha_g \rho_g Y_{tar}) dV \quad (83)$$

$$M_{feed} = \int_0^t \int_{inlet} (\alpha_b \rho_b \mathbf{u}_b) \cdot \mathbf{dA} dt' \quad (84)$$

where the subscript b denotes biomass. With these definitions, two measures for reactor performance are the yield (η) and the differential reactor efficiency (DRE), ϑ , cf. Miller and Bellan (1998):

$$\eta_{tar}(t) = \frac{\Omega_{tar} + M_{tar}}{M_{feed}} \quad (85)$$

$$\vartheta_{tar}(t) = \frac{\Omega_{tar} + M_{tar}}{\sum_{\xi} (\Omega_{\xi} + M_{\xi})} \quad (86)$$

where the summation is over the species tar, gas and char. These measures quantify the relative efficiency of reactor tar production relative to the biomass feed flow, and the relative proportion of tar produced compared to gas and char. Similar definitions are used for the reactor performance with respect to gas and char production.

Qualitative behavior To investigate the qualitative behavior of the reactor, snapshots of several variables have been plotted at $t=2.5$ s, representative for Run No 4.

Figure 8 illustrates contours of the volume fractions of the sand and biomass. The sand contours are similar to those obtained for isothermal simulations, as expected. The volume fraction of the biomass is generally very small due to the short simulation time. The biomass is fairly evenly distributed over the dense part of the bed, illustrating the effectiveness for solid mixing in fluidized beds.

In Figure 9, the partial macroscopic densities ($=\alpha\rho Y$) of the relevant gas and solid species are plotted. Therein, biomass refers to the sum of both virgin and active solid components. Both tar and gas densities are high at the same location which is a region where the biomass temperature has increased enough to produce large quantities of both gaseous products. The inhomogeneities in the partial densities are a result of both the inhomogeneous reaction rates and transport processes in the reactor. The char is almost uniform throughout the dense bed owing to the effective solid mixing.

Figure 10 shows contours of the temperatures of the gas, sand, and biomass. Both the gas and sand temperature are almost uniform and equal to the inlet gas temperature (and more importantly, the initial sand temperature), i.e. 800 K. The biomass temperature, however, varies significantly throughout the reactor, showing a distinctive pattern of biomass entering at the specified feed temperature (400 K), flowing clockwise, while at the same time heating up.

In Figure 11, the y -coordinate of the center of mass of the sand and biomass are plotted as a function of time. It shows the particular transient structure due to the bubbling of the bed (both sand and biomass fluctuate in phase). In general, the biomass is situated higher up in the bed than is the sand. This is caused by two effects: (i) the biomass density is much smaller than that of the sand due to its high porosity, and (ii) the general motion of the biomass is directed upwards right after feeding due to bubbling, while on downward motion the particles have already partially pyrolysed, before reaching the bottom of the bed (an exception being formed by the unreactive char which remains). This particle segregation may be detrimental to tar production, indicating the need to optimize this yield as a functions of reactor and feedstock parameters.

Parametric study This parametric study is devoted to finding optimum conditions for maximizing tar yield as function of the relevant operating parameters. The parameters investigated include the temperature of the inlet gas, the feed temperature of the biomass, the fluidization velocity (or flux), the location of the feedpoint(s), and the type of feedstock used for pyrolysis.

Figures 12 and 13 show the yield and differential reactor efficiency with respect to tar production, respectively. The strong dependence of both yield and DRE are noteworthy. Comparing the yield with the DRE, it can be concluded that the reactor efficiency is a more practical way of examining efficiency than is the yield which is, however, the quantity of ultimate industrial interest. Both figures indicate that the efficiency for tar production reaches a maximum at either 750 or 800 K; an extended simulation time is required to draw a stricter conclusion with respect to the optimum temperature. The abrupt decrease in tar DRE at small times corresponds to the large char DRE (see Fig. 17) resulting from the low biomass temperature. As the biomass temperature increases, so does the tar DRE concomitantly with the reduction in char DRE. The tar DRE is reduced by

the large char DRE at small gas temperatures, and by the large gas DRE at high gas temperatures (see Fig. 15). Figures 14 and 15 show similar results for the gas production. The yield indicates a monotonic increase as temperature is increased, however, the gas DRE seems to be minimized for $T_g = 750K$, indicating that this is the most likely optimal temperature for maximizing tar yield. Similarly, for the production of char, Figures 16 and 17 show that the of char production increases with T_g , as pyrolysis is more vigorous. However, the char DRE decreases with increasing T_g , in agreement with the known hindrance of char production at larger reactor temperatures.

Figures 18 to 23 show the effects of variations in biomass feed temperature, fluidization gas flux, and the biomass injection point, respectively on the tar yield and the tar differential reactor efficiency. The results show that the changes in these parameters cause only minor variations in the tar yield. The results should be interpreted accounting for the assumption of no pyrolysis before entering the reactor and uniform particle temperature (kinetically controlled regime).

Finally, Figures 24 and 25 show the effect of employing different biomass types as feedstock. Bagasse returns the highest tar yield due to the largest proportion of cellulose and the smallest proportion of lignin present in this feed, however its DRE is lowest due to the largest gas DRE (not shown). Basically, the formed tar decomposes to gas before it can be collected. This points out to the higher than optimal fluidizing gas temperature for this case.

5 Conclusions

A comprehensive mathematical model has been derived which is capable of predicting the thermo-fluid dynamics of dense reacting gas-solid mixtures. The model is based on a multifluid description obtained from systematic averaging of the local instantaneous equations using the kinetic theory of granular flows in combination with rigid sphere interaction models explicitly accounting for collisional transfer. Multiple solid classes are considered to enable a differentiation in either physical properties or thermochemical behavior of various particle types, e.g. fuel vs inert particles. Separate transport equations are used for each particle class, allowing for the independent acceleration of the particles in each class and non-equilibrium processes leading to momentum and energy exchange between respective classes, and between particles and the carrier gas. The model avoids heuristic extensions from monodisperse results which are common in literature (Syamlal, 1993; Mathiesen et al., 2000). To illustrate this general gas-solid reacting model, simulations are conducted for biomass pyrolysis in a fluidized bed. In this specific case, a previously validated, chemistry model for biomass particle pyrolysis (7 solid species, 2 gaseous species), capable of differentiating between different feedstocks is coupled to the hydrodynamics formulation.

The model has been applied to a variety of test cases in order to quantify its predictive capabilities. Comparison of shear and normal stress component predictions in a simple shear flow of a binary mixture ignoring frictional transfer, reveal that for the lower bulk fractions, the stresses are somewhat overpredicted, whereas for the higher bulk fractions they are underpredicted. A comparison has also been made for the time-averaged particle pressure along the wall of a bubbling fluidized bed for different values of the superficial gas velocity. Predictions are generally in reasonable agreement with the available experimental data. Additionally, predictions have been presented for a homogeneously aerated bed, both with sand particles and with a sand-biomass mixture. For the monodisperse case, predictions of the solids volume fraction in the lower part of the bed have been compared to an experimental correlation and agreement is fairly good. Computations of a mixture of sand and biomass have shown that the qualitative behavior of the flow is not changed. The binary mixture model predicted a significant amount of segregation, even during the short timespan here investigated. Finally, the model has been applied to high temperature particle py-

rolysis in a lab-scale fluidized bed reactor for which a parametric study has been performed. The major operating parameter, determining the tar yield is the temperature of the fluidization gas. Optimum yield was found for a fluidizing gas temperature of 750-800 K. Parametric variations in other process parameters, such as fluidization flux, biomass feed temperature, and feed position were found to be of relatively minor importance.

The results of this comparison further indicate that the model captures the key features of the pyrolysis process, and is general enough to be used for the optimization of reactor geometries and operating parameters, such as gas temperature, biomass injection procedures, etc. The model is presently used to optimize and scale up a biomass pyrolysis reactor for the National Renewable Energy Laboratory (NREL) (Lathouwers and Bellan, 2000b).

The present theory can be extended to more general situations. Two such obvious extensions are: (i) The consideration of gas phase turbulence, a model which has already been briefly outlined (Lathouwers and Bellan, 1999). (ii) The generalization of the single particle distribution function by seeking a solution to the Boltzmann equations that includes the effect of the surrounding gas on the velocity distribution function. This will lead to more accurate closure relations in the dilute region and would extend the applicability of the model to e.g. circulating beds. Both of these extensions can be made along the lines of Grad's theory (Grad, 1949; Jenkins and Richman, 1985; Peirano and Leckner, 1998), extended to a multiple-class granular mixture.

6 Acknowledgments

This research was conducted at the Jet Propulsion Laboratory (JPL) and sponsored by the U.S. Department of Energy (DOE), with Mr. Neil Rossmeisel (DOE Headquarters) and Mr. D. Hooker (DOE Golden Center) serving as contract monitors, under an agreement with the National Aeronautics and Space Administration. Computational resources were provided by the supercomputing facility at JPL.

7 Appendix A: Estimate of the ratio of heat transfer through direct particle contact to gas-particle heat transfer

The goal is here to estimate the relevant timescales associated with gas-particle and particle-particle heat transfer. To leading order, the averaged energy equation for particle class i is

$$(\alpha\rho C_p)_i \frac{dT_i}{dt} = \frac{6\hat{\alpha}_i\lambda_g Nu_i}{d_p^2} \Delta T_{gp} + \sum_k \chi_{ik}(\Delta E) \quad (87)$$

with the notation of the main text. To simplify the analysis, we assume non-porous particles ($\hat{\alpha}_i = \alpha_i$). The timescale for gas-particle heat-transfer is thus readily identified:

$$\tau_{gi} = \frac{\rho_i C_p d_i^2}{6\lambda_g Nu_i}. \quad (88)$$

The source integral for collisional transfer is

$$\chi_{ik}(\Delta E) = \sigma_{ik}^2 \int \Delta E(\mathbf{g} \cdot \mathbf{k}) h_{ik} f_i f_k d\mathbf{k} d\mathbf{c}_1 d\mathbf{c}_2 dT_1 dT_2 \quad (89)$$

where the expression for ΔE is given by eq. 28 and the integration over the particle masses has already been carried out. In reality, the particles are not perfectly spherical. The radius of curvature R (entering the expression for ΔE) therefore has a distribution associated with it. This does not affect the estimate of the collision integrals, especially since we are interested in order of magnitude estimates. The integrand depends on the relative velocity as well as on the temperature difference of the particles, and therefore consistent with the formulation of section 2.4.

$$f_i = \frac{n_i}{(2\pi\Theta_i)^{3/2}} \exp\left[-\frac{(\mathbf{c}_1 - \mathbf{u}_i)^2}{2\Theta_i}\right] \delta(T_1 - \tilde{T}_i(r, t)). \quad (90)$$

Simple estimates of the time-scale do not require the calculation of the source integral; it is sufficient to simply estimate it as $\nu_c \overline{\Delta E}$, where the overbar denotes the average energy exchange. $\overline{\Delta E}$ is estimated using the expression for ΔE , (eq. 28) and ν_c is the collision frequency. The collision frequency in the low-drift limit is

$$\nu_c = \pi n_i n_k h_{ik} \sigma_{ik}^2 \sqrt{8\pi(\Theta_i + \Theta_k)} \quad (91)$$

where σ_{ik} is the mean diameter and h_{ik} denotes the radial distribution function at contact. The integral is then readily estimated as

$$\chi_{ik}(\Delta E) \simeq \nu_c \frac{5(m/E)^{3/5} (Rg)^{7/10}}{(\rho C_p \lambda)_i^{-1/2} + (\rho C_p \lambda)_k^{-1/2}} \Delta T_{ik} \simeq \nu_c \frac{5(m/E)^{3/5} (R)^{7/10} (\Theta_2 + \Theta_3)^{7/20}}{(\rho C_p \lambda)_i^{-1/2} + (\rho C_p \lambda)_k^{-1/2}} \Delta T_{ik} \quad (92)$$

where we have approximated the relative velocity of the colliding particles as the square root of the sum of the granular temperatures. The timescale for particle-particle heat transfer is thus

$$\tau_{ik} = \frac{(\alpha \rho C_p)_i}{\pi n_i n_k h_{ik} \sigma_{ik}^2 \sqrt{8\pi(\Theta_i + \Theta_k)}} \times \frac{(\rho c_p \lambda)_i^{-1/2} + (\rho c_p \lambda)_k^{-1/2}}{5(m/E)^{3/5} (R)^{7/10} (\Theta_i + \Theta_k)^{7/20}} \quad (93)$$

To estimate the two time-scales we consider the following representative parameters appropriate for the dense regime (phases i and k denoting sand and biomass, respectively)

$$\begin{aligned} Nu_i &= 2 - 5 \\ \lambda_g &= 5 \cdot 10^{-2} \text{ J/msK (Miller and Bellan, 1997)} \\ \lambda_i &= 0.1 \text{ J/msK (CRC, 1992)} \\ \lambda_k &= 1 \text{ J/msK (CRC, 1992)} \\ \alpha_i &= \alpha_k = 0.25 \\ d_i &= d_k = 10^{-3} \text{ m.} \\ E_i &= 10^{10} \text{ Pa. (CRC, 1992)} \\ E_k &= 7 \cdot 10^{10} \text{ Pa. (CRC, 1992)} \\ \nu_i &= \nu_k = 0.16 \text{ (CRC, 1992)} \\ \rho_i &= \rho_k = 1000 \text{ kg/m}^3. \\ C_{p,i} &= C_{p,k} = 1000 \text{ J/kgK.} \\ \Theta_i &= 10^{-8} - 10^{-2} \text{ m}^2/\text{s}^2. \end{aligned}$$

The gas-particle heat transfer time-scale is then

$$\tau_{gi} = \frac{\rho_i C_i d_i^2}{6 \lambda_g Nu_i} \in [0.6, 1.5] \text{ s.} \quad (94)$$

On the other hand, the particle-particle heat transfer time-scale can be rewritten as

$$\tau_{ik} = \frac{K}{h_{ik}} (2\Theta)^{-17/20} s \quad (95)$$

where K is a constant of order 250. Taking the upper-limit for the granular temperature of $\Theta = 10^{-2}$ gives $\tau_{ik} = 7000/h_{ik} s$. As h_{ik} is of the order 5 for this packing, $\tau_{ik} \gg \tau_{gi}$ (even for this upper limit of granular temperature). The ratio τ_{ik}/τ_{gi} is even larger for lower granular temperatures. This analysis is, in principle, also valid for particle-wall collisions (except for a multiplicative constant arising from curvature differences). Considering the large ratio, τ_{ik}/τ_{gi} , the particle-particle heat transfer may be neglected in the regime where continuous frictional/rolling contacts prevail.

8 Appendix B: Calculation of collision integrals

The collision integrals for the source and flux contributions are

$$\chi_{ik}(\psi_i) = \sigma_{ik}^2 \int (\psi'_i - \psi_i)(\mathbf{g} \cdot \mathbf{k}) h_{ik} f_i f_k \left[1 + \frac{\sigma_{ik}}{2} \mathbf{k} \cdot \nabla \ln \frac{f_k}{f_i} \right] d\mathbf{k} d\mathbf{c}_1 d\mathbf{c}_2 dm_1 dm_2 dT_1 dT_2 \quad (96)$$

$$\theta_{ik}(\psi_i) = -\frac{1}{2} \sigma_{ik}^3 \int \mathbf{k} (\psi'_i - \psi_i)(\mathbf{g} \cdot \mathbf{k}) h_{ik} f_i f_k \left[1 + \frac{\sigma_{ik}}{2} \mathbf{k} \cdot \nabla \ln \frac{f_k}{f_i} \right] d\mathbf{k} d\mathbf{c}_1 d\mathbf{c}_2 dm_1 dm_2 dT_1 dT_2 \quad (97)$$

where the integration must be carried out over impending collisions ($\mathbf{g} \cdot \mathbf{k} \geq 0$). As mentioned in the main text, the single particle velocity distributions are Gaussians with their own temperature and mean velocity, and are assumed delta-peaked around the mean mass and temperature

$$f_i(\mathbf{c}, \mathbf{r}, t) = \frac{n_i}{(2\pi\Theta_i)^{3/2}} \exp\left[-\frac{(\mathbf{c} - \mathbf{u}_i)^2}{2\Theta_i}\right] \delta(m_i - \bar{m}_i) \delta(T_i - \tilde{T}_i). \quad (98)$$

Note that the term in the integrand containing the gradient of the distribution functions can now be expressed in terms of gradients of the mean fields:

$$\begin{aligned} \nabla \ln \left(\frac{f_k}{f_i} \right) &= -\nabla \ln \left(\frac{n_i}{n_k} \right) + \frac{3}{2} \nabla \ln \left(\frac{\Theta_i}{\Theta_k} \right) + \\ &\quad -\frac{1}{\Theta_i} \nabla \mathbf{u}_i \cdot (\mathbf{c}_1 - \mathbf{u}_i) + \frac{1}{\Theta_k} \nabla \mathbf{u}_k \cdot (\mathbf{c}_2 - \mathbf{u}_k) \\ &\quad -\frac{1}{2\Theta_i^2} (\mathbf{c}_1 - \mathbf{u}_i)^2 \nabla \Theta_i + \frac{1}{2\Theta_k^2} (\mathbf{c}_2 - \mathbf{u}_k)^2 \nabla \Theta_k. \end{aligned} \quad (99)$$

The most convenient way to calculate these integrals is to make a change of variables to $\mathbf{g} = \mathbf{c}_1 - \mathbf{c}_2$ and $\mathbf{c}_m = M_i \mathbf{c}_1 + M_k \mathbf{c}_2$. The Jacobian of the transformation equals unity

$$J = \frac{\partial(\mathbf{c}_1, \mathbf{c}_2)}{\partial(\mathbf{g}, \mathbf{c}_m)} = 1 / \frac{\partial(\mathbf{g}, \mathbf{c}_m)}{\partial(\mathbf{c}_1, \mathbf{c}_2)} = 1 / (M_i + M_k) = 1. \quad (100)$$

Through this transformation the integrals become

$$\begin{aligned} \chi_{ik}(\psi_i) &= \sigma_{ik}^2 h_{ik} \frac{n_i n_k}{(4\pi^2 \Theta_i \Theta_k)^{3/2}} \int (\psi'_i - \psi_i)(\mathbf{g} \cdot \mathbf{k}) \left[1 + \frac{\sigma_{ik}}{2} \mathbf{k} \cdot \nabla \ln \frac{f_k}{f_i} \right] \times \\ &\quad \exp\left\{-\frac{1}{2\Theta_g} (\mathbf{g} - \Delta \mathbf{u}_{ik})^2 - \frac{1}{2\Theta_{ik}} (\mathbf{c}_m - \mathbf{u}_0)^2\right\} d\mathbf{k} d\mathbf{c}_m d\mathbf{g} \end{aligned} \quad (101)$$

$$\begin{aligned} \theta_{ik}(\psi_i) &= -\frac{1}{2} \sigma_{ik}^3 h_{ik} \frac{n_i n_k}{(4\pi^2 \Theta_i \Theta_k)^{3/2}} \int \mathbf{k} (\psi'_i - \psi_i)(\mathbf{g} \cdot \mathbf{k}) \left[1 + \frac{\sigma_{ik}}{2} \mathbf{k} \cdot \nabla \ln \frac{f_k}{f_i} \right] \times \\ &\quad \exp\left\{-\frac{1}{2\Theta_g} (\mathbf{g} - \Delta \mathbf{u}_{ik})^2 - \frac{1}{2\Theta_{ik}} (\mathbf{c}_m - \mathbf{u}_0)^2\right\} d\mathbf{k} d\mathbf{c}_m d\mathbf{g} \end{aligned} \quad (102)$$

where the integration over m_1 , m_2 , T_1 , and T_2 have already been carried out and the terms in the integrand $\psi'_i - \psi_i$ and $\nabla \ln(f_k/f_i)$ must be expressed in the integration variables. For convenience, the following parameters have been introduced

$$\begin{aligned}
\Theta_g &= \Theta_i + \Theta_k \\
\frac{1}{\Theta_{ik}} &= \frac{1}{\Theta_i} + \frac{1}{\Theta_k}, \quad \Theta_{ik} = \frac{\Theta_i \Theta_k}{\Theta_i + \Theta_k} \\
\Delta \mathbf{u}_{ik} &= \mathbf{u}_i - \mathbf{u}_k \\
\mathbf{u}_0 &= \mathbf{u}_m + a_0 \mathbf{g} \\
\mathbf{u}_m &= \left(\frac{\mathbf{u}_i}{\Theta_i} + \frac{\mathbf{u}_k}{\Theta_k} \right) \Theta_{ik} \\
\mathbf{a}_0 &= (M_i \Theta_i - M_k \Theta_k) / \Theta_g.
\end{aligned} \tag{103}$$

The integrals over \mathbf{k} and \mathbf{c}_m are standard, and can be done with the help of standard integral tables (see Chapman and Cowling, 1970 and Jenkins and Richman, 1985). The integrals over \mathbf{g} are, however, very cumbersome to perform, at least for general $\Delta \mathbf{u}_{ik}$. These integrals are of the general form

$$I = \int N(\mathbf{g}) \exp\left\{-\frac{1}{2\Theta_g}(\mathbf{g} - \Delta \mathbf{u}_{ik})^2\right\} d\mathbf{g}. \tag{104}$$

Introducing the dimensionless variable $z = \frac{1}{2\Theta_g} \Delta \mathbf{u}_{ik}^2$, the integrals have a polynomial form in z combined with exponentials and errorfunctions. To avoid this algebraic complexity and since the relative velocity is generally small in dense beds, the integrals are approximated for small z (or small $\Delta \mathbf{u}_{ik}$). It is thus legitimate to expand the integrals in a Taylor series around $z = 0$ and retain the lowest orders in z . Recently, Gourdel et al. (2000) have calculated several collision integrals for general z , however, they only required the source terms in the case of homogeneous flows (no gradient integrals needed to be included). The integrals, calculated using the small z approximation, properly reduce to those of Jenkins and Mancini (1987) calculated in the limit of small drift and small temperature differences.

9 Appendix C: Derivation of the self-diffusion coefficient

The diffusive flux associated with fluctuations in particle velocity and a general variable Ψ reads $-\nabla \cdot (\alpha_i \bar{\rho}_i < \mathbf{C}_i \Psi'_i >)$. As the distribution for Ψ is unknown, we use mean free path theory to obtain a reasonable estimate of this flux (Chapman and Cowling, 1970). Following Chapman and Cowling we have

$$- < \mathbf{C}_i \Psi'_i > \approx \frac{1}{2} \bar{C}_i l_i \nabla \Psi_i$$

where \bar{C}_i is the average magnitude of C_i and l_i denotes the mean free path of particles in class i . Comparing this formulation with the original flux, we deduce the diffusion coefficient as

$$D_{ii} = \frac{1}{2} \bar{C}_i l_i$$

For a Gaussian distribution the average magnitude of the fluctuating velocity reads $\bar{C}_i = (8\Theta_i/\pi)^{1/2}$, while an expression for the mean free path in a dense binary suspension is given in Hsiao (2000). The above diffusion coefficient is only valid when the dynamics of the particle evolves relatively slow between collisions, i.e. $d\Psi/dt \approx 0$, i.e. the timescale for collisions is much smaller than a

characteristic timescale for particle dynamics. For dense systems, this condition is likely to be satisfied. Hsiau (2000) recently presented an analysis for heat conduction in granular flows where this assumption is relaxed.

References

- [1] Anderson, K. G. and Jackson, R., 1992. A comparison of the solutions of some proposed equations of motion of granular materials for fully developed flow down inclined planes. *J. Fluid Mech.* 241, 145-168.
- [2] Balzer, G., Boelle, A., Simonin, O., 1995. Eulerian gas-solid flow modelling of dense fluidized bed. *FLUIDIZATION VIII*, Proc. International Symposium of the Engineering Foundation, 1125-1134.
- [3] Barrett, R., Berry, M., Chan, T. F., Demmel, J., Donato, J., Dongarra, J., Eijkhout, V., Pozo, R., Romine, C., and Van der Vorst, H., 1994. Templates for the solution of linear systems: building blocks for iterative methods. SIAM, Philadelphia.
- [4] Bird, R. B., Stewart, W. E. and Lightfoot, E. N. 1960. *Transport Phenomena*, Wiley.
- [5] Boemer, A. and Renz, U., 1997. Eulerian simulation of bubble formation at a jet in a two-dimensional fluidized bed. *Int. J. Multiphase Flow.* 21(5), 927-944.
- [6] Campbell, C. S., 1990. Rapid granular flows. *Ann. Rev. Fluid Mech.* 22, 57-92.
- [7] Campbell, C. S. and Wang, D. G., 1991. Particle pressures in gas-fluidized beds. *J. Fluid Mech.* 227, 495-508.
- [8] Chapman, S. and Cowling, T. G., 1970. *The Mathematical Theory of Nonuniform Gases*. Cambridge University Press.
- [9] CRC handbook of chemistry and physics. 1992. CRC Press Inc.
- [10] Di Felice, R., Coppola, G., Rapagna, S., and Jand, N., 1999. Modeling of biomass devolatilization in a fluidized bed reactor. *The Can. J. Chem. Eng.* 77, 325-332.
- [11] Drew, D. A., 1983. Mathematical modeling of two-phase flow. *Ann. Rev. Fluid Mech.* 15:261-291.
- [12] Farrell, M., Lun, C. K. K and Savage, S. B., 1986. A simple kinetic theory for granular flow of binary mixtures of smooth, inelastic, spherical particles. *Acta Mechanica* 63, 45-60.
- [13] Goldhirsch, I., 1999. Scales and kinetics of granular flows. *Chaos* 9(3), 659-672.
- [14] Goldman, E. and Sirovich, L., 1967. Equations for gas mixtures. *Phys. Fluids* 10, 1928-1940.
- [15] Gourdel, C., Simonin, O. and Brunier, E., 2000. Eulerian Modelling of binary mixtures of colliding particles and validation from Lagrangian tracking coupled to Large Eddy Simulation of homogeneous gas-solid turbulent flow. Submitted to *Int. J. Multiphase Flow*.
- [16] Grad, H., 1949. On the kinetic theory of rarified gases. *Comm. Pure and Appl. Math.* 2, 331-407.

- [17] Gunn, D. J., 1978. Transfer of heat or mass to particles in fixed and fluidized beds. *Int. J. Heat Mass Transfer* 21, 467-476.
- [18] Gyarmathy, G., 1982. The spherical droplet in gaseous carrier streams: review and synthesis. In: *Multiphase science and technology*, Vol. 1. Eds. Hewitt, G. F., Delhaye, J. M., and Zuber, N. McGraw Hill, 99-279.
- [19] Brown, P. N., Byrne, G. D. and Hindmarsh, A. C., 1989. VODE: A Variable-coefficient ODE solver. *SIAM J. Sci. Stat. Comput.* 10(5), 1038-1051.
- [20] Hsiao, S. S., 2000. Effective Thermal Conductivities of a Single Species and a Binary Mixture of Granular Materials. *Int. Journal Multiph. Flow*, 387-419.
- [21] Jenkins, J. T. and Savage, S. B., 1983. A theory for the rapid flow of identical, smooth, nearly elastic, spherical particles. *J. Fluid Mech.* 130, 187-202.
- [22] Jenkins, J. T. and Richman, M. W., 1985. Grad's 13-moment system for a dense gas of inelastic spheres. *Arch. Ration. Mech. Anal.* 87, 355-377.
- [23] Jenkins, J. T. and Mancini, F., 1987. Balance laws and constitutive relations for plane flows of a dense, binary mixture of smooth, nearly elastic, circular disks. *Journal of Applied Mechanics* 54, 27-34.
- [24] Jenkins, J. T. and Mancini, F., 1989. Kinetic theory for binary mixtures of smooth, nearly elastic spheres. *Phys. Fluids A* 1(12), 2050-2057.
- [25] Johnson, P. C. and Jackson, R., 1987. Frictional-collisional constitutive relations for granular materials, with application to plane shearing. *J. Fluid Mech.* 176, 67-93.
- [26] Johnsson, F., Andersson, S., and Leckner, B., 1991. Expansion of a freely bubbling fluidized-bed. *Powder Technology* 68(2), 117-123.
- [27] Valiveti, P. and Koch, D. L., 1998. Instability of sedimenting bidisperse particle gas suspensions. *Appl. Sci. Res.* 58, 275-303.
- [28] Kumaran, V. and Koch, D. L., 1993a. Properties of a bidisperse particle-gas suspension Part 1. Collision time small compared with viscous relaxation time. *J. Fluid. Mech.* 247, 623-641.
- [29] Kumaran, V. and Koch, D. L., 1993b. Properties of a bidisperse particle-gas suspension Part 2. Viscous relaxation time small compared with collision time. *J. Fluid. Mech.* 247, 643-660.
- [30] Lathouwers, D., 1999. Modelling and Simulation of Bubbly Flows. PhD thesis, Delft University of Technology, The Netherlands.
- [31] Lathouwers, D. and Bellan, J., 1999. Fall Technical Meeting of the Western States Section of the Combustion Institute, Irvine, October 25-26.
- [32] Lathouwers, D. and Bellan, J., 2000a. Modeling and simulation of bubbling fluidized beds containing particle mixtures. *Proceedings of the Combustion Institute*, Vol. 28, in print.
- [33] Lathouwers, D. and Bellan, J., 2000b. Yield optimization and scaling of fluidized beds for tar production from biomass. In preparation for *Energy and Fuels*.

- [34] Louge, M., Yusof, J. M. and Jenkins, J. T., 1993. Heat transfer in the pneumatic transport of massive particles. *Int. J. Heat Mass Transfer* 36(2), 265-275.
- [35] Lun, C. K. K., Savage, S. B., Jeffrey, D. J. and Chepurniy, N., 1984. Kinetic theories for granular flow: inelastic particles in Couette flow and slightly inelastic particles in a general flowfield. *J. Fluid Mech.* 140, 223-256.
- [36] Ma, D., Eraslan, A. H. and Ahmadi, G., 1993. A computer code for analyzing transient three-dimensional rapid granular flows in complex geometries. *Computers & Fluids* 22(1), 25-50.
- [37] Mathiesen, V., Solberg, T. and Hjertager, B. H., 2000. An experimental and computational study of multiphase flow behavior in a circulating fluidized bed. *Int. J. Multiphase Flow* 26, 83-97.
- [38] Miller, R. S. and Bellan, J., 1997. A generalized biomass pyrolysis model based on superimposed cellulose, hemicellulose and lignin kinetics. *Combust. Sci. and Tech.* 126, 97-137.
- [39] Miller, R. S. and Bellan, J., 1998. Numerical simulation of vortex pyrolysis reactors for condensable tar production from biomass. *Energy and Fuels* 12(1), 25-40.
- [40] Miller, R. S., Harstad, K. and Bellan, J., 1999. Evaluation of equilibrium and non-equilibrium evaporation models for many-droplet-gas-liquid flow simulations. *Int. J. Multiphase Flow* 24(6), 1025-1055.
- [41] Ottino, J. M. and Khakhar, D. V., 2000. Mixing and segregation of granular materials. *Ann. Rev. Fluid Mech.* 32, 55-91.
- [42] Peirano, E. and Leckner, B., 1998. Fundamentals of turbulent gas-solid flows applied to circulating fluidized bed combustion. *Prog. Energy Combust. Sci.* 24, 259-296.
- [43] Savage, S. B. and Sayed, M., 1984. Stresses developed by dry cohesionless granular materials sheared in an annular shear cell. *J. Fluid Mech.* 142, 391-430.
- [44] Schiller, L. and Nauman, A., 1935. A drag coefficient correlation. *V.D.I. Zeitung*, 77, 318-320.
- [45] Scott, D. S. and Piskorz, J., 1982. The flash pyrolysis of Aspen-polar wood. *Can. Journal Chem Eng.* 60, 666-674.
- [46] Scott, D. S. and Piskorz, J., 1984. The continuous pyrolysis of biomass. *Can. Journal Chem Eng.* 62, 404-412.
- [47] Scott, D. S., Majerski, P., Piskorz, J., and Radlein, D., 1984. A second look at fast pyrolysis of biomass - the RTI process. *J. Anal. Appl. Pyrolysis* 51, 23-37.
- [48] Simonin, O., 1996. Combustion and turbulence in two-phase flows. Von Karman Lecture Series 1996-02, Von Karman Institute for Fluid Dynamics.
- [49] Strang, G., 1968. On the construction and comparison of difference schemes. *SIAM J. of Numer. Anal.* 5(3), 506.
- [50] Syamlal, M., 1993. MFIX Documentation Theory Guide. DOE Report No. DOE/METC-94/1004.

- [51] Sun, J. and Chen, M. M., 1988. A theoretical analysis of heat transfer due to particle impact. *Int. J. Heat Mass Transfer* 31(5), 969-975.
- [52] Tham, M. K. and Gubbins, K. E., 1971. Kinetic theory of multicomponent dense fluid mixtures of rigid spheres. *J. Chem. Phys.* 55(1), 268-279.
- [53] Young, J. B., 1995. The fundamental equations of gas-droplet flow. *Int. J. Multiphase Flow* 21(2), 175-191.
- [54] Zamankhan, P., 1995. Kinetic theory of multicomponent dense mixtures of slightly inelastic spherical particles. *Phys. Rev. E* 52(5), 4877-4891.

| Reaction | $A(1/s)$ | $E(J/kmol)$ |
|----------|----------------------|--------------------|
| K_1^c | $2.8 \cdot 10^{19}$ | $242.4 \cdot 10^6$ |
| K_2^c | $3.28 \cdot 10^{14}$ | $196.5 \cdot 10^6$ |
| K_3^c | $1.30 \cdot 10^{10}$ | $150.5 \cdot 10^6$ |
| K_1^h | $2.10 \cdot 10^{16}$ | $186.7 \cdot 10^6$ |
| K_2^h | $8.75 \cdot 10^{15}$ | $202.4 \cdot 10^6$ |
| K_3^h | $2.60 \cdot 10^{11}$ | $145.7 \cdot 10^6$ |
| K_1^l | $9.60 \cdot 10^8$ | $107.6 \cdot 10^6$ |
| K_2^l | $1.50 \cdot 10^9$ | $143.8 \cdot 10^6$ |
| K_3^l | $7.70 \cdot 10^6$ | $111.4 \cdot 10^6$ |
| K_4 | $4.28 \cdot 10^6$ | $108 \cdot 10^6$ |

Table 1: Rate constants and activation energy for the biomass pyrolysis kinetics scheme. The char formation ratios for reaction K_3 are: $X^c = 0.35$, $X^h = 0.60$, and $X^l = 0.75$.

| Specie | $W(kg/kmol)$ | $C_p(J/kgK)$ | $\lambda(J/msK)$ | $\mu(kg/ms)$ | $D(m^2/s)$ |
|--------|--------------|--------------|-----------------------|----------------------|----------------------|
| N_2 | 28.013 | 1120.91 | $5.63 \cdot 10^{-2}$ | $3.58 \cdot 10^{-5}$ | $8.52 \cdot 10^{-4}$ |
| Gas | 30 | 1100 | $2.577 \cdot 10^{-2}$ | $3.0 \cdot 10^{-5}$ | $1.1 \cdot 10^{-4}$ |
| Tar | 100 | 2500 | $2.577 \cdot 10^{-2}$ | $3.0 \cdot 10^{-5}$ | $1.1 \cdot 10^{-4}$ |

Table 2: Property values for the gas phase species. The properties for nitrogen are taken at $T = 800K$ and $p = 100kPa$.

| Species | $C_p(J/kgK)$ | $\rho(kg/m^3)$ |
|---------|--------------|----------------|
| Biomass | 2167 | 2300 |
| Char | 2333 | 1100 |
| Sand | 800 | 2600 |

Table 3: Specific heat and densities for solid species. Biomass refers to both virgin species and active species.

| Feed | cellulose | hemicellulose | lignin |
|------------|-----------|---------------|--------|
| bagasse | 0.36 | 0.47 | 0.17 |
| olive husk | 0.22 | 0.33 | 0.45 |
| maple | 0.40 | 0.38 | 0.22 |
| oak | 0.35 | 0.40 | 0.25 |

Table 4: Initial biomass composition by mass fractions (cf. Miller and Bellan, 1997).

| Run No | $T_g(K)$ | $T_b(K)$ | Feedpoint | Feedstock | Fluidflow(kg/m^2s) |
|--------|----------|----------|-----------|------------|------------------------|
| 1 | 600 | 400 | 1 | bagasse | 0.3 |
| 2 | 700 | 400 | 1 | bagasse | 0.3 |
| 3 | 750 | 400 | 1 | bagasse | 0.3 |
| 4 | 800 | 400 | 1 | bagasse | 0.3 |
| 5 | 850 | 400 | 1 | bagasse | 0.3 |
| 6 | 950 | 400 | 1 | bagasse | 0.3 |
| 7 | 750 | 450 | 1 | bagasse | 0.3 |
| 8 | 750 | 500 | 1 | bagasse | 0.3 |
| 10 | 750 | 400 | 1 | bagasse | 0.4 |
| 12 | 750 | 400 | 1 | olive husk | 0.3 |
| 13 | 750 | 400 | 1 | maple | 0.3 |
| 14 | 750 | 400 | 1 | oak | 0.3 |
| 16 | 750 | 400 | 1+2 | bagasse | 0.3 |

Table 5: Summary of operating parameters in the simulations performed.

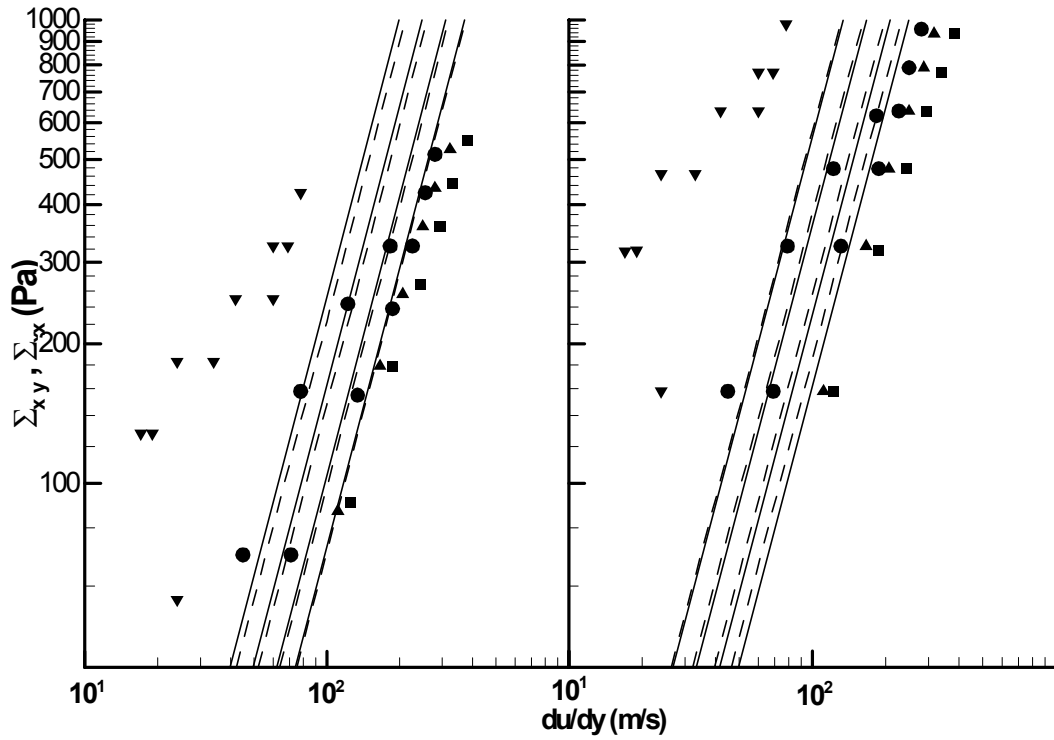


Figure 1: Predictions of the total shear (left) and normal stresses (right) generated in a simple shear flow of a binary mixture as function of shear rate for various bulk solids fractions, compared with the experimental data from Savage and Sayed (1984). Predictions: — binary model, - - -, monodisperse model. Experimental data: ■: $\alpha_{tot} = 0.498$, ▲: $\alpha_{tot} = 0.512$, ●: $\alpha_{tot} = 0.528$, ▼: $\alpha_{tot} = 0.542$.

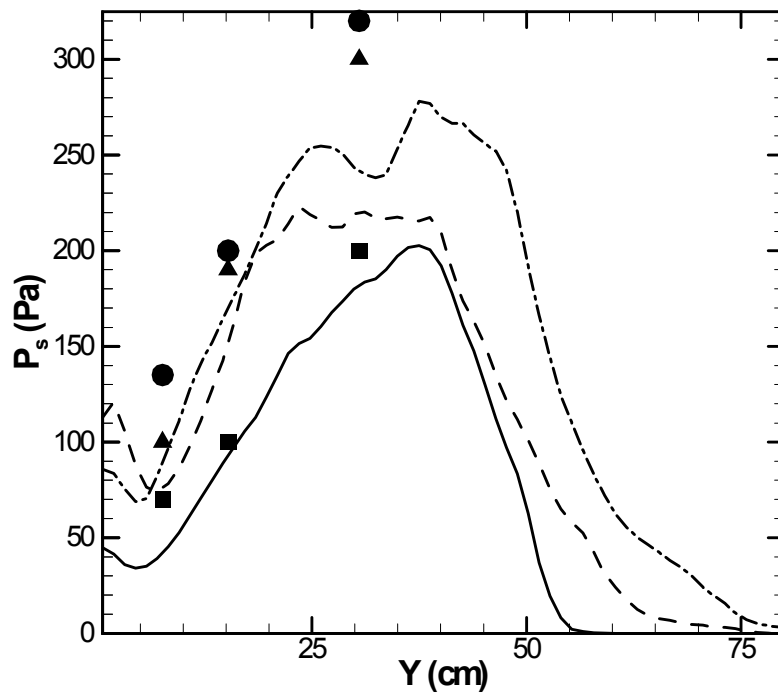


Figure 2: Predictions of the total time-averaged solids pressure along the wall compared to experimental data of Campbell and Wang (1991) at different superficial gas velocities. Predictions: $V_g = 0.4$: —; $V_g = 0.6$: - - - ; $V_g = 0.8$:-·-, Experimental data: $V_g = 0.4$: ■; $V_g = 0.6$: ▲; $V_g = 0.8$: ●.

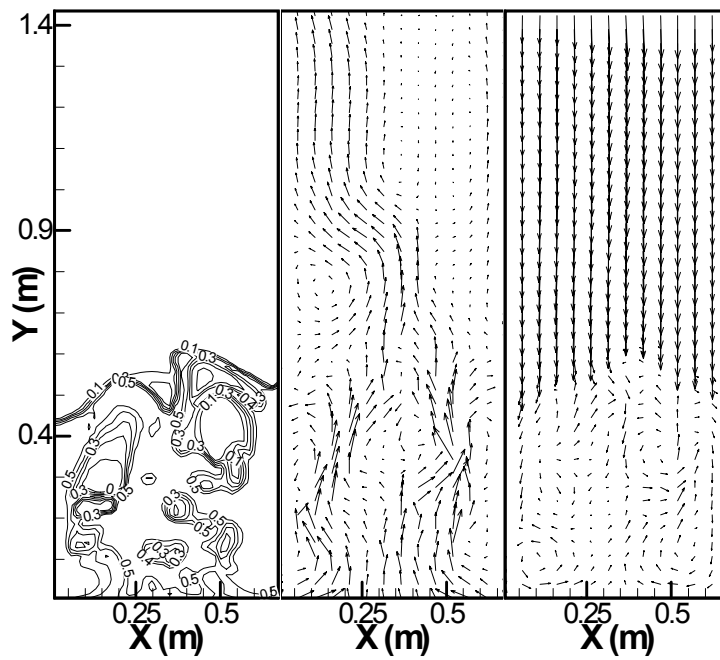


Figure 3: Instantaneous fields of the solid phase fraction (left), gas velocity (middle) and solids velocity (right) at $t = 3s$. (only 1 out of every 9 velocity vectors is shown).

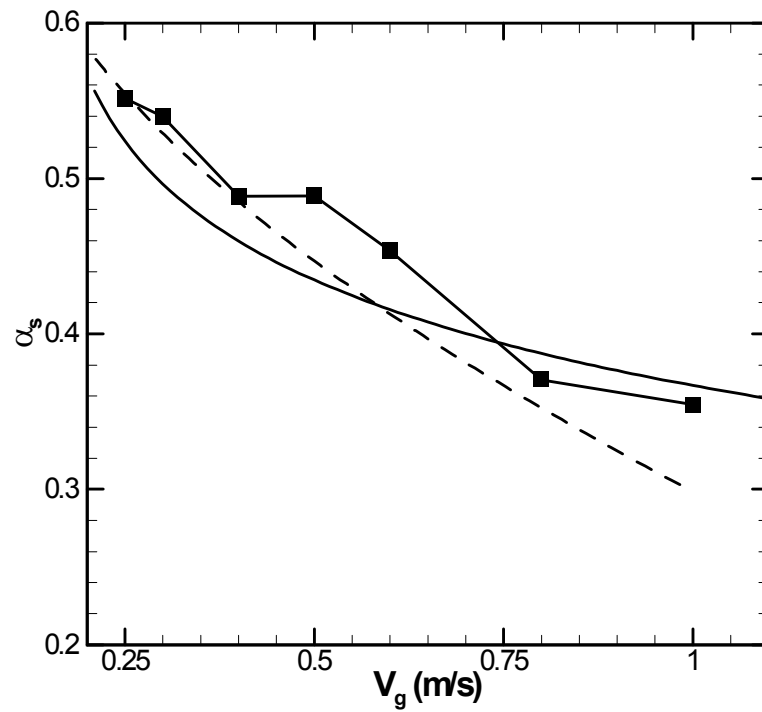


Figure 4: Solid phase volume fraction in the lower bed as function of the superficial gas velocity: ■ present model, — experimental correlation of Johnsson et al. (1991), - - - equilibrium solution of two-fluid equations.

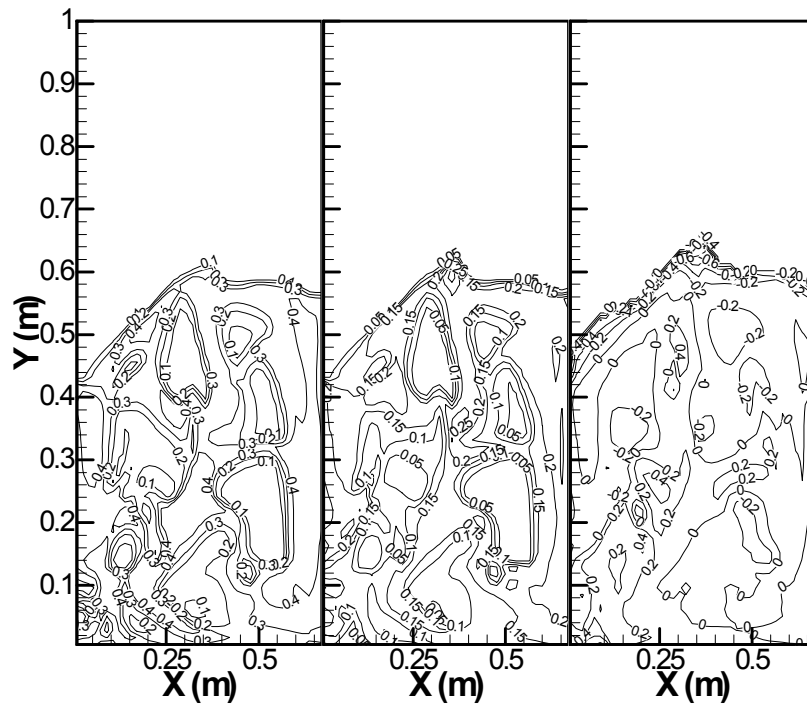


Figure 5: Instantaneous distributions of sand (left) and biomass (middle) concentrations, and of the segregation parameter (right) at $t = 6s$.

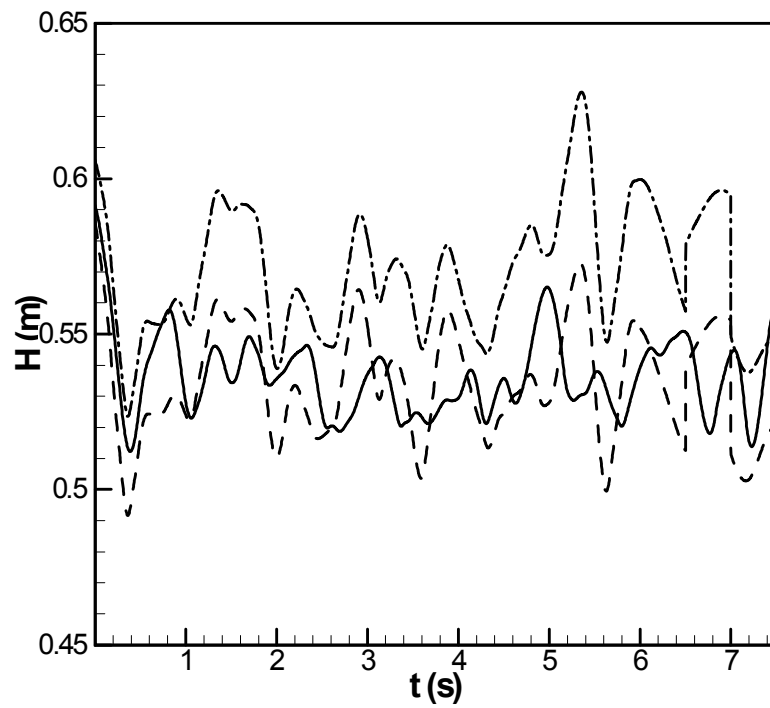


Figure 6: Time evolution of the y-coordinate of center of mass of sand and biomass compared to that of a monodispersed simulation: monodisperse:—, sand: - - - ; biomass: -.-.

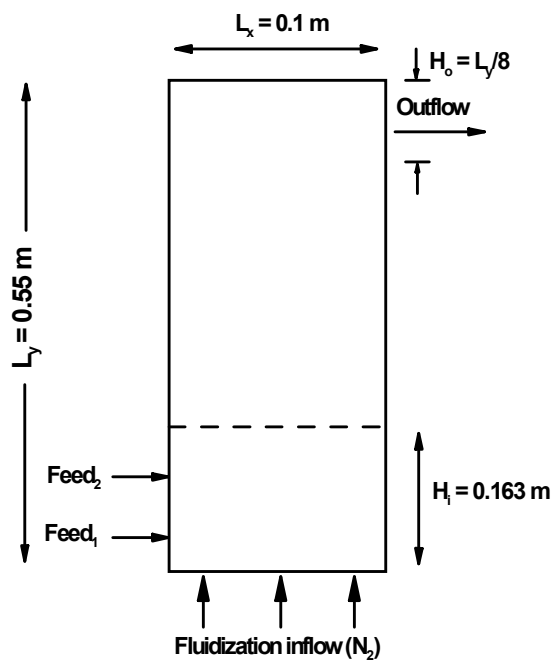


Figure 7: Schematic of the fluidized bed reactor.

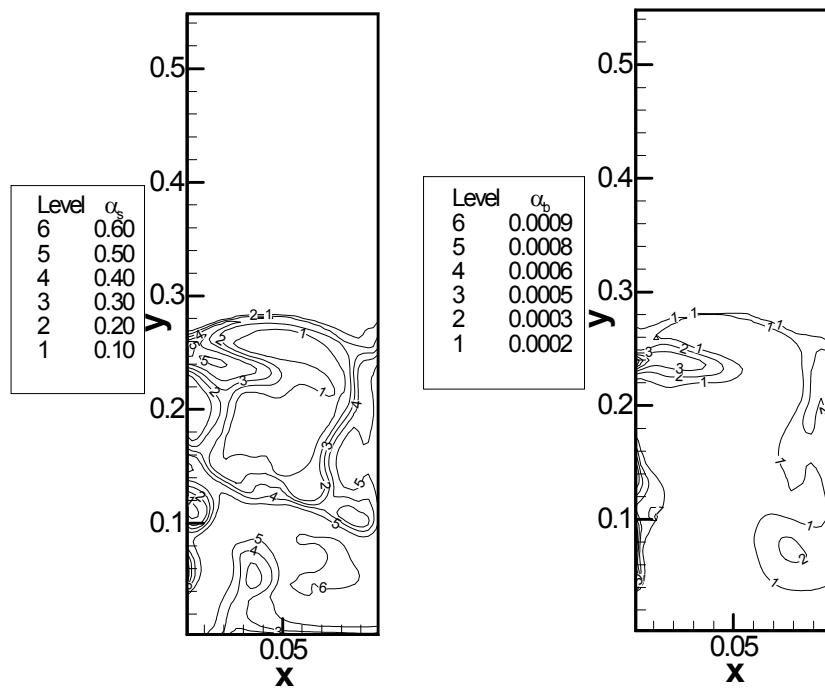


Figure 8: Contours of the volume fractions of sand (left) and biomass (right) at $t=2.5$ s.

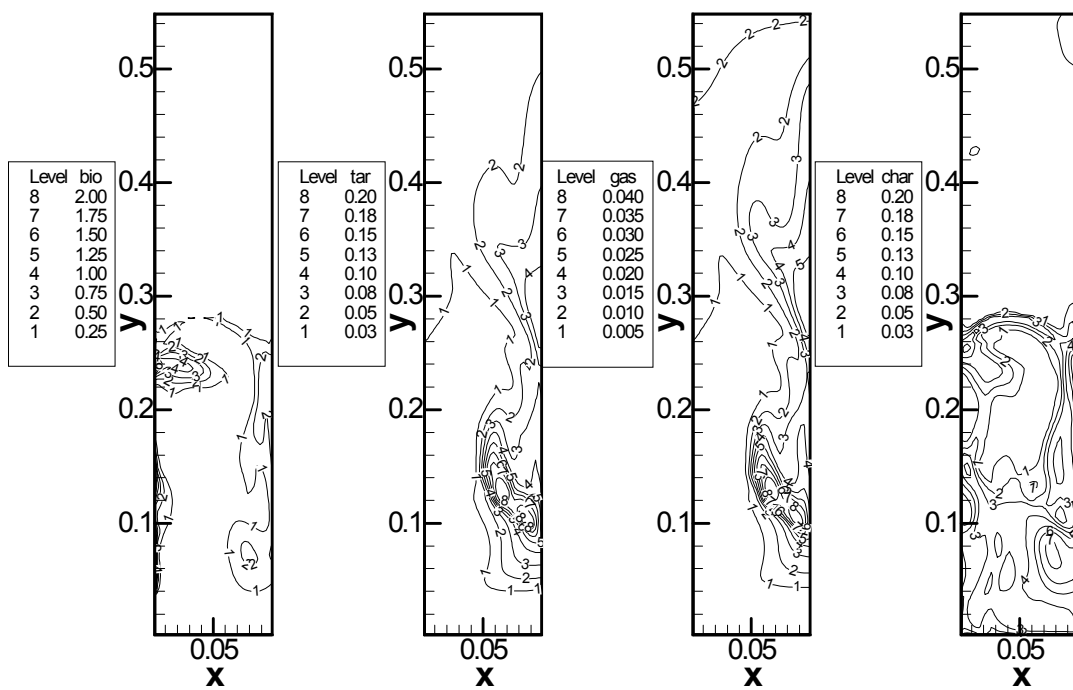


Figure 9: Contours of partial density of biomass, tar, gas and char at $t=2.5$ s.

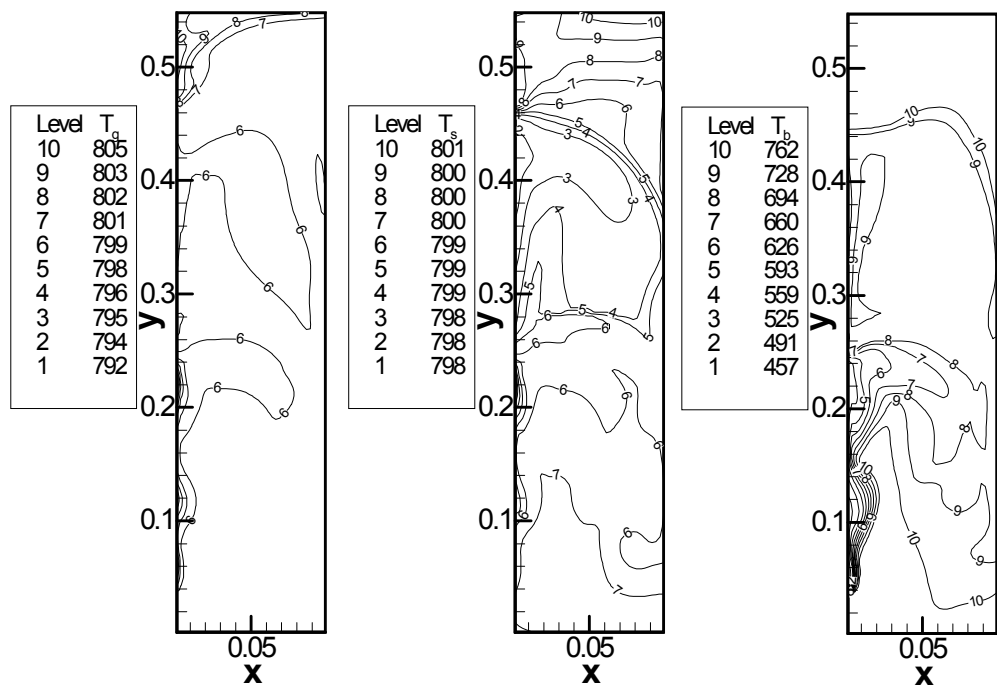


Figure 10: Contours of the temperatures of the gas (left), sand (middle), and biomass (right) at $t=2.5$ s.

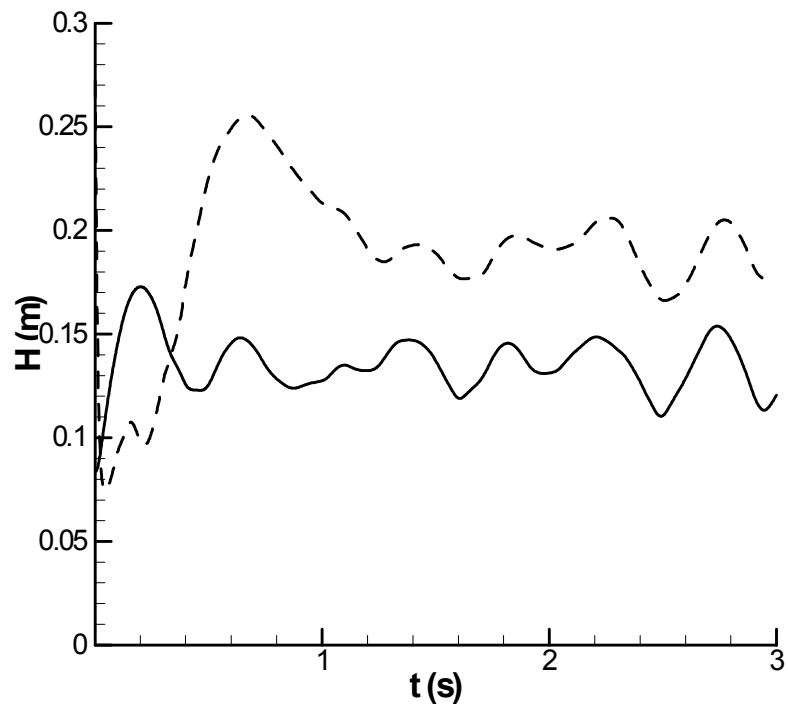


Figure 11: Averaged vertical coordinate of center of mass of sand (—) and biomass (- - - -) particles in the reactor. Data reflect case no 4.

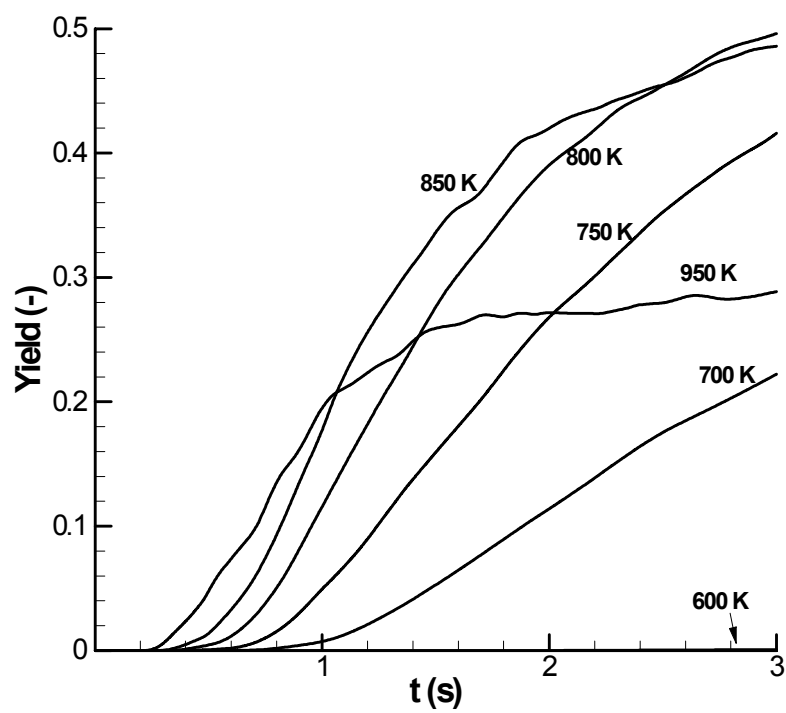


Figure 12: Tar yield as function of time for various gas temperatures; otherwise standard conditions.

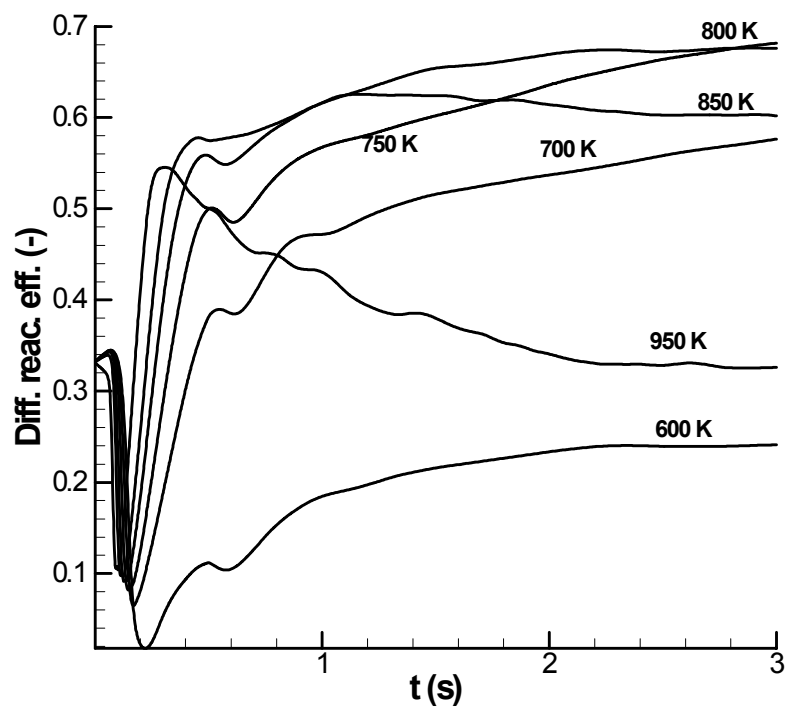


Figure 13: Tar differential reactor efficiency as function of time for various gas temperatures; otherwise standard conditions.

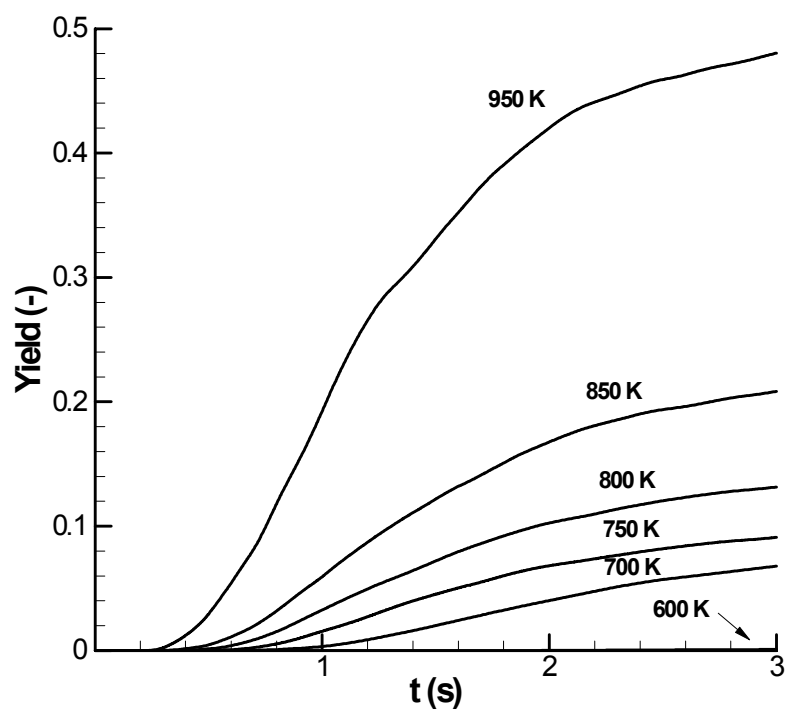


Figure 14: Gas yield as function of time for various gas temperatures; otherwise standard conditions.

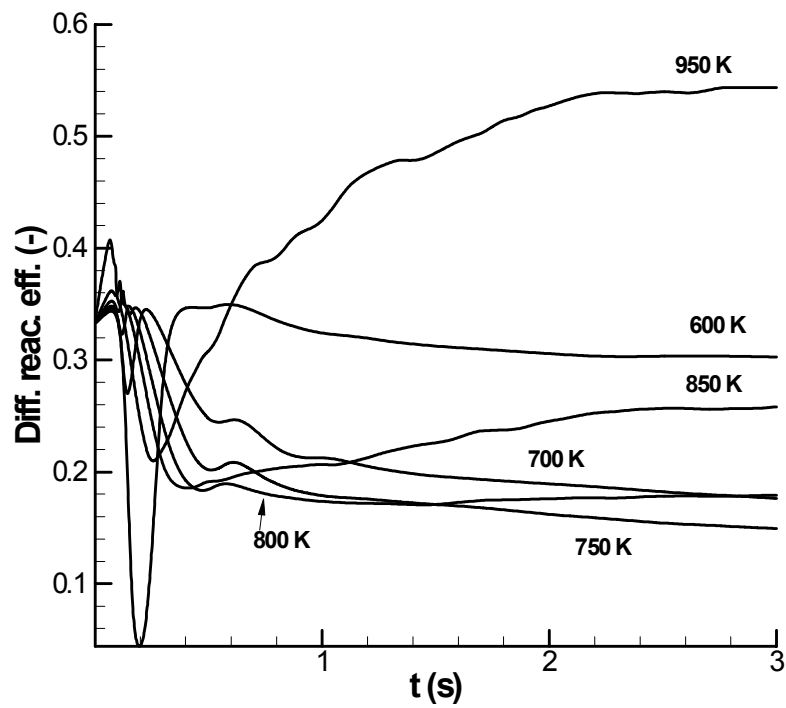


Figure 15: Gas differential reactor efficiency as function of time for various gas temperatures; otherwise standard conditions.

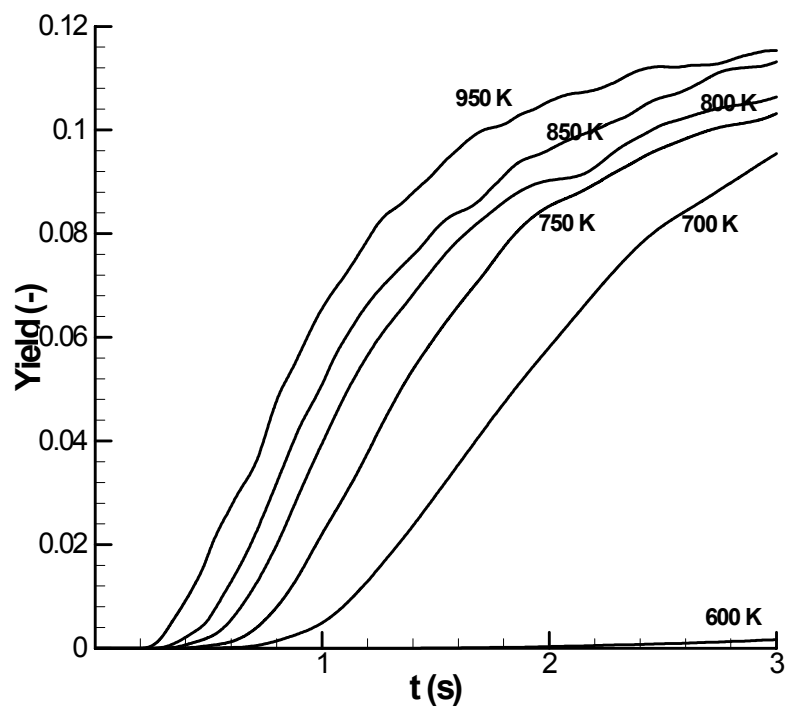


Figure 16: Char yield as function of time for various gas temperatures; otherwise standard conditions.

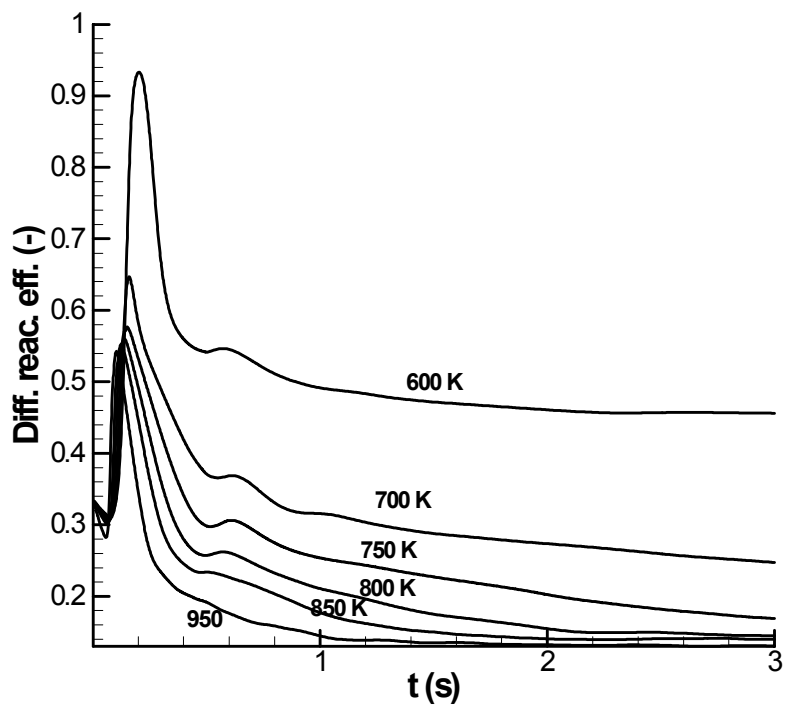


Figure 17: Char differential reactor efficiency as function of time for various gas temperatures; otherwise standard conditions.

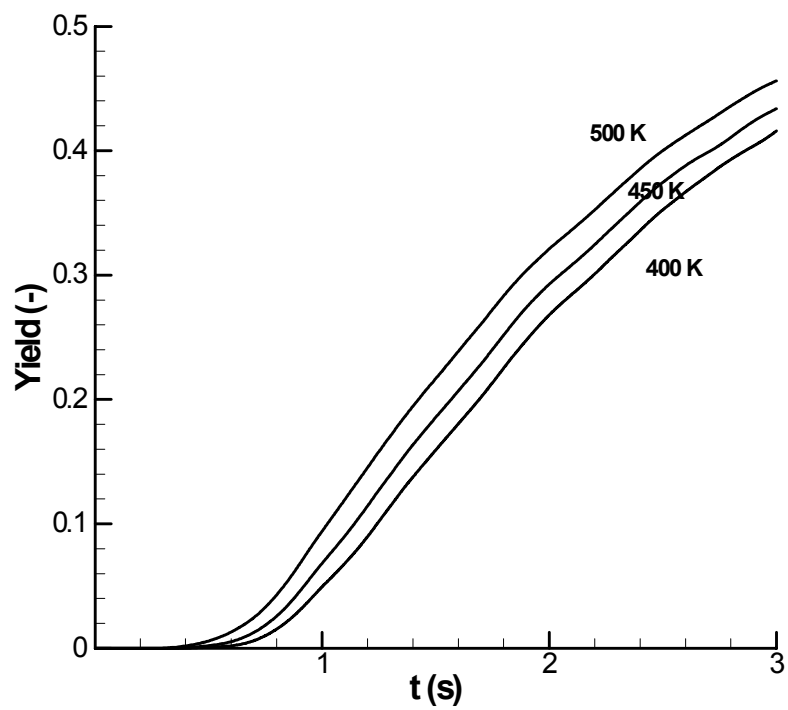


Figure 18: Tar yield as function of time for various biomass feed temperatures; otherwise standard conditions.

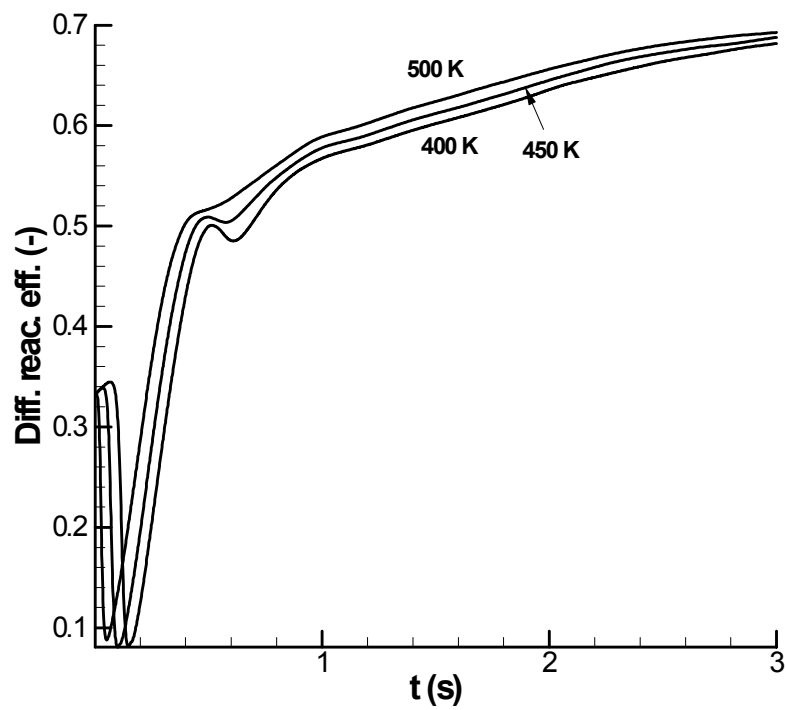


Figure 19: Tar differential reactor efficiency as function of time for various biomass feed temperatures; otherwise standard conditions.

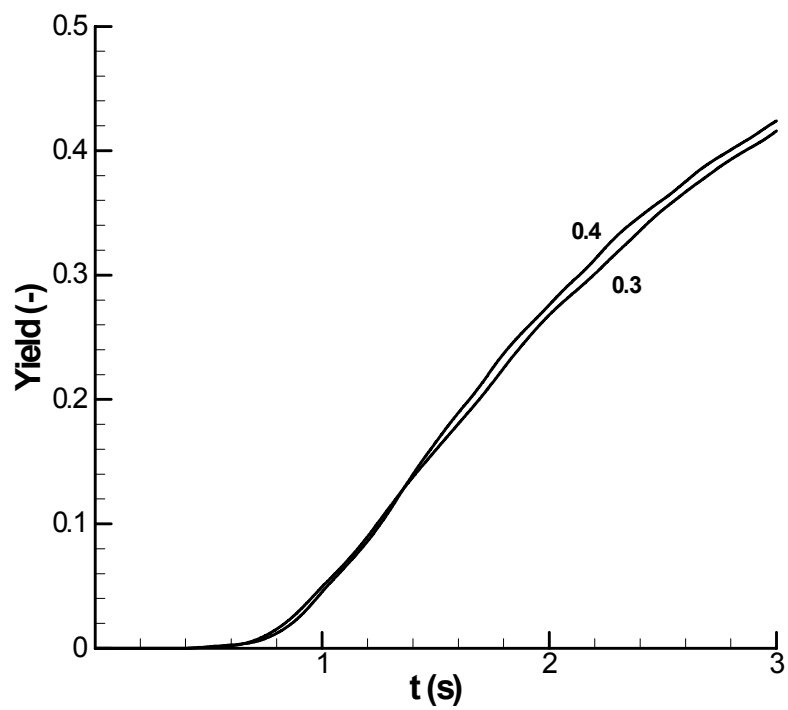


Figure 20: Tar yield as function of time for different fluidization fluxes; otherwise standard conditions.

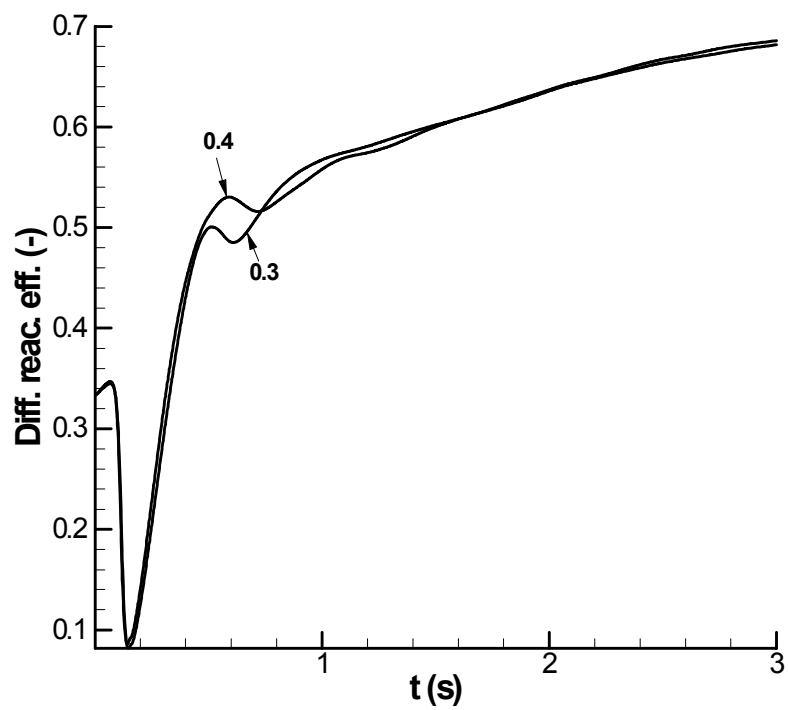


Figure 21: Tar differential reactor efficiency as function of time for different fluidization fluxes; otherwise standard conditions.

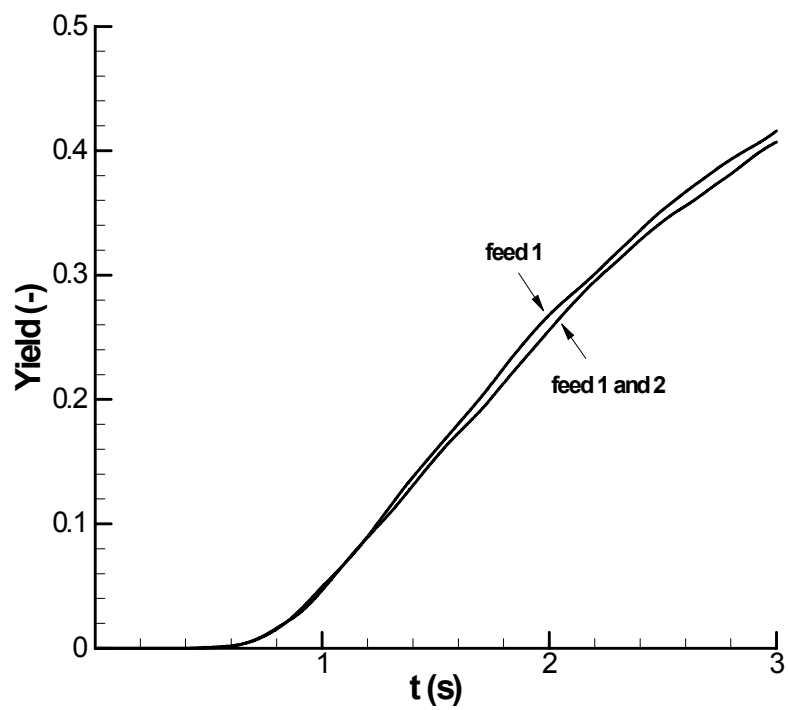


Figure 22: Tar yield as function of time for different feedpoint configurations; otherwise standard conditions.

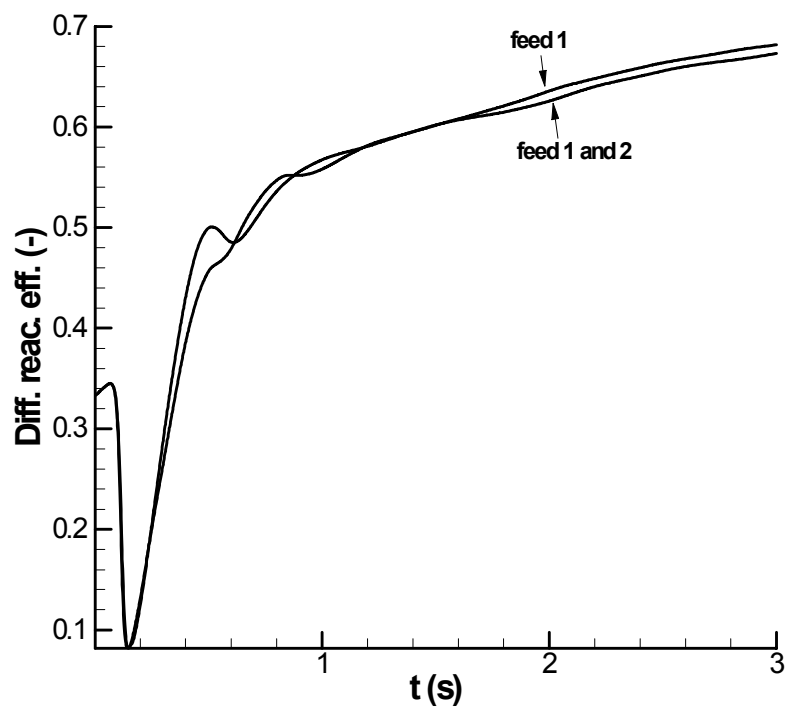


Figure 23: Tar differential reactor efficiency as function of time for different feedpoint configurations; otherwise standard conditions.

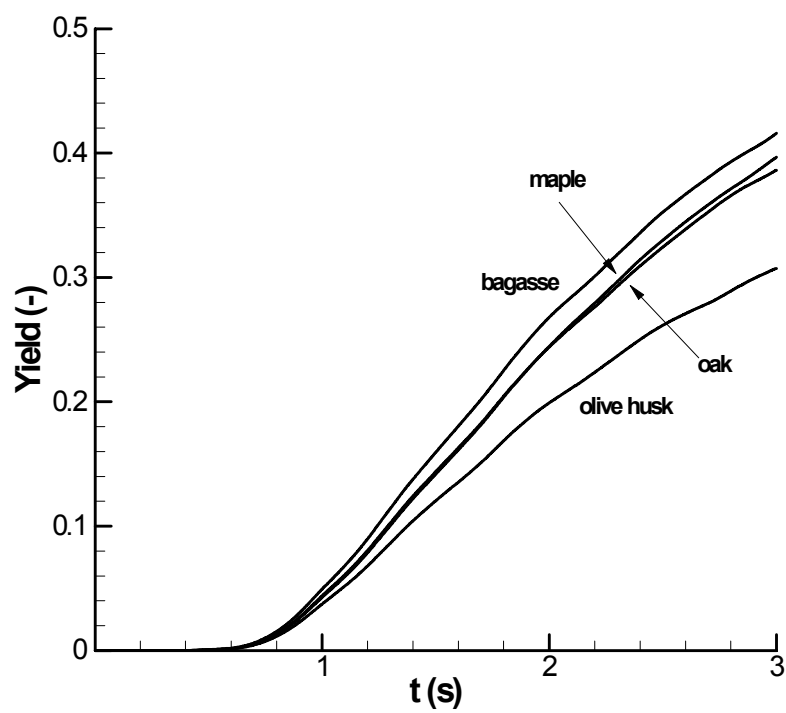


Figure 24: Tar yield as function of time for various biomass feedstock; otherwise standard conditions.

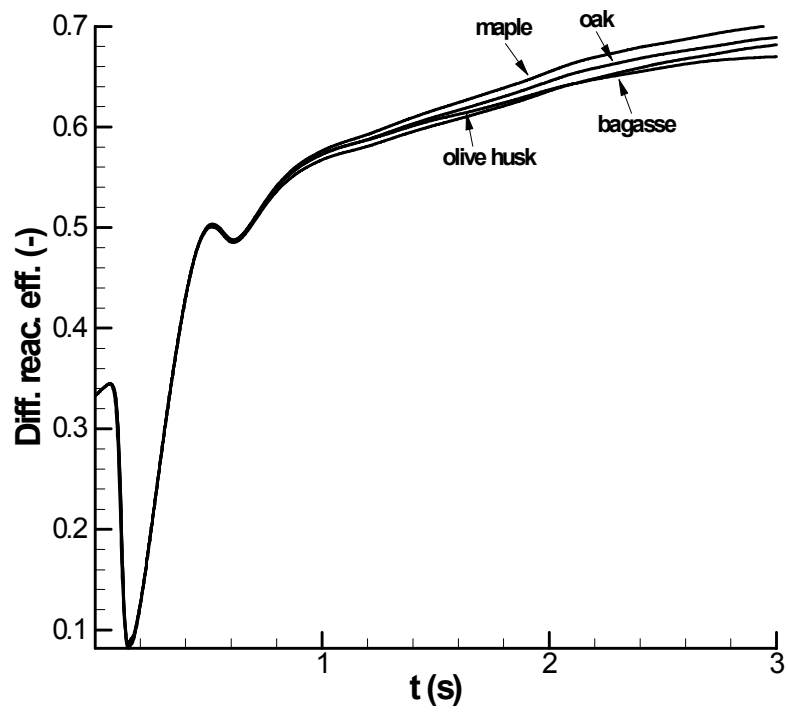


Figure 25: Tar differential reactor efficiency as function of time for various biomass feedstock; otherwise standard conditions.

SOLAR PHOTOCATALYTIC HYDROGEN PRODUCTION FROM WATER USING A DUAL BED PHOTOSYSTEM

Clovis A. Linkous
Darlene K. Slattery
Florida Solar Energy Center
University of Central Florida
Cocoa, FL 32922

Abstract

We have been investigating the use of organic pigments as semiconductor photocatalysts in a dual stage water decomposition scheme that would ultimately use solar energy to generate hydrogen from water. We have shown that by employing a combination of simple screening procedures on prospective compounds, such as semiempirical molecular orbital calculations and thin film voltammetry, we can quickly determine whether a compound will be capable of O₂ or H₂ evolution. A number of fused heteroaromatic compounds were identified as possible photocatalysts for O₂ evolution; we subsequently verified that various perylene, indanthrone, and quinacridone compounds do indeed evolve O₂ under Xe lamp illumination. A number of phthalocyanine compounds were shown to evolve H₂. Using a perylene diimide derivative as the O₂-evolving photocatalyst and copper phthalocyanine as the H₂-evolving photocatalyst, respective oxidative and reductive water decomposition was observed using the same IO₃⁻/I⁻ redox electrolyte, demonstrating that continuous closed cycle dual bed photocatalytic water-splitting is feasible.

Introduction

In this work we are attempting to perform the highly efficient storage of solar energy in the form of H₂ via photocatalytic decomposition of water. While it has been demonstrated that H₂ and O₂ can be evolved from a single vessel containing a single suspended

photocatalyst (Sayama 1994; 1997), we are attempting to perform net water-splitting by using two photocatalysts immobilized in separate containers, or beds. A schematic showing how the device would work is shown in Figure 1.

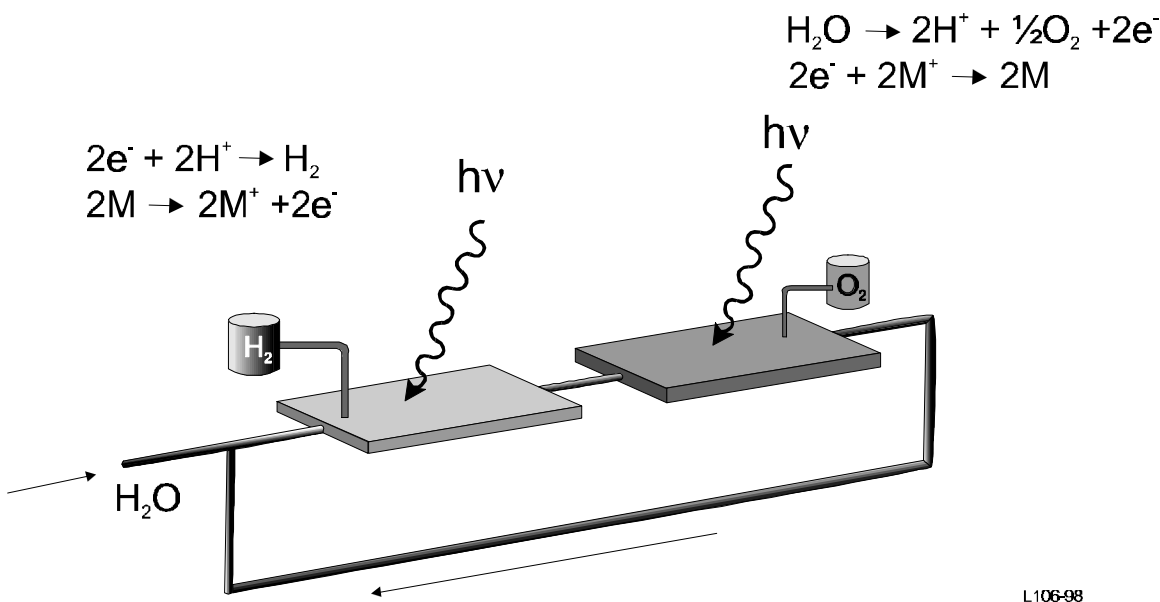


Figure 1. Schematic of a Dual Bed Photocatalytic Water-Splitting System.

Two pairs of photocatalytic reactions would occur. In one container, water is reduced to H_2 ; the electron equivalents for the reaction come from a redox mediator, M . In the second container, water is oxidized to evolve O_2 ; here the oxidized form of the mediator acts as electron acceptor. By circulating the mediator in an aqueous solution between the beds, the transfer of charge equivalents between the two water decomposition half-cell reactions is accomplished. While the maximum quantum efficiency for water-splitting is automatically cut in half, one is now able to utilize lower energy photons to perform less energetically demanding chemical steps, and so achieve better utilization of the solar spectrum.

The direction of reaction is controlled largely by the electronic structure of the photocatalysts. In order to perform H_2 evolution, the conduction band edge of the semiconductor must exceed, or on the electrochemical voltage scale, be more negative than, the electronic energy level for H_2 . The valence band edge must lie below the redox state of the mediator. A similar argument can be made for the O_2 -evolving photocatalyst.

One of the principle advantages of the photocatalytic approach to water-splitting is the module cost. Previous work has shown that photocatalyst dispersions at only a few milligrams per square centimeter can effectively collect the incoming light (Linkous 1995). To scale up the units, one would need $10 \text{ g photocatalyst/m}^2$, or $45 \text{ m}^2/\text{lb}$. With a projected cost of 10's of dollars per pound, the photocatalyst would have a negligible impact on overall system cost. In a comparative analysis of several semiconductor-

electrolytic H₂-generating systems (Block 1998), it was estimated that a dual bed reactor operating at 8.0% efficiency would be able to produce H₂ at \$13/Mbtu.

In earlier work on this concept, we tried to identify combinations of redox mediators and photocatalysts that would perform their respective functions. We identified the alkaline IO₃⁻/I⁻ redox couple as being optically transparent, highly soluble, and active for electron transfer in both Ox and Red states (Linkous 1996). For the O₂-evolving photocatalyst, we first studied TiO₂. While it was able to evolve O₂ under a variety of conditions, the 3.0-3.2 eV band gap absorbed too little of the solar spectrum. For the H₂-evolving photocatalyst, we identified indium phosphide, InP. While initial H₂ yields were good, it proved unstable under illumination in the alkaline solution. Moreover, it was eventually discovered that InP could be attacked by IO₃⁻ even in the dark.

That result led us to consider organic pigments as photocatalysts for the respective water-splitting reactions. The number of pigments commercially available is quite large, however, and so we sought to develop a battery of testing methods, both theoretical and experimental, for estimating whether a given compound could effectively absorb visible wavelength light and be able to either photooxidize or photoreduce water. As for a theoretical method, we evaluated several semi-empirical molecular orbital calculation methods and determined that the PM3 method gave the most reliable gas phase ionization potentials for fused ring compounds. The results were not necessarily accurate, but did yield a linear plot by which a correction factor could be obtained. The application of the PM3 method to pigments of interest, plus the development photoelectron and voltammetric methods of testing, are described below.

Experimental

Theoretical Calculations

Calculation of the HOMO (highest occupied molecular orbital in the ground state) and LUMO (lowest unoccupied molecular orbital) for each pigment was accomplished using CAChe 3.0 software from Oxford Molecular Group, run on a Pentium II, 233 MHz computer. The molecule was drawn within the program and the valence, hybridization, and initial geometry were corrected using the “beautify” option. After a preliminary geometry optimization by molecular mechanics, MM2, additional optimization was performed using PM3 parameters. The fully optimized molecule was then submitted for PM3 determination of the wavefunctions, including the HOMO and LUMO.

Ultraviolet Photoelectron Spectroscopy

The gas-phase ultraviolet photoelectron spectra were recorded using an instrument and procedures that have previously been described in detail (Westcott 1998). The argon ²P_{3/2} ionization at 15.759 eV was used as an internal calibration lock of the absolute ionization energy, and the difference between the argon ²P_{3/2} ionization and the methyl iodide ²E_{1/2} ionization at 9.538 eV was used to calibrate the ionization energy scale. During data

collection the instrument resolution (measured using FWHM of the argon $^{2}P_{3/2}$ peak) was 0.015-0.030 eV. Ionization peak positions are reproducible to ± 0.02 eV.

Voltammetry

The various pigments were largely intractable in aqueous solution and in most organic solvents as well, so that voltammetric data had to be obtained by casting pigment films directly onto the working electrode and performing the electrolysis on the film in a blank supporting nonaqueous electrolyte. The pigments were solubilized by making a Lewis acid complex with $AlCl_3$ which could then be subsequently acted on by organic solvents. Even though the pigments could be solubilized in this way, it was still necessary to cast films, because the ligand binding effect shifted the energy levels we were hoping to probe, and the organic solvents employed were electroactive themselves in the anodic potential region.

Solutions were prepared under an inert atmosphere in a glovebox. Using a process recently developed at Xerox (Hsieh 1998), 6 mL of nitromethane and 4 mL of methylene chloride were combined and 0.33 g of aluminum chloride was added. After stirring to dissolve the $AlCl_3$, 0.4 mmol of the pigment were added. The flask was stoppered and the solution allowed to stir for 6-18 hours.

The working electrode was a 1.0 cm^2 platinum foil. The electrode was passed through a hydrogen flame and then, under an inert atmosphere, was dipped in the pigment/nitromethane solution 1-7 times to coat, allowing time to dry between coats. After coating, the electrode was removed from the glove box and dipped in deionized water to remove any residual nitromethane, methylene chloride and aluminum chloride. It was then placed in a warm oven at approximately 110 $^{\circ}C$ until dry.

Voltammetric experiments were run using an EG&G Princeton Applied Research Potentiostat/Galvanostat model 273A with data being recorded using a Hewlett Packard 7015B chart recorder. A three electrode, single compartment configuration was used, with a platinum mesh counter electrode, and a $Ag/AgClO_4$ reference electrode. Solutions were 0.1 M tetraethylammonium perchlorate in DMSO when investigating reduction potentials or 0.1 M $LiClO_4$ in acetonitrile for oxidation potential studies. The solvents were Aldrich brand anhydrous and were used as received.

Results and Discussion

Semi-Empirical MO Calculations

As stated in the Introduction, we had shown that one could perform PM3 semi-empirical molecular orbital calculations on organic molecules, derive gas phase ionization potentials based on the calculated HOMO's of the molecules, and then plot these values versus the literature IP values to derive a linear equation containing the correction factor between theory and experiment. However, we soon found that good linear correlations could only

be obtained for structurally analogous series of compounds. The addition of heteroatoms in the fused aromatic rings of many of the more interesting pigments caused energy shifts that warranted a new correction factor. Unfortunately, rather little experimental ionization potential data exists for organic pigments. Plenty of optical spectral data is available, but IP is not recognized as a significant parameter for the dye and pigment industry, even though it undoubtedly correlates with factors of considerable interest, such as lightfastness.

Hence it became necessary to obtain experimental gas phase ionization potential data. This was done via ultraviolet photoelectron spectroscopy (see Experimental section). The values are shown for a number of pigments in Table 1 below. As expected, the experimental values were generally somewhat less than the calculated values. If nothing else, this is due to the fact that the experimental value is an “onset” of ionization, while the calculated value represents the maximum of the thermal Gaussian distribution of energies. It may also be true that PM3 typically overestimates some of the overlap integrals for fused aromatics. A plot of experimental versus theoretical ionization potential for a number of similar compounds (indanthrone, quinacridone, isoviolanthrone, indanthrene gold orange, perylene TCDA, and dimethoxyviolanthrone) are shown in Figure 2. Units are in electron volts (eV). The equation shown is a least squares fitting of the data. Our expectation is that we will now be able to take any prospective fused aromatic quinonoid structure, perform a 20 minute PM3 calculation on it, and then substitute the result into the fitted equation to derive the true ionization potential.

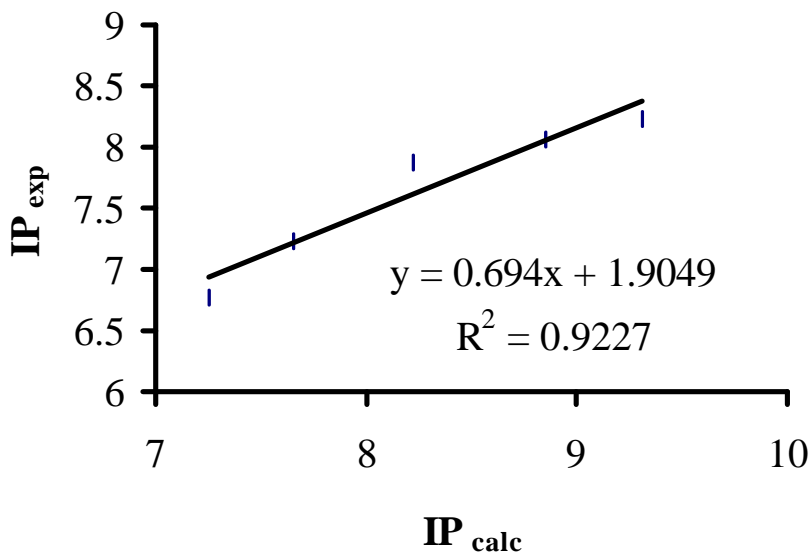


Figure 2. Plot of experimental versus theoretical ionization potential for photocatalytic pigments.

Table 1. Energy Levels of Various Organic Pigments as Determined by PM3 Semi-Empirical MO Calculation, UV-Photoelectron Spectroscopy, Voltammetry, and UV-Visible Spectrophotometry.

| PIGMENT | I.P. theory (eV) | I.P. exp (eV) | E°_{ox} (V)* | E°_{red}(V)* | (nm) | (eV) |
|----------------------------|-------------------------|----------------------|-----------------------------|-----------------------------|-------------|-------------|
| Indanthrone | 7.25 | 6.78 | 0.99 | -0.29 | 622 | 1.99 |
| Quinacridone | 7.65 | 7.23 | 1.39 | -1.11 | 595 | 2.08 |
| Dimethoxy Violanthrone | 7.90 | ~7.6 | 1.16 | -0.34 | 706 | 1.75 |
| Isoviolanthrone | 8.22 | 7.87 | 1.54 | -0.34 | 712 | 1.74 |
| Indigo | 8.34 | 7.23 | 1.19 | -0.37 | 737 | 1.68 |
| Bis(chlorophenyl) DPP | 8.50 | 7.47 | <1.49 | -0.70 | 600 | 2.06 |
| Pyranthrone | 8.54 | ---- | 1.39 | -0.30 | 585 | 2.12 |
| Indanthrene Black | 8.83 | ---- | ---- | ---- | ---- | ---- |
| Indanthrene Gold Orange | 8.84 | 8.07 | 1.50 | -0.03 | 562 | 2.20 |
| Perylene TCDA | 9.31 | 8.22 | <2.29 | -0.05 | 604 | 2.05 |
| Indanthrene Yellow | 9.41 | ---- | 1.09 | ---- | 510 | 2.43 |
| Perylene Diimide | 8.87 | ---- | <2.09 | -0.14 | 652 | 1.90 |

* vs NHE reference electrode

Voltammetric Studies

While UPS proved useful as a means of acquiring experimental ionization potential data, we also sought to develop an in-house method by which we could make the same determination. The first oxidation and reduction potentials in an electrochemical experiment can approximate the ionization potential and electron affinity, respectively, although a correction involving solvation energies would be necessary for a rigorous determination

The difficulty of preparing samples that would yield voltammetric data is described in the Experimental section. Even so, once the Lewis acid pigment solubilization technique was mastered, voltammetric data for nearly all the prospective organic photocatalysts could be obtained. These results are also shown in Table 1. In general, there was fair agreement between the ΔE value, based on the difference between the E_{ox} and E_{red} measurements, and the E_{HOMO} value based on spectroscopy. Sometimes the voltammetric wave was irreversible, so that the measured redox potential was more of an upper bound than the actual value. While the correlation between calculation and experiment was less than with the UPS measurements, it should be noted that the electrochemical experiment better reflects the solid state energy levels that would participate in the photocatalytic reaction. It is also true that there is no limitation having to do with structural analogues; the voltammetric waves are unambiguous indications of the energies where charge transfer would be expected from a given compound. Certainly the general trend of calculated HOMO increasing with E_{ox} was observed, especially for the perylenes.

O₂ Evolution Studies

Having established a number of methods for estimating the available oxidation potential of a photocatalyst, it was time to see whether water could indeed be oxidatively decomposed to evolve O₂. Accordingly, the prospective photocatalysts were suspended with 2.0 weight percent co-catalyst in a dichloroethane solution and deposited by painting onto an acrylic substrate.

This represented something of a departure from past methods. Formerly, we had made co-catalyst modifications of the primary photocatalysts by a number of methods, such as photoreduction or direct borohydride reduction of a noble metal salt. The direct chemical reduction method has been found to be difficult and counterproductive with the organic pigments. The reducing effect of the BH₄⁻ ion often served to irreversibly reduce and discolor the pigment.

Consequently, we have been directly physically mixing the photocatalyst and co-catalyst powders. While this does not make for as intimate a mixture as the aforementioned methods, nevertheless, related studies in photocatalytic detoxification studies with similarly intractable materials has shown that positive effects can indeed be observed by direct blending of the photocatalyst and co-catalyst powders (Linkous, 2000).

The O₂ evolution data from the photocatalytic experiments is shown in Table 2. Each value represents a 6-hour photolysis with a Xe lamp using iodate ion as electron acceptor in 1.0 M NaOH solution. The co-catalyst was iridium black.

Table 2. Volume of O₂ Evolved in Water-Splitting Experiments using Organic Pigments

| Photocatalyst | O ₂ Evolved (ml) |
|-------------------------|-----------------------------|
| Perylene Diimide | 4.4 |
| bis(p-chlorophenyl) DPP | 3.6 |
| Indanthrone | 3.3 |
| Perylene TCDA | 3.2 |
| Pigment Red 177 | 2.6 |
| Indanthrene Yellow | 2.0 |
| Quinacridone | 1.8 |
| Isoviolanthrone | 1.5 |
| Acrylic blank | 1.5 |
| Indigo | 1.4 |
| Dimethoxyviolanthrone | 1.3 |
| TiO ₂ | 1.3 |
| Indanthrene gold orange | 0.9 |
| Indanthrene Black | 0.7 |

Most of the pigments performed better than TiO₂ tested under the same conditions. The value obtained for the acrylic blank (which also included Ir co-catalyst) may represent a UV background effect that should be subtracted out. Even so, despite the modest yields of O₂, it is apparent that we have accomplished our goal in finding more active O₂-evolving photocatalysts than TiO₂.

Photocatalytic H₂ Evolution

Having achieved some measure of success with the O₂-evolving photocatalysts, it was time to turn our attention toward H₂-evolving photocatalysts. From the literature and

from our PM3 calculations, it was apparent that the phthalocyanine (Pc) family of compounds could serve as photocatalysts in this regard (Kearns 1961; Giraudeau 1980). A number of phthalocyanine compounds were acquired and submitted to testing in the same manner as the O₂-evolving photocatalysts above, except that the electrolyte contained 0.2 M iodide ion to serve as electron donor, and the co-catalyst was 2.0 weight percent platinum black.

These results are shown in Table 3 below. The chloro-aluminum Pc was chosen as a representative trivalent metal center. Earlier work had shown that these MPc-X's could perform well as electrode materials in a photoelectrochemical cell (Klofta 1985). Because of its above-plane central moiety, the vanadyl Pc has a unique crystal structure and optical spectrum, and so was of interest for this application (Griffiths 1976). As it turned out, the more common copper Pc evolved the most H₂. This may correlate with its superior extinction coefficient in the solid state (Moser 1963).

Table 3. Volume of H₂ Evolved in Water-Splitting Experiments using Phthalocyanine Organic Pigments

| photocatalyst | H ₂ evolved (l) |
|---------------|------------------------------|
| CuPc | 113.0 |
| VOPc | 25.6 |
| AlPc-Cl | 16.0 |
| NiPc | 22.6 |

While the amounts of gas evolved are considerably less than with the O₂-evolving photocatalysts, we are confident better photocatalysts will be identified with time. The challenge to date has been to identify organic materials whose HOMO was sufficiently positive on the voltage scale to oxidize water, but whose LUMO was also sufficiently positive so that the band gap energy could be surmounted using visible wavelength light. More often than not, LUMO levels for organic pigments are energetically capable of performing water reduction, and so with time more favorable materials will be found.

Proof of Concept Operation

Having found organic pigments that would support O₂ evolution and H₂ evolution, it was time for proof of concept, i.e., to show that the separate photocatalytic systems could evolve their respective gas using the same redox electrolyte. Our best O₂-evolving photocatalyst was the ditridecyl perylene diimide and our best H₂-evolving photocatalyst was copper phthalocyanine. Their structures are shown in Figures 3 and 4. The two photocatalysts were tested as before, except that instead of using entirely Ox or Red forms of the redox mediator, the experiment was begun at equal parts IO₃⁻ and I⁻. In each case,

the respective gas was obtained in ~80% of the amount obtained with 100% of Ox or Red, respectively, thus showing that net water-splitting would occur in closed cycle operation.

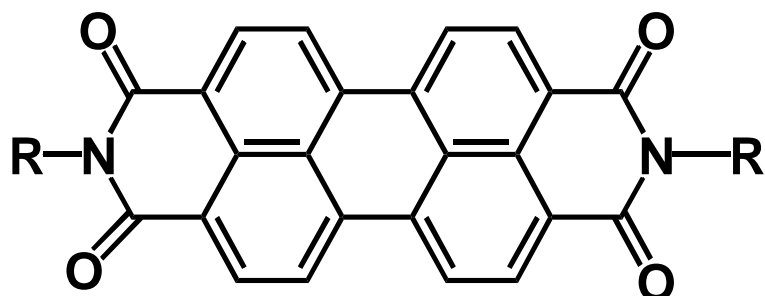


Figure 3. Structure of O₂-Evolving Photocatalyst N,N'-Ditriridecyl-3,4,9,10-Perylene Tetracarboxylic Diimide.

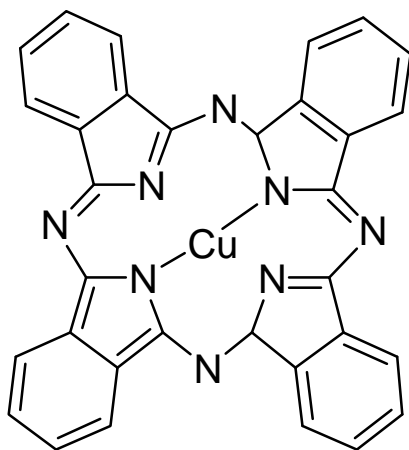


Figure 4. Structure of Copper Phthalocyanine.

In future work, modifications of the existing configuration will be attempted to increase system efficiency. We will attempt this objective in several ways. One is to demonstrate tandemized versions of the dual bed system using organic pigments and polymer membrane technology. Subsequently, we will introduce porosity or microperforations into the photocatalytic membranes. Finally, we will try to prevent back reaction by developing controlled conformation redox mediator complexes.

Acknowledgment

The authors wish to thank Dr. Nadine Gruhn of the Chemistry Department at the University of Arizona for her technical assistance in obtaining the UPS spectra and in their interpretation.

Our thanks also go to the US Department of Energy, Office of Solar Thermal, Biomass, and Hydrogen Technologies for financial support of this work.

References

Block, D.L. 1998. "Comparative Costs of Hydrogen Produced from Photovoltaic Electrolysis and from Photoelectrochemical Processes," In *Proceedings of the 12th World Hydrogen Energy Conference*, vol 1:185-194. Buenos Aires, Argentina: International Association for Hydrogen Energy.

Giraudeau, A., F.-R.F. Fan, and A.J. Bard. 1980. "Semiconductor Electrodes. 30. Spectral Sensitization of the Semiconductors n-TiO₂ and n-WO₃ with Metal Phthalocyanines," *J. Am. Chem. Soc.* 102:5137-5141.

Griffiths, C.H., M.S. Walker, and P. Goldstein,. 1976. *Mol Cryst. Liq. Cryst.* 33:149.

Hsieh, B.R., and A.R. Melnyk. 1998. *Chem. Mater.* 10:2313-2316.

Kearns, D.R., and M. Calvin. 1961. "Solid State Ionization Potentials of Some Aromatic Organic Compounds," *J. Chem. Phys.* 34: 2026-2030.

Klofta, T.J., P.C. Rieke, C.A. Linkous, W.J. Buttner, A. Nanthakumar, T.D. Mewborn, and N.R. Armstrong, "Tri- and Tetravalent Phthalocyanine Thin Film Electrodes: Comparison with Other Metal and Demetallated Phthalocyanine Systems," *J. Electrochem. Soc.* 132: 2134-2144.

Linkous, C.A., N.Z. Muradov, and S.N. Ramser. 1995, "Consideration of Reactor Design for Solar Hydrogen Production from Hydrogen Sulfide Using Semiconductor Particulates," *Int. J. Hydrogen Energy*, 20:701-710.

Linkous, C.A., D.K. Slattery, A.J.A. Ouelette, G.T. McKaige, and B.C.N. Austin. 1996. "Solar Photocatalytic H₂ from Water Using a Dual Bed Photosystem." In *Hydrogen Energy Progress XI: Proceedings of the 11th World Hydrogen Energy Conference*, vol. 3, 2545-2550.

Linkous, C.A., G.J. Carter, D.B. Locuson, A.J. Ouelette, D.K. Slattery, and L.A. Smitha. 2000. "Photocatalytic Inhibition of Algae Growth Using TiO₂, WO₃, and Co-catalyst Modifications," submitted to *Env. Sci. Technol.*

Moser, F.H., and A.L. Thomas. *Phthalocyanine Compounds*. New York:Reinhold Publishers.

Sayama, K., and H. Arakawa. 1994. "Effect of Na₂CO₃ Addition on Photocatalytic Decomposition of Liquid Water over Various Semiconductor Catalysts." *J. Photochem. Photobiol. A: Chem.*, 77: 243-247.

Sayama, K. and H. Arakawa. 1997. "Effect of Carbonate Salt Addition on the Photocatalytic Decomposition of Liquid Water over Pt-TiO₂ Catalyst." *J. Chem Soc., Faraday Trans.*, 93: 1647-1654.

Westcott, B.L., N.E. Gruhn, and J.H.J. Enemark. 1998. *J. Am. Chem. Soc.* 120:3382-3386.

Figure 1. Schematic of a dual bed water-splitting system.

Figure 2. Plot of experimental versus theoretical ionization potential for photocatalytic pigments.

Figure 3. Structure of O₂-Evolving Photocatalyst N,N'-Ditridecyl-3,4,9,10-Perylene Tetracarboxylic Diimide.

Figure 4. Structure of Copper Phthalocyanine.

PHOTOELECTROCHEMICAL HYDROGEN PRODUCTION

**Eric Miller and Richard Rocheleau
Hawaii Natural Energy Institute
School of Ocean and Earth Science and Technology
University of Hawaii at Manoa
Honolulu, HI 96822, USA**

Abstract

High efficiency photoelectrochemical (PEC) systems to produce hydrogen directly from water using sunlight as the energy source have been identified by DOE as one of the promising technologies to meet long-term hydrogen-production goals. In the PEC research at UH, our approach has been to compare alternate materials and system configurations using reactor modeling, and to identify and address the critical materials and photoelectrode-operation issues through extensive experiments in materials synthesis and in photoelectrode fabrication and testing. In 1996 we demonstrated direct solar-to-hydrogen conversion efficiencies of 7.8% using a photocathode fabricated from 10% efficient triple-junction amorphous silicon solar cells. These prototypes were configured with a separate anode connect by wire to a photocathode. In subsequent years, our focus shifted toward the development of photoelectrodes with fully integrated cathodes/anodes. This year, we advanced the design of a new fully integrated and self-contained photoelectrode fabricated entirely with thin film processing and demonstrated a process sequence to fabricate prototypes. The new photoelectrodes again used multi-junction a-Si cells and sputter-deposited catalyst, contact, and protective films developed at UH. We also continued the development of optimal transparent-conductive and protective films. A deposition system for copper-indium-gallium diselenide (CIGS) films was installed (cost shared with other projects and UH support) as part of a new effort to develop higher efficiency photoelectrodes. The encapsulated design with side-by-side series-connected CIGS junctions has the potential to achieve 15% solar to hydrogen conversion efficiency. Plans are underway to demonstrate hydrogen-production using the a-Si photoelectrodes and to develop a fabrication process for high efficiency CIGS-based photoelectrodes.

Introduction

One of most ambitious goals of the US Department of Energy's Hydrogen Program is the large-scale production of hydrogen utilizing a renewable energy source to split water. High efficiency photoelectrochemical (PEC) systems to produce hydrogen directly from water using sunlight as the energy source is one of the more promising technologies to meet this mission. A schematic illustration of a PEC hydrogen production using solar energy as the renewable source is shown in Figure 1a (Rocheleau et. al., 1989). Sunlight shining on a photoelectrode comprising a semiconductor photovoltaic generator coated with catalytic thin films produces electric current which drives the hydrogen and oxygen evolution reactions (HER, OER) at the respective surfaces. In one possible conceptual design for a large-scale reactor, shown in Figure 1b, arrays of photoelectrodes are arranged in tubular reactors which include gas-separating membranes to facilitate the collection of high-purity hydrogen and oxygen.

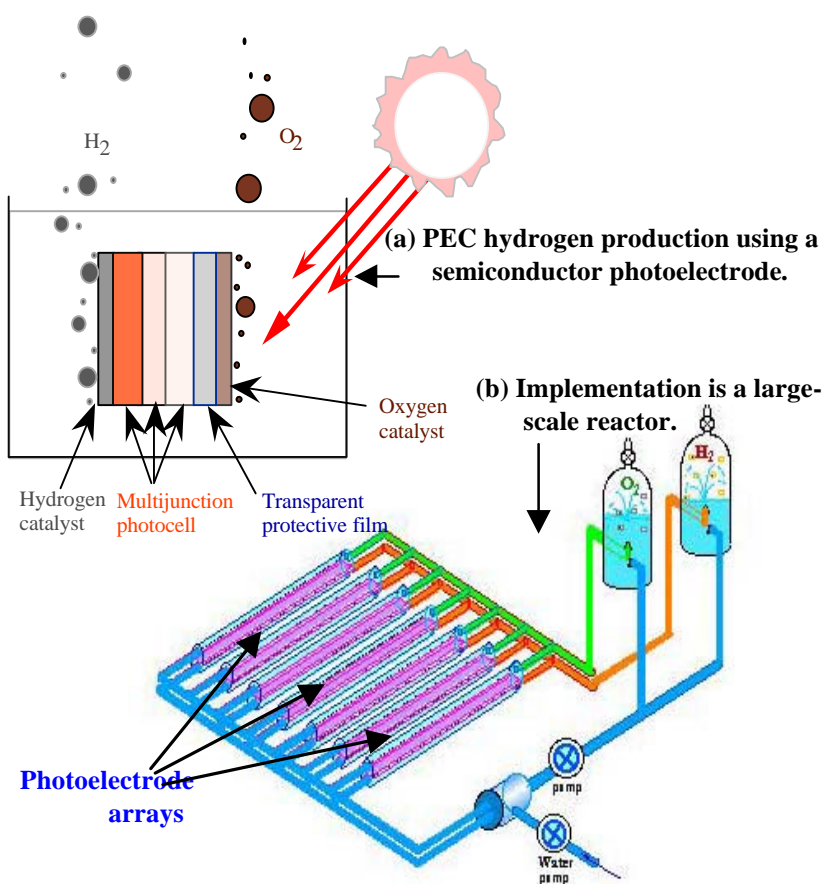


Figure 1 – Photoelectrochemical Hydrogen Production

In order to meet DOE goals, a PEC system must be low cost, must operate at solar-to-chemical conversion efficiencies greater than 10% and must have long operating lifetimes. Numerous approaches involving a variety of semiconductors have been explored since the early 1980's, but none have been successful. The high voltage required to dissociate water and corrosiveness of the aqueous electrolytes have been major hurdles. The use of multijunction PV devices provides sufficient voltage to split water and allows use of a wide range of catalytic and protective films. Modeling and proof-of-concept experiments conducted at UH have provided strong evidence that future direct solar-to-hydrogen conversion efficiency greater than 10% can be expected with photoelectrodes fabricated from low-cost, multijunction amorphous silicon (a-Si) solar cells (Rocheleau & Miller, 1997). Moreover, conversion efficiencies approaching 15% are possible using advanced photoelectrode designs (described in this paper) in which series-connected cells of high-efficiency materials, such as copper-indium-diselenide (CIS), can be stacked in a side-by-side configuration. Based on the very thin semiconductor layers involved and on compatibility with high-throughput manufacturing processes, both the a-Si and CIS photoelectrode systems have the potential for low cost.

Long Term Goals

The ultimate goal of this research is to develop high efficiency (greater than 10%), and low cost thin-film semiconductor photoelectrodes for PEC reactors to directly produce hydrogen from water using sunlight as the energy source. To reach this goal, our approach has included parallel research efforts in: 1) reactor modeling to compare alternate materials and system configurations (Rocheleau et al., 1994); 2) extensive experiments in materials synthesis and testing to identify critical materials issues (such as stability and catalytic activity); and 3) photoelectrode fabrication and testing to identify and address critical photoelectrode-operations issues. Work to date has identified promising high-efficiency PEC systems based on a-Si photoelectrodes coated with specially-developed thin-film catalysts (Rocheleau & Miller, 1997), and even higher efficiency systems based on CIS photoelectrodes. An important near-term goal is to identify which of the materials systems is best suited for achieving the long-term goals in efficiency, stability, scalability and cost.

Past Results

In the past, our effort was mainly focused on demonstrating the feasibility of the photoelectrochemical approach. Optimizing efficiency and stability of all necessary thin-film components of the photoelectrode, including semiconductor layers, the hydrogen and oxygen catalysts, and transparent contact and protective films, has been a significant part of the effort. Early demonstration prototypes were based the configuration shown in Figure 2 with a photoactive cathode and a separate anode. Potassium hydroxide (KOH) was chosen based on the demonstrated chemical activity and long-term stability of thin film HER and OER catalysts previously developed at UH for in this particular electrolyte (Miller & Rocheleau, 1997). For the cathode in the prototype, a triple-junction pinpinpin solar cell on a glass/SnO superstrate (Solarex Thin Film) was used. A CoMo HER thin-film catalyst was sputter-coated on the

backside. The separate anode, connected via wires to the SnO layer of the solar cell was sputter-coated with a Fe:NiOx OER catalyst.

The hydrogen production performance of the prototype system operated in Honolulu on a day with intermittent cloud coverage is shown in Figure 3. Solar-to-hydrogen efficiencies as high as 7.8% were achieved in this configuration using a 10.3% efficient a-Si solar cell (Rocheleau et. al., 1998).

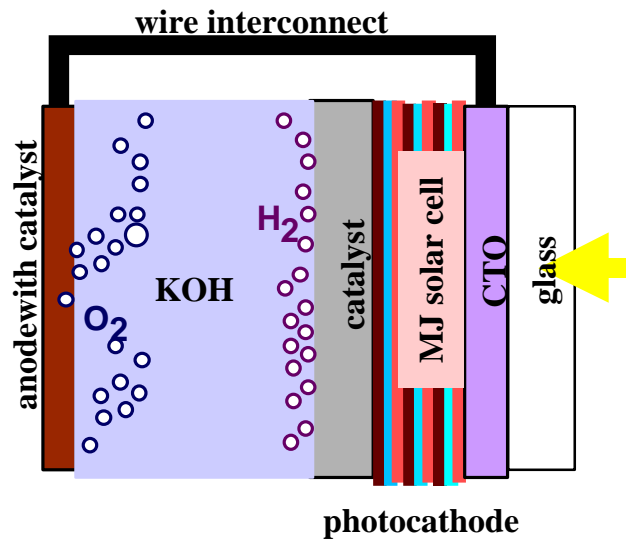


Figure 2 – Photocathode with Separate anode

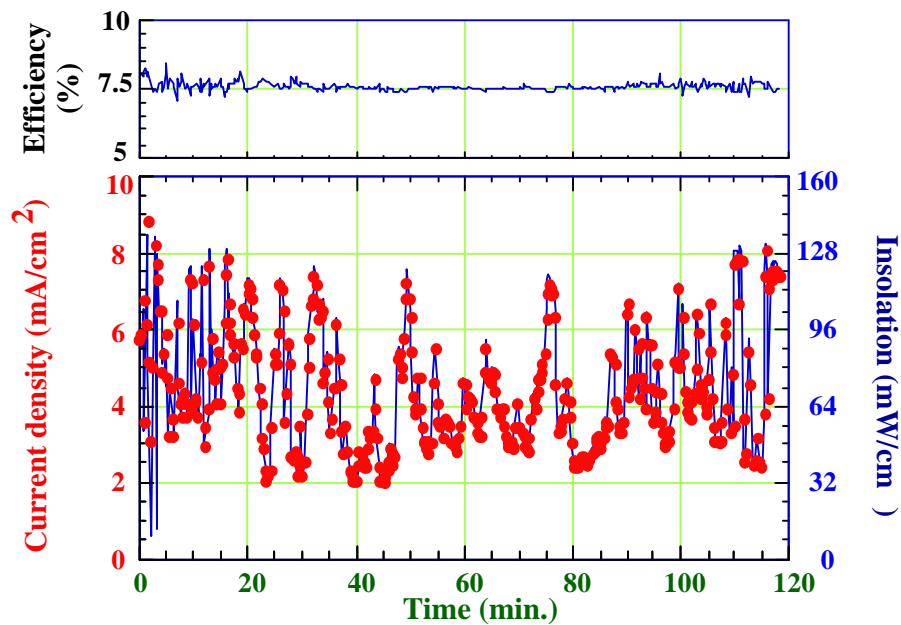


Figure 3 – Solar Hydrogen Production Data

After successful demonstration of proof of concept using the separated anode/cathode configuration, we focussed last year on the critical engineering issues for practical implementation. The primary goal was the development of fully integrated photoelectrode configurations based on planar fabrication of thin films onto inexpensive substrates. Design requirements included high solar-to-hydrogen efficiency, long term stability in aqueous electrolyte, and ease of scale-up. The first fully integrated photoelectrode design that was considered is shown in Figure 4. A nipnipnip a-Si cell (Energy Conversion Devices) on stainless steel substrate was used. The back surface of the SS substrate was coated with CoMo HER catalyst while the front surface of the solar cell was coated with Fe:NiOx OER catalyst. Unfortunately, the relatively thick (1 micron) Fe:NiOx layers introduced high optical losses (Miller, 1996), while thinner, more transparent films layers suffered from loss of catalytic activity and reduced corrosion protection.

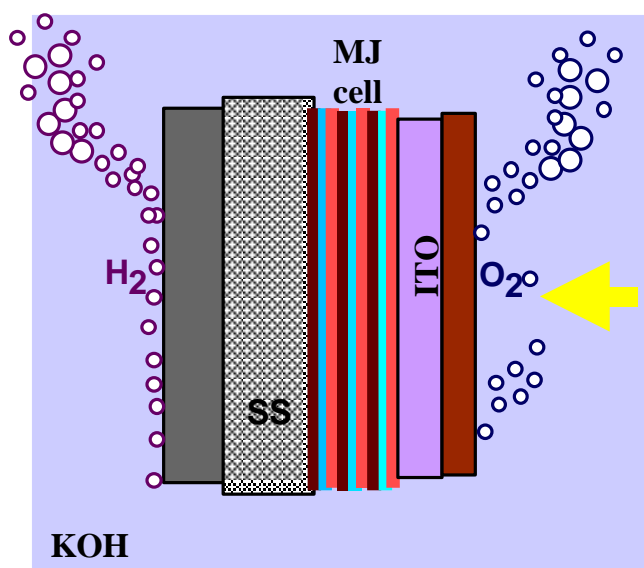


Figure 4 – Integrated Photoelectrode with Monolithic Stacked Cells

At the Hydrogen Program Review in May 1999 (Miller & Rocheleau, 1999), we introduced the conceptual design shown in Figure 5 for a new fully-integrated photoelectrode design structure incorporating planar, series connected solar cells. In this new structure, front surface regions for light collection and for oxygen evolution are separated laterally on the substrate eliminating the requirement for transparency in the OER catalyst material. A highly transparent and inert encapsulation film protects the solar cell under the light-collection area. Compared with the simple integrated structure in Figure 4, the new design has more intricate film geometries and therefore requires a more complex fabrication process. However, as described in the following sections, it opens the door to use of higher efficiency semiconductor materials, such as copper-indium-diselenide cells which have reported solar efficiencies exceeding 18% (Tuttle et al., 1995), previously not feasible for solar hydrogen production.

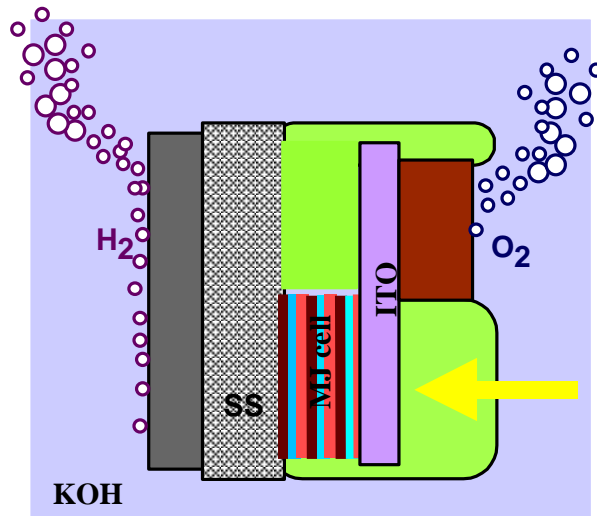


Figure 5 – New Lateral Photoelectrode with Encapsulated Cells

Along with the design of specific integrated photoelectrode configurations, the research last year continued to focus on optimization of the electronic and corrosion-resistance properties of the catalysts films, and of the underlying semiconductor and transparent contact films. Significant progress was made in enhancing the KOH-resistance of amorphous silicon, of transparent/conductive ITO, and of highly transparent TiO₂ encapsulation films.

Current Year Objectives/Tasks

The primary objective of the photoelectrode research effort this year was to identify fully-integrated configurations (i.e., no external wires to connect the anode and cathode) which could achieve high efficiency using thin film semiconductors and which would be compatible with large scale manufacturing.

Specific tasks included: 1) demonstrating a fabrication sequence for the new encapsulated photoelectrode design (i.e. Figure 5) using triple-junction a-Si cells supplied by the University of Toledo and thin-film catalyst and protective coatings developed at UH; 2) further optimization of the catalyst and protective coatings for use in the new photoelectrodes, primarily the indium-tin-oxide (ITO) transparent contact layer; 3) refinement of the new photoelectrode design to allow use of high efficiency CIGS (gallium-doped CIS) solar cells.

Current Year Progress

Photoelectrode Fabrication

Initial prototypes of the new encapsulated photoelectrode design were fabricated using triple-junction a-Si solar cells (University of Toledo). The contact layers, catalysts and encapsulation thin films were deposited in-house by sputtering. The process sequence including schematics of the shadow masks for the individual sputter steps is shown in Figure 6. Photoelectrodes were fabricated on 1" square substrates cut from the 2"x2" cells provided by the University of Toledo. A thin TiO₂ passivation layer was deposited onto the non-photo active regions of the front surface, followed by the ITO lateral conduction layer and the patterned Fe:NiOx OER catalyst. The photoactive region was encapsulated using transparent, chemically inert TiO₂. The final step in the process was deposition of a CoMo HER catalyst layer onto the back of the SS substrate. Photographs showing front and back sides of one of the fabricated photoelectrodes are seen in Figure 7.

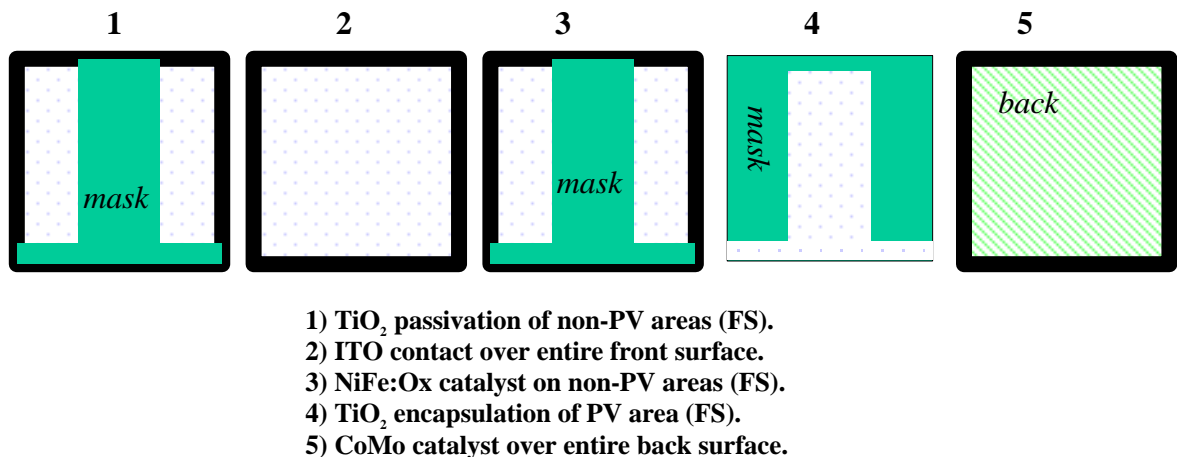


Figure 6 – Fabrication Sequence for Encapsulated Cells

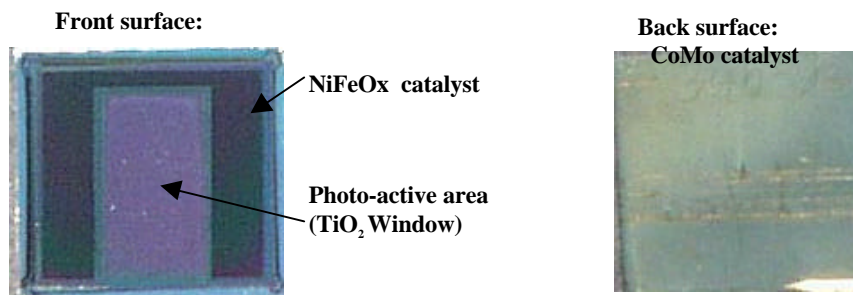


Figure 7 – Photographs of Fabricated Photoelectrodes

Preliminary tests were conducted on the fabricated photoelectrodes in 1N KOH under simulated solar light. The experimental setup is pictured in Figure 8. Observations from these early experiments indicate that hydrogen and oxygen gases are evolved at the photoelectrode surfaces, but performance is limited by device instabilities originating around the edges. The highest concentration of light-induced bubbles appears around the front surface edges of the photoelectrode. After about 15 minutes of operation, the front surface films begin to degrade, with the degradation initiating at these edge regions. Plausible explanations for the degradation include high electric fields occurring at the abrupt edges between the cathodic and anodic surfaces resulting in structural damage in the outer protective films or microcracks between the different lateral layers. Either problem could allow penetration of the corrosive KOH into the more vulnerable underlying a-Si layers. We plan to refine the fabrication sequence to produce a photoelectrode geometry that minimizes edge interfaces and eliminates the high-field edge effects.

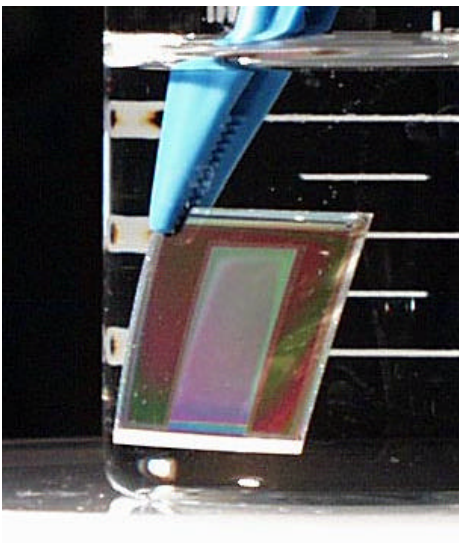


Figure 8 – Testing of Encapsulated a-Si Photoelectrode

ITO Optimization

The properties of the indium-tin-oxide (ITO) for use as a transparent conductive front contact are extremely important in the new photoelectrode design. The ITO must transmit light to the solar cell while laterally conducting photocurrent to the catalyzed areas. It should also assist in the protection of the underlying a-Si from chemical attack by KOH. Last year we initiated an extensive research effort to optimize the balance between conductivity, light transmission and chemical resistance in KOH in sputtered ITO films. This year, we completed the study (Chin, 2000), and are in the process of preparing publications to present our findings.

Central to the study, ITO films were RF sputter-deposited from a compound target under a range of process conditions. Variables in the test matrix of films included: sputter gas composition from 0 to 0.67% oxygen in argon; RF sputter power from 50 to 150W and substrate temperature from 50 to 200°C. For each set of conditions, films were deposited onto glass for conductivity (4-point probe), transparency (spectrophotometer) and structural (XRD) measurements; onto silicon for thickness (profilometer) and composition (EDX) measurements; and onto 302 stainless-steel to characterize corrosion rates in KOH. Electrical and optical properties varied significantly over the range of conditions used in the sputtering system. Optimal conductivity and transmittance (for the solar spectrum) were achieved in films deposited at 200°C with 0.25% oxygen in the argon sputtering gas. We attribute this result to the crystal orientation and grain sizes found in the polycrystalline films deposited under these conditions, which influence scattering mechanisms and optical bandgap in the material (Wu and Chiou, 1996).

Corrosion experiments revealed that the degree of chemical stability of the ITO films in KOH also depends strongly on process conditions during deposition. It was found that films deposited at 200°C exhibited the best corrosion resistance in KOH. Figure 9 shows the percentage weight loss of different ITO films (on SS302) as a function of time immersed in 1N KOH. A substantial fraction of the film was removed in the films deposited at 100°C, while little to no change was observed in the films deposited at 200°C. Again we attribute the result to film grain structure and orientations. Figure 10 shows SEM micrographs (40000x) of film surfaces for ITO on SS302 deposited at 100 and 200°C, before and after a 96-hour immersion in KOH. While the 200°C film appears unchanged, the 100°C film shows clear indications of chemical attack, particularly along grain boundaries. The fortunate result of this study is that corrosion-resistant ITO can be deposited under conditions also yielding high conductivity and transparency. We have thus identified a material well suited for the top conductive contact layer in the integrated photoelectrode structure.

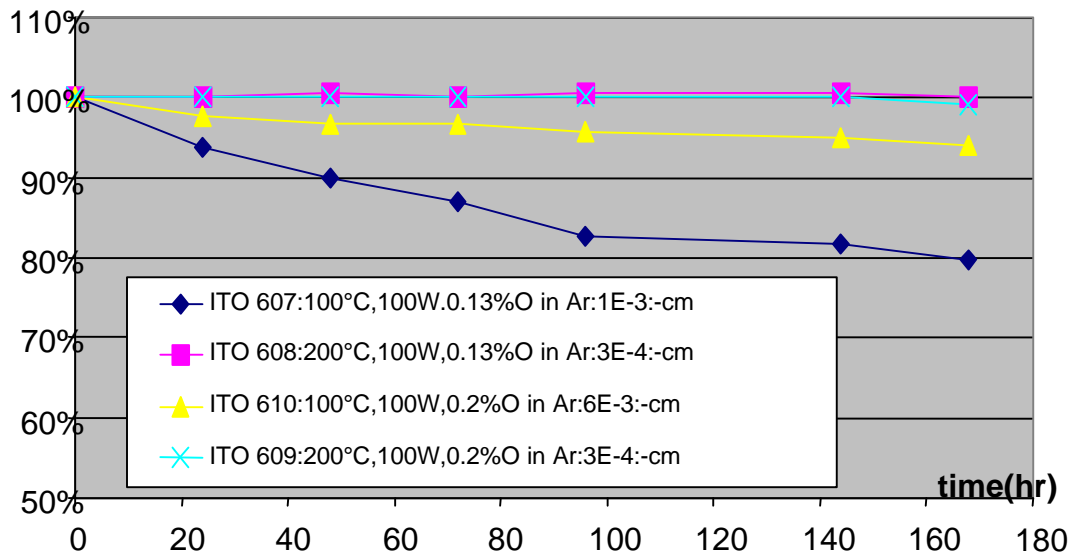


Figure 9 – Degradation of Different ITO Films in 1N KOH

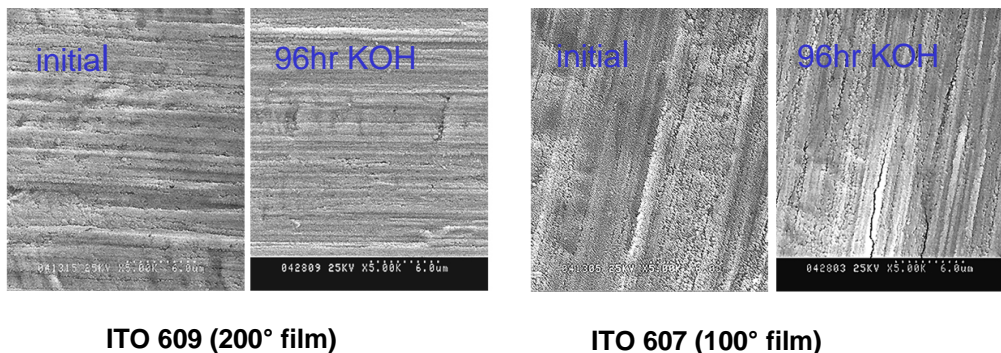


Figure 10 – SEM Surface Images of ITO Films Exposed to KOH

Photoelectrode Design for CIS

The new photoelectrode design allows use of side-by-side series-connected single-junction solar cells in addition to the stacked multijunction configuration. This has opened the door to using alternative low cost, high-efficiency thin film materials, such as copper-indium-diselenide, which have reported solar efficiencies exceeding 18%. These materials were not previously considered because of the low voltage of a single junction device and the inability to fabricate monolithic-stacked multi-junctions. However, the newly proposed encapsulated photoelectrode design was further developed to incorporate side-by-side CIS cells, taking advantage of the potential for efficiency enhancement. A cross sectional view of a CIS photoelectrode using three series-connected CIS/CdS junctions is shown in Figure 11.

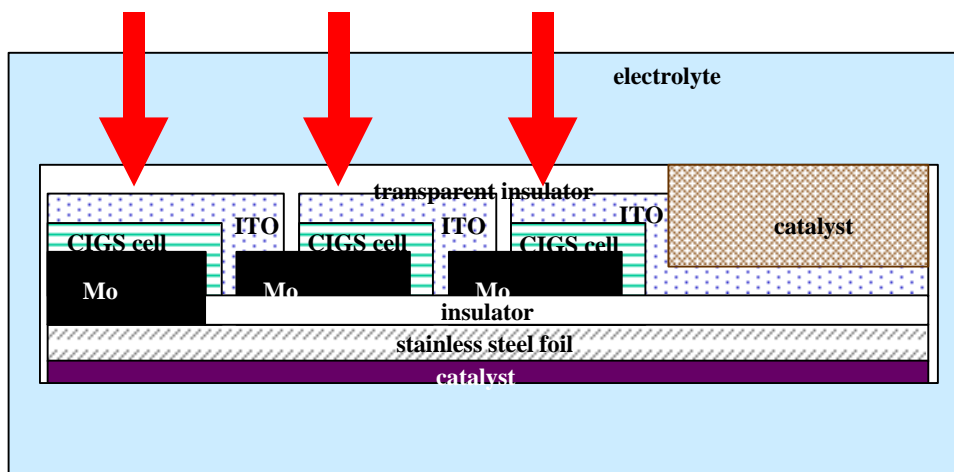


Figure 11 – Integrated Photoelectrode with 3 CIS Single-Junction Cells

In addition to the advancements in the photoelectrode design, progress was made this year in several areas necessary for the development of a practical CIGS photoelectrode. Most significantly, a thermal deposition system for CIGS was installed and tested at UH. CIS/CdS single-junction solar cells with efficiencies exceeding 10% were successfully fabricated on CIS films deposited in this system. Improved efficiencies are expected with incorporation of Ga and further optimization of the process conditions. Corrosion testing of CIGS devices is planned.

Summary and Plans

For the past several years, our approach has been to compare alternate materials and system configurations using reactor modeling, and to identify and address the critical materials and photoelectrode-operation issues through extensive experiments in materials synthesis and in photoelectrode fabrication and testing. We have demonstrated direct solar-to-hydrogen conversion efficiencies of 7.8% using a photocathode fabricated from low cost triple junction amorphous silicon solar cells with 10% photovoltaic efficiencies configured with a separated anode. Our focus has since shifted from the glass superstrate cells used in the separate anode/cathode configuration to devices grown on metal substrates for compatibility with proposed conceptual designs. These reactor designs, prepared in collaboration with NREL, indicated several important advantages of using the conductive (metal) substrates.

This year, we advanced the design of a fully integrated photoelectrode fabricated on a metal substrate using only thin film processing techniques. We demonstrated a process sequence to fabricate prototypes of the new photoelectrode using stacked triple-junction a-Si cells and sputter-deposited catalyst, contact, and protective films developed at UH. At the same time we continued optimization of the electronic properties and corrosion resistance of the semiconductor, transparent-conductor and transparent-protective films for the new photoelectrode. A deposition system for CIS and CIGS films was set up and tested as part of a new effort to develop higher efficiency photoelectrodes using the encapsulated design configured with side-by-side series-connected junctions.

The objective for FY2000-20001 is to demonstrate high efficiency, stable production of hydrogen using amorphous silicon photoelectrodes in the new encapsulated photoelectrode configuration and to evaluate the feasibility of using high efficiency copper-indium-gallium-diselenide cells in the side-by-side series-connected configuration. We plan to refine the specific processing steps for fabrication of the integrated a-Si photoelectrode to improve photoelectrode lifetime and to develop a processing sequence for the more complicated CIS photoelectrode.

During FY2000-2001, we will also continue the development of an integrated electrical/optical/electrochemical computer model to aid in the design and evaluation of alternate material systems and photoelectrode geometries. We plan to continue the optimization of catalyst and protective films integral to the encapsulated photoelectrode structure. To meet the objectives of a near-term hydrogen-producing demonstration, our strategy of working closely

with the solar cell manufacturers to obtain high-efficiency solar cell device structures tailored specifically for hydrogen production remains an important part of the planned research.

Acknowledgments

We wish to thank the US Department of Energy for support of this work under Grant DE-FG04-94AL85804. We also thank Solarex Thin Film, Energy Conversion Devices, and the University of Toledo for amorphous silicon samples and Maggie Mann of NREL for useful discussions and input in the development of conceptual designs for large-scale systems.

References

- Miller, E. L., and Rocheleau, R. E. 1997. "Electrochemical Behavior of Reactively Sputtered Iron-doped Nickel Oxide" *J. Electrochem. Soc.* 144(9):3072-3077.
- Miller, E. L., and Rocheleau, R. E. 1997. "Electrochemical and Electrochromic Behavior of Reactively Sputtered Nickel Oxide" *J. Electrochem. Soc.* 144(6):1995-2003.
- Miller, E. L., 1996. "A Study of the Electrochemical Behavior and Optical Properties of Reactively-sputtered Nickel Oxide and Nickel-Iron Oxide" University of Hawaii Ph.D. Dissertation in Electrical Engineering.
- Miller, E. L., and Rocheleau, R. E. 1999. "Photoelectrochemical Hydrogen Production" *Proceedings of the 1998 U.S. DOE Hydrogen Program Review*, Denver, CO, U.S. Department of Energy.
- Rocheleau, R. E., and Miller, E. L. 1997. "Photoelectrochemical Production of Hydrogen: Engineering Loss Analysis" *Int. J. Hydrogen Energy* 22(8):771-782.
- Rocheleau, R. E., Miller, E. L., and Misra, A.. 1997. "Photoelectrochemical Hydrogen Production" *Proceedings of the 1996 U.S. DOE Hydrogen Program Review*, 345-358. Miami FL. U.S. Department of Energy.
- Rocheleau, R. E., Miller, E. L., and Misra, A. 1998. "High-Efficiency Photoelectrochemical Hydrogen Production using Multijunction Amorphous Silicon Photoelectrodes" *Energy and Fuels* 12: 3-10.
- Rocheleau, R. E., and Vierthaler, M. 1994. "Optimization of Multijunction a-Si:H Solar Cells Using an Integrated Optical/Electrical Model" *Proceedings of the 21st World Conference on Photovoltaic Energy Conversion* , 567-570. Honolulu HI: IEEE.
- Wu, W. and Chiou, B. 1996 "Effect of Oxygen Concentration in the Sputtering Ambient on the Microstructure, Electrical and Optical Properties of Radio-Frequency Magnetron-Sputtered Indium Tin Oxide Films" *Semicond. Sci. Technol.* 11: 196-202.
- Tuttle, J. et al.,1995 "Thin Film Cu(In,Ga)Se₂ Materials and Devices: a Versatile Material for Flat Plate and Concentrator Photovoltaic Applications" *SPIE* 2531:194-200.
- Chin, G. P., 2000. "Characterization and Optimization of Indium-Tin-Oxide (ITO) for Hydrogen Photoelectrodes", University of Hawaii Masters Thesis in Electrical Engineering.

Figure Captions

Figure 1 – Photoelectrochemical Hydrogen Production

Figure 2 – Photocathode with Separate anode

Figure 3 – Solar Hydrogen Production Data

Figure 4 – Integrated Photoelectrode with Monolithic Stacked Cells

Figure 5 – New Lateral Photoelectrode with Encapsulated Cells

Figure 6 – Fabrication Sequence for Encapsulated Cells

Figure 7 – Photographs of Fabricated Photoelectrodes

Figure 8 – Testing of Encapsulated a-Si Photoelectrode

Figure 9 – Degradation of Different ITO Films in 1N KOH

Figure 10 – SEM Surface Images of ITO Films Exposed to KOH

Figure 11 – Integrated Photoelectrode with 3 CIS Single-Junction Cells

Photoelectrochemical System Studies

A. Bansal, O. Khaselev and J. A. Turner
National Renewable Energy Laboratory
1617 Cole Boulevard, Golden, Colorado 80401

ABSTRACT

The efficiency for any solar-to-hydrogen conversion process is particularly important because an area of land must be covered to collect the sunlight. Any efficiency losses in the system must be made up by an increase in the collector area. This will ultimately have a significant impact on the overall cost and siting ability of such a system. Section one of this report will explore the efficiency gains from a direct conversion system as compared to a separated PV/electrolysis system. Section two will discuss our results looking at the catalysis of hydrogen production on semiconductor electrodes.

EFFICIENCY OF PEC SYSTEMS

The energy efficiency of electrolysis can generally be defined as the chemical potential of hydrogen divided by the voltage required for electrolysis operation [1]. At the normal operating current density of commercial electrolyzers ($\sim 1 \text{ A/cm}^2$), this voltage ranges from 1.8—2.0 volts. Thus, an electrolyzer operating at 1.9 volts operates with an energy efficiency of 65% ($1.23/1.9$). Combining this electrolysis efficiency with a 12% PV array efficiency gives a solar-to-hydrogen efficiency of 7.8%. To increase the overall solar-to-hydrogen efficiency, the energy efficiency of electrolysis must be increased; thus, one must operate at a lower voltage. This requires better catalysts (particularly on the oxygen side), or a decrease in the current density (which results in a decrease in the rate of hydrogen production). Maintaining the rate of hydrogen production while reducing the current density could be done by increasing the area of the electrodes (or adding more electrolyzers), but costs would increase due to an increase in the amount of material used for the electrolyzer.

A photoelectrochemical (PEC) system combines the harvesting of solar energy with the electrolysis of water [2]. Depending on the type of semiconductor material and the solar intensity, the current density for electrolysis with a PEC system is 10-30 mA/cm^2 . Figure 1 presents a current-voltage curve for water splitting in an electrochemical cell consisting of two Pt electrodes of identical area. At a current density similar to short-circuit photocurrent from a solar cell, hydrogen and oxygen generation is achieved at an effective applied voltage of approximately 1.35 V, giving rise to an electrolysis efficiency of 91% [3]. One of the major advantages then of a direct conversion photoelectrochemical system is that the area available for electrolysis approximates that of the solar cell. A PEC hydrogen generation system not only eliminates most of the costs of the electrolyzer, but it also has the possibility of increasing the overall efficiency of the process leading to a further decrease in costs. Note, although this experiment was done with Pt electrodes, at this current density, less expensive nickel and metal oxide electrodes could be used with similar results.

We have previously shown a high solar-to-hydrogen PEC conversion device [4], but problems of semiconductor stability, and interfacial kinetics, make it difficult to quantify the efficiency gains from such a PEC system. For this work, we used an integrated PV/electrolysis design to emulate a PEC system. Unlike a direct-conversion PEC system, an integrated PV/electrolysis system has separated PV and electrolyzer parts. However, for an integrated system, the area of the electrolyzer system is identical to the area of the PV collector. These integrated systems allow us to study the issues involving the effects of current density, solar intensity variability, and light concentration on the overall efficiency for hydrogen production. In this study, we utilized an integrated PV/electrolysis design based on a low-cost amorphous silicon (a-Si) multijunction device. This cell is capable of generating a voltage sufficient for water splitting, and we note that its lower system cost, combined with the good efficiency, represents an important area of research for integrated hydrogen production systems. It is demonstrated that this monolithic PV/electrolysis configuration can lead to a higher solar-to-hydrogen conversion efficiency than coupled systems involving electrolyzers and photovoltaic solar cells alone.

For an integrated PV/electrolysis configuration to work properly, the solar cell must provide sufficient voltage to drive the water redox reactions, and also provide any additional voltage needed to overcome the overvoltage losses resulting from the hydrogen and oxygen evolution reactions. The total output photovoltage must include the thermodynamics for water splitting (1.23 volts at 25°C), polarization losses η_a and η_c , for the anodic and cathodic processes respectively, and the IR potential drop in the bulk of electrolyte, which can be significant when gas evolution occurs. A multijunction integrated PV/electrolysis configuration comprises either a tandem (or triple) pn-pn/metal/electrolyte cell, with water reduction occurring at the back-contact/electrolyte interface, and oxidation occurring at the electrolyte/counter electrode (anode) interface, or alternately, a tandem np-np/metal/electrolyte cell with water oxidation occurring at the back-contact/electrolyte interface and reduction occurring at the electrolyte/counter electrode (cathode) interface. Figure 2 shows the power curve for the triple junction p-i-n a-Si solar cell under 100 mW/cm² illumination, clearly indicating its ability to provide sufficient voltage for water splitting. Figure 3 shows the bias-voltage dependence of the photocurrent (hydrogen production) for a triple-junction a-Si(Pt)/2M KOH/Pt cell. The bias-voltage characteristics are consistent with that expected from the current-voltage characteristics shown in Figures 1 and 2. For the triple-junction a-Si(Pt)/2M KOH/Pt cells, the light-limited current was reached approximately at zero bias. Operated at zero bias, with shorted electrodes, the cell generated hydrogen and oxygen.

In operation, an ideal integrated PV/electrolysis system would operate under short-circuit conditions. For such configuration, the efficiency for hydrogen production can be calculated using the equation: efficiency = (power out)/(power in). The input power is the incident light intensity of 100 mW/cm². For the output power, assuming 100% photocurrent electrolysis efficiency, the hydrogen production photocurrent is multiplied by 1.23 volts, the ideal fuel cell limit at 25 °C (lower heating value [LHV] of hydrogen). Using this calculation, our experimental results for the hydrogen production efficiency for the triple junction a-Si(Pt)/2M KOH/Pt it is:

$$1.23V \cdot 6.4mA/cm^2 / 100mW/cm^2 = 7.8\%.$$

The value for the a-Si system is significant in that this efficiency is realized by a PV cell with only a 9% solar-to-electrical efficiency. Because of the lower current density, this system is performing water electrolysis with an equivalent efficiency of 86% (effective electrolysis voltage of 1.42 volts [LHV]). This means that the maximum operating voltage of the a-Si PV cell is close to that required for electrolysis.

To maximize solar-to-hydrogen efficiency of the PV/electrolysis system operating at short circuit condition, a multijunction photovoltaic cell should be specifically designed to match electrical parameters for water splitting. For any direct solar-to-hydrogen conversion system, the maximum voltage that can be used in an efficiency calculation is fixed by the chemical potential of hydrogen. In order to increase the conversion efficiency, the current (and therefore the rate of production of hydrogen) must be increased. The ideal system would reach maximum power at less than 1.6 V, and a current density more than 20 mA/cm². Although the solar-to-electrical conversion efficiency of such cell would be less, the solar-to-hydrogen efficiency of the integrated PV/electrolysis system (and an analogous PEC system) would benefit.

CATALYSIS FOR THE PHOTOELECTROCHEMICAL PRODUCTION OF HYDROGEN

For a practical, stable and efficient semiconductor based water splitting system, four criteria must be simultaneously satisfied. The bandgap of the semiconductor must be greater than 1.7 eV, the band edges of the semiconductor must overlap the H₂/H₂O and O₂/H₂O redox potentials under H₂/O₂ evolution condition and charge transfer across the semiconductor-liquid interface should be fast (Fig. 4). In addition, the semiconductor surface should be chemically stable in the aqueous media.

Although p-type GaInP₂ with a bandgap of 1.8-1.9 eV has been identified as a promising photocathode for water splitting, its band edges are 0.2-0.4 V too negative to effect photoelectrolysis.[5-7] Electrochemical investigations of GaInP₂ in aqueous media have found that the semiconductor surface is unstable and susceptible to corrosion [8]. Furthermore, it is not known if the charge transfer rate from p-GaInP₂ to water under illumination is sufficiently high or if this rate can be further catalyzed.

At present, there is no information on the energetic position of the band edges or on the kinetics of charge transfer at the p-GaInP₂/water interface under illumination i.e. under conditions of H₂ evolution. Several impedance measurements in the literature have previously reported that band edges of semiconductors are not fixed and are prone to migration under illumination [9-19]. These changes in flatband potential under illumination have been interpreted to indicate evidence of surface effects such as charge trapping, adsorption or changes in the surface chemistry. The band edge positions are also known to be strongly affected by interfacial kinetics under illumination [13,15]. Increased band edge migration as a result of illumination has been observed for interfaces with poor interfacial charge transfer ability and this migration has been suppressed by treating the semiconductor surfaces with transition metal catalysts [14,20].

In this report, we describe our work on evaluating the effect of interfacial kinetics on the band edge positions of the p-GaInP₂/water interface under illumination i.e. under conditions of H₂ evolution. In addition, we describe the results of C-V and I-V measurements on p-GaInP₂ surfaces modified with transition metal ions to evaluate their effectiveness as reagents for inducing band edge shifts in the dark and as electrocatalysts for suppressing band edge migration under illumination. In this study, the flow of photogenerated cathodic current at the semiconductor surface under illumination corresponds to generation of hydrogen from photoelectrolysis of water.

Note: A semiconductor surface treatment such as the adsorption of a transition metal ion, can have two distinct effects on the energetics of the interface. Due to change of net charge in the Helmholtz layer, adsorption of a transition metal as a charged species (ion) on the

semiconductor surface can change the band edge position relative to the band edge position for an underivatized surface - *in the dark*. This effect is referred to as band edge "shift" or flatband "shift" in this paper. On the other hand, the measured band edge position vs. a solution reference can also move as a result of illumination due to accumulation of photogenerated charges at the interface. This movement is not due to a change in the charge in the Helmholtz region. Its extent is determined by the level of illumination at the semiconductor surface and the interfacial charge transfer kinetics. This movement can be suppressed if the transition metal species acts as an electrocatalyst and catalyses charge transfer across the interface, thereby reducing the accumulation of charge at the interface. In this report, the movement of band edges due to photoelectron accumulation is referred to as "migration". In measuring the "migration" effect, the band edge position of a surface under a given level of illumination is compared with the band edge position for *the same surface* in the dark. Although both of these effects have been individually described in the literature as "shifts" of band edges, [9-19] we have used the terms "shift" and "migration" in this paper to distinguish between the two.

Impedance Data Analysis - A detailed impedance analysis of the p-GaInP₂/water system in the dark has been previously reported, in which capacitance data in the frequency range $500 < f < 10^5$ Hz, was attributed to the space charge layer of the semiconductor [7]. For the purpose of this study the series RC circuit (Scheme I) where R_S is the series resistance of the circuit and C_{SC} is the capacitance of the space charge region, was deemed as the simplest circuit that could adequately describe the trends in the movement of the flatband potential under illumination [21]. The slope and x-axis intercept of the Mott-Schottky plots were used to determine dopant density and the flatband potentials respectively.



Scheme I

Flatband potentials of etched p-GaInP₂/water interfaces - Figure 5 shows representative Mott-Schottky plots for etched p-GaInP₂ electrodes immersed in 0.20 M K₂SO₄ solutions of pH 1, 7 and 13. Data collected at each pH in the dark and compared to that under illumination show a negative migration of the flatband potential with increasing levels of light intensity. Figure 6a shows the corresponding flatband potentials calculated from similar Mott-Schottky plots for five different pH values, and the associated shifts from increased illumination. The curves for pH 1 and 13 were measured in unbuffered solutions of 0.20 M K₂SO₄, which were made acidic or basic using the necessary amount of H₂SO₄ or KOH, respectively. The curves for pH 4, 7 and 10 were measured in commercial phthalate (pH 4), phosphate (pH 7) and carbonate (pH 10) buffer solutions.

Figure 6b shows the same data as the net migration of the flatband potentials measured vs. the values observed in the dark. It is seen that even at low levels of illumination e.g. ~0.1 mA/cm², the GaInP₂ flatband potentials (band edges) move up to 0.3 V negative as compared to their positions in the dark. As the level of illumination is increased the negative migration of the band edges becomes more pronounced with values reaching almost one volt for some pHs at current densities of around 10 mA/cm².

Effect of transition-metal ions on the flatband potential of p-GaInP₂/water interface under illumination - Figure 7 shows Mott-Schottky plots for an untreated and a Ru^{III}-treated p- GaInP₂ surface, measured in the dark and under increasing illumination intensity in 3 M KOH solution. Figure 8a shows the corresponding flatband potentials calculated from similar Mott-Schottky plots of etched and metal-ion treated p- GaInP₂ electrodes in the 3 M KOH solution. In addition, the figure also shows flatband potentials measured with a GaInP₂ electrode modified with electrodeposited platinum. Figure 8b shows the same data plotted as the migration of the flatband potentials measured vs. the values observed in the dark. While the etched only (untreated) surface exhibits significant migration of the flatband potential under illumination, the migration is significantly suppressed for the metal-ion treated surfaces, with the Ru^{III} treated electrode showing the best overall behavior. Table I lists the flatband potentials (V_{fb}) observed for the underivatized and the metal-ion treated surfaces in the dark and under illumination. The 'light' data reported corresponds to a current density of 0.7-1.0 mA/cm².

Effect of transition-metal ions on the I-V properties of p- GaInP₂/water interface - Figure 9 shows the effect of metal-ion treatment on the current-voltage properties of the untreated (etched only) and metal-ion treated p-GaInP₂ electrodes in 3 M KOH solution. The metal-ion treated surfaces exhibit improved fill factors and decreased hysteresis as compared to the untreated surface. The open circuit voltages (V_{oc}) observed for the metal-ion treated surfaces were generally more positive than the untreated surface. The V_{oc} values observed for the underivatized and the metal-ion treated surfaces for the positive are also given in Table I.

A practical single semiconductor photoelectrochemical system for water splitting requires that the three conditions of bandgap, band edge overlap and fast kinetics must be simultaneously satisfied (Fig. 4). The first two conditions are determined, respectively, by the energetics of the semiconductor and the semiconductor/liquid junction, while the third condition is determined by the kinetics of the reaction of interest at the interface. In the present case, the reaction of interest is generation of hydrogen from photoelectrolysis of water. From the above description it would seem that in a p-type semiconductor/liquid junction cell, the first two conditions would be the only necessary and sufficient conditions for H₂ evolution at the semiconductor interface. However, we have shown here that fast interfacial kinetics is also a necessary condition for any significant amount of hydrogen evolution. The kinetics of interfacial charge transfer strongly affects the energetics of a semiconductor/liquid junction. Furthermore, we have shown (as also have others [7-15,18-20]) that it is erroneous to assume that the band edge positions of the semiconductors remain in the same position during current flow under illumination as in the dark, except perhaps for interfaces with extremely fast interfacial charge transfer rates. This realization is significant for GaInP₂ because it implies that any surface modification that is applied to shift semiconductor band edges to achieve band edge overlap must also not compromise interfacial kinetics or else any band edge shifts could be nullified by band edge migration under illumination [6,7].

The nature and amount of the catalyst at a semiconductor/electrolyte interface is very important in determining the activity of the electrocatalyst. The coverage should be high enough to affect a high rate of hydrogen production and yet should not be so high as to impede light absorption by the semiconductor. Although the exact nature and the amount of the transition metal species adsorbed on the p-GaInP₂ surface is presently unknown, a previous study on a similar substrate (GaAs) suggests that the metal ions may be deposited as complexes, in submonolayer to a few monolayers amounts, via a redox reaction with the surface semiconductor atoms [22]. In any case, the lack of flatband shifts in the dark upon metal-ion treatment suggests that the metal complexes are present as overall neutral species on the GaInP₂ surface. If precious metals are to be used as catalysts for photoelectrochemical hydrogen evolution, it is important that the

absolute minimum amount required for the highest catalysis be determined. Although the amount of catalyst deposited on the semiconductor surface has not been controlled or optimized in this study, it is clear that significant catalysis can be obtained even with near monolayer amounts of transition metal ions.

CONCLUSIONS

This work shows that the p-GaInP₂ band edges migrate negative under illumination in solutions with pH ranging from 1-14.5. The displacement is not due to a change in the pH of the semiconductor microenvironment but is caused by the accumulation of photogenerated electrons at the interface due to poor interfacial charge transfer kinetics. Differentiating between the two is important for developing appropriate surface modification strategies to realize an effective water-photoelectrolysis system. From the experiments described above, it becomes imperative that any surface modification scheme used to achieve the 'band edge overlap condition' must not compromise the charge transfer kinetics at the interface. Our observations indicate a less than optimal rate of charge transfer across the p-GaInP₂/water interface and underscore the necessity of catalysis at the p-GaInP₂/water interface.

Treatment with transition-metal ions is found to effectively electrocatalyse transfer of photogenerated electrons from the semiconductor to the liquid and to arrest the undesired band edge migration under illumination. p-GaInP₂ electrodes treated with Ru^{III}, Rh^{III}, Co^{III} and Os^{III} ions exhibit improved fill factors and small positive increases in the Voc. Light limited current levels are reached at lower applied voltages. Ru^{III} and Rh^{III} treatments are found to suppress band edge migration better than electrochemically deposited platinum treatment that is widely used as a hydrogen evolution catalyst in the literature. The observation that even the best catalysts of this study (Ru^{III} and Rh^{III}) show ~0.25 V band edge migration at a current density of ~10 mA/cm² suggests that other catalysts can be identified which can support higher currents through the interface without causing appreciable band edge migration.

Although the metal-ion treatment does not shift the band edges of p-GaInP₂ positive enough to affect unassisted photoelectrolysis, nevertheless, it can be applied to tandem cell designs where it can reduce the voltage assistance required by the p-GaInP₂ top layer to split water, thereby increasing the efficiency (by decreasing the energy input required) of photo-driven hydrogen production [4].

FOOTNOTES AND REFERENCES

- [1] *Energy efficiencies can really only be defined as power out/power in. In this case, we are assuming an ideal fuel cell running at the same current density as the electrolyzer.*
- [2] A. J. Bard and M. A. Fox, *Acc. Chem. Res.* 1995; **28**:141.
- [3] *Note that 1.35 volts is less than the thermodynamic potential required to split water. The additional energy needed for the reaction comes from the surrounding environment as heat. If one were to run a continuous electrolysis at 1.35 volts, the solution would cool down and eventually freeze. However, for this solar energy application, heat is available from the sunlight as infrared photons that are not being used by the semiconductor, so a continuous electrolysis at 1.35 volts is possible.*
- [4] O. Khaselev and J. Turner, *Science* 1998, 285, 425.
- [5] Kocha, S. S.; Turner, J. A.; Nozik, A. J. *J. Electroanal. Chem.* 1994, 367, 27.
- [6] Kocha, S. S.; Turner, J. A. *J. Electrochem. Soc.* 1995, 142, 2625.

- [7] Kocha, S. S.; Turner, J. A. *Electrochim. Acta* 1996, 41, 1295.
- [8] Khaselev, O.; Turner, J. A. *J. Electrochem. Soc.* 1998, 145, 3335.
- [9] Allongue, P.; Blonkowski, S. J. *Electroanal. Chem.* 1991, 316, 57.
- [10] Allongue, P.; Blonkowski, S.; Lincot, D. J. *Electroanal. Chem.* 1991, 300, 261.
- [11] Yoneyama, H.; Sakamoto, H.; Tamura, H. *Electrochim. Acta* 1975, 20, 341.
- [12] Nozik, A. J.; Memming, R. J. *Phys. Chem.* 1996, 100, 13061.
- [13] Allongue, P.; Cachet, H.; Horowitz, G. J. *Electrochem. Soc.* 1983, 130, 2352.
- [14] Allongue, P.; Cachet, H. J. *Electrochem. Soc.* 1984, 131, 2861.
- [15] Watts, D. K.; Koval, C. A. J. *Phys. Chem.* 1996, 100, 5509.
- [16] Uhlendorf, I.; Reineke-Koch, R.; Memming, R. *Ber. Bunsenges. Phys. Chem.* 1995, 99, 1082.
- [17] Allongue, P.; Blonkowski, S.; Souteyrand, E. *Electrochim. Acta* 1992, 37, 781.
- [18] Kelly, J. J.; Memming, R. J. *Electrochem. Soc.* 1982, 129, 730.
- [19] Koval, C. A.; Segar, P. R. *J. Am. Chem. Soc.* 1989, 111, 2004.
- [20] Kobayashi, H.; Mizuno, F.; Nakato, Y. *Jpn. J. Appl. Phys.* 1994, 33, 6065.
- [21] A preliminary analysis of impedance data using the series-parallel circuit between 40 Hz and 60 KHz indicated that the parallel resistor R_p was always greater than 30 Kohm. Moreover, Mott-Shottky ($1/C^2$ vs. V) plots made with capacitances calculated using both the series-parallel and the series circuits gave similar trends in migration of flatband potentials with illumination. The Mott-Shottky plots were made using capacitance values in the region where the current was light limited and was invariant with applied potential. In this potential range, the Mott-schottky plots were also found to be linear. Deviations from linearity occurred in potential regions (closer to V_{fb}) where the current changed with potential and capacitance data was not evaluated in this region.
- [22] Uhlendorf, I.; Reineke-Koch, R.; Memming, R. J. *Phys. Chem.* 1996, 100, 4930.
- [23] Tufts, B. J.; Abrahams, I. L.; Caley, C. E.; Lunt, S. R.; Miskelly, G.; Sailor, M. J.; Santangelo, P. G.; Lewis, N. S.; Hedman, B. M.; Roe, A. L.; Hodgson, K. O. *J. Am. Chem. Soc.* 1990, 112, 5123.

Table I. Capacitance-Voltage and Current-Voltage measurements on untreated and metal treated p-GaInP₂ surfaces in 3M KOH solution.

| | V _{fb} , dark | V _{fb} , light ^a | V _{fb} ^b | V _{oc} , p ^c | V _{oc} , n ^c |
|---------------|------------------------|--------------------------------------|------------------------------|----------------------------------|----------------------------------|
| | V vs. SCE | V vs. SCE | V | V vs. SCE | V vs. SCE |
| Untreated | -0.19 | -0.53 | -0.34 | -0.88 | -0.52 |
| Pt treated | -0.15 | -0.39 | -0.24 | -0.67 | -0.40 |
| RuIII treated | -0.15 | -0.24 | -0.09 | -0.67 | -0.41 |
| OsIII treated | -0.14 | -0.44 | -0.30 | -0.88 | -0.37 |
| CoIII treated | -0.15 | -0.38 | -0.23 | -0.77 | -0.43 |
| RhIII treated | -0.18 | -0.26 | -0.08 | -0.64 | -0.54 |

a. V_{fb} values measured at an illumination level corresponding to a current density of 0.7-1.0 mA/cm².

b. Band edge migration under illumination (V_{fb}, light - V_{fb}, dark)

c. V_{oc} values observed for positive (p) and negative (n) going scans corresponding to a current density of 0.7-1.0 mA/cm².

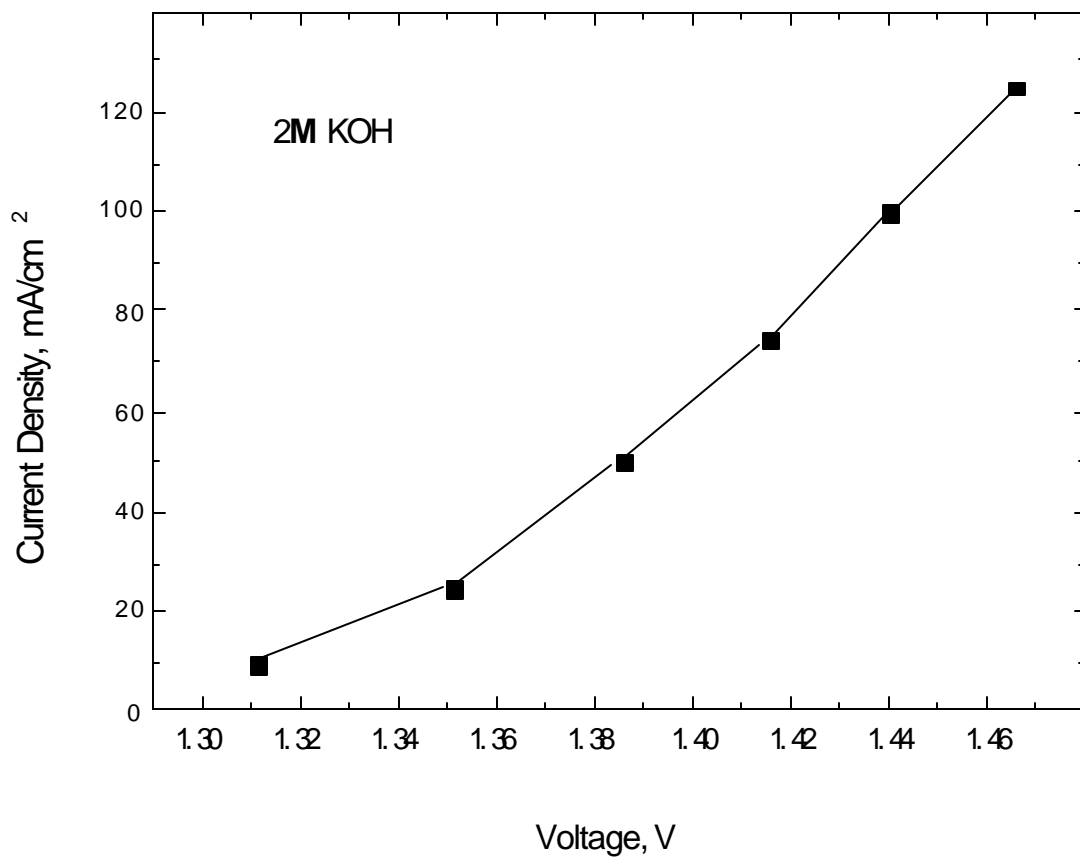


Figure 1. Current-voltage curve for water splitting in an electrochemical cell consisting of two Pt electrode mounted in the similar manner as in the PV/electrolysis system.

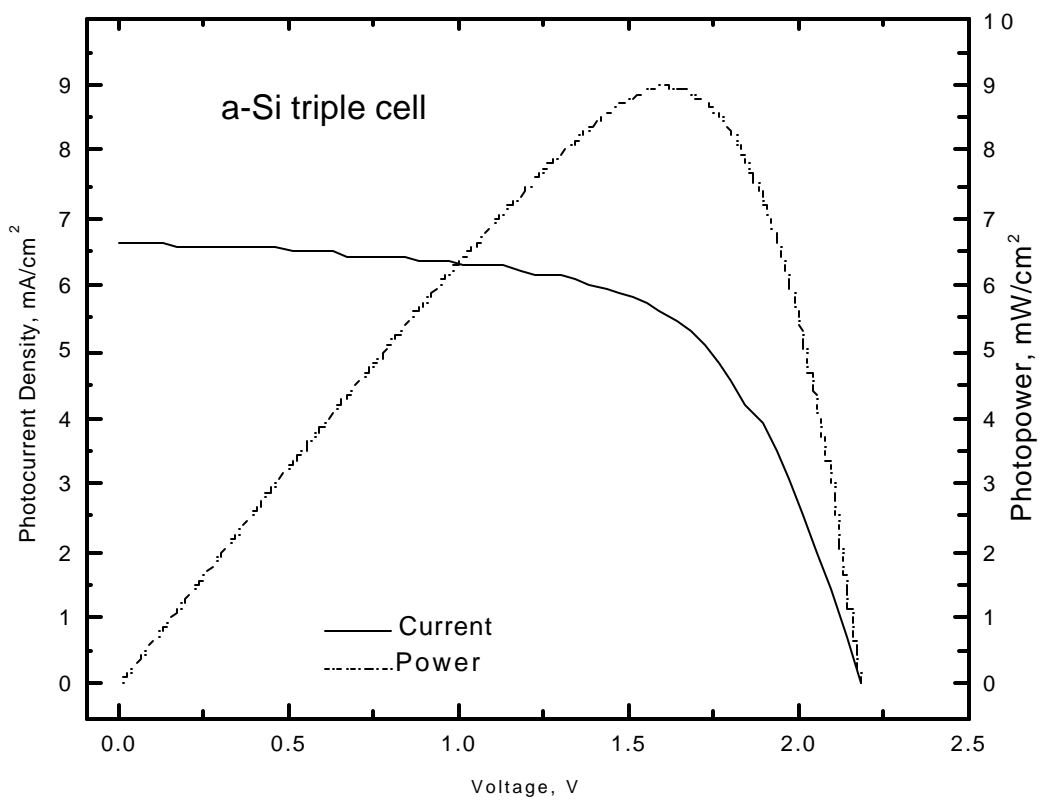


Figure 2. Measured indoor photocurrent and photopower/voltage characteristics for the triple p-i-n a-Si solar cell.

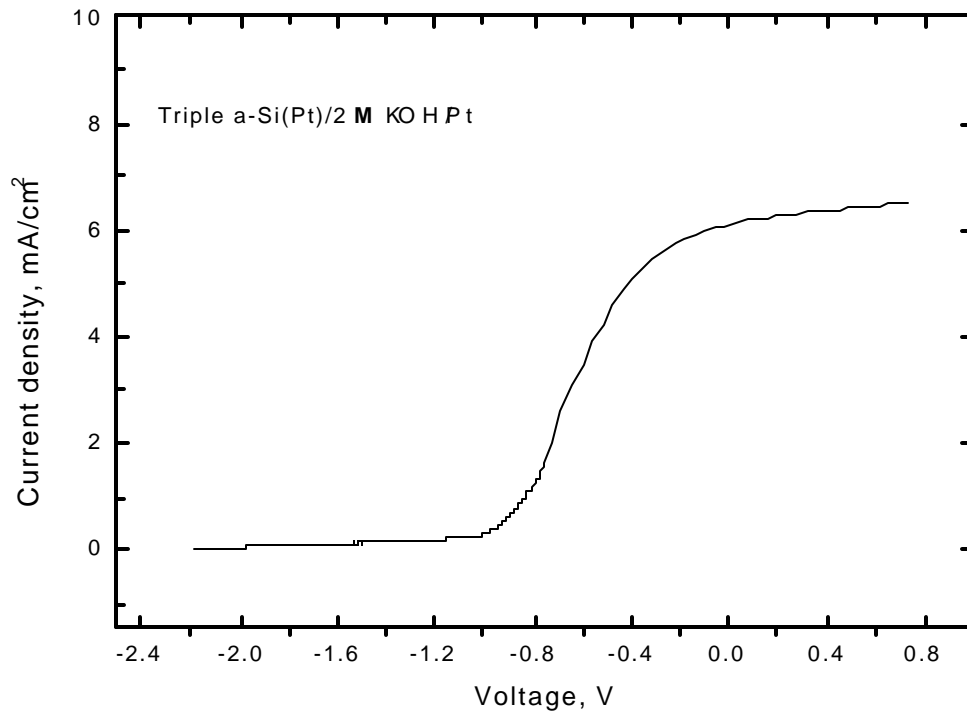
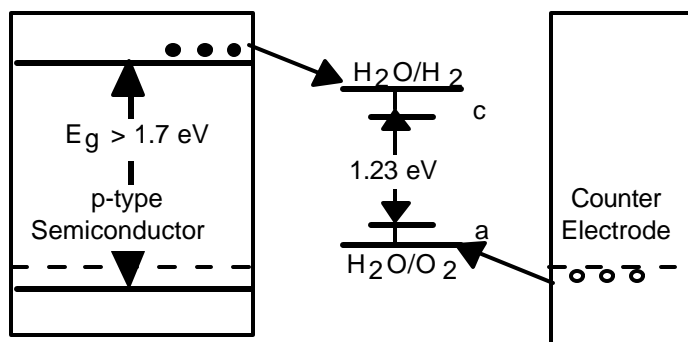
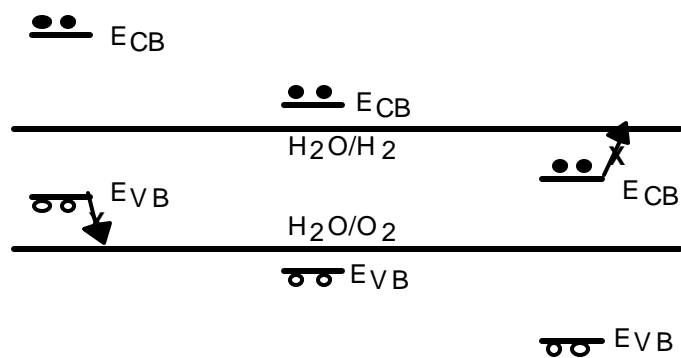


Figure 3. Measured indoor photocurrent/voltage characteristics of the triple p-i-n a-Si(Pt)/KOH/Pt PV/electrolysis solar cell.



(a)



(b)

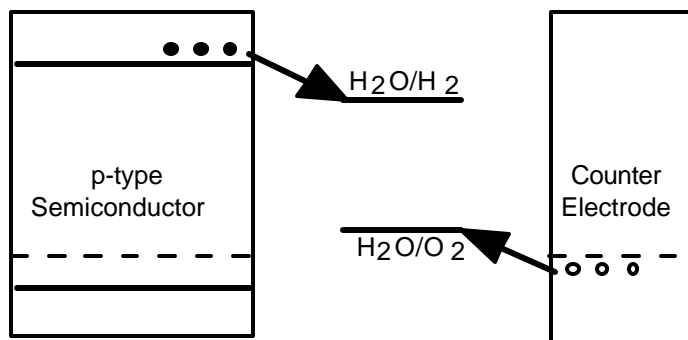


Figure 4. a) Bandgap criteria: The bandgap of the semiconductor must be greater than 1.7 eV. *a* and *c* indicate anodic and cathodic overpotentials for electrode reactions, respectively. b) Band Edge Overlap criteria: the band edges of the semiconductor must overlap the $\text{H}_2/\text{H}_2\text{O}$ and $\text{O}_2/\text{H}_2\text{O}$ redox potentials under H_2/O_2 evolution condition. c) Fast Kinetics criteria: Charge transfer across the semiconductor-liquid interface must be fast. For a successful hydrogen producing PEC system, all three criteria must be simultaneously satisfied.

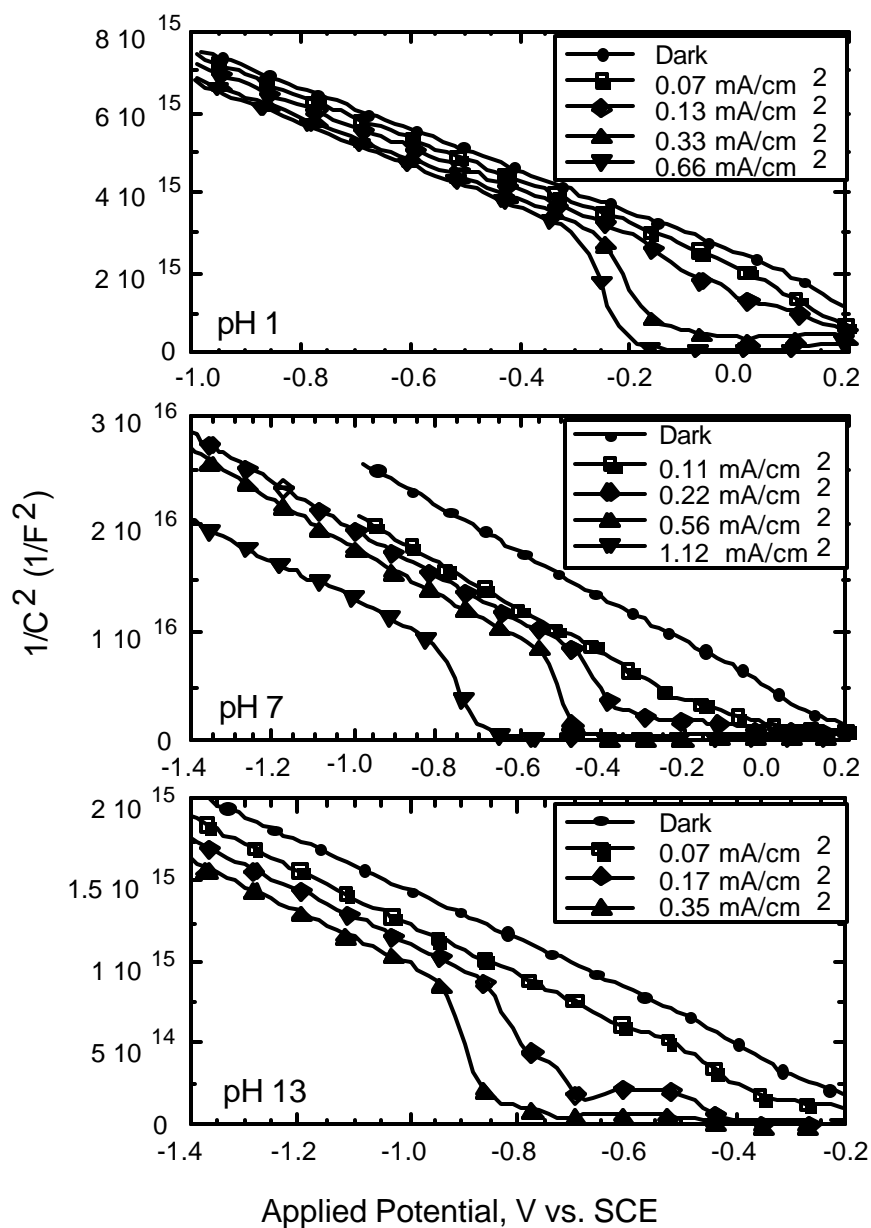


Figure 5. Mott-Schottky plots of p-GaInP₂ electrodes immersed in pH 1, 7 and 13, measured in the dark and under varying levels of illumination.

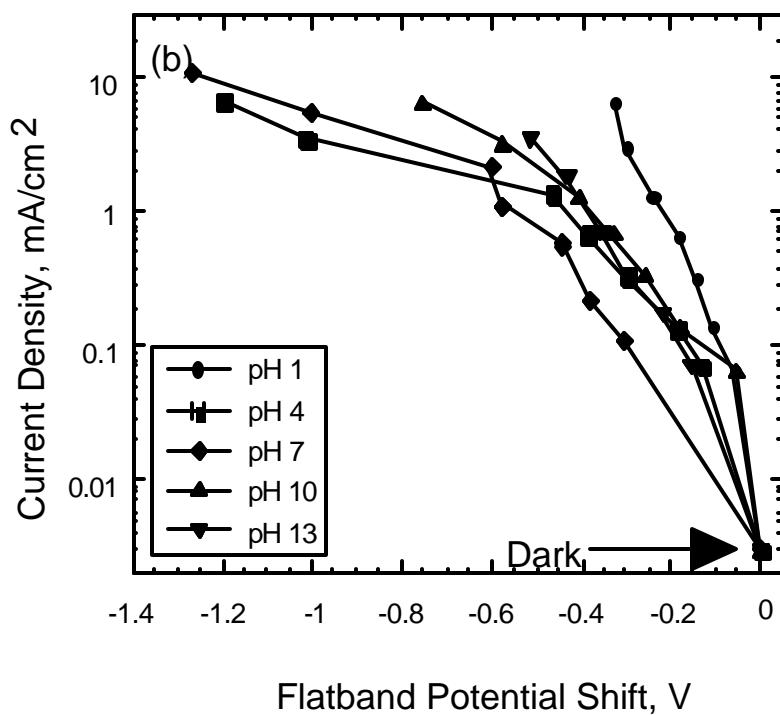
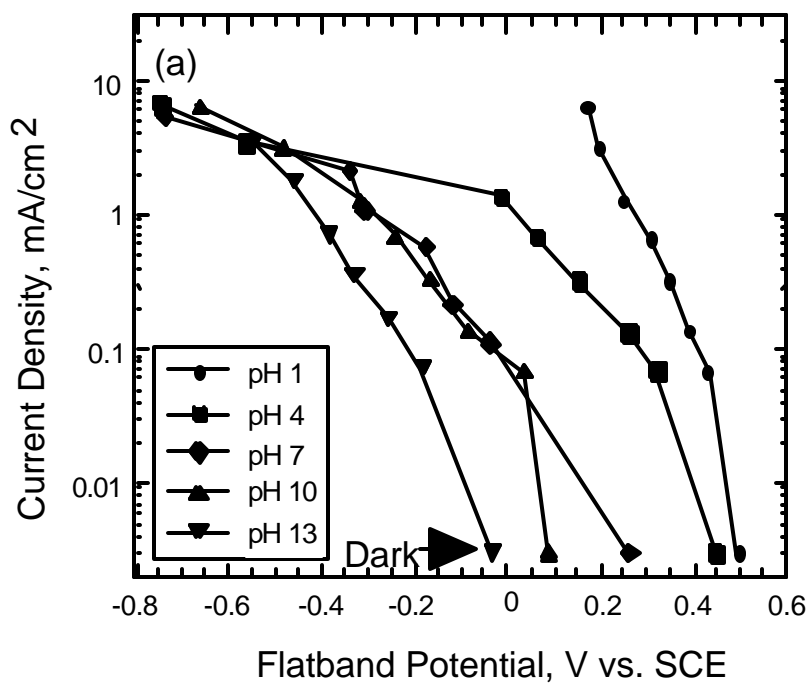


Figure 6. a) Flatband potentials of etched p-GaInP₂ electrodes, measured vs. SCE, at five different pH values for varying levels of illumination. b) Migration of flatband potentials vs. the V_{fb} values observed in the dark (V_{fb} , light - V_{fb} , dark) in solutions of 5 different pH

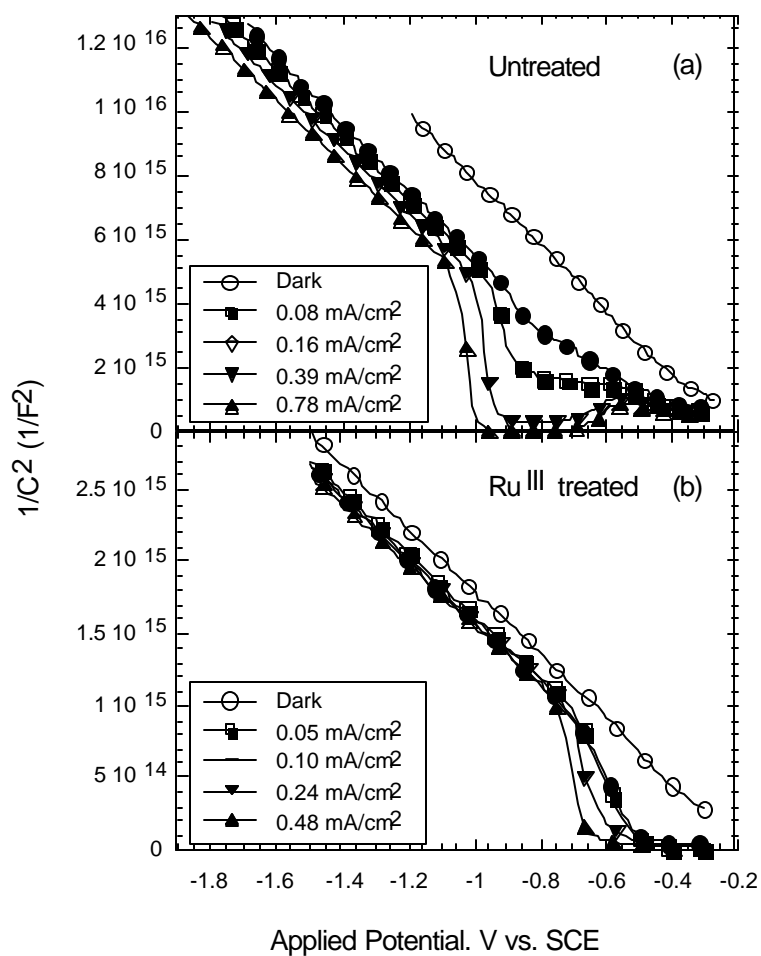


Figure 7. Mott-Schottky plots for a) an untreated and b) a RuIII-treated p-GaInP₂ surface, measured in the dark and under illumination in 3 M KOH solution.

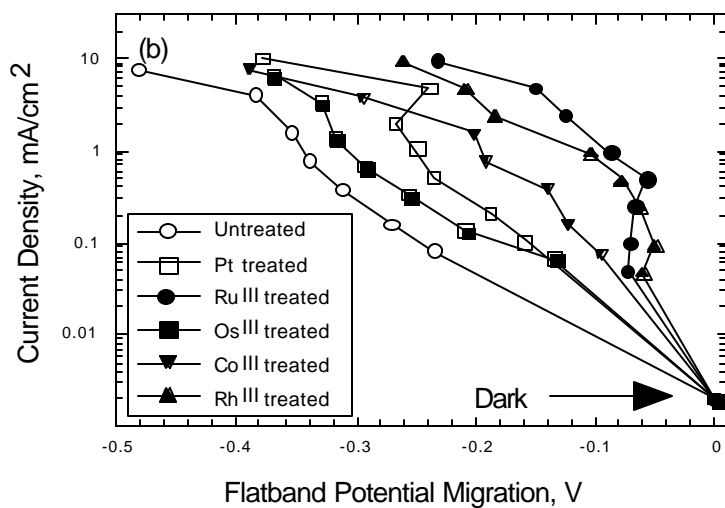
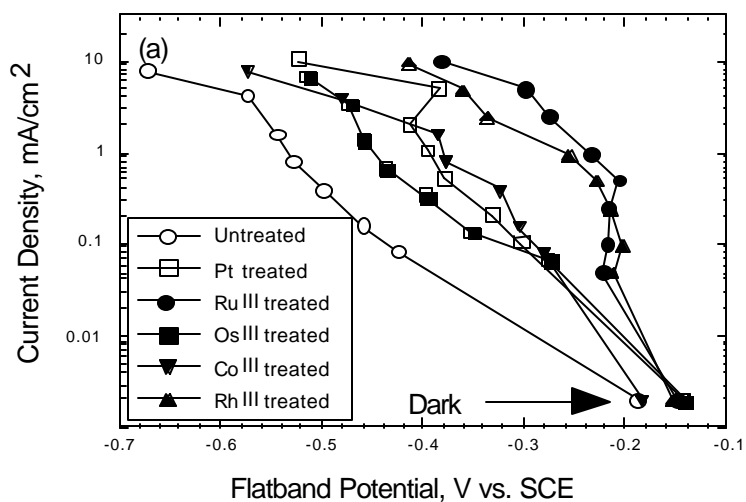


Figure 8. a) Flatband potentials of untreated (etched only) and metal-ion treated p-GaInP2 electrodes under illumination in the 3 M KOH solution. b) Migration of flatband potentials vs. the V_{fb} values observed in the dark (V_{fb} , light - V_{fb} , dark) in 3 M KOH solution.

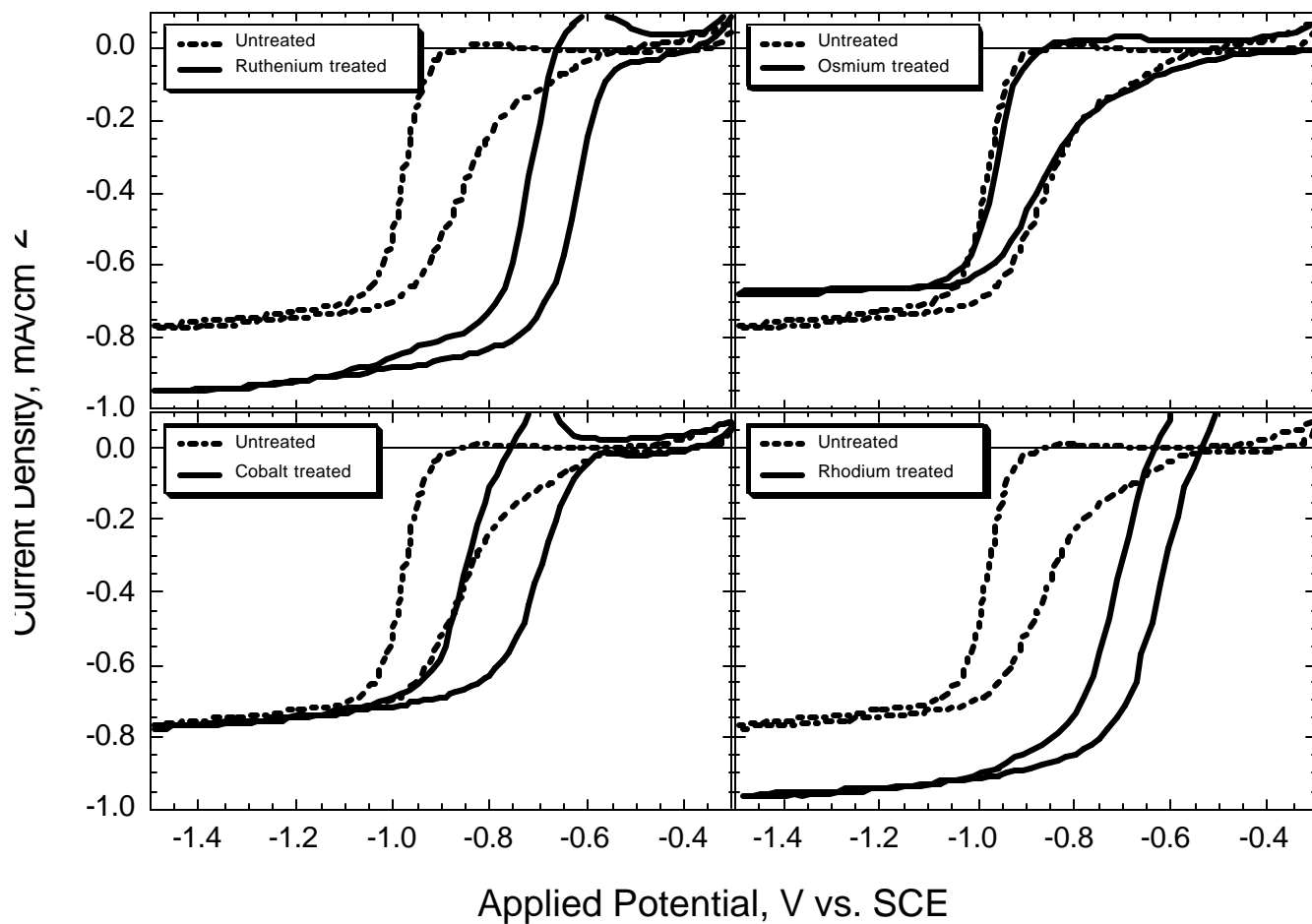


Figure 9. Current-Voltage (I-V) curves observed for untreated and metal-ion treated p-GaInP2 electrodes in 3 M KOH solution.

BIOLOGICAL H₂ FROM FUEL GASES AND FROM H₂O

**Pin-Ching Maness and Paul F. Weaver
National Renewable Energy Laboratory
Golden, CO 80401**

Abstract

When photosynthetic bacteria *Rhodocyclus gelatinosus* and *Rhodospirillum rubrum* were cultured under an atmosphere containing CO, a unique CO-linked pathway was quickly induced. These bacteria catalyze the water-gas shift reaction where CO (and H₂O) is oxidized to produce H₂ (and CO₂). The hydrogenase enzyme responsible for the H₂ production pathway is inducible only upon CO addition, and is a different enzyme from the formate-linked and the uptake hydrogenases in terms of induction criteria and electron mediator it can use. The CO-linked hydrogenase favors toward the H₂ evolution direction with a reaction rate-constant of greater than 60,000, therefore, is an ideal candidate for scale-up H₂ production. Water is ultimately the most abundant and inexpensive source of hydrogen on earth. A system of sustained H₂ production based on the photo-oxidation of water would be most economical. Since O₂ production is inherent in the oxidation of water, and the hydrogenase enzymes in most cyanobacteria and green algae are rapidly inactivated by O₂, the O₂-tolerant CO-linked hydrogenase enzyme is most suited if it can be transformed into a cyanobacterium where both O₂ and H₂ are produced simultaneously. To achieve this long-term goal of constructing a cyanobacterial-bacterial hybrid, we must devise assays to allow for the measurement of O₂ tolerance of the CO-linked hydrogenase with the simultaneous presence of O₂. This report documents an ongoing method development using a continuous sampling mass spectrometer to kinetically record the impact of O₂. Another issue needs to be addressed is the separation of the multiple hydrogenases in these organisms in order to specifically measure only the hydrogenase of interest. This report presents evidences on using the combinations of three strategies: via physiology, mutation and biochemical means, we achieve to spatially separate the three hydrogenase enzymes and to study the physiology of the enzymes and the electron mediators to which each can couple.

Introduction

Photosynthetic bacteria are versatile in their modes of H₂ metabolism. They have four terminal enzymes mediating the H₂ metabolism; they are nitrogenase, a classical uptake hydrogenase, a fermentative hydrogenase and a CO-linked hydrogenase. Nitrogenase is induced under N-free condition and catalyzes H₂ production while an abundance of energy is available (Stewart, 1973). This enzyme system is light-dependent and consumes 4 moles of ATP per mole of H₂ produced. A classical uptake hydrogenase has been isolated from various photosynthetic microbes and its main function is to break down H₂ to support CO₂ fixation (Colbeau *et al.*, 1983). A hydrogenase linking to formate oxidation has also been identified and its main function is to dissipate excess electrons under fermentative dark growth mode (Gorrell and Uffen, 1977; Schultz and Weaver, 1982). This enzyme is extremely O₂ sensitive, with a half-life of less than 1 min when whole cells were stirred in full air, it equilibrates at 10% partial pressure of H₂ (Maness and Weaver, unpublished data), and is not suitable for scale-up application.

The fourth enzyme, the CO-linked hydrogenase, is the most unique among all hydrogenase reported. It was first reported by Uffen in two strains of photosynthetic bacteria to shift CO (and H₂O) in darkness to H₂ (and CO₂) (Uffen, 1981). We have since isolated 450 strains of photosynthetic bacteria possessing this water-gas shift pathway. Among them, *Rhodocyclus gelatinosus* CBS-2 is most unique in that its hydrogenase is highly resistant to O₂, with a half-life of 19 hours when whole cells were stirred under full air. When the partially purified hydrogenase devoid of membrane was stirred in full air, a half-life of 4.5 hr was measured, clearly indicating that its O₂ tolerance is due to the intrinsic nature of the enzyme conformation, not owing to higher respiratory rates. This enzyme has a rate constant greater than 60,000 and is energetically more favorable toward the H₂ evolution direction. Compared to most hydrogenase systems, the CO-linked pathway is most robust and has great potential for commercial applications.

One requirement for economical H₂ production is to further enhance its O₂ tolerance in order to transform this enzyme system into a cyanobacterial hybrid, where H₂ is evolved using H₂O as the ultimate electron donor with the simultaneous production of O₂. Therefore, an ideal condition to quantify O₂ tolerance would be to measure the immediate impact of O₂ addition, and also to determine the rate and duration of H₂ production with O₂ present. Although we have determined previously that the CO-linked hydrogenase is quite tolerant to O₂, a drawback of the assay (using the Na-dithionite-reduced methyl viologen as mediator) prevents us from measuring activity while O₂ is present. Therefore we had routinely pre-exposed the hydrogenase to O₂ for a pre-determined amount of time, followed by the removal of O₂, and then conducted the assay using Na-dithionite as the reducing agent. One might also argue that the subsequent addition of a reducing agent such as Na-dithionite would re-activate the hydrogenase previously inactivated by O₂, as a result, an O₂ tolerance is falsely claimed. To take these issues into account, we must develop an assay that not only excludes a reducing agent, but also allows us to monitor the rate continuously. Hydrogenases from various sources have been reported to catalyze an H₂ and D₂O exchange reaction yielding HD without requiring a reducing agent (San Pietro, 1957; Fauque *et al.*, 1988; Vignais *et al.*, 1997). A continuous

sampling system using a mass spectrometer thus is an ideal technique to meet these criteria.

Another issue that complicates the O₂ tolerance determination is the existence of multiple hydrogenases, each having a varying degree of tolerance to O₂. Since multiple hydrogenases can be induced simultaneously under certain growth mode, it's confusing for one to conclude which hydrogenase is actually displaying the property. Ideally one would purify the hydrogenase of interest to physically insulate it. However, most hydrogenase is labile, the purification process is time-consuming, and the yield is low. Alternatively, one could devise growth condition where only one hydrogenase is preferentially induced to be studied. Most ideally will be to generate mutants lacking all hydrogenases except the one of interest. In this report, we document the induction conditions for each hydrogenase: through physiology by manipulating the growth condition, through mutant isolation to preclude uptake hydrogenase, and via biochemical means to partially purify the CO-linked hydrogenase. By combining all three strategies, we can selectively study the CO-linked hydrogenase without complications from others. We also report the on-going development of a kinetic mass spectrometer protocol to meet the goal of characterizing the O₂ tolerance of the CO-linked hydrogenase, applicable also to other hydrogenase enzyme systems.

Materials and Methods

Growth Conditions, Membrane Preparations and Assays

Rhodocyclus gelatinosus CBS-2, *Rhodospirillum rubrum* strains S1, G9 and P1 were cultivated in modified RCV medium (Weaver *et al.*, 1975). P1 was a mutant derived from G9 deficient in the H₂-uptake pathway (Maness and Weaver, 1999). Carbon source were 30 mM Na-malate or 15 mM fructose for photoheterotrophic growth, 16% CO along with 0.5% (w/v) yeast extract for CO-supported growth, or 30 mM Na-pyruvate for fermentative growth. Media were prepared by boiling and dispensing into anaerobe tubes under a stream of argon gas. NaCO₃ at 0.1% final concentration was added just prior to autoclaving.

To adapt cells to using higher concentration of CO for the CO/hemoglobin binding assay, approximately 160-ml of cells from a malate-grown photosynthetic culture were added to a 885-ml Parr pressure reactor. The headspace was replaced with argon gas, followed by adding 100% CO to 40 psig, and then to 68 psig with argon gas. The initial optical density (OD, at 660 nm) is 0.5. The suspension was then incubated in darkness with constant stirring under pressure. An aliquot of the suspension was withdrawn from the reactor outlet and diluted into 50 mM Tris buffer (pH 8.7) to approximately 0.1 OD for the CO uptake reaction.

Photosynthetic cultures were illuminated with a band of 40W incandescent lamps. Light intensity reaching the surface of cultures is approximately 100 W/m².

The preparations of cell-free hydrogenase extract, its partial purification, the hydrogenase assays, and dry weight determination were according to the Methods described in Maness and Weaver (1999).

CO/Hemoglobin Binding Assay

CO determination for the CO uptake reaction was measured by the CO/hemoglobin binding assay (Bonam *et al.*, 1984). Stoppered test tubes containing 2.5 ml hemoglobin solution was made anaerobic with argon gas. The CO uptake reaction was carried out inside a 5-ml glass syringe containing 2-ml cell suspension and pre-incubated inside a 45°C water bath to reach equilibrium. Two milliliter of 20% CO gas was then withdrawn into the syringe and shook vigorously for 10 seconds before the headspace was expelled to enhance mass transfer. At various intervals, 0.2 ml aliquot of the cell suspension containing various amounts of CO was injected into the hemoglobin solution. The total spectral changes between the peak at 419 nm and the trough at 433 nm were recorded with a Cary 4E spectrophotometer. A total change of 1.0 OD corresponds to 13.5 nmole of dissolved CO.

Results and Discussion

Variation in Hydrogenase Activities during Growth

A hydrogenase enzyme linking to CO oxidation has been reported by Uffen (1981) and Bonam *et al.* (1984) in two photosynthetic bacteria. We have observed a similar hydrogenase in both *Rhodospirillum rubrum* S1 and *Rhodocyclus gelatinosus* CBS-2 upon adding CO to the culture headspace. The appearance of this enzymes peaked when cells were in the mid-log phase of growth. No activity was measured when CO was not added. This CO oxidation pathway is postulated to play a role in either CO detoxification or in a novel CO-supported dark growth mode with the possible generation of energy (Champine and Uffen, 1987; Kerby *et al.*, 1995). A second hydrogenase activity was also detected in both organisms coupling to the reduction of methylene blue. This uptake hydrogenase activity paralleled cell growth and leveled off at the stationary-phase of cell growth. This uptake hydrogenase is postulated to be involved in the H₂-supported CO₂ fixation. A third hydrogenase has been identified in *R. rubrum* S1 when light was limiting, as the culture became denser. This activity was linked to formate oxidation, it appeared later, and peaked at early-stationary phase of cell growth. This enzyme was proposed to dissipate excess energy during fermentative growth in darkness (Schultz and Weaver, 1982). The appearance of all three enzymes at difference phases of growth strongly suggests that they are three separate enzymes, each has its own physiological function. The presence of multiple hydrogenases also complicates their characterization as one can harvest cells at any stage of growth and one or more enzymes will be present.

Growth Conditions to Induce Individual Hydrogenase Activities

In order to characterize the CO-linked hydrogenase of interest to us without complications from the other hydrogenases, we have to understand the criteria for their induction in order to devise conditions where only the CO-linked hydrogenase is induced. This is especially important for the quantification of O₂ tolerance since the uptake hydrogenase is known to be highly tolerant to O₂. If uptake hydrogenase is present along with the CO-linked hydrogenase, then the former enzyme could attribute some of the O₂ resistance measured. Formate-linked hydrogenase is known to be extremely sensitive to O₂ and could also confuse the measurement. We therefore carried out experiments to investigate the induction criterion of each hydrogenase activity. A general approach is to add a suspected enzyme inducer along with a protein-synthesis inhibitor to see if *de novo* protein synthesis is involved. If the result is positive, then we have identified the inducer for each enzyme. Once the identity of an inducer is known, we can add an inhibitor to prevent its synthesis during growth such that the specific enzyme is not made.

Fig. 1A shows that when exogenous formate was added, a hydrogenase activity linking to formate oxidation appeared rapidly when assayed by the formate-linked H₂ production pathway. A very low background activity was detected in the control culture where formate was not added. Formate produced through normal fermentative metabolism probably accounts for the low levels of activity in this culture. Chloramphenicol, an inhibitor at the protein translation level, immediately stopped the appearance of formate-induced hydrogenase activity when added along with formate as shown in Fig.1A. This indicates that formate is required to induce a hydrogenase involved in formate oxidation. Thereby, formate is the inducer for this pathway. In theory, if an inhibitor is added to inhibit formate synthesis completely during growth, formate-linked hydrogenase will not be synthesized at all.

Identical culture supplemented with CO exogenously similarly synthesized a chloramphenicol-sensitive, CO-dependent, H₂ production activity (Fig. 1B). The result suggests that CO is the inducer in expressing a hydrogenase enzyme that is linked to CO oxidation. Similar results of a CO-inducible hydrogenase in *R. rubrum* had been reported previously by Bonam *et al.* (1989). Since CO is not a natural byproduct of normal cell metabolism, at least not at any measurable quantity, CO-linked hydrogenase is generally not present during growth. Consequently, the appearance of CO-linked hydrogenase can be easily manipulated.

With the identification of the different inducers for various hydrogenases, we can then devise growth condition where only the hydrogenase of interest is selectively induced. Under light-limiting condition, the cellular fermentative pathway produces trace amounts of formate, responsible for the induction of the low-level of formate-linked hydrogenase. When higher level of formate-linked hydrogenase is desirable, we can supplement the culture medium with formate to induce it to a much higher level. To repress this enzyme entirely, we must use an inhibitor to repress the synthesis of formate. Sodium hypophosphite (HPP), a formate analog, has been reported as a potent inhibitor of the

enzyme responsible for the cellular production of formate (Gorrell and Uffen, 1977; Thauer *et al.*, 1972). With the addition of HPP, therefore, no formate should be produced. HPP had no effect on the formate-hydrogenlyase reaction in *R. rubrum* (Gorrell and Uffen, 1978). As expected, we have not detected any formate-linked hydrogenase activity in *R. rubrum* whenever 10 mM HPP was included during growth. The CO-linked hydrogenase activity can be selectively induced by supplementing 20% CO to the culture gas phase in the presence of HPP. Uptake hydrogenase activity can be maximally induced by growing cells photoautotrophically under H₂ and CO₂ in the presence of HPP. For all the experiments described below, cells were cultured under the appropriate condition (referred to as "induced" condition) so that each hydrogenase is singly induced. Table 1 summarized the induction conditions used to maximally induce the individual hydrogenase of interest through physiology manipulations.

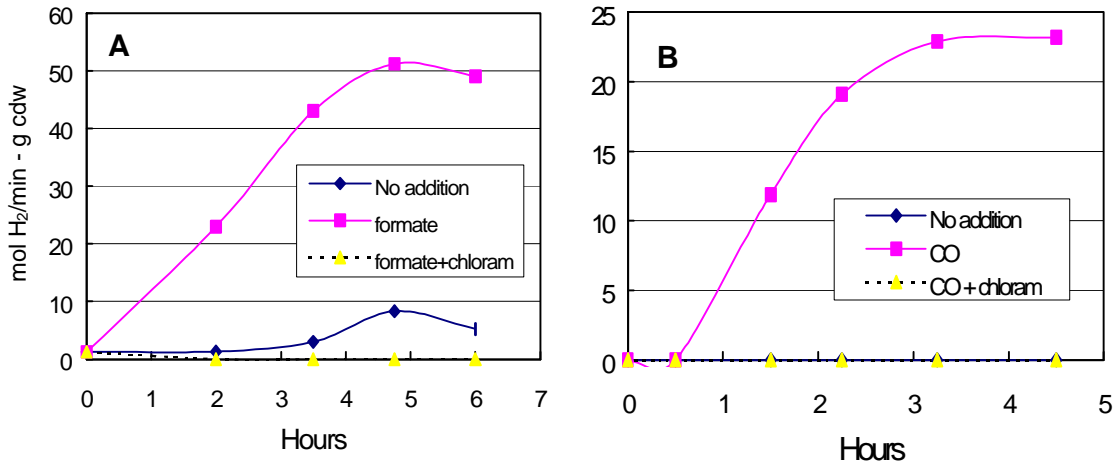


Figure 1 - The Effect of Chloramphenicol (chloram) on the Induction of the Formate-linked (A) and CO-linked (B) Hydrogenases

Table 1. Growth Conditions to Induce Individual Hydrogenase Activity

| Hydrogenase | Induction Condition |
|----------------------------|---|
| CO-linked Hydrogenase | Add CO to a photosynthetic culture with Na-hypophosphite |
| Formate-linked Hydrogenase | Fermentative conditions, or add formate to a photosynthetic culture |
| Uptake Hydrogenase | Malate or H ₂ /CO ₂ gas mixture with the presence of Na-hypophosphite |

Electron Donor/Acceptor Mediating Various Hydrogenase Activities

All three hydrogenases can use methyl viologen (-450 mV vs. NHE) to mediate both the production and uptake of H₂. Uptake hydrogenase is known to use methylene blue (+11 mV vs. NHE) as the terminal electron acceptor (Adams and Hall, 1977; Colbeau and Vignais, 1981). Yet it is not known whether the CO-linked hydrogenase can also use methylene blue as the electron acceptor. To examine this, we partially purified the CO-linked hydrogenase from *R. rubrum* P1, a mutant from which nearly 98% of the uptake hydrogenase has been removed previously, and obtained fractions enriched in CO-linked hydrogenase (Maness and Weaver, 1999). These fractions were then assayed for activity linking to various electron mediators. As expected, we detected good rate of H₂ evolution from reduced methyl viologen, low rate of H₂ uptake to methyl viologen (its backward reaction); yet no H₂ uptake to methylene blue was detected at all (Fig. 2). Identical results were obtained when we repeated the experiment. These data suggest that an evolving hydrogenase preferentially couples to a low-redox mediator to produce H₂ whereas an uptake hydrogenase favors a high-redox mediator such as methylene blue for the uptake of H₂. The methylene-blue reduction activity can thus be used to specifically detect the presence of the uptake hydrogenase activity only. We can, therefore, use this procedure to obtain only the CO-linked hydrogenase and study its O₂ tolerance without interference from the uptake hydrogenase, which is known for its higher O₂ tolerance. Any observed tolerance to O₂ can consequently be attributed entirely to the CO-linked hydrogenase only.

Although coupling well with reduced methyl viologen in the H₂-evolution direction, it is not known whether the formate-linked hydrogenase can couple to methylene blue. We have previously determined that this fermentative hydrogenase is extremely sensitive to CO, while the uptake hydrogenase is not. We decided to study the formate-linked hydrogenase from *R. rubrum* P1 since the bulk of its uptake hydrogenase has been removed by us. By culturing P1 with Na-pyruvate in darkness, the fermentative hydrogenase can be selectively induced. This culture still contains a low level of uptake hydrogenase coupling to methylene blue. We then determined that 14.8% of CO inhibits nearly 85% of the hydrogenase activity in the evolution direction using reduced methyl viologen; yet the traces of H₂ to methylene blue activity are not affected at all, even at 28% of CO. If the formate-linked hydrogenase were able to couple to methylene blue, CO would have affected its activity to the same extent. This result implies that the fermentative hydrogenase does not normally couple to methylene blue as the electron mediator. Since uptake hydrogenase is always induced in a growing culture, this finding allows one to use methylene blue as the electron mediator to specifically detect its presence. Table 2 summarizes the various electron mediators to which each hydrogenase couples.

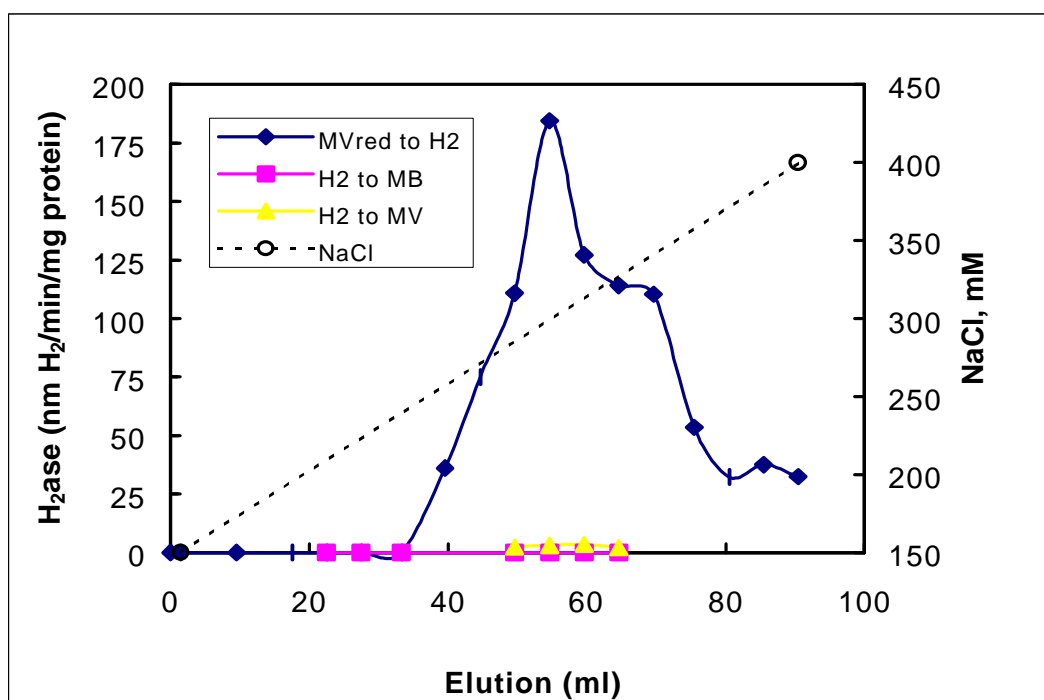


Figure 2 - Partial Purification of CO-linked Hydrogenase from *R. rubrum* P1

Table 2. Electron Mediators Mediating Various Hydrogenase Activities

| Hydrogenase | MV _{red} to H ₂ | H ₂ to MV | H ₂ to MB |
|----------------|-------------------------------------|----------------------|----------------------|
| CO-linked | + | + | |
| Formate-linked | + | + | |
| Uptake | + | + | + |

The Development of a H₂ – D₂O Exchange Assay

Using a mass spectrometer to measure a hydrogenase by its H₂-D₂O exchange activity, we have previously determined that the partially purified CO-linked hydrogenase from *R. rubrum* P1 was partially functional in the presence of 1% and 7% of O₂. The inhibition was more than 70% reversible upon the subsequent removal of O₂ from the headspace (Maness and Weaver, 1999). However, the assay was conducted during a 20-min incubation at batch mode with or without O₂. It will provide very valuable information if we were to develop a kinetic assay such that the impact of O₂ can be measured

immediately upon its addition. Knowing how to separate the three hydrogenases from each other, this year we set out to develop a kinetic assay. Preliminary work with a direct sampling mass spectrometer sampled at 5 second interval showed evidence of exchange, but at a very low level. This was partly due to the high flow rates of H₂ required (5 ml/min) for adequate sampling introduction, which dilute the reaction products in the headspace. The other explanation is that our CO-linked hydrogenase has a very high forward/backward ratio of reaction rates with regard to methyl viologen. The initiation of the exchange reaction mandates the H₂ molecule to be broken down first, a rate-limiting step for our hydrogenase, prior to exchange with the protons or deuterium ions in the medium to yield HD. Similar observations have also been recorded where a hydrogenase more favorable for H₂ production was reported to have a lower rate of D₂ exchange activity (Arp and Burris, 1981; Fox *et al.*,1996). To circumvent, we are presently developing techniques using a mass spectrometer equipped with a capillary leak for sample introduction. The capillary leak provides continuous sampling of reactor headspace at ambient pressure. An initial H₂ concentration of 3% was included in the headspace so that no continuous bubbling of H₂ is required. The work is currently in progress.

The Enhancement of the CO Shift Activity

To make this process for H₂ production more economical, one of our goals is to increase the rate of CO shift to H₂. We accomplished this by measuring the shift activity at very low cell density (< 0.1 OD) using cells adapted to higher CO concentration, by increasing mass transfer, and by conducting the assay at its optimal temperature of 45C using the CO/hemoglobin binding assay. Fig. 3 shows the kinetics of CO uptake by *R. gelatinosus* CBS-2 with a rate of 8.3 mmole/min-g cell dry weight, calculated from the data points between the 4 and 10 second interval. Zero time measurement was determined separately where no cells were added. Previously we determined that the *K_s* of the shift reaction is around 5.9 M of CO. Therefore the rate derived is an underestimation since even at 10 seconds the CO substrate is already at near the rate-limiting level. In future experiments, we will conduct multiple assays and for each we only measure CO concentration at one time interval. Kinetics are then constructed accordingly to a get more accurate rate.

Conclusion

Based on the data from cell physiology, biochemical purification and genetic studies, we have demonstrated that in *R. rubrum*, there are at least three separate hydrogenases, and each can be maximally induced at a different stage of growth. The induction study using a protein synthesis inhibitor chloramphenicol provides evidence that the induction initiates a *de novo* protein synthesis. Based on the induction conditions acquired for each hydrogenase, we were able to devise growth conditions to preferentially induce one hydrogenase over the others in order to characterize various physical and biochemical properties specific to the hydrogenase of interest without interferences from the others. The results of the mutant study of *R. rubrum* P1 further confirm that the induction of both the CO-linked and the formate-linked hydrogenases do not rely on the presence of the

uptake hydrogenase enzyme. Since the uptake hydrogenase co-induces with the CO-linked hydrogenase during the entire growth cycles on CO, and the uptake hydrogenase also co-purifies with the CO-linked hydrogenase, prior removal of the uptake hydrogenase in mutant P1 is critical in order to study the CO-linked hydrogenase only. Indeed, when the CO-linked hydrogenase is partially purified from P1, we were able to determine that the CO-linked hydrogenase does not couple to methylene blue, a high-redox dye known to be readily reducible by the uptake hydrogenase. This finding gives us a specific assay for the uptake hydrogenase and allows us to determine the purity of the CO-linked hydrogenase from the uptake hydrogenase enzyme.

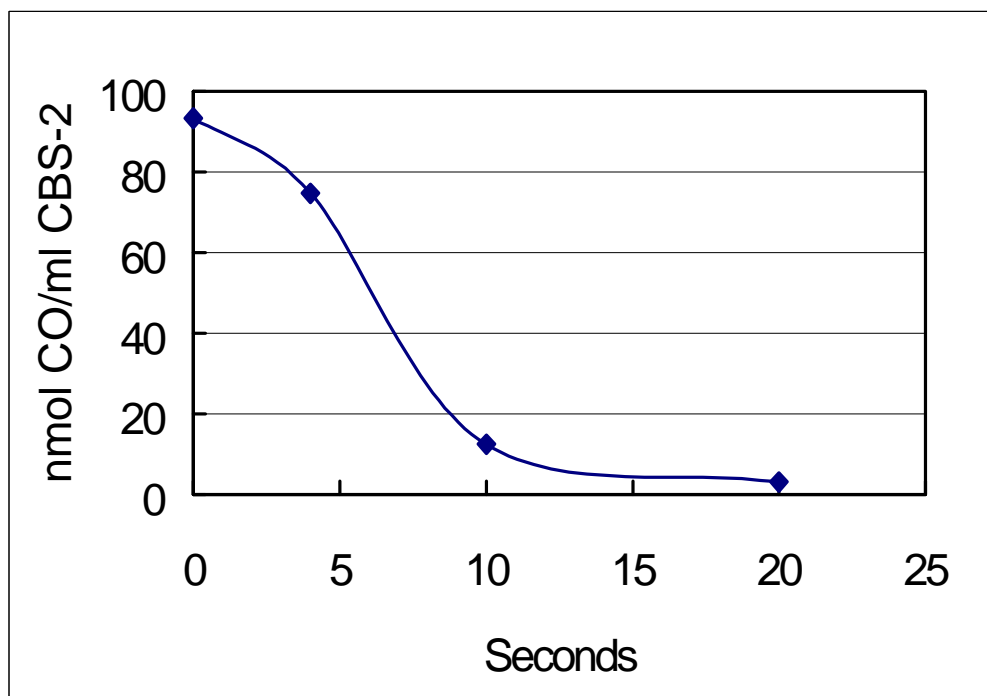


Figure 3 – Kinetics of CO Uptake by *Rhodocyclus gelatinosus* CBS-2

The development of a H₂-D₂O exchange assay using a mass spectrometer is essential for us to determine whether a hydrogenase can function in the presence of O₂. Knowing how to obtain a CO-linked hydrogenase fraction without complications from the other hydrogenases, this report documents preliminary findings on the exchange reaction. Due to the irreversible nature of the CO-linked hydrogenase favoring more in the H₂ evolution direction, this hydrogenase may not be the ideal candidate for the exchange assay. However, we can perhaps overcome this limitation by using a capillary mass spectrometer that provides continuous sampling of the reactor headspace without the constant flowing of a H₂ gas stream, which dilutes the signals significantly. This work is currently in progress.

Future Work

The long term goals of this project is to characterize the bacterial CO to H₂ shift reaction at both the biochemical and genetic levels so that both the reaction rates and durability of H₂ production can be enhanced. The characterization of the genetic systems of the hydrogenase complex also facilitates its subsequent transfer and expression into a cyanobacterium so that both H₂ and O₂ can be simultaneously produced from the water-splitting reaction. To enhance reaction rates and durability, we need to understand the regulation and physiology of the overall CO to H₂ pathway at the biochemical and physiological levels. By identifying the individual components involved, we can then determine the rate-limiting step. At the genetic levels, we plan to improve mutant selection/enrichment techniques in order to obtain a series of mutants deficient in the various components of the CO to H₂ pathway. By examining their revertants, we can then seek out those overly expressed mutants that synthesize the CO-linked hydrogenase enzyme constitutively. We will also initiate work in identifying and cloning the CO-linked hydrogenase gene in order to understand its regulation at the molecular genetics levels. This will allow us to manipulate the genetic capacity for H₂ production activity by making multiple copies of the hydrogenase gene. Cloning the hydrogenase gene will also enable us to construct a plasmid carrying this gene and later transform the plasmid into a cyanobacterium to meet our long-term goals of producing H₂ from the water-splitting reaction.

Acknowledgement

We thank Clark Fields, Kim Magrini-Bair, and Mike Looker at NREL for advice and for assistance with the mass spectrometer measurements.

References

- Adams, M.W.W. and D.O. Hall. 1977. "Isolation of the membrane-bound hydrogenase from *Rhodospirillum rubrum*." *Biochem. Biophys. Res. Comm.*, 77: 730-737.
- Arp, D.J. and R.H. Burris. 1981. "Kinetic mechanism of the hydrogen oxidizing hydrogenase from soybean nodule bacteroids." *Biochemistry*, 20: 2232-2240.
- Banam, D., A.M. Murrell, and P.W. Ludden. 1984. "Carbon monoxide dehydrogenase from *Rhodospirillum rubrum*." *J. Bacteriol.*, 159: 693-699.
- Bonam, D., L. Lehman, G. P. Roberts and P.W. Ludden. 1989. "Regulation of carbon monoxide dehydrogenase and hydrogenase in *Rhodospirillum rubrum*: effect of CO and oxygen on synthesis and activity." *J. Bacteriol.*, 171: 3102-3107.
- Champine, J.E. and R.L. Uffen. 1987. "Regulation of anaerobic carbon monoxide oxidation activity in *Rhodocyclus gelatinosus*". *FEMS Microbiol. Letters*, 44: 307-311.

Colbeau, A., J. Chabert, and P.M. Vignais. 1981. "The membrane-bound hydrogenase of *Rhodopseudomonas capsulata* stability and catalytic properties." *Biochim. Biophys. Acta.*, 662: 271-284.

Colbeau, A., J. Chabert, and P.M. Vignais. 1983. "Purification, molecular properties and localization in the membrane of the hydrogenase of *Rhodobacter capsulata*." *Biochimica et Biophysica Acta*, 748: 116-127.

Fauque G., H.D. Peck, J.J.G. Moura, B.H. Huynh, Y. Berlier, D.V. DerVartanian, M. Teixeira, A.E. Przybyla, P.A. Lespinat, I. Moura, and J. LeGall. 1988. "The three classes of hydrogenases from sulfate-reducing bacteria of the genus *Desulfovibrio*." *FEMS Microbiol. Rev.*, 54: 299-344.

Fox J.D., R.L. Kerby, G.P. Roberts, and P.W. Ludden. 1996. "Characterization of the CO-induced, CO-tolerant hydrogenase from *Rhodospirillum rubrum* and the gene encoding the large subunit of the enzyme." *J. Bacteriol.*, 178: 1515-1524.

Gorrell, T.E. and R.L. Uffen. 1977. "Fermentative metabolism of pyruvate by *Rhodospirillum rubrum* after anaerobic growth in darkness." *J. Bacteriol.*, 131: 533-543.

Gorrell, T.E. and R.L. Uffen. 1978. "Light-dependent and light-independent production of hydrogen gas by photosynthesizing *Rhodospirillum rubrum* mutant C." *Photochem. Photobiol.*, 27: 351-358.

Kerby, R.L., P.W. Ludden, and G.P. Roberts. 1995. "Carbon-monoxide-dependent growth of *Rhodospirillum rubrum*". *J. Bacteriol.*, 177: 2241-2244.

Maness, P.C. and P.F. Weaver. 1999. "Biological H₂ from fuel gases and from H₂O." In *Proceedings of the 1999 U.S. DOE Hydrogen Program Review*, NREL/CP-570-2693.

San Pietro, A., 1957. "The measurement of stable isotopes." In *Methods in Enzymology*, vol. IV, p. 473-488. Colowick, S. P. and N.O. Kaplan (eds.), Academic Press, Inc., N.Y.

Schultz, J.E. and P.F. Weaver. 1982. "Fermentation and anaerobic respiration by *Rhodospirillum rubrum* and *Rhodopseudomonas capsulata*." *J. Bacteriol.*, 181-190.

Stewart, W.D.P. 1973. "Nitrogen fixation by photosynthetic microorganisms." *Ann. Rev. Microbiol.*, p. 283-316.

Thauer, R.D., F.H. Kirchniway, and K.A. Jungermann. 1972. "Properties and functions of pyruvate-formate-lyase reaction in clostridia." *Eur. J. Biochem.*, 27: 282-290.

Uffen, R.L., 1981. "Metabolism of carbon monoxide." *Enzyme Micro. Technol.*, 3: 197-206.

Vignais, P.M., B. Dimon, N.A. Zorin, A. Colbeau, and S. Elsen. 1997. "HupUV proteins of *Rhodobacter capsulatus* can bind H₂: evidence from the H-D exchange reaction." *J. Bacteriol.*, 179: 290-292.

Weaver, P.F., J.D. Wall, and H. Guest. 1975. "Characterization of *Rhodopseudomonas capsulata*." *Arch. Microbiol.*, 105: 207-216.

Figure 1. The Effect of Chloramphenicol (chloram) on the Induction of the Formate-linked (A) and CO-linked (B) Hydrogenases

Figure 2. Partial Purification of CO-linked Hydrogenase from *R. rubrum* P1

Figure 3. Kinetics of CO Uptake by *Rhodocyclus gelatinosus* CBS-2

Table 1. Growth Conditions to Induce Individual Hydrogenase Activity

Table 2. Electron Mediators Mediating Various Hydrogenase Activities

BIOREACTOR DEVELOPMENT FOR BIOLOGICAL HYDROGEN PRODUCTION

Edward J. Wolfrum, Ph.D., Paul F. Weaver, Ph.D.
National Renewable Energy Laboratory
1617 Cole Boulevard
Golden, CO 80401

Abstract

This report summarizes the work on the development of bioreactors for the biological water gas shift reaction at the National Renewable Energy Laboratory. The motivation and long-term goals of the project are described, and the specific accomplishments of the past year are presented. In the section outlining the mathematical modeling efforts, a number of mathematical models that describe the mass-transfer properties of trickle-bed bioreactors for the biologically-mediated water-gas shift reaction are presented. The work performed to develop a computer-controlled Research/Demonstration Unit to provide a “real-world” synthesis gas source is also reviewed.

Introduction & Background

The biologically-mediated water-gas shift reaction may be a cost-effective technology for the conditioning of synthesis gas for storage or direct use within a hydrogen fuel cell. NREL researchers have isolated a number of photosynthetic bacteria that can perform the water-gas shift reaction, in which carbon monoxide is oxidized to carbon dioxide while water is simultaneously reduced to hydrogen. The overall stoichiometry of this reversible reaction is:



The current “state-of-the-art” water-gas shift technology is a two-stage, high temperature, high-pressure catalytic process. The reaction is equilibrium-limited at the temperatures required for it to operate sufficiently rapidly, preventing very high CO conversion efficiencies. Polishing steps using thermal catalysis can oxidize the residual CO, but such processes inevitably oxidize H₂ as well as CO.

One significant advantage to using photosynthetic bacteria to perform the water-gas shift reaction is the ability to operate at ambient temperature, where the reaction equilibrium is much

more favorable to hydrogen production. The advantages of low operating temperature, rapid reaction rate, and lack of equilibrium limitation make the biological shift reaction a promising alternative to conventional shift technologies.

Preliminary data already collected at NREL suggest that this reaction is far more rapid than the rate at which CO can be supplied to the bacteria. This is consistent with many other gas/liquid biological reaction systems, including most aerobic fermentations, where metabolic rates are commonly limited by the transfer rate of a gaseous substrate to the liquid media.

To increase the accuracy of economic estimates of the full-scale process, it is necessary to collect data from a laboratory-scale bioreactor whose mass transfer characteristics are well understood, and to incorporate these data into an appropriate bioreactor model. The model can then be used to predict the size of a full-scale system. The approach we are taking for this project is to collect laboratory performance data using common bioreactor designs, and then use these data in a bioreactor model to estimate the size of a full-scale system. During the course of the laboratory work (and through review of the literature), new bioreactor design ideas are developed for further testing.

Project Activities

Work on this project is divided into two parts. The first part involves the laboratory investigations of bioreactor designs, while the second part involves work on a research/demonstration unit (RDU) that combines syngas production with microbial CO shift for syngas cleanup. As part of the laboratory investigations, we have developed a comprehensive mathematical model of the bioreactor system, which is the principal subject of this report. For the RDU project, we are working to ready the RDU for long-term unattended operation as a supply of “real-world” syngas to a bioreactor.

Laboratory Bioreactor Model Development

We are investigating a number of different biological reactor designs to determine the maximum gas-liquid mass transfer rates we can achieve in the laboratory. In order to fully understand and interpret the laboratory results, we have developed a number of mathematical models to describe the operation of these reactors. This section of the report describes the operation and modeling of a trickle-bed reactor (TBR). TBRs are proven to be very effective for gas-liquid reactions where the mass transfer rate is limited by the resistance in the liquid phase. This is the case for biological processes utilizing sparingly soluble gases like carbon monoxide or oxygen. Figure 1 shows schematic diagrams of a co-current and counter-current TBR.

The reactor is filled with a high porosity support material, commonly called reactor packing. The liquid flows downward around the packing due to gravity, creating a thin film of liquid on the packing surface, and maximizing the amount of gas-liquid interfacial area. The liquid flow is low enough so that it “trickles” down the packing, giving the reactor its name. The gas can either flow upward or downward through the reactor. The relative flow directions of the gas and liquid phase give rise to the nomenclature “co-current” and “counter-current”.

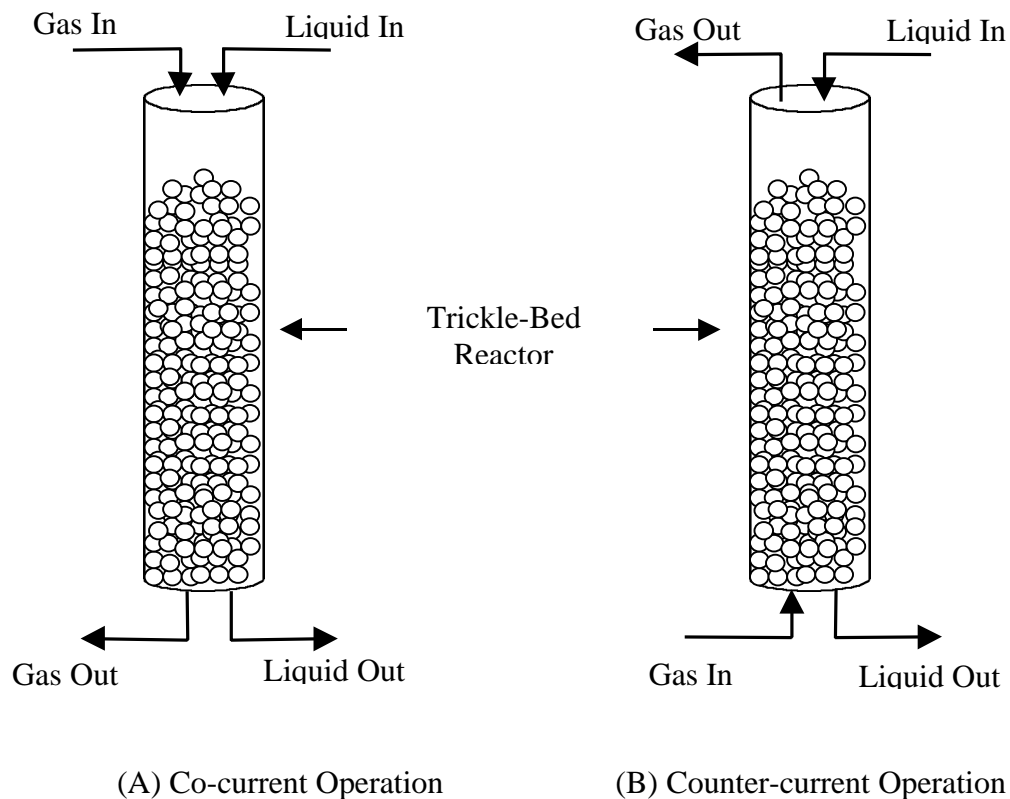


Figure 1. Schematic Diagram of Trickle Bed Reactors (TBRs) in (A) co-current and (B) counter-current operation. Liquid flow is downward in both cases.

The driving force for mass transfer between the gas and liquid phases is the concentration gradient across the interface. At equilibrium, Henry's Law describes the relationship between the gas and liquid phase concentrations:

$$yP = HC_L \quad (2)$$

Any deviation from this equality causes an interphase mass transfer driving force. The rate of gas-liquid mass transfer depends on many factors, including the hydrodynamics of the system in question, the chemical composition of the gas being transferred, and the shape and porosity of the reactor packing. In the situation where the majority of the mass transfer resistance is in the liquid phase, the mass transfer rate is characterized by the liquid-side overall mass transfer coefficient $K_L a$. However, this parameter cannot be measured directly, so we have developed a number of reactor models to help interpret the experimental data.

Mathematical models are useful for a variety of reasons. They are most commonly used to predict the size (and therefore cost) of larger reactor assemblies based on laboratory data, and thereby point out areas where more research could result in significant cost savings in the scaled-up systems. However, reactor models can also be useful as a framework to understand

experimental data, and to help guide the design of future laboratory experiments. This second use is the subject of this section.

Model Descriptions

A number of similar models have been developed for this work. Consider the reactor geometry in Figure 1, with a gas stream flowing at flowrate G containing the gas to be transferred with mole fraction y_{in} . The liquid phase is flowing at flowrate L , with inlet concentration C_L^{in} . As the gas and liquid flow through the column, the concentration gradient across the gas-liquid interface provides the driving force for mass transfer.

Co-current TBR Model

The differential equations that describe the co-current TBR are:

$$\frac{dN}{dz} = K_L a \times e_L \frac{yP}{H} C_L \quad (3)$$

$$\frac{dC_L}{dz} = \frac{K_L a \times e_L}{L} \frac{yP}{H} C_L \quad (4)$$

$$BC\#1: @ z = 0 \quad y = y_{in} \quad (5)$$

$$BC\#2: @ z = 0 \quad C_L = C_L^{in} \quad (6)$$

There is one equation for each phase, and two boundary conditions. Note that there is no reaction term included for the liquid phase differential equation (Eq. 4). That is, the liquid phase reaction rate is considered zero, and the gas concentration in the liquid phase will build up over time. In the opposite case, where the liquid phase reaction rate is significantly faster than the rate of gas-phase mass transfer, it is possible to simplify the model by assuming the liquid phase concentration C_L is essentially zero everywhere. In this case, Eq. 4 reduces to zero. These two cases (zero and infinite liquid phase reaction rates) bracket the range of possible liquid phase reaction rates.

These equations are easily solved numerically. For this work, a 4th Order Runge-Kutta technique was implemented in Microsoft Excel 97 Visual Basic for Applications (EXCEL/VBA).

Counter-current TBR Model

The model equations for the counter-current model are identical to the co-current model with one exception: the inlet boundary conditions of the gas phase are reversed:

$$BC\#1: @ z = Z \quad y = y_{in}$$

$$BC\#2: @ z = 0 \quad C_L = C_L^{in}$$

This adds slightly more complexity to the model, since the two boundary conditions are no longer co-located. Because of this, an iterative solution procedure is necessary. The outlet liquid phase concentration, $C_L(z=Z)$, is estimated, giving a new model with co-located boundary conditions. This new model is identical in formulation to the co-current model described above,

and is solved to give an estimate of the inlet liquid phase concentration $C_L(z=0)$. The model converges when this estimate is equal to the original boundary condition value.

In the case of infinitely fast liquid phase reaction rate, the model equations for the co-current and counter-current are identical, since the equation describing the liquid phase (Eq. 4) simplifies to zero. In reality, this means that if the reaction rate is limited by the rate of mass transfer, at a given value of K_La , operating the reactor in either co-current or counter-current mode will give identical results. It does not follow, however, that the two reactor modes are equivalent. That is, for the same gas and liquid flowrates (identical G and L), counter-current operation will always yield a higher value of K_La , since the relative velocity of the two phases is much higher than in co-current operation.

Model Results & Discussion

Figures 2 and 3 present some preliminary modeling results from the single-pass TBR models. The model parameter values for these simulations, unless otherwise stated, were as follows: $Z=100$ cm, $D=6$ cm, $L=3000$ cm³ min⁻¹, $V_H=400$ cm³, $G=2000$ cm³ min⁻¹, $K_La=0.20$ s⁻¹, $y_{in}=0.2$, $C_L^{in}=0$.

Figure 2 shows the effect of the inlet CO concentration on the CO conversion at a fixed value of the mass transfer coefficient K_La . The conversion is almost 50% in the limit of very low CO mole fractions, and decreases to approximately 45% at CO mole fractions close to 0.5. This decrease is caused by an increase in the volume of the gas phase. The reaction stoichiometry states that the reaction of one mole of CO with water will form two moles of product, CO₂ and H₂. The model assumes that these gases are essentially insoluble in the liquid phase, and are transferred immediately to the gas phase. At CO mole fractions close to 0.5, this increase in gas volume becomes significant, and the residence time in the reactor drops slightly, causing the decrease in conversion. Effects of CO₂ dissolution in the liquid phase (gas volume changes, pH effects, etc.) will be examined in future work.

The co-current and counter-current TBR models with no liquid phase reaction show different behavior from the infinite reaction rate case. Since the liquid phase reaction rate is zero for these cases, CO transferred from the gas phase accumulates in the liquid phase. At high inlet CO mole fractions, enough CO gas is transferred to the liquid phase to appreciably decrease the total gas flowrate. As the gas flowrate drops, the residence time of the gas in the reactor increases, leading to higher conversions for high mole fractions. The equilibrium conversion for the counter-current model is slightly higher than for the co-current case for all inlet mole fraction values, since the exiting liquid phase is in equilibrium with the higher concentration inlet gas stream rather than the lower concentration exiting gas stream.

Figure 3 shows the effect of varying the overall mass transfer coefficient at a fixed value of the inlet CO mole fraction y_{in} . With infinitely fast liquid phase reaction kinetics, conversion increases steadily with the mass transfer coefficient, and will reach 100% at very high K_La values. For the case of no liquid phase reaction rate, the conversion is equilibrium-limited at high K_La values, with the conversion higher for the counter-current model than for the co-current model. Thus, the extent to which the chemical reaction is limited by equilibrium considerations depends on the relative values of the mass transfer rate and the liquid-phase reaction rate. It is

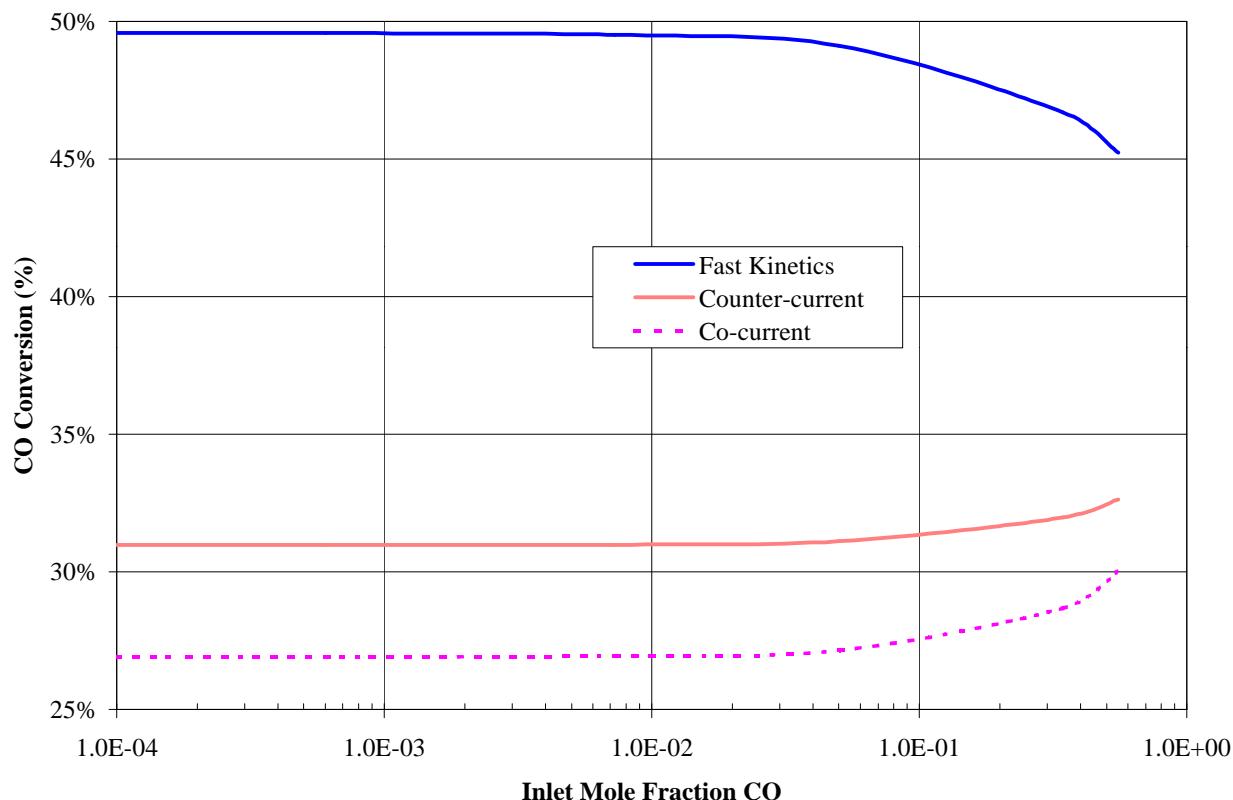


Figure 2. Effect of Inlet CO Mole Fraction (y_{in}) on CO conversion. Conversion is higher for the case with infinitely fast liquid phase kinetics, and the co-current and counter-current models are identical for this case. Conversion is lower for the case with no reaction in the liquid phase, and the co-current and counter-current models do not provide the same results.

entirely possible that the rate of the same reaction can be limited by mass transfer in one reactor assembly, and equilibrium-limited in another.

The models can be used to extract a mass transfer parameter from experimental data. Figure 4 shows experimental CO conversion by the photosynthetic bacterium *Rhodocyclus gelatinosus* CBS-2 in a counter-current TBR at fixed gas and liquid flowrates, but varying inlet CO mole fraction. The CO conversion is approximately 20%, and independent of the three different inlet CO mole fractions examined. These conversion data were used, along with the counter-current TBR model, to extract a value of the mass transfer coefficient $K_La=0.032 \text{ s}^{-1}$. This is in good agreement with literature data for similar reactor assemblies.

Modeling Conclusions & Future Work

The TBR models developed in this work demonstrate that in the limit of infinitely fast liquid phase reaction rate, the extent of CO conversion is not sensitive to the concentration of CO in the gas stream, except at very high concentrations ($y_{in} \sim 0.5$) when the gas phase residence time is affected. The limited experimental data currently available support this conclusion.

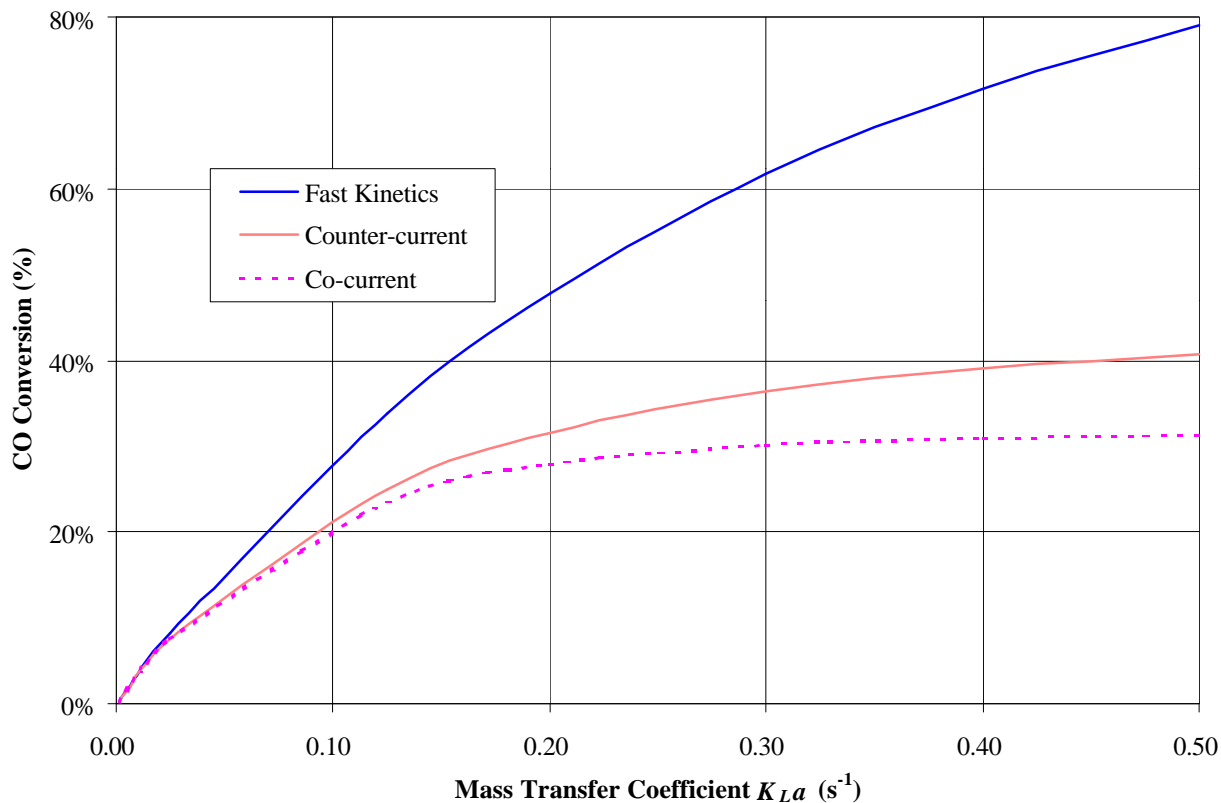


Figure 3. Effect of Mass Transfer Coefficient K_{La} on CO conversion. Conversion in the case of infinitely fast liquid phase kinetics increases steadily with K_{La} . Conversion is lower for the case of no liquid phase reaction, and reach equilibrium-limited values for both the co-current and counter-current models.

This result means that a reactor of a given size and overall throughput will convert the same fraction of carbon monoxide in the inlet feedstream, whether the stream contains 10% CO, 1% CO, or .01% CO. Another way of expressing this so-called “first-order behavior” is that the volumetric productivity of the reactor (the amount of CO converted per unit reactor volume per unit time) is directly proportional to the CO concentration.

The extent to which the reaction will be limited by equilibrium considerations depends very strongly on the relative rates of mass transfer and reaction. In particular, as new reactor designs with enhanced mass transfer rates are developed, it will be important to understand very clearly the maximum reaction rate required, since there is little reason to develop reactors that have mass transfer rates in excess of the maximum intrinsic reaction rate.

The TBR models allow the extraction of a mass transfer coefficient K_{La} from experimental conversion data, but not the *a priori* prediction of K_{La} . A number of correlations exist in the literature, but these have somewhat limited utility since the scatter in the data is quite significant.

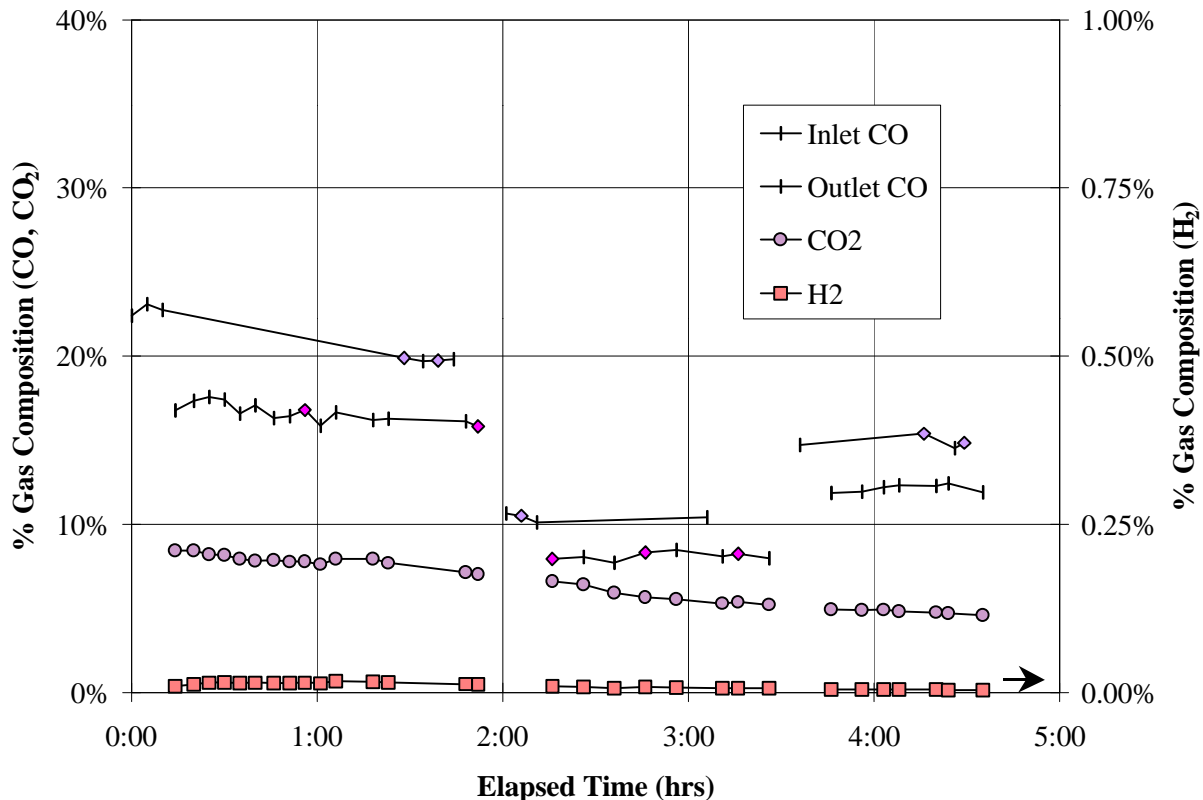


Figure 4. Representative CO conversion data from TBR assembly. $G=1$ SLPM, $L=2$ LPM. CO conversion was $\sim 20\%$ and independent of inlet CO concentration, but only very small amounts of H_2 were evolved.

A better technique for characterizing reactors is to perform experiments in the absence of chemical reaction. Measuring the rate of interphase mass transfer in the absence of reaction provides a conservative estimate of the mass transfer coefficient. A hypothetical experiment of this type would consist of operating the TBR reactor at a given set of reaction conditions with the liquid phase containing the required nutrients but without a microbial culture. These experiments, and the slightly more complex reactor modeling required to interpret the experimental data, are underway.

Research/Demonstration Unit (RDU)

Most work that has been reported in the literature on the use of photosynthetic bacteria to perform the water-gas shift reaction has involved experiments using synthetic CO/H_2 feedstreams. In a real-world application, the syngas will be supplied to the bioreactor either by reforming a gaseous or liquid hydrocarbon fuel, or by biomass gasification. The syngas produced by either of these processes will contain other species besides CO and H_2 . For example, syngas produced by propane reforming will likely contain uncracked propane and other hydrocarbons, while syngas from biomass gasification is known to contain quantities of ash and tar. The ability

of the bacterial conditioning system to handle “real” syngas streams has not yet been demonstrated. We are developing a computer-controlled research/demonstration unit (RDU) to supply “real” syngas by reforming methane.

Current Year Results

During the last year, we made a number of modifications to the RDU, including modifying the LabView interface program, repairing the reactor, replacing the steam generator, and making improvements to the flow measurement and control system. We also modified the thermal reactor to hold a catalyst charge (the catalyst was kindly provided by Dr. Stefan Czernik of NREL). Figure 5 shows the effect of varying the steam/methane molar ratio on the performance of the RDU with a catalyst bed temperature of 850°C. At a steam/methane ratio of 1, the outlet CO concentration is 25%, which is in agreement with the theoretical stoichiometry. As the steam/methane ratio is increased, significant amounts of carbon dioxide are produced, again in agreement with theoretical stoichiometry.

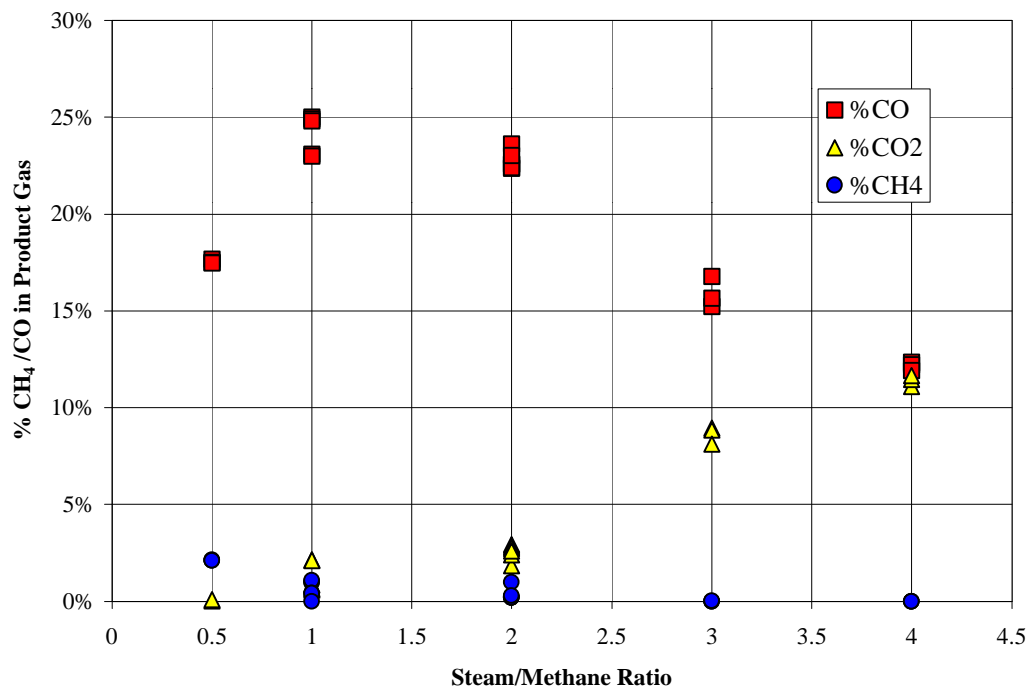


Figure 5. Effect of Steam/Methane Ratio on the Performance of the RDU.

RDU Conclusions & Future Work

As the data in Figure 5 suggest, the RDU is now ready for use as a source of syngas to test different bioreactor designs with a “real-world” feedstock. We will couple the RDU to a bioshift reactor to demonstrate the ability of the bacteria to perform the water-gas shift reaction on a syngas stream that may contain a number of different components besides hydrogen and carbon monoxide. Our longer-term goal is to modify the RDU to produce syngas from the pyrolysis of biomass, which should provide an even more realistic feedstream than methane reforming.

Nomenclature

| Symbol | Description | Units |
|------------|---|---|
| a_s | Reactor cross-sectional area | cm^2 |
| C_L | Liquid-phase concentration | mol cm^{-3} |
| C_L^{in} | Initial liquid-phase concentration | mol cm^{-3} |
| G | Volumetric gas flowrate | $\text{cm}^3 \text{s}^{-1}$ |
| H | Henry's Law coefficient | $\text{cm}^3 \text{mol}^{-1} \text{atm}^{-1}$ |
| K_{La} | Overall mass transfer coefficient | s^{-1} |
| K | Chemical reaction equilibrium constant | -- |
| L | Volumetric liquid flowrate | $\text{cm}^3 \text{s}^{-1}$ |
| N | Molar flux of gas | $\text{mol cm}^{-2} \text{s}^{-1}$ |
| P | ambient pressure | atm |
| Q_L | volumetric flowrate of liquid | $\text{cm}^3 \text{s}^{-1}$ |
| Q_G | volumetric flowrate of gas | $\text{cm}^3 \text{s}^{-1}$ |
| u_L | superficial liquid velocity (Q_L/a_s) | cm s^{-1} |
| u_G | superficial gas velocity (Q/a_s) | cm s^{-1} |
| V_L | liquid holdup volume | cm^3 |
| V_R | total reactor volume | cm^3 |
| V_{res} | reservoir volume | cm^3 |
| V_T | total system volume | cm^3 |
| y | gas-phase mole fraction of gas | -- |
| y_{in} | inlet gas-phase mole fraction of gas | -- |
| Z | reactor length | cm |
| z | axial dimension of reactor | cm |
| e_L | void fraction liquid phase (V_L/V_R) | --- |

DEVELOPMENT OF AN EFFICIENT ALGAL H₂-PRODUCTION SYSTEM

**Maria L. Ghirardi, Zheng Huang, Marc Forestier, Sharon Smolinski,
Matthew Posewitz and Michael Seibert
National Renewable Energy Laboratory
Golden, CO 80401**

Abstract

The ultimate goal of our research is to generate *Chlamydomonas reinhardtii* mutants that are sufficiently O₂ tolerant to produce H₂ under aerobic conditions. We have been addressing this goal by means of both classical genetics and molecular biology approaches.

The classical mutagenesis/selection approach that we have developed to obtain such mutants takes advantage of the reversible activity of the algal hydrogenase. We have designed two selective pressures that require mutagenized algal cells to survive by either metabolizing (H₂-uptake selective pressure) or evolving (H₂-production selective pressure) H₂ in the presence of O₂ concentrations that inactivate the wild-type (WT) enzyme. The surviving organisms are subsequently subjected to a positive screen using a chemochromic sensor that detects H₂ evolved by the algae. Clones that are found to exhibit high H₂-evolution activity in the presence of O₂ are characterized in more detail using biochemical assays. The strategy currently employed consists of re-mutagenizing, re-selecting and re-screening first and second generation mutants under higher selective stringency in order to accumulate single-point mutations, and thus, to further increase the O₂ tolerance of the organism.

Current year's results include (i) the isolation of a second-generation H₂-uptake mutant with an O₂ I₅₀ over 5 times higher than the WT strain, and (ii) the observation that the H₂-evolution activity of H₂-uptake mutants is more easily re-activated upon removal of O₂ and subsequent addition of reductant to the assay medium than that of the WT strain or of the H₂-production mutants.

In order to enhance the probability of ultimately obtaining a commercially-viable organism, we have also been pursuing a molecular biology approach, which is synergistic with the classical genetic strategy described above. Our purpose is to first clone the hydrogenase gene and then to use site-directed mutagenesis to further increase the O₂ tolerance of the enzyme. The types of site-directed mutants that we will attempt to generate will be based on sequence information gathered from the O₂-tolerant mutants described above. Two techniques are currently being used to clone the gene, namely RT-PCR (which allows for the amplification of a specific DNA sequence out of a population of expressed sequences) and insertional mutagenesis (which consists of interrupting genes by introduction of a tagged plasmid, followed by screening for mutants unable to evolve H₂; the tag allows identification and sequencing of the interrupted gene).

Current results include: (i) identification of two partial clones by RT-PCR, using primers based either on the published N-terminal sequence of the algal hydrogenase or on regions of conserved homology between a variety of Fe-only hydrogenases and (ii) isolation of 4 insertional mutants with reduced H₂ evolution activity but WT rates of photosynthesis and respiration.

Introduction

The ability of green algae such as *Chlamydomonas reinhardtii* to photoproduce H₂ from water depends on the activity of the reversible hydrogenase enzyme (Gaffron and Rubin, 1942). In the light, electrons released by the oxidation of water molecules are transferred through photosystems II and I to the low-redox potential carrier, ferredoxin. Normally, reduced ferredoxin supplies electrons to the CO₂ fixation pathway, to cyclic electron transport, and to a variety of secondary pathways. However, following an anaerobic treatment in the dark, algal cells induce the reversible hydrogenase (Ghirardi et al., 1997b), an enzyme that can re-combine photosynthetically-generated electrons and protons to evolve H₂ gas. The hydrogenase competes with the other ferredoxin-dependent pathways for photosynthetic electrons. This competition is normally short-lived, though, due to the prompt deactivation of hydrogenase by O₂ that is concomitantly released by photosynthetic water oxidation (Schulz, 1996). The O₂-sensitivity problem associated with the hydrogenase has precluded the use of green algae in a direct biophotolysis H₂-production system (Benemann, 1996).

Mutant organisms containing hydrogenases that are able to operate at higher O₂ concentrations have been described (Gogotov, 1986; McTavish et al., 1995; Maness et al., 1999), suggesting that the enzyme is amenable to manipulations that may affect its O₂ tolerance. These observations led us initially to investigate several classical genetic approaches to generate and isolate *C. reinhardtii* mutants that can produce H₂ in the presence of O₂. Figure 1 is a summary of these approaches. They involved using random mutagenesis, followed by application of selective pressures under gradually increasing O₂ concentrations. The two selective pressures (McBride et al., 1977; Ghirardi et al., 1996, 1997a, 1997b; Flynn et al., 1999) were based on the reversible activity of the algal hydrogenase, e.g., H₂-production and H₂-uptake. Due to the lack of specificity of the selective pressures, a chemochromic sensor was also developed to allow us to quickly screen the survivors of the selective pressures for H₂-producing clones. Using this combination of mutagenesis, selection and screening, we isolated two generations of H₂-production mutants, 76D4 and 141F2, with, respectively, 4 and 9 times higher tolerance (see later for explanation) to O₂ compared to the WT

parental strain (Flynn et al.,1999; Ghirardi et al., 1999; Seibert et al., in press). We also isolated a H₂-uptake mutant, 104G5, with 13 times higher tolerance to O₂ (Ghirardi et al., 1999; Seibert et al., in press). These results have confirmed the validity of the designed approach for the isolation of the desired phenotype.

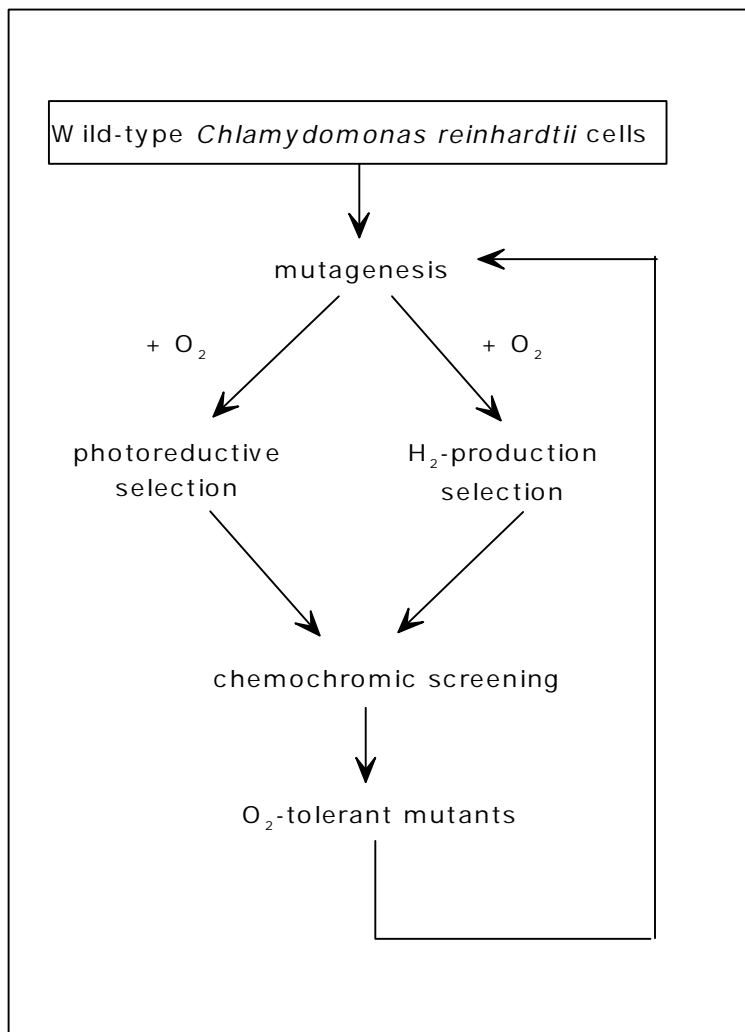


Figure 1. Strategy for the generation of O₂-tolerant algal mutants that produce H₂ under aerobic conditions.

The classical genetics approach described above is the best choice if one is interested in isolating an O₂-tolerant, H₂-producing *organism*, independent of whether the mutation affects the hydrogenase gene or some other gene that confers the same phenotype to the organism. Indeed, genetic crosses involving our different O₂-tolerant mutants in the future will indicate whether more than one locus is involved in the isolated phenotypes. However, if one proposes to generate an O₂-tolerant *hydrogenase* (instead of an O₂-tolerant, H₂-producing *organism*), the ideal approach is site-directed

mutagenesis. The algal hydrogenase has been isolated to purity by Happe and Naber (1993), who also sequenced 24 amino acid residues from the N-terminal portion of the enzyme. However, at this point, the DNA sequence of the gene encoding the hydrogenase enzyme in *C. reinhardtii* has not been reported, and site-directed mutagenesis is not possible at present. We are currently exploring two techniques to clone the algal hydrogenase gene. The first one, RT-PCR (reverse transcriptase polymerase chain reaction), is based on the specific amplification of nucleic acid sequences upon introduction of primers that hybridize to the desired gene. The second technique utilizes insertional mutagenesis, followed by screening for mutants that have lost the capacity to photoevolve H₂. This procedure depends on the insertion of a tagged plasmid in the *Chlamydomonas* genome, which interrupts genes at random. Using the chemochromic sensor, we can pick out those clones in which the plasmid interrupts genes required for photoevolution of H₂. Using the tag in the plasmid, one can then recover sequences of the interrupted gene near the plasmid insertion site and use this information to further sequence the gene. Our expectation is that either of the techniques will lead us to cloning the hydrogenase gene, which in turn will allow us to use molecular biology techniques to specifically target the hydrogenase gene for changes in O₂-tolerance.

Materials and Methods

Cell Growth

Wild-type (WT) *C. reinhardtii* (137c⁺) was a gift from Prof. S. Dutcher, Washington University, St. Louis, MO. Algal cells were grown photoautotrophically in basal salts (BS) (Flynn et al., 1999), a modification of Sueoka's high salt medium (Harris, 1989) that includes citrate to prevent salt precipitation during autoclaving. This medium can be solidified with 1.5% w/v agar and amended with 0.5 g/l yeast extract (Difco) for plates, and may be supplemented with 10 mM sodium acetate depending on the experiment. Liquid cultures were grown under continuous cool white fluorescent lamp illumination (70 E·m⁻²·s⁻¹ PAR) at 25°C and agitated on a shaker. Cells were harvested by centrifugation at 2000 x g for 10 min and resuspended in liquid BS medium.

Mutagenesis

Liquid BS medium (550 ml) was inoculated with 20 ml of mid-log phase cells to give an initial density of 4.9 x 10⁴ cells/ml. The culture was grown overnight under cool white fluorescent illumination (70 μE·m⁻²·s⁻¹) and then sparged with 2% CO₂ in air (50 ml/min). A filter-sterilized stock solution of 5-bromouracil (dissolved in BS) was then added to the culture to a final concentration of 1 mM. The culture was incubated under the same conditions for another 72 h, at which point the cells were harvested, washed, and resuspended in 50 ml of BS medium. Liquid cultures from 5BU mutagenesis were grown in the light as above for at least 7 days before submitting them to H₂-uptake selective pressure.

H₂-Uptake Selection Procedure

Liquid cultures of mutagenized algal cells (250 ml, 2.8×10^5 cells/ml) in BS were treated with 15 μ M each of DCMU and atrazine, and the flasks were placed in anaerobic jars. The gas phase contained 16.5% H₂, 2% CO₂, 30% O₂, and balanced with Ar. The cultures were grown for a couple of weeks with stirring and illuminated with fluorescent light (70 $\text{E}\cdot\text{m}^{-2}\cdot\text{s}^{-1}$ PAR). At the end of the selection period, the cells were washed with BS medium and revived in liquid BS medium plus 10 mM sodium acetate.

Chemochromic screening

Individual colonies surviving mutagenesis and selection were transferred to square petri dishes that can easily accommodate an 8 x 8 colony matrix and a square chemochromic sensor (Seibert et al., in press). Following a 7-14 day growth period, the agar plates were made to go anaerobic overnight, to order to induce the algal hydrogenase and then pre-exposed to 21% O₂ for different periods of time in the dark to deactivate any remaining WT phenotype. The plates were immediately transferred to an anaerobic glove box, the sensor applied, and the colonies illuminated for 3 minutes to photoevolve H₂. At the end of the illumination period, the sensors were analyzed for the location of blue dots, corresponding to the algal colonies that still evolved H₂ following the O₂ pretreatment. The identified clones were then transferred from the original plate to liquid BS + 10 mM acetate and were cultivated for further characterization.

H₂-Evolution Assays

Anaerobic Induction

Mid-log phase algal cells were harvested to give 200 μ g/ml Chl in phosphate buffer (Ghirardi et al., 1997b) supplemented with 15 mM glucose and 0.5% v/v ethanol. Concurrently, an enzymatic oxygen-scrubbing system (Packer and Cullingford, 1978) that consisted of 1mg/ml glucose oxidase (Sigma, St. Louis, MO) and 27720 units/ml catalase (Sigma, St. Louis, MO) was prepared, and 2 ml of the enzymatic mixture was dispensed into dialysis tubing (6-8 kD MW cutoff). In an anaerobic glove box, the dialysis bags were added to the cell suspensions in small vials, and the vials were sealed, covered with aluminum foil to ensure darkness, and incubated at room temperature for 4 h. Following this induction treatment, the cell suspensions were kept at 4 °C overnight and assayed for H₂-evolution activity using either the light-Clark electrode or the dark methyl viologen/gas chromatography assay.

Light – Clark Electrode assay (L-CE)

MOPS buffer (50 mM, pH 6.8) was added into a water-jacketed chamber (a 2.5 ml volume held at 25° C) and equipped with two Clark electrodes (YSI 5331, Yellow Springs, OH), one poised for the measurement of H₂ and the other for O₂ production (Ghirardi et al., 1997b). The O₂ concentration in the cuvette was set to the desired initial concentration by bubbling with Ar, 200 μ l of anaerobically induced cell suspension was injected into the buffer, and the cells were exposed to the pre-set O₂

concentrations for two minutes in the dark. Some respiratory oxygen consumption did take place in the dark, so that the O₂ concentration was not absolutely constant over time. Following O₂ deactivation, the cell suspension was illuminated (320 E m⁻² s⁻¹, PAR incandescent light filtered through 1% CuSO₄) for three minutes. The initial rates of H₂ production were plotted as a function of initial O₂ concentration.

Methyl Viologen-Gas Chromatography assay (MV-GC)

The assay reaction consisted of exposing the anaerobically-induced cells to various levels of O₂ for two minutes, re-establishing anaerobiosis, and adding reduced methyl viologen to serve as the electron donor to the hydrogenase. The reaction mixtures were incubated in the dark for 15 minutes at 30°C in a shaking water bath. The reaction was then stopped by the addition of trichloroacetic acid, and the presence of H₂ was detected by gas chromatography.

Results and Discussion

In the past, we used ethyl-methane sulfonate (EMS) to generate random mutants of *C. reinhardtii*, from which we isolated first (76D4) and second generation (141F2) H₂-production mutants (Ghirardi et al., 1999; Flynn et al., 1999; Seibert et al., in press). We also used 5-bromouracyl (5-BU) to generate another population of mutants, from which the first generation H₂-uptake 104G5 mutant was isolated (Ghirardi et al., 1999; Seibert et al., in press). These results are shown in Figure 2.

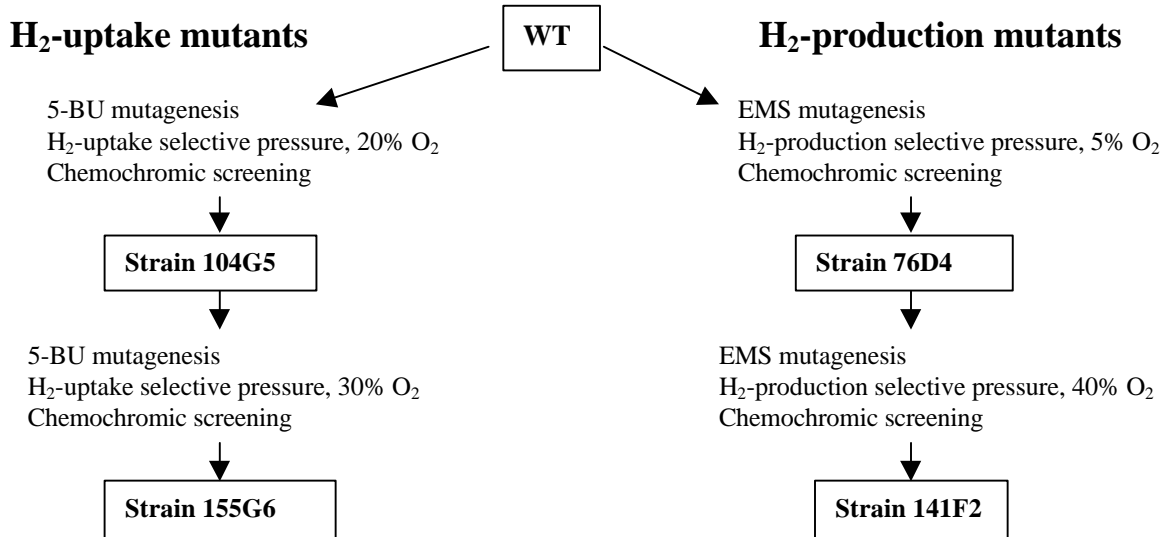


Figure 2. Histories of the different algal strains used in our past and current work.

In order to further improve the O₂-tolerance of the 104G5 mutant, we re-mutagenized it with 5-BU and re-submitted the resulting mutant population to H₂-uptake selective pressure. Selection was done

in the presence of 30% O₂, conditions that are more stringent than those used to isolate the 104G5 mutant (20% O₂). The survivors from this selective pressure were then chemochromically screened, following inactivation by O₂. Clones that produced the best signal during the screening procedure were characterized in a more detailed manner as described below. The best mutant was strain 155G6, as indicated in Fig.2.

Measurements of the O₂ tolerance of all of the isolated clones was done by determining an O₂ I₅₀ for H₂ evolution, that is, the concentration of O₂ added to the gas phase that inhibited the rate of algal H₂ evolution by half of the value measured in the absence of inactivation by O₂ (Ghirardi et al. 1996, 1997, 1997b, 1998; Seibert et al. 1998). Rates of H₂ evolution were measured by either of two techniques: (i) polarographically with a Clark-type electrode, poised for the detection of light-induced H₂ evolution (L-CE) or (ii) by gas chromatography, using dark-reduced, methyl-viologen-induced H₂ evolution (MV-GC). In the past, the validity of data obtained from the L-CE measurement assay had been questioned, due to the consumption of the added O₂ by the O₂-scrubbing enzymes present in the sample suspension. Since then, we have modified the assay by separating the O₂-scrubbing system from the sample by using a dialysis membrane (see Anaerobic Induction in the Materials and Methods Section). The two assays are described in detail in the Materials and Methods Section. Figure 3 shows the O₂ I₅₀s, of the different mutants that we have isolated thus far, determined by both of the assays.

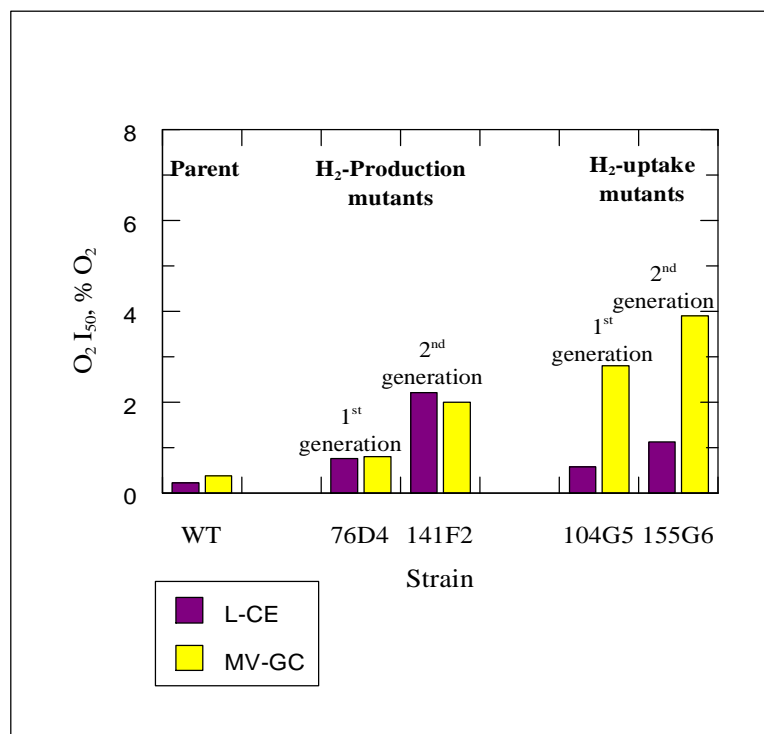


Figure 3 . Estimates of O₂ I₅₀s determined for each of the 4 isolated O₂-tolerant algal mutants. The O₂ I₅₀s were determined by two types of assays, as indicated.

It is clear from Fig. 3 that the two assays give different O₂ I₅₀ values for the H₂-uptake mutants, but same values for the WT strain and H₂-production mutants. Moreover, the segregation of the O₂-scavenging enzymes in a dialysis bag does not seem to have changed the estimated O₂ I₅₀ values (Ghirardi et al., 1999; Flynn et al., 1999; Seibert et al., in press), suggesting that the inactivation of the enzyme by O₂ must be a process that occurs as soon as the enzyme comes in contact with O₂. Given the different nature of the two assays (see above), it appears that the H₂-uptake mutants, besides their tolerance to some O₂, are also able to reactivate their O₂-inhibited hydrogenase enzyme once the O₂ is removed and a reductant is added (as is done in the MV/GC assay). This trait may have given the cells an advantage during the application of the H₂-uptake selective pressure, if the initial dark starvation period was not long enough to deprive the cells of all their internal metabolic reserves. In this case, when the mixture of H₂/CO₂/O₂ is added, the cells will initially respire the added O₂ and only then will shift to a H₂ consumption mode. This situation would be repeated each time the gases are replaced, until the cells run out of substrate for respiration. Evidently, mutants with a hydrogenase that is reactivated more quickly in the presence of a reductant, following consumption of added O₂, will start metabolizing H₂/CO₂ for their metabolism more rapidly (and thus outgrow the competitors).

Conclusions

Based on their responses to the removal of O₂ and addition of reductants to the assay, we conclude, at least on a preliminary basis, that the observed O₂-tolerant phenotypes of the H₂-production mutants were probably caused by mutations affecting the hydrogenase enzyme only, while the phenotypes of the O₂-uptake mutants could be explained by either a hydrogenase mutation or mutations affecting other genes. For example, it is possible that the H₂-uptake mutations involve the activation of protective mechanisms that shield the WT hydrogenase from O₂, such as changes in membrane permeability to O₂. Also, it is conceivable that some of the O₂-tolerance phenotypes are due to an increase in the activity of the chloroplast O₂-scavenging system. We find, however, that it is not necessary to invoke mutations in other genes to explain the phenotype of all of our mutants. These phenotypes could all be due to single point mutations in the hydrogenase gene, that improve its tolerance to O₂, since previous work (McTavish et al., 1995) demonstrates that single amino acid changes can improve the O₂ tolerance of hydrogenases from non-photosynthetic organisms. Future work will be necessary to clarify this point.

Acknowledgements

We are grateful to Dr. T. Flynn, a former post-doctoral fellow for generating the mutants described in this work. The work was supported by the U.S. DOE Hydrogen Program.

References

- Benemann, J. 1996. "Hydrogen Biotechnology: Progress and Prospects". *Nature Biotechnol.* 14:1101-1103.
- Flynn, T., M.L. Ghirardi and M. Seibert. 1999. "Isolation of *Chlamydomonas* Mutants with Improved Oxygen-Tolerance". In *Division of Fuel Chemistry, 1999 ACS Meeting, New Orleans, LA*, vol. 44, pp. 846-850.
- Gaffron, H. and J. Rubin. 1942. "Fermentative and Photochemical Production of Hydrogen in Algae". *J. Gen. Physiol.* 26:219-240.
- Ghirardi, M.L., S. Markov and M. Seibert. 1996. "Development of an Efficient Algal H₂-Producing System". In *Proceedings of the 1996 U.S. DOE Hydrogen Program Review*, 285-302, NREL/CP-430-21968.
- Ghirardi, M.L., T. Flynn, S. Markov and M. Seibert. 1997a. "Development of an Efficient Algal H₂-Producing System". In *Proceedings of the 1997 U.S. DOE Hydrogen Program Review*, 11-24, NREL/CP-430-23722.
- Ghirardi, M.L., R.K. Togasaki and M. Seibert. 1997b. "Oxygen Sensitivity of Algal H₂-Production". *Appl. Biochem. Biophys.* 63-65:141-151.
- Ghirardi, M.L., T. Flynn, M. Forestier and M. Seibert. 1998. "Development of an Efficient Algal H₂-Producing System". In *Proceedings of the 1998 U.S. DOE Hydrogen Program Review*, 43-60, NREL/CP-570-25315.
- Ghirardi, M.L., T. Flynn, M. Forestier and M. Seibert. 1999. "Development of an Efficient Algal H₂-Producing System". In *Proceedings of the 1999 U.S. DOE Hydrogen Program Review*, 16-29, NREL/CP-570-26938.
- Gogotov, I.N. 1986. "Hydrogenases of Phototrophic Microorganisms". *Biochimie* 68:181-187.
- Happe, T. and J.D. Naber. 1993. "Isolation, Characterization and N-terminal Amino Acid Sequence of Hydrogenase from the Green Alga *Chlamydomonas reinhardtii*". *Eur. J. Biochem.* 214:475-481.
- Harris, E.H. 1989. *The Chlamydomonas Sourcebook*, Academic Press, New York.
- Maness, P.-C. and P.F. Weaver. 1999. "Biological H₂ from Fuel Gases and from H₂O". In *Proceedings of the 1999 U.S. DOE Hydrogen Program Review*, 111-124, NREL/CP-570-26938.
- McBride, A.C., Lien, S., Togasaki, R.K. and San Pietro, A. 1977. "Mutational Analysis of *Chlamydomonas reinhardtii*: Application to Biological Solar Energy Conversion". In *Biological Solar Energy Conversion* (A. Mitsui et al., eds.), Academic Press, New York.

McTavish, H., L.A. Sayavedra-Soto and D.J. Arp. 1995. "Substitutions of *Azotobacter vinelandii* Hydrogenase Small-Subunit Cysteines by Serines Can Create Insensitivity to Inhibition by O₂ and Preferentially Damages H₂ Oxidation over H₂ Evolution". *J. Bacteriol.* 177:3960-3964.

Packer, L. and W. Cullingford. 1978. "Stoichiometry of H₂ Production by an *in vitro* Chloroplast, Ferredoxin, Hydrogenase Reconstituted System". *Z. Naturforsch.* 33c, 113-115.

Schulz, R. 1996. "Hydrogenases and Hydrogen Production in Eukaryotic Organisms and Cyanobacteria". *J. Mar. Biotechnol.* 4:16-22.

Seibert, M. T. Flynn, D. Benson, E. Tracy and M. Ghirardi. 1998. "Development of Selection and Screening Procedures for Rapid Identification of H₂-Producing Algal Mutants with Increased O₂ Tolerance". In *Biohydrogen* (O. Zaborsky et al., eds.), Plenum Press, New York, p. 227-234.

Seibert, M., T. Flynn and M. Ghirardi. "Strategies for Improving Oxygen Tolerance of Algal Hydrogen Production". In *Biohydrogen 99*, in press.

TWO-PHASE PHOTOBIOLOGICAL ALGAL H₂-PRODUCTION SYSTEM

**Maria L. Ghirardi, Sergey Kosourov, Anatoly Tsygankov and Michael Seibert
National Renewable Energy Laboratory
1617 Cole Blvd.
Golden, CO 80401**

Abstract

Continuous production of large volumes of H₂ by algal cells has been achieved by depleting the cells of sulfur (Melis et al., 2000). The operation of this novel algal H₂-production system occurs in the light with acetate-supplemented medium. Investigations are under way to simplify the system and determine the metabolic pathways involved in the process.

Current year results include the observation that: (i) depletion of nutrients other than sulfur will also inactivate O₂ evolution but at slower rates, (ii) light and acetate are required for rapid inactivation of O₂ evolution, suggesting an energy-dependent process, and (iii) inhibitors of Photosystem II also inhibit H₂ evolution, indicating that residual water-oxidation activity is an important source of reductant for H₂ production.

An automated photobioreactor experimental system was also developed at NREL. We report the design being used and the parameters found important to monitor sulfur deprivation. The automated system will be utilized in the future to measure the effect of a variety of parameters on the H₂-evolution activity of sulfur-depleted cells.

Introduction

Microbial H₂ photoevolution is catalyzed either by nitrogenases or hydrogenases, enzymes that can only function under anaerobic conditions due to their extreme sensitivity to O₂. Since O₂ is a by-product of photosynthesis, nitrogenase-containing organisms have developed the following spatial and temporal strategies to protect the enzyme from inactivation by O₂: (a) heterocyst-containing cyanobacteria physically

separate O₂ evolution from nitrogenase activity by segregating oxygenic photosynthetic activity in vegetative cells and nitrogenase activity in heterocystis with reduced O₂-permeability (Fay, 1992) and (b) non-heterocystous cyanobacteria separate O₂-evolution from nitrogenase activity by performing these functions during, respectively, light and dark periods (Bergman et al., 1997).

Similar strategies cannot be found in phototrophic hydrogenase-containing organisms in nature. In order to sustain H₂ production by green algae in the light, researchers have used a variety of methods to keep the cultures free of O₂. These include addition of O₂ scavengers such as chromous chloride (Healey, 1970) or dithionite (Randt and Senger, 1985), or purging the cultures with inert gases such as nitrogen (Gfeller and Gibbs, 1984) or helium (Greenbaum et al., 1999). Benemann (1996) has advocated the use of the principle of temporal separation of H₂ and O₂ evolution in green algae (“indirect biophotolysis”), triggered by an unspecified reversible inactivation of Photosystem II (PSII) O₂-evolution activity. In his proposed model, H₂ photoevolution in the absence of PSII would require the break-down of starch to provide reductants for Photosystem I (PSI) through the chlororespiratory pathway. These reductants would then be used by ferredoxin to reduce protons to H₂, in a reaction catalyzed by the hydrogenase enzyme. Based on his proposal, we identified and used sulfur depletion to reversibly inactivate PSII (Melis et al., 2000), achieving apparent temporal separation of O₂ and H₂ evolution in the green alga *Chlamydomonas reinhardtii*. In the absence of sulfur and in the presence of acetate, the cells shut off most (but not all) of their O₂-evolving activity, respire all measurable remaining O₂ in a closed environment, and induce the expression of the hydrogenase enzyme. At this point, they can evolve H₂ in the light for up to 4 days. Subsequently, if sulfur is added back to the cultures, they will recover PSII activity and return to a normal growth mode. Cycles of O₂ and H₂ production can be repeated at least 3 times without significant loss of activity. Our results also showed that protein degradation, rather than starch breakdown, correlated with H₂ production by the algal cells. The rates of H₂ evolution by our system were much lower than its potential for electron transport (Melis et al., 2000), suggesting that the system is being limited by some factor other than enzyme activity. Possible limitations include: (a) the rate of substrate degradation, (b) redox control of the rate of electron transport by reducing conditions, (c) limited supply of electrons from residual water oxidation, and (d) competition between the hydrogenase and other physiological pathways.

Currently, both light and acetate are present during the H₂-production phase. However, the development of a commercial system for algal H₂ production using sulfur-depleted cells will require the elimination of superfluous nutrients and/or procedures to bring down the cost. Light is required for H₂ evolution. Acetate, however, is not consumed during the time in which H₂ is actually produced, and is thus not necessary for that step (Melis et al., 2000). In the current report, we have examined the requirement for light and acetate during the O₂-inactivation phase, before H₂ evolution commences. We also examined the effect of inhibiting the residual water oxidation activity (using DCMU) on the H₂-evolution activity of the sulfur-depleted cells. Finally, we present initial results on a new automated photobioreactor system that can continuously monitor 5 key parameters in algal cultures during sulfur-depletion treatment.

Materials and Methods

Cell Growth and Sulfur Depletion

Wild-type *C. reinhardtii* C137⁺ cells were initially grown photoheterotrophically in Tris-acetate-phosphate (TAP) medium, pH 7, and bubbled with 3% CO₂ in air at about 25° C. The photobioreactors consisted of flat bottles with stirring capability and placed under continuous cool-white fluorescent illumination at about 100-200 E m⁻² s⁻¹. The cultures were grown to late log phase, harvested by centrifugation, washed three times in TAP minus sulfur medium, and resuspended in 1.2 l of the same medium to a concentration of 11-18 g Chl /ml. The sulfur-depleted cell suspension was placed back in the light for up to 150 h.

Oxygen and Hydrogen Evolution Measurements

Oxygen- and hydrogen-evolution activities of the cultures were measured as previously described (Melis et al., 2000) with two different Clark-type electrodes, each poised for the optimal measurement of each gas.

Gas Collection Measurements

The reactor bottles were fitted with a #25 Ace thread and with smaller side-ports for liquid sampling. A threaded glass stopper with capillaries for gas sampling was fitted with a Viton O-ring and used to seal the reactor. Threaded side-arm and gas sampling ports were sealed with rubber-laminated Teflon septa. Figure 1 shows how teflon tubing (HPLC, Aminco), attached to one of the gas ports, was used to conduct gas evolved by the algae in the culture bottles to an upside-down graduated cylinder filled with H₂O. The gas collection tubing was detached from the culture bottle during liquid and gas sampling to avoid disturbance of gas volume readings in the graduated cylinder.

Results

Effect of depletion of nutrients other than sulfur on inactivation of O₂ evolution

It is known that, besides sulfur, depletion of nutrients such as phosphorus (Wykoff et al., 1998) or nitrogen (Kumazawa and Mitsui, 1981) from the medium also inactivates the photosynthetic O₂-evolution activity of algae. However, inactivation by phosphorus depletion is slower than that by sulfur (Wykoff et al., 1998). We investigated the effect of depleting algal cultures of nutrients other than sulfur on the rate of inactivation of PSII activity. Figure 2 (left side) shows the half-life for inactivation of O₂ evolution from algal

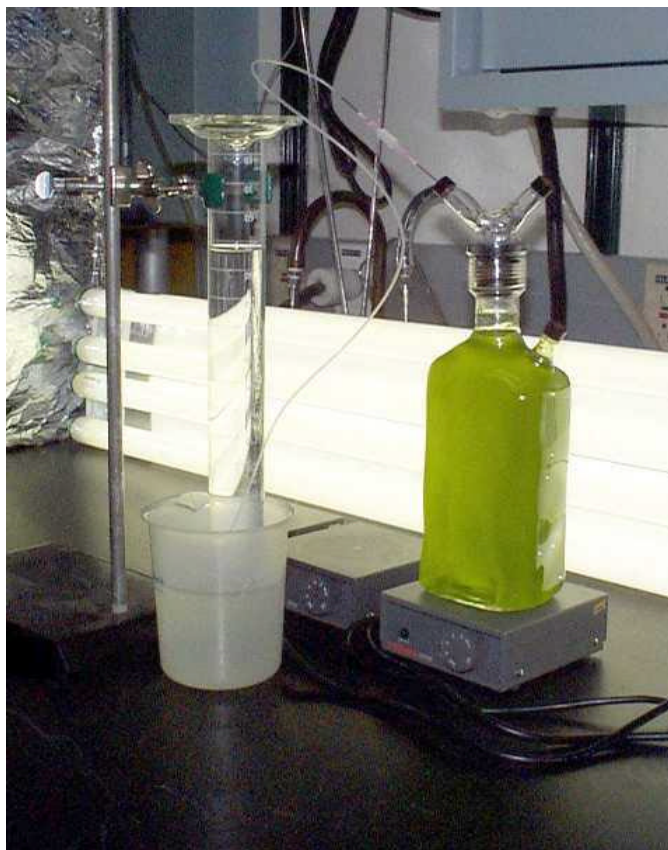


Figure 1. Photobioreactor for algal H₂-production and system for gas collection

cultures resuspended in media depleted of different nutrients. It is clear that PSII can be inactivated by removing either S, Fe, or Mn from the medium. However, the inactivation is 3 to 4 times faster when sulfur is removed. Figure 2 also shows the effect of combining sulfur depletion with Fe or Mn depletion. The combined depletions do not result in faster inactivation of O₂ evolution, and gave similar rates of subsequent H₂ production (not shown).

Effect of light and acetate on inactivation of O₂ evolution

We also investigated the need for both acetate and light during inactivation of O₂ evolution. The right side of Figure 2 shows that both acetate and light accelerate the inactivation of PSII. In the presence of acetate but in the dark (D+A), the cultures are inactivated two times slower than in the light; in the absence of acetate but in the light (L-A), inactivation takes four times as long. These results support the notion of an energy-dependent protease contributing to the inactivation of O₂ evolution. Energy-dependent proteases are involved in specific inactivation of various proteins in *E. coli* and other

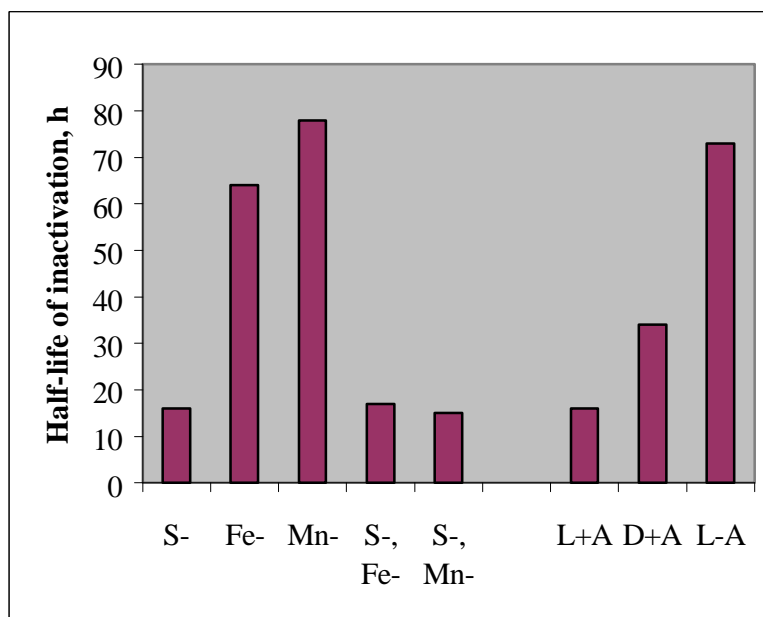


Figure 2. Effect of different nutrient and light parameters on the rate of inactivation of O₂ evolution.

organisms (Wilson et al., 2000; Wang et al., 1999; Hilliard et al., 1998; Laachouch et al., 1996).

Source of reductant for H₂ evolution

Sulfur depletion for 24 h inhibits more than 90% of the O₂-evolution activity in algal cells (Melis et al., 2000). Our previous observation that protein consumption alone could potentially provide the reductant needed for the amount of H₂ evolved by sulfur-depleted algal cells seemed to indicate that at least some of the reductant for H₂ evolution originated from protein degradation. However, given that the subsequent rate of H₂ evolution is only 10% of the capacity of electron transport chain (based on the O₂ evolution rate measured at the beginning of the sulfur-deprivation experiment), it is also possible that the electrons used to reduce protons to H₂ come from residual PSII activity. In order to test this idea, we added DCMU, a specific inhibitor of PSII activity, to the algal cultures following onset of H₂ evolution. This treatment resulted in inhibition of about 80% of the rate of H₂ evolution, suggesting that most of the reductant required for H₂ production by the algal hydrogenase originated from residual water-oxidation activity.

Automated Photobioreactor Experimental System

We have developed an automated system that allows us to continuously monitor a series of physical and electrochemical parameters in our sulfur-depleted, algal H₂-production system, as shown in Figure 3. Preliminary experiments showed that pH, eH (redox

potential), pO_2 (dissolved O_2), temperature, and quantity of evolved gas are important parameters to record.

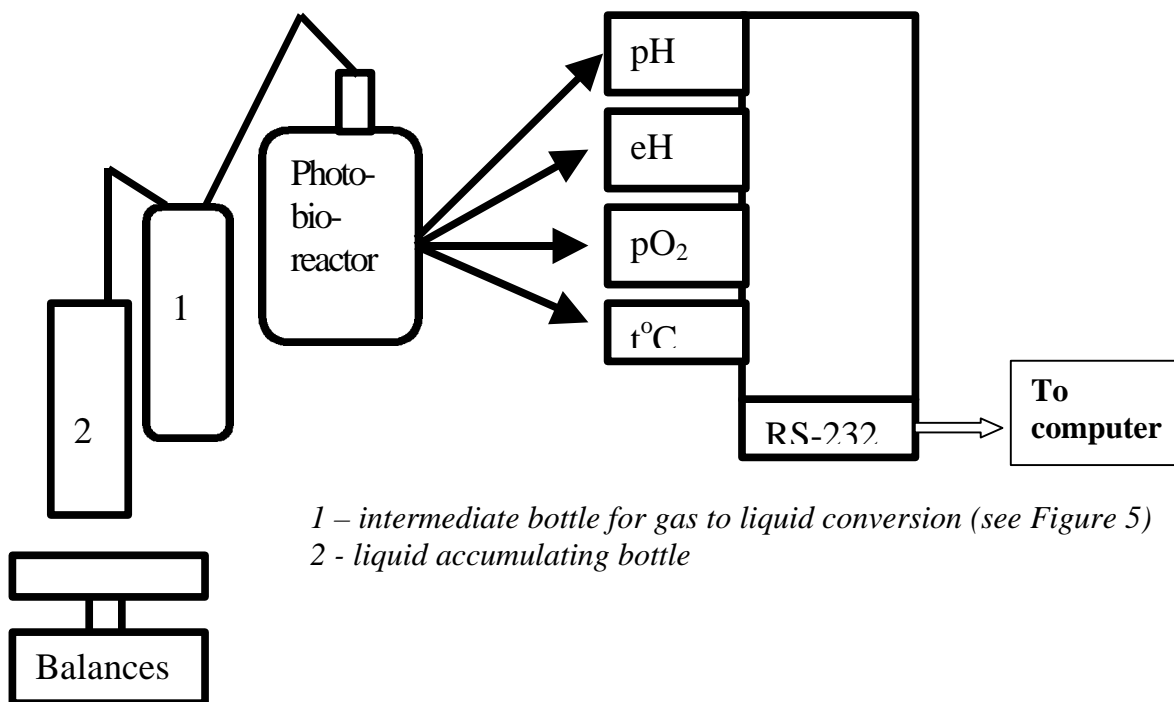


Figure 3. Schematic of an automated system to monitor algal H_2 -production

In order to test this design, photobioreactors with additional ports for each of the sensors were fabricated. Each photobioreactor has 3 ports for the sensors, one for culture sampling or chemical injection, and one for gas outlet, as shown in Figure 4.

The method adopted for gas-to-liquid volume conversion is described in Figure 5. It consists of an intermediate bottle (bottle 1 in Fig. 3) full of water that collects the gas evolved by the photobioreactor cultures. The collected gas displaces the liquid in the intermediate bottle, which in turn is syphoned to a second bottle (bottle 2 in Fig. 3). Bottle 2 is located on an electronic balance. The changes in the weight of bottle 2 are a measure of the rate of gas evolution by the algal cultures. We found that the inside diameter of the connecting tubes had to be no less than 0.5 mm, otherwise the time response of the system was excessively high. This type of gas-to-liquid conversion and measurement system is temperature and pressure sensitive but under properly controlled conditions gives an error of less than 3%.

Finally, an integrated microprocessor system that simultaneously monitors four separate algal culture vessels was assembled, according to the schematic shown in Figure 6.

Preliminary experiments have been conducted in order to confirm consistent changes in all the monitored parameters in all four vessels (not shown).

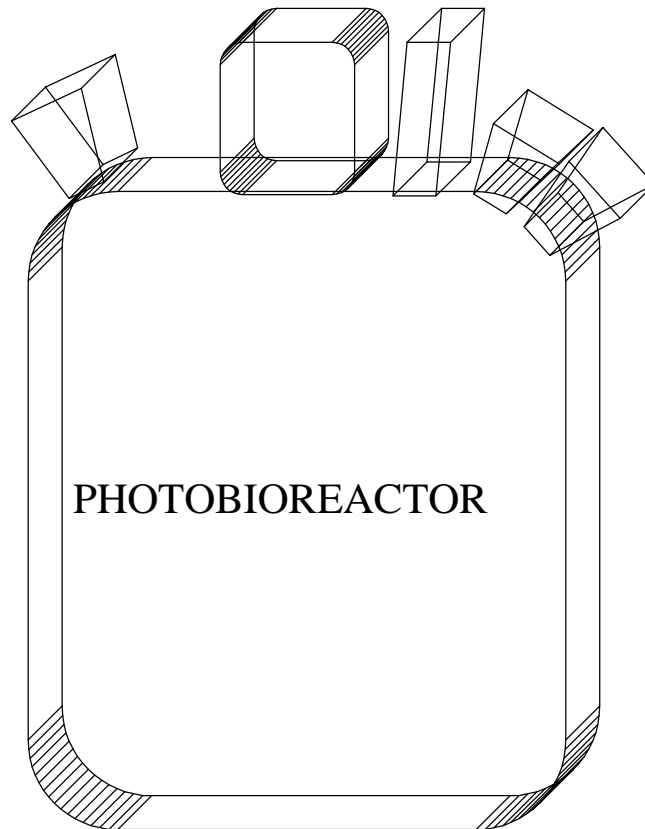


Figure 4. Design of a photobioreactor for the automated algal H₂-production system.

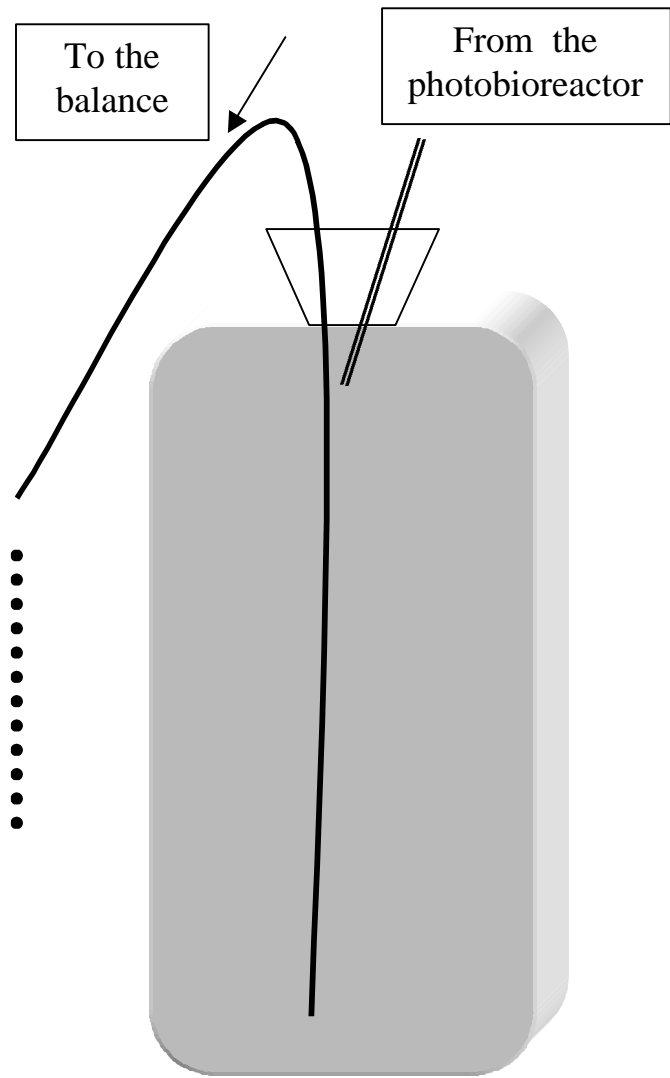


Figure 5. Vessel for gas-to-liquid conversion.

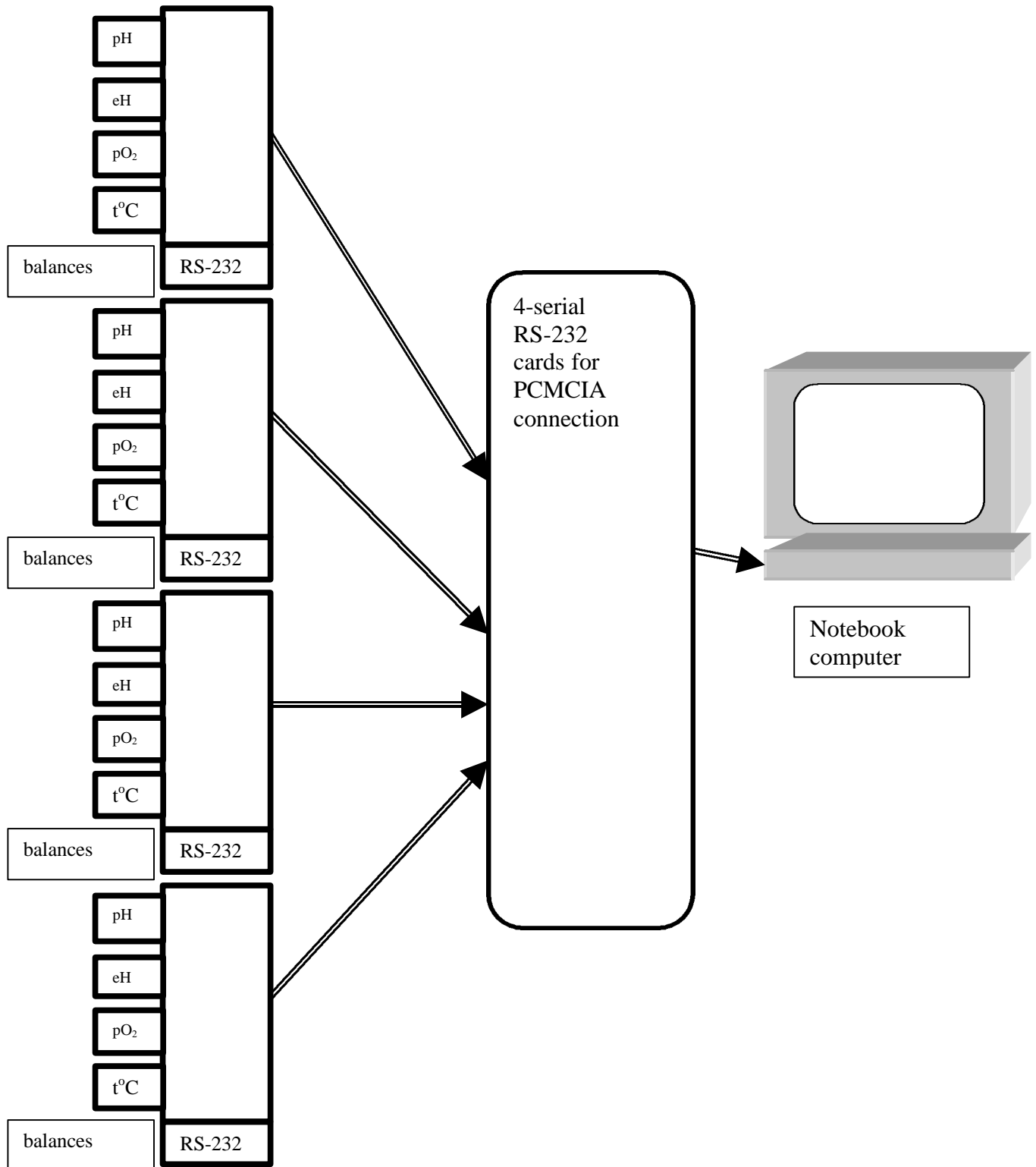


Figure 6. Schematic of an integrated system for simultaneously monitoring five parameters from four photobioreactors in an algal H₂-production system.

Summary and Conclusions

Since algal H₂ photoproduction from water was discovered almost 60 years ago (Gaffron and Rubin, 1942), H₂ could be collected only if O₂, produced by photosynthesis, was removed continuously by chemical or mechanical means. Earlier this year, we described a physiological method (sulfur depletion) to reversibly inactivate O₂-evolution activity in an algal culture; this inactivation leads to the induction of hydrogenase activity and subsequent production of large quantities of H₂ for 3-4 days (Melis et al., 2000). We now report that, while depletion of a number of other nutrients besides sulfur can also inactivate O₂-evolution, their rate of inactivation is slower (Fig. 2). We also provide evidence that this inactivation must involve energy-dependent proteases (Fig. 2), since it occurs much more slowly in the dark and/or in the absence of acetate. Finally, we present preliminary evidence suggesting that residual water-oxidation activity may be the source of most of the reductant for the H₂ evolution process (Fig. 3). Clearly, much more detailed work will be required to clarify the metabolic pathways involved in the process, and the inter-relationship between H₂ evolution and protein degradation.

Even without a clear knowledge of all the pathways involved in the transport of reductant to hydrogenase in sulfur-depleted cells, it is evident that H₂ production can be sustained for up to 4 days (Melis et al., 2000). Moreover, the system can be recycled back and forth between photosynthetic growth and H₂ production (data not shown). This algal H₂-production system does not seem to be a pure “indirect biophotolysis” system, as proposed by Benemann (1996). Indeed, it is similar in concept to systems in which photosynthetically-produced O₂ is removed by addition of O₂ scavengers or by purging with neutral gases. The significant difference is that sulfur-depleted cells operate with only 10% of their normal oxygenic PSII activity, while previous systems (listed in Table I), presumably operate with 100% functional PSII. Nevertheless, this does not seem to make a large difference in terms of the actual rates of steady-state H₂ production, as shown in Table I. Indeed, sulfur-depleted cells produce H₂ at rates comparable to systems in which 100% of the PSII are operational, with the additional advantage that O₂ is removed by physiological means, not by the introduction of extraneous chemical reductants or inert gases.

Up until now, only nitrogenase-based systems were capable of sustained H₂ photoproduction without expensive O₂-removal systems (Benemann, 1996). Indeed, cyanobacteria, in the absence of fixed nitrogen sources can produce H₂ for months, particularly if their uptake hydrogenase activity is concomitantly inactivated (Markov et al., 1996). Table II shows a comparison of the rates of H₂ production by a variety of nitrogenase-containing cyanobacteria, and our sulfur-depleted algal system. Given the different pigment composition of cyanobacteria and green algae, we show the data on a per mg dry weight basis. The sulfur-depleted algal cells evolve H₂ at rates higher than most optimized cyanobacterial systems. This is not surprising, given that nitrogenases are known to be sluggish enzymes that, besides reductants, require ATP.

Table I. Comparison of Rates and Volumes of H₂ Collected from Different Algal Systems and Methods Used to Sustain High H₂ Evolution Rates

| Organism | Initial rate (moles H ₂ mg Chl ⁻¹ h ⁻¹) | Steady-state rate (moles H ₂ mg Chl ⁻¹ h ⁻¹) | Total volume H ₂ collected | Culture volume and Chl content |
|--|--|---|---|--------------------------------------|
| <i>Chlamydomonas moewusii</i> (Healey, 1970) | - | 5 [chromous chloride]* | - | - |
| <i>Chlamydomonas reinhardtii</i> F60 (Gfeller & Gibbs, 1984) | - | 5.7 [N ₂ purging] | 0.25 ml in 3.5 h | 0.3 mg Chl in 3 ml |
| <i>Scenedesmus obliquus</i> (Randt & Senger, 1985) | 54 | 13 [Na dithionite] | - | - |
| <i>Chlamydomonas reinhardtii</i> (Greenbaum, personal communication) | 50 | 10 [He purging] | | |
| <i>Chlamydomonas reinhardtii</i> (this work) | 90 | 10 [Sulfur depletion] | 325 ml in 95 h | 18 mg Chl in 1 liter |

* Values in brackets indicate the means by which O₂ was removed from the cultures.

Table II. Comparison of the Rates of H₂ Evolution among Different Nitrogenase-Based Systems and our Sulfur-Depleted Green Algal System.

| Organism | Rate of H ₂ evolution (ml mg dry weight ⁻¹ d ⁻¹) | Reference |
|---|---|---------------------------|
| <i>Anabaena cylindrica</i> | 0.09-0.03 | Miyamoto et al., 1979 |
| <i>Oscillatoria</i> sp. Miami BG7 | 0.14 | Kumazawa and Mitsui, 1981 |
| <i>Anabaena variabilis</i> (no uptake hydrogenase) | 0.22 | Markov et al., 1996 |
| Sulfur-depleted <i>Chlamydomonas reinhardtii</i> | 0.34 | This work |

In conclusion, we have shown that green algae can produce significant amounts of bulk H₂ gas at rates comparable to other oxygenic photosynthetic organisms, when their O₂-evolving capability is reduced by physiological means. Hydrogen production depends on the depletion of sulfur from the medium, is reversible, and results in the generation of pure H₂ (co-evolved CO₂ stays in solution). We are currently investigating in more detail the metabolic pathways involved in the evolution of H₂ under sulfur-depletion conditions.

Acknowledgements

We would like to acknowledge a very fruitful collaboration with Prof. A. Melis, University of California, Berkeley, CA, and with Drs. E. Greenbaum and J. Lee, Oak Ridge National Laboratory, Oak Ridge, TN. This work was supported by the U.S. DOE Hydrogen Program.

References

- Benemann, J. 1996. "Hydrogen Biotechnology: Progress and Prospects". *Nature Biotechnol.* 14:1101-1103.
- Bergman, B., J.R. Gallon, A.N. Rai and L.J. Stal. 1997. "N₂ fixation by Non-Heterocystous Cyanobacteria". *FEMS Microbiol. Rev.* 19: 139-185.
- Chen, Z.Y., M.D. Burow, C.B. Mason and J.V. Moroney. 1996. "A Low-CO₂-Inducible Gene Encoding an Alanine -Ketoglutarate Aminotransferase in *Chlamydomonas reinhardtii*". *Plant Physiol.* 112: 677-684.
- Fay, P. 1992. "Oxygen Relations of Nitrogen Fixation in Cyanobacteria". *Microbiol. Rev.* 56: 340-373.
- Gaffron, H. and J. Rubin. 1942. "Fermentative and Photochemical Production of Hydrogen in Algae". *J. Gen. Physiol.* 26: 219-240.
- Gfeller, R.P. and M. Gibbs. 1984. "Fermentative Metabolism of *Chlamydomonas reinhardtii*. 1. Analysis of Fermentative Products from Starch in Dark and Light". *Plant Physiol.* 75: 212-218.
- Greenbaum, E. 1982. "Photosynthetic Hydrogen and Oxygen Production: Kinetic Studies". *Science* 196: 879-880.
- Healey, F.P. 1970. "The Mechanism of Hydrogen Evolution by *Chlamydomonas moewusii*". *Plant Physiol.* 45: 153-159.
- Hilliard, J.J., Simon, L.D., Van Melderren, L. and M.R. Maurizi. 1998. "PinA Inhibits ATP Hydrolysis and Energy-Dependent Protein Degradation by Lon Protease". *J. Biol. Chem.* 273: 524-527.

Kumazawa, S. and A. Mitsui. 1981. "Characterization and Optimization of Hydrogen Photoproduction by a Saltwater Blue-green Alga, *Oscillatoria sp.* Miami BG7. I. Enhancement through Limiting the Supply of Nitrogen Nutrients". *Int. J. Hydrogen Energy* 6: 339-348.

Laachouch, J.E., L. Desmet, V. Geuskens, R. Grimaud and A. Tooussaint. 1996. "Bacteriophage Mu Repressor as a Target for the *Escherichia coli* ATP-Dependent Clp Protease". *The EMBO J.* 15: 437-444.

Markov, S., P.F. Weaver and M. Seibert. 1996. "Hydrogen Production using Microorganisms in Hollow-Fiber Bioreactors". *Hydrogen Energy Progress XI*, Proceedings of the 11th World Hydrogen Energy Conference, Stuttgart, Germany, 23-28 June 1996 (ed. T.N. Verziroglu et al.), Vol. 3, 2619-2624, Schon & Wetzell GmbH, Frankfurt am Main, Germany.

Melis, A., L. Zhang, M. Forestier, M.L. Ghirardi and M. Seibert. 2000. "Sustained Photobiological Hydrogen Gas Production upon Reversible Inactivation of Oxygen Evolution in the Green Alga *Chlamydomonas reinhardtii*". *Plant Physiol.* 122: 127-136.

Miyamoto, K., P.C. Hallenbeck and J.R. Benemann. 1979. "Solar Energy Conversion by Nitrogen-Limited Cultures of *Anabaena cylindrica*". *J. Ferment. Technol.* 57: 287-293.

Randt, C. and H. Senger. 1985. "Participation of the Two Photosystems in Light Dependent Hydrogen Evolution in *Scenedesmus obliquus*". *Photochem. Photobiol.* 42: 553-557.

Wang, L., M. Elliott and T. Elliott. 1999. "Conditional Stability of the HemA Protein (Glutamyl-tRNA Reductase) Regulates Heme Biosynthesis in *Salmonella typhimurium*". *J. Bacteriol.* 181: 1211-1219.

Wilson, H.L., M.S. Ou, H.C. Aldrich and J. Maupin-Furlow. 2000. "Biochemical and Physical Properties of the *Methanococcus jannaschii* 20S Proteasome and PAN, a Homolog of the ATPase (Rpt) Subunits of the Eucaryal 26S Proteasome". *J. Bacteriol.* 182: 1680-1692.

Wykoff, D.D., J.P. Davies, A. Melis and A.R. Grossman. 1998. "The Regulation of Photosynthetic Electron Transport during Nutrient Deprivation in *Chlamydomonas reinhardtii*". *Plant Physiol.* 117: 129-139.

DISCOVERY OF AN ALTERNATIVE OXYGEN SENSITIVITY IN ALGAL PHOTOSYNTHETIC H₂ PRODUCTION

James Lee and Elias Greenbaum
Oak Ridge National Laboratory
Chemical Technology Division
Oak Ridge, TN 37831-6194

Abstract

Characterization of O₂-tolerance in H₂-producing photosynthetic organisms is essential to the development of this renewable energy source, since application of green algae for H₂ production is confronted with the problem of oxygen sensitivity. During current reporting period, we observed a new oxygen sensitivity in *Chlamydomonas reinhardtii* that is clearly distinct from the oxygen sensitivity of the hydrogenase. This distinct O₂ sensitivity indicates that there is an alternative electron transport pathway that can take electrons away from the hydrogenase-catalyzed H₂ production pathway to O₂. Our experiments demonstrated that this alternative mechanism is more sensitive to O₂ than the oxygen sensitivity of the hydrogenase. These findings redefine the meaning of “oxygen tolerance” in algal H₂ production. Future work will focus on mapping this alternative electron transport pathway and on developing a technique to control this pathway to enhance the production of H₂.

Introduction

Algal photosynthetic hydrogen (H_2) production is a potential future clean energy resource. In green algae, photoevolution of H_2 and O_2 occurs in the same cell where the photosynthetically produced O_2 can inhibit the production of H_2 .¹ Therefore, application of green algae for H_2 production is confronted with the problem of oxygen sensitivity. In the past, this O_2 -sensitive phenomenon was generally interpreted as the O_2 -inhibition effect on hydrogenase activity.² During this reporting period, we discovered that this classic interpretation of O_2 sensitivity needs to be revised. In our recent experiments that characterized O_2 -tolerance in H_2 -producing wild-type *Chlamydomonas reinhardtii*, we observed a new oxygen sensitivity that is clearly distinct from the oxygen sensitivity of the hydrogenase. This distinct O_2 sensitivity indicates that there is an alternative electron transport pathway that can take electrons away from the hydrogenase-catalyzed H_2 production pathway to O_2 . Our experiments demonstrated that this alternative mechanism is more sensitive to O_2 than the oxygen sensitivity of the hydrogenase. Therefore, these findings represent an important progress in algal H_2 production studies. This paper reports the detailed experimental results.

Materials and Methods

In our recent O_2 -tolerance assays, we discovered a new oxygen sensitivity that is an alternative to the oxygen sensitivity of hydrogenase in wild-type *Chlamydomonas* strain 137c. The wild-type alga was grown under light intensity of about $20 \mu E \cdot m^{-2} \cdot s^{-1}$ in minimal plus acetate medium. When the culture grew to a cell density of about 10^6 cells/ml, the algal cells were harvested by gentle centrifugation (3000 RPM). It was then washed and re-suspended in fresh minimal medium for O_2 -tolerance hydrogen production assays. The O_2 -tolerance assays were performed under atmospheres of research grade helium (purity >99.9999%, zero oxygen) and 0.1000% O_2 in helium using our unique dual-reactor-flow detection system. The 0.1000% O_2 in helium was a primary standard purchased from Matheson Gases and Equipment, Inc.

As illustrated in Fig. 1, the assays were conducted using a laboratory-built dual-reactor flow detection system.³ For each assay, 35 ml of 137c algal sample ($3 \mu g$ Chl/ml) was placed and sealed in each of the two reactors that are water-jacketed and held at $20^\circ C$ with a temperature controlled water bath (Lauda RM6, Brinkmann Instruments, Germany). The algal sample was then purged by helium flow (50 ml gas /min) through the liquid reaction medium. This helium flow serves two purposes: 1) to remove O_2 from the algal sample to establish and maintain anaerobic condition that are necessary for induction of the algal hydrogenase synthesis and production of H_2 ; and 2) to carry the any H_2 gas product to the hydrogen sensors. After induction of hydrogenase and establishment of steady-state photoevolution of H_2 under the helium atmosphere (it normally took about 8 hr or more), the primary standard 0.1000% O_2 in helium was introduced into the reactors by replacing the pure helium at the same flow rate (50 ml/min) to characterize the oxygen sensitivity of photoevolution of H_2 . The actinic illumination at $120 \mu E \cdot m^{-2} \cdot s^{-1}$ (about 6% of the full LED intensity) for the H_2 photoevolution

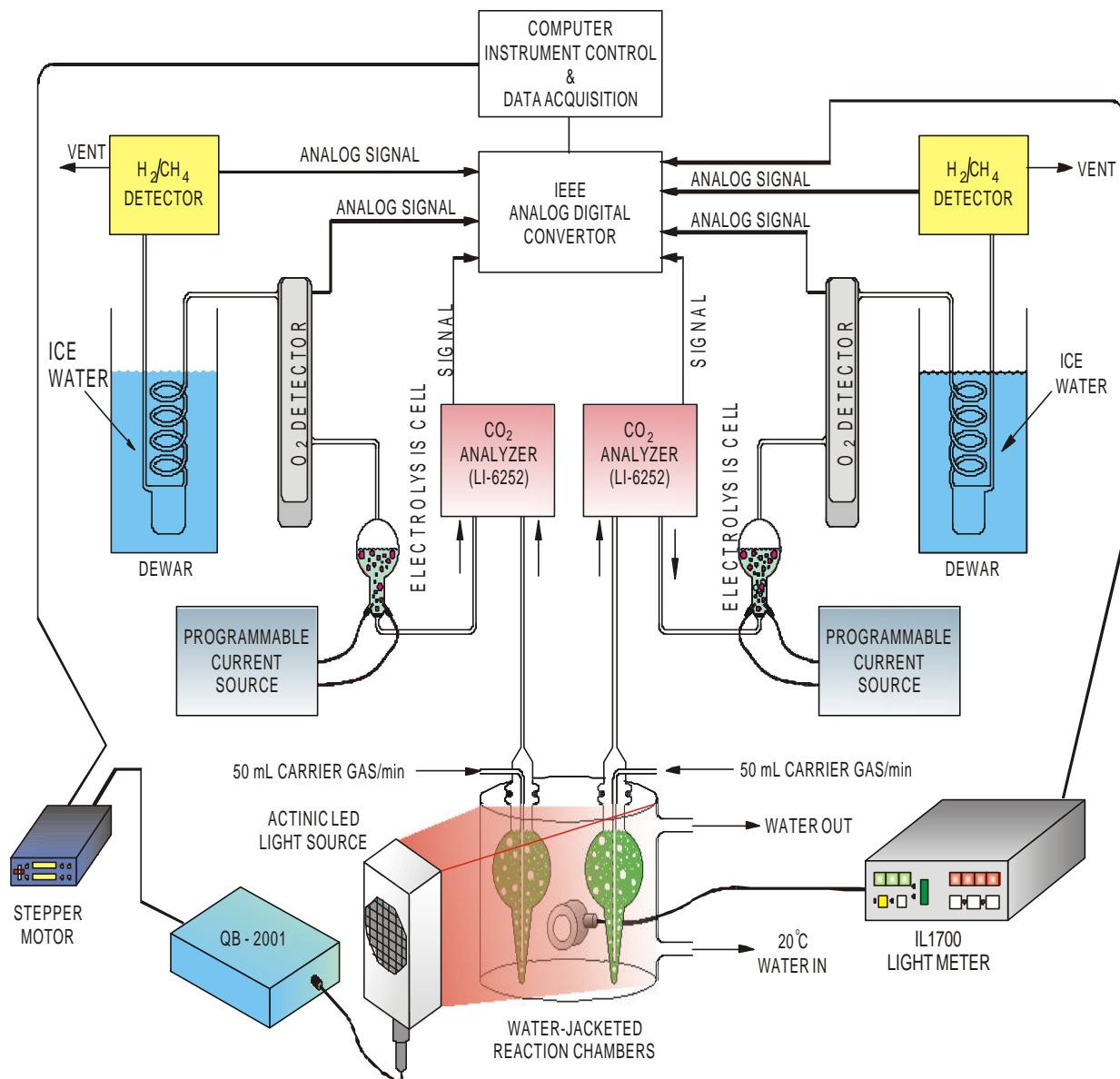


Figure 1. Schematic of a Dual-Reactor Flow Detection System for Simultaneous Detection of CO₂, H₂, and O₂.

assay was provided by an electronically controlled LED light source with its full (100%) intensity of about $2000 \mu\text{E}\cdot\text{m}^{-2}\cdot\text{s}^{-1}$ at 670 nm. The actinic intensity was measured with a IL-1700 light meter. Both the rate of H₂ production and the actinic intensity were recorded simultaneously by a PC computer.

Results and Discussion

The results of the assays are very intriguing. As illustrated in Fig. 2, introduction of 0.1000% O₂ dramatically reduced the rate of algal H₂ photoevolution. The steady-state H₂ production rate in the presence of 0.1000% O₂ was 0.33 : moles H₂ mg chl⁻¹·hr⁻¹ which is only about 2.8% of the full steady-state rate (12 : moles H₂ mg chl⁻¹·hr⁻¹) before the introduction of the 0.1000% O₂. In the past, this type of H₂ production decay was commonly interpreted as the inhibition of O₂ on hydrogenase activity. Our experimental results have now proved that this classic interpretation of oxygen sensitivity on algal H₂ production is not consistent with the data. According to the classic interpretation, the reduction of H₂ production after the introduction of 0.1000% O₂ is due to O₂ inhibition on hydrogenase per se. That is, hydrogenase activity would be the limiting factor for the rate of H₂ photoevolution. If this interpretation were correct, one would expect the rate of H₂ photoevolution to be no higher than the inhibited rate (0.33 : moles H₂ mg chl⁻¹·hr⁻¹) after a brief dark period in the presence of 0.1000% O₂. However, the experimental data turned out to be very different from the classic expectation. As shown in Fig. 2, there was a surge of H₂ photoevolution after a 2-hr dark period in the continued presence of 0.1000% O₂. The peak rate of H₂ photoevolution was about 15 : moles H₂ mg chl⁻¹·hr⁻¹ which is about 45 times higher than the classically predicted rate (0.33 : moles H₂ mg chl⁻¹·hr⁻¹). This assay has now been repeated for more than 6 times. All the assay results were consistent with the observation presented in Fig. 2.

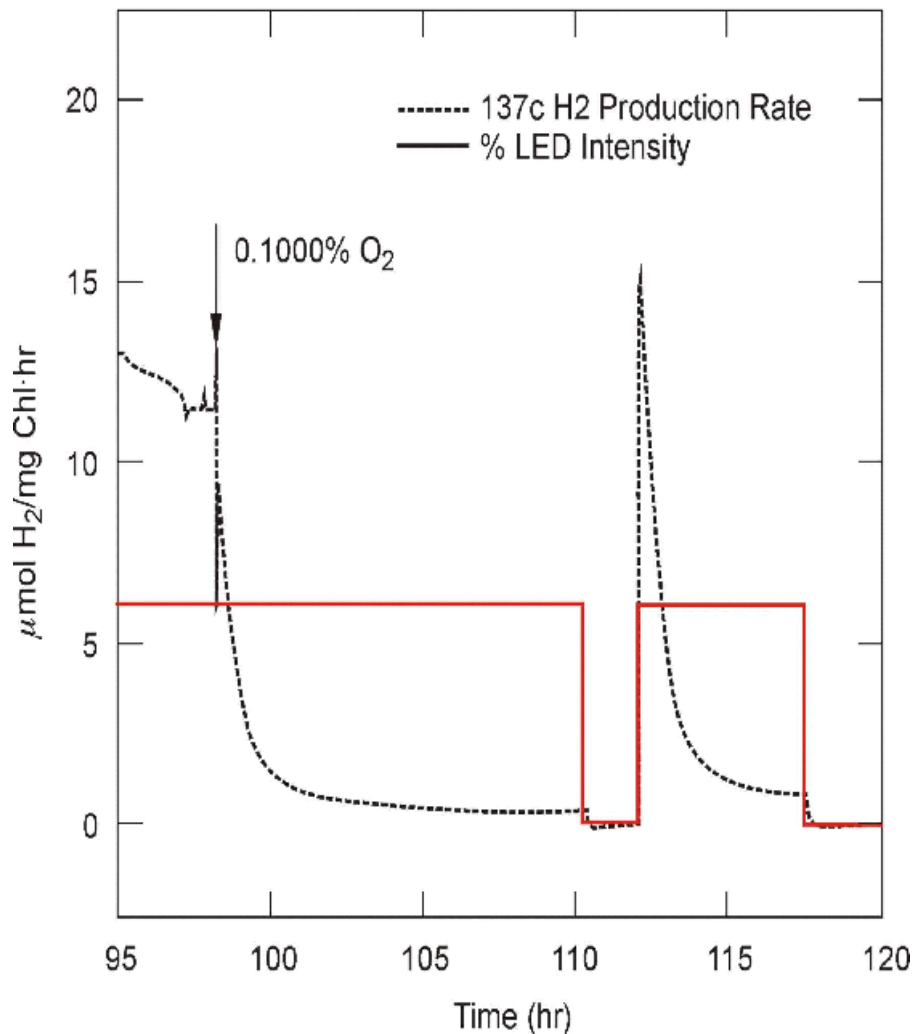


Figure 2. Observation of a new oxygen sensitivity to algal H₂ production in *Chlamydomonas reinhardtii*.

This observation clearly indicated that hydrogenase activity was not the limiting factor for photoevolution of H₂ at this O₂ level. There must be an alternative electron transport pathway that takes the photogenerated electrons away from ferredoxin to O₂. The observed reduction of H₂ production after the introduction of 0.1000% O₂ can be explained by this alternative pathway that competes for electrons with the hydrogenase-catalyzed H₂ production pathway. This is an important discovery since it really redefines the meaning of “oxygen tolerance” in algal H₂ production. Our future work will focus on mapping this alternative electron transport pathway and on developing a technique to control this pathway to enhance the production of H₂.

Acknowledgments

The authors thank S. L. Blankinship for technical support; C. A. Woodward and B. Forbes for culture media preparation; M. K. Savage for editorial assistance; C. D. King and V. W. Purdue for technical illustrations. This research was supported by the U.S. Department of Energy Hydrogen Program, the DOE Office of Science Young Scientist Award (to J. W. Lee), and the Research Institute for Innovative Technology for the Earth. Oak Ridge National Laboratory is managed by UT-Battelle, LLC, for the U.S. Department of Energy under contract DE-AC05-00OR22725.

References

1. Greenbaum, E. and J. W. Lee 1998. “Photosynthetic hydrogen and oxygen production by green algae.” In *BioHydrogen*, Edited by O. R. Zaborsky et al., pp. 235–241. Plenum Press, New York.
2. Ghirardi, M. L., R. K. Togasaki, and M. Seibert 1997. “Oxygen sensitivity of algal H₂-production” *Applied Biochemistry and Biotechnology*, 63-65:141-151.
3. Lee, J.W., S. L. Blankinship, and E. Greenbaum 1995. “Temperature effect on production of hydrogen and oxygen by *Chlamydomonas* cold strain CCMP1619 and wild-type 137c” *Applied Biochemistry and Biotechnology*, 51/52:379-385.

PHOTOSYNTHETIC SOLAR CONVERSION EFFICIENCY IN WILD TYPE AND TRUNCATED Chl ANTENNA TRANSFORMANT (Chl *b*-less MUTANT) OF THE GREEN ALGA *Chlamydomonas reinhardtii*

Juergen E.W. Polle¹, John R. Benemann¹, Ayumi Tanaka², Anastasios Melis¹

¹ Department of Plant and Microbial Biology, 411 Koshland Hall, University of California, Berkeley, CA
94720-3102, USA

² *Permanent Address:* The Institute of Low Temperature Sciences, Hokkaido University,
Sapporo 0600819, Japan

Abstract

The assembly, organization and function of the photosynthetic apparatus was investigated in wild type and a chlorophyll (Chl) *b*-less mutant of the unicellular green alga *Chlamydomonas reinhardtii*, generated via DNA insertional mutagenesis. Comparative analyses were undertaken with cells grown photoheterotrophically (acetate), photomixotrophically (acetate and HCO₃⁻) or photoautotrophically (HCO₃⁻). It is shown that lack of Chl *b* diminished the photosystem-II (PSII) functional Chl antenna size from 320 Chl (*a* and *b*) to about 95 Chl *a* molecules. However, the functional Chl antenna size of PSI remained fairly constant at about 290 Chl molecules, independent of the presence of Chl *b*. Western blot and kinetic analyses suggested the presence of inner subunits of the Chl *a-b* light-harvesting complex of PSII (LHCII) and the entire complement of the Chl *a-b* light-harvesting complex of PSI (LHCI) in the mutant. It is concluded that Chl *a* can replace Chl *b* in the inner subunits of the LHCII and in the entire complement of the LHCI. Growth of cells on acetate as the sole carbon source imposes limitations in the photon use efficiency and capacity of photosynthesis. These are manifested as a lower quantum yield and lower light-saturated rate of photosynthesis, and as a lower variable to maximal (F_v/F_{max}) chlorophyll fluorescence yield ratios. This adverse effect probably originates

because acetate shifts the oxidation-reduction state of the plastoquinone pool, and also because it causes a decrease in the amount and/or activity of Rubisco in the chloroplast. Such limitations are fully alleviated upon inclusion of an inorganic carbon source (e.g., bicarbonate) in cell growth medium. Further, the work provides evidence to show that transformation of green algae can be used as a tool by which generate mutants exhibiting a permanently truncated Chl antenna size and a higher (per Chl) photosynthetic productivity of the cells.

Abbreviations

Chl = chlorophyll; CP24, CP26 and CP29 = chlorophyll proteins of 24, 26 and 29 kDa, respectively; I_s = saturating irradiance; LHC = light harvesting complex; PMSF = phenylmethylsulfonyl fluoride; PSII = photosystem II; PSI = photosystem; PAGE = polyacrylamide gel electrophoresis; SDS = sodium dodecyl sulfate

Introduction

The process of photosynthesis is initiated upon absorption of light energy by pigments in the light-harvesting chlorophyll (Chl) antenna complexes. Two distinct photosystems in the chloroplast of higher plants and green algae possess, in addition to their Chl *a*-containing core antenna, an auxiliary light-harvesting antenna consisting of specific Chl *a*- and Chl *b*-binding light-harvesting proteins (LHC). The light-harvesting Chl-proteins of photosystem I (PSI) and photosystem II (PSII) are encoded for by the large nuclear *Lhc* gene family and are referred to by the LHCI and LHCII abbreviations, respectively (Jansson 1994).

In higher plants, Chl *b* is specifically required for the assembly and function of several LHC proteins. Studies of Chl *b*-less strains of barley (Thornber and Highkin 1974; Harrison and Melis 1992; Harrison et al. 1993; Krol et al. 1995), rice (Terao and Katoh 1989) and *Arabidopsis thaliana* (Murray and Kohorn 1991) revealed that these strains either lack or have significantly lower amounts of LHCII and LHCI in their thylakoid membranes. Therefore, Chl *b*-less mutants of higher plants have a highly truncated auxiliary light-harvesting antenna of PSII and a smaller PSI antenna size (Ghirardi et al. 1986; Harrison et al. 1993; Terao and Katoh 1996). In contrast to higher plants, Chl *b*-less strains of the green alga *Chlamydomonas reinhardtii*, when grown on acetate in the light, appear to contain in their thylakoid membrane all apoproteins of the LHC (Picaud and Dubertret 1986; Allen and Staehelin 1994). However, it was reported that trimeric LHCII does not assemble and that the PSII Chl antenna size is truncated in the Chl *b*-less *C. reinhardtii* (Michel et al. 1983; Picaud and Dubertret 1986; Allen and Staehelin 1994).

The interplay between presence of Chl *b* and source of carbon during cell growth in the regulation of *Lhc* gene expression is not understood. The presence of acetate in the medium of light-grown *C. reinhardtii* is reported to down-regulate transcription of *Lhcb* genes (Kindle 1987). It was also reported that low levels of CO₂ up-regulate the transcription of *Lhc* genes (Somanchi et al. 1998). Therefore, differentially regulated transcription and expression of *Lhcb* genes would be expected when cells are grown under different carbon conditions. Different levels of LHC would affect the Chl antenna size of the photosystems and the photosynthetic

apparatus organization and function, depending on the primary carbon source available during cell growth.

In the present work, we investigated the photochemical apparatus organization and function in *Chlamydomonas reinhardtii* cultivated in the presence of either acetate, a mixture of acetate and bicarbonate, or bicarbonate alone in the growth medium. Since Chl *b*-less mutants of higher plants have been used successfully as model organisms in the study of the assembly of the light-harvesting complex, we extended these studies to include the photochemical apparatus organization and function in a Chl *b*-less mutant of *Chlamydomonas reinhardtii*. This strain was derived via DNA insertional mutagenesis in which the chlorophyll *a* oxygenase gene was affected (Tanaka et al. 1998). The advantage of tagged genetic transformation for the generation of mutants is that genes responsible for a given property can be later isolated. This work shows that it is possible to employ genetic transformation of green algae for the isolation of strains with a truncated Chl antenna size. Our results show that the photochemical apparatus organization and function in *C. reinhardtii* are strongly influenced by the carbon source during cell growth. In addition, we show that the light-harvesting Chl antenna size of PSI and PSII are not affected in the same manner by the absence of Chl *b*.

Materials and Methods

Growth Conditions of the Algae

Chlamydomonas reinhardtii wild type strain *cw15* and the chlorophyll *b*-less mutant *cbs3* (Tanaka et al. 1998) were grown in liquid cultures in flat 1 L Roux bottles at 22°C under continuous illumination at 200 mol photons m⁻² s⁻¹ of cool-white fluorescent light. Cultures were stirred to ensure uniform illumination and to prevent cell settling. Cells were grown to the mid-logarithmic phase either photoheterotrophically in Tris-Acetate-Phosphate medium (TAP, pH 7.0) (Gorman and Levine 1965), photomixotrophically in TAP medium supplemented with 25 mM sodium bicarbonate and 40 mM Tris-HCl, pH 7.4 (TABP medium), or photoautotrophically in modified 40 mM Tris-HCl-phosphate-medium, pH 7.4, supplemented with 25 mM sodium bicarbonate (TBP medium).

Cell Count and Chlorophyll Determination

Cell density was monitored by counting the number of cells per milliliter of culture using a Neubauer ultraplane hemacytometer. Cells or thylakoid membranes were extracted in 80% acetone and debris was removed by centrifugation at 10,000g for 5 min. The absorbance of the supernatant was measured with a Shimadzu UV-160U spectrophotometer. The chlorophyll (*a* and *b*) concentration of the samples was determined according to Arnon (1949), with equations corrected as in Melis et al. (1987).

Thylakoid Membrane Isolation

Cells were harvested by centrifugation at 1,000g for 3 min at 4°C. Pellets were resuspended in 1-2 ml of growth medium and stored frozen at -80°C until all samples were ready for processing. Samples were thawed on ice and diluted with ice-cold sonication buffer containing 50 mM Tricine (pH 7.8), 10 mM NaCl, 5 mM MgCl₂, 0.2% polyvinylpyrrolidone 40, 0.2% sodium ascorbate, 1 mM aminocaproic acid, 1 mM aminobenzamidine and 100 M phenylmethylsulfonylfluoride (PMSF). Cells were broken by sonication in a Branson 250 Cell

Disrupter operated at 4°C for 30 s (pulse mode, 50% duty cycle, output power 5). Unbroken cells and starch grains were removed by centrifugation at 3,000g for 4 min at 4°C. The thylakoid membranes were collected by centrifugation of the supernatant at 75,000g for 30 min at 4°C. The thylakoid membrane pellet was resuspended in a buffer containing 50 mM Tricine (pH 7.8), 10 mM NaCl, 5 mM MgCl₂ for spectrophotometric measurements, or 250 mM Tris-HCl (pH 6.8), 20% glycerol, 7% SDS and 2 M urea for protein analysis. Solubilization of thylakoid membrane proteins was carried out for 30 min at room temperature, a procedure designed to prevent the formation of protein aggregates during denaturation. Samples were centrifuged in a microfuge for 4 min to remove unsolubilized material, -mercaptoethanol was added to yield a final concentration of 10% and the samples were stored at -80°C.

SDS-PAGE and Western blot analysis

Samples were brought to room temperature prior to loading for electrophoresis and diluted accordingly to yield equal Chl concentrations. Gel lanes were loaded with an equal amount of Chl (2 nmol Chl per lane). SDS-PAGE analysis was carried out according to Laemmli (1970), with resolving gels containing 12.5% acrylamide, at a constant current of 9 mA for 16 h. Gels were stained with 1% Coomassie brilliant blue R for protein visualization. Electrophoretic transfer of the SDS-PAGE resolved proteins onto nitrocellulose was carried out for 3-5 h at a constant current of 800 mA, in transfer buffer containing 50 mM Tris, 380 mM glycine (pH 8.5), 20% methanol and 1% SDS. Identification of thylakoid membrane proteins was accomplished with polyclonal antibodies raised against the LHC complex of *Zea mays*, kindly provided by Dr. R. Bassi (Di Paolo et al. 1990; Bassi et al. 1992). Cross-reaction with the antibodies was visualized by a chromogenic reaction with anti Ig-G secondary antibodies conjugated with alkaline phosphatase (BioRad, Hercules, CA) and it was quantified by densitometry. For densitometry, a HP-ScanJet 6100C optical scanner was employed, on-line with a PowerMacintosh/G3 computer. DeskScanII software in combination with Adobe Photoshop were used for scanning of the western blots, whereas NIH Image version 1.6 software was employed for the deconvolution and quantification of the bands.

Chlorophyll Fluorescence, Oxygen Evolution and Spectrophotometric Analyses

The initial (F_0), variable (F_v) and maximum (F_{max}) chlorophyll fluorescence yield of intact cells was measured at 690 nm (combination of CS 2-60, CS 2-64 Corning and 690 nm interference filter). Actinic excitation of the cultures was provided by green light (CS 4-96 and CS 3-69 Corning Filters, intensity of 75 mol photons m⁻² s⁻¹) (Melis and Hart 1980). For these measurements an aliquot from the culture was incubated in the dark for 10 min prior to the measurement and the chlorophyll fluorescence was recorded in the absence or presence of DCMU (2.5 M final concentration).

Oxygen evolution activity of the cultures was measured at 22°C with a Clark-type oxygen electrode illuminated with a slide projector lamp. Yellow actinic excitation was provided by a CS 3-69 Corning cut-off filter in combination with an Ealing 35-5453 VIQ5-8 filter. An aliquot of 5 ml cell suspension (2 M Chl) was transferred to the oxygen electrode chamber. To ensure that oxygen evolution was not limited by the carbon source available to the cells, 100 l of 0.5 M sodium bicarbonate solution (pH 7.4) was added to the suspension prior to the oxygen evolution measurements. Measurement of the light-saturation curve of photosynthesis was implemented with the oxygen electrode, beginning with the registration of dark respiration in the cell suspension, and followed by measurements of the rate of oxygen evolution in steps at 36, 70,

140, 260, 360, 500, 620, 1,750 and 2,600 mol photons m⁻² s⁻¹. Registration of the rate (slope) of oxygen evolution at each light intensity step was recorded for about 2.5 min.

The concentration of the photosystems in thylakoid membranes was estimated spectrophotometrically from the amplitude of the light *minus* dark absorbance difference signal at 700 nm (P700) for PSI, and 320 nm (Q_A) for PSII (Melis and Brown 1980). The functional light-harvesting Chl antenna size of PSI and PSII was measured from the kinetics of P700 photo-oxidation and Q_A photoreduction, respectively (Melis 1989).

Results

Organization of the Photosynthetic Apparatus in Wild Type and Chl *b*-less Mutant

C. reinhardtii cells of the wall-less strain *cw15* (referred to as the wild type in this work) showed a Chl *a*/Chl *b* ratio of 2.7:1 when grown in the presence of acetate as the sole carbon source (Table 1).

Table 1. Chlorophyll content and Chl *a*/Chl *b* ratios in wild type (*cw 15*) with the Chl *b*-less mutant of *C. reinhardtii*. Values represent means ±SD.

| Parameter | wild type | | | Chl <i>b</i> -less | | |
|---------------------------------------|-----------|---------|----------|--------------------|---------|---------|
| | TAP | TABP | TBP | TAP | TABP | TBP |
| Chl <i>a</i> / Chl <i>b</i> | 2.7±0.14 | 3.2±0.2 | 3.0±0.12 | - | - | - |
| mol Chl/cell (x10 ⁻¹⁵) | 3.5±1.1 | 2.4±0.1 | 2.4±0.5 | 3.6±0.6 | 4.0±0.6 | 3.8±1.1 |

When grown in the presence of a mixture of acetate and bicarbonate (TABP medium), or bicarbonate alone (TBP medium), the Chl *a*/Chl *b* ratio of the cells was slightly higher to about 3.1:1. Table 1 also shows the Chl content of the wild type cells under the three growth conditions. The Chl content of the cells was slightly lower when the growth medium contained bicarbonate (TABP or TBP media) than acetate alone (TAP). In the Chl *b*-less mutant, the Chl content of the cells did not change as a function of the growth medium. Interestingly, and in spite of the lack of Chl *b*, the Chl content of the mutant was relatively high compared to the wild type. This result suggests a higher chloroplast concentration of PSI and PSII units in the mutant than in the wild type (see below).

Table 2 presents the thylakoid membrane content in Q_A (PSII) and P700 (PSI). Quantitation of the functional PSII and PSI reaction centers was obtained from the light-induced absorbance change at 320 (Q_A) and 700 nm (P700), respectively (Melis and Brown 1980).

Table 2. Photochemical apparatus characteristics of wild type and Chl *b*-less strain of *C. reinhardtii* (n = 3-5).

| Parameter | wild type | | | Chl <i>b</i> -less | | |
|--|-----------|-----------|-----------|--------------------|----------|----------|
| | TAP | TABP | TBP | TAP | TABP | TBP |
| Q _A / total Chl (mmol:mol) | 1.83±0.06 | 2.76±0.23 | 2.86±0.09 | 3.0±0.27 | 3.1±0.03 | 4.1±0.6 |
| P700/ total Chl (mmol:mol) | 2.14±0.13 | 1.87±0.1 | 1.63±0.17 | 3.1±0.24 | 2.3±0.08 | 2.2±0.16 |
| Q _A / cell (mol/cellx10 ⁻¹⁸) | 6.4 | 6.6 | 6.9 | 10.8 | 12.4 | 15.6 |
| P700 / cell (mol/cellx10 ⁻¹⁸) | 7.5 | 4.5 | 3.9 | 11.2 | 9.2 | 8.4 |
| PSII / PSI | 0.86 | 1.48 | 1.75 | 0.97 | 1.35 | 1.86 |

The wild type contained about 1.8 mmol Q_A per mol Chl in the TAP grown cells, a value that increased to about 2.8 mmol Q_A per mol Chl when bicarbonate was present in the growth medium. The wild type had about 2.1 mmol P700 per mol Chl in the TAP-grown cells, a value that decreased to about 1.9 (TABP) and about 1.6 mmol P700 per mol Chl in the TBP-grown cells. Translated on a per cell basis, the concentration of Q_A was fairly constant and at about 6.6x10⁻¹⁸ mol Q_A/cell, independent of the carbon source (Table 2). However, the amount of PSI was substantially lower in the TABP and TBP-grown cells. The dissimilar dependence of PSII (Q_A) and PSI (P700) content on the carbon source during cell growth made for substantially different PSII/PSI ratios in the thylakoid membrane of these samples. A wild type PSII/PSI ratio of 0.86:1 in TAP increased to 1.48:1 in TABP and was 1.75:1 in TBP. Interestingly, a quantitatively and qualitatively similar dependence of the PSII/PSI ratio was also observed in the Chl *b*-less mutant (Table 2).

Table 2 also shows that, on a per cell basis, the Q_A and P700 contents in the Chl *b*-less mutant were greater (by a factor of about 2) than those in the wild type, irrespective of the carbon source during growth. These results are consistent with the higher Chl content in mutant vs. wild type (Table 1) and show that a truncated Chl antenna size in the mutant may have been compensated by a correspondingly higher density of PSI and PSII units in the mutant thylakoids. The results in Table 2 further suggest that, irrespective of the photosynthetic apparatus pigment content, the PSII/PSI ratio is highest when the cells are grown in the presence of bicarbonate (TBP medium) and that growth in acetate (TAP) tends to suppress the functional PSII/PSI ratio. The effect of the mutation on the functional Chl antenna sizes of PSII and PSI was further addressed in detail (see below).

Photosystem Chlorophyll Antenna Size

Estimates of the functional Chl antenna sizes of PSI and PSII were obtained with the so-called kinetic and spectrophotometric method (Melis and Anderson 1983). In this approach, Chl molecules are functionally assigned to PSI and PSII in direct proportion to the rate of light

absorption/utilization by the two photosystems, measured from the kinetics of P700 oxidation and Q_A reduction in isolated and DCMU-poisoned thylakoids (Melis 1989).

Figure 1 (left panels) shows examples of light-induced changes in the absorbance of the reaction center P700 at $\lambda = 700$ nm, occurring as a result of P700 photooxidation in thylakoid membranes of wild type and the Chl *b*-less mutant grown on TAP. Fig. 1 (right panels) shows the respective semilogarithmic plots of the A_{700} kinetics, revealing single exponential functions of time with rate constants K_{PSI} of 9.0 s^{-1} for wild type and 7.5 s^{-1} for the Chl *b*-less mutant. The slower P700 photooxidation kinetics for the Chl *b*-less mutant suggests a slightly smaller PSI Chl antenna size than in the wild type.

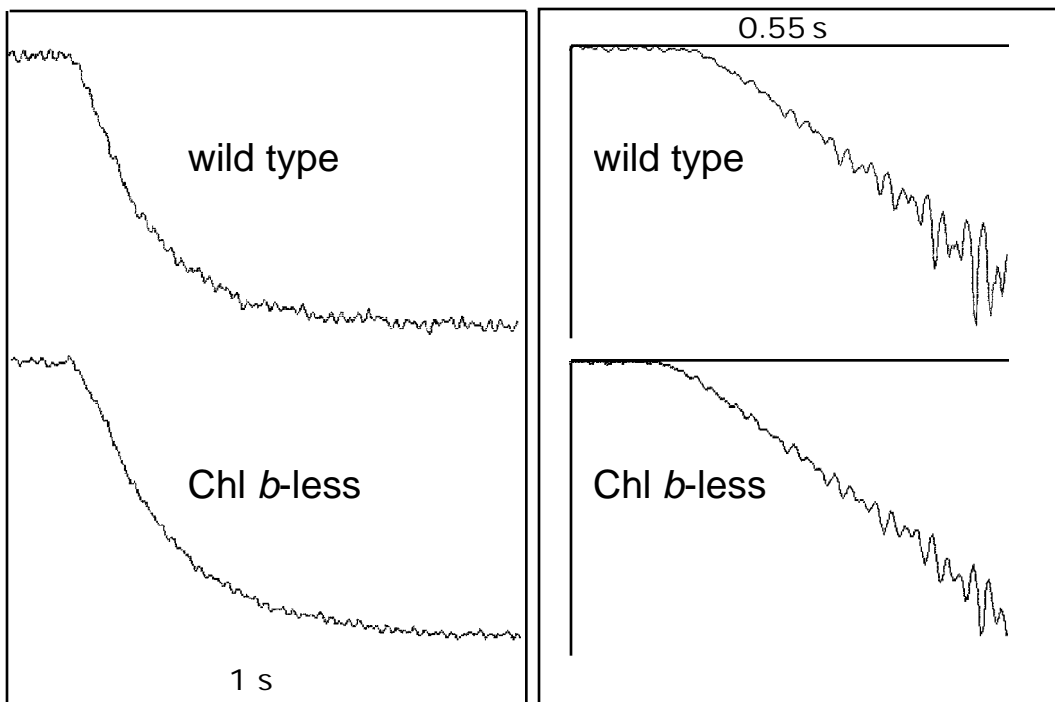


Figure 1 - Light-induced absorbance change measurements. (Left panel) Kinetics of P700 photooxidation(A_{700}) with thylakoid membranes of wild type and a Chl *b*-less mutant of *C. reinhardtii*. Upper trace, wild type; lower trace, Chl *b*-less mutant. (Right panel) Corresponding semilogarithmic plot of the A_{700} kinetics.

Figure 2 (left panels) shows examples of light-induced fluorescence induction kinetics, the variable part of which reflects the photoreduction of Q_A (Melis and Duysens 1979) in the thylakoid membranes of wild type and the Chl *b*-less mutant grown on TAP.

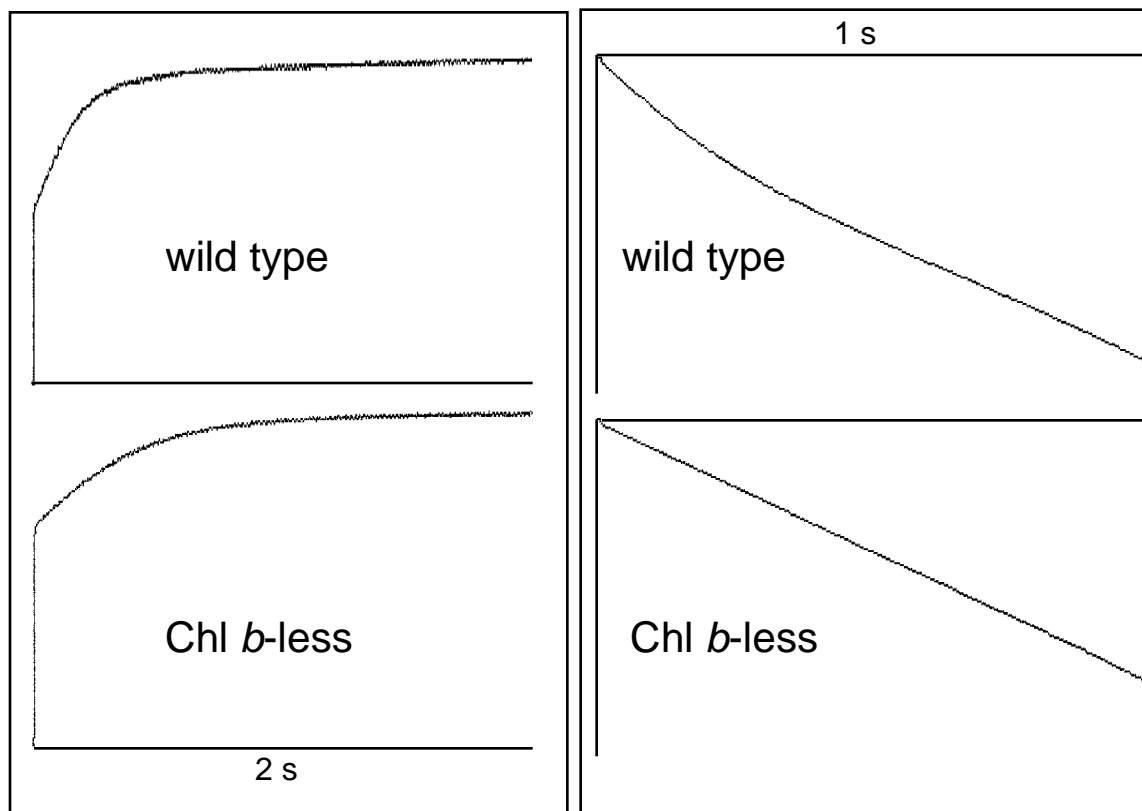


Figure 2 - Chlorophyll fluorescence induction kinetics. (Left panel) Chl fluorescence induction traces of wild type (upper) and a Chl *b*-less mutant (lower). (Right panel) Corresponding semilogarithmic plots of the area over the fluorescence induction curve.

The fluorescence induction kinetics of the wild type strain were faster than those of the Chl *b*-less mutant, suggesting a larger PSII Chl antenna size for the former. Fig. 2 (right panels) shows the respective semilogarithmic plots of the area over the fluorescence induction kinetics. This parameter (area over fluorescence) is directly proportional to the amount of Q_A that becomes photoreduced (Melis and Duysens 1979, Melis 1989). The analysis (Fig. 2, right panels) revealed biphasic Q_A reduction kinetics for the wild type, reflecting a PSII heterogeneity and the existence of two populations of PSII (PSII₁ and PSII₂) with significantly different Chl antenna sizes (Melis 1991, Lavergne and Briantais 1996). In the Chl *b*-less mutant, Q_A photoreduction occurred as a single exponential function of time with significantly slower kinetics, suggesting lack of PSII heterogeneity and the occurrence of a uniform and small Chl antenna size for the mutant (Ghirardi et al. 1986).

From the measured kinetics of P700 photooxidation and “area over fluorescence induction” we determined the functional chlorophyll antenna size of PSI and PSII, respectively, for the wild type and Chl *b*-less mutant (Table 3).

Table 3. Chlorophyll antenna sizes of PSII and PSI in wild type and Chl *b*-less mutant. The concentration of the various forms of PSII is given as a % of total PSII in the thylakoid membrane. The antenna size of PSII and PSI is given as the number of Chl molecules functionally associated with a photosystem. The value of N_{PSII} in parenthesis (325) is based on the assumption of PSII /PSII = 50:50. The values given are the mean \pm SD.

| Parameter | wild type | | | Chl <i>b</i> -less | | |
|---------------------|--------------|---------------|-----------------------|--------------------|-------------|--------------|
| | TAP | TABP | TBP | TAP | TABP | TBP |
| PSII | 42 \pm 7.4 | 53 \pm 10.5 | 29 \pm 9.5 | - | - | - |
| PSII | 58 \pm 7.4 | 47 \pm 10.5 | 72 \pm 9.5 | - | - | - |
| $N_{(\text{PSII})}$ | 322 \pm 7 | 284 \pm 49 | 474 \pm 49 (325) | - | - | - |
| $N_{(\text{PSII})}$ | 127 \pm 3 | 141 \pm 3 | 119 \pm 3 | - | - | - |
| $N_{(\text{PSII})}$ | | | | 93 \pm 3 | 107 \pm 9 | 88 \pm 7 |
| $N_{(\text{PSI})}$ | 291 \pm 17 | 217 \pm 8 | 204 \pm 4 | 245 \pm 14 | 284 \pm 6 | 289 \pm 12 |

In wild type grown in the presence of acetate (TAP and TABP), PSII accounted for about 50% of the total PSII, whereas it accounted for only about 30% of the total PSII in cells grown in the presence of bicarbonate as the sole carbon source (TBP). Table 3 also shows values for the respective functional Chl antenna sizes N of the photosystems. In wild type grown with TAP or TABP, PSII contained about 300 Chl (*a* and *b*) ($N_{\text{PSII}} = 300 \pm 28$), whereas PSII contained about 130 Chl molecules ($N_{\text{PSII}} = 130 \pm 11$). PSII Chl antenna size for the samples grown on TBP ($N_{\text{PSII}} = 474 \pm 49$) was significantly larger than that of the other growth media. However, the larger Chl antenna size, along with the relatively smaller fraction of PSII centers in these samples, suggests a dissociation of PSII centers from the statistical pigment bed of the LHClI normally associated with PSII (Melis and Duysens 1979), leaving behind a peripheral light-harvesting Chl antenna to be shared by fewer PSII centers. This dissociation could be an artifact occurring during the isolation of the thylakoid membranes. Indeed, if one assumed a PSII /PSII ratio of about 50:50 in the TBP samples, then the calculated Chl antenna size of PSII (N_{PSII}) would be about 325 Chl molecules, i.e., similar to that of cells grown on TAP or TABP. On the basis of this assumption, it would appear that the average PSII functional Chl antenna size (N_{PSII}) is fairly constant and independent of the carbon source in the growth medium. In the wild type, the PSI Chl antenna size appeared to decline somewhat from $N_{\text{PSI}} = 291 \pm 17$ in the TAP-grown cells to $N_{\text{PSI}} = 204 \pm 4$ in the cells grown in TBP media.

In contrast to the wild type, PSII in the Chl *b*-less mutant did not display Chl antenna size heterogeneity, a characteristic also seen in the Chl *b*-less mutant of barley (Ghirardi et al. 1986). The PSII Chl antenna size in the mutant ($N_{\text{PSII}} = 96 \pm 10$) was substantially smaller compared to that of the wild type. However, at about 96 Chl *a* molecules per reaction center, it is significantly larger than the minimum Chl antenna size of the PSII-core, which is known to contain only about 37 Chl *a* molecules (Manodori et al. 1984, Glick and Melis 1988). This difference suggests that, in the Chl *b*-less *C. reinhardtii* mutant, a number of the auxiliary LHC proteins are assembled and functionally associated with the PSII-core complex.

Surprisingly, the PSI Chl antenna size in the Chl *b*-less mutant ($N_{\text{PSI}} = 245\text{-}290$ Chl *a* molecules per reaction center) was essentially as large as that of the wild type. Thus, the absence of Chl *b* appears not to have had a pronounced effect on the Chl antenna size of PSI, irrespective of the growth conditions (Table 3). This observation suggests that LHCI in *C. reinhardtii* assembles fully and functions normally in the total absence of Chl *b*. It may be concluded that Chl *a* can effectively substitute for Chl *b* in the LHCI of this green alga.

LHC Polypeptide Composition in Wild Type and Chl *b*-less Mutant

The analysis of the functional Chl antenna size in the Chl *b*-less mutant suggested a significant presence of LHCI and LHCII proteins, which assemble and function irrespective of Chl *b*. This observation warrants further analysis of the LHC apoprotein composition in wild type and Chl *b*-less mutant. Western blot analysis of the protein composition in thylakoid membranes of *C. reinhardtii* (Fig. 3) revealed the presence of several LHCII (Bassi and Wollman 1991; Allen and Staehelin 1994) and LHCI proteins (Bassi et al. 1992).

The LHCII apoproteins were distinguished according to their abundance in the thylakoid membrane into major (LHCII) and minor (the so-called CP24, CP26 and CP29). The polyclonal antibodies used in this study cross-reacted with most of the LHC proteins of *C. reinhardtii* (Bassi et al. 1992). Several distinct protein bands were discerned (Fig. 3), with arrows indicating the position of the apoproteins for CP26, CP29, the major LHCII as well as that of a composite band consisting of CP24 and LHCI. The minor protein band indicated by a star at about 15 kDa most likely originates from partial degradation of a LHC (Allen and Staehelin 1994). It is evident from the results in Fig. 3 that, irrespective of the growth conditions, wild type and Chl *b*-less mutant qualitatively contain essentially the same LHC apoproteins in their thylakoid membranes. Quantitatively, the abundance of the various LHC forms depends on the carbon source used for cell growth.

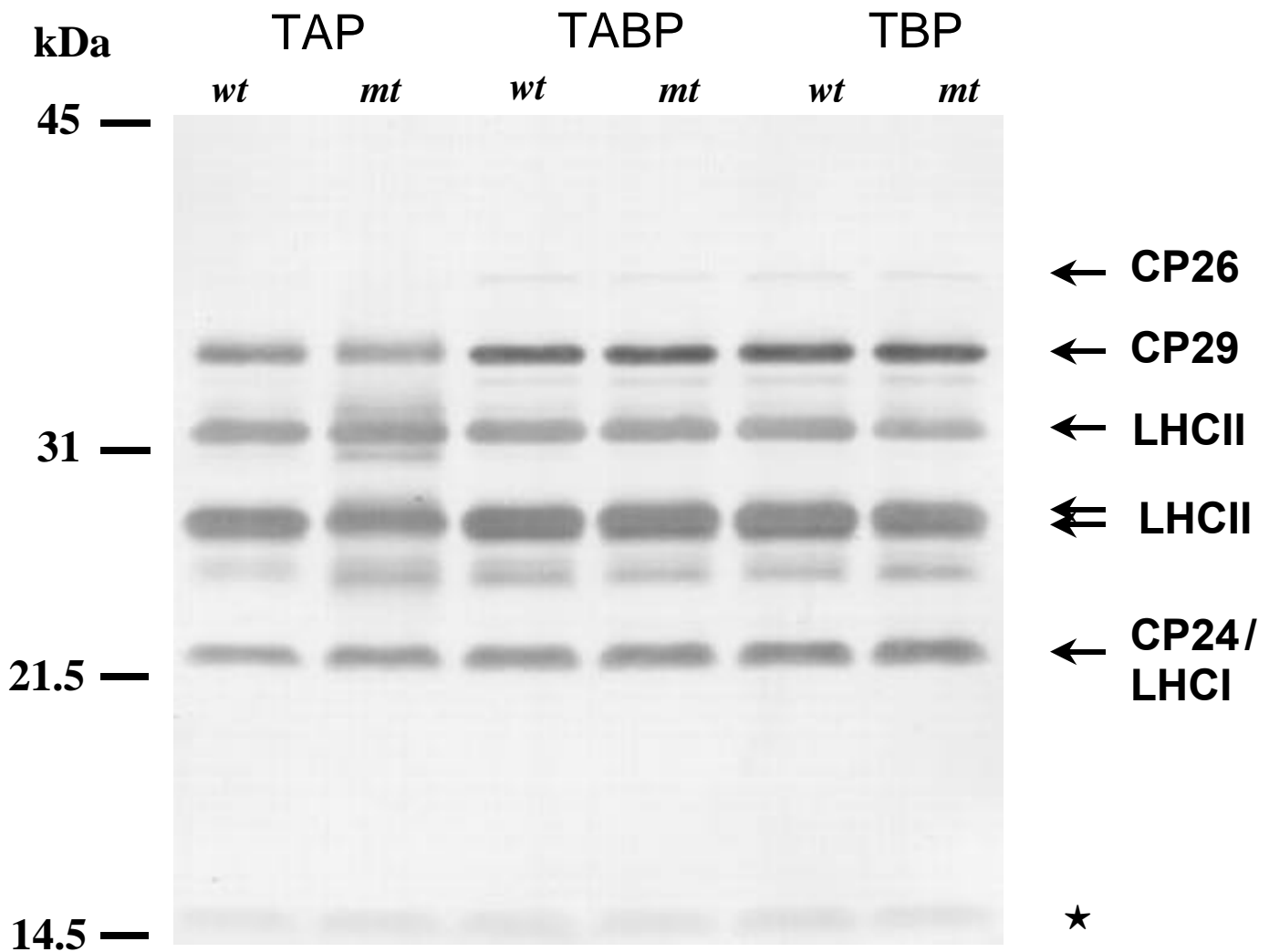


Figure 3 - Western blot analysis of electrophoretically separated thylakoid membrane proteins of wild type (wt) and Chl *b*-less mutant (mt) *C. reinhardtii* grown on acetate (TAP), a mixture of acetate and bicarbonate (TABP), or bicarbonate (TBP) as the source of carbon to the cells. Lanes were loaded on an equal Chl basis (2 nmol Chl per lane) and probed with polyclonal LHC antibodies. The electrophoretic mobility position of the various LHC apoproteins of PSII are shown. Asterisk indicates the presence of a probable LHC degradation product.

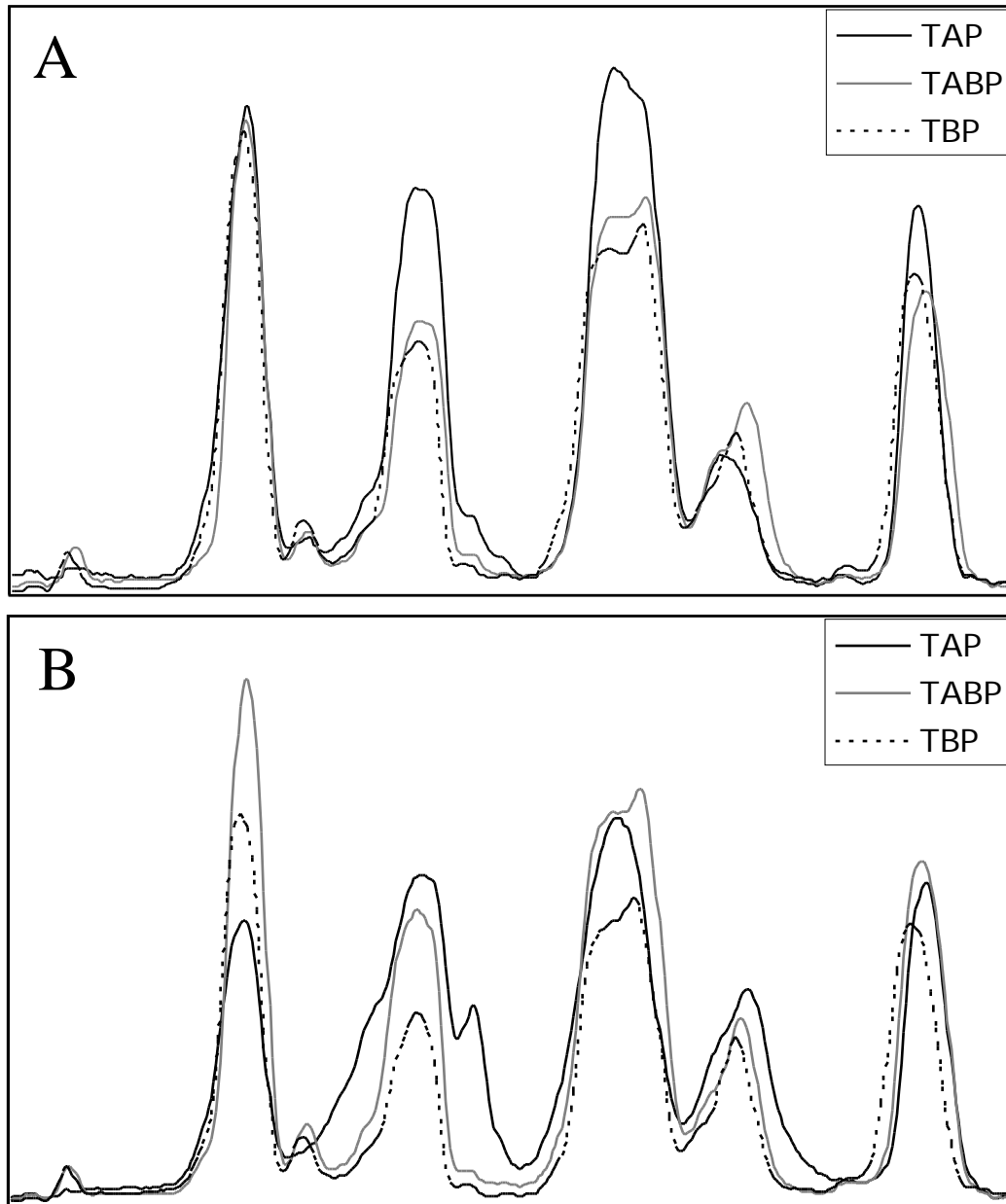


Figure 4 – A, B: Densitometric scan of Western-blot lanes from wild type (A) and Chl *b*-less mutant (B) as shown in Figure 3. Superimposed scans were normalized on the basis of equal Q_A loading. The peaks of CP26 and CP29 are indicated. Arrows show the position of the major LHCII apoproteins.

A quantitative comparison of the relative abundance of light-harvesting proteins associated with PSII in wild type and Chl *b*-less mutant under the different growth conditions was obtained upon densitometric scanning of the lanes in Fig. 3. Figure 4A shows results for the wild type grown in TAP, TABP or TBP, normalized to the amount of Q_A in the respective sample (equal PSII content). Table 4 presents a numerical analysis of the combined results, normalized to the CP29 per Q_A content of the wild type grown in TAP (100%).

Table 4. Relative amounts of LHC proteins of PSII and PSI as measured by densitometry of Western blots similar to those shown in Figure 3. Protein band densities were estimated on the basis of equal Q_A loading and normalized to the amount of CP29 measured in the wild type, TAP-grown cells.

| LHC | wild type | | | Chl <i>b</i> -less | | |
|-----------|-----------|------|-----|--------------------|------|-----|
| | TAP | TABP | TBP | TAP | TABP | TBP |
| CP26 | 2 | 4 | 4 | 1 | 3 | 3 |
| CP29 | 100 | 86 | 91 | 55 | 81 | 65 |
| LHCII | 94 | 62 | 54 | 68 | 54 | 32 |
| LHCII | 180 | 145 | 139 | 114 | 129 | 91 |
| LHCI/CP24 | 71 | 66 | 70 | 56 | 64 | 54 |

In the analysis of Table 4, valid comparisons can be made horizontally in each one of the rows, but not vertically in the various columns. It is evident from the results in Fig. 4A and Table 4 that wild type *C. reinhardtii* thylakoids contain approximately equal amounts of CP29 per Q_A under the various growth conditions. However, the major LHCII content appeared to be somewhat lower in the presence of bicarbonate (TABP and TBP media) relative to that in TAP. Since the Chl antenna sizes of PSII were largely independent of the carbon source in the growth medium (Table 3), the results indicate the presence of LHCII apoproteins that are not functionally associated with PSII in the thylakoid membrane of the TAP-grown cells.

Figure 4B shows the corresponding results for the Chl *b*-less mutant. In this case, the relative amount of CP29 per Q_A was lower than that of the wild type, albeit somewhat variable under the different growth conditions. Further, the relative amount of LHCII per Q_A was significantly lower than that of the wild type. This decrease was more pronounced in cells grown in TBP medium (Table 4).

Measurements of Photosynthetic Capacity

Information about the capacity and efficiency of photosynthesis can be obtained from the light-saturation curve (the so-called *photosynthesis* versus *irradiance* curve), in which the rate of O_2 evolution is measured and plotted as a function of the actinic light intensity. In these measurements, the rate of O_2 evolution first increases linearly with irradiance and then levels off as the saturating irradiance (I_s) is approached (Neale et al. 1993). The slope of the initial linear increase provides information about the photon use efficiency of photosynthesis (Bjorkman Demmig 1987; Neale 1993), whereas the light-saturated rate (P_{max}) provides a measure of the capacity of photosynthesis for the particular sample (Powles and Critchley 1980). Figure 5 shows light-saturation curves of photosynthesis for wild type and Chl *b*-less mutant, grown in media with different sources of carbon.

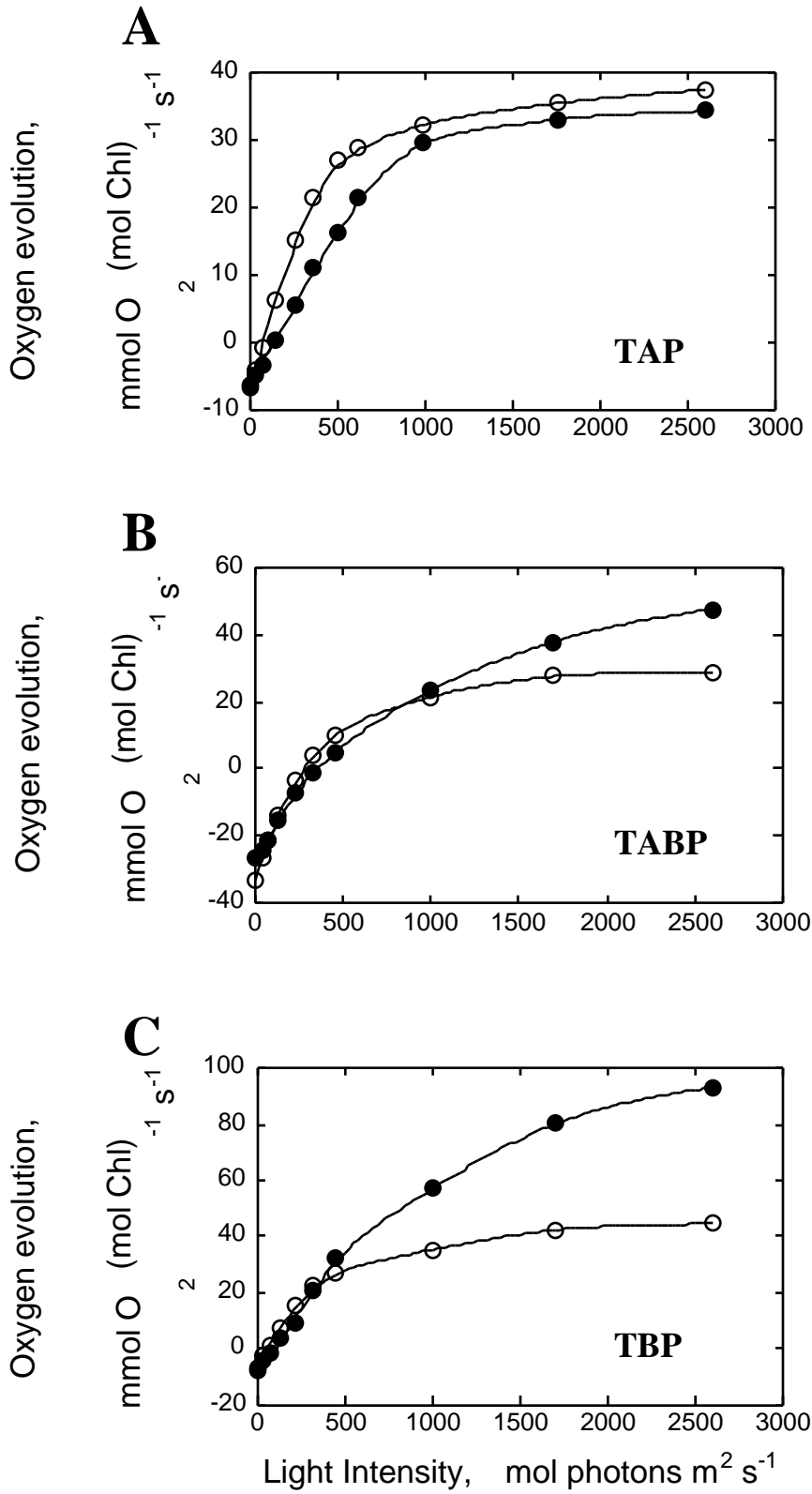


Figure 5 A-C: Light-saturation curves of photosynthesis in wild type (open circles) and a Chl *b*-less mutant (closed circles) of *C. reinhardtii*.

When grown on TAP (Fig. 5A), wild type and Chl *b*-less had similar P_{\max} values at 39 and 34 mmol O₂ (mol Chl)⁻¹ s⁻¹, respectively (Table 5).

Table 5. Oxygen exchange rates and photon use efficiency in the photosynthetic apparatus of *C. reinhardtii* wild type and the Chl *b*-less mutant. The values shown represent the mean ±SD.

| Parameter measured | wild type | | | Chl <i>b</i> -less | | |
|---|-----------|-----------|-----------|--------------------|-----------|-----------|
| | TAP | TABP | TBP | TAP | TABP | TBP |
| Respiration (mmol O ₂ (mol Chl) ⁻¹ s ⁻¹) | 6 ±1.1 | 33 ±1.8 | 6.5 ±2.1 | 7 ±2.1 | 26 ±1.6 | 7 ±3.6 |
| P_{\max} (mmol O ₂ (mol Chl) ⁻¹ s ⁻¹) | 39 ±7.8 | 34 ±6.0 | 39 ±8.8 | 34 ±2.2 | 48 ±2.8 | 97±31.1 |
| photon use efficiency (, arbitrary units) | 0.091 | 0.137 | 0.125 | 0.05 | 0.086 | 0.091 |
| F_v / F_{\max} | 0.65±0.04 | 0.73±0.02 | 0.73±0.02 | 0.56±0.02 | 0.55±0.03 | 0.57±0.04 |

However, the slope of the initial linear increase for the Chl *b*-less mutant (=0.05), which provides information about the photon use efficiency of photosynthesis, was only about half that for the wild type (=0.091). These results indicate a similar photosynthetic capacity of wild type and Chl *b*-less mutant grown on acetate but, at the same time, a strongly reduced photon use efficiency for the mutant.

When grown on TABP (Fig. 5B), the wild type had a P_{\max} (34 mmol O₂ (mol Chl)⁻¹ s⁻¹) similar to that in TAP-grown cells. However, the value (=0.137) was greater than that measured in TAP (=0.091, Table 5). In TABP medium, the Chl *b*-less mutant showed a higher P_{\max} (48 mmol O₂ (mol Chl)⁻¹ s⁻¹) than that measured in TAP. Moreover, the value (=0.086) was also significantly greater than that measured in TAP (0.05). Thus, both types of measurement indicate greater photochemical efficiency in the presence of bicarbonate than in the presence of acetate as the sole carbon source. Interestingly, when grown in TABP, both wild type and mutant exhibited strongly enhanced rates of dark respiration, compared to those measured in acetate only or bicarbonate only media (Fig. 5). This unusual observation corroborates results in a recent study, which showed a 4-fold increase in the rate of dark respiration upon addition of acetate to a CO₂-grown culture of *C. reinhardtii* (Endo and Asada 1996).

When grown on TBP, the wild type had a P_{\max} of 39 mmol O₂ (mol Chl)⁻¹ s⁻¹, i.e., similar to that in TAP-grown or TABP-grown cells (Fig. 5C). The photon use efficiency was high (=0.125) as in cells grown on acetate/bicarbonate (TABP) media. The photon use efficiency of the Chl *b*-less mutant (=0.091) was only slightly lower than that of the wild type and almost twice that measured in the TAP-grown mutant (Table 5).

Moreover, the Chl *b*-less mutant grown on TBP had a greatly enhanced P_{\max} value of 97 mmol O₂ (mol Chl)⁻¹ s⁻¹ (Table 5). On a per chlorophyll basis, this light-saturated rate was approximately 2.5 times greater than that of the wild type. Under these conditions, the light saturation curve of photosynthesis for the mutant showed a saturating irradiance significantly

higher than that of the wild type, consistent with the differences observed in the Chl antenna size of PSII. Taken together, the results in Figs. 5A-5C suggest that PSII determines the properties of the light-saturation curve of photosynthesis in TBP-grown cells. In TAP-grown cells, and to some extent in TABP-grown cells, the rate and capacity of photosynthesis are defined (and probably limited) not by PSII but either by PSI or by the carbon fixing reactions in the chloroplast (see below).

Table 5 also shows the *in vivo* F_v/F_{max} ratio, which is a measure of the photochemical efficiency of PSII in the chloroplast (Butler and Kitajima 1975). It is evident that F_v/F_{max} of the wild type depends on the growth medium of the cells. In the wild type, the presence of bicarbonate improves the photochemical efficiency of PSII ($F_v/F_{max}=0.73$) over that in the presence of acetate as the sole carbon source ($F_v/F_{max}=0.65$). We conclude, that PSII operates with a lower photochemical efficiency when acetate is the sole carbon source. Interestingly, cells of the Chl *b*-less mutant displayed a lower F_v/F_{max} ratio of about 0.56, independent of the carbon source (Table 5). This lower PSII photochemical efficiency of the mutant is probably a consequence of the replacement of Chl *b* by Chl *a* in the minor LHCII in this mutant (see below).

Discussion

Earlier studies from this laboratory with the green alga *Dunaliella salina* demonstrated a novel method for maximizing solar use efficiencies and photosynthetic productivity in microalgal mass cultures by minimizing the number of the light-harvesting antenna pigments of the photosystems (Neidhardt et al. 1998; Melis et al. 1999). Small Chl antenna sizes in *Dunaliella salina* were generated physiologically, upon continuous exposure of the cells to irradiance stress (Smith et al. 1990). Spontaneous mutants with a truncated Chl antenna size have not been identified in green algae as this property does not confer a competitive advantage to the algae in the wild. In higher plants, however, there have been numerous reports of Chl deficient and Chl *b*-less mutants (Falbel and Staehelin 1996; Harrison and Melis 1992; Harrison et al. 1993; Krol et al. 1995; Murray and Kohorn 1991; Terao and Katoh 1989; Thornber and Highkin 1974). These proved invaluable in the study of the assembly and organization of the photosynthetic apparatus. In this report, we provide a detailed analysis of the photosynthetic apparatus organization and function in a Chl *b*-less mutant of *Chlamydomonas reinhardtii*, generated by DNA insertional mutagenesis (Tanaka et al. 1998). We report a number of similarities and distinct differences in the Chl antenna assembly, size, organization and function in the Chl *b*-less *C. reinhardtii* and that of higher plants.

The Chl *b*-less mutant of *C. reinhardtii* had a significantly truncated Chl antenna size for PSII and a slight or no reduction in the Chl antenna size for PSI (Table 3). In spite of the significant loss of Chl from the light-harvesting antenna of PSII, we noted that the Chl content of the mutant cells was equal to, or even greater than that of the wild type (Table 1). More important, the Q_A and P700 content of the mutant cells were, on the average, twice as high as those of the wild type (Table 2). This observation suggests the presence and functioning of a greater number of photosynthetic units per chloroplast in the mutant, probably a response of the cells by which to mitigate against the lower light-harvesting capacity introduced by the smaller Chl antenna size in the thylakoid membrane. In higher plants, a distinct aspect of the acclimation response of the photosynthetic apparatus to Chl deficiency in general, and lack of Chl *b* in particular, is an upward adjustment of the PSII/PSI ratio in thylakoids (Ghirardi et al. 1986, Glick and Melis 1988, Harrison et al. 1993). Increased PSII/PSI ratios in Chl-deficient and Chl

b-less mutants were thought to compensate for the disproportionate reduction in the Chl antenna size of PSII and to restore balanced electron transport between the two photosystems in the chloroplast thylakoids (Melis 1991; 1996). In *C. reinhardtii*, however, independent of the growth conditions, the PSII/PSI ratio in the Chl *b*-less mutant was similar to that of the wild type, i.e., no upward adjustment of the PSII/PSI ratio was observed. It may be concluded that the Chl *b*-less mutant of *C. reinhardtii* lacks the dynamic photosystem stoichiometry compensation mechanism, which functions to restore balanced electron transport by adjustment of the photosystem ratio in thylakoids. In consequence, Chl *b*-less *C. reinhardtii* showed slightly lower photon use efficiency values () than the wild type (Table 5, TBP), probably due to the fact that a portion of the light-energy absorbed by PSI could not be efficiently utilized in the linear photosynthetic electron transport process.

To better understand the organization of the photochemical apparatus in the Chl *b*-less mutant of *C. reinhardtii*, we measured the functional Chl antenna sizes of PSII and PSI as well as the composition of the LHC proteins in the thylakoid membrane. Such studies were extended to include measurements with cells grown under a variety of carbon sources, including acetate, a mixture of acetate and bicarbonate, or bicarbonate alone in the growth medium. Results showed that the PSII antenna sizes of wild type and Chl *b*-less mutant were largely independent of the carbon source used for growth. However, the PSII Chl antenna size of the mutant was only 30% of that measured for PSII and about 70% of that measured for PSII in the wild type. This is evidence that pigment deficiency in a green alga can be generated by DNA insertional mutagenesis and can result in a permanently truncated Chl antenna size of PSII.

The PSII antenna size found in the Chl *b*-less mutant (N= \sim 96 Chl molecules) was, nevertheless, significantly larger than that of the PSII-core antenna (N= \sim 37 Chl molecules, Glick and Melis 1988). Our polypeptide analysis confirmed the presence of CP26, CP29 and a portion of the major LHCI proteins in the thylakoid membrane of the Chl *b*-less mutant (Figure 3). Obviously, there is stable integration of these LHC polypeptides in the thylakoid membrane of *C. reinhardtii* in the absence of Chl *b*, consistent with previous reports on this matter (Allen and Staehelin 1994; Chunaev et al. 1991; Michel et al. 1983; Picaud and Dubertret 1986; Plumley and Schmidt 1995). In contrast to PSII, the Chl antenna size of PSI in the Chl *b*-less mutant was similar to that of the wild type. In agreement, LHCI proteins that were present in the wild type were also found to comparable levels in the Chl *b*-less mutant. It is concluded that the PSI auxiliary light-harvesting Chl antenna can fully assemble and be functionally connected with the reaction center P700, even in the absence of Chl *b*.

This work provided information about the impact of the carbon source during growth on the photosynthetic capacity and photon use efficiency of *C. reinhardtii*. Acetate grown cells of the wild type exhibited a lower PSII photochemical efficiency, measured as F_v/F_{max} *in vivo* and, concomitantly, lower overall photosynthetic electron transport efficiency () than cells grown in the presence of bicarbonate (Table 5). A lower F_v/F_{max} *in vivo* in the presence of acetate as the sole carbon source might originate from an acetate-induced partial reduction of the plastoquinone pool (and hence of Q_A) in the thylakoid membrane. Similarly, growth strictly in the presence of acetate as the sole carbon source may also impose limitation in the capacity of photosynthesis at the carbon fixation level (low levels and/or activity of Rubisco), evidenced in the case of the mutant by the relatively suppressed level of P_{max} (Fig. 5, TAP). However, when bicarbonate is present in the growth medium, such limitations are alleviated, and cells exhibit maximum photosynthetic efficiencies and productivities. Noteworthy in this respect is the observation of a P_{max} that is 2.5-fold greater in the Chl *b*-less mutant than in the wild type (Fig. 5, TBP),

suggesting that mutants with a truncated Chl antenna size are good candidates for mass culture of algae in which a high photosynthetic efficiency and productivity is required (Melis et al. 1999). This notion is also consistent with recent results with pigment (phycocyanin)-deficient cyanobacteria, which exhibited higher photosynthetic productivities when compared to those of the normally pigmented wild type (Nakajima and Ueda 1997; Nakajima and Ueda 1999).

In summary, direct experimental evidence is provided in this work to show that transformation of green algae can be used as a tool by which generate mutants exhibiting a permanently truncated Chl antenna size and a higher (per Chl) photosynthetic productivity.

Acknowledgments

The work was produced under DOE-UCB Cooperative Agreement Number DE-FC36-98GO10278.

References

- Allen KD, Staehelin LA (1994) Polypeptide composition, assembly and phosphorylation patterns of the photosystem II antenna system of *Chlamydomonas reinhardtii*. *Planta* 194: 42-54
- Arnon DI (1949) Copper enzymes in isolated chloroplasts. Polyphenoxidase in *Beta vulgaris*. *Plant Physiology* 24: 1-15
- Bassi R, Wollman F-A (1991) The chlorophyll-*a/b* proteins of photosystem II in *Chlamydomonas reinhardtii*. *Planta* 183:423-433
- Bassi R, Soen SY, Frank G, Zuber H, Rochaix J-D (1992) Characterization of chlorophyll-*a/b* proteins of photosystem-I from *Chlamydomonas-reinhardtii*. *Journal of Biological Chemistry* 267: 25714-25721
- Bjorkman O, Demmig B (1987) Photon yield of O₂ evolution and chlorophyll fluorescence characteristics at 77 K among vascular plants of diverse origins. *Planta* 170: 489-504
- Butler WL, Kitajima M (1975) Fluorescence quenching in photosystem II of chloroplasts. *Biochimica Biophysica Acta* 376: 116-25
- Chunaev AS, Mirnaya ON, Maslov VG, Boschetti A (1991) Chlorophyll *b*- and Loroaxanthin-deficient mutants of *Chlamydomonas reinhardtii*. *Photosynthetica* 25 (2): 291-301
- Di Paolo ML, Dal Belin Peruffo A, Bassi R (1990) Immunological studies on chlorophyll-*a/b* proteins and their distribution in thylakoid membrane domains. *Planta* 181: 275-286
- Endo T, Asada K (1996) Dark induction of the non-photochemical quenching of chlorophyll fluorescence by acetate in *Chlamydomonas reinhardtii*. *Plant Cell Physiology* 37: 551-555
- Falbel TG, Staehelin LA (1996) Partial blocks in the early steps of the chlorophyll synthesis pathway: A common feature of chlorophyll *b*-deficient mutants. *Physiologia Plantarum* 97: 311-320
- Ghirardi ML, McCauley SW, Melis A (1986) Photochemical apparatus organization in the thylakoid membrane of *Hordeum vulgare* wild type and chlorophyll *b*-less *chlorina-f2* mutant *Biochimica Biophysica Acta* 851: 331-339
- Glick RE, Melis A (1988) Minimum photosynthetic unit size in System-I and System-II of barley chloroplasts. *Biochimica Biophysica Acta* 934: 151-155
- Gorman DS, Levine RP (1965) Cytochrome *f* and plastocyanin: their sequence in the photosynthetic electron transport chain of *Chlamydomonas reinhardtii*. *Proceedings of the National Academy of Sciences USA* 54: 1665-1669

- Harrison MA, Melis A (1992) Organization and stability of polypeptides associated with the chlorophyll *a-b* light-harvesting complex of photosystem-II. *Plant Cell Physiology* 33: 627-637
- Harrison MA, Nemson JA, Melis A (1993) Assembly and composition of the chlorophyll *a-b* light-harvesting complex of barley (*Hordeum vulgare* L.): Immunochemical analysis of chlorophyll *b*-less and chlorophyll *b*-deficient mutants. *Photosynthesis Research* 38: 141-151
- Jansson S (1994) The light-harvesting chlorophyll *a/b*-binding proteins. *Biochimica Biophysica Acta* 1184: 1-19
- Kindle KL (1987) Expression of a gene for a light-harvesting chlorophyll *a/b*-binding protein in *Chlamydomonas reinhardtii*: effect of light and acetate. *Plant Molecular Biology* 9: 547-563
- Krol M, Spangfort MD, Huner NPA, Oquist G, Gustafsson P, Jansson S (1995) Chlorophyll *a/b* binding proteins, pigment conversions, and early light-induced proteins in a chlorophyll *b*-less barley mutant. *Plant Physiology* 107: 873-883
- Laemmli UK (1970) Cleavage of structural proteins during the assembly of the head of bacteriophage T4. *Nature* 227: 680-685
- Lavergne J, Briantais J-M (1996) Photosystem II heterogeneity. In: Ort DR, Yocum F (eds) *Advances in Photosynthesis Vol. 4. Oxygenic Photosynthesis: The Light Reactions*. Kluwer Academic Publishers, Dordrecht, The Netherlands pp.265-287
- Manodori A, Alhadeff M, Glazer AN, Melis A (1984) Photochemical apparatus organization in *Synechococcus* 6301 (*Anacystis nidulans*). Effect of phycobilisome mutation. *Archive Microbiology* 139: 117-123
- Melis A (1989) Spectroscopic methods in photosynthesis: photosystem stoichiometry and chlorophyll antenna size. *Phil Trans R Soc Lond B* 323: 397-409
- Melis A (1991) Dynamics of photosynthetic membrane composition and function. *Biochimica Biophysica Acta* 1058: 87-106
- Melis A (1996) Excitation energy transfer: Functional and dynamic aspects of *Lhc (cab)* proteins. In Ort DR, Yocum CF (eds) *Advances in Photosynthesis Vol. 4. Oxygenic Photosynthesis: The Light Reactions*. Kluwer Academic Publishers, Dordrecht, The Netherlands, pp. 523-538.
- Melis A, Anderson JM (1983) Structural and functional organization of the photosystems in spinach chloroplasts: Antenna size, relative electron transport capacity, and chlorophyll composition. *Biochimica Biophysica Acta* 724: 473-484
- Melis A, Brown JS (1980) Stoichiometry of system I and system II reaction centers and of plastoquinone in different photosynthetic membranes. *Proceedings of the National Academy of Sciences USA* 77: 4712-4716
- Melis A, Duysens LNM (1979) biphasic energy conversion kinetics and absorbance difference spectra of PS II of chloroplasts. Evidence for two different PS II reaction centers. *Photochemistry and Photobiology* 29: 373-382
- Melis A, Hart RW (1980) A laboratory-constructed sensitive difference spectrophotometer for the ultraviolet, visible and far-red region of the spectrum. *Carnegie Yearbook* 79: 170-172.
- Melis A, Spangfort M, Andersson B (1987) Light-absorption and electron-transport balance between photosystem II and photosystem I in spinach chloroplasts. *Photochemistry and Photobiology* 45: 129-136
- Melis A, Neidhardt J, Benemann JR (1999) *Dunaliella salina* (Chlorophyta) with small chlorophyll antenna sizes exhibit higher photosynthetic productivities and photon use efficiencies than normally pigmented cells. *Journal of Applied Phycology* 10: 515-525

- Michel H-P, Tellenbach M, Boschetti A (1983) A chlorophyll *b*-less mutant of *Chlamydomonas reinhardtii* lacking in the light-harvesting chlorophyll *a/b* protein complex but not in its apoproteins. *Biochimica Biophysica Acta* 725: 417-424
- Murray DL, Kohorn BD (1991) Chloroplasts of *Arabidopsis thaliana* homozygous for the *ch-1* locus lack chlorophyll *b*, lack stable LHCP II and have stacked thylakoids. *Plant Molecular Biology* 16: 71-79
- Nakajima Y, Ueda R (1997) Improvement of photosynthesis in dense microalgal suspension by reduction of light harvesting pigments. *Journal of Applied Phycology* 9: 503-510
- Nakajima Y, Ueda R (1999) Improvement of microalgal photosynthetic productivity by reducing the content of light harvesting pigment. *Journal of Applied Phycology* 11: 195-201
- Neale PJ, Cullen JJ, Lesser MP, Melis A (1993) Physiological bases for detecting and predicting photoinhibition of aquatic photosynthesis by PAR and UV radiation. In: Yamamoto HY, Smith CM (eds) Photosynthetic responses to the environment. Current topics in Plant Physiology, Vol. 8. American Society of Plant Physiologists Publication Series, pp. 61-77
- Neidhardt J, Benemann JR, Zhang L, Melis A (1998) Photosystem-II repair and chloroplast recovery from irradiance stress: relationship between chronic photoinhibition, light-harvesting chlorophyll antenna size and photosynthetic productivity in *Dunaliella salina* (green algae). *Photosynthesis Research* 56:175-184
- Picaud A, Dubertret G (1986) Pigment protein complexes and functional properties of tetratype resulting from crosses between CP1 and CP2 less *Chlamydomonas* mutants. *Photosynthesis Research* 7: 221-236
- Plumley FG, Schmidt GW (1995) Light-harvesting chlorophyll *a/b* complexes: Interdependent pigment synthesis and protein assembly. *The Plant Cell* 7: 689-704
- Powles SB, Critchley C (1980) Effect of light intensity during growth on photoinhibition of intact attached bean leaflets. *Plant Physiology* 65: 1181-1187
- Smith BM, Morrissey PJ, Guenther JE, Nemson JA, Harrison MA, JF Allen, Melis A (1990) Response of the photosynthetic apparatus in *Dunaliella salina* (Green Algae) to irradiance stress. *Plant Physiology* 93: 1433-1440
- Somanchi A, Handley ER, Moroney JV (1998) Effect of low CO₂ growth on *psaE* and *des6* cDNAs in *Chlamydomonas reinhardtii*. In: Garab G (ed) Photosynthesis: Mechanisms and Effects Vol. 5. Kluwer Acad Publ, Netherlands, pp. 3487-3490
- Tanaka A, Ito H, Tanaka R, Tanaka N, Yoshida K, Okada K (1998) Chlorophyll *a* oxygenase (CAO) is involved in chlorophyll *b* formation from chlorophyll *a*. *Proceedings of the National Academy of Sciences USA* 95: 12719-12723
- Terao T, Katoh S (1989) Synthesis and breakdown of the proteins of light-harvesting chlorophyll *a/b* proteins in chlorophyll *b*-deficient mutants of rice. *Plant Cell Physiology* 30: 571-580
- Terao T, Katoh S (1996) Antenna sizes of photosystem I and photosystem II in chlorophyll *b*-deficient mutants of rice. Evidence for an antenna function of photosystem II reaction centers that are inactive in electron transport. *Plant Cell Physiology* 37: 307-312
- Thornber JP, Highkin HR (1974) Composition of the photosynthetic apparatus of normal barley leaves and a mutant lacking chlorophyll *b*. *European Journal of Biochemistry* 41: 109-116

Efficient Production of Hydrogen from Glucose-6-Phosphate

Jonathan Woodward,* Mark Orr, Kimberley Cordray, and Elias Greenbaum

Chemical Technology Division
Oak Ridge National Laboratory**
P.O. Box 2008
Oak Ridge, TN 37831-6194

U.S. DOE Hydrogen program
Annual Review Meeting
May 9-11, 2000
San Ramon, California

* To whom correspondence should be addressed

** Managed by UT-Battelle, LLC under contract DE-AC0500OR22725 with the U.S. Department of Energy

EFFICIENT PRODUCTION OF HYDROGEN FROM GLUCOSE-6-PHOSPHATE

Jonathan Woodward, Mark Orr, Kimberley Cordray, and Elias Greenbaum
Chemical Technology Division
Oak Ridge National Laboratory
P.O. Box 2008
Oak Ridge, TN 37831-6194

Abstract

The maximum molar yield of hydrogen that can be obtained from a renewable sugar such as glucose is 12 mol H₂ per mole glucose. In this work it has been shown that the enzymes of the oxidative cyclic pentose phosphate pathway coupled to hydrogenase, using NADP⁺ as the electron carrier, is capable of generating 11.6 mol H₂ per mole of glucose-6-phosphate (G6P). These results provide the first evidence to indicate that the maximum molar yield of hydrogen from a renewable sugar, such as glucose, is possible enzymatically, and, as such, could lead to an efficient process for biohydrogen production.

Introduction

The development of alternative sources of energy to oil, is essential as geologists have predicted that oil shortages will begin in about 10 to 20 years. Even with the discovery of new major oil fields such as those of the Caspian Basin, oil shortages are still inevitable within a generation (Kerr, 1998). Introduction of a hydrogen economy into society now seems even more important than a generation ago. Biohydrogen production *in vivo* and the enzymatic conversion of glucose to H₂ has been demonstrated as a method for H₂ production (Zaborsky, 1998, Woodward et al., 1996, Hershlag et al. 1998). Glucose, a sugar produced by photosynthesis, is renewable, unlike fossil fuels such as oil. Examples of other renewable sugars include xylose, lactose and sucrose (Goyal et al., 1991, Woodward, 1984) all of which have the potential to be converted into hydrogen gas utilizing two enzymes, glucose dehydrogenase (GDH) and hydrogenase from the extremophiles *Thermoplasma acidophilum* and *Pyrococcus furiosus* respectively (DeLong, 1998, Bonete et al., 1996, Smith et al., 1989, Woodward and Orr, 1998). In this enzymatic pathway for H₂ production, GDH catalyzes the oxidation of glucose to gluconic acid (via the lactone) using NADP⁺ as the electron acceptor.

NADPH simultaneously reduces hydrogenase and H₂ is evolved. The maximum stoichiometric yield of hydrogen possible from glucose by this procedure is only 1 mol per mole sugar which can be achieved (Woodward et al., 1996). However, this value represents only 8.3% of the theoretical yield. We postulated that the enzymatic conversion of glucose to H₂ might result in the maximum yield (~12 mol of H₂ per mole of glucose) if hydrogenase was included with the enzymes of the oxidative cyclic pentose phosphate pathway. This was based on results from the pioneering experiments of Horecker and Racker who showed, respectively, that the oxidation and decarboxylation of 6-phosphogluconate (6PG) resulted in the formation of pentose phosphate and demonstrated the cyclic nature of the complete oxidation of glucose-6-phosphate (G6P) to NADPH and CO₂ (Horecker and Smyrniotis, 1950, Couri and Racker, 1959).

Methods

Yeast enzymes of the pentose phosphate pathway were obtained from Sigma Chemical Company. In experiments measuring NADPH (NADH) or hydrogen production the reaction mixture contained 1 manufacturer's unit of G6P dehydrogenase, 6PG dehydrogenase, phosphoribose isomerase, Ru5P-epimerase, transaldolase, transketolase, aldolase, phosphoglucoisomerase, fructose-1,6-bisphosphatase and 50 units of triosephosphoisomerase. Other details are given below. Fructose 1,6 diphosphatase was dialyzed against buffer, pH 7.5 prior to use because the commercial preparation was shown to contain an inhibitor of the G6P/6PG dehydrogenase couple. Hydrogenase was purchased from the University of Georgia, Athens. Hydrogen evolution was measured using an in-line hydrogen sensor with a flow-detection system described in detail previously (Greenbaum, 1984). The reaction mixture for measuring Hydrogen production by enzymes of the oxidative branch of the pentose phosphate cycle contained 2 μmol of G6P, 1 unit each of G6P and 6PG dehydrogenases, 63 units of *Pyrococcus furiosus* hydrogenase, and 4 μmol of NADP⁺ in 2.0 mL 50 mM sodium phosphate buffer, pH 7.5, at 40°C. The reaction mixture for measuring the enzymatic conversion of G6P to H₂ by enzymes of the oxidative and regenerative branch of the pentose phosphate cycle contained 1 μmol of G6P, each of the enzymes of the pentose phosphate cycle (see ref. 6), 1 μmol of co-carboxylase, 1.0 μmol of NADP⁺, and 63 units of hydrogenase in 2.0 mL of 200 mM Hepes buffer, pH 7.5, containing 10 mM MgCl₂, at 30°C. The starting pH was measured at 7.4; and after 92 h of reaction, the pH was 7.2.

Production of reductant and regeneration of G6P by the oxidative pentose phosphate cycle was measured in a reaction mixture containing 3.0 mL of 0.2 M Hepes buffer, pH 7.5 at 23°C, contained 0.05 μmol of G6P, each of the enzymes of the oxidative pentose phosphate cycle, 1.0 μmol of thiamine pyrophosphate (cocarboxylase), 1.0 μmol of NADP⁺, and 100 μg of the antibiotic spectomycin. An increase in absorbancy at 340 nm due to the formation of NADPH was monitored over time. For measuring G6P formation from Ru5P, the reaction mixture (total volume, 3.19 ml) consisted of 3.0 ml of hexokinase assay reagent, containing G6P dehydrogenase (Sigma), each of the enzymes of the oxidative pentose phosphate cycle except G6P and 6PG dehydrogenases, 1.0 μmol of cocarboxylase, 1.5 μmol of Ru5P, and 100 μg of spectomycin. The increase in absorbance at 340 nm due to the formation of NADH by the action of G6P dehydrogenase in the hexokinase reagent was measured at 23°C.

The simultaneous production of H₂ and CO₂ by the oxidative branch of the oxidative pentose phosphate cycle was measured in a reaction mixture (2.0 ml) containing 1 μmol G6P, 2 μmol EDTA, 10 μmol MgCl₂, 1 unit each of G6P dehydrogenase and 6PG dehydrogenase, 4 μmol of NADP⁺, and 63 units of hydrogenase in 0.2 M HEPES, pH 7.5 in 2.0 mL 0.2M HEPES buffer, pH 7.5, at 30°C. For further details see Lee et al. (1996).

Results and Discussion

We conducted experiments to determine whether the oxidative pentose phosphate cycle could be utilized to improve the molar yield of H₂ from glucose by using G6P as the starting substrate. First, G6P dehydrogenase, 6PG dehydrogenase and hydrogenase were employed to convert G6P to ribulose-5-phosphate (Ru5P). Since, in these reactions, 2 mol of NADPH and 1 mol CO₂ are formed per mole G6P, it follows that if hydrogenase is present, 2 mol of hydrogen could also be generated since NADPH is the physiological electron donor to *P. furiosus* hydrogenase (Ma et al., 1994). This was indeed the case and the oxidative branch of the pentose phosphate pathway was capable of generating the maximum theoretical yield of hydrogen possible (i.e. 2.0 H₂ mol/mole G6P). The yield of CO₂ (0.85 mol/mole G6P) gives a ratio of H₂ to CO₂ of 2.3 and agrees quite well with the expected theoretical value (Fig. 1).

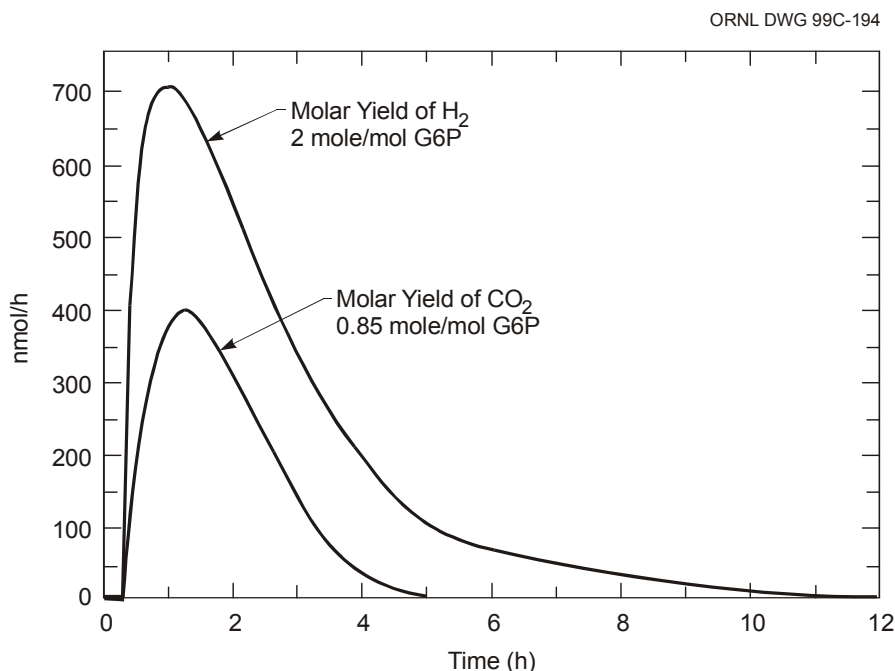


Fig. 1. Simultaneous production of H₂ and CO₂ by the oxidative branch of the oxidative pentose phosphate cycle.

A maximum rate of hydrogen evolution of ~700 nmol/h was observed and the reaction rate declined to zero after 5 h. No inhibition of G6P dehydrogenase by NADPH (Zubay, 1993) would be likely since it is oxidized by hydrogenase as soon as it is formed. The kinetics of these reaction remain to be optimized.

In an experiment to determine whether or not the non-oxidative branch of the pentose phosphate pathway was capable of regenerating G6P from Ru5P, enzymes of the pathway were incubated with 0.05 μmole G6P and 1.0 μmole NADP^+ and the formation of NADPH monitored. If the pathway is kinetically capable of cyclic behavior, a theoretical maximum of 0.6 μmole NADPH could be produced. The data of Fig. 2A show that after 80 min 0.16 μmole of NADPH was produced indicating 27% efficiency after this time. After 17 h of the reaction the 0.36 μmole of NADPH was produced (60% efficiency). This observed efficiency is expected if G6P is regenerated and indicates that greater than 3 cycles of the pathway have occurred after 17 h. The kinetics of this reaction are such that 0.1 μmole NADPH is formed rapidly (within 5 min) after the initiation of the reaction and can be explained by the rapid conversion of G6P to Ru5P with the concomitant generation of NADPH. Further production of NADPH is slow and limited by the enzyme-catalyzed reactions of the non-oxidative branch of the pathway. This would not be surprising since the pool of sugar phosphates is at equilibrium in cells containing transketolase and transaldolase (Glasser and Brown, 1955). The conversion of Ru5P to G6P suggested a similar kinetic pattern to that observed above in that there was an initial faster rate of G6P production in the first hour of the reaction. After 48 h, an initial 1.5 μmol Ru5P had led to the generation of 0.97 μmole G6P which represents $\sim 65\%$ of the maximum theoretical amount possible (Fig 2B). Other reasons for the slow kinetics of either NADPH or G6P production after the initial burst of activity could be product inhibition or enzyme inactivation over time. Inorganic phosphate is an inhibitor of G6PDH and triosephosphate isomerase (Zubay, 1993, Oesper and Meyerhof, 1950). NADPH is a potent inhibitor of yeast G6PDH with a K_i of 27 μM (Zubay, 1993). The concentration of NADPH reached 120 μM after 17 h of reaction and might suggest a reason for the slow production of NADPH (Fig. 2A). The G6DH/6PGDH enzyme couple was also determined to be unstable when heated at 35.5 $^\circ\text{C}$ losing all of its activity after 60 h.

Hydrogen was evolved upon the addition of NADP^+ when the enzymes of the pentose phosphate pathway were mixed together with hydrogenase and 1.0 μmole G6P. The rate of hydrogen evolution reached a maximum of 425 nmol/h (Fig. 3, Curve A). These data are significant because 11.6 μmol hydrogen per mole of G6P were evolved after 92 h and are compared to the maximum yield of 2.0 mol H_2 from the oxidative branch of the cycle (Fig. 3, Curve B). This represented 97% of the maximum yield of hydrogen possible. Such high stoichiometric yields of hydrogen have never been obtained from glucose fermentation by anaerobic bacteria because most of the reducing potential produced by such cells is needed for ATP synthesis with subsequent growth and maintenance of the organism (Thauer et al., 1977). Typically, the molar yield of hydrogen from glucose is 1–4 mol H_2 per mole of glucose by anaerobic fermentation (Solomon, 1995). However, yields of 8.0 and 9.8 mol H_2 per mole of glucose have been reported by a combination of *Clamydomonas* and *Rhodopseudomonas* and by *Oscillatoria* sp. respectively (Miura, 1995). If glucose is the starting substrate, the requirement of ATP to generate G6P must be taken into consideration when calculating the energy efficiency of the process. The high molar yields of hydrogen obtained using enzymes of the pentose phosphate pathway coupled via NADP^+ with hydrogenase gives a thermodynamic efficiency of 98%. This value is much higher than the 25–50% energy efficiency common to the majority of anaerobic bacteria that ferment glucose (Thauer et al., 1977). Two other observations are noteworthy. Firstly, no G6P was detected in the reaction mixture at the completion of the experiment. Secondly, the cofactor NADP^+ was recycled 11.6 times during the experiment. This is important because co-factor requiring reactions are

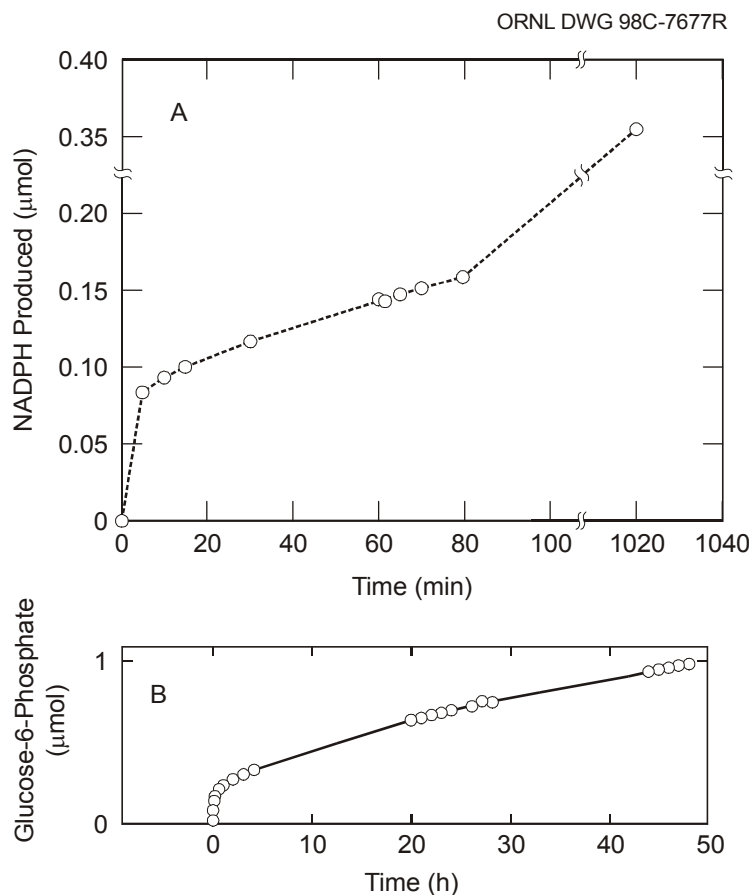


Fig. 2. Production of reductant (A) and regeneration of G6P (B) by the oxidative pentose phosphate cycle.

generally considered to be uneconomical if utilized on an industrial scale. The cost of NADP^+ could be reduced drastically if it was recycled. An example whereby the co-factor NAD^+/NADH is recycled on a practical scale is the commercial production of *L-tert-leucine*. In this case, polymer enlarged NADH was recycled 125,000 times reducing the co-factor costs by several orders of magnitude. It should also be noted that cofactors in bulk quantities are commercially available e.g. ATP \$0.33/g, NADP^+ \$2.06/g (Kragl, 1996). The production of G6P enzymatically, therefore, even without the regeneration of ATP from ADP and P_i should be commercially feasible.

A process for the efficient production of hydrogen using enzymes of the pentose phosphate pathway coupled to hydrogenase could become practically feasible if they were isolated from thermophilic microorganisms (extremophiles). This could result in higher rates of hydrogen evolution and faster yields because *Pyrococcus furiosus*, the source of hydrogenase used in these studies, is a hyperthermophile whose hydrogenase activity is optimal at 85°C (Bryant and Adams, 1989). Pentose phosphate enzymes from yeast used in this study are rapidly inactivated above 45°C , hence the necessity for maintaining a reaction temperature of 30°C at which the activity of hydrogenase is an order of magnitude lower than that at 80°C . In this regard, the complete genome sequence has been determined for *Aquifex aeolicus*, one of the most thermophilic bacteria known and genes encoding most of the enzymes of the pentose phosphate pathway have been identified. The cloning

and expression of these genes from *A. aeolicus* could provide enzymes that are active and stable at 60°C and above. Also, plasmids containing genomic *Methanococcus jannaschii* DNA fragments encoding transaldolase, glucose-6-phosphate isomerase and triose phosphate isomerase have been cloned into expression vectors and expressed in active form. Obtaining thermally stable forms of the enzymes of the pentose phosphate pathway active at higher than ambient temperatures in large quantities therefore, is technically feasible. The possibility of producing hydrogen utilizing these enzymes in immobilized form also exists including a polymer enlarged NADP⁺ co-factor. Although this process also generates CO₂ as a by product (6 mol/mole G6P), it should not be considered as contributing to global warming but rather as green technology that recycles the CO₂ that was reduced to sugar by the process of photosynthesis. This is in contrast to fossil fuel utilization for the production of fuels and chemicals that simply adds CO₂ to the atmosphere.

ORNL DWG 99C-193

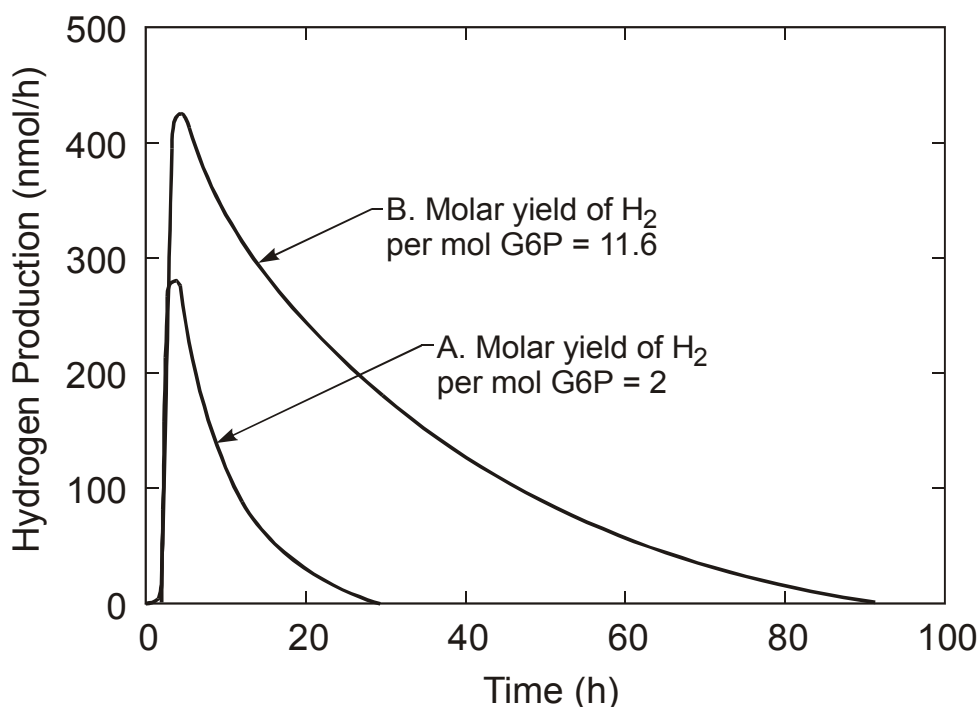


Fig. 3. Hydrogen production by enzymes of the oxidative pentose phosphate cycle.

Acknowledgements

We thank S. Blankinship for technical assistance, H. O'Neill, M. Danson and M. Gibbs for comments and criticism, L. Wagner for administrative assistance and M. Savage for editorial assistance. This work was supported by the Office of Energy Efficiency and Renewable Energy, Office of Basic Energy Sciences, Office of Science, U.S. Department of Energy, the Office of Research and Development and the Christopher Columbus Fellowship Foundation. Oak Ridge National Laboratory is managed by Lockheed Martin Energy Research Corporation for the U.S. Department of Energy under contract DE-AC0500OR22725.

References

- Bonete, M-J, Pire, C., Llorca, F. I., and Camacho, M. L. 1996. *FEBS Lett.* **383**, 227–231.
- Bryant, F. O. and Adams, M. W. W. 1989. *J. Biol. Chem.*, **264**, 5070–5078.
- Couri, D. and Racker, E. 1959. *Arch. Biochem. Biophys.* **83**, 195–205.
- Delong, E. 1998. *Science*, **280**, 542–544.
- Glasser, L. and Brown, D.H. 1955. *J. Biol. Chem.* **216**, 67–75.
- Goyal, A., Ghosh, B., and Eveleigh, D. 1991. *Bioresource Technol.* **36**, 37–52.
- Greenbaum, E. 1984. *Photobiochem. Photobiophys.* **8**, 323–332.
- Herslag, N., Turner, I., and Woodward, J. 1998. *J. Chem. Ed.* **75**, 1270–1274.
- Horecker, B. L., and Smyrniotis, P. Z. 1950. *Arch. Biochem.* **29**, 232–241.
- Kerr, R.A. 1998. *Science*, **281**, 1128.
- Kragl, U. 1996. *Industrial Enzymology*, T. Godfrey, S. West eds., London, Macmillan Press Ltd 2nd edition, p. 273.
- Lee, J. W. et al., 1996. *Science* **273**, 364–367.
- Ma, K., Zhou, Z. H., and Adams, M. W. W. 1994. *FEMS Microbiol. Lett.* **122**, 245–250.
- Miura, Y., 1995. *Process Biochem.* **30**, 1–12.
- Oesper, P. and Meyerhof, O. 1950. *Arch. Biochem. Biophys.* **27**, 223–234.
- Smith, L. D., Budgen, N., Bungard, S. J., Danson, M. J., and Hough, D.W. 1989. *Biochem. J.* **261**, 973–979.
- Solomon, B.O. et al., 1995. *J. Biotechnol.* **39**, 107–115.
- Thauer, R. K., Jungermann, K., and Decker, K. 1977. *Bacteriol. Rev.* **41**, 100–166.
- Woodward, J. 1984. *Topics in Enzyme and Fermentation Biotechnology* 8, Wiseman, A. ed. Chichester, Ellis Horwood, p. 9.
- Woodward, J. et al., 1996. *Nature Biotechnol.* **14**, 872–874.
- Woodward J., and M. T. Orr, 1998. *Biotechnol. Prog.* **14**, 897–902.
- Zaborsky, O. R., ed. 1998. *Biohydrogen*. New York, Plenum Press.
- Zubay, G. 1993. *Biochemistry*. Dubuque, Iowa, Wm. C. Brown Publishers, 3rd edition, chap. 13.

Legends to Figures

Fig. 1. Simultaneous production of H_2 and CO_2 by the oxidative branch of the oxidative pentose phosphate cycle.

Fig. 2. Production of reductant (A) and regeneration of G6P (B) by the oxidative pentose phosphate cycle.

Fig. 3. Hydrogen production by enzymes of the oxidative pentose phosphate cycle.

INTEGRATED RENEWABLE HYDROGEN UTILITY SYSTEM

Robert J. Friedland
Proton Energy Systems, Inc.
Rocky Hill, CT 06067

Abstract

This paper describes the plans for a Phase II program recently awarded to Proton Energy Systems, Inc. (Proton) under cooperative agreement DE-FC36-98GO10341 with the Golden Field Office of the Department of Energy (DOE).

The ultimate goal of this project is to enable the link to sustainability by converting excess renewable power into hydrogen and having that hydrogen available for conversion back to power, on demand. Furthermore, the cost of this capability must be less than \$1000 per kW and allow for a variety of renewable inputs.

Since the inception of the program on April 15, 1998, Proton has successfully demonstrated a fully functioning integrated renewable hydrogen utility system. The system, installed at Arizona Public Service (APS) in Tempe, AZ couples a solar concentrating dish, an external combustion engine and a Proton HOGEN 300 hydrogen generator. The system was installed and operating from May of 1999 through the end of the Phase I program in December of 1999. A description of the technical performance of the system and a market assessment is detailed in the Final Technical Report ¹.

Approach

The Phase I demonstration efforts and market evaluation has shown that a hydrogen generator coupled with some form of renewable power and some form of energy conversion device has a distinct advantage over a battery system backing up the same renewable application. Proton cannot determine which renewable technology will win out in the end, nor predict which energy conversion device will be the most cost effective. However, it is clear that the link to these

HOGEN is a registered trademark of Proton Energy Systems, Inc.

alternatives lies in the ability to convert excess renewable power into hydrogen and have the hydrogen available for conversion back to power, on demand.

To that end, Proton will utilize Phase II funding to begin significant cost reduction efforts on the hydrogen generator product line that will reduce the cost of the hydrogen generator family by 50% in the next two years and show evidence of further reductions in the years beyond. Cost reduction efforts will focus on three key elements of the electrolyzer: the electrolysis cell stack, the power conditioning and renewables interface, and the system components. These reductions will be implemented on the smaller HOGEN 40 (6 kW electrical power in) electrolyzer first and expanded to the larger HOGEN 380 (60 kW electrical power in) electrolyzer towards the end of the program. All of the improvements undertaken on this program will benefit the full line of electrolyzers so that the cost to large and small energy storage applications will be reduced.

Long Term Goals

All of Proton’s cost reduction goals are focused on the long term markets associated with sustainable power. However, there are three other markets where the hydrogen generator technology fits well and where products can move into commercial applications while the renewable technologies mature, come down in cost and become more commercially available.

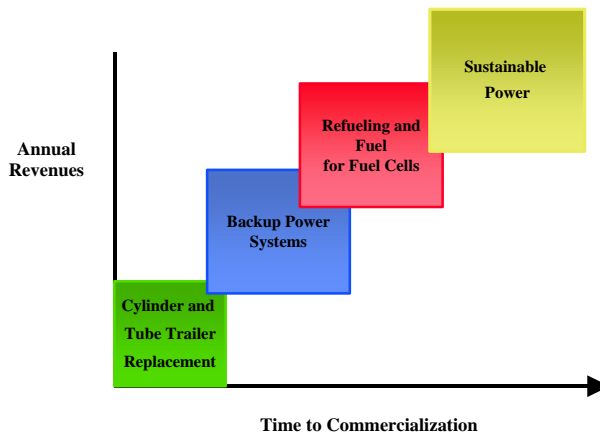


Figure 1 – Market Scope and Timing

These markets all have unique attributes that require different cost structures and pricing to compete effectively. Based on these markets and Proton’s internal projections for numbers of units, market share and earnings, a detailed cost reduction plan was developed. The plan, as it pertains to hydrogen generators, focused on the HOGEN 40 and the HOGEN 380 sized units with the near term emphasis on the HOGEN 40.

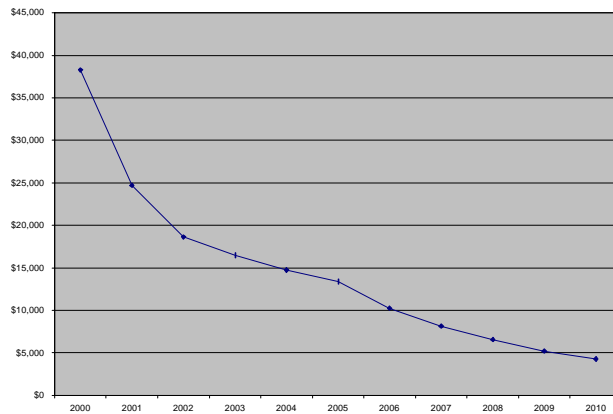


Figure 2 –HOGEN 40 (6kW) Ten Year Cost Projection

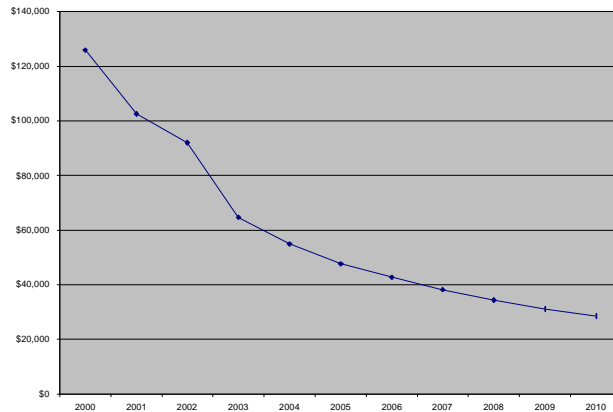


Figure 3 –HOGEN 380 (60kW) Ten Year Cost Projection

The hydrogen program has a goal of hydrogen production at the lowest possible cost. To that end, Proton has established a cost goal of \$1000 per kW in the near term and \$500 per kW within ten years. The goal of \$1000 per kW is achieved rather quickly on the larger generator, but requires a few more years on the HOGEN 40. This is not unexpected, as the economies of scale on the larger unit are much more favorable than on the smaller unit. Regardless, both units project costs that are comfortably under \$1000 per kW by 2010. The following sections will discuss in further detail the areas of cost reduction under the current agreement.

Electrolysis Cell Stack

The cell stack is the heart of the system and requires the most amount of technology development to realize significant cost reduction. Although significant government-sponsored research has focused on component cost reduction in fuel cell stack designs, there has been little emphasis on similar cost reduction efforts for PEM electrolysis stack components. This task will focus on addressing the electrolysis cell stack on a component-by-component basis using strategies that have been substantially proven in fuel cell hardware. Subtasks will address support components, membrane and electrode assemblies and flow fields. Individual component-level activities are further described below.

Support Components

The electrolysis cell stack has traditionally used machined endplates and a spring washer configuration on tie rods to maintain proper mechanical compression on the individual cell components. Work will be done to redesign the endplates for implementation of a near-net-shape process such as casting or powder metallurgy that minimizes the amount of material that is used and further reduces process time. Different materials of construction of the compression hardware will be explored and the required tooling will be purchased for the 0.1 square foot cell stack design (smaller stack) and then expanded to include the 1.0 square foot cell design (larger stack) upon successful prove out of the smaller design. In addition, design work to investigate alternate methods of mechanical compression will be conducted and evaluated on the smaller stack. If successful, this design approach will then be applied to include the larger stack.

Membrane & Electrode

This task will optimize the membrane and electrode assembly (MEA's). This will include optimization of the amount of catalyst applied to both the hydrogen and oxygen sides of the electrode as well as the method of those applications. Techniques for catalyst application that will be investigated will include certain approaches utilized in the manufacture of fuel cell MEA's such as silk screening of inks and application of dry powders. State-of-the-art electrolyzer oxygen electrodes that are generally proprietary precious metal formulations will be used instead of typical fuel cell grade platinum/carbon materials. Membrane materials showing significant cost savings and performance enhancement opportunity will be evaluated as part of this program task. These materials may include thinner perfluoroionomers, modified styrene based materials, and composite structures. The targeted evaluation protocol will determine if these materials can withstand the life requirements and high differential pressures associated with electrolysis operation. This evaluation will include cycle testing of these materials in small test cells as well as non-operational performance characterization tests such as MEA resistance and gas diffusion.

Flow Fields

This task will further development of a lower cost electrode support material and implement advanced configurations previously conceived by Proton. This involves the characterization of materials that are electrically conductive, corrosion resistant, mechanically robust and offer the proper fluids carrying capability required for high performance. Testing will include short-term corrosion and performance testing in cells as well as benchtop characterization testing which includes porosity, tensile, resistivity, and thickness testing.

Power Conditioning and Renewables Interface

Power Electronics

This task will look for innovative ways to reduce the cost of the cell stack power supply and associated electronics as well as improving its efficiency. The power supply currently represents about 10-15% of the system material cost. Overall system efficiencies such as cells vs. current will be investigated in order to determine the optimum cost per kW we can provide. Design work will look to integrate many of the parts of the current power electronics design into the two systems to eliminate redundant framework and components.

Alternate Energy Inputs

It is imperative that the HOGEN be able to ultimately operate with a number of different renewable technologies. This task will look at various types of renewable inputs and the potential impacts on interface and operations. Various technologies and sources of supply will be contacted including the Phase I partners.

System Cost Reductions

Circuit Board

This task will evolve the controllers that are currently used on-board the electrolyzers into a circuit board design that will also serve to eliminate many of the electrical control monitoring that currently requires many discrete components and quite a bit of labor to wire. This will involve use of an outside board design house to take a baseline design used on Proton's smallest electrolyzer and add the required functionality first to the HOGEN 40 and then to the HOGEN 380. The complex nature of the system safety controls and functionality as the unit gets larger requires that this be done in a two step process.

Component Cost Reductions through Casting and Manifolds

Pressure vessels in the HOGEN system, including the hydrogen-water separator, are machined from 316 stainless steel plate and pipe stock and welded to make the completed assembly. Valves, gauges and other small hydrogen and water components are plumbed together in a discrete manner with many fittings. The goal of this task is to effect significant cost reductions in the HOGEN fluid system by going to a powdered metal 316SS casting for the hydrogen-water separator. Use of manifold mounting of components on the hydrogen water phase separator or by using an alternate component manifold will eliminate fittings and permit use of less costly manifold mount valves and components.

Project Status and Plans for Next Year

The Phase II efforts were awarded May 1, 2000. Proton has been initiating efforts on the electrical control board, low cost endplates and spring washer designs, testing of various cell stack component configurations and characterization of various renewable inputs. Other efforts as previously described will be initiated in the coming months.

As the project advances into the coming years, all cost reductions will be verified on the HOGEN 40 to ensure that they meet the product life and integrity requirements, and that they also result in the expected cost reduction. As this occurs, the item will be introduced into production and the cost reduction effort will be advanced to the HOGEN 380 product. Cell stack cost reduction efforts will be introduced as they mature to the point where their life and performance data can be adequately characterized.

In addition, Proton will research additional methods to reduce the cost curves presented above to target costs of under \$500 per kW before 2010.

References

1. Friedland, R., Smith, W., Speranza, A., January 2000. *Integrated Renewable Hydrogen Utility System*, Phase I Final Technical Report and Market Assessment PES-T-99014.

Listing of Figures

1. Market Scope and Timing
2. HOGEN 40 (6kW) Ten Year Cost Projection
3. HOGEN 380 (60kW) Ten Year Cost Projection

HIGH EFFICIENCY STEAM ELECTROLYZER

Ai-Quoc Pham
Lawrence Livermore National Laboratory
7000 East Avenue, L-350, Livermore, CA 94550

Abstract

A novel steam electrolyzer has been developed. In conventional electrolyzers, oxygen produced from electrolysis is usually released in the air stream. In our novel design, natural gas is used to replace air in order to reduce the chemical potential difference across the electrolyzer, thus minimizing the electrical consumption. The oxygen from the electrolysis is consumed in either a total oxidation or a partial oxidation reaction with natural gas. Experiments performed on single cells shown a voltage reduction as much as 1 V when compared to conventional electrolyzers. Using thin film materials and high performance cathode and anode, electrolysis could be done at temperatures as low as 700°C with electrolytic current as high as 1 A/cm² at a voltage of 0.5 V only. The 700°C operating temperature is favorable to the total oxidation of natural gas while minimizing the need for steam that is otherwise necessary to avoid carbon deposition. A novel tubular electrolyzer stack has been developed. The system was designed to produce hydrogen at high pressures, taking advantage of the simplicity and high efficiency of the electrochemical compressors. A complete fabrication process was developed for making electrolyzer tubes with thin film coatings. A 100 W stack is being built.

Introduction

Currently, most of the total hydrogen demand is met by hydrogen production from fossil fuels, i.e., by steam reforming of natural gas and by coal gasification. However, most of these central plants are located in remote areas. The produced hydrogen must then be delivered to the users either by trucks or by using hydrogen pipelines. Because of the inherently low energy density of hydrogen, hydrogen transportation is not a viable option. Hydrogen delivery using pipelines is not cost effective neither because of the high cost of the hydrogen pipelines (about \$1 million/mile). Thus, the ideal hydrogen production for the future hydrogen economy is likely to be a distributed system where hydrogen is produced close to where it is used. Such a distributed hydrogen production using distributed small conventional steam reforming reactors is not possible due to the very high cost of the reactors at small scales.

Hydrogen can be produced from water or steam electrolysis using much simpler technology. Due to the modularity of the electrolyzer, electrolysis can be done at a central plant as well as at a refueling station or at home. In addition, electrolysis using renewable electricity offers the possibility to produce hydrogen without any greenhouse gas emissions. However, water electrolysis has not had significant commercial impact because it has not been possible to make it cost effective.

The main drawback of the electrolyzers is the high electricity consumption. Electricity is known to be by far the most expensive form of energy. As a result, electrolytic hydrogen is more expensive than the steam-reformed hydrogen by a factor of at least two to three (Donitz 1990). Moreover, electricity is not a primary energy but must be produced using fossil fuels, nuclear fuels or renewable energy. Considering the fact that the production of electricity has an average efficiency of less than 40% with respect to primary energy, the overall efficiency of the electrolyzer in general is low. In addition, currently, less than 20% of the overall electricity production in the United States involves renewable energy. As a consequence, electrolysis using electricity coming from the grid is not a carbon-free process, but actually involves a large amount of greenhouse gases due to the use of electricity that is mostly produced from burning coal and natural gas. On the other hand, electrolysis using exclusively renewable energy would have limited applications since they must be linked directly to a renewable energy source.

The long-term objective of this project is to develop a high efficiency steam electrolyzer for carbon-free production of hydrogen. This approach will be viable only when renewable energy becomes the major source for electricity production. The short-term goal is to develop a transitional electrolyzer technology that takes into account the current situation of electricity production and the current economic infrastructure. The goal for the transitional electrolyzer technology is a distributed hydrogen production system with lower electricity consumption, higher overall efficiency and lower greenhouse gas emissions.

Background

From the thermodynamic viewpoint of water decomposition, it is more advantageous to electrolyze water at high temperature (800-1000°C) because the energy is supplied in mixed form of electricity and heat (Donitz 1980). In addition, the high temperature accelerates the

reaction kinetics, reducing the energy loss due to electrode polarization, thus increasing the overall system efficiency. Typical high temperature electrolyzer such as the German HOT ELLY system achieves 92% in electrical efficiency while low temperature electrolyzers can reach at most 85% efficiency only (Donitz 1990). Despite this high efficiency with respect to electricity, the German system still produces hydrogen at about twice the cost of the steam-reformed hydrogen (Donitz 1990). According to the German analysis of the HOT ELLY system, about 80% of the total hydrogen production cost comes from the electricity cost (Donitz 1990). Therefore, to make the electrolytic hydrogen competitive versus the steam-reformed hydrogen, the electricity consumption of the electrolyzer must be reduced. Currently, there is no solution because the high electricity consumption is dictated by the thermodynamic of the decomposition of water.

In conventional steam electrolyzers, the gas supplied to the cathode side (where water is decomposed) is usually a mixture of steam and hydrogen, while the gas supplied to the anode side is usually air. At zero current, the system has an open-circuit voltage of 0.8 to 0.9 V, depending on the hydrogen/steam ratio and on operating temperatures. This open-circuit voltage is even higher for water electrolysis. In order to electrolyze water, a voltage that opposes and is higher than the open circuit voltage must be applied in order to pump oxygen from the steam side to the air side. Clearly, much of the electricity used, 60 to 70% of the total electrical power, is wasted forcing the electrolyzer to operate against the high chemical potential gradient for oxygen. In addition, the liberation of oxygen coming from the decomposition of water into the air stream at the anode side is clearly a waste.

Approach

In order to lower the open circuit voltage, and thus the electricity consumption, our approach is to replace air in the anode side by natural gas (Pham 2000). The reducing character of natural gas will help to bring down the chemical potential difference between the two sides of the electrolyzer. One can distinguish two different modes of operation: total oxidation or partial oxidation of natural gas. In the first case, natural gas is used in the anode side of the electrolyzer to burn out the oxygen coming from the electrolysis, thus reducing or eliminating the potential difference across the electrolyzer membrane. The products of the reaction will be CO₂ and steam. The role of natural gas is just to lower the chemical potential gradient, thus the electricity consumption. This mode replaces one unit of electrical energy by one equivalent energy unit of natural gas at one-fourth the cost. Due to the thermodynamic, the total oxidation mode is restricted to temperatures lower than 700°C. Above 800°C, carbon monoxide becomes more stable and total oxidation is not possible.

In the second operation mode, an appropriate catalyst on the anode side will promote the partial oxidation of natural gas to carbon monoxide and hydrogen. The resulting gas mixture, also called syn-gas can be used in important industrial processes such as the synthesis of methanol, liquid fuels... Most important of all, CO can also be shifted to CO₂ to give additional hydrogen. In this process, hydrogen is produced at both sides of the steam electrolyzer. The overall reaction is equivalent to the steam reforming of natural gas. As opposed to the steam reforming reactors, the modular characteristics of the electrolyzer, together with the absence of the extensive heat exchangers, make possible the small-scale hydrogen production units. However,

we chose to focus our effort on the total oxidation mode because it is simpler and does not require any additional water-shift nor CO clean-up units.

In both cases, the key point of the approach is to use natural gas directly on the electrolyzer instead of using natural gas to make electricity at the central plant, then to use that electricity to split water. The efficiency and the carbon emissions will be lower than in conventional electrolysis. The Natural-Gas-Assisted Steam Electrolyzer or NGASE is not a carbon free hydrogen production system because it still involves natural gas. However, by combining both natural gas and electricity, which have existing infrastructures, the NGASE is an ideal transitional technology for distributed hydrogen production.

Summary of last year accomplishments

During FY99, we demonstrated the feasibility of the NGASE concept. Using small disk samples having yttria-stabilized-zirconia (YSZ) as thin film electrolyte, Ni/YSZ as composite anode and cathode, we shown that the use of methane in the anode side reduced the electrolyzer voltage by as much as 1 V. The open-circuit voltage actually became negative, indicating that the methane side had lower oxygen partial pressure than the steam/hydrogen side. In the low current region, the cell operated in a fuel cell mode, i.e. the splitting of water molecules occurred spontaneously. The use of thin film was shown to be of great benefit to the overall cell performance. The effect of steam and methane concentrations on the electrolyzer performance was studied. We found that both electrodes could still be improved. One of the major problems found was that significant carbon deposition occurred at the 900°C operating temperature, unless a large amount of steam is mixed with methane.

Preliminary analysis shown that the electricity consumption for the NGASE is almost an order of magnitude lower than that of the HOT ELLY, the remaining energy requirement being supplied by natural gas. The system efficiency with respect to primary energy can be higher than 60% while that of conventional electrolyzers is below 40%.

Accomplishments

Development of improved electrode/catalysts

Early characterization has shown that the anode performance is mainly diffusion-limited. Therefore, improving the anode porosity should improve the gas phase diffusion and thus the anode performance. Various pore former materials, including carbon, polymers and starches have been tested. The optimum pore former amount has also been identified. Figures 1a and 1b shows the Scanning Electron Microscopy (SEM) pictures of the cross-section view of the anode materials without (last year cells) and with pore former respectively. The black dots correspond to the pores. Clearly, sample in figure 1b is significantly more porous than sample in figure 1a. The pores introduced are homogeneous and uniformly distributed in the matrix of the anode. Figure 2 shows the performance of the new cells with optimum porosity. The I-V curve of the HOT ELLY steam electrolyzer (Donitz 1990) as well that of last year data are reproduced for comparison. The performance of last year NGASE cell is similar to that of the HOT ELLY as indicated by the same slope. However, the voltage is about 1 V lower due to the use of methane

depolarizer. The new NGASE cell with optimum anode porosity outperforms the other cells. At only 0.5 V, the electrolytic current is as high as 2.8 A/cm², compared to 1 A/cm² for last year cell. The introduction of pore former has thus improved the electrolytic current by almost a factor of three. This is probably the highest electrolytic current per unit area ever reported to date.

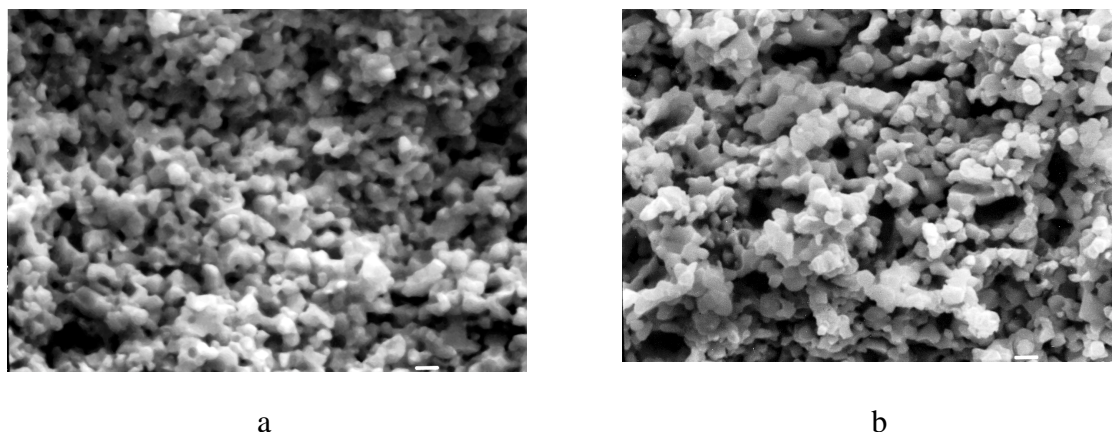


Figure 1 — SEM pictures of: a. 1999 anode with low porosity, b. 2000 anode with optimized porosity

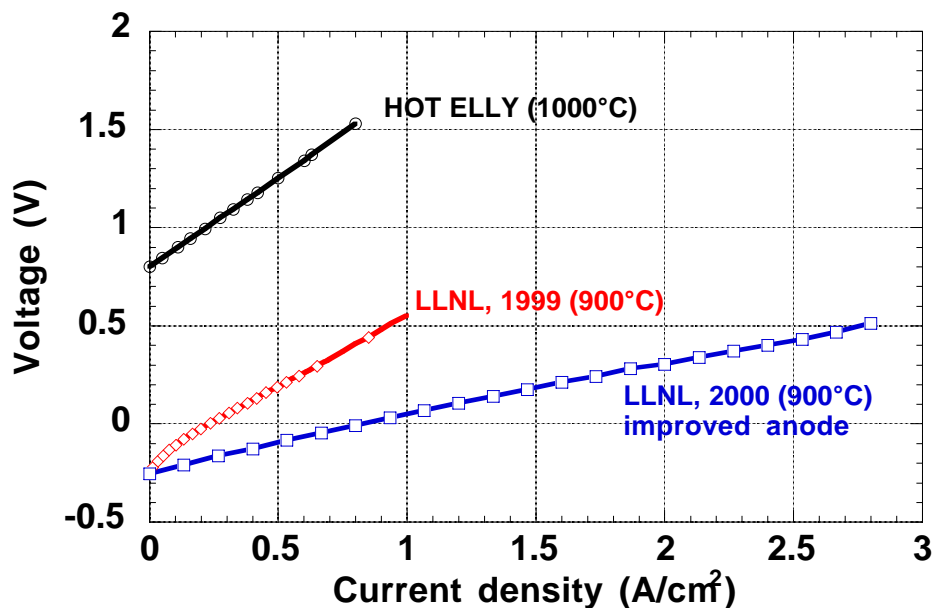


Figure 2 — Current-Voltage characteristics of various steam electrolyzer cells

However, as mentioned above, the operation at 900°C requires significant amount of steam in the methane side in order to avoid carbon deposition. The presence of excess steam can cause excessive steam-reforming of methane, which is undesirable because of the reaction is highly endothermic. Thus, it is highly desirable to reduce the operating temperature to minimize the

amount of steam and also to favor the total oxidation of methane. Figure 3 shows the I-V plot of the new cell with improved anode at 700°C. The performance drops significantly, the electrolytic current at 0.5 V is down from 2.8 A/cm² at 900°C to 0.35 A/cm². This poor performance has been identified as due essentially to the cathode. The cathode material, Ni/YSZ, was then replaced with a better electrode/catalyst. The I-V curve of the cell with both improved anode and cathode is also shown in figure 3. At 0.5 V, the current increases to 1 A/cm², about three times the current of the cell with the old cathode. Overall, the development of the improved cathode and anode has allowed to reduce the operating temperature from 900°C to 700°C while preserving excellent cell performance. The main advantage is that carbon deposition is suppressed even with steam concentration as low as 10% only.

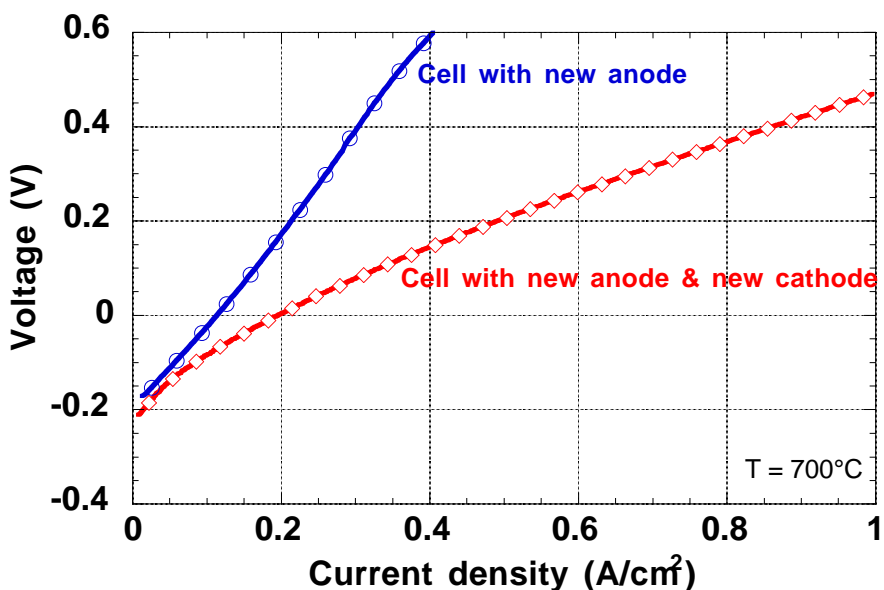


Figure 3 — Current-Voltage characteristics at 700°C

Development of electrolyzer stacks

Most of the actual uses of hydrogen require hydrogen under some pressure. Thus the cost consideration of various hydrogen production methods must take into account the need to pressurize hydrogen. If hydrogen is produced at low pressure and a hydrogen compressor must be used for pressurization, then the overall production cost could be high due to the high cost, high maintenance and low reliability of the hydrogen compressors.

As mentioned above, pure electrolysis is not attractive due to the high electricity consumption from the hydrogen production standpoint. However, when used as a compressor, electrochemical devices are known to be the most efficient devices for the pressurization of hydrogen. One of the most attracting features is that electrochemical compressors just require an extra 100 mV or so to pressurize hydrogen from ambient pressure to 5000 psi. Therefore, the

design of the electrolyzer stack must take advantage of the possibility to pressurize hydrogen in-situ.

Since the electrolyzer is basically a fuel cell operating in reverse mode, the various stack designs developed for fuel cells can be considered for use for the electrolyzer. There are two major stack designs depending on the tubular or planar configurations. The planar configuration can be made compact and is potentially cheaper than the tubular design. However, it is much more difficult to pressurize the planar stack because the planar configuration is more subject to mechanical fractures, had there be a slight pressure differential across the plates. We chose to pursue the tubular configuration since this design allows to pressurize the exterior compartment while having ambient pressure inside the tubes. Figure 4 shows the drawing of the tubular electrolyzer stack with four tubes. The electrolyzer stack is located inside a metal vessel that can withstand high pressures. Natural gas flows inside the tubes at ambient pressure while the outside compartment is exposed to steam/hydrogen mixture at pressure. We have developed a novel process for efficient compression of hydrogen (DiCarlo 2000). Figure 5 shows the experimental reactor where the electrolyzer stack will be tested. Although the objective for this current year is hydrogen production at ambient pressure only, the system was designed for pressure operation up to 150 psi.

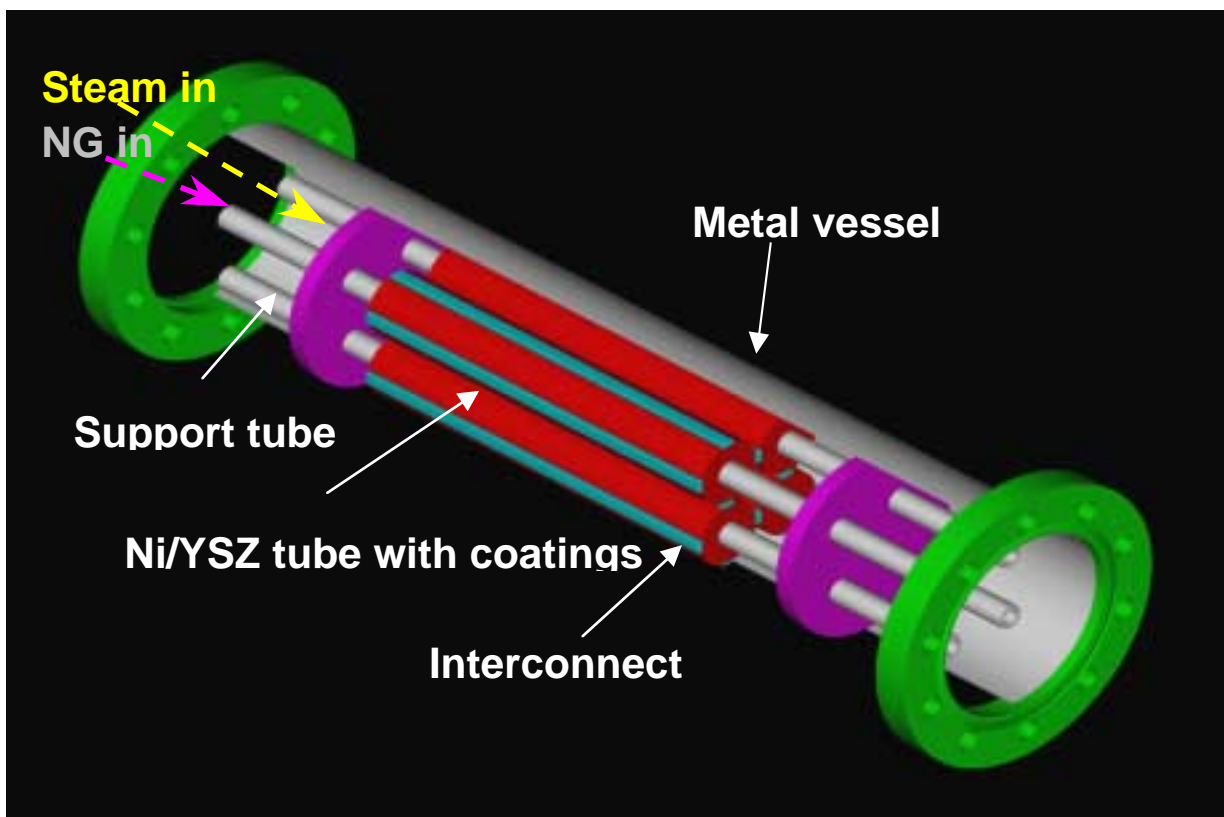


Figure 4 — Drawing of a four-tube electrolyzer stack



Figure 5 — Bench-scale reactor for a 100 W electrolyzer stack

Development of a tube fabrication process

A complete tube fabrication process has been developed. NiO/YSZ anode support tubes were made by cold isostatic pressing or by extrusion. The green tube was masked, and an interconnect thin film was deposited in form of a thin stripe along the tube. YSZ electrolyte thin film was then coated on the tubes, followed by sintering at high temperatures (Pham 1999). The thin film cathode was subsequently deposited. All thin films were processed using the Colloidal Spray Deposition, a low cost thin film deposition technique that we have developed recently (Pham 2000). Figures 6a and 6b show the tube after cold isostatic pressing and after completion respectively. A SEM cross-section view of the electrolyzer tube is shown in figure 7. The performance of the individual tubes is currently evaluated.



a



b

Figure 6 - Electrolyzer tubes: a. green tube after cold isostatic pressing, b. after completion

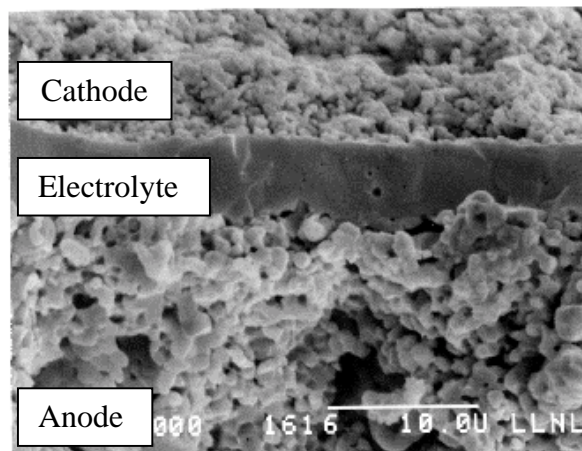


Figure 7 — SEM cross-section view of an electrolyzer tube

Conclusion and future work

We have significantly improved our electrolyzer performance using new and optimized electrode materials. The electrolyzer operating temperature has been lowered down to 700°C to favorize total oxidation process while minimizing carbon deposition. We have developed a tubular electrolyzer stack that can be used to efficiently pressurize hydrogen in-situ. A fabrication process has also been developed for making ceramic tubes with thin film coatings.

We plan to demonstrate a 100 W electrolyzer stack operating at ambient pressure by September 2000. For FY01, we will develop an improved prototype with twice higher capacity and capable of operating at high pressures. We plan to explore the possibility to use the electrolyzer to produce both hydrogen and electricity on demand (one product at a time). Preliminary experiments have indeed shown that, granted some modifications, the electrolyzer system can also be used as a solid oxide fuel cell to produce electricity using natural gas as a fuel. The power density is still low, in the range of 300 mW/cm² at 800°C. However, we expect to be able to significantly increase the performance in the fuel cell mode. Both the high-pressure operation and the co-production of hydrogen and electricity are interesting features that will set the NGASE as a unique device for the distributed generation of hydrogen and electricity.

References

- Donitz, W., Schmidberger, R., Steinheil, E., Streicher, R., *Int. J. Hydrogen Energy*, **5**, 55 (1980).
 Donitz, W., Erdle, E., Streicher, R., 1990. *Electrochemical Hydrogen Technologies.*, Wendt, H., Editor. Elsevier. p 213.
 Pham, A.Q., Lee T.H., and Glass, R.S., 1999, Colloidal Spray Deposition Technique for the Processing of Thin Film Solid Oxide Fuel Cells, In *Proceedings of the 6th International Symposium on Solid Oxide Fuel Cells*, edited by S. C. Singhal and M. Dokiya, The Electrochemical Soc., Pennington, NJ. USA p.172.
 Pham, A.Q., Wallman, H., Glass, R.S., US patent n°6051125 (April, 2000).

Figure captions

Figure 1 — SEM pictures of: a. 1999 anode with low porosity, b. 2000 anode with optimized porosity

Figure 2 — Current-Voltage characteristics of various steam electrolyzer cells

Figure 3 — Current-Voltage characteristics at 700°C

Figure 4 — Drawing of a four-tube electrolyzer stack

Figure 5 — Bench-scale reactor for a 100 W electrolyzer stack

Figure 6 - Electrolyzer tubes: a. green tube after cold isostatic pressing, b. after completion

Figure 7 — SEM cross-section view of an electrolyzer tube

“FILLING UP WITH HYDROGEN 2000”

**Matthew J. Fairlie, Paul B. Scott
Stuart Energy USA
3360 East Foothill Blvd
Pasadena, California
91107-3111**

Abstract

“Filling Up with Hydrogen 2000” is Stuart Energy’s prototype deployment program to develop Hydrogen Fuel Appliances, purpose built on-site electrolytic hydrogen generators for refueling gaseous hydrogen vehicles. The general objective of this prototype deployment program is to demonstrate that electrolysis based hydrogen generators can meet market cost and performance targets. The program is in year 2 of Phase 2.

In Phase 2 of the Stuart/DOE program Stuart Energy will deploy two types of appliances called Fleet Fuel Appliances and Personal Fuel Appliances. The Fleet Fuel Appliance targets buses, trucks and other centrally fuelled fleet vehicles where fuel production rates in excess of 400 scfh (10 Nm³/h) are required. The Personal Fuel Appliance is geared towards consumers’ vehicles at the home or office, and can be supported by the utility infrastructure of the typical North American home. The production rate of these units is in the range of 50 scfh (1.5 Nm³/h). Both types of appliances will be capable of delivering gaseous hydrogen at high pressure (up to 5000 psig) to the vehicle. The goals of the program are to demonstrate the performance and cost objectives projected in the Phase 1 commercialization plan while accomplishing a safe and convenient refueling process.

Introduction

The objectives of the past year were to demonstrate operation of Stuart's new CST electrolytic cell stack technology in large-scale application as part of a hydrogen bus refueling station at SunLine Transit in 1000 Palm, California and in small sizes through the prototyping program for the personal fuel appliance. The CST cell stack is key to achieving the cost targets in both product lines. The experience from the demonstrations will provide an experience base for the cell stack technology for later commercialization, and is a cost effective approach for equipment testing in that the user picks up operating costs.

In addition to testing the cell technology, Stuart's prototype development plan provides public exposure to the fuel appliance concept, introducing customers to the idea of distributed on-site hydrogen production as well as providing valuable precedents for the development of codes and standards and hydrogen project risk assessment. The operation of the bus fuel appliance (P3-1A) at SunLine Transit provides public access to the technology through SunLine. The low-pressure fueler (P3-1B LP) provides a demonstration of a system, which can refuel metal hydrides. The high-pressure fueler (P3-1B HP) demonstrates the concept of a distributed "community fueler". Prototyping of the personal fuel appliance (PFA P1 Model 25) at major automakers will provide the auto industry the opportunity to evaluate the concept of a small onsite hydrogen generator and potential home based fueling appliance.

While the design and manufacture of the P3 prototypes provides a proving ground for component technology, primarily the cell stack, the design emphasis in the next 12 months will be development of the P4 systems. The P4 prototypes will realize a projected 50% reduction in appliance footprint and will be the basis for achieving manufacturing cost targets.

Stuart Fleet Fuel Appliance Program

The Fleet Fuel Appliance targets the refueling needs of hydrogen buses, trucks and other centrally fuelled fleet vehicles. Conceived to be a scalable product, 1 to over 30 vehicles can be supported with one appliance. By combining the purchasing power of a number of distributed fuel appliances off-peak power can be purchased at rates of less than 3 cents/kWh, which will make hydrogen from fleet fuel appliances competitive with other transportation fuels. The development of Fleet Fuel Appliance prototypes follows a four-phase product development program, which is now in its third phase. The 17.7 million-dollar program will be completed by 2003. The ultimate cost target for the fleet fuel appliance is \$3000 per scfm hydrogen production/refueling capacity. Relationships with bus operators and hydrogen bus companies will be developed during the prototype deployment period from 1999-2001. Commercialization will occur from 2001 to 2004 and will probably be led by fuel cell urban buses.

Fleet Fuel Appliance Cost Targets

Through the building of prototypes, practical experience has been gained to give a more accurate system analysis of the fleet fuel appliances. The data gained from factory testing the units has aided in establishing reliable, unattended operation. Also from this experience, a more accurate account of the costs in mass manufacturing has been acquired. These revised cost models show

\$400 per kW can be achieved for the entry bus fueller (10 buses) and \$300 per kW for 30 bus fleets. The electricity consumption would be 60kWh per kg of hydrogen produced.

P3 Fleet Fuel Appliance Progress

Prototype P3-1A

Following testing reported in last years report an extensive redesign of the cells of the P3-1A prototype was undertaken, involving the eventual replacement of the cell blocks. P3-1A demonstrates Stuart's new MW-CST or multi stack electrolyser cell technology, which is targeting bus fleets and large retail outlets. The new cells were factory tested up to full current (12000 amps) or a hydrogen production rate of approximately 1500 scfh. Not only were hydrodynamic stabilities corrected but so were earlier reported problems with foaming in the cell. The foaming was identified to be due to contamination in the cell assembly. The unit was delivered to Sunline Transit in 1000 Palms, California on February 24, 2000. Within 24 hours of landing in SunLine the unit was producing and pumping gas, demonstrating the quick deployment feature of the Stuart fuel appliance concept.



Figure 1 – The P3-1A Fleet Fuel Appliance at SunLine

The unit has been connected to a high-pressure storage system (approx. 100,000 scf) and an external dispenser, which is part of a public access hydrogen fueling station. The dispenser was designed by Stuart and built by Fueling Technologies Inc. High-pressure hydrogen is delivered through one hose and high pressure Hythane, a mixture of 20% by volume hydrogen in natural gas, from the other. Gas mixture is controlled dynamically by mass flow sensors and mixture is checked using a thermal conductivity sensor. The P3-1A will continue to fill buses and trucks at the SunLine site for a three year process evaluation. The hydrogen bus fleet consisting of one fuel cell bus and two Hythane buses are expected to enter revenue service in late summer 2000.



Figure 2 - The Hythane/Hydrogen Dispenser at the SunLine Public Filling Station

Prototype P3-1B LP

The low pressure fleet fuel appliance, P3-1B LP, delivers a rated hydrogen output of 400 scfh at 200psig. It uses Stuart's new H-CST single stack electrolyser technology on a standard design platform. In factory testing the P3-1B LP fueler has operated continuously for over 750 hours (32 days) at 120% of rated output (Figure 3). In total, the unit has operated for over 2800 hours. Subsequent disassembly and examination of the cell stack showed no significant deterioration of cell parts. The hydrogen purity is better than 99.99% with less than 20ppm of oxygen. The water vapour dew point of the delivered hydrogen is better than -70°C expanded meeting the purity requirements for metal hydride gas storage ($\text{M-Ni}_{4.5}\text{Al}_{1.5}$). In the coming year, the hydrogen from the prototype will be used to demonstrate refueling hydrogen vehicles in underground mining applications.

Prototype P3-1B HP

Construction of the P3-1B HP fleet fuel appliance has been completed. Based on the same platform as P3-1B LP the unit uses H-CST technology. The commissioning of the unit was completed recently and testing has started. The hydrogen production rate is rated at 400scfh at a maximum pressure of 5000psig with plans to increase pressure to 6000 psig. Once factory tests have been completed, the unit will be deployed at a customer site.

Prototype P3-5 Cell Stack Assembly

The construction of the P3-5 fuel appliance, capable of fueling 5 buses or approximately 10000 scfh has been taken to the design stage of the cell stack assembly only. The cell stack assembly will be constructed in 2- block cell platforms. The blocks are mounted back to back so that in an assembly the units form a U shaped bank, which can be assembled in an enclosure. The cell stack assembly design will be used in future bus fueler prototypes.



Figure 3 – P3-1B-LP Factory Test



Figure 4 – P3-1B-HP Prototype

P4 Fleet Fuel Appliance Future Goals

The design of the P4 prototypes are underway; the build schedule is shown below. Among the improvements will be the use of a new process, which pressurizes the stack and eliminates the need for a water seal. A P4 stack similar to that being used in these appliances has been under test for about 500 h.

Other improvements to be built into the P4 series of prototypes will be: reducing the number of cell stacks in H-CST appliances from two to one by increasing the size of the stack and increasing current density, reducing dryer costs by using an interstage drier, and using a switching mode power supply rather than conventional rectifier to reduce size and improve power factor. Once constructed the unit will be factory tested and eventually deployed in the field at a prototyping partner site.

Table 1. Schedule for Fleet Fuel Appliance Prototypes

| PROTOTYPE | PROTOTYPING PARTNER | DELIVERY DATE |
|-------------------------|---------------------------------|----------------------|
| Fleet Fuel Appliance | | |
| P3-1A | SunLine Transit | Q1 2000 |
| P3-1B (High Pressure) | CA Fuel Cell Partnership* | Q4 2000 |
| P3-1B (Low Pressure) | Fuel Cell Propulsion Institute* | Q4 2000 |
| P4-1 | TBA | Q1 2001 |
| P4-10 | TBA | Q4 2001 |
| Personal Fuel Appliance | | |
| PFA-P1-99 | Ford Motor Company | Q4 2000 |

* proposal under consideration

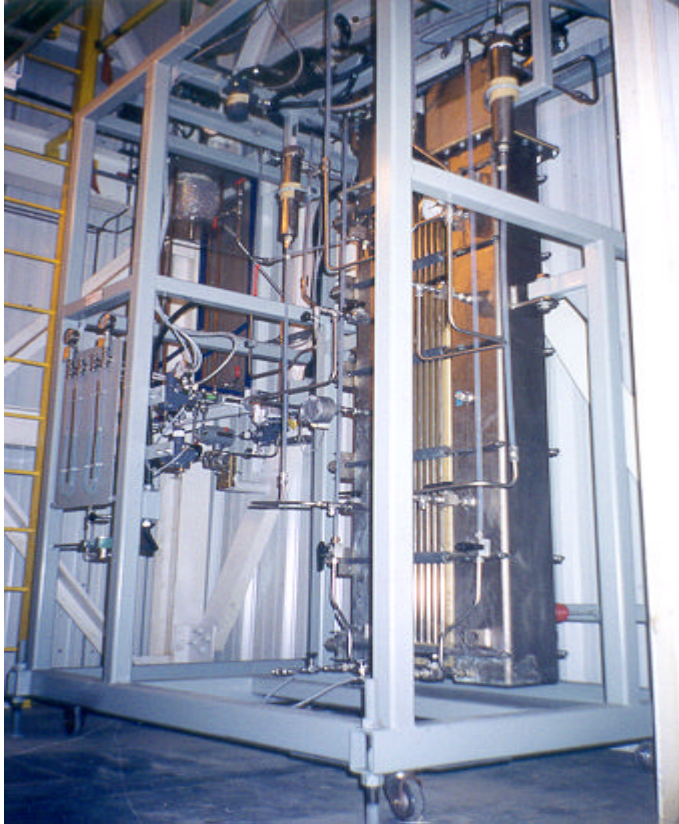


Figure 5 – Phase 4 Prototype Cell Under Test

Personal Fuel Appliance

Stuart Personal Fuel Appliance Program

The aim of the PFA program is to develop a viable solution to the problem of production and storage of hydrogen for the average consumer's vehicle. The PFA allows refuelling to take place at home or at a place of business, using household utilities, water and electricity and is designed to be as simple to operate as a battery charger. The PFA program includes all necessary equipment for supplying high-pressure fuel for "time filling" hydrogen vehicles. The only inputs are water and electricity; the only outputs are vehicle-ready hydrogen and oxygen. The product development program will be completed by 2003 at an expense of 15.2 million dollars. Commercialization will occur from 2003 to 2004.

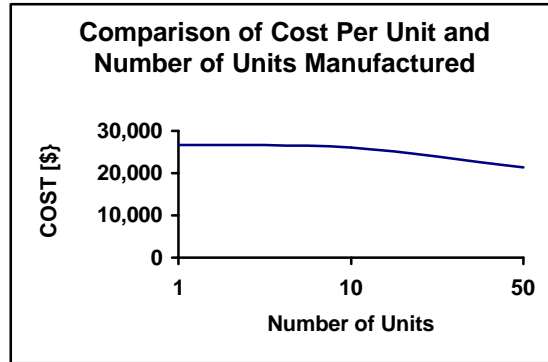
The Personal Fuel Appliance family of products can be marketed as part of a hydrogen vehicle purchase, as a choice of an alternative fuel supply, or as a portable hydrogen maker for more than just a car. This concept of a widely dispersed hydrogen fuel supply infrastructure presents new energy control alternatives and prepares the way for extensive integration of renewable sources into the power mix.

Personal Fuel Appliance Cost Model Targets

Near-term cost projections for the prototypes are shown below. These are on track with cost projections presented in earlier studies to achieve a cost of \$1500 at production volumes of

100,000 per year. The near term plan calls for assembly of a fleet of ten prototypes for limited release to automakers and strategic fleet operators.

Table 2 – Near-Term PFA Costs



Personal Fuel Appliance Results and Future Goals

PFA P1 1999 Unit E delivers 3600psig hydrogen at a rate of 40 scfh. In December of 1999 it was demonstrated to the auto industry at Ford Motor Company at the Dearborn headquarters for the Think group and Daimler Chrysler at Auburn Hills, and at the beginning of this year at National Hydrogen Association Annual Meeting in Washington DC.

The second unit, PFA P1 1999 Unit D, is improved from Unit E in several ways. The system is much more reliable, and approximately 120 pounds lighter. This unit is currently on a tour of California, CARB, SCAQMD, and at SunLine Transit.

Ford Motor Company, Dearborn will be ready to accept a unit for testing in Q3 2000. The evaluation of this unit by a major automaker is the last deliverable of the PFA segment to this project.



Figure 6 – P1 Model 25 Refueling NRG Hythane Vehicle at the NHA Meeting, Washington, DC



Figure 7 – Model of 2003 PFA

Conclusion

The objectives for next year are to deploy all three of the P3 type prototypes and begin field evaluation of the cell stack technology. In the next year we hope to complete the design, and build a P4 appliance incorporating improvements to the cell stack, higher current density and incorporate the new pressure controls, which will elevate pressure in the cell and eliminate water seals in the process. For the personal fuel appliance program, through joint evaluation with major North American automakers, we hope to prove the fuel appliance concept.

References

Stuart Energy USA, *Filling Up With Hydrogen*, 1998, under DOE Cooperative Agreement No. DE-97GO10221

Ford Motor Company, Directed Technologies Inc., Air Products and Chemicals, BOC Gases, The Electrolyser Corporation Ltd., and Praxair Inc. 1997. *Hydrogen Infrastructure Report*, under DOE Prime Contract No. DE-AC02-94CE50389

List of Figures

- Figure 1 - The P3 Fleet Fuel Appliance at SunLine**
- Figure 2 - The Hythane/Hydrogen Dispenser at the SunLine Public Filling Station**
- Figure 3 - P3-1B-LP Factory Test**
- Figure 4 - P3-1B-HP Prototype**
- Figure 5 - Phase 4 Prototype Cell Under Test**
- Figure 6 - P1 Model 35 Refueling NRG Hythane Vehicle at the NHA Meeting, Washington, DC**
- Figure 7 - Model of 2003 PFA**

TECHNOLOGY DEVELOPMENT AND VALIDATION OF INDUSTRIAL FUEL CELL VEHICLES - PHASES II/III

James M. Morrison
Southeastern Technology Center
Augusta, GA 30906-3381

Abstract

The status and plans to develop and validate a light industrial vehicle powered by a fuel cell with on-board storage of hydrogen fuel as a metal hydride are described. Work began in August 1998 and this phase of the project is scheduled to end in September 2000. The first of two prototype vehicles has been assembled and is undergoing testing and evaluation. Performance agrees well with a steady state computer model developed to aid in evaluation and design. Several opportunities have occurred for display and demonstration of the first vehicle. A number of operating problems have been encountered requiring modifications or repair. Lessons learned from this experience are being factored into the design of the second prototype vehicle which employs more advanced fuel cell and metal hydride storage technologies. Assembly of the second vehicle is in progress and expected to be complete in early summer 2000. A market evaluation is being performed by Deere & Co., the vehicle manufacturing participant in the project, to determine the prospects for an ultimate commercial version of the vehicle. Technical and business plans leading to commercialization will be developed as warranted by the outcome of this evaluation, also scheduled for completion this summer.

Project Status and Plans

Project Participants

A total of seven organizations are participating in the Phase II/III Industrial Fuel Cell Vehicle (IFCV) Project. These include, together with their individual areas of interest and expertise:

- Deere & Company IFCV manufacturing and sales
- Energy Partners PEM fuel cells

- Westinghouse Savannah River Co. Metal hydride hydrogen storage system
- Teledyne Brown Engineering Hydrogen generator design and sales
- University of South Carolina-Center for Electrochemical Engineering Performance modeling & testing, H2 storage/refueling testing
- York Technical College IFCV validation testing
- Southeastern Technology Center Project management and integration

As project manager, Southeastern Technology Center (STC) serves as the applicant for the DOE Cooperative Agreement under which the project is sponsored and funded. The non-federal participants provide nominally a 50% cost share of the total Phase II/III project budget, which is approximately \$1.25 million.

Long-Term Goals

The fundamental goal of the project is to develop and validate small commercial electric vehicles utilizing hydrogen fuel cell power and on-board storage of fuel as a metal hydride. The concept of solid state storage of hydrogen is being employed to provide inherent safety advantages. This technology, developed originally for national defense purposes, is provided by the Westinghouse Savannah River Co. (WSRC) as a technology Transfer initiative.

A corollary goal is to develop and validate a compatible hydrogen generator system that could be used to provide refueling for limited numbers of IFCVs in commercial service locations. The generator used for this purpose in the project is an electrolyzer designed and manufactured by Teledyne Brown Engineering Energy Systems (TBES), one of the project participants.

A number of potential applications are envisioned for a commercial IFCV, such as in landscaping, airports, warehouses, maintenance, and various other off-road uses.

FY 2000 Objectives and Rationale

The Phase II/III IFCV Project has a number of objectives to be accomplished during FY 2000. The first is to complete design, assembly, testing, and evaluation of the first prototype IFCV, designated Gator 1 (“Gator” is a trademark of Deere & Co., which manufactures and sells a line of small Gator vehicles for a variety of customer applications). The purpose of Gator 1 is not only to determine the validity of the IFCV concept, but also to provide feedback to improve the design of the more advanced second prototype.

The second major objective in FY 2000 is to design, build, and test Gator 2, which employs more advanced designs for the fuel cell power system and the metal hydride storage system. The purpose of testing and evaluating Gator 2 is to provide a basis for a reference design of a commercial vehicle.

The third major objective this year is to evaluate the readiness of the IFCV concept to enter the pre-commercialization phase of the long-term program. A number of factors will affect this

evaluation, such as design, performance, reliability, cost, market prospects, and business criteria important to the ultimate vehicle manufacturer. The last major objective, then, following the readiness determination is to decide the path forward beyond FY 2000 and to define the business strategy and plan for ultimate IFCV commercialization.

FY 2000 Tasks

The tasks in place for FY 2000 are designed to accomplish the project objectives. Two prototype vehicles, Gator 1 and Gator 2 are scheduled to be built and tested. Gator 1 represents an extension of the technology demonstrated when two previous vehicles were built and tested with fuel cell power systems and on-board pressurized gas storage. Gator 1 incorporates a more advanced fuel cell than the previous units as well as a solid state metal hydride storage system with inherent safety advantages. In turn, Gator 2 includes yet more advanced designs of both the fuel cell and the metal hydride storage units, and its scheduled completion is later than Gator 1 to permit incorporating design improvements suggested by experience with the first prototype.

Several tasks are designed to help evaluate the readiness of the IFCV concept for pre-commercialization. Results from the design and testing activities are major inputs. Both performance and reliability will be evaluated. The market evaluation of the prospects for a commercial IFCV constitutes an extremely important task, as does other business factors to be weighed by Deere & Co. The outcome of these considerations by Deere is expected to be definition of the corporate position, strategy, and long-term business plan for commercialization. When available, all these inputs will determine the recommendations for the path forward beyond FY 2000 that will be made by the project.

Progress and Accomplishments

Significant progress has been made this year. Assembly of Gator 1 was completed by Energy Partners and the vehicle successfully passed the checkout tests of all on-board systems. Refueling tests were run at the University of South Carolina-Center for Electrochemical Engineering (USC-CEE). Two types of tests were conducted. The first was on a sample of the metal hydride material (a La-Ni-Al compound) used in Gator 1 which was provided by WSRC in a test bed. The bed was connected to the TBEES electrolyzer and runs were made at different rates, pressures and temperatures to define the adsorbing/desorbing characteristics of the hydride material. The electrolyzer was subsequently connected to the metal hydride beds in Gator 1 to check refueling times. Gator 1 performance tests were conducted by USC-CEE to verify the output of the fuel cell, parasitic loads of auxiliary equipment (primarily the air compressor), overall vehicle performance, and benchmark the steady state computer model developed by USC-CEE.

Gator 1 was then transferred to York Technical College (York Tech) for reliability testing, which is still in progress. These tests, to determine range, operating time, speed, endurance and other characteristics have been extremely valuable in identifying problems for feedback into the Gator 2 design process. Many of these problems have been of a systems integration nature, very difficult to predict in advance, and this validated the original project plan to design and build the two prototypes sequentially rather than simultaneously. Some typical examples of problems encountered to date are:

- High compressor noise levels
- Overheating of the compressor motor during idling
- High fuel cell temperatures due to a faulty cooling water bypass valve
- Starting difficulties caused by excessive hydrogen purging
- Fuel cell shutdowns on low voltage, due to flooding

There has been considerable public and corporate exposure of Gator 1 this year. The IFCV concept was reviewed in a paper presented by Energy Partners in Switzerland (F. Barbir et. al., 1999). Additional information is contained in another Energy Partners paper scheduled for presentation in Las Vegas in July 2000 (F. Barbir et. al., 2000). Gator 1 was displayed in two technical exhibits. The first was by WSRC in Augusta, GA in February 2000 in connection with Savannah River Site Engineers Week. The second was by York Tech during the Earth Day celebration at Fort Mill, SC in April 2000, attended by both South Carolina Gov. Jim Hodges and U.S. Representative John Spratt from South Carolina. Also in April, Gator 1 was shipped to Aguila, AZ for demonstration to senior corporate and engineering management at an internal Deere & Co. review of developmental agricultural equipment. This latter event will undoubtedly prove to be of high importance in the management decisions within Deere regarding the future of the IFCV concept.

Much progress has also been made this fiscal year on Gator 2, assembly of which is in progress. The fuel cell and stack design and system configuration have been finalized. The fuel cell stack and related support systems are being built. A more advanced, higher capacity metal hydride material was selected and procurement of the material from the German company GfE is in process. This material, called Hydralloy C, is a Ti-Mn-V compound capable of storing 1.8% hydrogen by weight as opposed to about 1.3% for the material in Gator 1.

An IFCV market evaluation was undertaken by Deere & Co., which assembled an interdisciplinary team for that purpose. Results from this evaluation are expected to be available in the summer of 2000. An interim update of the potential unit cost of a commercial IFCV produced in large numbers was made in January 2000. This estimate showed that progress is being made toward the cost goal of about \$5,000 per vehicle, but the overall cost is still higher than the goal. The cost estimate ranged from about \$13,000 to \$19,000 per vehicle depending on manufacturing volume. The projected costs of both the fuel cell and the metal hydride storage systems appear to be satisfactorily approaching their targets. The two areas most responsible for the current high cost estimate are the fuel cell support systems (electrical, humidification, etc.), which ranged from \$5,000 to \$9,000, and the base vehicle cost which was about \$5,000. These areas are planned to be addressed in the ongoing market evaluation, particularly from the standpoint of potential cost reductions that might be achieved using manufacturing engineering techniques for the support system subassemblies. A subsequent update is planned based on Gator 2 performance.

Basic Design Requirements

Some of the more important design requirements for Gator 1 and Gator 2 are compared in Table 1.

Table 1. IFCV Design Requirements

| | <u>Gator 1</u> | <u>Gator 2</u> |
|--------------------------------------|----------------|----------------|
| <u>Power System:</u> | | |
| Fuel cell type | PEM | PEM |
| Nominal stack power | 8 kw | 8 kw |
| Fuel cell operating temperature | 60 °C | 60 °C |
| Fuel cell operating pressure | 15 psig | 8 psig |
| Air compressor type | Twin screw | Vane type |
| Nominal bus voltage | 40 VDC | 40 VDC |
| <u>Environmental:</u> | | |
| Gaseous emissions | Zero | Zero |
| Noise | 90 dBA | 80 dBA |
| <u>Storage System:</u> | | |
| Metal hydride material | La-Ni-Al | Ti-Mn-V |
| Discharge temp./press. @ 50% loading | 43 °C/100 psig | 57 °C/100 psig |
| H ₂ storage capacity | 4.3 lbs | 4.0 lbs |
| Max. refueling time @ 300 psig | 60 minutes | 60 minutes |

Status of Business Plan and Safety Review

The original business plan for the commercialization of an Industrial Fuel Cell Vehicle was incorporated in the Phase II/III Project proposal issued in January 1998. However, that plan was developed by a different vehicle manufacturer that participated in the Phase I Feasibility Study, thereby preceding Deere & Co.'s involvement in the project. Updating the plan is one of the principal goals of the project in FY 2000, and it depends on business decisions currently pending at Deere & Co. Management feedback is expected in the near future as a result of the Gator 1 demonstration in Arizona during April. Further, the results of the IFCV market evaluation, expected in the summer of 2000, will play a major role in shaping the management decision on pursuing the concept beyond 2000.

A preliminary safety review of the IFCV metal hydride system was proposed by WSRC as a task in FY 2000, but was not funded due to budget constraints. The present plan is to propose this task again for FY 2001.

Plans and Objectives for FY 2001

The overall objective of the project is to continue the development, validation, and commercialization of an IFCV with on-board metal hydride storage of hydrogen fuel. Initial results from the first prototype have been encouraging, problems notwithstanding, and a wide

variety of potential applications are envisioned. Specific objectives will be developed that appropriately reflect the corporate strategy now under consideration at Deere & Co. Commensurate with that decision, an important objective is to begin the transition from project management to a corporate management structure. The main technical goal remaining is to continue developing the power and hydrogen storage systems, together with the supporting infrastructure, to the point where commercialization appears viable with a satisfactory level of confidence.

As stated earlier, updating the business plan for IFCV commercialization to reflect Deere & Co.'s decisions and preferences is expected to be one of the major activities in FY 2001. Within the overall business plan a range of specific plans potentially exists, depending on corporate feedback. At one end, for example, the plan might be to simply continue reliability testing of Gator 2 to gain additional confidence on performance and endurance and perhaps to identify and implement minor improvements. A more comprehensive plan might be to develop a third generation prototype, or "Gator 3," designed for high volume manufacturing, perhaps for more rapid refueling, and with which to address safety issues including applicable codes and standards. A still more ambitious plan would be to target specific potential customers and applications and take steps toward small fleet testing of IFCVs. When the corporate response is available from Deere, the actual plan that will be created may contain elements of any or all of these possibilities. At that time, decisions will be made concerning the appropriate participants, schedule, budget and funding for continuation of the IFCV Project.

References

F. Barbir, M. Nadal, and M. Fuchs, 1999, "Fuel Cell Powered Utility Vehicles," in Proceedings Fuel Cells 1999 Conference, Lucerne, Switzerland.

F. Barbir, M. Nadal, and M. Fuchs, 2000, "Fuel Cell Powered Utility Vehicle with Metal Hydride Fuel Storage," in Proceedings GlobeEx 2000 Conference, Las Vegas, NV, July 23-28, 2000.

Hydrogen-Enriched Natural Gas Bus Demonstration

**Ranson Roser
NRG Technologies, Inc.
681 Edison Way
Reno, NV 89502**

Abstract

This paper provides a project overview of a recently awarded contract for the development of a hydrogen-enriched natural gas engine and its demonstration in up to six heavy-duty transit buses. The purpose of the project is to demonstrate the applicability and benefits of hydrogen as a contributing automotive fuel in a heavy-duty bus application. NRG Technologies, Inc. in Reno, Nevada will build an engine to its specifications using off-the-shelf components suitable for transit bus operation. Engine components will be selected based on engine output goals as well as the need for high durability and efficiency to meet the expectations of heavy-duty engine users. The electronic engine management system employed will provide the sophistication required to fully realize the low-emissions potential of hydrogen-enriched natural gas. The project will evolve through sub-systems experimentation, engine dynamometer emissions and power development, field demonstration of one engine in a bus, and finally the demonstration of up to six buses in the City of Las Vegas' transit fleet. No engine data, field data, or conclusions are presented here due to the embryonic status of project.

Introduction

Supplementation of hydrogen into natural gas (herein HCNG) extends the lean-burn, or charge-dilution limit of combustion in engines. Extremely low oxides of nitrogen (NO_x) and carbon monoxide (CO) emissions can be achieved when a combined lean-burn and exhaust gas recirculation (EGR) combustion strategy is employed with HCNG. The excess air from lean-burn can be used to reduce CO and non-methane hydrocarbons with an oxidation catalyst. The EGR is intended to be the primary charge dilution agent to

reduce peak combustion temperatures thus leading to extremely low NO_x emissions. Without the hydrogen enhancement, natural gas would not be able to combust with the amount of charge dilution necessary to achieve the targeted NO_x reductions without unacceptable sacrifices in fuel consumption, torque fluctuation, and hydrocarbon emissions. Hydrogen itself is not considered a low-NO_x fuel. Due to higher combustion temperatures than natural gas at equivalent air/fuel ratios, hydrogen actually produces higher NO_x emissions. It is important that the hydrogen supplementation be significant enough to extend the charge-dilution limit to levels sufficient to reduce NO_x emissions beyond what is capable with three-way catalyst technology at stoichiometric air/fuel ratios. It has been the experience of NRG staff that it takes at least 30_{vol}% hydrogen to consistently achieve impressive improvements in NO_x emissions compared to natural gas alone with catalytic exhaust aftertreatment.

NRG Technologies, Inc. has been co-funded by the Department of Energy and the Gas Research Institute to develop an engine platform to demonstrate the advantages of hydrogen-enriched natural gas (HCNG) in heavy-duty transit bus applications. This is the natural extension of previous success NRG has had demonstrating HCNG in a light-duty vehicles. The scope of the three-year project is intended to progress through three major phases; engine development, single-bus demonstration, and multi-bus demonstration. The transit buses for the field demonstration will be new 26-passenger, 30 ft coaches being procured by the City of Las Vegas. The buses will be delivered to the City of Las Vegas with commercially available Cummins 5.9L 195 HP natural gas engines. The OEM engine will be removed by NRG and replaced with an HCNG engine built to its specifications and thoroughly tested on an engine dynamometer in Phase I. The intent at this time is to operate the engine on an HCNG mixture of 30% hydrogen by volume. However, NRG may use up to 60% hydrogen supplementation if it enhances the technical achievements of the engine and boosts the Department of Energy's hydrogen efforts in Las Vegas as a whole. In Phase II the HCNG repowered bus will be emissions tested at an independent CARB/EPA certified laboratory to document the emissions reductions achievable with HCNG fuel. Finally, the bus will be delivered back to Las Vegas and integrated into the City of Las Vegas transit operations for field evaluation.

Assuming the Phase II single-bus field demonstration is generally successful over an eight month evaluation period, the project will expand to include up to six total HCNG buses for Phase III. Any engine improvements deemed necessary as a result of the first evaluation phase, whether they be for hardware components or the electronic engine control strategy, can be incorporated into all of the engines during the demonstration expansion. Although the emissions capabilities of the HCNG engines are a primary driver for the project, they will not undermine the importance of the transit fleet operator's acceptance of the technology as its performance, fuel consumption, and reliability is compared to their existing diesel and natural gas powered buses.

It is important to note that the demonstration of these HCNG buses will provide benefits to the Department of Energy's Hydrogen Program and the interests of the "Hydrogen Community" in general. It will introduce fleet managers, safety regulators, air quality agencies, and the public at-large to hydrogen as a transportation fuel. It will also exercise

the hydrogen generation and refueling infrastructure being constructed in Las Vegas for this and other demonstrations of hydrogen technologies.

DISCUSSION

Engine Platform Selection

Matching Performance

The performance goal of the HCNG demonstration project is to match the engine performance that is normally expected by the bus market. This criteria alone is too vague since fleets with hills need more powerful engines than fleets servicing flat geographies. For the Las Vegas project it is most appropriate to simply look at the power and torque specifications on the natural gas engine that the transit district ordered and deemed appropriate for its needs. NRG will build an engine to those same specifications in order to achieve a seemingly transparent shift in fuel technology.

Originally it was expected that the OEM CNG engine of choice was going to be a 250 hp John Deere 8.1L natural gas engine. The John Deere performance specifications, shown in Figure 1, show it to be capable of 800 lb-ft peak torque at 1350 rpm and 250 hp at 2200 rpm. This became the original performance target to base engine development around, although it will be evident in the report that the engine target eventually changed to a lower output Cummins model.

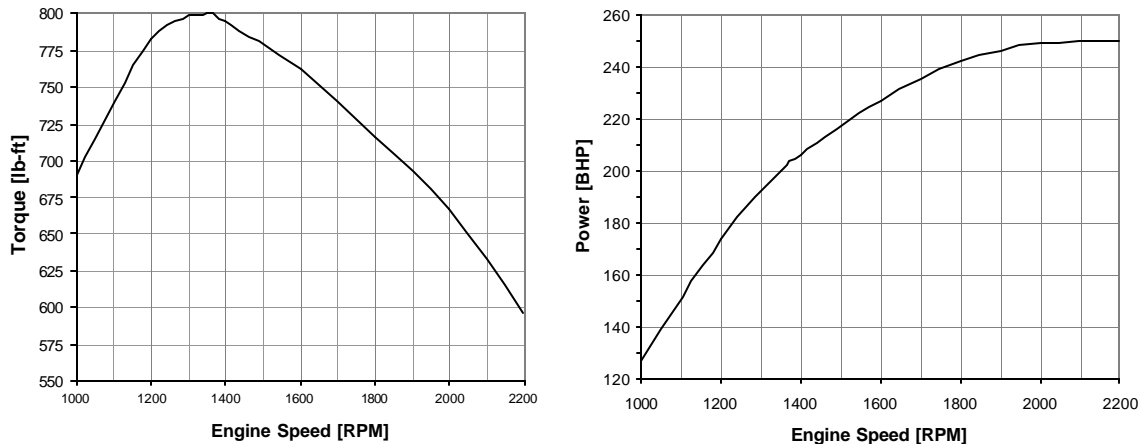


Figure 1 – John Deere 8.1L CNG Output Specifications

With the 250 hp John Deere in mind, NRG identified four base block and cylinder head configurations available from the racing industry suitable for evaluation as HCNG replacement candidates. These were:

GM based 8.0L (489 in³) with cast iron block and aluminum heads with stock valve and rocker positions

Chrysler based 7.95L (485 in³) with cast iron block and aluminum hemispherical four-valve heads with two spark plugs per cylinder

GM based 9.4L (572 in³) aluminum block and heads with stock valve and rocker positions

GM based 13.2L (805 in³) aluminum block and heads with stock valve and rocker positions

A spreadsheet was developed to evaluate each base configuration using reasonable assumptions regarding thermal efficiency, volumetric efficiency, expected equivalence ratios and other engine parameters to determine four general profiles for each engine configuration. The spreadsheet gave an indication of:

1. The engine speeds required to achieve power and torque specs naturally aspirated.
2. The intake air boost required to achieve power and torque specs at identical engine speeds to the peak power and torque speeds of the John Deere.
3. The engine speeds required to achieve power and torque specs with 1 atm (14.7 psi) of intake air boost.
4. The engine speeds required to achieve power and torque specs with 1.5 atm (22 psi) of intake air boost.

Table 1 shows an example of this type of spreadsheet analysis for the 572 in³ (9.4L) candidate engine platform. Careful observation of the results in Table provides insights into the trade-offs that occur with engine selection and one can draw the following conclusions from each scenario assessed for the 9.4L.

1. It would take unacceptably high engine speeds to achieve the raw performance requirements without turbocharging since frictional losses increase with engine speed. Although rated power at 4740 rpm does not represent a structural liability to the engine, it would result in a large sacrifice in fuel economy in a highly loaded heavy-duty bus application. Also, it would be more desirable to reach peak torque much before 3,900 rpm in the engine's acceleration (Scenario 1).
2. It would require undesirably high boost pressure (35 psi) to achieve peak torque at the John Deere's rated torque speed of 1350 rpm (Scenario 2).
3. A very reasonable boost pressure of 1 atm would achieve the peak torque at 2150 rpm and peak power at 3500 rpm. Each speed is reasonable for spark ignition engines. However, frictional losses and their impact on fuel consumption make rated power speeds above 3,500 rpm undesirable. The lower the speed the better for maintaining high fuel economy.
4. Finally, 1.5 atm of boost, still reasonable, achieves peak torque at 1760 rpm and peak power at 2870 with the turbo reduced to 0.8 atm of boost. This represents a very legitimate configuration and shows the 9.4L engine to be a viable platform.

Table 1 – Engine Power Analysis Scenarios

| Engine Power Estimator | Chevy 572 ci aluminum block platform | | | | | | | |
|---|--------------------------------------|--------------|--------------|--------------|--------------|--------------|--------------|--------------|
| | Scenario 1 | | Scenario 2 | | Scenario 3 | | Scenario 4 | |
| Inputs | | | | | | | | |
| Engine Displacement [in3]: | 572 | 572 | 572 | 572 | 572 | 572 | 572 | 572 |
| Engine Speed [rpm]: | 3900 | 4740 | 1350 | 2200 | 2150 | 3500 | 1760 | 2870 |
| Gear Ratio: | none | none | none | none | 1.592 | 1.592 | 1.303 | 1.303 |
| Shaft Speed [rpm]: | | | | | 1350 | 2200 | 1350 | 2200 |
| Fuel: | 30% H2 | 30% H2 | 30% H2 | 30% H2 | 30% H2 | 30% H2 | 30% H5 | 30% H6 |
| Fuel LHV [Btu/lb]: | 23007 | 23007 | 23007 | 23007 | 23007 | 23007 | 23007 | 23007 |
| Stoichiometric AFR: | 18.03 | 18.03 | 18.03 | 18.03 | 18.03 | 18.03 | 18.03 | 18.03 |
| Lambda: | 1.9 | 1.9 | 1.9 | 1.9 | 1.9 | 1.9 | 1.9 | 1.9 |
| Brake Efficiency: | 34.0% | 34.0% | 34.0% | 34.0% | 34.0% | 34.0% | 34.0% | 34.0% |
| Volumetric Efficiency: | 0.8 | 0.8 | 0.8 | 0.8 | 0.8 | 0.8 | 0.8 | 0.8 |
| Altitude [ft above sea level]: | 0 | 0 | 0 | 0 | 0 | 0 | 0 | 0 |
| Air Temperature [C]: | 25 | 25 | 25 | 25 | 25 | 25 | 25 | 25 |
| Intercooling medium: | none | none | ATAAC | ATAAC | ATAAC | ATAAC | ATAAC | ATAAC |
| Cooling medium temperature [C]: | 32 | 32 | 32 | 32 | 32 | 32 | 32 | 32 |
| Intercooler Effectiveness: | 0 | 0 | 0.75 | 0.75 | 0.75 | 0.75 | 0.75 | 0.75 |
| Boost Pressure [psi]: | 0 | 0 | 35.2 | 21 | 14.7 | 6.6 | 22 | 11.6 |
| T. Exhaust [C]: | 700 | 700 | 700 | 700 | 700 | 700 | 700 | 700 |
| P. Exhaust [kPa]: | 107 | 107 | 107 | 107 | 107 | 107 | 107 | 107 |
| Compressor Efficiency: | 0.65 | 0.65 | 0.65 | 0.65 | 0.65 | 0.65 | 0.65 | 0.65 |
| Calculations | | | | | | | | |
| Atmospheric pressure [kPa]: | 101.4 | 101.4 | 101.4 | 101.4 | 101.4 | 101.4 | 101.4 | 101.4 |
| P_{amb} [lb/ft ³]: | 0.0740 | 0.0740 | 0.0740 | 0.0740 | 0.0740 | 0.0740 | 0.0740 | 0.0740 |
| Atm. Power CF: | 0.97 | 0.97 | 0.97 | 0.97 | 0.97 | 0.97 | 0.97 | 0.97 |
| T. Charge (compressed) [C]: | 25.0 | 25.0 | 214.4 | 155.9 | 124.4 | 75.7 | 160.5 | 107.0 |
| T. Charge (compressed & cooled) [C]: | 25.0 | 25.0 | 77.6 | 63.0 | 55.1 | 42.9 | 64.1 | 50.8 |
| Pressure Ratio: | 1.00 | 1.00 | 3.39 | 2.43 | 2.00 | 1.45 | 2.50 | 1.79 |
| Density Ratio: | 1.00 | 1.00 | 2.89 | 2.15 | 1.82 | 1.37 | 2.21 | 1.65 |
| Air Flow Naturally Aspirated [cfm]: | 516 | 628 | 179 | 291 | 285 | 463 | 233 | 380 |
| Air Flow Naturally Aspirated [lb/min]: | 38.20 | 46.43 | 13.22 | 21.55 | 21.06 | 34.28 | 17.24 | 28.11 |
| Air Flow Boosted [cfm]: | 516 | 628 | 516 | 627 | 517 | 633 | 514 | 626 |
| Air Flow Boosted [m ³ /sec]: | 0.244 | 0.296 | 0.243 | 0.296 | 0.244 | 0.299 | 0.243 | 0.295 |
| Air Flow Boosted [lb/min]: | 38.20 | 46.43 | 38.15 | 46.42 | 38.26 | 46.86 | 38.04 | 46.29 |
| Corr. Comp Map Air Flow [lb/min]: | 36.01 | 43.77 | 35.96 | 43.76 | 36.06 | 44.17 | 35.86 | 43.64 |
| Mitsub. Corr. Comp Map Air Flow [kg/sec]: | 0.272 | 0.331 | 0.272 | 0.331 | 0.273 | 0.334 | 0.271 | 0.330 |
| Exhaust Flow [cfm]: | 1642 | 1996 | 1640 | 1995 | 1644 | 2014 | 1635 | 1990 |
| Exhaust Flow [m ³ /sec]: | 0.775 | 0.942 | 0.774 | 0.942 | 0.776 | 0.950 | 0.772 | 0.939 |
| Power Output [hp]: | 205.7 | 250.0 | 205.4 | 249.9 | 206.0 | 252.3 | 204.9 | 249.3 |
| Engine Output [kw]: | 153.4 | 186.4 | 153.2 | 186.4 | 153.6 | 188.1 | 152.8 | 185.9 |
| Engine Output BMEP [psi]: | 73.0 | 73.0 | 210.7 | 157.3 | 132.7 | 99.8 | 161.2 | 120.3 |
| Deere Target Output [kw]: | 153 | 186 | 153 | 186 | 153 | 186 | 153 | 186 |
| | Peak Torque | Peak Power | Peak Torque | Peak Power | Peak Torque | Peak Power | Peak Torque | Peak Power |

One of these power analyses was performed for each engine. The analyses also provided the means for assessing appropriate compressor and turbine wheel selections for turbocharger assemblies. Ultimately it was determined that all four candidate engines were capable of meeting power and torque requirements with varying levels of turbocharging and engine speed.

The next consideration process was to look at the whole engine, its component availability, cost, and level of technical risk for a heavy-duty bus demonstration. The intent of evaluating the four candidate engine designs was to maximize the likelihood of achieving the performance and emissions goals with an engine that is commercially viable. It is important during the strategic development of the project to make sure the demonstration is a test of HCNG and high level of charge dilution and not a test of the reliability of specialty engine components. To replace the John Deere engine, NRG had concluded that the GM based 9.4L engine was the platform of choice after assessing the compromises between each of the factors mentioned above. However, the engine target changed.

In June 2000, it was announced that the engines to be supplied with the buses were going to be the 5.9L 195 hp natural gas engines manufactured by Cummins. Figure 2 shows the performance characteristics of the Cummins 5.9-195G. Notice that the performance target compared to the John Deere became much easier and the reduced requirement created more flexibility into the engine platform selection process. The new criteria was input into each engine profile in NRG's power analysis spreadsheets and new trade-off relationships were examined. In the end, NRG chose the 8.0L GM based engine with an aluminum block and cylinder heads, and two valves per cylinder with stock valve and rocker arm orientation. The power analysis showed that the 8.0L could achieve the Cummins 5.9-195G power specifications at the same rated speeds with no more than 1 atm of boost at peak torque. The 8.0L represents a very nice solution because it is the smallest of the candidate engines, it is compatible with friction-reducing cylinder coatings, and the fact that the power specifications could be met at the same engine speeds as the Cummins eliminated the need for an additional gear box.

AUTOMOTIVE ENGINES AND DURABILITY

Whereas the Cummins natural gas engine was originally derived from a diesel based engine, the NRG HCNG engines will be built from what are generally considered to be automotive gasoline components. The following discussion addresses the issue of durability that may arise regarding this strategy. The discussion of durability here and throughout the scope of the project will remain largely qualitative due to the fact that both 500,000 miles of real world mileage accumulation and expensive accelerated engine fatigue testing are both beyond the scope of this project.

The physical structure of heavy-duty engines for transit buses are characterized by the compression ignition diesel engines that have historically dominated the industry. The overall structure of the block and the reciprocating components of diesel engines are more massive than those of spark ignition engines due to higher peak cylinder pressures and the market demand for durability that allows 500,000 miles of operation before major

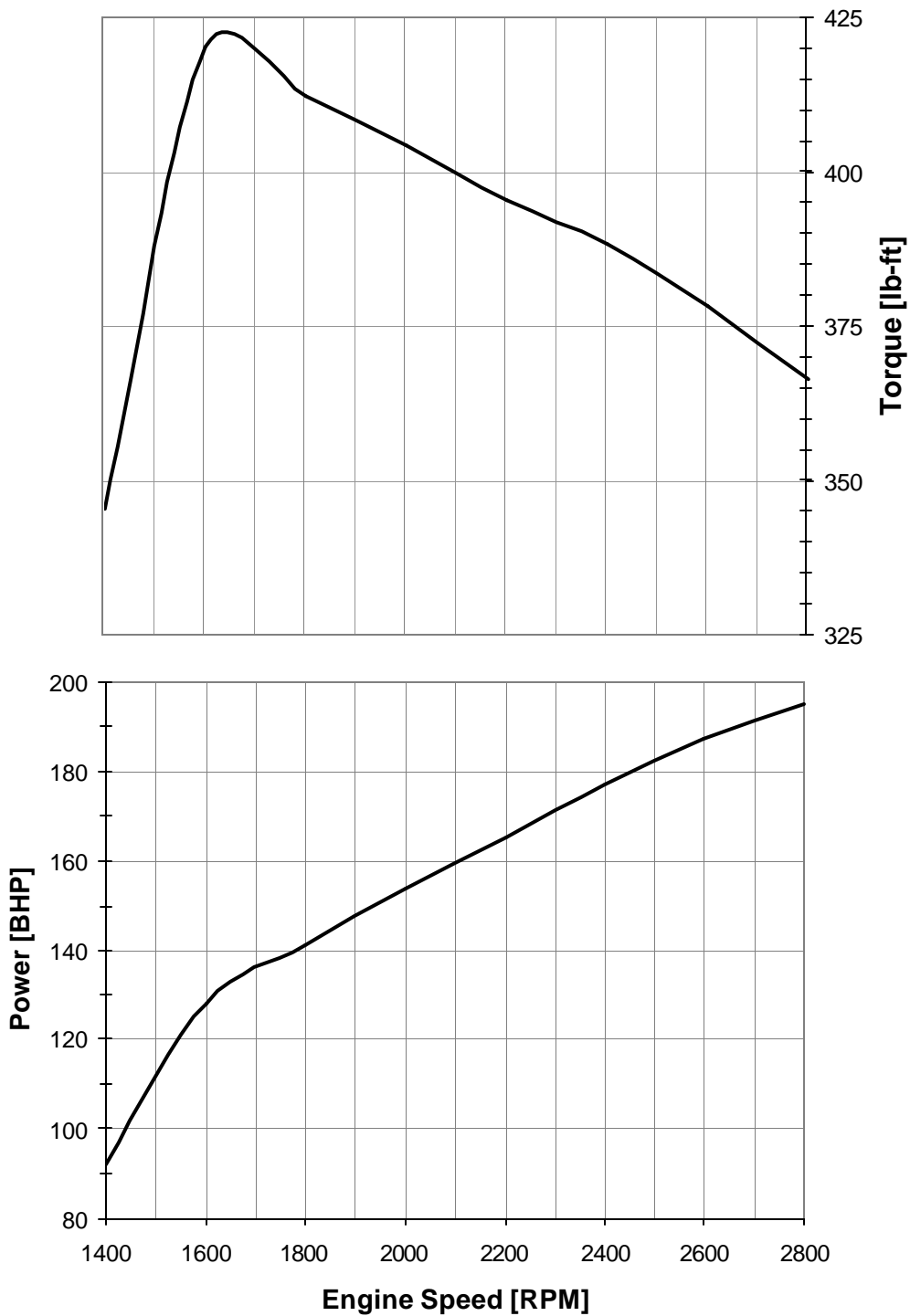


Figure 2 – Cummins 5.9L NG Output Specifications

engine overhauls. Fundamentally, the durability is not dictated by the massiveness of the engine components, but rather the massiveness of the diesel engine components are necessary to achieve the durability expectations in lieu of the extreme pressure induced

stresses from the compression ignition process. Automotive gasoline based engines are generally thought to have less durability capabilities than diesel engines, but that judgement is heavily flawed by the consumer markets that drive their development. The heavy-duty trucking and transit industry demands, and pays the price for, durability because of the number of miles traveled per year and the high cost of down time when goods or services cannot be delivered. The automotive market, dominated by purchases for personal use, only demands 200,000 mile engine lifetimes, is far more sensitive to up front capital costs, and does not necessarily expect those engines to be rebuilt. Thus the engine manufacturers select major reciprocating components that cost less to manufacturer and are not as durable as they could be for the light-duty car and truck market. So, in most cases it is true that automotive based spark ignition engines are less durable, but it need not be true if the engine components are selected with durability as a primary consideration. The high performance racing industry is one that demands durability out of engine components under extreme conditions. The popularity of the performance industry has created an extensive aftermarket for components that have been developed with intensive engineering efforts placed on component durability for spark ignition engines. These are the components that NRG will incorporate into the HCNG engine and with far lower peak cylinder pressures than diesel engines, and even the Cummins CNG engine, it is expected that the durability of the HCNG engine could ultimately be a highlight feature of the technology.

Engine Development on Engine Dynamometer

Emissions Goals

The stated goal of the project is to demonstrate the ability of HCNG fueled heavy-duty engines to achieve a 75% reduction in HC, CO, and NO_x emissions based on 1998 HDV US EPA Emissions Standards. These emissions goals, shown in Table 1, are to be met without sacrificing industry expectations in driveability or fuel economy.

Table 1.

| Emissions Standards and Goals | | | |
|---------------------------------------|----------------------------|--------------------------|--------------------------------------|
| | NMHC [g/bhp-hr] | CO [g/bhp-hr] | NO_x [g/bhp-hr] |
| 1998 U.S. EPA Standard for HDE | 1.7 | 37.1 | 5 |
| 75% Reduction Goal | 0.4 | 9.28 | 1.25 |

Engine Emissions and Control Development

Engine testing will take place on a 500 hp eddy-current engine dynamometer. First the engine will be evaluated under maximum output conditions to determine whether or not it can meet the target performance criteria at the equivalence ratios that it was designed for. If not, then hardware modifications, such as turbocharger configuration, can be made as needed. Once the engine is known to be able to meet its maximum output objectives then it will undergo an extensive array of equivalence ratio and timing mapping at various speeds and load.

Figure 3 will be used as an example maximum output Torque Vs. RPM curve for the HCNG engine. Emissions and efficiency mapping will be performed at various engine

speeds at 25, 50, 75, and 100% load. At each speed/load point an equivalence sweep will be performed to determine its characteristics as a function of air/fuel ratio. Additionally, each speed/load/equivalence point will be assessed at three ignition timing intervals to map the influence of ignition timing on the system. The timing intervals will include minimum timing advance to achieve best torque (MBT), timing retard to 97.5% of maximum torque, and timing retard to 95% or best torque. The timing intervals are intended to evaluate the trade-off between NOx emissions and brake efficiency.

The goal of mapping is to characterize the trade-offs between output, emissions, and fuel consumption so “optimized” electronic engine control strategies can be defined. Once a few air/fuel ratio and timing strategies have been identified, they can be individually evaluated under further steady-state tests to develop a reasonable projection of how the engine would perform if evaluated using the official transient testing protocol for EPA and CARB emissions certification.

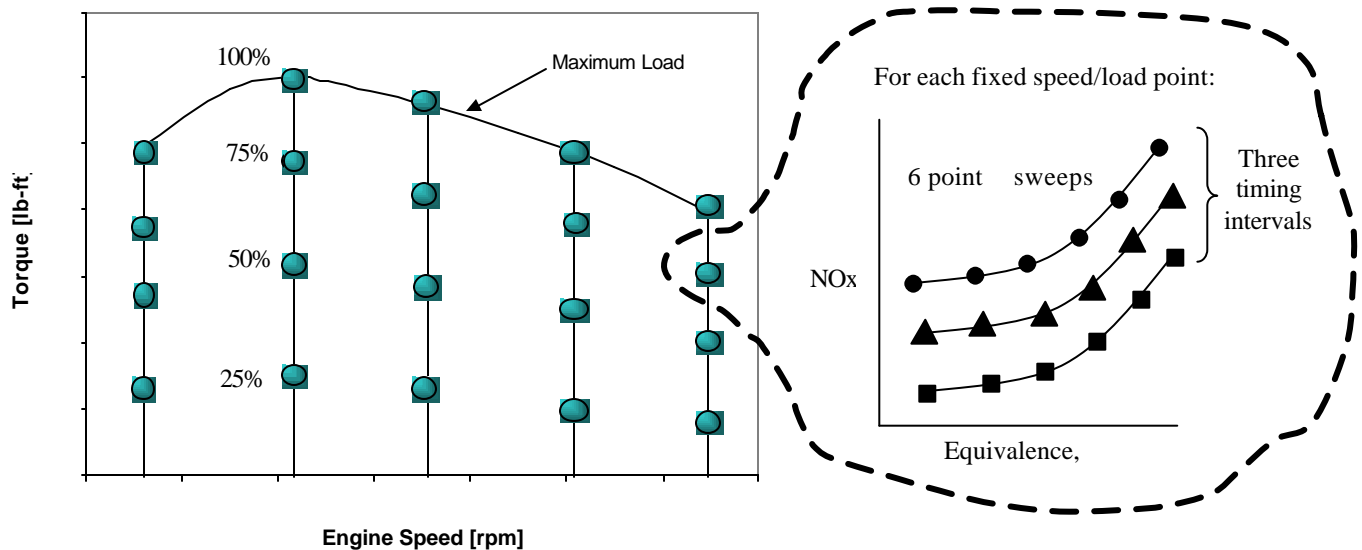


Figure 3 – Sample Equivalence Ratio and Spark Timing Mapping

Projecting FTP Emissions Using Steady-State Protocol

The 1998 US EPA Emissions Standards and the goals set forth for this project are based on a transient testing protocol that is performed on an engine dynamometer, known as the US EPA Heavy-Duty Engine Federal Test Procedure (HD FTP) illustrated in Figure 4. The test is so time and equipment extensive that even the engine manufacturers do not use it during an engine’s development phase.

Instead, the emissions are typically quantified at about eight specific steady-state conditions and then the emissions at these specific points are weighted. The final processed emissions value is intended to represent the same value that would result if the engine were to be run through the FTP. OEM engine manufacturers will typically use a weighted steady-state process that has been developed through proprietary in-house studies and has shown to provide good correlation between the final weighted steady-

state numbers and actual FTP tests. A similar strategy will be used by NRG in assessing the emissions performance of the HCNG engine. NRG will use the eight-mode steady-state protocol developed by AVL (Table 2) to obtain a reasonable approximation of what the US EPA FTP emissions would be for each engine. Only NO_x and THC will be evaluated with the eight-mode test. There are currently no steady-state processes that are adequate for simulating transient PM and CO. This is not expected to play a role in the evaluation process, however, because CO emissions for the HCNG engine will be practically eliminated with an oxidation catalyst and PM emissions should be consistent with natural gas technology in general.

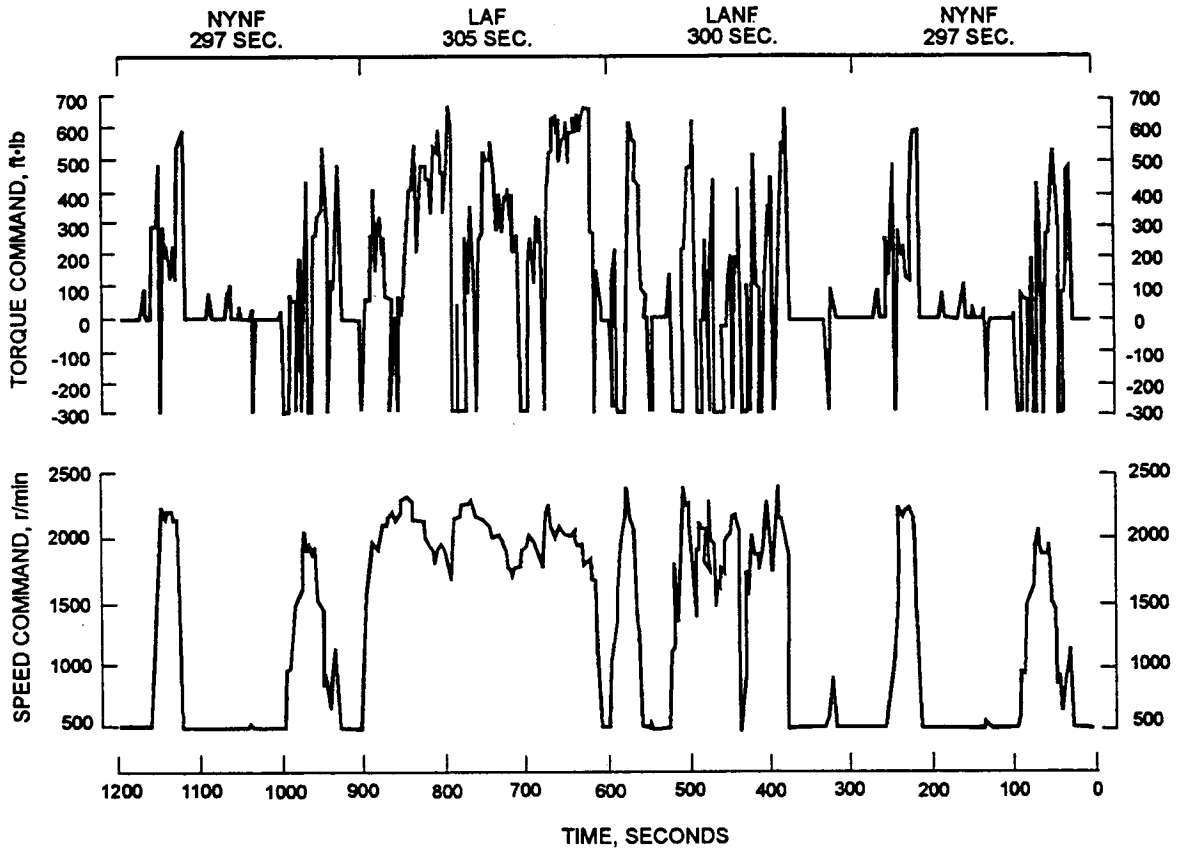


Figure 4 – The U.S. EPA Heavy-Duty Federal Test Procedure

The eight-mode test will be used as a development tool to define the best fuel and spark control strategy and it will provide one level of comparison between HCNG and natural gas capabilities. It will not be used, though, as the final comparison between the HCNG engine and current natural gas technology. Chassis dynamometer evaluations will be conducted under one of the heavy-duty bus driving cycles that have been developed for emissions testing purposes. This will provide an in-use comparison of NG and HCNG bus emissions. The chassis dynamometer testing process will be discussed later in this report.

Table 2 - Eight-Mode Steady-State Protocol & Weight Factors

| AVL Eight-Mode Test For Predicting US EPA FTP Emissions | | | |
|--|------------------------|-------------------------|------------------------------|
| Mode | Speed % ⁽¹⁾ | Torque % ⁽²⁾ | Weight Factor ⁽³⁾ |
| 1 | 0 | 0 | 35.01 |
| 2 | 11 | 25 | 6.34 |
| 3 | 21 | 63 | 2.91 |
| 4 | 32 | 84 | 3.34 |
| 5 | 100 | 18 | 8.4 |
| 6 | 95 | 40 | 10.45 |
| 7 | 95 | 69 | 10.21 |
| 8 | 89 | 95 | 7.34 |
| (1) Speed % means percent between idle and rated | | | |
| (2) Torque % means the percent of maximum torque at a given speed. | | | |
| (3) The weight factors are not supposed to add to 100%. | | | |

Emissions Measurement at NRG

Emissions of NO_x, CO, and THCs will be measured with the engine on NRG's 500 HP eddy-current dynamometer in Reno. NO_x, CO, and THC emissions will be measured using chemiluminescence, non-dispersive infra-red, and flame-ionization detection equipment, respectively . . . all manufactured by Thermo Environmental Instruments. These measurement techniques are the industry standard for automotive emissions testing. The instruments provide data in parts per million which will then be converted to g/bhp-hr. Particulate measurement will not be addressed for two reasons. First, PM measurement for automotive applications requires transient testing equipment that is outside the scope of this project. Second, PM regulations for heavy-duty engines are set at levels that reflect the state of the art of diesel fueled engines. Diesel engines produce inherently higher levels of PM because of the nature of diffusion flame combustion using a liquid hydrocarbon fuel. The PM produced by any gaseous-fueled engine comes predominately from lubricating oil, This is far less than from diesel engines and is not expected to play a role in assessing the viability of hydrogen-enriched natural gas as a fuel. The project participants can be assured that NO_x reduction techniques for this project are not going to come at the expense of PM, a common trade-off relationship with diesel systems.

Transient Compensation and Feedback Control Development

The final phase of engine dynamometer development will be to define the deviations in air/fuel ratio that occur with sharp accelerations and decelerations. Once the nature of the deviations is defined, NRG will develop, test, and implement transient compensation algorithms into the electronic engine control strategy in-order-to further enhance the stability of the emissions control system. Furthermore, a feedback control system will be implemented and tested. Oxygen sensor feedback control allows tighter control of air/fuel ratio, protection against the effects of faulty or aging sensors, and protection from variations in fuel hydrogen content. The methodology of this test phase is proprietary to NRG and will not be outlined in detail. However, examples of the benefits of these

compensating elements can be demonstrated from laboratory data subsequent to the development work.

At the completion of Phase I, NRG will have a 8.0L V8 engine that has been fully characterized for emissions and achieves the same performance as the Cummins 5.9 – 195G. The project will then progress into Phase II which includes integration of the engine into the bus and chassis dynamometer evaluation of the emissions at an independent laboratory.

Initial On-Road Assessment In Reno

The NRG bus engine will have been thoroughly tested and the electronic engine control (EEC) strategies developed on NRG's engine dynamometer in Phase I. However, further EEC strategy modifications are often necessary when transitioning an engine from the dynamometer to the street. Using properly licensed NRG personnel, the bus will be evaluated for initial driver perception in Reno. If appropriate, NRG will modify the air/fuel ratio, spark advance, transient control parameters, and shifting algorithms to optimize bus accelerations and decelerations. In this fashion the bus can be delivered to the City of Las Vegas with confidence that it will be accepted by the drivers in the bus fleet.

Chassis Dynamometer Testing

Once NRG has finalized any EEC strategy modifications for on-road driving the whole bus will be emissions tested as a system. The testing will be performed at California Truck Testing Services (CATTS) in Richmond, CA. CATTS is run by the Clean Air Vehicle Technology Center (CAVTC) and jointly owned by CAVTC and Arcadis/Geraghty & Miller (formerly Acurex Environmental). The CATTS facility's features and capabilities include the following:

- Emissions testing over any programmable drive cycle
- Electric dynamometer with tandem 48" rolls
- Vehicle weight, power, and speed: GVW from 6,000 to 85,000 lbs, power absorption up to 500 hp at rolls, speeds up to 75 mph
- Vehicle size: Up to 65 feet long with single or tandem drive axles
- Axle dead load: hydraulic simulator
- Temperature-controlled engine air supply
- Bag-dilute modal emissions analysis capabilities for CO, NO_x, CO₂, HC, and CH₄.
- Particulate mass measurement and size distribution capability

In the early stages of Phase II, one of the CNG buses in operation with the City of Las Vegas will be instrumented with a data logging system supplied by NRG to assist with the chassis dynamometer emissions evaluation of an HCNG bus. The purpose of the data logging system is to characterize the typical engine and bus operating characteristics within real routes of the Las Vegas transit system. Operating profiles may be generated for more than one bus route if deemed appropriate. The bus operating profiles will be compared against standard heavy-duty bus driving schedules for chassis dynamometer emissions testing. The driving protocol that best represents the real world usage of the Las Vegas buses will be used for performing chassis dynamometer emissions evaluations

of the NRG HCNG engine. Examples of these heavy-duty bus driving schedules are shown in Figure 5.

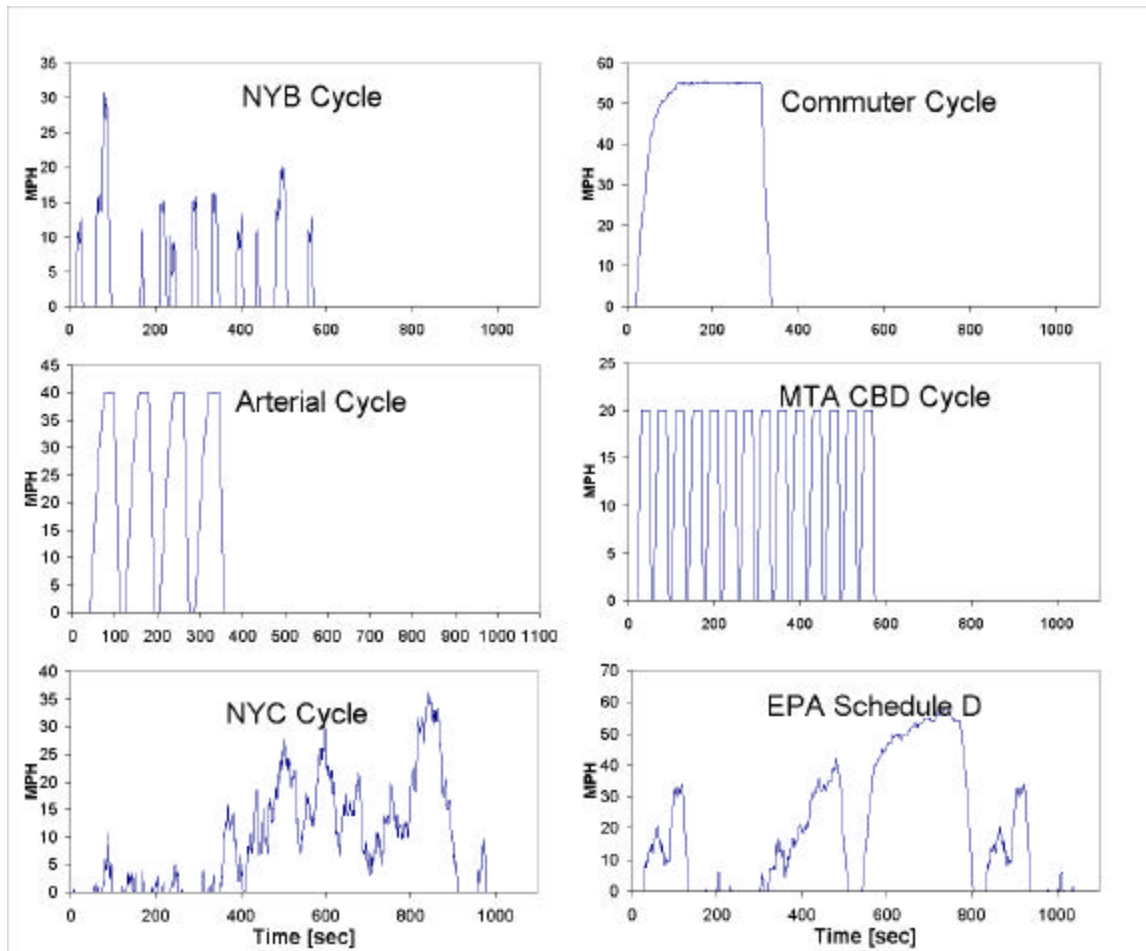


Figure 5 – Heavy-Duty Bus Driving Cycles

The bus with the first integrated HCNG engine will be tested on a chassis dynamometer using a driving schedule, or protocol, that will have been specified after reviewing data logging information from a real bus in the Las Vegas fleet as described. Emissions of CO, NO_x, and THC will be collected in tedlar bags and measured in terms of grams per mile over the whole test. Real-time emissions in parts per million will also be measured. The grams per mile data is useful for making composite comparisons of HCNG with other fuel technologies whereas the real-time ppm data is useful as a development tool for analyzing the engine's emissions performance during specific driving conditions such as cruise, accelerations, and decelerations.

The chassis dynamometer testing will give NRG the opportunity to make further EEC strategy modifications if transient emissions performance warrants such changes. The chassis dynamometer is the final forum in a controlled environment for determining the trade-offs between emissions, driveability, and fuel consumption. Once a final engine control strategy has been decided upon, then a final "official" driving cycle test will be

performed for documenting the emissions reduction capability of the NRG HCNG engine. Between the NRG engine dynamometer data and CATTs chassis dynamometer data, there will be a solid characterization of the HCNG engine's emissions performance allowing a comparison between it and commercially available CNG technology.

Las Vegas Field Demonstration

After the emissions testing is completed at CATTs, the HCNG powered bus will be operated in the Las Vegas public transit system for a period of several months. During that time detailed records will be kept on fuel usage, oil consumption, maintenance, and driver perception for evaluation before progressing with the demonstration expansion proposed for Phase III. Oil samples will be taken at regular maintenance intervals for tracking of wear metals.

NRG will install a data logging system on the bus for monitoring parameters such as oil, coolant, and intake air temperature, engine and vehicle speed, boost pressure, and throttle position. The system will be accessible remotely at NRG's facilities via an on-board modem with cellular phone access. This will allow NRG to obtain daily feedback on the engine's performance for record keeping and diagnostic troubleshooting if necessary.

It will be the responsibility of the bus operators to perform the standard maintenance as prescribed by NRG. NRG will provide training on the engine and its maintenance procedures to all appropriate personnel when the bus is delivered to Las Vegas operating on HCNG.

Phase II Completion – Engine Teardown

At the end of the three-month field test in Las Vegas, the bus will be shipped by a commercial carrier to NRG in Reno. NRG will then remove, disassemble, and inspect the engine for abnormal wear conditions. Measurements of valve seat recession and bore wear will be made in order to begin tracking the durability of the engine during the life of the whole project. If any abnormalities are identified, then NRG will be able to make design modifications to the engine package before progressing with Phase III. Ultimately, the engine will be reinstalled into the bus as one of up to six Phase III repowers.

PHASE III – HCNG DEMONSTRATION EXPANSION

The HCNG demonstration with the City of Las Vegas will expand to include up to six total buses running on hydrogen mixtures assuming the first bus in Phase II proved successful. Phase III will provide the more meaningful data with regards to fuel consumption and reliability because the data will become more statistical rather than singular in nature. The bus expansion will also be important for the hydrogen refueling infrastructure being developed in Las Vegas. Fast-fill gaseous fueling systems are capital intensive and it becomes important for the owners of the station to bring the equipment up to reasonable capacity as quickly as possible.

At the end of Phase III it will be up to the project participants to decide the fate of the HCNG engines. The demonstration period could be extended or the City of Las Vegas

may wish to have the Cummins engines reinstalled if the fast-fill HCNG station poses long-term problems to the operation of the fleet.

CONCLUSION

NRG Technologies, Inc. has initiated work on a three-year plan to demonstrate hydrogen-enriched natural gas in the City of Las Vegas bus fleet. The project is only in its early stages of development so no technical results are available for discussion within this paper. Based on initial engine modeling, NRG has decided to use a General Motors based 8.0L aluminum block with aluminum wedge style cylinder heads. The larger displacement compared to the base Cummins engine is necessary to maintain output goals while achieving significant emissions reductions with extreme charge dilution compared to conventional fuels. Two engine simulation software packages are also being used to optimize intake, exhaust, valve, and camshaft geometry. The project is the natural extension of previous success with HCNG fuels in light-duty demonstrations.

Progress on Improvements to a Hydrogen/Electric Hybrid Bus

Y. Baghzouz, J. Fiene, J. Van Dam, L. Shi, E. Wilkinson, R. Boehm
Center for Energy Research, University of Nevada, Las Vegas
Las Vegas, Nevada
and
T. Kell, Kell's Automotive
Las Vegas, Nevada

Abstract

The primary goal of the reported work is to extend the range of the bus in a cost-effective manner. Among the modifications underway are the development of a new engine, upgrading the power control system, rewiring critical elements, adapting a supercapacitor regenerative braking system, devising more effective changes to the hydrogen safety systems, and adding a high pressure gas storage system to supplement the existing hydride bed hydrogen storage. All of this work is being supplemented with the use of a dynamic simulation code to determine optimal operational strategies.

Introduction

The hydrogen-powered bus was constructed for the Atlanta Summer Olympics. This bus began as an all-electric vehicle that carried four battery packs in under-vehicle compartments. Two of the battery packs were removed and replaced by two metal-hydride beds for hydrogen storage. Then the rear portion of the bus was modified so that a large, industrial V-8 engine with large electrical generator could be installed in that location. This engine was modified from its standard gasoline form to one that was specially designed for hydrogen fuel.

The system is designed so that all of the electrical energy went through the batteries. When the battery state-of-charge reaches sufficiently low levels, the driver starts the engine to accomplish a recharge. When the state-of-charge in the battery bank is restored to a predetermined level, the driver turns off the engine. More complete information on the initial vehicle design can be found in Jacobs et al. (1999a, b) at the end of the paper.

Several problems were encountered with the bus operation. One of these was that the range was deemed to be too small. Another was that oil consumption of the engine was reported to be particularly high. Premature battery system failure was observed. This may have been related to the operation of the regenerative braking system that came with the bus. The electrical power

controller was found to overheat. In addition, the flammable gas sensors that were an integral part of the hydrogen safety system of the bus did not have the appropriate hydrogen selectivity necessary.

This project began after the bus was shipped to Nevada in 1999.

Electrical System

The current electrical system of the H2 Bus consists of three main components the auxiliary power unit, the battery bank, and the electric drive system. A fourth major component that is currently under development is the supercapacitor bank.

Auxiliary Power Unit

The auxiliary power unit consists of an engine (described in a later section of this paper) that drives a 4-pole, 277 V, 80 Hz, 70 kVA synchronous generator. The generator AC voltage is converted to DC through a diode rectifier. The generator performance characteristics were determined by conducting laboratory tests last summer. The generator-rectifier efficiency at full load was estimated near 83% with a voltage regulation of 8%. Plans are made to replace the generator unit with a larger and more efficient one.

Battery Bank

The battery bank consists of two parallel sets of deep-cycle VRLA batteries, each containing a series connection of 28 units. Each unit is rated at 12 V, 85 Ah @ C/3. The total battery system operates at 336 V with a capacity of 170 Ah @ C/3. The equivalent maximum energy storage is 57 kWh, but only 80% of this energy (i.e., 46 kWh) can actually be used since VRLA batteries are not allowed to be discharged below 20 state-of-charge (SOC).

The original bus batteries reached their life cycle prior to the bus transfer from Georgia. Consequently, new batteries have recently been installed. Monitoring of the battery cells is accomplished by a battery management system that provides several advantages including charging of individual units to help restore them to normal state. When the bus is not in operation, the battery bank state of charge is maintained with an external battery charger which requires 480V, 100 A, 3-phase power supply. The new batteries are equipped with internal thermistors to determine the temperature of each battery. One of the current tasks related to bus improvements is considering aspects of battery thermal management that would extend battery life.

Electric Drive System

The electric drive system is composed of an IGBT-based inverter that converts the DC voltage to three-phase pulse-width-modulated (PWM) AC voltages. These voltages are fed to an AC induction motor that is capable of producing 230 hp in addition to its 250 ft-lb of torque. The traction motor is wound with dual 3-phase windings and is capable of continuous operation at a

maximum speed of 12,500 rpm. Both the motor and inverter electronic switches are oil cooled. Drive motor and traction battery current flow are monitored and controlled by an electronic subsystem known as the chassis vector controller (CVC). Due past thermal problems which limited the maximum power demand, the inverter has been upgraded to a more efficient and more heat-tolerant one.

Supercapacitor Bank

The bus came equipped with a regenerative braking system that converts the vehicle kinetic energy back to electrical energy during braking. This feature is known to increase the driving range by up to 20%. Currently, the regenerative braking uses the battery bank to store the energy gained. Since VRLA batteries are not designed to accept large, short bursts of power, especially when near full charge, conventional regenerative braking may cause them to overcharge and result in battery damage. For this reason, the existing regenerative braking system is temporarily disabled.

A supercapacitor bank in series with a DC/DC chopper (currently at the design stage) is being developed to act as an energy buffer: It has the ability to store energy as quickly as needed, and then supply back this energy when required during acceleration.

Miscellaneous

Much of the originally modified bus wiring was found to be very poorly documented as well as poorly installed. In many cases violations with the NEC code were found. Much of the electrical wiring has been corrected, re-wired, and documented.

A data acquisition system (DAS) was included in the original bus system. This apparently is not designed for the expected rugged condition in normal service, its ports and connectors are not standard, and its programs run on a special computer. The entire DAS is being analyzed for further improvements.

Engine

The Original Engine

An area that is being closely examined for increasing bus performance is the hydrogen-fueled engine. The necessary power output for the engine was established as 70 kilowatts at a speed of 2500 revolutions per minute. This was determined as a function of the operating range of the generator. Changes that had been made to the engine for the conversion to hydrogen gas included the addition of an HCI Constant Volume Injection system (see Jacobs et al. 1999a, b), the addition of exhaust gas recirculation, and modifications to the heads and pistons.

The Constant Volume Injection system is a unique sequential multi-port fuel injection method to meter the flow of hydrogen into each cylinder. The system is based upon the ideal gas relationship between pressure, volume and temperature. Not only do the pressure and volume

effect the flow of gas into the engine, but changes in temperature can have adverse effects. To combat this, an electronic control system was incorporated into the injection arrangement.

An exhaust gas recirculation system was employed to reduce emissions. The system drew the exhaust from one bank (four of the eight cylinders) of the engine through four parallel coolers, into a condenser and then into a mixer at the intake manifold. This did increase the load on the engine but it was assumed that it would not drop the power output below the desired level.

The engine heads were replaced to increase the compression ratio to then improve the brake thermal efficiency. In an attempt to increase further the compression ratio and to reduce the excessive amounts of oil lost during operation, new pistons and rings were installed.

Test Results, Modifications and Improvements

Shortly after acquisition of the bus from Georgia, extensive research was performed to determine what needed to be improved. It was decided that substantial changes needed to be made to achieve the desired performance, efficiency and emissions results. Of primary concern was increasing the operational range of the bus, which could be accomplished by improving the performance of the engine, among other aspects described in this paper.

To study what improvements could be made to the engine, it was first removed from the bus and mounted on an engine dynamometer. Extensive diagnostic tests were then performed in a controlled environment.

The use of hydrogen as a fuel for internal combustion engines has been researched greatly in recent years primarily because of its 'clean' burning properties. The greatest concern involved with emissions control is the production of NO_x.

Nitrous oxide production is commonly triggered by high temperature 'hot spots' located within each combustion chamber. Coupled with high pressures within the cylinders and a relatively rich air-to-fuel ratio, levels of this harmful pollutant can easily become a problem. It was found that the rate of NO_x produced by the engine was unstable and varied between 6 and 55 parts per million as measured at the tailpipe. Reviewing the emissions data gathered via a synchronized dynamometer/exhaust analyzer in conjunction with thermistors located within each cylinder, the largest production of NO_x occurred while the greatest difference between cylinder temperatures existed.

The conclusion inferred from the correlation between increased NO_x production and temperature variance between cylinders was the assumption that non-uniform burns were occurring within cylinders. Mixtures of fuel and air abnormally rich were believed to be increasing the temperatures of some of the cylinders. While the NO_x readings generally registered below 6 PPM, they subsequently increased to figures as high as 45 PPM at points where cylinder temperature differences reached 106°F.

In an attempt to locate the cause of this non-uniformity, a pressure transducer was installed to measure the line pressure of the hydrogen upstream of the constant-volume injector pump.

Readings from this sensor revealed violent oscillations in the pressure of the fuel supply. The design of the injection system did not allow for the compensation of this anomaly; in actuality it caused large variations in the amount of fuel delivered to each cylinder. This was most likely due to the compressibility of the gaseous fuel as it passed through the volumetric metering chambers of the injector pump. The excess hydrogen introduced to the cylinders may have been the catalyst for the production of the 'hot spots' and thus the high levels of nitrous oxide.

It was then determined that further analysis of the exhaust elements would be more useful once the engine's air/fuel supply could be more accurately controlled. It was assumed that the engine would exhibit less variable emissions readings once the combustion inside each of its cylinders could be more accurately predicted and controlled.

Fuel Delivery

In order to determine the possible power output of the existing engine and to evaluate its integrity, dynamometer tests were performed while the engine was run with several fuels. A performance test was conducted on the engine in its original condition using hydrogen fuel. In order to compare the output of the engine with its gasoline fueled counterpart, a carburetor (Holley 833 CFM) was mounted to the intake manifold and the engine was run on VP-C12 (108 octane) gasoline. To study the performance of the engine as run on gaseous fuels in general, Compressed Natural Gas (CNG) was introduced through the carburetor for the next test. These two initial tests were to evaluate the performance of the engine to comparable engines for which data was already available. The engine was then returned to its original setup for hydrogen with the addition of an electronic control unit capable of adjusting the overall air/ fuel mixture. The engine was then run with a leaner mixture.

Results of these tests indicated performance derating typical of the use of gaseous fuels. Comparative (at least generally so, since different types of fuel input systems were used) maximum outputs (in kW) were found at 3000 rpm as follows: gasoline-170; natural gas-130; hydrogen (A/F ratio of 30)-75; and hydrogen (stoichiometric)-45. It was desired to have higher outputs with higher efficiency than what was demonstrated with this engine.

Several characteristics of the existing Constant Volume Injection (CVI) system gave cause for concerns related to good performance. First and foremost, the mass of hydrogen metered by the CVI was directly dependant on the line pressures upstream and downstream from the pump. Secondly, the presence of petroleum-based lubricants in the piston/ cylinder design of the CVI allowed for the contamination of the hydrogen gas before it reached the combustion chamber.

These factors made the possibility of utilizing an Electronic Fuel Injection (EFI) system an appealing one. If electronic fuel injectors could be used, little or no contaminants would be introduced to the fuel supply and the amount of fuel delivered to each cylinder could be far more accurately controlled. Furthermore, the air/fuel ratio and the injection timing could be easily optimized. The concentration of fuel within each intake of air could be controlled so that the occurrence of the aforementioned 'hot spots' might be eliminated.

Research showed that fuel injectors designed for metering hydrogen gas were not generally available. The use of injectors designed for the delivery of petroleum-based fuel raised two concerns. Because the energy density of hydrogen is much less than that of gasoline, significantly larger volumes of hydrogen must be delivered at each injection interval. And, as opposed to a petroleum-based fuel, pure hydrogen gas exhibits 'dry' properties that do not provide the lubrication needed to keep the internal mechanisms of a standard fuel injector working properly.

A testing apparatus was constructed to determine if the necessary volumes of hydrogen could be passed through a large bore fuel injector commonly used in the racing industry. Given proper upstream pressures, it was found that the fuel injectors were capable of providing the necessary mass flow rates.

Similar studies performed using electronic fuel injectors to control hydrogen flow revealed that the mechanism failed after a remarkably short duration of operation. The 'dry' hydrogen had caused the contacting metal surfaces within the injector to seize in the open position and hydrogen was allowed to flow continuously through the injector. This situation was not acceptable for many reasons, including the safety risks involved with hydrogen gas.

In an attempt to find commercially available injectors capable of operating in a hydrogen environment, injectors intended for use with Compressed Natural Gas (CNG) were then obtained. The major point of interest concerned with this type of injector was the method by which they delivered larger volumes of fuel. While the same seizure problem was likely to occur in these injectors as well, the design methodology used to obtain higher flow rates was noted and the engineering of a new injector specifically designed for hydrogen was begun. This development included considerations for the larger flow rates as developed by the CNG injectors as well as novel methods to resist the premature failure of the mechanism.

Concurrent with the aforementioned development of a new injector, the investigation for a commercially available injector continued. Custom fuel injectors further along in development were discovered that allowed us to focus our efforts on the implementation of the injection and intake systems.

Intake and Exhaust Systems

The new hydrogen-fueled engine was a converted internal combustion engine with high flow cylinder heads. The intake manifold, cylinder heads, and exhaust manifold were originally designed for use at variable engine speeds. Since we intend to run the engine at a constant speed (in the general range of 2500-3000 RPM), it was decided to develop manifolds and head porting with a geometry that would provide the maximum efficiency and power at the desired operational speed.

Intake and exhaust geometries are generally designed to provide the maximum efficiency of airflow over a wide bandwidth that will include all engine-operating speeds. Since the APU must only run at a single speed, the method by which air is delivered to and removed from the engine could be optimized.

Using fluid flow principles, intake runners were designed that use the inertia of the air flowing to the individual intake ports on the cylinder heads to pressurize the inlet air. When the intake valve is closed, the mass of air flowing through the tube above it compresses until the next opening of the valve. By carefully timing the valve opening, the air/fuel mixture can be introduced to the cylinder at the point of maximum upstream pressure. As will be discussed below when addressing the camshaft aspects, this has multiple benefits for our application.

We treated the exhaust headers in a similar fashion. Each exhaust runner was designed such that the mass of the air flowing through it creates a pressure drop behind each exhaust valve while the valve is closed. When the valve is opened, the exhaust gasses in each cylinder escape to pressures less than that of ambient. Engines employing similar intake and exhaust methods have yielded volumetric efficiencies greater than 120%.

Cylinder heads were then designed to accommodate the intake and exhaust runners, and to provide a higher compression ratio so that a greater thermal efficiency could be achieved.

To mate the custom fuel injectors to the new intake manifold, special mounting hardware was developed. The design consisted of four individual mounts, each of which holds two injectors. These mounts are interconnected using reservoirs of ample internal volume so that the cyclic firing of injectors will not induce any substantial pressure variations.

In addition, higher precision cylinder surfaces and corresponding piston interfacing has been accomplished. This was done to minimize oil consumption and the resulting negative impacts upon exhaust emissions.

Cam

A new camshaft was designed to meet the custom needs of the hydrogen application. The variables with the most significant impact on the design of the cam profile are the range of speeds of operation and the combustion characteristics of the fuel being used. Since the engine was intended for operation at a constant speed, the valve actuation could be designed in such a way that the most efficient cycle could be obtained.

The burn properties of hydrogen differ significantly from those of gasoline, and thus several special considerations were made in the camshaft design. The original engine exhibited frequent 'flash backs' that were presumably caused by the high flame speed and low ignition temperature of hydrogen. Unstable fuel delivery and the existence of 'hot spots' within the cylinders undoubtedly contributed to their prevalence as well. To eliminate 'flash backs' and to better control the combustion of the fuel, the valve timing was altered to fit the characteristics of hydrogen.

The amount of time that the exhaust valve remains partially open while the intake valve is being opened, otherwise known as overlap, also needed to be addressed. While overlap is commonly used on variable speed engines to control the amount of exhaust remaining in the cylinder after combustion, our methods of introducing fuel and air and extracting it once burned allowed us to more closely time the valve actuation and to use the fuel more efficiently. To prevent the

escape of unburned fuel and air and to reduce the possibility of premature ignition, the degree of overlap was significantly reduced.

Predicted Results

Utilizing custom driver software for the electronic fuel injection system, very precise metering of hydrogen delivery can be achieved. Herein may lie the largest improvements that will be realized over the existing engine design. With the ability to control accurately the amount of fuel entering each cylinder during the cycle, the optimum control system can be developed to provide the greatest overall efficiency.

An emissions-testing apparatus has been designed with special attention to two key elements in the exhaust, namely NO_x and unburned hydrogen. With predicted nitrous oxide levels falling below the detectable range of most automotive analyzers, a special, high sensitivity analyzer was required. Along with this, a flow-through hydrogen sensor was acquired for the detection of any unburned hydrogen in the exhaust stream. This will insure that any parametric changes made to the engine during development have not led to the presence of unburned hydrocarbons in the exhaust stream and will aid in the optimization of the control systems.

The concept of the hydrogen powered engine shows that there should not be any significant amount of carbon compounds in the exhaust (the only possible source being the combustion of engine oil). Nevertheless, a standard automotive analyzer will be employed to ensure that any possible exhaust emissions are within accepted levels.

The intended nominal running speed of the existing engine was determined by the efficiency and the maximum output of the generator to which it was coupled. A more efficient generator that can operate at higher speeds will be incorporated into the modifications on the bus. Since the efficiency of the engine increases proportionately with its operating speed over a specified range, the new generator will allow us to operate the engine at a more efficient speed. The APU, consisting of the engine and the generator, can now be run at its combined peak efficiency.

Fuel Storage System

Existing System

The existing storage system on the bus is by means of a metal hydride system that is mounted under the bus. In this case a Lanthanum-Nickel-Aluminum (LANA) type alloy is used. The system consists of two separate beds that are cooled (usually by an external source of cool water) when hydrogen is to be added, and heated (with engine coolant in this case) when hydrogen is to be used. In its present configuration, the bed is estimated to be able to hold 15.2 kg of hydrogen. A great deal of additional information about the existing system can be found in Heung (1997) and Jacobs et al. (1999a, b).

Planned System

Plans are currently underway to install additional storage on the bus. This will take advantage of some new technology being developed by DOE: high-pressure composite material tanks. Current plans are to mount six 48" long x 18" diameter tanks on the top of the bus in the 2001 time frame. These tanks will allow a substantially increased amount of hydrogen fuel to be carried with the bus.

One of the design criteria for the modified fuel storage system is to have access to both a high-pressure-tank system and the low-pressure-hydride system by simple adjustments between the two. As new and more promising hydride bed systems are developed, it is hoped that the bus can serve as a test bed for evaluations.

System Modeling

Introduction

To enhance the system performance, a study of the system dynamics is being carried out. In this study, the special code is being used. This software, developed by the National Renewable Energy Laboratory (NREL) and called ADVISOR (ADvanced VehIcle SimulatOR), is available from the www (see the References section at the end of the paper). This is used to simulate and analyze the performance and fuel economy of this hybrid vehicle. In ADVISOR, this vehicle is handled in a series mode, which includes a fuel converter, a generator, batteries, and a motor. The fuel converter (an engine in this case) does not drive the vehicle shaft directly. Instead, it converts mechanical energy directly into electrical energy via the generator. All torque used to move the vehicle comes from the electric motor. The control strategy is a series power follower. The hybrid accessories are assumed to be a constant electrical power load.

Overall Performance Estimates and ADVISOR Simulation

For the H₂-fuel bus system, we know the energy capacity of hydrogen and the battery, the efficiencies of engine, generator and motor, and the electrical power load at certain speed, we can use the energy equation (1) to calculate the total load and ranges vs. speed

$$(R_b + R_p) \eta_m = TL \quad (1)$$

where R_b is the rate of battery draw down, R_p is the rate of power produced from engine, η_m is the motor efficiency, TL is the total load.

In the bus system: the total hydrogen available = 15.2 kg; engine efficiency = 30%; generation efficiency = 95%; the battery starts at 100% state of charge (SOC) and ends at 20% SOC; motor efficiency = 88%. The load vs. speed is found in ADVISOR 2.2.1 as shown in Figure 1. The range vs. speed is shown in Figure 2 based on the energy balance, equation (1). The results are bus operation at constant speed.

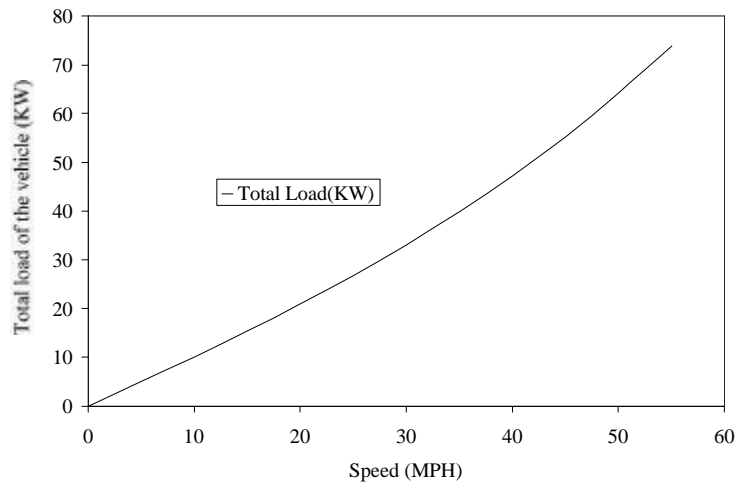


Figure 1. Electrical power load vs. speed for constant speed operation.

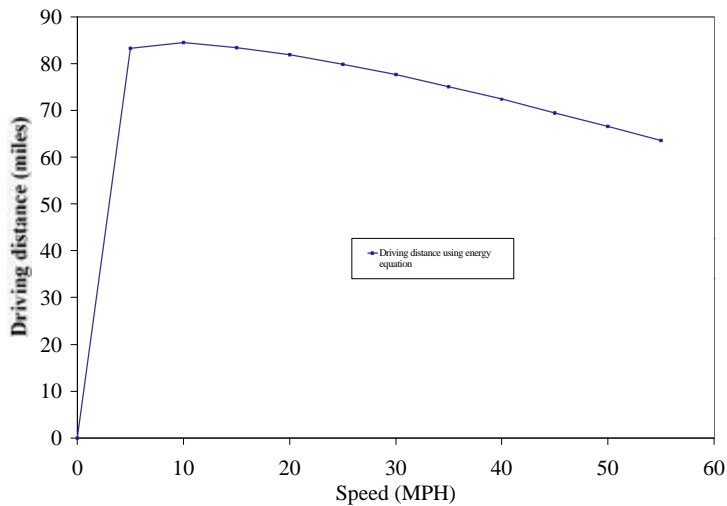


Figure 2. Maximum bus range at constant speed.

Implications of Different Driving Cycles

On a given trip, the bus may travel at a constant speed, or it may drive with many stops and starts. In the simulation using ADVISOR, the former case can be implemented using **CYC_constant**, and the latter is implemented using **CYC_FUDS** where FUDS stands for Federal Urban Driving Schedule. In Figure 3, the simulation results determining the battery-state-of-charge is given for a constant speed constant speed of 55 mph. The bus runs solely with the electrical battery for the first 27 minutes. The engine is on when the SOC of battery is at 40%. The power from the engine and the battery is used to drive the bus at 55 mph until all the hydrogen is used up. Then the bus runs only using the battery until the SOC reaches 20% which is assumed to be the lowest SOC the battery can tolerate before requiring recharging.

Now compare Figure 3, for constant speed, with Figure 4, which are related results but for the FUDS driving cycle schedule. The corresponding temporal use of fuel for the FUDS driving cycle is shown in Figure 5.

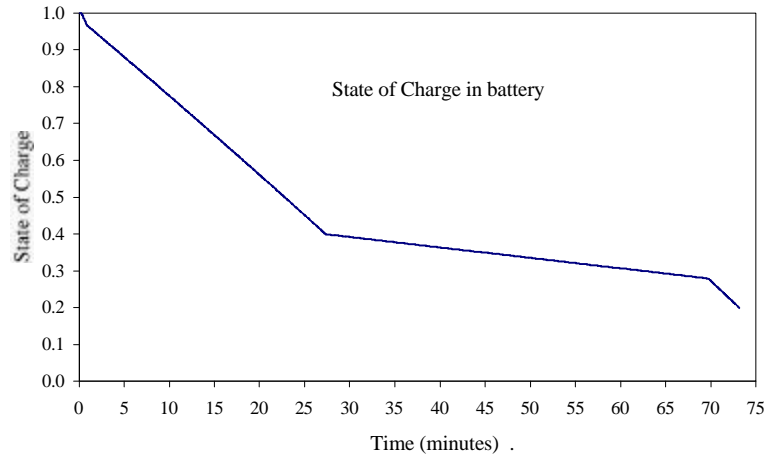


Figure 3. State of charge of battery at constant speed (55 mph).

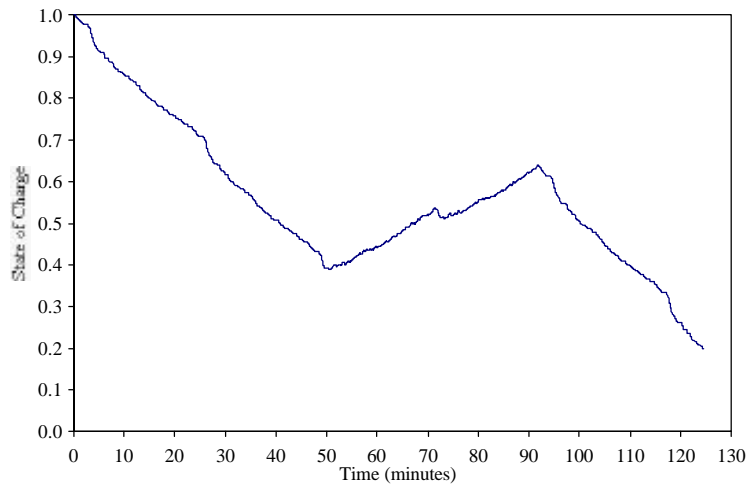


Figure 4. State of charge of battery using the FUDS driving cycle.

Regenerative braking is the process by which some of the kinetic energy stored in the vehicle's translating mass is stored in the vehicle during decelerations. In most electric and hybrid electric vehicles on the road today, this is accomplished by operating the traction motor as a generator, providing braking torque to the wheels and recharging the batteries.

In the system we are considering here, the regenerative braking will be by supercapacitors. Other than the dynamics of the two regenerative braking systems being different, the general energy considerations are similar. The energy provided by regenerative braking can then be used for propulsion or to power vehicle accessories. All scenarios were analyzed considering credit for regenerative braking or no credit.

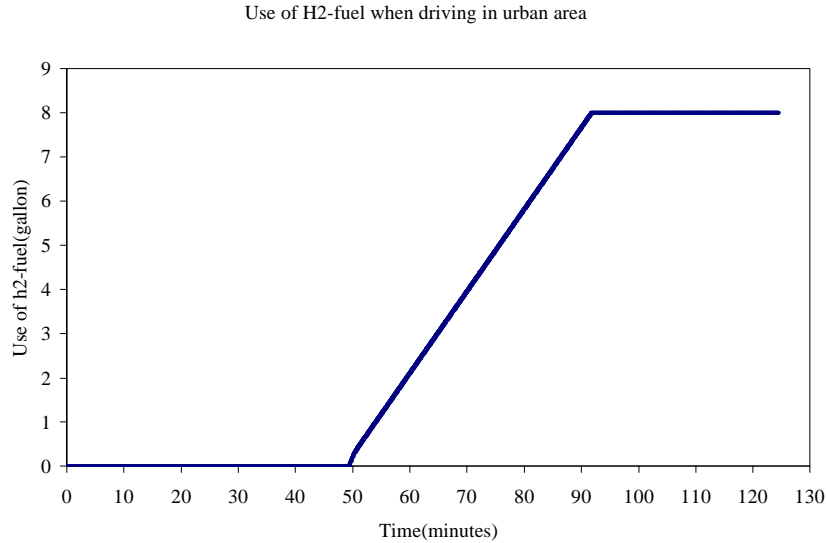


Figure 5. The temporal use of fuel during the FUDS driving cycle.

From Table 1, it can be seen that the bus with regenerative braking has a longer range. But note that the recharging time is not affected by regenerative braking. This is a result of the fact that the engine runs at full speed after it is turned on, and it is turned off when the total fuel is used up.

Table 1 Effects of Using Regenerative Braking

| | With reg braking | Without reg braking |
|----------------------|------------------|---------------------|
| Trip elapsed time | 155 min | 124 min |
| Trip mileage | 48.7 mi | 39.3 mi |
| Recharging starts at | 60 min | 49 min |
| Recharging ends at | 102 min | 91 min |
| Recharging time | 42 min | 42 min |

Concluding Comments

A project involving the development of a hybrid electric bus powered by a hydrogen fueled internal combustion engine has been described. This project is a continuation of some earlier work done by others. Extensive modifications are being made to the fuel system, engine, electrical system, and operation of the bus. All of these aspects are directed toward generally improving the performance of the bus.

Future Work

- Complete the modifications on the data acquisition system.
- Develop, install, and test the supercapacitor system

Design, install, and checkout the hydrogen safety sensor system.
Configure, design, and install the high pressure hydrogen storage system.
Complete the design and fabrication of the new hydrogen engine.
Test the engine and modify it to meet the performance goals, including total power, fuel efficiency, exhaust emissions.
Install the engine into the bus.
Operate the bus in a test mode.
Perform additional system simulations and compare to actual operation.
Detail a list of further modifications that would result in bus performance.

Acknowledgement

This paper is based on the paper: Y. Baghzouz, J. Fiene, J. Van Dam, L. Shi, E. Wilkinson, R. Boehm, and T. Kell, "Modifications to a Hydrogen/Electric Hybrid Bus," AIAA Paper 2000-2857, to be presented at the 2000 IECEC, July 2000.

The assistance of Bob Golden (Nevada Operations Office of DOE) and Tom Van Sittert (Bechtel-Nevada) with many constructive recommendations is appreciated.

References

ADVISOR Documentation, NREL website: http://www.ctts.nrel.gov/analysis/advisor_doc

Heung, L. K., 1997. "On-Board Hydrogen Storage System Using Metal Hydride," *Proceedings of the Hypothesis II Conference*. Grimstad, Norway, August 18-22.

Jacobs, W. D., Heung, L. K., Motyka, T., Summers, W. A., and Morrison, J. M., 1999a. *Final Report for the H2Fuel Bus*, Report WSRC-TR-98-00385, Westinghouse Savannah River Company, Aiken, SC.

Jacobs, W. D., Heung, L. K., Motyka, T., Summers, W. A., and Morrison, J. M., 1999b. "Final Report for the H2Fuel Bus," SAE Paper 1999-01-2906.



H₂ Reformer, Fuel Cell Power Plant, & Vehicle Refueling System

Venki Raman

Air Products and Chemicals Inc.

Allentown, Pennsylvania, USA

DOE Hydrogen Program Annual Review

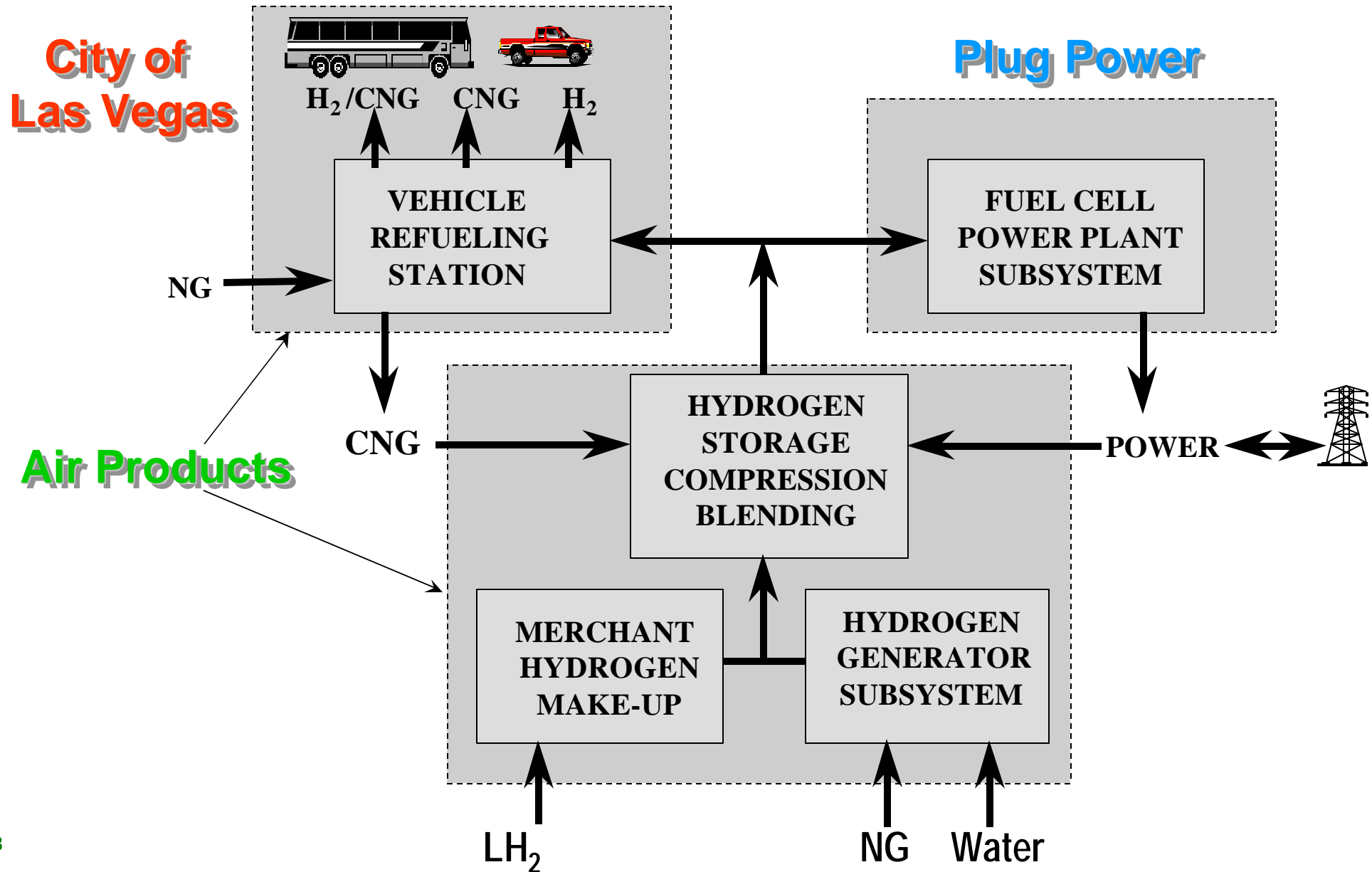
San Ramon, CA

May 9-11, 2000

Long-Term Goals/Project Objectives

- **Resolve design issues & demonstrate small, on-site H₂ production for fuel cells and H₂ fuel stations**
- **Design/construct/operate multipurpose refueling station**
 - Dispense CNG, H₂/CNG blends, and pure H₂ to 27 vehicles
 - Ultimately serve as a link in a national H₂ corridor
- **Design/construct/operate 50kW fuel cell**
- **Evaluate operability/reliability/economic feasibility, and certify integrated power generation and vehicle refueling designs**

Overall Project Scope



Project Partners

- **Plug Power Inc., Latham, NY**
 - Major owners/ strategic partners: MTI Inc., DTE Energy , General Electric, SoCal Gas (Sempra)
 - Developing a 7 kW home fuel cell
 - Developing 50 kW fuel cells for vehicles and buildings under separate DOE funding
- **City of Las Vegas (CLV)**
 - Host site for the project
 - 120 CNG vehicles operated by the RTC in Las Vegas
 - Purchasing 6 new buses for conversion to CNG/ H₂

Task 1 Design & Development

- **1.1 Finalize Project Plan (May 2000)**
- **1.2 Reformer Design & Development**
 - Preliminary Prototype Testing
 - Prep. Prototype for relocation to Las Vegas
 - Scaled-up H₂ Generator design
- **1.3 50 kW PEM Fuel Cell System**
- **1.4 CLV Fueling Station/Subsystem Integration**

Task 2 - Construction & Installation

- **2.1 Reformer Subsystem**
 - Phase 2 - Prototype installation
 - Phase 3 - Scale-up unit installation

- **2.2 50 kW PEM Fuel Cell**
 - Off-site assembly & testing
 - Installation at CLV site (July 2001)

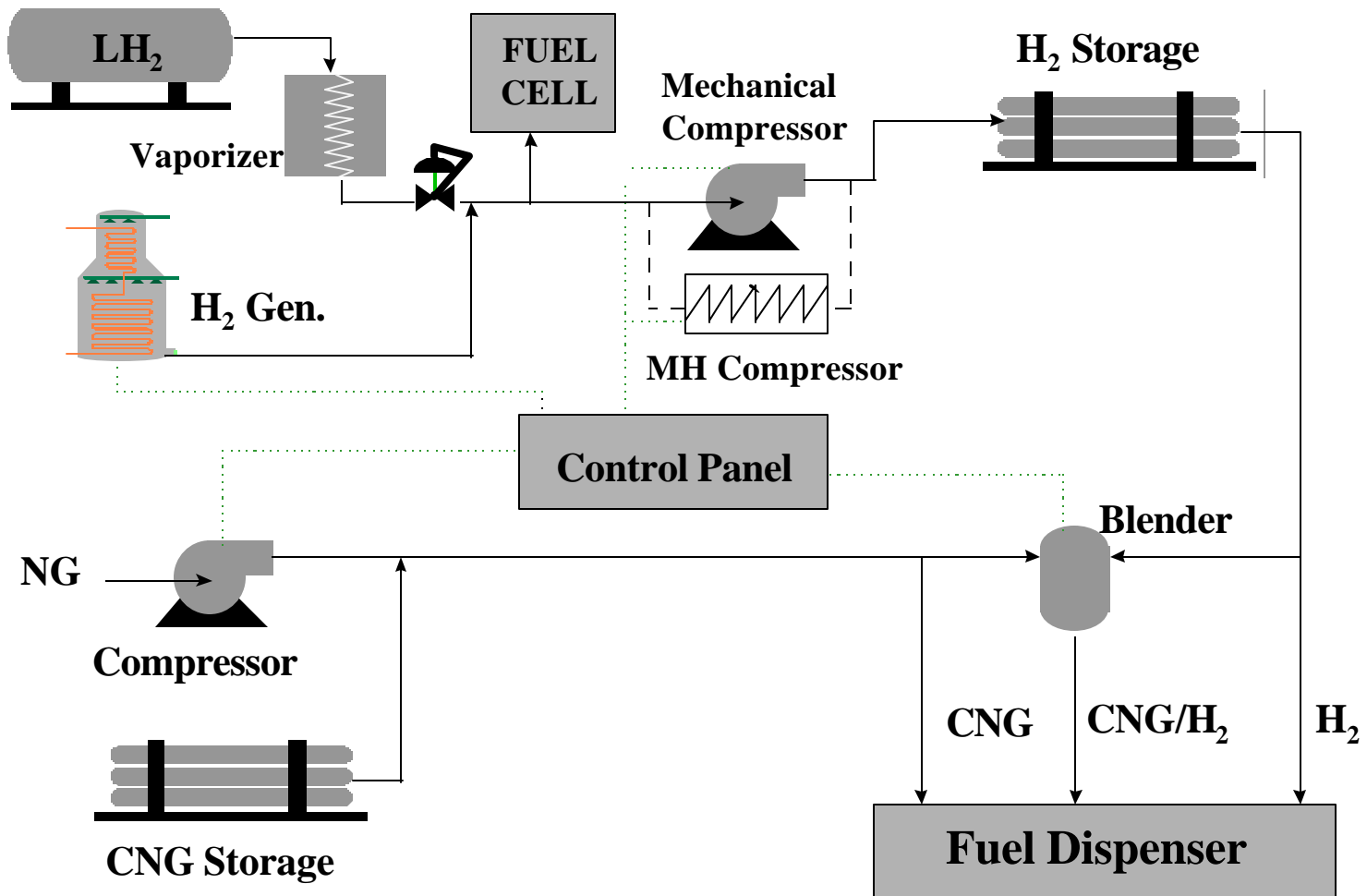
- **2.3 CLV Refueling Station**
 - Phase 1: Merchant H₂ supply
 - Phase 2 & 3 : Integration of reformers

Task 3 - System/Station Operations

- **3.1 Permitting & Safety Review**
- **3.2 Start-Up Testing**
- **3.3 Facility O & M**
 - Phase 1: 3 - 5 vehicles
 - Phase 2: 9 - 18 vehicles + 50 kW Fuel Cell
 - Phase 3: 18 - 27 vehicles

Task 4 - Project Management & Reporting

Fuel Station



Projected H₂ Demand

| <u>Operations Phase</u> | <u>Hydrogen Applications</u> | <u>H₂ Demand SCFD</u> | <u>Proposed Hydrogen Supply</u> |
|--|---|--|--|
| Phase 1 Sept 2000 - Jun 2001 | 1 - 3 H ₂ /CNG LDVs 1 H ₂ Hybrid Elec. bus 1 H ₂ /CNG Bus - Jan 2001 | 1,000 - 3,000 | Install LH ₂ tank and fueling equipment initially Install H ₂ generator Prototype as available |
| Phase 2 Jul 2001 - Dec 2001 | 6 - 11 H ₂ /CNG LDVs 1 H ₂ Hybrid Elec. bus 2- 6 H ₂ /CNG Buses 50kW Fuel Cell @ 25 - 50% rate | Vehicle 3,000 - 15,000 Fuel Cell 9,000 - 21,000 | H ₂ Generator prototype -24,000 SCFD LH ₂ is used as backup/peak shave. Fuel Cell balances H ₂ generator production |
| Phase 3 Jan 2002 - Sept 2004 | 11 - 20 H ₂ /CNG LDVs 1 H ₂ Hybrid Elec Bus 6 H ₂ /CNG Buses 50kW Fuel Cell @ 100% rate | Vehicle 15,000 - 17,000 Fuel Cell 39,000 | Install scaleup H ₂ generator, provided bus fleet buildup meets targets. |

FY2000 Objectives & Rationale

- **Achieve acceptable commercial operation of prototype H₂ generator (1000 SCFH) for integration with 50 kW fuel cell and fuel station.**
- **Begin conceptual development of a commercial design for scaled-up H₂ generator.**
 - To realize the potential for commercial economics as vehicle usage increases.

FY2000 Objectives & Rationale (continued)

- **Begin design and manufacture of a 50 kW PEM Fuel Cell Power Plant.**
 - Integration with the H₂ production and compression system, and with the power needs of the site.
- **Install H₂ and H₂/CNG mixed-fuel station for the City of Las Vegas.**

Current Year Tasks/Progress

- **Task 1.1 - Firm Plan** - nearing completion
- **Task 1.2.1.1 - Preliminary Testing** - nearing completion
- **Task 1.3 - 50 kW Fuel Cell Design** - initiated April 2000
- **Task 1.4 - Refueling Station Design** - pending completion of Task 1.1

Status of Business Plan & Safety Review

- **Business plans will follow installation and routine operation of the integrated systems**
 - Partners are interested in total integrated system as well as individual components
- **Safety is top priority in design, construction and operation**
 - All safety and industry codes are addressed in designs
 - Reviews at each phase - design, construction, and operation
 - Follow philosophy of CTA and Ford H₂ fueling facilities
 - Air Products' 40 years of experience in commercial H₂

Objectives for FY2001

- **Achieve integrated operation and improve reliability.**
 - Collect information on the reliability of the subcomponents for any corrective actions required.
- **Gain operating experience on the fuel station and determine needs for improvement.**
- **Determine the feasibility and need for construction of the scaled-up hydrogen generator.**

THE REMOTE AREA POWER PROGRAM (RAPP)

Dennis Witmer
Ronald Johnson
Thomas Johnson
University of Alaska Fairbanks
Fairbanks, AK 99775

Jay Keller
Andy Lutz
Sandia National Laboratories
Livermore, CA

Abstract

In this paper we discuss the motivation and program structure for the Remote Area Power Program for Alaskan Villages. Rural Alaskan Villages are typified by small populations (many of less than 100 people), no road access to places outside the village, no access to the national (or even an Alaskan) electrical grid. Most of the Villages have electrical power typically generated by diesel generators providing power to each dwelling by a small very local micro grid. This system is difficult to maintain, very inefficient, and subject to frequent outages. To protect against power outages due to mechanical breakdowns, redundant generators are frequently in place, resulting in higher capital costs. Maintenance work is most often done by skilled workers from outside the village. Fuel must also be transported to the village. All of this results in a very high cost of power (up to 80 cents a kilowatt hour), currently subsidized by the state government to about ten cents a kilowatt for residential users through "Power Cost Equalization".

Recent advances in Proton Exchange Membrane (PEM) fuel cell technology have created the hope that these devices can be used in reliable, affordable remote power applications. Higher electrical conversion efficiency and heat recovery for residential use results in higher fuel utilization, high reliability results in lower maintenance costs, and networking a small microgrid allows reduction in the redundancy necessary for reliable power, leading to lower capital costs. The long-term goal is to work towards a carbonless infrastructure based on renewable energy.

Goals and Basis for Goals

The goals of this program are to accelerate the development of PEM fuel cells for distributed power applications, significantly reduce the consumption of fossil fuels, begin development of a power generation system based on hydrogen as an energy carrier. The basis for this goal is to work towards a carbonless energy infrastructure based on renewable energy.

Summary of Approach and Rationale

The cost of generating electrical power in remote areas is much higher than in grid connected areas. In remote rural villages in Alaska, these costs can rise as high as \$.80 per kilowatt-hour. Conservation does not reduce the fixed cost of operating a utility, and so other ways to reduce the cost of electricity are sought.

In order for a new technology to be successful in this market, it must reduce the total system cost of energy. The system must be highly reliable in order to reduce O&M expenses. The capital cost must be low. And the system should be efficient, so that less fuel needs to be transported to the remote location. In Alaska, there is an added criterion, the system must work in the severe arctic climate.

Based on these criteria, stationary distributed power systems based on PEM fuel cells are attractive. They provide distributed power generation capability, heat can be recovered to increase fuel utilization, system reliability can be provided by networking units together, and capital costs can be reduced due to the lower excess capacity needed to cover outages.

Economic Analysis

In thermodynamics, it is essential to define a system boundary in order to define system efficiency. In order to compare PEM Fuel Cell systems with conventional power systems in the 5kW range, we have selected for this work an overall system boundary that looks at hydrocarbon fuel into the system and the AC electricity out. This boundary includes the reformer, fuel cell, inverter, and any batteries that are part of the system, and all of the parasitics necessary to perform the internal functions necessary to keep the system working. Note that this is a significantly different definition of fuel cell efficiency than used by this program last year, when the system boundary was defined around the fuel cell system only, using pure hydrogen as the feed stock, and DC electricity as the output.

When this program began in 1998, the fuel cell industry was claiming that net electrical efficiencies of over 40% based on the lower heating value were possible in PEM fuel cell systems running on hydrocarbons. In order for this number to be true, efficiencies of individual components had to be high. A system with a reformer efficiency of 75%, a fuel cell efficiency of 58%, and an inverter efficiency of 94% meets this overall efficiency target. It should be noted that this efficiency value can still be found on the web sites of fuel cell companies.

An analysis of a PEM system specifically designed for the Alaskan Environment was done in the spring of 1998 by Phil DiPietro. This analysis used slightly more conservative estimates of efficiencies for the system: the reformer at 70%, the fuel cell at 55% (the DOE OTT target efficiency), the inverter at 90%, plus a reduction in power out due to load leveling using lead acid batteries at 80% for part of the electrical load. These assumptions give an overall electrical efficiency of 31.5%. This analysis also included a cost analysis, showing that given reductions in capital cost due to decreased redundancy in the system, credit for heat recovery, and some fairly optimistic projections about fuel cell system costs, the PEM fuel cell system would lead to lower energy costs in remote villages.

Program Plan

The RAPP program began in July of 1998, and was divided into three phases. Phase I involved delivery and verification of system components, and was successfully completed, with fuel cells delivered and operating in September of 1998, and a reformer delivering fuel cell quality hydrogen. Phase II was intended to result in a laboratory integrated system capable of converting diesel to grid

quality AC power. Phase III was intended to result in a fully automated system suitable for field demonstration of the technology in a remote arctic site, but this phase is currently on hold.

Past Results

The past results in this program have been encouraging, as Phase I and Phase II goals have been met. Three hydrogen PEM fuel cells were delivered to the program and made operational by September 30, 1998. Two additional fuel cells have been tested since then. A steam reformer operating on kerosene was delivered by December 30, 1998, and a POX reformer was delivered on April 5, 1999. Three fuel cell benches were constructed and made operational by February 15, 1999. Systems efficiency data was collected on three PEM FC systems, and a paper was presented at the 10th Annual NHA meeting in April 1999.

Current Year Effort

During the past year, much of the effort of this program has been transferred to the University of Alaska Fairbanks, with completion of a new laboratory facility there in the summer of 1999. The dedication of this laboratory occurred in August, and was attended by DOE Assistant Secretary Dan Reicher. As part of this dedication, a demonstration of the technology being tested was given. Kerosene was fed into the Northwest Power reformer (with a paladium membrane), fuel cell quality hydrogen (less than 1 PPM CO) was produced and fed to the Schatz Energy Research Center fuel cell, DC electricity was fed into an inverter, and AC electricity was produced to run the lights in the lab for two hours. It was a fine demonstration, but it should be noted that the fuel used was a desulfurized bio diesel, the reformer burner was operating on propane, and the reformer required the attention of an experienced operator.

The UAF Energy Center has developed an automated control system for the diesel reformer. This control system requires maintaining accurate control over two independent low flow liquid streams, and requires numerous decision points for start up, steady state operation, and shut down procedures. UAF is currently working with Sandia Livermore and NPS to further develop this control system.

Much of the work in the past year has focused on the performance of the diesel reformer. The first diesel unit delivered to the program and use for the demo in August, but had some materials problems in the burner area due to the high temperatures required for diesel reforming, and failed after about 50 hours on the bench. A second diesel reformer was delivered in late December 1999, with different materials, and is currently providing clean data on the laboratory bench.

The test bench at UAF was designed to provide a mass and energy balance for the reformer. Inputs of air, water, diesel fuel, electrical power (for pumps, blowers, and control solenoids), propane (sometimes used to supplement the burner) were measured, as well as hydrogen flow and heat in the combustion exhaust. In most cases at least two independent measurements were made to assure the accuracy of the data set.

In order to assess the performance of the reformer, measurements were made of the composition of the raffinate gas. These measurements were then compared to equilibrium thermodynamic calculations done by Andy Lutz at SNL. Results showed significant departure from equilibrium conditions.

Results

The most significant result to date has been the encouraging demonstration that it is possible to run a pure hydrogen PEM fuel cell on hydrogen produced from a heavy hydrocarbon fuel. The reformer

has been operated in a self-sustained mode (diesel fuel only) using a control algorithm developed at UAF. Energy Balance data and reformer gas composition measurements have been made.

However, system efficiency measurements have not been encouraging to date. The energy balance data collected show that the overall efficiency of the reformer is less than expected, in the range of 36% (LHV) of the energy leaving the system in the hydrogen stream. Much of the energy leaves the system in the combustion exhaust (about 43%), and additional losses occur due to radiation and convection from the reformer surfaces.

Using the experimentally obtained values for reformer (36%), fuel cell (49%), and power conditioning (80% with inverter and batteries) and subtracting off the electrical parasitic losses for the reformer yields an overall systems efficiency of 12.8%. This is not a very satisfactory result, being considerably lower than what can be obtained by conventional technology.

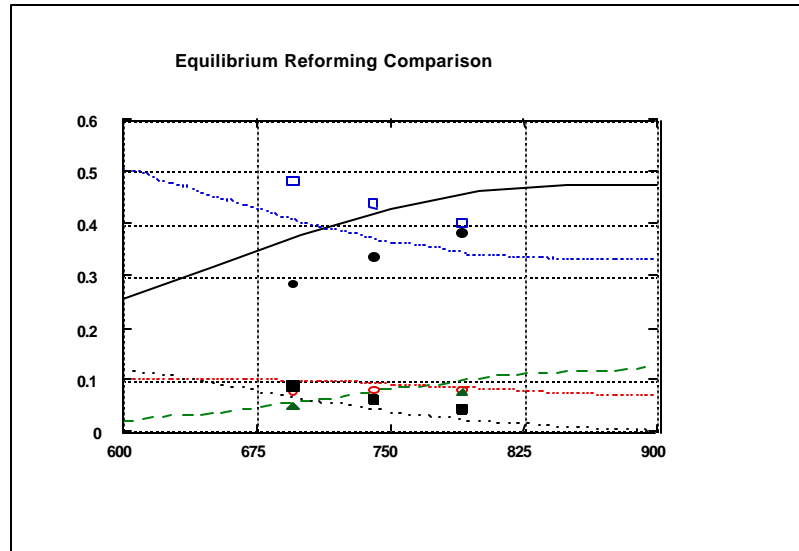
It must be noted that the reformer is still in the prototype stage, and that the experience to date with the reformer does suggest possible improvements in the reformer design. In particular, the deviation from thermodynamic equilibrium suggests that reducing the space velocity in the catalyst area is necessary to improve performance. Heat recovery from the combustion exhaust is also necessary. While it is hard to predict exactly how much improvement can be made in the performance, of the unit, the improvements should be considerable. However, the smaller the reformer, the greater the surface to volume ratio, and the greater the relative heat loss.

As part of our evaluation of reformer efficiency, we also calculated efficiencies based on various system boundaries, as well as attempting to differentiate between efficiency and hydrogen yield. In tests designed to evaluate catalyst performance, hydrogen yield is often the parameter given, but these measurements are often done at a constant temperature without regard for the heat losses in the system. Since the purpose of this work is to evaluate total system efficiency, these heat losses become an important energy flux, and cannot be ignored. Results of this analysis are shown in the figure below.

Based on the results to date, it is apparent that the current level of performance of the reformer is significantly lower than had been hoped at the beginning of the program. Therefore the decision has been made to delay phase III of the program until this issue can be resolved.

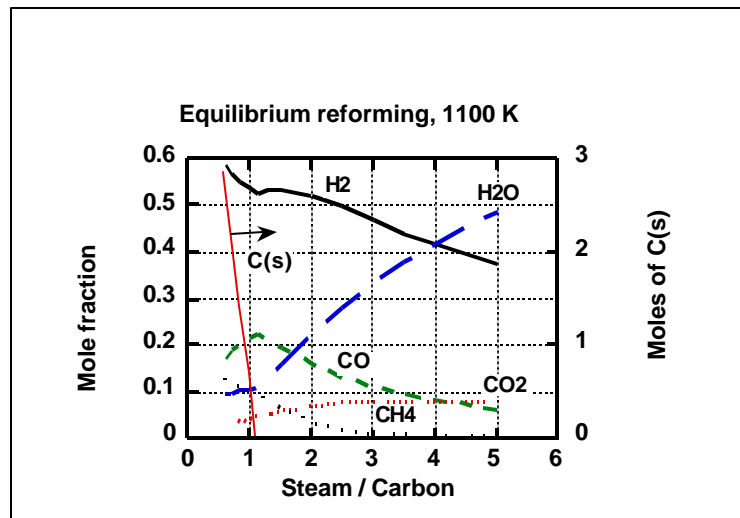
The issue of reformation is an important one for the fuel cell industry. Small-scale reformation allows use of conventional hydrocarbon fuels in widely distributed power generation systems, but forces the development of small-scale reformers. This technology requires careful attention to heat management, fuel vaporization, catalysts, and combustion technology, and represents a difficult problem. Diesel reforming is a problem that has a long history, and will likely require significant additional effort and resources to solve.

It is widely recognized that, due to the long hydrocarbon chains and the sulfur content, diesel represents one of the hardest fuels to reform. It may be that the only logical way to progress with the rural power program at this point is to switch fuel feedstocks to a fuel easier to reform, such as propane or methanol, and continue development of the integrated system with one of these fuels. Development of the small-scale diesel reformer could continue on a parallel track, and be introduced into the field when ready.



- **Equilibrium reforming of heptane at 1100 K, including solid carbon.**
- **$C_7H_{16} + 14 H_2O \rightarrow 7 CO_2 + 22 H_2$**
- **Vary steam/carbon ratio; stoichiometric is 2.**
- **C(s) appears below steam/carbon ratio of 1.**
- **The cycle efficiency computations neglect C(s), for a minimum steam/carbon ratio of 1.5.**

| Comparison of Thermal Efficiencies for Reformer Systems | | | | |
|---|--|--------------------|----------------|--|
| Reaction Balance | Energy Balance | Thermal Efficiency | Hydrogen Yield | |
| Complete reaction: | Balance Energy using H2 at HHV | 100 | 78 | |
| $\text{CH}_4 + 2\text{H}_2\text{O} \rightarrow \text{CO}_2 + 4\text{H}_2$ | Balance Energy using H2 at LHV | 90 | 74 | |
| | Adiabatic System; | | | |
| Chemical equilibrium at 900 C | Balance Energy using reformat at LHV | 88 | 73 | |
| | Exhaust products at 100 C (liquid) | | | |
| | Adiabatic System; | | | |
| Chemical equilibrium at 700 C | Balance Energy using reformat at LHV | 56 | 47 | |
| | Exhaust products at 100 C (liquid) | | | |
| | Adiabatic System; | | | |
| Equilibrium at 900 C for Heptane | Balance Energy using reformat at LHV | 81 | 68 | |
| | Exhaust products at 100 C (liquid) | | | |
| Experimental on Kerosene 800C | Heat provided by suplimental fuel | 65 | 52 | |
| Self Sustained on Kerosene | Energy Loss in Combustion Exhaust and Radiation and Convection | 40 | 33 | |



FUEL-CELL MINE VEHICLE — DEVELOPMENT AND TESTING

Arnold R. Miller, PhD
Fuelcell Propulsion Institute
Denver, CO 80226-0130

Abstract

Underground vehicle applications — tunneling and mining — may be the first fuelcell-vehicle markets that succeed solely on economic merit. Providing traction power in these enclosed, highly regulated workplaces is a difficult challenge, and the inadequacies of conventional power are the basis of economic stress in the industries. Clean, safe, and productive fuelcell vehicles, while higher in capital cost, offer cost offsets that can make them the first commercially successful products. The Locomotive Project of the Fuelcell Propulsion Institute is developing and testing the world's first fuelcell-powered underground vehicle, a mine locomotive. The 25-month project involves more than 20 international partners, including mining companies, mine vehicle companies, mine regulators, organized labor, and national laboratories, and is internationally funded by two governments and the mining industry.

Introduction

Tunneling and mining offer the most immediate markets for successful fuelcell vehicle commercialization. The enclosed, underground operating environment exacerbates problems of vehicle emissions and noise. Despite high capital cost of the fuelcell, powerful cost offsets arising from solving these problems will make the fuelcell vehicle cost-competitive

several years before surface applications (Gaibler and Miller, 1998; Miller, 2000). These offsets allow the fuelcell vehicle to compete strictly on economic merit.

The mining industry faces economic losses resulting from the health and safety deficiencies of conventional underground traction power. Because workers are constrained to an underground workplace, mining is one of the most regulated industries. Conventional power technologies — tethered (including trolley), diesel, and battery — are not simultaneously clean, safe, and productive. For instance, tethered vehicles are power-dense and clean, but the tether is unsafe and interferes with mobility and productivity. Diesel vehicles, nearly as power-dense, are more mobile and theoretically more productive, but government emissions regulations hamstring actual productivity. Emissions and noise regulations (Wilson, 2000) in the process of implementation will further increase vehicle capital and operating costs and lower mine productivity. Because the market price of metals and coal is low, the problem of underground power production places the industry in economic stress — downward forces on price and upward forces on costs.

Tunneling is even more hampered by inadequate traction power. A tunnel under development is a tube, perhaps 10 km long, closed at one end. Because ventilation is poor, operations may use staged vehicles: battery locomotives working near the face that hand off a train to diesel locomotives operating in better ventilation near the tunnel entrance. Multiple battery locomotives may be required — whereas one is sufficient for power, the others transport batteries. The potential economic value of solving the problem of traction power in tunneling exceeds that of mining.

Fuelcells offer a solution — and underground vehicles offer the opportunity that they will be the first commercially successful products. A fuelcell type well-suited to underground applications is the “hydride fuelcell” — the coupling of a fuelcell system with metal-hydride onboard energy storage. Benefits of fuelcells include zero emissions, low noise, high power density, low temperature/pressure operation, and long life. The PEM (Proton Exchange Membrane) fuelcell type, coupled with hydride storage, provides additional benefits critical to heavy-duty, underground applications: safety, compactness, simplicity, and ruggedness. Although hydride storage is heavy, weight is of no consequence in counter-balanced vehicles (e.g., loaders) or steel-wheeled vehicles (locomotives).

ECONOMIC ANALYSIS

Analyses by the Fuelcell Propulsion Institute show that hydride fuelcells will provide improved health and safety, enhanced performance, and reduced mine operating costs. We project that these cost offsets will make fuelcell vehicles cost-competitive at least three years earlier than projected for surface vehicle applications (Gaibler and Miller, 1998). The cost analysis addresses rubber-tired vehicles in coal mining, but similar results are expected for vehicles in hardrock metal mining and tunneling.

Current purchase costs are high for both fuelcells and metal hydrides because they are

largely hand-built, manufacturing volume is low, manufacturing experience is limited, and development costs must be recovered. Labor is the largest component of manufacturing costs. The analysis focuses on replacement of the diesel vehicle because its productivity is the benchmark that the fuelcell vehicle must equal or exceed.

Application of diesel-powered equipment in coal mines is a difficult technical challenge. Because the vehicle operates in a potentially explosive environment, regulations require that no surface temperature exceed 150 C (302 F). This necessitates water-jacketed exhaust manifolds and water-scrubbed exhaust. Frequent emissions tests and system complexity lower vehicle availability and increase capital cost. Complete diesel systems for coal mining cost more than \$500/kW, far above the cost for surface applications.

The diesel engine is not inherently well-suited to underground operation. Constituents of diesel exhaust are known to be carcinogenic, and underground diesel operations require extensive ventilation. Noise is excessive. Proposed regulations require filtration of the exhaust to eliminate 95% of particulate matter. A consequence of compensating for the diesel's inherently poor health and safety characteristics is that complexity and cost will continue to rise and availability will fall. Hydride fuelcell systems obviate the complexity of underground diesel engines.

This study estimates the year when the hydride fuelcell vehicle is cost-competitive with the diesel version of three coal vehicles. It compares both recurring and capital costs of diesels with projections for hydride fuelcells. Recurring costs include (a) fuel, (b) tires, (c) driver and maintenance labor, (d) labor to assure conformance to diesel regulations, e.g., exhaust-gas sampling lost time, (e) consumable parts such as filters, (f) drivetrain maintenance due to breakdown and rebuild, and (g) engine control system (safety system) breakdown and rebuild costs. Capital cost projections were obtained via a survey of the fuelcell and metal-hydride industries and from the known cost of diesel vehicles. Projected capital costs assume production volumes that have substantial components other than mine vehicles. Capital costs include financing costs. Although diesel costs, both recurring and capital, will rise over the same time period, we conservatively assume a constant diesel cost. Since fuelcell costs are expected to fall, the study's objective is to determine at what time the falling fuelcell vehicle costs cross the constant diesel costs.

Although the fuelcell production vehicle will probably be more productive than a diesel vehicle — because of higher allowed vehicle density, higher availability, and substantially higher performance — and may lower non-vehicle subsidiary mine operating costs — e.g., ventilation costs — the scope of the study was limited to costs directly attributable to operation and purchase of the vehicle.

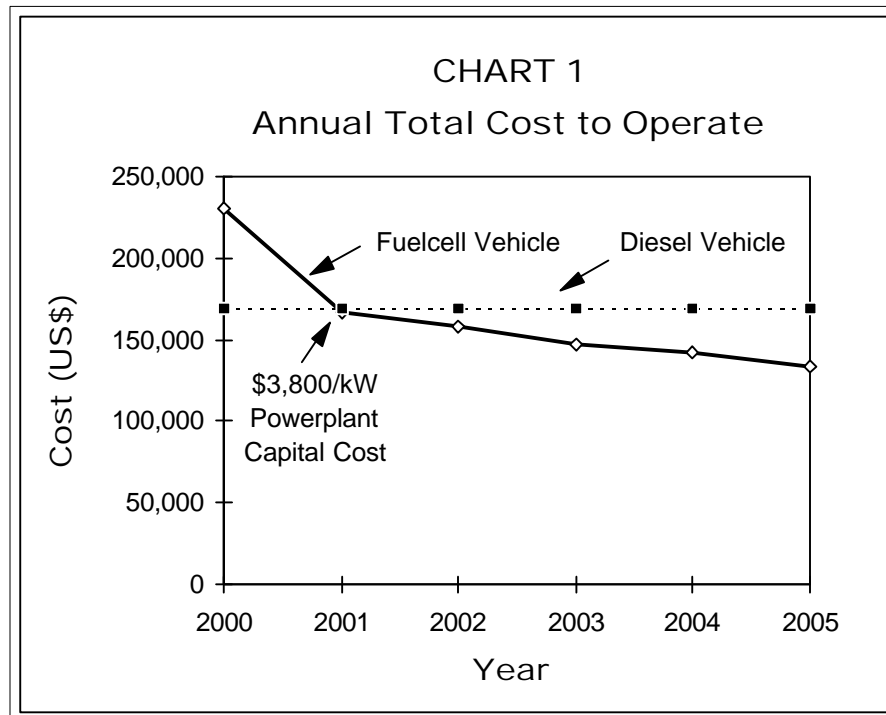


Chart 1 shows the trends for annual total costs for a typical coal vehicle (a scoop). When viewed in terms of the sum of annualized capital costs and annual recurring costs, the fuel-cell vehicle is cost-competitive even while the capital cost of its hydride fuelcell powerplant is quite high. We predict that when the powerplant capital cost is as high as \$3,800/kW, compared to about \$500/kW for the diesel counterpart, it will nonetheless be cost-competitive. This follows because there are important cost components besides the purchase cost of an industrial vehicle, and these are lower for the fuelcell vehicle: Diesels are expensive to maintain and operate because they are inherently ill-suited to operate underground. It is primarily the reduction in recurring costs in the underground application that make the fuelcell vehicle cost-competitive so soon.

Accordingly, we believe the rate-limiting factors to commercialization are not capital cost but government regulations, acceptance by organized labor, and ramp-up time for product development.

Locomotive Project

During the past four years, the Fuelcell Propulsion Institute, an international technical and

educational consortium¹, has proposed and analyzed hydride fuelcells as a solution to the growing problem of providing underground traction power. The Institute, comprised of technology developers, manufacturers, and end-users, is structured as a nonprofit membership organization. Its mission is to spearhead industry-specific transitions to fuelcell propulsion by bringing together an industry's major stakeholders, applying their in-depth knowledge, developing the technology, and educating the public.

The principal business of the Institute is the development of fuelcell vehicles for applications with high commercialization potential. The Fuelcell Propulsion Institute itself, a nonprofit corporation, has no commercial objectives and acts as a facilitator for the ultimate benefit of the public-at-large.

Under the guidance of its primary customer, the mining industry, the Institute's 25-month Locomotive Project (Miller, et al, 2000) involves all major players in North American mining — more than 20 international partners, including mining companies, mine vehicle companies, mine regulators, organized labor, and national laboratories. The world's first fuelcell locomotive is scheduled for completion by 9 October 2000, the starting date for its display at MINExpo INTERNATIONAL 2000SM in Las Vegas, NV, USA. MINExpo is the largest event of its kind in the world and features the newest equipment and technology available in the mining and tunneling industries. It occurs only every four years.

Power

Because of the well-behaved characteristics of steel wheels on steel rails, we have established the power requirements of the vehicle analytically (Miller, 2000; Miller, et al, 1999). The track system of underground metal mines is almost universally on a 0.5% grade, with the mine face being uphill of the dump point: Ore is loaded into the cars at the top of the grade, they are pulled downhill, dumped, and returned uphill empty. This operational method provides two benefits: (a) The system exploits gravity to assist the removal of ore from the mine and (b) water drains out of the mine rather than into it.

¹Atlas Copco Wagner Inc, Barrick Gold Corporation, Bituminous Coal Operators' Association (BCOA), Canada Centre for Mineral and Energy Technology (CANMET), Cast Resource Equipment Ltd, H Power Corporation, Inco Limited, Long-Airdox Company, McNally International Inc, Mining Technologies International Inc, National Mining Association, National Renewable Energy Laboratory, National Rural Electric Cooperative Association (NRECA), Noranda Inc, Pennsylvania State University, Placer Dome Inc, RA Warren Equipment Ltd, Sandia National Laboratories/California, Sandia National Laboratories/New Mexico, Sandvik Tamrock Corporation, Société de Recherche et Développement Minier (SOREDEM), South Dakota State University, Stuart Energy Systems, U.S. Department of Agriculture/ARS (in process), Virginia Tech, Westinghouse Safety Management Solutions, Inc, Westinghouse Savannah River Company

The maximum power in the duty cycle of the locomotive is the power developed during the initial stall condition of startup (acceleration from rest) for the fully loaded train on a 0.5% grade. While a benefit of rail vehicles is the low coefficient of friction between steel wheels and steel rails, startup torque is also limited by wheel slippage during acceleration. The vehicle employs a programmable, smart motor controller that limits startup torque to a value below that causing wheel slippage. Because stall current is limited by the controller, the locomotive maximum power requirement is in fact determined by the motor controller rather than limited by the power source. We estimate 6 kW as the average power over the duty cycle.

The locomotive manufacturer has developed equations and tables of empirical parameters (Miller, et al, 1999) that allow computation of the maximum allowed tractive effort at startup that is simultaneously consistent with wheel adhesion. The calculations below first compute this maximum allowable tractive effort (TE_{max}). From TE_{max} , we derive the traction-motor shaft torque, and from the torque-versus-current curve of the traction motor, the corresponding motor current. By estimating the corresponding battery voltage, we determine the maximum power P_{max} that the fully loaded locomotive can develop — at stall on a 0.5% grade — and avoid wheel slippage. P_{max} is the required maximum power of the fuelcell.

Definitions and values of parameters used in the analysis are collected in the accompanying table.

Total motion resistance RT to the train is a function of four resisting forces: rolling resistance R_r , grade resistance G_r , inertia A_r , and resistance due to curvature of the tracks C_r . Thus,

$$RT = R_r + G_r + A_r + C_r. \quad (1)$$

Substituting the values from the table gives

$$\begin{aligned} RT &= 25 \text{ lb/ton} + 10 \text{ lb/ton} + 5 \text{ lb/ton} + 0 \text{ lb/ton} \\ &= 40 \text{ lb/ton} \end{aligned} \quad (2)$$

Define the trailing load TL as the weight of the loaded train cars. When the locomotive wheel adhesion force (friction) is in balance with the total motion resistance (RT) force, we have the equilibrium described by equation (3):

$$L(Ad - RT) = TL \times RT. \quad (3)$$

DEFINED AND CALCULATED PARAMETERS

| Parameter | Value |
|--|--|
| L Locomotive weight | 4.0 ton (U.S.) |
| Rr Rolling resistance of train (lb/ton) | 25 lb/ton for steel wheels at startup |
| Gr Grade resistance — gravity (lbs/ton) | 10 lb/ton for 0.5% grade |
| Ar Acceleration resistance or inertia (lb/ton) | 5 lb/ton for standard acceleration of 0.05 m/s ² |
| Cr Curvature resistance of track (lb/ton) | Assume zero |
| Ad Wheel adhesion (lb/ton) | 400 lb/ton for steel wheels at startup |
| Tw locomotive gear-reduction ratio | 17 (i.e., 17:1) |
| Wr Wheel radius (m) | 0.23 m |
| TL Trailing load weight (ton) | Calculate |
| RT Total motion resistance (lb/ton) | Calculate |
| TE Tractive effort (lb, N) | Calculate |
| Ts Torque at traction motor shaft (Nm) | Calculate |
| P Power (kW) | Calculate |

Solving this for TL, we find the acceptable trailing load for our conditions:

$$\begin{aligned}
 TL &= L(Ad - RT)/RT && (4) \\
 &= 4.0 \text{ ton } (400 \text{ lb/ton} - 40 \text{ lb/ton})/40 \text{ lb/ton} \\
 &= 36 \text{ ton.}
 \end{aligned}$$

The maximum startup tractive effort, without wheel slip, is the product of the total motion resistance force (lb/ton) and the total acceptable weight of the train (ton):

$$\begin{aligned}
 TE_{\max} &= RT(L + TL) && (5) \\
 &= 40 \text{ lb/ton } (4.0 \text{ ton} + 36 \text{ ton}) \\
 &= 1600 \text{ lb} \\
 &= 7100 \text{ N.}
 \end{aligned}$$

Working backward, the traction-motor shaft torque Ts necessary to provide this tractive effort is given by

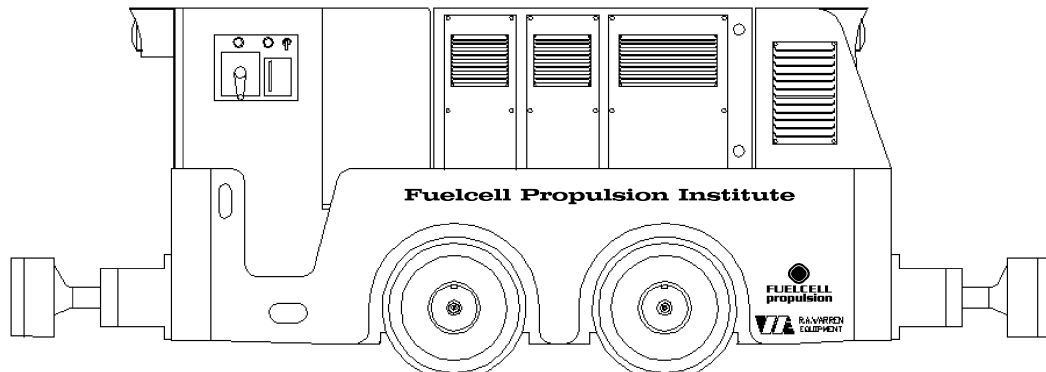
$$Ts = TE_{\max} \times Wr/Tw \quad (6)$$

$$\begin{aligned} &= (7100 \text{ N} \times 0.23 \text{ m})/17 \\ &= 96 \text{ Nm.} \end{aligned}$$

From the traction-motor performance curves, the current required to produce 96 Nm of torque is determined. By estimating the traction battery's corresponding voltage, the maximum power P_{max} consistent with wheel adhesion is computed as 13.3 kW net at startup stall (Miller, 2000; Miller, et al, 1999).

Fuelcell Locomotive

The base vehicle for the project is a commercial four-ton battery locomotive manufactured by consortium member RA Warren Equipment. The vehicle employs a 52-cell lead-acid battery (104 V nominal), series traction motor with interpoles, smart motor controller, double-enveloping gear drive, hydraulically assisted disc brakes, and unitized body/chassis. An illustration of the derived fuelcell locomotive is shown below; the front of the vehicle is to the right.



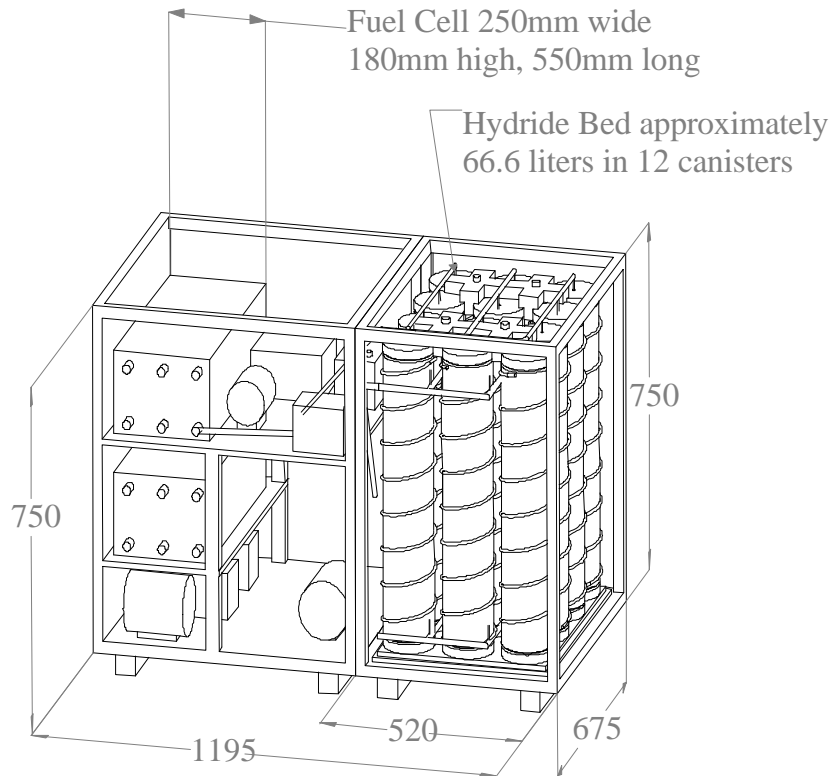
The locomotive's powerplant uses a proton-exchange membrane (PEM) fuelcell. No traction battery is employed, and the vehicle is thus a pure fuelcell vehicle. The stacks, undergoing fabrication, are a rugged industrial design, using metal bipolar plates, that has been tested under extreme conditions by the Ecole des Mines in France. Two stacks in electrical series give 104 V and 135 A at the continuous rated power of 14 kW gross. Each stack, with integral humidifier, weighs 30 kg and has a volume of 25 L. The air cathode operates at 0.5 bar above ambient pressure. Because the overload capacity of the fuelcell is at least as great as the parasitic load of system ancillaries, the 14 kW gross-power stacks can provide at least the 13.3 kW net required during the transient overload of startup stall.

The state-of-the-art hydride storage system, under development by consortium member Sandia/CA, will store 3 kg of hydrogen, sufficient for eight hours of locomotive operation at the 6 kW average power of its duty cycle. The bed uses approximately 200 kg of C-15 alloy (an alloy of manganese, titanium, zirconium, iron, and other constituents from GfE) stored in 12 cylinders, each having an outside diameter of 12.7 cm, inside diameter of 11.4 cm, and height of about 65 cm. Weight of each loaded cylinder is 25 kg, and outer volume of the group is 100 L. The C-15 alloy was chosen for its room-temperature performance characteristics, with pressure ranging from 1 to 10 bars over the temperature range 20 - 60 C. Bed capacity is 1.8 weight per cent. System pressure is limited by a relief valve to 10 bar and system pressure capability will be tested at 40 bar.

Hydride system design allows for rapid change-out (swapping) of a discharged bed with a freshly charged unit. The radiator is designed to maintain bed temperature below 50 C and allow recharging, either onboard or offboard, in 30 minutes. Recharging will utilize gaseous hydrogen at seven bars.

The proprietary powerplant is being developed for the consortium by member Sandia/CA. The complete system — stacks, fuelcell balance-of-plant, hydride storage system, and all system controls — packaged in a stand-alone subframe is illustrated below. A heat exchanger links two isolated thermal systems: (a) the hydride-bed heating/cooling loop and (b) stack cooling loop. The bed loop uses a circulating anti-freeze medium, whereas the stack loop uses demineralized water. Stack cooling water also passes through a forced-air excess-heat radiator. Coolant pumps and the stack air pump are powered at system startup by an auxiliary battery recharged by the stacks.

The fuelcell locomotive will match or exceed the battery vehicle in performance while having greater availability. Its calculated power and tractive effort are equal or greater. Vehicle operating time on a full hydride charge is eight hours, versus a practical battery operating time of six hours. It can be refueled in 30 minutes rather than eight hours. The complete hydride fuelcell powerplant (see illustration) is one-third the weight of the battery, and ballast must be added to bring vehicle weight to the four tons assumed in the power analysis. The powerplant has half the water-displacement volume of the battery. By relaxing power density, available chassis volume should accommodate two additional hydride beds and allow continuous locomotive operation for 24 hours. Comparisons of the battery and hydride fuelcell power sources are given in the accompanying table.



Comparison of Battery and Fuelcell Powerplant

| Parameter | Battery | Powerplant |
|------------------------------|-----------------|----------------|
| Power, continuous | 7.1 kW (net) | 14 kW (gross) |
| Current, continuous | 71 A | 135 A |
| Voltage at continuous rating | 101 V | 104 V |
| Weight of components | 1650 kg | < 550 kg |
| Volume of components | 520 L | < 250 L |
| Energy capacity, electrical | 43 kWh | 48 kWh |
| Operating time | 6 h (available) | 8 h |
| Recharge time | 8 h | ½ h (expected) |

Although low-temperature hydride storage is often considered too heavy for light-duty vehicles, our entire powerplant (fuelcell plus storage) is one-third the weight of the corresponding lead-acid battery. The powerplant will be somewhat heavier than a diesel engine, including fuel tank, but weight is not an issue for many underground vehicles, e.g., loaders, lift-trucks, and locomotives. Far more important is safety and minimum volume: workers are highly confined and all available space had to be dug out of rock. Thus, the combination of metal-hydride storage and PEM fuelcells is an ideal solution for underground traction power.

Vehicle Evaluation

Under the direction of the Mine Safety and Health Administration (MSHA), the agency within the US Department of Labor responsible for safeguarding the safety and health of the mining workforce, the vehicle will be tested aboveground for safety. Objective is to validate the safety of various features, listed below, before the vehicle is taken into operating mines for the productivity tests:

- Integrity of fittings, piping, and fuelcell with respect to gaseous hydrogen
- Guarding of components within the machine frame
- Routing of piping and wiring between components
- Hydride-bed refueling by gaseous transfer
- Refueling by bed change-out (swapping)
- Vulnerability of refueling to mud, water, air, and other contaminants
- Effects of shock and vibration on system integrity
- Training requirements of mining personnel
- Acceptance of hydrogen storage and refueling by workers and regulators.

The vehicle will also be tested for performance at the aboveground site. Objective is to demonstrate that its performance is adequate to not disrupt mine operations during underground evaluation:

- Tractive effort
- Grade climbing
- Tram speed
- Operating duration on a full charge
- Refueling time
- Shock and vibration resistance
- Overload capacity
- Ergonomics and human control characteristics.

Under the direction of the Canada Centre for Mineral and Energy Technology (CANMET), a Canadian national laboratory and consortium member, the locomotive will be evaluated while working in four underground metal mines. Besides evaluating produc-

tivity in actual underground working conditions, the tests will lay the foundation for subsequent development of vehicles for coal mining. Specific field assessments include productivity, reliability, availability, practicality, and safety of the hydride fuelcell locomotive. It will be compared directly with battery versions of the vehicle.

Conclusions

Fuelcells coupled with metal-hydride storage, by solving the problem of underground traction power, offer cost offsets — higher productivity and lower operating costs — making them cost-competitive sooner than surface applications. Compared to the battery vehicle from which it is derived, the fuelcell locomotive has equivalent power and tractive effort, at least twice the volumetric energy density, and greater availability. By relaxing power density, chassis volume should accommodate two additional hydride beds, giving a vehicle that can operate continuously for 24 hours. Because weight is not an issue for many key production vehicles, safe and compact metal-hydride storage is an ideal storage solution for underground vehicle applications.

Acknowledgments

The Locomotive Project is funded by the US Department of Energy, Office of Power Technologies, through Hydrogen Program cooperative agreement DE-FC36-99GO10458; Natural Resources Canada through CANMET/IERD contract 23440-991022; and Vehicle Investment Partners LLC, Denver, CO, USA. Funding for powerplant development is provided by direct funding of Sandia National Laboratories/CA by the DOE Hydrogen Program. The Fuelcell Propulsion Institute and its projects are managed and operated by TransConsortia LLC, Denver, CO, USA. Lead partners in the Locomotive Project are RA Warren Equipment, North Bay, ON, Canada (provision of the base locomotive and vehicle design); Nuvera Fuel Cells, Cambridge, MA, USA, and Milan, Italy (fabrication of stacks); Sandia National Laboratories, Livermore, CA, USA (powerplant development, including hydride storage); Atlas Copco Wagner, Portland, OR, USA (vehicle integration and aboveground evaluation site); MSHA, Arlington, VA, USA (safety evaluation); and CANMET, Ottawa, ON, Canada (underground productivity evaluation). RA Warren Equipment provided the locomotive illustration and Sandia/CA provided the powerplant illustration. I thank my co-authors of earlier papers (see below) for their contributions to this summary.

References

- Gaibler, D. W., and A. R. Miller, 1998. *Cost Model for Fuelcell Mine Vehicles: Conservative Analysis of Recurring and Capital Costs*. Denver, CO: Fuelcell Propulsion Institute.
- Miller, A. R., 2000. "Commercialization of Fuelcell Underground Locomotives." In *Proceedings of the Conference Commercializing Fuel Cell Vehicles 2000*. Berlin, Germany:

Intertech.

Miller, A. R., H. A. Bursey, A. I. Attia, and W. D. Muir, 1999. *Maximum Power of the Fuelcell Propulsion Institute's Mine Locomotive*. Denver, CO: Fuelcell Propulsion Institute.

Miller, A. R., H. A. Bursey, G. C. Story, M. C. Bétournay, and G. J. Thomas, 2000. "Underground Fuelcell Locomotives and their Applications." In *Proceedings of the Conference Fuel Cell 2000*. Lucerne, Switzerland.

Wilson, J. 2000. "MSHA Speaks Out: New Standard to Control Occupational Noise Exposures." *Safety and Health*, April, 2-7.

PROCEEDINGS OF THE 2000 DOE/NREL HYDROGEN PROGRAM REVIEW

MAY 8-10, 2000

CARBON NANOTUBE MATERIALS FOR HYDROGEN STORAGE

A.C. Dillon, T. Gennett, J. L. Alleman, K.M. Jones, P.A. Parilla,
and M.J. Heben

National Renewable Energy Laboratory
Golden, CO 80401-3393

Abstract

Carbon single-wall nanotubes (SWNTs) are capable of adsorbing hydrogen quickly, to high density, at ambient temperatures and pressures. Last year, we showed that hydrogen storage densities on SWNTs made by laser vaporization ranged from 3.5 to 4.5 wt% after a new cutting procedure was performed. We present the details of the cutting procedure here and show that, when optimized, hydrogen storage densities up to 7 wt% can be achieved. Infrared absorption spectroscopy measurements on pristine and H₂-charged samples indicate that no C-H bonds are formed in the hydrogen adsorption process. These experiments are in agreement with an earlier temperature programmed desorption analysis which showed that hydrogen molecules are not dissociated when bound to the SWNT surfaces¹. This conclusion is further supported by the first neutron scattering measurements which were performed through collaboration with researchers at NIST and University of Pennsylvania². We also developed methods to tune SWNT diameters during synthesis so that mechanistic aspects of H₂ storage can be probed³, and learned how to de-tangle and organize individual tubes to form "superbundles" that will afford high volumetric storage densities⁴. Finally, we wish to report that we have performed first synthesis experiments with a new laser which recently arrived at NREL. Raman spectroscopy indicated that the as-produced materials were ~ 50 wt% pure SWNTs, in contrast to the 20 to 30 wt% usually seen with the previous laser, and the production rate for raw soot appears to be significantly greater than the 150 mg/hr observed previously, even though the current performance is probably far from optimal.

Statement of the Problem / Relevance of the Work

Background

With the 1990 Clean Air Act and the 1992 Energy Policy Act, the United States recognized the need for a long-term transition strategy to cleaner transportation fuels⁵. This realization comes while the U.S. continues to increase petroleum imports beyond 50% of total oil consumption, with nearly 50% of the total oil consumed being used in the transportation sector⁶. Because of the potential for tremendous adverse environmental, economic, and national security impacts, fossil fuels must be replaced with pollution-free fuels derived from renewable resources. Hydrogen is an ideal candidate as it is available from domestic renewable resources, and usable without pollution. It could therefore provide the long-term solution to the problems created by the Nation's dependence on fossil fuel.

Interest in hydrogen as a fuel has grown dramatically since 1990, and many advances in hydrogen production and utilization technologies have been made. However, hydrogen storage technology must be significantly advanced in performance and cost effectiveness if the U.S. is to establish a hydrogen based transportation system. As described in the U.S. DOE Hydrogen Program Plan for FY 1993 - FY 1997, compact and lightweight hydrogen storage systems for transportation do not presently exist.

Hydrogen provides more energy than either gasoline or natural gas on a weight basis. It is only when the weight, volume, and round-trip energy costs of the entire fuel storage system and charging/discharging cycle is considered that hydrogen's drawbacks become apparent. New approaches enabling more compact, lightweight, and energy efficient hydrogen storage are required in order for the wide-spread use of hydrogen powered vehicles to become a reality.

Research and development geared towards implementation of a national hydrogen energy economy has many indirect economic benefits. With almost 600 million vehicles in the world in 1992 - double the number in 1973 - the conflict between energy requirements, power generation, and environmental concerns is felt on a worldwide basis ⁷. Thus, in addition to providing domestic energy alternatives, investment in hydrogen energy research will result in opportunities for U.S. technologies in over-seas markets.

Currently Available Hydrogen Storage Technologies

Hydrogen can be made available on-board vehicles in containers of compressed or liquefied H₂, in metal hydrides, or by gas-on-solid adsorption. Hydrogen can also be generated on-board by reaction or decomposition of a hydrogen containing molecular species⁸. Although each method possesses desirable characteristics, no approach satisfies all of the efficiency, size, weight, cost and safety requirements for transportation or utility use. The D.O.E. energy density goals for vehicular hydrogen storage call for systems with 6.5 wt % H₂ and 62 kg H₂/m³.

Gas-on-solid adsorption is an inherently safe and potentially high energy density hydrogen storage method that should be more energy efficient than either chemical or metal hydrides, and

compressed gas storage. Consequently, the hydrogen storage properties of high surface area "activated" carbons have been extensively studied^{9,10,11}. However, activated carbons are ineffective in hydrogen storage systems because only a small fraction of the pores in the typically wide pore-size distribution are small enough to interact strongly with gas phase hydrogen molecules.

The first measurements of hydrogen adsorption on carbon single-wall nanotubes (SWNTs) were performed here at NREL with highly impure samples. The room-temperature stabilization that was demonstrated at atmospheric pressures suggested the possibility of 5-10 wt % hydrogen storage in SWNT-based systems¹. Contradictory results from purified SWNTs indicated that such high storage densities could only be achieved with cryogenic temperatures (80 K) and high pressures (158 atm)¹², consistent with theoretical consideration of van der Waals interactions between H₂ and SWNTs^{13,14,15}. However, we showed last year that SWNTs can adsorb between 3.5 and 4.5 wt% at room temperature and room pressure when un-optimized preparation procedures were employed¹⁶, and large-diameter SWNTs were recently shown to adsorb 4.2 wt % hydrogen at room temperature and ~100 atm¹⁷. This year we show that hydrogen storage densities can be optimized to values as high as 7 wt%, and present results from experiments designed to elucidate the mechanisms responsible for the unique hydrogen adsorption properties.

Technical Approach and Summary of Past Work

We have been working on the idea that aligned and self-assembled single wall carbon nanotubes could serve as ideal hydrogen adsorbents since 1993. The concept was motivated by theoretical calculations¹⁸ which suggested that adsorption forces for polarizable molecules within SWNTs would be stronger than for adsorption on ordinary graphite. Thus, high H₂ storage capacities could be achieved at relatively high temperatures and low pressures as compared to adsorption on activated carbons.

In the Proceedings of the 1994 Hydrogen Program Review, we presented microbalance data which demonstrated gravimetric hydrogen storage densities of up to 8.4 wt% at 82 K and 570 torr on samples containing carbon nanotubes. This substantial uptake at low hydrogen pressures demonstrated the strong interaction between hydrogen and these materials, consistent with higher heats of adsorption than can be found with activated carbons.

In the 1995 Hydrogen Program Review Proceedings, we presented the results of our temperature programmed desorption (TPD) studies which showed significant H₂ adsorption near room temperatures. The adsorption energies on nanotube materials were estimated to be a factor of 2-3 times higher than the maximum that has been observed for hydrogen adsorption on conventional activated carbons. These were the first results which demonstrated the existence of stable adsorbed hydrogen *on any type of carbon at temperatures in excess of 285 K*. We also analyzed the nanotube production yields versus rod translation rate in the electric arc.

In 1996 we performed a detailed comparative investigation of the hydrogen adsorption properties of SWNT materials, activated carbon, and exfoliated graphite. We also determined that the cobalt nanoparticles present in the arc-generated soots do not play a role in the observed hydrogen uptake. We determined the amount of hydrogen which is stable at near room

temperatures on a SWNT basis is between 5 and 10 wt%, and found that an initial heating in vacuum is essential for producing high temperature hydrogen adsorption. Further experiments suggested that SWNTs are selectively opened by oxidation during this heating, and that H₂O is more selective in oxidation than O₂ due to hydrogen termination of dangling bonds at the edges of opened nanotubes. Purposeful oxidation in H₂O resulted in hydrogen storage capacities which were improved by more than a factor of three. We also correlated the measured nanotube densities produced by specific synthesis rod translation rates during arc-discharge with hydrogen storage capacities determined by TPD. Finally, we utilized NREL's High Flux Solar Furnace to form nanotubes by a new and potentially less expensive route for the first time.

In 1997, the desorption of hydrogen was found to fit 1st order kinetics as expected for physisorbed H₂, and the activation energy for desorption was measured to be 19.6 kJ/mol. This value is approximately five times higher than the value expected for desorption of H₂ from planar graphite and demonstrates that SWNT soots can provide very stable environments for H₂ binding. We also employed diffuse reflectance Fourier transform infrared (DRFTIR) spectroscopy to determine the concentrations and identities of chemisorbed species bound to the carbon surface as a function of temperature, and determined that “self-oxidation” allows high-temperature adsorption of hydrogen to occur in the arc-generated SWNT materials. We also began synthesizing SWNT materials in much higher yield than is currently possible with arc-discharge by using a laser vaporization process. We determined that the very long SWNTs made by this method could not be activated towards high-temperature H₂ physisorption by the same oxidative methods that were found to be effective for tubes produced by arc-discharge.

In 1998 we made significant advances in synthesis and characterization of SWNT materials so that we could prepare gram quantities of SWNT samples and measure and control the diameter distribution of the tubes by varying key parameters during synthesis. By comparing continuous wave (c.w.) and pulsed laser techniques, we learned that it is critical to stay in a vaporization regime in order to generate SWNTs at high yield. We also developed methods which somewhat purified the nanotubes and cut them into shorter segments. We performed temperature programmed desorption spectroscopy on high purity carbon nanotube material obtained from our collaborator Prof. Patrick Bernier, and finished construction of a high precision Seivert's apparatus which will allow the hydrogen pressure-temperature-composition phase diagrams to be evaluated for SWNT materials.

Last year we improved our laser-based method so that material containing between 20 - 30 wt% SWNTs could be generated at a rate of ~ 150 mg/hr or ~ 1.5 g/day. A simple 3-step purification technique was developed which resulted in single walled carbon nanotubes of greater than 98 wt% purity. A thermal gravimetric analysis (TGA) method was developed to allow the accurate determination of nanotube wt% contents in carbon soots. We also established a process for reproducibly cutting purified laser-generated materials. This advance was necessary since laser-produced tubes were found to be unresponsive to the oxidation methods that successfully opened arc-generated tubes. TPD spectroscopy demonstrated that purified cut SWNTs adsorbed between 3.5 – 4.5 wt% hydrogen under ambient conditions in several minutes and that the adsorbed hydrogen was effectively “capped” by CO₂

This year we present the details of the new cutting procedure and show that, when optimized, hydrogen storage densities up to 7 wt% can be achieved. Infrared absorption spectroscopy measurements on pristine and H₂-charged samples indicate that no C-H bonds are formed in the hydrogen adsorption process. These experiments are in agreement with an earlier temperature programmed desorption analysis which showed that hydrogen molecules are not dissociated when bound to the SWNT surfaces¹. This conclusion is further supported by first neutron scattering measurements of hydrogen adsorbed onto SWNTs which were performed through collaboration with researchers at NIST and University of Pennsylvania². We also developed methods to tune SWNT diameters during synthesis so that mechanistic aspects of H₂ storage can be probed³, and learned how to de-tangle and organize individual tubes to form "superbundles" that will afford high volumetric storage densities⁴. Finally, we wish to report that we have performed first synthesis experiments with a new laser which recently arrived at NREL. Raman spectroscopy indicated that the as-produced materials were ~ 50 wt% pure SWNTs, in contrast to the 20 to 30 wt% usually seen with the previous laser, and the production rate for raw soot appears to be significantly greater than the 150 mg/hr observed previously, even though the current performance is probably far from optimal.

Experimental

Pulsed Laser Synthesis of SWNTs

SWNT materials were synthesized by a laser vaporization method similar to that of Thess et al.¹⁹. A single Molelectron MY35 Nd:YAG laser was used which produced gated laser light ranging in duration from 300 to 500 ns at a frequency of 10 Hz. The gated laser light contained numerous short laser pulses of about 5 to 15 ns. The emission wavelength was 1064 nm at an average power of 20 - 30 W/cm². An electronically rastered beam enabled material generation at rates of 75 - 150 mg / h. Typically, production is ~ 1.5 g / day. It is important to stay in a vaporization regime²⁰ during synthesis so that graphite particles are not ejected. Targets were made by pressing powdered graphite (~ 1 μ particle size) doped with 0.6 at % each of Co and Ni in a 1 1/8" inch dye at 10,000 psi. Crude soot was produced between 850 - 1200 °C with 500 Torr Ar flowing at 100 sccm. Raw materials were estimated to contain ~ 20 - 30 wt% SWNTs by both a detailed analysis of numerous different TEM images²⁰ and an accurate thermal gravimetric analysis method. SWNT diameters were between 1.1 - 1.4 nm [3]. Inductively coupled plasma spectroscopy (ICPS) was performed after complete air-oxidation of the carbon soots and thorough digestion of the residue in concentrated HNO₃. The same metal content was found in both the laser-generated crude and the initial target to be ~6 wt%.

Purification of Laser-generated SWNTs

Approximately 80 mg of the above laser-generated crude was refluxed in 60 ml of 3M HNO₃ for 16 h at 120 °C. The solids were collected on a 0.2 μm polypropylene filter in the form of a mat and rinsed with deionized water. After drying, an ~ 82 wt % yield was obtained. The weight lost is consistent with the digestion of the metal and an additional ~ 12 wt % of the carbon impurities. The carbon mat was then oxidized in stagnant air at 550 °C for 10 min., leaving behind pure SWNTs. The SWNTs were shown to be > 98 wt% pure with thermal gravimetric

analysis. Also, TGA revealed that no significant SWNTs were consumed in the purification process²¹.

Cutting of Laser-generated SWNTs

Purified 1-3 mg samples were sonicated in 20 ml of 4M HNO₃ with a high-energy probe for 10 minutes to 24 hrs at powers ranging from 25 – 250 W/cm². Figure 1 displays a typical transmission electron microscopy (TEM) image of purified SWNTs following ultrasonication in 4M HNO₃ for 16 hrs, and shows that the very long ropes found after purification²¹ have been cut and re-assembled. The large-scale cutting observed here is consistent with the generation of cuts and defects that have been observed by others^{22, 23, 24}. We find that cutting with a high-energy probe in HNO₃ is necessary to achieve high-capacity ambient H₂ adsorption, explaining why other studies have not seen the high room-temperature capacities observed here.¹² Other TEM images of cut samples revealed metal particles ranging in size from several nanometers to several microns. X-ray patterns of the particles in the cut samples were consistent with an alloy of nominal composition TiAl_{0.1}V_{0.04} as expected for disintegration of the ultrasonic probe.

Temperature Programmed Desorption

Details of the ultra high vacuum (UHV) chamber employed for the TPD studies have been reported previously^{1,8}. Briefly, carbon samples weighing ~1 mg were placed in a packet formed from 25 μm thick platinum foil and mounted at the bottom of a liquid nitrogen cooled cryostat. The packet could be resistively heated with a programmable power supply. Pinholes in the foil enable gas diffusion into and out of the packet. An ion gauge and capacitance manometer are employed to monitor pressure. Gas exposures are controlled with a variable conductance leak valve. Isolation gate valves separate the sample compartment during high-pressure gas exposures. A mass spectrometer measures species with an m/e up to 300 a.m.u. and insures that only hydrogen is involved in adsorption/desorption cycles. Signals were sufficiently large that the ion current could provide low-noise spectra without multiplication. The instrument was easily calibrated²⁵ by thermally decomposing known amounts of CaH₂. The amount of evolved hydrogen was linear with the weight of decomposed CaH₂, and the calibrations were performed with amounts of CaH₂ that yielded a TPD signal similar to the SWNT samples. The charged hydrogen could also be desorbed under flowing helium during thermal gravimetric analysis (TGA). The hydrogen uptake measured by TPD and TGA was within 10%. Samples were initially degassed by heating in a vacuum of ~ 10⁻⁷ torr to 823 - 973 K at 1 K/s. The sample temperature was measured with a thin thermocouple spot-welded to the platinum packet. Room temperature H₂ exposures for ~ 1 minute at pressures between 10–500 torr saturated the hydrogen adsorption. Capacity determinations in the TPD were done by cooling the sample to 130 K prior to evacuation of the chamber.

Infrared Absorption Spectroscopy

Transmission Fourier transform infrared (FTIR) studies of single walled carbon nanotubes were performed on a Nicolet 690 spectrometer with a liquid nitrogen cooled MCT-B detector at a resolution of 4 cm⁻¹. Thin SWNT films were prepared employing an Anthem airbrush to spray SWNT/acetone mixtures onto silicon wafers. Approximately 4 mg of various SWNT materials

were suspended in ~ 15 ml acetone by sonication with an ultra sonic probe for several minutes. The resulting solution was sprayed onto the silicon for ~ 10 s. at 30 p.s.i., and the acetone was allowed to evaporate at room temperature in air. A uniform thin SWNT film on the IR transparent silicon substrate was thus obtained. Infrared spectra were ratioed to a background spectrum of a clean silicon wafer. A minimum of 500 scans were collected.

Results and Discussion

Hydrogen Adsorption on Cut SWNTs

Upon degassing the purified cut SWNT samples in vacuum, the high capacity hydrogen adsorption was activated. Figure 2 displays the H₂ TPD spectrum of a degassed sample following a brief room temperature H₂ exposure at 500 torr. The spectrum is characterized by two separate desorption signals peaked at ~ 375 and 600 K indicating at least two different types of sites for hydrogen adsorption. The peak desorption temperatures of these signals can be as much as 100 K lower depending on the SWNT sample and the specific cutting conditions. The hydrogen adsorption capacity, as measured by calibrated TPD, was ~ 6.5 wt% on a total sample weight basis after sonication for 16 hrs at 50 W/cm² and degassing to 825 K. This sample was found to contain ~ 15 wt% TiAl_{0.1}V_{0.04} by combusting the carbon fraction in flowing air and accounting for the oxidation of the metals. In addition to being used in the construction of ultrasonic probes, TiAl_{0.1}V_{0.04} is also employed in fusion reactor components. The latter application has led to numerous studies of the interactions between the alloy and hydrogen. A maximum of ~3 wt % hydrogen is observed^{26,27,28}, while virtually no adsorption is seen for T < 373 K due to poor kinetics²⁸. We generated TiAl_{0.1}V_{0.04} samples with the ultrasonic probe for 16 hrs in 4M HNO₃ without the addition of SWNTs. The generated particles exhibited X-ray patterns consistent with the alloy found in the SWNT samples. After a normal degas and H₂ exposure, the TiAl_{0.1}V_{0.04} sample exhibited only ~ 2.5 wt% hydrogen adsorption as measured by both TPD and volumetric techniques. Assuming that the alloy in the SWNT sample behaves like the pure alloy sample, the hydrogen uptake on the SWNT fraction is ~ 7.2 wt%. Samples with higher alloy contents had reduced overall hydrogen capacities, but the value of ~ 7 wt% on the SWNT fraction was relatively constant. The total adsorption capacity of the cut samples varied between 2-7 wt% depending on the material, the sonication power, sonication time, the hydrodynamics of the sonication vessel and the sample degas temperature. Adjustments in these parameters also affected the temperatures of the hydrogen desorption signals, but these results will be discussed in detail later²⁹. The storage results were highly reproducible within 10-20% for a given set of experimental conditions. The samples are stable to cycling with no apparent degradation when the vacuum and the hydrogen are relatively clean and the sample temperature does not exceed ~825 K.

Mechanism of Hydrogen Adsorption

We worked at length this past year to elucidate the mechanism of H₂ adsorption on SWNTs. This type of work is critical to the growing community that has been attempting to understand how SWNTs - as well as other types of nanostructured carbons - interact with hydrogen. There is considerable debate over the issue in the scientific community, and it is important to obtain a

deeper understanding so that; (i) accurate theoretical models and predictions may be developed, (ii) specific SWNT diameters and chiralities may be targeted for synthesis, and (iii) capacities and performance characteristics may be optimized. We have previously shown that hydrogen is not dissociated when adsorbed on arc-generated SWNTs even though the binding energy is 19.6 k/mol¹. In this report we present new evidence that H₂ is non-dissociatively adsorbed on laser-generated materials. Additional evidence pointing at the true nature of the stabilizing interaction cannot be discussed here as this work has been submitted for publication elsewhere³⁰. All-in-all, we find that the interaction between H₂ and single-wall nanotubes is mid-way between conventional van der Waals adsorption and chemical bond formation. A detailed understanding of the mechanism coupled with a high degree of control during synthesis should allow useful hydrogen adsorbents to be designed and constructed.

Figure 3 displays TPD data from a sample which displays hydrogen desorption peaks at ~ 425 and 600 K. The low-temperature peak occurs at a slightly higher temperature in comparison to the spectrum in Fig 2. due to the specifics of nanotube diameter and chirality and alterations in the cutting procedure. The hydrogen corresponding to the signal peaked at 425 K can be mostly evolved by holding the sample at room temperature overnight in vacuum, or completely evolved after 1 hr at 373 K (Fig. 3). Also in Fig. 3 it is apparent that all but the most stable hydrogen is liberated after heating in vacuum for 1 hr at 550 K. Qualitatively, the data show a distribution of binding energies for hydrogen, with the existence of at least two different sites.

Last year we learned that SWNT samples could be removed from vacuum after dosing with hydrogen and that the adsorbed hydrogen was retained on the sample³¹. Consequently, we are now able to perform spectroscopic experiments on H₂ charged samples outside of the controlled environment of the dosing chamber. Figure 4 displays infrared spectra of a cut and a cut, degassed and H₂ charged SWNT film. The spectrum of the cut sample displays a broad infrared absorbance between 942 and 1251 cm⁻¹ consistent with Si-O stretching vibrations due to slightly different concentrations in the native oxide layer of the silicon before and after coating with the cut SWNT film. Features at 1478 and 1630 cm⁻¹ which may be attributed to SWNT vibrational modes are also apparent. The feature at 1317 cm⁻¹ is consistent with an N-O stretching vibration attributed to the presence of intercalated HNO₃ species following cutting in nitric acid. Features between 2810 – 2970 cm⁻¹ consistent with C-H_x stretching vibrations of chemisorbed hydrogen most likely introduced during cutting are also observed. Temperature programmed desorption data of the cut samples indicates that this chemisorbed hydrogen constitutes an amount less than 0.1 wt%. Following infrared spectroscopy the cut SWNT film was loaded into the TPD chamber, degassed to 550 °C and charged with hydrogen at 500 Torr. The amount of adsorbed hydrogen then corresponded to approximately 3.5 wt%. The infrared spectrum subsequently obtained for the charged SWNT sample displays a loss in the N-O stretching feature consistent with the desorption of intercalated nitric acid species during the degas (Fig. 4). However, a significant increase in the C-H_x stretching region is not observed suggesting that the 3.5 wt% adsorbed hydrogen is not chemically bound to the nanotube walls. Changes in the infrared spectrum between 3100 - 3200 cm⁻¹ and at ~1600 cm⁻¹ are consistent with slightly different Si-OH and adsorbed H₂O species present at different locations on the silicon substrate.

During the past year we also worked with collaborators at the National Institute of Standards and Technology and the University of Pennsylvania to perform inelastic neutron scattering

measurements on our hydrogen-loaded SWNT samples². Figure 5 shows the signal associated with the ortho to para conversion as a function of temperature for the unprocessed material. Surprisingly the transition is observed at temperatures as high as 65K, indicating a binding energy of ~ 6 kJ/mol. These first measurements were performed on raw (unpurified and uncut) SWNT samples grown by laser vaporization, and the dosing and degassing procedures were not fully controlled. Although we do not expect to see strongly-bound H₂, these experiments serve as a basis for future work on samples which have been more carefully activated and charged with hydrogen. The reader is referred to the publication² for a detailed explanation of these neutron scattering measurements.

Diameter Tuning and Increased Production Rates by Controlled Laser Vaporization

This year we have demonstrated, for the first time, that SWNT diameter distributions can be tuned through variation in laser pulse power. This advance is important to furthering progress towards the goals of the Hydrogen Program since there is growing evidence in our lab as well as in others¹⁷ that the diameter of a given SWNT can effect the capacity, thermodynamics, and kinetics of hydrogen storage. The production of SWNTs was investigated at room temperature with a porous target, and at 1200 °C with a dense target. The tube diameters were shifted to smaller sizes with increasing pulse power in both cases. The SWNT size distributions and yields were studied with Raman spectroscopy and transmission electron microscopy, and the evolution of the material quality with laser energy parameters was investigated. The smaller fragments generated by the higher peak pulse powers result in the formation of smaller tubes. Conversely, larger tubes are generated when larger fragments are produced at lower peak pulse powers. The overall yield of nanotubes is low unless thermal energy for assembly is provided by an external furnace. The study offers a unique view of SWNT formation mechanisms, and should aid in the development methods for the rational control of SWNTs. The full, peer-reviewed study was recently published in Chemical Physics Letters³. Some key findings are reproduced here.

A Molelectron Nd:YAG laser was operated in both a Q-switched (10 ns) and long-pulsed (450 ns) mode. The pulse repetition rate was fixed at 10 Hz, and experiments were performed with an external furnace surrounding the target at a temperature of 1200 °C. Figure 6 shows Raman spectra in the radial breathing mode region for SWNT materials produced with three different types of laser pulses. Spectrum 6a shows data from material produced at an average power of 200 W/cm² in long-pulse mode where the pulse power is 45 MW/cm². Three signals are present at 164, 177 and 182 cm⁻¹ consistent with populations of (10,10), (16,0), and (9,9) tubes³². Much weaker signals at 193 and 202 cm⁻¹ may also be discerned. The Raman spectrum is dramatically shifted to higher frequencies corresponding to smaller tubes when the average power is maintained at 200 W/cm² but the laser is Q-switched to yield a pulse power of 2 GW/cm² (Fig 6b). The 164 cm⁻¹ peak is no longer observed, and the signals at 177 and 182 cm⁻¹ are significantly reduced in intensity. Two new strong bands found at 202 and 193 cm⁻¹ can be associated with (8,8) tubes and a slightly larger non-armchair tube such as the (14,0) tube, respectively.

The data is consistent with the shift to smaller tubes seen with increasing peak pulse power in room temperature experiments³. However, with the Molelectron laser, the comparison can be made at different peak powers when the average power and pulse repetition rate are the same.

The shift to smaller tubes is clearly due to the increased pulse power. The point is proven further by considering the size distribution of SWNTs when the average power, and thus the pulse power, are reduced while the pulse width and repetition rate are held constant. Figure 6c shows the radial breathing modes for SWNTs produced at an average power of 80 W/cm² and a 10 ns pulse width so the peak power is 0.8 GW/cm². The SWNT size distribution is shifted to larger values in comparison to the distribution obtained at a peak power of 2 GW/cm², and is in fact similar to the size distribution found at an average power of 200 W/cm² in the long-pulse mode. Two major features are present at 164 and 182 cm⁻¹ as expected for (10,10) and (9,9) tubes, and weaker modes at 193 and 202 cm⁻¹ are also seen.

In addition to learning how to control nanotubes size distributions we have also learned how to de-tangle and order nanotubes on a larger scale. This capability eventually may be important for achieving high packing densities, and therefore high volumetric hydrogen storage densities. Figure 7 shows a SWNT "superbundle" prepared using our methods. The relevant discussion is beyond the scope of this report, but is reported completely in an article published in Chemistry of Materials⁴.

Finally, we wish to report that we have performed the first synthesis experiments with a new laser which recently arrived at NREL. The Molelectron MY35 laser which had been in use was more than 20 years old and had been failing more and more regularly. Additionally problematic was the fact that the laser spot itself was very inhomogenous and irreproducible after required flash lamp changes. The TEM images of Figure 8 show the quality of the raw materials produced using a) old Molelectron MY35 and b) the new Light Age, Inc., laser operating at ~ 0.5 J/pulse. Raman spectroscopy indicated that the as-produced materials were ~ 50 wt% pure SWNTs, in contrast to the 20 to 30 wt% usually seen with the Molelectron laser. The new laser will be much more stable and require less maintenance than the Molelectron laser, and the production rate for raw soot appears to be significantly greater than the 150 mg/hr observed previously, even though the current performance is probably far from optimal. The fact that we can easily produce gram quantities of this quality material everyday will greatly facilitate our development of a carbon nanotube based hydrogen storage system.

Conclusions / Future Work

This year we have presented the details of our recently developed cutting procedure for laser generated SWNTs and have shown that, when optimized, hydrogen storage densities up to 7 wt% can be achieved. Briefly, purified 1 - 3 mg samples are sonicated in 20 ml of 4M HNO₃ with a high-energy probe for 16 hrs at a power of 50 W/cm². We have employed TPD measurements to show that at least two unique binding sites are present for hydrogen adsorption on SWNTs. We have also employed infrared absorption spectroscopy measurements on pristine and H₂-charged samples to show that no C-H bonds are formed in the hydrogen adsorption process. These experiments are in agreement with an earlier temperature programmed desorption analysis which showed that hydrogen molecules are not dissociated when bound to the SWNT surfaces¹. This conclusion is further supported by the first neutron scattering measurements which were performed through collaboration with researchers at NIST and University of Pennsylvania². We also developed methods to tune SWNT diameters during

synthesis so that mechanistic aspects of H₂ storage can be probed³, and learned how to de-tangle and organize individual tubes to form "superbundles" that will afford high volumetric storage densities⁴. Finally, we wish to report that we have performed the first synthesis experiments with a new laser which recently arrived at NREL. The as-produced materials are ~ 50 wt% pure SWNTs, in contrast to the 20 to 30 wt% usually seen with the old laser, and the production rate for raw soot appears to be significantly greater than the 150 mg/hr observed previously, even though the current performance is probably far from optimal.

The fact that we can easily produce gram quantities of ~ 50 wt% SWNT material everyday will facilitate future large-scale measurements with volumetric techniques. These experiments will more closely simulate the anticipated on-board hydrogen storage system. In the future we will also employ our laser diameter tuning techniques to better establish a correlation between materials properties and hydrogen adsorption behaviors. For example, is the adsorption site that may be depopulated at 300 K for cut and purified laser-generated SWNTs located on larger diameter tubes rather than smaller diameter tubes? Is it also possible that either semi-conducting or metallic SWNTs are better suited for hydrogen adsorption? Raman studies at multiple wavelengths which enable the differentiation between semi-conducting and metallic nanotubes³³ may enable an answer to this question. If a preference is determined, synthetic methods for the production of specifically metallic or semiconducting tubes will need to be developed. Our current state of the art production and purification techniques provide gram quantities of high quality material per day. We will of course continue to focus on up-scaling the production and purification of SWNT adsorbent materials.

References

- (1) Dillon, A.C., Jones, K.M., Bekkedahl, T.A., Kiang, C.H., Bethune, D.S. and Heben, M.J., *Nature* **1997**, 386, 377.
- (2) Brown, C.M., Yildirim, T., Neumann, D.A., Heben, M.J., Gennett, T., Dillon, A.C., Alleman, J.L. and Fischer, J.E., *Chem. Phys. Lett.* **2000**, 329, 311.
- (3) Dillon, A.C., Parilla, P.A., Alleman, J.L., Perkins, J.D. and Heben, M.J., *Chem. Phys. Lett.* **2000**, 316, 13.
- (4) Gennett, T., Dillon, A.C., Alleman, J.L., Hassoon, F.S., Jones, K.M. and Heben, M.J., *Chem. of Mat.* **2000**, 12, 599.
- (5) Cannon, J.S. in *Harnessing Hydrogen* INFORM, Inc., New York, **1995**
- (6) N.E.S., **1991/1992**,
- (7) Flavin, C. and Lessen, N. in *Power Surge* W.W. Norton & Co., New York, **1994**
- (8) Dillon, A.C., Bekkedahl, T.A., Cahill, A.F., Jones, K.M. and Heben, M.J. *Carbon Nanotube Materials for Hydrogen Storage* 1-521 (Coral Gables, FL, 1995).
- (9) Carpetis, C. and Peschka, W., *Int. J. Hydrogen Energy* **1980**, 5, 539.
- (10) Schwarz, J.A. *Modification Assisted Cold Storage (MACS)* .
- (11) Schwarz, J.A. *Activated Carbon Based Storage System* 1-271 (Honolulu, HI., 1992).
- (12) Ye, Y., Ahn, C.C., Witham, C., Fultz, B., Liu, J., Rinzler, A.G., colbert, D., Smith, K.A. and Smalley, R.E., *Appl. Phys. Lett.* **1999**, 74, 2307.
- (13) Wang, Q. and Johnson, J.K., *J. Phys. Chem.* **1999**, 103, 4809.

- (14) Wang, Q. and Johnson, J.K., *J. Chem Phys.* **1999**, *110*, 577.
- (15) Rzepka, M., Lamp, P. and de la Casa-Lillo, M.A., *J.Phys. Chem* **1998**, *102*, 10894.
- (16) Dillon, A.C., Gennett, T., Alleman, J.L., Jones, K.M., Parilla, P.A. and Heben, M.J. *Carbon Nanotube Materials for Hydrogen Storage* (San Ramon, CA, 2000).
- (17) Liu, C., Fan, Y.Y., Liu, M., Cong, H.T., Cheng, H.M. and Dresselhaus, M.S., *Science* **1999**, *286*, 1127.
- (18) Pederson, M.R. and Broughton, J.Q., *Phys. Rev. Lett.* **1992**, *69*, 2689.
- (19) Thess, A., Lee, R., Nikolaev, P., Dai, H., Pitit, P., Robert, J., Xu, C., Lee, Y.H., Kim, S.G., Rinzler, A.G., Colbert, D.T., Scuseria, G.E., Tomanek, D., Fischer, J.E. and Smalley, R.E., *Science* **1996**, *273*, 483.
- (20) Dillon, A.C., Parilla, P.A., Jones, K.M., Riker, G. and Heben, M.J., *Mater. Res. Soc. Conf. Proc.* **1998**, *526*, 403.
- (21) Dillon, A.C., Gennett, T., Jones, K.M., Alleman, J.L., Parilla, P.A. and Heben, M.J., *Adv. Mat.* **1999**, *11*, 1354.
- (22) Shelimov, K.B., Esenaliev, R.O., Rinzler, A.G., Huffman, C.B. and Smalley, R.E., *Chem. Phys. Lett.* **1998**, *282*, 429.
- (23) Liu, J., Rinzler, A.G., Dai, H., Hafner, J.H., Bradley, K.R., Boul, P.J., Lu, A., Iverson, T., Shelimov, K., Huffman, C.B., Roderiguez-Macias, F., Shon, Y.-S., Lee, T.R., Colbert, D.T. and Smalley, R.E., *Science* **1998**, *280*, 1253.
- (24) Lu, K.L., Lago, R.M., Chen, Y.K., Green, M.L.H., Harris, P.J.F. and Tsang, S.C., *Carbon* **1996**, *34*, 814.
- (25) Wang, J. and McEnaney, B., *Thermochimica Acta.* **1991**, *190*, 143.
- (26) Davis, J.W. and Smith, D.L., *J. Nuc. Mat.* **1979**, *85*, 71.
- (27) Jiao, J. and Seraphin, S., *J. Mater. Res.* **1998**, *13*, 2438.
- (28) S. Ishiyama, K. Fukaya, M. Eto and Miya, N., *Journal of Nuclear Science and Technology* **2000**, *37*, 144.
- (29) Gennett, T., Dillon, A.C., Alleman, J.L., Parilla, P.A., Jones, K.M. and Heben, M.J., (*in preparation*)
- (30) Dillon, A.C., Gennett, T., Alleman, J.A., Jones, K.M., Parilla, P.A. and Heben, M.J., (*submitted to Nature*)
- (31) Dillon, A.C., Gennett, T., Alleman, J.L., Jones, K.M., Parilla, P.A. and Heben, M.J. *Carbon Nanotube Materials for Hydrogen Storage* (Herndon, VA, 1999).
- (32) Rao, A.M., Richter, E., Bandow, S., Chase, B., Eklund, P.C., Williams, K.A., Fang, S., Subbaswamy, K.R., Menon, M., Thess, A., Smalley, R.E., Dresselhaus, G. and Dresselhaus, M.S., *Science* **1997**, *275*, 187.
- (33) Brown, S.D.M., Corio, P., Marucci, A., Dresselhaus, M.S., Pimenta, M.A. and Kneipp, K., *Phys. Rev. B* **2000**, *61*, R5137.

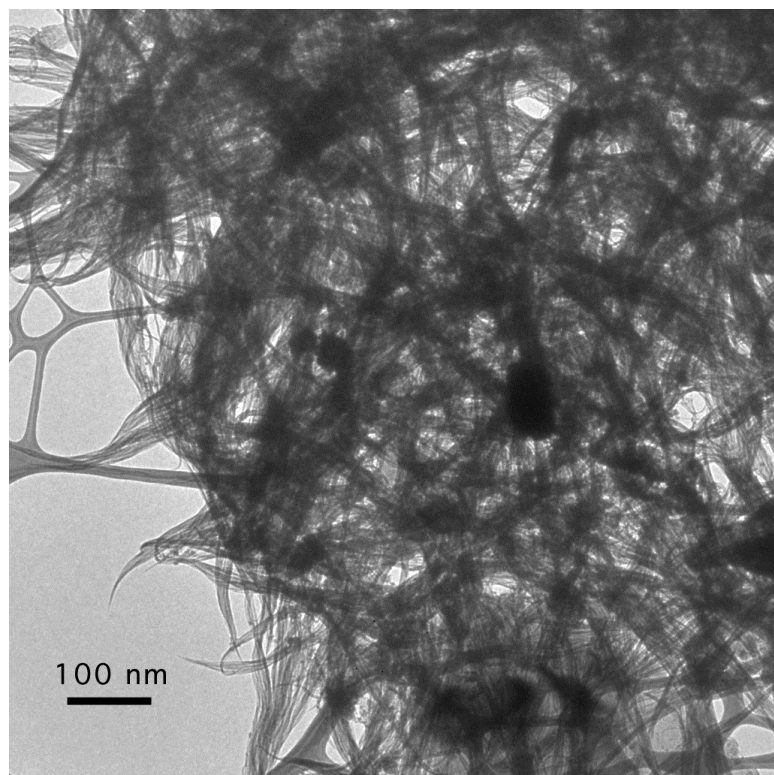


Figure 1: TEM image of purified SWNTs following ultrasonication in 4M HNO₃ for 16 hrs.

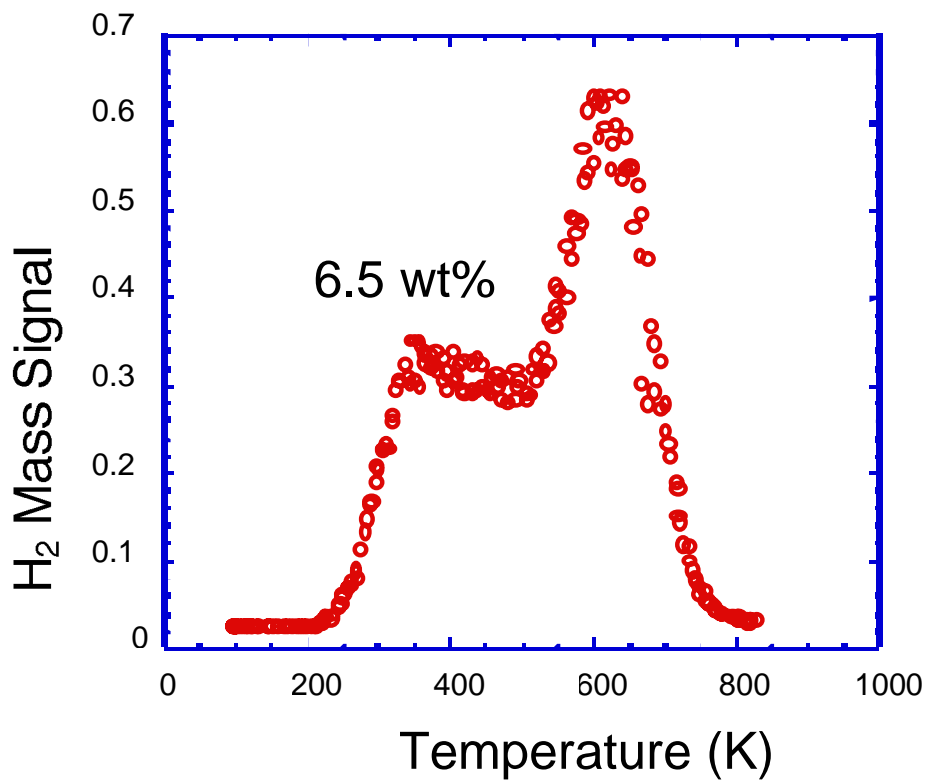


Figure 2: Hydrogen TPD spectrum of a degassed sample following a brief room temperature H₂ exposure at 500 torr. The adsorbed hydrogen corresponds to 6.5 wt%.

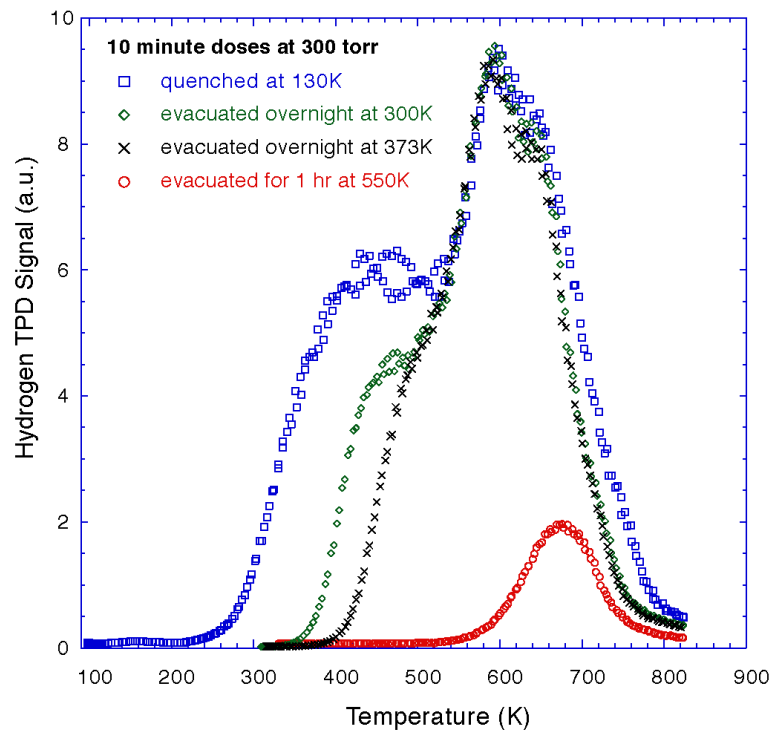


Figure 3: Hydrogen TPD data from an SWNT sample that was exposed to hydrogen at 300 Torr for 10 minutes followed by a variation in post-dosing conditions.

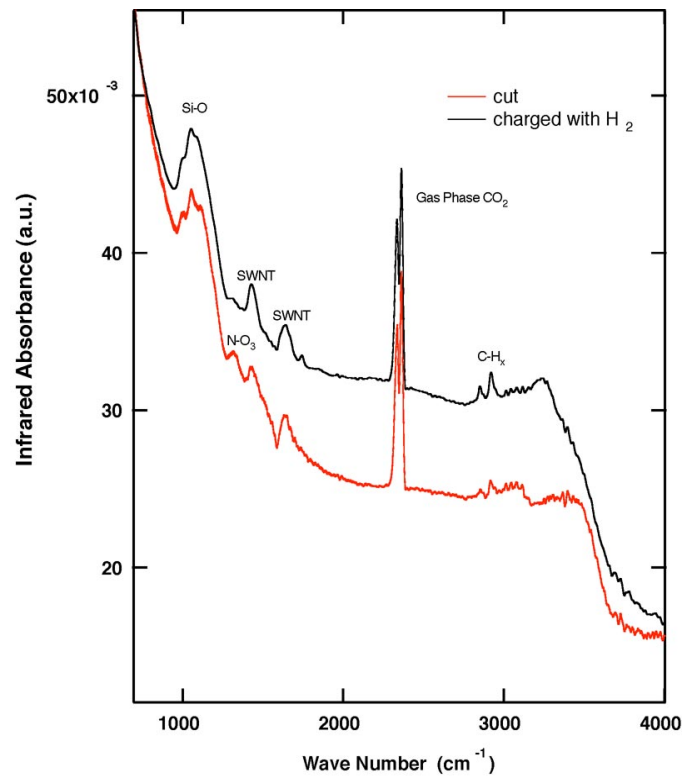


Figure 4: FTIR spectra of a cut and a cut, degassed and H_2 charged SWNT film.

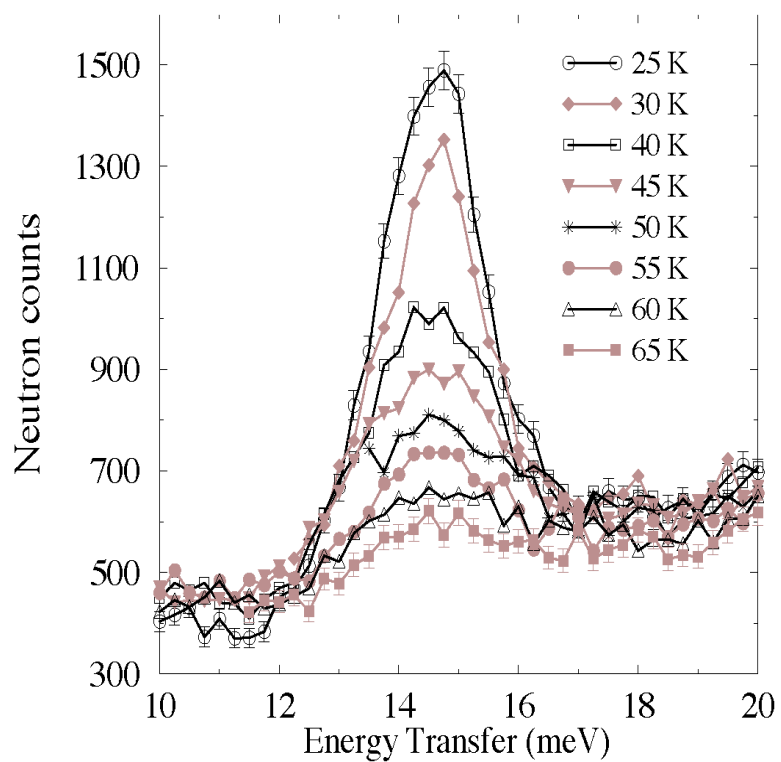


Figure 5: The signal from inelastic neutron scattering measurements on our hydrogen-loaded SWNT samples associated with the ortho to para conversion as a function of temperature.

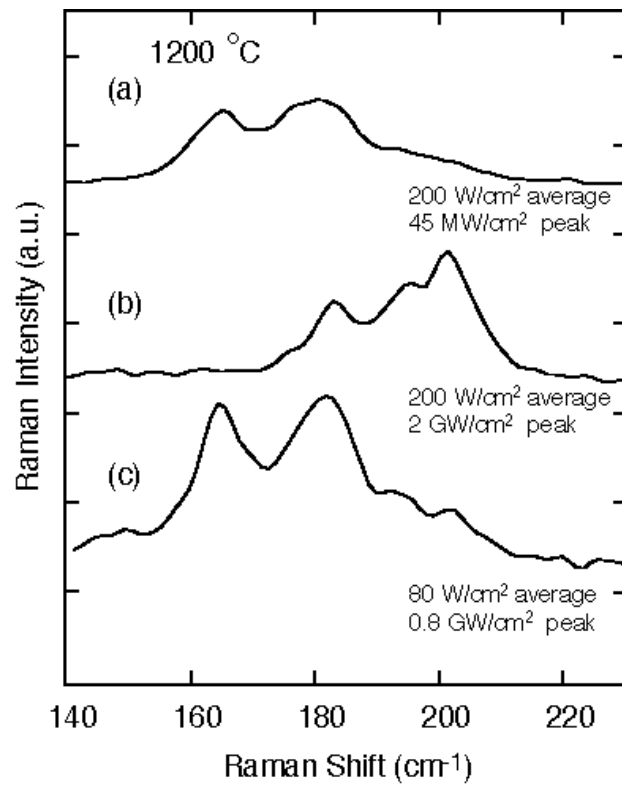


Figure 6: Raman spectra in the radial breathing mode region for SWNT materials produced with three different types of laser pulses.

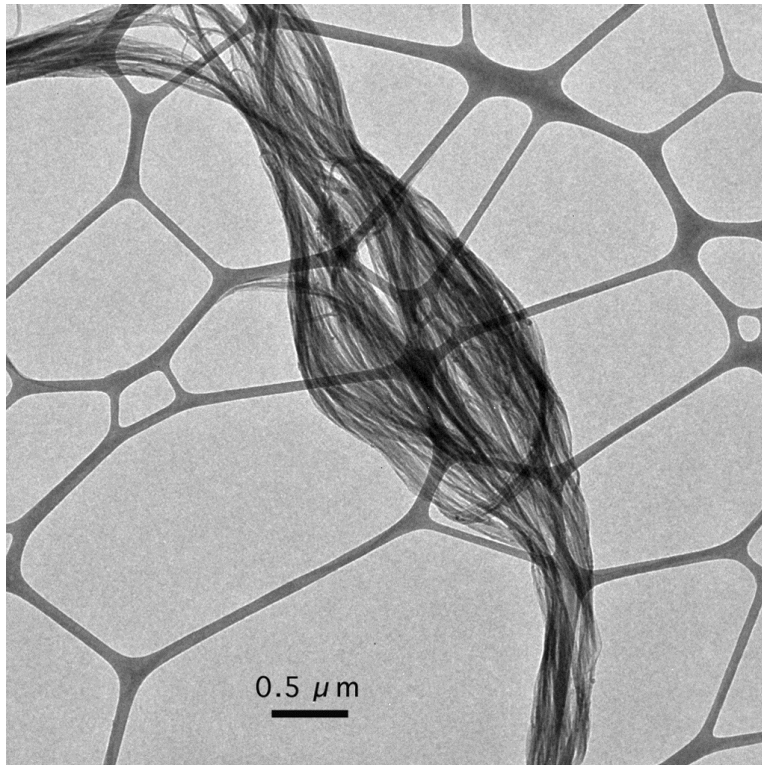


Figure 7 : An SWNT "superbundle". The large bundle of well-aligned tubes should enable higher capacity hydrogen storage.

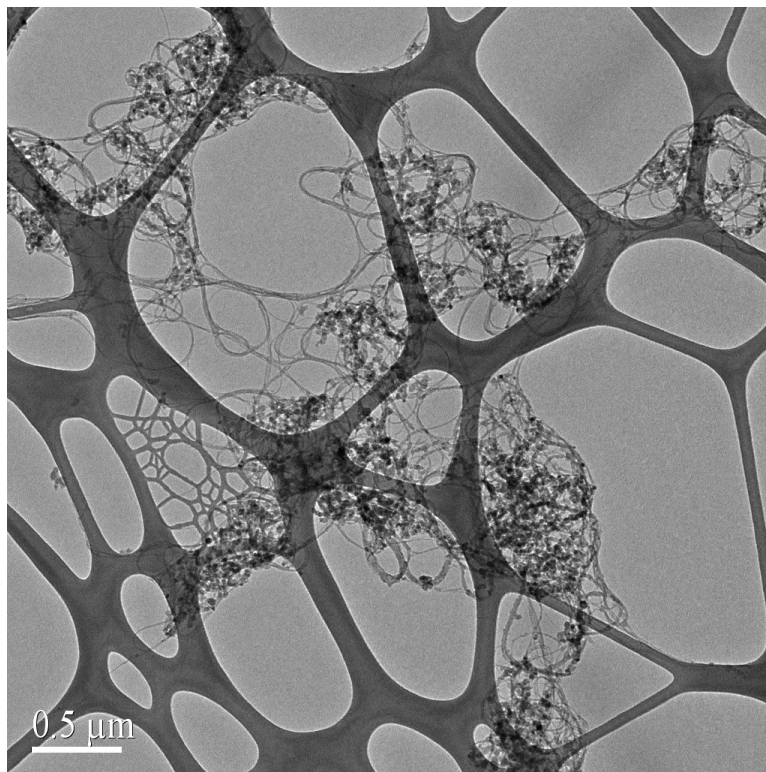
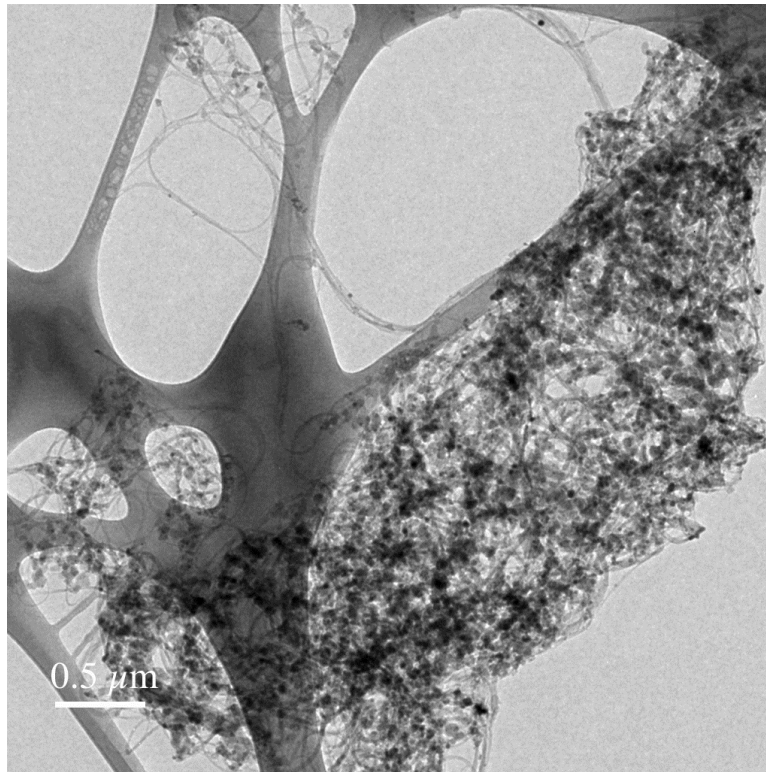


Figure 8: TEM images of the raw materials produced using a) the old Molectron MY35 laser and b) the new Light Age, Inc. laser. The SWNT density was improved from ~20-30 wt% to 50 wt%.

**HYDROGEN TRANSMISSION/STORAGE WITH
METAL HYDRIDE-ORGANIC SLURRY
AND
ADVANCED CHEMICAL HYDRIDE/HYDROGEN
FOR PEMFC VEHICLES**

Andrew W. McClaine, Dr. Ronald W. Breault, Christopher Larsen,
Dr. Ravi Konduri, Jonathan Rolfe, Fred Becker, Gabor Miskolczy
Thermo Technologies, a Thermo Electron Company
45 First Avenue, Waltham, MA 02454-9046

Abstract

This paper describes the work performed on two programs supported in part by the U.S. Department of Energy. These programs are aimed at evaluating the potential of using slurries of chemical hydrides and organic liquids to store hydrogen. The projects have been very successful in meeting all project objectives. After a detailed analysis of chemical hydrides, lithium hydride was selected for use in these programs. Lithium hydride has been prepared as a slurry with light mineral oil and a dispersant and has been found to be stable for long periods of time at atmospheric temperatures and pressures. We have demonstrated that the lithium hydride slurry can be mixed with water to produce hydrogen on demand. Reactions between the lithium hydride slurry and water take place rapidly and completely. The resulting lithium hydroxide can be recycled either by electrolytic methods or by a carbo-thermal process. Experiments with the carbo-thermal process indicate that the regeneration of lithium hydride can be accomplished at temperatures of 1500°K or less enabling the use of economically acceptable furnace materials. A cost analysis of the regeneration process indicates that the process should be cost competitive with hydrogen produced from natural gas and stored as a liquid or a highly compressed gas.

NOTICE

This Technical Progress report was prepared with the support of the U.S. Department of Energy (DOE) Award Nos. **DE-FC02-97EE50483**, “Advanced Chemical Hydride -Based Hydrogen Generation/Storage System For PEM Fuel Cell Vehicles”, and **DE-FC36-97GO10134**, “Hydrogen Transmission/Storage With A Metal Hydride/Organic Slurry”. However, any opinions, findings, conclusions, or recommendations expressed herein are those of the author(s) and do not necessarily reflect the views of DOE.

This report was prepared as a result of work sponsored, in whole or in part, by the South Coast Air Quality Management District (AQMD). The opinions, findings, conclusions, and recommendations are those of the author and do not necessarily represent the views of AQMD. AQMD, its officers, employees, contractors, and subcontractors make no warranty, expressed or implied, and assumes no legal liability for the information in this report. AQMD has not approved or disapproved this report, nor has AQMD passed upon the accuracy or adequacy of the information contained herein.

INTRODUCTION

Objective

We refer to these two programs as the Transportation/Storage Program and the Vehicle Program. The objective of the Transportation/Storage Program is to demonstrate the technical viability and economic attractiveness of chemical hydride slurry based hydrogen generation/storage systems. This program is intended to take a broad view of the entire chemical-hydride hydrogen-storage cycle. Technical validations and economic analyses are the primary focus of the program.

The objective of the Vehicle Program is to demonstrate a prototype storage and delivery system for vehicular applications. In this program, we are taking a more detailed look into the ability of the chemical hydride slurries to store hydrogen for PEM fuel cell applications in vehicles.

The programs are intended to answer the following questions:

Can the reaction rate of a chemical hydride with water be controlled to provide a safe and stable storage and hydrogen production process utilizing a slurry based approach?

Are the physical properties of the reactants and products acceptable for transportation and bulk storage systems?

Can a cost effective design of a storage and hydrogen production system be made to meet the energy density criteria for transportation applications?

Can a hydroxide-to-hydride regeneration system design be identified that is able to produce hydrogen at a cost competitive with present fuels?

Technical Concept

The concept behind the use of chemical hydrides is that when the chemical hydrides are mixed with water they will produce hydrogen. Table 1 displays several of the chemical hydrides evaluated for use as part of these investigations. Lithium hydride produces hydrogen with a relatively high gravimetric density. In considering a recyclable process, one of the important issues is the ability to regenerate the chemical hydride. We selected lithium hydride because it was a mono-metal hydride rather than a bi-metal hydride. We felt that it would be easier to reduce a mono-metal hydroxide than to separate and reduce a multi-metal hydroxide. An additional consideration is that many of the hydroxides form hydrates. Lithium hydroxide forms a mono-hydrate. Many of the bi-metal hydrides form multi-hydrates when reacted with water. The lithium hydroxide hydrate decomposes when it is heated above the temperature of boiling water. Many of the bi-metal hydroxide hydrates do not decompose until they are heated to quite high temperatures.

Table 1 - Chemical Hydrides and Their Gravimetric Densities

| Chemical Reaction | Gravimetric Density, %H₂ (Hydride Only) |
|---|--|
| $\text{CaH}_2 + 2 \text{H}_2\text{O} \longrightarrow \text{Ca(OH)}_2 + 2 \text{H}_2$ | 9.6% |
| $\text{MgH}_2 + 2 \text{H}_2\text{O} \longrightarrow \text{Mg(OH)}_2 + 2 \text{H}_2$ | 15.3% |
| ★ $\text{LiH} + \text{H}_2\text{O} \longrightarrow \text{LiOH} + \text{H}_2$ | 25.2% |
| $\text{LiBH}_4 + 4 \text{H}_2\text{O} \longrightarrow \text{LiOH} + \text{H}_3\text{BO}_3 + 4 \text{H}_2$ | 37.0% |
| $\text{NaBH}_4 + 4 \text{H}_2\text{O} \longrightarrow \text{NaOH} + \text{H}_3\text{BO}_3 + 4 \text{H}_2$ | 21.3% |

The process envisioned is that lithium hydride will be prepared as a slurry at centralized plants. The slurry will be pumped into tanker trucks or pumped through pipes to distribution centers where it will be loaded into vehicles or carried to storage vessels in homes, business, or industry. When hydrogen is required, the chemical hydride slurry will be mixed with water to produce a high quality hydrogen that can be used in fuel cells. The resulting hydroxide waste product will be picked up when the next delivery is made and transported back to the regeneration plant where it will be separated from the mineral oil and where the lithium hydroxide will be regenerated to lithium hydride.

Slurry Concept

A slurry is a mixture of a solid and a liquid to make a pumpable mixture. The main issue in preparing a slurry of a solid is to distribute the solid in the liquid in such a way that the solid does not settle out. We have selected light mineral oil in which to suspend finely ground lithium hydride. A dispersant is used to prevent the particles from settling out of the suspension. Figure 1 displays a conceptual view of the dispersant action. The dispersant is made with an anchor group and a lyophile. The anchor group attaches to the particle and the lyophile streams outward forming a set of tendrils that fend off other particles and slow the movement of the particles within the mineral oil. Particles are typically about 20 microns in diameter.

A major feature of the use of mineral oil to form the slurry is that it forms a protective coating around the particle that slows the movement of water toward the particle. Figure 2 diagrams this effect. This protective coating allows the lithium hydride to be safely handled and stored in the air without absorbing moisture from the air. It also slows the kinetics of the reaction allowing the development of reaction vessels to mix the hydride with water for releasing hydrogen.

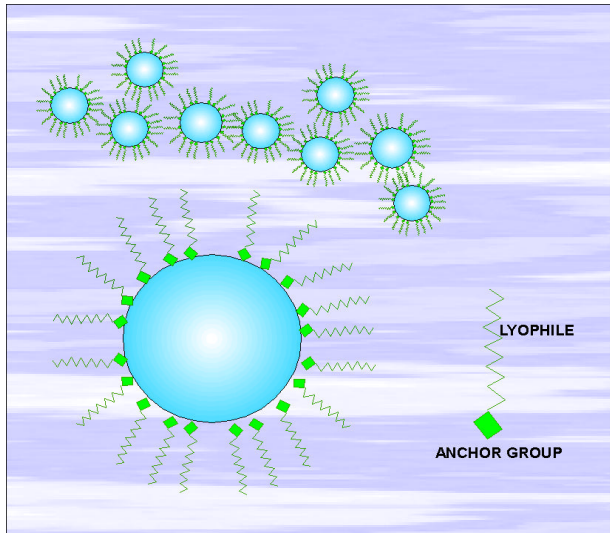


Figure 1 - Chemical Hydride Slurry

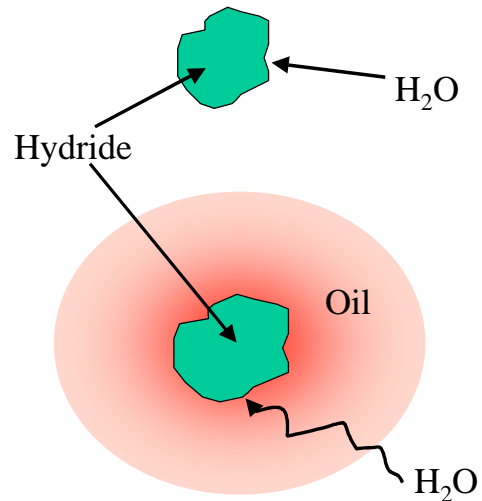


Figure 2 - Rate Limiting Reaction Kinetics

Over the past couple of years, we have developed the ability to produce lithium hydride slurries in a nearly continuous operation. Figure 3 is a picture of a 3 gallon batch of lithium hydride slurry being poured into a storage vessel that we were using in the vehicle program. This is 60% lithium hydride in mineral oil with a dispersant to maintain the slurry properties. The viscosity of the slurry is about 2000 cp. This slurry is stable for several weeks or more.



Figure 3 - Lithium Hydride Slurry

An important feature of the slurry is its ability to protect the lithium hydride from inadvertent exposure to water or water vapor. If allowed to, powdered lithium hydride will absorb water

vapor from the air. The reaction of the water vapor and the hydride produces hydrogen and heat. If the day is sufficiently humid, the heat will build up until it ignites the hydrogen. When mixed with mineral oil, the hydride cannot absorb moisture rapidly enough to be a hazard. In addition, because mineral oil has such a high vapor pressure, the mineral oil actually prevents the ignition of the lithium hydride from open flames. Figure 4 is a sequence of photographs of a test performed with a propane torch. A spoon full of lithium hydride slurry was placed in our fume hood. The flame from the torch did not light the slurry when passed near. Gasoline would have ignited. When the flame was held on the slurry for sufficient time, some of the mineral oil evaporated and burned. But the flame went out when the torch was removed.

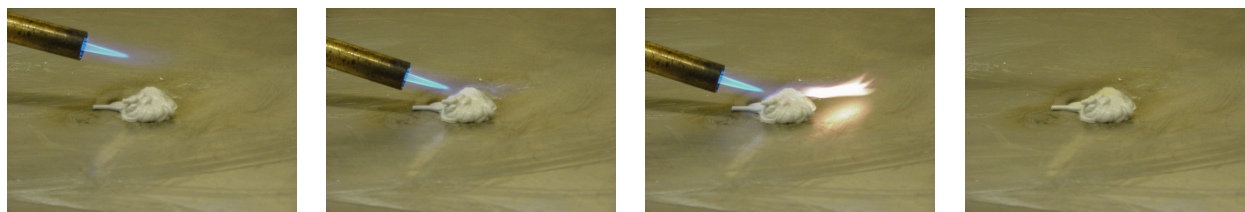


Figure 4 - Flame Test with LiH Slurry

TRANSPORTATION/STORAGE PROGRAM

The focus of our attention in the Transportation /Storage Program during the past year has been to better understand the regeneration process. We have performed a large number of tests with a controlled atmosphere high-temperature furnace that we built for this application. We have also performed a preliminary system design and economic analysis of the regeneration process to identify the relative cost of hydrogen that can be expected from a chemical-hydride hydrogen-storage system.

Regeneration Process

The proposed regeneration process is a carbo-thermic reduction process based on the use of low cost carbon from coal or biomass. The objective is to have zero net carbon dioxide emissions from the regeneration plant by capturing the highly concentrated carbon dioxide stream leaving the plant for sequestration. Regeneration will be performed in centralized plants much like refineries using technologies synergistic with blast, aluminum reduction, and glass furnaces. Figure 5 is a diagram showing the regeneration process that was evaluated. Figure 6 shows a simplified ASPEN Plus process flow diagram. Lithium hydroxide and carbon are fed to a radiant reduction reactor where they are heated to 1350°K. During this reaction, hydrogen and carbon monoxide are released and lithium is melted. We have assumed that this reduction process is about 50% effective so the lithium oxide that is not reduced is returned to the reactor. Hydrogen and carbon monoxide are separated from the lithium and from each other. Carbon monoxide is put through a shift reaction to form carbon dioxide and hydrogen. The hydrogen is used to produce electric power and lithium hydride.

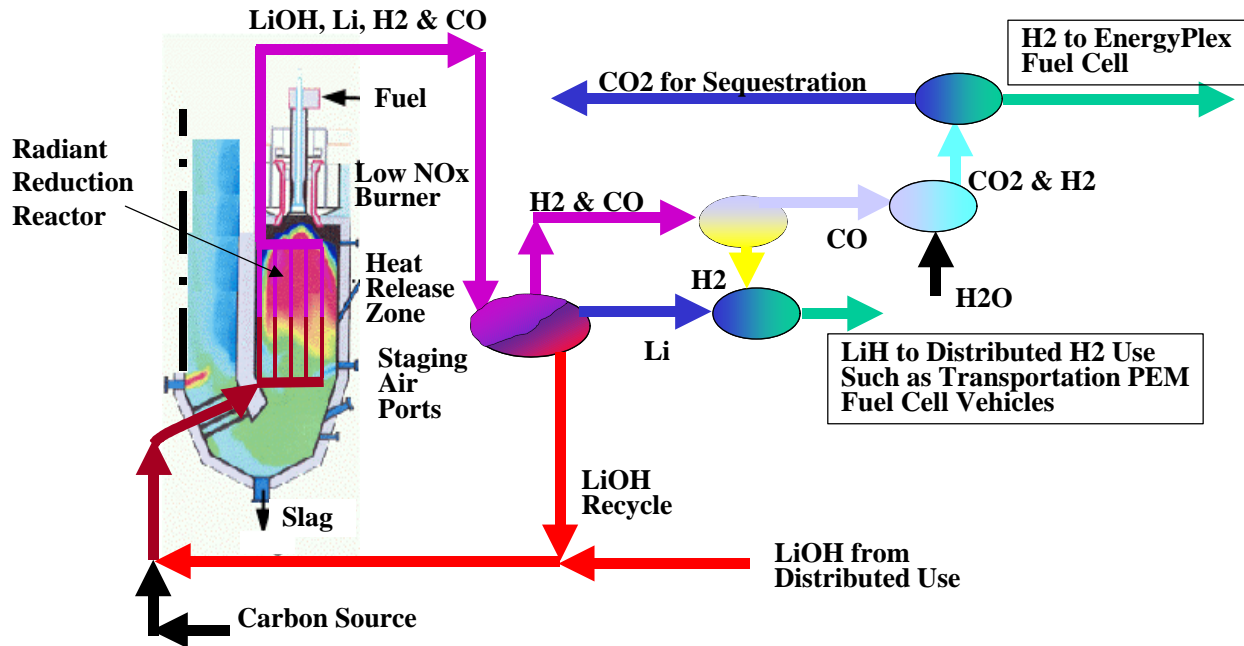


Figure 5 - Lithium Hydride Regeneration Process

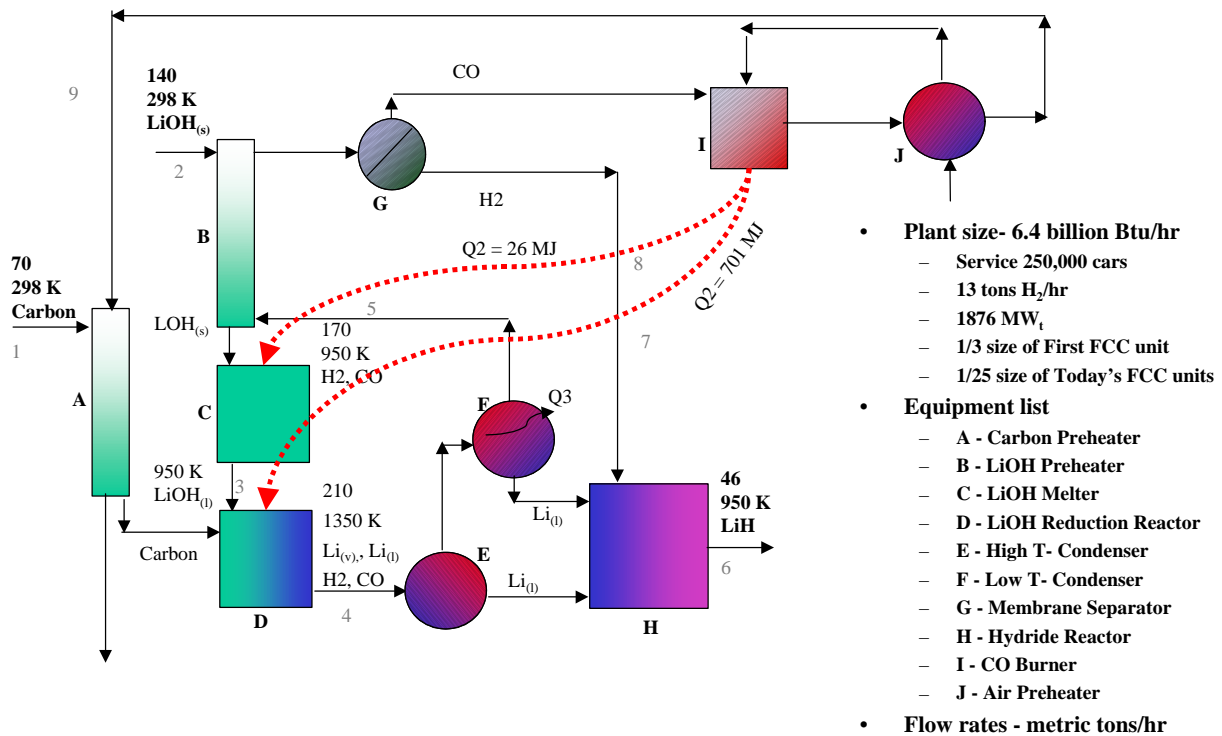


Figure 6 - Simplified ASPEN Plus Process Flow Sheet

A series of experiments were performed to verify that regeneration takes place at the temperatures desired. Equilibrium thermochemical calculations showed that the reduction of lithium hydroxide with carbon typically takes place at temperatures above 1800°K except when the carbon monoxide formed is swept away from the reaction. Figure 7 shows pictorially the effect of removing CO from the reaction zone. By removing the CO, the reaction is allowed to proceed toward completion at lower temperatures. Figure 8 shows the high temperature controlled atmosphere furnace used for the experiments.

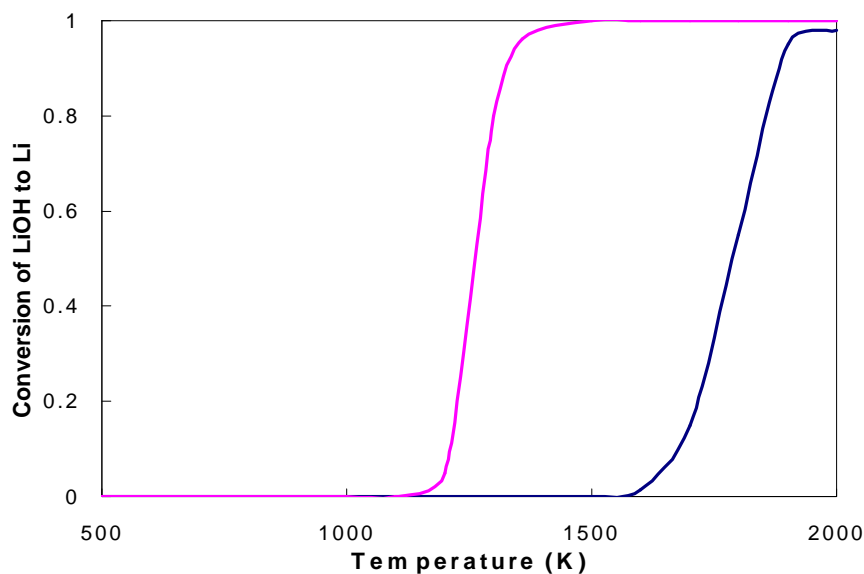


Figure 7 - Effect of Removing CO from LiOH/C Reaction

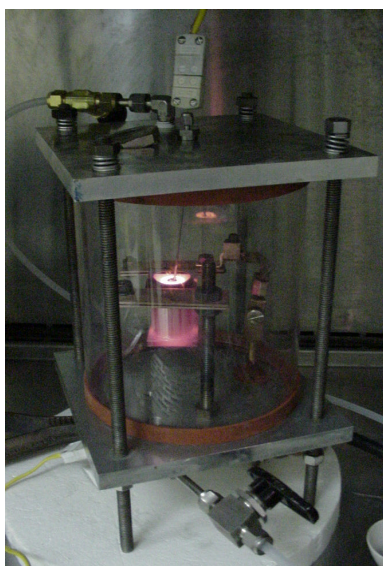


Figure 8 - High Temperature Controlled Atmosphere Furnace

Figure 9 displays some of the data collected during the test program and confirms the hypothesis of the regeneration process. It can be seen that the analytical result appears to be supported by the data collected.

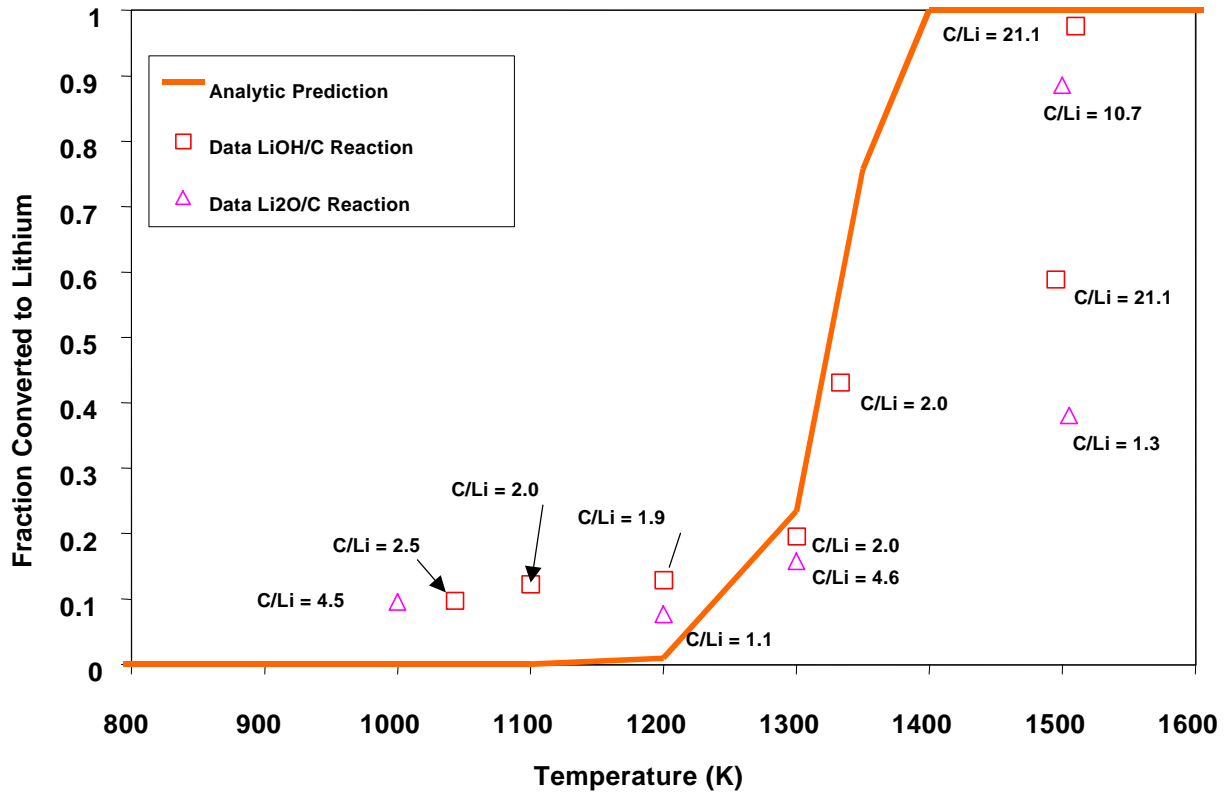


Figure 9 - Data Collected from High Temperature Furnace Experiments

Economic Analysis

An economic analysis was performed for the regeneration process described above to determine the cost of hydrogen to be expected. Table 2 displays the assumptions used in the economic analysis. The analysis began with a preliminary design of the various components required in the process.

Table 2 - Assumptions Used in Economic Evaluation

| | |
|--------------------|--------------------------|
| Capital | \$ 58.8 Million |
| Carbon | Variable |
| Labor | |
| Operators | 25 at \$35,000/yr |
| Super. & Cleric. | 15% of Operators |
| Mainten. & Repairs | 5% of Capital |
| Overhead | 50% of Tot. Lab. + Mtnc. |
| Local Tax | 2% of Capital |
| Insurance | 1% of Capital |
| G&A | 25% of Overhead |
| Fed. and State Tax | 38% of Net Profit |

We found this process to be sensitive to the cost of carbon. However, carbon sources appear to be available at costs that will make this process economical. Figure 10 displays the results of our analyses for two size plants. The first plant would serve about 250,000 cars per day. The larger plant would serve about 2,000,000 cars per day.

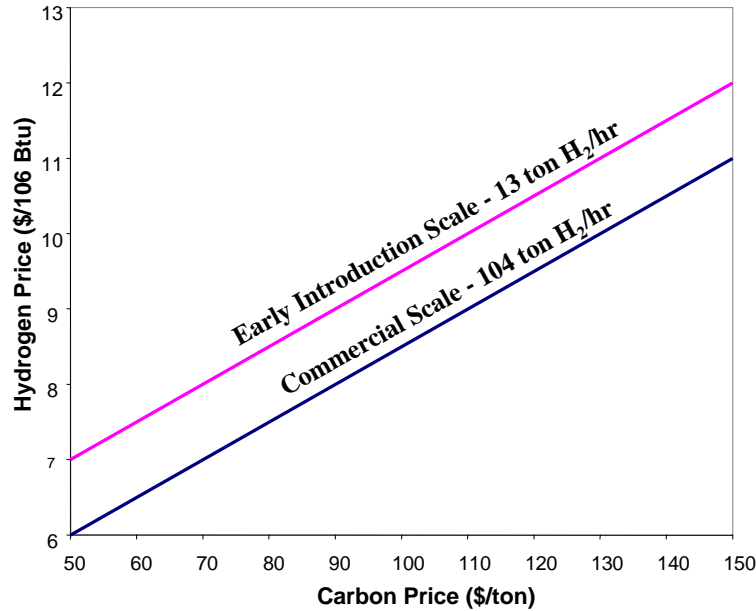


Figure 10 - Results of Economic Analysis

Figure 11 displays the cost of hydrogen from the lithium hydride slurry system and other systems. When compared to the cost of stored hydrogen form other production methods, the chemical hydride slurry approach appears to be very competitive. It is even competitive to the cost of tax free gasoline.

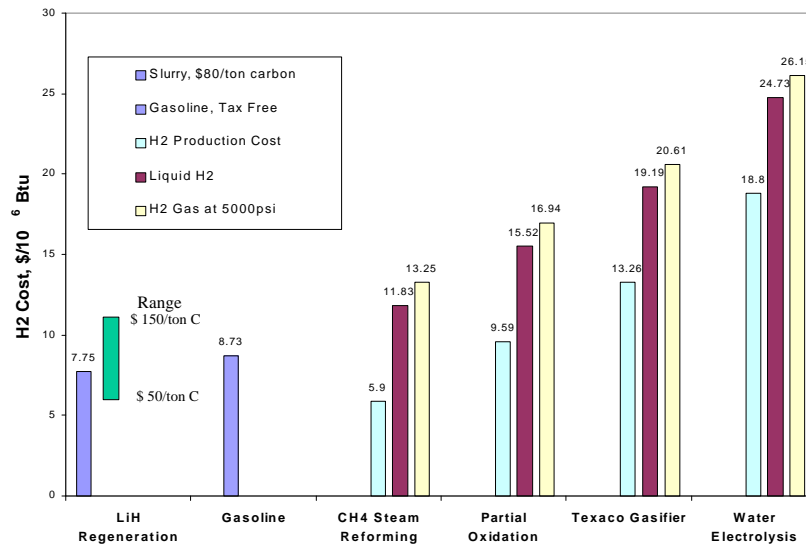


Figure 11 – Cost of Stored Hydrogen as a Chemical Hydride and by Conventional Methods

VEHICLE PROGRAM

The focus of our attention in the Vehicle Program during the past year has been the completion of the demonstration of the mobile chemical-hydride hydrogen generator. To satisfy the goals of the program, the hydrogen generator must demonstrate that it can produce 3 kg/hr of hydrogen, and that it can meet or exceed the gravimetric density goal of 3355 Wh/kg and the volumetric density goal of 929 Wh/l.

The chemical-hydride hydrogen-storage system developed during this program has achieved all its goals. An advanced system design based on the developed system and recycling water from the fuel cell would have a gravimetric energy density of 3364 Wh/kg and a volumetric energy density of 1954 Wh/l. The system has been demonstrated to follow the hydrogen demand rapidly and to produce in excess of the 3 kg/hr hydrogen flow rate target.

Hydrogen Generator Design

The hydrogen generator design is made up of storage vessels for the lithium hydride slurry and a small amount of water, pumps for both the slurry and the water, a mixing reactor, a heat exchanger, and a hydroxide storage tank. Figure 12 is a diagram of the design. Figure 13 is a picture of the prototype hydrogen generator after one of its final test sequences. The reactor is a tube with an auger/mixer running through it. Hydride slurry and water are pumped into the reactor at one end. The auger/mixer moves this mixture through the reactor and mixes it as it is being moved. Excess water is evaporated, absorbing and carrying the heat of reaction out of the reactor with the hydrogen. Hydrogen and water vapor are separated from the hydroxide product in the head of the hydroxide tank. The water vapor is condensed in the heat exchanger. Condensed water is returned to the water circuit and hydrogen is delivered to the fuel cell.

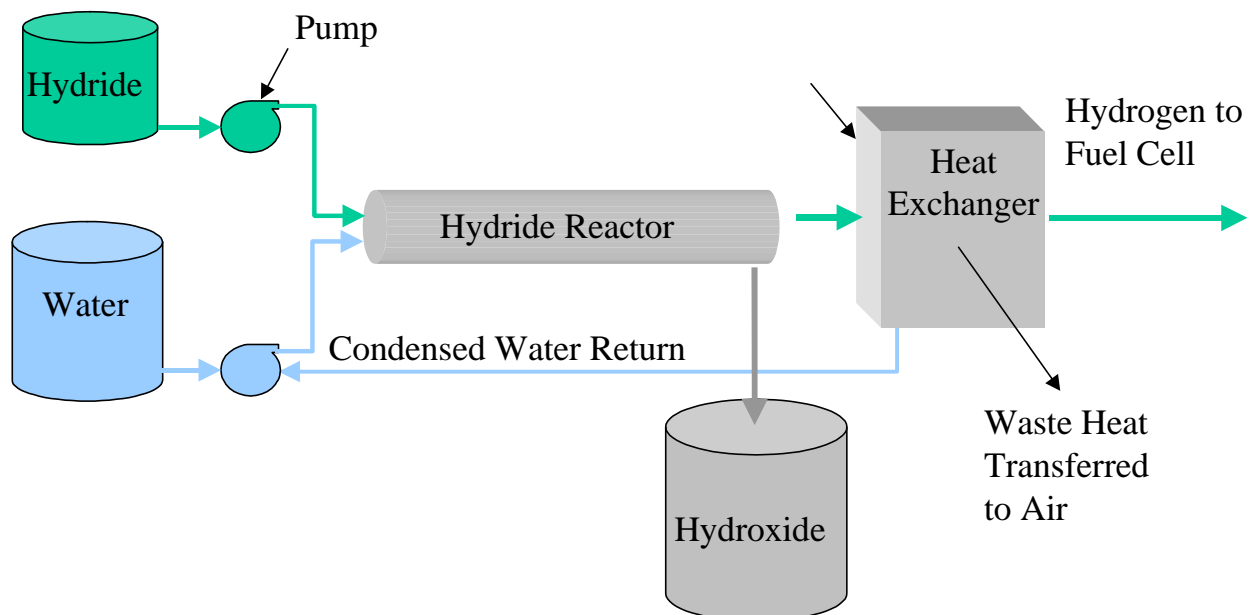


Figure 12 - Diagram of the Hydrogen Generation System

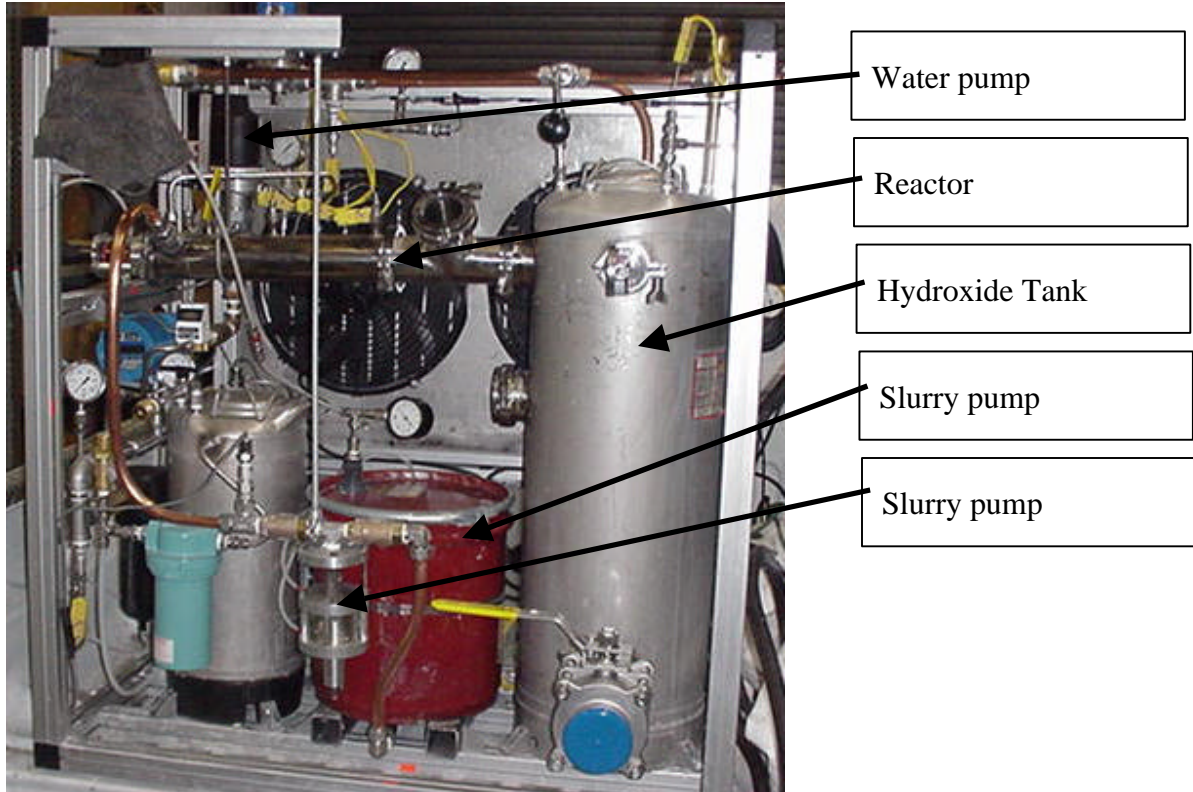


Figure 13 - Picture of the Prototype Hydrogen Generator

Hydrogen Generator Performance

Figure 14 shows the hydrogen and hydride slurry flow rates during a typical test of the system. During this test, the maximum flow rate was a little over 2 kg/hr of hydrogen. An important thing to note is the rapid rise in hydrogen flow rate with increases of the slurry and the rapid drop in the hydrogen flow rate with decreases of the slurry. By having the hydrogen flow stop when the hydride slurry flow stopped, we were assured that the mixing and reaction in the reactor were complete.

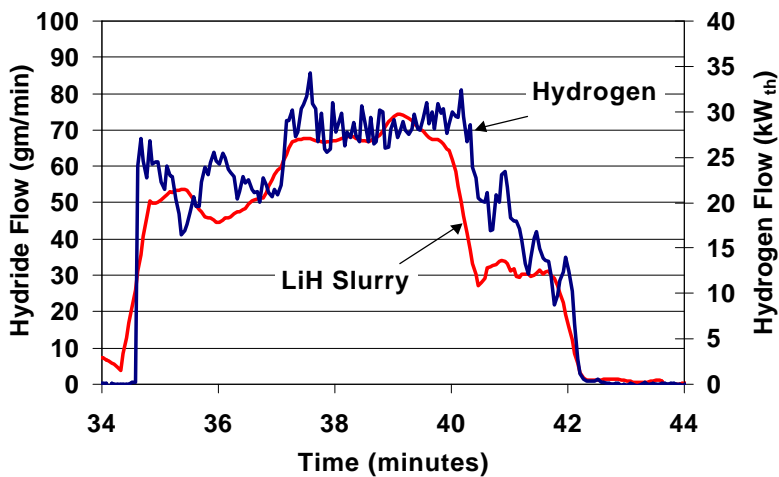


Figure 14 - Data Showing the Slurry and Hydrogen Flow Rates

Quality of the Hydrogen

In order to be acceptable in a fuel cell, the hydrogen produced from the lithium hydride slurry reactor must have very low concentrations of carbon monoxide. Fuel cell researchers have noted that the concentration of carbon monoxide must be less than 10 ppm.

Measurements were made during one test of the hydrogen leaving the system at points before and after a carbon filter. Table 3 displays the results of these measurements. In both measurements, the carbon monoxide measurements showed that levels were well below the tolerable levels of a PEM fuel cell. Also measured were concentrations of oxygen, nitrogen, carbon dioxide, mineral oil, and hydrocarbons. The ratio of oxygen to nitrogen was the same as that of air and was different in each measurement indicating that air contamination may have occurred during the measurement process. Measurements of mineral oil and hydrocarbons were both low. Carbon dioxide was also low. One possible source of the carbon dioxide is from the water used in the system. Untreated tap water was used in all our experiments.

Table 3 - Measured Contaminants in Hydrogen

| | | | | |
|----------------------|-------------------|---------|-------|---------|
| Before Carbon Trap - | CO ₂ = | 2.4 ppm | CO = | 1.5 ppm |
| | O ₂ = | 25 ppm | Oil = | 0.1 ppm |
| | N ₂ = | 95 ppm | HC = | 1.2 ppm |
| After Carbon Trap - | CO ₂ = | 0.7 ppm | CO = | 0.1 ppm |
| | O ₂ = | 10 ppm | Oil = | 0.1 ppm |
| | N ₂ = | 40 ppm | HC = | 0.8 ppm |

As expected the carbon monoxide and hydrocarbons were lower after having passed through a carbon filter. The results of this test indicate that a carbon filter is probably not necessary for this system.

SUMMARY/CONCLUSIONS

In summary, the lithium hydride slurry approach for storing hydrogen provides a viable alternative to hydrogen storage as liquid hydrogen or highly compressed hydrogen. Storage densities are higher than those for metal hydrides. The gravimetric energy density of 60% lithium hydride slurry is 5110 Wh/kg or 15.3% hydrogen. The volumetric energy density is 3937 Wh/l or 118 kg H₂/m³. This is more than twice the volumetric energy density of liquid hydrogen and it is at ambient pressure and temperature. The slurry is easily pumped and can be reacted with water with mixing to produce hydrogen on demand.

The mobile generator developed for the vehicle program has been shown to produce hydrogen on demand with complete reaction occurring in the reactor volume. Hydrogen production has been measured up to 3 kg/hr. Based on the prototype generator design, an advanced design is anticipated to provide a gravimetric energy density of 3361 Wh/kg and a volumetric energy

density of 1954 Wh/l assuming that the water from the fuel cell is condensed and used to produce hydrogen in the hydride reactor.

The cost of hydrogen resulting from the carbo-thermal regeneration of the lithium hydroxide to lithium hydride is estimated to range from \$6.04 for carbon costing \$50/ton to \$11.30 for carbon costing \$150/ton. This is competitive with hydrogen produced by natural gas and stored as a liquid.

The chemical hydride slurry approach provides other desirable features. The slurry protects the hydride from accidental contact with moisture in the atmosphere or otherwise. Hydrogen produced by the reaction of the slurry with water can be performed at elevated pressures allowing additional power to be generated from the exhaust hydrogen/steam from the reactor and/or allowing the exhaust hydrogen/steam to be used to pressurize air for a more compact fuel cell. Production of hydrogen at elevated pressures also allows the components of the hydrogen generator to be reduced in size.

ACKNOWLEDGMENTS

The authors would like to thank DOE for its support on these two programs. We would also like to thank the Southern Illinois University and Thermo Technologies for co-funding the Hydrogen Transportation/Storage Program and the California South Coast Air Quality Management District and Thermo Technologies for co-funding the Hydrogen Vehicle Program.

We would also like to thank Ford Motor Company, Air Products, and Morton International for participating in our technical review panel.

An Integrated PV – Electrolysis Metal Hydride Hydrogen Generation and Storage System

Krishna Sapru, S. Ramachandran, Z. Tan

Energy Conversion Devices Inc

Troy, MI 48084, USA

Abstract

This project deals with the use of renewable electricity to generate hydrogen for large scale use in developing countries such as India. The hydrogen ICE scooter market in India was identified as a potential near-term application for hydrogen/metal hydride technology. India not only represents a large two wheeler market but also one that is growing the fastest. The hydrogen can come from the electrolysis of water using two sources of renewable, distributed electrical energy, PV and bagasse based cogenerated power. Bagasse is a byproduct of the sugar industry. We show how both of these scenarios are economically viable. Ovonic metal hydrides are used to store the hydrogen on-board and for transportation. Other uses of hydrogen/metal hydrides include distributed power generation to replace polluting kerosene or diesel generator sets and for portable power use. The renewable hydrogen thus produced can also be used as cooking fuel.

Introduction

The objective of the program is to introduce renewable hydrogen in the worldwide energy scene and pave way for the widespread use of metal hydride technology for storage. Before large scale use of hydrogen can be implemented, at least the following four issues need to be addressed:

1. Identification of the near-term market
2. Address the issues of storage, safety, distribution and refueling infrastructure
3. Cost and availability of hydrogen, and
4. Establishment of appropriate/strategic business alliances using a global approach

The market:

Two and three wheelers are a major consumer of petroleum and major source of air pollution in India. The global two wheeler fleet in year 2000 is estimated to be approximately 200 million units. Asia represents approximately 67% of global fleet and India being the largest market in Asia with an annual growth rate ~14%. We have identified the hydrogen –ICE two wheelers as an initial application for hydrogen because it permits transition to a clean alternative and will permit early large-scale use of hydrogen. The ICE manufacturing and maintenance infrastructure is available. This would minimize capital expenditure on the part of the OEM. When fuel cells become available, H₂ infrastructure will already be in place.

There are other promising markets for hydrogen/metal hydride technology and these include: distributed power generation to replace highly polluting kerosene and diesel generator sets, portable power, and use of hydrogen for cooking.

Storage:

Safety and compactness of the metal hydride storage system (MHSS) will ease transition to a hydrogen economy, especially when dealing with consumer applications.

ECD has extensive expertise in the science and technology of metal hydrides. Figure 1 shows the desorption PCT behaviour of a low temperature alloy with hydrogen absorption capacity ~ 2 wt% and a reversible desorption capacity of 1.5 wt%. This alloy is manufactured in large quantities. The plateau pressures of the alloy is suitable for use in storage systems for H-ICE and H-PEM Fuel Cell applications. The alloy exhibits excellent cycle life and resistance to CO poisoning.

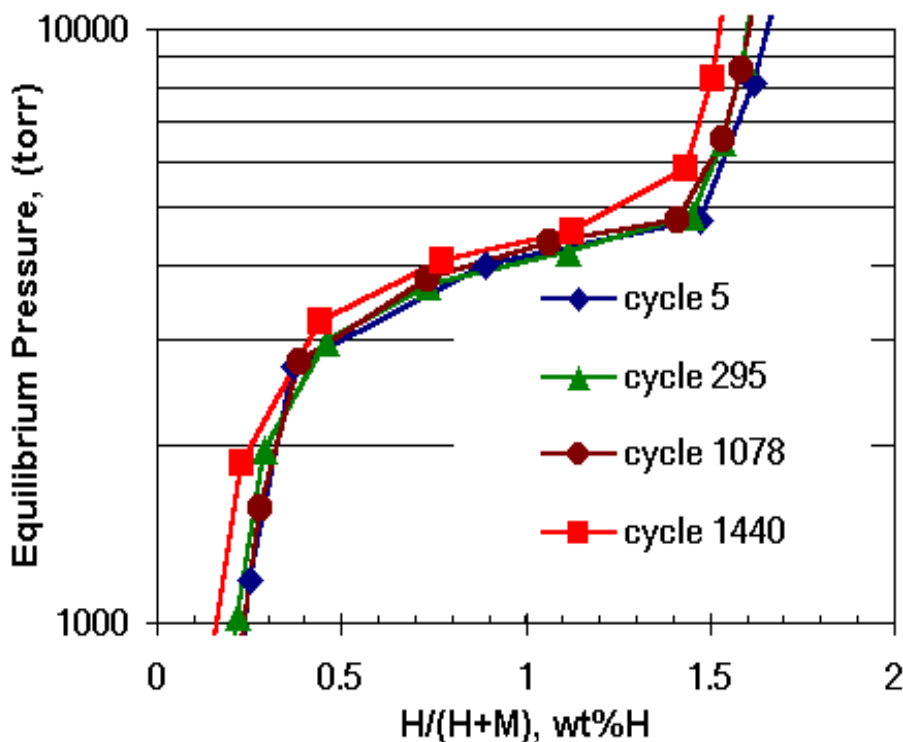


Figure 1. Desorption P-C Isotherms of TA-1b at 30°C. Cycles 1080-1429, H₂ / 0.1% CO

Figure 2 shows the desorption PC-isotherm of an alloy having a hydrogen absorption capacity of 3.5 wt%, and a desorption capacity of 2 wt% at 30 °C. Further work is required on this alloy to improve its plateau pressure, reversible capacity, cycle life, poison resistance and stability to moisture.

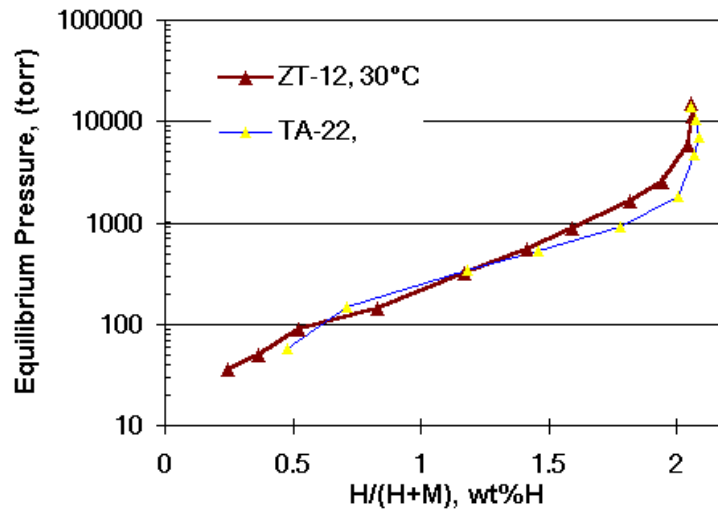
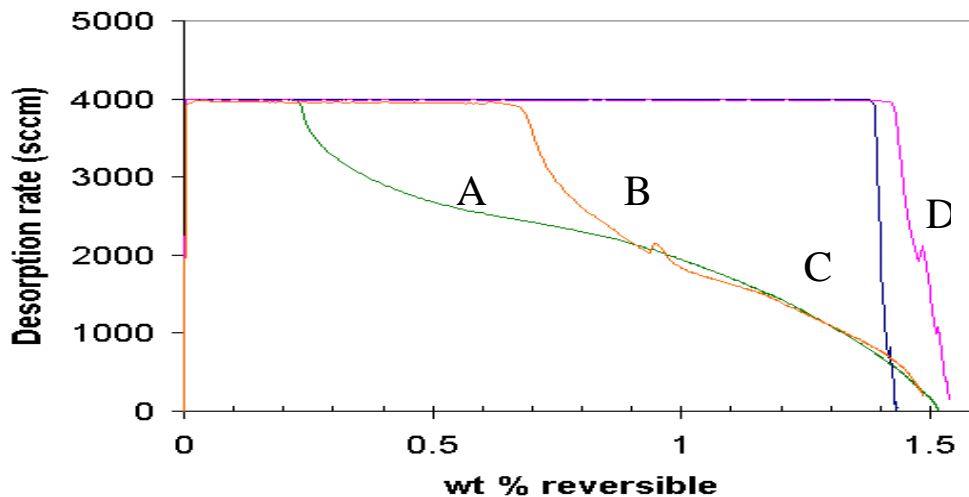


Figure 2. Desorption P-C Isotherms of TA-22 and ZT-12 at 30°C

The Storage System

While the metal hydride is the heart of a metal hydride storage system, the design and engineering of the complete system is critical for optimized performance. Figure 3 illustrates the effects of packaging on the hydrogen desorption characteristics of a metal hydride storage system. Four different canisters A, B, C, and D were packaged with alloy from the same production batch. The mass of the alloy and the desorption parameters (surrounding temperature, desorption pressure and desorption rate) were the same. The graph clearly shows the effect of heat and mass transfer on the hydrogen desorption characteristics. Storage systems C and D were able to sustain the desired discharge rate of 4000 sccm more effectively than systems A and B, which were packaged differently.

Figure 3. Effect of packaging on performance of a MHSS



MHSS for HICE Scooter for India

| | |
|--------------------------------|--------------------|
| Fuel (H ₂) use | 5 gm/ km (assumed) |
| Avg. daily driving distance | 20 km |
| Avg. driving speed | 20 kmph |
| Onboard H ₂ storage | 100 gms |
| Mass of alloy (@ 1.5 w/o) | 7 Kg |

Figure 4 shows a prototype metal hydride storage module for H-ICE application. The module is designed to derive the heat of desorption from the hot exhaust of a H-ICE.

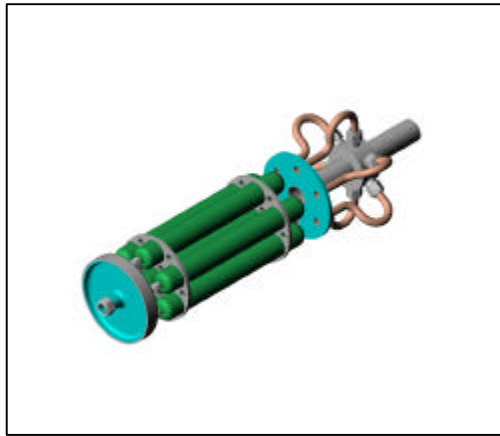
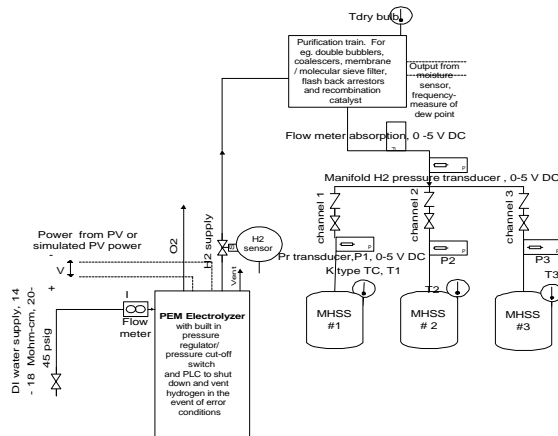


Figure 4. Prototype MHSS system for H-ICE scooter application

Fuel generation requirement is met with a USSC - 12 V, 1.66 kW_p a-Si PV array, 7.5 % panel. efficiency, 42 sq.m area, and a 1.25 kW water electrolyzer. On a typical July day in Detroit a PEM electrolyzer generated 134 grams of hydrogen, sufficient to run a scooter for one day. The metal hydride storage system was charged with hydrogen from the electrolyzer.

Figure 5: Schematic of a PV-Electrolysis Metal Hydride System



Preliminary test results

Heat of desorption from exhaust gas in a H-ICE scooter was determined by doing a mass balance to find exhaust gas volume (V_{exhaust} in scfm). Using the hydrogen consumption at 20 kmph, the power at the rear wheel and the fuel -air ratio for a stoichiometric reaction a simple energy balance at the H-ICE determines the thermal energy lost to the exhaust (Q_{exhaust} in Watts). It was assumed that about 30 % of the energy lost is in the form of thermal energy to the exhaust. The heat transfer medium used is air. The assumed range and hydrogen consumption data were used to determine the mass of the alloy required (total in the 7-tube bundle) to be 7 Kg.

In the absence of a HICE, we designed bench-top experiments simulating the exhaust heat. A simple exhaust gas – metal hydride storage system heat exchanger was designed and built. The hydrogen was desorbed at a fixed discharge rate and the hot air volumetric flow rate and the temperature were varied. It was found that about 80 % of the total reversible hydrogen could be released at the constant rate of 15 slm at 10 psig pressure. Figure 6 below shows the discharge characteristics and the temperature of the module surface as a function of time.

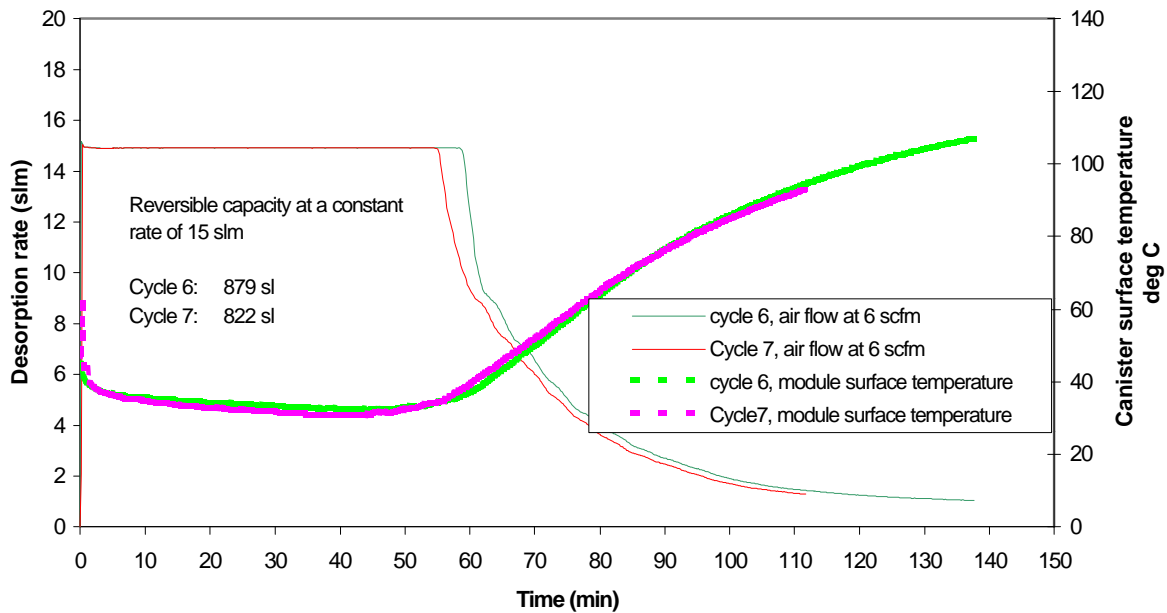


Figure 6. Hydrogen desorption from a tube bundle comprising of seven 140 sl modules. Desorption at 10 psig, 15-slm maximum, and airflow at 6 scfm

Renewable Hydrogen

a. PV/Electrolysis

India has a severe power shortage (greater than 11 GW), and a central power system that is highly unreliable and unable to meet the demand in remote areas. About 70% of the population lives in the villages. Decentralized renewable energy is the only option. India has approximately 39 MW installed PV capacity, the largest in Asia, and is the third largest in terms of installed Wind Power in the world. The country is receptive to renewable technologies, including hydrogen. India has established Independent Renewable Power Producers (IRPP's) organizations to accelerate the commercialization of decentralized power. PV can be placed anywhere and presently 50% subsidy is being offered on many PV products. We looked closely at the cost of hydrogen produced by PV –Electrolysis as a part of our current year effort. A 2 kW PV-Electrolysis system represents a distributed, and renewable hydrogen generation system. It was demonstrated that a Ovonic metal hydride (TA-1) can be readily charged with electrolytic hydrogen from a PEM electrolyzer.

A preliminary cost analysis (Figure 7) was carried out for a PV- Electrolysis System producing hydrogen

The following assumptions were made

electrolyzer 65%

Cost of electrolyzer not included

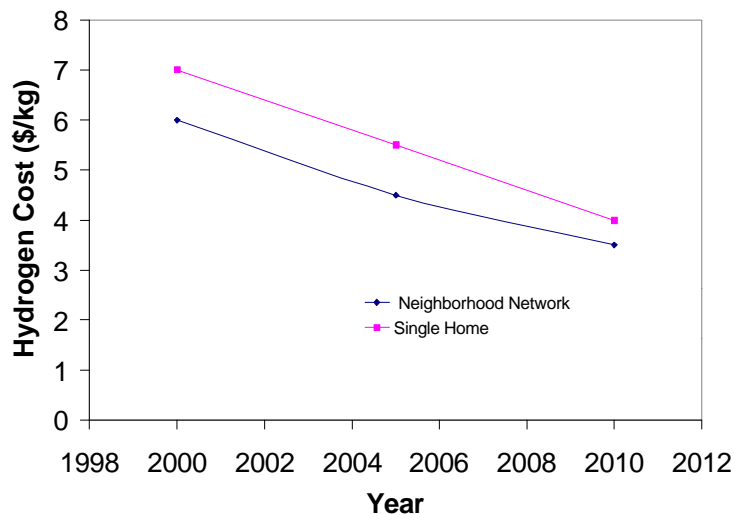


Figure 7. Cost of hydrogen from PV¹ – Electrolysis

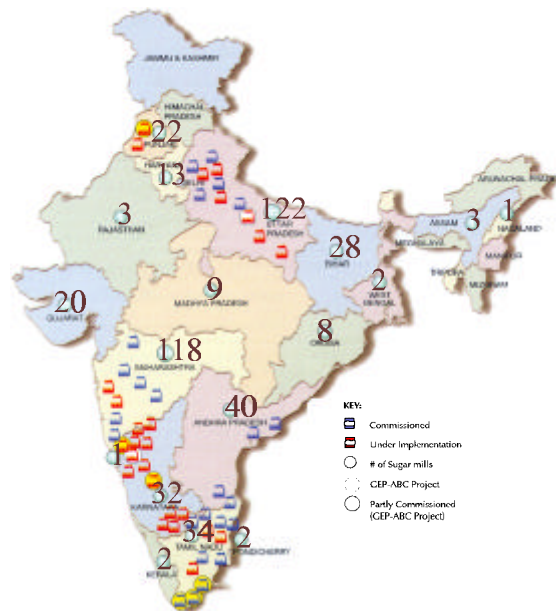
Cost of PV – electrolytic hydrogen was calculated for both a-Si and crystalline Si PV panels in the kW range. Both the present cost and performance (efficiency) of the PV panels as well as the

¹ PV cost from report titled 'Overview of Photovoltaic technologies'

projected data were used to determine the cost. PV- Electrolyzer system can be tailored to meet the power and fuel requirement (hydrogen) in remote locations that are not grid connected and

India is the largest cane sugar producer in the world, producing about 13 million metric tons / year and bagasse is a by-product of this process with high density of thermal energy. The cogen power in India is 3,800 MW. Of this, 180 MW cogeneration is consumed internally for sugar manufacture and the rest is available for sale at a price of 2-4 cents/

Figure 8 shows a map of India with the number and location of existing sugar mills. mills are located next to the cane fields and are distributed all over the country. This minimizes the cost of transporting cane and will also reduce the cost of transporting the product hydrogen.



Cogen distribution in India

Shown below in Figure 9 is a concept of the proposed hydrogen production using bagasse based

The power available will be used to run the electrolyzers onsite. Hydrogen will be produced

tankers to ‘filling stations’. In addition, Ovonic metal hydrides would be charged at the hydrogen plants and distributed to the applications.

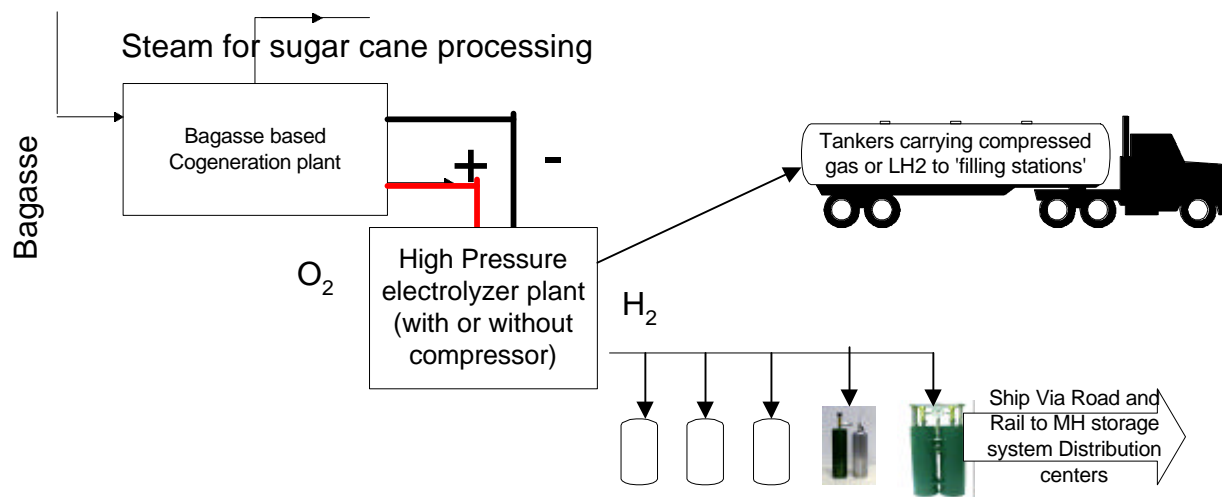


Figure 9 : Concept for bagasse based cogeneration electrolysis for hydrogen production and its distribution

Case study - three sugarcane processing mills in India ²

| Available low cost Power (GWh/yr) | H ₂ Energy (Gwh/ yr) (electrolysis =0.5) | H ₂ production (tonnes/year) | # Scooters fueled/year [!] |
|-----------------------------------|---|---|-------------------------------------|
| 295 | 147.5 | 4470 | 122457 |
| 166 | 83 | 2515 | 68908 |
| 89 | 44.5 | 1348 | 36945 |

[!] The fuelling capacity assumes 5 gm H₂/Km and 100 gm / day per scooter and 365 driving days / year

Based on private discussions with Proton Energy Systems, the capital cost of an electrolyzer was included in the cost of cogeneration powered - electrolytic hydrogen. The plant is assumed to produce ~ 14.2 Tonnes H₂ / year assuming 300 days/ year and 19 hour operation per day.

| Cost of power | Cost of hydrogen |
|----------------|------------------|
| 2 cents / kWhr | US \$ 1.76/ Kg |
| 4 cents / kWhr | US \$ 2.81 / Kg |

We see that the low cost of cogeneration power reduces the cost of electrolytic hydrogen. Bulk hydrogen can be dispensed to the application directly at a 'hydrogen filling station' while the charged metal hydrides can be distributed to customer directly through retail outlets.

² USAID/NewDelhi and the Office of Energy and Infrastructure study (Report No. 93-02) titled 'Advancing Cogeneration in the Indian Sugar Industry'

High-Pressure Conformable Hydrogen Storage for Fuel Cell Vehicles

Thiokol Propulsion
Point of Contact: Andrew Haaland
P.O. Box 707, M/S 230
Brigham City, UT 84302-0707
(435) 863-6373; Fax (435) 863-8782; Email: haalaac@thiokol.com

Abstract

Thiokol Propulsion is currently developing conformable tanks for gaseous hydrogen storage at 5,000 psig. These tanks have a water volume of 68 liters and have external dimensions of approximately 12.8 in. x 21.2 in. x 27.9 in. At an operating pressure of 5,000 psig, this volume will allow storage of 3.4 lb. of hydrogen, providing 23% more capacity than two cylinders in the same volume envelope. The tanks are fabricated using carbon fiber TCR[®] prepreg, plastic liners, and aluminum polar bosses. During the past five years, a significant technology development effort has been completed that has resulted in a baseline tank design that has passed many of the tests outlined in the NGV2-1998¹ standard for natural gas modified for 5,000 psig hydrogen storage. This paper will summarize the design process as well as provide a complete synopsis of tank testing.

Introduction

Fuel cell-powered vehicles have the potential to provide a solution to air quality problems as well as to reduce U.S. dependence on foreign fuel sources. A fuel cell combines hydrogen with air to produce electricity to power a vehicle, with water vapor as the primary by-product. A key issue for fuel cell operation is the availability of hydrogen on-board the vehicle. Hydrogen can be provided either as a compressed gas, as a cryogenic liquid, or as an adsorbed element using metal hydride storage. Alternatively, an on-board reformer can be used to generate hydrogen from gasoline, diesel, natural gas, or methanol. Of these alternatives, compressed hydrogen is considered the best near-term solution for hydrogen storage on a motor vehicle due to the relative simplicity of gaseous

hydrogen, rapid refueling capability, excellent dormancy characteristics, low infrastructure impact, and low development risk.²

Despite these advantages, on-board high-pressure hydrogen storage must overcome several technical challenges in order to be viable in the long term. The energy density of hydrogen is significantly less than that of competing fuels as shown in Figure 1. Even with the high efficiencies projected for fuel cell vehicles, up to three times the current fuel efficiencies for internal combustion engines, a large volume of gaseous hydrogen storage will be required for acceptable vehicle range.

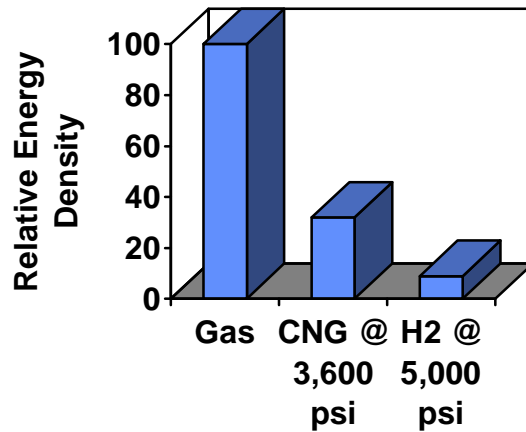


Figure 1. Comparison of fuel energy densities

With increased fuel requirements, the size of the fuel storage system becomes an issue. Liquid fuels such as gasoline and diesel can be stored in tanks that closely conform to the available space on the vehicle without reducing cargo capacity. For a gaseous fuel, the added requirement of pressurized storage constrains the geometry of the fuel tank. Because cylindrical tanks provide near-optimum pressure vessel structural efficiency, vehicles currently utilizing gaseous fuel systems employ one or more compressed storage cylinders. However, the cylindrical geometry of these tanks often does not lend itself to efficient use of the normally rectangular fuel storage volumes available on a vehicle as shown in Figure 2. In a rectangular envelope with an aspect ratio (width/height) equal to an integer, cylinders occupy less than 75% of the available storage volume. For non-integer aspect ratios, this figure can be as low as 50%.

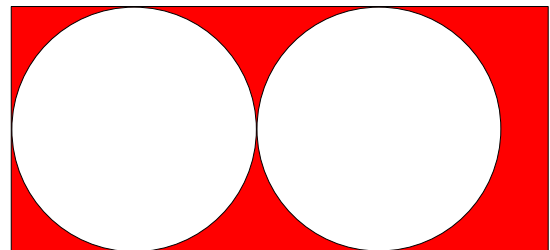


Figure 2. Cylindrical tanks in a rectangular envelope

The twin issues of energy density and packaging efficiency combine to exact a significant range penalty for gaseous-fueled vehicles. A lower energy density fuel dictates that a larger volume of fuel will be required for the same range as a conventionally fueled vehicle. However, the requirements of pressurized storage dictate that a smaller volume of fuel can be stored in the same envelope used for a conventional gasoline tank. This situation typically results in the location of additional gaseous fuel storage cylinders in the vehicle cargo area. This results in an increased vehicle range at the expense of vehicle payload.

The problem of maximizing on-board gaseous fuel storage is being addressed through the development of a conformable pressurized tank. Based on the physical principle that cylinders efficiently contain internal pressure via membrane response, the fundamental concept for the conformable tank consists of adjoining cell segments with internal web

reinforcements. The general approach is shown in the cross-section in Figure 3. The result is a multi-cell pressure vessel. The number of internal cells is optimized for volume and pressure capacity and depends in large part on the aspect ratio of the envelope.

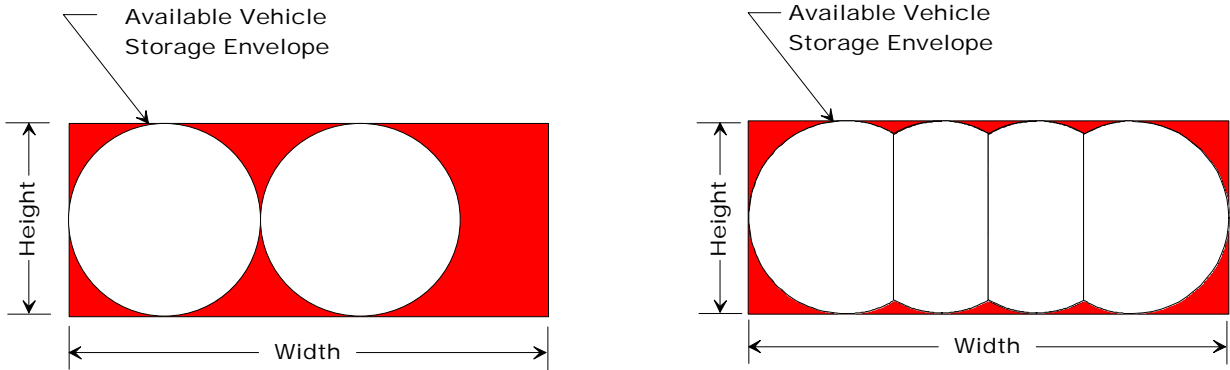


Figure 3. Cylinders vs. a conformable tank in a rectangular envelope

The expected benefits in volumetric efficiency of the conformable tank concept compared to multiple cylinders in a rectangular envelope are shown in Figure 4. Regardless of aspect ratio, the internal volume of the multiple cylinders never exceeds 70% of the envelope volume; except for aspect ratios close to 1.0, the conformable tank provides significantly increased storage volume.

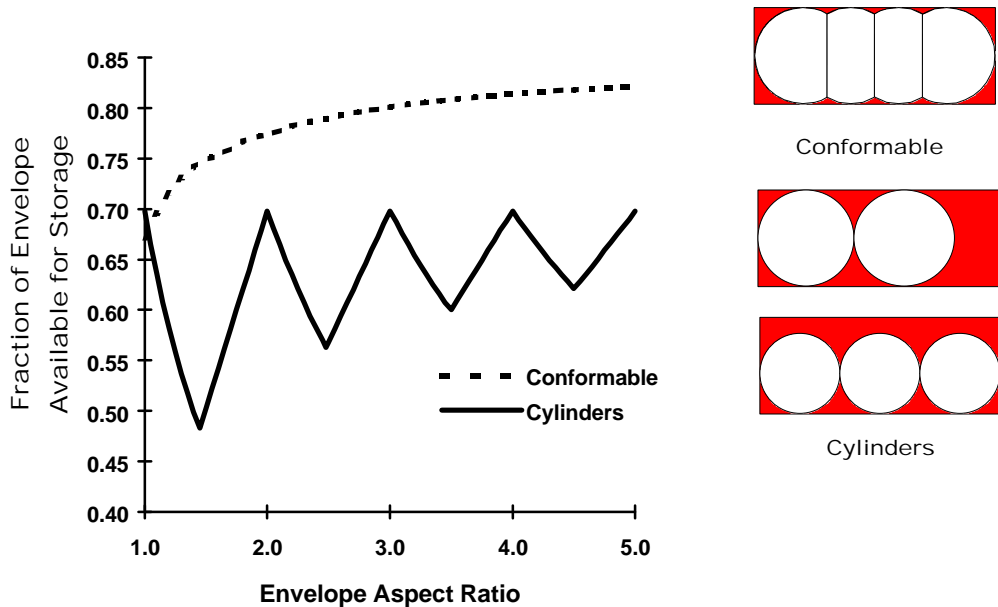


Figure 4. Comparison of storage efficiencies as a function of storage envelop

Discussion

To sustain the service pressures required for conformable hydrogen storage, material and process trade studies dictated the use of a carbon fiber composite tank design that employed a plastic liner and aluminum polar bosses. Use of the carbon composite material also allows the tank design to meet structural, cost, weight, and volume constraints. The plastic liner must prevent permeation of the stored gas through the structural composite while also serving as the mandrel for filament winding. From both weight and cost considerations, a plastic liner manufactured using a rotational molding process was selected for use in the baseline tank design. Rotational molding provides the dual benefits of low-cost tooling requirements for prototype development as well as the capability for molding non-symmetrical shapes.

The initial tank designs strove to exploit the advantages inherent in the use of carbon composite materials. The tailorability of filament-wound composites offers the opportunity to optimize tank wall thickness by applying less material in the lower-stressed axial direction, and by applying more material in the higher-stressed hoop direction. Finite element analysis combined with Thiokol's experience in winding composite rocket motor cases allowed for the completion of the initial conformable composite tank designs. The individual cells comprising the tank were wound with a combination of hoop and helical composite layers. These cells were then joined together to form a complete tank using winding tooling that allowed a final hoop overwrap to be wound over all of the cells. Careful control of the transition radius between the curved outer wall and the flat internal web allowed elimination of most of the bending and peel stresses at the joint between the cells. The geometry of the tank cross-section is shown in Figure 5. A U.S. Patent³ has been obtained for the design and fabrication approach.

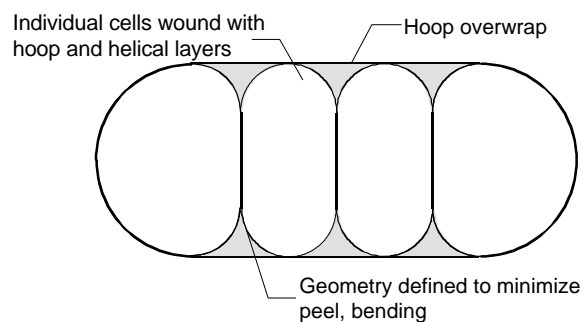


Figure 5. Conformable tank configuration

In efforts prior to FY1999, the structural capabilities of the resulting composite conformable tank design, were demonstrated using a sub-scale, two-cell prototype tank design. The prototype, pictured in Figure 6, occupies a storage envelope of 10.5 in. x 15.5 in. x 19 in. and has a capacity of 7.5 gallons. Mandrels for winding the individual cells were fabricated from sand mixed with a water soluble binder. The sand was cast and cured in a metal mold, and a thin layer of elastomeric material was applied to the surface of the mandrel for containing the pressurizing fluid. Following winding of the carbon/epoxy hoop overwrap and oven cure of the tank, the sand was washed out of the interior. Winding of an individual cell is shown in Figure 7. The finished prototype tank had a weight of 23 lb., including 15 lb. of composite. Prototypes were fabricated using Toray's M30S carbon fiber with Thiokol's TCR® prepreg resin system. Considerable

trial and error was required to develop filament winding procedures for the non-axisymmetric conformable geometry.

The target burst pressure for the prototype tank was 11,250 psig, corresponding to a safety factor of 2.25 for a 5,000 psig service pressure tank. This was consistent with qualification requirements for CNG fuel tanks¹. A burst pressure of 10,950 psig was achieved, verifying the capability of the composite conformable tank concept to meet the strength requirements for a hydrogen fuel tank. This design served as a baseline for the development of a full-scale hydrogen conformable storage tank that would have a service pressure of 5,000 psig and a service life of 20 years.



Figure 6. Prototype two cell conformable tank



Figure 7. Filament winding a conformable cell

Conformable hydrogen storage tank design activities completed in FY1999 included full-scale tank design, structural capability demonstration, and liner material evaluation and selection. Successful completion of FY1999 activities demonstrated the primary functional requirement for a full-scale high-pressure conformable hydrogen tank: the capability for safely withstanding the service pressure of 5,000 psi. However, additional requirements must be satisfied in order to demonstrate safe and reliable operation of the tank within the motor vehicle environment. Over a lifetime of service, the tank will experience cyclic loading due to repeated fills, extremes of temperature, exposure to corrosive fluids, potential damage both during handling and vehicle operation, and possible creep and stress rupture due to sustained high pressure loading.

The ANSI/AGA NGV2-1998 standard provides a comprehensive set of design and qualification test requirements for compressed natural gas (CNG) vehicle fuel tanks to ensure safe operation over the tank lifetime. In the absence of a comprehensive standard for hydrogen vehicle fuel tanks, and because of their similarity with CNG tanks, Thiokol will use NGV2-1998 qualification requirements modified for tank operation at 5,000 psig as the basis for safety and durability testing and evaluation under the present program.

The primary approach employed in FY2000 efforts is to subject a total of 6 tanks produced using the technology developed in FY1999 to qualification testing based on

NGV2-1998 modified for 5,000 psig tank operation in order to identify and address critical safety and durability issues. Accordingly, a total of 6 two cell conformable tanks were fabricated and delivered to Powertech Laboratories in Surrey, British Columbia, Canada for testing during the month of March 00. The tests conducted are defined in the NGV2-1998 standard and included temperature cycling, accelerated stress rupture, drop, environmental, penetration, and permeation. Test criteria for the complete NGV2-1998 standard and results obtained on the 6 tanks are summarized in Table 1 below;

Table 1: Conformable Hydrogen Tank Test Criteria and Results

| Test | Criteria for Successful Test* | Result |
|----------------------------|---|--------------|
| Burst | Safety Factor 2.25 * 5,000 psig = 11,250 psig | Pass |
| Ambient Cycle | 15,000 cycles without failure: 45,000 cycles without rupture to 1.25 safety factor * 5,000 psig = 6,250 psig | Pass |
| Environmental Cycling | Subject to fluid exposure, pendulum impact, gravel impact, high low, ambient temperature cycling, burst above 9,000 psig | Pass |
| Flaw Tolerance | Machined flaws followed by cycling (15,000 cycles to 6,250 psig) | Not Tested** |
| Drop | A total of 6 drops from a height of 6 feet followed by ambient cycling of 15,000 cycles to 6,250 psig | Pass |
| Penetration | Bullet penetration of tank pressurized to 5,000 psig with hydrogen. Tank must not fragment | Pass |
| Permeation | Specified leak rate for hydrogen | 1.2 scc/l/hr |
| Bonfire | Must safely vent | Not tested |
| Hydrogen Gas Cycling | 1,000 cycles with hydrogen to 5,000 psig, followed by leak test and destructive inspection | Not tested |
| Accelerated Stress Rupture | Tank pressurized to 6,250 psig and held at pressure for 1,000 hours at 149 F. At conclusion, tank must burst above 8,438 psig | Pass |

* Requirements for a tank with 5,000 psig service pressure and a 20 year service life. Burst test results were conducted at Thiokol on additional conformable tanks that were not a part of the lot of 6 tanks sent to Powertech.

** Tank expected to pass this test based on positive results for a compressed natural gas tank of similar design operating at 3,600 psig.

Conclusions

Thiokol has successfully designed and demonstrated a two cell conformable tank capable of storing hydrogen at 5,000 psig that will meet most of the design criteria of the NGV2-1998 standard. Additional testing will be required to certify the design to the NGV2-1998 standard. Additional challenges for this effort include increasing the tank operating

pressure to 10,000 psig and incorporation of lower cost manufacturing components and techniques.

Future Work

Thiokol has currently completed all of its existing contract efforts for the DoE. An additional proposal has been submitted for a follow-on effort. Future tasks will either be completed on the follow-on contract or using Thiokol discretionary funding. Additional future efforts are defined below;

- 1.) Complete the remaining tests on the full-scale tank outlined in the NGV2-1998 standard.
- 2.) Extend the conformable tank design to operate at 10,000 psig.
- 3.) Incorporate component and manufacturing cost improvements into the existing tank design.

Acknowledgments

Thiokol Propulsion wishes to acknowledge the technical support and oversight provided by Joanne Milliken and Sig Gronich at DOE Headquarters; Fred Mitlitsky and Andrew Weisberg at Lawrence Livermore National Laboratory, and Walt Podolsky at Argonne National Laboratory throughout the entire conformable hydrogen storage tank development program. Jim Wegrzyn and Wai-Lin Litzke at Brookhaven National Laboratory have also provided technical support for concurrent conformable CNG tank development. Thiokol would also like to acknowledge the efforts and technical expertise of team members Peter Regna and Al Baris at Aero Tec Laboratories, and Eric Stokes at Southern Research Institute.

References

1. American National Standards Institute, "American National Standard for Basic Requirements for Compressed Natural Gas Vehicle (NGV) Fuel Containers," Standard ANSI/AGA NGV2-1992.
2. B. D. James, G. N. Baum, F. D. Lomax, Jr., C. E. Thomas, I. F. Kuhn, Jr., "Comparison of Onboard Hydrogen Storage for Fuel Cell Vehicles," Task 4.2 Final Report under Subcontract 47-2-R31148, prepared for Ford Motor Co. under DOE Prime Contract DE-AC02-94CE50389, Directed Technologies, Inc., 1996.
3. "Composite Conformable Pressure Vessel," U.S. Patent No. 5,566,630, Nov. 26, 1996.

VEHICULAR HYDROGEN STORAGE USING LIGHTWEIGHT TANKS

Fred Mitlitsky, Andrew H. Weisberg, and Blake Myers
Lawrence Livermore National Laboratory
7000 East Avenue, L-174, Livermore, CA 94551-0808

Abstract

Lightweight hydrogen storage for vehicles is enabled by adopting and adapting aerospace tankage technology. The weight, volume, and cost are already acceptable and improving. Prototype tankage was demonstrated with 11.3% hydrogen by weight, 1.74 million inch (44.3 km) burst performance factor ($P_b V/W$), and 3.77 kWh/kg specific energy for the tank and hydrogen (LHV).

DOE cannot afford full scale aerospace development costs. For example, it costs many tens of \$M to develop a rocket motor casing with a safety factor (SF) of 1.25. Large teams of experts are required to design, develop, and test new processes. Car companies are buying existing technology with only modest investments in research and development (R&D).

The Lawrence Livermore National Laboratory (LLNL) team is maximizing the leverage from DOE funding by joining with industry to solve technical risks at the component level. LLNL is developing fabrication processes with IMPCO Technologies, Thiokol Propulsion, and Aero Tec Laboratories (ATL). LLNL is creating commercial products that are close to adoption under DOE solicitation. LLNL is breaking ground to achieve greater than 10% hydrogen by weight tankage with safety that exceeds the requirements of NGV2 standards modified for hydrogen.

Risk reduction is proceeding along three axes:

- Commercializable products will be available next year with ~90% confidence.
- R&D progress is pushing the envelope in lightweight tankage for vehicles.
- Integration challenges are being met with partners in industry and DOE demo programs.

This project is a key part of LLNL's effort to develop high cycle life energy storage systems with >600 Wh/kg specific energy for various applications, including: high altitude long endurance solar rechargeable aircraft, zero emission vehicles, hybrid energy storage/propulsion systems for spacecraft, energy storage for premium power, remote power sources, and peak shaving.

Long-Term Goals

There are eight long-term goals in this project:

1. Demonstrate tankage with 12% hydrogen by weight (5,000 psi [34.5 MPa] service, 300 K, safety factor [SF] 2.25) and 700 Wh/liter.
2. Certify tankage for operation on vehicles (e.g., NGV2 standards modified for hydrogen).
3. Modify designs for easy manufacturability and have industry adopt lightweight tankage designs.
4. Work with industry to reduce the cost of hydrogen tankage.
5. Work with industry to develop lightweight hydrogen tankage with service pressure ratings up to 10,000 psi (69 MPa).
6. Work with large auto manufacturers to demonstrate lightweight hydrogen tanks on fuel cell vehicles.
7. Suggest modifications to hydrogen tankage codes and standards (e.g., hydrogen permeation standards for modified NGV2 or ISO/TC 197).
8. Develop fast filling operations, tankage, and fueling infrastructure that mitigate overtemperature/overpressure issues.

This list of eight tasks will appear throughout this Annual Report. It provides a common framework to organize the presentation of many related accomplishments. Expertise and contacts are shared between these tasks, and an accurate picture of present or future activities cannot be obtained from viewing particular tasks in isolation.

The recurrence of these eight tasks reflects the LLNL team's attempt to answer the DOE required project reporting format for the 2000 Hydrogen Program Annual Review Meeting (San Ramon, CA, May 9-11, 2000). All LLNL lightweight tankage research activities have been organized into these eight categories. Within each category, extensive presentations of the LLNL team's activities will be found largely in the Current Year Progress section. All current and planned activities derive from the list of long term goals above, reflecting LLNL's dedication to aggressive pursuit of this pivotal hydrogen storage technology.

LLNL interest in lightweight hydrogen storage derives from several aggressive aerospace vehicle projects (Carter 1999, de Groot 1997, Kare 1999, McElroy 1998, Mitlitsky 2000, Mitlitsky 1999-a,b,c,d,e Mitlitsky 1998-a,b,c,d,e,f, Mitlitsky 1997, Mitlitsky 1996-a,b,c,d, Mitlitsky 1994, Mitlitsky 1993) whose feasibility relied heavily on the availability of advanced pressure vessels to hold gaseous hydrogen and oxygen. Attempts to dramatically improve mass performance of aerospace vehicle tanks had obvious spinoffs in automotive and utility applications of interest to DOE (Mitlitsky 1999-c,d,e, Mitlitsky 1998-b,d,e,f, Mitlitsky 1997,

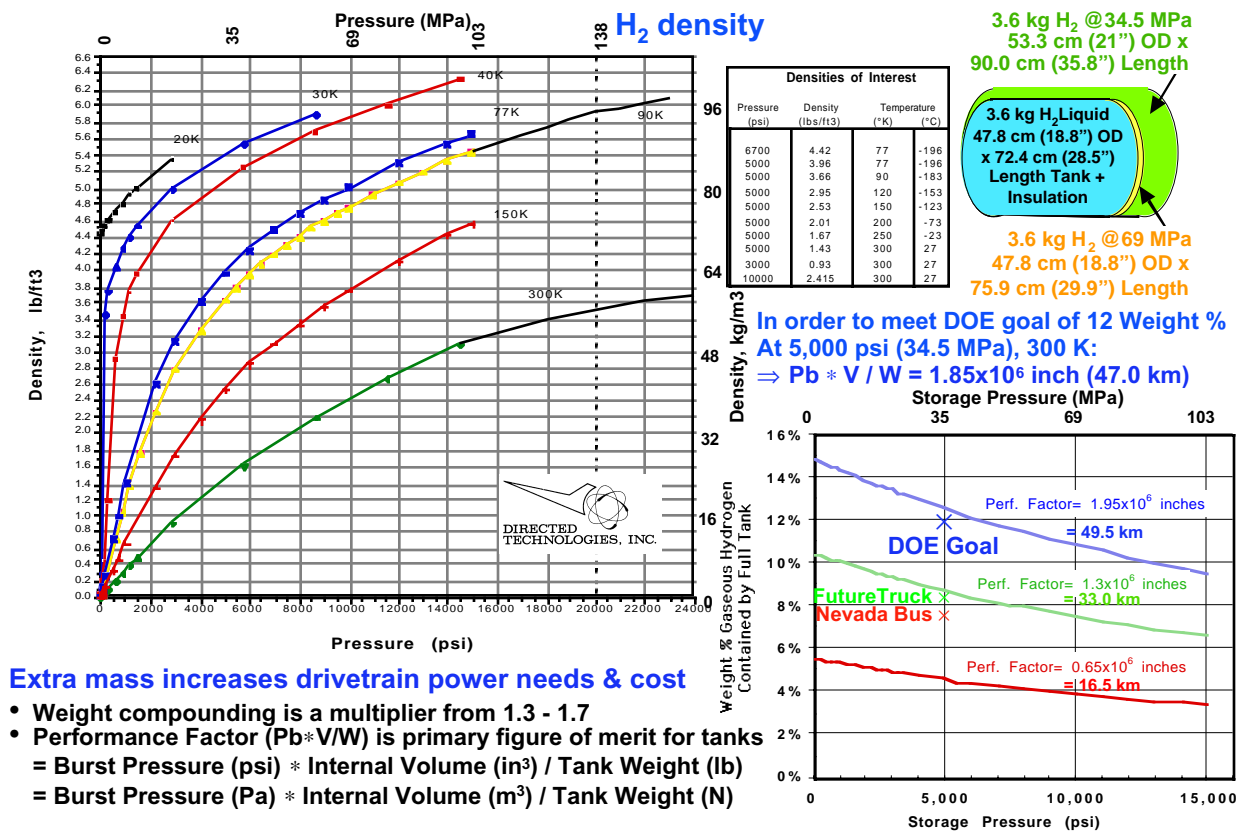
Mitlitsky 1996-a,c, Mitlitsky 1994). Of the potential applications, automotive fuel tanks is by far the most important to DOE, as written into the Hydrogen Program's enabling legislation (Gronich 2000).

Mass-sensitivity may be reduced in automobiles compared to aircraft or spacecraft, but it cannot be ignored. The mass of fuel a vehicle can afford to carry directly limits its range. The reason why battery-powered automobiles are not capable of the ~380 mile (610 km) range desired for electric vehicles is due to the mass compounding effect of the energy storage system. Each kg of energy storage on the vehicle results in a 1.3-1.7 kg increase in vehicle mass, due to the additional powerplant and structure required to suspend and transport it (Mitlitsky 1999-e). Large mass fractions devoted to energy storage ruin a vehicle design, devoting too much costly hardware to transport a smaller fraction available for passengers and payload. Although the entire power train mass should be minimized to save costly components, fuel mass cannot be pitched overboard without sacrificing vehicle range. Therefore, lightweight tankage is required for vehicular energy storage systems that can store sufficient specific energy in order to achieve a market-acceptable vehicle driving range.

Lightweight vehicular hydrogen tankage has recently advanced to the threshold of application in demonstration vehicles. Competition with other ways to store hydrogen, or to produce hydrogen from other fuels onboard a vehicle, is intense. Various vehicle designs are being fueled by hydrogen stored in various technologies. Only the technology investigated herein, Type IV pressure vessels, is currently capable of furnishing adequate vehicle range with percent hydrogen by mass performance adequate for the ~380 mile range drivers appear to insist on. The research reported herein can essentially double the range performance of this lowest-mass hydrogen storage alternative.

Volume restrictions are an additional constraint on hydrogen-fueled vehicles, but only in the near term when the relatively few demonstration vehicles cannot afford designs that depart from conventional vehicle layouts. Vehicles that are not designed from the ground up to accommodate enough hydrogen can fail to achieve attractive vehicle range. The relatively low density of energy stored in the form of compressed hydrogen requires significant volume devoted to hydrogen tanks. Increasing storage pressure reduces the storage volume required, at the expense of increased compression losses and infrastructure complexity.

These vehicle design issues have been studied extensively by Directed Technologies, Inc. (DTI) and LLNL. Figure 1 (Mitlitsky 1999-e) shows how hydrogen density is related to temperature and pressure, and its impact on the DOE 2000 tankage goals. Three overlays of tank external volumes show the relative sizes of tanks (and insulation) which store 3.6 kg of hydrogen at 34.5 MPa (300 K), 69 MPa (300 K), and low pressure liquid hydrogen (20 K) (Aceves 2000). The non-ideal compressibility of hydrogen at high pressures is shown by the decreasing slopes of the density curves (at constant temperature) and the sag in the weight percent curves (at constant tank performance factor). The DOE goal of 12 weight percent H₂ at 5,000 psi (34.5 MPa), 300 K translates directly into the need for a tank with a performance factor of 1.85 million inch (47.0 km). The team of LLNL and its industrial partners reports achieving almost all of this goal in the Current Year Tasks section below.



Extra mass increases drivetrain power needs & cost

- Weight compounding is a multiplier from 1.3 - 1.7
- Performance Factor ($Pb \cdot V / W$) is primary figure of merit for tanks
 - = Burst Pressure (psi) * Internal Volume (in³) / Tank Weight (lb)
 - = Burst Pressure (Pa) * Internal Volume (m³) / Tank Weight (N)

Figure 1 – DOE 2000 Tankage Goals

LLNL has served, and will continue to serve as a conduit for tankage design information between DTI, DOE demonstration programs, and LLNL's industrial partners who are producing high performance hydrogen tanks (IMPCO Technologies and Thiokol Propulsion). Besides technical management of the DOE-funded hydrogen tankage development at IMPCO Technologies (program start May 2000), and Thiokol Propulsion (Haaland-2000), LLNL is funded directly by DOE to develop advanced tankage with significantly better mass performance. Tanks are being built to LLNL specifications, with LLNL design and materials selections, which realize the DOE 2000 Goals. The hydrogen storage mass of 3.6 kg is required for a PNGV-like fuel cell vehicle with a range of 380 miles (610 km) for the EPA Combined Cycle (Mitlitsky 1999-e).

This Year's Objectives and Rationale

1. Prototype tankage with ~12% hydrogen by weight (5000 psi [34.5 MPa] service, 300 K, safety factor 2.25). This will set a tank performance record ($P_b V/W = 1.85$ million inch = 47.0 km) for high cycle life tankage and demonstrate the feasibility of certifying tankage for vehicular operation with >10% hydrogen by weight.
2. Specify a ~1 year program to certify tankage with 7.5-8.5% hydrogen by weight (5000 psi, 300 K, SF 2.25). This will rapidly demonstrate certified hydrogen tankage that has significantly better mass performance (by 50-80%) than industry has demonstrated to date.
3. Develop a lightweight liner fabrication process and permeation reduction coatings that are easily adopted by industry. Variable thickness rotomolded liners are lightweight and easily adopted. Permeation reduction coatings enable lightweight liners to meet proposed permeation specifications, but increase fabrication complexity.
4. Develop lightweight tankage with SF 2.25 and accumulate cost projections from DOE tank solicitations. Lightweight tank liners enable weight goals to be achieved with less expensive fiber. Tankage with SF 2.25 uses ~75% of the fiber required for tankage with SF 3. This is important because fiber cost dominates tankage cost, especially in high volume production.
5. Work with car companies and tank manufacturers to understand prospects for adopting higher pressure (up to 10,000 psi [69 MPa] service pressure). Higher pressure improves storage density of hydrogen at the expense of hydrogen compression cost/inefficiency and infrastructure complexity.
6. Design tankage for Nevada Bus (7.5% hydrogen by weight certified tankage) and FutureTruck 2001 (8.5% hydrogen by weight certified tankage) hydrogen fueled demonstration vehicles. Certify lightweight tankage and illustrate to a wide audience that this technology is ready for adoption. Feasible tank designs can then be developed with and acquired from industry.
7. Scrutinize the proposed specification for hydrogen permeation in the modified NGV2 standard (< 1 standard cc / hr / liter of water capacity at service pressure, room temperature, beginning of life). Overly stringent standards increase cost and preclude attractive technology options without improving safety.
8. Collect data on overtemperature/overpressure issues with fast filling procedures. Overtemperature issues in fast filling are greater than anticipated and might not allow hydrogen tanks to be rapidly filled to capacity without exceeding temperature limits in some cases.

Current Year Tasks

1. Prototype tankage with ~12% hydrogen by weight (5000 psi [34.5 MPa], 300 K, safety factor 2.25). Design hydrogen tanks with lightweight liners, fabricate liners and tanks, burst test tanks, and recommend improvements.
2. Specify a ~1 yr program to certify tankage with 7.5-8.5% hydrogen by weight (5000 psi, 300 K, SF 2.25). Write, modify, and review a solicitation to develop lightweight hydrogen tankage. Technically direct the program that commenced in May 2000 (IMPCO Technologies).
3. Develop a lightweight liner fabrication process and permeation reduction coatings that are easily adopted by industry. Optimize fabrication of variable thickness rotomolded liners. Develop metal and plastic permeation coatings, permeation test coatings, fabricate tanks with coated liners (if funding permits).
4. Develop lightweight hydrogen tankage with SF 2.25 and accumulate cost projections from DOE tank solicitations. Demonstrate plastic lined composite tankage (cylinders and conformable) with safety factor 2.25.
5. Technically direct a 10,000 psi (69 MPa) tankage development effort (pending a DOE/OTT funding award and/or additions to the current DOE/Golden contract DE-AC36-GO10494).
6. Design tankage for Nevada Bus (7.5% hydrogen by weight) and FutureTruck 2001 (8.5% hydrogen by weight) hydrogen fueled vehicles. Design Nevada Bus tankage around existing government tooling for rapid development and demonstration. Design FutureTruck 2001 tankage for a GM Suburban (K 15906) modified for hydrogen fuel.
7. Scrutinize the proposed specification for hydrogen permeation in the modified NGV2 standard and/or the ISO/TC 197 standard. Less than 1 standard cc / hr / liter of water capacity at service pressure, room temperature, beginning of life has been proposed by others. Review the basis for the proposed hydrogen permeation specification and propose a modification if necessary.
8. Collect data on overtemperature/overpressure issues with fast filling procedures. Propose alternatives to mitigate overtemperature/overpressure issues.

Recent progress on each of these eight tasks will be presented in the following section.

Current Year Progress

1. Prototype tankage with ~12% hydrogen by weight (5000 psi [34.5 MPa] service, 300 K, safety factor 2.25). Design hydrogen tanks with lightweight liners, fabricate liners and tanks, burst test tanks, and recommend improvements.

By the beginning of FY00, designs were in hand at LLNL and contracts were in place to realize tank designs at the ~12% hydrogen by weight performance level. Such high performance results were anticipated to set a world record and nearly double the available levels of tank mass efficiency (for high cycle life tankage). All pieces and processes believed necessary to attempt prototyping stood ready to assemble and debug: Special rotational mold tooling had been procured and built in FY99 in an earlier attempt to produce a tank relevant to a Ford demonstration program. Sizing issues for that earlier vehicle program will be discussed in the Task #2 subsection of Current Year Progress (starting on page 17). The availability of this advanced liner production tooling allowed the research this section describes to commence swiftly at the beginning of FY00 under a tank fabrication subcontract with Thiokol that had also been put in place in FY99.

LLNL subcontracted with Thiokol Propulsion to wind tanks on advanced liners produced by ATL. Thiokol's final report to LLNL under that contract has been appended as a major contribution to this report (Appendix 1). The lightweight liners LLNL directed Thiokol to wind around employed a tapered sidewall technology that assists tanks in this design family to achieve the highest percent hydrogen by mass performance levels, using processes that industry might adopt almost immediately.

Tapered thin liners using the technology developed by LLNL at ATL were produced in three batches at the start of FY00. The first batch was employed primarily for process research, and produced several lightweight units that were used in initial winding trials at Thiokol. The second batch completed LLNL's contract with ATL and produced five tanks each in five different wall thickness, ranging in total liner weight from 5 to 10, 15, 20, 25, and 30 pounds. Subsequently a last batch of five liners (6 lb each) with additional processing was built under a small additional LLNL subcontract to ATL. ATL attempted to duplicate a new process step that Thiokol's earliest prototyping attempts found to be necessary on this last batch. Without this thermal preconditioning process step, unacceptable and unexpectedly large liner shrinkage was encountered later in the manufacturing sequence: up to 8% shrinkage occurred during composite cure. By subjecting the liner to thermal cycling similar to its upcoming cure cycling, this shrinkage was found to be stable after just one cycle, so prototypes turned out to be up to ~8% undersized (compared to their designs) and the liner-overwrap interfaces that resulted appeared to be very well adhered (as designed).

Burst tests were performed on four of the five tanks prototyped in this research program. Several attempts to wind on thin liners produced rejects before the process sequence was ironed out early in calendar 2000. The first successful prototype is shown immediately below in Figure 2, next to the thin-wall liner from the same first lot it was wound on. The success of this manufacture in overcoming risky process steps prompted LLNL to reject the entire second batch of fabricated liners in favor of those which duplicated the successful 6 pound prototype liner for

Tank #1, with the additional post-molding thermal process step being applied in the third batch of liners produced and treated at ATL. Prototype Tanks #4 and #5 were wound on parts from this last batch of thermally preconditioned liners.



Figure 2 – First Composite Wrapped Tank Prototype Next to Thin-Wall Liner

Figure 2 above shows a thin-wall liner next to finished Tank #1. The Thiokol boss design employed throughout this research, and built into the tapered thickness rotational mold tooling with 18 inch diameter, is visible at the top of the finished tank in Figure 2, and is sketched in cross section in Appendix 1 (see Appendix C therein). Tank #1 proved to be a useful showpiece, as the LLNL team investigated coating methods in hopes of adopting further process improvements this year. Coating and permeation barrier research is described in Task #3. Although encouraging coating results were obtained with permeation test coupons, neither funds nor time were available to scale candidate coating processes up to pretreat 48 inch long liners. As the Annual Performance Review approached and prospects for scaling up a coating process dwindled, the decision was taken to build more tanks like Tank #1 and obtain burst data confirming the team's P_bV/W performance predictions.

Tank #2 did not pass the leak test prior to proof testing, and its manufacturing failure prompted LLNL to seek ATL help by duplicating Thiokol's preshrinking process step. That prototype

leaked through spiral cracks that formed around just one of its bosses during a Thiokol attempt to heat treat its tank liner horizontally. One boss was driven in the oven by a motor, but the other was retained on a ball bearing fixture which had slight rotational drag. That end developed the spiral cracks, whereas the 'successful' Tank #1 had been heat treated in a vertical orientation. ATL retained the rotational mold tooling and set it up again to perform a heat treat after molding without removing the part from its mold. The rotational mold's motion capabilities provided a superior substitute to horizontal spindle support, avoiding the slumping and hub drag problems encountered at Thiokol in horizontal heat treat process development. Tank #2 was sawed in half perpendicular to its long axis for debugging purposes, and subsequently furnished two demonstration articles (one was shown at the Annual Review).



Figure 3 – Remains of Test Tank #3 after Premature Burst

Figure 3 shows the remains collected after prototype Tank #3 was burst. Tank #3 was built with ATL's first heat treated 6 pound liner, and passed its 7500 psig proof test without any problems. Initially its burst test was thought to be a successful milestone in this research effort's performance goals. It burst at a pressure initially thought to be several percent above predictions. Subsequent recalibration of that test pressure sensor uncovered a test site operator error. The wrong sensor/preamplifier combination was reading pressures at 2/3 of actual. This calibration error triggered a full scale fact finding investigation at Thiokol Propulsion.

Direct evidence from the carcass shown in Figure 3 and the video frame shown below in Figure 4 helped to explain why Tank #3 burst at 70% of design pressure. The accidental canceling of human errors on the test stand and this premature failure mode obscured the dismal results for several days, until the confirmed mismatch of pressure sensor and preamp established the low actual value for burst pressure of Tank #3. Understanding why the burst pressure fell so far below predictions sent Thiokol fact finders in two directions: detailed failure analysis and reverse engineering of what had been built. Winding patterns of the as-built tank were extracted and resubmitted to Thiokol design codes.

Figure 4 shows a video frame captured at the instant when Tank #3 was burst. This evidence agreed with the location of the end dome separation visible in Figure 3, confirming that premature failure occurred near the tangent line between cylindrical section and end dome. Reverse engineering with Thiokol design codes showed great sensitivity to the exact pattern of winding in that region. The Thiokol investigation uncovered a number of problems, including subtle but significant differences between what was modeled and what was actually built in this sensitive region of the tank design. Great detail and a record of this extensive simulation effort that reverse engineered hoop wound fiber termination patterns and their consequences is given in Appendix 1 (see Appendix C therein).



Figure 4 – Video Captures Localized Failure During Tank #3 Burst Test

Additional modeling and oversight was put in place in order to improve the design of Tank #4 and Tank #5, which provided the only affordable attempts to rectify implementation errors presumed to be built into Tank #1 and the sectioned halves of Tank #2. These measures were deemed adequate to assure that the last two prototype tanks to be built would match an improved design. The fate of Tank #1 was decided in the few days before the Annual Review, it was worth more as a burst data point of a design known to be defective than as a showpiece that needed apologies. It burst at 85% of its design burst pressure, confirming the process variability and the sensitivity to details of tank designs with the wrong hoop wound fiber termination locations. This result confirmed the pattern observed at Thiokol by other tank designers – that failures in the tangent line are much less repeatable than failures in the sidewall. Avoidance of premature dome failures and boss failures constrained the improved designs and their prevention appeared to require additional weight, but an added wafer incorporated during winding in the end domes kept the improved design weight growth below 0.1 kg.

Tank #4 was fabricated and burst at 10,464 psi, which is 93% of its 11,250 psi design prediction for burst. The failure mode was not conclusively isolated, although the dome and boss regions did not appear to fail. It was not clear whether failure was in the cylindrical section or the transition from the cylindrical section to the dome. Very little of this tank was left as a helpful carcass, and no dramatic moment was captured on video to indicate where failure initiated. Thirty three

milliseconds between video frames was clearly too long to capture the failure event, one frame showed a complete tank and the next showed no tank left!

Tank #4 had an estimated internal volume at ambient pressure of 8,600 in³ (or 8,800 in³ at 5,000 psi working pressure). The tank weight was 52.8 lb (excluding 1.2 lb of fiberglass used to hold a label). This corresponds to a burst performance factor (P_bV/W) of 1.74 million inches (44.3 km) or 11.3% H₂ by weight. However, the safety factor of this design is only 2.09 compared to 2.25, if tanks identical to Tank #4 were operated at 5000 psig. This roughly 7% loss in performance is significant, and the data remaining from the burst test of Tank #4 was insufficient to resolve how the performance was lost or what to do in order to recover it.

The unsatisfactory state of understanding after Tank #4 burst would have left this highly visible research effort inconclusive. IMPCO Technologies agreed to pay for design and test of Tank #5 as a means of helping the entire DOE-funded tankage program and acquiring technology from Thiokol Propulsion, who recently became their strategic partner. Therefore, the final report from Thiokol to LLNL (Appendix 1) only discusses Tanks #1-4.

Design of Tank #5 explored numerous options, but ended up close to the design of Tank #4 to minimize the risk of new problems. A single additional hoop wrap was added to bring the new design towards the desired burst pressure with a slight improvement in projected P_bV/W . Higher speed video (~400 frame/second compared to the ~30 frame/second that was affordable for earlier testing of Tanks #3, #1, and #4), redundant pressure and strain sensors, “belly band” sensors at both tangent lines and mid-tank, and standard test video were all used to monitor the burst of Tank #5.



Figure 5 – Condition of Tank #5 before Highly-Instrumented Burst Test

Figure 5 shows the initial condition for the burst test of Tank #5. It was digitized from the early frames captured by one of six high speed cameras employed in this highly instrumented test. These six cameras were set up to record ~400 frames/second and were run in pairs, with slight overlap to ensure that both sides of the tank under test were covered for almost 3000 psi of final filling time at the pumping rate of Thiokol Test Slab #9. These cameras were fast enough to capture the failure event that was missed during the burst of Tank #4. Many frames from the middle pair of cameras show water being ejected and the painted grid (visible on the outside of tank, with 2 inch grid spacing, in Figure 5), but the frame shown in Figure 6 best shows the failure event. As with tank #4, very little for Tank #5 remained after burst, and 30 frame/second video was useless because the tank failed in less than the two frames of the high speed camera (~5 milliseconds). Expert observers were impressed by the speed and thoroughness of the burst.

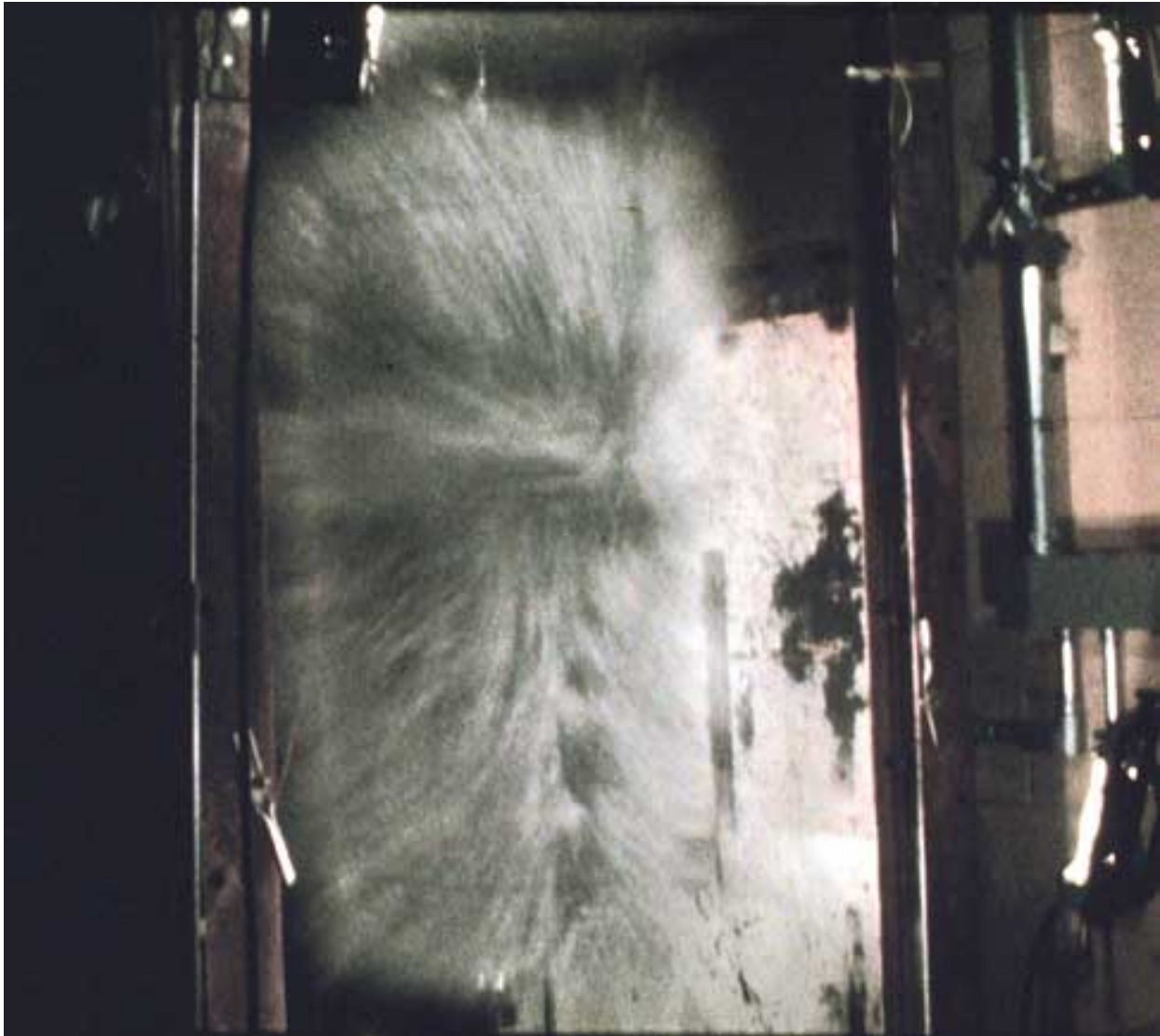


Figure 6 – Best High Speed Camera Frame Captures Tank #5 At Burst

Figure 6 shows the burst of Tank #5 on July 13, 2000. Performance was again ~7% below the performance that was expected for T1000G fiber, quite consistent with the results from Tank #4. Although it is not clear what caused this ~7% performance loss, it may be due to the pressurization sequence used for winding on inflatable mandrels that has not yet been optimized. The additional hoop wrap in Tank #5 delivered increased burst pressure, with comparable volume, and increased weight (compared to Tank #4). The burst pressure was 95.55% of the 11,250 psig design. Tank #5 had a comparable P_bV/W to Tank #4, but the measurement errors are known more precisely (specifically the internal volume measurement).

The importance of this published record, prompted LLNL researchers to seek traceable accuracy on all the measurements reported and inferred in Table 1. If the service pressure for Tank #5 is considered to be 5,000 psig, then the safety factor is only 2.15 (as opposed to the desired 2.25). The percent hydrogen by weight and specific energy shown in Table 1 assumed a service pressure of 4777 psig (32.94 MPa) to keep the safety factor fixed at 2.25.

Table 1. 11.3% H₂ by Weight was Demonstrated for a High Cycle Life Cylinder

| Performance Variable | Unit | Measurement | Std. Deviation | 3 Sigma Error |
|---|-----------------|--------------|----------------|---------------|
| Burst Pressure (P _b) | psig | 10,749 | 14 | 42 |
| Internal Volume at 5000 psig (V) | in ³ | 8,758 | 7.6 | 23 |
| Tank Weight (W) | lb | 54.0 | 0.018 | 0.054 |
| Performance Factor P _b V/W | inch | 1.743 E6 | 0.0028 E6 | 0.0083 E6 |
| Specific Energy (tank + H ₂ , LHV) | Wh/lb | 1708 | 2.4 | 7.3 |
| Percent Hydrogen by Weight | % | 11.31 | 0.016 | 0.048 |

| Performance Variable | SI Unit | Measurement | Std. Deviation | 3 Sigma Error |
|---|----------------|--------------|----------------|---------------|
| Burst Pressure (P _b) | Pa | 74.112 E6 | 0.097 E6 | 0.290 E6 |
| Internal Volume at 34.5 E6 Pa (V) | m ³ | 0.1435 | 0.00013 | 0.00038 |
| Tank Weight (W) | N | 240.2 | 0.080 | 0.240 |
| Performance Factor P _b V/W | m | 44.27 E3 | 0.070 E3 | 0.211 E3 |
| Specific Energy (tank + H ₂ , LHV) | Wh/kg | 3767 | 5.2 | 16 |
| Percent Hydrogen by Weight | % | 11.31 | 0.016 | 0.048 |

Considerable discussion and several alternative approaches were considered to calculate tank internal volume at service pressure. IMPCO makes use of a superior and simple technique to measure water volume by weighing additional water before it is pumped into a tank being hydrotested to maximum expected operating pressure (MEOP). Since Thiokol test facilities were not rapidly reconfigured to weigh the water going in to their high pressure pump, the entire tank was weighed by a load cell during its cycle through proof pressure, and weight was noted particularly at MEOP of 5000 psig. Internal volume calculations at 5000 psig were performed using the methodology described by the Compressed Gas Association (CGA 1996). The volume calculations using this methodology were within 1% of volume estimated by Thiokol design codes, and within 1% of geometry models used by LLNL spreadsheets. All the error analysis of measured and derived performance parameters given above assumes Gaussian-distributed independent random error contributions from multiple calibrated error processes in each sensor/instrument employed.

Although the volume of Tank #4 is expected to be very similar to that of Tank #5, it was not measured directly with water. If the volume measurement from Tank #5 (8758 in³ at 5000 psig) is used for Tank #4, instead of the 8800 in³ estimated by geometry and strain, then the P_bV/W for Tank #4 is 1.74 E6 inch (44.1 km). By this criterion, the percent hydrogen by weight for Tank #4 is 11.2%.

Recommendations based on preliminary fact-finding after the Tank #5 burst test are still being developed in detail. A list of suggestions is included in the final section (Conclusion and Recommendations).

More detail on the recent progress in this task is in the report from Thiokol Propulsion to LLNL, which is included as Appendix 1.

2. Specify a ~1 yr program to certify tankage with 7.5-8.5% hydrogen by weight (5000 psi, 300 K, SF 2.25). Write, modify, and review a solicitation to develop lightweight hydrogen tankage. Technically direct the program that commenced in May 2000 (IMPCO Technologies).

The technical advantages of lightweight pressure vessels for vehicular hydrogen storage are not in doubt, but eventual adoption depends on high volume price reductions as well as public acceptance. Industrial partners are vital to the production of near-term tank technologies in quantities sufficient to support demonstration projects. Only tank technologies that can be reduced to commercial manufacturability over the next year or two can advance the entire hydrogen powered vehicle effort through the integration phases that lead to vehicle demonstrations and public acceptance. Two DOE funded demonstration vehicle projects are almost ready to adopt such near-term lightweight pressure vessels for onboard hydrogen storage. DOE/Golden contract DE-AC36-GO10494 that LLNL is directing will demonstrate vehicle ranges acceptable to the public.

Because of the low density of hydrogen, tanks that give acceptable range are difficult to fit within existing vehicle designs. The problem of how to best accommodate hydrogen storage aboard vehicles has generated numerous solutions over the past few years. DTI has extensive experience working on this problem for Ford, and has advocated a single large tank under the rear seat for a Ford demonstration vehicle. Figure 7 illustrates some of the packing issues DTI captured in the specification process for tankage and suggested to LLNL roughly two years ago, which led LLNL to direct its research toward the 18 inch diameter by 48 inch length tankage that was explored by the research effort described in Task #1.

Single Cylinder is Lowest Tankage System Cost & Complexity but Requires Car to be Designed from the Ground Up with that Priority

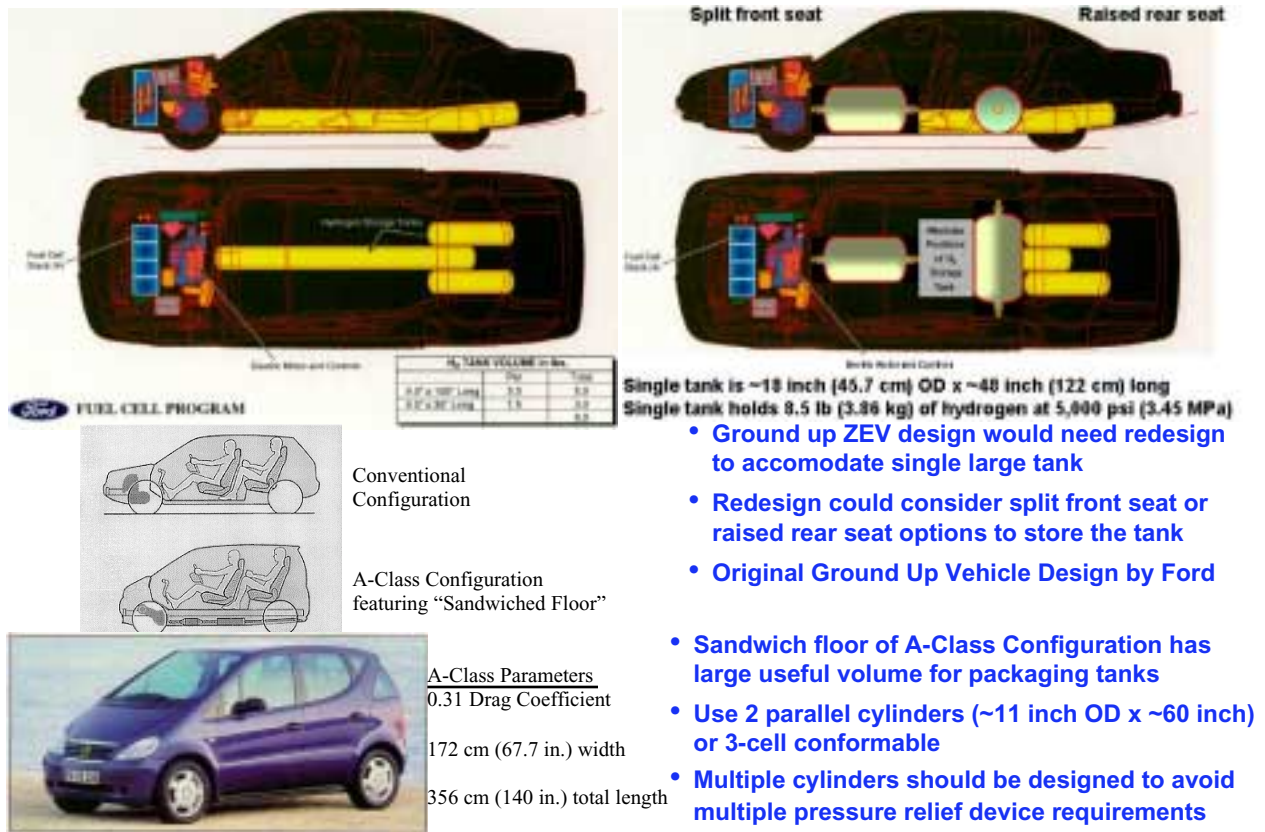


Figure 7 – Tank Size and Location Considerations for Vehicular H₂ Storage

Figure 7 illustrates the problem of packing 3.6 kg of hydrogen at 5000 psi into a passenger car, if sufficient volume has not been designed in from the ground up. A single large cylinder (~46 cm OD x 122 cm long) can be placed under a raised rear seat or between split front seats. Alternatively a ~30 cm OD x ~270 cm long tank can run the length of the car. If the OD is kept to ~30 cm or less, packaging can be done into a sandwich floor construction, like that found in the A-Class configuration. Preliminary design information on GM’s recently unveiled hydrogen-powered Opal appears to use a similar under-the-floor tank configuration.

Besides finding the volume for both tanks and passengers, a complex number of safety and regulation issues remain to be resolved before new hydrogen storage technology can be deployed in widespread applications. The first demonstration vehicle project for lightweight tanks is the Nevada Bus project, which operated as the Savannah River bus in previous years. Any moderate advance in Type IV hydrogen pressure vessels will give this bus a significant range increase.

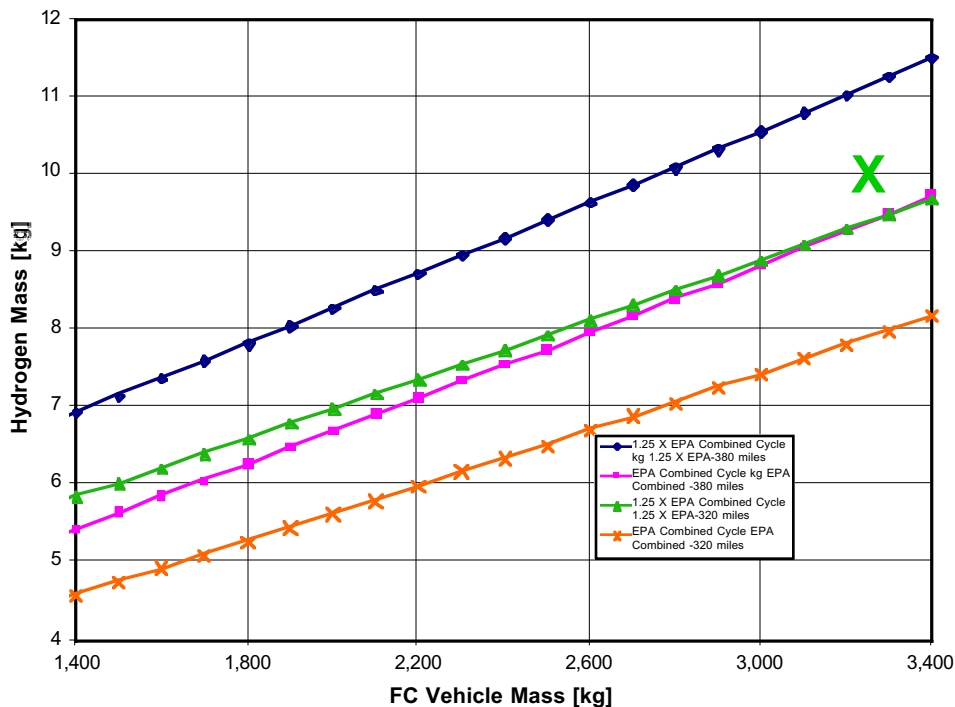
Design of near-term producible tanks for DOE to solicit from industry for the Nevada Bus project was straightforward because the demonstration vehicle project is already underway (linked to a DOE hydrogen infrastructure demonstration in Las Vegas), and because it can accept and benefit from uncertified tanks that provide a modest advance in performance. Plenty of room on the roof of the bus avoided many of the cramped vehicle configuration issues posed by modifying existing automobiles. Various configurations of rooftop tankage this demonstration

vehicle might install are shown in the brief discussion of Task #6. Essentially all of the vehicle installation design for this project was supplied by the Nevada Bus team, once LLNL decided in the interests of delivery time to base early phases of the DOE 2000 tankage solicitation on existing 18 inch tooling.

The other DOE hydrogen vehicle demonstration project that LLNL specified when the DOE tankage solicitation was written in early FY00 is known as FutureTruck, and it involved much more design attention. This SUV is bigger than a car, but still based on an existing automotive design, and its range will be set by to the amount of hydrogen that can be stored onboard. Volume constraints in the underside of the SUV chosen for FutureTruck limit the tank outside diameter to ~11 inches, as opposed to the 18 inch diameter tooling that was already available. Since new tooling will be required, initial lightweight tankage developments will be done for delivery to the Nevada Bus program on existing tooling.

Extensive assistance from DTI, General Motors, and Argonne National Laboratory staff who oversee the FutureTruck competition helped in setting the tank design requirements. Foremost was the specification of the amount of hydrogen such a heavy vehicle (3265 kg ‘curb’ weight) would need to carry. DTI performed the sizing analyses that are shown in Figure 8. Due to volume constraints and a programmatic desire to keep maximum storage pressure to 5000 psi (35 MPa), LLNL chose a configuration with ~10 kg hydrogen storage (marked with a green X on Figure 8). This specification should enable modified SUVs to exceed the minimum requirement of 320 mile range (assuming 1.25 x EPA Combined driving cycle).

DTI analysis of H₂ mass requirement vs. FC vehicle mass



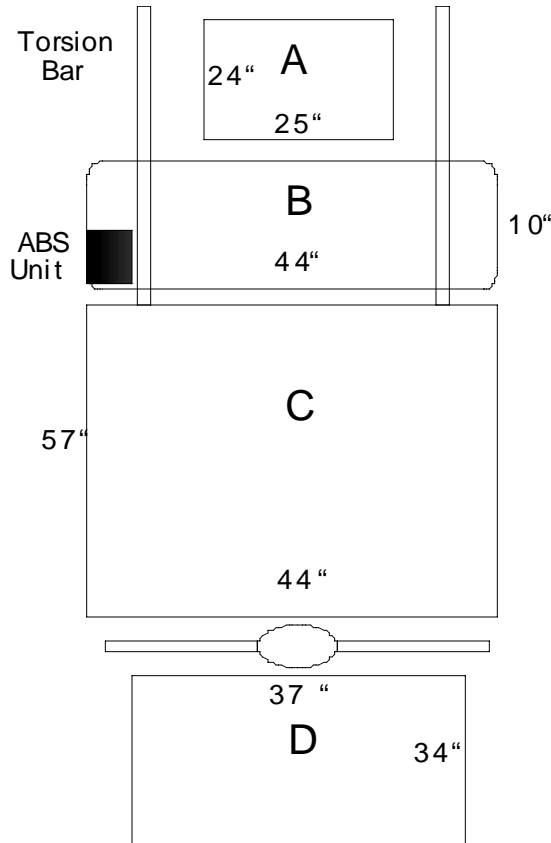
X – Design point for GMT 830 K 15906 (3265 kg GVW prior to retrofit)

Figure 8 – Hydrogen Requirements for FutureTruck

After selecting the amount of hydrogen FutureTrucks ought to carry, a level playing field among solicitation bidders required the detailed specification of tank sizes and masses. Mass specifications were set to percent hydrogen by weight levels that would be truly enabling for hydrogen fueled vehicles, that were still low enough to give multiple bidders high likelihood of developing safety certifiable tanks in the short time available (before the FutureTruck competitions moved on to a different vehicle design in 2002). LLNL's earlier experience with the DOE/Ford demonstration project argued strongly against trying to hit a moving target whose geometric requirements could be very different, and thus technical ambition on these tanks was held to 8.5% hydrogen by weight in order to deliver certified tanks with >90% probability early enough for at least two competing teams to integrate on their vehicles (before May 2001, with the contest scheduled in July 2001).

Because the academic teams modifying FutureTrucks do not have the engineering manpower resources to undertake safety modifications, tanks delivered by the solicitation had to be fully safety certified before delivery to avoid any DOE liability. Although LLNL is advocating modification of the hydrogen safety standard for permeation (as discussed below in Task #7), the success of that advocacy could not be foretold when the solicitation was written, so its terms merely include the possibility of relaxing the required hydrogen loss rate in this one safety test. Similar safety uncertainties precluded installing hydrogen tanks anywhere besides inside a raised vehicle floor, since roll and side-impact safety could not have been developed within available human resources and time. With sufficient installation engineering manpower, some of the experts in LLNL-directed conference calls with ANL and GM would have preferred roof mounted tanks.

Figure 9 summarizes the tank placement issues that constrain possible tank geometries for FutureTruck SUVs modified to store ~10 kg of hydrogen. Although lifting the vehicle with an after-market "lift kit" modification was a straightforward way to gain safely in tank diameter, safe ground clearance and a maximum GM-recommended lift of 3 inch restricted under-the-floor tank outside diameters to ~11 inch. It initially appeared that tanks must occupy most of the crowded volume inside the vehicle frame shown below in Figure 10 in order to store 10 kg of hydrogen at 5000 psi. LLNL experts designing the solicitation sought interest in higher pressure designs from both auto manufacturers and FutureTruck contest staff, but late in 1999 the hydrogen demonstration vehicle community remained skeptical of pressure ratings above 5000 psi. By mid-2000 this situation has changed dramatically, and can only be mentioned briefly in the discussion of Task #5 below because an increased scope for the ongoing solicitation is being prepared as this report goes to 'press'.



Area 'A' would require **removing the Transmission and Transfer case**, but without a prop shaft - what good are they anyway? The assumption here being at least two motors (1 driving each axle). **Redesign of the Transmission crossmember** is required to allow for tanks to pass further forward in the chassis.

Area 'B' would require moving the Torsion bar hanging cross member and the tank shield. These would need to be relocated forward and reattached. This requires **new torsion bars** (due to the change in length). The **ABS unit would need to be relocated** as well, but without the converters from the IC engine, there should be room.

Area 'C' in the Diagram is currently available with **removal of the Prop shaft and Exhaust**. There needs to be some additional dimensional checking to insure that the 11" OD tanks would not protrude beneath the frame line.

Lifting a "Body on Frame" vehicle is not a difficult design task, and after-market companies will most likely have kits available very soon.

Area 'D' would require **relocating the spare tire**. A very simple design change, though probably not as pleasing to the Marketing group. Also the volume in area 'D' may not allow use of the 11" diameter tank.

Figure 9 – Hydrogen Tankage Placement Issues for FutureTruck

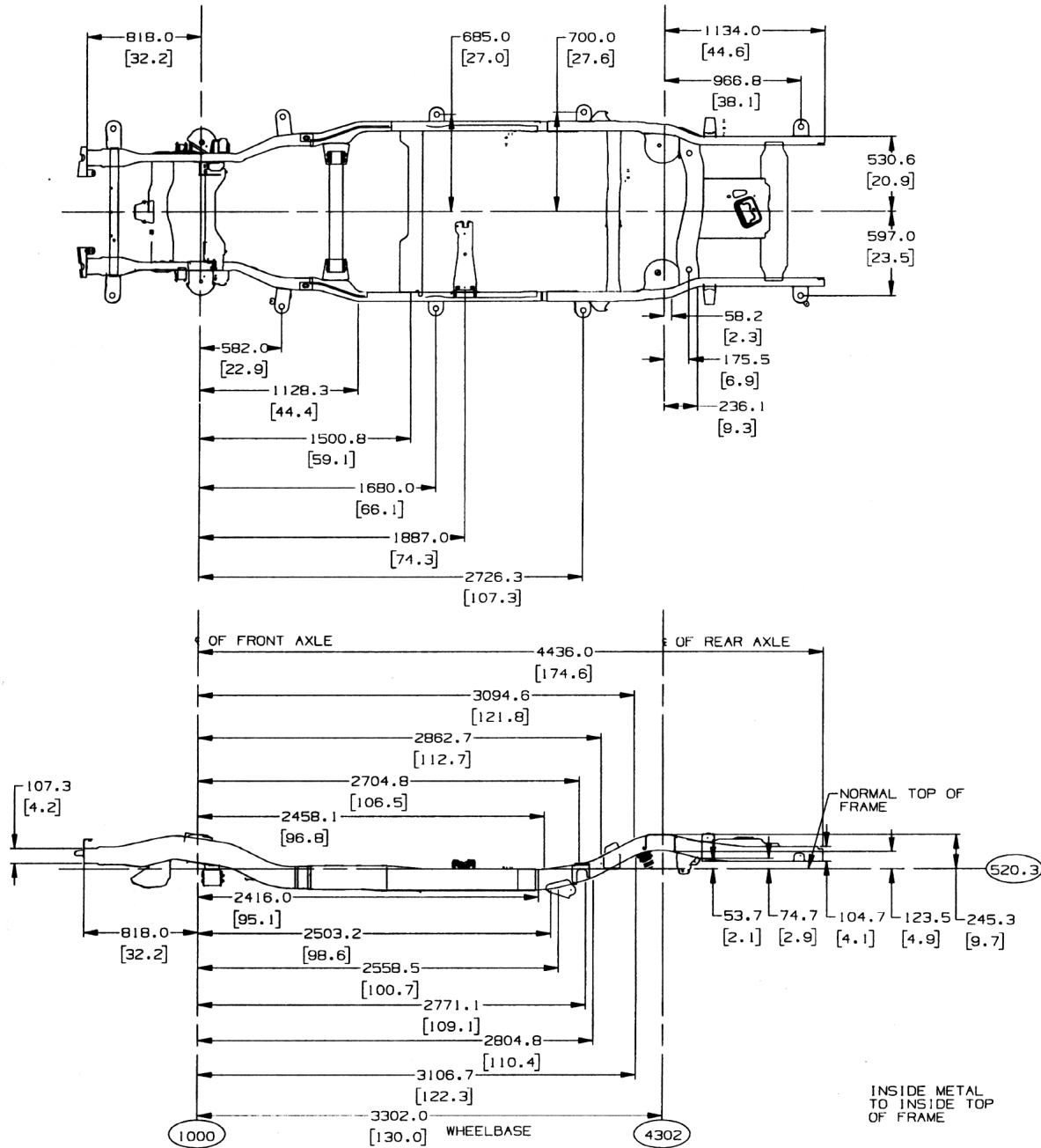


Figure 10 – Preliminary GM Suburban Rail and Crossmember Arrangement

Some cleverness and detailed consideration of the certification requirements of two tank designs that differ only in length allowed two length specifications to join with the 11 inch maximum diameter specification and totally describe the shape of tanks that multiple bidders would be required to quote. This pair of lengths contains the requisite 10 kg of hydrogen in four tanks with MEOP of 5000 psi, in the configuration shown below on Figure 11.

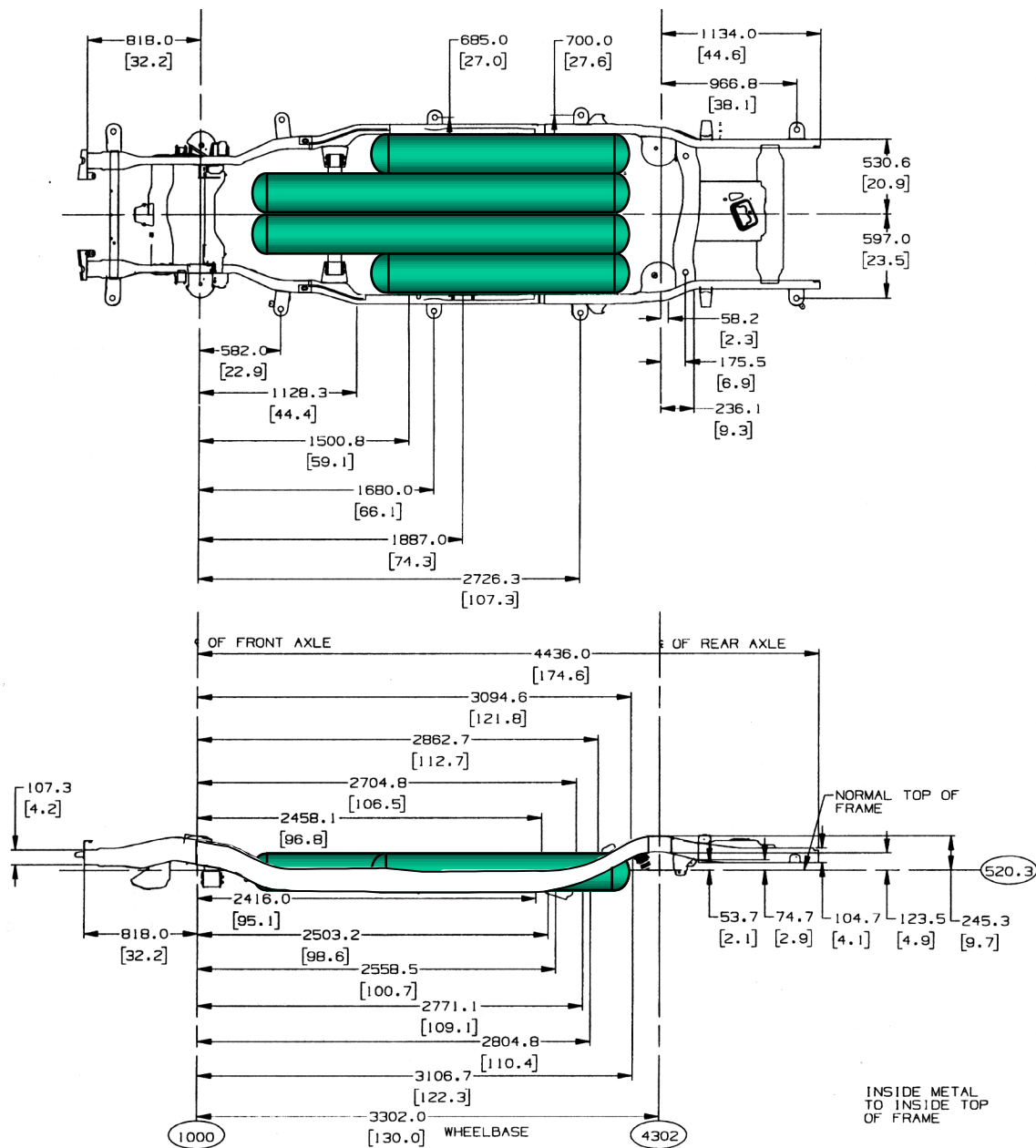


Figure 11 – Proposed H₂ Tank Placement for FutureTruck (GMT 830 K 15906)

Many other considerations applied to the design of tanks and program. These had to be captured in the requirements wording of the Solicitation itself. Figure 12 below reproduces the crucial information from the Solicitation, which assembled all specifications for the four phases chosen to structure this effort. The desire to solicit competing bidders precluded contract language that would have allowed non-cylindrical pressure vessels to occupy the same tank envelopes. Since only Thiokol would be able to deliver such ‘conformable’ tank technology (Golde 1999, Haaland 2000), its advantages for hydrogen storage were specifically not addressed by this solicitation. Thiokol did not respond to the Solicitation directly.

Carbon fiber cost barriers and perceived safety risks and consumers' desire for vehicle ranges typical of gasoline powered vehicles are issues that apply to conformable as well as cylindrical tanks. Although cylindrical tanks could provide lighter weight, less expensive storage, the design traditions and existing practices/tooling/workforce puts significant burdens on the kind of "ground up" vehicle design that could benefit from single large cylinders of the sort DTI advocated in 1998, for which LLNL had already developed advanced, government-owned tooling.

The scheduling of four phases was very tight, allowing the bare minimum of time to innovate on cylindrical tank mass performance, test to reduce risks of failing safety certification, and then produce batches large enough to deliver multiple test articles to the demonstration projects after 14 identically-manufactured tanks pass safety certification tests. The lower performance Nevada Bus phases were designed to accelerate learning and deliver the lessons of manufacturing and testing from the easier first two phases to the more challenging mass performance requirements of the final two (FutureTruck) development phases. Man months of detailed attention, rewritings, and conference calls between LLNL and the DOE/Golden contracting office further stress this contracts schedule with the real work of hammering out a Federal Contract.

| | Phase 1 | Phase 2 | Phase 3 | Phase 4 |
|---|-------------------------|-------------------------------|--|------------------------------------|
| Vehicle requiring tanks | Nevada Bus | | FutureTruck | |
| Acquired Tank Generation | First Generation | | Second Generation | |
| Phase Begins | Apr '00 | Oct '00 | Oct '00 | Jan '01 |
| Mission of Phase | Risk Reduction, Tooling | NGV2 certify for H2, Demo Bus | Risk Reduction, New Tooling | NGV2 certify for H2, Demo Suburban |
| Tank Diameter (O.D.) | 18 inch (46 cm) | | 11 inch (28 cm) | |
| Tank Length (approximate) | 48 inch (122 cm) | | 69 inch (175 cm) (A) 93 inch (236 cm) (B) | |
| Tank Service Pressure | 5,000 psi (34.5 MPa) | | 5,000 psi (34.5 MPa) | |
| Burst Pressure (minimum) | 11,250 psi (77.6 MPa) | | 11,250 psi (77.6 MPa) | |
| Hydrogen Contained (34.5 MPa, 300 K) | 7.9 lb (3.6 kg) | | 4.6 lb (2.1 kg) 6.3 lb (2.9 kg) | |
| Quantity of Tanks Produced | 10 | 22 | 10 (A) 4 (B) | 20 (A) 8 (B) |
| Quantity of Tanks Tested | 10 | 14 | 10 (A) 4 (B) | 14 (A) 2 (B) |
| Minimum %H ₂ by weight (34.5 MPa, 300 K) | 7.5% | | 8.5% | |

(A) Applicable to the 69-inch length

(B) Applicable to the 93-inch length

Figure 12 – H₂ Tankage for Nevada Bus Program and FutureTruck Competition

Figure 12 compresses the contractual requirements of four phases into a concise list of technical requirements. Many other contractual clauses had to be adapted from standard government practice. Economic performance of the resulting tankage was not included explicitly in the solicitation, but plays a strong implicit role due to the “modified step-and-half” form of Solicitation that the LLNL/Golden team chose. That form awarded the contract to the lowest bidder only after bidders had been downselected for competence to deliver the very stringent technical requirements. Low cost manufacturers would win this solicitation, but only if they were capable of delivering the requisite high (7.5% and 8.5% hydrogen by weight) mass performance requirements.

This contract was awarded to a team of IMPCO and Thiokol in May of 2000. Since that time, considerable technology transfer has infused IMPCO's future product line with Thiokol's aerospace (high performance) tank fabrication expertise, and the transfer of LLNL thin-wall rotational molded liner technology into Phase 1 efforts is proceeding on schedule. A loan agreement (LLNL Loan Agreement # 101-2485) was generated to enable IMPCO to borrow and modify the government-owned mold, which is being supplied as government furnished equipment. A preliminary design for the boss and shell of tanks in Phase I has been established. Capital equipment for testing and fabrication has been specified and ordered. Process trials with tow-preg materials (Thiokol Propulsion's method of winding) have commenced at IMPCO. The high probability of success plans built into the solicited tank development program production and test schedules are on track, and should soon be generating risk reduction test data such as the extra stringent (hydrogen fill not required by safety certification) bullet test conducted and passed by Thiokol on one of their conformable tanks shown in Figure 13. The Thiokol conformable tank program was technically directed by LLNL and is discussed in (Haaland-2000).



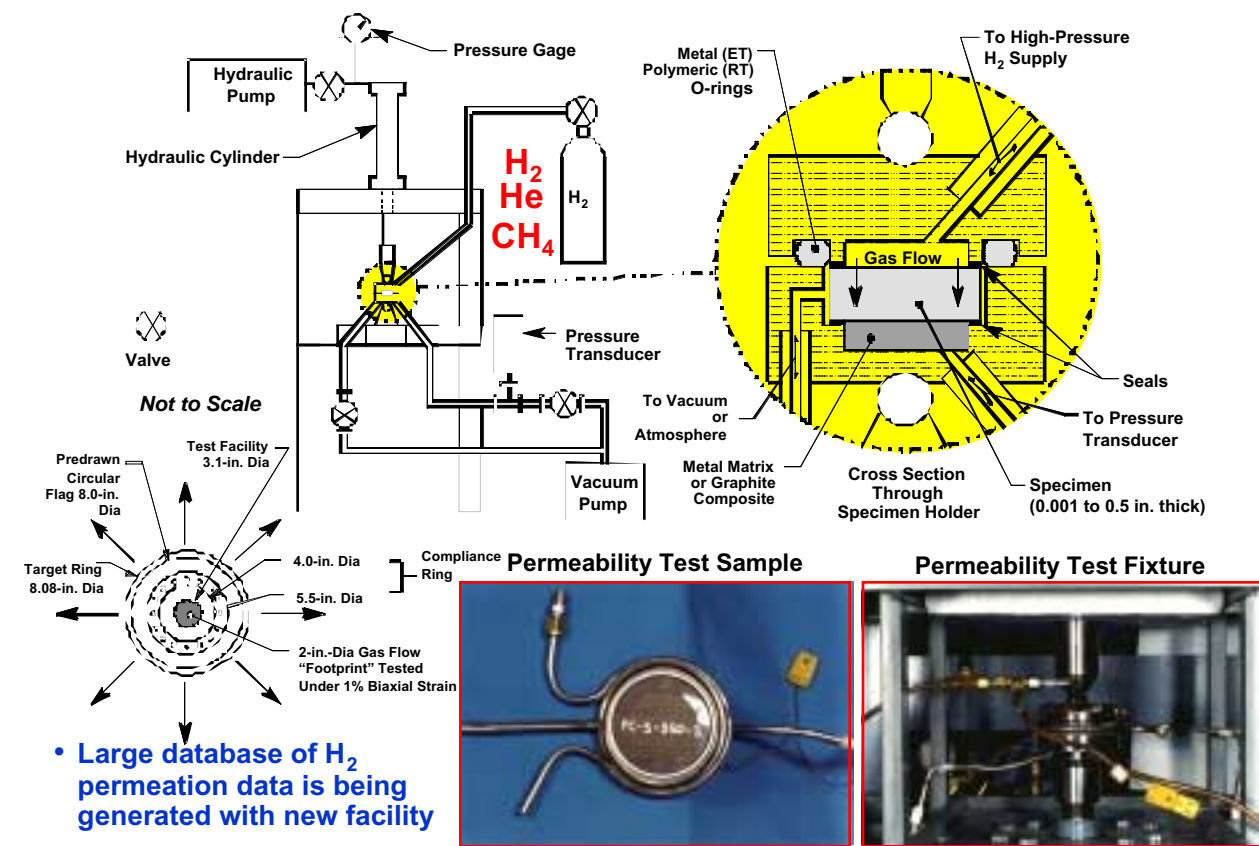
.030 caliber armor piercing bullet impact at 45° to one cell side wall of a conformable tank pressurized to 5000 psi (34.5 MPa) using hydrogen gas caused **no fragmentation failure**

Test with 5000 psi Hydrogen – No Deflagration

Figure 13 – Conformable Tankage Fabricated by Thiokol Passed Bullet-Test

3. Develop a lightweight liner fabrication process and permeation reduction coatings that are easily adopted by industry. Optimize fabrication of variable thickness rotomolded liners. Develop metal and plastic permeation coatings, permeation test coatings, fabricate tanks with coated liners (if funding permits).

The LLNL effort to develop the next generation of advanced hydrogen tankage was able to take advantage of existing SRI capability to further a broader understanding of hydrogen permeability. Thiokol internally funded (in 1998-1999) a new facility at SRI capable of permeation testing at high pressure (up to 5000 psi or 34.5 MPa) with hydrogen, as well as an unprecedented fixturing arrangement that enabled the first-ever collection of permeation test data under controllable biaxial strain at the levels anticipated in tank liner service (Golde 1999, Haaland 2000). This test capability has been made available with Thiokol's permission for LLNL research, and is illustrated in Figure 14.



Tests with gas ΔP up to 5 ksi (34.5 MPa) as a function of temperature & biaxial strain

Figure 14 – Schematic and Photos of Permeability Test Fixture at SRI

LLNL took advantage of an earlier hiatus in Thiokol's testing to procure ASTM-traceable calibration for all subsequent measurements, confirming previous measurements made at LLNL on LLNL-developed liners. LLNL, the USAF, and Thiokol IR&D funded significant additional hydrogen permeation testing on a variety of candidate liner materials, as a function of pressure (Mitlitsky 2000, Mitlitsky 1999-a,b,e, Souers 1986). The graph in Figure 15 not only confirms the hydrogen permeability of several previously employed liner materials, it extends the sparse earlier results to a much wider range of pressures, temperatures, and materials. This new

database, and the literature survey summarized in (Mitlitsky-1999) have been used to assess many relevant materials' acceptability as thin liners for high pressure tankage. Downselection is currently proceeding in parallel with rotational molding process development to produce LLNL's next generation of advanced liners (sufficient to enable DOE 2000 Goals).

A permeability of 1×10^{-14} corresponds to a "half-life" of 6 months for 0.15 inch (3.8 mm) thick liner

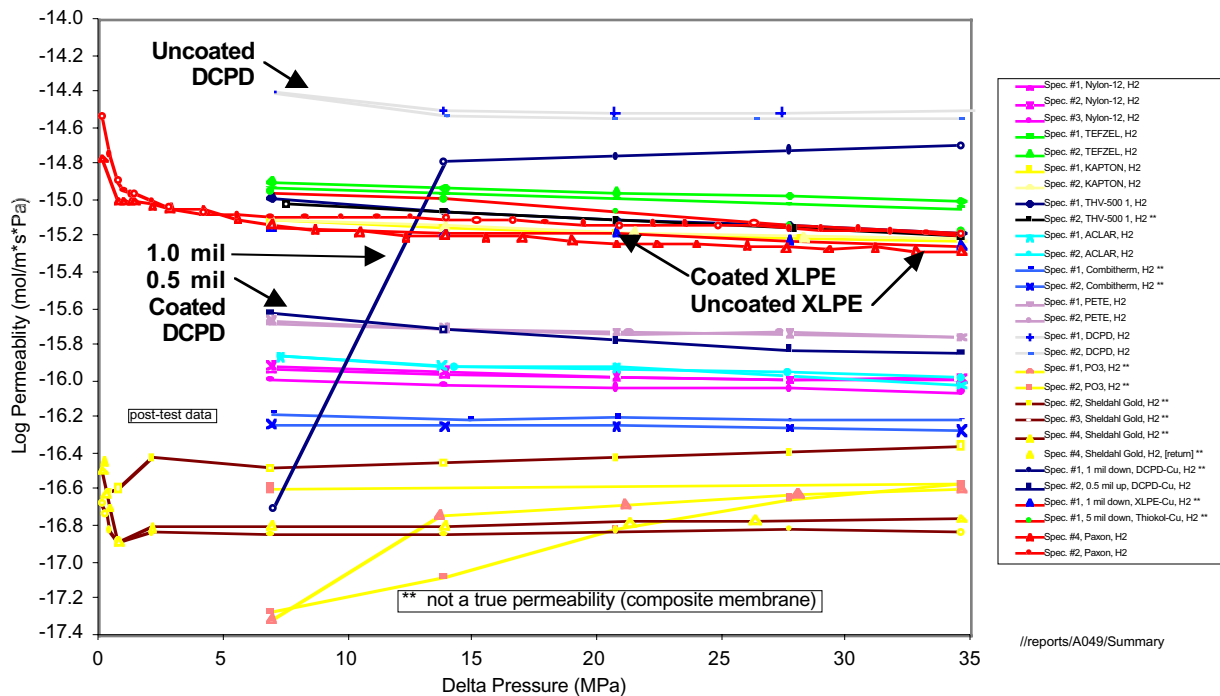


Figure 15 – Measured Hydrogen Permeability of Several Candidate Liner Materials

Metalized samples of dicyclopentadiene (DCPD) and cross-linked polyethylene (XLPE) that were manufactured by Epner Technology were subjected to permeation testing at Southern Research Institute (SRI). Metalized samples of XLPE that were manufactured by Thiokol were also tested at SRI. All samples were screened for pinholes using bright light illumination through the back of the samples. All of the XLPE samples from Epner Technology and two of the DCPD (one of the 0.5 mil thick and one of the 1.0 mil thick metal coated) samples have visible holes/cracks through the coating as detected with back lighting. SRI measured one of the remaining 1.0 mil thick metal-coated DCPD samples that has no visible holes. This sample showed a ~2 order-of-magnitude decrease in H₂ permeation at 1000 psi (7 MPa) delta-pressure compared with an uncoated DCPD sample. However, at 2000-5000 psi (14-35 MPa), the sample showed only modest improvement compared to uncoated DCPD samples. The curve from this sample is labeled in Figure 15 “1.0 mil Coated DCPD” and shows a rapid rise in log permeability as a function of pressure between 7 and 14 MPa.

Examination of the metalized sample when removed from the permeation test rig showed that trapped H₂ bubbles between the DCPD and the film caused delamination and tearing of the film. The tearing is consistent with the 2 order of magnitude increase in permeation measured at 2000 psi (14 MPa) compared to 1000 psi (7 MPa) delta-pressure.

Metal-coated XLPE samples from Thiokol did not appear to have pinholes when examined with bright light illumination through the backside. Permeation testing of metal-coated XLPE samples from Thiokol did not show an improvement compared to uncoated XLPE at any delta-pressures that were measured (7-35 MPa). Examination of the metalized XLPE sample when removed from the permeation test rig showed that trapped H₂ bubbles between the XLPE and the film caused delamination and tearing of the film, which must have occurred at delta-pressure below 1000 psi (7 MPa). Both of these metalized substrates were measured with the metal coating toward vacuum (high pressure applied from the uncoated side of the substrate).

LLNL and SRI decided to test the 0.5 mil thick metalized DCPD substrate with the metal oriented towards the high pressure H₂ supply (uncoated side of the substrate towards vacuum). This sample showed > 1 order-of-magnitude reduction in H₂ permeation at all pressures from 1000-5000 psi (7-35 MPa). There were no signs of film delamination or tearing when this sample was removed from the permeation test rig. This sample serves as an existence proof that metalization of plastic samples (such as DCPD) can achieve sufficiently low H₂ permeation at 5000 psi (35 MPa) to enable thin liners (< 3 mm thickness) to meet the stringent permeation specifications that have been proposed for hydrogen pressure vessels. This experiment also shows that initial pressure cycling of such a metal coated plastic sample does not fail the permeation reduction capability of the coating.

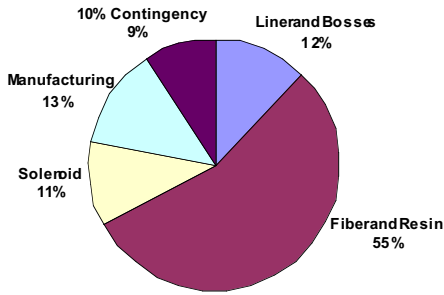
Designs of lightweight tankage using metal-plated molded plastic liners were further refined using the latest results from coating experiments and permeation tests. Methods for addressing issues of liner shrinkage during cure were successfully. Specifically, a post-annealing step of the liners prior to metalization was performed on an additional set of liners procured by LLNL and fabricated by ATL. A cross-linked polyethylene (XLPE) liner (12 inch diameter x 20 inch length) was prepared and coated with a permeation reduction coating by Thiokol Propulsion in May. This work will be put on hold until additional funds are available.

4. Develop lightweight hydrogen tankage with SF 2.25 and capture cost projections from DOE tank solicitations. Demonstrate plastic lined composite tankage (cylinders and conformable) with safety factor 2.25.

Lightweight tank liners enable weight goals to be achieved with less expensive fiber. Tankage with safety factor of 2.25 uses ~75% of the fiber required for tankage with safety factor of 3. Since fiber cost dominates tankage cost, it is important to keep the safety factor low, while improving storage system safety in other ways. Revised economic evaluations are summarized in Figure 16, and show that high volume tankage (>500,000 unit per year) will cost ~\$640/unit for tanks that hold 3.6 kg H₂ at 5,000 psi service pressure using T700S carbon fiber (assuming \$6/lb cost of fiber). This result is significant because tankage now appears to be both less expensive and lighter weight when using T700S (at \$6/lb fiber), compared to Panex-33 (at \$5/lb fiber) because the strength-to-weight advantage of T700S requires sufficiently less fiber per tank to more than compensate for its higher cost per pound.

- Economic evaluations have been performed in conjunction with Thiokol Propulsion, Directed Technologies Inc. (DTI), Toray Composites, and colleagues at LLNL.
- The major cost driver is the cost of various grades of carbon fiber; large uncertainties remain in the projected fiber costs that may be achievable with high volume production, especially for T1000G (currently the highest strength-to-weight carbon fiber commercially available).
- Although use of T1000G will result in the lightest weight tanks, its current cost of ~\$70/lb (\$154/kg) must be compared to lower strength/less expensive carbon fibers, such as M30SC with current cost of ~\$28/lb (\$62/kg), or even lower strength/less expensive fibers, such as T700S with current cost of \$9-14/lb (\$20-31/kg) or Panex-33 with current cost of ~\$6-6.5/lb (\$13-14/kg).
- High volume cost projections for these fibers (500,000 units/yr) have been estimated by DTI (with new input from manufacturers) to be \$15-25/lb (\$33-55/kg) for T1000G (<\$40/lb will be very difficult according to Toray), \$6-7/lb (\$13-15/kg) for T700S, and ~\$5/lb (\$11/kg) for Panex-33; M30SC would have an estimated high volume cost of \$15-20/lb (\$33-44/kg).
- Assuming Panex-33 at \$5/lb (\$11/kg) with a high density polyethylene (HDPE) liner, the cost of a tank that is capable of storing 8.0 lb (3.6 kg) of hydrogen has been estimated by DTI to be \$841 (\$78 for liner and bosses, \$500 for fiber & resin, \$69 for solenoid, \$117 for manufacturing, and a 10% cost contingency).
- These assumptions project costs of \$105/lb (\$231/kg) of hydrogen stored or \$6.93/kWh.
- Repeating this analysis for a tank with similar capacity using new cost estimates for T700S, assuming a fiber cost of \$6/lb (\$13/kg), the estimated tank cost in high volume production would be ~\$640/unit (~\$80/lb or ~\$176/kg of hydrogen stored or ~\$5.28/kWh).

Tank Cost Breakdown (T700S)



Direct H2 Fuel Tank Subsystem

3.58 kg (7.9 lb) of H2 at 34.5 MPa (5,000 psi) stored in carbon fiber tank, integral solenoid and pressure relief device (PRD)

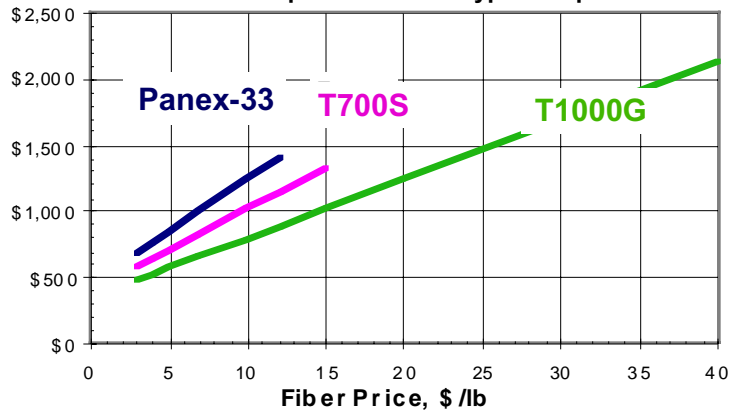
| | |
|-----------------------|-------------|
| Liner and Bosses | \$78 |
| Fiber & Resin | \$352 |
| Solenoid | \$69 |
| Manufacturing | \$83 |
| 10 % Cost Contingency | <u>\$58</u> |

Tank System Cost **\$640**

Major Assumptions

- Use Toray T700S carbon fiber with manufacturer projected future price of **\$6/lb**
- Pressure vessels overwrapped on HDPE liner
- High production volume manufacturing (500,000 units/year)

Tank System Cost (pressure vessel & solenoid) as a function of fiber price with fiber type as a parameter



| Fiber Type | Current Price \$/lb | Projected Price \$/lb |
|------------|---------------------|-----------------------|
| Panex-33 | 6-6.5 | 5 |
| T700S | 9-14 | 6-7 |
| M30SC | 28 | 15-20 |
| T1000G | 70 | 15-25 (40) |

- Tank System Cost of **\$640** corresponds to **\$5.28/kWh** (DOE 2000 goal was **\$20/kWh**)
- Tank System Cost of **\$1015** corresponds to **\$8.24/kWh** using similar assumptions for **T1000G** with a future price of **\$15/lb**

Figure 16 – Economic Analysis of Carbon Fiber Tanks in High Volume Production

5. Technically direct a 10,000 psi (69 MPa) tankage development effort (pending a DOE/OTT funding award and/or additions to the current DOE/Golden contract DE-AC36-GO10494).

Addition of phases 5-8 to the four phase DOE/Golden contract DE-AC36-GO10494 has been discussed with the sponsor. Modifications to the technical specifications for that contract's Phases 1 through 4 allow timely development of 10,000 psi, safety-certifiable tanks that can drop in to a modified FutureTruck vehicle, and either extend the projected range by up to 2/3 or allow a 3-tank configuration (instead of 4), with all tanks chosen to be the same ~69 inch length (instead of the 2 different lengths chosen for the configuration shown in Figure 11). Design of the new phases includes the development and certification of in-tank regulator/valve/pressure-relief devices rated for 5,000 psi and 10,000 psi service. These ancillaries will contribute significantly to the safety of demonstration projects by sparing project team members the rigors of designing and protecting such high pressure plumbing. A draft Statement Of Work for phases 5-8 of the ongoing contract has been written, and is being seriously considered for DOE funding.

A demonstration vehicle for tankage fabricated under this extended program is being sought. FutureTruck 2002 is one possible candidate. The vehicle for this year-after-next competition will not be the same GM Suburban SUV, but 11 inch diameter tankage is likely to be applicable to it, as well as other demonstration vehicles by large auto manufacturers. Length modifications are relatively inexpensive to safety certify at a fraction of the cost of a diameter retooling. The near-term provision (perhaps within a year of Phase 4 completion) of commercial products derived from DOE funded developments under this solicitation by IMPCO makes the 11 inch diameter envelope very attractive for future vehicle integrators and for the development of "drop-in upgrade" tanks with up to 10,000 psi service pressure.

6. Design tankage for Nevada Bus (7.5% hydrogen by weight) and FutureTruck 2001 (8.5% hydrogen by weight) hydrogen fueled vehicles. Design Nevada Bus tankage around existing government tooling for rapid development and demonstration. Design FutureTruck 2001 tankage for a GM Suburban (K 15906) modified for hydrogen fuel.

Four possible configurations for mounting hydrogen tanks on the Nevada bus rooftop are shown in Figure 17 (Boehm 2000). The rightmost configuration is preferred because there are nominally 6 tanks available for this program (plus 2 spares) and all 6 tanks in this configuration can be plumbed easily through a single manifold. Design efforts are ongoing in collaboration with the Nevada bus team.

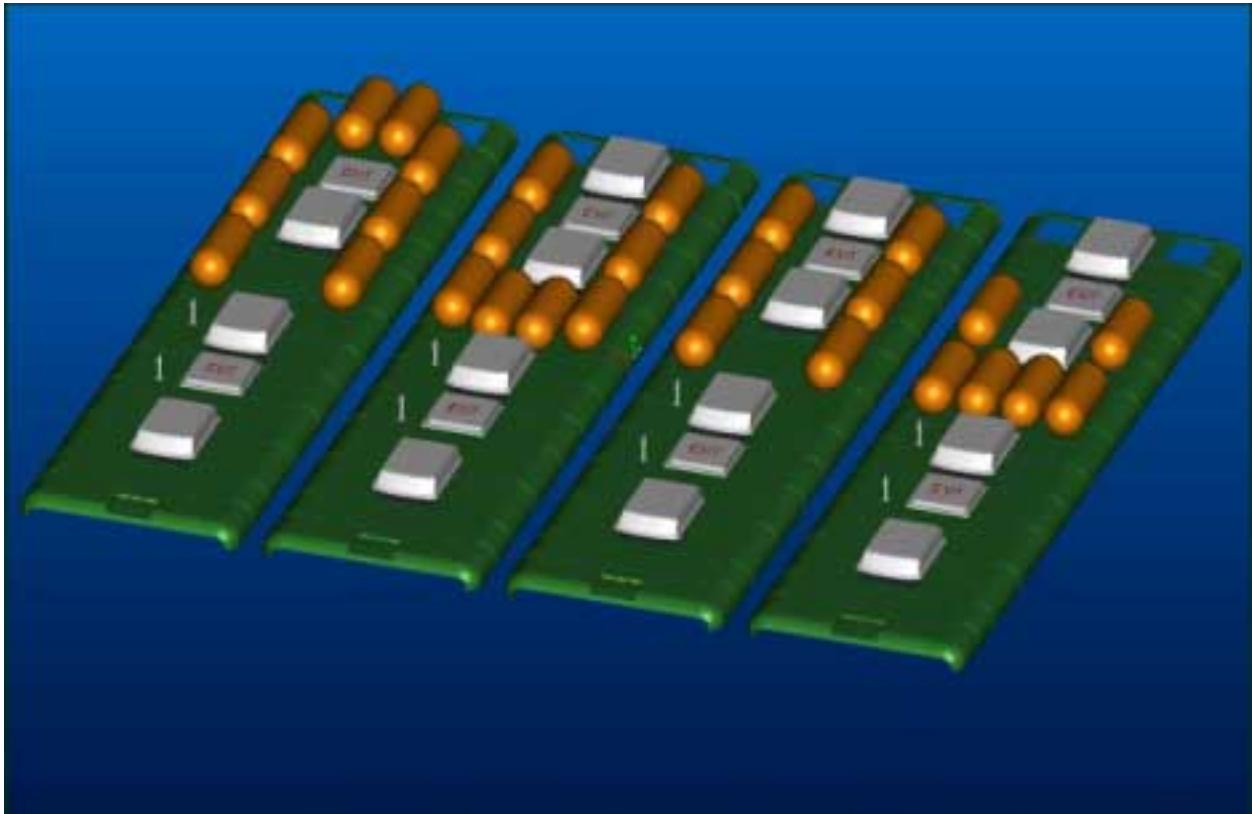


Figure 17 – Possible Tank Configurations for Nevada Bus

7. Scrutinize the proposed specification for hydrogen permeation in the modified NGV2 standard and/or the ISO/TC 197 standard. Less than 1 standard cc / hr / liter of water capacity at service pressure, room temperature, beginning of life has been proposed by others. Review the basis for the proposed hydrogen permeation specification and propose a modification if necessary.

LLNL and a team of experts reviewed a Committee Draft version of ISO/TC 197 N 148 and ISO/TC 58/SC 3 N 907. The following information was sent to the ISO/TC 197 Committee for comment:

Thank you for sending the Committee Draft version of ISO/TC 197 N 148 and ISO/TC 58/SC 3 N 907. After review of this document by a team of experts from LLNL and industry, we are proposing two changes to this document before it becomes an accepted standard.

The first change relates to the permeation test (A.20). Specifically, we propose that the permeation rate shall be less than 10.0 standard ml of hydrogen per hour per liter water capacity of the tank at room temperature, instead of the draft value of 1.0 ml of hydrogen per hour per liter water capacity of the tank. We further propose that verification of this permeation rate can be accomplished by monitoring for 50 hours instead of 500 hours for the test apparatus that is already used for verification. Documentation for this proposed change is provided below.

The second change relates to the stress ratio and burst pressure ratios for Type IV carbon fiber tanks, as described in Table 9 (of the Committee Draft). Although the team agrees that a stress ratio of 2.25 (burst pressure of 2.25 times the working pressure) should be chosen (as it was for CNG), we did not have adequate time to further justify this position with calculations. The team would be very interested to hear the rationale for why a draft value of 2.35 is being considered, since this will result in more expensive tanks without improving safety.

Documentation for proposed change to “A.20 Permeation test” of the Committee Draft:

It is the opinion of the review group that the draft specification for the A.20 permeation test is overly stringent, which will result in increased tank weight and cost without improving safety. LLNL has constructed a worst case scenario for safety issues resulting from excessive permeation of hydrogen through a tank wall. We evaluated the permeation level that could create a hazard under such a scenario and have proposed a specification which offers a safety margin adequate to prevent a hazardous situation even in such an extremely rare worst case scenario.

Background information is required to understand the basis for the worst case scenario. Permeation losses can be modeled as a very slow leak, which can cause a hazardous situation in a closed residential garage without forced ventilation or catalytic conversion of hydrogen. Hydrogen permeation rates through a tank wall are roughly linear with pressure, exponential with temperature (Souers 1982), and may be marginally worse near

the end of life of a tank, compared to the “as built” tank. Hydrogen concentration in a garage can increase most rapidly in small garage volumes with limited air exchange rates.

The worst case scenario results when a large vehicle (e.g., an SUV) which has a very large hydrogen capacity, is completely fueled (e.g., 12 kg hydrogen), is parked in a very small one car garage (e.g., 30 m³), the garage has poor ventilation (0.18 air changes per hour), the garage is very hot (180 degrees F) for sustained periods, and the tank is near end of life. We would like to keep the hydrogen concentration in this worst case garage safely below the lower flammability limit for hydrogen in air (4.1%) with a margin of safety of 2.

For reference on garage ventilation rates, the American Society of Heating, Refrigerating, and Air Conditioning Engineers, Inc. (ASHRAE) Standard 62-1989, “Ventilation for Acceptable Indoor Air Quality”, Atlanta, (1989), recommends an air exchange rate of 3.73 air changes per hour. Assuming a Poisson distribution of air exchange rates for 1 billion garages, the worst case would be $3.73/\text{LN}(1 \text{ billion}) = 0.18$ air changes per hour. Coincidentally, 0.18 air exchanges per hour is also the worst case air exchange rate for a residential garage that was measured in a study “Modeled and Measured Infiltration: a Detailed Study of Four Electrically Heated Homes”, prepared by ECOTOPE, Inc., Seattle, WA, EPRI Report No. CU-7327, May 1991 and “Air Infiltration and Interzonal Airflow Measurements in Research Houses”, prepared by GEOMET Technologies, Inc., Germantown, MD, EPRI Report No. EM-5968, August (1988), as referenced in “Addendum to Hydrogen Vehicle Safety Report: Residential Garage Safety Assessment”, analysis conducted by M.R. Swain, under subcontract to Directed Technologies, Inc., August (1998).

We assumed a 5000 psi working pressure for the hydrogen tank, which has 540 liter water capacity. In order to achieve the 4.1% lower flammability limit, the 30 m³ (30,000,000 ml) garage must have 1,230,000 ml (30,000,000 ml * 4.1%) of hydrogen present. This level requires a hydrogen permeation rate of 221,389 ml/hr (1,230,000 ml * 0.18 air change/hr). This requires a permeation rate from the hydrogen tank of 410 ml/hr/liter water capacity (221,389 ml/hr / 540 liter water capacity). Note that this is the permeation specification at the elevated temperature, for the “near end of life” tank without a margin of safety.

Hydrogen permeation experiments at elevated temperatures (180 degrees F) have been performed on plastic liners for tank walls and have shown a factor of 10 increase in permeation compared with similar measurements at room temperature (75 degrees F), F. Mitlitsky, A.H. Weisberg, and B. Myers, “Vehicular hydrogen storage using lightweight tanks (Regenerative fuel cell systems),” DOE Hydrogen Program Annual Review, Lakewood, CO, May 4-6 (1999); UCRL-JC-134540. In order to account for this difference (assuming that tank permeation qualification measurements will be done at room temperature), then the permeation specification must be reduced by this factor. This requires a permeation rate from the hydrogen tank of 41 ml/hr/liter water capacity (410 ml/hr/liter water capacity / 10). Note that this is the permeation specification at room temperature, for the “near end of life” tank without a margin of safety.

Hydrogen permeation experiments have been performed on plastic liners for tank walls at room temperature and compared with permeation tests for entire tanks that have undergone the 500 hour tests as described in the draft specification for A.20 permeation test. Entire tanks at beginning of life have hydrogen permeation that is approximately a factor of 2 lower than what would be expected for the permeation rate of the liner only. This implies that the composite overwrap is responsible for a permeation reduction of approximately a factor of 2 near the beginning of life. Near the end of life the composite overwrap matrix material will generally have a large density of microcracks. Although this will not effect the structural integrity of the tank, it will provide little (if any) permeation barrier to hydrogen. In order to account for this difference (assuming a worst case where the composite overwrap supplies no barrier to hydrogen permeation near end of life, and assuming that permeation measurements will be done at “beginning of life”), then the permeation specification must be reduced by a factor of 2. This requires a permeation rate from the hydrogen tank of 20.5 ml/hr/liter water capacity ($41 \text{ ml/hr/liter water capacity} / 2$). Note that this is the permeation specification at room temperature, for the “beginning of life” tank without a margin of safety.

Finally, the permeation specification should be reduced to account for a margin of safety below the lower flammability limit if the worst case as described above is achieved. A margin of safety of 2 requires a permeation rate from the hydrogen tank of 10.2 ml/hr/liter water capacity ($20.5 \text{ ml/hr/liter water capacity} / 2$). Note that this is the permeation specification at room temperature, for the “beginning of life” tank with a margin of safety.

Based on these calculations we believe that 10 ml/hr/liter water capacity is a very conservative, but reasonable specification for qualifying hydrogen tanks. Arbitrarily setting the specification any tighter does not appear to have any merit and will result in heavier, more expensive tanks, that are not any safer. Qualification of these tanks could be done as specified in the draft standard using a 500 hour test. However, the rationale for such a long test time was based on the sensitivity of detecting low permeation rates (0.25 ml/hr/liter water capacity as specified for CNG). Since we are proposing a permeation specification that is a factor of 40 higher than this rate, it makes sense to decrease the test time by an order-of-magnitude in order to reduce testing time and cost. We therefore suggest a 50 hour test.

8. Collect data on overtemperature/overpressure issues with fast filling procedures. Propose alternatives to mitigate overtemperature/overpressure issues.

Some initial work has been done to suggest an efficient way to efficiently precool the hydrogen during fast fills in order to keep the tanks from exceeding overtemperature limits. Discussions with Directed Technologies Inc. (DTI) on the subject have occurred (Daney 1995, James 1999, Jasionowski 1992, Kountz 1994, Mitlitsky 1996-c).

The facilities that might collect such data are currently being competitively costed out at IMPCO. Within the next few months, fully decided and approved tests plans should be in place at IMPCO, which include the downselection of this facility from among 3 subcontractors and potential in-house facility construction efforts.

Further LLNL efforts to collect thermal data independent of IMPCO are contingent on FY01 funding, and would require sample tanks of a relevant design to explore this issue with hardware. Computer modeling methods are considered unlikely to resolve the real heat transfer issues of particular tank designs and materials. Experimental characterization of tank fill thermodynamics would be possible with portable instrument accompanying research-instrumented tanks into one of the test cells at LLNL's High Pressure Laboratory, but spare pressure vessels suitable for instrumentation will probably not be available in calendar 2000.

Plans for Next Year

1. Design and test hydrogen tanks with >10% hydrogen by weight (5000 psi [34.5 MPa] service, 300 K, safety factor 2.25) and 700 Wh/liter.
2. Direct a ~1 year program to deliver certified tankage with 7.5-8.5% hydrogen by weight (5000 psi, 300 K, safety factor 2.25).
3. Test lightweight liners with the best permeation reduction coatings that offer easily adopted fabrication processes.
4. Demonstrate lightweight tankage with safety factor 2.25 and improve cost projections based on input from industry.
5. Work with car companies and tank manufacturers to advance the adoption prospects of 10,000 psi H₂ tankage. Technically direct 10,000 psi tankage development effort (pending a DOE/OTT funding award and/or additions to the current DOE/Golden contract DE-AC36-GO10494).
6. Oversee operation of delivered tankage on Nevada Bus (7.5% H₂ by weight) and FutureTruck 2001 (8.5% H₂ by weight) hydrogen fueled vehicles.
7. Recommend alternative specifications (e.g., H₂ permeation) to NGV2 and/or ISO/TC 197 standards committee.
8. Construct models to demonstrate reduction of fast filling overtemperature and overpressure transients.

Objectives for Next Year

1. Demonstrate a prototype hydrogen tank that can be certified to modified NGV2 standards while achieving >10% hydrogen by weight (5000 psi [34.5 MPa] service, 300 K, safety factor 2.25) and 700 Wh/liter.
2. Demonstrate certified tankage with 7.5-8.5% hydrogen by weight (5000 psi, 300 K, safety factor 2.25) for delivery to Nevada Bus and FutureTruck 2001 programs.
3. Work with industry to adopt lightweight liners with the best permeation reduction coatings.
4. Demonstrate that safety factor of 2.25 is adequate for plastic lined composite hydrogen tankage and publish improved cost projections.
5. Demonstrate 10,000 psi hydrogen tankage (pending a DOE/OTT funding award and/or additions to the current DOE/Golden contract DE-AC36-GO10494).
6. Support Nevada Bus and FutureTruck 2001 hydrogen fueled vehicle demonstration programs that use onboard compressed H₂ storage.
7. Persuade NGV2 and/or ISO/TC 197 standards committee to adopt safe but not overly stringent specifications for hydrogen.
8. Recommend a procedure to reduce fast filling overtemperature and overpressure transients.

Conclusions and Recommendations

Hydrogen storage with Type IV pressure vessels is advancing rapidly, and is approaching adoption by automotive demonstration vehicles over the next year. Last year DTI concluded that, a fuel cell powered vehicle fueled with compressed H₂ (at 5,000 psi) was the system to beat (James 1999). Such vehicles offer: low weight (with >10% hydrogen by weight feasible), while storing hydrogen in an acceptable volume, at an acceptable cost. The other advantages of advanced Type IV hydrogen tanks include high system simplicity, high safety, the potential for faster refills than their competitors, as well as expected support by a feasible H₂ infrastructure (in both start-up and mature phases). Over the next year, LLNL lead efforts are poised to turn this prediction into reality.

Efforts at LLNL have made progress toward significant weight and cost improvements over the last year in two directions: research leading to fundamental improvements and facilitating the commercialization of recent advances. Thin liner technology pioneered by LLNL is already being folded into commercializable tank designs, while permeation barrier coatings have been pushed into the preliminary-encouraging regime that might lead to near-term adoption. Safe hydrogen tankage is already commercially available at ~5 % hydrogen by weight. By the conclusion of the LLNL-directed DOE/Golden contract DE-AC36-GO10494, 8.5% hydrogen by weight tankage should be at the threshold of commercialization in 2001. Research prototyping efforts by LLNL and its industrial partners have proven performance levels above 11% hydrogen by weight are feasible.

Further research on the weight frontier could establish manufacturing processes capable of >12% by weight hydrogen storage, and/or modify record-breaking designs for high confidence of meeting safety certification with >10% hydrogen by weight. Technical direction of expert industrial contractors under LLNL subcontracts remains a viable option for pursuing progress further than one year from revenue generation on this crucial frontier.

LLNL technical direction of ongoing and planned DOE solicitations involves technology much closer to adoption than innovating directly on the weight frontier. This effort is part diplomatic and highly technical, and is vital to rapid adoption of hydrogen fueled vehicles. It must execute the glorious demonstration projects that have already been planned by developing, delivering, and competently installing proven tanks. Those tanks are currently numbers converging on a detailed set of designs. Over the next few months, stabilized designs will be manufactured in batches, subjected to risk reduction testing, manufactured in more batches, and safety certified. Success in meeting the solicitations aggressive weight goals depends on careful attention to mass allocation, design decisions, test plans, and every decision based on test conclusions.

In late 1999, the LLNL team crafting technical specifications of the 7.5-8.5% hydrogen by weight DOE solicitation currently underway sought industrial interest in higher pressure tank technology. Higher pressure designs would be easier to package aboard demonstration vehicles (e.g., FutureTruck), and could dramatically increase (by ~2/3) the range of vehicle already fitted with 5,000 psi tanks. After initial skepticism, increasing interest has been circulating among automobile companies, DTI, and other interested parties across the hydrogen community. Thus

there is a new constituency for progress on the density frontier. This new constituency encourages DOE funding to extend LLNL-directed, near-commercializable tank technology development to deliver 10,000 psi tankage.

Understanding of the engineering and economic issues on the weight, cost, safety, and density frontiers is rudimentary at present. The world's experts can barely account for the failure phenomena that have emerged on the LLNL-subcontracted weight frontier research. Aerospace expertise has spent few man years on the frontiers of hydrogen tankage, and DOE can't afford much of this expense. Commercial expertise has largely chased aerospace out of the non-aerospace tankage business, offering lower costs but relying on empirical methods and much less sophisticated engineering. Neither commercial nor aerospace experts can model many of the phenomena that LLNL-lead research has encountered.

Academic researchers should be capable of debugging many of the process and material phenomena that advanced tank development has and will uncover, but they have seldom been able to afford the refined state of the art in composite manufacturing. Neither solid rocket motor cases, nor aircraft wings, nor automotive driveshafts have much of an academic research community despite being frontiers for composite materials. This leaves only national laboratories with the research means and incentives to make progress that won't show a profit in the next two years. The alternative is to let industry declare artificial performance limits, deliver 'research' that turns into products that were already possible without government funding, and to employ non-innovators to disburse taxpayers funds that entrench premature monopolies.

Industrial policy ought to be off limits for purely technical efforts at National Laboratories, yet recent progress in the hydrogen community makes it nearly impossible to ignore interest groups. DOE and the taxpayers and hydrogen technologies in general will be well served by LLNL-lead initiatives to remove confusion in international safety regulations for hydrogen, especially those related to hydrogen permeation. The fate of liquid hydrogen and natural gas infrastructures in Europe could determine the outcome of LLNL's recent regulatory initiative. Without some experts' time and ability to travel, such important 'diplomatic' frontiers will wither before many months elapse, and long before accidents of regulatory history (that heavily penalize a near-monopoly for the U.S. in Type IV tanks) can be reversed.

Without real research to extend our understanding of what progress to pursue next, staff devoted to contracts between DOE and industry must follow rather than lead. In the absence of a research community dedicated to understanding the utmost that industry can do (and what might profitably lie just beyond that 'utmost'), industry's arguments that they already know their business best are true.

If leadership on any of these frontiers is justified, there is already a strong case to be made for process research on smaller (perhaps 5 inch diameter) pressure vessels. Only affordable process research can sort out the unknown failure mechanisms encountered recently on the weight performance frontier. Small tanks may need to be produced and integrated-performance tested in statistically significant quantities (batches of at least 6 identical units). It probably makes sense to attempt correlating failure modes with microstructure, but much more expert advice should be tapped to determine how best to probe composite microstructures. More permeation barrier and

coating research could be very cost-effective in speeding adoption of advanced liners. The first exploration (at small scale) of blow molding could discover the superior cost and quality and performance liner options many experts anticipate. Permeation should also be studied as a function of cycling, to know rather than guess the permeation consequence of the relatively huge cycle lives required by safety certification. It is also not premature to begin design studies of 10,000 psi ancillaries.

Acknowledgments

This work was performed under the auspices of the U.S. Department of Energy by University of California Lawrence Livermore National Laboratory under contract No. W-7405-Eng-48. This work was funded in part by: Ballistic Missile Defense Organization (BMDO), Ford Motor Company, LLNL Laboratory Discretionary Research and Development Funds, NASA, U.S. Air Force (USAF), the Defense Advanced Research Projects Agency (DARPA), and U.S. Department of Energy (DOE). This work was performed in conjunction with various organizations, including: Aero Tec Laboratories (Ramsey, NJ), Air Force Research Laboratory (AFRL), Directed Technologies Inc. (Arlington, VA), EDO Fiber Science Division (Salt Lake City, UT), Epner Technology (Brooklyn, NY), IMPCO Technologies (Irvine, CA), and Thiokol Propulsion (Corinne, UT). The authors are grateful to IMPCO Technologies for expediting the design, fabrication, and test of Tank #5.

References

- Aceves, S.M., J. Martinez-Frias, and O. Garcia-Villazana. 2000. "Low temperature and High Pressure Evaluation of Insulated Pressure Vessels for Cryogenic Hydrogen Storage," (in these proceedings).
- Boehm, R. 2000. "Hybrid Hydrogen Electric Bus Development," (in these proceedings).
- Carter II, P.H., F. Mitlitsky, A.H. Weisberg, J.C. Whitehead, and R.W. Humble. 1999. "Design Trade Space for a Mars Ascent Vehicle for a Mars Sample Return Mission," *Acta Astronautica*, 45 (4-9), 311-318; UCRL-JC-130277.
- CGA. 1996. *Methods for Hydrostatic Testing of Compressed Gas Cylinders 7th edition*, Compressed Gas Association, Inc., Pamphlet CGA C1-1996.
- Daney, D.E., F.J. Edeskuty, M.A. Daugherty, F.C. Prenger, and D.D. Hill. 1995. *Cryogenic Engineering Conference*, July 17-21, 1995.
- de Groot, W.A., L.A. Arrington, J.F. McElroy, F. Mitlitsky, A.H. Weisberg, P.H. Carter II, B. Myers, and B.D. Reed. 1997. "Electrolysis Propulsion for Spacecraft Applications," AIAA 97-2948, 33rd AIAA/ASME/SAE/ASEE Joint Propulsion Conference, July 7-9, 1997.
- Golde, R., B. McQuivey, R.K. Kunz. 1999. "Conformable Hydrogen Storage Development," DOE Hydrogen Program Annual Review, Lakewood, CO, May 4-6, 1999.
- Gronich, S. 2000. "Hydrogen Program Goals and Outcomes," (in these proceedings).
- Haaland, A. 2000. "High Pressure Conformable Hydrogen Storage for Fuel Cell Vehicles," (in these proceedings).

James, B.D., C.E. Thomas, and F.D. Lomax, Jr. 1999. Directed Technologies, Inc., "Onboard Compressed Hydrogen Storage," presented at the 1999 Canadian Hydrogen Association Meeting, February 1999.

Jasionowski, W., K.J. Kountz, and C.F. Blazek. 1992. Gas Research Institute Report #GRI-92/0350, July 1992.

Kare, J.T., F. Mitlitsky, and A.H. Weisberg. 1999. "Preliminary Demonstration of Power Beaming with Non-Coherent Laser Diode Arrays," Space Technology & Applications International Forum (STAIF-99), Albuquerque, NM, January 31-February 4, 1999; UCRL-JC-133428.

Kountz, K.J. 1994. *Proc. 207th ACS-Division of Fuel Chemistry*, March 13-17, 1994.

McElroy, J.F. (Hamilton Standard); R.W. Humble (US Air Force Academy); W.A. de Groot and S.R. Oleson (FDC, Inc., NASA LeRC); and F. Mitlitsky, A.H. Weisberg, B. Myers, and P.H. Carter II (LLNL). 1998. "Unitized Electrolysis Propulsion and Fuel Cell Power for Selected Satellite Missions," *33rd Intersociety Energy Conversion Engineering Conference (IECEC)*, Colorado Springs, CO, August 2-6, 1998 (IECEC-98-339).

Mitlitsky, F., A.H. Weisberg, P.H. Carter, B. Myers, and J.T. Kare. 2000. "Applications of Water Refuelable Spacecraft," Final Report to DARPA/TTO, Agreement #99-G527, January 5, 2000; UCRL-ID-137296.

Mitlitsky, F., A.H. Weisberg, B. Myers, et al. 1999-a. "Water rocket – Electrolysis Propulsion and Fuel Cell Power," AIAA-99-4609, AIAA Space Technology Conference, Albuquerque, NM, September 28-30 (1999); UCRL-JC-135315

Mitlitsky, F., and A.H. Weisberg. 1999-b. "Water-Based Spacecraft," invited presentation, JASONS Program Office, La Jolla, CA, July 12, 1999.

Mitlitsky, F., B. Myers, A.H. Weisberg, and A. Leonida. 1999-c. "Applications and Development of High Pressure PEM Systems," invited presentation, Portable Fuel Cells International Conference, Lucerne, Switzerland, June 21-24, 1999; UCRL-JC-134539.

Mitlitsky, F., B. Myers, A.H. Weisberg, T.M. Molter, and W.F. Smith. 1999-d. "Reversible (Unitized) PEM Fuel Cell Devices," invited presentation, Portable Fuel Cells International Conference, Lucerne, Switzerland, pp. 3-16, June 21-24, 1999; Feature Article, Fuel Cells Bulletin, No. 11, August, 1999; UCRL-JC-134538.

Mitlitsky, F., A.H. Weisberg, and B. Myers. 1999-e. "Vehicular hydrogen storage using lightweight tanks (Regenerative fuel cell systems)," DOE Hydrogen Program Annual Review, Lakewood, CO, May 4-6, 1999; UCRL-JC-134540.

Mitlitsky, F. 1998-a. "Water Rocket Technologies," invited presentation, US Embassy, Paris, France, December 10-11, 1998; UCRL-MI-132628 Rev 1.

Mitlitsky, F., B. Myers, A.H. Weisberg, and T.M. Molter. 1998-b. "Unitized regenerative fuel cell systems," *1998 Fuel Cell Seminar*, Palm Springs, CA, November 16-19, 1998; UCRL-JC-130198 (paper) and UCRL-MI-130198 (viewgraphs).

Mitlitsky, F., P.H. Carter, M.D. Dittman, R.W. Humble, J.T. Kare, B. Myers, and A.H. Weisberg. 1998-c. "Water Rocket Design Trade Analysis," whitepaper to Air Force Research Lab, October 29, 1998.

Mitlitsky, F. 1998-d. "Regenerative Fuel Cell Systems," Invited Presentation, Joint DOE/EPRI/GRI Workshop on Fuel Cell Technology, San Francisco, CA, May 18-20, 1998.

Mitlitsky, F., B. Myers, and A.H. Weisberg. 1998-e. "Regenerative Fuel Cell Systems R&D," DOE Annual H₂ Program Peer Review, Alexandria, VA, April 28-30 (1998); UCRL-JC-131087.

Mitlitsky, F., A.H. Weisberg, and B. Myers. 1998-f. "Regenerative Fuel Cell Systems," *Energy & Fuels*, 12 (1), 56-71, January 12, 1998; UCRL-JC-128267 Rev 1; <http://pubs.acs.org/subscribe/journals/enfuem/jtext.cgi?enfuem/12/i01/html/ef970151w.html>

Mitlitsky, F., B. Myers, and A.H. Weisberg. 1997. "Regenerative fuel cell systems," DOE Annual H₂ Program Peer Review, Herndon, VA, May 22, 1997.

Mitlitsky, F., B. Myers, and A.H. Weisberg. 1996-a. "Lightweight Pressure Vessels and Unitized Regenerative Fuel Cells," *1996 Fuel Cell Seminar*, Orlando, FL, November 17-20, 1996; UCRL-JC-125220 (paper) and UCRL-MI-125220 (viewgraphs).

Mitlitsky, F., W.A. de Groot, L. Butler, and J.F. McElroy. 1996-b. "Integrated Modular Propulsion and Regenerative Electro-Energy Storage System (IMPRESS) for Small Satellites," *AIAA Small Satellite Conference*, September 16-20, 1996; UCRL-JC-125242.

Mitlitsky, F. and B. Myers. 1996-c. "Development of an Advanced, Composite, Lightweight, High Pressure Storage Tank for On-Board Storage of Compressed Hydrogen," *Fuel Cells for Transportation TOPTEC: Addressing the Fuel Infrastructure Issue*, Alexandria, VA, April 1-2, 1996; UCRL-MI-123802.

Mitlitsky, F. 1996-d. "Rechargeable Solar Powered Aircraft Using Regenerative Fuel Cells," *High Altitude Long Endurance (HALE) Roundtable Meeting, European Space Research and Technology Centre (ESTEC)*, invited presentation, Noordwijk, The Netherlands, January 17, 1996; UCRL-MI-122808.

Mitlitsky, F., N.J. Colella, and B. Myers. 1994. "Unitized Regenerative Fuel Cells for Solar Rechargeable Aircraft and Zero Emission Vehicles," *1994 Fuel Cell Seminar*, November 28-December 1, 1994; UCRL-JC-117130 (paper) and UCRL-MI-117130 (viewgraphs).

Mitlitsky, F., N.J. Colella, B. Myers, and C.J. Anderson. 1993. "Regenerative Fuel Cells for Solar Powered Aircraft," *28th Intersociety Energy Conversion Engineering Conference (IECEC)*, August 9-13, 1993; UCRL-JC-113485.

Souers, P.C. 1986. *Hydrogen Properties for Fusion Energy*, University of California Press: Berkeley, CA, pp 370-373.

List of Figures

- Figure 1 – DOE 2000 Tankage Goals
- Figure 2 – First Composite Wrapped Tank Prototype Next to Thin-Wall Liner
- Figure 3 – Remains of Test Tank #3 after Premature Burst
- Figure 4 – Video Captures Localized Failure During Tank #3 Burst Test
- Figure 5 – Condition of Tank #5 before Highly-Instrumented Burst Test
- Figure 6 – Best High Speed Camera Frame Captures Tank #5 At Burst
- Figure 7 – Tank Size and Location Considerations for Vehicular H₂ Storage
- Figure 8 – Hydrogen Requirements for FutureTruck
- Figure 9 – Hydrogen Tankage Placement Issues for FutureTruck
- Figure 10 – Preliminary GM Suburban Rail and Crossmember Arrangement
- Figure 11 – Proposed H₂ Tank Placement for FutureTruck (GMT 830 K 15906)
- Figure 12 – H₂ Tankage for Nevada Bus Program and FutureTruck Competition
- Figure 13 – Conformable Tankage Fabricated by Thiokol Passed Bullet-Test
- Figure 14 – Schematic and Photos of Permeability Test Fixture at SRI
- Figure 15 – Measured Hydrogen Permeability of Several Candidate Liner Materials
- Figure 16 – Economic Analysis of Carbon Fiber Tanks in High Volume Production
- Figure 17 – Possible Tank Configurations for Nevada Bus

List of Tables

- Table 1. 11.3% H₂ by Weight was Demonstrated for a High Cycle Life Cylinder

Appendix 1

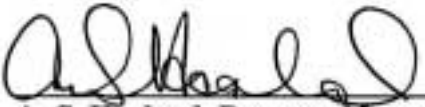
DOC NO.: TR12153 VOL: REV: B
TITLE: Lawrence Livermore National Laboratory 18 X
48-inch Lightweight Hydrogen Cylinder – Final
Report

6 JULY 2000


Prepared by:


D. J. Son
Case Design/Analysis

Approved by:


A. C. Haaland, Program Manager
Technical Programs


C. P. Pulver, Supervisor
Case Design/Analysis


Released by Data Management
7/6/2000



**Thiokol
Propulsion**

From Cordant Technologies

P. O. Box 707 Brigham City, UT 84302-0707 (435) 863-3511

Appendix 1

TABLE OF CONTENTS

| | | |
|-------|---------------------------------------|----|
| 1.0 | INTRODUCTION | 47 |
| 2.0 | OBJECTIVES | 47 |
| 3.0 | SUMMARY..... | 47 |
| 4.0 | TANK DEVELOPEMENT | 48 |
| 4.1 | Requirements..... | 48 |
| 4.2 | Tank Design and Analysis..... | 48 |
| 4.3 | Liner Tests..... | 49 |
| 4.4 | Fabrication and Testing..... | 50 |
| 4.4.1 | Tank #1 | 50 |
| 4.4.2 | Tank #2 | 50 |
| 4.4.3 | Tank #3 | 51 |
| 4.5 | Failure Analysis | 51 |
| 4.5.1 | Tank #1 Hydroburst Test | 56 |
| 4.6 | Redesign | 56 |
| 4.6.1 | Hoop Termination Pattern Design | 56 |
| 4.6.2 | Wafer Design..... | 60 |
| 4.6.3 | Tank #4 Fabrication and Testing..... | 62 |
| 5.0 | CONCLUSION | 63 |

FIGURES

| | | |
|------------|--|----|
| Figure 1: | Tank #3 after hydroburst test | 51 |
| Figure 2: | Tank #3 failure initiation..... | 52 |
| Figure 3: | Finite element model geometry..... | 53 |
| Figure 4: | Fiber Strain Plot..... | 54 |
| Figure 5: | Modeled vs. as-built hoop termination..... | 55 |
| Figure 6: | Modeled vs. as-built fiber strain plot | 55 |
| Figure 7: | Measured vs. estimated fiber strain plot (Tank #1) | 56 |
| Figure 8: | Redesigned hoop termination pattern..... | 57 |
| Figure 9: | Redesigned hoop pattern fiber strain plot..... | 57 |
| Figure 10: | FEM with hardware..... | 58 |
| Figure 11: | Fiber strain plot with hardware | 58 |
| Figure 12: | FEM with smoothed composite..... | 59 |
| Figure 13: | Fiber strain plot with smoothed composite | 60 |
| Figure 14: | Wafer FEM | 61 |
| Figure 15: | Wafer design fiber strain plot | 61 |
| Figure 16: | Tank #4 before hydroburst test..... | 62 |
| Figure 17: | Tank #4 after hydroburst test..... | 63 |

Appendix 1

TABLES

| | |
|--|----|
| Table 1: Test Results..... | 47 |
| Table 2: Design Requirements..... | 48 |
| Table 3: Tank Design Estimates..... | 48 |
| Table 4: T1000G Properties | 49 |
| Table 5: CLT Stress/Strain Estimates..... | 49 |
| Table 6: Measured vs. CLT strains for Tank #3..... | 52 |
| Table 7: CLT vs. isotropic strain estimates | 52 |

APPENDICES

- APPENDIX A: Tank Drawings
- APPENDIX B: Hoop Termination Design Iterations
- APPENDIX C: Wafer Design Iterations
- APPENDIX D: Test Plan TTP528

Appendix 1

1.0 INTRODUCTION

Thiokol designed, fabricated and tested 18-inch diameter by 48-inch length gaseous hydrogen cylinders for Lawrence Livermore National Laboratory (LLNL) under sub-contract #B503790. The program was conducted from 15 Mar 99 to 30 June 00. Plastic liners for the tanks were supplied by LLNL as government furnished material and was manufactured by Aero Tec Laboratories Inc. (ATL) of Ramsey, NJ.

2.0 OBJECTIVES

The goal of the program was to fabricate high performance tanks for the storage of hydrogen for vehicular applications. Main design issues to be addressed by this program included maximum volume and minimum weight. The designed service pressure for the tank was 5,000 psig, with a safety factor of 2.25. The primary performance metric for the tank was expressed as burst pressure * internal volume / total tank weight. The design goal for this metric was a value of 1.8 million inches.

3.0 SUMMARY

Four tanks were fabricated using T1000G TCR-prepreg because of its high strength to weight ratio. The tanks used plastic liners and aluminum polar bosses. One tank leaked following cure and was subsequently sectioned prior to delivery to LLNL. Three tanks were hydroburst tested at Thiokol. Results are given in Table 1. Tanks 1-3 employed the same design; tank 4 was a redesign. An annealed liner was used to fabricate tank 4, which lead to a volume decrease. Tank 4 reached 94.4% of the performance goal of 1.8 million inches.

Table 1: Test Results

| Tank # | 1 | 2 | 3 | 4 |
|---|--------|-------|---------|---------|
| Test Date | 5/8/00 | -- | 4/28/00 | 6/16/00 |
| Burst Pressure (psig) | 9,503 | -- | 7,872 | 10,464 |
| Meas. Hoop Strain (in./in.) | .01444 | -- | .01192 | .01518 |
| Ambient Internal Volume (in ³) ¹ | 9,240 | 9,240 | 9,240 | 8,600 |
| Total Tank Weight (lbs.) | 53.5 | 56.8 | 55.7 | 54.0 |
| Adjusted Tank Weight (lbs.) ² | 53.5 | 54.4 | 54.5 | 52.8 |
| Liner Weight (lbs.) | 5 | 6 | 6 | 6 |
| Polar Boss Weight (lbs.) | 1.5 | 1.5 | 1.5 | 1.5 |
| P _b V/W (X 10 ⁶ in.) | 1.64 | -- | 1.33 | 1.70 |

¹ Water volume measured for Tank 1. Tanks 2 & 3 similar to Tank 1. Tank 4 (annealed liner) estimated with CAD program (conservative value).

² Total tank weight minus glass overwrap weight (1.2 lbs./ply). Tank 2 had two glass hoop plies, Tanks 3 & 4 had one ply.

Appendix 1

4.0 TANK DEVELOPMENT

4.1 Requirements

The requirements for the hydrogen tank are listed in Table 2. The main goal was to obtain a greater than 1.8 million inches P_bV/W , where P_b is the burst pressure, V is the internal volume, and W is the total weight of the tank including the composite, liner, and polar bosses.

Table 2: Design Requirements

| Parameter | Requirement |
|---|---------------------|
| Outside Diameter (in.) | 18.0 |
| Length, boss to boss (in.) | 48.0 |
| Liner Material | Plastic |
| Service Pressure (psig) | 5,000 |
| Safety Factor | 2.25 |
| Minimum Burst Pressure (psig) | 11,250 |
| H ₂ Storage Capacity (lbs.) | 8.5 |
| P_bV/W (in.) | $> 1.8 \times 10^6$ |
| H ₂ by Total Tank Weight (%) | 12 |

4.2 Tank Design and Analysis

The 18-inch tank design was scaled up from standard IR&D 12-inch diameter cylinders. The polar boss to liner interface was unchanged except for the boss being thickened for the higher design pressure (see Appendix A for boss drawing). The first tank was made with an plastic liner. The design parameters for the tank are listed in Table 3.

Table 3: Tank Design Estimates

| | |
|------------------------------------|--------------------------------------|
| Liner (Plastic) | |
| Liner O.D. (in.) | 17.25 |
| Liner Length (in.) | 46.0 |
| Internal Volume (in ³) | 9482 |
| Liner Weight (lbs.) | 5.0 |
| Polar Boss (AL6061-T6) | |
| Total Boss Weight (lbs.) | 1.6 |
| Composite (T1000G) | |
| Total Composite Thickness (in.) | .352 |
| Composite O.D. (in.) | 17.95 |
| Stress Ratio | .70 |
| Composite Weight (lbs.) | 47.5 |
| Total Tank Weight (lbs.) | |
| | 54.5 |
| P_bV/W (in.) | 1.96×10^6 |

Appendix 1

The composite case was designed using classical lamination theory (CLT). Lamina properties are given in Table 4 (ref. TR10958), and the stress and strain estimates based on CLT are provided in Table 5. The lower 3σ value was used for the allowable fiber stress.

Table 4: T1000G Properties

| Property | Value |
|------------------------------|---------|
| E_{11} (Msi) | 22.70 |
| E_{22} (Msi) | 1.05 |
| ν_{12} | .337 |
| G_{12} (Msi) | .606 |
| Allowable Fiber Stress (psi) | 740,000 |

Table 5: CLT Stress/Strain Estimates

| Laminate Strain | 5,000 psig | 11,250 psig |
|-------------------------------|------------|-------------|
| Hoop (in./in.) | .00859 | .0193 |
| Axial (in./in.) | .00586 | .0132 |
| Fiber Stress | | |
| Hoop (ksi) / Safety Factor | 330 / 2.24 | 743 / .996 |
| Helical (ksi) / Safety Factor | 234 / 3.16 | 525 / 1.40 |

The finite element model for the composite was generated using FWIND and STACKER, both in-house codes. Hardware was added using I-DEAS MS 7.0 and ABAQUS 5.8 was used as the solver. In the initial analysis, much time was taken to determine a suitable helical step-back pattern to avoid dome failure. After numerous iterations, a winding sequence was chosen. The analysis is covered in Section 4.5.

4.3 Liner Tests

The first liner from ATL made of plastic material weighed 6 pounds and had a thin area in the sidewall. The liner was pressurized to 2 psi with air at Thiokol's I-10 test facility without significant deformation. The liner was being pressurized to 4 psi when it ruptured in the thin area and resulted in a longitudinal split down the entire cylindrical length.

The second liner from ATL made of plastic material weighed 5 pounds and had more uniform thickness distribution. The liner was threaded and polar bosses with smaller diameter flanges were installed and torqued to a level of 15 ft-lbs. (180 in-lbs.). The liner was pressure tested with air at M-9 on June 11, 1999 to 4 psi for five minutes without any significant deformation. It was then considered safe to wind with an operator next to the liner with an internal pressure of 2 psi.

The correctly sized polar bosses for the second liner were installed and torqued, but not to the full 180 in-lbs. It seemed that the torque was not getting increasingly higher. It was decided to do some additional torque evaluations with the first liner that burst. The closed end of the burst liner was torqued to 180 in-lbs., and then increased to 270 in-lbs. with an additional 1/2 revolution. The open end was torqued to 180 in.-lbs. After a few minutes, it was torqued again to 180 in-lbs. with an additional 1/2 revolution.

Appendix 1

The results indicated that additional applications of the same torque could cause significant revolutions between the polar boss and the plastic liner. It was decided to not do any additional tightening, except as would be performed by the winding operations.

The second liner was installed in the winding machine. Four tows at 6 lbs./tow tension were attempted in a hoop winding mode. The polar boss continued to turn so the hoop winding was terminated. Helical layers were applied with 4 tows per winding band. There was no more turning of the polar boss on the liner. After part of the first helical layer was applied, it was noted that the polar boss to polar boss length was reducing. The compressive force of the helical layer was more than the internal pressure (2 psig) would withstand. Additional helicals were wound using two tows per bandwidth. There was no further reduction in length. It was also noted that during the helical winding operations, the right side axis of the liner that is held by the tail stock in the winding machine was raising about 3/4 to 1 inch when the winding was being performed at this end of the liner. The support rod in the tail stock is much longer than what is needed, and there was some "play" between the support rod and the tail stock live center. These features allowed the right end of the liner to be able to move. It was decided to wind with two tows/band for first helical layer, then determine if additional winding can be accomplished with four tows per band without anymore turning of the polar boss on the liner.

Scotch-Weld DP-8005 was evaluated for use as an adhesive between the polar boss and liner. The material was mixed and applied to the threads and flat recess for the polar boss on one of the ends of the first liner. After the adhesive had cured overnight, the polar boss was torque tested. A torque of 600 in-lbs. was achieved without movement between the polar boss and the plastic liner.

4.4 Fabrication and Testing

4.4.1 Tank #1

The first tank was used as a demonstration piece for LLNL. The liner weighed 5 lbs. and the outside diameter measured 17.12 inches (2 psig). The tank was cured horizontally with rotation. No glass hoop plies were applied to the tank, but shrink-wrap was used. The tank weighed 53.5 lbs. and the internal volume was measured to be 9,240 cu. in. The tank was successfully proof tested to 7,500 psig, with a two-minute hold, on June 23, 1999. The tank was then delivered to LLNL.

4.4.2 Tank #2

Tank two was fabricated on April 14, 2000. The liner weighed 6 lbs. and the outside diameter measured 17.21 inches (2 psig). The tank was built and cured using the same process as the first tank, with the exception that two glass hoop plies were applied to secure a label. The total tank weight was 56.8 lbs. The tank failed to hold pressure, with air leaking around the polar boss. Dissection revealed cracks in the liner in the polar boss flange region. The liner also showed radial folds, most likely caused by the rotation of the tank during cure. It was decided to cure vertically with no rotation for subsequent tanks. A section of the tank was delivered to LLNL for further evaluation.

Appendix 1

4.4.3 Tank #3

Tank three was fabricated on April 27, 2000. The tank was vertically cured with no rotation. A heavier 6-lb. liner was used and the outside diameter measured 17.06 inches (2 psig). One glass hoop ply held the label, and the total tank weight was 55.7 lbs. The tank was hydrostatically tested on April 28, 2000 according to test plan TTP528 (attached in Appendix D). The burst pressure was 7,872 psig, 70% of the required minimum burst pressure. The measured fiber strain at burst was 1.192%. The tank after burst is pictured in Figure 1.



Figure 1: Tank #3 after hydroburst test

4.5 Failure Analysis

Following the low burst pressure of Tank #3, a failure analysis ensued. The tank was inspected by the manufacturing engineers for possible fabrication problems. The correct material was used, no wrinkled fibers were observed, and the winding drawing had been followed. In reviewing the video footage taken of the burst test, it was determined that failure initiated at the tangent line. Figure 2 shows the tank setup and the frame from the video showing water sprays from the tangent line.

Appendix 1



Figure 2: Tank #3 failure initiation

The design was also reviewed. The measured hoop strains was compared to the CLT hoop strains in Table 6. In a prior rocket motor program, a fiber direction modulus of 24.8 Msi was used. This value gave better CLT estimates compared to the measured strain values.

Table 6: Measured vs. CLT strains for Tank #3

| Pressure (psig) | Measured Strain (in./in.) | CLT Strain with E1=22.7 Msi | Ratio | CLT with E1=24.8 Msi | Ratio |
|-----------------|---------------------------|-----------------------------|-------|----------------------|-------|
| 5000 | 0.00793 | 0.00859 | 0.92 | 0.0079 | 1.00 |
| 3333 | 0.00532 | 0.00573 | 0.93 | 0.00527 | 1.01 |
| 7500 | 0.0115 | 0.0129 | 0.89 | 0.0119 | 0.97 |
| 7872 | 0.0119 | 0.0135 | 0.88 | 0.0124 | 0.96 |

As a quick check of the CLT numbers, simple isotropic calculations were done using the hoop thickness in Table 7. This verified the right material thickness was used.

Table 7: CLT vs. isotropic strain estimates

| Pressure (psig) | CLT | | Isotropic | | Ratio Stress | Ratio Strain |
|-----------------|--------------|------------------|--------------|------------------|--------------|--------------|
| | Stress (ksi) | Strain (in./in.) | Stress (ksi) | Strain (in./in.) | | |
| 11250 | 743 | 0.0193 | 793 | 0.0186 | 0.94 | 1.04 |
| 7500 | 495 | 0.0129 | 528 | 0.0124 | 0.94 | 1.04 |
| 5000 | 330 | 0.00859 | 352 | 0.00825 | 0.94 | 1.04 |

The focus then shifted to the finite element analysis. Upon reviewing the axisymmetric model results, a problem was discovered in the tangent line. In the initial analysis, only the first five helical layers were looked at. The focus of the analysis was the step-backs to avoid a dome failure, where the highest strains occurred in the inner helical layers. Similar to previous cylinders, the tangent line was not thoroughly analyzed. Standard 12-inch cylinders have been used extensively for burst tests, cycle tests, etc. without any problems in the tangent line area. Because of this history, the 18-inch tank followed the 12-inch cylinders in design. Unfortunately in the 18-inch tank, the highest strained helical was at the tangent line of the outside layer, which was above the level of the hoops. The

Appendix 1

higher 0.7 stress ratio design, compared to 0.55 for M30S cylinders, further attributed to the problem. The model geometry is pictured in Figure 3 and the fiber strain plot for the 18-inch tank is shown in Figure 4.

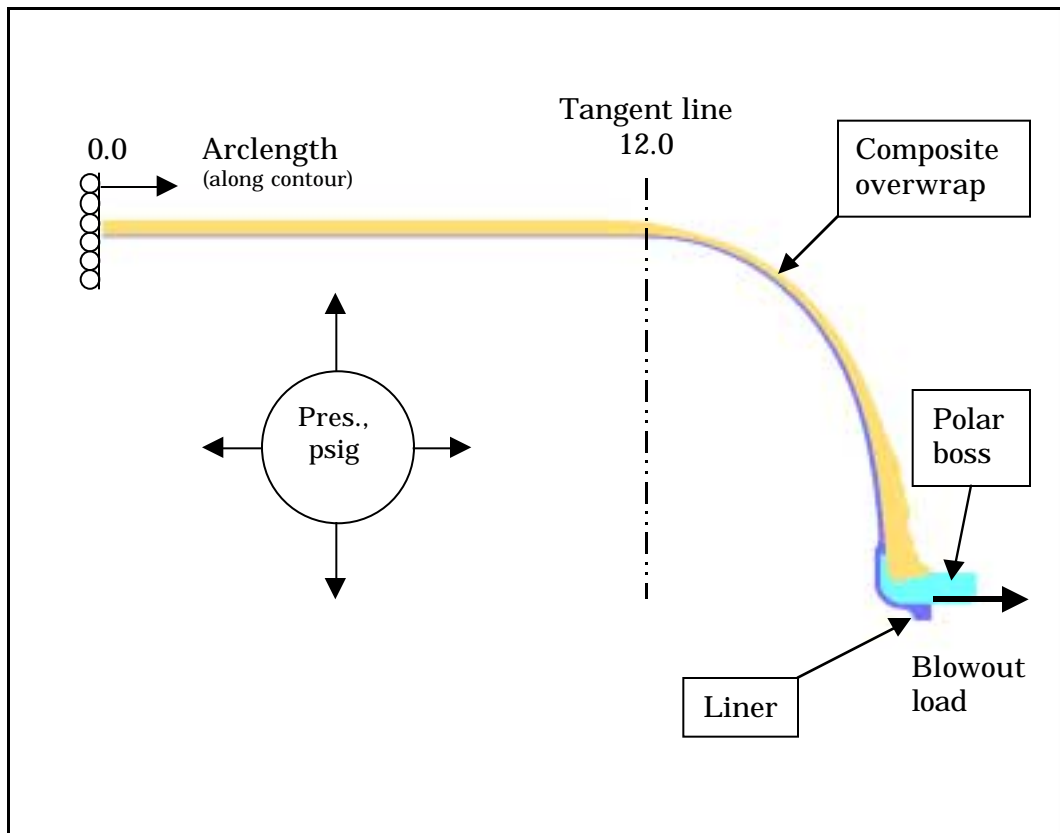


Figure 3: Finite element model geometry

Appendix 1

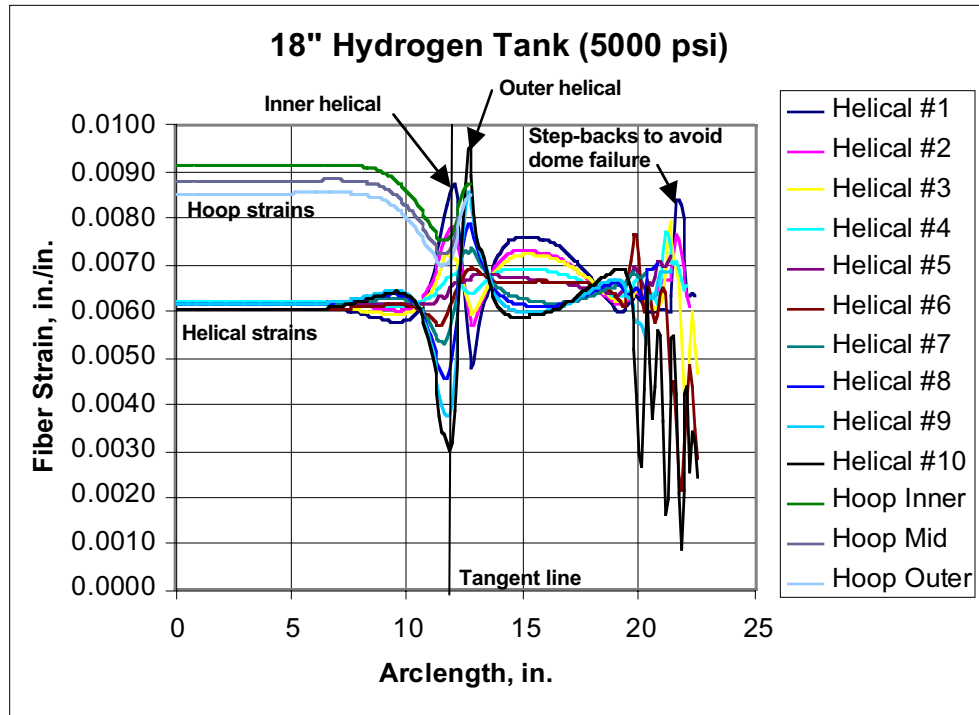


Figure 4: Fiber Strain Plot

Since the failure mode was determined to be the tangent line, the hoop terminations were analyzed. As in previous drawings, the hoop terminations were not specified, and establishing the position for the terminations was left to the manufacturing engineer. The hoop termination in the model is compared to the as-built in Figure 5. The hoop terminations were modeled as a “V”, extending 0.5 inches past the tangent line down the dome. The as-built tank did not have hoops extending past the tangent line. The fiber strain plot comparison between the two is given in Figure 6.

Appendix 1

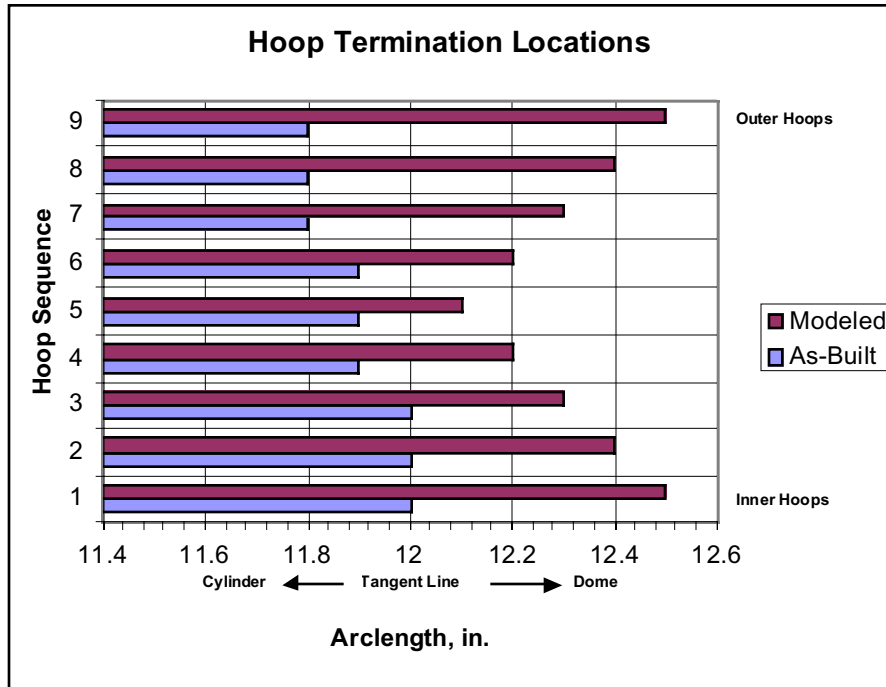


Figure 5: Modeled vs. as-built hoop termination

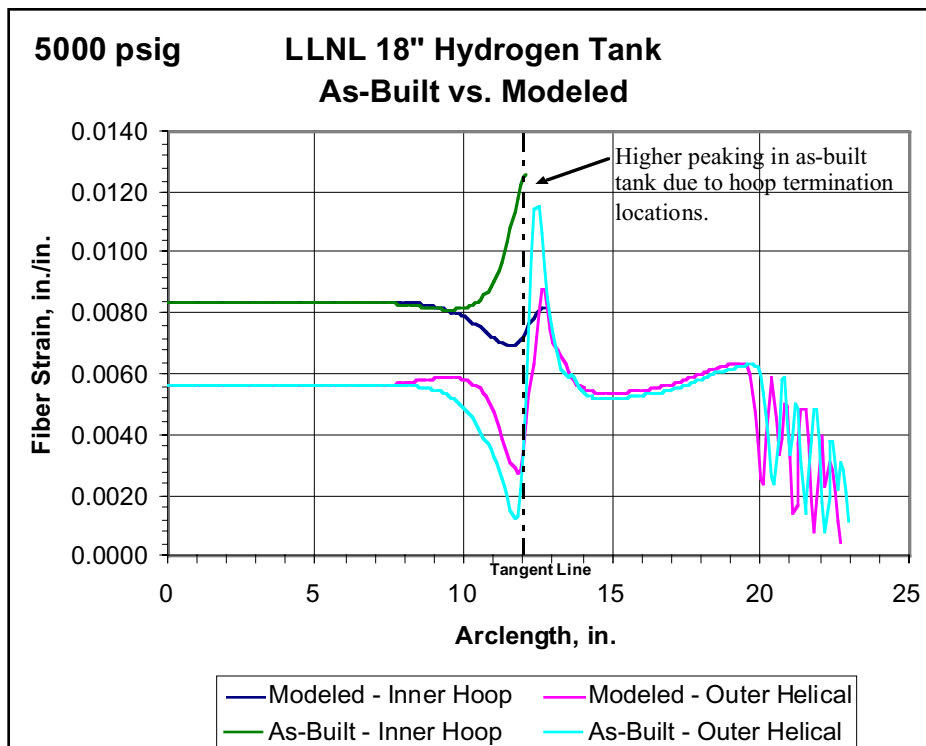


Figure 6: Modeled vs. as-built fiber strain plot

Appendix 1

4.5.1 Tank #1 Hydroburst Test

Tank #1 was returned to Thiokol for burst testing to address variability of the burst pressure and to verify the failure analysis findings. The tank was fitted with six strain gages, three along each tangent line over a 1-inch length. The tank was burst tested on May 8, 2000 at a pressure of 9,503 psig, 20.7% higher than the first tank, with a measured fiber strain of 1.444%. The tank also failed in the tangent line. The high variation is typical with bending failures. The recorded strains at 5,000 psig are plotted with the estimated strains in Figure 7. The measured strains agreed well with the estimates, although the peak helical strains were missed.

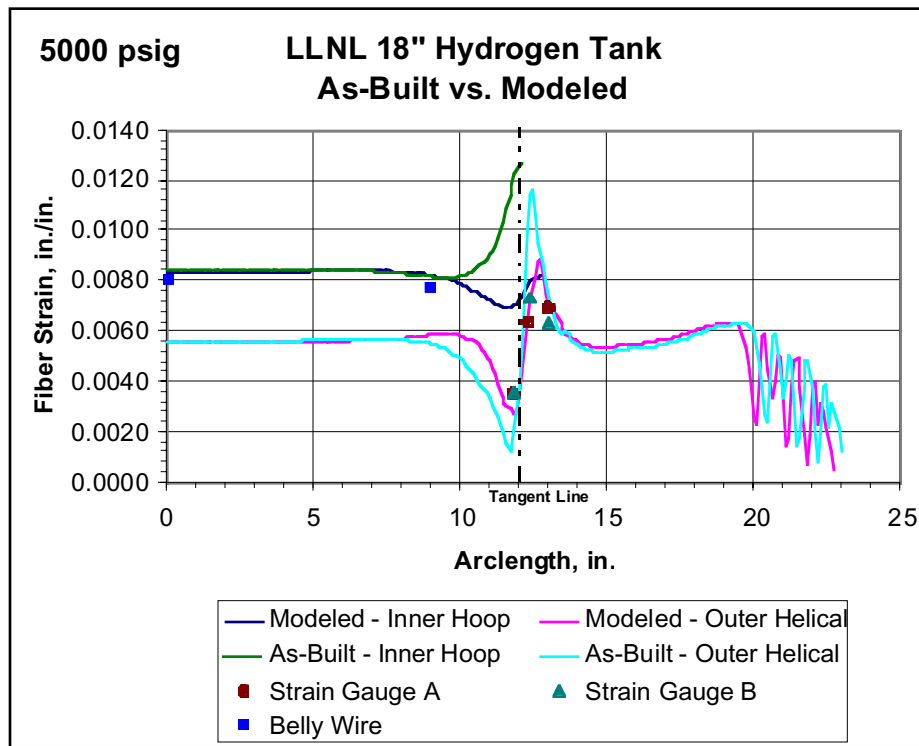


Figure 7: Measured vs. estimated fiber strain plot (Tank #1)

4.6 Redesign

The redesign effort first focused on finding a hoop termination pattern that dropped helical strains at the tangent below the level of the hoop strain. Some iterations were done to investigate the sensitivity of the termination points. After a suitable pattern was determined, the polar boss and liner was added to the model to see whether dome failure would be an issue.

4.6.1 Hoop Termination Pattern Design

In trying to find the optimum hoop termination pattern, only the composite was modeled. The target was to get a peak helical strain at the tangent line to be 10-15% lower than the hoop strains. The pattern in Figure 8 achieved the target (see Appendix B for the complete iteration summary). The fiber strain is plotted in Figure 9.

Appendix 1

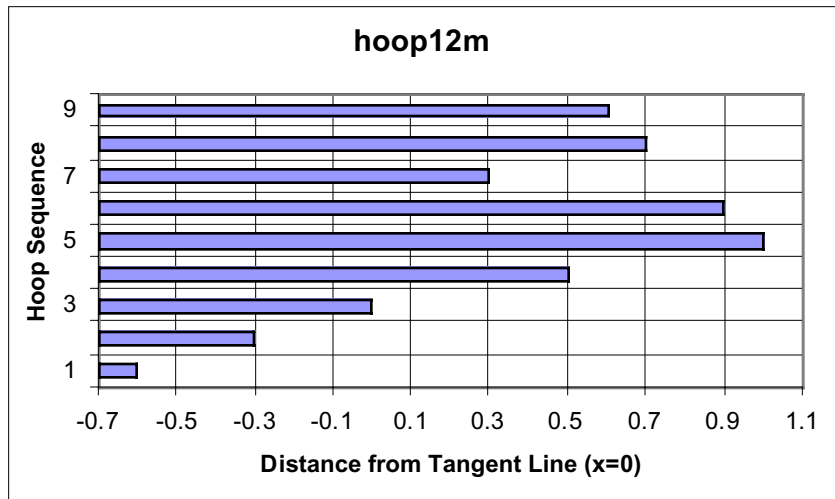


Figure 8: Redesigned hoop termination pattern

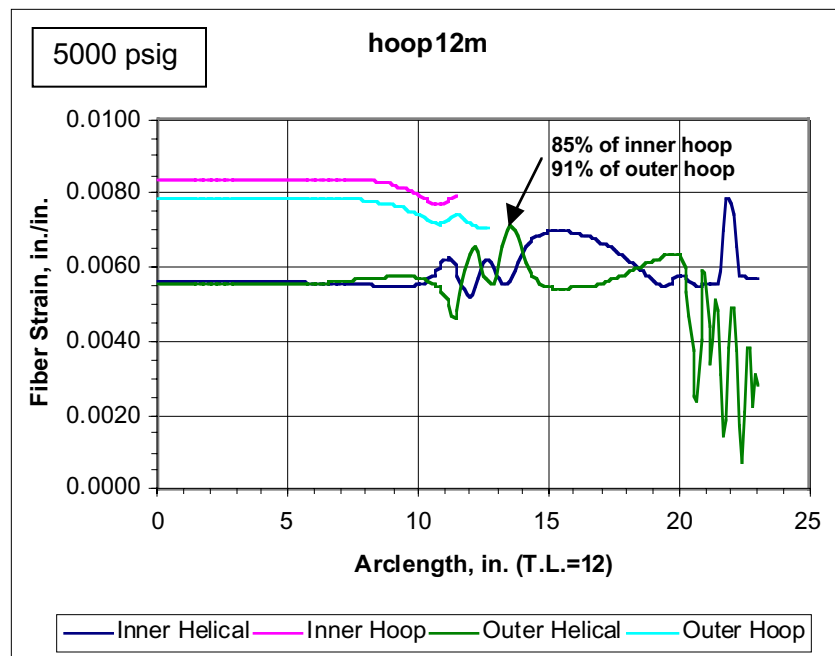


Figure 9: Redesigned hoop pattern fiber strain plot

Sensitivity was also looked at, where all the hoop terminations were offset ± 0.3 inches from the tangent line. An offset forward of the tangent line had minimal impact, however, offsetting aft of the tangent line increased helical strains considerably. The drawing was dimensioned to err on the side of the dome.

The tangent line strains were judged to be acceptable based on experience with rocket motor designs employing similar stress ratio. However, the peak strain in the inner helical layer near the boss was a concern. Generally, when the polar boss is added into the model,

Appendix 1

the peaks decrease. To check this, the liner and polar boss were added into the FE model. The close-up of the boss region of the model is pictured in Figure 10. The model failed to converge at ultimate pressure (11,250 psig) but reached 10,940 psig. The fiber strain plot at this pressure is given in Figure 11.

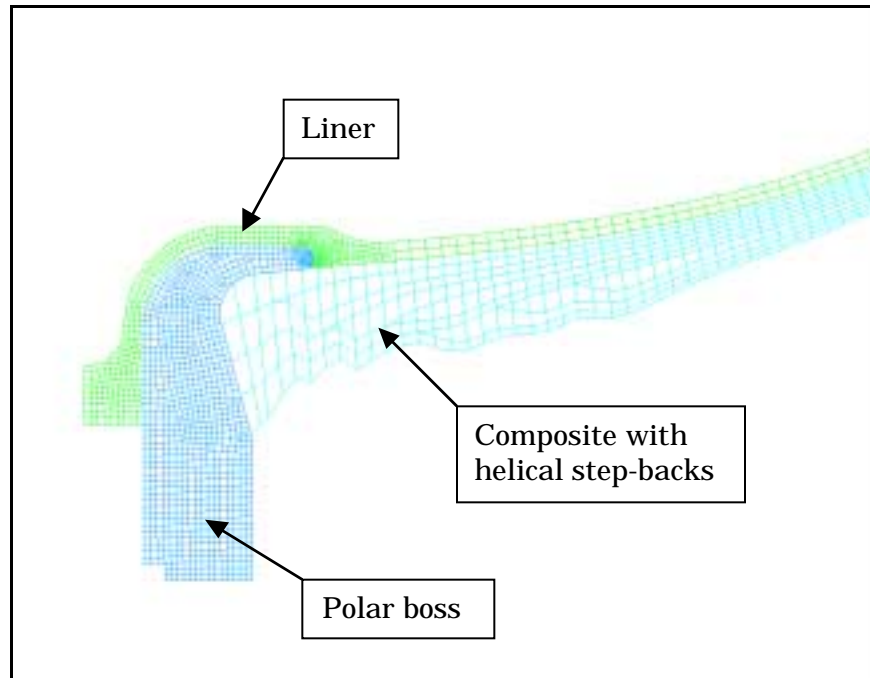


Figure 10: FEM with hardware

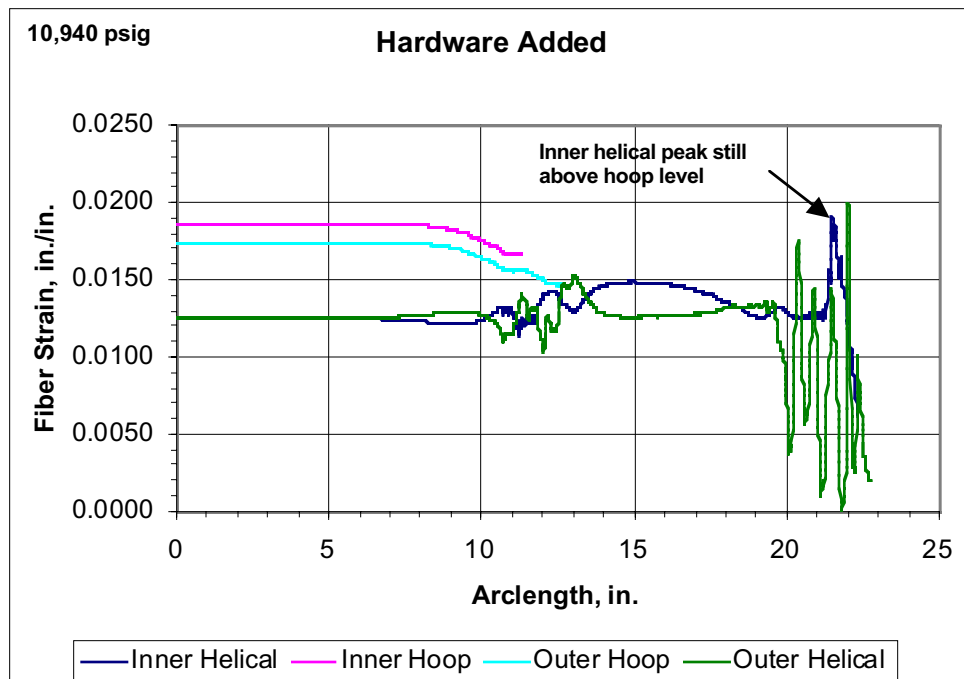


Figure 11: Fiber strain plot with hardware

Appendix 1

The addition of the boss did not bring down the peak inner helical strain. The level is above the hoop strain level, which would indicate a dome failure upon burst testing. The peaks in the outer helical layer were also high, however, it was felt that those peaks were artificial and were a function of the element mesh. As can be seen in Figure 10, the composite mesh is quite jagged on the outer helical layer. To verify this, the composite mesh was manually smoothed in the polar boss region, from about where the furthest step-back is to the boss. The element smoothing was done by moving nodes to simulate an actual build-up, and then degrading properties where resin pools would be located. The smoothed model is shown in Figure 12. The buildup is smoother, but the outer helical is still rougher than what would actually be wound. The fiber strain plot at ultimate pressure is shown in Figure 13. Comparing the fiber strain in the outer helical to the un-smoothed plot in Figure 11, the peaks have drastically decreased. Thus, the outer helical peaks were deemed artificially caused by the mesh geometry.

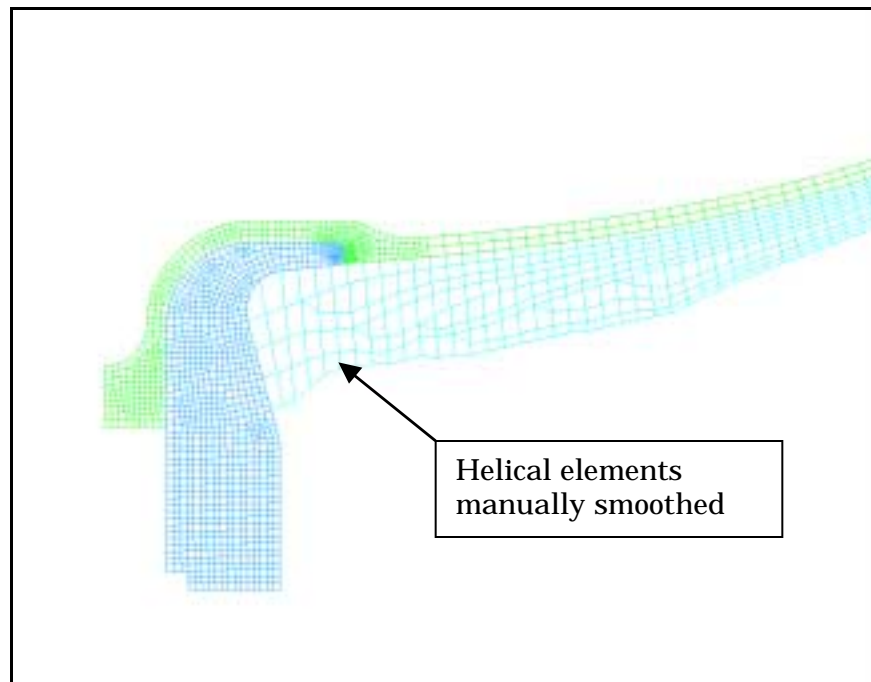


Figure 12: FEM with smoothed composite

Appendix 1

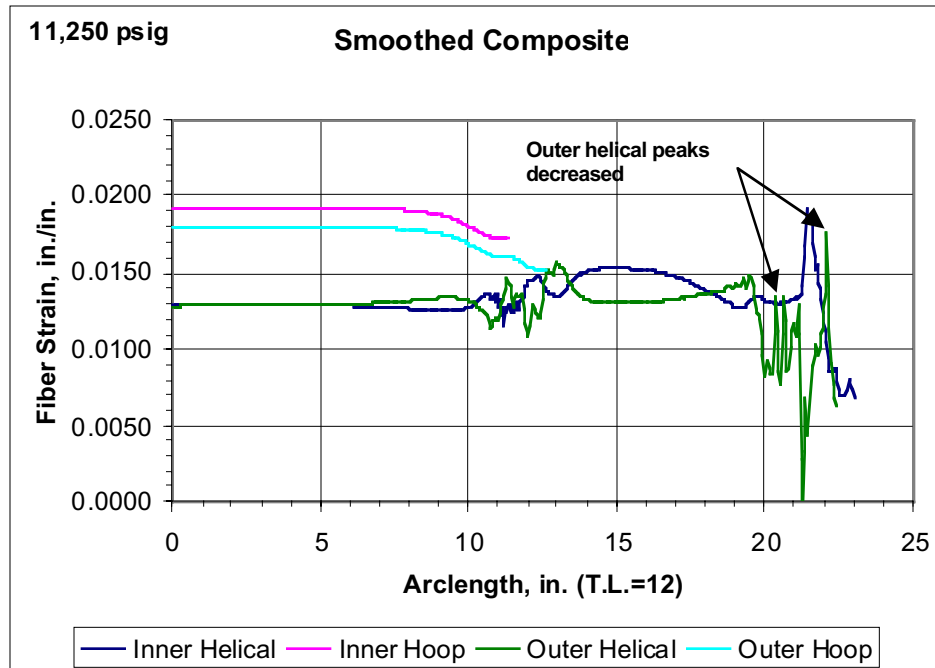


Figure 13: Fiber strain plot with smoothed composite

4.6.2 Wafer Design

The full analysis with all the hardware indicated a dome failure was a high possibility. Several design options were considered to minimize this failure mode.

1. Build a tank with just the new hoop termination pattern – the helical peak could not be as high as predicted.
2. Add one more helical layer to decrease the stress ratio.
3. Use a wafer to decrease the helical peak.

Since the next tank to be built required a high probability of meeting the burst strength target, option 1 was dismissed. Likewise, it was felt that option 2 would not bring the strain peak low enough. Also, the extra weight was undesirable since performance was key. Option 3 seemed to be the best choice. The weight would be minimally impacted by the addition of a wafer, plus, it had the most potential to bring the helical peak down.

The finite element model was modified to include a wafer. Analyses were done with various wafer dimensions, number of wafers, and locations of wafers. The design iterations are attached in Appendix C. The final design used one wafer between the 1st and 2nd helical layers. This location proved optimal in that the wafer would be positioned on a smooth surface contour compared to an outer layer where step-backs would cause bumps under the wafer. Also, the location greatly impacted the helical strain. The wafer model is pictured in Figure 14. The wafer is made of T1000 prepreg, same as the case, and includes an adhesive backing to hold it in place. The basic dimensions are a 2.9-inch inside diameter and a 6.6-inch outside diameter. The thickness increases from the inside diameter to the full 0.1-inch thickness over 0.25 inches, remains constant for 0.6 inches, then tapers down

Appendix 1

to the outside diameter. The model was run at ultimate pressure, and the fiber strain plot is given in Figure 15.

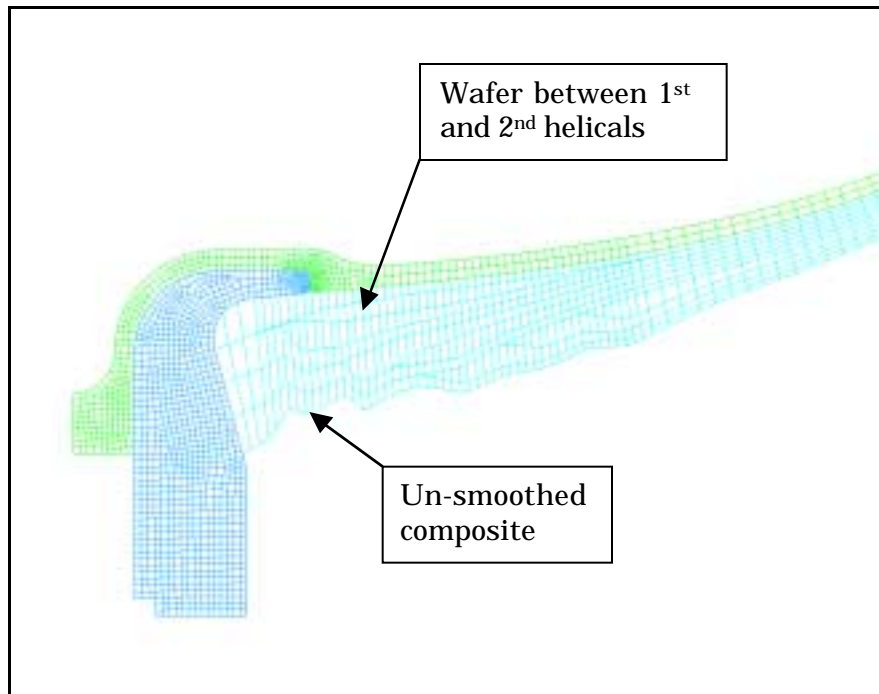


Figure 14: Wafer FEM

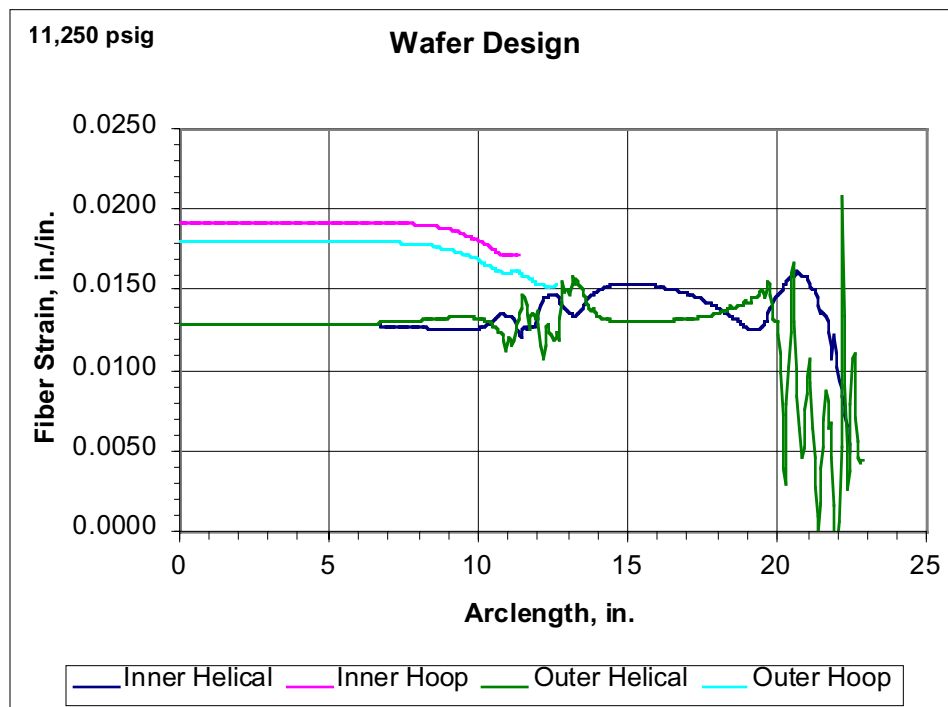


Figure 15: Wafer design fiber strain plot

Appendix 1

Compared to Figure 10, the wafer drastically decreased the fiber strain in the inner helical layer. As before, the outer helical peaks were deemed artificial.

With the new hoop termination pattern and the addition of the wafer in the dome, the design looked promising. The original winding drawing was revised to include the changes and is attached in the appendix.

4.6.3 Tank #4 Fabrication and Testing

Tank four was built incorporating the new design aspects. An annealed liner from ATL was used. The liner weighed 6 lbs. with an outside diameter measuring 16.54 inches (2 psig), about a half-inch smaller than the first three liners. The cylinder length measured 32.51 inches. Each wafer weighed 0.11 lbs., and the total tank weight was 54 lbs. One glass hoop ply secured the label. The internal volume was conservatively estimated to be 8,600 cu. in.

The tank was hydroburst tested on June 16, 2000 per TTP528 Rev. A. The burst pressure was 10,463 psig, 93% of the minimum burst pressure. The measured fiber strain at burst was 1.518%. Figure 16 shows the tank before burst, and Figure 17 shows the tank following the test. The failure was much more catastrophic compared to the previous bursts. The tank failed along the entire length of the cylinder. Whether the failure initiation location was mid-cylinder or at the tangent line is unknown. The domes in the polar boss region looked good with no evidence of fiber breakage except due to secondary impacts.



Figure 16: Tank #4 before hydroburst test

Appendix 1



Figure 17: Tank #4 after hydroburst test

5.0 CONCLUSION

Tanks 1-3 had a design flaw that made the tangent line the failure mode. Tank 4 was redesigned to fix the problem at the tangent line and improve the dome characteristics by adding a wafer; the stress ratio remained unchanged. The redesigned tank reached 93% of the minimum burst pressure requirement (11,250 psig), and 94.4% of the performance goal (1.8×10^6 inches). The fiber strain did not meet expectations. The lower than expected burst pressure was not resolved as a part of this effort.

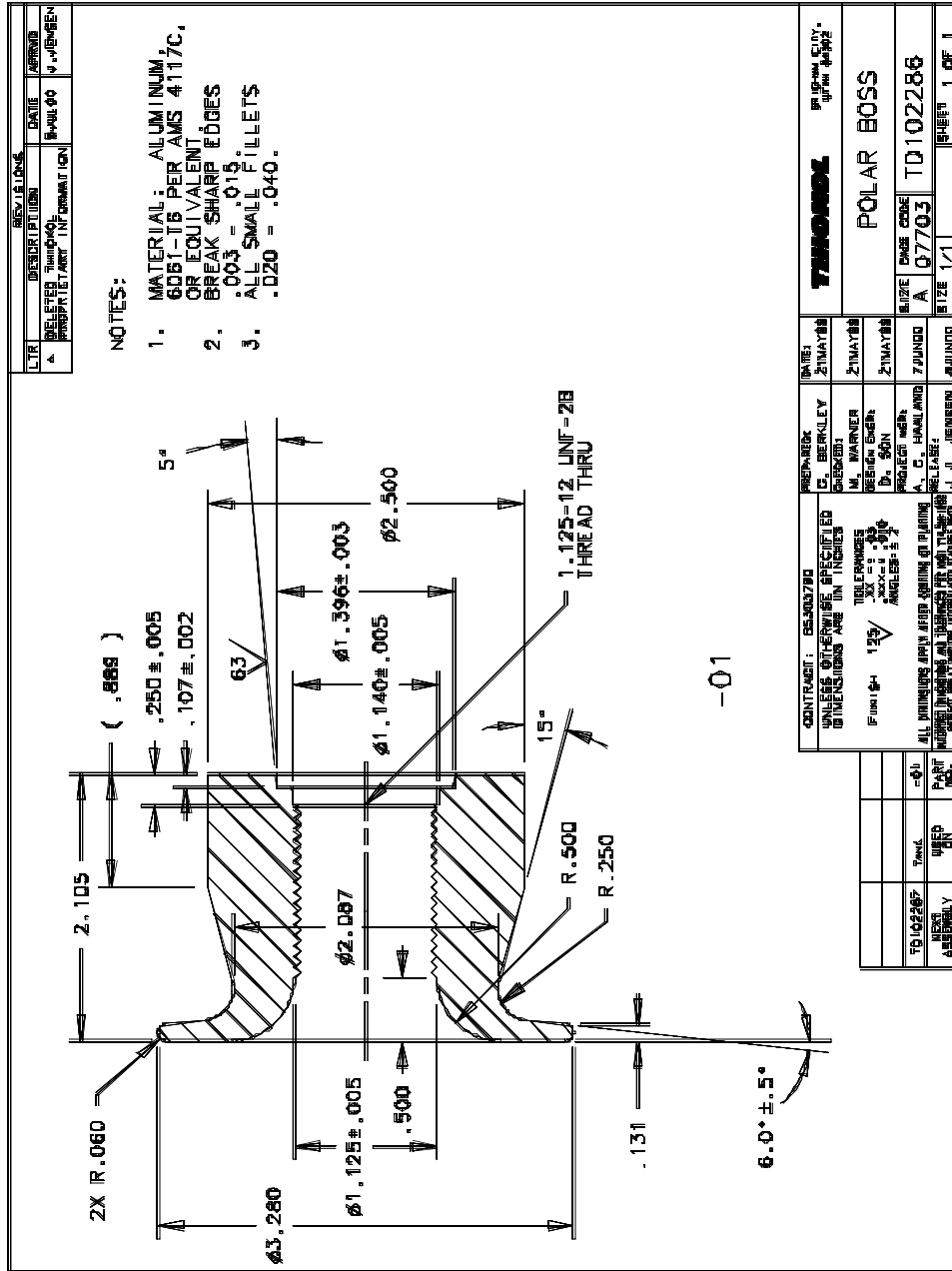
If tank 4 failed in the cylinder region, more hoops could be added to the design to increase the burst pressure and performance goal, but this would increase the stress ratio and may move the failure mode to the domes. The cause of the low burst needs to be investigated so that the design can be modified or the material property allowables can be changed accordingly. Also, if liners are to be annealed, the mold needs to account for the shrinkage so that the designed internal tank volume is not decreased.

Appendix 1

APPENDIX A Tank Drawings

TD102286 Rev A - Polar Boss
TD102288 Rev A - Plastic Liner
TD102287 Rev B - Tank Drawing

Appendix 1



Appendix 1

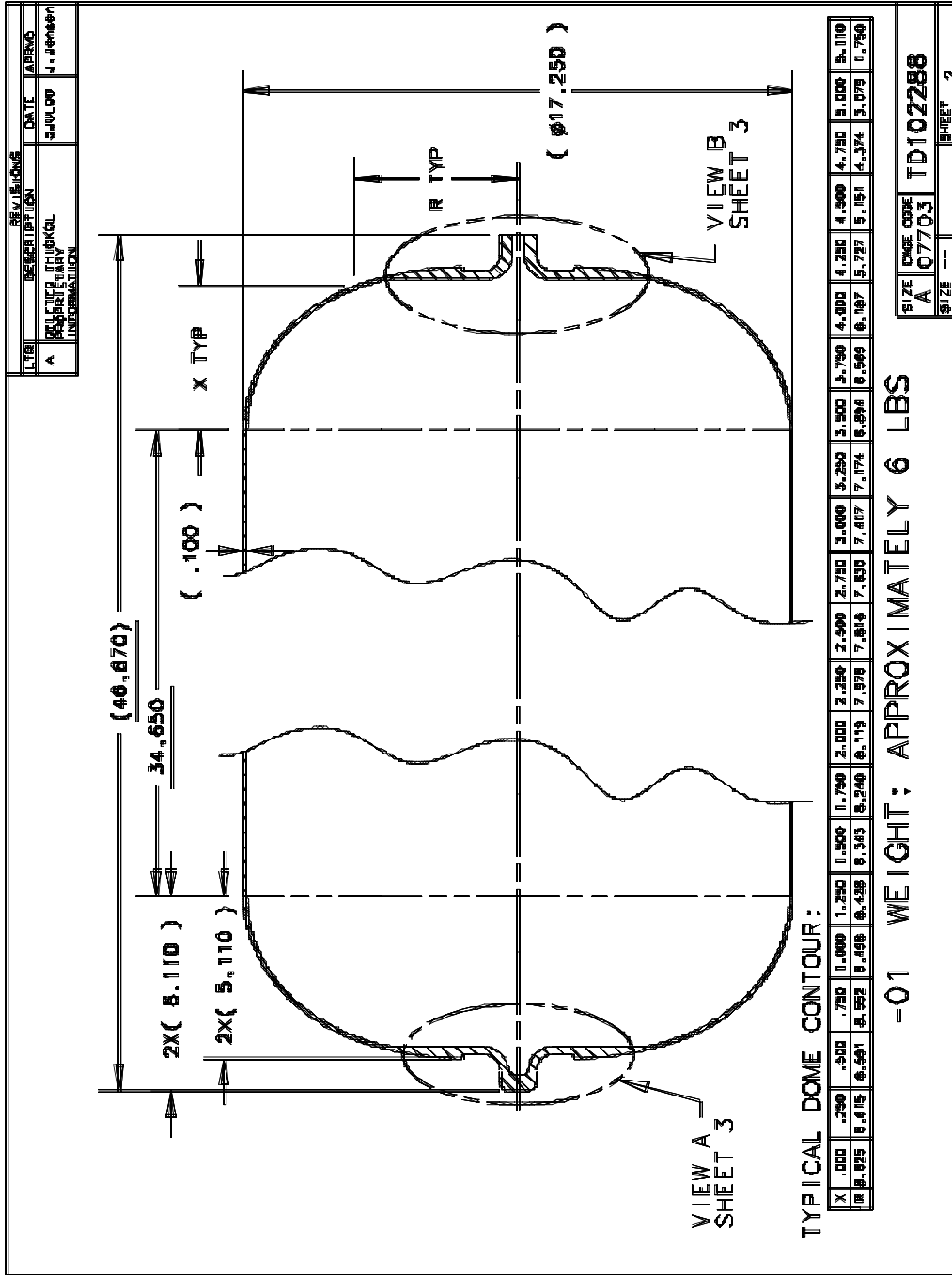
| ITEM | DESCRIPTION | DATE | APPROVAL |
|------|--|--------|-----------|
| A | REVISION TO ORIGINAL PROGRAM DRAWING INFORMATION | 8/1/00 | J. JENSEN |

NOTES:

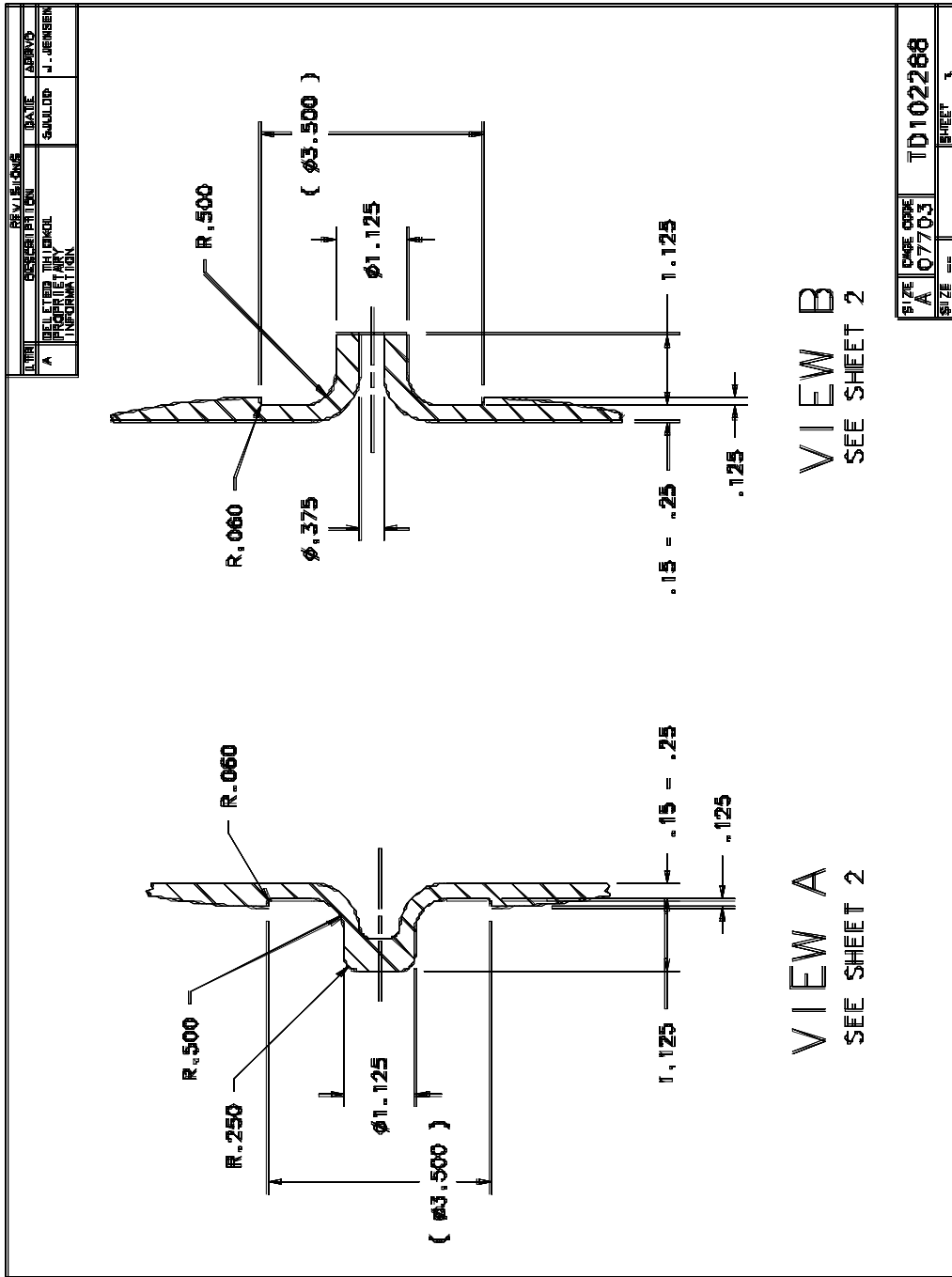
- 1 ACCEPTABLE MATERIAL: FOR -01: TBD.
- 2 OUTSIDE CONTOUR DIMENSIONS ARE FOR TOOLING INSPECTION ONLY. THICKNESS DIMENSIONS APPLY TO MOLDED PARTS.
- 3 MARK CASE CODE, PART NUMBER SERIAL NUMBER, AND MFG DATE USING .25 MIN HEIGHT LETTERS WITH BLACK PERMANENT INK.

| CITY | REQD | FIND | PART NUMBER | DESCRIPTION | MATERIAL SPECIFICATION | NOTE |
|--|------|---------------|---------------------|-------------|------------------------|------|
| <p>CONTRACT: -</p> <p>UNLESS OTHERWISE SPECIFIED DIMENSIONS ARE IN INCHES</p> <p>FINISH: ---√---</p> <p>TELEPHONE: ---</p> <p>FAX: ---</p> <p>ADDRESS: ---</p> <p>ANGLE: ---</p> <p>ALL DIMENSIONS APPLY TO THE COATING OR FINISH</p> <p>INTERFERENCES TO BE SHOWN ON THE DRAWING</p> <p>OTHER INFO AT THE BOTTOM OF DRAWING</p> | | | | | | |
| PARTS LIST | | | | | | |
| D. A. BERKLEY | | DATE: 22DEC98 | FINISH: BIRMAN CITY | | | |
| CHECKED: | | | LINER, 18-INCH DIA | | | |
| SEE LIST FOR: | | 22DEC98 | X 48-INCH LENGTH | | | |
| R. K. KUENZ | | 22DEC98 | SIZE CASE CODE | | | |
| DRAWN BY: | | | A 07703 | | | |
| D. R. MCGUIRE | | 22DEC98 | SIZE --- | | | |
| CHECKED: | | | TD102288 | | | |
| J. J. JENSEN | | 22DEC98 | SHEET 1 OF 3 | | | |

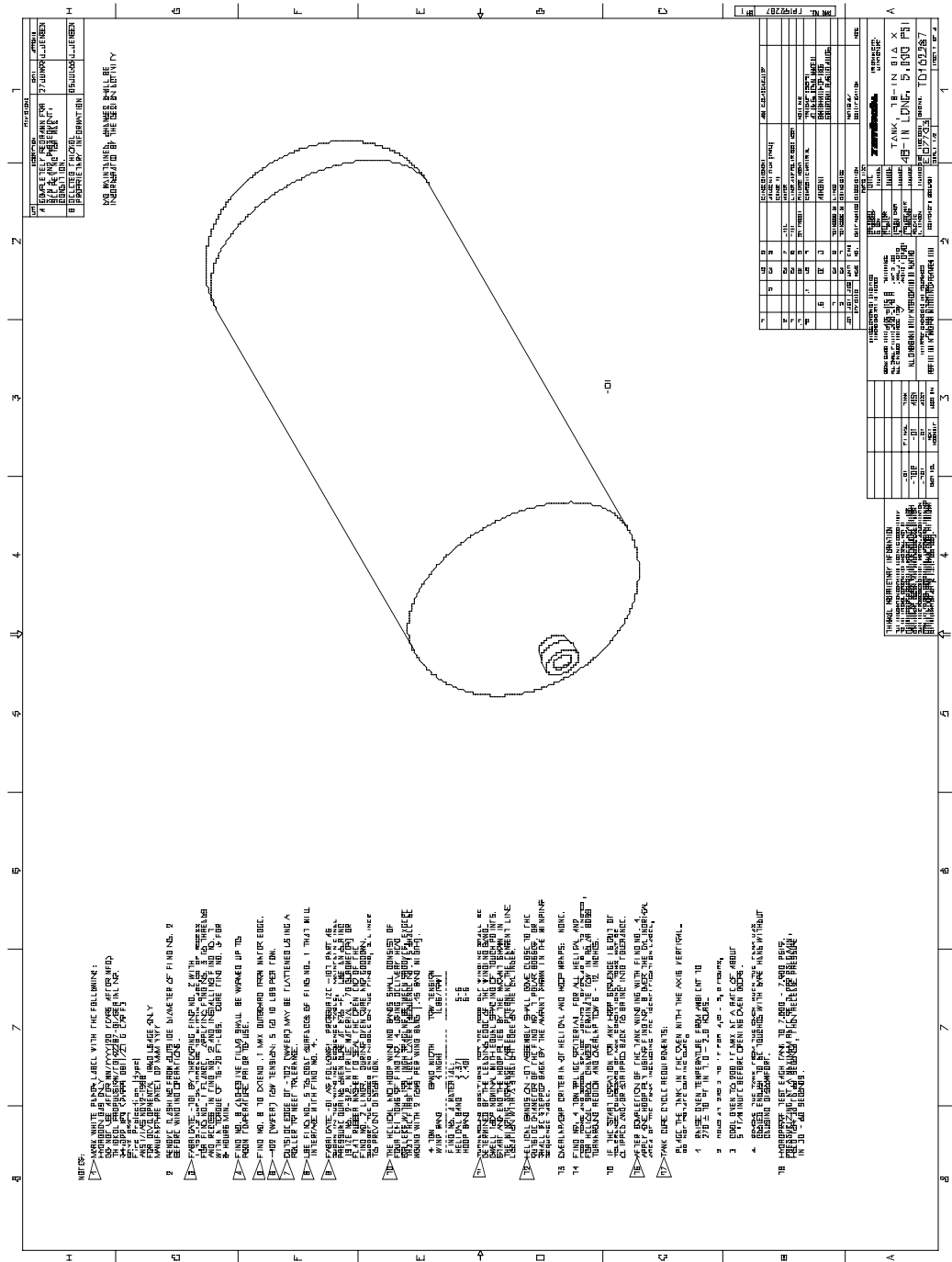
Appendix 1



Appendix 1



Appendix 1

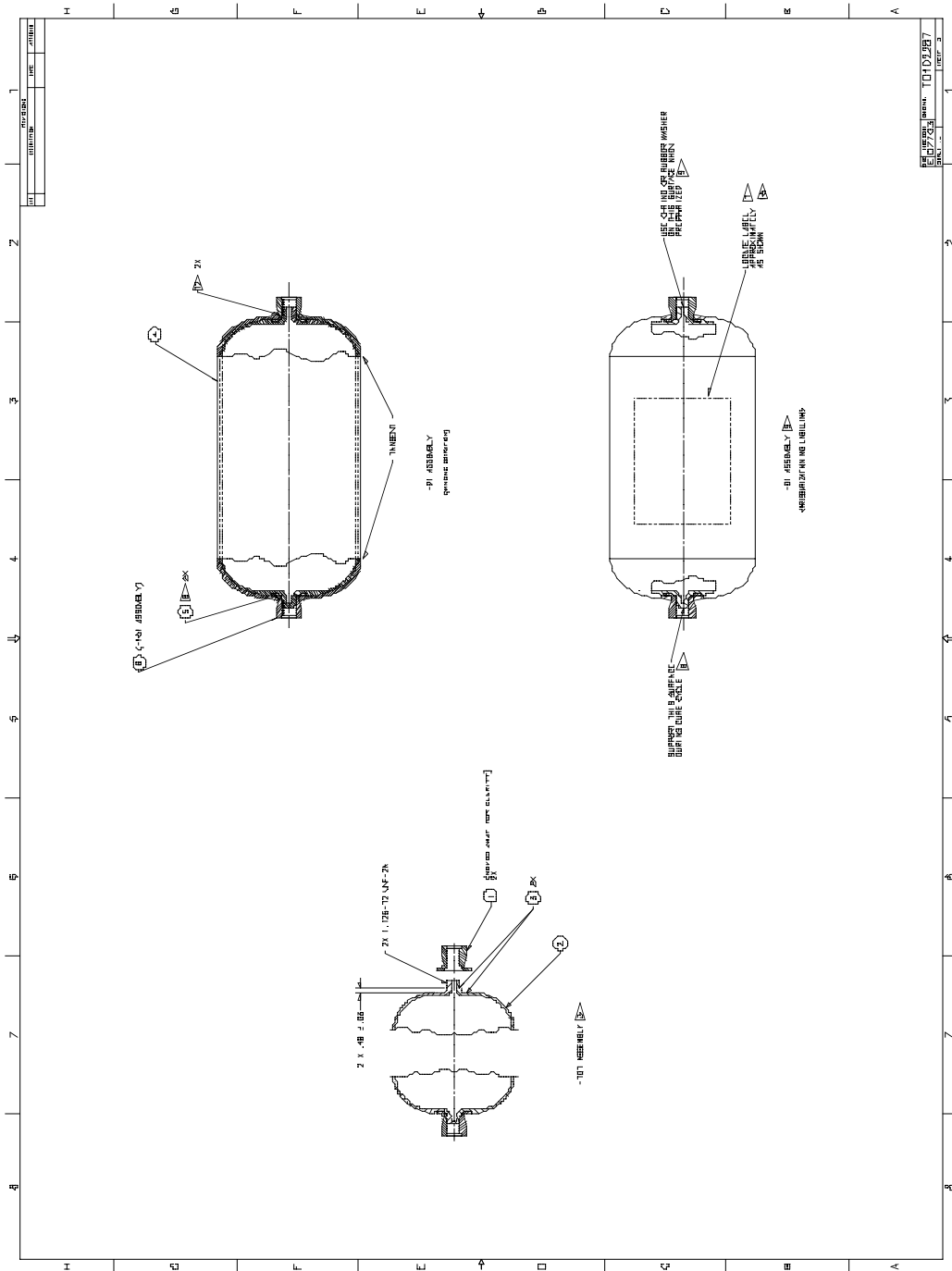


NOTES:

- 1 MARK WHITE PAINT LABEL WITH THE FOLLOWING:
 1. PART NUMBER: 27100001100000
 2. PART NAME: ROTOR HUB
 3. PART NUMBER: 27100001100000
 4. PART NAME: ROTOR HUB
 5. PART NUMBER: 27100001100000
 6. PART NAME: ROTOR HUB
 7. PART NUMBER: 27100001100000
 8. PART NAME: ROTOR HUB
 9. PART NUMBER: 27100001100000
 10. PART NAME: ROTOR HUB
 11. PART NUMBER: 27100001100000
 12. PART NAME: ROTOR HUB
 13. PART NUMBER: 27100001100000
 14. PART NAME: ROTOR HUB
 15. PART NUMBER: 27100001100000
 16. PART NAME: ROTOR HUB
 17. PART NUMBER: 27100001100000
 18. PART NAME: ROTOR HUB
- 2 HOLE DIA. 0.1250 ± 0.0005
- 3 HOLE DIA. 0.1250 ± 0.0005
- 4 HOLE DIA. 0.1250 ± 0.0005
- 5 HOLE DIA. 0.1250 ± 0.0005
- 6 HOLE DIA. 0.1250 ± 0.0005
- 7 HOLE DIA. 0.1250 ± 0.0005
- 8 HOLE DIA. 0.1250 ± 0.0005
- 9 HOLE DIA. 0.1250 ± 0.0005
- 10 HOLE DIA. 0.1250 ± 0.0005
- 11 HOLE DIA. 0.1250 ± 0.0005
- 12 HOLE DIA. 0.1250 ± 0.0005
- 13 HOLE DIA. 0.1250 ± 0.0005
- 14 HOLE DIA. 0.1250 ± 0.0005
- 15 HOLE DIA. 0.1250 ± 0.0005
- 16 HOLE DIA. 0.1250 ± 0.0005
- 17 HOLE DIA. 0.1250 ± 0.0005
- 18 HOLE DIA. 0.1250 ± 0.0005

| REV | DATE | DESCRIPTION |
|-----|----------|-----------------------|
| 1 | 10/10/00 | ISSUED FOR PRODUCTION |
| 2 | 10/10/00 | ISSUED FOR PRODUCTION |
| 3 | 10/10/00 | ISSUED FOR PRODUCTION |
| 4 | 10/10/00 | ISSUED FOR PRODUCTION |
| 5 | 10/10/00 | ISSUED FOR PRODUCTION |
| 6 | 10/10/00 | ISSUED FOR PRODUCTION |
| 7 | 10/10/00 | ISSUED FOR PRODUCTION |
| 8 | 10/10/00 | ISSUED FOR PRODUCTION |
| 9 | 10/10/00 | ISSUED FOR PRODUCTION |
| 10 | 10/10/00 | ISSUED FOR PRODUCTION |
| 11 | 10/10/00 | ISSUED FOR PRODUCTION |
| 12 | 10/10/00 | ISSUED FOR PRODUCTION |
| 13 | 10/10/00 | ISSUED FOR PRODUCTION |
| 14 | 10/10/00 | ISSUED FOR PRODUCTION |
| 15 | 10/10/00 | ISSUED FOR PRODUCTION |
| 16 | 10/10/00 | ISSUED FOR PRODUCTION |
| 17 | 10/10/00 | ISSUED FOR PRODUCTION |
| 18 | 10/10/00 | ISSUED FOR PRODUCTION |

Appendix 1



Appendix 1

APPENDIX B Hoop Termination Design Iterations

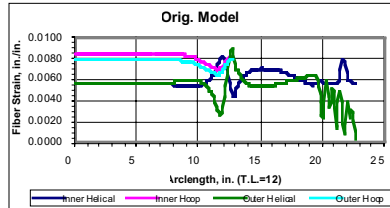
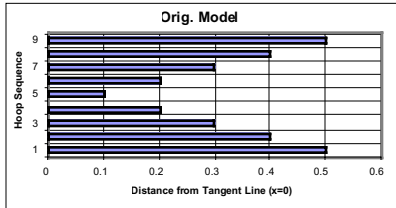
Appendix 1

LLNL 18" Hydrogen Tank Hoop Termination Design Iteration

Pressure = 5000 psi

Orig. Model

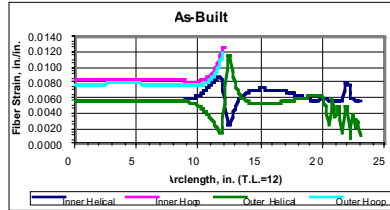
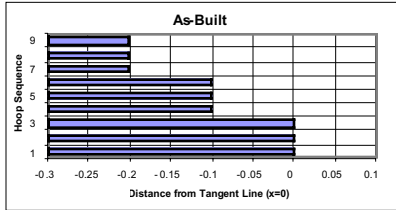
| Seq. | Term. |
|------|-------|
| 1 | 0.5 |
| 2 | 0.4 |
| 3 | 0.3 |
| 4 | 0.2 |
| 5 | 0.1 |
| 6 | 0.2 |
| 7 | 0.3 |
| 8 | 0.4 |
| 9 | 0.5 |



| | | | |
|----------------|---------|-------------|--------|
| inner hoop | 0.0084 | outer hoop | 0.0078 |
| T.L. max. hel. | 0.00882 | | |
| hel./l.hoop | 1.05 | hel./o.hoop | 1.13 |

As-Built

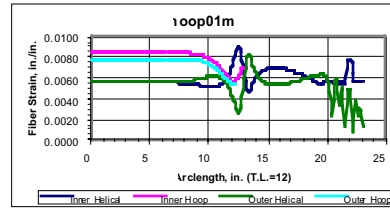
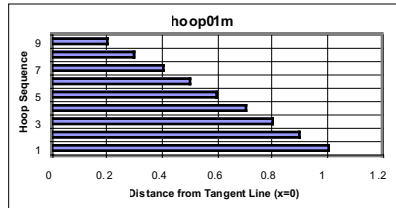
| Seq. | Term. |
|------|-------|
| 1 | 0 |
| 2 | 0 |
| 3 | 0 |
| 4 | -0.1 |
| 5 | -0.1 |
| 6 | -0.1 |
| 7 | -0.2 |
| 8 | -0.2 |
| 9 | -0.2 |



| | | | |
|----------------|---------|-------------|--------|
| inner hoop | 0.0084 | outer hoop | 0.0078 |
| T.L. max. hel. | 0.01157 | | |
| hel./l.hoop | 1.38 | hel./o.hoop | 1.48 |

hoop01m.stk

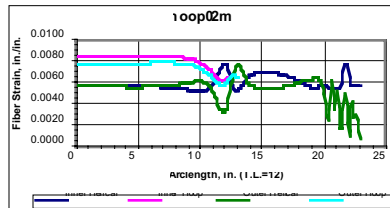
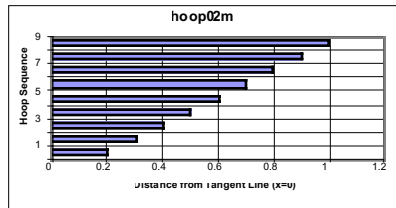
| Seq. | Term. |
|------|-------|
| 1 | 1 |
| 2 | 0.9 |
| 3 | 0.8 |
| 4 | 0.7 |
| 5 | 0.6 |
| 6 | 0.5 |
| 7 | 0.4 |
| 8 | 0.3 |
| 9 | 0.2 |



| | | | |
|----------------|---------|-------------|--------|
| inner hoop | 0.0084 | outer hoop | 0.0078 |
| T.L. max. hel. | 0.00910 | | |
| hel./l.hoop | 1.08 | hel./o.hoop | 1.16 |

noop02m.stk

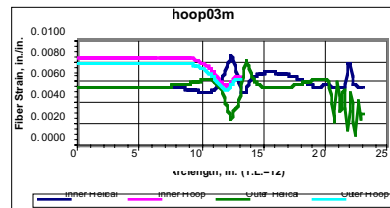
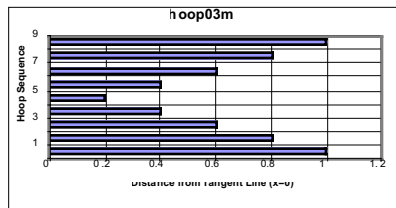
| Seq. | Term. |
|------|-------|
| 1 | 0.2 |
| 2 | 0.3 |
| 3 | 0.4 |
| 4 | 0.5 |
| 5 | 0.6 |
| 6 | 0.7 |
| 7 | 0.8 |
| 8 | 0.9 |
| 9 | 1 |



| | | | |
|----------------|---------|-------------|--------|
| inner hoop | 0.0084 | outer hoop | 0.0078 |
| T.L. max. hel. | 0.00778 | | |
| hel./l.hoop | 0.93 | hel./o.hoop | 0.99 |

hoop03m.stk

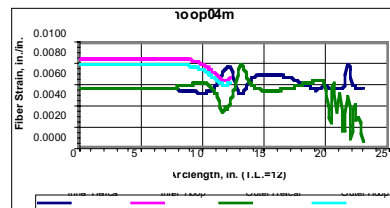
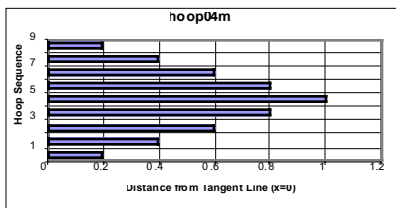
| Seq. | Term. |
|------|-------|
| 1 | 1 |
| 2 | 0.8 |
| 3 | 0.6 |
| 4 | 0.4 |
| 5 | 0.2 |
| 6 | 0.4 |
| 7 | 0.6 |
| 8 | 0.8 |
| 9 | 1 |



| | | | |
|----------------|---------|-------------|--------|
| inner hoop | 0.0084 | outer hoop | 0.0078 |
| T.L. max. hel. | 0.00846 | | |
| hel./l.hoop | 1.01 | hel./o.hoop | 1.08 |

hoop04m.stk

| Seq. | Term. |
|------|-------|
| 1 | 0.2 |
| 2 | 0.4 |
| 3 | 0.6 |
| 4 | 0.8 |
| 5 | 1 |
| 6 | 0.8 |
| 7 | 0.6 |
| 8 | 0.4 |
| 9 | 0.2 |

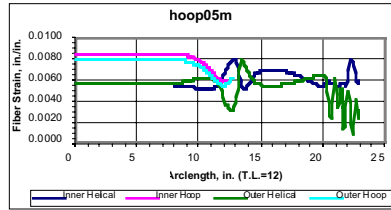
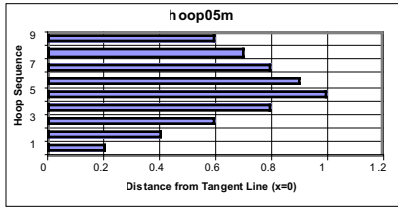


| | | | |
|----------------|---------|-------------|--------|
| inner hoop | 0.0084 | outer hoop | 0.0078 |
| T.L. max. hel. | 0.00779 | | |
| hel./l.hoop | 0.93 | hel./o.hoop | 0.99 |

Appendix 1

hoop05m.stk

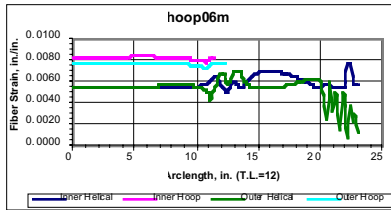
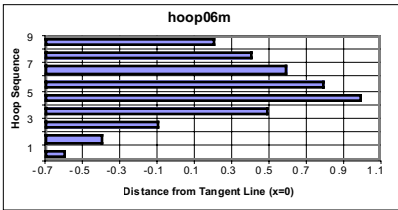
| Seq. | Term. |
|------|-------|
| 1 | 0.2 |
| 2 | 0.4 |
| 3 | 0.6 |
| 4 | 0.8 |
| 5 | 1 |
| 6 | 0.9 |
| 7 | 0.8 |
| 8 | 0.7 |
| 9 | 0.6 |



| | | | |
|----------------|---------|-------------|--------|
| inner hoop | 0.0084 | outer hoop | 0.0078 |
| T.L. max. hel. | 0.00795 | | |
| hel./l.hoop | 0.95 | hel./o.hoop | 1.02 |

hoop06m.stk

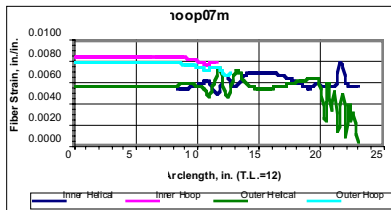
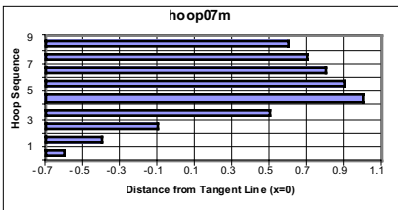
| Seq. | Term. |
|------|-------|
| 1 | -0.6 |
| 2 | -0.4 |
| 3 | -0.1 |
| 4 | 0.5 |
| 5 | 1 |
| 6 | 0.8 |
| 7 | 0.6 |
| 8 | 0.4 |
| 9 | 0.2 |



| | | | |
|----------------|---------|-------------|--------|
| inner hoop | 0.0084 | outer hoop | 0.0078 |
| T.L. max. hel. | 0.00710 | | |
| hel./l.hoop | 0.85 | hel./o.hoop | 0.91 |

hoop07m.stk

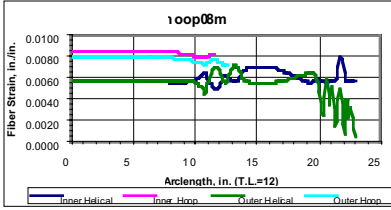
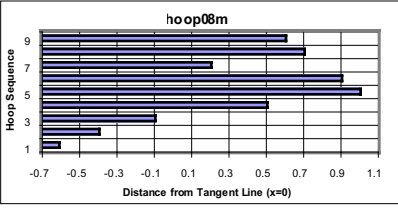
| Seq. | Term. |
|------|-------|
| 1 | -0.6 |
| 2 | -0.4 |
| 3 | -0.1 |
| 4 | 0.5 |
| 5 | 1 |
| 6 | 0.9 |
| 7 | 0.8 |
| 8 | 0.7 |
| 9 | 0.6 |



| | | | |
|----------------|---------|-------------|--------|
| inner hoop | 0.0084 | outer hoop | 0.0078 |
| T.L. max. hel. | 0.00727 | | |
| hel./l.hoop | 0.87 | hel./o.hoop | 0.93 |

hoop08m.stk

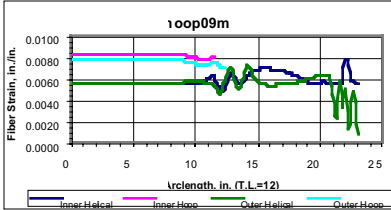
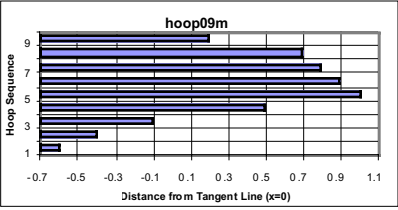
| Seq. | Term. |
|------|-------|
| 1 | -0.6 |
| 2 | -0.4 |
| 3 | -0.1 |
| 4 | 0.5 |
| 5 | 1 |
| 6 | 0.9 |
| 7 | 0.2 |
| 8 | 0.7 |
| 9 | 0.6 |



| | | | |
|----------------|---------|-------------|--------|
| inner hoop | 0.0084 | outer hoop | 0.0078 |
| T.L. max. hel. | 0.00709 | | |
| hel./l.hoop | 0.84 | hel./o.hoop | 0.90 |

hoop09m.stk

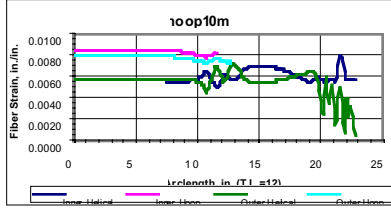
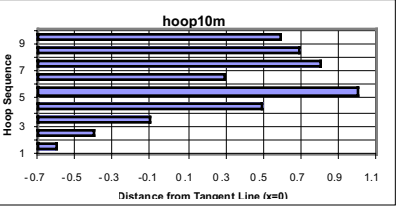
| Seq. | Term. |
|------|-------|
| 1 | -0.6 |
| 2 | -0.4 |
| 3 | -0.1 |
| 4 | 0.5 |
| 5 | 1 |
| 6 | 0.9 |
| 7 | 0.8 |
| 8 | 0.7 |
| 9 | 0.2 |



| | | | |
|----------------|---------|-------------|--------|
| inner hoop | 0.0084 | outer hoop | 0.0078 |
| T.L. max. hel. | 0.00720 | | |
| hel./l.hoop | 0.86 | hel./o.hoop | 0.92 |

hoop10m.stk

| Seq. | Term. |
|------|-------|
| 1 | -0.6 |
| 2 | -0.4 |
| 3 | -0.1 |
| 4 | 0.5 |
| 5 | 1 |
| 6 | 0.3 |
| 7 | 0.8 |
| 8 | 0.7 |
| 9 | 0.6 |

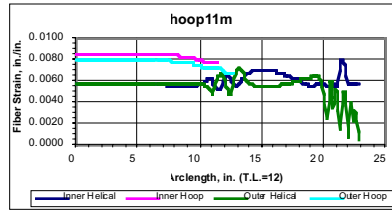
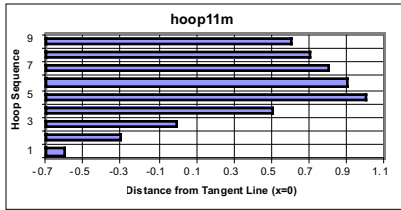


| | | | |
|----------------|---------|-------------|--------|
| inner hoop | 0.0084 | outer hoop | 0.0078 |
| T.L. max. hel. | 0.00710 | | |
| hel./l.hoop | 0.85 | hel./o.hoop | 0.91 |

Appendix 1

hoop11m.stk

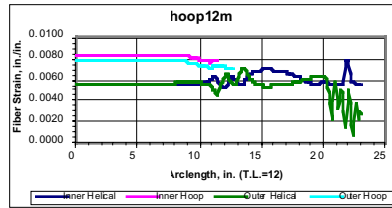
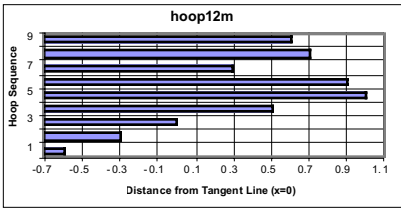
| Seq. | Term. |
|------|-------|
| 1 | -0.6 |
| 2 | -0.3 |
| 3 | 0 |
| 4 | 0.5 |
| 5 | 1 |
| 6 | 0.9 |
| 7 | 0.8 |
| 8 | 0.7 |
| 9 | 0.6 |



| inner hoop | outer hoop |
|------------------------|-------------|
| 0.0084 | 0.0078 |
| T.L. max. hel. 0.00721 | |
| hel./l.hoop | hel./o.hoop |
| 0.86 | 0.92 |

hoop12m.stk

| Seq. | Term. |
|------|-------|
| 1 | -0.6 |
| 2 | -0.3 |
| 3 | 0 |
| 4 | 0.5 |
| 5 | 1 |
| 6 | 0.9 |
| 7 | 0.3 |
| 8 | 0.7 |
| 9 | 0.6 |



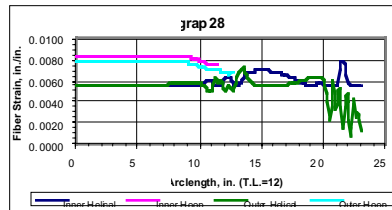
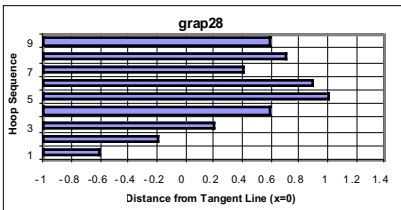
| inner hoop | outer hoop |
|------------------------|-------------|
| 0.0084 | 0.0078 |
| T.L. max. hel. 0.00713 | |
| hel./l.hoop | hel./o.hoop |
| 0.85 | 0.91 |

NOTE: hoop12m chosen over hoop08m because there is more margin between the hoop strain in the cylinder and near the termination where it peaks up (arclength 11-12).

Sensitivity for hoop12m.stk

grap28.stk

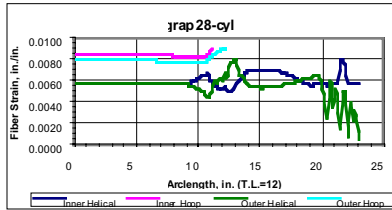
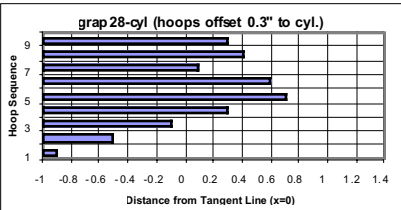
| Seq. | Term. |
|------|-------|
| 1 | -0.6 |
| 2 | -0.2 |
| 3 | 0.2 |
| 4 | 0.6 |
| 5 | 1 |
| 6 | 0.9 |
| 7 | 0.4 |
| 8 | 0.7 |
| 9 | 0.6 |



| inner hoop | outer hoop |
|------------------------|-------------|
| 0.0084 | 0.0078 |
| T.L. max. hel. 0.00719 | |
| hel./l.hoop | hel./o.hoop |
| 0.86 | 0.92 |

grap28-cyl.stk

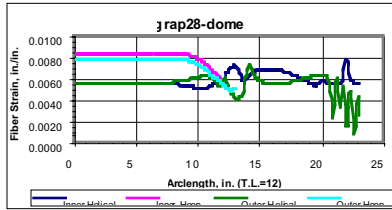
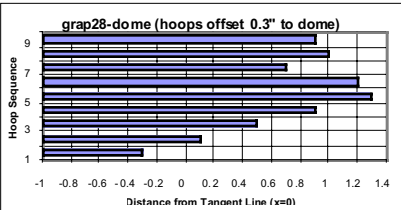
| Seq. | Term. |
|------|-------|
| 1 | -0.9 |
| 2 | -0.5 |
| 3 | -0.1 |
| 4 | 0.3 |
| 5 | 0.7 |
| 6 | 0.6 |
| 7 | 0.1 |
| 8 | 0.4 |
| 9 | 0.3 |



| inner hoop | outer hoop |
|------------------------|------------------------|
| 0.0084 | 0.0078 |
| T.L. max. hel. 0.00783 | T.L. max. hoop 0.00902 |
| hel./l.hoop | hel./o.hoop |
| 0.93 | 1.00 |

grap28-dome.stk

| Seq. | Term. |
|------|-------|
| 1 | -0.3 |
| 2 | 0.1 |
| 3 | 0.5 |
| 4 | 0.9 |
| 5 | 1.3 |
| 6 | 1.2 |
| 7 | 0.7 |
| 8 | 1 |
| 9 | 0.9 |



| inner hoop | outer hoop |
|------------------------|-------------|
| 0.0084 | 0.0078 |
| T.L. max. hel. 0.00731 | |
| hel./l.hoop | hel./o.hoop |
| 0.87 | 0.93 |

hoops cannot vary towards the cylinder!

Appendix 1

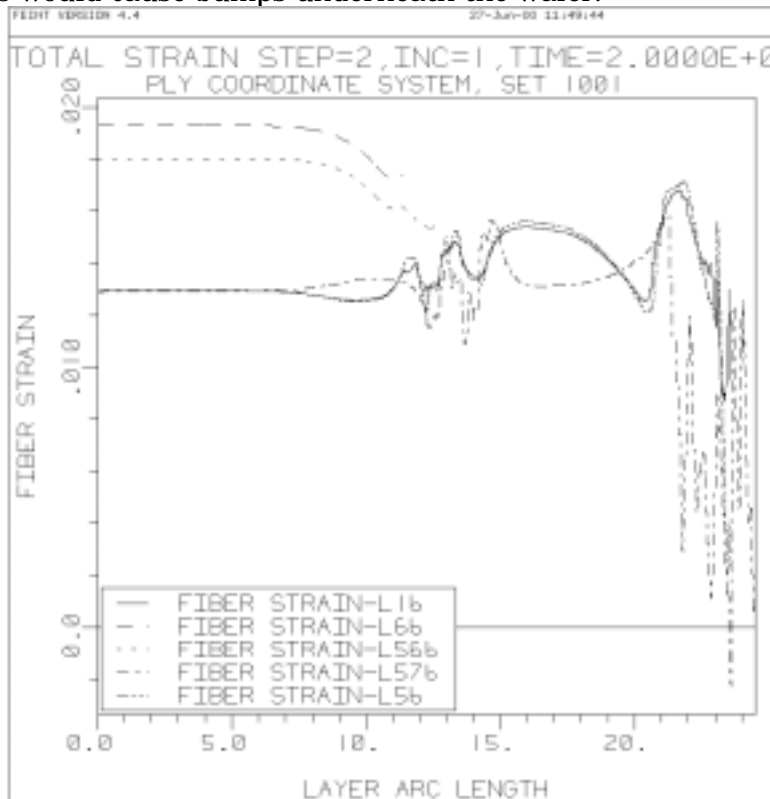
APPENDIX C Wafer Design Iterations

Appendix 1

Wafer Design Iteration

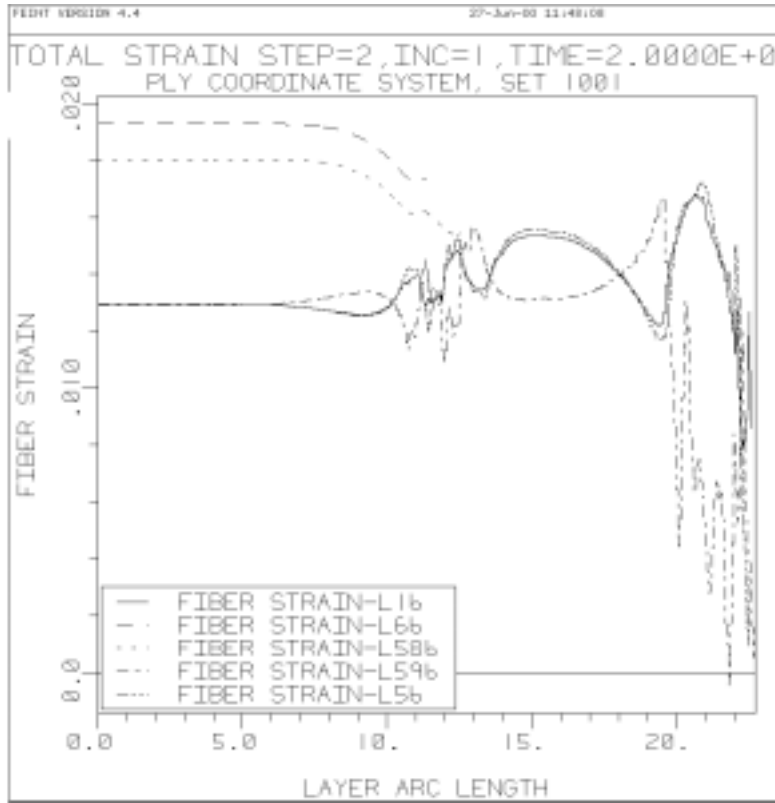
Fiber Strain Plots at 11,250 psig (Composite only)

Run 6 was used as the baseline design. Runs 4 and 7 were comparable to Run 6 and showed that the design could tolerate dimensional changes with little impact to the peak helical fiber strain. Runs 1,2, and 8 showed slightly higher strain peaks, while Runs 3 and 5 were unacceptable. The two wafer design in Run 2 did not give better performance compared to using just one wafer. Placing the wafer between the 1st and 2nd helical layers was desirable since the surface contour was smoother compared to outer layers where helical step-backs would cause bumps underneath the wafer.

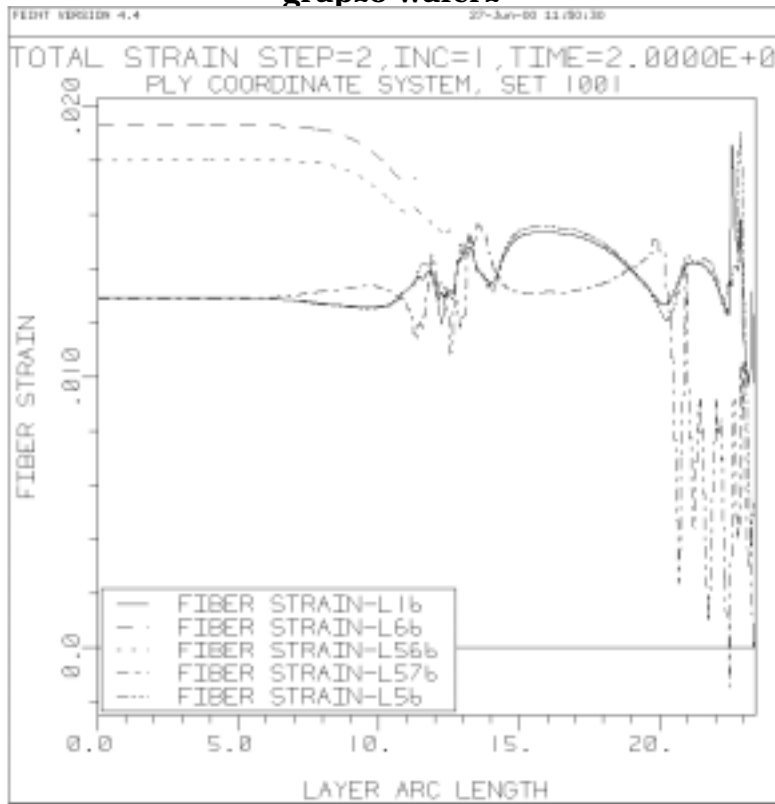


grap28-wafer1

Appendix 1

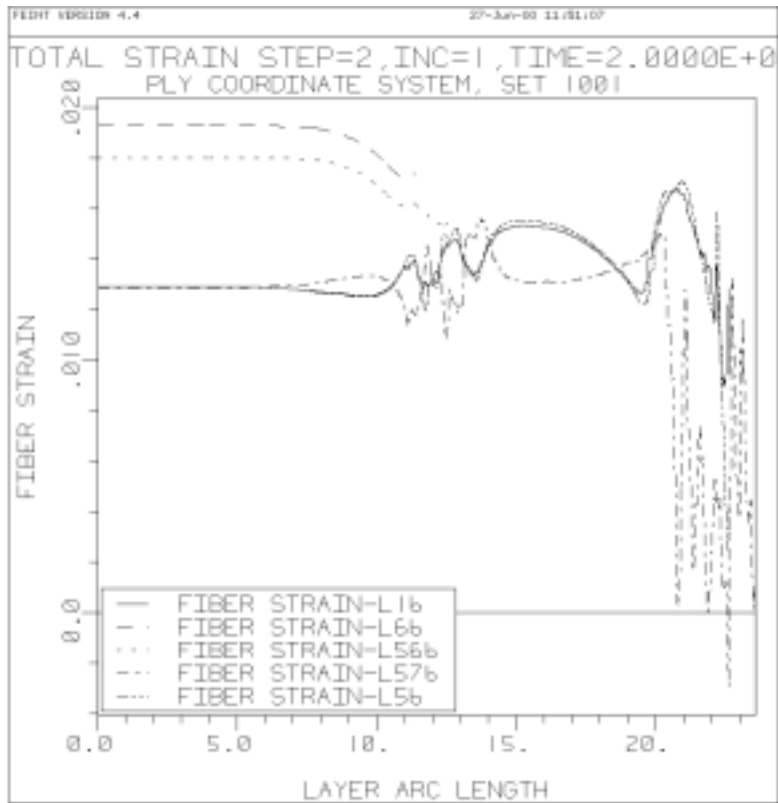


grap28-wafer2

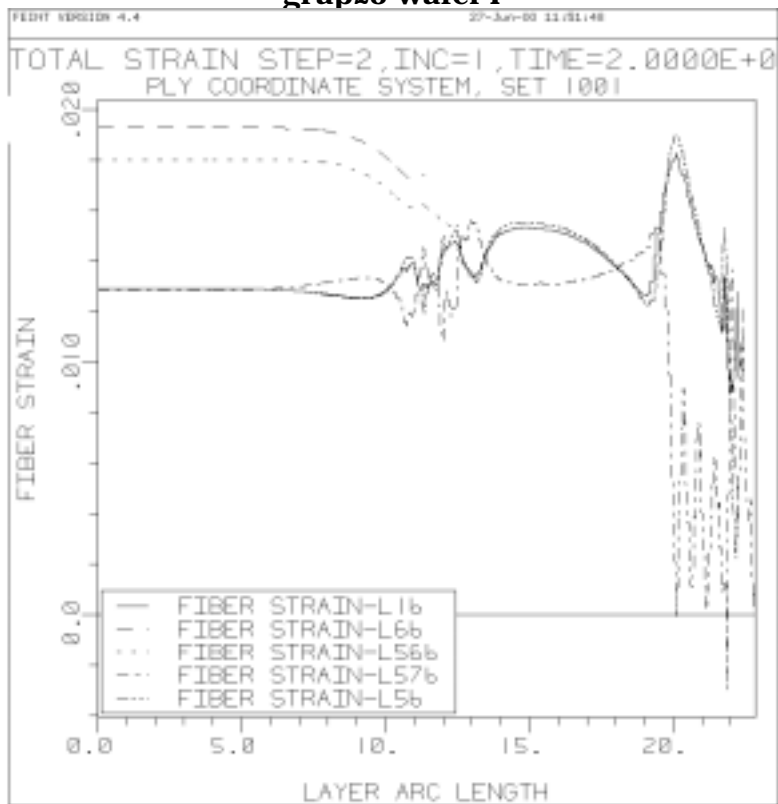


grap28-wafer3

Appendix 1

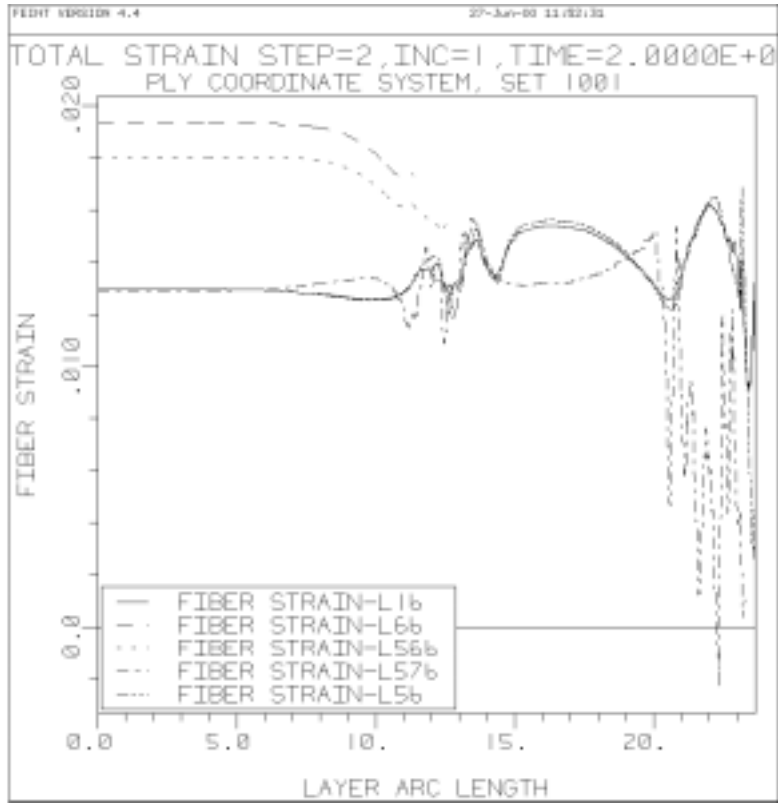


grap28-wafer4

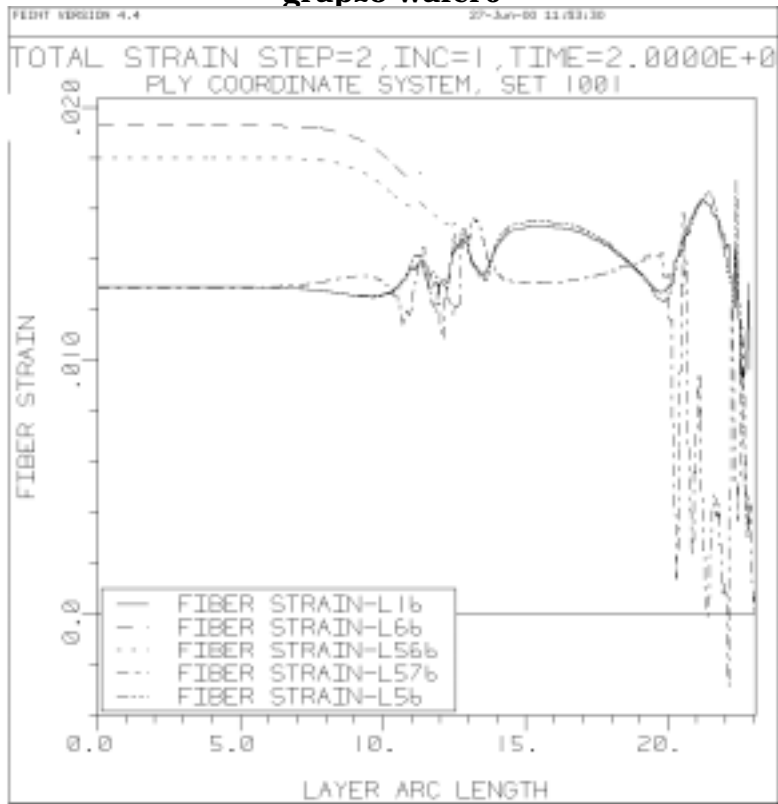


grap28-wafer5

Appendix 1

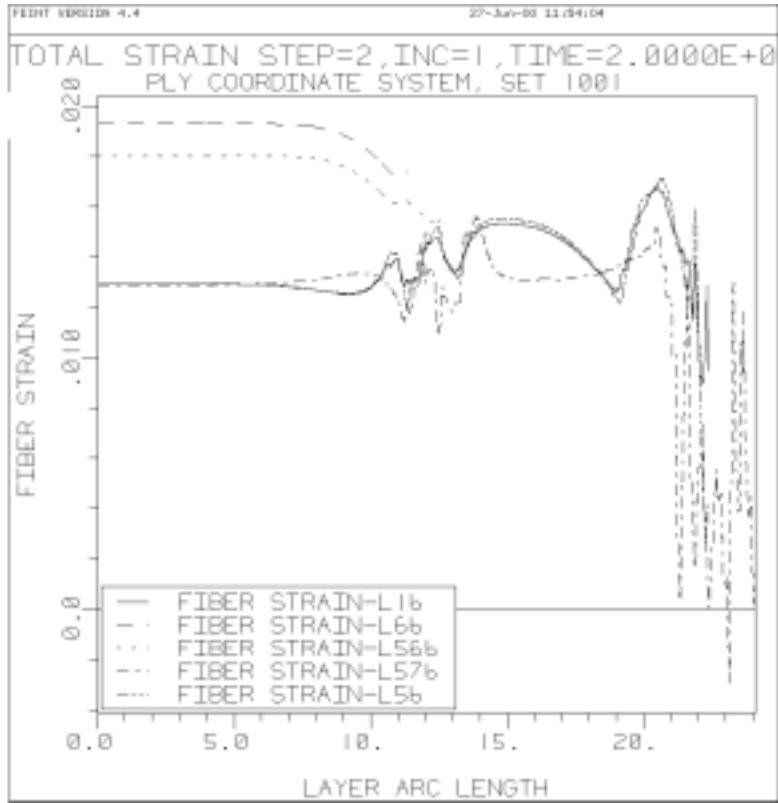


grap28-wafer6



grap28-wafer7

Appendix 1



grap28-wafer8

Appendix 1

APPENDIX D Test Plan TTP528

Appendix 1

DISTRIBUTION

| Name | # Copies | Mail Stop |
|-----------------|-----------------|------------------|
| Fred Mitlitsky | 1 | LLNL |
| Andrew Weisberg | 1 | LLNL |
| Andy Haaland | 1 | 230 |
| Dave Nelson | 1 | 242 |
| David Son | 4 | 254 |

LOW TEMPERATURE AND HIGH PRESSURE EVALUATION OF INSULATED PRESSURE VESSELS FOR CRYOGENIC HYDROGEN STORAGE

S. M. Aceves,
Lawrence Livermore National Laboratory
7000 East Ave., L-641
Livermore, CA 94551, USA
saceves@llnl.gov

J. Martinez-Frias
Centro de Ingenieria y Desarrollo Industrial
Queretaro, Qro., Mexico
jmartinez@cidesi.mx

O. Garcia-Villazana
FIMEE, Universidad de Guanajuato
Salamanca, Gto. Mexico
villa@salamanca.ugto.mx

Abstract

Insulated pressure vessels are cryogenic-capable pressure vessels that can be fueled with liquid hydrogen (LH₂) or ambient-temperature compressed hydrogen (CH₂). Insulated pressure vessels offer the advantages of liquid hydrogen tanks (low weight and volume), with reduced disadvantages (fuel flexibility, lower energy requirement for hydrogen liquefaction and reduced evaporative losses). The work described here is directed at verifying that commercially available pressure vessels can be safely used to store liquid hydrogen. The use of commercially available pressure vessels significantly reduces the cost and complexity of the insulated pressure vessel development effort. This paper describes a series of tests that have been done with aluminum-lined, fiber-wrapped vessels to evaluate the damage caused by low temperature operation. All analysis and experiments to date indicate that no significant damage has resulted. Required future tests are described that will prove that no technical barriers exist to the safe use of aluminum-fiber vessels at cryogenic temperatures.

Introduction

Hydrogen-fueled vehicles present features that make them serious candidates as alternatives to today's petroleum-powered vehicles. Hydrogen vehicles can use the advanced technology of electric vehicles to improve environmental quality and energy security, while providing the range, performance, and utility of today's gasoline vehicles.

Probably the most significant hurdle for hydrogen vehicles is storing sufficient hydrogen on board. Hydrogen storage choices can determine the refueling time, cost, and infrastructure requirements, as well as indirectly influence energy efficiency, vehicle fuel economy, performance, and utility. There are at least three viable technologies for storing hydrogen fuel on cars. These are compressed hydrogen gas (CH_2), metal hydride adsorption, and cryogenic liquid hydrogen (LH_2). Each of these has significant disadvantages.

Storage of 5 kg of hydrogen (equivalent in terms of energy to 19 liters; 5 gallons of gasoline) is considered necessary for a general-purpose vehicle, since it provides a 640 km (400 mile) range in a 34 km/liter (80 mpg) hybrid vehicle or fuel cell vehicle. Storing this hydrogen as CH_2 requires a volume so big that it is difficult to package in light-duty cars (Pentastar Electronics, 1997). The external volume for a pressure vessel storing 5 kg of hydrogen at 24.8 MPa (3600 psi) is 320 liters (85 gal). Hydrides are heavy (300 kg for 5 kg of hydrogen, Michel et al., 1996), resulting in a substantial reduction in vehicle fuel economy and performance.

Low-pressure LH_2 storage is light and compact, and has received significant attention due to its advantages for packaging (Braess and Strobl, 1996). Significant recent developments have resulted in improved safety (Pehr, 1996a, 1996b), and fueling infrastructure (Hettinger et al., 1996). Disadvantages of low-pressure LH_2 storage are the substantial amount of electricity required for liquefying the hydrogen (Peschka, 1992); the evaporation losses that may occur during fueling low-pressure LH_2 tanks (Wetzel, 1996); and the evaporative losses that occur during periods of inactivity, due to heat transfer from the environment.

An alternative is to store hydrogen in an insulated pressure vessel that has the capacity to operate at LH_2 temperature (20 K), and at high pressure (24.8 MPa; 3600 psi). This vessel has the flexibility of accepting LH_2 or CH_2 as a fuel. Filling the vessel with ambient-temperature CH_2 reduces the amount of hydrogen stored (and therefore the vehicle range) to about a third of its value with LH_2 .

The fueling flexibility of the insulated pressure vessels results in significant advantages. Insulated pressure vessels have similar packaging characteristics as liquid hydrogen tanks (low weight and volume), with reduced energy consumption for liquefaction. Energy requirements for hydrogen liquefaction are lower than for liquid hydrogen tanks because a car with an insulated pressure vessel can use, but does not require, cryogenic hydrogen fuel. A hybrid or fuel cell vehicle with 34 km/l (80 mpg) gasoline-equivalent fuel economy could be refueled with ambient-temperature CH_2 at 24.8 MPa (3600 psi) and still achieve a 200 km range, suitable for the majority of trips. The additional energy, cost, and technological effort for cryogenic refueling need only be undertaken (and paid for) when the additional range is required for longer trips. With an insulated pressure vessel, vehicles can refuel most of the time with ambient-temperature

hydrogen, using less energy, and most likely at lower ultimate cost than LH₂, but with the capability of having 3 times the range of room-temperature storage systems. Use of compressed hydrogen in all trips under 200 km (which represent 85% of all the distance traveled in the USA, (Klinger and Kuzmyak, 1984) reduces the total energy consumption by 16% over the energy consumed by a vehicle that is always filled with LH₂.

Insulated pressure vessels also have much reduced evaporative losses compared to LH₂ tanks. This has been demonstrated in a previous work (Aceves and Berry, 1998), which presents a thorough analysis of evaporative losses in cryogenic pressure vessels based on the first law of thermodynamics. Figure 1 illustrates some of the main results. This figure shows hydrogen losses during vehicle operation. The figure assumes that two vehicles are fitted with cryogenic hydrogen storage tanks with the same capacity (5 kg). One vehicle has a low-pressure (0.5 MPa; 70 psia maximum) conventional liquid hydrogen tank, and the other has an insulated pressure vessel. The vehicles are identical in every respect, except for the tanks. The vessels are filled to full capacity with liquid hydrogen, and then the vehicles are driven a fixed distance every day. When the fuel runs out, the amount of fuel burned by the engine and the amount of fuel lost to evaporation are calculated, and the results are shown in Figure 1. The figure shows total cumulative evaporative hydrogen losses out of a full tank as a function of the daily driving distance, for a high-efficiency vehicle (34 km/l or 80 mpg gasoline equivalent fuel economy). As expected, evaporative losses increase as the daily driving distance is reduced, because less driving results in a longer time for hydrogen evaporation. The figure shows that a low-pressure LH₂ tank loses hydrogen even when driven 100 km per day. Losses from a LH₂ tank grow rapidly as the daily driving distance drops. A vehicle driven 50 km per day (the average for the USA, Aceves and Berry, 1998) loses almost 1 kg (20%) of the fuel to evaporation. On the other hand, insulated pressure vessels lose hydrogen only for very short daily driving distances (less than 5 km/day). Most vehicles are driven considerably more than this distance, so that most vehicles equipped with an insulated pressure vessel would never lose any hydrogen to evaporation.

The low losses in insulated pressure vessels are the result of the flow work (work required to extract the hydrogen from the vessel, VanWylen and Sonntag, 1978). The hydrogen stored in the vessel does work as the hydrogen is being extracted, cooling down in the process. This effect is very significant for hydrogen, due to its low molecular weight.

From an engineering and economic perspective, insulated pressure vessels strike a versatile balance between the cost and bulk of ambient-temperature CH₂ storage, and the energy efficiency, thermal insulation and evaporative losses of LH₂ storage.

Considering all the potential benefits of insulated pressure vessels, it is important to determine what type of pressure vessel could be operated at both high pressure and cryogenic temperature. Of the available pressure vessel technologies commonly used for vehicular storage of natural gas (Institute of Gas Technology, 1996), it appears that aluminum-lined, composite-wrapped vessels have the most desirable combination of properties for this application (low weight and affordable price). However, commercially available aluminum-composite pressure vessels are not designed for low temperature applications.

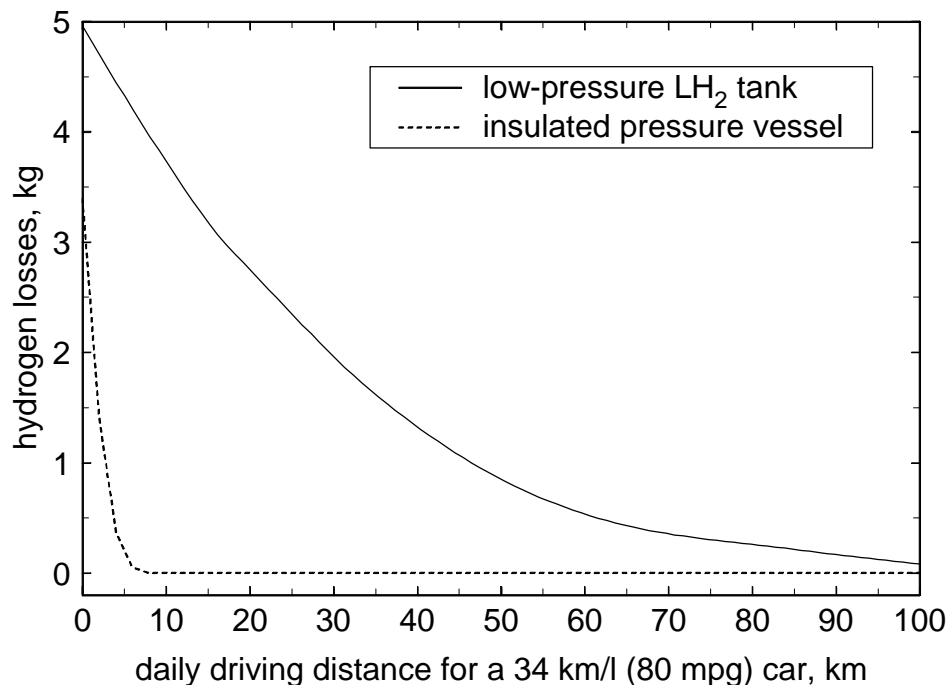


Figure 1. Cumulative hydrogen losses in kg as a function of daily driving distance, for vehicles with 17 km/liter (40 mpg); or 34 km/l (80 mpg) fuel economy, for three cryogenic hydrogen storage vessels.

This paper describes work in progress directed at evaluating the possibility of using commercially available aluminum-fiber pressure vessels at cryogenic temperatures and high pressures, as would be required for vehicular hydrogen storage in insulated pressure vessels. The paper gives a description of previous and ongoing tests, followed by a list of future tests. The purpose of these tests is to demonstrate that no technical barriers exist that prevent the use of aluminum-fiber pressure vessels at cryogenic temperatures. However, it is recognized that further tests may be necessary for certification, which is required for commercialization of insulated pressure vessels. Certification also requires subjecting several pressure vessels to the required tests, to determine the statistical significance of the results (Bauer, 1996). Obtaining vessel certification is beyond the scope of this work. It is the authors' belief that the current work will provide vessel manufacturers with an additional option for vehicular hydrogen storage. It would then be left to manufacturers to conduct the required tests to achieve certification and guarantee safety under all possible conditions. It is worth pointing out that the aluminum-fiber pressure vessels used in all these tests have been certified according to the DOT standards (CFR-

DOT, Title 49, 1996a) for storage of compressed natural gas. The current tests are being performed because these pressure vessels are being used outside their typical range of operation, and also because they are being modified to attach a vacuum insulation to them.

Previous and Ongoing Tests

Pressure and Temperature Cycling

Pressure vessels have been cycled through 900 high-pressure cycles and 100 low-temperature cycles. The cycles are alternated, running 9 pressure cycles followed by a temperature cycle, and repeating this sequence 100 times. This test is expected to replicate what would happen if these vessels were used in a hydrogen-fueled car. Liquid nitrogen is used for low-temperature cycling and gaseous helium for high-pressure cycling. To accomplish the required testing, an experimental setup has been built inside a high-pressure cell. A schematic is shown in Figure 2. The valves shown in the schematic are controlled by computer, which allows the system to run with no supervision, resulting in fast cycling. An aramid-aluminum and a carbon fiber-aluminum pressure vessel have been cycled. The characteristics of these are listed in Table 1.

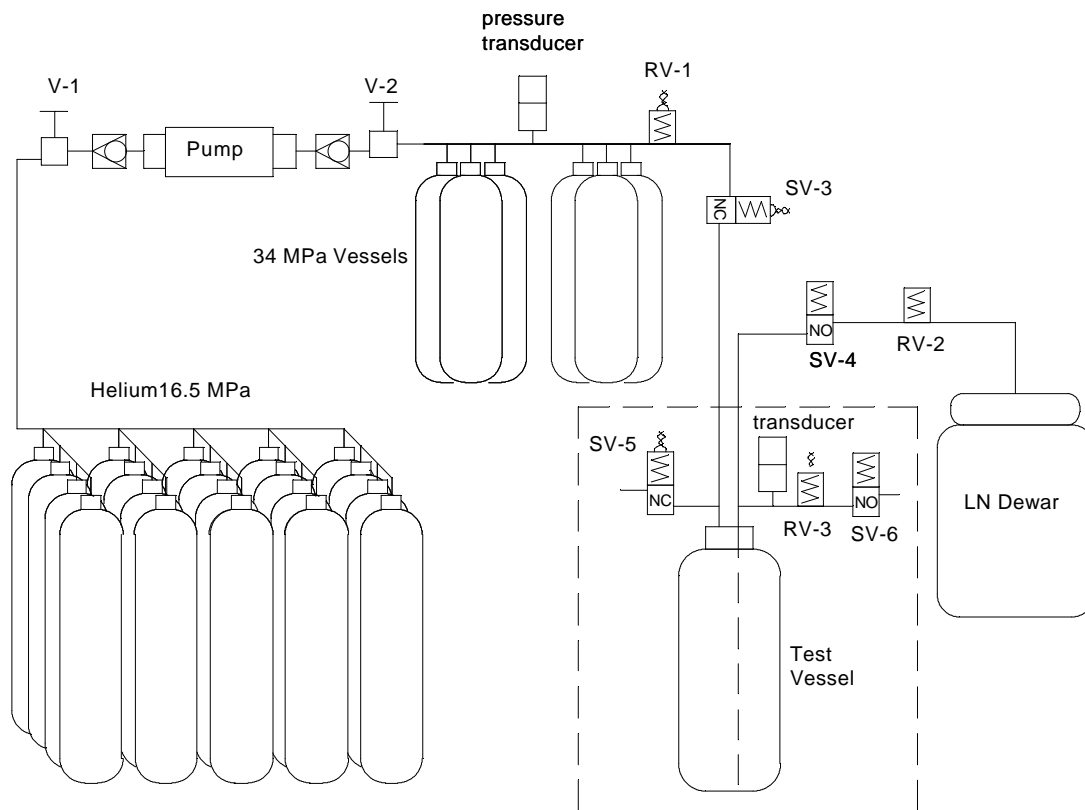


Figure 2. Schematic of the experimental setup for temperature and pressure cycling of pressure vessels.

Table 1. Characteristics of the Tested Hydrogen Vessels and Their Planned Insulation

| | Aramid-Aluminum | Carbon Fiber-Aluminum |
|--|-----------------|-----------------------|
| Mass of hydrogen stored, kg | 1.13 | 0.44 |
| Vessel weight, kg | 10 | 4.1 |
| Internal volume, liters | 17.6 | 6.8 |
| Internal diameter, m | 0.2 | 0.17 |
| Internal surface area, m ² | 0.48 | 0.25 |
| Design pressure, MPa (psi) | 24.1 (3500) | 31 (4500) |
| Performance factor ¹ , m (10 ⁶ in) | 13000 (0.5) | 13115 (0.51) |
| Safety factor | 3.0 | 2.5 |

¹ defined as burst pressure*volume/weight.

Two cyclic tests have been completed, one on an aramid-aluminum pressure vessel and other on a carbon fiber-aluminum pressure vessel. The vessels have not failed during the test, and they have not shown superficial evidence of damage under observation. The carbon fiber-aluminum vessel was instrumented with strain gages in addition to the thermocouples and pressure sensor. Results from the strain gages will be used for validating the finite element analysis.

Burst Test

The aramid-aluminum and the carbon fiber-aluminum pressure vessels were burst-tested after being cycled and ultrasound-tested. The burst test was conducted according to the Code of Federal Regulations-Department of Transportation standards for pressure vessel certification (CFR-DOT, 1996a). Figure 3 shows the variation of pressure as a function of time for the aramid-aluminum vessel. Failure occurred by hoop mid cylinder separation, which is the preferred mode of failure. The burst pressure was 94.2 MPa (13.7 ksi), which is substantially higher than the minimum burst pressure of 72.4 MPa (10.5 ksi). The very high value of the burst pressure compared to the minimum burst pressure may be due in part to work hardening that took place during the cold cycling of the vessel. The carbon fiber-aluminum also failed at a pressure higher than the minimum required.

Finite Element Analysis

Cyclic, ultrasound and burst testing of the pressure vessels is being complemented with a finite element analysis, which will help to determine the causes of any potential damage to the vessel during low temperature operation. Finite element analysis is currently in progress. A mesh has been built and preliminary runs have been made. Physical properties of fiber-epoxy laminae were obtained from available literature at ambient and cryogenic temperatures (Reed and Golda, 1994, Morgan and Allred, 1989). Lamina properties are then converted into properties of the composite matrix. This is done by using a computer program (Hull and Clyne, 1996). This program

assumes that the matrix is a homogeneous, orthotropic material. The properties of the matrix will be used in the finite element thermal and stress analysis. Results of the finite element analysis will be validated by comparison with the strain gage measurements.

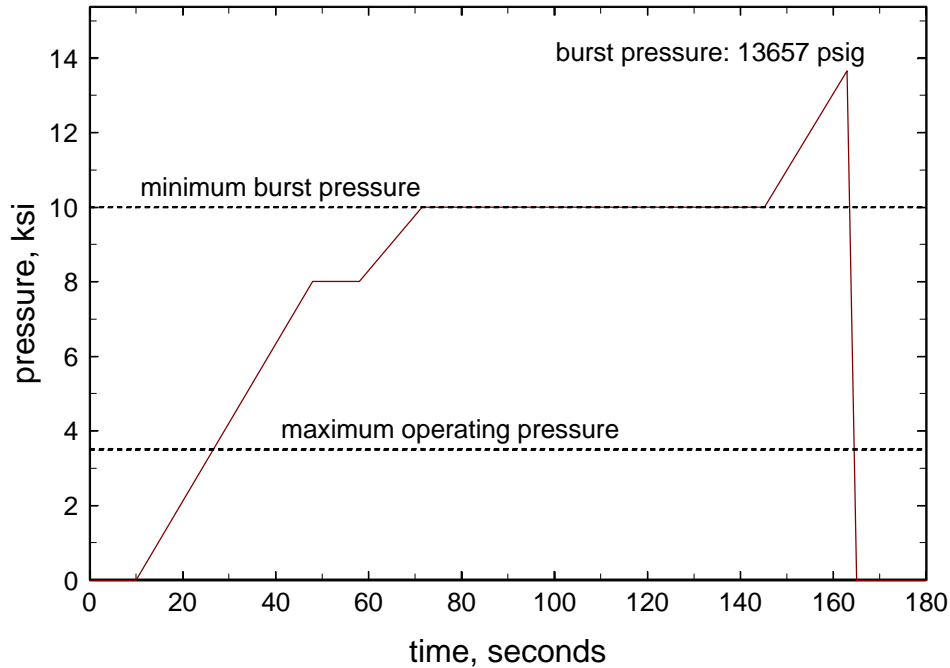


Figure 3. Pressure as a function of time during the burst test of the aluminum-lined, aramid-wrapped vessel. The burst pressure was 94.17 MPa (13657 psig).

Insulation Design and Insulated Pressure Vessel Construction

Insulated pressure vessels have been designed to operate with multilayer vacuum superinsulation (MLVSI). MLVSI has a good thermal performance only under a high vacuum, at a pressure lower than 0.01 Pa (7.5×10^{-5} mm Hg; Kaganer, 1969). Therefore, the use of MLVSI requires that an outer jacket be built around the vessel. Two designs for the insulation have been built: a first-generation design and a second-generation design. The first-generation vessel is a 1/5-scale vessel that stores about 1 kg of liquid hydrogen, and it is shown in Figure 4. This design has been built for cyclic testing and for DOT certification tests. The insulation design includes access for instrumentation for pressure, temperature and level, as well as safety devices to avoid a catastrophic failure in case the hydrogen leaks into the vacuum space. Five pressure vessels have been built according to the first-generation pressure vessel design. One of these has been extensively cycled at a high-pressure cell, and has also been tested with liquid hydrogen. The remaining 4 insulated pressure vessels have been delivered to the pressure vessel manufacturer to verify compliance with DOT standards.

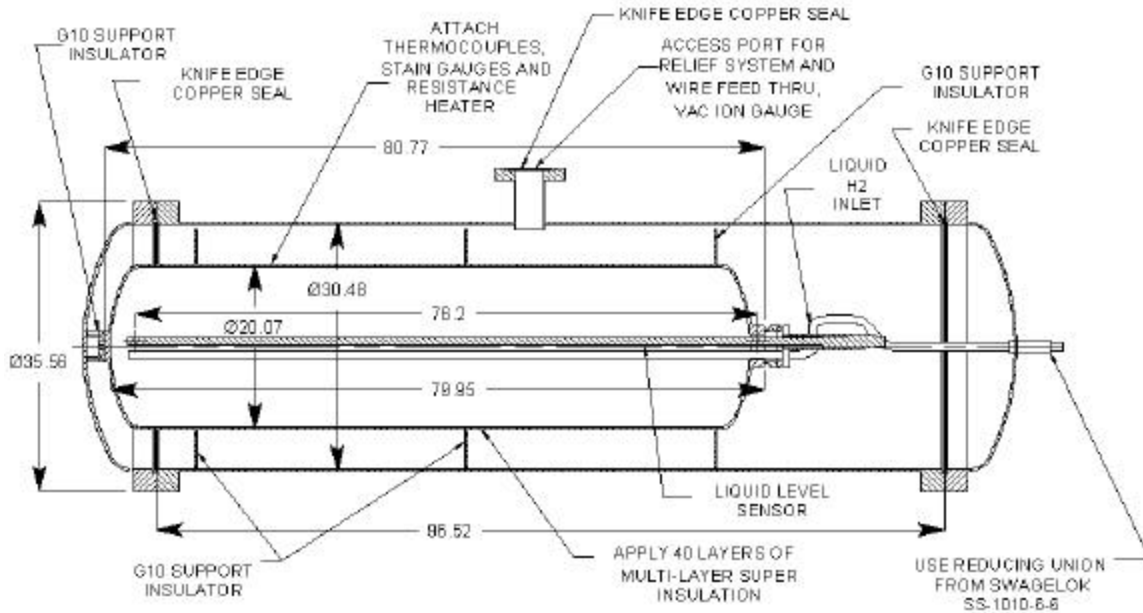


Figure 4. Insulation design for first-generation pressure vessel. The figure shows a vacuum space, for obtaining high thermal performance from the multilayer insulation, and instrumentation for pressure, temperature and level. Dimensions are given in cm.

The second-generation pressure vessel design is shown in Figure 5. This vessel can store about 6 kg of liquid hydrogen. This design includes a vapor shield to reduce evaporative losses in addition to the instrumentation and safety devices that exist in the first generation vessel. These vessels are currently being built. The second generation of pressure vessels will be used for DOT and SAE tests, and for incorporation into a demonstration vehicle.

Cyclic Testing of Insulated Pressure Vessels

The insulated pressure vessels of the first generation (Figure 4) have been cycle tested. This is done to verify that the pressure vessel or the outer jacket does not develop leaks during repeated stresses that occur during cycling. One of these first-generation pressure vessels has been subjected to 1000 cycles, following the same procedure as previously used for the pressure vessels with no insulation (see “Pressure and Temperature Cycling” above). The remaining four first-generation pressure vessels have been subjected to a cold shock and pressure test before being delivered to the vessel manufacturer for DOT testing. The experimental setup for this test is the same as previously used for cyclic testing (Figure 2). The test procedure is as follows: The vessel is pressurized with compressed helium to 1.2 times the Maximum Allowable Working Pressure (MAWP). The pressure is held for a minimum of 30 minutes. Then, the pressure vessel is shock conditioned by cycling it 3 times to low temperature with liquid nitrogen. Finally, The vessel is leak tested with helium to 0.25 times the MAWP. Any leakage detected with a mass spectrometer leak detector is unacceptable.

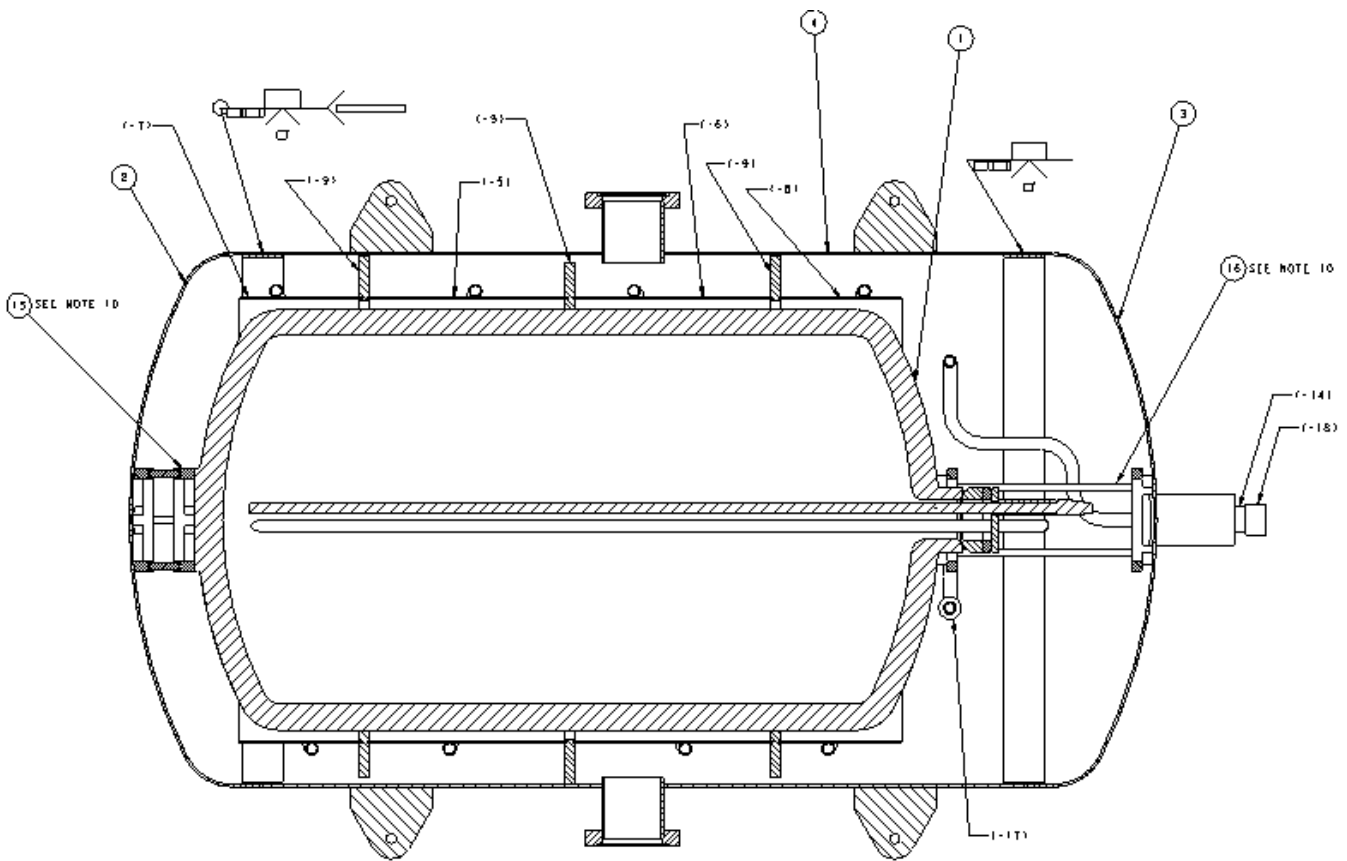


Figure 5. Insulation design for second-generation pressure vessel. The figure shows a vacuum space, for obtaining high thermal performance from the multilayer insulation, instrumentation for pressure, temperature and level, and a vapor shield for reducing hydrogen evaporative losses.

The same shock conditioning test procedure will be used for the second-generation, full-size pressure vessel before being tested according to the DOT and the SAE standards.

Liquid and Gaseous Hydrogen Testing

A first-generation insulated pressure vessel has been tested with liquid and gaseous hydrogen. The vessel was first shock-tested and leak-tested. The insulated pressure vessel was then transported to a remote facility for testing with liquid hydrogen. Testing involved filling the vessel with LH₂ to study the insulation performance, the performance of the sensors, and the problems involved with pumping the LH₂ into the vessel. This test is expected to replicate what would happen to the vessel during fueling and operation in an LH₂-fueled car. The test was conducted successfully. There was no damage to the vessel due to the low temperature operation, all the instrumentation operated properly at the low temperature, and there was no hydrogen ignition or explosions.

Future Work

Future work includes performing additional tests on insulated pressure vessels. A list of tests has been obtained from standards issued by institutions dedicated to pressure vessel and vehicular safety, including the Department of Transportation (DOT), the Society of Automotive Engineers (SAE) and the National Fire Protection Association (NFPA). These institutions have established test procedures for pressure vessels that guarantee safety under regular operating conditions. Successful completion of these tests by insulated pressure vessels will demonstrate that no significant safety problems exist with pressure vessel operation at low temperature. However, additional tests (and multiple execution of any individual test) will be still required for insulated pressure vessel certification. The list of planned tests is:

Cycling, ambient temperature. 10000 cycles from less than 10% of the service pressure to the service pressure, 10 cycles per minute maximum (CFR-DOT, Title 49, 1996a). Each test cylinder must withstand the cycling pressurization test without any evidence of visually observable damage, distortion, or leakage.

Cycling, environmental. 10 cycles per minute maximum. 1) 5000 cycles from zero to service pressure with tank at 60°C (140°F) and air at ambient temperature and 95% humidity, 2) 5000 cycles from zero to service pressure with tank at -51.1°C (-60°F) and air at ambient temperature, 3) 30 cycles from zero to service pressure, ambient conditions 4) burst test the cycled vessel (CFR-DOT, Title 49, 1996a). Each test cylinder must withstand the cycling pressurization test without any evidence of visually observable damage, distortion, or leakage.

Cycling, Thermal. 10 cycles per minute maximum. 1) 10 000 cycles from zero to service pressure at ambient temperature, 2) 20 thermal cycles with tank temperature varying from 93.3°C (200°F) to -51.1°C (-60°F) at service pressure, 3) burst test the cycled vessel (CFR-DOT, Title 49, 1996a). Each test cylinder must withstand the cycling pressurization test without any evidence of visually observable damage, distortion, or leakage.

Gunfire. Pressurize vessel with air or nitrogen to service pressure, and impact the vessel with a 0.30 caliber armor-piercing projectile with a speed of 853 m/s (2800 ft/s). The cylinder is positioned in such a way that the impact point is in the cylinder side wall at a 45° angle with respect to the longitudinal axis of the cylinder. The distance from the firing location to the cylinder may not exceed 45.7 meters (150 feet) (CFR-DOT, Title 49, 1996a). The cylinder shall not fail by fragmentation.

Bonfire. Pressurize cylinder with air or nitrogen to service pressure. Set pressure relief devices to discharge at 83% of the cylinder test pressure. The cylinder shall be exposed to fire until the gas is fully vented. The temperature measured on the surface tank exposed to the fire has to be between 850 and 900°C (CFR-DOT, Title 49, 1996a). The venting of the gas must be predominantly through the pressure relief device.

Drop Test from 3 m (10 ft). 1) The cylinder is dropped vertically onto the end, 2) the cylinder is dropped horizontally onto the side wall, 3) the cylinder is dropped onto a 3.8 x 0.48 cm (1 ½ x 3/16 inch) piece of angle iron, 4) after the drops, the vessel is cycled over 1000 pressure cycles from 10% of service pressure to the service pressure, at 10 cycles per minute (CFR-DOT, Title 49, 1996). The cylinder then has to be burst tested; the burst pressure of this vessel has to be at least 90 % of the minimum burst pressure.

Drop tests from 10 m and 3 m. 1) Drop from 10 m. The drop test subjects a full-size vehicle fuel tank to a free-fall impact onto an unyielding surface from a height of 10 m. The fuel tank is released by firing one or more explosive cable cutters simultaneously. The fuel tank impacts the outer shell on the critical area as determined by the manufacturer. The fuel tank is filled with an equivalent full weight of liquid nitrogen saturated to at least 50% of the maximum allowable working pressure of the fuel tank. 2) Drop from 3 m. The drop test subjects a full-size vehicle fuel tank to a free-fall impact onto an unyielding surface from a height of 3 m. The fuel tank is released by firing one or more explosive cable cutters simultaneously. The fuel tank impacts the outer shell on the critical area as determined by the manufacturer. The fuel tank is filled with an equivalent full weight of liquid nitrogen saturated to at least 50% of the maximum allowable working pressure of the fuel tank (SAE J2343, 1997). There shall be no loss of product for a period of 1 hour after the drop other than relief valve operation and loss of vapor between the filler neck and the secondary relief valve in the case of a test involving the filler neck. Loss of vacuum, denting of the vessel, piping and piping protection, and damage to the support system are acceptable.

Flame test. The tank should contain an equivalent full level of liquid nitrogen saturated at one half the maximum allowable working pressure (MAWP). The tank should be inverted and subjected to an external temperature of 538°C (1000°F) for 20 minutes without the vessel reaching relief pressure (SAE J2343, 1997).

Insulated pressure vessels for the first four tests have already been delivered to the vessel manufacturer. These will be tested shortly. Additional plans include the installation of insulated pressure vessels into demonstration hydrogen-powered vehicles. For this application, the NFPA (NFPA 57, 1996; NFPA 52, 1998), and CFR-DOT (Title 49, 1996) standards will be reviewed to prepare the required tests to guarantee the safety of the operation. Future work will also focus on developing a testing procedure for achieving certification of insulated pressure vessels.

Conclusions

Insulated pressure vessels are being developed as an alternative technology for storage of hydrogen in light-duty vehicles. Insulated pressure vessels can be fueled with either liquid hydrogen or compressed hydrogen. This flexibility results in advantages compared to conventional hydrogen storage technologies. Insulated pressure vessels are lighter than hydrides, more compact than ambient-temperature pressure vessels, and require less energy for liquefaction and have less evaporative losses than liquid hydrogen tanks.

For reduced cost and complexity it is desirable to use commercially available aluminum-fiber pressure vessels for insulated pressure vessels. However, commercially available pressure vessels are not designed for operation at cryogenic temperature. A series of tests has been carried out to verify that commercially available pressure vessels can be operated at cryogenic temperature with no performance losses. All analysis and experiments to date indicate that no significant damage has resulted. Required future tests are described that will establish that no significant safety issues exist with pressure vessel operation at cryogenic temperature.

Acknowledgments

This project is funded by the DOE Hydrogen Program, Sig Gronich and Neil Rossmeis, Program Managers. The authors also express their appreciation for the significant contributions of Structural Composites Industries (SCI) to this project. Work performed under the auspices of the U.S. Department of Energy by Lawrence Livermore National Laboratory under Contract W-7405-ENG-48.

References

Aceves, S. M., Berry, G.D., 1998, "Thermodynamics of Insulated Pressure Vessels for Vehicular Hydrogen Storage," ASME Journal of Energy Resources Technology, June, Vol. 120, pp. 137-142.

Baur L., 1995, "Composite Pressure Vessel with Metal Liner for Compressed Hydrogen Storage," Proceedings of the 1st IEA Workshop on Fuel Processing for Polymer Electrolyte Fuel Cells, Paul Scherrer Institut, Villigen, Switzerland, International Energy Agency, Swiss Federal Office of Energy, September 25-27, 1995, p. 45-69.

Braess, H.H., and Strobl, W., 1996, "Hydrogen as a Fuel for Road Transport of the Future: Possibilities and Prerequisites," Proceedings of the 11th World Hydrogen Energy Conference, Stuttgart, Germany.

Code of Federal Regulations, Department of Transportation (CFR-DOT), 1996a, "Basic Requirements for Fully Wrapped Fiber Reinforced Aluminum Lined Cylinders," Title 49, CFR 107.105 Standard.

Hettinger, W. Michel, F., Ott, P., and Theissen, F., 1996, "Refueling Equipment for Liquid Hydrogen Vehicles," Proceedings of the 11th World Hydrogen Energy Conference, Stuttgart, Germany, pp. 1135-1143.

Hull, D., and Clyne, T.W., 1996, "An Introduction to Composite Materials," Cambridge University Press, Cambridge, Great Britain.

Institute of Gas Technology, 1996, "Compressed Natural Gas Storage Optimization for Natural Gas Vehicles," Gas Research Institute Report GRI-96/0364, Des Plaines, IL.

Kaganer, M.G., 1969, "Thermal Insulation in Cryogenic Engineering," Israel Program for Scientific Translation Ltd., Jerusalem, Israel.

Klinger, D., Kuzmyak JR., 1984, "Personal Travel in the United States," Vol. 1, 1983-1984, Nationwide Personal Transportation Study, Report PB89-235378, prepared for the US Department of Transportation, Office of Highway Information Management, Washington, DC.

Michel, F., Fieseler, H., Meyer, G., and Theissen, F., 1996, "Onboard Equipment for Liquid Hydrogen Vehicles," Proceedings of the 11th World Hydrogen Energy Conference, Stuttgart, Germany, pp. 1063-1077.

Morgan, R.J. and Allred, R.E., 1989, "Aramid fiber reinforcements," in "Reference Book for Composite Technology," Edited by Lee, S.M., pp. 143-166, Technomic Publishing, Lancaster, PA.

National Fire Protection Association (NFPA), 1998, "NFPA 52: Compressed Natural Gas (CNG) Vehicular Fuel System Code," Quincy, MA.

National Fire Protection Association (NFPA), 1996, "NFPA 57: Liquefied Natural Gas (LNG) Vehicular Fuel System Code," Quincy, MA.

Pehr, K., 1996a, "Experimental Examinations on the Worst Case Behavior of LH₂/LNG Tanks for Passenger Cars," Proceedings of the 11th World Hydrogen Energy Conference, Stuttgart, Germany.

Pehr, K., 1996b, "Aspects of Safety and Acceptance of LH₂ Tank Systems in Passenger Cars," International Journal of Hydrogen Energy, Vol. 21, pp. 387-395.

Pentastar Electronics, 1997, "Direct-Hydrogen-Fueled Proton-Exchange-Membrane Fuel Cell System for Transportation Applications, Conceptual Design Report," Report DOE/CE/50390-9, prepared for U.S. Department of Energy, Office of Transportation Technologies, under contract DE-AC02-94CE50390.

Peschka, W., 1992, "Liquid Hydrogen, Fuel of the Future," Springer-Verlag, Vienna, Austria.

Reed, R.P., and Golda, M., 1994, "Cryogenic Properties of Unidirectional Composites," Cryogenics, Vol. 34, No. 11, pp. 909-928.

Society of Automotive Engineers (SAE), 1997, "Recommended Practices for LNG Powered Heavy-Duty Trucks," SAE.J2343.

Wetzel, F.J., 1996, "Handling of Liquid Hydrogen at Filling Stations," Proceedings of the 11th World Hydrogen Energy Conference, Stuttgart, Germany, pp. 1123-1134.

Figure Captions

Figure 1. Cumulative hydrogen losses in kg as a function of daily driving distance, for vehicles with 17 km/liter (40 mpg); or 34 km/l (80 mpg) fuel economy, for three cryogenic hydrogen storage vessels.

Figure 2. Schematic of the experimental setup for temperature and pressure cycling of pressure vessels.

Figure 3. Pressure as a function of time during the burst test of the aluminum-lined, aramid-wrapped vessel. The burst pressure was 94.17 MPa (13657 psig).

Figure 4. Insulation design for pressure vessel. The figure shows a vacuum space, for obtaining high thermal performance from the multilayer insulation, and instrumentation for pressure, temperature and level. Dimensions are given in cm.

Figure 5. Insulation design for second-generation pressure vessel. The figure shows a vacuum space, for obtaining high thermal performance from the multilayer insulation, instrumentation for pressure, temperature and level, and a vapor shield for reducing hydrogen evaporative losses.

HYDRIDE DEVELOPMENT FOR HYDROGEN STORAGE

K. J. Gross, G. J. Thomas and G. Sandrock
Sandia National Laboratories
Livermore, CA 94550

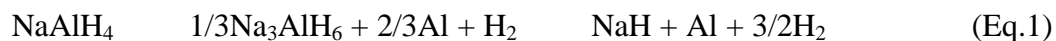
Abstract

The hydrogen storage properties of NaAlH_4 mechanically catalyzed with 2 mol % each of the liquid alkoxides $\text{Ti}(\text{O}i\text{Bu})_4 + \text{Zr}(\text{OPr})_4$ have been studied using a small (1.5 g sample) reactor and a 100 g “scaleup” reactor. The aim was to assess the potential for using this new hydride family for fuel-cell vehicle applications and to identify potential problems. Studies included low temperature equilibrium thermodynamic measurements, discharging and recharging kinetics and thermal effects, cyclic capacity, room temperature desorption kinetics, H_2 purity analysis and other practical properties. For the first time, low temperature equilibrium pressure measurements were made which showed that a hydrogen pressure of 1 atm can be obtained at 33°C by desorbing NaAlH_4 to Na_3AlH_6 . Also, recharging was possible at lower temperatures and pressures than generally reported. Cycling tests, however, indicated a much lower than expected capacity after the first desorption. The use of alkoxide-based Ti and Zr catalysts introduces oxygen and hydrocarbon impurities into the sample which were still present after several cycles and may contribute to the observed low reversible capacity. For this reason we have started to investigate inorganic catalysts as well as dry doping processes. Our latest results show reversible capacities close to the theoretical value of 5.6 wt.% (note added in proof).

Introduction

The need remains for safe, lightweight and compact means of hydrogen storage for vehicles. Liquid, compressed gas and reformer-derived hydrogen as well as metal hydride hydrogen storage systems all have well-known disadvantages. In the case of hydrides, metallic (interstitial) hydrides such as LaNi_5H_6 have excellent thermodynamic properties but suffer from low reversible gravimetric capacity (generally < 2 wt.% H). On the other hand, covalent hydrides such as Mg_2NiH_4 and other Mg-alloys offer good H-capacity (3-7 wt.%), but have unfavorable thermodynamics that require 250-300 C for positive desorption pressures. Overcoming this thermodynamic-capacity dilemma has been the hydride R&D objective of Sandia National Laboratories for the last few years.

Although alkali metal alanates have been known for many years as nonreversible “chemical hydrides” for the one-time hydrolysis generation of H_2 , recent demonstrations of catalyzed reversibility offer the distinct possibility of a new family of low-temperature hydrides. Bogdanovic et al (Bogdanovic' 1997) demonstrated that the well-known alkali metal alanate-complex hydride, NaAlH_4 , readily released and absorbed hydrogen when doped with a TiCl_3 or Ti-alkoxide catalysts according to the following two-stage reaction:



The net reaction represents a theoretical 5.6 wt.% reversible gravimetric H-storage, with the potential of liberating this hydrogen at less than 100 C. Such an achievement would be of significant practical value for on-board H_2 storage for a low-temperature fuel-cell vehicle.

There are two areas of R&D that are needed to develop Na-alanate into a practical vehicular system:

1. The optimization of the catalyst as to (a) type, (b) doping process and (c) mechanistic understanding.
2. Engineering development and determination of practical properties.

These are being addressed within the DOE Hydrogen Program by a cooperative effort between the University of Hawaii (with emphasis on area 1) and Sandia (with emphasis on area 2).

It is important to understand the history of catalyzed Na-alanate development and how it relates to the work to be presented here. The concept of catalyzed Na-alanate reversibility was first developed at the Max-Planck Institute für Kohlenforschung (Germany) using solution chemistry to add the catalyst and control the alanate particle size (Bogdanovic' 1997, 2000). The technique developed at Hawaii was quite different, with liquid Ti- and Zr-alkoxide catalysts added directly to the Na-alanate by mechanical ball-milling (Jensen 1999, Zidan 1999). Very recent work at Hawaii has also suggested that liquid TiCl_4 catalyst can also be added to NaAlH_4 by ball-milling (Jensen 2000). Ball-milling also offers the ability to control particle size and introduce solid catalysts or “activators”, such as carbon (Zaluska 2000). Sandia work with Ti- and Zr-alkoxide catalyzed NaAlH_4 (ball-mill-doped) began two years ago with detailed dynamic X-ray

diffraction studies to delineate the complex reaction sequence, along with some preliminary kinetic measurements (Gross 1999, Thomas 1999). During the last reporting year we continued with this same material with the aim of quantifying the engineering it's behavior, as well as identifying possible problems for the practical use of these materials.

There are a number of engineering problems that must be understood and/or solved before the catalyzed alanates can be applied to practical H-storage. For example, *low-temperature kinetics* may be slow because, unlike the interstitial hydrides, alanate H₂ absorption and desorption reactions take place by a series of disproportionation and repropotionation reactions (Eq.1) that must involve at least localized metal atom diffusion. Will low temperature kinetics be high enough for application in vehicles and other devices? Because of low kinetics, *low temperature equilibrium plateau pressures* have not been properly measured, causing us to rely on van't Hoff extrapolation from higher temperatures. A priority has been to gather experimental thermodynamic data. Most importantly, a *macroscopic* "engineering-scale" *catalyzed alanate bed* has never been made and tested. Are there any problems with large beds? What are the *reaction heat effects* (exothermic and endothermic)? Can the alanate bed be melted or sintered during exothermic charging and what are the resultant changes in gas impedance effects? What are the *volume changes* associated with hydriding and dehydriding? What effects on capacity and kinetics result from *cycling*? Do the liquid organometallic catalysts decompose in service, resulting in *contamination of the desorbed H₂*? These are the issues we address in this paper.

Experimental Basics

Most of the work reported here was done with NaAlH₄ to which was added 2 mol % each of Ti(OBuⁿ)₄ and Zr(OPr)₄ in liquid form by mechanical mixing. The use of this formula was based on the University of Hawaii observation that combined Ti- and Zr-doping resulted in maximum desorption kinetics for both steps of Eq.1 (Zidan 1999).

Hydrogen absorption/desorption studies were done using two experimental reactors. The one shown in Figure 1 represents what we call the "100 g scaleup reactor" designed to simulate the heat transfer and gas impedance conditions of a larger engineering bed. This 316 SS reactor has a 4.6cm OD, 0.38cm wall thickness, about 11.4cm internal length and was pressure rated to 3000 psia (204 atm) at 350 C. It was loaded with about 100 g of bicatalyzed NaAlH₄ as described above (78 g of NaAlH₄ and 22 g of Ti(OBuⁿ)₄ + Zr(OPr)₄). The NaAlH₄ was synthesized at University of Hawaii and blended with the catalysts at SNL using a few minutes ball-milling. The reactor had internal thermocouples but no internal heat exchange structure. The reactor was heated with an air furnace. Absorption kinetics and capacity were measured volumetrically and desorption measured with flow meters backed up by a wet test meter. The data below is presented in terms of wt.% H₂ normalized to the alanate weight only (i.e., not including the 22 wt.% catalyst).



Figure 1 – Scaleup (100 g) reactor with end cap removed in Ar-glovebox to show catalyzed alanate

Low temperature kinetics and plateau pressures were obtained volumetrically with a smaller 316 SS reactor (1.3 cm OD and 0.12 cm wall thickness) containing about 1.5 g of catalyzed sample. This reactor also had a fine internal thermocouple located in the middle of the bed. This unit was heated with electrical heating tape, and of course had better heat exchange than the scaleup reactor described above. This reactor was also used for lower pressure data (below 100 atm H₂). Other experimental details will be given with the data presentations.

Scaleup (100 g) Bed Results

The 100 g bed was evaluated through five instrumented absorption/desorption cycles. (The synthesis of the starting NaAlH₄ is artificially considered the first absorption half-cycle). Absorption H₂ pressures generally ranged from 100-200 atm and nominal absorption temperatures ranged from 125-165 C. Desorption was generally performed at 150-165 C against a 1 psig (1.07 atma) backpressure. In addition to capacity and rate measurements, exothermic (charging) and endothermic (discharging) thermal effects could be recorded. Exit hydrogen was monitored semiquantitatively for possible gaseous impurities. Samples were examined by XRD and SEM/EDS surface analysis. The alanate volume change was measured for the last desorption half-cycle.

Cyclic Capacity

The measured absorption and desorption capacities of the 100 g scaleup bed are shown as a function of cycle number in Figure 2. Generally good agreement was found between absorbed gas quantities and the amounts subsequently desorbed. However, cycle 1D (first discharge) showed a capacity of 6.0 wt.% H₂, in significant excess of the 5.6 wt.% theoretical value from Eq.1. This is believed to be an indication of substantial quantities of non- H₂ impurities coming out of the bed during the first desorption (see impurities discussion below). In cycle 2 only a partial absorption was made. The charge pressure used was 14 atm. This is well below the NaAlH₄ plateau pressure at 125 °C and, hence, only the Na₃AlH₆ phase was formed.

Cycles 3-5 demonstrates a serious capacity problem encountered not only with the scaleup bed but with all other samples we have tested with the liquid alkoxide catalysts. Cyclic capacity (both absorption and desorption) was only about 3 wt.%, well below the 5.6 wt.% expected for this system. X-ray diffraction measurements clearly showed that the low capacity is due to an inability to completely recharge to 100% NaAlH₄ (Eq.1, full left reaction). There was no problem discharging to NaH+Al (Eq.1, full right reaction). A mechanism for this incomplete recharging phenomenon is uncertain at the present time, although it may involve the uniformity of catalyst distribution or impurity effects to be discussed later. This reversible capacity problem must be solved if this material is to be a viable candidate for hydrogen storage. (See Note added in Proof at the end of this paper)

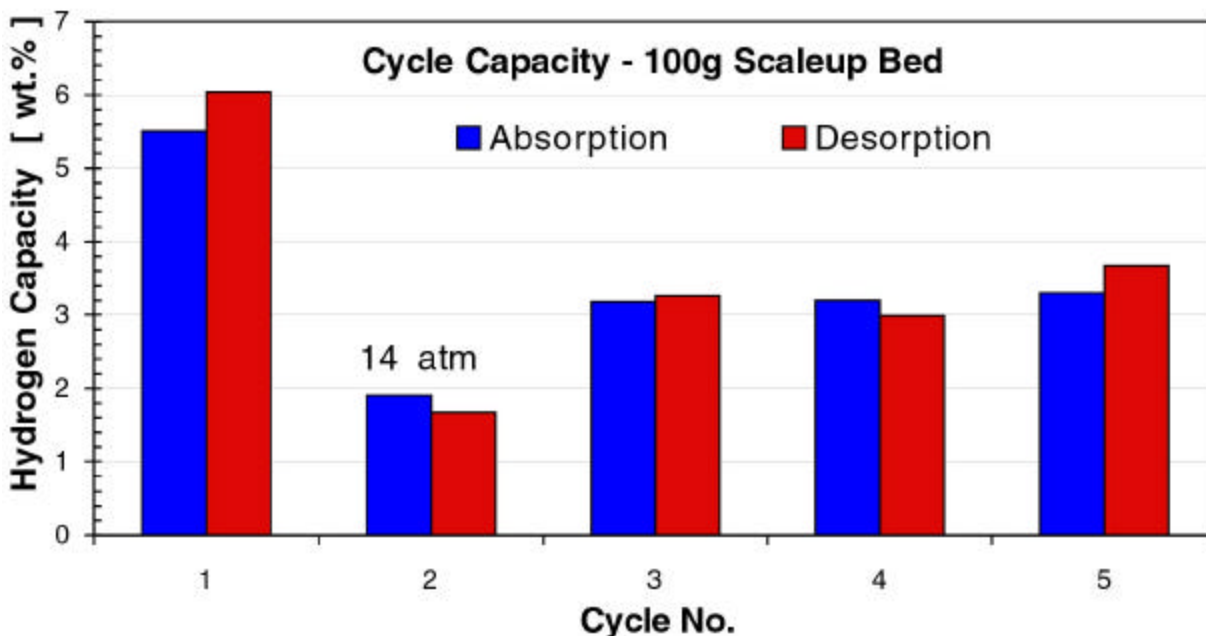


**Figure 2 – Cyclic capacities of the 100 g scaleup bed.
Charging was done at 100-200 atm and 125-165 °C,
except for cycle 2 which charged only through the low P phase.**

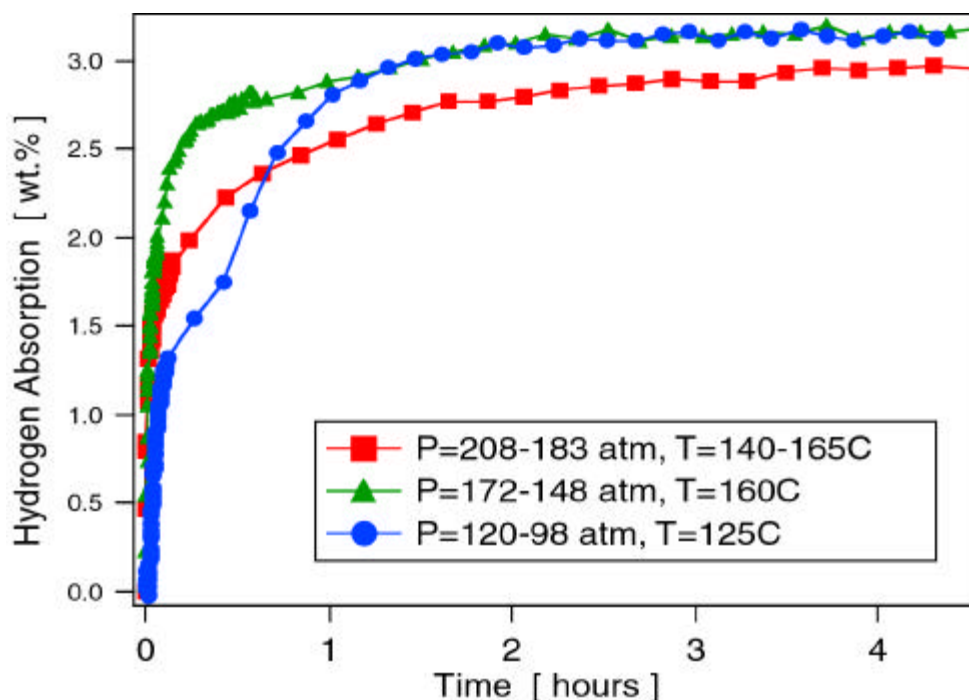


Figure 3 – Charging curves for the 100 g scaleup bed at various applied H₂ pressures and initial temperatures

Charging/Discharging Rates

Charging curves for half-cycles 3A-5A are shown in Figure 3. Although a range of applied pressures and starting temperatures were tried, in all cases charging was more rapid than we had expected from the literature and from University of Hawaii results, albeit with the lower than expected capacity discussed above. Most of the H₂ uptake was accomplished in the first hour or two, even for the lowest pressure and starting temperature. Although not shown, discharge was nearly as fast at 150-165 °C; most of the charge was desorbed in about 3 hours. Using the small test bed (with better heat transfer), we have been able to achieve desorption times of 4-5 hours at 125 °C. We need to achieve such rates at 100 °C or less by improvements in particle size, catalyst and/or engineering design.

Thermal Effects

The higher than expected initial charging kinetics, combined with limited heat transfer, results in exothermic temperature excursions, as is common with all “fast” hydrides. An example is shown in Figure 4 for half-cycle 4A. At time zero, 172 atm H₂ was quickly applied to the fully dehydrided 100 g bed which had been equilibrated at 155 °C. Within one minute, the exothermic hydriding reaction resulted in an internal temperature of 234 °C. This is essentially the van’t Hoff temperature for NaAlH₄ at this applied pressure (see Figure 9, later). It is

important to recognize that the melting point of NaAlH_4 is only 182 °C (Dymova 1974); thus, any NaAlH_4 formed during the first 0.5 hr of Fig.4 would do so directly into the liquid phase. As one can see that during the absorption (Fig.4), a 182 °C thermal arrest occurs due to solidification during cooling (about $t = 0.6-0.8$ hr). This is precisely as expected and shows that liquid NaAlH_4 was formed during the exothermic temperature excursion associated with the rapid initial charge.

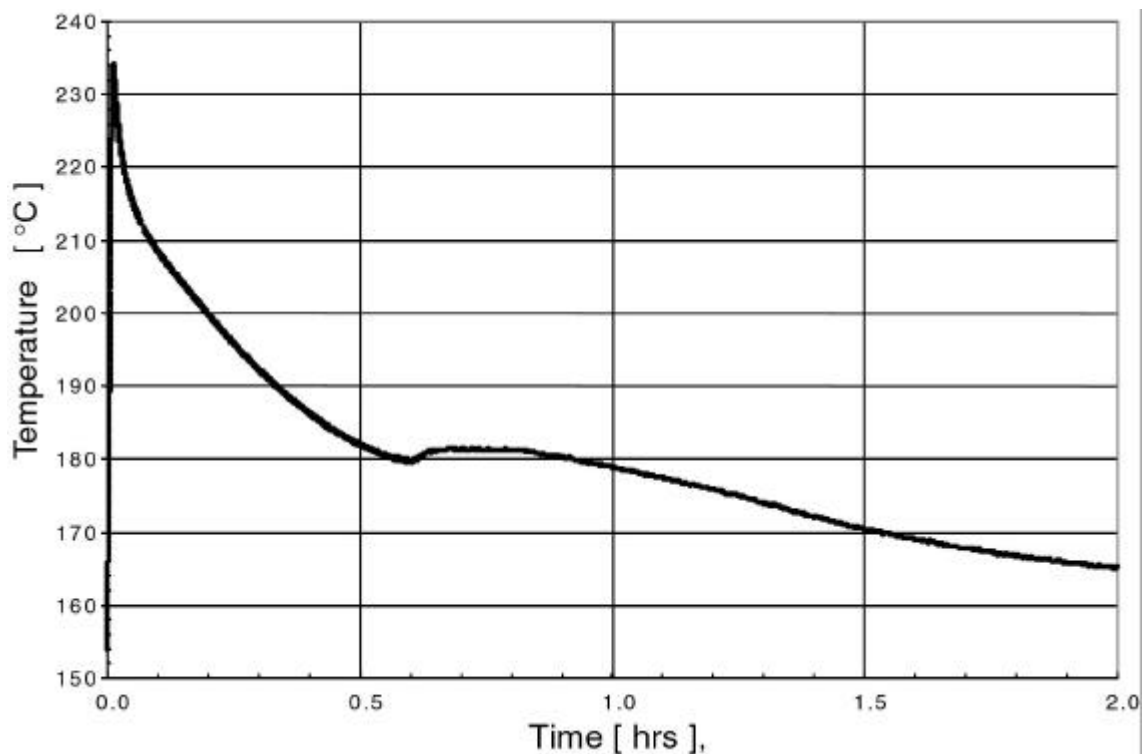


Figure 4 – Exothermic temperature excursion during scaleup bed charge half-cycle 4A ($P_i = 172$ atm, $T_i = 155$ °C)

It is natural to ask if such melting could be detrimental to the subsequent performance of the alanate bed. The answer seems to be “no” or at least “not much”. We have not observed any negative effects of partially melting the bed at least three times. It is interesting to note that there was a furnace malfunction late in the half-cycle 3A that led to an increase in the temperature to 234 °C with the material essentially in the fully charged state. This seemed to have had no significant negative effect on kinetics or capacity for subsequent half-cycle 3D, as well as cycles 4 and 5. In fact, there may be a benefit of partial melting. We opened the reactor between cycles 4 and 5 (the time at which the photograph shown in Fig.1 was taken) and found the bed to be sintered into a porous, solid mass. Such a structure may have distinct advantages for actual applications. In particular, such a sintered structure should reduce particulate migration, increase

packing densities, allow expansion, and provide a constant internal gas impedance and enhanced safety.

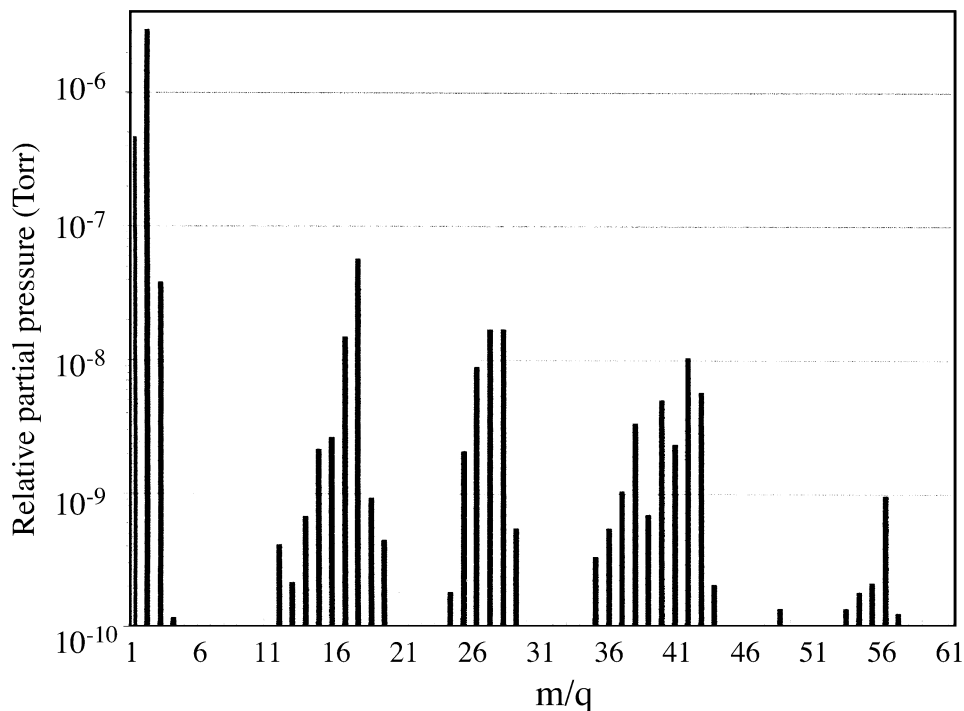


Figure 5 – Typical RGA pattern of H₂ desorbed from the Ti-Zr-alkoxide catalyzed NaAlH₄ 100 g scaleup bed

Gaseous Impurities

The direct addition of the catalysts in the form of liquid organometallic alkoxides (the University of Hawaii method) seems to result in serious problems relative to the purity of the desorbed H₂ and may be a contributing factor to the low cyclic capacity we see (cf. Figures 2 and 3). During the first desorption (1D) of the 100 g scaleup bed the measured quantity of gas indicated a capacity above the stoichiometric 5.6 wt.% H₂. Hence, during subsequent desorption half-cycles, semiquantitative analyses of the desorbed gas composition were done by RGA (Residual Gas Analysis [Mass Spectroscopy]) and occasionally by GC (Gas Chromatography).

A typical RGA pattern of the desorbed H₂ is shown in Figure 5. For pure H₂, one would expect only the mass 2 peak (with satellites m 1 and m 3), along with the ubiquitous background RGA peaks for H₂O (m 18,17,16), CO (m 28) and CO₂ (m 44). In fact, many more impurity peaks present. A GC analysis taken of cycle 2D desorbed gas showed that butane (Bu) and propane (Pr) were present in the hydrogen. Both of those species can be deduced from the Fig.5 RGA pattern. Thus the Ti(OBuⁿ)₄ and Zr(OPr)₄ wet catalysts seem to be decomposing into O-free Bu and Pr. As shown in Figure 6, EDS (X-ray Energy Dispersive Spectroscopy) surface analysis clearly shows that most of the oxygen introduced by the Ti(OBuⁿ)₄ + Zr(OPr)₄ catalysts remain on the hydride surface after both stages of the desorption reaction (Eq.1). It may be that surface

damage associated with this oxygen is a contributing factor to the lower than stoichiometric cyclic capacity.

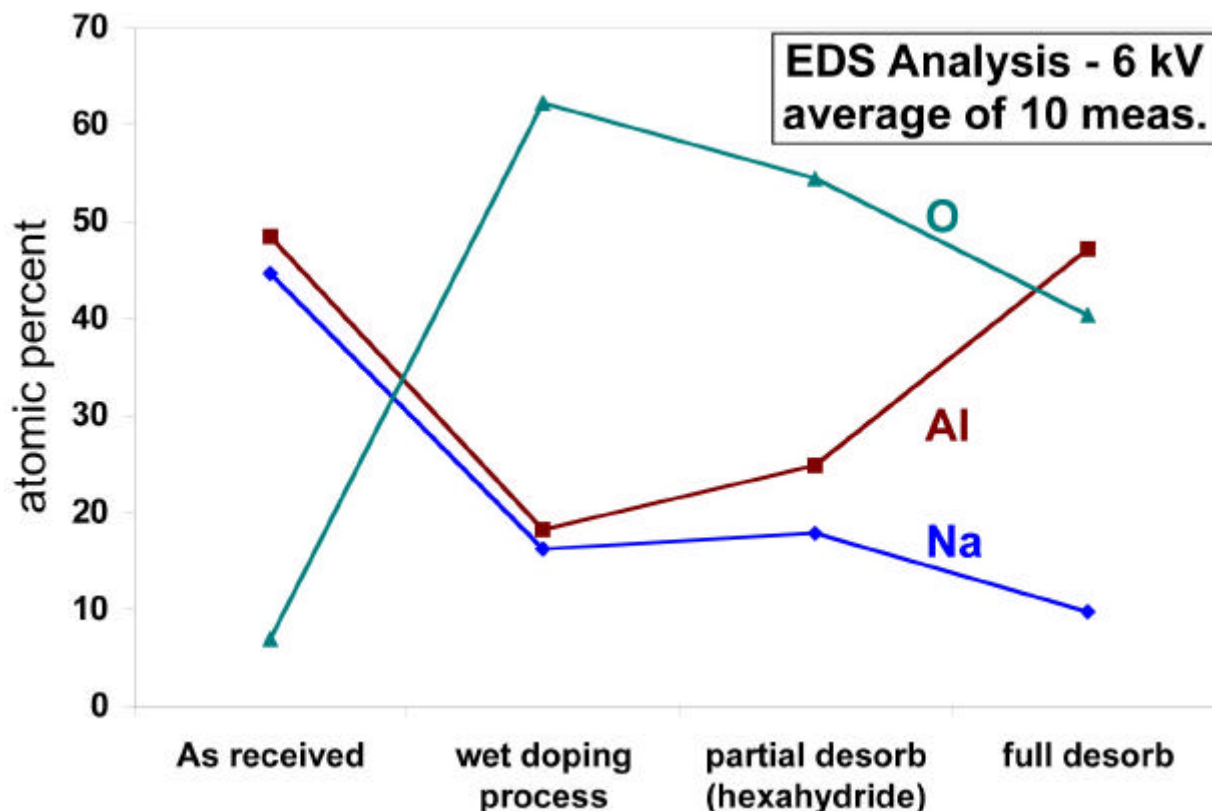


Figure 6– EDS analysis of NaAlH_4 sample before and after wet doping with Ti and Zr alkoxide catalysts, after desorbing to Na_3AlH_6 , and fully desorbing to NaH .

We believe the high level of impurities in the desorbed H_2 (not to mention possible surface damage from the catalysts) constitutes a fatal flaw in the University of Hawaii process of wet mechanical catalyst-alanate homogenization. One likely application for an onboard storage bed will be the PEM fuelcell which is not very tolerant of impurities in the H_2 fuel, especially carbonaceous species that might include or lead to CO. It might be argued that the wet-alkoxide-catalyzed beds can be cleaned up by vacuum baking and repeated cycling, but we feel this will be expensive and not easy. We observed significant impurity levels even after 5 cycles and temperature excursions above 200 C. Furthermore, if the capacity loss is really due to damage

by the catalysts, that problem will be particularly hard to surmount. Thus, we plan to direct our future work toward inorganic catalyst species.

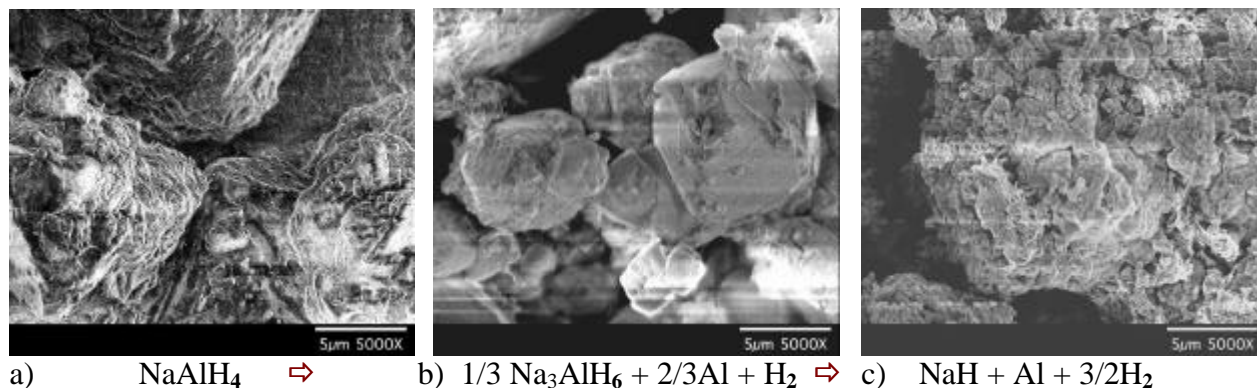


Figure 7 – SEM images showing the morphology changes during the two-step dehydriding reaction

Packing Densities and Hydriding Volume Changes

For the traditional metallic hydrides typically experience volume expansions on the order of 25% during hydriding. Because such large volume changes pose engineering problems (e.g., bed packing, expansion, deformation, etc.), it is important to know how the complex alanates behave. As shown by the SEM (Scanning Electron Microscopy) images in Figure 7, Na-alanate exhibits rather pronounced changes in morphology during the two stages of decomposition (Eq.1). From published X-ray densities the first stage of decomposition ($\text{NaAlH}_4 \rightarrow \frac{1}{3}\text{Na}_3\text{AlH}_6 + \frac{2}{3}\text{Al}$) would be expected to give a contraction of -30.3 % and the second stage ($\frac{1}{3}\text{Na}_3\text{AlH}_6 + \frac{2}{3}\text{Al} \rightarrow \text{NaH} + \text{Al}$) an expansion of 13.8 %. The net ΔV for the complete dehydriding reaction of Eq.1, including the excess Al produced in both stages, would then be expected to be -16.5 %. The actual volume change measured from the beginning to the end of the dehydriding cycle 5D was -14.7%. This large measured volume change is presumably due to the incomplete reaction to the final phases as shown by the low capacity (3.3 wt.%) of the bed. Unlike the traditional metallic hydrides, the alanates have the distinct advantage of starting with the material in it's fully hydrided state. This means that fully packed beds can be constructed which makes engineering the container easier and allows a higher volumetric density to be achieved compared to traditional hydrides. The aforementioned ability to liquid-phase-sinter the alanates into porous structures is also an engineering plus.

Results of Small Reactor Studies

We performed a number of parallel experimental studies on alkoxide catalyzed NaAlH_4 using the small 1.5 g reactor. In general, the kinetics and capacity data were very similar to that reported above for the 100 g scaleup bed and so it will not be presented here. We also did synthesis studies and testing of the Norway-Hawaii catalyst Ti_3Al (Maeland 1999) which is said to increase the rehydriding kinetics when added as a third component to the Ti-Zr-alkoxide bicatalyst system. The results of that work is included in the University of Hawaii contribution

to these Proceedings (Jensen 2000). The unique results obtained from the small reactor studies we report here are low temperature NaAlH_4 kinetics (especially room temperature) and low temperature NaAlH_4 van't Hoff (plateau pressure) data that were obtained experimentally for the first time.

Room Temperature Desorption Measurements

It was our original intent to perform detailed absorption and desorption kinetic measurements, starting at 100 °C and down to the lowest measurable temperature. This effort was discontinued after our capacity and impurity observations suggested the liquid-alkoxide-catalyzed alanate system was probably not practical. Before that, however, we made the rather surprising observation that desorption kinetics could be measured even down to room temperature. Examples of room temperature desorption data are shown in Figure 8. As shown in Fig.8b, the initial kinetics are strongly dependent on particle size, as would be expected. The sample designated “large particles” represents the bicatalyzed sample used in the 100 g scaleup bed where the NaAlH_4 and catalysts were simply mixed with relatively brief ball-milling. The “fine particle” data were taken with an identical blend that was ball-milled for 3 hours (Spex-mill). There was nearly an order of magnitude difference in initial desorption kinetics between these two samples.

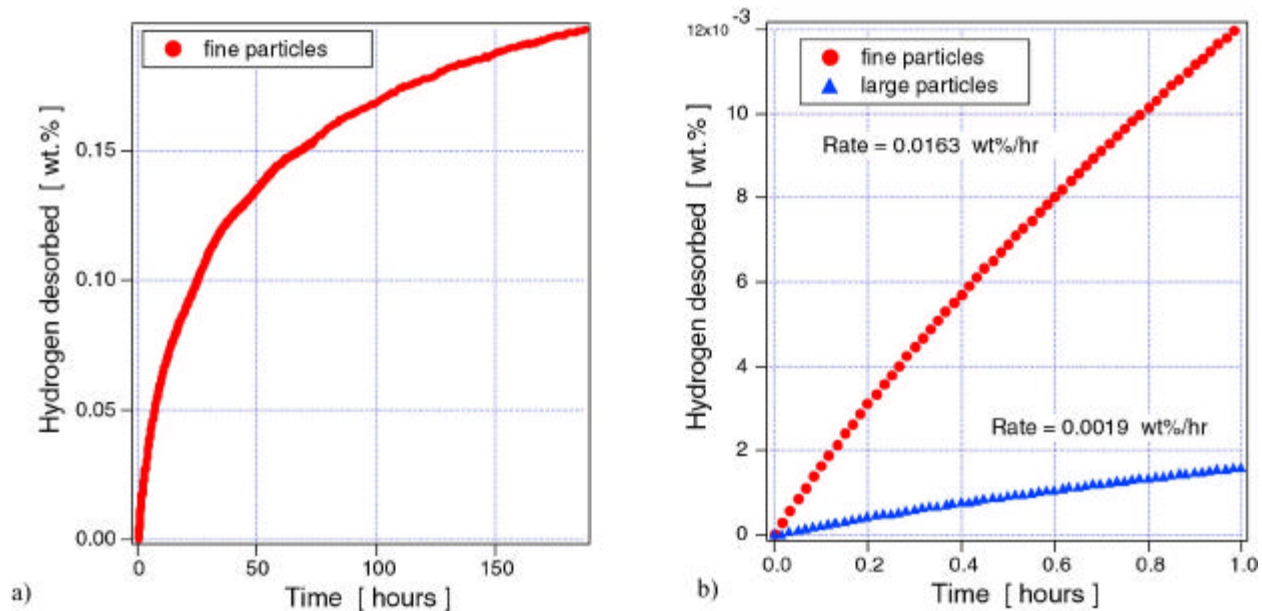


Figure 8 – Room temperature H_2 desorption from Ti- + Zr-alkoxide catalyzed NaAlH_4

We believe that, this is the first time that NaAlH_4 has been reported to decompose at room temperature, and that quantitative low temperature H_2 desorption kinetics have been measured. This has practical significance for applications. For example, high-capacity catalyzed- NaAlH_4 could be used for long-term, low-demand devices that use H_2 . Examples might be low-power remote fuel-cells or portable gas analyzers that use H_2 .

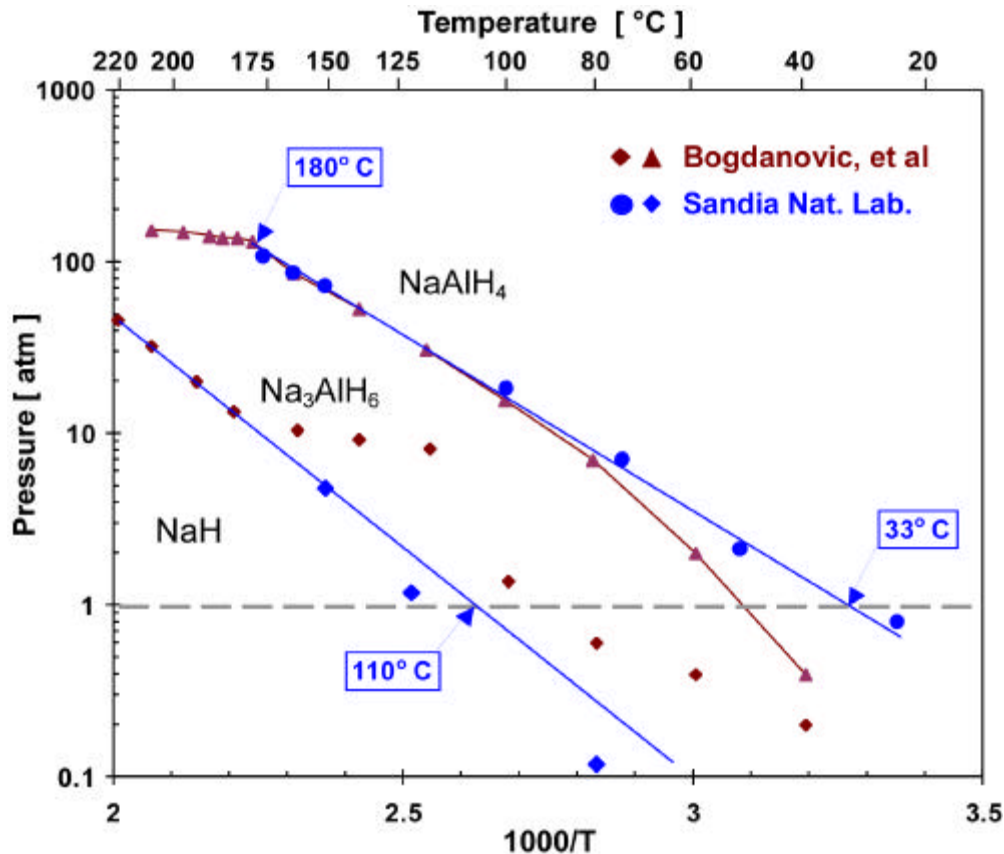


Figure 9 – Van't Hoff Diagram showing equilibrium pressures as a function of temperature for both hydride phases

Low Temperature van't Hoff Data

The reasonably high kinetics at low temperatures allowed the reliable determination of equilibrium desorption plateau pressures down to room temperature for the NaAlH₄ phase. These data are plotted in Figure 9 in the form of a van't Hoff plot (lnP vs 1/T) and compared to the data previously published by the Bogdanovic' and co-workers (Bogdanovic'2000). The low temperature SNL data looks more reasonable because it falls along the extrapolation of the high temperature data. It has now been accurately shown that the temperature for 1 atmosphere absolute desorption pressure is 33 C. This is a very convenient temperature for fuel-cell applications.

The Na₃AlH₆ plateau pressure is also shown in Figure 9. Included are the MPI data (Bogdanovic'2000) and the previously published SNL data (Thomas 1999). Because of the relatively low pressures and kinetics involved, the low-temperature Na₃AlH₆ van't Hoff data are not as reliable as the NaAlH₄ data. Be that as it may, the 1 atma van't Hoff temperature for Na₃AlH₆ is estimated to be about 110 C. This temperature is somewhat higher than desired for a PEM fuel-cell and future work will have to aim at lowering that temperature well below 100 C. This can be accomplished only by modification of the alanate thermodynamics.

Summary and Conclusions

Studies of a 1.5 g experimental and a 100 g scaleup bed of NaAlH₄ wet catalyzed with 2 mol % each of the alkoxides Ti(OBuⁿ)₄ + Zr(OPr)₄ have indicated some promising engineering properties:

1. H₂ absorption/desorption kinetics for the scaleup bed were surprisingly fast, at least at 125 °C, and certainly good enough for some practical applications.
2. Rehydriding could be accomplished at lower pressures and temperatures than originally thought.
3. We were not been able to achieve full capacity after the first cycle. Instead of the 5.6 wt.% theoretical reversible H₂ capacity, we consistently achieved only about 3 wt.%.
4. The reason for the low H-capacity is associated with difficulty rehydriding all the Na₃AlH₆ to NaAlH₄.
5. NaAlH₄ has measurable desorption kinetics down to room temperature, and thus, may be useful in its present state for practical applications where H₂ rate demands are low.
6. Because of 5, we have been able to measure plateau pressures of NaAlH₄ down to room temperature and, therefore, experimentally complete the van't Hoff plot. The temperature required for 1.0 atma desorption plateau pressure is 33 °C.
7. The initial absorption kinetics were so high that reaction self-heating was significant, easily exceeding the 182 °C melting temperature of NaAlH₄. This means that, like all other known hydrides, adequate heat transfer will be important for achieving the best hydrogen absorption and desorption rates.
8. Partial melting of the alanate bed did not appear to hinder subsequent A/D kinetics. On the contrary, partial melting of the alanate results in a moderately sintered porous structure that effectively fixes the particulates, thus simplifying large bed design.
9. The A/D volume change of alanate beds is nearly zero which is much lower than conventional metallic hydrides. This also simplifies large bed design and allows far more material to be used in storage beds.
10. The current Ti+Zr alkoxide catalyst doping procedure has significant drawbacks:
 - A. The alkoxide based catalysts are too heavy. Standard loadings of 2 mol % each results in a 22 wt.% burden on the bed.
 - B. The liquid organometallic catalysts contribute substantially to hydrocarbon contamination of the exit H₂, in particular with butane and propane.
 - C. A large amount of oxygen from the alkoxide catalysts remains in the bed, perhaps damaging the bed and causing the less than ideal cyclic capacity.

Future Work

Our principal plan for the coming year is to continue work on the catalyzed complex hydrides, with an emphasis on moving these materials toward practical storage applications and devices. Our focus on advanced studies of the engineering properties of these materials will also be complimented by efforts to develop improved methods of materials preparation, as well as some mechanistic studies on the reaction processes. More specifically, we will focus on the following list of objectives:

1. Understand the factors that lead to the much lower than ideal capacity in the alanate beds.
2. Work with the University of Hawaii to optimize chloride-catalyzed beds.
3. Investigate other inorganic and non-chloride catalysts.
4. Complete engineering data (especially low-temperature kinetics) on an optimized inorganic catalyst-alanate system.
5. Develop substituted alanates and characterize their hydriding properties.
6. Begin safety studies and economic analyses.

Acknowledgements

This is an extension of work originally started at Sandia by S. Guthrie. We gratefully acknowledge all of his contributions and are saddened by his untimely death. We also acknowledge the valuable collaboration of C. Jensen and S. Takara of the University of Hawaii. We wish to thank D. Meeker of SNL for his expert technical help in all aspects of the experimental measurements.

Note added in proof:

Recent experiments using an inorganic catalyst have achieved reversible hydrogen capacities nearly at the theoretical limit with no degradation in kinetic properties or gas impurities. Reversible capacities in this material have been measured for a small number of cycles at this time. In addition, analysis of the material has identified the source of the small loss in capacity and work is in progress leading to the attainment of essentially full hydrogen capacity.

References

- Bogdanovic', B. and Schwickardi, M. 1997. *J. Alloys and Compounds*, **253**:1.
- Bogdanovic', B., Brand, R.A., Marjanovic', A., Schwikardi, M., and Tölle, J. 2000. *J. Alloys and Compounds*, **302**:36.
- Dymova, T.N., Dergachev, Y.M., Sokolov, V.A., and Grechanaya, N.A. 1974. *Doklady Akademii Nauk SSSR, UDC 546.11*, **224**(3):591.
- Gross, K.J. , Guthrie, S.E., Takara, S., and Thomas, G.J. 1999. *J. Alloys and Compounds*, **297**:270.
- Jensen, C.M., Zidan, R.A., Mariels, N., Hee, A.G., and Hagen, C. 1999. *Int. J. Hydrogen Energy*, **24**:461.
- Jensen, C.M., Takara, S. 2000. "Catalytically Enhanced Systems for Hydrogen Storage", these Proceedings.
- Maeland, A.J., Hauback, B., Fjellvåg, H., and Sørby, M., 1999. *International Journal of Hydrogen Energy*, **24**: 163.
- Thomas, G.J., Guthrie, S.E., and Gross, K. 1999. in *Proceedings U.S. DOE Hydrogen Program Review*, NREL/CP-570-26938,452. Denver CO.
- Zaluska, A., Zaluski, L., and Ström-Olsen, J.O. 2000. *J. Alloys and Compounds*, **298**:125.
- Zidan, R.A., Takara, S., Hee, A.G., and Jensen, C.M. 1999. *J. Alloys and Compounds.*, **285**:119.

HYDRIDE BED/FUELCELL PROJECT

G. Cook Story, Ph.D.
Sandia National Laboratories
Livermore, CA 94551

Abstract

The Hydride Bed/Fuelcell Project will result in the development and production of a prototype Fuelcell Powerplant for Mining/Tunneling Locomotives. This powerplant will replace and outperform batteries, currently utilized for mining and tunneling. The Mine Locomotive Project is a project of the Fuelcell Propulsion Institute (FCPI) consortium.

Introduction

Mining/Tunneling Locomotives are a highly regulated resource essential to mining and tunneling. Powerplants for these Locomotives currently utilize batteries, tethered electric and diesel. The utilization of diesel fuel is highly regulated and very cost intensive due to the required air exchange in the enclosed spaces. Tethered electric resolves the exhaust issues but presents operational constraints and worker safety issues. Batteries are widely used; however, the power density of a battery is not as high as desired and a great deal of time and effort is utilized in maintenance and recharging.

The Mine Locomotive Fuelcell Powerplant prototype under development will represent an improvement over batteries by providing power over a longer use period, allowing rapid refueling, and increased productivity. The powerplant waste products are hot water and warm air. The Proton Exchange Membrane (PEM) Fuelcell Stacks produce DC electricity by combining hydrogen with oxygen from the ambient air (pumped through the Stack) with low-pressure gaseous hydrogen from the Hydride Bed. The waste products are water and heat. Part of the waste heat will be utilized to warm the hydride bed, making up for the negative heat of desorption of hydrogen from the metal-hydride.

The Fuelcell Propulsion Institute determined that a conventional battery powered Mine Locomotive could be powered by a Fuelcell Powerplant having the capability to produce 14 kW of peak electrical power. The storage of approximately 3 kg of hydrogen in the metal-hydride will provide more than 8 hours of operation for mining operations (Warren Electric).

Mining/Tunneling Locomotive powerplants represent a niche market for the Fuelcell Powerplant that is cost competitive with current technologies in use. A downside to the Fuelcell Powerplant, for many applications, is the weight of the metal hydride bed; however, Mine/Tunnel Locomotives are usually ballasted to enhance tractive efficiency. Fuelcell Stack costs are currently high due to limited demand; however, the cost benefits (productivity, safety and pollution) for Mine/Tunnel Locomotives outweigh these capital costs. Economic evaluation by FCPI predicts cost savings from the utilization of the Fuelcell Powerplant for Mine Locomotives (Gaibler and Miller, 1998).

The Hydride Bed/Fuelcell Project requires:

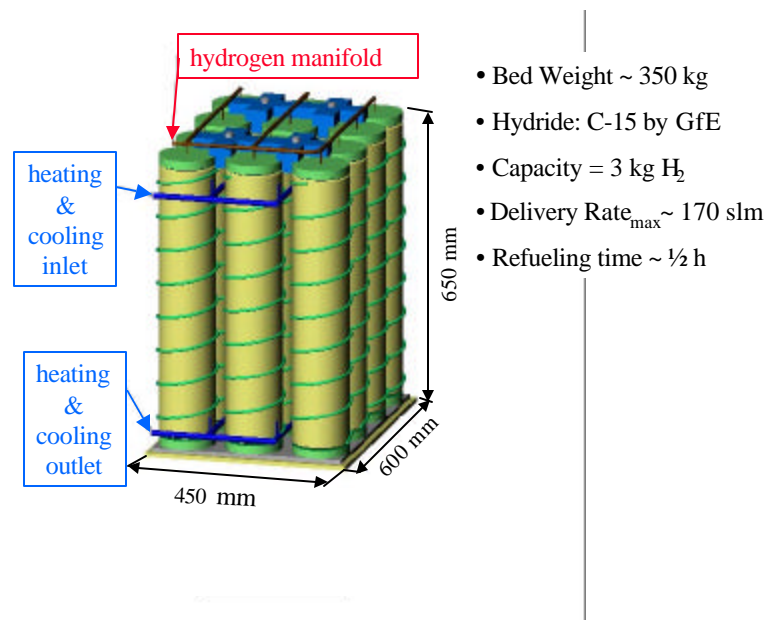
- (1) The design, development and fabrication of a metal-hydride bed,
- (2) The design and fabrication of Fuelcells (utilizing Fuelcell Stacks provided by Nuvera, of Milan, Italy), and
- (3) The design, development and fabrication of a powerplant control system to integrate the Hydride Bed and the Fuelcells into a Mine Locomotive Fuelcell Powerplant.

Hydride Bed

A metal-hydride was chosen as the hydrogen storage media for the Mine Locomotive Fuelcell Powerplant to provide a safe, low pressure and large capacity storage of fuel. Hydrogen may be stored at approximately 1.5 weight percent in the metal-hydride. The goal of 3 kgm of hydrogen storage thus requires approximately 200 kgm of metal-hydride. The metal-hydride chosen for this prototype is Hydralloy C15 (a product of GfE, Nuremberg, Germany). Hydralloy C15 exhibits a plateau pressure of approximately two atmospheres at room temperature and has a good record of consistency after many recharges.

The Hydride Bed utilizes twelve aluminum cylinders having a proprietary internal configuration to control packing density and heat transfer. The bed will be warmed during operation via a recirculating warming system utilizing water as the heat transfer fluid. Recharging will be likely accomplished by exchanging hydride beds (due to regulatory concerns about gaseous hydrogen underground). A conceptual picture of the Hydride Bed is shown in Figure 1. The recharging goal of 30 minutes is quite ambitious and may require further design modifications to effectively remove the heat of formation and keep the bed temperature to less than 50 degrees Celsius during charging at these high rates. The increase in Hydride Bed temperature increases the equilibrium overpressure of hydrogen, thus disallowing the Bed to absorb more hydrogen at the charging pressure of approximately 30 bars.

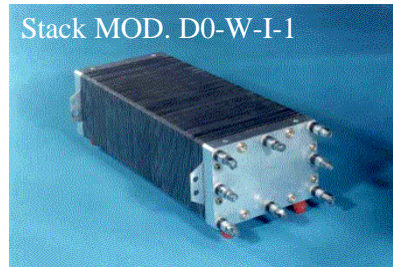
Figure 1. Mine Locomotive Hydride Bed



Fuelcells

The Fuelcell Stacks (see Figure 2.) are designed to produce 7 kW (52 volts at 135 amps) from each stack at peak power. The powerplant will contain two stacks, wired in series, to produce 14 kW (104 volts at 135 amps) at peak power. The peak power design requires air supplied at 1.5 bars and hydrogen supplied at 1.8 bar, the airflow rate at peak power is 24 cubic meters per hour for each stack. The air handling equipment to produce these pressures and flows is fairly large and power intensive (2 kW of electric power can easily be consumed at peak output). The demineralized cooling/humidifying water supplied to the Stacks is also at maximum flow rate during peak power demands. Fortunately, peak power demands are very short-term for the Mine Locomotive, the usual power demand will be 7 kW or less. Lower power requirements should allow the lowering of the air pressure, airflow rate and hydrogen pressure. The utilization of DC motors for the air pumps and water pumps allow pump speed/flow rate to be changed as power demand requirements vary.

Figure 2. Nuvera Fuelcell Stack



Courtesy Nuvera (De Nora)

Mine Locomotive Powerplant Fuelcells

- Stacks Required: 2
- Stack Voltage: 54 V
- Stack Current: 135 A
- Air Required: 400 slm/stack
- Air Pressure: 1.5 bar
- Hydrogen Required: 85 slm/stack
- Hydrogen Pressure: 1.7 bar
- Coolant Water Required: 100 lm/stack

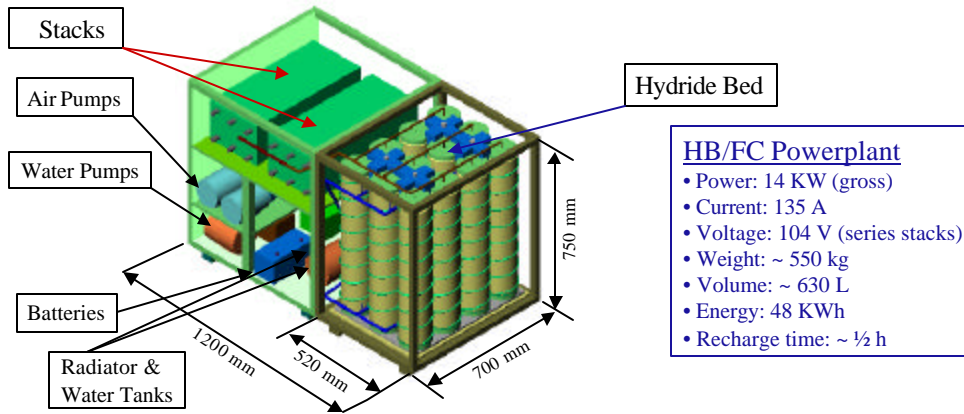
Fuelcell Powerplant

The Fuelcell Powerplant (see Figure 3. for conceptual layout) requires the integration of the Hydride Bed and Fuelcells through the use of a Control System that monitors power demand from the locomotive and adjusts air flow rate and pressure, hydrogen pressure, water flow rates and cooling fan speeds to optimize the efficiency of the powerplant and meet the Locomotive's demands. This portion of the project is in the early development stage.

Mine Locomotive

The Mine Locomotive with the prototype Fuelcell Powerplant will be displayed at MINExpo 2000 in Las Vegas, NV, October 9-12, 2000. Complete integration and test of the Mine Locomotive with the Fuelcell Powerplant will commence after it returns from the show. The Mine Locomotive and comparisons with battery power and the Fuelcell Powerplant are shown in Figure 4.

Figure 3. Mine Locomotive Powerplant



Powerplant Concept Drawing--Work in Progress

- Designed for Battery Powered Mine Locomotives to aid in customer evaluation
- Will be interchangeable with a Four-Ton Mine Locomotive's Battery
- Hydride Bed may be easily replaced with a recharged one

Figure 4. Mine Locomotive

Four-Ton Mine Locomotive



Courtesy of R.A. Warren Equipment

Performance Capability
Favors the Hydride Bed/
Fuelcell Powerplant!

Battery Power

| | |
|-----------------------|-----------------------|
| • Power: 7.1 KW (net) | • Volume: 520 L |
| • Current: 76 A | • Energy: 43 KWh |
| • Voltage: 94 V | • Operating time: 6 h |
| • Weight: 1650 kg | • Recharge time: 8 h |

HB/FC Powerplant

- Power: 14 KW (gross)
- Current: 135 A
- Voltage: 104 V
- Weight: <550 kg
- Volume: <650 L
- Energy: 48 KWh
- Operating time: 8 h
- Recharge time: ~½ h

Conclusions

The economic benefits of utilizing Fuelcell technology in mining and tunneling have generated serious industry interest in Fuelcell Powerplants. Progress to date has shown the viability of this technology for Mining/Tunneling Locomotive Powerplants. Future work includes the completion of the Fuelcell Powerplant and the Control System, followed by considerable testing above and below ground in the United States and Canada. Refueling processes must be worked out and the safety assessment completed by the Mine Safety and Health Administration (MSHA). Additional work is also planned on the design of the Hydride Bed to improve its refueling performance and with the air pump manufacturers to optimize the design required to supply the required air to the Fuel Stacks.

Acknowledgements

1. The contributions of Sandia National Laboratories personnel Ray Baldonado, Design Engineer; Tim Sage, Mechanical Technologist; and, George Thomas, Project Manager have made this progress possible.
2. Special thanks to: Arnold Miller, Mine Locomotive Project Manager and Director of FCPI; Harry Bursey, President of R. A. Warren Equipment; Casper Swart, Engineering Manager, Atlas Copco Wagner, Inc.; and, their many colleagues and fellow workers.
3. The Fuelcell Propulsion Institute, a multinational consortium of government and private companies, has provided leadership and assistance in this project.
4. Funds for this project are provided by the Hydrogen Program of the US Department of Energy.

References

Gaibler, D.W. And Miller, A.R., 7 December 1998, *Cost Model for fuelcell mine vehicles: conservative analysis of recurring and capital costs*, Fuelcell Propulsion Institute, Denver, CO, USA.

CATALYTICALLY ENHANCED SYSTEMS FOR HYDROGEN STORAGE

Craig M. Jensen and Satoshi Takara
Department of Chemistry
University of Hawaii
Honolulu, HI 96822

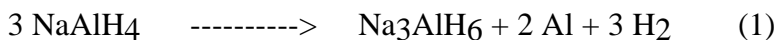
Abstract

A new catalyst has been discovered for the rehydriding of NaH and Al to NaAlH₄. The kinetics of this process in the presence of this catalyst is improved by a factor of ~5 over that of Ti/Zr doped hydride. The problem of hydrocarbon contamination of the hydrogen evolved from catalytically enhanced NaAlH₄ can be eliminated by doping the hydride with TiCl₄ in place of Ti(OBu)₄. Partial substitution of sodium cation by potassium results in a lowering of the plateau pressure associated with the dehydriding of X₃AlH₆ to XH and Al.

Introduction

For decades, hydrogen has been targeted as the utopian fuel of the future due to its abundance and environmental friendliness. A major difficulty in the utilization of hydrogen as a fuel is the problem of onboard hydrogen storage. High pressure and cryogenic hydrogen storage systems are impractical for vehicular applications due to safety concerns and volumetric constraints. This has prompted an extensive effort to develop solid hydrogen storage systems for vehicular application. Metallic hydrides (Sandrock et al. 1992; Sandrock 1995), activated charcoal (Carpetis and Peshka, 1980; Agarwal et al., 1987) and carbon nanotubes (Dillon et al., 1997) have been investigated as hydrogen carriers. Unfortunately, despite decades of extensive effort, especially in the area of metallic hydrides, no material has been found which has the combination of a high gravimetric hydrogen density, adequate hydrogen dissociation energetics, and low cost required for commercial vehicular application (Suda and Sandrock, 1994). The

dehydrogenation of NaAlH₄ is known to occur by a multistep process involving the reactions seen in equations 1 and 2 (Dymova et. al., 1975). This process is thermodynamically mically favorable at moderate



temperatures. However, it is characterized by very slow kinetics (Dymova et. al., 1975) and reversibility only under severe conditions (Dymova et. al., 1974). Thus despite favorable thermodynamics and a high available hydrogen weight percentage, NaAlH₄ was precluded from consideration as a potential hydrogen storage material until it was recently discovered that titanium doping of NaAlH₄ significantly enhances the kinetics of hydrogen desorption and renders the dehydriding process reversible under moderate conditions (Bogdanovic and Schwickardi, 1997; Jensen et al., 1999; Zidan et al., 1999). Bogdanovic found that the onset of the initial dehydriding was lowered by 50 °C upon titanium doping by evaporation of an ether suspension of NaAlH₄ which contained 2 mol % of titanium tetra-*n*-butoxide, Ti(OBuⁿ)₄ (Bogdanovic and Schwickardi, 1997). We subsequently found that homogenization of NaAlH₄ with Ti(OBuⁿ)₄ resulted in a material that undergoes rapid dehydriding at temperatures as low as 100 °C and proceeds at an appreciable rate even at 80 °C (Jensen et al., 1999; Zidan et al., 1999). The cyclable hydrogen capacity is also improved in the advanced titanium doped material. Over 4.0 wt % hydrogen can be evolved through 10 dehydriding-rehydriding cycles. We have found that the dehydriding of NaAlH₄ is also kinetically enhanced by doping the hydride with zirconium through our procedure (Jensen et al., 1999; Zidan et al., 1999). The zirconium doped material has a further improved, 4.5 wt % cyclable hydrogen capacity. In contrast to the titanium doped material, the catalytic effect is most pronounced for the second rather than the first dehydriding process. We have found that titanium and zirconium can act in concert to optimize dehydriding/rehydriding kinetics while achieving a 4.5 wt % cyclable hydrogen capacity. These findings represented a breakthrough in the application of this class of hydrides to hydrogen storage and suggested that our materials might be developed as practical onboard hydrogen carriers. In order to assess this possibility, we have extended our studies to large scale (100 g) hydrogen cycling tests that are being conducted in collaboration with Sandia National Laboratory. Additionally, Honda, General Motors, Toyota, Japan Steel Works and Motorola have expressed interest in the commercial application of these materials. However, further kinetic enhancement, especially for the rehydriding process, is required to produce a material that is suitable for practical vehicular applications. It was therefore of interest to investigate whether further improvement of the kinetics of the reversible dehydriding of NaAlH₄ could be achieved by other catalysts. Additionally, there is a thermodynamic limitation on the release of hydrogen from sodium aluminum hydride at the 80-100°C temperatures that can be supplied from the exhaust of a PEM fuel cell. The 3.6 wt % hydrogen released by first dehydriding reaction (in which NaAlH₄ is converted to Na₃AlH₆ and Al) establishes a practical plateau pressures in the range of 3-10 atm. However, in this temperature range the plateau pressure of the second reaction, in which (Na₃AlH₆ is converted to NaH and Al) is insufficient for utilization in a PEM fuel cell system. In order to harness the additional 1.9 wt % hydrogen available from this reaction

at moderate temperatures, sodium must be at least partially substituted by an alternate cationic species that would favorably alter the thermodynamics of hydrogen release.

Results

Screening of Advanced Catalysts. We have explored the dehydriding and rehydriding kinetics of NaAlH_4 doped with a variety of potential catalysts and catalyst precursors. The catalytic enhancement resulting from doping the hydride with the vanadium alkoxide complex, $\text{V}(\text{O})(\text{OPr}^i)_3$, Ti_3Al , and TiAl , were inferior in all respects to that produced by the titanium and zirconium catalyst precursors. We have, however, found two catalyst precursors that significantly improve the reversible dehydriding process. Most notably, we have discovered a new catalyst (composition can not be disclosed at this time due to proprietary reasons) whose principal effect is to vastly improve rehydriding kinetics. As seen in Figure 1, the kinetics of hydrogen uptake by dehydrided material are vastly

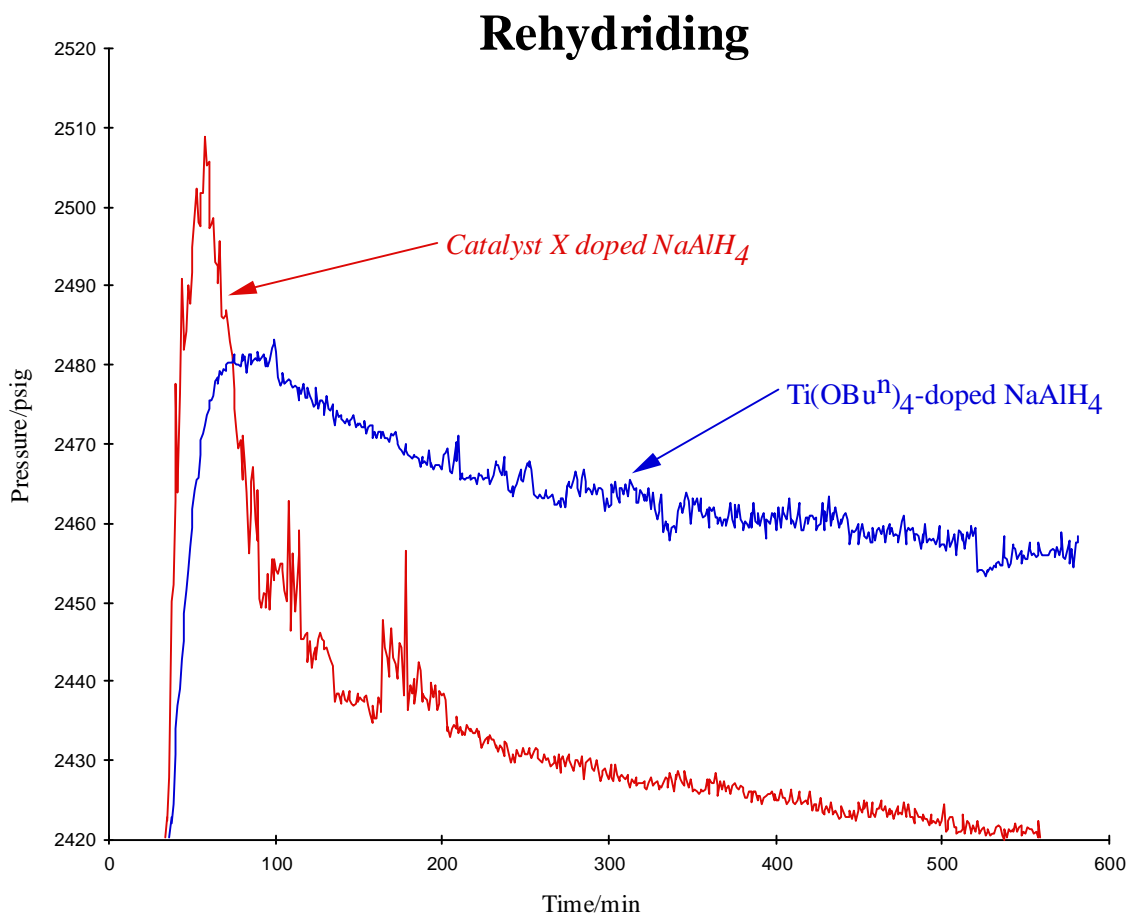


Figure 1. Comparison of hydrogen uptake by mixture of NaH + Al doped with “catalyst X” vs. $\text{Ti}(\text{OBu})_4$.

improved in material doped with “catalyst X” beyond those resulting from doping with Ti/Zr. In the presence of the new catalyst, hydrogen recharging occurs in less than 2 h at

150 °C under 170 atm of hydrogen as opposed to the 10 h required for NaAlH₄ that is doped with the titanium and/or zirconium alkoxide catalyst precursors. The combined benefit of the new, Ti, and Zr catalysts have been realized in a sample of NaAlH₄ that was doped with a ternary mixture of catalysts.

As mentioned above, large scale hydrogen cycling tests of Ti/Zr doped NaAlH₄ are being conducted in collaboration with Sandia National Laboratories. These studies have shown that the hydrogen evolved from hydride doped with Ti(OBu)₄ and/or Zr(Oi-Pr)₄ contaminated with the gaseous hydrocarbons, butane and propane. Concerns that such contamination of hydrogen might impair the operation of a fuel cells lead us to explore the doping of the hydride with the inorganic catalyst precursor, TiCl₄. As seen in Figure 2, the catalytic enhancement of the dehydriding process was seen to be similar, and in fact slightly improved when TiCl₄ was used in place of Ti(OBu)₄. Thus the problem of hydrocarbon contamination of the hydrogen evolved from catalytically enhanced NaAlH₄ has been eliminated.

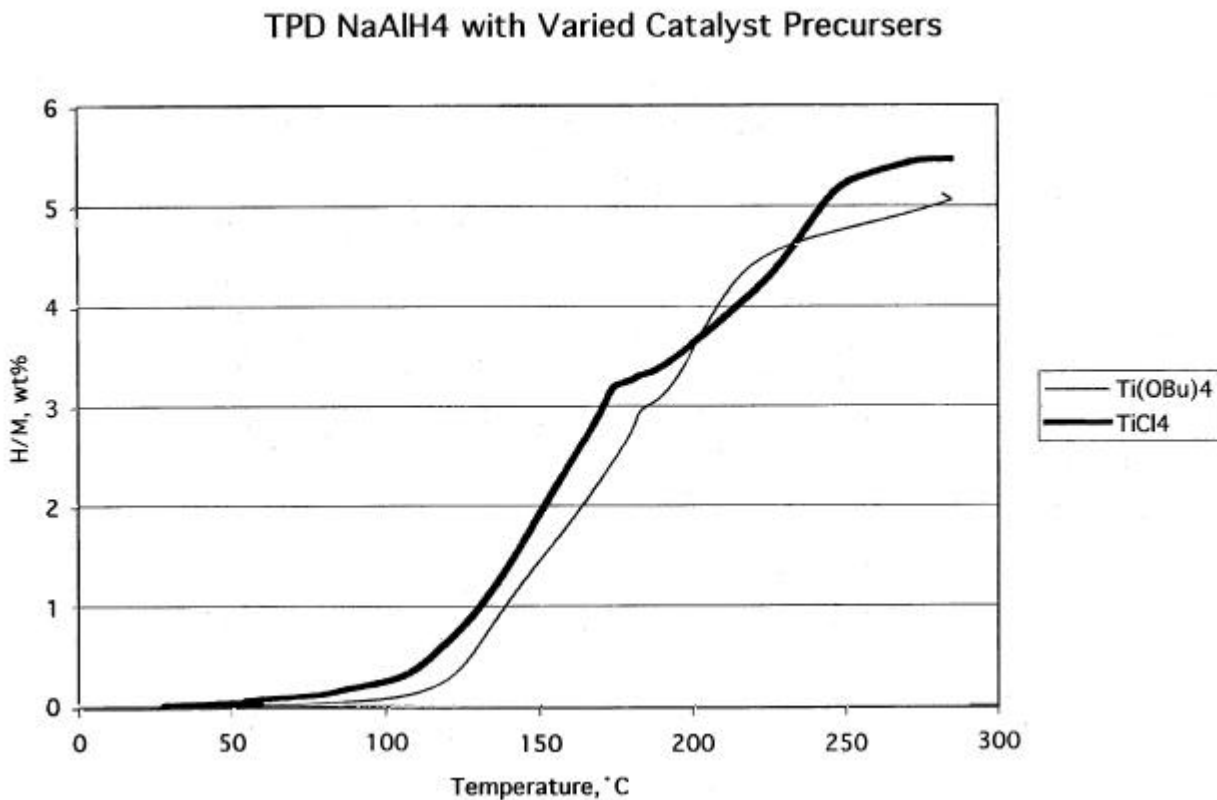


Figure 2. Comparison of the thermal programmed desorption (2 °C min⁻¹) of hydrogen from NaAlH₄ doped with TiCl₄ vs. Ti(OBu)₄.

Synthesis and Evaluation of Salts with Partial Substitution of the Sodium Cation. We have synthesized Na₂KAlH₆ through the mechanical alloying of a stoichiometric combination of KH and NaAlH₄. Unfortunately, we have found that the

potassium substitution results in an increase of the hydrogen desorption temperature to about 170 °C and decreases the hydrogen capacity by about 50%. Similar attempts to prepare the magnesium substitution compound were unsuccessful. Our studies revealed that the material resulting from energetic mechanical alloying of either MgH₂ or Mg powder with NaAlH₄ is simply a mixture of MgH₂ and NaAlH₄.

Conclusions

Two important advances have been made in the development of improved catalysts for the reversible dehydriding of NaAlH₄. We have discovered a new catalyst for the rehydriding of NaH and Al to NaAlH₄. The kinetics of this process in the presence of this catalyst is improved by a factor of ~5 over that of Ti/Zr doped hydride. Thus the time required to recharge dehydrided material has been reduced from 10 h to 2 h. Additionally, we have found that the problem of hydrocarbon contamination of the hydrogen evolved from catalytically enhanced NaAlH₄ can be eliminated by doping the hydride with TiCl₄ in place of Ti(OBu)₄.

We have determined that partial substitution of sodium cation by potassium results in a lowering rather than the hoped for raising of the plateau pressure associated with the dehydriding of X₃AlH₆ to XH and Al. Our attempts to prepare NaMgAlH₆ through mechanical alloying techniques were unsuccessful. These results, in conjunction those previously obtained for Na₂LiAlH₆ (Bogdanovic and Schwickardi, 1997), indicate that the partial substitution of sodium by alkali metal or alkaline earth cations are not a means of raising the plateau pressure the 1.9 wt % hydrogen available from this reaction such that it could be utilized for fuel cell applications below 100 °C.

Future Work

Further improvement in the rates of the dehydriding and, more crucially, the rehydriding of NaAlH₄ are required in order for this material to achieve commercial viability. With this goal in mind, we plan to test a variety of bimetallic, aluminum-transition metal hydride complexes as catalysts for these processes. Our search for improved catalysts would be greatly aided by the characterization of the active catalysts in our materials and a fundamental understanding to of the mechanism of the fundamental dehydriding and rehydriding reactions. In order to gain such insight, we propose to study the reversible dehydriding of NaAlH₄ by solid state nuclear magnetic resonance spectroscopy.

We have also found a class of catalysts that could provide the key to a practical hydrogen storage system based on the reversible dehydrogenation of cycloalkanes to arenes. Such a system meets the criteria of low cost and high hydrogen density (~7.0 wt %). The PCP pincer complex, IrH₂{C₆H₃-2,6-(CH₂PBu^t)₂} is the first reported homogeneous catalysts for the dehydrogenation of cycloalkanes to arenes (Gupta et. al., 1997). Unlike the heterogeneous catalysts for this reaction, it shows appreciable activity at low concentrations at temperatures as low as 100 °C. We have also found that the pincer complex also catalyzes the hydrogenation of arenes to cycloalkanes under

moderate (10 atm) pressures of hydrogen. The two-way, hydrogenation/dehydrogenation activity of the catalyst suggests its application in a hydrogen storage system. The major obstacle to the practical application of the pincer catalyst is that pronounced product inhibition occurs after about 10% dehydrogenation of cycloalkanes. In order to eliminate this problem we plan to synthesize and test an improved catalyst, $\text{IrH}_2\{\text{C}_6\text{H}_3\text{-2,6-(CH}_2\text{AsBu}^t\text{)}_2\}$.

References

- Agarwal, R.K., J.S. Noh, J.A. Schwarz, and R. Davini, 1987. *Carbon* 25:219.
- Bogdanovic, B. and M. Schwickardi, 1997. *J. Alloys and Compounds* , 1-9:253.
- Carpentis, C. and W. Peshka, 1980. *Int. J. Hydrogen Energy* , 5: 539.
- Dillon, A.C., K.M. Jones, T.A. Bekkedahl, C.H. Kiang, D.S. Bethune and M.J. Heben, 1997. *Nature* , 386:377.
- Dymova, T.N., Y.M. Dergachev, V.A. Sokolov, and N.A. Grechanaya, 1975. *Dokl. Akad. Nauk USSR*, 224:591.
- Dymova, T.N., N.G. Eliseeva, S.I. Bakum, and Y.M. Dergachev, 1974. *Dokl. Akad. Nauk USSR*, 215:1369.
- Gupta, M., C. Hagen, W.C. Kaska, R.E. Cramer, C.M. Jensen, 1997. *J. Am. Chem. Soc.*, 119: 840.
- Jensen, C.M., R. Zidan, N. Mariels, A. Hee, C. Hagen, 1999. *Int. J. Hydrogen Energy*, 24:461.
- Sandrock, G., S. Suda, and L. Schlapbach, 1992. *Topics in Appl. Phys.*, 67:197.
- Sandrock, G. 1995. *Application of Hydrides in Hydrogen Energy Systems* (ed Yurum), 253-280. Netherlands: Kluwer Academic Publishers.
- Suda, S. and G. Sandrock, 1994. *Z. Phys. Chem.*, 183:149.
- Zidan, R.A., S. Takara, A.G. Hee, C.M. Jensen, 1999. *J. Alloys and Compounds*, 285:119.

The Corrosion of Metallic Components in Fuel Cells

J. A. Turner

National Renewable Energy Laboratory
1617 Cole Boulevard, Golden, Colorado 80401

When one is considering the mass production of fuel cells, the manufacturability of each component is very important. To obtain the economy of mass production, approximately one million fuel cell systems need to be manufactured each year, that is almost 100,000 per month. Assuming 120 bipolar plates per stack, that is 12 million bipolar plates per month or 400,000 per day! That means these plates must be injection molded or stamped from metal stock. Injection molding requires a cycle time of less than 10 seconds and conductivity similar to POCO graphite. Because of the need for rapid production, and high conductivity, metal stock is a good possibility. However when considering metal stock, a number of problem arise from the possibility of corrosion leading to failure of the stack. Because of the unique and complex environment in a fuel cell stack, the importance of corrosion testing cannot be understated. A fuel cell stack has a humid environment that includes both oxidizing and reducing atmospheres, small amounts of fluoride leach from the membrane, and other halides, as well as SO_x, and NO_x are available from the atmosphere. These conditions can interact in a complex way to attack the metal plates leading to corrosion. Additionally, if the metal plates contain iron, it can leach out into the membrane blocking the sulfonic acid sites, thereby reducing the conductivity of the membrane. Iron can also act as a catalytic poison to degrade the membrane. The goal of this research is to determine corrosion mechanisms for various metal alloy compositions, and to develop techniques for long term corrosion protection for thin metal foils.

The usual way in which stainless steels and titanium are protected is from an inert oxide coat that naturally forms on the surface. Unfortunately, these oxides are typically insulating, leading to ohmic losses within the cell. Additionally, the surface resistance also affects the force needed to hold the cell plates together. Higher resistivity requires a higher force and corresponding thicker and more massive endplates. If these oxides could be made conducting, then perhaps they would not only protect the underlying metal plates from corrosion, but also provide a conducting pathway for the flow of current. This would also reduce the size of the endplates, increasing the energy density of the fuel cell.

Various groups have looked at the corrosion resistance of a number of stainless steel formulations. Hornung and Kappelt (from Siemens) studied Fe-based alloys for construction of bipolar plates (1). Their goal was to replace gold-coated nickel bipolar plates with low cost Fe-based alloys. They concluded, with regards to corrosion resistance, that Fe-based alloys have similar characteristics as the nickel-based alloys, However, only the gold-coated plates gave contact resistances that were low enough for fuel cell performance. Davies, et.al., looked at electrical resistance of the surface oxide films for three stainless steel alloys, 310, 316, and 904L (2). All these films were shown to be resistive and the resistive losses could be correlated with the thickness of the film. The performance increased (due to a lower surface film resistance) in the order $316 < 310 < 904L$. They concluded that the thickness of the film was thinner in alloys containing higher concentrations of nickel and chromium. They also mention a proprietary low surface resistant coating for 316 stainless steel that increased cell performance. As expected they determined that the bulk resistivity is insignificant as compared to the resistivity of the passivating film.

Most of the testing of these plates has been in the 1000-3000 hour range, and for automotive use the lifetime needs to be at least 5000 operational hours and for stationary systems greater than 50,000 hours. Cleghorn et. al., commented that while stainless steel systems showed no apparent effects from corrosion after 1000 h of testing, some form of surface treatment may be required to achieve extended long-term stability (3).

Developing a conducting passivating film for metal based bipolar plates would greatly enhance the performance of the fuel cell and address the issue of the bipolar plate manufacturability (4). It may also be possible, with proper choice of conductive coating, to protect the Nafion membrane from transition metal ion poisoning. NREL is unique in having a long experience in conducting

oxides due to their use in various types of solar cells. For example, conductive tin oxide, used as the current collector for solar cells, may offer the appropriate protection and give high conductivity. This includes SnO:F which would likely be stable in the presence of fluoride. Other coatings of interest are ITO (indium tin oxide), ZnO and SnO₂. Tungsten trioxide, used in electrochromic devices, becomes conducting in the presence of hydrogen and perhaps could be used as a protective coating for the hydrogen side of the plate. In solar cells, these coatings are deposited on glass and on stainless steel in large areas and at high volume. For this work, NREL is combining its expertise in corrosion testing with its unique capability in conducting oxides.

A laboratory has been set-up to test the corrosion resistance of these coating and experiments are underway.

References

1. R. Hornung and G. Kappelt, *J. Power Sources*, **72**, 20 (1998).
2. D.P. Davies, P.L. Adcock, M. Turpin, and S.J. Rowen, *J. Power Sources*, **86**, 237 (2000).
3. S. J. C. Cleghorn, X. Ren, T.E. Springer, M.S. Wilson, C. Zawodzinski, T. A. Zawodzinski, and S. Gottesfeld, *Int. J. Hydrogen Energy*, **22**, 1137 (1997).
4. R. L. Borup, N.E. Vnaderbourgh, *Materials Research Society Proceedings Series*, **393**, 151 (April 1995).

SMALL BATTERY — FUEL CELL ALTERNATIVE TECHNOLOGY DEVELOPMENT

**Mahlon S. Wilson, Erik B. Brown, Christine Zawodzinski
and Mark Daugherty (Enable Fuel Cell Corp.)
Materials Science and Technology Division, MS D429
Los Alamos National Laboratory, Los Alamos, NM 87545**

Abstract

A compelling market segment for the introduction of fuel cells is in small battery types of applications. While in other applications (e.g. transportation), fuel cells need to compete with relatively effective and low-cost technologies, batteries are easier to compete with because they are expensive and have low energy densities. Even with modest hydrogen storage densities such as metal hydrides, fuel cells can provide higher energy densities than batteries and the values can increase substantially further with an increase in the energy to power ratio of the system (which is fixed for batteries). However, the fuel cells will still have to compete with batteries on reliability and cost. As such, the typical polymer electrolyte fuel cell system with its heavy reliance on subsystems for cooling, humidification and air supply would not be practical in small battery applications. Instead, the fuel cell system should ideally be simple, inexpensive, and reliable. In response, Los Alamos National Laboratory (LANL) conceived of a novel, passive, self-regulating, "air-breather" fuel cell stack that requires no moving parts (fans or pumps) and still maintains sufficient hydration of the polymer electrolyte membrane to provide stable and reliable power. Enable Fuel Cell Corp. (a subsidiary of DCH Tech.) has been partnered with LANL to further technological development and commercialize the air-breather. Development has reached the point where a 12 W system has officially become a commercial product. Nevertheless, understanding of the approach is continually improving and the design is being refined and adapted for various applications. It would appear that the primary factor now affecting market penetration is the fuel storage issue.

Introduction

Depending upon the fuel storage technology, fuel cell systems can provide substantially higher energy densities than similar-sized battery packs. Correspondingly, interest in fuel cells for portable power applications is rapidly increasing and now global electronics companies are pursuing the possibilities. In this program, LANL and Enable Fuel Cell Corporation are developing a unique low-power portable fuel cell and system inexpensive and reliable enough to eventually compete head-to-head with batteries in electronics-type applications. The advantage of this fuel cell system over current competing fuel cell designs is that it does not require the use of peripherals such as cooling or reactant flow fans and can operate effectively with no active humidification, no active cooling, and no pressurization or forced flow of the cathode air. The system is inherently stable and self-regulating. A passive scheme is used that relies on diffusion limited oxygen access to maintain a positive water balance. The oxygen in the air must diffuse into the stack from the periphery of the flow-field plates. For this reason the stack is often described as "air-breathing." Given that the oxygen must diffuse in, twice as much water (as there are two molecules formed per O_2 that reacts) must diffuse out to maintain an even balance. While it first appears that a surplus of water is obtained, the fuel cell stacks quickly heat up and the water removal is greatly facilitated. Overall, the balance remains fairly even such that the polymer electrolyte membranes do not dry out, even at relatively high continuous operation temperatures ($+60^\circ C$). Thus, the diffusion supply scheme results in simple stacks with reliable and stable performance. To operate this type of fuel cell stack only a low pressure hydrogen supply is required which can be provided from a pressurized source (such as metal hydride canisters) via a compact low-pressure regulator.

Discussion

Since the oxygen needs to diffuse in from the periphery of the cathode flow-field plate, the fuel cell assumes the unique configuration shown in Figure 1 that utilizes circular flow-field plates with an annular hydrogen feed manifold and a single tie-bolt extending up through the central axis of the stack (Wilson 1996). With this geometry, the hydrogen supply to the unit cells is radially outward, and the air supply is from the periphery inward. This configuration has several advantages. The entire periphery is free to air access and allows greater heat conduction to enhance cooling and the diffusion path lengths are minimal for both the hydrogen from the annular region and the oxygen from the periphery. Furthermore, all of the components in the stack (e.g., the flow-fields, seals and membrane/electrode assemblies), are radially symmetrical, so part fabrication is simple and the entire system is potentially low-cost. The reactant flow-fields are typically reinforced carbon paper and membrane/electrode assemblies (MEA) are of conventional design. Seals are located at the inner edge of the air flow-field and the outer edge of the hydrogen flow-field. Stainless steel foil separators prevent the reactants in the back-to-back flow-fields from mixing. As shown in the right hand side figure, end-plates compress the collection of unit cells together with the use of the tie-bolt projecting up through the middle. The use of a single tie-bolt decreases the footprint and helps provide a configuration that is compact and lightweight. In multi-cell stacks, the separators can be of a larger diameter than the flow-fields to provide cooling fins, which gives the stack the appearance of a finned tube.

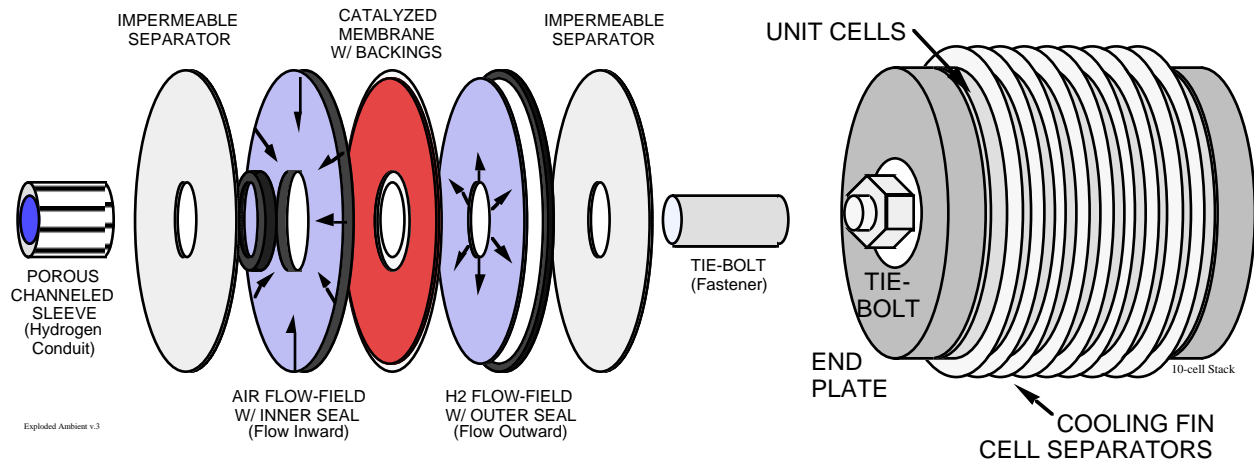


Figure 1 - Configuration and key components of a unit cell in an air-breather stack.

When the cells are stacked, not only do the structures heat up more but water accumulation in the annular region actually becomes a problem. Since the hydrogen supply is dead-ended, condensate can collect undisturbed and block the hydrogen from accessing the cells furthest from the hydrogen supply. The accumulation can be alleviated by introducing a wicking material in the annular region that draws the condensate away from the downstream cells (Wilson and Neutzler 1997).

Not surprisingly, cell performance is substantially affected by the thickness of the cathode flow-field because oxygen must diffuse in from the periphery through this structure. While the thicker flow-fields provide high powers at low temperatures, too much water is lost as the stack heats up to higher temperatures, especially at the relatively high altitude of LANL (2,250m or 7,300'). The optimum flow-field thickness for both power and stability at LANL is about 3 mm, but can be greater at low altitude. With the high altitude, the ambient pressure is only about 0.76 atm. Not only is the oxygen partial pressure lower (and hence kinetics poorer), but the stacks also tend to run much drier because the higher volume fraction of water vapor that can occur results in a greater driving force for removing water from the stack. Another aspect of high altitude operation is that cooling by free convection is much less effective than at sea level, which naturally exacerbates the drying effect. For these various reasons, a stack that stably produces 25 W at LANL can produce up to 35 W at sea level while actually operating cooler, and excess water may actually be accumulated. Thus, more leeway is afforded designs provided they are operated at lower altitudes. Conversely, products that are oriented towards camping or backpacking impose even more stringent design limitations.

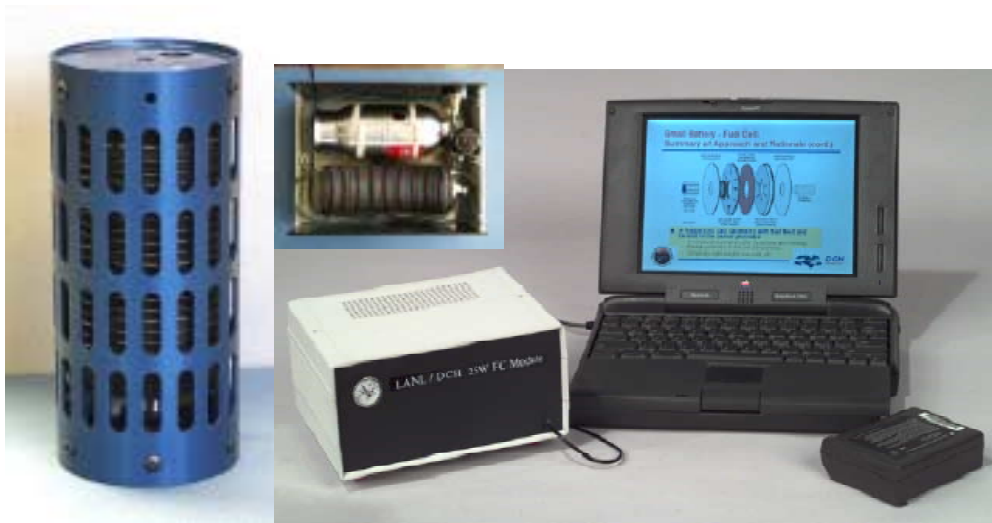


Figure 2 — Various Air-Breather Packages — The Enable Commercial Product and a Fully Integrated Module Operating a Laptop.

The versatility of the air-breather allows it to be packaged in various ways. Two examples are shown in Figure 2. On the left is the initial Enable FCC product which has recently become commercially available. As can be seen, the air-breather is mounted vertically and is protected by a shroud with elongated openings that allow air to freely convect upward and over the stack to provide cooling. While capable of more power, the stack is conservatively rated at 12 Watts at roughly 12 V and is design to be affixed atop the hydrogen supply in a tower configuration that is then suitable for supporting a camping lantern. On the right is a fully integrated module containing both the stack and a metal hydride canister, as is shown in the top view in the inset in Figure 2. A small pressure gage indicates the status of the fuel supply. Positioned side-by-side, air convection thermally couples the 36-cell stack and the hydride canister to provide cooling air for the stack and to heat the hydride to facilitate the desorption process. The module supplies 25 W at LANL's altitude and can operate the laptop shown scrolling through a slide presentation for almost 12 hours. Although the energy density of the system depends upon the stack power, at approximately 25W it works out to a relatively modest 75 Wh/kg (still better than most rechargeable battery technologies), because the metal hydride canister is at best only about 1% hydrogen by weight. The true promise of fuel cells will be realized only when more effective hydrogen storage technologies are developed. For example, the same system with 4% hydrogen storage would obviously yield a 300 Wh/kg package and operate the laptop for nearly 48 h.

Much of the effort over the past year has continued to concentrate on optimizing the air-breather design in improving performance, lowering component costs and facilitating manufacture. One of the simpler improvements is to use a more open annular region. The performance improvement is most likely attributable to better and more uniform access of the hydrogen to the entire inner edge of the hydrogen flow-fields. Since the system operates dead-ended, a certain amount of diffusion transfer probably has to occur as inerts accumulate in the hydrogen distribution network. In our particular experimental stack design at LANL, we simultaneously changed the design of the "hub" not only to open up the free area but also to improve the effectiveness of the inner edge seals for the air flow-fields. The individual "hubs" for each separator plate provide alignment, hydrogen and wicking passages for each cell and also facilitate disassembly for swapping out components. The hub also effectively replaces the porous channeled sleeve depicted in Figure 1, which was a particularly problematic component. Since the carbon paper air flow-fields can compress

substantially, the seal area basically varies as a function of the end-plate compression. Many times a cell or two in a stack would not seal until the entire assembly was further compressed, probably due to small differences in the various material thicknesses, compressibilities, etc. The seal design was modified to allow the hub to float, thus minimizing the effect of the variations. Since this change has been implemented, stacks have all sealed the first time, which naturally improves manufacturability and reproducibility.

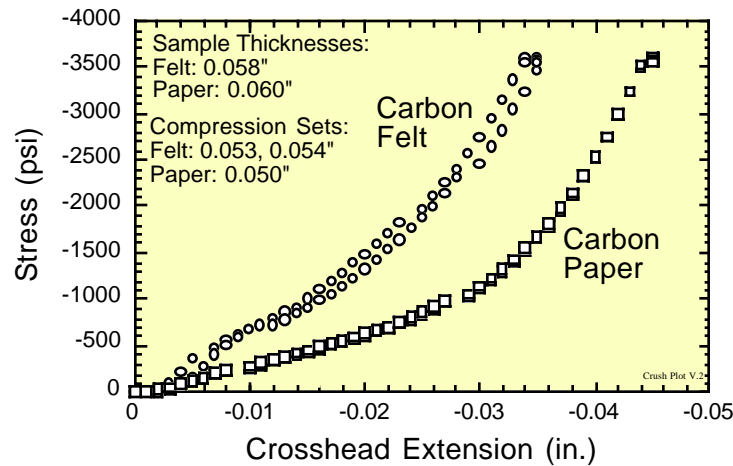


Figure 3 — Compressibilities of carbon papers and felts.

Much of the optimization is of a proprietary nature but the issue of accommodating the compressibility of the carbon paper air flow-fields leads to an example of component optimization vis-à-vis performance and manufacturability. Carbon papers have been a staple component in fuel cells for many years but they are relatively expensive. More recently, carbon felts have become commercially available, and already they appear to be less expensive. As shown in Figure 3, the felts are less compressible and take less of a set than a paper of the equivalent thickness, which improves the manufacturing aspect. On the other hand, edgewise permeability measurements using the classic Stefan Diffusion Tube configuration suggests that the papers are slightly more permeable. Thus, a somewhat thicker sheet will in principle be needed to provide the same performance. As is often the case, changing one component then has ramifications on the other elements in the system, and optimizing the system fully around price and performance becomes all the more difficult because of it.



Figure 4 — A Miniature 1 W Air-Breather Alongside a 9 V Alkaline Battery.

The global electronics industries that are entering the fuel cell arena are primarily interested in personal electronics applications such as cellular phones, hand-held computers, etc. The power requirements are more on the watt level rather than the tens of watts appropriate for the air-breather scale we have thus far been employed. Figure 4 is a picture of our first effort on a watt-level air-breather. While successful, the design was rather primitive and hence not of the possibly highest performance and also not particularly amenable to commercialization. The annular and tie-bolt region is very cramped and it appeared that there were hydrogen access limitations. One of the challenges on such a small scale is to obtain a reasonable fraction of active area with such small diameters because so much of the plate area is lost to seals, the tie bolt and the hydrogen feed region. The area taken up by the outer (hydrogen) seal is roughly equal to the active area. Although the current densities are already higher than the larger stacks (as expected), further performance increases should be readily attainable as the designs are improved.

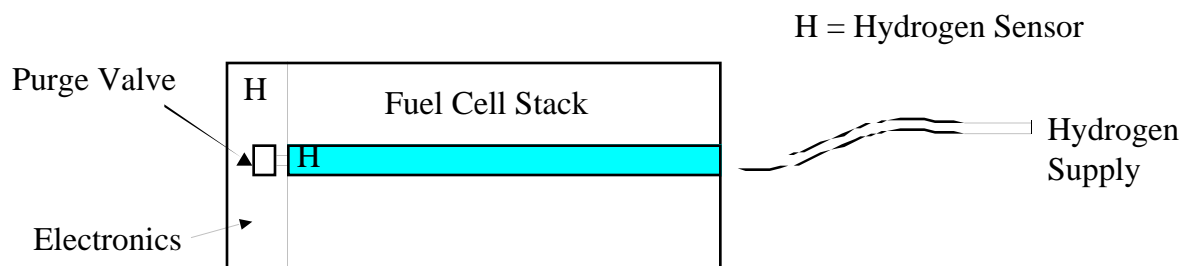


Figure 5 — Integration of Hydrogen Sensors into the System.

Many potential applications for the air-breather will require some level of remote status monitoring and operability or safety assurance. In addition, the buildup of inerts may be more challenging with some hydrogen sources or stack configurations. Hydrogen sensors may be advantageous in these cases. The parent company of Enable FCC, DCH Technology, has licensed and successfully commercialized state-of-the-art hydrogen sensor technologies including the Robust Hydrogen Sensor (RHS), from Sandia National Laboratories. These technologies are being integrated into the fuel cell system as depicted in Figure 5. One sensor is located within the stack to detect inert build-up, and would then trigger a brief purge. A second sensor is installed for safety and to detect leaks or excess build-up from the purges. The compact control electronics and the miniature purge valve are cleanly incorporated onto one end of the stack.

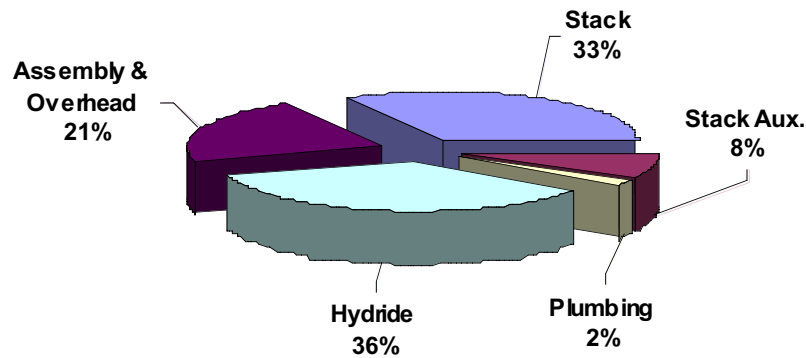


Figure 6 — System Component Costs (from Enable FCC)

As anticipated, a major issue coming into the forefront is hydrogen storage. In order to realize the energy density potential of the system, the metal or chemical hydrides need to be packaged particularly effectively. An overly complex or peripheral-burdened system would not be viable for portable power applications. Ideally, the fuel would be available in a cartridge that could be returned and recycled, or if it must be disposed (say, on foreign travel), it should not be an overly expensive loss. The economics element of the fuel supply issue is illustrated in Figure 6. As shown, the hydride storage system for this 4 W, 10 h system costs at least as much as the fuel cell, even though the latter involves numerous costly and special order components that have not yet had the benefit of high production levels to lower prices. While hydride production levels are not particularly enormous either, the business does have fairly large and established markets (e.g., Ni-metal hydride batteries). Costs for the hydride also may not be expected to decrease much further considering that the system is not particularly parts intensive, especially compared to the fuel cell. How the hydrogen is stored and supplied will naturally depend upon the application, but the overall system (storage + fuel cell) needs to be integrated and optimized. Portable power possibly provides some unique opportunities as to how this can be accomplished that would not be practicable on larger scale systems.

Conclusions

The air-breather has been shown to be an effective and versatile design over a wide range of sizes and packaging possibilities. Designs, understanding of the mechanics, and performances all continue to evolve. Although a number of aspects can be still further improved, the air-breather provides the durability and reliability necessary to become a commercial product and has demonstrated the performance and utility necessary to provide a successful fuel cell product. On the other hand, the complete system is still wanting, and the missing element is a cost-effective fuel storage system and its integration with the fuel cell.

Future Work

We plan to continue collaborating with Enable FCC in further evolving air-breather technology. As the fundamentals and optimal designs become better understood and more functional, opportunities arise to implement newer ideas and approaches that will bring the air-breather to the next technical levels. Already, Enable is pursuing new directions that can be particularly advantageous in many applications.

Since the interest in power supplies for personal electronics is particularly strong, more emphasis will be spent on the watt-level air-breathers. Because of the high surface area to volume ratios inherent in small objects, it should be possible to attain relatively high power densities and correspondingly develop some compelling devices.

As the air-breather design and understanding continue to evolve, additional issues are becoming more pressing. Paramount of these is the remainder of the overall system, namely the fuel storage and supply subsystem. The extent to which portable power fuel cells can be commercialized will be contingent on the safety, energy density and user-compatibility of the overall system, and we perceive that the weak link now is the fuel subsystem. Substantial progress has been accomplished with the fuel cell side of the system but now we believe that the emphasis also needs to encompass the fuel issues. Consequently, increased attention will be directed toward the hydrogen supply for the fuel cells. In this new aspect of the portable fuel cell effort, we intend to collaborate with Enable FCC and others to help develop and demonstrate portable storage technologies. Some of the challenges and opportunities inherent in a portable unit for commercial applications are very different than conventional storage requirements. As such, fairly conventional chemical hydrides that are not particularly attractive for large scale applications are possibly advantageous for portable systems. Thus, we are not trying to develop new chemistries so much as effectively and inexpensively adapt existing approaches and repackage them for portable power.

References

Gottesfeld, S. and M. S. Wilson. 2000. "Polymer Electrolyte Fuel Cells as Potential Power Sources for Portable Electronic Devices," in *Energy Storage Systems in Electronics*, Tetsuya Osaka and Madhav Datta (Editors), Gordon & Breach Science Pub; ISBN: 90-5699-176-0.

Wilson, M. S., 1996. "Annular Feed Air Breathing Fuel Cell Stack." *U. S. Patent No. 5,514,486*.

Wilson, M. S., D. DeCaro, J. K. Neutzler, C. Zawodzinski and S. Gottesfeld, 1996. "Air-Breathing Fuel Cell Stacks for Portable Power Applications." In *Abstracts of the Fuel Cell Seminar*, 331-335, Orlando, FL: Courtesy Associates, Inc. / Fuel Cell Seminar Organizing Committee.

Wilson, M. S. and J. K. Neutzler, 1997. "Annular Feed Air Breathing Fuel Cell Stack." *U. S. Patent No. 5,595,834*.

PEMFC STACKS FOR POWER GENERATION

**Mahlon S. Wilson, Christine Zawodzinski, Guido Bender,
Thomas A. Zawodzinski, and Deanna N. Busick
Materials Science and Technology Division, MS D429
Los Alamos National Laboratory, Los Alamos, NM 87545**

Abstract

Industries promoting polymer electrolyte membrane (PEM) fuel cells for stationary and auxiliary power applications are receiving considerable attention because of the attractiveness of the primary markets, such as small, home-based power generation on the roughly 3 – 5 kW level. More recently, interest in auxiliary power applications down to about the 1 kW level has also been steadily increasing. Plug Power, LLC, a fuel cell manufacturer, is primarily pursuing the development of the home-based power systems. Technological advances in PEM fuel cells at Los Alamos National Laboratory (LANL) are of potential utility for the development of readily manufacturable, low-cost and high performance fuel cell systems operating at near-ambient reactant pressures. As such, the two parties are collaborating on addressing some of the more pressing needs as well as some longer term issues. The primary tasks involve the investigation of both stainless steel and composite bipolar plates, CO tolerant anodes, and novel fuel cell system operation schemes.

Introduction

Fuel cells for home-based stationary power applications are attracting ever greater attention. Some of the possible reasons for this increased attention are the recent demonstrations and development successes of the PEM fuel cell, the deregulation of the utilities and the subsequent power difficulties in California this summer, and finally, the slow maturation and competitiveness of the transportation market for fuel cells. While the majority of funding and interest in PEM fuel cells has historically been for transportation applications, meaningful penetration of that market will be difficult for many years yet to come because the competitive technologies are well-entrenched and inexpensive. Despite the significant environmental advantages, fuel cell systems will still need to cost on the order of \$50/kW for transportation which will require at the least enormous production

levels. Until then, many of the fuel cell companies have been attracted to home-based stationary power as a possible fuel cell market that should still be sizable, should accommodate much higher unit costs and does not involve entrenched competition. Most domestic fuel cell companies have teamed up with utilities to explore such possibilities. The majority of home-based units will be designed to operate on natural gas because of the extensive distribution network in place. By installing home-based units, utilities can increase generation capacity without needing to site and license new plants or build new power lines, both of which have become ever more costly and problematic due to public resistance and tightening regulations. Natural gas suppliers might also be interested in the home-based systems because of the possibilities of competing in a new market and relieving their susceptibility to natural gas prices.

Operating the home-based system on natural gas will require a fuel processor to provide hydrogen to the fuel cell. The reforming and/or partial oxidation fuel processor reactions produce byproducts such as CO and CO₂. If the CO is not removed from the fuel stream in some manner before it reaches the fuel cell it will severely affect performance, especially with standard anode designs. The typical strategy is to remove the CO through a series of additional steps, but removing the last tens of ppms can not always be routinely assured with typical systems. Therefore, anodes that can tolerate higher levels of CO than conventional electrodes are of interest to withstand excursions that may occur with start-up of the fuel processor or during variations in load levels. Another issue with the use of natural gas is the operating pressure of the fuel processor system. Most other hydrocarbon fuels are liquids that can be efficiently pumped to allow the use of a pressurized fuel processor. This decreases the fuel processor volume (and cost) and increases the pressure of the hydrogen delivered to the fuel cell stack, which alleviates dilution effects. However, domestic natural gas is typically delivered into the house at less than 1 psig. Compressing the natural gas incurs a considerable power penalty and requires an additional piece of expensive equipment. The preferable option is to operate a low-pressure fuel processor, however, the fuel cell anode will then need to operate at near ambient pressures. Anodes then need to be designed and optimized for both the low-pressure operation and CO tolerance.

The balance of the fuel cell system is inordinately complex and expensive. Conventional systems rely upon a multitude of subsystems, e.g., cooling, reactant humidification, water recovery, pressurization, etc., that introduce a parasitic power draw that compounds the size of the stack and/or lowers efficiency. If the subsystems can be combined or eliminated, often the lesser complexity and lower power draw more than compensate for any stack performance penalty once the entire system is taken into account.

Regardless of the fuel cell system or stack technology, one of the major limitations has been the bipolar plate technology. Historically, machined graphite plates have been the material of choice, but are clearly too expensive for mass production. The bipolar plates also need to be highly electrically conductive, durable, impermeable and corrosion resistant, a surprisingly difficult combination to realize. Metal hardware is of interest because of its toughness and the versatile fabrication options, but corrosion is a significant difficulty. Composites have therefore been the preferred option, but even then they have generally been too expensive.

Discussion

Metal Bipolar Plates

As previously discussed here, most of our work with metal hardware in this program has focused on the development of non-machined low-cost bipolar plates based on the use of untreated metal alloy screens and foils (Wilson and Zawodzinski 1998 & 2000, Zawodzinski et al. 1998). In general, the hardware performed well in several fuel cell tests including a 2000 h life-test and appeared to be corrosion resistant, in that cell performance and the high frequency resistance

remained quite stable over the test period. When the membrane-electrode assembly (MEA) was subsequently examined by x-ray fluorescence (XRF) spectroscopy, it was found that metals such as iron and nickel were indeed present in appreciable quantities. While the cell performance was not yet unduly affected, significant losses can be expected over the much longer lifetimes that would be expected of stationary applications. While the membrane has some tolerance, eventually its active sites would be tied up by the polyvalent ions and ionic conductivity would be seriously impaired. Consequently, we commenced screening more “noble” stainless steel and nickel rich alloys that might provide better corrosion resistance than 316 SS but are still relatively low-cost. Many types of alloys have been developed for applications where common stainless steels such as 304 or 316 SS do not provide adequate corrosion resistance. In general, the compositions of these alloys are similar to their stainless steel or nickel-base counterparts except that certain stabilizing elements, such as nickel, chromium and molybdenum, are added and/or are present in much higher concentrations in order to obtain desirable corrosion properties. Different combinations of these elements and their concentrations can dramatically change the nature of the alloy and thus, alloy compositions are usually tailored for quite specific applications, such as marine water service. This poses a problem in choosing suitable materials for fuel cells because of the variety of conditions present that are all conducive to corrosion yet are very different in nature, i.e. chemical and electrochemical oxidizing and reducing environments, humidity, and possibly slightly acidic environments.

For example, nickel, which is common to all of these families of alloys, provides corrosion resistance in neutral and reducing environments and is essential to prevent chloride stress corrosion cracking. Thus, for applications such as seawater or caustic service, a high Ni content is required and most of the nickel-base alloys have been developed for these types of applications. In neutral to oxidizing media, however, a high chromium content (which is often accompanied by the addition of molybdenum) is necessary. Many of the stainless steel alloys have been developed along this vein and are used in a variety of corrosive environments, i.e. nitric acid service. Since both oxidizing and reducing conditions exist in a typical fuel cell environment, we screened a number of stainless steel and nickel alloy samples representing several categories of corrosion-resistant materials as possible improvements to 316 SS. The alloys were evaluated using individual immersion testing in pH 2 and 6 sulfuric acid solutions held at 80°C that were either sparged with hydrogen or air to simulate anode and cathode conditions, respectively. Although severe, the pH 2 conditions tend to accelerate corrosion of the materials and thus differences in the corrosion resistance of numerous alloys can be assessed relatively quickly (on the order of a few weeks). As a result, only the most promising alloys need be made into bipolar plates and tested in fuel cells, which is a time-consuming and much more expensive process. The “corrosion” was quantified by gravimetric weight loss and by measuring the metal ion uptake in Nafion membranes placed in the solution during the test. The latter is used to anticipate the severity of ion uptake in operating fuel cell membranes. As reported last year, roughly a half dozen promising alloys were identified, both of the stainless steel and of the nickel-based types. The preferred Ni-based alloys were intriguing because although their pH 2 corrosion tolerances were only mediocre, their pH 6 tolerances were the best surveyed.

Consequently, over the past year, the down-selected alloys were tested on the anode side of 50 cm² pressurized and humidified PEM fuel cells. Unfortunately, the Ni-based alloys showed appreciable corrosion after only a short time in the fuel cells. Even though the cell effluents were in the pH 6 range, the fuel cell is enough different from the immersion testing that the pH 2 results appear to be a better indicator. Nevertheless, two of the stainless steel-type alloys, described as “B” and “F”, provided very promising results. In order to see how the cells responded to optimum as well as severe conditions each cell was put through cycles of operation at 0.5 V and at open-circuit voltage (OCV), which was about 0.94 V. During the course of operation, the cells underwent shutdowns due to unplanned circumstances such as power outages as well.

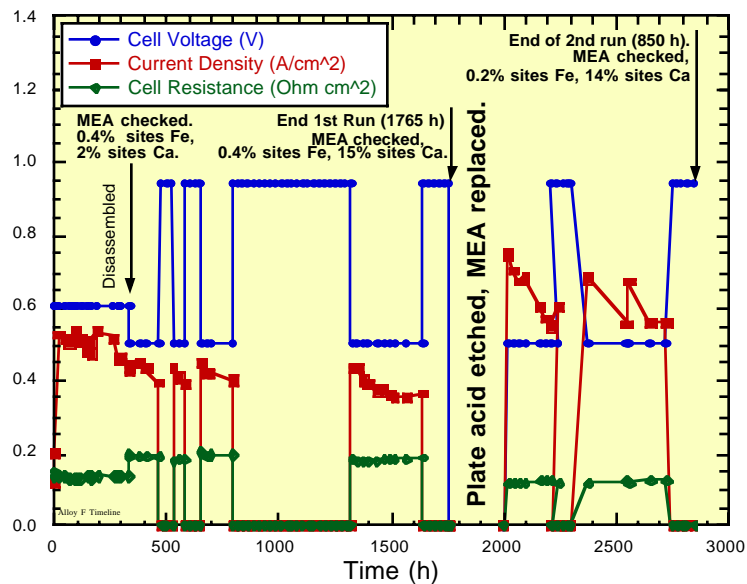


Figure 1 — Timeline for an Alloy F Fuel Cell Anode Corrosion Test.

For example, an alloy F test is shown in Figure 1. The cell incurred a total of approximately 1766 h at 0.5 V operation and 1253 h at open-circuit voltage (OCV). Extensive OCV conditions are included as the cell conditions can be particularly aggressive for many alloys. After the first 1151 h of 0.5 V operation and 1068 h at OCV, the MEA was analyzed by XRF and found to contain calcium and only a trace of iron. More susceptible alloys will result in a more extensive array of metal ions and a higher degree of exchange. The calcium probably comes from the water despite the use of deionized water and the iron may have come from other carbon components in the fuel cell where we have detected iron in the past. However, the high frequency resistance (HFR) of the cell was relatively high possibly due to extensive passivation layers on the untreated alloy's surface. Passivation layers are less conductive than a clean metal surface and thus increase its resistance, but are beneficial in terms of promoting corrosion resistance.

To test this, the alloy was acid-etched to strip off any passivation layers and was put back into the fuel cell with a new MEA. The HFR lowered to a reasonable value suggesting that passivation layers were indeed the cause of the higher values previously obtained. The cell was operated for another 615 h at 0.5 V and 185 h at OCV before the MEA was analyzed and again found some calcium and only a trace of iron. Thus it appears that removing the passivation layers was not detrimental, the material is still corrosion resistant. Tests for a second alloy, "B", were performed for roughly similar durations. As with the "F" tests, the MEA contained calcium and a trace amount of iron. Though roughly comparable, the results of B are more promising because the alloy gave a very low HFR from the start making pretreatment unnecessary. In terms of bipolar plates, any treatment steps that can be eliminated result in lower costs.

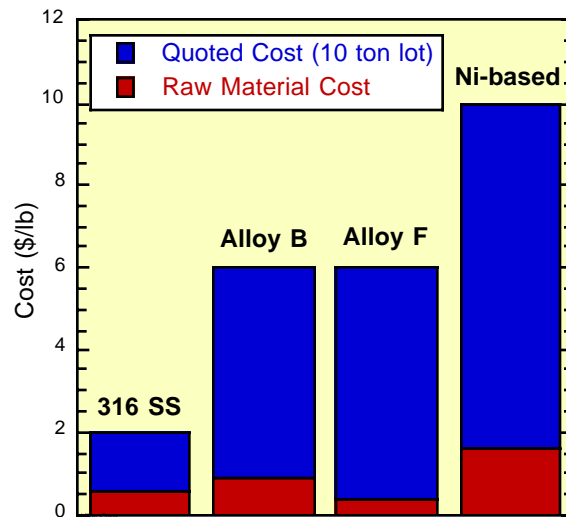


Figure 2 — Comparison of Raw Material and Quoted Costs for Various Alloys.

A natural concern is the cost of the more “noble” stainless steel type alloys. While some of these alloys may use several percent of relatively exotic elements, the primary factor affecting costs is typically demand. Shown in Figure 2 is a bar-chart comparing the costs of Alloys B and F with 316 SS and a generic Ni-based alloy. Also shown are the raw material costs calculated from recent market prices for the various constituent elements. The quoted costs for 10 ton lots of B and F are similar even though the raw material costs of one is more than twice the other. The single biggest factor affecting the raw material cost is the amount of nickel used, as demonstrated by the cost of the Ni-based alloy. Also illustrated is the high mark-up of these specialty alloys over the raw material cost compared to 316 SS. In short, alloys B and F should not be intrinsically any more expensive than 316 SS, but it will require large-scale production in order to get a price break on the alloying cost. Both are available in strip and plate form, however, alloy B is presently available in some foil thicknesses as well.

Due to these promising results cathode plates of each alloy will be tested. If cathode testing is successful, alloy B, which is available in a variety of forms and provides a low cell resistance without pretreatment is presently the favorite to utilize in future short stack testing. Stack testing of promising alloys is essential as success on the single-cell level does not necessarily promise success on the stack level, as possible shunt and/or stray currents can result in significantly more challenging environment. Future work will also include immersion testing of alternative untreated alloys that come from the same respective families as B and F, in case even more promising variations can be identified.

Composite Bipolar Plate Materials

Composite materials offer the potential advantages of lower cost, lower weight, and greater ease of manufacture than traditional graphite or coated metal plates. For instance, flow fields can be molded directly into these composites, thereby eliminating the costly and difficult machining step required for graphite. Most of the composites used in fuel cell bipolar plates have employed graphite powder in a thermoplastic matrix such as polyethylene, polypropylene, or, most commonly, poly(vinylidene fluoride) (PVDF). Unfortunately, PVDF is relatively expensive, and any thermoplastic composite must be cooled before its removal from a mold, resulting in long cycle times. On the other hand, thermosetting resins (e.g., phenolics, epoxies, polyesters, etc.) generally

offer shorter process cycle times than thermoplastics because, once cured, they become sufficiently rigid and can be removed from the mold while still hot. Furthermore, injection molding, or at least injection compression molding may be possible with the “wet” (albeit thixotropic) resin mix which would be very difficult if not impossible with the dry thermoplastic mixtures, which are probably limited to compression molding. In either case, cost-effective mass production would tend to be more readily achievable with thermosets rather than thermoplastics because of their shorter cycle times. With the proper combination of resin additives and temperature, a compression molded thermoset composite can cure in comfortably less than about two minutes, resulting in cycle times an order of magnitude less than those required for thermoplastics. One particular family of thermoset resins, vinyl esters, seems especially well-suited to bipolar plates (Busick and Wilson 1998). Vinyl esters are methacrylated epoxy difunctional polyesters, and as such are often described as a cross between polyester and epoxy resins. In addition to being noteworthy for their excellent corrosion resistance, vinyl esters are lightweight, strong, tough, and commercially available at surprisingly low cost. By capitalizing on these properties of vinyl ester resins, we have developed new material formulations for producing low-cost, high-performance, easy-to-manufacture composite bipolar plates.

The most widely used conductive filler for composite bipolar plates is graphite powder and it is employed in the vinyl ester composites described here as well, although early tests revealed that the choice of graphite powder influences the conductivity of molded parts. Thus, the relationship between filler loading and electrical conductivity appears to depend somewhat on graphite particle size and particle size distribution. We have identified a particular type of graphite powder with a fairly narrow particle size distribution that offers relatively high conductivity for a given volume fraction and is reasonably easy to combine with the liquid resin to form a homogeneous mixture.

Early development with Plug Power resulted in relatively crude but successful formulations that provided plates that were stronger and tougher than other commercially available composites and conceivably much less expensive due to the lower cost binder and the faster cycle times. Fuel cell testing at Plug Power provided results that were comparable to machined graphite in their hardware as reported here last year. Compounders, companies that specialize in formulating composite resin mixtures, Premix, Inc. and Bulk Molding Compounds, Inc. (BMC), refined and improved the formulations using their proprietary additives and expertises. Plug Power has subsequently obtained good stack results with plates molded to shape with compounds provided by these companies. Our primary role became characterizing the properties of the molded plates (conductivity, corrosion-tolerance and mechanical properties) to assist the compounders in optimizing their formulations. Since, Premix and BMC have sampled or sold products to a number of potential customers. Consequently, our role is diminishing and will probably cease altogether with the exception of legacy issues such as intellectual property, etc.

Over this past year, the major issue addressed was the effect of exposure testing under aggressive conditions on the mechanical properties of the composites. The primary concern is that although the “ester” in vinyl ester is not a component of the polymer backbone, it will conceivably hydrolyze nonetheless (a weakness with polyesters under such conditions) with unknown consequences on the durability of the plates. Naturally, the hydrolysis rate depends upon the presence of water. As such, some samples were immersed in 1 or 6 M methanol not only to improve wetting of the plate and hence exacerbate the hydrolysis problem, but also to gauge the suitability for the composites for direct methanol fuel cells (DMFCs) should a market-viable product ever be developed. As such, flat-molded plaques (nominally 0.1 in. thick) of promising bipolar plate materials were provided by Premix, Inc. for the exposure testing. Material 1 contained 75% graphite powder in a proprietary formulation of the thermosetting resin and various additives. Material 2 contained 65% graphite powder in a resin formulation identical to that of Material 1. Material 3 contained 75% graphite in a resin that is a possible alternative to the “preferred” resin used in Material 1 and Material 2. After the electrical conductivities of the materials were measured,

rectangular mechanical test coupons were cut from the plaques. Six coupons of each material were immersed in each of five different liquids for 1000 hours at 80°C. These liquids (water, 1M and 6M methanol, and pH 2 and pH 6 sulfuric acid) ranged from expected to unduly aggressive environments for hydrogen or direct methanol fuel cells. Small squares of Nafion 112 membranes were immersed with the samples; following the 1000-hour exposure period, the membranes were analyzed using x-ray fluorescence spectroscopy to identify any ionic leachant species. All of the exposed mechanical test coupons, plus six unexposed coupons, were tested for flexural strength according to ASTM D638.

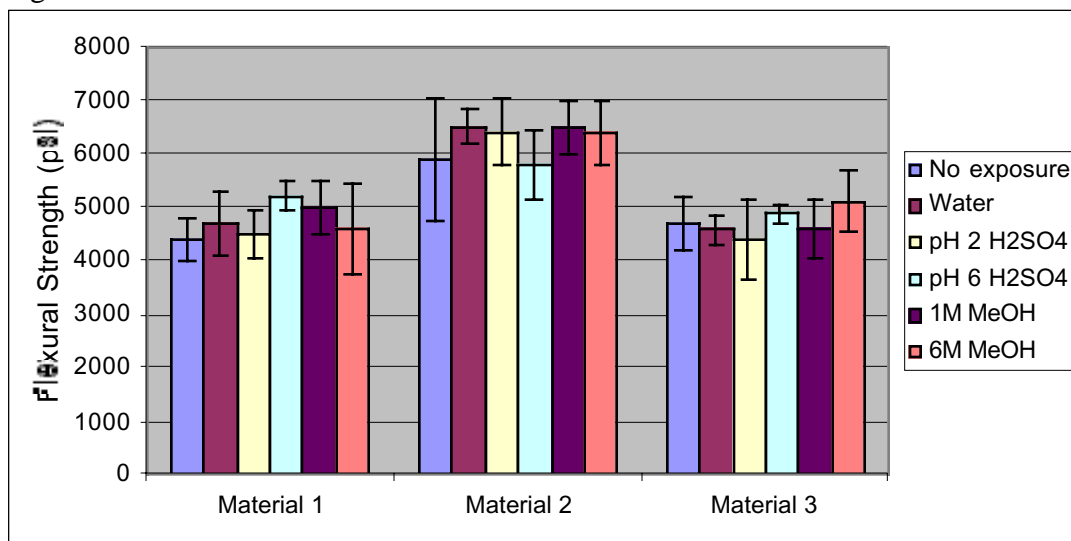


Figure 3 — Flexural Strengths of Test Samples after Aggressive Immersion Testing.

The XRF analysis of the Nafion membranes immersed with the composite samples indicated the presence of calcium. This was to be expected, since previous immersion tests conducted by both LANL and Premix revealed similar results. Calcium is present in the ash component of the graphite powder, and is able to leach out of finished plates when they are immersed in liquid. When the test liquid is not circulated or changed, noticeable amounts of calcium can accumulate. However, in an operating fuel cell with the liquid continuously flushed, calcium does not appear to be any greater of a problem than with machined graphite plates.

The results of the flexural strength tests are shown in Figure 3. There is a significant difference in strength between Material 1 and Material 2. This difference was expected, since the materials contain the same resin binder but different relative amounts of resin and graphite. With its lower graphite content, Material 2 is stronger than Material 1 since most of the strength of a particulate composite is derived from the resin binder. However, the lower graphite content of Material 2 also lowers its electrical conductivity to a level that is currently considered "borderline acceptable" for bipolar plates. Based on a comparison between Material 1 and Material 3, the preferred and alternative resins are equivalent in terms of flexural strength imparted to the bipolar plate. It is important to note that the test coupons were cut from molded plaques, not directly molded to shape. This introduces edge roughness effects in the 3-point bending test. The flexural strength of an uncut, molded-to-shape plate is anticipated to be 10-20% higher than the values shown in Figure 3.

A prime motivator for investigating various alternatives to the "preferred" resin binder was the potential susceptibility of the resin to chemical attack, especially when facilitated by methanol. However, for each material, the flexural strengths of the exposed samples are at least equivalent to the strength of unexposed samples, within experimental scatter. Thus, the most important and encouraging result of this study is that the strengths of the various materials investigated are

unaffected by exposure to various conditions including those much more aggressive than a fuel cell environment. Clearly, any chemical attack or hydrolysis that may be occurring is not affecting the structural component of the matrix.

CO Tolerant Anodes

The majority of home-based stationary power systems will need to be designed for operation on natural gas, primarily due to its extensive distribution network. The simplest home-based units will use near-ambient pressure steam reforming to avoid the requirement of pressurizing the feedstock when converting the natural gas to a hydrogen rich fuel stream. The thermodynamic reaction equilibrium at the high temperature steam reforming (e.g., 700°C) yields a roughly 10% concentration of CO by-product. As a result, the reformat is relayed through high and low temperature (HT and LT) water-gas shift reactors to further lower the CO concentration. Since even 0.1 % CO (1000 ppm) is easily enough to thoroughly poison the fuel cell anode, the effluent from the LT shift reactor is sent to a preferential oxidation (PROX) reactor. Here, the CO is selectively oxidized using oxygen from injected air to lower the CO to a level that can ideally be tolerated by the fuel cell. Unfortunately, it is difficult to assure sufficiently low CO levels so air bleeding into the fuel cell stack anode inlet is used to increase the anode tolerance. Another means of increasing CO tolerance is merely by increasing cell temperature, which lowers the CO sticking coefficient. However, it is not possible to increase the operating temperatures much over the standard 80°C with near-ambient pressures. In any case, the amount of bleed air required to recover performance as well as the upper level CO tolerance of the anode is strongly dependent upon the anode design and catalysts.

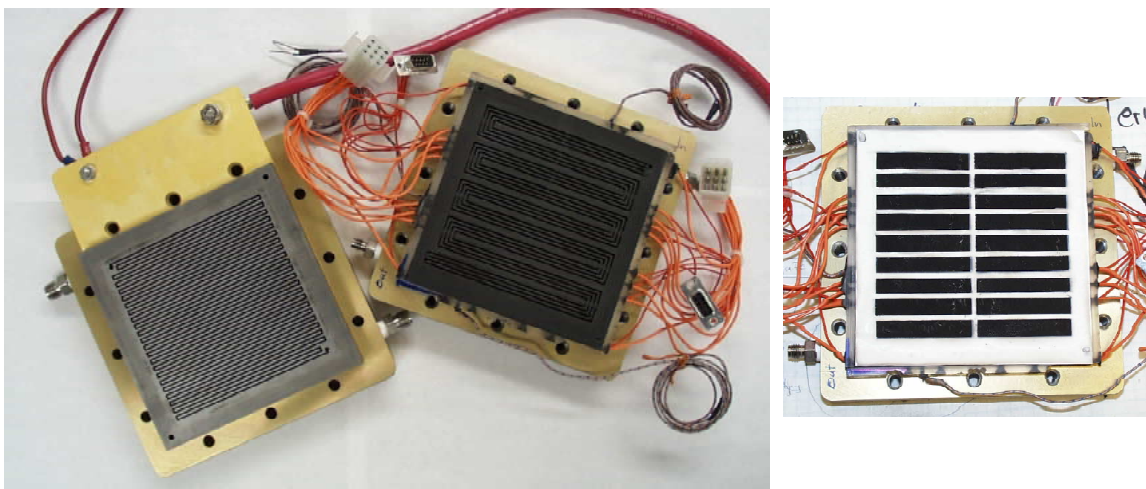


Figure 4 — 100 cm² Segmented Cell Hardware and a Segregated MEA

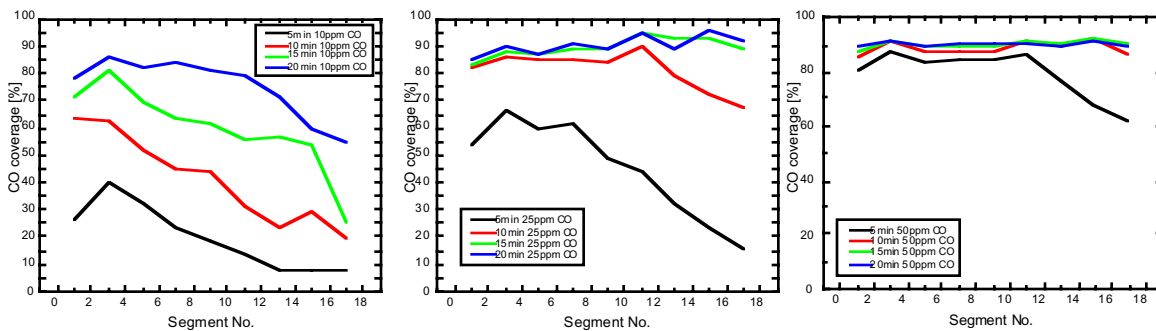


Figure 5 — CO Coverages Along the Anode Flow-Field as Functions of Time and Concentration

At Los Alamos, we previously developed a "reconfigured anode" (RCA) for pressurized transportation applications that demonstrated substantially increased anode tolerance compared to conventional anodes. Last year, we showed results for ambient pressure attained in a LANL 50 cm² single cell at Plug Power which surprisingly showed very modest losses compared to a neat hydrogen stream. Unfortunately, as is so often the case, it has not been possible to replicate the small cell results on larger single cells or in stacks with either ambient or pressurized anode operation. Characterizing the dynamics of the CO poisoning and the RCA within the cell is consequently important in order to understand the link between the small and the larger cells and stacks. The most straightforward method of elucidating the various mechanisms as the reactant progresses through the cell is possibly to use a "segmented" fuel cell. In such a cell, one of the flow-field plates of a conventional 100 cm² single-cell is sectioned into numerous small, electrically isolated sections to provide numerous small individual fuel cells within the same flow-field plate. It is consequently possible to map the performance over the active area and "follow" the effects of CO poisoning as the reactant gasses pass through the flow-field. The segmented cell used over the past year is shown in Figures 4a and b. Unfortunately, various difficulties with the design and electronics allow the segments to cross-talk an undue amount at higher current densities, so the most useful experiments are to perform voltammograms on each segment to effectively "titrate" the CO adsorbed on each segment as a function of time and CO concentration. The series of graphs in Figure 5 qualitatively portrays one such family of curves on a conventional (non-RCA) anode. Not surprisingly, at lower CO concentrations the upstream segments shield the downstream to a large degree but are quickly overwhelmed at the higher concentrations. On the other hand, the amount of CO gettered appears to be greater than attributable to the active area, which may not be a real effect due to the cross-talk and other problems with the experimental set-up. Consequently, a new segmented cell is being designed and fabricated to hopefully perform better and provide additional features, such as gas sample taps and thermocouples at each element. The segmented cell approach is of interest not only to characterize CO poisoning but to also generically understand the effects of various operating conditions (e.g., humidity levels and temperatures) and configurations (e.g., counter- vs. co- vs. cross-flow) and flow-field designs (and their effects on CO tolerance).

Adiabatic Stack Operation Scheme

Near ambient pressure operation is of interest for the air or cathode side for much the same reason as the anode side, that is, to minimize parasitic power losses and lower the component costs. If pressures can be kept low, a blower can be used to provide the air flow through the fuel cell. While not particularly efficient, a blower is obviously much less expensive than a turbine or positive displacement compressor, and with very low pressures, the PV work required is minimal and the

device efficiency is not particularly critical. Since the cathode kinetics are roughly first order with respect to oxygen partial pressure, the stack power densities are not as high as with the pressurized cells. However, we demonstrate below that once the parasitic losses are taken into account, the net power densities are not very different. A number of issues arise with very low-pressure operation. Low-pressure operation often results in drier operating conditions due to both lower current densities (less water produced) and the higher water vapor volume fractions (more water removed with the air effluent compared to pressurized). As such, the effectiveness of the membrane hydration scheme becomes more significant at the lower pressures. The technique for direct liquid water hydration of the membranes that we use (Wilson 1999) appears to have advantages over the classical means of cell hydration, namely, reactant humidification. Avoiding reactant humidification also eliminates the pressure drop required to force the reactant air through the humidification module, which further decreases the parasitic power requirements. A consequence of introducing ambient temperature air into the humid environment provided by the direct liquid water hydration is that the stack is readily evaporatively cooled. Cooling plates, coolant and radiators, etc., are then eliminated which further simplifies the system. Since the airstream heats up substantially as it passes through the stack, a temperature gradient is established from inlet to exit sides. In contrast to typical “isothermal” stack designs, this temperature increase is encouraged in order to avoid condensation and the two-phase flow pressure drop problem. For such reasons, this approach is described as “adiabatic” operation. This past year, we have demonstrated the utility of the adiabatic approach on a roughly 1.5 kW level. The system was operated with less than 2% parasitic power and full water self-sufficiency at a 56% overall system efficiency and 350 W/L net power density.

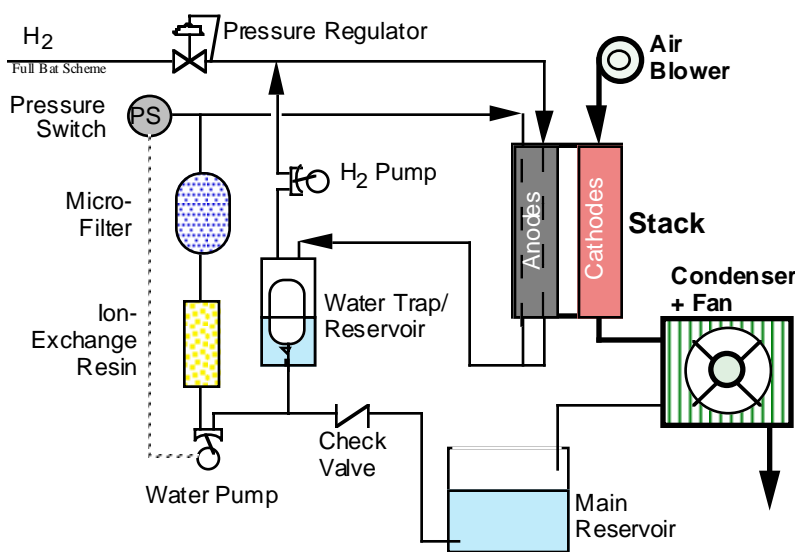


Figure 6 — Schematic of the Adiabatic Stack System

Over the past year, the adiabatic stack system was also further simplified. A current schematic of the roughly 1.5 kW system is depicted in Figure 6. Water recirculation through the stack (for the direct liquid hydration) and make-up from the ambient-pressure main water reservoir are now accomplished using a single water pump in conjunction with a pressure switch and float valve. With this scheme, a second pump, liquid level sensor and motor controller are eliminated or replaced by lower-cost and non-powered components.

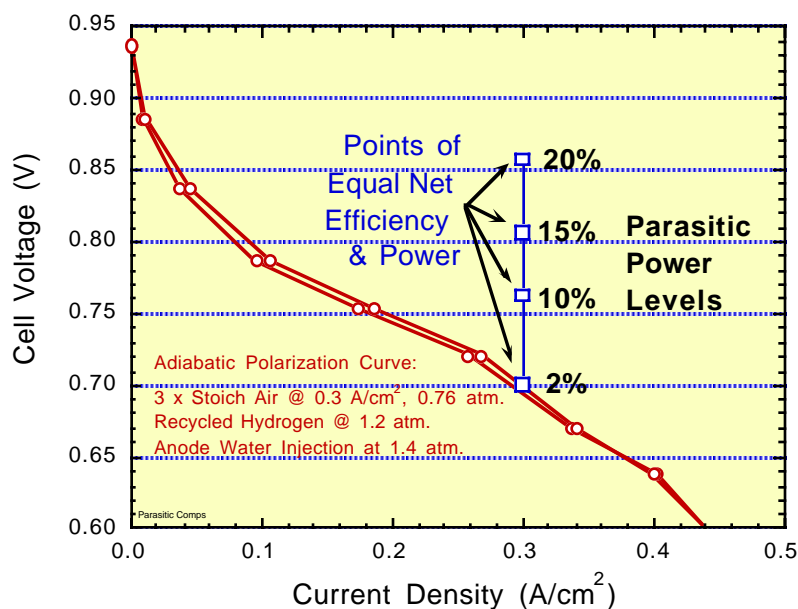


Figure 7 - Polarization Curve Illustrating the Effect of Parasitic Power on Net Efficiency and Power

The less than 2% parasitic power level is of critical importance to allow the modest performance of the adiabatic stack to compete favorably with higher pressure fuel cell stacks in terms of net power density and efficiency. The parasitic power significance is illustrated in Figure 7. Here, a polarization curve depicting the rather modest performance of the adiabatic stack is depicted. However, for a higher parasitic power (e.g., pressurized) system to match the net efficiency of the adiabatic stack, it must operate at a higher cell voltage. For example, if a competing system has a 15% parasitic power level (quite optimistic for a 30 psig stack, reasonable for a 2 – 3 psi stack with no PV recovery), then it must operate at about 0.81 V/cell to attain the same net efficiency. The unit cells in the competing stack will actually need to be thinner to achieve the same net power density, because the stack must also accommodate cooling plates, etc.

Conclusions

Commercialization of home-based stationary power PEM fuel cells will require reliable and inexpensive components and systems. Consequently, a common theme uniting the various tasks and efforts in this program is that they are all oriented towards overall system simplicity, with the belief that ultimately the long term commercial viability of fuel cell systems will depend upon their simplicity (and hence cost and reliability). Major steps to realizing these criteria can be achieved with the development of low-cost and reliable bipolar plates, stable and effective CO tolerant anodes, and highly efficient and simple fuel cell systems. Clear progress has been made this past year in meeting these objectives, particularly with the commercial attention enjoyed by the composite bipolar plate approach and the low parasitic power system demonstration of the adiabatic stack. While not quite as fast paced as the above tasks, we are developing the fundamental underpinnings for future advances in the more challenging metal alloy bipolar plate and CO tolerant anode tasks.

Future Work

If upon further testing promising cathode results are obtained in the single cell tests with Alloys B or F, the next step in the metal alloy bipolar plate effort will be to procure foils appropriate for the fabrication of an internally manifolded short stack. This step is necessary to definitively demonstrate the viability of uncoated metal alloy fuel cell hardware because of the additional corrosion challenges that a stack presents such as stray and shunt currents. Because the technology is now basically in commercial hands, the composite bipolar plate component of the project is winding down, although the work involved with the other tasks more than make up for the amount of resources made available. The work on CO tolerant anodes based on the LANL reconfigured anode approach will enter a more fundamental phase of understanding in order to better design and optimize anodes for larger cells and stacks. The segmented cell will be instrumental in characterizing the poisoning and mitigation processes. While the reconfigured anode CO mitigation strategies have improved tolerance substantially, the overall system is remarkably complex merely to supply low CO levels. Entirely new CO tolerant anode approaches are needed and will be considered. Cost will always be a critical issue even though the net performance levels of the adiabatic stack system compare favorably with more complex systems developed elsewhere, so we would like to increase the power produced per cell at the 0.7 V/cell level. We anticipate that we may be able to increase the current density (i.e., power) about 50% using new flow-field and gas-diffusion structures (plus some additional improvements), which obviously decreases costs/kW substantially. While the system is already quite simple, the next step to work on in further simplifying the system is to eliminate the hydrogen recirculation pump. This is necessary to flush condensate from the anode side, but judiciously altering the anode water supply scheme may alleviate the condensation difficulties.

References

Busick, D. N. and M. S. Wilson, 1998. "Composite Bipolar Plates for Fuel Cells," In *Proton Conducting Membrane Fuel Cells II, Vol. 98-27*, 435-445, Boston, MA: The Electrochemical Society.

Wilson, M. S., 1999. "Fuel Cell Membrane Humidification," *U.S. Patent No. 5,952,119*.

Wilson, M. S. and C. Zawodzinski, 1998. "Fuel Cell with Metal Screen Flow-Field," *U.S. Patent No. 5,798,187*.

Wilson, M. S. and C. Zawodzinski, 2000 "Fuel Cell with Metal Screen Flow-Field," *U.S. Patent No. 6,037,072*.

Zawodzinski, C., M. S. Wilson and S. Gottesfeld, 1998. "Metal Screen and Foil Hardware for Polymer Electrolyte Fuel Cells," In *Proton Conducting Membrane Fuel Cells II, Vol. 98-27*, 446-456, Boston, MA: The Electrochemical Society.

LOW COST REVERSIBLE FUEL CELL SYSTEM

Dr. Robert C. Ruhl
Vice President, Technology
Technology Management Inc.
4440 Warrensville Center Road
Cleveland, Ohio 44128

June 15, 2000

Contract No. DE-FC36-99GO10455
DOE Golden Field Office
POC: Doug Hooker

Abstract

TMI has studied a reversible solid-oxide fuel cell/electrolyzer system which would be capable of storing electrical energy generated from renewable sources at projected round-trip efficiencies over 80% and also of providing backup power generated from propane at lower heating value efficiencies over 60%. The systems would utilize a single set of stacks for all electrochemical functions together with a unique system design which stores both gases and thermal energy. The total system capital and operating costs are projected to be lower than comparable lead-acid battery plus backup generator systems.

Summary

1.1 Problem Statement

Grid-independent electric power systems based upon renewable power sources (chiefly solar, wind, and water) offer the promise of drastically reducing CO₂ emissions as well as offering unmatched siting flexibility and other advantages. However, the installed cost of complete, practical systems of this type is currently very high. Due to the intermittent and variable nature of renewable generation, such systems must have both a large energy storage capacity and backup generation for use when energy storage becomes depleted. The storage must be highly efficient in order to minimize renewable capacity needed. Currently, the only practical choice for these systems is deep-cycle lead acid batteries for storage plus an engine-generator for backup. Although these batteries can achieve high energy storage efficiencies near 80%, the battery/generator combination is quite expensive (first cost plus maintenance costs). Additionally, currently available generators are highly polluting, noisy, and have low fuel efficiencies (usually averaging below 30% lower heating value).

Based upon public literature, systems using Proton Exchange Membrane (PEM) fuel cell and electrolyzer technology are inherently incapable of achieving competitive energy storage efficiencies: known systems require electrolysis voltages which are far above their fuel cell voltages.

1.2 Proposed New Systems

Technology Management Inc. (TMI) has performed conceptual designs and simulations on a new low cost, reversible solid-oxide fuel cell/electrolyzer system which would use hydrogen and oxygen for energy storage and would also incorporate highly efficient backup power generation from propane and ambient air. A single solid oxide cells subassembly (which includes electrochemical stacks, heat exchange, fuel reformer, etc.) would be designed to operate in three (3) different modes:

1. Electrolysis mode (electrical energy to H₂ and O₂)
2. H₂/O₂ fuel cell mode (power from stored gases)
3. Propane/air fuel cell mode (power from propane and air)

The hydrogen and oxygen would be stored as gases at near-ambient temperature. Predicted energy storage efficiency (electrical energy out/electrical energy in) is near 80% (similar to lead acid batteries). Predicted propane efficiency is near 60% LHV, with negligible air pollutant emissions.

The system design utilizes multiple independent complete system modules for superior reliability. Thermal energy storage devices built into each module would provide a

delayed transfer of excess thermal energy generated as a product of fuel cell mode operation to supply the required thermal input during electrolysis mode. Projected initial and maintenance costs of these systems are significantly below existing options.

2. Introduction

TMI has studied possible system and subsystem options for small, grid-independent electric power generating systems. Three classes of options were investigated: those using available existing equipment, those using the planned TMI fuel cell systems for fossil fuels, and those using potential TMI systems having reversible fuel cells.

Grid-independent systems are viable markets because of one or more of the following reasons:

Grid power is unavailable

The cost of extending grid power to the site is too expensive

Grid power has unacceptable reliability (too many power outages)

Avoidance of unsightly and potentially dangerous overhead lines

Grid power quality is unacceptable

Traditional utilities cause considerable pollution

Antipathy towards the local utility company

Costly additional equipment is required by the utility for interconnection

A large number of existing grid-independent systems in this size range employ both a renewable power source (usually solar photovoltaic, wind turbine, or water turbine) and an engine-generator.

2.1 Example Requirements Summary

The example application used in this study is based upon a hypothetical remotely sited residence of 2500 square feet located near Boulder, Colorado. The power requirement is limited to 120 volts AC, 60 Hertz, single phase. Good power quality is needed (true sine wave with low total harmonic distortion, good voltage and frequency regulation) for computers, home entertainment, noise minimization, and other reasons. A high degree of reliability is also needed (system outages being very infrequent and brief). The residence is assumed to use propane fuel for all significant heating needs: space heating, cooking, hot water, and clothes drier. It has no air conditioning, but does use cooling fans (and possibly evaporative coolers) and many other types of small kitchen and household

appliances. The maximum instantaneous peak AC demand (to handle motor starting, etc.) is 3000 Watts and 4000 Volt-Amperes (VA).

The assumed average daily AC net power usage (averaged over 365 days) is 15,360 Watt-hours/24 hr (an average of 640 Watts and a total of 5606 kWh/year). This average usage is about 85% of the assumed worst case day. If 640 Watts is divided by the specified system peak capacity of 3000 Watts, the annual load factor of 21.3% is obtained. This value is typical for residences without air conditioning.

The assumed average cost of propane fuel is \$1.00 per gallon delivered, including tank rental charges for propane (also called liquefied petroleum gas or LPG). Its lower heating value (LHV) is assumed to be 84,300 BTU/gallon thereby giving a cost of \$11.86 per million BTU. Diesel fuel is assumed to cost \$1.50 per gallon delivered with a LHV of 128,000 BTU/gal.

2.2 Technical Background Notes

Solid Oxide Fuel and Electrolysis Cells

Solid oxide fuel cells and electrolysis cells are electrochemical devices consisting of an impervious oxide-ion conducting solid oxide electrolyte, two porous electrodes (which perform charge transfer between electrons and oxygen ions), an electronically conductive impervious cell separator, and seals to confine the fuel and oxidizing gases to desired regions of the cell. In fuel cell mode, electric power is generated from a fuel gas (e.g. an H₂/H₂O mixture) and an oxidizing gas (normally air or oxygen). In typical electrolysis mode, steam is decomposed into hydrogen and oxygen, which are collected separately.

Design Philosophy

Energy balances for reversible systems must consider thermal, electrical, and chemical energies. Thermal energy can spontaneously flow only from higher to lower temperature. High efficiency reversible systems require that electrochemical and thermal processes are performed under conditions as close to equilibrium as practical. Prior experimental work at TMI has demonstrated electrochemical H₂/O₂/H₂O cells operating with only small differences between their electrolysis and fuel cell voltages.

3. Proposed Reversible Solid-Oxide System

The proposed reversible system for the above example requirements would provide both energy storage (using H₂ and O₂) and backup generation from propane fuel. They would utilize two (2) identical reversible fuel cell/electrolyzer modules having the following preliminary specifications.

Table 1. Reversible Fuel Cell/Electrolyzer Module Specifications

| Parameter | Value | Units |
|-----------------------------------|---------|-----------|
| Nominal Output Power | 1000 | Watts |
| Maximum Surge Power | 4800 | VA |
| Nominal Energy Storage | 6500 | Wh |
| Output AC Voltage (60 Hz) | 120 | Volts rms |
| Typical Net Propane Efficiency | 62% | LHV |
| Typical Energy Storage Efficiency | 81% | Wh |
| Noise @ 1 meter | < 50 | dbA |
| Retail Price (est. 2009) | \$3400. | |
| Average Annual Maintenance | \$170. | |

Each module would contain the following components:

1. A triple-purpose solid-oxide stack, capable of operating in three (3) different modes:
 - Electrolysis mode for energy storage,
 - H₂/O₂ mode for recovering stored energy, and
 - Propane/air mode for supplemental generation
2. A hydrogen and oxygen gas storage system
3. A liquid water storage system
4. A multifunction power conditioning circuit
5. A small lead-acid battery for instantaneous load following
6. Required balance of system components, including compact heat exchangers, pump, blowers, valves, insulation, startup heater, control system, sensors, enclosure, etc.

Two modules would be connected as shown in Figure 1 below.

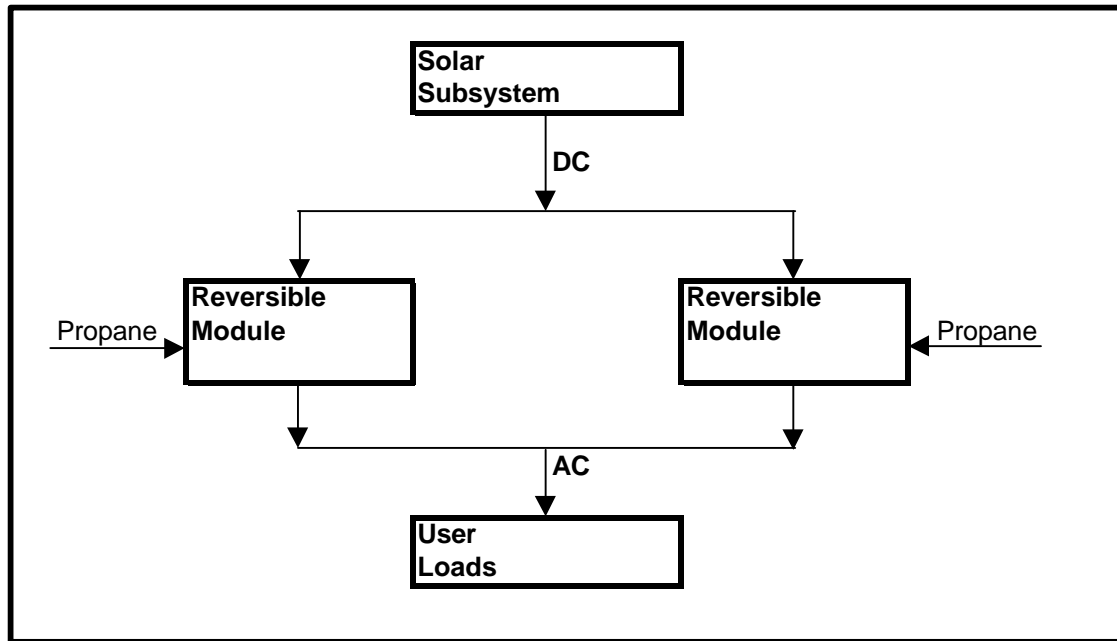


Figure 1: Connection of Two Reversible Modules

In the event of an outage of one module, the remaining module would supply the full user loads (at reduced efficiency).

4. Comparisons

The following table compares seven (7) cases analyzed in detail (using estimated 2009 selling prices for the new-technology systems). The installed costs in the table were computed using the specified system peak power requirement of 3.0 kW and are rounded to the nearest \$100. The fuel cell systems in Cases D and E are the TMI high-efficiency type (these have no reversible storage capability). The fuel cell systems in Cases F and G are the previously described reversible type. Cases D through G each use two fuel cell modules. The percent solar power row refers to the share of user power requirements generated by solar. System comparisons using wind turbines would have different numbers, but similar relative positioning.

Table 2. Systems Comparison

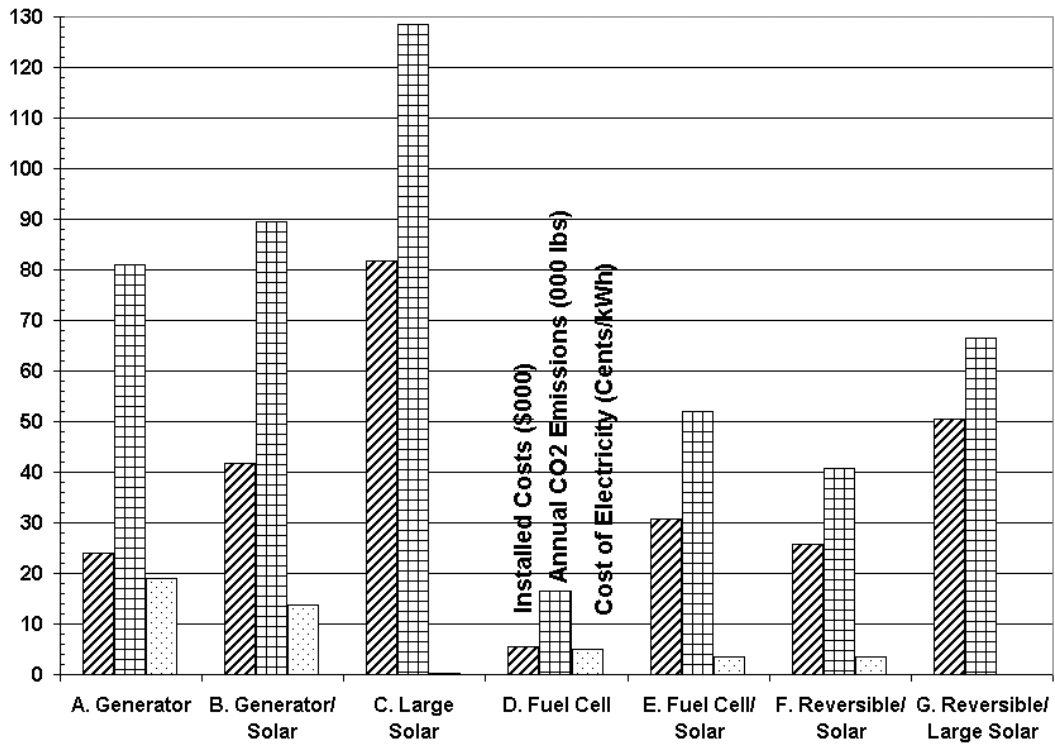
| Case | A | B | C | D | E | F | G |
|-------------------------------|----------------|----------------|---------------|-------------------|-------------------|-------------------|-------------------|
| Percent Solar Power | 0 | 33 | 99 | 0 | 33 | 33 | 99 |
| Primary Generation | propane engine | propane engine | none | propane fuel cell | propane fuel cell | propane fuel cell | none |
| Backup Generation | diesel engine | diesel engine | diesel engine | propane fuel cell | propane fuel cell | propane fuel cell | propane fuel cell |
| Primary Storage | lead-acid | lead-acid | lead-acid | lead-acid | lead-acid | hydrogen | hydrogen |
| Pollution | highest | high | low | ~ 0 | ~ 0 | ~ 0 | ~ 0 |
| Noise | highest | high | low | very low | very low | very low | very low |
| Installed Cost per kW | \$ 8,000 | 13,900 | 27,300 | 1,800 | 10,300 | 8,600 | 16,800 |
| Fuel, c/kWh | 26.9 | 19.3 | 0.2 | 7.1 | 5.1 | 4.9 | 0.1 |
| Maintenance, c/kWh | 32.9 | 33.0 | 55.5 | 4.6 | 19.6 | 12.9 | 21.5 |
| Cost of Electricity, c/kWh | 81.1 | 89.5 | 128.6 | 16.6 | 52.1 | 40.7 | 66.6 |
| Annual CO ₂ , tons | 9.5 | 6.9 | 0.07 | 2.5 | 1.8 | 1.7 | 0.021 |

System D (TMI high efficiency fuel cell) has the lowest installed cost and the lowest cost of electricity. Systems F and G (using the TMI reversible fuel cell stacks) have the lowest installed cost for their respective solar capacities.

The reduction in CO₂ by using System G (reversible) instead of D (non-reversible) costs about \$1000. per ton of CO₂ eliminated: a very high figure. By comparison, if System D were to be substituted for grid power made from coal, it would cost only about \$100. per ton of CO₂ eliminated (in an application of this size).

Although the example application used in this report is based upon a good-sized residence, most of the considerations cited would also apply to smaller and larger systems having average power requirements anywhere from about 500 to at least 5000 Watts. The new technologies recommended would be applicable for both new installations and upgrades of existing systems. The following figure compares key values from Table 2.

Figure 2. Systems Comparison



5. Other Possibilities

The proposed new energy storage/fuel cell systems could also be used with wind or water power as the renewable source. The storage capacities for hydrogen, oxygen, and heat could be varied to match application needs.

Wherever natural gas is available, its typical cost is considerably lower than propane, leading to lower cost of electricity in fossil fuel mode.

6. Conclusions and Recommendations

The TMI reversible solid-oxide system is environmentally and economically attractive for renewable applications having various renewable capacities

TMI high efficiency fuel cell systems offer low predicted costs and could be a transitional technology en route to renewable-based systems

A proposal for a follow-on development program is being prepared (see below)

Commercial introduction of the proposed systems could be possible as early as 2005.

A detailed report on the present study is now in preparation.

7. Proposal for Follow-On Development Program

The proposed high-efficiency fuel cell and reversible fuel cell/electrolyzer 1 kW modules and systems will require a technology development program to extend existing TMI technology and design concepts into a working hardware demonstration. The key questions about technical feasibility (proof of concept) can be answered by this program.

A draft proposal for the follow-on program will be available soon.

8. Acknowledgements

TMI would like to acknowledge the Department of Energy, NREL , Golden Field Office for their support during the first Phase of this project.

List of Tables

Table 1. Reversible Fuel Cell/Electrolyzer Module Specifications

Table 2. Systems Comparison

List of Figures

Figure 1: Connection of Two or More Modules

Figure 2. Systems Comparison

GALLIUM NITRIDE INTEGRATED GAS/TEMPERATURE SENSORS FOR FUEL CELL SYSTEM MONITORING FOR HYDROGEN AND CARBON MONOXIDE

**Stephen C. Pyke, PhD
Peterson Ridge, LLC
P.O. Box 1257
Sisters, OR 97759**

**Jehn-Huar Chern, R. Jennifer Hwu and Laurence P Sadwick
University of Utah Electrical Engineering Department
50 S Central Campus Dr. Room 3280
Salt Lake City, UT 84112-9206**

Abstract

High-temperature electrical performance of thermally stable GaN-based MESFETs and MODFET sensors is presented. Data on Ti/Al ohmic contacts, with Cr(TiWN)/Au protection layers, to n-type GaN and $\text{Al}_{0.3}\text{Ga}_{0.7}\text{N}$ grown by MBE is presented. Preliminary data is also presented on the current-voltage and capacitance-voltage characteristics of the gas sensing structure (Schottky contacts to both n-type GaN and $\text{Al}_{0.3}\text{Ga}_{0.7}\text{N}$). Electrical performance was measured from room temperature to 400°C.

Introduction

Need for Gas Sensors for Fuel Composition in Fuel Cell Systems

The electrodes in solid polymer electrolyte fuel cell systems require hydrogen fuel free from carbon monoxide (CO), otherwise the platinum electrodes are poisoned and fuel efficiency is degraded. Steam reforming of hydrocarbon fuels produces a mix of hydrogen, carbon dioxide and enough by-product CO to poison the electrodes. Preferential oxidation (PROX) of CO to reduce this contaminant is accomplished over a noble metal catalyst typically platinum by adding oxygen to the hydrogen fuel upstream of the PROX catalyst (Mann, et al 1993 and Krumpelt 1999). An inexpensive monitor to confirm the PROX catalyst efficiency and ultimately control the PROX system conditions is useful if not necessary to avoid the risk that PROX catalyst degradation could lead to reduced fuel efficiency or failure of the fuel cell due to contaminated hydrogen. Since the environment for a PROX monitor is rich in hydrogen, the problem is developing a sensor that can monitor carbon monoxide at high temperature without the sensor output being dominated by hydrogen or temperature. This proposal will cover preliminary research to prove this concept by fabricating and testing prototype sensors. The requirements for a prototype sensor include: successful high temperature operation (ca 100-400 C) and the resolution of CO (ca. 2-200 ppm) in the presence of hydrogen (ca 35-75% vol), oxygen, hydrocarbons and water vapor. Monitoring the concentration of hydrocarbons and reactive sulfur (H₂S) may also important in some systems (DOE 1999).

Science and Technology

We are exploring an approach combining the advantages of the sensing capabilities of the catalytic metal gate with a wide bandgap GaN semiconductor metal semiconductor field effect transistor (MESFET) and modulation doped field effect transistor (MODFET) transducers for high temperature measurement of carbon monoxide in hydrogen. The choice of the catalytic metals for the device is based on the metals used in FET detectors for lower temperature applications and based on data for metals used in the three-way automobile catalytic converter: platinum, palladium/silver and rhodium. The reasons for three different metals and the sensor architecture and materials is discussed later in the introduction.

GaN high temperature electronics background

GaN based devices and circuits have the potential to operate at 600°C or higher temperatures owing to the wide band gap (e.g. ~ 3.4 eV). The interface between the semiconductor and the first metallization layer is the most important for it controls the transport mechanism(s) in solid state devices. In a FET low resistance (ohmic) contacts are made for the source and drain regions. The FET is a switch, and current flows through these contacts when the switch is “turned on” (Sze 1983). The voltage applied to the gate metal in a MESFET or MODFET determines whether the switch is on or off. A large electrical impedance is typically sought for the gate contact as it is important that little or no current flows through the gate electrode. For GaN and other highly ionic semiconductors, evidence has suggested that electrical transport properties of metal to Group III-nitride contacts strongly depends on the difference between the work function of the metal and the electron affinity of the semiconductor (Sze 1983). In a GaN

MESFET or MODFET with metal contacting the semiconductor directly, the so called Schottky barrier is the electric field produced by the difference between the work function of the metal gate and the electron affinity of the semiconductor and any chemical interaction of the metal with the semiconductor that can change the resistivity of the material. Theory suggests that metals with lower work functions form ohmic contacts on n-GaN. In fact, Ti, Al, and Cr are common metals for ohmic contact to n-GaN. Similarly, metals with higher work function, such as Pt, Rh and PdAg are expected to form high impedance gate Schottky contacts to n-GaN.

As with other semiconductor systems, especially compound semiconductor systems, the formation of an alloyed semiconductor/contact is usually the most straightforward method to achieve ohmic behavior. This is most certainly true for other group III-V semiconductors such as the well-studied and characterized GaAs semiconductor (Chern 2000). Almost all known, successful contacts to III-V semiconductors consist of bi-level to multi-level metallization schemes. Usually, chemical or thermal reactions, solid-state diffusion and interdiffusion, and/or other methods produce an alloy and possibly material damage that reduces the resistivity of the semiconductor and concomitantly the penetration depth of the barrier electric field region under the first metal layer.

Gate Metal Adhesion and Barrier metals

The adhesion of catalytic noble metals to GaN is typically improved with a metal or nitride intermediate layer, because the noble nature of the catalytic gate metals reduces the reactivity toward other materials and the strength of bonds otherwise made strong by alloying, compound formation, or intermetallic oxides or nitrides. The stresses inherent in the sputter deposited metal films often results in the noble metals lifting off the substrate. Temperature coefficients of expansion mismatch between the metal films and substrate exacerbate this problem, and mechanical reliability is an important consideration. Tungsten or titanium nitride or tantalum nitride are potential adhesion layers that also help prevent contamination and sensor drift caused by interdiffusion of the substrate components and metal films. Phase diagrams for the nine combinations of Pt, PdAg and Rh with TiWN, TiN and TaN are lacking. A priori calculations by (Niessen 1983) suggest a small enthalpic driving force for solvation of W and Ta by platinum and palladium but a zero or slightly positive enthalpy for solvation by rhodium. The enthalpic driving force for Ti solvation by any of these metals is expected to be smaller because of the size mismatch compared to W and Ta. The fact that Ta, W and Ti are nitrides further reduces the driving force for solid solutions and interdiffusion with the overlying catalytic metal layer, but the driving force for interdiffusion of TaN, WN and TiN with GaN is not well known.

Catalytic gate FET sensor background

The development of gas sensing and analysis using the well-known effect on surface potential of gas adsorption on a metal surface has been extensively explored using chemically sensitive semiconductor devices (Lundstrom 1989). Recent work on field effect devices using catalytic metal gates on silicon carbide substrates has been reviewed (Lundstrom 1996) and suggests the promising application of the field effect technology for monitoring the composition of automobile emissions and the efficiency of the catalytic converter.

The field effect technology using catalytic metal electrodes on a semiconductor exploits dissociative chemisorption on the surface. The effect of hydrogen was reported (Lundstrom 1975) on a palladium gate FET on silicon. Other work (Poteat 1983) demonstrated sensitivity to ethylene and carbon monoxide hydrogen sulfide, propylene oxide, ethylene, formic acid, carbon monoxide and NO₂. More recently, hydrogen, carbon monoxide, ethylene and acetylene effects have been observed on metal-insulator-semiconductor (MIS) diodes with electrodes of pure platinum and platinum and palladium compositions with small amounts (ca. 5-10%) of transition metals such as copper (Feinstein 1998 and Pyke 1993). These electrodes were suspended above a silicon nitride/silicon dioxide barrier dielectric covering a silicon substrate.

The theory behind the effect, in a FET or diode sensor, is that hydrogen and other gases chemisorb on the catalytically active metal electrodes, and in the process yield a species which alters the surface component of the metal work function. The change in work function alters the population distribution of carriers in the semiconductor under the metal by changing the surface potential of the semiconductor. The consensus in the literature is that gases other than hydrogen cannot be detected directly on a solid electrode. Without a pathway for the molecules to penetrate to the metal insulator interface, the effect on the work function produced on the outside of the electrode (exposed to gas) does not influence the surface potential of the semiconductor. In the case where a solid electrode does show a response, it is usually in the presence of hydrogen. The catalytic interaction of gases adsorbed on the surface affects the steady state surface chemical composition changing the metal work function and surface potential of the semiconductor. Thus, it is thought gases reacting with hydrogen on a catalytic surface can be measured indirectly through the effect they have on hydrogen at the metal dielectric interface (Hughes 1987). The observations above on NO₂ and CO were explained in this way. The current hypothesis is gases that do not dissolve and diffuse through the metal can be detected only by sensors with a perforated or ultrathin porous catalytic metal electrode (Cassidy 1985, Dobos 1990, Hedborg 1994 and Lundstrom 1996), and perforations or pores must extend down through the metallic layer to the metal dielectric interface for electric field penetration of the semiconductor. The resulting surface potential distribution would have a two-dimensional fine structure depending on the morphology of the metal film, but the average surface potential will change with the adsorption of gas, and for a FET, the gate voltage will change accordingly.

Owing to their large bandgap, the III-V nitrides are attractive for high temperature, high power electronics applications. For GaN and other highly ionic semiconductors, evidence has suggested that the Schottky barrier height of metal to III-nitride contacts strongly depend on the difference between the work function of the metal and the electron affinity of the semiconductors. Metals with lower work functions form ohmic contacts on n-GaN. This explains why Ti, Al, W, and Cr are chosen as ohmic contacts on n-GaN. Similarly, metals with higher work function, such as Pt, Ni, Pd, and Au are expected to form good Schottky barriers to n-GaN.

Platinum and palladium have been used in the catalytic metal FET before, and both metals are used in the three-way catalytic converter this product is designed to monitor. Rhodium was chosen, because of its use in the catalytic converter and selectivity to NO over O₂ in the catalytic oxidation of CO (Shelef 1994) and the probability that in a sensor, Rh will add some selectivity to the analysis of the exhaust gases. Each of these metals is refractory and as such do will not

sublime or corrode under the operational conditions of high temperature and exhaust gas exposure.

The adhesion of these catalytic metals to GaN is typically improved with a metal or nitride intermediate layer, because the unreactive nature of the catalytic gate metals with Pd a possible exception (Oelhafen 1983) makes the bond to other materials weak. The stresses inherent in the deposited metal films often result in the noble metals lifting off the substrate. Temperature coefficients of expansion mismatch between the metal films and substrate exacerbate this problem, and an adhesion metal layer is an important component in the design. In the case of one design for a suspended gate GasFET (Cassidy 1984) where a sacrificial metal is etched away from under the catalytic metal to form a metal bridge for gas access, compressive stress in the catalytic metal films (usually sputter deposited) caused the films to buckle when the sacrificial metal is etched away (Pyke 1993). At the very least, the buckling resulted in a gap capacitance that was highly variable and resulted in an unacceptably wide distribution in sensor performance.

Tungsten or titanium nitride or tantalum nitride are potential adhesion layers that also help prevent contamination and sensor drift caused by interdiffusion of the substrate components and metal films. At the high temperatures proposed for this work, a barrier is necessary to impede any potential alloying reactions of the catalytic metal with gallium. A priori calculations (Niessen 1983) suggest a small enthalpic driving force for solvation of W and Ta by platinum and palladium but a zero or slightly positive enthalpy for solvation by rhodium. Recent data suggests significant solvation of Pd by W. The enthalpic driving force for Ti solvation by any of these metals is expected to be smaller because of the size mismatch compared to W and Ta. The fact that Ta, W and Ti are nitrides further reduces the driving force for solid solutions and interdiffusion with the overlying catalytic metal layer. A small positive enthalpic contribution to solid solutions of the two metals has the corresponding potential detrimental effect of a mechanically unreliable combination. Our approach will be to deposit a thin layer (10-100 nm) of the barrier nitrides described above then an ultrathin film (5-20 nm) of the catalytic metal. Film formation is expected to give rise to island or clusters connected on the corners of the nanocrystallites for conduction but sufficiently separated to form a porous film and to relieve the intrinsic stress.

Choice of Pt, Rh and PdAg as Catalytic Gate Materials

Platinum and palladium were selected because each has shown sensitivity in the ppm range for ethylene, acetylene, CO. Both metals are PROX catalyst candidates, and both metals have been used in metal-semiconductor junctions on GaN. PdAg was selected, because the mechanical integrity is better than pure Pd at these hydrogen concentrations and because PdAg has been used successfully in hydrogen purification membranes. Rhodium was selected, because of its PROX catalytic activity and to help resolve the effects of the multiple gases in combination with platinum and palladium-silver. Each of these metals is expected to adsorb CO preferentially in the fuel stream just as in the PROX catalyst. The reaction of CO and hydrogen with oxygen on the surface of the catalyst produces a steady state surface composition that can be detected through the work function change of the catalyst. Our expectation is that with a higher affinity for CO, the three metals chosen for this work should show a higher resolution for changes involving CO and a more accurate and precise analysis in a parallel sensor array.

Experimental

Fabrication

GaN-MESFET and MODFET structures were grown on sapphire substrates using MBE. The cross sections of these two structures are illustrated in Figure 1. All structures had a buffer layer consisting of a 20 nm AlN layer on a sapphire substrate, followed by a 3 μm unintentionally-doped GaN layer. The active layers were then grown on the 3 μm -thick GaN layer. The MESFET consisted of 100 nm thick, $1 \times 10^{17} \text{cm}^{-3}$ Si-doped channel thinned from an originally 2 μm layer and without a n^{++} capping layer. The MODFET had a 20 nm thick, Si-doped AlGaIn epilayer with an Al composition of 30% and a 1 μm thick, undoped GaN channel layer. The sheet carrier concentration and Hall mobility were measured as $1.3 \times 10^{12} \text{cm}^{-2}$ and 960 cm^2/Vsec , respectively. All FETs were fabricated with a source-drain spacing of 6 μm . The gate length was 2 μm and the width varied from 100 μm to 200 μm . The wafer was first covered with a 200 nm-thick, sputtered, Ti layer as the mask prior to the photolithography. Processing steps were similar to that have been described for GaAs-based devices. The major difference in processing between the GaN-based devices and GaAs-based devices is that the wet etching was ruled out in the former case.

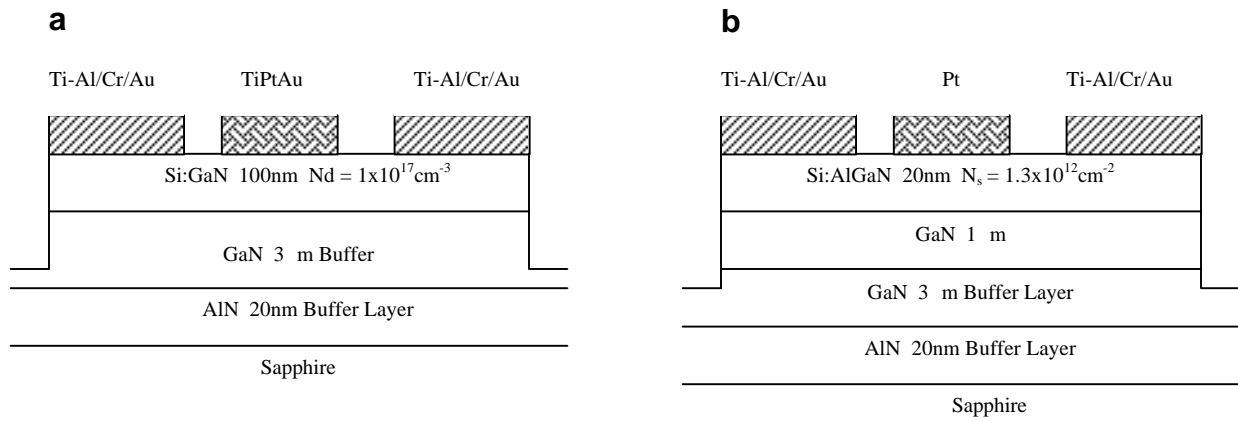


Fig.1 GaN FET cross-section (a) Si-doped MESFET and (b) AlGaIn/GaN MODFET.

The trench etching for device isolation was carried out by reactive ion etching (RIE) using Cl plasma. The final depth of the mesa is close to 2 μm . The Ti mask is then removed in HF solution and contact windows were exposed. The wafer received plasma etching for 30 sec in CF_4 and Ar plasma. Then, the Ti-Al ohmic contacts were deposited using e-beam evaporation. For MESFET, TiPtAu gate contacts were deposited by sputtering, while Pt gate was used for MODFET structure. The annealing condition was optimized at 600°C for 5 min in forming gas (10% vol H_2 in N_2) ambient.

Electrical Measurements

All the current-voltage (I-V) measurements were conducted using a test system comprised of a HP 4145B parameter analyzer, a Micromanipulator HSM hot stage and chuck controller, and an IBM PC compatible computer. The data was acquired via an IEEE 488 HPIB data bus and stored electronically for further analysis. The capacitance-voltage characteristics were obtained with an EG&G PAR 410/4108 CV system also controlled by the PC. If the slope of the C^{-2} vs V plot obtained is linear, one can obtain an independent measurement of barrier height using the method of least squares fit, from the intercept of the voltage axis V_{int} through the use of the relationship (Goodman 1999)

$$f_b = V_{\text{int}} + f_o + kT/q \quad (1)$$

where $f_o = (kT/q)\ln(N_d/n)$ can be determined from the donor density which in turn can be calculated from the slope of the C^{-2} vs V plot. The density of states in conduction band of $\text{Al}_x\text{Ga}_{1-x}\text{As}$ can be found in (Missous 1990)

Results

Ohmic Contacts

We have found that Cr/TiW/Ti-Al and Cr/Ti-Al to n-GaN are both suitable ohmic contact systems to n-GaN for prolonged use in air ambients to temperatures of at least 500°C. We chose Cr as a capping layer to protect the Ti-Al ohmic contacts since TiW intended to oxidize during the aging tests. The Cr cap layer has a high electrical conductivity and high thermal resistance to oxidation and also does not diffuse through the TiW layer. A final layer of Au (Cr acts as a blocking layer to interdiffusion) improves the chemical and oxidation resistance of the contacts and is amenable standard packaging techniques and equipment. Considering the work function effect on the Schottky barrier height, the contact resistance is not expected to degrade much in case of further diffusion of Cr from the capping layer to the interface between GaN and Ti-Al because of the low work function of Cr. The specific contact resistance was 2.0×10^{-6} Ohm-cm² and remained unchanged after annealing in air at 350°C for over 120 hours.

GaN MESFET with TiPtAu Gate

Figure 2 shows poor transistor performance. The ideal curve should rise steeply and then be insensitive to V_{ds} . The inflection point (e.g. typically $V_{ds} \sim 1-2V$) is called the pinch off voltage.

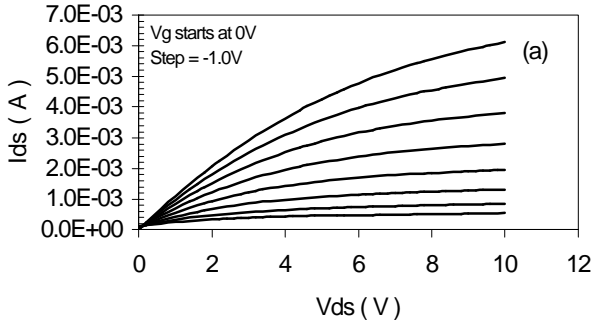


Fig. 2: Current-voltage characteristics at 300°C for a representative GaN MESFET with a TiPtAu gate

This can be explained on the basis of severe leakage currents between the gate electrode and the buffer layer shown by the I_g-V_g characteristics as a function of temperature of the gate diode are shown in Figure 3. The weak rectifying property (low ratio of forward to reverse current) of the gate diode is ascribed to the defects in the doped-GaN layer, which is close to the buffer layer. It is well known that the threading dislocations may have a high density in or near the channel that may provide leakage paths at elevated temperatures. It is worth pointing out that the GaN structure was grown ~4 years ago and the material properties for GaN-based semiconductors were not as good compared to that of currently grown ones and had considerably more defects.

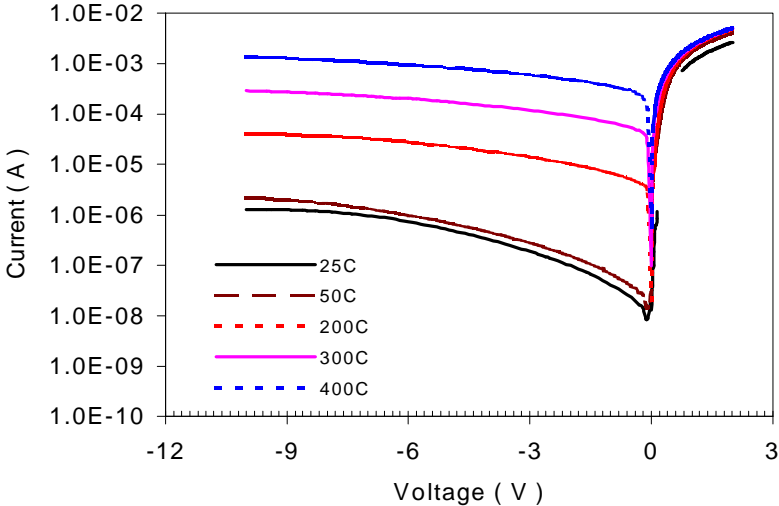


Fig. 3: Current voltage plot of a representative TiPtAu/n-GaN diode as a function of temperatures.

AlGaN/GaN Modulation Doped Field Effect Transistor (MODFET)

Figure 4 shows the characteristic I_d - V_{ds} curves for a representative MODFET. The current when the channel was fully open was 33 mA and the breakage voltage was ~ 70 V (not shown in the figure). Self-heating was observed in this type of device as reflected by the decrease in drain current with respect to increased drain voltage. Another reason for such behavior is, at higher fields, the electron mobility is reduced due to the scattering of electrons (Bykovski 1997 and Asbeck 1997).

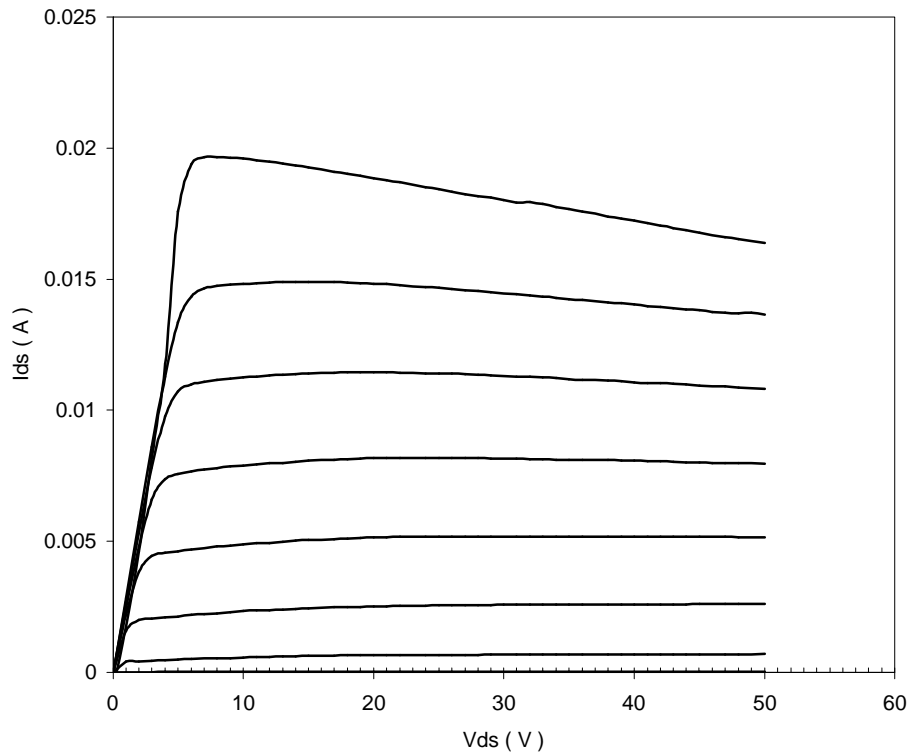


Fig. 4: I_{ds} - V_{ds} for a representative Pt gate AlGaN/GaN MODFET at 35°C

The elevated temperature characteristic curves of representative MODFETs still show the ideal shape as shown in Figs.5 and 6 for temperatures of 300°C and 400°C, respectively. The current ratios of gate leakage to total drain leakage at $V_{ds}= 5$ V and $V_{gs}= -2$ V at 300°C and 400°C are 22.4 A/48 A and 271 A/225 A, respectively.

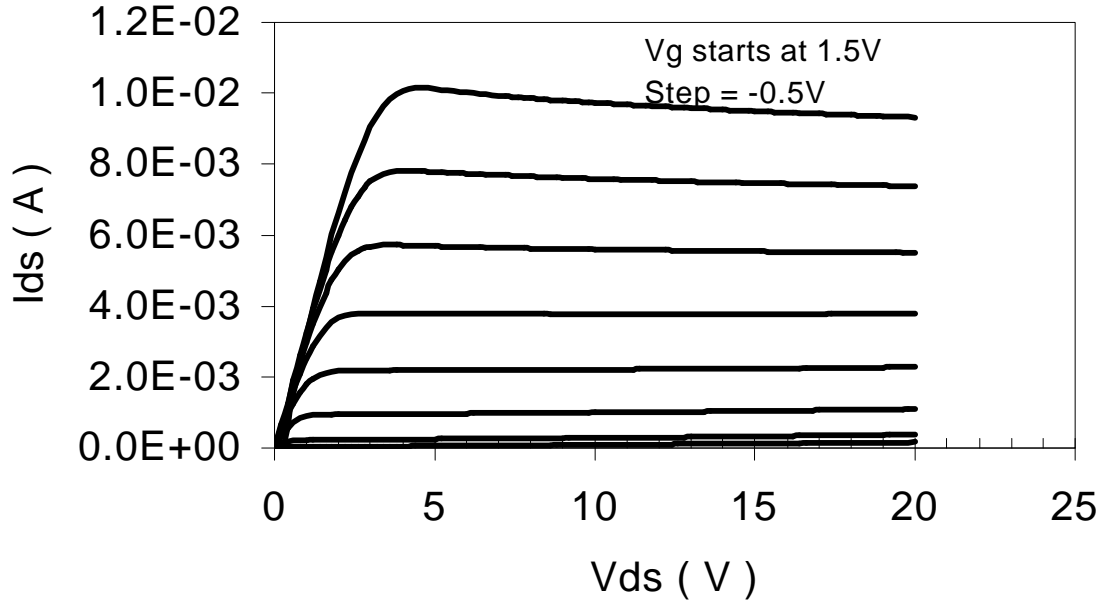


Fig. 5: I_{ds} - V_{ds} for a representative Pt gate AlGaIn/GaN MODFET at 300°C

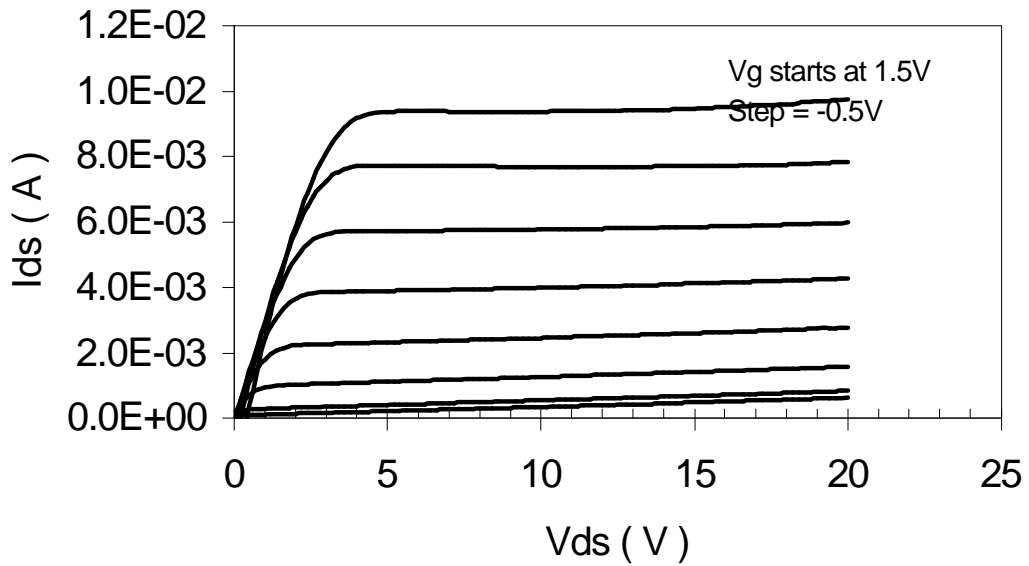


Fig. 5: I_{ds} - V_{ds} for a representative Pt gate AlGaIn/GaN MODFET at 400°C

Discussion and Conclusions

While Figure 5 and 6 show the ideal shape gate leakage current has to be reduced for a sensitive FET detection circuit. The fact that the gate current became the dominate leakage source is not surprising because the barrier height characterized from forward I-V curves and $1/C^2$ vs V plots for the gate diode at 35°C was ~1.0 eV. This is not sufficient to eliminate gate leakage at temperature higher than 350°C as been shown in all GaAs-based devices studied (Chern 2000).

Typical control and signal processing circuitry might try to maintain the I_{ds} by controlling the V_g . If gate leakage is a significant load and thermally generated, the chemical effect on V_g would be confounded by temperature. This leakage load depends exponentially on temperature and could easily dominate the relatively small (e.g 100mV-700mV) changes due to a chemical effect on V_g . Reducing the gate leakage current in the FET structure is necessary and should be the focus achieving sensitive and cost effective high-temperature sensing applications for GaN catalytic gate FET sensors using traditional signal processing. The barrier height may be improved by choosing metals having a large work function. Pt is already among the highest work function metals. Rh and Pd/Ag have slightly smaller work functions, however comparisons of the differences in electron affinity and work functions have yielded crude correlations at best (Sze, 1981). There is a need for a more accurate picture of the Schottky barrier height dependence on the metal work function and the relatively unknown chemical effect of the metal on the semiconductor electrical properties. An insulating layer between the metal and semiconductor is another way to reduce the gate leakage current. The AlGaN layer in the MODFET structure has this effect, and the performance comparison above suggests improvement consistent with this hypothesis. If this can be done with additional nitride or insulating oxide without adversely affecting the transconductance of the source drain channel, the layer could also have the effect of chemical passivation of the semiconductor in more aggressive chemical environments. These issues will be addressed in further work pending demonstration of the ability to detect and measure carbon monoxide in a hydrogen ambient.

In conclusion, using wide band-gap semiconductors such as AlGaN reduces the substrate leakage current at elevated temperatures and makes high temperature sensors based on GaN within reach of near term development. For this potential to be realized, defect levels must be reduced, and improvement of semi-insulating buffers and Schottky contacts is needed to optimize high temperature operation.

Acknowledgments

The authors wish to acknowledge the support of the Department of Energy Hydrogen Research Program (Contract # GO10453) to Peterson Ridge, LLC, for the majority of the support of this research and Chanh Nguyen at Hughes Research Laboratories, LLC for some of the materials used in this study.

REFERENCES

- Allison, E.G. and G.C. Bond. 1972. *Catal. Rev.*, 7, 233.
- Asbeck, P.M., E.T. Yu, S.S. Lau, G. J. Sullivan, J. Van Hove, and J. Redwing. 1997. *Electron. Lett.*, **33**, 1230.
- Bykhovski, A.D., B. L. Gelmont, and M.S. Shur. 1997. *J. Appl. Phys.*, **81**, 6332.
- Cassidy, J., S. Pons and J. Janata, *Anal. Chem.*, 58, 1757.
- Chern, Jehn-Huar. 2000. PhD Dissertation, The University of Utah and references therein.
- Department of Energy STTR Solicitation, No. DOE/ER-0728. Topic No. 1 Subtopic C. 1999.
- Dobos, K., et al.1990. *Sensors and Actuators*, B1, 25.
- Feinstein, D.I., C. Renn, M. Scharff and S.C. Pyke. 1997. "Metal-Insulator-Semiconductor (MIS) Gas Sensor Array for Gas Analysis and Diagnosing Faults in Oil-Filled Power Transformers", *Proceedings of the 191st Meeting of the Electrochemical Society*, Montreal, Quebec, Canada.
- Goodman, S.A., F.K. Koschnick, Ch. Weber, J.-M. Spaeth, and F.D. Auret. 1999. *Solid State Comm.*, 593.
- Hedborg, E., F. Winquist and I. Lundstrom. 1994. *Appl. Phys. Lett.*, 64(4), 420.
- Hughes, R.C., W.K. Schubert, T.E. Zipperian, J.L. Rodriguez and T.A. Plut. 1987. *J. Appl. Phys.*, 62,1074
- Krumpelt, M. 1999. Argonne National Labs, private communication.
- Lundstrom, I., M.S. Shivaraman, C. Svensson, and L. Lundqvist. 1975. *J. Appl. Phys.*, 26, 55.
- Lundstrom, I. and L.G. Petersson. 1996. *J. Vac. Sci. Technol.*, A, 14(3), 1539.
- Lundstrom, I., M. Armgarth and L.-G. Petersson. 1989. *CRC Critical Reviews in Solid State and Materials Sciences*, 15, 201-278.
- Mann, R.F., J.C. Amphlett, and B.A. Peppley. 1993. *Frontiers Sci. Ser.* 7, 613 .
- Missous, M., W.S. Truscott and K.E. Singer. 1990. *J. Appl. Phys.*, **68**(5), 2239.
- Niessen, A.K. and A.R. Miedema. 1983. *Ber. Bunsenges. Phys. Chem.*, 87, 717 and references therein.
- Oelhafen, P., J.L. Freeouf, T.S. Kuan, T.N. Jackson and P.E. Batson. 1983. *J. Vac. Sci. Technol.* B 1 (3), 588.
- Poteat, T.L., B. Lalevic, B. Kuliyeu, M. Yousef and M. Chen. 1983. *J. Electron. Mater.*, 12, 181.
- Pyke, S.C. 1993. "Transformer Fault Gas Analyzer," (invited paper) *Proceedings of the First Annual Substation Equipment Diagnostic Conference*, The Electric Power Research Institute, Palo Alto, CA.
- Shelef, M., and G.W. Graham. 1994. *Catal.Rev. Sci. Eng.*, 36(3) 433-457.
- Spetz, A., F. Winquist, H. Sundgren and I. Lundstrom. 1992. "Field Effect Gas Sensors", in G. Sberveglieri (ed.), *Gas Sensors*, Kluwer, Dordrecht, 219-279.
- Sze, S.M. 1981. " *Physics of Semiconductor Devices*", 2nd ed., New York, Wiley
- Wormeester, H., E. Huger and E.Bauer. 1996. *Phys. Rev. B.*, 54(23) 17108.

ADVANCED INTERNAL COMBUSTION ENGINE RESEARCH

Peter Van Blarigan
Sandia National Laboratories
Livermore, CA 94550

Abstract

In this manuscript, research on hydrogen internal combustion engines is discussed. The objective of this project is to provide a means of renewable hydrogen based fuel utilization. The development of a high efficiency, low emissions electrical generator will lead to establishing a path for renewable hydrogen based fuel utilization. A full-scale prototype will be produced in collaboration with commercial manufacturers.

The electrical generator is based on developed internal combustion engine technology. It is able to operate on many hydrogen-containing fuels. The efficiency and emissions are comparable to fuel cells (50% fuel to electricity, ~ 0 NO_x). This electrical generator is applicable to both stationary power and hybrid vehicles. It also allows specific markets to utilize hydrogen economically and painlessly.

Introduction

Two motivators for the use of hydrogen as an energy carrier today are: 1) to provide a transition strategy from hydrocarbon fuels to a carbonless society and 2) to enable renewable energy sources. The first motivation requires a little discussion while the second one is self-evident. The most common and cost effective way to produce hydrogen today is the reformation of hydrocarbon fuels, specifically natural gas. Robert Williams discusses the cost and viability of natural gas reformation with CO₂ sequestration as a cost-effective way to reduce our annual CO₂ emission levels. He argues that if a hydrogen economy was in place then the additional cost of natural gas reformation and subsequent CO₂ sequestration is minimal (Williams 1996).

Decarbonization of fossil fuels with subsequent CO₂ sequestration to reduce or eliminate our CO₂ atmospheric emissions provides a transition strategy to a renewable, sustainable, carbonless society. However, this requires hydrogen as an energy carrier.

The objectives of this program for the year 2000 are to continue to design, build, and test the advanced electrical generator components, research hydrogen based renewable fuels, and develop industrial partnerships. The rationale behind the continuation of designing, building, and testing generator components is to produce a research prototype for demonstration in two years. Similarly, researching hydrogen based renewable fuels will provide utilization components for the largest possible application. Finally, developing industrial partnerships can lead to the transfer of technology to the commercial sector as rapidly as possible.

This year work is being done on the linear alternator, two-stroke cycle scavenging system, electromagnetic/combustion/dynamic modeling, and fuel research. The Sandia alternator design and prototype will be finished, and the Sandia and Magnequench designs will be tested. Work on the scavenging system consists of learning to use KIVA-3V, and designing the scavenging experiment. Ron Moses of Los Alamos National Laboratories is conducting the modeling; modeling of the alternator is being performed. Hydrogen based renewables, such as biogas and ammonia, are the fuels being researched. Outside of modeling and research, an industrial collaboration has been made with Caterpillar and Magnequench International, a major supplier of rare earth permanent magnet materials. A collaborative research and development agreement (CRADA) has been arranged with Caterpillar, and Magnequench is designing and supplying a linear alternator. In addition, the prestigious Harry Lee Van Horning Award presented by the Society of Automotive Engineers (SAE) was awarded in October 1999 for a paper concerning homogeneous charge compression ignition (HCCI) with a free piston (SAE 982484).

Background

Electrical generators capable of high conversion efficiencies and extremely low exhaust emissions will no doubt power advanced hybrid vehicles and stationary power systems. Fuel cells are generally considered to be ideal devices for these applications where hydrogen or methane are used as fuel. However, the extensive development of the IC engine, and the existence of repair and maintenance industries associated with piston engines provide strong incentives to remain with this technology until fuel cells are proven reliable and cost competitive. In addition, while the fuel cell enjoys high public relations appeal, it seems possible that it may not offer significant efficiency advantages relative to an optimized combustion system. In light of these factors, the capabilities of internal combustion engines have been reviewed.

In regards to thermodynamic efficiency, the Otto cycle theoretically represents the best option for an IC engine cycle. This is due to the fact that the fuel energy is converted to heat at constant volume when the working fluid is at maximum compression. This combustion condition leads to the highest possible peak temperatures, and thus the highest possible thermal efficiencies.

Edson (1964) analytically investigated the efficiency potential of the ideal Otto cycle using compression ratios (CR) up to 300:1, where the effects of chemical dissociation, working fluid

thermodynamic properties, and chemical species concentration were included. He found that even as the compression ratio is increased to 300:1, the thermal efficiency still increases for all of the fuels investigated. At this extreme operating for instance, the cycle efficiency for isoctane fuel at stoichiometric ratio is over 80%.

Indeed it appears that no fundamental limit exists to achieving high efficiency from an internal combustion engine cycle. However, many engineering challenges are involved in approaching ideal Otto cycle performance in real systems, especially where high compression ratios are utilized.

Caris and Nelson (1959) investigated the use of high compression ratios for improving the thermal efficiency of a production V8 spark ignition engine. They found that operation at compression ratios above about 17:1 did not continue to improve the thermal efficiency in their configuration. They concluded that this was due to the problem of non-constant volume combustion, as time is required to propagate the spark-ignited flame.

In addition to the problem of burn duration, other barriers exist. These include the transfer of heat energy from the combustion gases to the cylinder walls, as well as the operating difficulties associated with increased pressure levels for engines configured to compression ratios above 25:1 (Overington and Thring 1981, Muranaka and Ishida 1987). Still, finite burn duration remains the fundamental challenge to using high compression ratios.

The goal of emissions compliance further restricts the design possibilities for an optimized IC engine. For example, in order to eliminate the production of nitrogen oxides (NO_x), the fuel/air mixture must be homogeneous and very lean at the time of combustion (Das 1990, Van Blarigan 1995). (It is subsequently possible to use oxidation catalyst technologies to sufficiently control other regulated emissions such as HC and CO.) Homogeneous operation precludes diesel- type combustion, and spark-ignition operation on premixed charges tends to limit the operating compression ratio due to uncontrolled autoignition, or knock. As well, very lean fuel/air mixtures are difficult, or impossible to spark ignite.

On the other hand, lean charges have more favorable specific heat ratios relative to stoichiometric mixtures, and this leads to improved cycle thermal efficiencies. Equivalence ratio is no longer required to be precisely controlled, as is required in conventional stoichiometric operation when utilizing tree way catalysts. Equivalence ratio is defined here as the ratio of the actual fuel/air ratio to the stoichiometric ratio.

Combustion Approach

Homogeneous charge compression ignition combustion could be used to solve the problems of burn duration and allow ideal Otto cycle operation to be more closely approached. In this combustion process a homogeneous charge of fuel and air is compression heated to the point of autoignition. Numerous ignition points throughout the mixture can ensure very rapid combustion (Onishi et al 1979). Very low equivalence ratios ($\phi \sim 0.3$) can be used since no flame propagation is required. Further, the useful compression ratio can be increased as higher temperatures are required to autoignite weak mixtures (Karim and Watson 1971).

HCCI operation is unconventional, but is not new. As early as 1957 Alperstein et al. (1958) experimented with premixed charges of hexane and air, and n-heptane and air in a Diesel engine. They found that under certain operating conditions their single cylinder engine would run quite well in a premixed mode with no fuel injection whatsoever.

In general, HCCI combustion has been shown to be faster than spark ignition or compression ignition combustion. And much leaner operation is possible than in SI engines, while lower NO_x emissions result.

Most of the HCCI studies to date however, have concentrated on achieving smooth releases of energy under conventional compression condition ($\text{CR} \sim 9:1$). Crankshaft driven pistons have been utilized in all of these previous investigations. Because of these operating parameters, successful HCCI operation has required extensive EGR and/or intake air preheating. Conventional pressure profiles have resulted (Thring 1989, Najt and Foster 1983).

In order to maximize the efficiency potential of HCCI operation much higher compression ratios must be used, and a very rapid combustion event must be achieved. Recent work with higher compression ratios ($\sim 21:1$) has demonstrated the high efficiency potential of the HCCI process (Christensen et al 1998, Christensen et al 1997).

In Figure 1, the amount of work attained from a modern 4-stroke heavy duty diesel engine is shown at a 16.25 : 1 compression ratio. The results show that under ideal Otto cycle conditions (constant volume combustion), 56% more work is still available. This extreme case of non-ideal Otto cycle behavior serves to emphasize how much can be gained by approaching constant volume combustion.

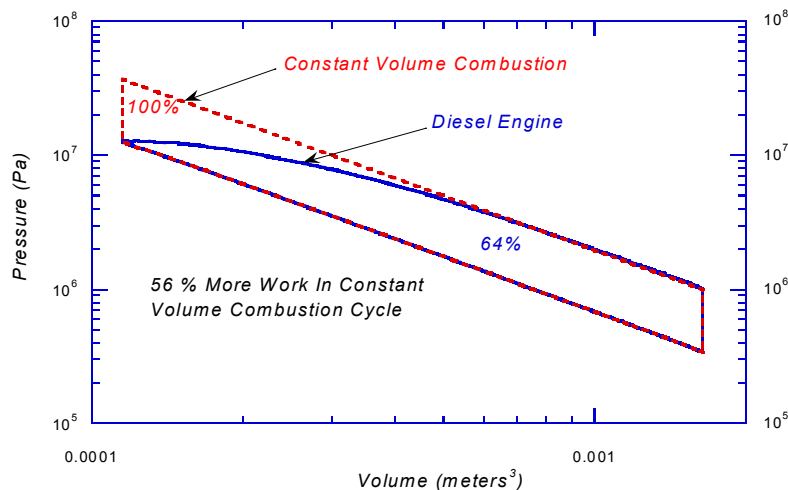


Figure 1 – Modern 4-Stroke Heavy Duty Diesel Engine

Engineering Configuration

The free piston linear alternator illustrated in Figure 2 has been designed in hopes of approaching ideal Otto cycle performance through HCCI operation. In this configuration, high compression ratios can be used and rapid combustion can be achieved.

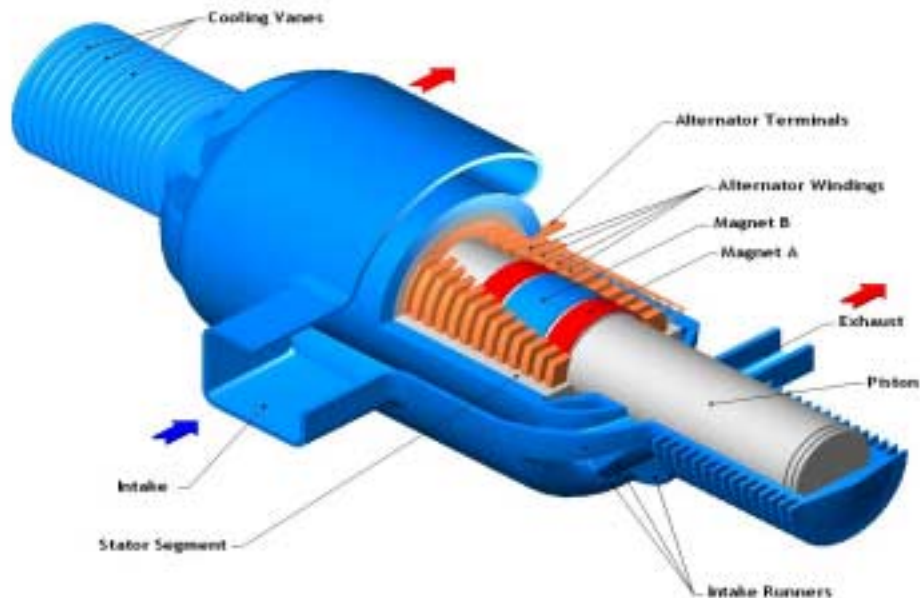


Figure 2 – Free piston linear alternator

The linear generator is designed such that electricity is generated directly from the piston's oscillating motion, as rare earth permanent magnets fixed to the piston are driven back and forth through the alternator's coils. Combustion occurs alternately at each end of the piston and a modern two-stroke cycle scavenging process is used. The alternator component controls the piston's motion, and thus the extent of cylinder gas compression, by efficiently managing the piston's kinetic energy through each stroke. Compression of the fuel/air mixture is achieved inertially and as a result, a mechanically simple, variable compression ratio design is possible with sophisticated electronic control.

The use of free pistons in internal combustion engines has been investigated for quite some time. In the 1950's, experiments were conducted with free piston engines in automotive applications. In these early designs, the engine was used as a gasifier for a single stage turbine (Underwood 1957, Klotsch 1959). More recent developments have integrated hydraulic pumps into the engine's design (Baruah 1988, Achten 1994).

Several advantages have been noted for free piston IC engines. First, the compression ratio of the engine is variable; this is dependent mainly on the engine's operating conditions (e.g., fuel type, equivalence ratio, temperature, etc.). As a result, the desired compression ratio can be achieved through modification of the operating parameters, as opposed to changes in the engine's hardware.

An additional benefit is that the mechanical friction can be reduced relative to crankshaft driven geometries since there is only one moving engine part and no piston side loads. Also, combustion seems to be faster than in conventional slider-crank configurations. Further, the unique piston dynamics (characteristically non-sinusoidal) seem to improve the engine's fuel economy and NO_x emissions by limiting the time that the combustion gases spend at top dead center (TDC) (thereby reducing engine heat transfer and limiting the NO_x kinetics). Finally, one researcher (Braun 1973) reports that the cylinder/piston/ring wear characteristics are superior to slider/crank configurations by a factor of 4.

The combination of the HCCI combustion process and the free piston geometry is expected to result in significant improvements in the engine's thermal efficiency and its exhaust emissions. The following advantages should be found:

1. For a given maximum piston velocity, the free piston arrangement is capable of achieving a desired compression ratio more quickly than a crankshaft driven piston configuration. This point is illustrated in Figure 3 where the piston position profiles of both configurations are plotted. The reduced compression time should result in higher compression of the premixed charge before the onset of autoignition.

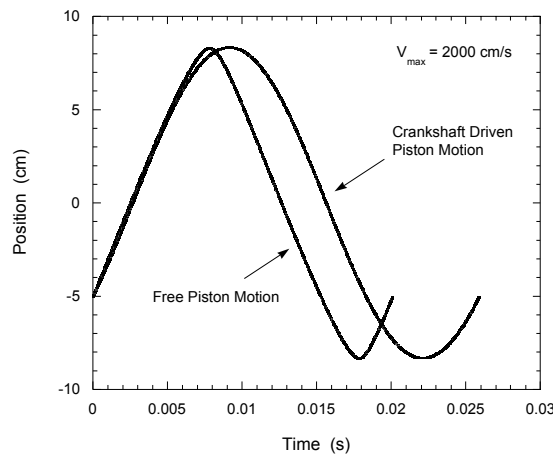


Figure 3 – Piston position vs. time

2. High compression ratio operation is better suited to the free piston engine since the piston develops compression inertially, and as such there are no bearings or kinematic constraints that must survive high cylinder pressures or the high rates of pressure increase (shock). The use of low equivalence ratios in the HCCI application should further reduce the possibility of combustion chamber surface destruction (Lee and Schaefer 1983, Maly et al 1990).
3. The free piston design is more capable of supporting the low IMEP levels inherent in low equivalence ratio operation due to the reduction in mechanical friction.

Integration of the linear alternator into the free piston geometry provides further benefits to the generator design. In this arrangement mechanical losses in the system are dramatically reduced since there is essentially one moving part, and this allows engine operation at a more or less constant piston speed. These points aid in the generator design, and further improve the fuel-to-electricity generation efficiency of the device.

The linear alternator itself is based on technology developed for brushless DC motors. This class of motors is characterized by high efficiency and high power density, typically 96% efficiency and 1 hp per pound density. Put simply, the rotary configuration is unrolled until flat, then rolled back up perpendicular to the first unrolling to arrive at the linear configuration. Relative to the rotary geometry the linear device is approximately 30% heavier due to not all of the coils being driven at the same time. Efficiency will be comparable.

2-Stroke Cycle

Inherent in the configuration selected is the need to scavenge the exhaust gases out of the cylinder and replace them with fresh fuel/air charge while the piston is down at the bottom of the cylinder. This requirement is due to the need to have trapped gases in the cylinder to act as a spring, as well as to provide the next combustion event.

Conventional 2-stroke cycle engines have developed a reputation for low fuel efficiency and high hydrocarbon emissions due to short-circuiting of the inlet fuel/air mixture directly to the exhaust port. The typical 2-stroke application stresses power density over efficiency and emissions – chain saws, weed whackers, marine outboard motors. These devices must operate over a wide speed and power range.

In this case the requirements are quite different. The speed of the free piston oscillation is essentially fixed. Power is varied by modification of the equivalence ratio, not the quantity of gas delivered. Power density is not a driving requirement. As a result, the design of this system can be optimized within tight constraints utilizing computational fluid dynamics and experimental gas dynamics techniques.

Experimental Results - FY 2000

Figure 4 shows the results of experimental combustion studies completed with hydrogen. In this investigation, a single-stroke rapid compression-expansion machine has been used to compression ignite hydrogen. Hydrogen is the fastest burning fuel out of all the fuels tested. The high rate of combustion does approach constant volume combustion. Figure 3 shows a typical logarithmic P/V diagram for hydrogen combustion at top dead center at 33:1 compression ratio. The piston has, for all practical purposes, not moved during the combustion event. In the free piston configuration high pressure-rise rates can be handled without difficulty since there are no load bearing linkages, as in crankshaft-driven engines. Additionally, operation at equivalence ratios less than 0.5 reduces the need to consider piston erosion, or other physical damage (Maly et al. 1990).

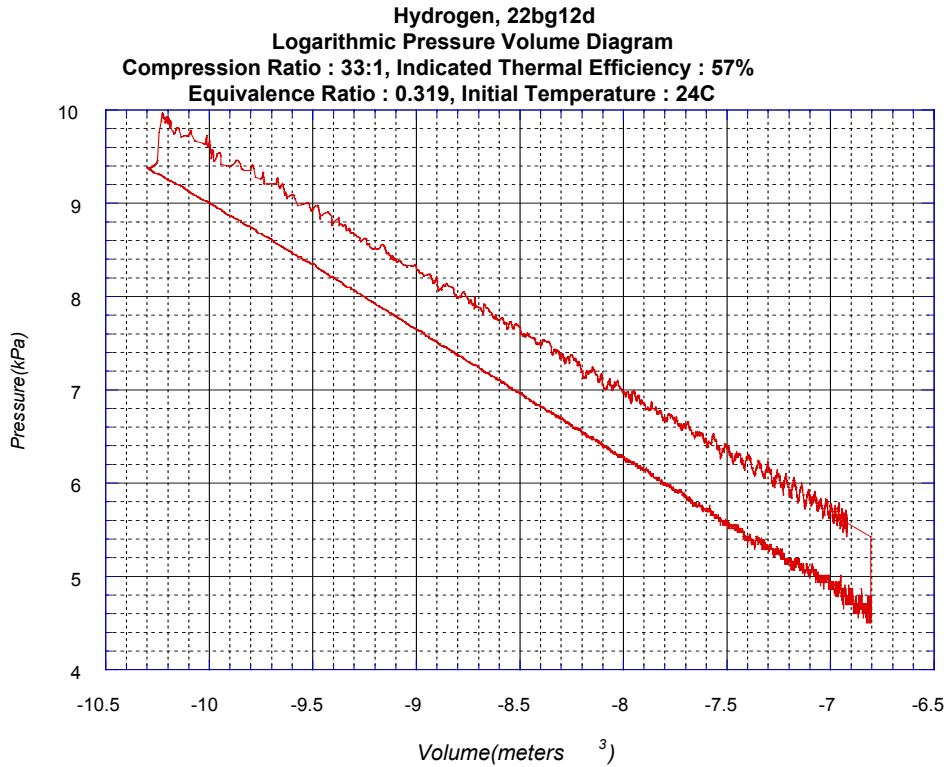


Figure 4 - Hydrogen Combustion

Figure 5 shows the free piston generator again. The overall length of the generator is 76 centimeters, its specific power is 800 watts per kilogram, and it has a power density of 800 watts per liter. Hydrogen based renewable fuels such as bio-gas (low BTU producer gas H_2-CH_4-CO), ammonia (NH_3), methanol (CH_4O), and/or hydrogen (H_2) can be used directly.

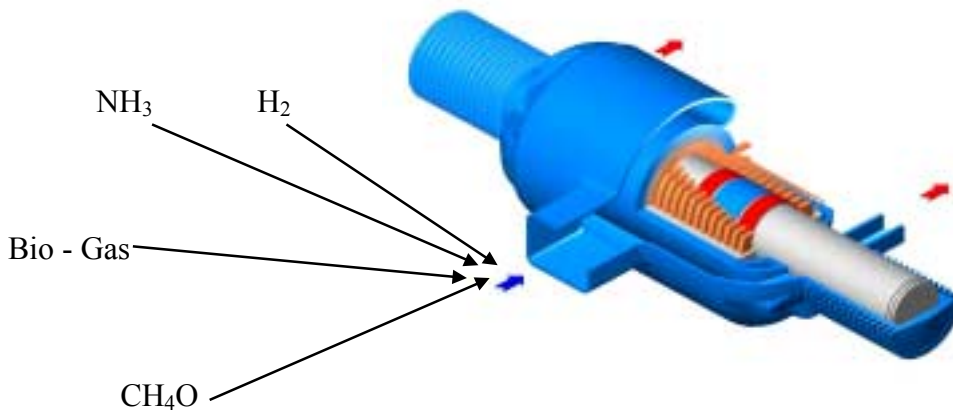


Figure 5 – Free Piston Generator

The alternator consists of moving rare earth permanent magnets and stationary output coils and stator laminations. The design is similar to a conventional rotary brushless DC generator.

Figure 6 shows the magnetic flux path for the linear alternator. It can be seen that the flux through the coils changes direction as the permanent magnet assembly moves down the alternator core. This changing flux induces current in the coils.

Two parallel paths are being pursued to develop the linear alternator. An alternator is being built and tested in house. As a design tool, we are utilizing a two dimensional finite element computer code to solve Maxwell's equations of electromagnetism. The code, called FLUX2D, is produced by MagSoft Corporation. We have investigated various design configurations, and have optimized a design with respect to maximizing efficiency and minimizing size. In parallel Magnequench, a commercial development partner, is also designing and fabricating an alternator. Both alternator designs are being fabricated and will be tested under full design output conditions on a Sandia designed Caterpillar engine based tester. The tester will measure both power output and mechanical to electrical conversion efficiency.

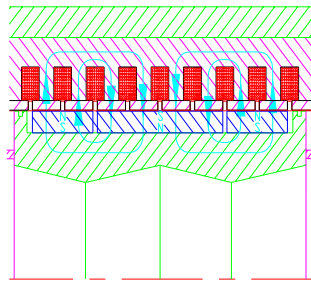


Figure 6 – Alternator Design

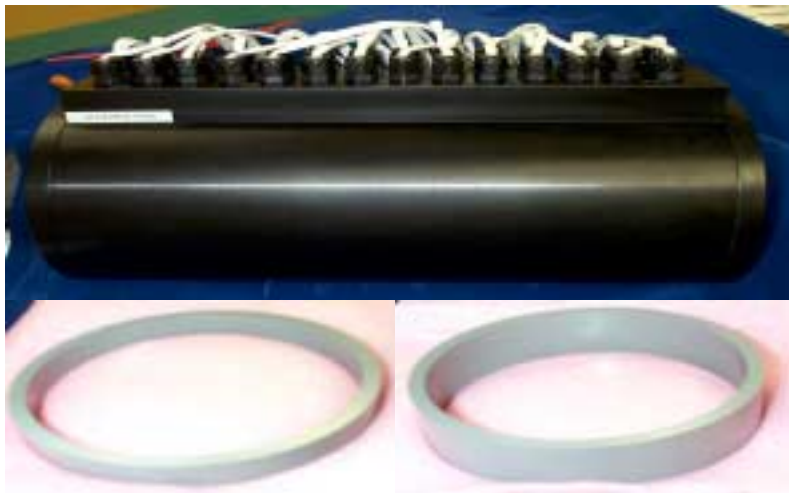
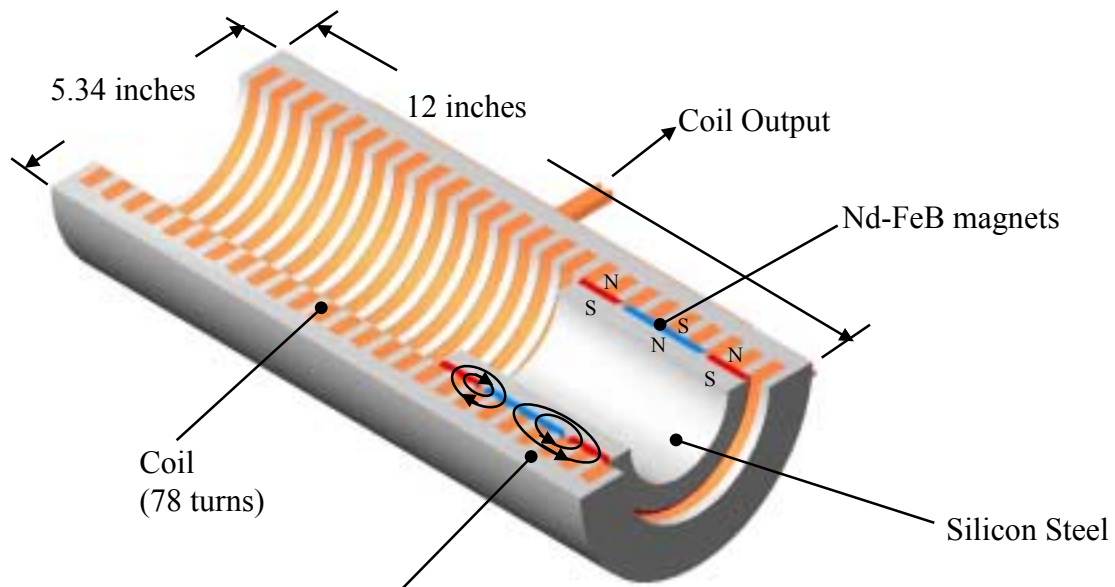


Figure 7 – Magnequench Linear Alternator Stator Assembly

Magnequench has delivered three stator assemblies to Sandia, one of which is shown in Figure 7. Also shown in Figure 7 are a short and a long magnet ring. These magnets are pressed from neodymium-iron-boron rare earth material and magnetized in the radial direction. Sandia will assemble the Magnequench supplied magnets to the moving part back iron and provide linear bearing supports. One assembly will then be returned to Magnequench for their own testing.



Power Output : 40kW
 Efficiency : 96%
 Weight 60 pounds

Oriented Grain Silicon steel Laminations
 (1600 each)

Figure 8 – Sandia Linear Alternator Design

Figure 8 shows a cut away of the Sandia alternator design. The power output of the linear alternator is 40 kW, and has an efficiency of 96%. The Magnequench design is very similar; the differences are primarily in the coil configuration, magnet fabrication and stator material. The Sandia magnet assembly is fabricated from 10 degree arc magnet segments, which are magnetized in a linear direction.

The Sandia stator is an assembly of 1600 laminations punched from anisotropic oriented grain silicon steel. Each lamination has a small angle ground so the assembly stacks into a cylinder. The Magnequench stator material is pressed iron powder in an adhesive matrix.

The Magnequench coils consist of a single row winding of flat wire. The Sandia coils contain 78 turns of square cross section wire. The Magnequench coils must be connected in moving groups of five as the magnet assembly moves in the stator. The Sandia design isolates each coil from the other coils with a Wheatstone bridge. This has the advantage of not requiring an active magnet assembly following switching network.

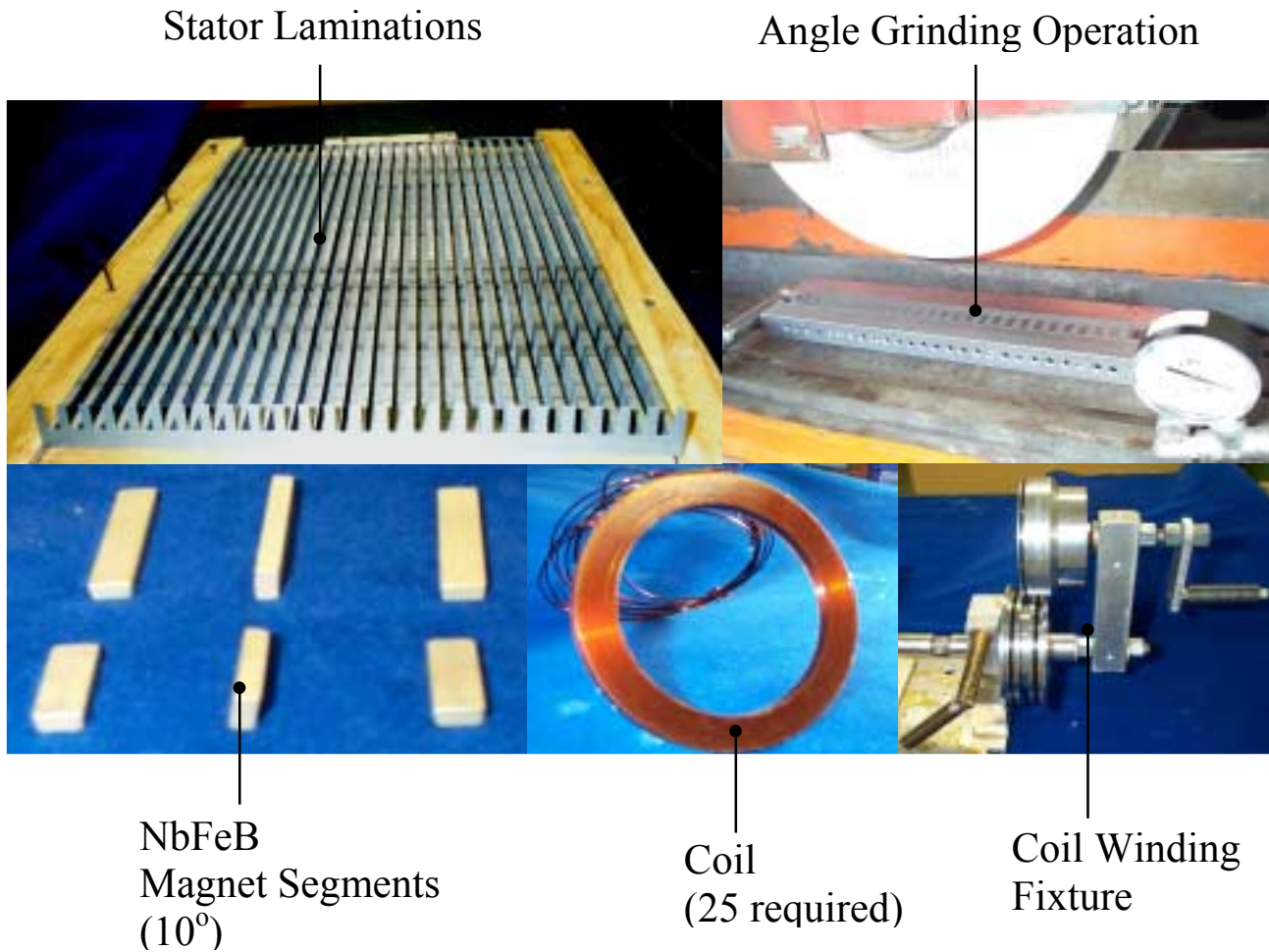


Figure 9 – Linear Alternator Design Components

Some of the components and fabrication tools for the Sandia linear alternator are shown in Figure 9.

Alternator Modeling

In preparation for designing the generator control algorithms a comprehensive mathematical model of the entire physical system is required. One of the challenging aspects of the system model is the electromagnetic performance of the linear alternator. The finite element model (FLUX2D) utilized in the design process is too cumbersome for use in a real time system model.

To circumvent this situation we have contracted with Ron Moses of Los Alamos National Laboratory to derive a simplified alternator model. Ron is an expert in electromagnetic systems and excited to be part of our project team. We intend to have Ron develop, with our input, a total system model capable of predicting control system response.

Two Stroke-Cycle Scavenging System Design

Conventional two-stroke cycle engines are designed to maximize power density at the expense of efficiency and emissions. They also must operate over a wide speed and power range.

Our design intent is to maximize efficiency while minimizing emissions at a narrow power output operating condition. As a result, the configuration of the scavenging ports and operating pressures is likely to be unique to this design.

Our approach is to utilize KIVA-3V to design the scavenging system and to validate the KIVA-3V predictions at selected conditions. Towards this goal we have designed an add-on scavenging experiment for our free piston combustion test facility. Figure 10 shows the scavenging experiment on the upper left side connected to the existing combustion experiment on the lower right side. The experiment will reproduce combustion cylinder pressure and temperature conditions immediately prior to scavenging port opening and replicate piston motion during one scavenging cycle. By measuring gases in the cylinder and in the exhaust collector we will be able to discern trapping efficiency and scavenging efficiency during realistic operating conditions.

Figures 11 and 12 show the KIVA-3V modeling results for one particular configuration being investigated. We are striving to design a loop scavenged flow system due to the simplicity it possesses. We are also designing a uniflow system with an exhaust valve in the cylinder head. This approach is thought to be a more confident solution from a fluid mechanics viewpoint.

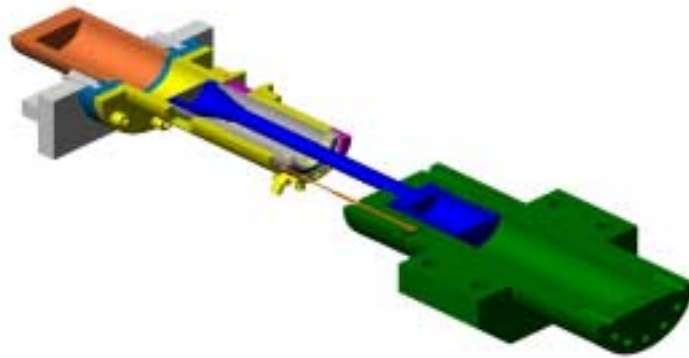


Figure 10 – Scavenging Experiment

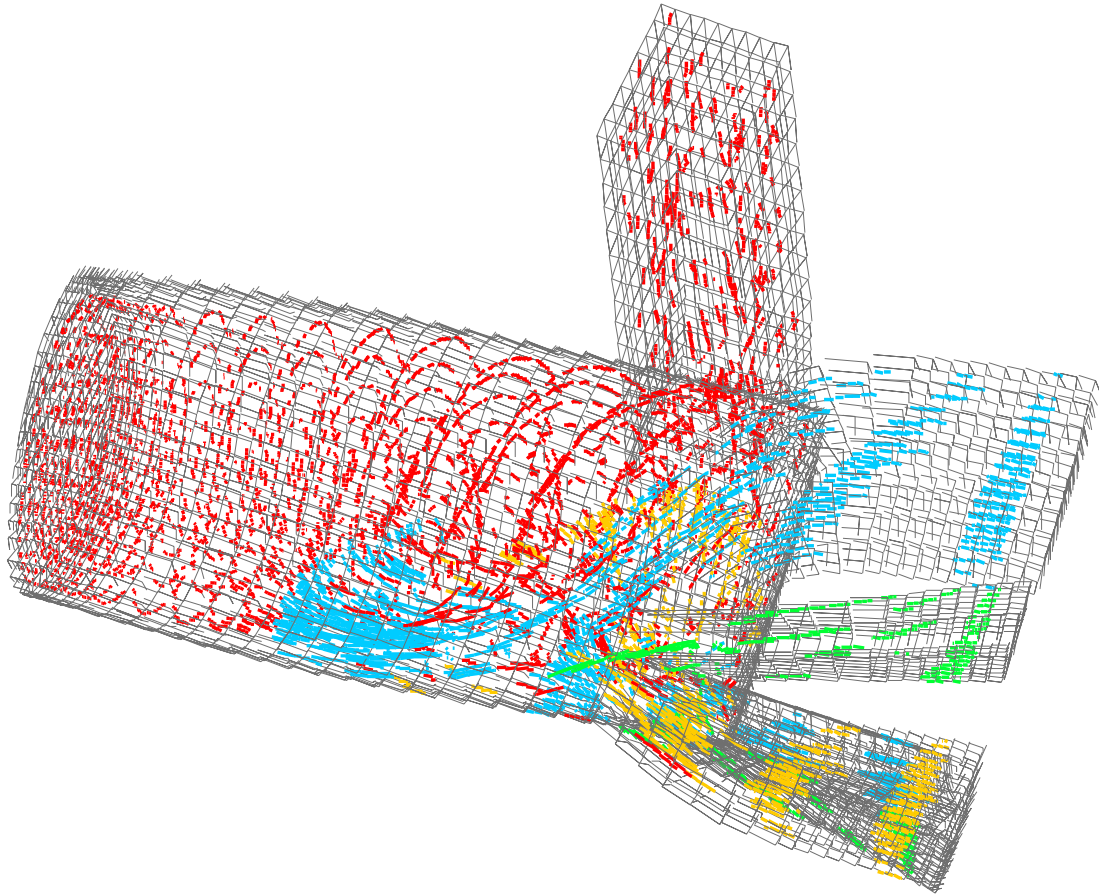


Figure 11 – KIVA-3V flow pictorial

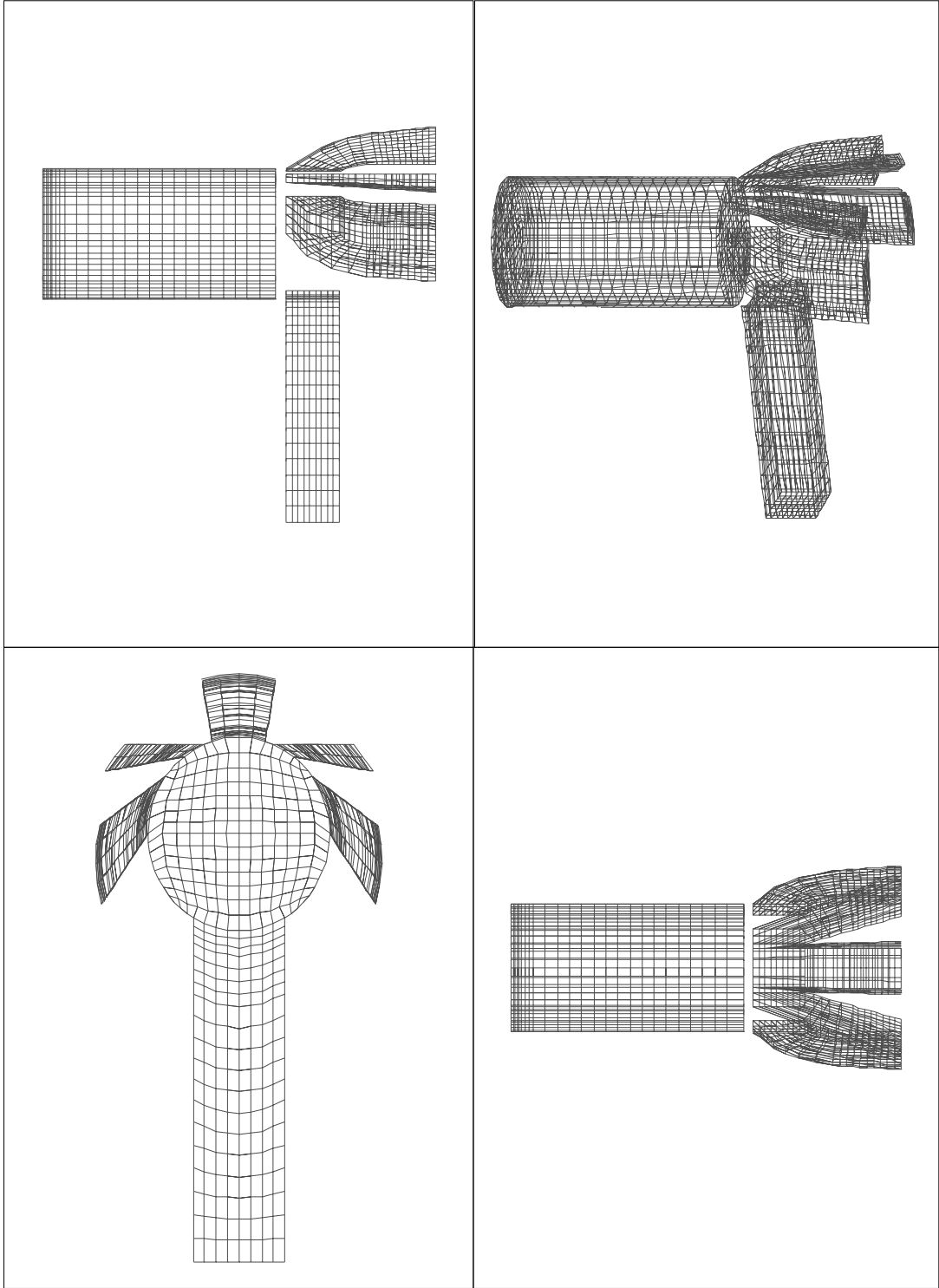


Figure 12 – KIVA-3V grid

Hydrogen Based Renewable Fuels

Bio-gas

One of the unique characteristics of HCCI combustion with a free piston is the ability to combust extremely lean mixtures. In the field of gasification of biomass the simplest approach is to combust the material in an oxygen-starved environment. The resultant gas is a mixture of hydrogen, carbon monoxide, carbon dioxide, methane, and nitrogen. The mixture is too lean for utilization in spark-ignition engines and requires a pilot diesel fuel injection when fumigated into a diesel engine.

Figure 13 shows the results of combustion of a typical low BTU producer gas as would be produced from a crude gasifier as would be found in a developing country. The formulation was kindly supplied by William Hauserman of Hauserman Associates. The results indicate excellent performance in the free piston experiment. In fact, this lean mixture is ideal for achieving the NO_x control our concept is based upon.

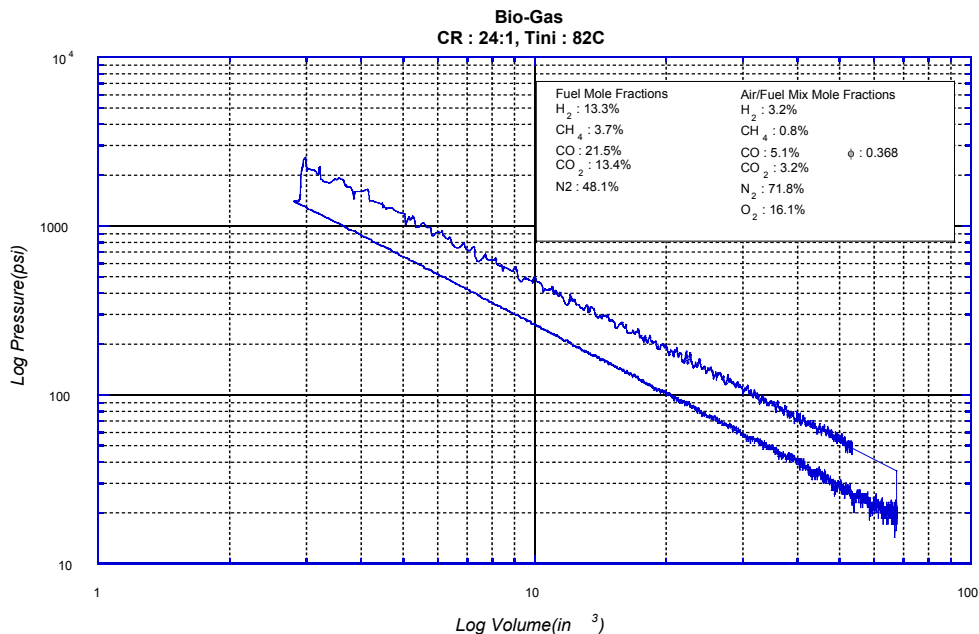


Figure 13 – Bio-gas Ideal Otto Cycle Performance

Ammonia

The two most challenging aspects of widespread hydrogen application are the storage of hydrogen for mobile applications and the distribution infrastructure. In the United States approximately 1,000,000 farms have access to anhydrous ammonia. The distribution infrastructure already exists to deliver approximately 8 billion pounds of anhydrous ammonia to

these farms for direct use as a nitrogen soil supplement. The farmers are already handling anhydrous ammonia and could easily use it as a fuel for their farm equipment if an efficient utilization device was available.

In Figure 14, the combustion of ammonia exhibits ideal Otto cycle performance in our free piston combustion experiment, and produces conversion efficiencies comparable to hydrogen (see Figure 15). Ammonia is an ideal hydrogen based renewable fuel to use in our free piston generator for several reasons. Ammonia is widely available. 35,000,000,000 pounds of anhydrous ammonia are produced in the United States per year. Ammonia contains no carbon, and can be easily made from hydrogen or natural gas.

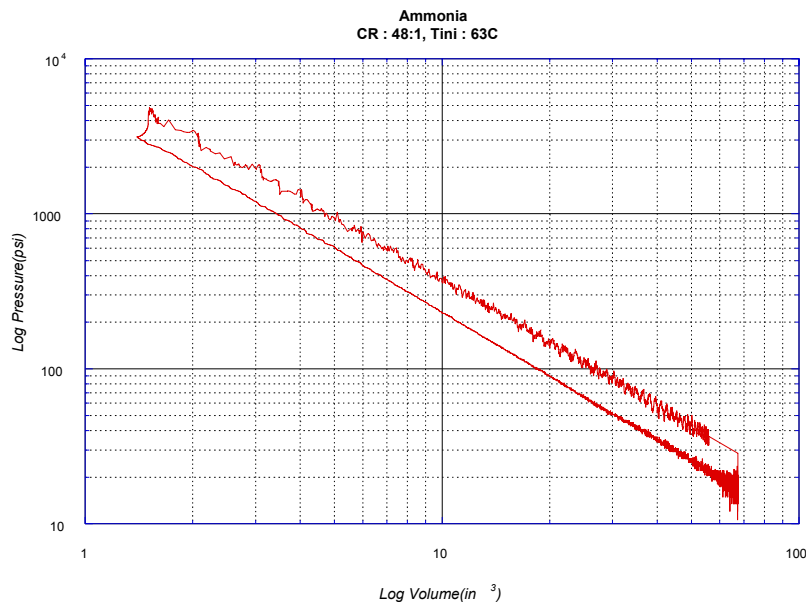


Figure 14 – Ammonia Ideal Otto Cycle Performance

Anhydrous ammonia is stored in the same manner as propane, as a liquid under approximately 100 pounds per square inch vapor pressure at room temperature. If released into the atmosphere, ammonia's density is lighter than that of air and thus dissipates rapidly. In addition, because of its characteristic smell the nose easily detects it in concentrations as low as 5 ppm. Finally, ammonia has such a narrow flammability range that it is generally considered non-flammable when transported.

Ammonia is comparable to gasoline as a fuel for combustion engines. Three gallons of ammonia is equivalent to one gallon of gasoline in energy content. In other terms, 2.35 pounds of ammonia is equivalent to one pound of gasoline in energy content. Cost wise in 1998, bulk ammonia was \$1.13 per gallon gasoline equivalent.

In using ammonia as a fuel, ammonia and air would enter the free piston generator through the intake port. After combustion, any generated NO_x emissions can be readily reduced by reaction with ammonia over a zeolite according to one of the following two reactions:

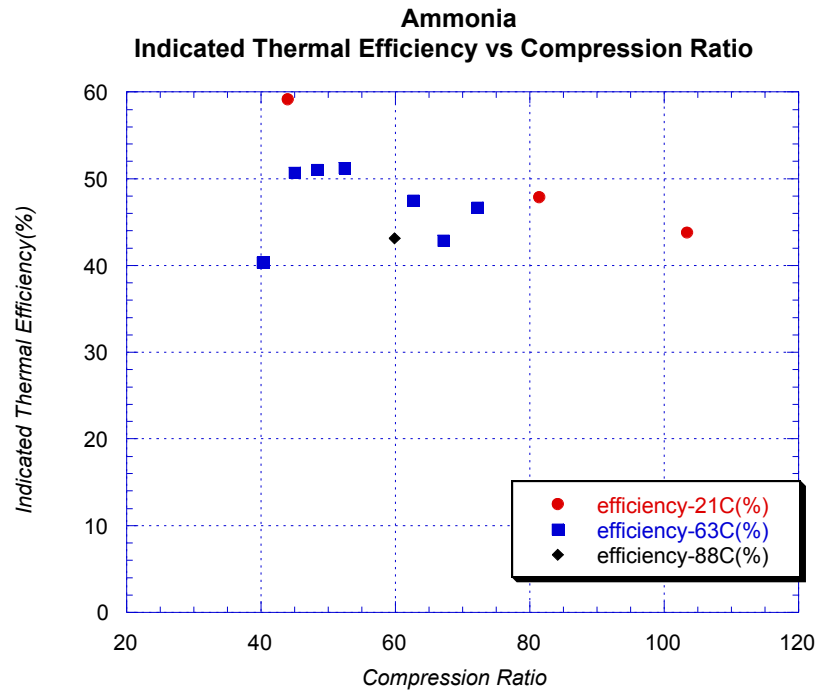
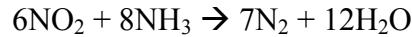
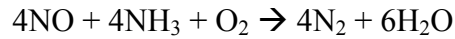


Figure 15 – Ammonia Combustion

Industrial Collaboration

As previously discussed Magnequench International, Incorporated is supplying a linear alternator at no cost in order to develop new applications for rare earth permanent magnets. In addition, Caterpillar Corporation is entering into a cooperative research and development agreement (CRADA) with our group. The purpose of the collaboration is for CAT to share their free piston lubrication and sealing technology with Sandia while in return applying our linear alternator technology to their free piston hydraulic pump program.

Both of these collaborations will ease the transfer of this exciting new technology to the industrial sector.

Future Work

Plans for the 2001 fiscal year include completing the two-stroke scavenging system design, developing a comprehensive system model, designing a prototype starting system, investigating alternative funding, and quantifying performance of both alternator designs. The principal

objectives are to select a prototype scavenging system, obtain a predictive model of electrical and mechanical components, select a starting system, and collaborate with industrial partners in pursuing other funding.

References

- Achten, P. A. J. 1994. "A Review of Free Piston Engine Concepts," SAE Paper 941776.
- Alperstein, M., Swim, W. B. and Schweitzer, P. H. 1958. "Fumigation Kills Smoke – Improves Diesel Performance," SAE Transactions, vol. 66, pp.574 – 588.
- Baruah, P. C. 1988. "A Free Piston Engine Hydraulic Pump for an Automotive Propulsion System," SAE Paper 880658.
- Braun, A. T. and Schweitzer, P. H. 1973. "The Braun Linear Engine," SAE Paper 730185.
- Caris, D. F. and Nelson, E. E. 1959. "A New Look at High Compression Engines," SAE Transactions, vol. 67, pp. 112-124.
- Christensen, M., Johansson, B. and Einewall, P. 1997. "Homogeneous Charge Compression Ignition (HCCI) Using Isooctane, Ethanol, and Natural Gas – A Comparison With Spark Ignition Operation," SAE Paper 972874.
- Christensen, M., Johansson, B., Amneus, P. and Mauss, F. 1998. "Supercharged Homogeneous Charge Compression Ignition," SAE Paper 980787.
- Das, L. M. 1990. "Hydrogen Engines: A View of the Past and a Look Into the Future," International Journal of Hydrogen Energy, vol. 15, no. 6, pp. 425 – 443.
- Edson, M. H. 1964. "The Influence of Compression Ratio and Dissociation on Ideal Otto Cycle Engine Thermal Efficiency," Digital Calculations of Engine Cycles, SAE Prog. in Technology, vol. 7, pp. 49-64.
- Karim, G.A. and Watson, H.C. 1971. "Experimental and Computational Considerations of the Compression Ignition of Homogeneous Fuel-Oxidant Mixtures," SAE Paper 710133.
- Klotsch, P. 1959. "Ford Free-Piston Engine Development," SAE Paper 590045.
- Lee, W. and Schaefer, H. J. 1983. "Analysis of Local Pressures, Surface Temperatures and Engine Damages under Knock Conditions," SAE Transactions, vol. 92, section 2, pp. 511 – 523.
- Maly, R. R., Klein, R., Peters, N. and Konig, G. 1990. "Theoretical and Experimental Investigation of Knock Induced Surface Destruction," SAE Transactions, vol. 99, section 3, pp. 99 – 137.

- Muranaka, Y. T. and Ishida, T. 1987. "Factors Limiting the Improvement in Thermal Efficiency of S.I. Engine at Higher Compression Ratio," SAE Transactions, vol. 96, section 4, pp. 526 – 536.
- Najt, P. M. and Foster, D. E. 1983. "Compression – Ignited Homogeneous Charge Combustion," SAE Paper 830264
- Onishi, S., Jo, S. H., Shoda, K., Jo, P. D. and Kato, S. 1979. "Active Thermo– Atmospheric Combustion (ATAC) – A New Combustion Process for Internal Combustion Engines," SAE Paper 790501.
- Overington, M. T. and Thring, R. H. 1981. "Gasoline Engine Combustion – Turbulence and the Combustion Chamber," SAE Paper 810017.
- Thring, R. H. 1989. "Homogeneous-Charge Compression-Ignition Engines," SAE Paper 892068.
- Underwood, A. F. 1957. "The GMR 4-4 'Hyprex' Engine – A Concept of the Free-Piston Engine for Automotive Use," SAE Paper 570032.
- Van Blarigan, P., and Green R. 1995. "NO_x Emission Data Verified in a Hydrogen Fueled Engine," Combustion Research Facility News," vol.17, no.4, January/February.
- Williams, Robert. January 1996. "Fuel Decarbonization for Fuel Cell Applications and Sequestration of the Separated CO₂," PU/CEES Report No. 295.

DEVELOPMENT OF LOW-COST HYDROGEN SENSORS

Robert J. Lauf
Oak Ridge National Laboratory
Oak Ridge, TN 37831-6085

Carlton Salter and R. D. Smith II
DCH Technology
Valencia, CA 91355

Abstract

We describe ongoing research aimed at understanding and improving the speed and reproducibility of our resistive hydrogen sensor, along with complementary efforts in manufacturability and further design improvements. Maskworks were designed to allow for the printing and firing of multi-sensor layouts (15 per substrate) and a large batch of these sensors was produced using standard thick-film manufacturing lines. Piece-to-piece variations of both the as-made resistance and the response of these sensors to hydrogen were within acceptable tolerances, and the sensor design has now been released for commercial prototyping. Automated testing has begun in order to develop long-term performance data. Dynamic response of selected sensors was measured before and after exposures to methane, hydrogen sulfide, and carbon monoxide, in order to assess the effects of interference gases and surface poisoning. As expected, H₂S degrades the sensor somewhat, whereas CH₄ and CO do not create significant interference when air is present.

Introduction

The goal of the program is to develop rugged, reliable, and cost-effective thick-film resistive sensors in order to encourage widespread use within a developing National hydrogen infrastructure. This project supports that goal by continuing the development

of optimized materials and designs while maintaining good manufacturability by conventional processes. Performance testing under cyclic conditions provides data on speed and sensitivity that will define appropriate applications and guide the engineering design of sensor packages and electronics. Also, understanding issues associated with cross-sensitivity, contamination, and poisoning will help us to develop strategies to mitigate these effects and improve sensor reliability and lifetime.

Our resistive hydrogen sensor (Hoffheins 1995) was designed for conventional thick-film manufacturing techniques. The sensor uses four Pd-containing resistors in a Wheatstone bridge arrangement. Two of the resistors are exposed to the atmosphere and when hydrogen is present, H₂ dissociates on the surfaces of these uncovered Pd resistors and atomic H diffuses into the Pd. The resulting increase in the electrical resistance of the Pd (Lewis 1967, Barton 1963) is measured by the shift in the bridge voltage. The other two Pd resistors are covered by a dense hermetic dielectric film, thereby forming reference resistors to eliminate the effect of temperature fluctuations (the temperature coefficient of resistivity of Pd is $\sim 3 \times 10^{-3}/^{\circ}\text{C}$).

The sensor is fabricated by screen printing three distinct materials on an alumina substrate. The Pd resistors are DuPont Conductor Composition 12345-67A fired at 1000°C; solderable pads at the junction points are DuPont Conductor Composition 4093 fired at 900°C; the hermetic passivation layer covering the reference Pd resistors is DuPont Dielectric Composition 5704 fired at 850°C. All firings are done in air using the manufacturer's recommended temperature profile.

Experimental Activities

Manufacturing Scaleup and Evaluation

During the early stages of development, experimental sensors were made by printing them individually on standard 1" x 1" substrates, using a small benchtop screen printer. These samples were adequate for evaluating the basic design, but the next step toward a commercially viable product was to make a large number of identical sensors, using commercial equipment, for statistical evaluation and long-term testing. A prototype batch was fabricated at DuPont (Research Triangle Park, NC) using perforated substrates designed to accommodate 15 sensors, which are snapped apart after firing (Figure 1). An initial run of 420 sensors was made using this setup. The Pd metallizations were 10 mil wide with 10 mil spacing, giving each of the four resistors a nominal resistance of ~ 100 ohms. Profilometry data on the fired sensors indicated the average film thickness of the Pd metallization was about 4-6 μm .

Characterization and testing of these sensors included analysis of the piece-to-piece variation in as-fired resistances of the individual resistors. The bridge resistances showed better than $\pm 5\%$ repeatability of resistances within a substrate and among substrates. The consistency is more than adequate. Limited testing of sensors exposed to hydrogen shows consistent response from sensor to sensor.

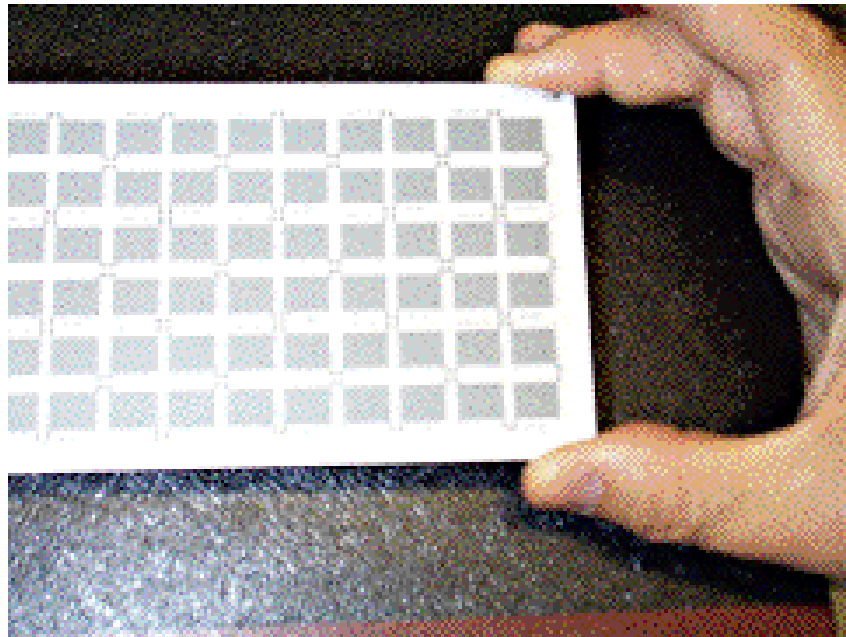


Figure 1 - Multiple Sensor Layout, 15 per Substrate

Based on the good reproducibility of the multisensor layout, a prototype design has been released for a short commercial manufacturing run. This new design uses 7.5 mil lines at 7.5 mil spacing. The bridge circuit is 1/2" x 1/2" and will be fabricated on a 1/2" x 1" substrate, with some additional electronics (including temperature sensing circuitry) fabricated on the other half of the substrate.

Development of More Rugged Designs

In previous work, sensors exposed to very harsh conditions (up to 30% hydrogen at temperatures up to 200°C) exhibited severe delamination of the exposed Pd metallization from the substrate as shown in Figure 2. We have begun to explore two alternate methods (U. S. Patent Pending) for mitigating this effect with minimal added cost.

The first approach is to extend the pattern of the passivation layer so that it completely covers the reference Pd resistors and also extends in thin bands, crossing the sensing resistors at selected points, Figure 3. This is intended to help hold them down to the substrate while leaving most of their area exposed to the atmosphere. The advantage of this approach is that it requires only a modification of the maskwork, with no added printing or firing steps.

The second approach is to completely cover the sensing resistors with a dielectric layer that is substantially continuous but porous enough that the underlying metallization is accessible to the atmosphere. This layer must obviously be different from the hydrogen-impermeable layer covering the reference resistors, so one more print step is added;

however, the porous dielectric can be formulated to be cofirable with the dense dielectric so that no added firing step is needed. To test this idea, we added 10, 20, and 30%

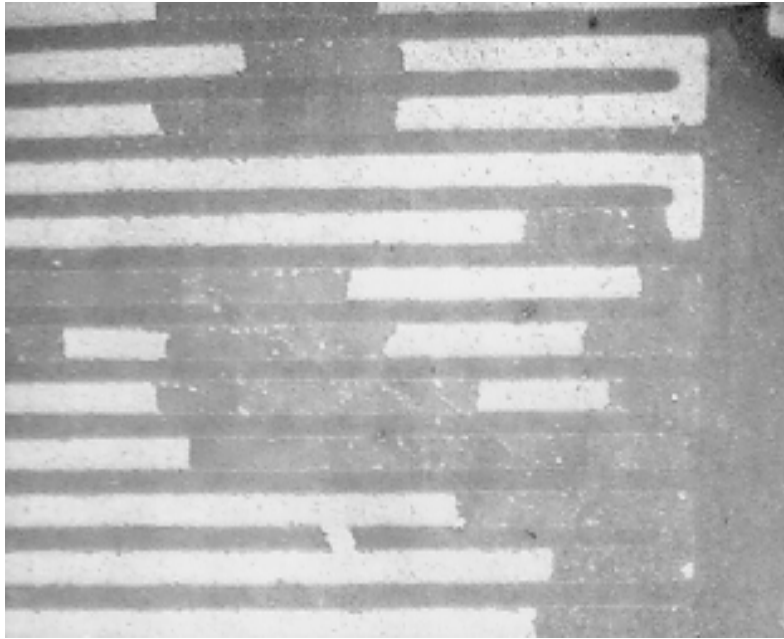


Figure 2 - Failure of Pd Metallization Under Harsh Conditions

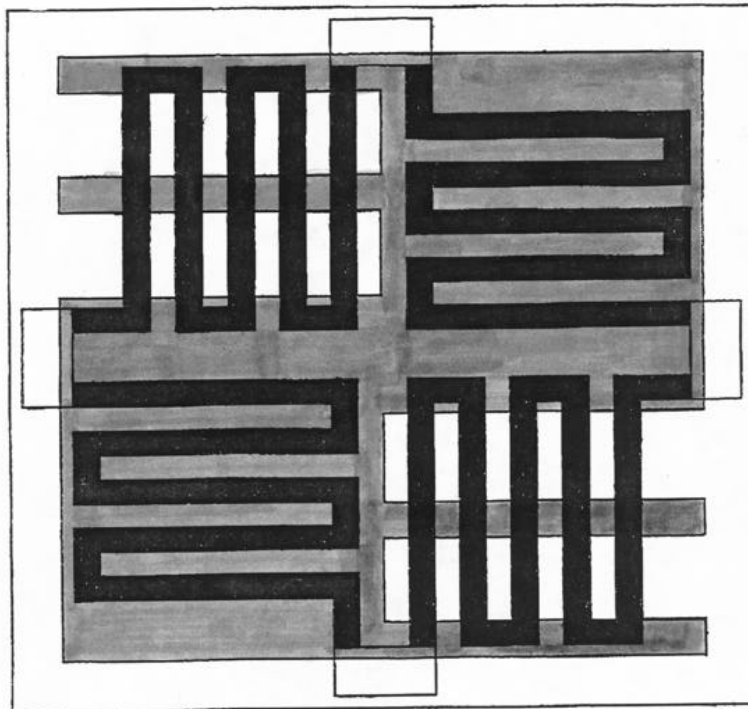
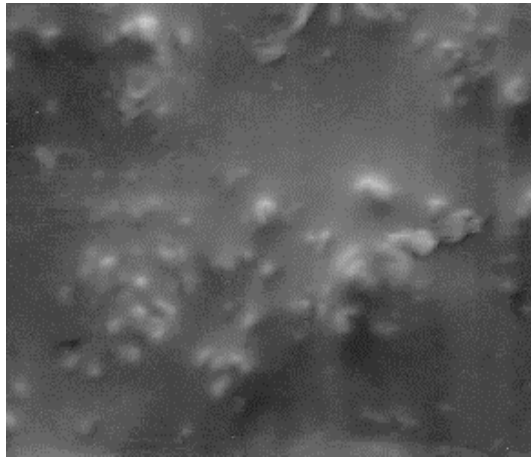
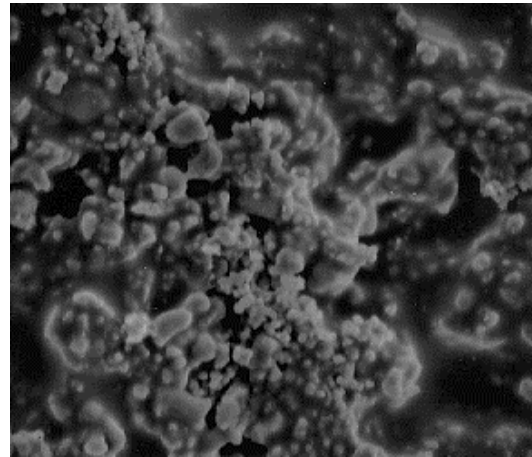


Figure 3 - Modified Sensor Design with Added Support Structures

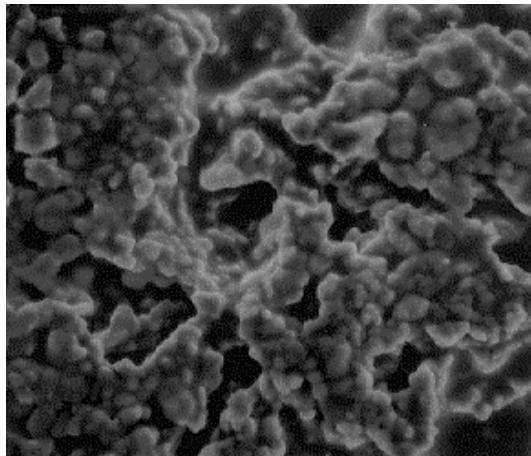
alumina powder (Baikowski CR-6) to the DuPont 5704 dielectric composition, thinning as needed with DuPont 8672 thinner. These materials were printed onto bare alumina substrates and fired at 850°C in air. The fired layers adhered well to the substrates, and as expected they had significant porosity, which increased with increasing alumina content as shown in Figure 4. Current plans call for fabricating some sensors using these modified designs and materials, and determining the effect of the added structures on response time.



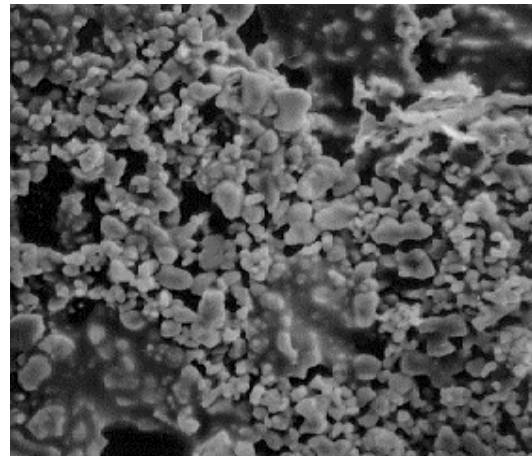
5704



5704 + 20% Al₂O₃



5704 + 10% Al₂O₃



5704 + 30% Al₂O₃

Figure 4 - Fired Dielectric with Alumina Additions (SEM 10,000X)

Testing and Characterization

Two types of testing have been started: Life testing and repeatability testing. Prior to use, the sensors must be “awakened”. These processes and results are summarized below.

The wake-up procedure is to expose a sensor to a gas mixture of 4% hydrogen and 96% argon for an hour. Prior to wake-up, a sensor will not respond to hydrogen. The wake-up process reduces a deep oxide layer that is picked up during manufacture (the firing process).

Awakened sensors were first exposed to some limited life testing. The test equipment periodically and automatically exposes groups of sensors to different levels of hydrogen. The levels are 0%, 0.4%, and 2%. The balance of the gas is dry air. Three channels, each with different exposure periodicity, are used. Initially, a group of sensors are exposed every four hours, 24 hours a day, for a week. If the sensors are stable after that period, then they are moved to a second channel in which they are exposed once a week for a month. Then they are moved to the third channel that exposes them only once a month. The sensors will stay in the latter channel for at least a year. To date, an initial batch of sensors have passed channels one and two and are in the third channel. The responses of the sensors are stable.

All working gas sensors must be able to accommodate various impurities and interference gases that will always be present in the environment. Knowing the effects of likely interference gases (especially organics, CO, and moisture) and surface poisons (particularly sulfur) will allow us to understand and predict how the sensors will behave in real applications and to design protective strategies when needed. Dynamic response of selected sensors (to 2% hydrogen) was measured before and after exposures to CH₄, H₂S, and CO, in order to assess the effects of these species.

The response of a sensor to 2% hydrogen, before and after exposure to 10 ppm H₂S (in nitrogen), Figure 5, shows that H₂S degrades the sensor. The observed slowing of the dynamic response does not recover with subsequent exposures to either air or hydrogen. We attribute this to irreversible poisoning of the catalytic properties of the Pd surface by sulfur.

The dynamic response to 2% H₂ for a sensor as received, after 1 hr in air, and after 1 hr in 100 ppm CH₄ (in nitrogen) is shown in Figure 6. It can be seen that CH₄ has no significant effect on rise time in 2% H₂.

Figure 7 shows the response of the sensor in the as-received condition and after a 1 minute exposure to a high concentration of CO, after which the rise time in 2% H₂ went from less than a minute to about four minutes. Following a brief exposure to air (at about 6 minutes into the run), the dynamic response to H₂ returned to its original behavior. We attribute these results to high surface coverage of CO on the Pd, which slows the uptake of hydrogen but does not prevent it from ultimately reaching its equilibrium value. A brief exposure to air removes the CO, possibly by oxidizing some of it to CO₂, after which the original rise time of the sensor is restored. (A similar, but somewhat less dramatic effect is seen after a purge with nitrogen, suggesting that adsorbed CO is fairly readily removed from the Pd surface.) This implies that for a safety monitor intended to detect concentrations of H₂ in air, reasonable concentrations of CO will not interfere or slow the response.

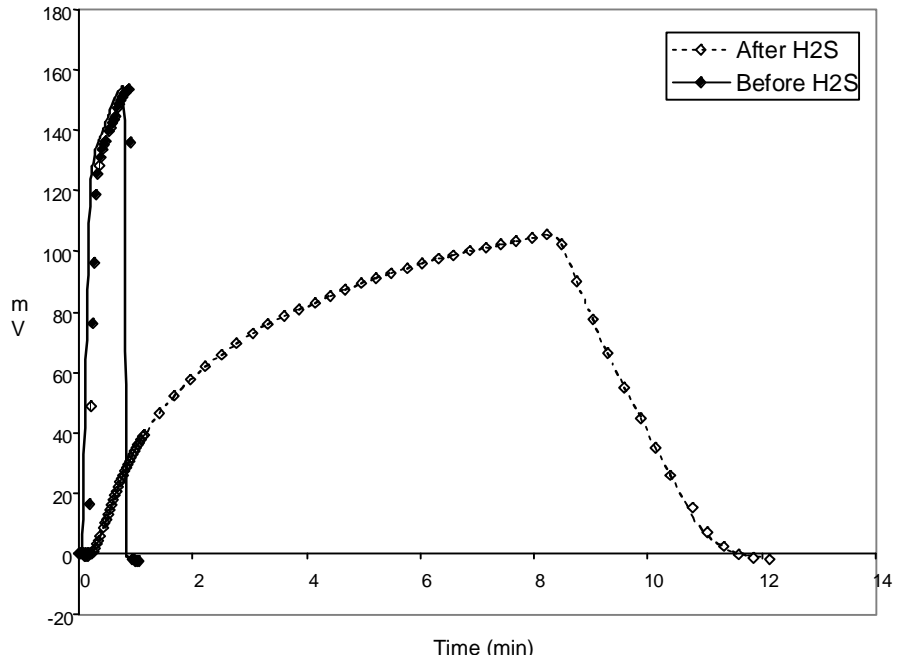


Figure 5 – Response to 2% H₂ Before and After Exposure to 10 ppm H₂S

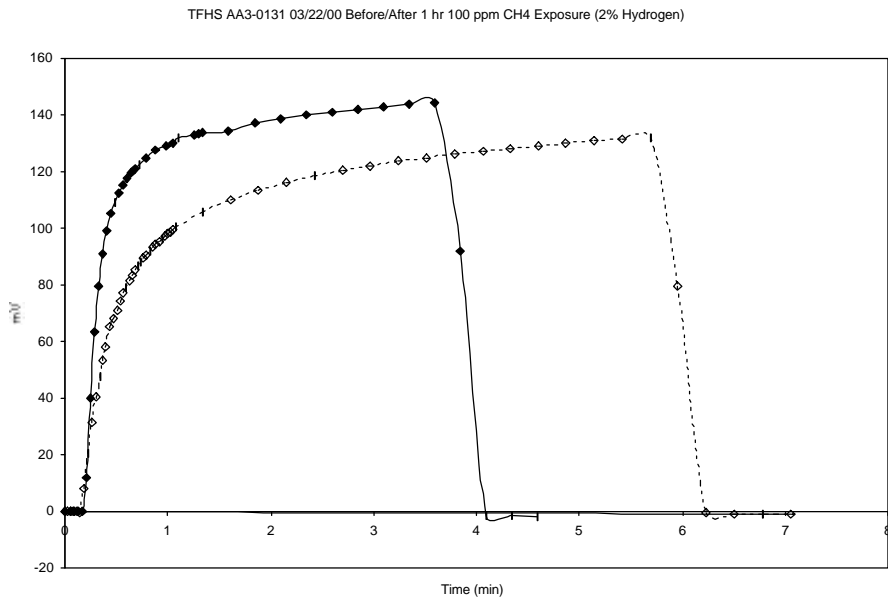


Figure 6 – Response Before and After Exposure to 100 ppm CH₄

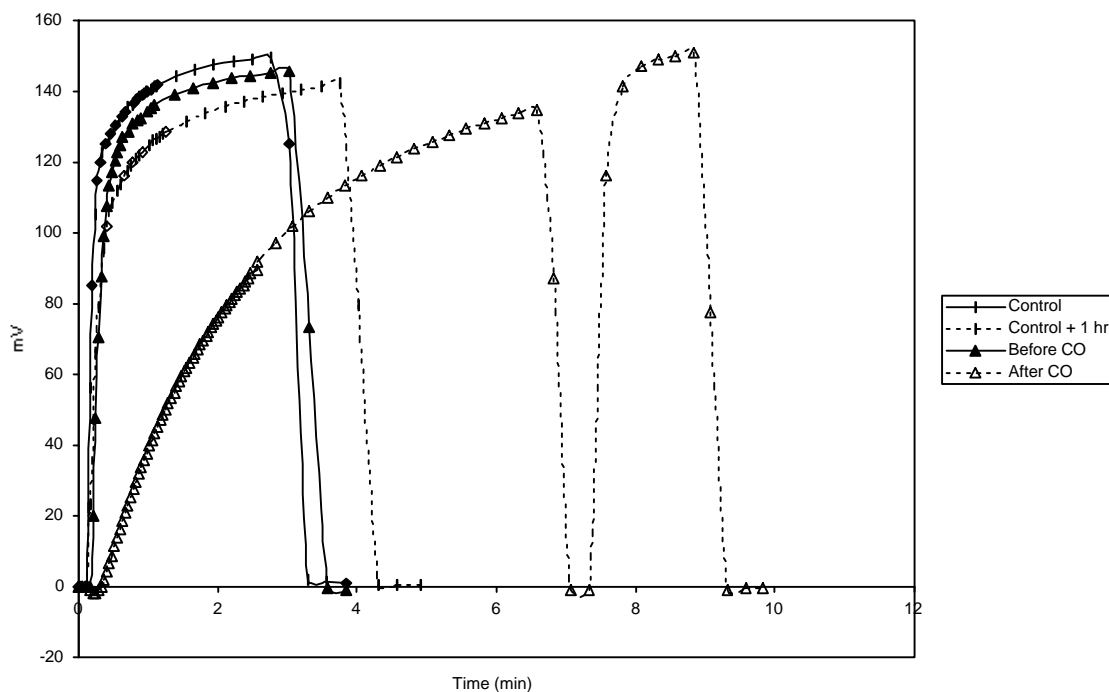


Figure 7 – Response After Exposure to CO and After 1 min in Air

SEM analysis was done on selected samples before and after exposures. XPS analysis on the as-fired sensor detected an oxygen-rich layer, as well as significant amounts of carbon, much of which was removed by the "wake-up" process. This indicates that the hydrogen may be performing a cleaning mechanism on the Pd surface (and would also explain the cyclic testing data in which we observed that the response time only degrades after a prolonged period without hydrogen exposure). The SEM photographs themselves reveal a subtle change in morphology, notably an edge rounding effect that is most likely due to the volume expansion of the Pd after H absorption. The change in specular properties has also been attributed to this expansion (J. R. Pitts, personal communication), although the removal of a native palladium oxide layer could also play a role in the color change (dark gray to silver) observed upon first exposure to H₂.

Market Analysis and Commercialization

DCH Technology continues to conduct economic analyses in collaboration with end users in several fields.

For the automotive market, low cost is important as well as rapid response. Strategies are being developed for heating the sensor in order to help meet performance specifications that include very low ambient temperatures. It is important to

emphasize that the automotive industry needs a significantly faster response. To provide this, with any Pd-based hydrogen sensor, the dynamics of the surface under exposure must be understood. This is not just a good thing to do; it is necessary and if this isn't done, the Nation will not have an acceptable sensor for hydrogen cars. For personal safety monitors (badge) or distributed area sensors (wireless) DCH has designed appropriate electronics and packaging for battery-powered applications. Second-generation electronics are in conceptual design. For battery boxes, long-term reliability is a key performance attribute because of limited accessibility of many installations. DCH will institute alpha testing with battery box customers using “badge” electronics.

Conclusions

1. The thick-film hydrogen sensor is inherently manufacturable by standard processes. Sensors made on standard production equipment using multiple-sensor layout (15 per substrate) are uniform and reproducible.
2. Rise time of the sensor output (in response to 2% hydrogen) is less than 1 minute at ambient temperature.
3. Carbon monoxide slows the response in the absence of air, but in the presence of air CO does not appear to have an effect on response time. Methane has no significant effect on response to hydrogen.
4. Hydrogen sulfide greatly degrades the performance of the sensor, most notably by increasing the response time. This is attributed to poisoning of the surface catalytic properties of the Pd by sulfur.

Future Work

All hydrogen-specific sensors that rely on the unique properties of Pd share many issues in common. Among these are:

Chemisorbed oxygen or the formation of a PdO film on the surface after long times in ambient air can slow the response when hydrogen is first encountered.

The processes that occur during first exposure to hydrogen are sensitive to small changes in the catalytic properties of the Pd surface. The role of processing variables, contaminants, etc. must be better understood.

Mechanical stability of the films will be influenced by volumetric changes during repeated exposures to moderate hydrogen concentrations or during a single exposure to a high concentration of hydrogen.

Kinetics of hydride formation and decomposition will affect the observed time constants whenever hydrogen concentrations are high enough to create small amounts of hydride phases.

Our plan is to continue our scientific studies of the foregoing issues in support of the ongoing commercialization activities at DCH Technology. Specifically, we plan to conduct *in situ* X-ray diffraction on the sensors, during exposures to various concentrations of hydrogen at various temperatures. This will help to elucidate the degree to which hydride formation occurs, its effect on stresses in the Pd film, and the speed with which the hydride decomposes. We also hope to study the existence of surface oxides and their removal during hydrogen exposures. Last, we plan to continue surface analyses of samples after exposure to interference gases, contaminants, and poisons.

Acknowledgments

Roland Pitts at NREL has graciously made space and equipment available for R. D. Smith to perform testing and characterization. John Felten provided invaluable assistance in the prototype run at DuPont and with ongoing commercialization/manufacturing advice. Dixie Barker provided SEM photographs at ORNL and Amy Swartzlander did the SEM/Auger work at NREL.

Oak Ridge National Laboratory is operated by UT-Battelle, LLC under contract DE-AC05-00OR22725 with the U. S. Department of Energy.

References

Barton, J. C., F. A. Lewis, and I. Woodward 1963, "Hysteresis of the Relationships between Electrical Resistance and the Hydrogen Content of Palladium." *Trans. Faraday Soc.* 59:1201-1208

Felten, J. J. 1994. "Palladium Thick-Film Conductor" U. S. Patent 5,338,708.

Hoffheins, B. S., and R. J. Lauf 1995. "Thick Film Hydrogen Sensor" U. S. Patent 5,451,920.

Lewis, F. A. 1967. *The Palladium Hydrogen System*. New York: Academic Press.

INTERFACIAL STABILITY OF THIN FILM HYDROGEN SENSORS

J. R. Pitts, P. Liu, S. -H. Lee, and C. E. Tracy
National Renewable Energy Laboratory
1617 Cole Blvd.
Golden, CO 80401

R. D. Smith and C. Salter
DCH Technology
27811 Ave. Hopkins, Unit 6
Valencia, CA 91355

Abstract

The real and perceived hazards of hydrogen fuel use, its production, and storage require extensive safety precautions and codes to be put in place before any serious movement can be made towards a hydrogen based energy future. Currently, commercial hydrogen detectors are not useful for widespread use, particularly in transportation, because they are too bulky, expensive, and dangerous. Recent work sponsored by the DOE Hydrogen Program has developed promising technologies for satisfying the future demands. Sensors that exhibit physical or optical changes when exposed to hydrogen have been fabricated and tested, and promise to provide inexpensive hydrogen detection. For example, there are thick film and thin film metallic sensors that exhibit a conductivity change when hydrogen adsorbs on the surface and is incorporated into the lattice. There are thin film sensors that are deposited as a part of a field-effect transistor, where accumulation of atomic hydrogen at the metal/insulator interface results in a change of response from the circuit. Finally, there are chemochromic sensors, where reaction of thin films with hydrogen gas results in an optical change that can be sensed by a probe beam of light. All of these sensors have the potential for degradation in their performance over time due either to mechanisms that are inherent in their construction, a result of their cyclic interaction with hydrogen, or contamination from impurities in the environments in which they will be used. Research to study those issues in order to rank their importance to the various sensor concepts, to determine the relevant mechanisms, and to mitigate these factors is reported here.

Introduction

The ability to detect hydrogen gas leaks economically and with inherent safety is an important technology that could facilitate commercial acceptance of hydrogen fuel in various applications. In particular, hydrogen-fueled passenger vehicles will require hydrogen leak detectors to signal the activation of safety devices such as shutoff valves, ventilating fans, and alarms. Such detectors may be required in several locations within a vehicle—wherever a leak could pose a safety hazard. It is therefore important that the detectors be very economical. This paper reports on progress in the development of low-cost hydrogen detectors intended to meet the needs of a hydrogen-fueled passenger vehicle and then treats stability issues in optical sensors specifically.

There are four candidate sensor configurations that look particularly attractive for the transportation applications. These are termed the HFET, the Thick Film, and the Thin Film, and the Fiber-Optic sensors. The HFET construction uses a thin film of Pd as the metal contact controlling the device. The presence of hydrogen results in the migration of atomic hydrogen to the interface between the metal film and the insulator, which results in a change in the output of the device that is scaled to the hydrogen concentration. The Thick Film device uses thick film Pd alloy paste to form a four resistor network (Wheatstone bridge) on a ceramic substrate. Two opposed resistors are covered to isolate them from the ambient atmosphere. The exposure of the uncovered resistors to hydrogen results in a change in resistivity of the thick film material and a shift in the balance point of the bridge, which can be scaled to the hydrogen concentration. The thin film device is equivalent in design to the thick film, only much thinner films (typically vacuum deposited) are used as the resistors.

The Fiber-Optic sensor consists of coatings at the end of an optical fiber that sense the presence of hydrogen in air. When the coating reacts with the hydrogen, its optical properties are changed. Light from a central electro-optic control unit is projected down the optical fiber where it is either reflected from the sensor coating back to central optical detector, or is transmitted to another fiber leading to the central optical detector. A change in the reflected or transmitted intensity indicates the presence of hydrogen. The fiber-optic detector offers inherent safety by removing all electrical power from the test sites and reduces signal-processing problems by minimizing electromagnetic interference. Critical detector performance requirements (for all four configurations) include high selectivity, response speed, and durability as well as potential for low-cost fabrication.

Fiber optic sensors have been made in a variety of configurations, all using one or more thin films coating the end of the cable. Butler (1991, 1994) suggested using a thin film of Pd as a mirror on the end of a fiber optic cable. Garcia (1996) and Mandelis (1998) describe a more sensitive (and much more complex) method of sensing hydrogen optically. They use a diode laser and beam splitters to illuminate reference flats in a gas flow chamber. One flat is coated with Pd, while the other is coated with Al. Reaction of hydrogen at concentrations above 0.2% in nitrogen is registered by the optical changes of the Pd film.

Ito (1984) originally proposed using the palladium-catalyzed reaction of amorphous tungsten oxide with hydrogen in a fiber-optic hydrogen detector. The reaction causes partial reduction of the tungsten oxide and introduces a strong optical-absorption band near 800 nm. The increase in

absorption reduces the intensity of the light beam reflected by the coated optical fiber. We found this sensor design to be adequately sensitive, but too slow for the intended use.

A different sensor design using a surface-plasmon resonance (SPR) configuration was also evaluated (Raether, 1988 and Chadwick, 1993). Chemochromic materials, such as tungsten oxide and certain Lanthanide hydrides (Griessen, 1997) were used in thin film stacks on a sensor head at the end of an optical fiber (Benson, 1998). A layer of silver was deposited first, in which the surface plasmon was generated. The chemochromic layer was deposited upon the silver, followed by a thin layer of palladium, which acted as the hydrogen dissociation catalyst. When hydrogen comes in contact with the sensor head, small amounts of atomic hydrogen change the optical properties of the chemochromic layer. The SPR shifts in response to very subtle changes in the refractive index of the coating and is detected as a change in intensity of the reflected beam of light. This shift can be monitored to provide a faster response than was evident in the first tungsten oxide sensors.

Yet another variation of this sensor design uses Pd deposits on the sides of the fiber optic cable, after the jacketing material in a section of the fiber is removed (Tabib-Azar, 1999). In this configuration the Pd interacts with the evanescent field as the light beam propagates down the fiber via total internal reflection. When exposed to hydrogen, the complex index of refraction of the Pd film changes, affecting the transmission of light down the fiber. Detection of variations of light intensity at the end of the fiber signals changes in the Pd film due to the incorporation of hydrogen. This construction allows multiple sensors to be deposited along a single strand of fiber-optic cable. However, to allow this concept to identify the sensing station that has detected hydrogen, fiber optic Bragg gratings (FBGs) must be etched into the fiber at each station (Sutapun, 1999). The individual gratings are tuned to specific wavelengths. Then, they are coated with Pd. Hydrogen incorporated into the Pd causes an expansion of the film that results in a stretch of the fiber and an alteration in the spacing of the FBG. The FBG acts as a strain gage and shows a linear response in the shift in Bragg wavelength with hydrogen concentration over a range from 0.3% to 1.8% hydrogen in nitrogen. Thus, multiplexed hydrogen sensors may be fabricated on a single fiber.

Key Issues

There are a series of key issues for any hydrogen detector, if it is to gain wide acceptance for use within the hydrogen infrastructure (production, storage, transportation, and utilization).

Performance – sensors must respond to the presence of hydrogen well before the explosive limit (4% H₂ in air) is reached. This requirement dictates that a premium is placed on detecting small quantities of hydrogen in the ambient atmosphere (prefer detection limit of 0.5% or better). The sensor must also respond quickly (prefer response time of 1 second or less), so that corrective action or evacuation can occur before the explosive limit is reached. Fast response times are also desired for diagnostic study of hydrogen transportation systems (vehicles, electrolyzers, storage containers, etc.).

Lifetime – sensors must have a usable lifetime consistent with the application for which it is intended. For transportation applications that must be at least the time between scheduled

maintenance (minimum 6 months, prefer 1 year or more). In this respect the sensor must be operational with no active effort for a minimum of that period, while exposed to ambient conditions.

Reliability – sensors must indicate the presence of hydrogen reliably. That is, they must perform to some specification, each and every time they are exposed to hydrogen over the lifetime of the sensor. Response must not drift outside acceptable limits over that lifetime. Functionality of the sensors should be easily verifiable, but there will be a low tolerance for false alarms. Sensors should be able to survive multiple excursions to hydrogen concentrations above the explosive limit without damage.

Cost – sensors and their controllers must be reasonably priced, so that their inclusion within the hydrogen infrastructure can be ubiquitous. A worthy goal is \$5 per sensor and \$30 per controller. As long as performance, lifetime and reliability are not compromised, less expensive is better.

The common link in all of the hydrogen sensor concepts is that they all use Pd as a catalyst, because of its superior properties among the noble and semi-noble metals for dissociating and transporting hydrogen. Molecular hydrogen dissociates on the Pd surface, and atomic hydrogen diffuses rapidly through the film. Physical or optical changes in the Pd film itself, or in adjacent films or interfaces, are used to detect the presence of hydrogen. All of the current sensor concepts share Pd as the catalyst. Therefore, we have chosen to focus on stability issues related to ambient exposure of Pd and cyclic exposure of Pd to hydrogen. Additional work reported here has focused upon performance issues related to fiber-optic sensors (response time, reliability, and lifetime).

Experimental

Thin films of the active layers of the optical sensors were fabricated by standard techniques of vacuum deposition. Thermal evaporation was carried out on a Varian Model 3118 evaporator. Sputtered films were prepared on a Leybold magnetron sputter coater, and plasma enhanced chemical vapor deposition was done on a Plasma Technology system. Thick film sensors were prepared either at Oak Ridge National Laboratory or at DuPont by the thermal decomposition of metalorganic pastes.

Performance testing of the completed articles was carried out at the National Renewable Energy Laboratory (NREL) or at DCH Technology (Valencia, CA). Analytical investigations of failed articles were carried out in the Device Characterization Laboratory at NREL.

The experimental set-up for testing of thick film components is detailed by the photographs in Fig. 1. The apparatus consists of a cylindrical Plexiglas test enclosure, a regulated power supply, and a Kiethley electrometer to measure imbalances in the Wheatstone bridge. A typical experiment would consist of balancing the bridge under an ambient flow of synthetic air (dry). Airflow is turned off, then a hydrogen in nitrogen mixture is admitted into the test enclosure. Changes in the resistivity of the exposed Pd resistors upon admission of the hydrogen mixtures were then measured as an offset in the voltage across the bridge.

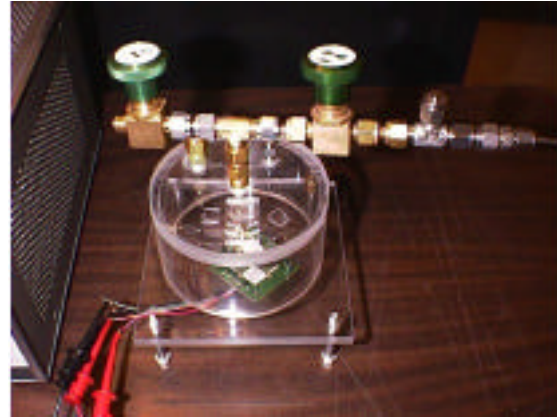
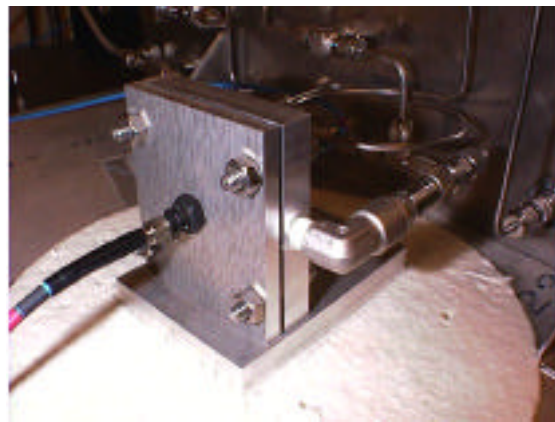


Figure 1. Test Apparatus for Thick Film Hydrogen Sensors.

For the fiber-optic sensor test station, we constructed a gas flow manifold that could be switched automatically from gas mixtures containing hydrogen to air. Switching is controlled by the same computer used to acquire optical spectra. The manifold fed the test gas stream into a test chamber, constructed so that the dead volume was minimal (0.1 cm^3). In addition the chamber was constructed so that we could measure either spectral transmittance or reflectance. The spectrometer used for the optical measurements was an Ocean Optics S2000 spectrometer, measuring flux from 300 nm to 800 nm. Either fiber-optic tips or small glass slides coated with the active layers could be used as test articles. Glass slides were often used to simplify deposition and analysis after testing. The details of this measurement system appear in Fig. 2 and Fig. 3.

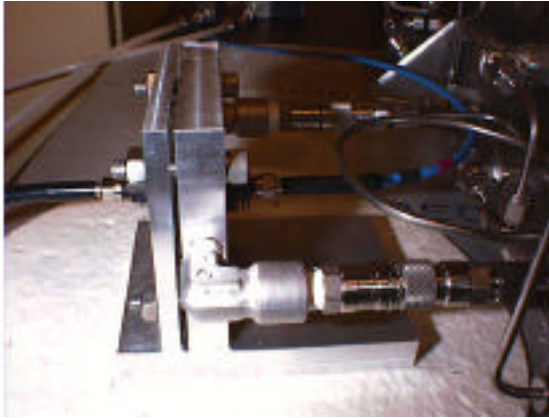


Manifold and Test Station

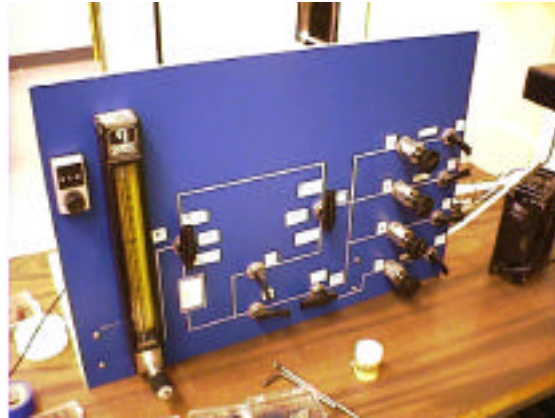


Test Chamber

Figure 2. Fiber-Optic Sensor Test Station



Test Chamber, Transmission Mode



Gas Manifold

Figure 3. Transmission Mode and Gas Manifold Details

Analytical work on functional and failed specimens was carried out with an array of tools available in the Characterization Laboratories at NREL. These included optical microscopy with Nomarski phase contrast (Neophot 21), electron microscopy (JEOL JSM-5800 and JSM-6320), Auger electron spectroscopy (Physical Electronics 670 Auger Nanoprobe), and X-ray photoelectron spectroscopy (Physical Electronics 5600 ESCA System).

Results

Research activities covered in this report were conducted in the second half of FY 1999 and the first half of FY 2000. These activities consisted of diagnostics and analysis of state-of-the art sensor materials. We quickly determined that the prior optical sensor configurations were unstable to repeated exposures to hydrogen. Signal response was slow, recovery was slow, and repeatability in response was poor. Furthermore, exposure of these sensors to concentrations greater than 2% hydrogen in nitrogen resulted in permanent damage to the Pd catalyst. Adhesion of the hydride sensor materials (YH_2 and GdH_2) to both glass substrates and polymer fiber faces was poor. Cyclic exposure to hydrogen resulted in severe cracking of the thin films and eventual delamination of the entire structure from the substrate material. New, improved materials were needed.

Work on the resistive sensor elements has shown that these sensors exhibit a decrease in response time after extended periods in air with no hydrogen, or may show no response for low concentrations of hydrogen in air. It is possible to restore the performance of these sensors by exposing them to hydrogen concentrations exceeding 2% in air for periods in excess of 2 h. There appears to be a surface reaction that inhibits the dissociation of the hydrogen molecule on the surface, or its propagation into the film.

Having determined the most important issues for durability and reliability in the field for the current sensor concepts, it appears that the relevant issues, broken down by sensor type are:

Optical Thin Films

Primary issue is durability and repeatability of response for the chemochromic layers at ambient exposure conditions.

Stability of the hydrogen dissociation catalyst (Pd) to cyclic exposures to hydrogen.

Fouling of the catalyst due to impurities and pollutants in or reaction with the air.

Thick Film and Thin Film Resistive

Stability of the Pd films after long (days) exposures in ambient air.

Stability of the films to repeated exposures to hydrogen, or excessive concentration of hydrogen once.

Fouling of the film surface due to impurities and pollutants in or reaction with the air.

Thin Film Electronic

Fouling of the film (Pd) surface due to impurities and pollutants in or reaction with the air.

We believe that we have a fundamental understanding of the first two issues for optical thin films and proceeded with work to mitigate those issues. We also worked on the issue of fouling of the Pd surface by pollutants and have proposals for methods of mitigation.

Three new material configurations were created to solve the problems associated with the previous optical sensors. A high sensitivity configuration exhibits superior performance properties. It displays the best sensitivity and response times of any material evaluated to date, at least down to hydrogen concentrations of 200 ppm. Typical response curves are shown in Fig. 4, and we have measured response times of 15 seconds at concentrations of 0.1%. While its high sensitivity and fast response time make this the best candidate as a safety device in such applications as transportation, further work is needed to address stability issues. However, it would function very well for applications where a new sensor is required for each test. The material is already the leading candidate for these applications, such as the detection of diffusible hydrogen in welds (Smith, 2000).

High Sensitivity Film Exposed to 1% Hydrogen

(02/10/00)

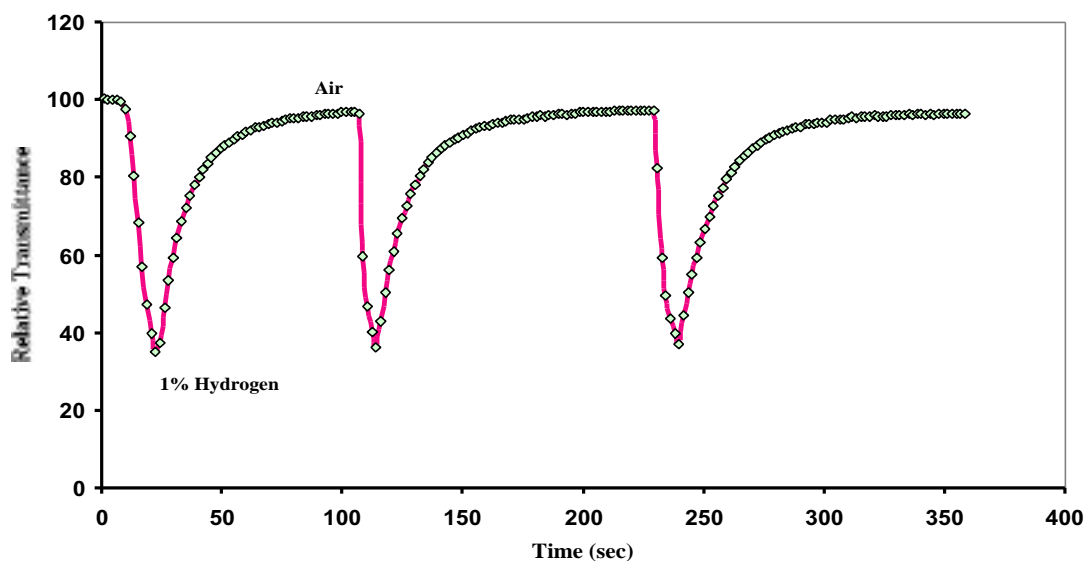


Figure 4. Cyclic Response of High Sensitivity Film to 1% Hydrogen in Nitrogen

The other two materials provide much enhanced performance (not quite as good as the high sensitivity material) and much enhanced reliability and lifetime. Examples of the performance over extended periods of time and many cycles of coloration and bleaching are shown in Fig. 5 (for Type 1 durable sensor) and in Fig. 6 (for a Type 2 durable sensor). Both of these films become more transparent with the addition of hydrogen and color as the hydrogen is removed. Some irreversible changes occur in the optical properties of the films with the first few cycles of hydrogen, but they remain stable thereafter. Both films become stable in response after a few cycles; however, long term drift in baseline is noted. This drift is the subject of further study.

Durable Sensor Type 1, Cycled in 4% Hydrogen

1/29/00

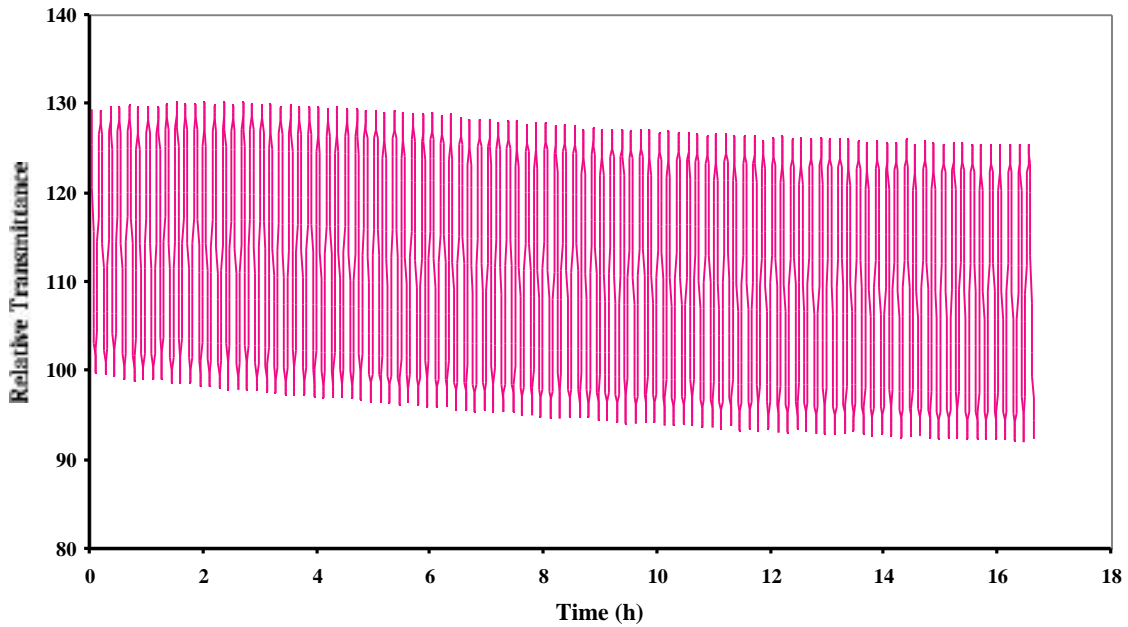


Figure 5. Type 1 Sensor Cycled Between 4% Hydrogen and Synthetic Air.

Durable Sensor Type 2, Cycled in 4% Hydrogen

2/13/00

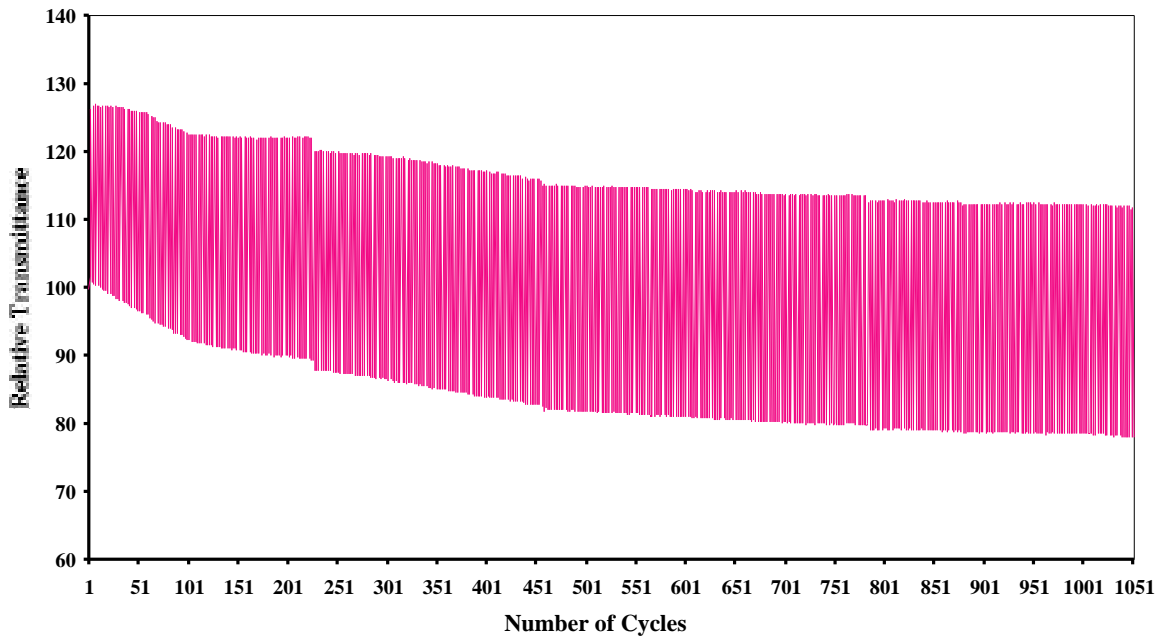


Figure 6. Type 2 Sensor Cycled Between 4% Hydrogen and Synthetic Air.

During the testing of these sensor elements, we observed that exposure to ambient versus synthetic air (even for relatively short periods of time) caused a loss of sensitivity. However, after a few cycles of exposure to hydrogen, sensitivity returned. We speculate that the active Pd surface sites involved in the dissociation of the hydrogen molecule become covered with contaminant species, such as hydrocarbons. These species occlude those sites from participation in the dissociation reaction and inhibit hydrogen transfer into and out of the films. Evidence obtained from X-ray Photoelectron Spectroscopy (XPS) and Auger Electron Spectroscopy (AES) support this speculation. Air exposure of the clean Pd surface results in the buildup of a monolayer of carbon bearing compounds. These compounds are easily removed by light ion bombardment or by less destructive techniques ex situ.

In order to study more carefully the role of contamination in air, we did a number of controlled experiments, where small concentrations of contaminant gases were allowed into the test chamber during a testing sequence. In this way we could examine the deterioration of the signal and see whether it would recover or would remain desensitized. In Fig. 7 the response of a Type 1 sensor is presented before and after exposure to carbon monoxide (CO). The contaminant dosing significantly slowed the response and recovery of the sensor.

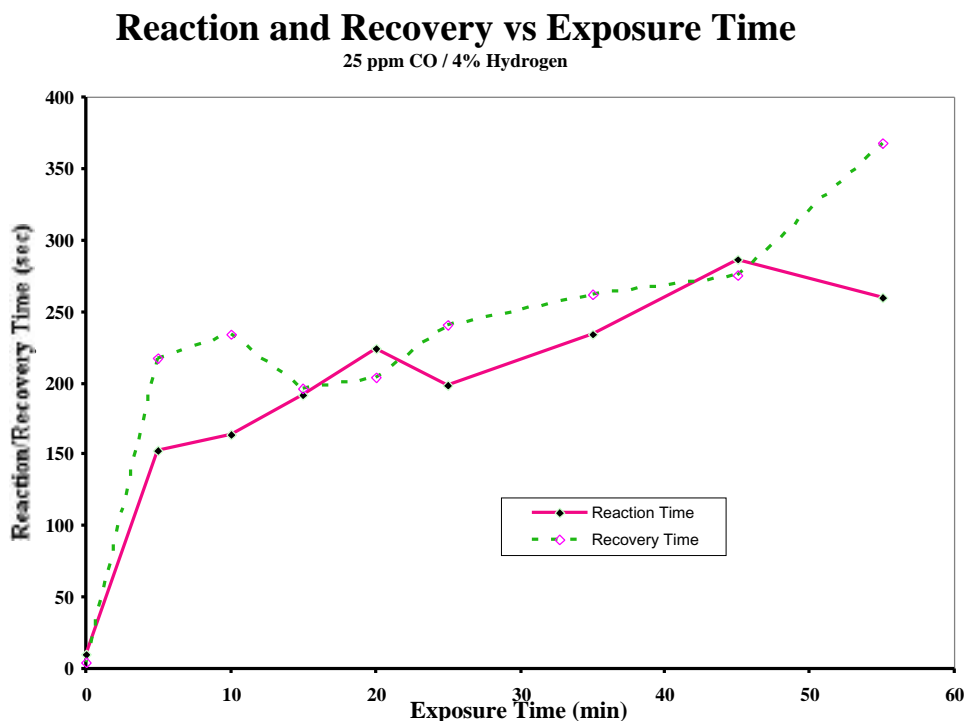


Figure 7. Effect of CO Adsorbed on Sensor Surface.

Similar experiments were performed using methane (CH₄) and hydrogen sulfide (H₂S) as the contaminant gases. Similar results were obtained, except the magnitude of the effect on the sensor varied dramatically for each contaminant gas. Figure 8 illustrates the effect from CH₄, and Fig. 9 illustrates the effect from H₂S.

Response and Recovery Time vs Exposure Time

100 ppm CH₄ / 4% Hydrogen

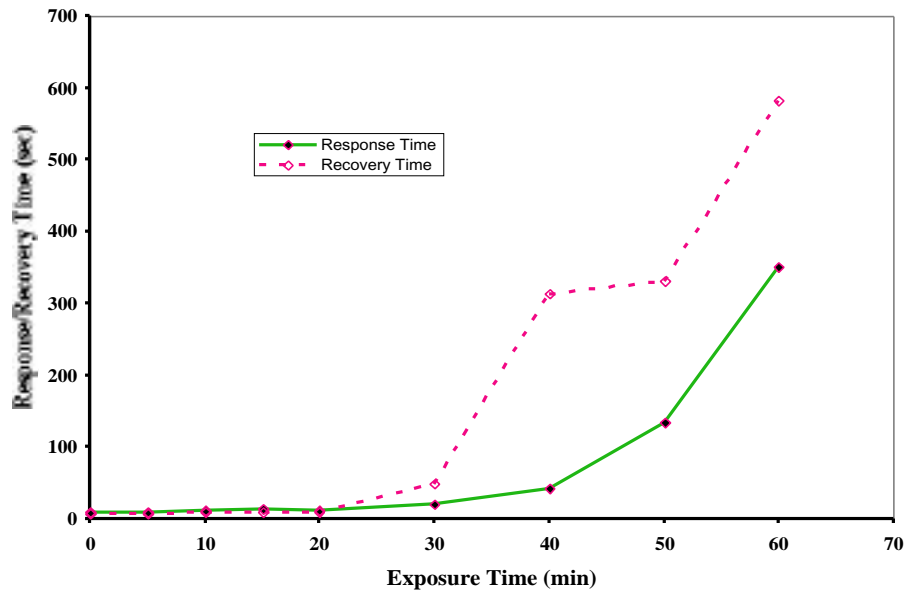


Figure 8. Effect of CH₄ Adsorption on Sensor Surface.

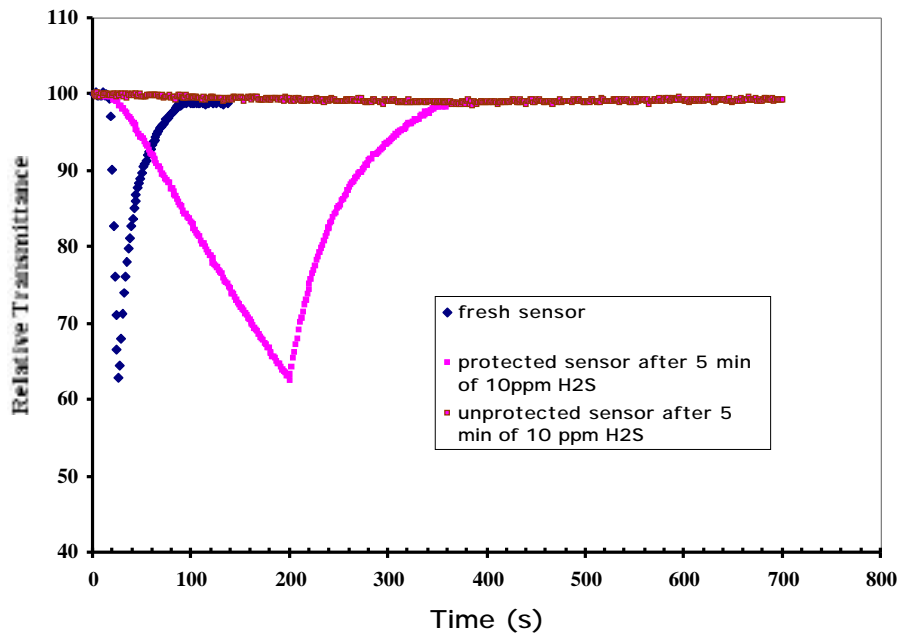


Figure 9. Effect of H₂S Adsorbed on Sensor Surface.

Both CH_4 and CO physisorb to the surface of the Pd so as to block the active sites for H_2 dissociation, as evidenced by the fact that the optical response of the sensor is significantly slowed by exposure to either of these gases. However, the sensor response is never killed, and exposing the sensor films to synthetic air for several hours is sufficient to restore the original response of the sensor. This indicates that the adsorption is weak enough to allow the pollutant molecules to exchange with N_2 and O_2 and diffuse away from the surface. The H_2S adsorption is very different. As is evident in Fig. 9, this molecule adsorbs onto the Pd surface and can completely block all of the active surface sites for the H_2 dissociation in 5 minutes. There is no recovery in clean air without extra measures to clean the H_2S off the surface. We conclude that the H_2S is chemisorbed to the Pd surface. This conclusion is consistent with much literature in the binding of sulfur bearing compounds to noble and semi-noble metal surfaces.

It is clear that for these sensors to survive for any significant period in ambient atmospheres contaminated with automobile or industrial emissions, the Pd surface must be protected in some way to prevent it from losing sensitivity. A simple option is to encase the sensor head within a canister of activated carbon. This is represented in a sketch of the sensor head package and electronic control unit in Fig. 10. Activated carbon is an efficient way to absorb polar molecules, thus removing most of the contaminants before they can approach the clean Pd surface. Less expensive and more effective means are needed for keeping the Pd surface active for H_2 dissociation.

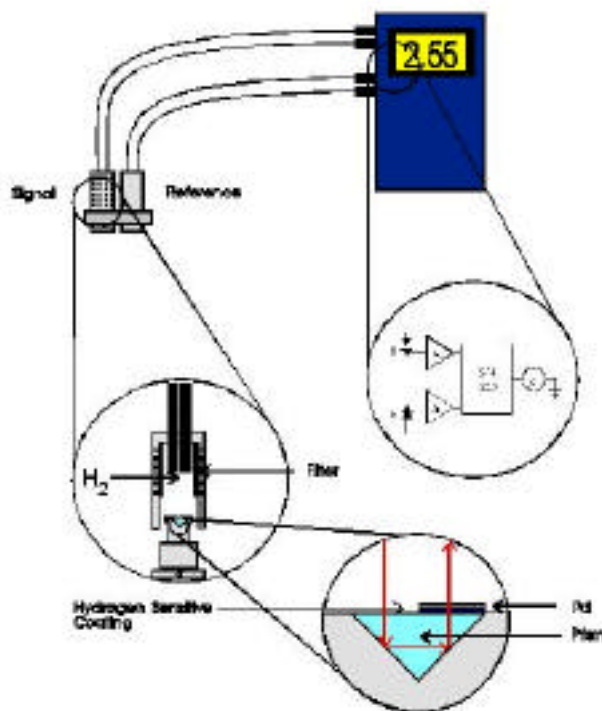


Figure 10. Schematic of Encased Sensor, Transmission Mode.

A final observation about the active Pd surface is that some experimental evidence obtained recently, as well as some investigations reported in the literature (Huang, 1999), suggest that at least of monolayer of PdO_x forms after extended inactive periods in air (natural or synthetic). It may be that this oxide monolayer is responsible for the loss in sensitivity observed in sensors that have been stored in air for extended periods of time. It has been noted that this loss of sensitivity is not permanent and sensor performance can be restored by exposure to H₂. This phenomena needs to be investigated thoroughly in the coming year.

Summary and Conclusions

We have researched the issues regarding performance and durability of thick film, thin film, and fiber-optic sensors. For the fiber-optic sensors that used metal hydrides for the detection of hydrogen, we found adhesion problems during cyclic exposure to hydrogen, most likely related to the expansion and contraction of the metal hydrides. Lifetimes of these sensors did not exceed 10 cycles. For the surface plasmon based sensors, we found that the response time was slow and that the repeatability of signal upon cyclic exposure was poor. Therefore, we concentrated most of the work on issues related to the metal oxide based sensors.

New optical materials have been developed that show great promise for the fiber-optic sensor development. One material has demonstrated high sensitivity and a response time of less than 1 second. Unfortunately, its sensitivity decreases with time over periods of storage of about 1 month. Other materials have shown good sensitivity and cyclic stability to over 1000 cycles. Long term stability of these sensors is now dependent upon the properties of the hydrogen dissociation catalyst (Pd).

Common air pollutants found in exhaust streams of current internal combustion engines seriously affect the palladium catalyst material. In particular, CO and CH₄ adsorb on the surface and restrict access to hydrogen dissociation sites. This adsorption appears to be weak and reversible when the sensor is exposed for extended periods in synthetic air. The effect observed with exposure to H₂S is much more dramatic. Exposure to 10 ppm H₂S for 5 minutes is sufficient to completely kill the sensor for the detection of hydrogen. This effect is not reversible after exposure to synthetic air, indicating that the H₂S has chemisorbed to the surface.

Finally, we have indications that residence times longer than one day in air (even synthetic) can significantly slow the response of the thick film, thin film, and the fiber-optic sensors. Subsequent exposure to hydrogen for periods up to 2 hours allows the sensors to recover their original performance. We suspect that a surface or near subsurface oxide is the basis of this effect. This will be a topic of continued research.

Future Work

Research this year has led to the development of some improved sensor materials. However, there are important questions remaining about the material performance for applications in the hydrogen infrastructure.

Can the hydrogen dissociation catalyst be protected from common pollutants found in the transportation environment?

Does the surface of the dissociation catalyst react with atmospheric oxygen, and, if so, can the surface be modified to mitigate the slow response that has been attributed to this reaction?

Can the multi-layered thin film be stabilized for concentrations of hydrogen in air exceeding the lower explosive limit?

Work will continue to understand the behavior of the optical films and catalyst and resolve these issues.

Acknowledgements

The authors want to thank the DOE Hydrogen Program for financially supporting this work under Contract No. DE-AC36-99GO10337 and DCH Technology for its significant contribution under a Cooperative Research and Development Agreement (CRD-96-046). We also wish to thank Dr. Robert Lauf, Oak Ridge National Laboratory for his contributions on the thick film sensors.

References

- Benson, D. K., C. E. Tracy, G. A. Hishmeh, P. A. Ciszek, Se-Hee Lee, and D. P. Haberman, "Low-cost, fiber-optic hydrogen gas detector using guided-wave, surface-plasmon resonance in chemochromic thin films," Proceedings of the SPIE International Symposium on Industrial and Environmental Monitors and Biosensors, Boston, MA, November 2-5, 1998.
- Butler, M. A., "Fiber Optic Sensor for Hydrogen Concentrations near the Explosive Limit," J. Electrochem. Soc. **138**, L46 (1991).
- Butler, M. A., "Micromirror optical-fiber hydrogen sensor," Sensors and Actuators **B 22**, 155 (1994).
- Chadwick, B., and M. Gal, "Enhanced optical detection of hydrogen using the excitation of surface plasmons in palladium," Applied Surface Science **68**, 135 (1993).
- Garcia, J. A., and A. Mandelis, Study of the thin-film palladium/hydrogen system by an optical transmittance method," Rev. Sci. Instrum. **67** (11), 3981 (1996).
- Griessen R., et al., "Yttrium and Lanthanum Hydride Films with Switchable Optical Properties," *J. Alloys and Compounds*, 253–254:44–50. 1997.
- Huang, W., R. Zhai, and X. Bao, "Direct observation of subsurface oxygen on the defects of Pd(100)," Surf. Sci. Lett. 439, L803 (1999).
- Ito, K., and T. Kubo, "Gas Detection by Hydrochromism," In *Proceedings of the 4th Sensor Symposium, Tsukuba, Japan, Dec. 1984*, pp. 153–156. 1984.
- Mandelis, A., and J. A. Garcia, "Pd/PVDF thin film hydrogen sensor based on laser-amplitude-modulated optical-transmittance: dependence on H₂ concentration and device physics," Sensors and Actuators **B 49**, 258 (1998).
- Raether, H., *Surface Plasmons on Smooth and Rough Surfaces and on Gratings*, Springer-Verlag, Berlin, p. 21, 1988.
- Smith II, R. D., D. L. Olson, T. R. Wildeman, and D. K. Benson, "Fiber Optic Sensor for Diffusible Hydrogen Determination in High Strength Steel," Proceedings from Phonics West 2000 Conference, Jan. 25-28, 2000, SPIE, San Jose, CA.
- Sutapun, B., M. Tabib-Azar, and A. Kazemi, "Pd-coated elasto-optic fiber optic Bragg grating sensors for multiplexed hydrogen sensing," Sensors and Actuators **B 60**, 27 (1999).
- Tabib-Azar, M., B. Sutapun, R. Petrick, and A. Kazemi, "Highly sensitive hydrogen sensors using palladium coated fiber optics with exposed cores and evanescent field interactions," Sensors and Actuators **B 56**, 158 (1999).

List of Figures

Figure 1. Test Apparatus for Thick Film Hydrogen Sensors.

Figure 2. Fiber Optic Sensor Test Station.

Figure 3. Transmission Mode and Gas Manifold Details.

Figure 4. Response of High Sensitivity Film to 1% Hydrogen in Nitrogen.

Figure 5. Type 1 Sensor Cycled Between 4% Hydrogen and Synthetic Air.

Figure 6. Type 2 Cycled Between 4% Hydrogen and Synthetic Air.

Figure 7. Effect of CO Adsorbed on Sensor Surface.

Figure 8. Effect of CH₄ Adsorption on Sensor Surface.

Figure 9. Effect of H₂S Adsorbed on Sensor Surface.

Figure 10. Schematic of Encased Sensor, Transmission Mode.

Hydrogen Pressure Vessel Testing Program

Ben C. Odegard Jr. and George J. Thomas
Sandia National Laboratories
Livermore, California, USA

Abstract

The Hydrogen Pressure Vessel Testing Program has been designed to meet two objectives, including: 1) providing visual and quantitative information to OEM's, regulatory agencies, and the public, regarding the consequences of on-board high pressure hydrogen as a fuel source and 2) through a collaborative effort with experts in the field, use the data generated from this project to provide a predictive, validated model to use in evaluating on-board accidents scenarios involving compressed gases. An Oversight Committee of experts in the field of hydrogen storage and pressure vessel testing has been assembled to monitor all aspects of the project. Pressure vessels have been procured and testing is to begin in the July-August time frame. Test objectives will be completed by the end of the FY00 time period. The test data will be documented and distributed in written form and in film through a collaborative effort with the H2000 project.

Introduction

The long term goal of this project is to gain acceptance of on-board compressed hydrogen storage for use in hydrogen powered vehicles. To meet this goal, we are conducting a comparative study between hydrogen and other fuels which are widely accepted, such as gasoline, natural gas, and propane. The data from this study will be documented and distributed both in written form and in film through a collaborative effort with the H2000 project. Further, with this data, we will develop a predictive, validated model for use in determining the response of composite cylinders in accident scenarios. These models may in turn be used by federal agencies and insurance companies. This work builds on previous hydrogen safety studies conducted by M. R. Swain et al (ref: 1-4).

The project consists of testing, modeling, documentation, and dissemination of the results. An Oversight Committee, consisting of experts in the field of hydrogen storage and pressure vessel testing has been formed to monitor all aspects of the work. The committee membership is as follows:

Robert Mauro - National Hydrogen Association
Mahendra Rana - Praxair
George Schmauch - Air Products / Hydrogen Technical Advisory Panel
John Smith - National Institute of Standards and Testing
Robert Zalosh - Worcester Polytech
W. Hoagland - Hydrogen-2000 Project

Test Program Description

State-of-the-art, composite cylinders (Type IV) were manufactured by the IMPCO company in Carson, California specifically for these tests. These are polymeric lined, graphite/glass reinforced epoxy cylinders which were tested to 96 MPa without visible damage. The internal volume is 24 liters with an outside diameter of 23 cm and a total outside length of 35 cm (figure 1). These cylinders are compatible with both hydrogen and natural gas. Tank features include a steel (4340 HSLA) single collar with an attached valve. An integrated pressure relief device is not included in these tanks. A small number of similarly constructed cylinders (Type IV) were purchased from another vendor (Lincoln Composites, Lincoln, Nebraska). The current test matrix does not include these tanks.

The objective of this project is to determine the response of these pressure vessels to extreme conditions, compare the results of hydrogen gas to other fuels, quantify the results, and document the results for public awareness. It is hoped that the results will aid in fostering acceptance by the general public.

This year, we have acquired the cylinders for testing and shipped them to the test site. The test facility will be Sandia National Laboratory-New Mexico, Test Site III. Engineering support is being supplied by the test site staff. The test site staff have prepared the equipment and cameras necessary to begin testing. In preparation for this project, we have reviewed the literature and certification documents on pressure vessel testing (ref: 5-10), formed an Oversight Committee, and established a test matrix that meets our objectives. Testing will begin during the months of July-August, '00. Several delays have occurred in the test schedule because of the drought conditions in New Mexico and the awareness raised by the Los Alamos fire.

Oversight Committee

A meeting was held in Albuquerque, NM on March 15, 2000 with the Oversight Committee to review the initial test matrix, generate feedback from the committee, and tour the test site. From

this meeting several modifications were made to the initial test matrix. Test diagnostics were also reviewed and modified during this important meeting. A film crew from the Hydrogen-2000 project was also in attendance both as consultants and to plan their activities in documenting the test results on film.

Further, suggestions made during the DOE Hydrogen Program Review and the Hydrogen Codes and Standards Workshop were considered and integrated into the modified test matrix.

Test Description

The test matrix for FY00 is shown in the table below.

Hydrogen Pressure Vessel Test Matrix

| Manuf. | Pressure (MPa) | Fuel | Penetration | Flame |
|--------|----------------|------------------|-------------|-------|
| IMPCO | 35 | N ₂ * | 1 | 1 |
| IMPCO | 35 | H ₂ | 2 | 2 |
| IMPCO | 25 | H ₂ | 2 | 2 |
| IMPCO | 25 | CH ₄ | 2 | 2 |

*Preliminary testing will be conducted to determine the energy required to penetrate the tank using nitrogen as the fill gas.

The test diagnostics include: temperature, pressure, high speed video, IR video, spatial and temporal distribution of shrapnel, magnitude of shock wave, and standard video. Both standard and high speed video will be used to provide a real time record of the test event from a minimum of two angles; perpendicular and parallel to the container axis of symmetry. An additional camera will be used by the H2000 film crew. An IR camera will be employed to record the temperature profile during the test event. Spatial and temporal distributions will be determined by visual evidence following the test sequence. Post-test examination of the fracture region will yield information on the failure characteristics of the materials used in the fabrication of the cylinders.

The penetration test will be done using a 5 cm diameter steel rod with a hemispherical end configuration. The cylinder will be fixed in a horizontal position and the rod positioned at a pre-determined distance above the cylinder. Initially, the drop distance will be adjusted to determine the energy required for penetration. Preliminary testing with nitrogen gas will provide the actual energy requirements for penetration and yield additional information on the strength and fracture properties of the material. A cable-guided drop tower (figure 2) will be used to guide the weighted rod from the pre-determined height to the cylinder. The penetration tests will also include an external spark ignition source placed in a position which presents the highest probability of ignition.

Initial calculations indicate a penetration energy between 1630-1900 joules. The higher value is based on information from the manufacturer (ref: 11) which came from firing a 50 caliber, 163 grain (10.6 gm) bullet with a muzzle velocity of 850 m/sec. The kinetic energy of this bullet generates 3800 joules which was sufficient to penetrate both sides of the tank. Approximately half that value should be sufficient to penetrate a single wall thickness. The lower value is based on the rod diameter and an estimate for the shear strength of the material. If the rod diameter is 5 cm and the tank wall is 1.27 cm, the shear area for a 5 cm diameter plug is 20.25 cm². A typical shear strength for a graphite epoxy structure is 64 MPa which translates to a 13,280 kg (force) acting on the rod. Thus the work required to act against that force over a 1.27 cm wall is approximately 1630 joules. These two calculated values for penetration energy are sufficiently close to give us some confidence in choosing a starting value for the penetration tests. As mentioned earlier, preliminary tests to determine the experimental value for penetration will be conducted using compressed nitrogen.



Figure 1- Type IV cylinder: IMPCO



Figure 2- Drop Tower

The flame test will be conducted in an open flame pit with the cylinder in a horizontal position approximately 10 cm above the fire source. For the flame tests, the container (and thermocouples) will be shielded from the flame source using a thin metal plate to prevent direct contact with the flame. The test will proceed until rupture of a pressure relief device occurs. In this case, a pressure relief device such as a burst disc will provide a closer comparison with other fuel containers such as propane or gasoline tanks.

Impact of Project

The impact of the project will be two-fold: 1) providing visual and quantitative information to OEM's, regulatory agencies, and the public, regarding the use of on-board high pressure hydrogen as a fuel source and 2) through a collaborative effort with experts in the field, use the data generated from this project to provide a predictive, validated model to use in evaluating on-board accidents scenarios involving compressed gases. This second point has the potential for use by both the US government and insurance companies.

Future Studies

Plans for next year include testing other fuels including propane, CNG, and gasoline, and completing any additional testing indicated by test results from this year. We have several cylinders in inventory for additional testing including both IMPCO and Lincoln. Further, if warranted, we will include tests on new tank designs such as conformable tanks and the cryotank design from LLNL using the facilities, staff, and test procedures developed this year. These test results will be combined with the tests from this year.

Acknowledgements

Special thanks to the efforts of Timothy Brown with the Sandia National Laboratories-New Mexico test site. Mr. Brown is responsible for setting up the facilities and directing the tests for the hydrogen pressure vessel project. This has been a particular challenging project in New Mexico with the current drought conditions and the increased awareness caused by the fire in Los Alamos, New Mexico. Also, we would like to acknowledge the assistance of the Oversight Committee members mentioned in the text. Their efforts have been most helpful and appreciated. Bill Hoagland and Geoffrey Holland from the H2000 Project have also been major contributors during the planning stages for the tests. Their film documentation should be a valuable contribution to the acceptance of hydrogen for vehicle applications.

References

1. M. R. Swain, 1995, "Safety Analysis of High Pressure Gaseous Fuel Container Punctures", In *Proceedings from DOE Hydrogen Program Review*.
2. M. R. Swain and M. N. Swain, 1996, "Task D: Hydrogen Safety Analysis", In *Proceedings from DOE Hydrogen Program Review*.
3. M. R. Swain, E. S. Grilliot, and M. N. Swain, 1997, "Risks Incurred by Hydrogen Escaping from Containers and Conduits", In *Proceedings from DOE Hydrogen Program Review*.
4. M. R. Swain, J. Shriber, and M. N. Swain, 1998, "Comparison of Hydrogen, Natural Gas, Liquified Petroleum Gas, and Gasoline Leakage in a Residential Garage", *Energy and Fuels*, 12: 83-89.
5. NGV2, 1992, "Basic Requirements for Compressed Natural Gas Vehicle (NGV) Containers", NSSN.
6. DOT FRP-1 Standard, 1981, "Basic Requirements for FRP Type 3FC Cylinders".
7. ISOTC 197/ISO TC 58/SC 3 N, 2000, "Gaseous Hydrogen and Hydrogen Blends - Land Vehicle Fuel Tanks".
8. ISO/TC 58/SC 3, 1999, *Report of the Meeting of ISO/TC 58/SC 3 - Gas Cylinders*, Venice, Italy, September 20-22.
9. CGA Docket 77-8, 1982, "Cylinder Specification Subcommittee Report on Basic Considerations for Composite Cylinders".
10. DOT-CFFC, 1996, "Basic Requirements, Basic Requirements for Fully Wrapped Carbon-Fiber Reinforced Aluminum Lined Cylinders".
11. Private Communication, 2000, Neel Sirosh, Director of Research, IMPCO Technologies Inc., Carson, CA, USA

Dispersion of Hydrogen Clouds

**Michael R. Swain
Eric S. Grilliot
Matthew N. Swain
University of Miami
Coral Gables, FL 33124**

Abstract

The following is the presentation of a simplification of the Hydrogen Risk Assessment Method previously developed at the University of Miami. It has been found that for simple enclosures, hydrogen leaks can be simulated with helium leaks to predict the concentrations of hydrogen gas produced. The highest concentrations of hydrogen occur near the ceiling after the initial transients disappear. For the geometries tested, hydrogen concentrations equal helium concentrations for the conditions of greatest concern (near the ceiling after transients disappear). The data supporting this conclusion is presented along with a comparison of hydrogen, LPG, and gasoline leakage from a vehicle parked in a single car garage. A short video was made from the vehicle fuel leakage data.

Simplification of the Hydrogen Risk Assessment Method to reduce the need for CFD modeling.

A method is being developed that can be used to determine the potential health and safety implications of a hydrogen release. The method allows the user to establish changes to venting in buildings and home refueling areas to minimize or eliminate any serious threats. Additionally, the method can be used to determine optimum hydrogen sensor locations for active safety systems. It is the objective of this portion of the work to simplify the risk assessment method to eliminate or reduce the need for computer modeling in the method.

Gaseous fuel escapes can be classified by enclosure geometry and a hydrogen flow quantity description. This is done as follows:

1. Gas escapes into enclosed spaces
 - a. Total volume of escaped hydrogen.
 - b. Flow rate of escaping hydrogen.
2. Gas escapes into partially enclosed spaces.
 - a. Total volume of escaped hydrogen.
 - b. Flow rate of escaping hydrogen.
3. Gas escapes into unenclosed spaces.
 - a. Total volume of escaped hydrogen.
 - b. Flow rate of escaping hydrogen.

General descriptions of the type of risks incurred can be made for each of the above mentioned classifications. For leaks into enclosed (non-vented) spaces, the risk incurred is most strongly affected by the total volume of hydrogen escaping rather than the flow rate of hydrogen escaping. This is because ignition can occur soon after the gas escape begins or be delayed. The overpressure created by the delayed ignition of an accumulating combustible mixture typically produces a greater risk than does early ignition resulting in a standing flame.

Ignition early in the escape results in a burning jet or standing flame. The size of the standing flame is dependent on hydrogen flow rate.

If ignition is delayed, the magnitude of the potential overpressure, due to ignition of the accumulating combustible mixture, is a function of the gas motion in the enclosed space. The escaping hydrogen will rise to the ceiling (or any overhead barrier) within seconds and then diffuse back toward the lower section, which takes hours. If the total volume of hydrogen escaping is less than 4.1% of the volume of the enclosure, the resulting risk of combustion will decrease to zero as the hydrogen becomes homogeneously distributed into the enclosure. If the total volume of hydrogen escaping is greater than 4.1% of the volume of the enclosure, the resulting risk of combustion will continue until the enclosure is vented or combustion occurs.

For leaks into unenclosed spaces, the risk incurred is most strongly affected by the flow rate of the hydrogen escape rather than the total volume of hydrogen escaped. Without an enclosure, hydrogen rises and the risk of hydrogen accumulation is removed. For hydrogen escaping into an unenclosed space, steady state combustible gas cloud size is typically reached within 15 seconds. If the hydrogen flow is stopped, combustible mixtures of hydrogen are typically gone in 10 seconds. The risk of large overpressures caused by ignition of the hydrogen-air mixture is small due to the lack of an enclosure to constrain the expanding products of combustion. Additionally, the hydrogen jet produced is very inhomogeneous and the volume of hydrogen-air mixtures that produce high flame speeds is typically small. It is near stoichiometric and rich mixtures of hydrogen and air that burn rapidly enough to produce appreciable overpressures.

For leaks into partially enclosed spaces (buildings with vents) the risk incurred is affected by the total volume of hydrogen escaping and the flow rate of escaping hydrogen. The relative importance of the total volume and flow rate is dependent on the geometry of the partially enclosed space and the location of the hydrogen escape. Proper design of the partial enclosure reduces the risk incurred due to hydrogen escape.

Hydrogen's low density causes it to rise after escaping from a container or conduit. Vents near the top of the enclosure can allow hydrogen to exit the enclosure efficiently, as long as vents are also provided near the bottom of the enclosure. Vents near the bottom of the enclosure allow fresh air to enter and replace the hydrogen enriched mixture exiting from the top vents. If fresh air must enter through the same vent that the hydrogen is exiting, the efficiency of hydrogen removal is substantially reduced.

The design of ventilation in structures, which might potentially produce partial enclosures for escaping hydrogen, can be facilitated by using a risk assessment method that simulates potential hydrogen escape scenarios with helium escapes. Both hydrogen and helium are low-density gases and behave in similar a fashion when released into partial enclosures. Helium concentrations, versus time, can be measured in the partial enclosure during a simulated hydrogen escape scenario. Last year's work has shown that accurate descriptions of hydrogen behavior can be obtained by creating a verified CFD model using the helium escape data and then using the model to predict hydrogen escape behavior.

The method of risk assessment, previously developed, utilizes four steps.

1. Simulation of the accident scenario with leaking helium (measure helium concentration versus time at various locations while leaking helium at the expected hydrogen leakage rate).
2. Verification of a CFD model of the accident scenario (modeling helium) using the helium data.
3. Prediction of the behavior of hydrogen using the CFD model (modeling hydrogen).
4. Determination of risk from the spatial and temporal distribution of hydrogen.

It appears that by determining the manner in which helium and hydrogen behave in various geometries, it will be possible to directly interpret helium release data, thereby replacing steps 2 and 3 with a simple procedure.

The ongoing work deals with gas escapes into partially enclosed spaces. The spaces investigated were defined as simple enclosures (six-sided rectangular structures). The simple enclosures studied were of the single vent and double vent configuration. A single case of two interconnected simple enclosures was also studied.

General findings were as follows:

1. For simple enclosures, whether single or double vented, the concentration of hydrogen and helium were the same for areas of bulk flow near the ceiling but not in close proximity to the leak origin or a vent. This was particularly true when

steady state conditions were reached. These are the same areas of high concentration and large volume that are of the greatest safety concern. Figure 1 is a plot of 20 data sets representing the helium/hydrogen concentration ratio for all the geometries modeled to date. The data sets are from locations near the ceiling of the enclosures modeled. Half of the enclosures were of the single vent type and half were of the double vent type.

2. For areas near a vent the concentration of either gas (hydrogen or helium) may fluctuate wildly due to instabilities in flow. This is most noticeable in flow up a "chimney". Figures 2 and 3 show the instability when pure hydrogen or helium is allowed to enter the bottom of a 1 by 1 foot chimney that is 6 feet tall. The figures show a surface of constant 5% concentration versus time for helium and hydrogen. The low-density gas (helium or hydrogen) rises, entrains air, and forms a flow that attaches itself randomly to the four walls of the chimney. The concentration at a specific point is not predictable. Therefore, the helium to hydrogen ratio fluctuates wildly and rapidly. Fortunately, the volume of gases affected is typically small compared to the volume of the enclosure.
3. For areas near the leak origin the concentration of either gas (helium or hydrogen) may fluctuate wildly due to instabilities in the flow. However, concentration gradients in a horizontal direction are typically large, near the leak, so stable readings of zero percent helium are generally an indicator of zero percent hydrogen.
4. Regarding the simulation of an accident scenario with helium: if helium detectors are properly placed, or if a sufficient number of helium detectors are employed, measured helium concentrations can be used as a direct indicator of hydrogen concentrations for the high concentration, high-volume locations of most concern.
5. For two interconnected simple enclosures, one above the other, there appears to be more hydrogen in the lower enclosure than would be predicted by helium concentration measurements in the bulk flow near the ceiling.

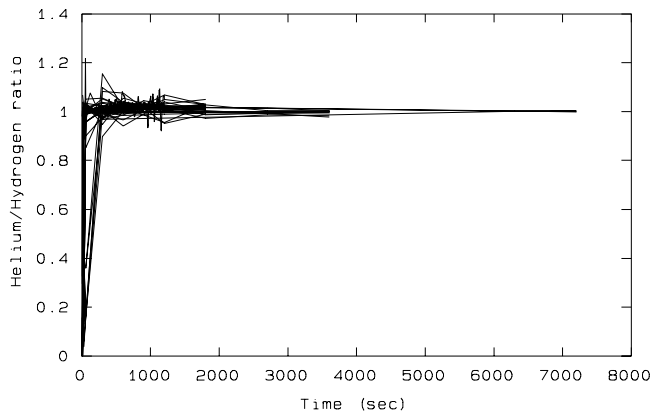


Figure 1 - Data from the 20 enclosures modeled to date. The ratio between helium and hydrogen concentration values near the ceiling are plotted.

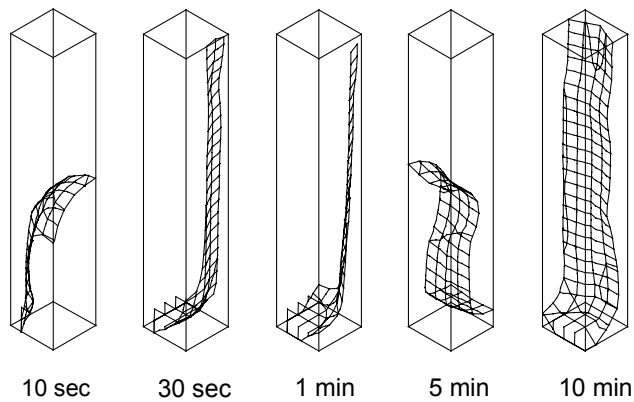


Figure 2- CDF results for helium in chimney

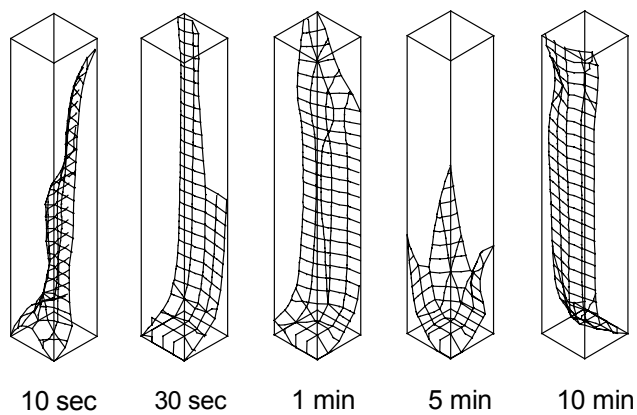


Figure 3 - CDF results for hydrogen in chimney

Explanation of Results

The following experimentally verified computer models of hydrogen leakage into simple enclosures are presented to give examples of the general findings. The results are presented in a schematic of the simple enclosure, and as pairs of graphs: on the left a graph of the ratio of helium to hydrogen concentration at the ceiling and floor, and on the right the percentage concentration of hydrogen at the ceiling and floor. The ratio of helium to hydrogen concentration indicates the accuracy of predicting hydrogen concentrations from measured helium concentrations. Values less than 1.0 indicates under prediction of hydrogen concentrations and would be of greater concern than values greater than 1.0. The graph of hydrogen concentration is presented to show the actual values predicted by the computer model.

The first example is shown in Figures 4 and 5. Fig. 4 shows a single car garage with a single vent in the garage door, and a sheet of plywood mounted above the middle of the floor. The hydrogen is leaking from under the middle of the plywood (all figures are drawn to scale). The hydrogen rose from under the sheet of plywood, and flowed out of the garage door vent while fresh air flowed in the same vent. Hydrogen concentration was higher at the ceiling and lower at the floor. The ratio of helium concentration to hydrogen concentration was approximately 1.0 after 4,000 seconds of leakage. The leakage rate for hydrogen and helium were identical at 7,200 l/hr. As the measured concentration of helium near the ceiling began to stabilize at concentrations above 6%, helium concentration was a good predictor of hydrogen concentration.

Figures 6 through 10 show the effects of increased flow rate on hydrogen concentration and helium to hydrogen concentration ratio, as leakage rate is increased from 7,200 l/hr to 43,200 l/hr. The model shows a home refueling unit leaking in the back of the garage. Note that there were vents at the top and bottom of the garage door to reduce the risks incurred during hydrogen leakage. Separate vents locations, high and low in the room, are more effective than a single vent. Hydrogen concentration increases with leakage rate but doubling the flow rate does not double the concentrations. Helium concentrations near the ceiling are a good predictor of hydrogen concentrations.

Figures 11 through 14 shows the effects of moving a single large vent up and down in the garage door. Though placing the vent low in the garage door increases hydrogen concentrations near the ceiling slightly, little change occurs as long as the vent size does not change. Helium concentrations near the ceiling are a good predictor of hydrogen concentrations.

Figures 15 and 16 show what happens when the leaking unit is placed next to the garage door and the garage door has a single vent across the bottom of the garage door. This is a very inefficient location for a garage door vent. Though hydrogen concentration increases rapidly helium concentrations near the ceiling are still a good predictor of hydrogen concentrations.

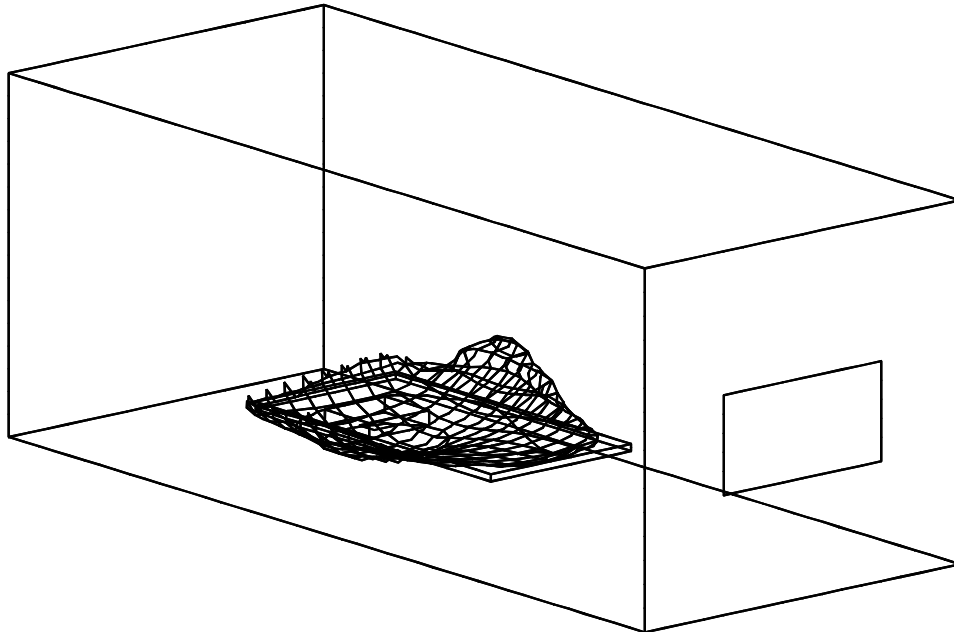


Figure 4 - Surface of constant 6.5% hydrogen concentration after leakage at 7200 l/hr for 25 minutes

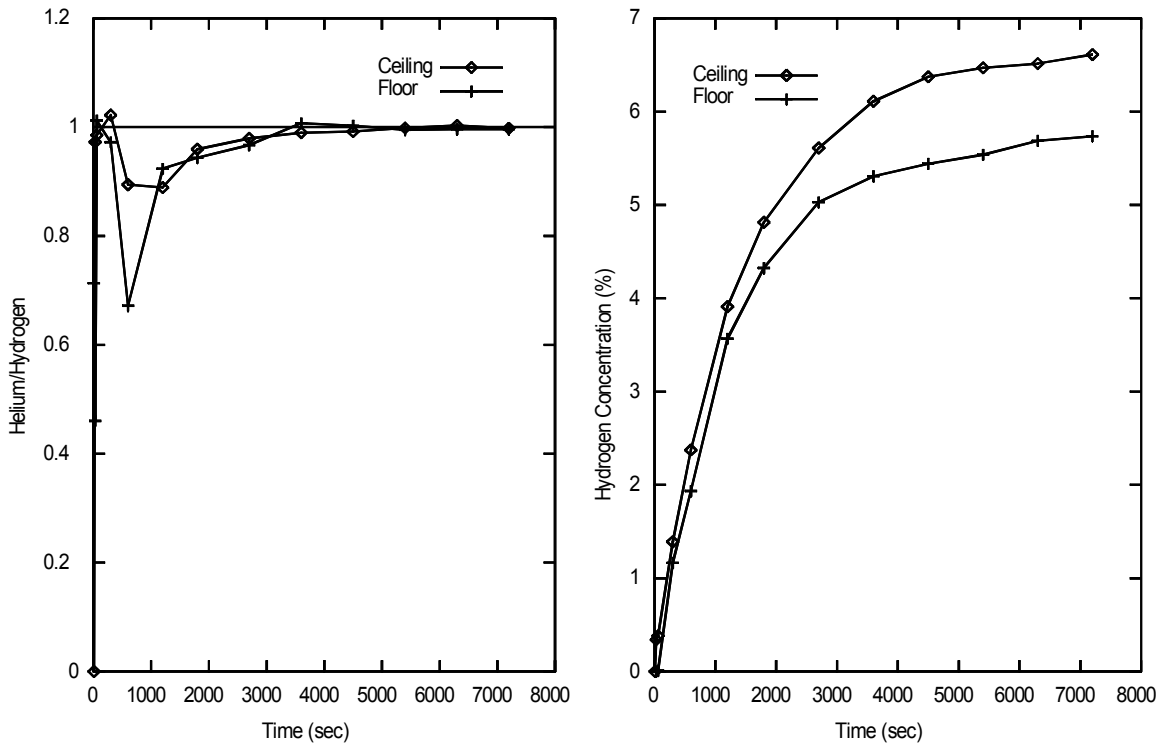


Figure 5 - Leakage in garage. Single vent garage door. Plywood in center of floor. Leakage rate: 7200 l/h

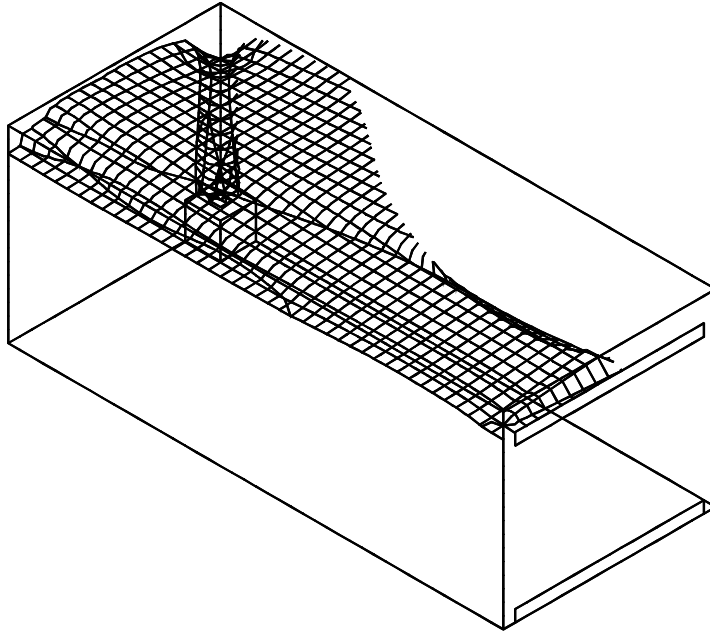


Figure 6 - Surface of constant 1.7% hydrogen concentration after leakage at 7200 l/hr for 10 minutes

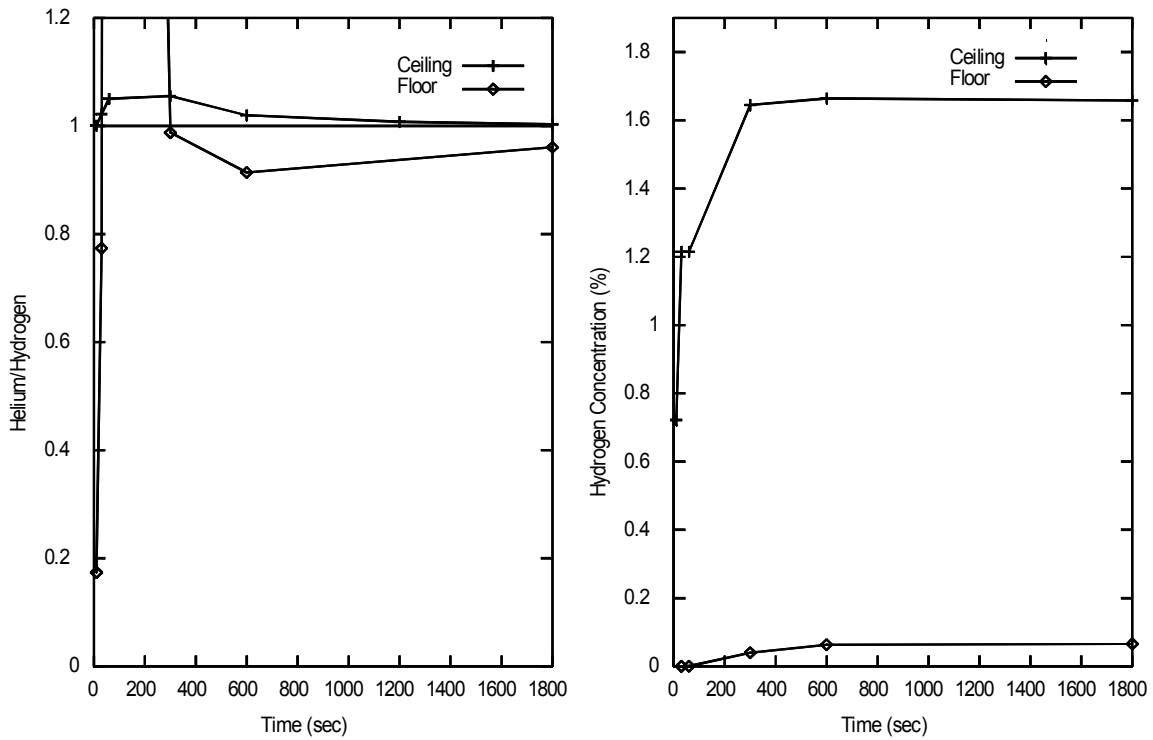


Figure 7 - Leakage in garage. Double vent garage door. Home refueling unit opposite garage door. Leakage rate: 7200 l/hr

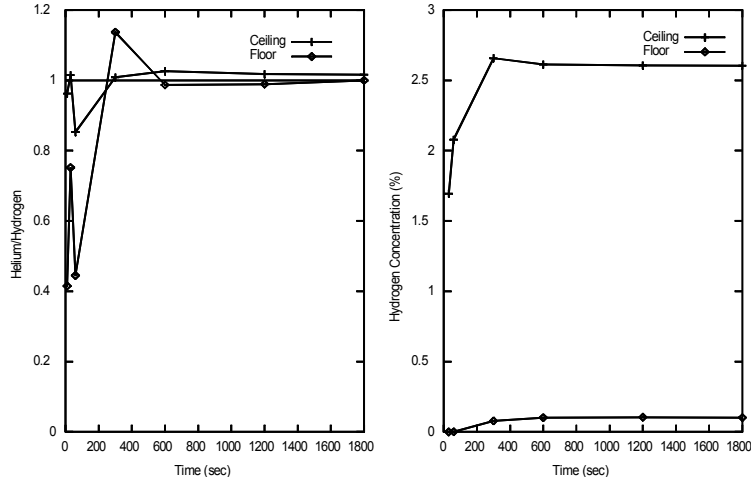


Figure 8 - Leakage in garage. Double vent garage door. Home refueling unit opposite garage door. Leakage rate: 14,400 l/hr

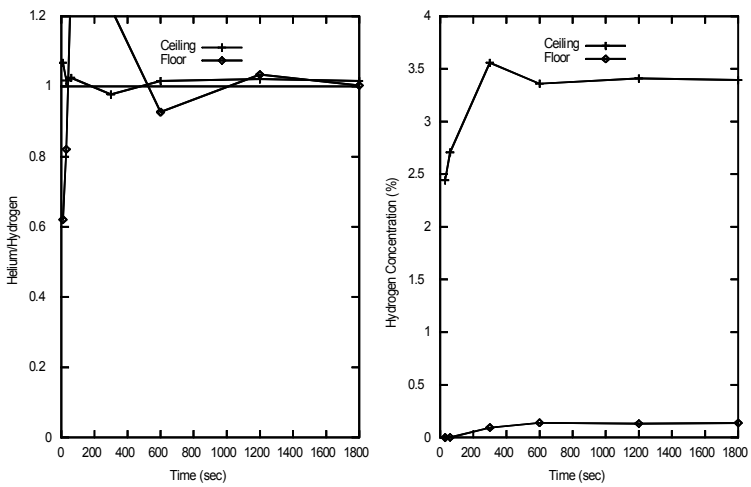


Figure 9 - Leakage in garage. Double vent garage door. Home refueling unit opposite garage door. Leakage rate: 21,600 l/hr

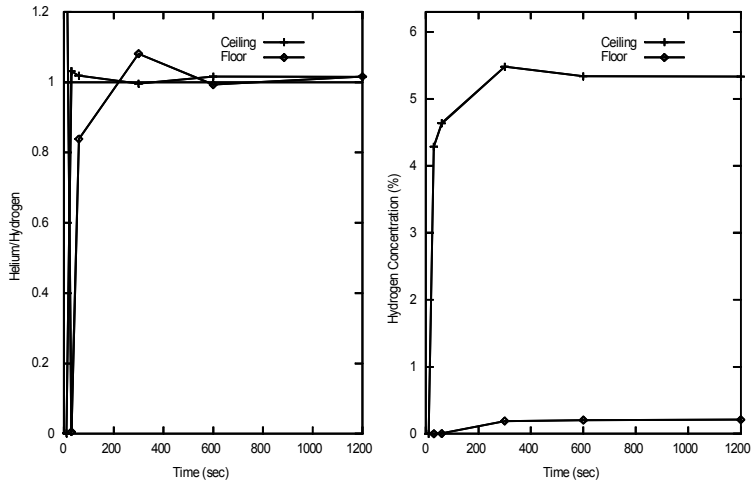


Figure 10 - Leakage in garage. Double vent garage door. Home refueling unit opposite garage door. Leakage rate: 21,600 l/hr

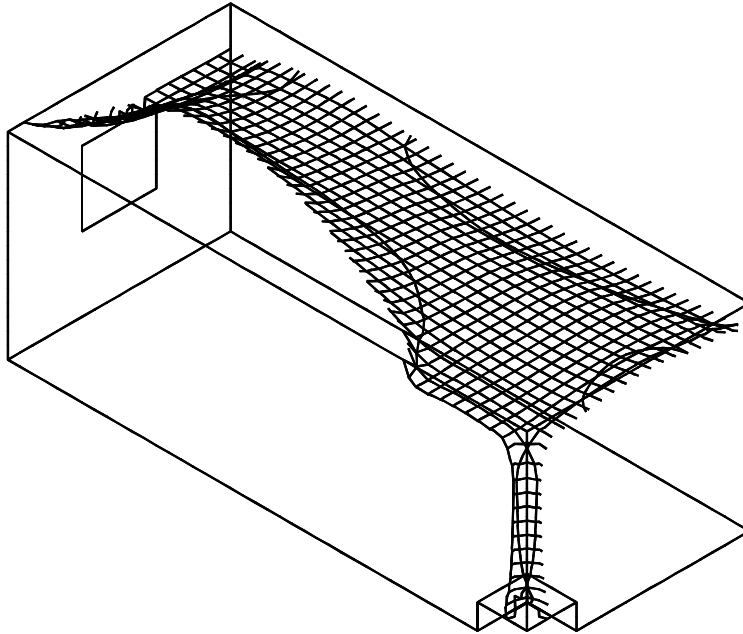


Figure 11 - Surface of constant 7.5% hydrogen concentration after leakage at 6796 l/hr for 20 minutes

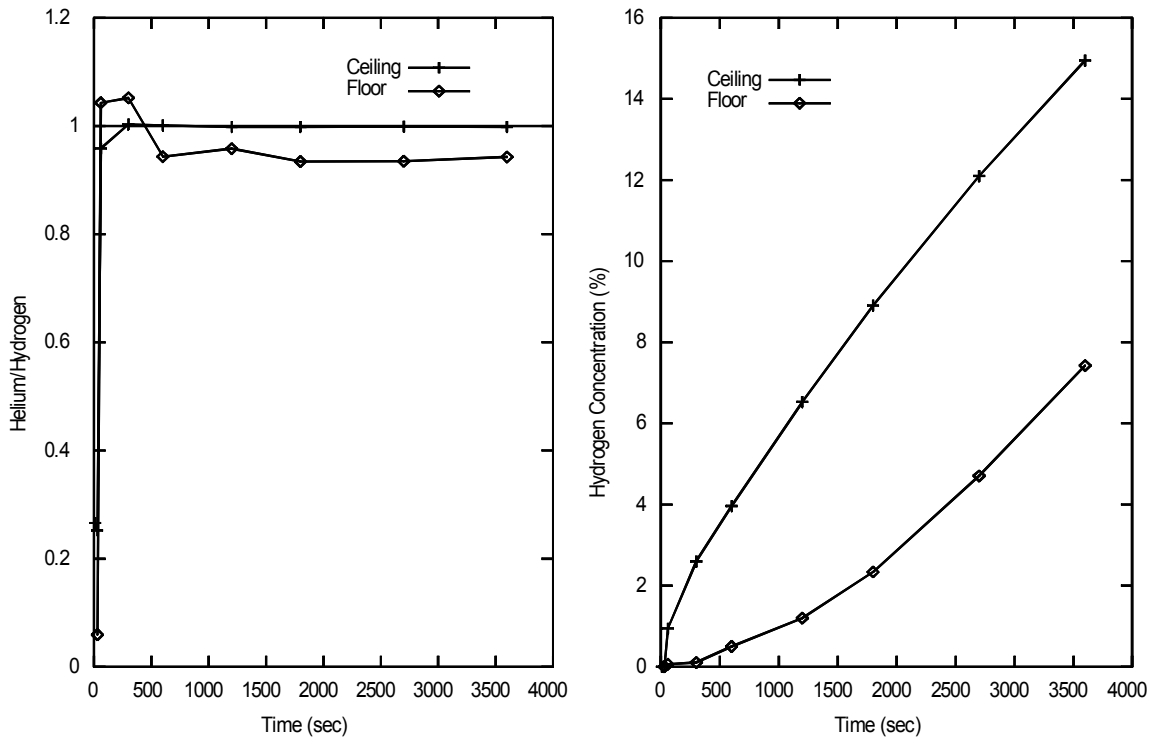


Figure 12 - Leakage in garage. Single vent garage door. Home refueling unit opposite garage door. Leakage rate: 6796 l/hr

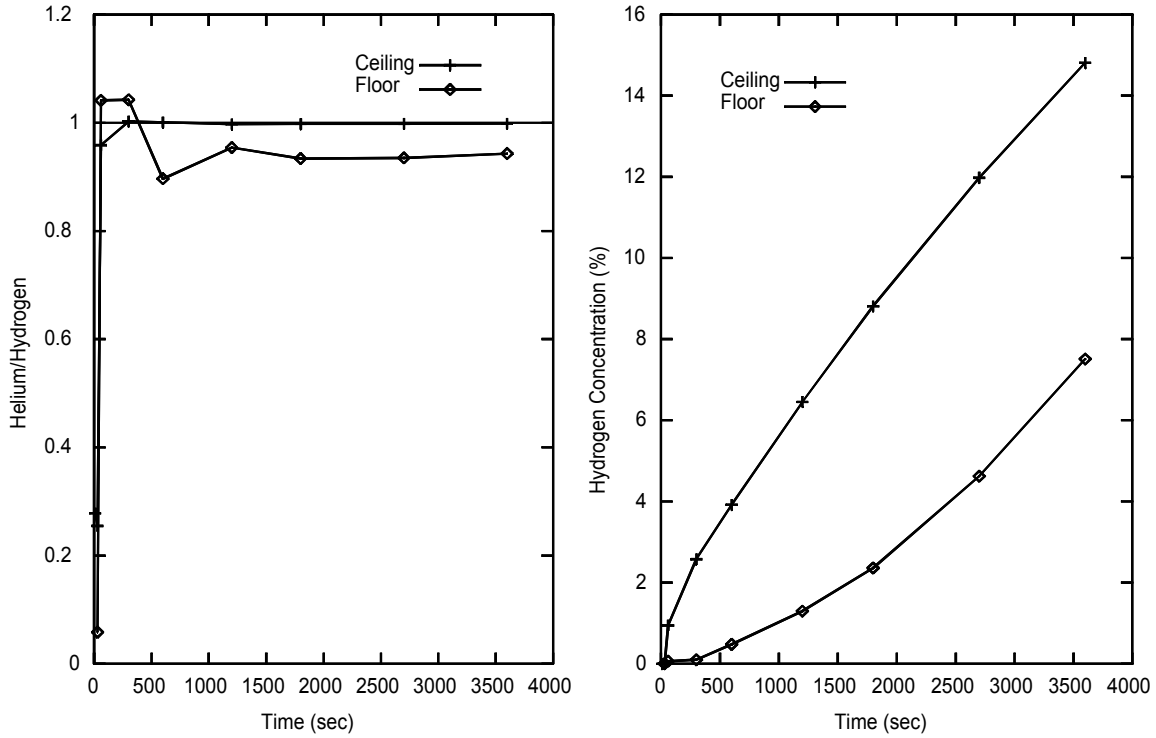


Figure 13 - Leakage in garage. Single vent high in garage door. Home refueling unit opposite garage door. Leakage rate: 6796 l/hr

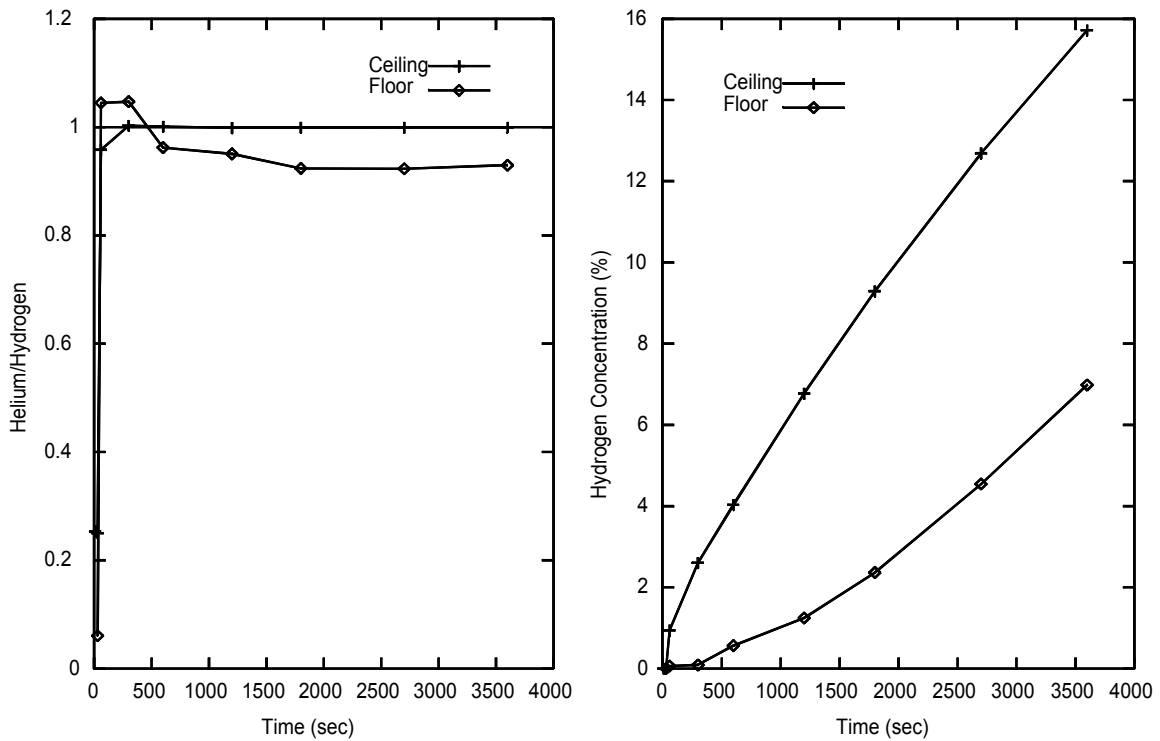


Figure 14 - Leakage in garage. Single vent low in garage door. Home refueling unit opposite garage door. Leakage rate: 6796 l/h

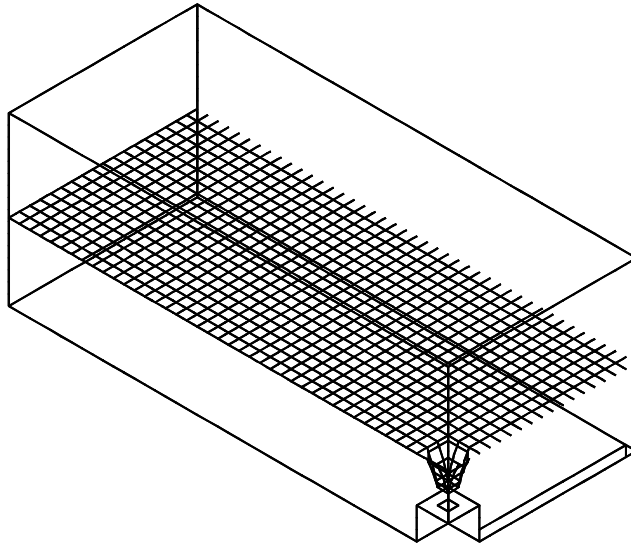


Figure 15 - Surface of constant 34% hydrogen concentration after leakage at 43,200 l/hr for 20 minutes

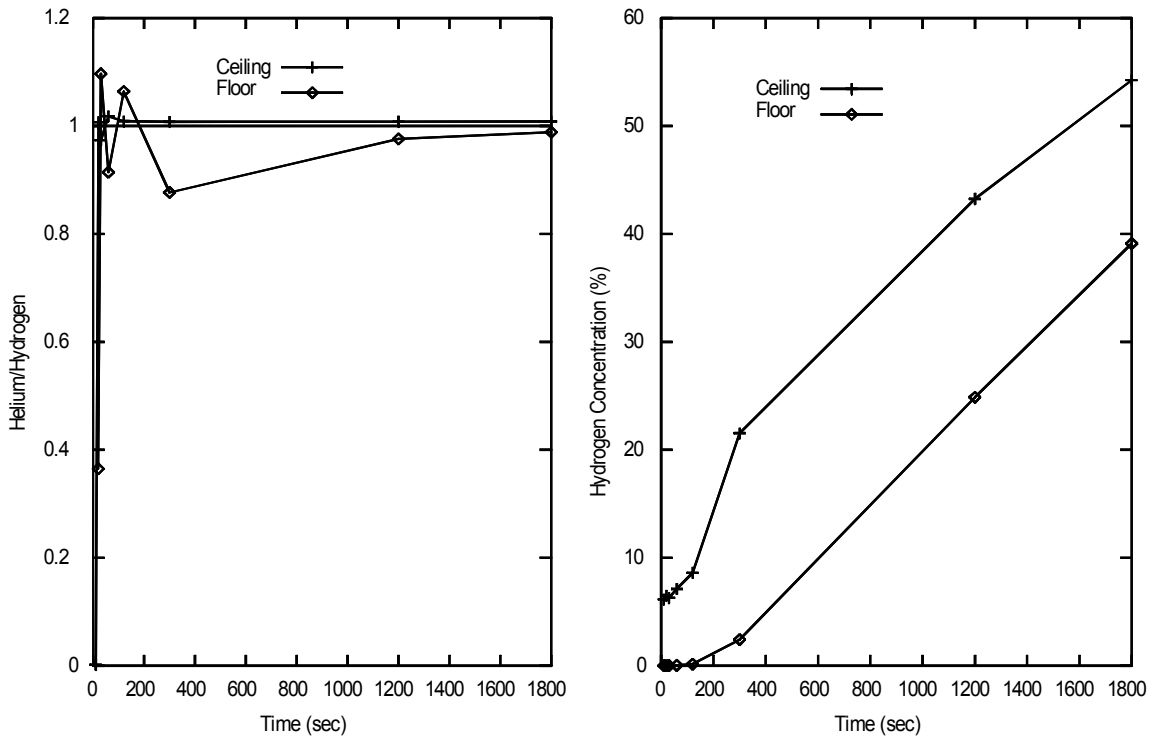


Figure 16 - Leakage in garage. Single vent low in garage door. Home refueling unit opposite garage door. Leakage rate: 43,200 l/hr

Figures 17 through 20 show the results from a van parked in a garage. The effects of moving the single garage door vent location and van position are shown. Moving the van near the garage door or raising the vent location had little effect on hydrogen concentration. Helium concentrations near the ceiling are still a good the predictor of hydrogen concentrations.

Figures 21 and 22 show the effects of hydrogen leakage into a hallway. The hydrogen leaks from the floor at one end of the hallway while two vents exist at the other end the hallway. One vent is in the ceiling and the other vent is in the bottom of the door at the end of the hallway. Because there are lower and upper vents, the enclosure produces a steady state condition after 300 seconds. Helium concentrations near the ceiling are a good predictor of hydrogen concentrations.

Figures 23 and 24 show the effect of adding a "chimney" to the upper vent. Hydrogen concentrations are reduced. Helium concentrations continue to be a good predictor of hydrogen concentrations.

Moving the leak to the middle of the hallway produces slight decreases in hydrogen concentration as the leak is closer to the vents as shown in Figures 25 and 26. Helium concentrations are a good predictor of hydrogen concentrations.

Shortening the hallway but retaining both vents results in large fluctuations in hydrogen concentration near the floor (Figures 27 and 28). This is because the leak and lower vent are in close proximity to the measurement locations. Eddies created at the leak produce large fluctuations in hydrogen concentration. Helium concentrations near the ceiling are a good predictor of hydrogen concentrations.

Figures 29 and 30 show the effects of leakage into a hallway with a single small vent in the ceiling at the opposite end of the hallway. Hydrogen concentrations slowly rise toward 100% because the vent size is small enough, and leakage rate large enough, to prevent flow of air back into the hallway from the single vent. Helium concentrations are a good predictor of hydrogen concentrations.

If a single ceiling vent is increased in size, back flow of air did occur as shown in Figures 31 and 32. Hydrogen concentration levels off at a concentration below 100%. Helium concentrations are a good predictor of hydrogen concentrations. There is a tendency to predict hydrogen concentrations greater than actually existed.

Figures 33 and 34 show that moving the single vent to a lower position in the door does not prevent back flow of air into the room. Helium concentrations were a good predictor of hydrogen concentrations.

The addition of a "chimney" reduces hydrogen concentrations as can be seen comparing Figures 35 and 36 to Figures 31 and 32. The "chimney" does not prevent the back flow of air through the vent. Helium concentrations near the ceiling are good predictor of hydrogen concentration.

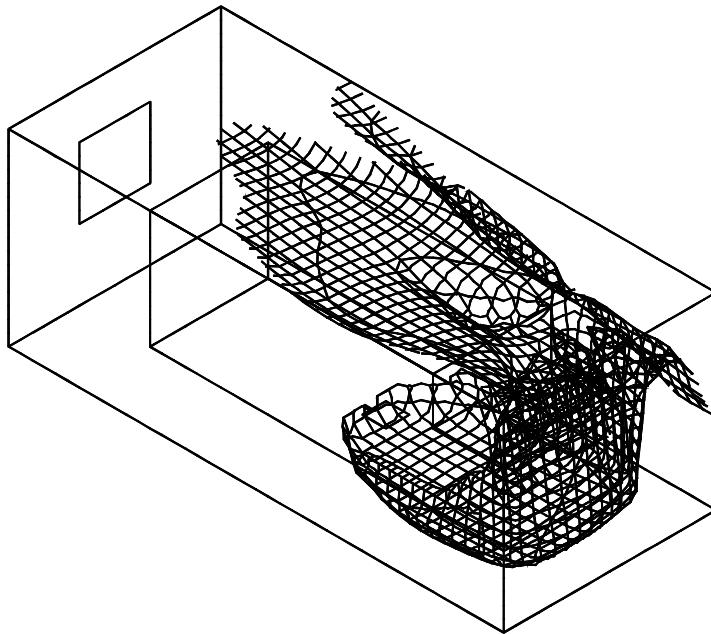


Figure 17 - Surface of constant 6.5% hydrogen concentration after leakage at 6796 l/hr for 20 minutes

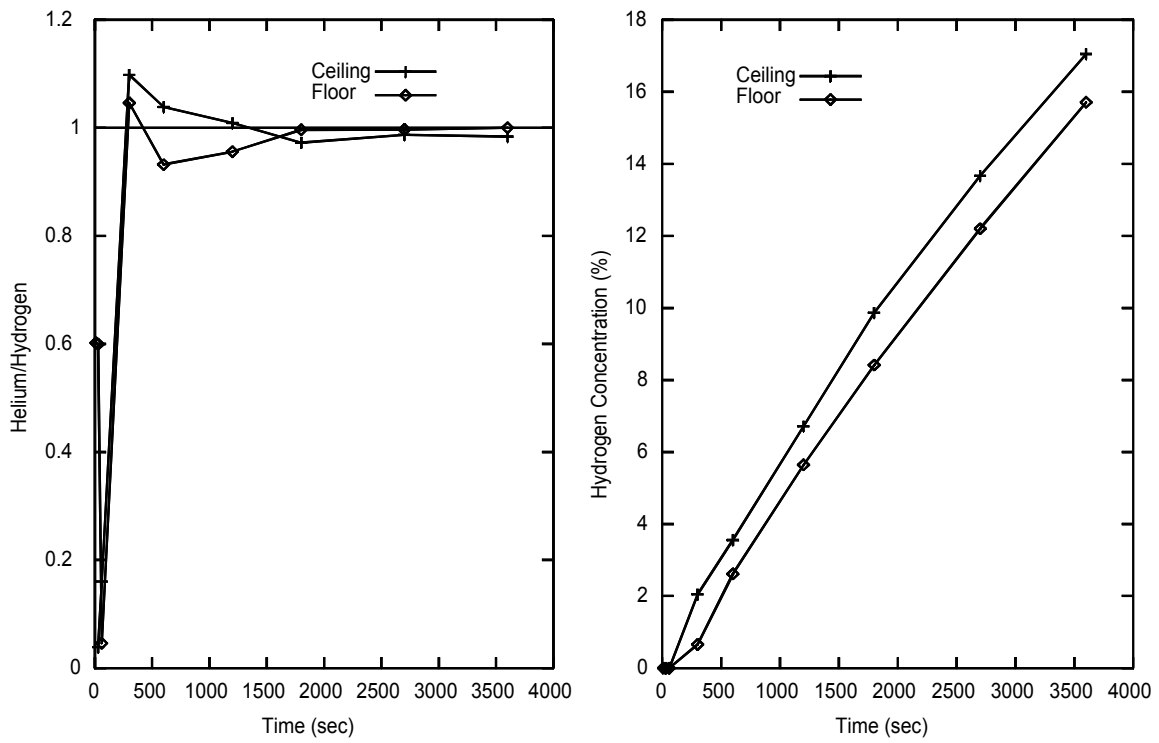


Figure 18 - Leakage in garage. Single vent garage door. Van in standard position. Leakage rate: 6796 l/h

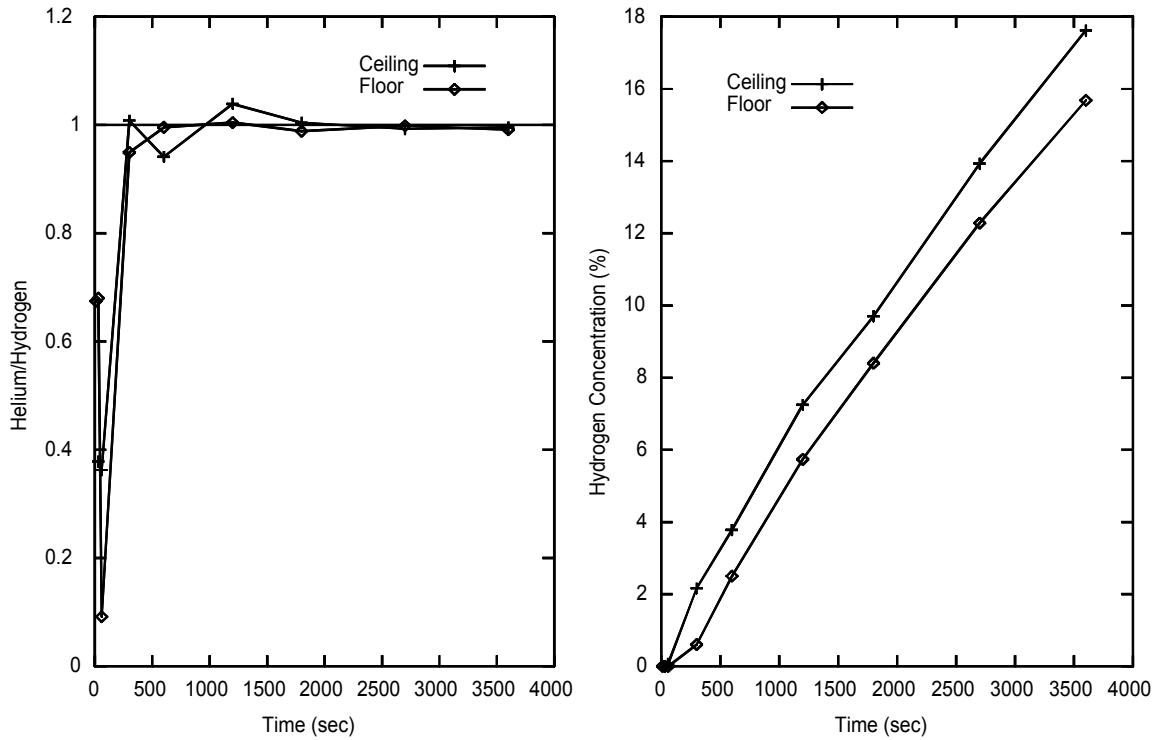


Figure 19 - Leakage in garage. Single vent garage door. Van near garage door. Leakage rate: 6796 l/h

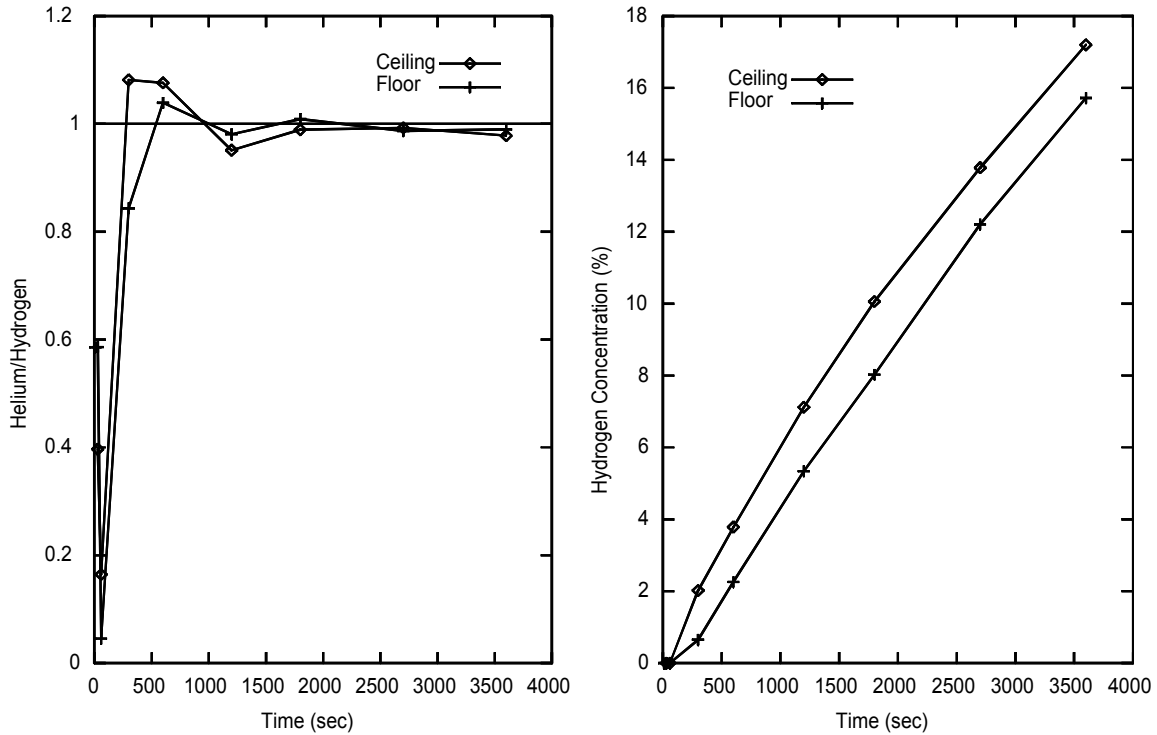


Figure 20 - Leakage in garage. Single vent high in garage door. Van in standard position. Leakage rate: 6796 l/h

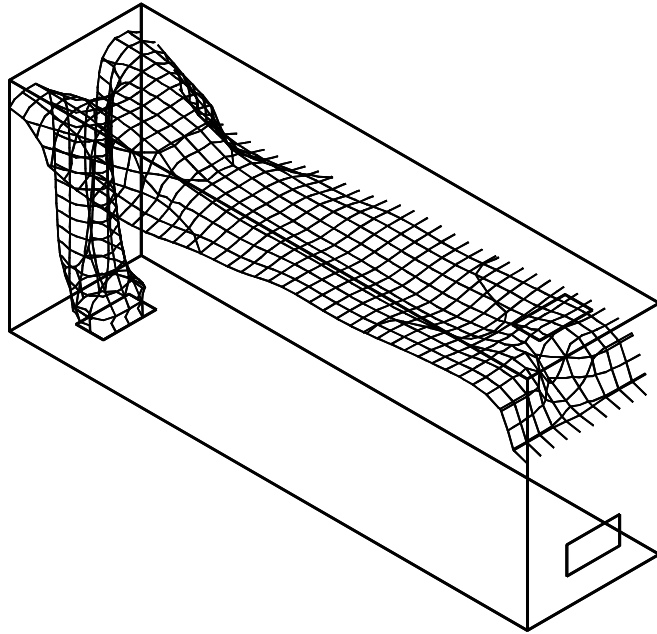


Figure 21 - Surface of constant 3.0% hydrogen concentration after leakage at 27,184 l/hr for 1 minute

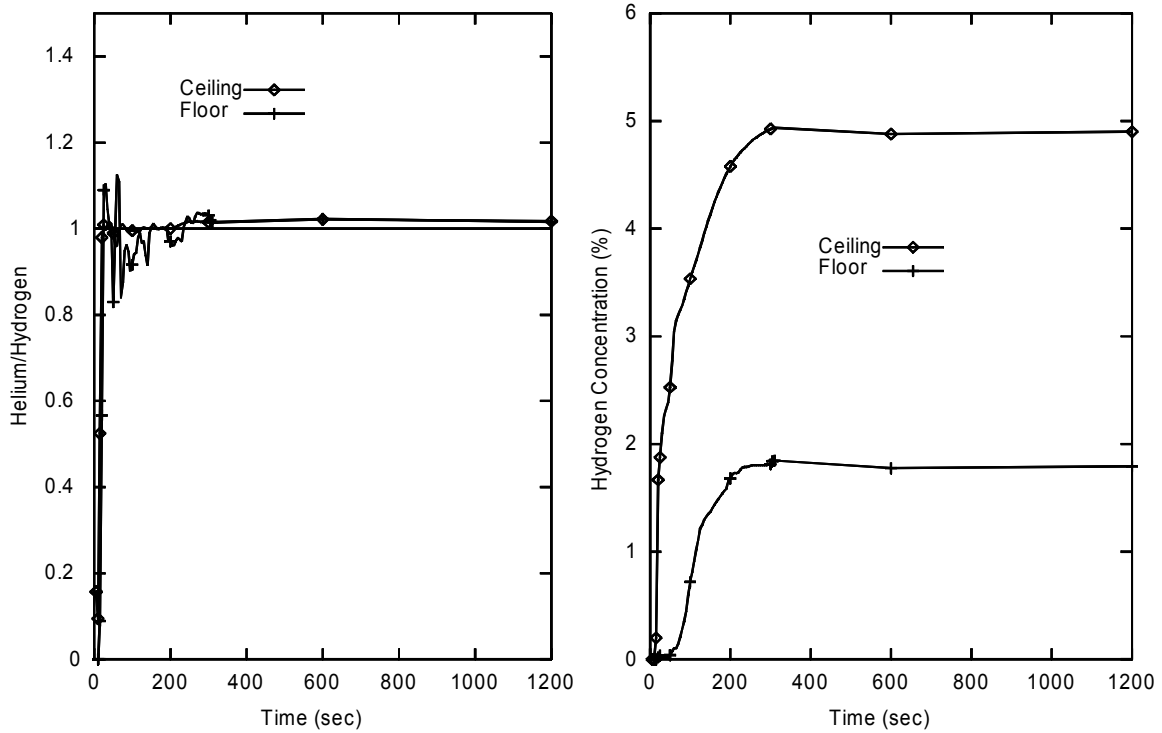


Figure 22 - Leakage at end of hallway. Double vent opposite leak. Leakage rate: 27,184 l/hr

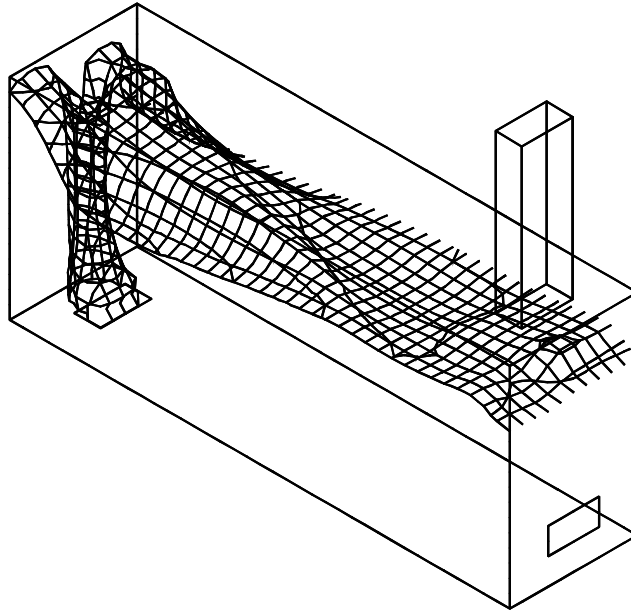


Figure 23 - Surface of constant 4.0% hydrogen concentration after leakage at 27,184 l/hr for 20 minutes

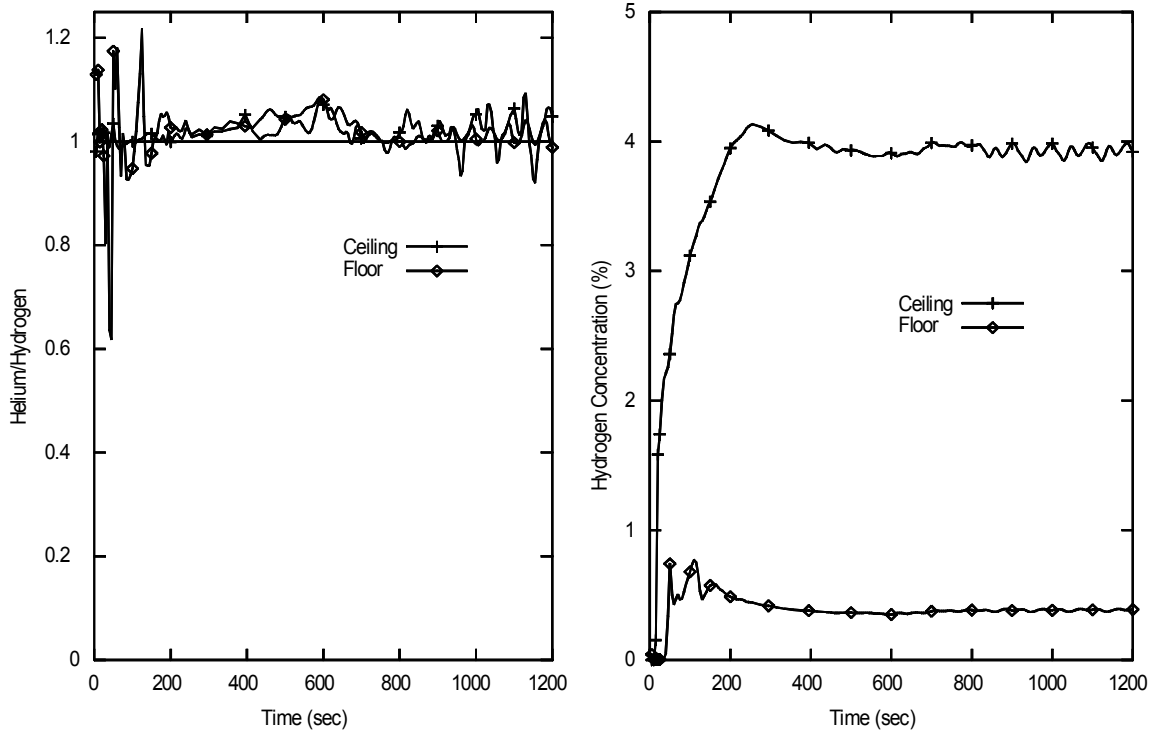


Figure 24 - Leakage at end of hallway. Double vent opposite leak. Chimney on roof vent. Leakage rate: 27,184 l/hr

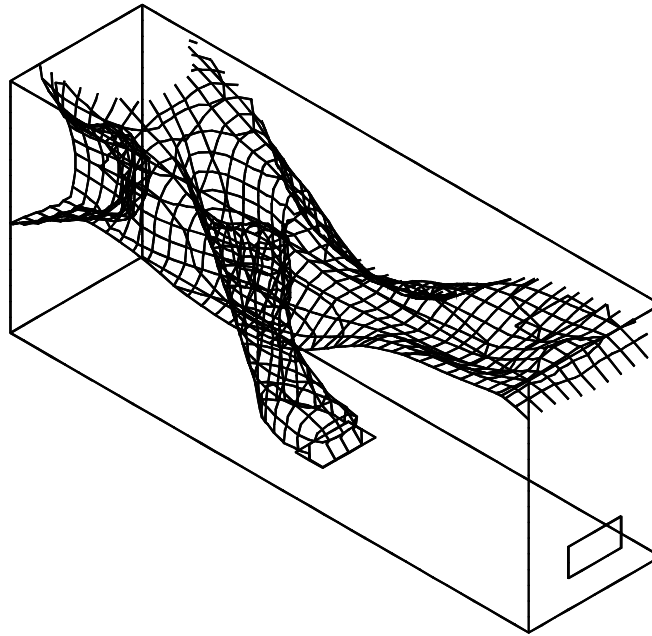


Figure 25 - Surface of constant 4.8% hydrogen concentration after leakage at 27,184 l/hr for 20 minutes

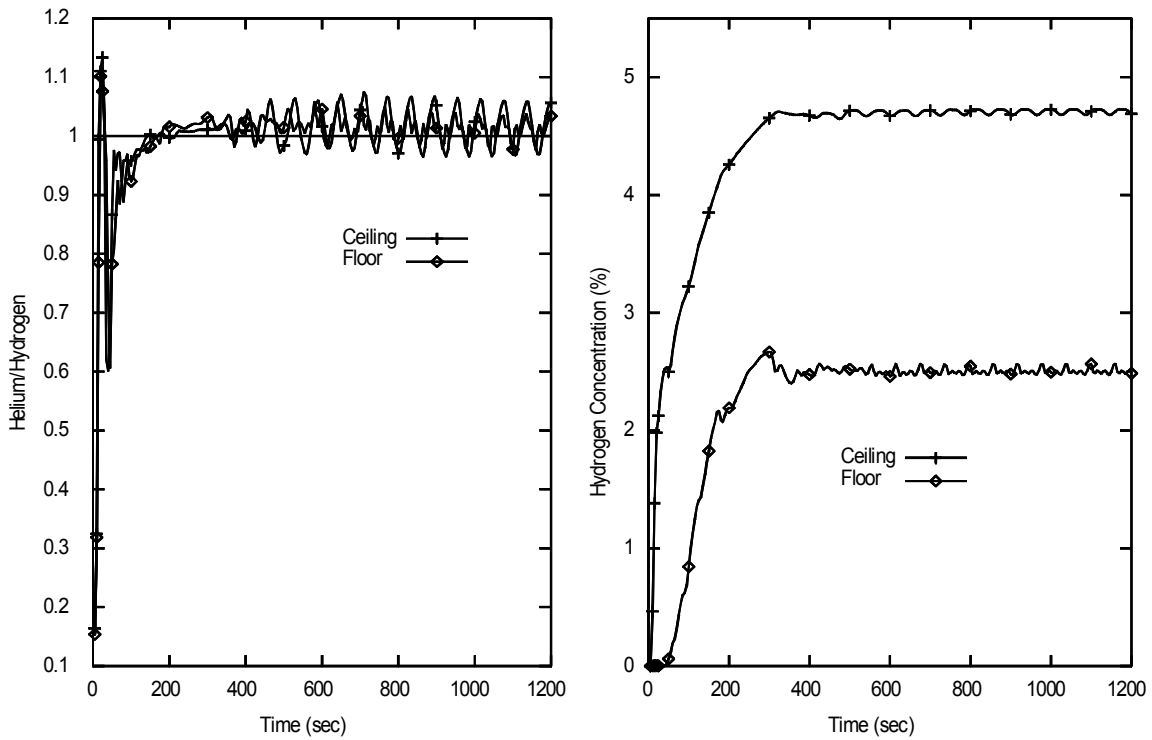


Figure 26 - Leakage in middle of hallway. Double vent at end of hallway. Leakage rate: 27,184 l/hr

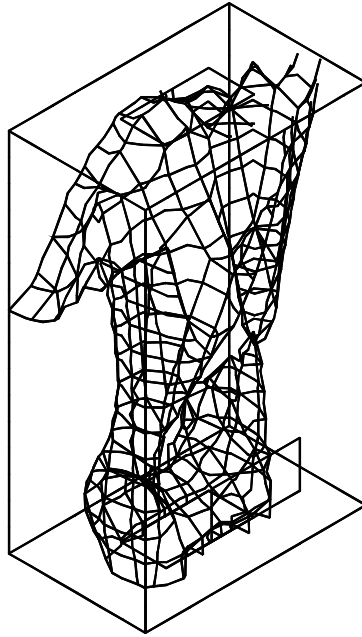


Figure 27 - Surface of constant 4.1% hydrogen concentration after leakage at 27,184 l/hr for 20 minutes

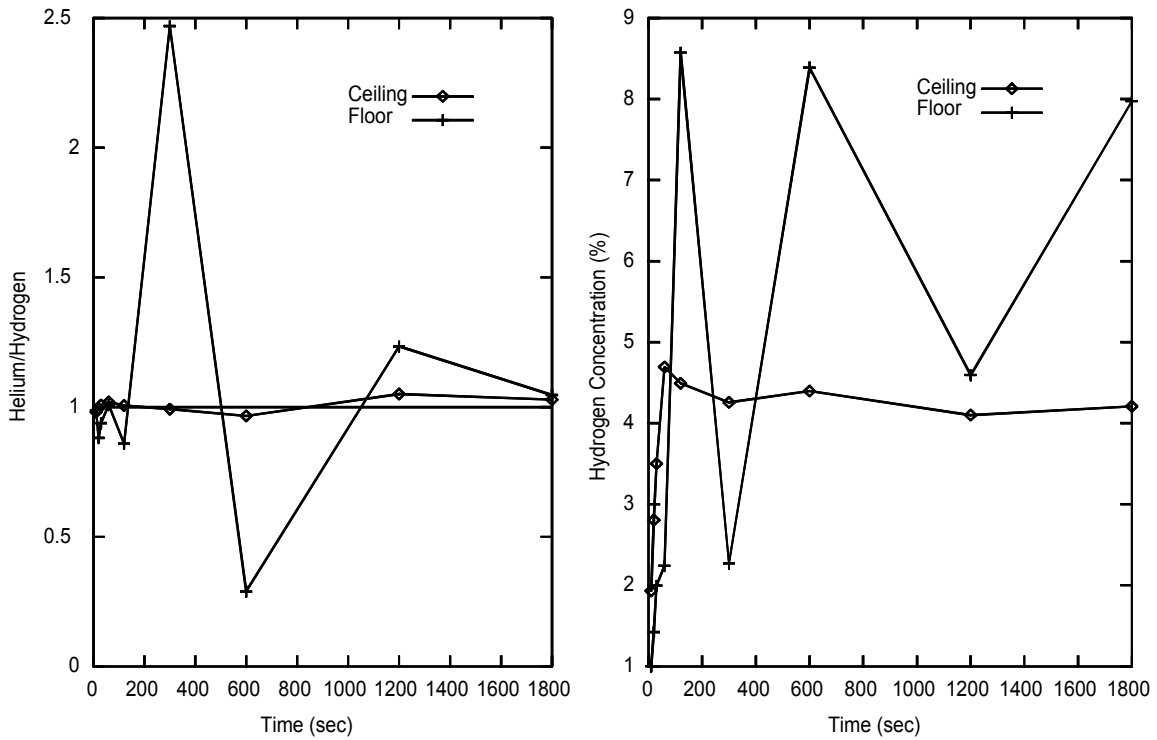


Figure 28 - Leakage in middle of hallway. Double vent at end of hallway. Leakage rate: 27,184 l/hr

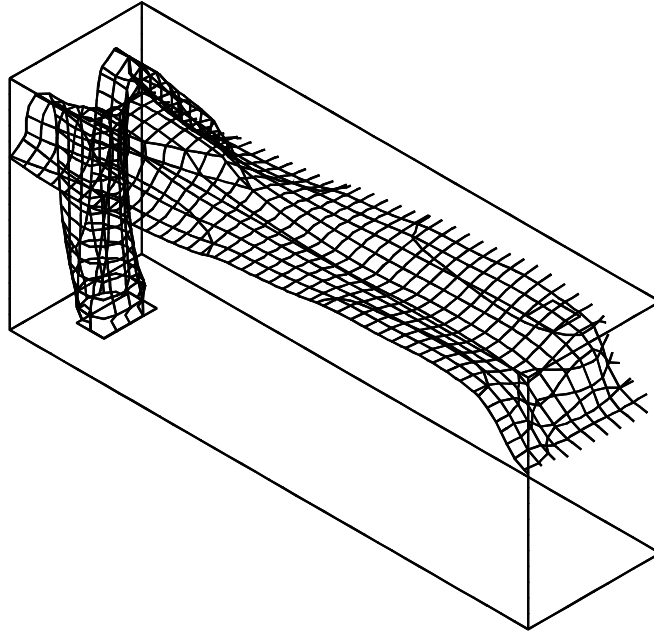


Figure 29 - Surface of constant 36% hydrogen concentration after leakage at 27,184 l/hr for 20 minutes

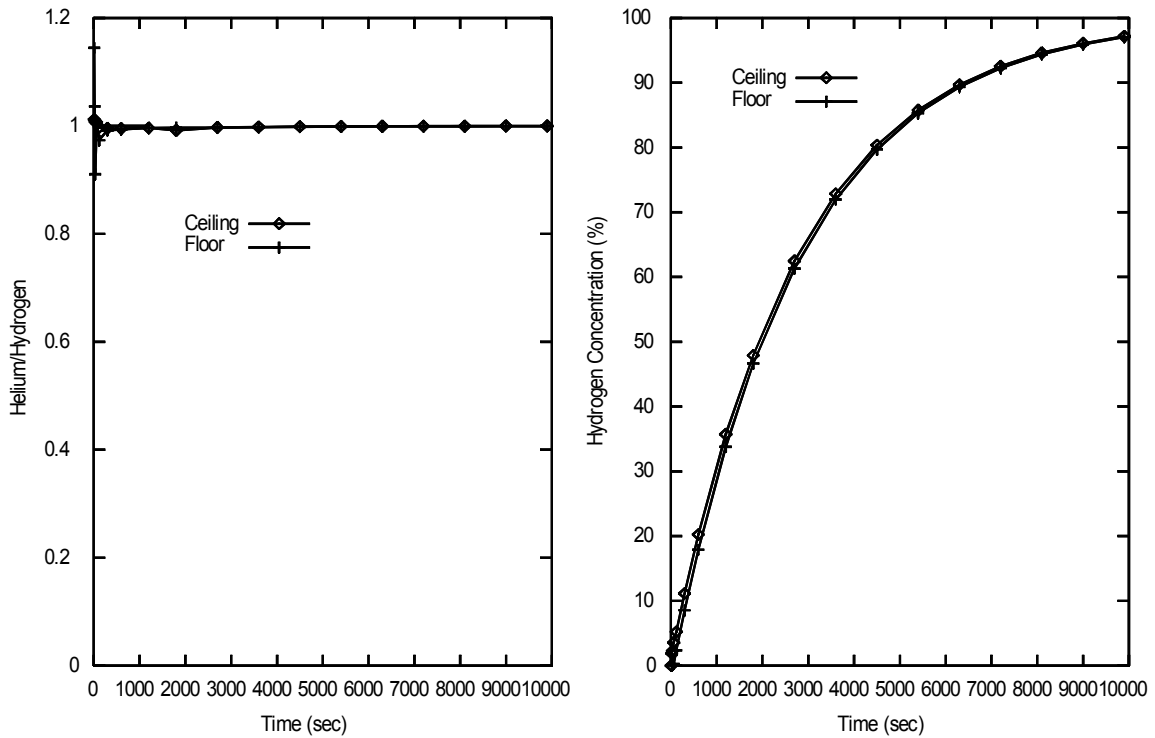


Figure 30 - Leakage at end of hallway. Single vent high at opposite end of hallway. Leakage rate: 27,184 l/hr

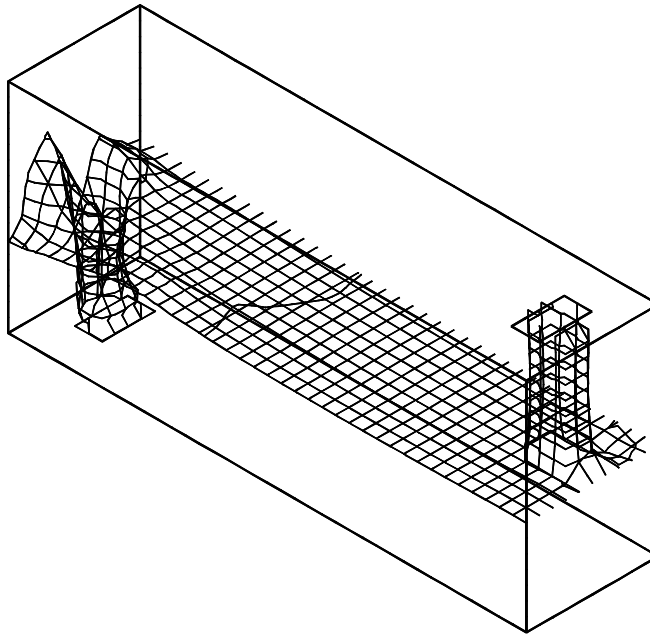


Figure 31 - Surface of constant 22% hydrogen concentration after leakage at 27,184 l/hr for 20 minutes

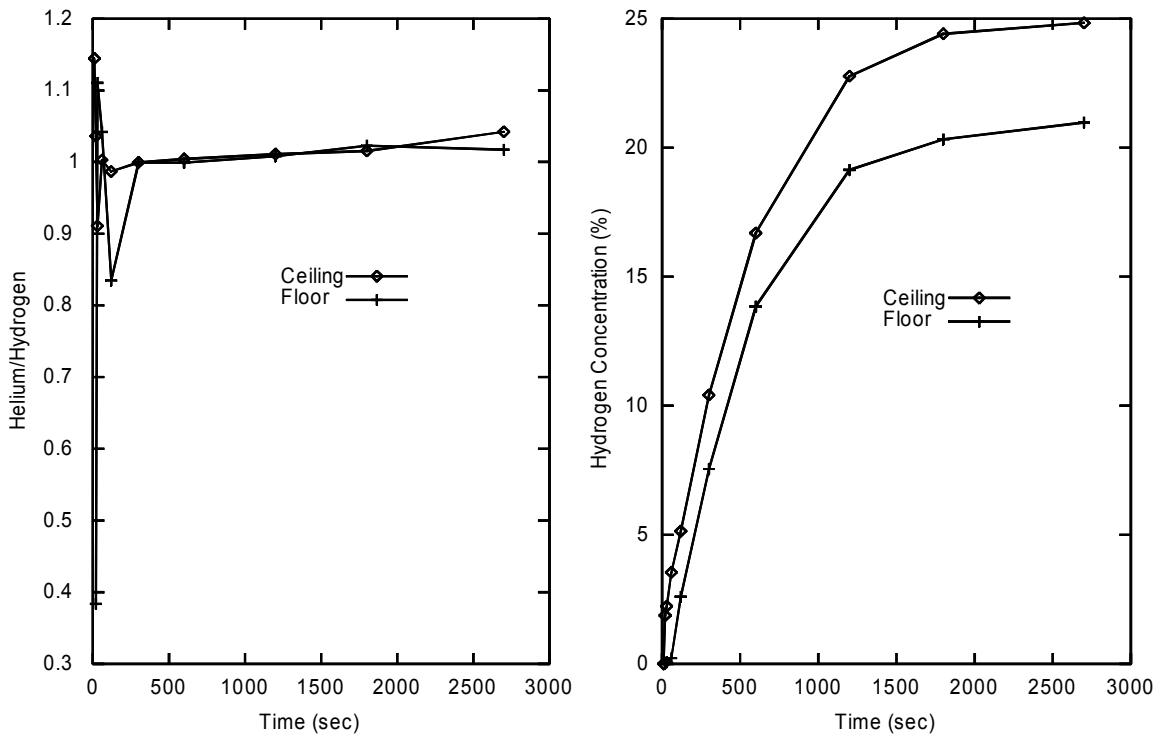


Figure 32 - Leakage at end of hallway. Single vent high at opposite end of hallway. Leakage rate: 27,184 l/hr

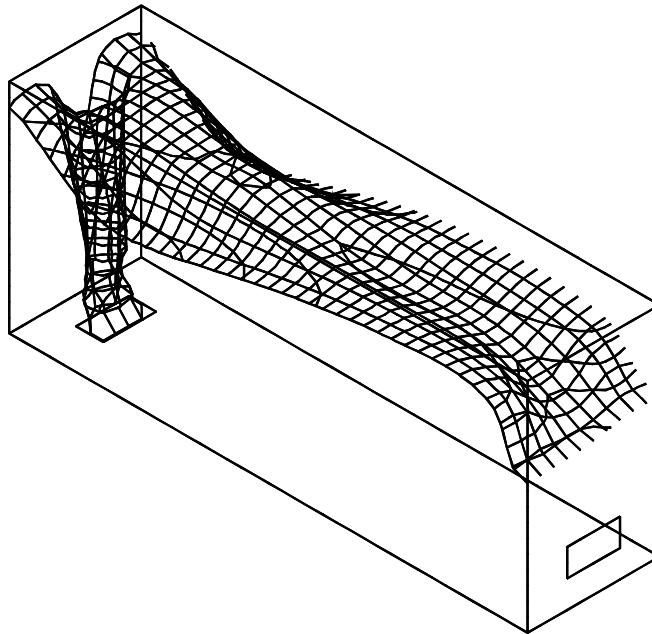


Figure 33 - Surface of constant 24% hydrogen concentration after leakage at 27,184 l/hr for 20 minutes

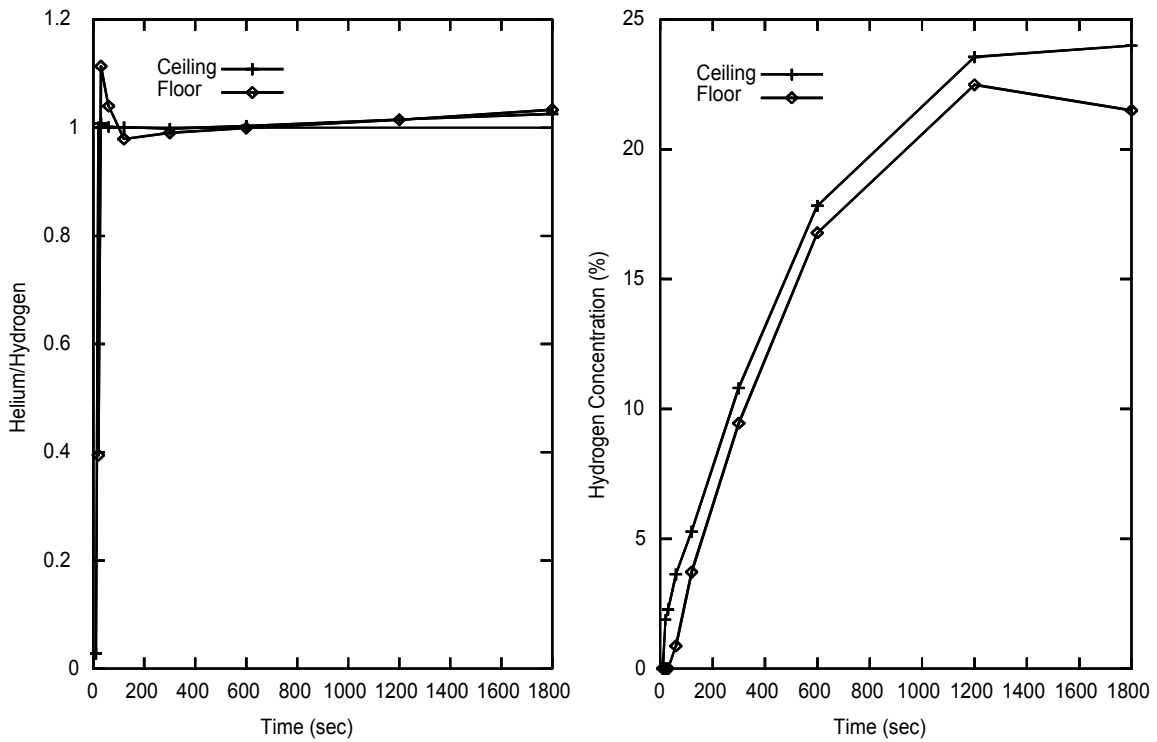


Figure 34 - Leakage at end of hallway. Single vent low at opposite end of hallway. Leakage rate: 27,184 l/hr

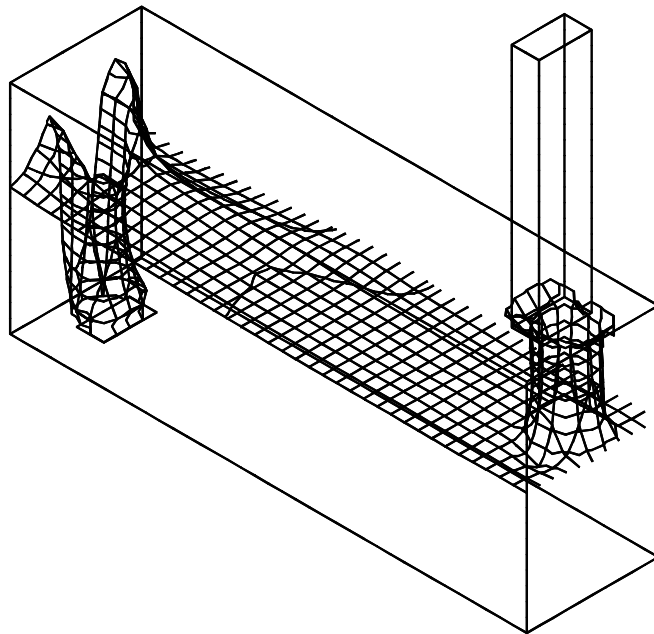


Figure 35 - Surface of constant 12% hydrogen concentration after leakage at 27,184 l/hr for 20 minutes

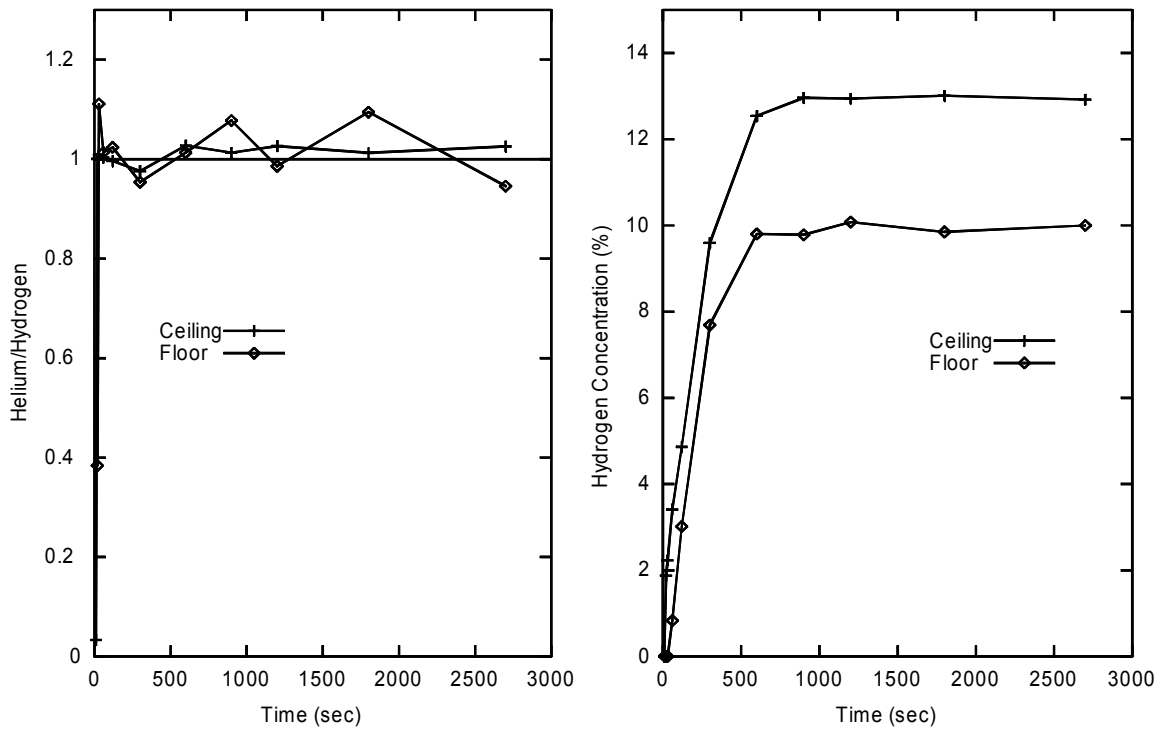


Figure 36 - Leakage at end of hallway. Single vent, with chimney, at opposite end of hallway. Leakage rate: 27,184 l/hr

Interconnected simple enclosures do not necessarily show a one-to-one relationship between helium and hydrogen concentration. Figures 37 through 40 show two interconnected hallways, one above the other in a two-story structure. In the downstairs hallway the helium to hydrogen ratio is less than 1.0. This would result in hydrogen concentrations that were 15% higher than predicted if the helium values were used as a direct indicator. The method is still an accurate predictor of behavior in the upstairs hallway but since higher hydrogen concentrations are reached in the downstairs hallway, the downstairs hallway is of greater concern.

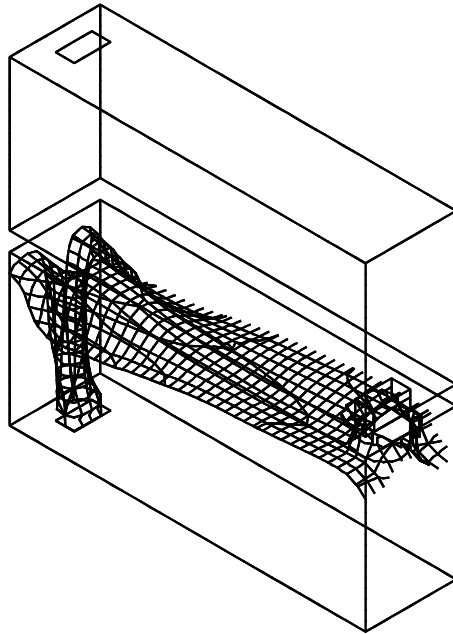


Figure 37 - Surface of constant 25% hydrogen concentration after leakage at 27,184 l/hr for 20 minutes

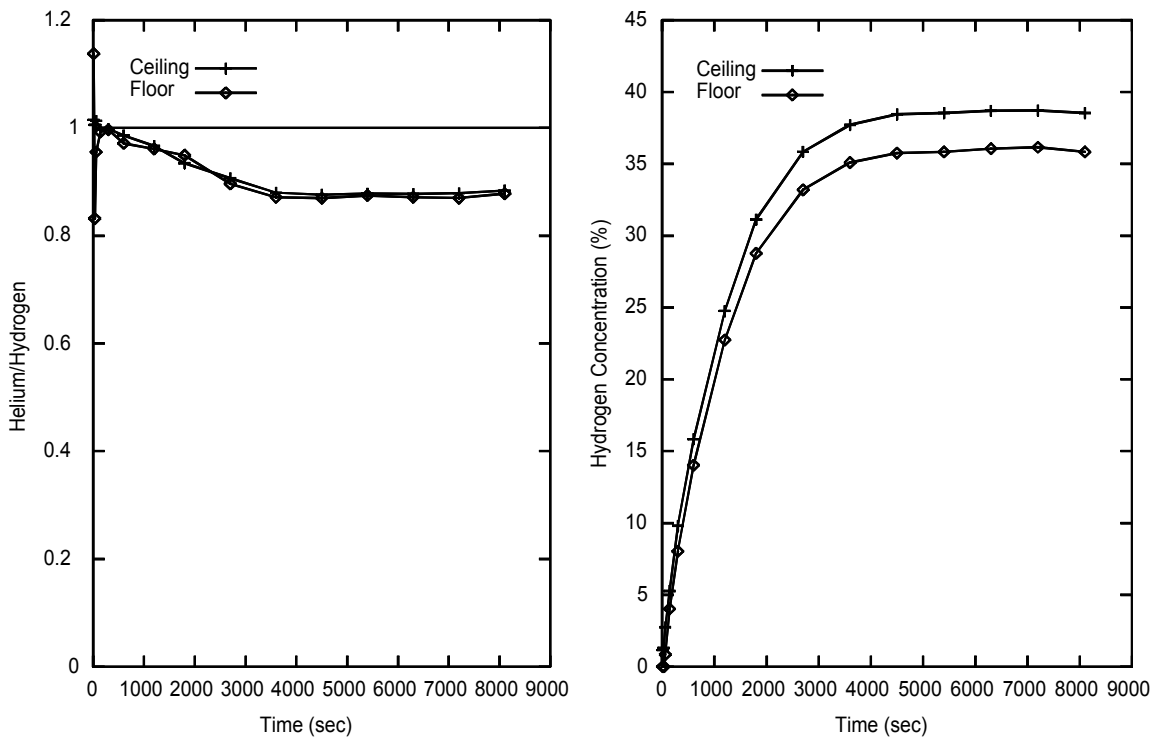


Figure 38 - Downstairs: Leakage at end of hallway (downstairs). Vent at opposite end of hallway (downstairs). Vent in ceiling (upstairs). Leakage rate: 27,184 l/hr

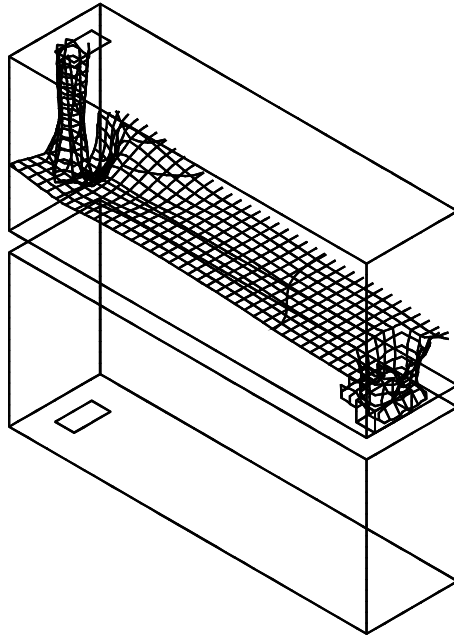


Figure 39 - Surface of constant 13% hydrogen concentration after leakage at 27,184 l/hr for 20 minutes

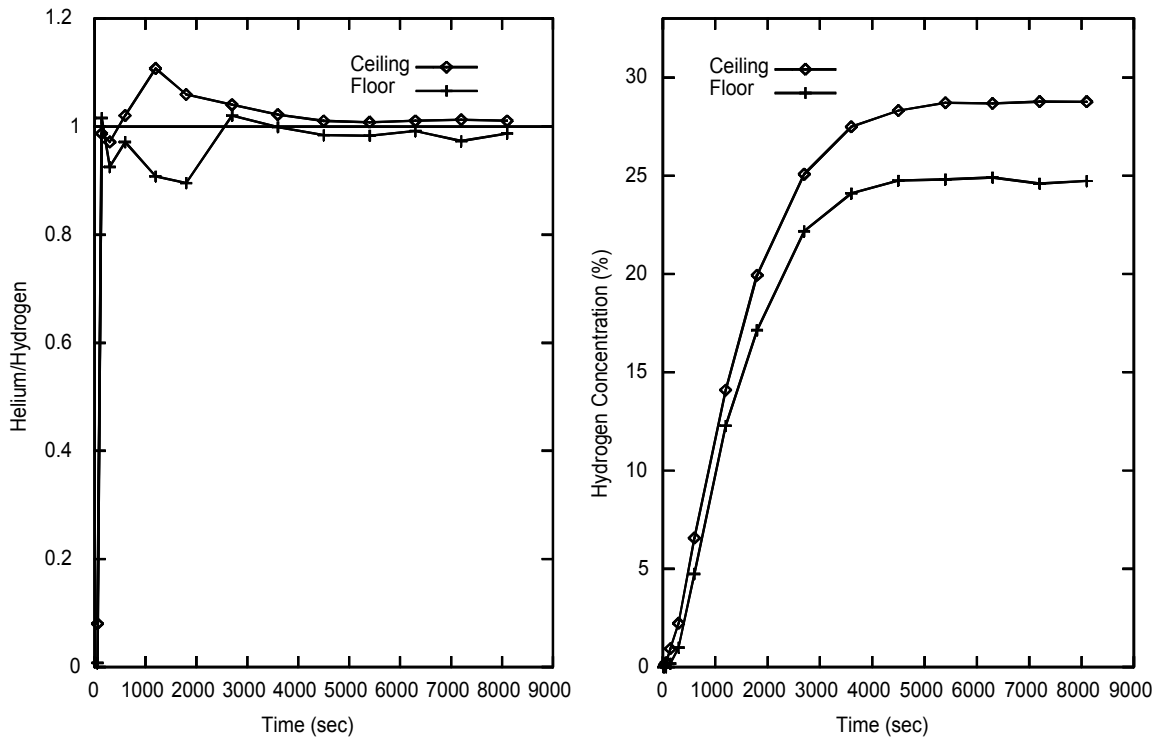


Figure 40 - Upstairs: Leakage at end of hallway (downstairs). Vent at opposite end of hallway (downstairs). Vent in ceiling (upstairs). Leakage rate: 27,184 l/hr

Hydrogen Safety Information Dissemination to Groups Outside the Hydrogen Community

This research effort has resulted in production of two BetaCAM videos and a personal interview video for the H2000 Project Safety video. Discussions began in the middle of June 1999 with Geoffrey Holland of Cognizant Media to establish the subject matter to be covered by the University of Miami. It had been previously decided to present animation of hydrogen leakage into a hallway to demonstrate hydrogen gas cloud motion. By mid-July, the subject matter of the first video to be provided to the H2000 project was established. It was decided that it was preferable to model a vehicle in a single car garage. This allowed a comparison of the leakage of hydrogen to the leakage of LPG or gasoline from that vehicle to be made.

The following accident scenario was modeled. A family size vehicle was parked in a single car residential garage. The accident scenario began when a fuel line leak released fuel after the vehicle was parked in the garage. The modeling was done assuming the vehicle was powered by gasoline, hydrogen, or LPG. In the cases of hydrogen and LPG the fuel pressure cutoff solenoids that would normally shut off with the ignition key were assumed to have also failed. The leak was assumed to be a circular hole producing a turbulent leak. This assumption was least favorable for hydrogen. If the leak was assumed laminar, as would be the case with a leak caused by corrosion, the hydrogen flow rate would have been 80% lower. The leakage rate for gasoline was experimentally determined for a circular hole in a standard gasoline fuel line. The leakage rates were 7200 liters/hr for hydrogen, 848 liters/hr for LPG, and 2.6 liters/hr for gasoline. The clouds of combustible gas produced by the leak were plotted using the lean limit of combustion for each fuel. The lean limits were 4.1% for hydrogen, 2.1% for LPG, and 1.3% for gasoline. The topic of fuel leakage into a garage has been addressed previously at the University of Miami. This work effort required additional modeling of the leakage

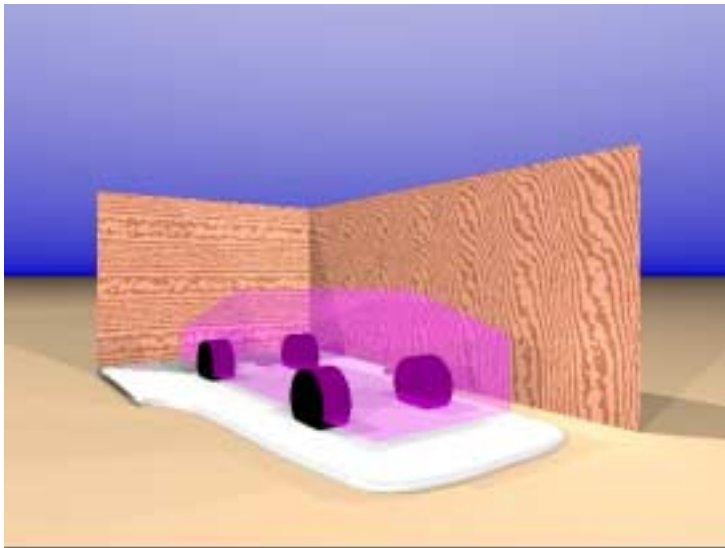


Figure 41 - Draft animation frame of combustible LPG cloud growing under vehicle

of gasoline together with animation of the previous computational results. Figure 41 shows a draft frame of the animation of a combustible LPG cloud growing from a fuel line leak in an LPG fueled vehicle. Figure 41 shows the size of the combustible cloud produced by LPG leaking at a rate of 848 liters/hr. The cloud was defined by the lean limit of combustion for LPG (2.1%) and is shown after 30 minutes of leakage.

It was decided in late November that the format of the video needed additional detail, showing the relative position of the garage to the house and the vents in the garage door. The video of fuel leakage (H₂, LPG, and Gasoline) into a residential garage was updated to the format shown in Figures 42 through 46. Figure 42 shows the residential home that has a single car garage. The subject vehicle is shown moving up the driveway.



Figure 42 - Residential home with single car garage

Figure 43 shows the vehicle parked in the garage with the garage door almost completely closed. Note that there are a strip of 7-in. tall louvered and screened vents at the top and bottom of the garage door.



Figure 43 - Vehicle parked in garage (Note garage door vents)

Figure 44 shows the size of the combustible cloud formed by gasoline leaking at a rate of 2.6 liters/hr for 30 minutes.



Figure 44 - Combustible cloud produced by gasoline

Figure 45 shows the size of the combustible cloud formed by LPG leaking at a rate of 848 liters/hr for 30 minutes.



Figure 45 - Combustible cloud produced by LPG

Figure 46 shows the size of the combustible cloud formed by hydrogen leaking at a rate of 7200 liters/hr for 30 minutes.



Figure 46 - Combustible cloud produced by hydrogen

In February, Geoffrey Holland came to Miami to videotape interviews for H2000 and see the results of the animations. While he was in Miami it was decided to also provide a video of hydrogen leakage and ignition from a 1985 Mercury Cougar tested in previous DOE research.

The final BetaCAM form of the leakage into a single car garage was sent to Cognizant Media on March 22nd. The BetaCAM copy of hydrogen leakage and ignition from a 1985 Mercury Cougar was sent on April 12th. Figure 47 is a frame from that video that shows hydrogen leaking at 3000 cubic feet per minute.



Figure 47 - Hydrogen release and ignition

Acknowledgements

The authors would like to acknowledge the Department of Energy without whose support this work would not have been possible.

ADVANCED THERMAL HYDROGEN COMPRESSION

David H. DaCosta
Ergenics, Inc.
247 Margaret King Ave.
Ringwood, NJ 07456

Abstract

Ergenics, Inc. has developed a novel thermal hydrogen compressor that may offer advantages for compressing hydrogen produced from renewable resources using advanced production techniques. Ergenics' thermal compressor is an absorption based system that uses the properties of reversible metal hydride alloys. Hydrogen is absorbed into an alloy bed at ambient temperature and is desorbed at elevated pressure when the bed is heated with hot water. Two recent innovations strongly suggest that thermal compressors can be used for non-pure hydrogen streams likely to result from advanced production methods. The first involves a combination of processes that permit the absorption of impure hydrogen streams by hydride alloys. The second is a modular alloy bed design that permits rapid hydrogen absorption kinetics, enabling a reduction in compressor size with an associated reduction in capital cost.

The long term goal of this project is to develop a thermal hydrogen compressor that operates in conjunction with advanced hydrogen production technologies and improves the efficiency and economics of the compression process.

Introduction

An important element of large scale hydrogen production, storage and utilization infrastructure is hydrogen compression. Ergenics is examining the application of advanced thermal hydrogen compression to hydrogen produced from renewable resources. The compressor would be used in conjunction with physical storage (e.g. storage as a high pressure gas) or other advanced storage system that requires hydrogen to be supplied at elevated pressure. The advanced thermal compressor can be powered by either waste heat from a hydrogen production process or solar hot water. It has overwhelming advantages compared to mechanical hydrogen compressors, including smaller size, lower capital, operating and maintenance costs, no rotating hydrogen seals, and nearly silent operation.

Ergenics, Inc. has been supplying thermal hydrogen compressors for pure hydrogen gas streams for more than 15 years. Recent developments in moisture tolerant metal hydride alloy storage systems strongly suggest that thermal compressors can be used for non-pure hydrogen streams likely to result from advanced production methods. Additional developments in rapid hydrogen absorption alloy bed design and modular construction now enable systems that can economically process the high flow rates associated with large-scale hydrogen production facilities.

In the thermal compressor, hydrogen is absorbed in a reversible metal hydride alloy at low pressure in a water-cooled container. The container is subsequently heated with hot water which releases the hydrogen at higher pressure. The pressure increases exponentially with increasing temperature, so large pressure increases can be affected with only moderate temperature increases. To obtain even higher pressures, several containers are connected in series, with each container using a different hydride alloy with successively higher operating pressures. Continuous compression is achieved with two identical containers in a parallel configuration; one container cooled by water absorbs hydrogen while the other is heated with hot water to release hydrogen at the same rate. The cool and hot water streams are periodically switched and simple check valves keep hydrogen moving through the compressor (Golben 1983).

The hydride alloys are active metal powders that are affected by gaseous impurities. Certain active gas species such as water vapor, oxygen and carbon monoxide can gradually poison the alloy, reducing its hydrogen sorption capabilities. Inert species such as noble gases and nitrogen can blanket the alloy, slowing hydrogen absorption until the blanket is swept away. Ergenics pioneered research into alloy poisons in the early 1980s. In the early 1990s, corrosion resistant alloys were developed for nickel-metal hydride batteries. In connection with its recent metal-hydrogen battery development, Ergenics has invented and patented a process that enables hydride alloys to store hydrogen saturated with water vapor. Related processes and alloying techniques can eliminate performance degradation from other active gas species.

The work completed to date includes three elements:

- We classified the hydrogen composition and operating conditions expected to result from various advanced production techniques to determine which processes would be good candidates for thermal compression.
- We identified three techniques that can mitigate the effect that impurities have on thermal compressor operation.
- We prepared a preliminary design for a 3,600 psia, 2,000 scfh refueling station thermal compressor, compared the thermal compressor with a mechanical compressor and performed a hazardous operation analysis.

Discussion

Hydrogen Composition Expected From Advanced Production Processes

The advanced hydrogen production processes analyzed for this work were selected from projects funded by the DOE Hydrogen Program in 1999. Production processes included:

- algal hydrogen production (photobiological)
- biomass via fast pyrolysis
- biomass in supercritical water
- plasma catalytic reforming of natural gas
- PEM electrolysis
- photoelectrochemical direct conversion
- sodium borohydride production

Information about hydrogen compositions attained to date and the availability of waste or solar heat was gathered from the Proceedings of the 1999 U.S. DOE Hydrogen Program Review. Where necessary, follow up calls were made to the principal investigators for clarification or updated information.

Hydrogen impurities include air, H₂O, N₂, O₂, CO, CO₂, and CH₄ over wide concentration ranges. Production pressures range from atmospheric to very high. For example, a hydrogen compressor will not be required for biomass in supercritical water because the process produces hydrogen near supercritical (water) pressure. The availability of waste heat or solar heat is application specific.

Table 1 presents a summary of hydrogen compositions, conditions, availability of heat and conclusions about which processes are candidates that can take advantage of the benefits of thermal compression.

Table 1. Hydrogen Quality and System Compatibility Summary

| H₂ Production Process | H₂ Purity | Waste Heat | H₂ Pressure | Comments |
|--|---|-------------------|-------------------------------|--|
| Algal H ₂ Production (Photobiological) | H ₂ : >90% N ₂ : <10% Air: trace | Solar | Atmospheric | Good Application for Thermal Compression |
| Hydrogen from Biomass via Fast Pyrolysis/Catalytic Steam Reforming | H ₂ : 60-70% CO ₂ : 20-30% CO: 5% | Yes | Moderate | Good Application for Thermal Compression |
| PEM H ₂ Electrolyser | H ₂ : >99% H ₂ O: sat. | Mod. | Moderate | Will need heat assist |
| Plasma Catalytic Reforming of Natural Gas | H ₂ : 25-38% CO ₂ : 5-8% CO: 8-17% CH ₄ : 2-12% | Yes | Moderate | Incomplete Data |
| Biomass in Supercritical Water | H ₂ : .57mf CO ₂ : 0.34mf CO: 0.03mf CH ₄ : 0.06mf (see below) | Yes | High | No need for Compressor |
| Supercritical Water Pyrolysis (Purification for Biomass SCW) | H ₂ : 9mf CO ₂ : 5mf CO: 0.25mf | Yes | High | No need for Compressor |
| Photoelectrochemical Based Direct Conversion Systems for H ₂ Production | H ₂ : >99% | Solar | Atmospheric | Good Application for Thermal Compression |
| Sodium Borohydride | H ₂ : >99% H ₂ O: sat. | Mod. | Moderate | Will need heat assist |

Thermal Compressor Purification Processes

Impurities interact with hydride alloys with varying effects (Sandrock 1984). *Poisoning* results in a rapid decrease in hydrogen capacity with cycling. Damage from poisoning tends to be localized on the alloy particle surface, so it is often possible to restore performance with little, if any, loss in capacity. *Retardation* is manifested by a reduction in absorption kinetics without loss in ultimate capacity. With enough time, full capacity can be achieved. *Reaction* causes irreversible capacity loss through bulk corrosion of the alloy. Reaction results in the formation of very stable chemical compositions that do not reversibly hydride and cannot be easily returned to their original state.

Although hydrogen purification systems can be used to remove impurities, the purification systems themselves are often complex, expensive to maintain, and, for hydrogen produced at atmospheric pressure, would require their own motive force in the form of a mechanical compressor or blower. These disadvantages offset most benefits that could be derived from thermal compression.

It is possible to engineer alloys and containment systems that can withstand impurities without degradation. Ergenics has invented and patented a process that enables hydride alloys to store hydrogen saturated with water vapor (Golben 1999). This alone opens many new possibilities to apply hydride process technology to commercial hydrogen production. In addition, nickel-metal hydride battery alloy development by Ergenics and others stimulated a large body of research into the corrosion of hydride electrodes submersed in electrolytes. A number of corrosion inhibiting additives, such as cobalt and tin, have been identified for submersed alloys, and Ergenics has found these to have positive impact on gaseous systems as well.

Previously, reversible metal hydride alloys would sustain damage from hydrogen impurities at low levels of ~ 50 ppm. Ergenics has developed three processes, summarized in Table 2, that permit hydride alloy beds to tolerate higher levels of impurities, in some cases up to 10,000 ppm or more. Passive Purification is used for water vapor and oxygen, Elevated Temperature Desorption is used for CO and CO₂, and Automatic Venting can clear inert gas blanketing caused by N₂ and CH₄. The advanced thermal hydrogen compressor will include the three purification processes.

Table 2 – Thermal Compressor Purification Processes

| Impurity | Process | Comments |
|----------------------------------|---------------------------------|--|
| H ₂ O, O ₂ | Passive Purification | Hydride Heat Exchanger in-situ process prevents retardation and poisoning. Removes O ₂ from hydrogen. |
| CO, CO ₂ | Elevated Temperature Desorption | Over 115°C desorption removes CO impurities from alloy surface. |
| N ₂ , CH ₄ | Automatic Venting | Clears inert gas blanketing and removes impurity from hydrogen. |

Miniature Modular Hydride Heat Exchangers

Thermal hydrogen compressors produced to date are a superior alternative to diaphragm compressors when there is a source of hot water. However, they have been limited to applications with relatively low flow rates (400 scfh) due to heat transfer limitations associated with large alloy beds. Another important innovation from Ergenics will permit economical scale up to production-sized units competitively superior to piston compressors. Ergenics has developed and patented an advanced hydride bed design with rapid heat transfer capabilities. The hydride bed is essentially a miniature high

surface area hydride heat exchanger, which permits the construction of large compressors of small size and cost. The small hydride beds can be thermally cycled at a rapid rate (<1 minute) in order to process high hydrogen flow rates. The unique hydride heat exchanger design is modular and lends itself to high volume, low cost production.

Thermal Compressor For A Hydrogen Service Station

Design

A thermal compressor sized for duty at a hydrogen service station to refuel vehicles has been preliminarily designed and compared with a mechanical compressor. The compressor employs the three purification processes and the miniature hydride heat exchanger design. A detailed Piping and Instrumentation Diagram and a Layout Drawing were prepared for cost estimating purposes. The layout appears in Figure 1.

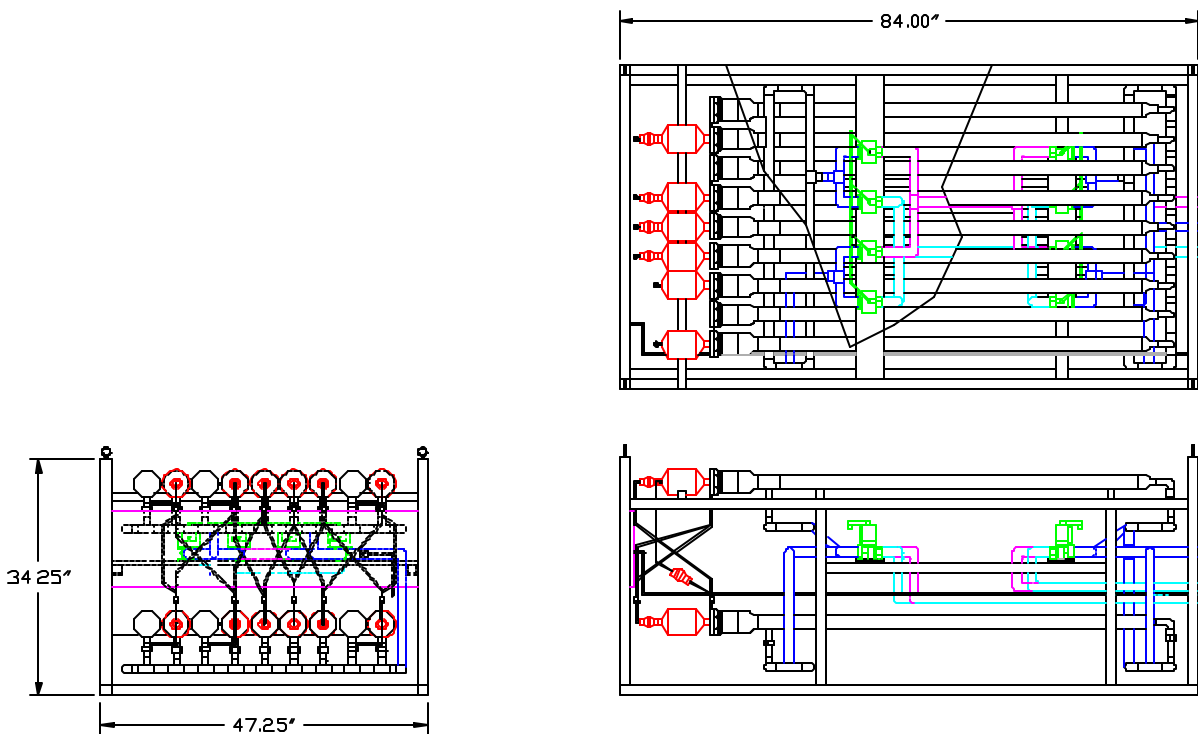


Figure 1 - Advanced Thermal Compressor Layout

Economic Analysis

An economic analysis comparing a thermal compressor with a mechanical compressor was performed and is summarized in Table 3. Assumptions used for the analysis are:

- Operating Conditions: 2,000 scfh, Inlet P=100 psia, Outlet P=3,600 psia

- Capital costs: Mechanical compressor quotation; Thermal compressor detailed cost estimate.
- Operating Costs: Power @ \$0.10/kWh, Waste heat @ \$0.00
- Maintenance Costs: Mechanical compressor annual rebuild; Thermal compressor valve replacement every other year

Table 3. Comparison of Advanced Thermal and Mechanical Hydrogen Compressors

| | Thermal Compressor | Mechanical Compressor |
|--|---------------------------|------------------------------|
| Hydrogen Flow | 2,000 scfh | 2,000 scfh |
| Inlet Pressure | 100 psia | 100 psia |
| Outlet Pressure | 3,600 psia | 3,600 psia |
| Number of Stages | 5 | 3 |
| Weight | 100 kg | 3,600 kg |
| Volume | 400 liters | 6,000 liters |
| Hot Water Flow (waste heat) | 50 gpm @ 90 C | - |
| Heat Energy Required | 240 kBTU/h | - |
| Cooling Water Flow | 50 gpm @ 30 C | 20 gpm @ 30 C |
| Electrical Power | 500 watts | 20,000 watts |
| Estimated Capital Cost | \$130,000 | \$145,000 |
| Annual Power Cost (2,000 h/y, \$0.10/kWh) | \$100 | \$4,000 |
| Annual Maintenance Cost | \$1,000 | \$8,000 |

Safety Analysis

The compressor system was subjected to a complete Hazardous Operation Review in conjunction with a major supplier of hydrogen. The review divided the compressor system into six nodes and each node was reviewed for startup, normal operation, shutdown, failure modes, controls, design pressure, pressure relief, and materials.

Conclusions

Thermal hydrogen compression appears to offer significant advantages over mechanical compression for large scale hydrogen production from renewable resources.

Future Work

In order to validate the conclusions reached to date, we plan to construct and demonstrate a single stage thermal compressor that employs miniature hydride heat exchangers and an associated test apparatus that will verify thermal compressor performance while processing hydrogen with impure gas species. The test apparatus will be flexible enough to vary inlet impurity levels to determine threshold contamination levels (levels at which compressor performance is affected). Three purification technologies will be demonstrated: passive purification for oxygen and water, inert gas purification, and elevated temperature desorption for CO and CO₂.

In the case of impurities that can adversely affect fuel cell operation (e.g. nitrogen, CO), outlet hydrogen purity will be monitored to verify the degree to which a thermal compressor can perform the dual function of compressing and purifying hydrogen. This will allow the evaluation of trade-offs between hydrogen purity and compressor and fuel cell operating efficiencies necessary for the design and integration of full-scale systems

Acknowledgement

This material is based on work partially funded by the United States Department Of Energy's Hydrogen Program under Cooperative Agreement No. DE-FC36-99GO10448.

References

- Golben, P.M. 1983. "Multi-stage Hydride Hydrogen Compressor." In *Proceedings of the 18th Intersociety Energy Conversion Engineering Conference*, 1746-1753. New York, NY: American Institute of Chemical Engineers.
- Golben, M. 1999. "Advanced Thermal Hydrogen Compression." In *Proceedings of the 34th Intersociety Energy Conversion Engineering Conference*. Warrendale, PA: SAE International.
- Sandrock, G.D.; Goodell, P.D. 1984. "Cyclic Life of Metal Hydrides with Impure Hydrogen: Overview and Engineering Considerations." *Journal of Less-Common Metals* 104, 159-173

MICROHOTPLATE BASED H₂ GAS SENSORS

Frank DiMeo Jr., and Barry Chen
ATMI
Danbury, CT 06810

Abstract

The United States Department of Energy has been mandated by Congress to develop the critical technologies required for the implementation of hydrogen based energy. A common need in every technology area is the ability to detect and monitor gaseous hydrogen. Hydrogen gas sensors that can quickly and reliably detect hydrogen over a wide range of oxygen and moisture concentrations are not currently available, and must be developed in order to facilitate the transition to a hydrogen based energy economy

This paper reports our recent progress in developing MEMS (Micro-Electro-Mechanical Systems) based H₂ gas sensors. These sensors couple novel thin films as the active layer with a MEMS structure known as a Micro-Hotplate. This coupling results in a H₂ gas sensor that has several unique advantages in terms of speed, sensitivity, stability and amenability to large scale manufacture. Our preliminary results are extremely encouraging, and suggest that this technology has substantial potential for meeting the sensing requirements of a hydrogen based energy economy.

Introduction

"Hydrogen will join electricity in the 21st Century as a primary energy carrier in the nation's sustainable energy future."(DOE 1995) This bold statement was made as part of

the 1995 Hydrogen Vision and reflects the tremendous potential of hydrogen as an energy system. The abundance and versatility of hydrogen suggests that it can provide solutions to problems encountered with current fossil fuel energy systems, such as declining domestic supplies, air pollution, global warming, and national security.

Significant research and development efforts are currently underway to make the widespread use of hydrogen technically and economically feasible. These efforts are directed toward creating the basic building blocks of a hydrogen economy: production, storage, transport and utilization. An underlying need of each of these building blocks is the ability to detect and quantify the amount of hydrogen gas present. This is not only required for health and safety reasons, but will be required as a means of monitoring hydrogen based processes. For example, if hydrogen were to be introduced as an automobile fuel additive, several sensors would be needed to detect potential hydrogen gas leaks, as well as to monitor and provide feedback to regulate the air/fuel/hydrogen mixture.

Although the safety record of the commercial hydrogen industry has been excellent, it is estimated that undetected leaks were involved in 40% of industrial hydrogen incidents that did occur. (HRI/NREL 1998) Emerging hydrogen based energy systems will require hydrogen sensors that are as ubiquitous as computer chips have become in our factories, homes, and in our cars. This means that the ability to produce large volumes of sensors at a low cost is paramount. It follows naturally that the same technology that has enabled computer chips to proliferate could be used to advantage for fabrication of hydrogen sensors: namely, solid state integrated circuit technology.

In order to support an effective hydrogen detection and monitoring system, the hydrogen sensor element must fulfill several requirements. It needs to be selective to hydrogen in variety of atmospheres (including the oxygen-rich high-humidity environments found in fuel cells). It must have a good signal to noise ratio and a large dynamic range. Speed of detection is a critical requirement to ensure rapid response to potentially hazardous leaks. Long lifetimes between calibrations are desirable in order to minimize maintenance. Low power consumption is requisite for use in portable instrumentation and personnel monitoring devices. Ultimately, these must all be achieved by a safe sensor element that is affordable to manufacture in large numbers, so that safe design principles, and not costs, are the deciding factor in the number and locations of detection points.

This paper reports on our recent progress in developing MEMS (Micro-Electro-Mechanical Systems) based H₂ gas sensors. These sensors couple novel thin films as the active layer with a MEMS structure known as a Micro-Hotplate. This coupling was expected to result in a H₂ gas sensor that has several unique advantages in terms of speed, sensitivity, stability and amenability to large scale manufacture. To date, we have demonstrated a speed of response of < 0.5 s to 1% H₂ in dry air, and the ability to detect < 200 ppm. Our preliminary manufacturing analysis suggests that these can readily and inexpensively be produced at quantities of >1 million.

Experimental

Sensor Fabrication

MEMS based hydrogen gas sensors have been produced at ATMI using a 5 step process. The realization of micro-machined suspended structures via a CMOS foundry process has been described by several laboratories, (Suehle, Cavicchi et al. 1993; Cavicchi, Suehle et al. 1995; Baltes, Paul et al. 1998) and the process used in this work is as follows. First the microhotplate device structures were designed using a commercial CAD layout software package. These designs were then sent out for fabrication through the MOSIS foundry service. The as-received chips were etched at ATMI using XeF_2 to create suspended micro-hotplate device structures. The functionalization step of this process involves applying a H_2 sensitive coating to the surface of structures. The precise nature of both the materials and deposition process for this coating are proprietary to ATMI, but for the purposes of this report can be thought of as a rare-earth based film, overcoated with a palladium based layer.(Bhandari and Baum 1999) The final fabrication step was the dicing and packaging of the chips, which was done by an external vendor. Figure 1 shows a group of packaged sensors devices, and Figure 2 is a picture of an individual packaged sensor.

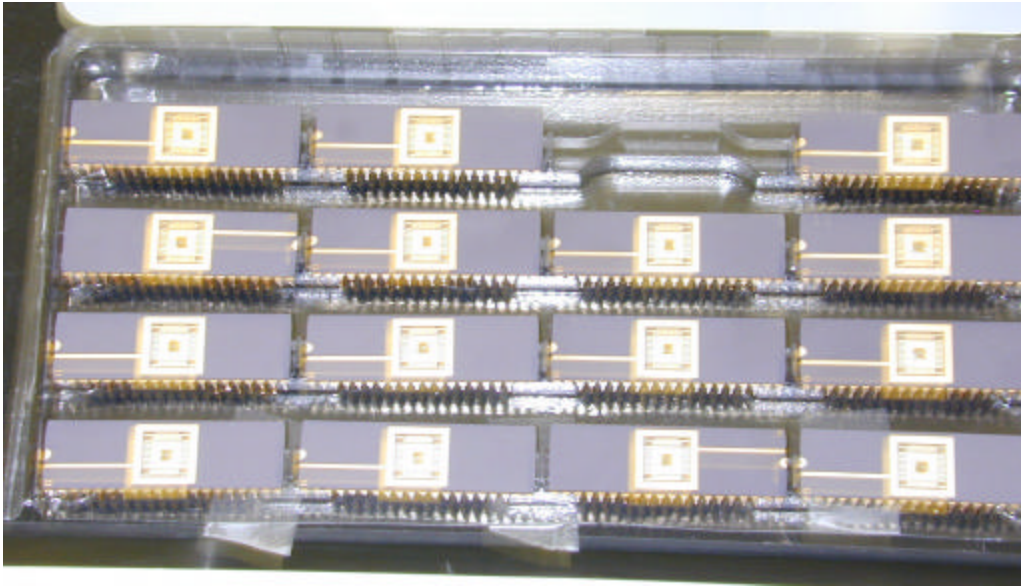


Figure 1. Optical digital photograph of several packaged microhotplate based H_2 gas sensors.

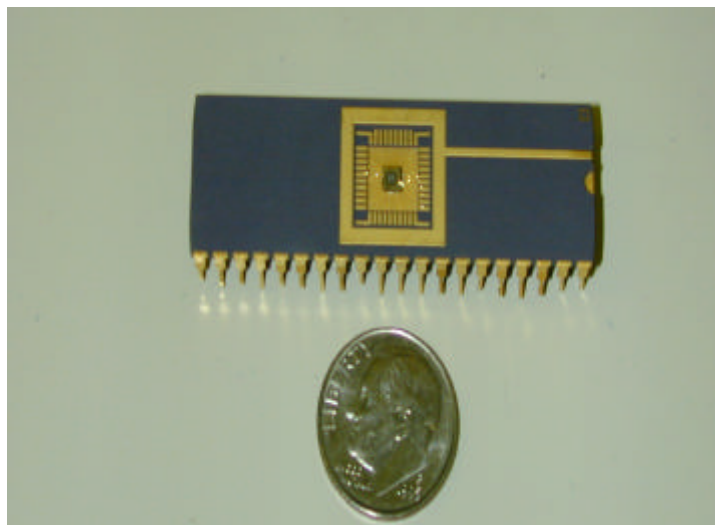


Figure 2. Optical digital photograph of an individual microhotplate based H₂ gas sensor.

H₂ Response Testing

The measured response of these gas sensors is the change in resistance that occurs in the active layer film stack when exposed to hydrogen, where the resistance of the film increases with increasing hydrogen concentration. Based on the design flexibility of the micro-hotplate, the resistance of these films can be measured in either a 2-wire or a 4-wire configuration.

Accurately measuring the speed of response to H₂ of the gas sensors was an important design consideration for both the data collection system and the gas handling manifold constructed for this program. For the data collection, we constructed an automated system based on an HP 34970A DMM data logger with an HP 34902A scanning card. This system is capable of a scanning speed of 250 channels/s. In order to achieve fast gas switching speeds, the gas handling manifold used low volume gas chromatography valves in combination with 1/8" tubing and a small test chamber size.

The ambient gas used for the experiment was triple filtered compressed air that was passed through a membrane drier, with a dewpoint specification of -40°C. Grade 5.0 hydrogen was used and blended with the air using mass flow controllers with ranges of 200 and 5000 sccm respectively.

Discussion

H₂ Gas Sensing Results

Figure 3 shows the resistive response of a micro-hotplate based H₂ gas sensor. The measurement was made in a 2-wire configuration, and the micro-hotplate was held at an

elevated temperature by passing current (< 5 mA) through the embedded polysilicon heater. In this experiment, the sensor was cyclically exposed 10 times to 0.25% H_2 in dry air. Figure 4 focuses on the transition of one particular cycle with an expanded scale. From this figure, a rise time of < 0.44 s was measured. It should also be noted that the magnitude of the response was greater than 120%. This can be compared with the typical change in response of palladium alloy resistors, which is on the order of 10% when exposed to 1 atm of H_2 . (Hunter 1996)

Figure 5 shows the response of a microhotplate to different concentrations of H_2 . In this experiment, the initial concentration was 1%, and it was decreased by a factor of 2 with each step until a final concentration of $\sim 0.01\%$ (150 ppm) was reached. The sensor was exposed two times at each concentration. The exposure time was 300 s and the time between exposures was also 300 s. The sensor exhibited detectable responses to nearly two orders of magnitude of H_2 concentration. The temperature of the hotplate was not intentionally varied in this experiment. It seems likely that the minimum detectable gas concentration can be further improved by optimizing the operation conditions at lower H_2 concentrations. Figure 6 is a plot of the responses from Figure 5 as a function of H_2 concentration. For this plot, the response was taken as the absolute change in resistance as measured from the beginning base line resistance. The H_2 concentration is plotted on a logarithmic axis, and shows that the response does not follow a simple dependence on the H_2 concentration. The reasons for the behavior of the resistivity as a function of H_2 are not currently well understood. One factor influencing the behavior of the curve in Figure 6 is the fact that at the lower H_2 concentrations, the films response does not appear to have come to equilibrium within the exposure time. In addition to this, the influence of contact resistance in a two probe configuration should be considered. Further testing is required to obtain a more accurate understanding of this behavior.

Stability is an important requirement of any type of sensor. To begin the investigation in this area, the resistance as a function of time without H_2 exposure was examined for a period of several days in dry air, as shown in the top panel of Figure 7. There was no flow over the sensor at this time. During the first day or so there is a small steady reduction in resistance, which eventually leveled out. This small drift was on the order of an ohm, which represents hydrogen in the sub-200 ppm range, and may either be due to outgassing from the sensing film, or from the chamber wall. After this, the resistance reached steady state, with a standard deviation of ~ 0.05 ohms. This resulted in a signal to noise ratio of ~ 1200 (average value/standard deviation). The middle panel of Figure 7 shows the power consumed by the polysilicon heater element of the microhotplate over the same time frame, which is expected to be representative of the operating temperature. There appeared to be cyclical variation in the power, which has a ~ 24 hour period, i.e. a day/night difference. When the resistance is multiplied by the power consumed, which, to first order, compensates for temperature, the variation appears much reduced. The signal to noise now increases to nearly 3000, and a jump in resistance on day 6, which was lost in the noise, becomes noticeable.

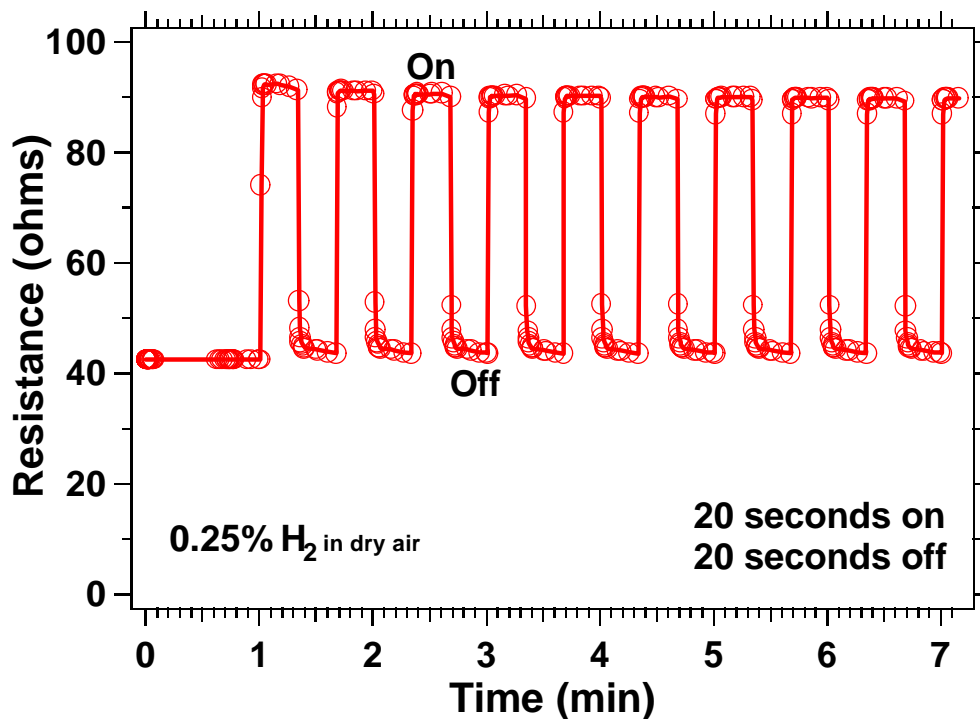


Figure 3. Resistive response of a microhotplate based H₂ gas sensor to repeated exposure to 0.25% H₂ in air. The magnitude of response is greater than 120% of the pre-exposure baseline.

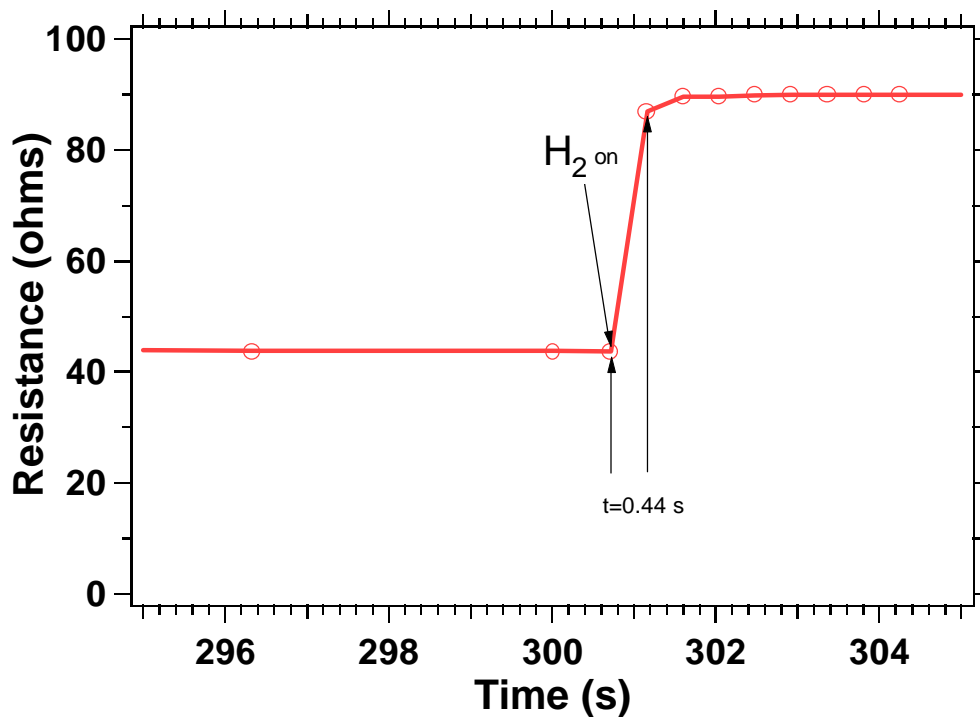


Figure 4. Expanded scale plot of the resistive response of a microhotplate based H₂ gas sensor to exposure to 0.25% H₂ in air, with a demonstrated speed of response < 0.5 sec.

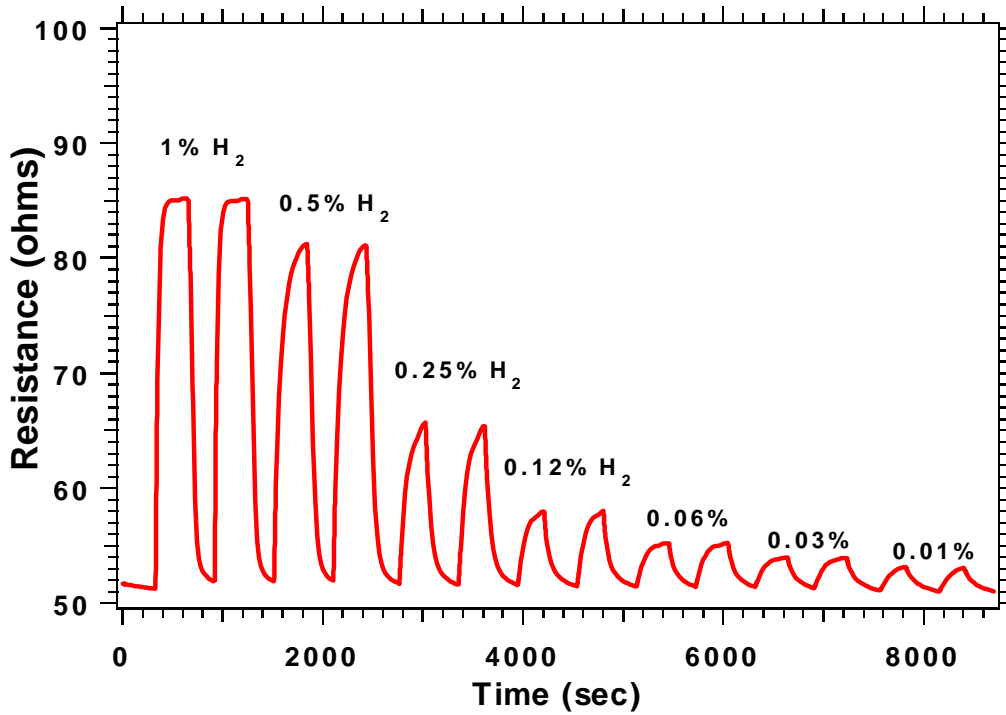


Figure 5. Resistive response of a microhotplate based H₂ gas sensor to concentrations of H₂ in air ranging from 1% to 0.01%.

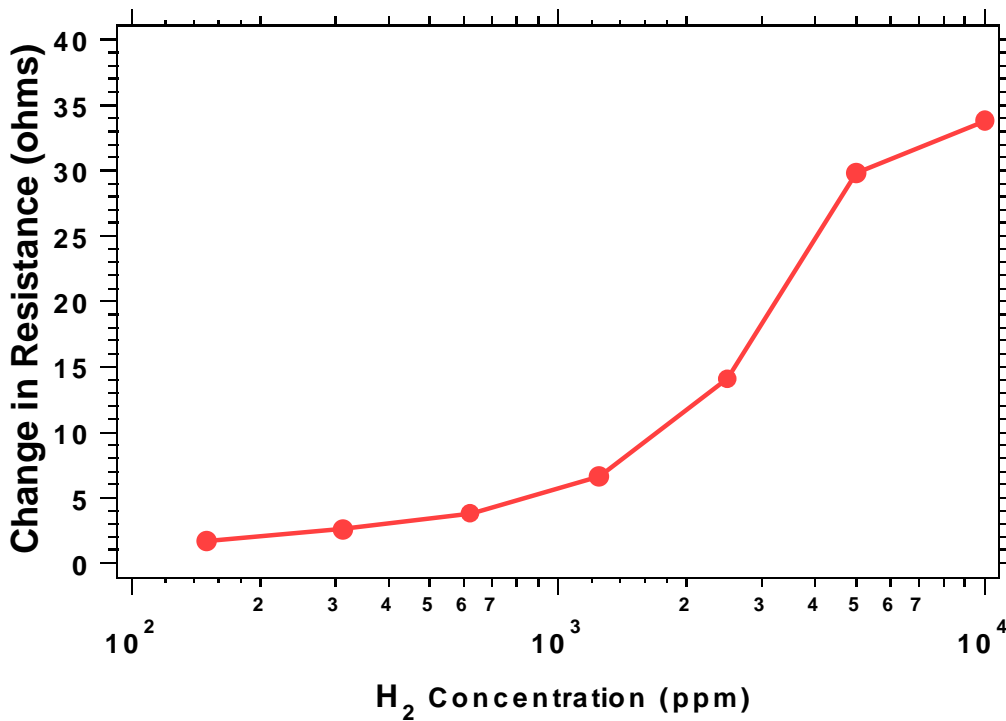


Figure 6. The resistive response from the previous figure, plotted as function of H₂ gas concentration.

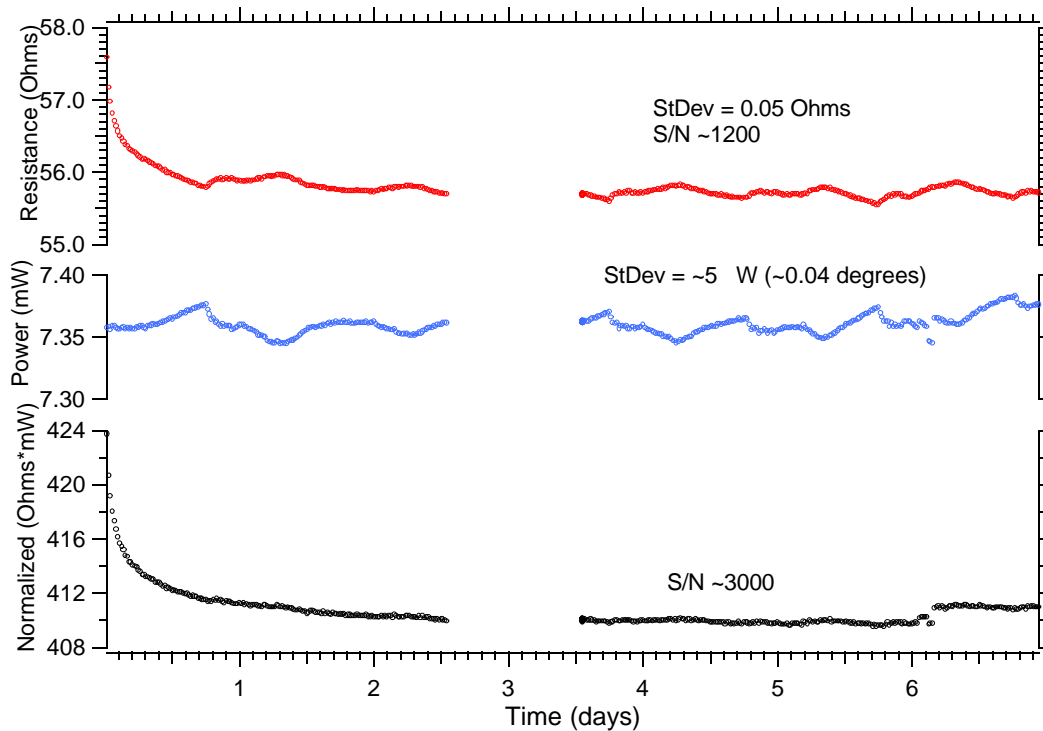


Figure 7. Stability results over a 7 day time frame. Top: H₂ sensor resistance in air. Middle: Measured poly silicon heater power. Bottom: Normalized sensor response (Resistance * Heater Power).

Economic Analysis

A significant advantage to the microhotplate based approach for H₂ gas sensing is that it is based on commercially available semiconductor processing technology. This technology is readily accessible through a number of integrated chip foundry facilities. The small size and simplicity of the microhotplate device can further leverage this advantage, and we therefore estimate that more than 1 million devices could be produced on a single lot of 25 six-inch wafers. Our analysis further indicates that at these quantities, the final device cost becomes dominated by the packaging costs.

Conclusions

In our work to date, we have successfully demonstrated a novel hydrogen gas sensing technology based on a MEMS device platform known as a microhotplate. These sensors have shown exceptional responsivity. Changes in resistance of >120% to 0.25 % H₂ concentrations have been measured, with response times <0.5 sec. These sensors have demonstrated a dynamic range of two orders of magnitude, detecting H₂ from >200ppm to > 1%. In the area of stability, we have demonstrated an un-corrected baseline signal to noise ratio of ~1200, and a temperature compensated signal to noise of ~3000. From a commercialization standpoint, our preliminary analysis indicates that this technology is

readily scalable to quantities > 1 million devices. These results are extremely encouraging and suggest that this technology has substantial potential for meeting the sensing requirements of a hydrogen based energy economy.

Future Work

Based on the successful demonstration of these devices, we plan to continue to focus our efforts on exploring the potential of these devices. We would like to continue to investigate the effect of sensor fabrication on sensor performance, as well as begin hydrogen response testing under different environment conditions, e.g. humid vs dry. We will also continue to investigate the long-term stability of these sensor materials under these different environments

Acknowledgements

The contributions of Frank Tamweber and Ed Hutchins of ATMI in the fabrication of the sensor devices and gas testing manifold respectively are gratefully acknowledged. Conversations with researchers at NIST, Steve Semancik and Dick Cavicchi, are also gratefully acknowledged. This work, performed at ATMI, was supported in part by the U.S. Department of Energy, under contract #DE-FC36-99GO10451. This support, however, does not constitute an endorsement by the DOE of the views expressed in this article.

References

- Baltes, H., O. Paul, et al. (1998). "Micromachined Thermally Based CMOS Microsensors." Proceedings of the IEEE **86**(8): 1660-1678.
- Bhandari, G. and T. H. Baum (1999). "Hydrogen sensor utilizing rare earth metal thin film detection element." US Patent 6,006,582
- Cavicchi, R. E., J. S. Suehle, et al. (1995). "Fast Temperature Programmed Sensing for Micro-Hotplate Gas Sensor." IEEE Electron Device Lett. **16**: 286-288.
- DOE (1995). Vision Statement, The Green Hydrogen Report; The 1995 Progress Report of the Secretary of Energy's Hydrogen Technical Advisory Panel., DOE.
- HRI/NREL (1998). The Sourcebook for Hydrogen Applications, Hydrogen Research Institute, National Renewable Energy Laboratory.
- Hunter, G. W. (1996). "PdTi Metal Alloy as a hydrogen or hydrocarbon sensitive metal." US Patent 5520753
- Suehle, J. S., R. E. Cavicchi, et al. (1993). "Tin Oxide Gas Sensor fabricated using CMOS Micro-hotplates and In Situ Processing." IEEE Electron Device Lett. **14**: 118-120.

PROCESS ANALYSIS WORK FOR THE DOE HYDROGEN PROGRAM - 1999

Margaret K. Mann, Pamela L. Spath, Wade A. Amos, Janice M. Lane
National Renewable Energy Laboratory
Golden, CO 80401

Abstract

In 1999, process analysis work conducted at the National Renewable Energy Laboratory for the Department of Energy's Hydrogen Program included updating previous analyses, performing new cost analyses, identifying system integration issues, and conducting the first in a series of life cycle assessments. The goal of this work is to provide direction, focus, and support to the development and introduction of renewable hydrogen through evaluation of the technical, economic, and environmental aspects of hydrogen production and storage technologies. The advantages of performing analyses of this type within a research environment are several fold. First, the economic competitiveness of a project can be assessed by evaluating the costs of a given process compared to the current technology. These analyses can therefore be useful in determining which projects have the highest potential for near-, mid-, and long-term success. Second, the results of a technoeconomic analysis are useful in directing research toward areas in which improvements will result in the largest cost reductions. Finally, as the economics of a process are evaluated throughout the life of the project, advancement toward the final goal of commercialization can be measured. Life cycle assessment (LCA) is used to identify and evaluate the environmental impacts of emissions and resource depletion associated with a specific process. When such an assessment is performed in conjunction with a technoeconomic feasibility study, the total economic and environmental benefits and drawbacks of a process can be quantified. Material and energy balances are used to quantify the emissions, resource depletion, and energy consumption of all processes required to operate the process of interest, including raw material extraction, transportation, processing, and final disposal of products and by-products. The results of this inventory are then used to evaluate the environmental impacts of the process so that efforts can be focused on mitigating negative effects.

The studies that were conducted this year are summarized below. The actual milestone report for each study is available from the authors. Analyses were conducted on the following:

- C Update of the analysis of photoelectrochemical hydrogen production to include a Monte Carlo sensitivity analysis (Mann)
- C Update of the analysis of hydrogen from biomass to include new experimental data and a Monte Carlo sensitivity analysis (Spath, Lane, Mann, Amos)
- C Analysis of hydrogen production from low-Btu coal, including CO₂ sequestration and coalbed methane recovery (Spath and Amos)
- C Analysis of hydrogen from PV and wind, with storage required to meet a constant load (Mann, Putsche, Amos)
- C Comparison of on-board hydrogen storage options (Lane)
- C Study on the use of a reversible fuel cell for storage of wind-generated electricity (Amos)
- C Analysis of supercritical water gasification of high-moisture content biomass (Amos)
- C LCA of steam methane reforming (Spath and Mann)

Sensitivity Analysis of Photoelectrochemical Hydrogen Production

A 1998 study of the economic viability of photoelectrochemical (PEC) hydrogen production was revised to include advanced sensitivity analysis algorithms. Using Decisioneering's Crystal Ball[®], a Microsoft Excel add-in, probability distributions for the major variables were incorporated into the analysis to determine the most likely cost of hydrogen and the uncertainty in that value. Probability distributions were determined from research projections and historical data. This type of detailed sensitivity study presents a clearer picture of the important research elements for success of this technology. Furthermore, the likelihood of research success and progress can be more accurately measured once an analysis of this nature is performed and used as the baseline for future studies.

This type of detailed sensitivity study is often referred to as risk analysis or stochastic modeling. Using various sampling techniques, numerous combinations of variable values can be tested to assess the most likely result. This differs from parametric sensitivity analyses, where only one parameter is varied at a time to assess its affect on the final result. Parametric analyses serve to highlight the most important variables, but do not present best or worse cases that would result from several parameters varying from the base case values. Additionally, the contribution to the uncertainty in the analysis cannot be determined. With parametric analysis, there isn't any opportunity for studying the likelihood that the final answer obtained in the base case will occur given uncertainty in the different inputs. In the context of a hydrogen research project, this type of economic analysis answers questions like: What is the probability that the cost of hydrogen will be less than a given amount? Which parameters contribute the most uncertainty to the final price? What are the likely best and worst cases that could be expected? What is the effect of research goals on the final hydrogen price?

The mean hydrogen selling price result is \$5.0/kg (\$37.0/GJ, HHV basis) for a 15% internal rate of return (IRR). For a 20% IRR, which may be required for investment in a new technology, the mean hydrogen selling price rose to \$6.7/kg. At 10% IRR, the price was \$3.5/kg, while the pre-tax production cost (0% IRR) was \$1.2/kg. Equity financing and standard U.S. tax structures were assumed. The analysis shows that there is an 80% certainty that the hydrogen will cost less than \$41.3/GJ with a 15% after-tax IRR. For a 95% confidence level, the hydrogen will cost less than \$46.4/GJ.

The statistical parameters generated by Crystal Ball[®] serve to describe the variability in this analysis. The standard deviation, or distribution of values around the mean, was about 15% of the mean. This indicates

a fair amount of uncertainty. The kurtosis, or shape of the curve, was 3.84. This is slightly higher than what would be expected of a normal distribution, meaning that the curve is more narrow than the standard. It's important to note that the accuracy of this risk analysis is only as good as the assumptions used to construct the probability distributions.

Determination of the parameters that contribute most to the uncertainty in this analysis allows us to better focus research efforts on areas that will result in cost reductions. As expected, system efficiency has the largest impact on hydrogen selling price, at 30% contribution to variance. Capacity factor holds second place, and demonstrates that the reliability of the system to operate when the sun is shining is crucial to success. Siting the PEC units where there is good solar insolation is important, as demonstrated by its 17.5% contribution to variance. The housing unit, while ranked as fourth, still contributes a very significant 12.4% to the uncertainty of this analysis. Contingency and photocatalyst cost each account for less than 5% of the uncertainty. The support structure, or linear concentrator assembly, is responsible for less than 2%. Other variables accounted for less than 1% each, and 1.3% combined.

Sensitivity Study of the Delivered Cost of Hydrogen from Biomass

The purpose of this analysis was to assess the economic feasibility of producing hydrogen from biomass via two thermochemical processes: 1) gasification followed by reforming of the syngas, and 2) fast pyrolysis followed by reforming of the carbohydrate fraction of the bio-oil. In each process, water-gas shift is used to convert the reformed gas into hydrogen, and pressure swing adsorption is used to purify the product. This study was conducted to incorporate recent experimental advances and any changes in direction from previous analyses. The systems examined are based on the Battelle/FERCO low pressure indirectly-heated biomass gasifier, the Institute of Gas Technology (IGT) high pressure direct-fired gasifier, and fluidized bed pyrolysis followed by coproduct separation. The pyrolysis case assumes a bio-oil feed which is shipped from remote locations to the hydrogen production plant. Following water extraction, the carbohydrate-derived fraction of the bio-oil is reformed while the lignin-derived fraction is sold as a phenol substitute for phenolic resins manufacture.

The delivered cost of hydrogen, as well as the plant gate hydrogen selling price, were determined using a cash flow spreadsheet and Crystal Ball[®] risk assessment software. Several cases were run for each of the biomass conversion technologies at varying plant sizes and internal rate of return (IRR) values. Three hydrogen production rates were examined for the gasification technologies: 22,737 kg/day, 75,790 kg/day, and 113,685 kg/day. For the pyrolysis case, because some of the bio-oil is used in the production of the coproduct, only the small and medium plant sizes were studied. Even with several remote pyrolysis plants, the feed required for the large plant would likely be more than could be economically secured.

For any given IRR, the plant gate hydrogen selling price is lowest for the pyrolysis case (\$1.1-1.3/kg for a 15% after-tax IRR), followed by the Battelle/FERCO gasifier plant (\$2.0-2.4/kg for a 15% after-tax IRR), and then the IGT gasifier system (\$2.3-2.9/kg for a 15% after-tax IRR). As the plant size increases, the hydrogen selling price decreases due to economy of scale. The delivered cost is important because even if the hydrogen is produced cheaply, the cost to store and transport the hydrogen will make a difference in determining if the hydrogen is economical. Six likely scenarios for hydrogen use were examined, and the cheapest storage and delivery methods were identified. For these six options, storage and delivery adds between \$0.1 and \$1.7/kg to the plant gate cost, resulting in a delivered cost of hydrogen between \$1.3/kg and \$4.6/kg (using a 15% after-tax IRR) for all cases studied.

For both of the gasification options (Battelle/FERCO and IGT), the two variables having the largest effect on the uncertainty in the hydrogen selling price are hydrogen production factor and operating capacity. Combined, these two variables account for roughly 51-76% of the uncertainty in the hydrogen selling price depending on the plant size and IRR. For the pyrolysis case, the bio-oil feedstock cost, pyrolytic lignin selling price, and yield of carbohydrate from the bio-oil are the largest contributors to variance, and combine to account for 82-95% of the variability. Roughly 40-44% of the contribution comes from the bio-oil feedstock cost alone.

Hydrogen from Low-Btu Western Coal - Incorporating CO₂ Sequestration and Coalbed Methane Recovery

A hydrogen production process using pressure swing adsorption (PSA) for purification results in a concentrated CO₂ gas stream. In a typical natural gas steam reforming process, this stream is used to fuel the reformer. However, because coal gasification takes place at high temperatures, the synthesis gas contains very little CH₄ and other hydrocarbons, therefore, reforming is not required. An analysis was performed to examine hydrogen production via gasification of low sulfur western coal with CO₂ sequestration of the PSA off gas. This stream is then used to displace methane from unmineable coalbeds and the methane is utilized within the gasification-to-hydrogen system. The work was performed as a collaborative effort between the National Renewable Energy Laboratory and the National Energy Technology Laboratory. The purpose of the analysis was to examine the technoeconomic feasibility, CO₂ emissions, and energy balance of these systems. Several processing schemes, as outlined in Table 1, were evaluated.

Table 1: Cases Examined for Hydrogen from Low-Btu Coal

| Case | Title | Description |
|------|------------------------------------|--|
| 1 | reference case | coal gasification, shift, & H ₂ purification |
| 2 | CO ₂ sequestration only | reference case with CO ₂ sequestration only added |
| 3 | maximum H ₂ production | H ₂ production via the syngas, CO ₂ sequestration, & additional H ₂ production via steam methane reforming of the coalbed methane |
| 4 | H ₂ /power coproduction | H ₂ production via the syngas, CO ₂ sequestration, & power production via the coalbed methane |

For this study, because the hydrogen plant is assumed to be sited far from any users, two likely storage and transportation options were examined: (1) bulk delivery for a distance of 1,610 km (one way) and (2) pipeline delivery with 3 km to nearest infrastructure, no storage, and an additional 1,610 km pipeline, shared by five companies, for delivery to end user. Bulk delivery adds \$8.78/GJ to the plant gate cost and pipeline delivery adds \$4.67/GJ

The economics favor sequestering CO₂, recovering coalbed methane, and making hydrogen or power (case 3 and 4). The plant gate H₂ selling price for these cases are \$8/GJ for maximum H₂ (case 3) and \$14/GJ for H₂/power coproduction (case 4). However, due to the CO₂ emissions generated from the steam methane reformer, additional hydrogen production via natural gas is not necessarily the most environmentally friendly option from a CO₂ standpoint (case 3). Coal fired power plants emit large quantities of CO₂; therefore, optimizing hydrogen production with electricity generation, as in case 4, is a means of lowering the CO₂ emissions from power generation in the U.S. Because of the high temperatures, coal gasification to hydrogen production does not require a steam reforming step, and adding

CO₂ sequestration only (case 2), results in almost no CO₂ being emitted to the atmosphere for a minimal cost. However, for all of the cases examined in the analysis it should be noted that there is much debate about the fate of the sequestered CO₂ and its long term environmental effects.

Hydrogen from PV and Wind, with Storage Required to Meet a Constant Load

A study of the production, storage, and transportation of hydrogen from sunlight and wind was conducted. The basic system was designed to provide enough hydrogen to fuel 100 cars per day at a filling station, with each car requiring approximately 3 kg. Because delivery to the filling station would likely occur at regular intervals, the load was assumed to be constant. Four scenarios were examined for both PV and wind:

- Case 1: the size of the renewable is minimized, while the storage is sized to meet the load each week
- Case 2: the renewable is oversized to meet the load during the worst resource week of the year, while storage requirements are minimized, and the excess electricity is sold over the grid
- Case 3: same as Case 2 except that excess hydrogen rather than excess electricity is produced and sold to a customer other than the filling station
- Case 4: same as Case 1 except that the renewable is located at the filling station, so transportation costs are avoided.

This study had three purposes: (1) To identify possible situations for low-cost hydrogen production from PV and wind, (2) to identify problems associated with using hydrogen to store PV and wind energy, and finally, (3) to test the integration of three models previously developed for hydrogen analysis. Three different models were used to evaluate the four cases. The first model matched hydrogen demand with production from PV and wind, and was used in studies performed for the International Energy Agency. The second model calculates the cost to store and transport hydrogen using different storage devices and transportation modes, over varying distances. The third model was used in an earlier study to determine the cost of hydrogen produced from PV and wind.

Because the model developed for the IEA annex uses actual resource data and existing PV module and wind turbine performance data, present day costs were calculated for these systems. Therefore, as technology improvements in the PV and wind fields improve, the costs of hydrogen will come down. Future studies will incorporate projected performance data into the IEA model. Cost results in this study should be examined for trends rather than projected hydrogen cost. The analysis was performed in three distinct steps. From wind and sunlight resource data, the renewable power output to meet the hydrogen demand was calculated for each case. From these data, the necessary selling price of the hydrogen for an internal rate of return (IRR) of 15% was determined. To this price, the lowest cost to store and transport the hydrogen, was added. Transportation over distances of 10, 100, and 1,000 miles was tested.

Several conclusions about storage and transportation costs with regard to these systems were made. First, liquid storage is favored for long-term storage of hydrogen. For highly variable flows, gas storage should be used because it's cheaper to oversize a compressor than a liquefier. Finally, rail delivery was found to be the cheapest option for long distances. Transportation costs range between \$5.4 and \$14.0/GJ of hydrogen delivered. Storage costs were found to be as low as \$3.7/GJ for Wind Case 3, but as high as \$76.9/GJ for Wind Case 1.

For both the PV and wind systems, the lowest cost hydrogen is obtained in Case 3. The total cost for this case is dominated by the hydrogen production costs; storage and transportation costs are minimal. The lowest delivered hydrogen costs for this case are \$10.4/kg and \$17.3/kg for wind and PV, respectively. The plant-gate selling price of hydrogen in Cases 1 and 4 is slightly lower than in Case 3, but storage costs in these cases are much higher. Case 2, where the electricity not used to produce hydrogen is sold as a byproduct, is less attractive than Case 3. The main reason for this is that hydrogen is worth more than electricity, even if peak prices can be obtained for all of the excess electricity. Additionally, it is conceivable that an electric utility grid, to which the power could be sold, may not be available in all locations where one would like to produce hydrogen from renewables.

In general, and as expected, the hydrogen from the PV systems is more expensive than that from the wind systems. New understanding of the viability of producing hydrogen from PV and wind can be drawn from this study. Principally, systems designed to meet a constant load cannot be economical. Rather, hydrogen sold through larger markets, similar to the way electricity is brokered today, will reduce costs. The important implication of this conclusion is that unless the load matches the resource profile, the economic viability of using hydrogen to meet village and remote energy needs is limited. Minimizing the size of the renewable and using storage to meet the demand results in extremely high storage costs. Sizing the system such that storage costs are minimized creates excess hydrogen and/or electricity, for which a market must exist. Earlier studies have demonstrated that with appropriate grid interaction and moderate technology and cost improvements, hydrogen from PV and wind can be a viable future energy option. Interacting with the grid would reduce the cost of the hydrogen, but would also add a non-renewable energy component to the system. Additionally, this situation will only be possible where an electricity grid is available.

Comparison of On-board Hydrogen Storage Methods

Wide-spread adoption of fuel cell vehicles depends on safe, reliable, and cost-effective hydrogen storage. At the present time, there is no single hydrogen storage option that stands out among the others in terms of a definite alternative to a gasoline storage system in terms of weight, size, maximum speed, mileage range, and cost. The three traditional hydrogen storage methods are compressed hydrogen, liquid hydrogen, and metal hydrides. Several other storage methods are still at the laboratory stage and include carbon adsorption systems, liquid hydrides, nonclassical polyhydride metal complexes (PMCs), glass microspheres, slush hydrogen, and sponge iron. The purpose of this study was to review the characteristics of the storage options found in the literature, and compare them to the current gasoline storage system.

Compressed gas hydrogen storage vessels require a large volume, whereas slush and liquid hydrogen storage vessels require much less space for the same amount of energy. The advantages of a compressed gas system are its simple design, rapid refueling capability, low cost, safety benefits, and the fact that natural gas vessels can be easily adapted for hydrogen storage. In addition to a smaller volume, liquid hydrogen also offers a high hydrogen mass fraction, fast refueling, and sound safety characteristics. However, liquefaction of hydrogen is an expensive process and requires the use of special insulated vessels and pumps for cryogenic on-board storage. Liquid hydrogen boil-off losses can be as high as 2% per day, even in a well-insulated system. Slush hydrogen is similar to liquid hydrogen because it has a high storage density (15% more than a liquid storage system) and requires a cryogenic storage vessel. However, slush hydrogen has specific temperature and pressure requirements, causing this system to be very expensive for passenger vehicle application.

Metal hydrides are extremely safe, but have a high cost, slow refueling time, large weight, and moderate system volume. A metal hydride storage system weighs twice as much as a compressed gas system and four times as much as a liquid hydrogen or gasoline system of an equivalent energy capacity. Carbon adsorption systems operate in a manner similar to metal hydride systems, except hydrogen is bonded to high surface area carbon at extremely low temperatures. Research at the National Renewable Energy Laboratory in single-walled carbon nanotubes is offering great potential for hydrogen storage at ambient conditions. Liquid hydrides have a high volumetric density, are easy to store and transport, but require additional equipment for reforming or oxidation. Nonclassical PMCs may overcome the weight density problem of hydride storage systems and are able to release hydrogen at virtually any rate and temperature. Glass microspheres are porous to hydrogen at high temperature and pressure conditions. These miniature pressure vessels are safe and of moderate weight, but their bulky volume and long refueling time are some of the research obstacles being faced. Sponge iron, a porous form of iron with a high surface area for hydrogen liberating reactions to take place, is safe and has a reasonable cost, however, the weight of iron and water in the system and high temperature requirement for operation do not appear promising for vehicular applications.

Each of these options have benefits and drawbacks, making the decision for an on-board hydrogen storage system very difficult. The three near-term options, gaseous hydrogen, liquid hydrogen, and metal hydrides, have already been tested in passenger vehicles with some success. Both compressed hydrogen and metal hydrides have a much greater volume and weight requirement than a gasoline system, for the same driving range. Liquid hydrogen storage comes very close to a gasoline system's weight and volume, but substantial costs result from liquefaction of the hydrogen. To obtain public acceptance of hydrogen-fueled vehicles, there is a need to further develop hydrogen storage systems in order to bring their weight, volume, vehicle range, and cost to levels comparable to gasoline storage.

Reversible Fuel Cell for Storage of Wind-Generated Electricity

A study was conducted to examine the economic benefit of using a reversible hydrogen bromide fuel cell to store energy generated by wind for sale to the wholesale power market during times when it would produce more revenue. Although the per kWh selling price of electricity was higher in all cases, the annual income from electricity sales was generally lower due to process inefficiencies. When the additional cost of the extra energy storage equipment was considered, the technology was not competitive, even when considering the avoided cost of adding additional transmission line capacity. Electricity prices would need to reach \$0.45/kWh before hydrogen bromide storage would be economical.

A supply-demand curve was constructed using wholesale electricity prices from the New England Power Pool, then hourly wind data were used to determine the amount of wind power that could be produced each hour. A variety of equipment sizes and storage algorithms were considered to optimize revenue and/or power supply efficiency. Hourly demand data for 1998 were used to estimate the electricity sales for each hour of the year and to determine the annual income from electricity sales.

Four different scenarios were examined. In the first case, the costs and income associated with supplying wind power directly to the grid around the clock were determined. This information was used as a baseline comparison of the value of the wind power without any storage system. The analysis showed that selling power on the wholesale market would result in an average selling price of \$0.026/kWh. However, the average selling price would need to be \$0.059/kWh in order to obtain a 15% internal rate of return.

The second case examined storing power produced during off-peak periods and selling the power during peak periods to produce higher revenues. While the average per kWh selling price was higher (as much as \$0.032/kWh), the annual revenues were lower because less power was available for sale. This is because using the hydrogen bromide system results in a loss of approximately one third of the energy passing through storage. Power produced from the wind turbine during peak times can, however, flow directly to the grid without going through storage. Even with projected advances in fuel cell technology, the electricity selling price would need to be \$0.45/kWh to recover the investment in the storage system and wind turbine.

The last two cases assumed that the power transmission lines from the wind site to the consumer were overloaded and constrained during peak periods, so power could only be transmitted during off-peak times (i.e., nights, weekends and holidays). If no storage is used, power can only be transmitted during off-peak periods and will sell for a very low price. If storage is used, the power can be transmitted during off-peak times and stored near the point of consumption so it can be sold during peak periods without passing through any long-distance transmission lines. These two cases were not favorable because no power from the wind turbines could be used during peak periods and all power sold using the storage system was subject to the one-third efficiency losses. Based on the analysis, construction of new transmission lines is a more economical alternative for providing peak wind power than using a power storage system.

Supercritical Water Gasification of High-Moisture Content Biomass

Two analyses were performed on the cost of hydrogen production from supercritical water gasification of wet biomass. In the first analysis, the design was based upon information supplied by Professor Michael Antal of the University of Hawaii and Robert Divilio of Combustion Systems, Inc. For the second analysis, some design changes were made to reduce capital and operating costs. However, in both cases, the hydrogen selling price was several times higher than the current price of hydrogen from steam methane reforming.

In the initial analysis using the Antal/Divilio design, three different plant sizes were examined: 9, 90 and 180 Mg biomass/day. The hydrogen selling price with no feed credit or tipping fee ranged from \$603/GJ for the smallest plant to \$205/GJ for the 180 Mg/day size. The effect of feed cost or credit was then examined for the 180 Mg/day plant. For a feed credit (waste disposal fee) of \$22/Mg, the hydrogen selling price was \$188/GJ and for a feed cost of \$10/Mg, the hydrogen selling price was \$214/GJ. Because the capital costs have such a large impact on the hydrogen selling price, the effect of cutting the capital costs in half with a zero feed cost was examined. The resulting hydrogen selling price was \$116/GJ. There were a number of concerns with the original Divilio design, such as high electricity consumption, unrealistic cooling water temperatures and the potential for calcium precipitation in the scrubbing section.

In the second analysis, the carbon dioxide scrubber, meant to reduce the load on the hydrogen purification section, was removed and the option of producing power was considered. The 180 Mg/day plant size was used in four different power generation cases with the altered design. The same feed credits and feed costs from the first analysis were used in the second analysis.

In Case 1 of the second study, only hydrogen was produced, with no electricity generation. The hydrogen selling price varied from \$89/GJ-\$110/GJ, depending on the feed credit/cost. For all analyses, a 20-year plant life was assumed along with a 15% internal rate of return. In Case 2, a combustion turbine was used to generate electricity using the off-gas from the purification module. A \$0.04/kWh credit was taken for

all electricity generated and sold. The hydrogen selling price for Case 2 ranged from \$92/GJ-\$114/GJ. For Case 3, additional equipment was added to capture heat from the combustion turbine exhaust in a steam cycle to generate electricity. While the electricity production increased 77% for the same hydrogen production rate, the hydrogen selling prices actually increased to \$98-\$119/GJ because of the higher capital investment. The additional income from electricity production in Case 2 and Case 3 did not justify the added capital expense for the power production equipment.

One last case examined a power production only case, with no hydrogen sales. This was a scenario of interest to Professor Antal and had a lower capital investment because no hydrogen purification equipment was needed. However, the high capital equipment costs associated with the high-pressure, high-temperature supercritical gasification equipment resulted in an electricity selling price that ranged from \$0.53-\$0.68/kWh, which is eight to ten times higher than the average electricity price of \$0.068/kWh in the United States.

Life Cycle Assessment of Hydrogen from Steam Methane Reforming

Although hydrogen is the cleanest burning fuel, it is important to recognize that there are environmental impacts that occur during the production process. The system studied in this life cycle assessment (LCA) is hydrogen production via catalytic steam reforming of natural gas, which is a mature technology and is the route by which most hydrogen is made today. In recognition of the fact that the processes required for the operation of the steam methane reforming (SMR) plant also produce pollutants and consume energy and natural resources, this LCA was performed in a cradle-to-grave manner. Therefore, the emissions, resource consumption, and energy use of the upstream processes necessary to convert the natural gas to hydrogen were included in the study. The system was divided into the following subsystems: natural gas production and distribution, electricity generation, plant construction and decommissioning, hydrogen plant operation, and avoided operations.

The size of the hydrogen plant is 1.5 million Nm³/day (57 million scfd), which is typical of the size that would be found at today's major oil refineries. The natural gas is reformed in a conventional steam reformer, the resulting synthesis gas is shifted in both high and low temperature shift reactors, and purification is performed using a pressure swing adsorption (PSA) unit. Although the plant requires some steam for the reforming and shift reactions, the highly exothermic reactions result in an excess amount of steam produced by the plant. For the base case, this steam is assumed to be used by some other source. Therefore, the stressors that would have resulted from producing and transporting natural gas and combusting it in a boiler are avoided because the other process/facility is not required to produce this steam. In extracting, processing, transmitting, storing, and distributing natural gas, some is lost to the atmosphere. The base case of this LCA assumed that 3.96% of the natural gas that is produced is lost to the atmosphere.

The operation of the hydrogen plant itself produces very few emissions with the exception of CO₂. On a system basis, CO₂ is emitted in the largest quantity, accounting for 98 wt% of the total air emissions and 77% of the system global warming potential (GWP), defined as a weighted combination of CO₂, CH₄, and N₂O emissions expressed on a CO₂-equivalent basis for a 100 year time frame. Methane, which is primarily emitted as lost natural gas during production and distribution, accounts for 22.3% of the GWP because of its higher radiative forcing. The overall GWP of the system is 13,745 g CO₂-equivalent/kg of hydrogen produced. Table 2 contains a breakdown of the sources, showing that the hydrogen plant itself accounts for 64.7% of the greenhouse gas emissions.

Table 2: Sources of System Global Warming Potential

| Source of system greenhouse gases | | | | |
|---|------------------------------------|------------------------|--------------------------------|-----------------------------------|
| Construction & decommissioning ^(a) | Natural gas production & transport | Electricity generation | H ₂ plant operation | Avoided operations ^(b) |
| 0.3% | 36.6% | 2.0% | 64.7% | -3.6% |

(a) Construction and decommissioning include plant construction and decommissioning as well as construction of the natural gas pipeline.

(b) Avoided operations are those that do not occur because excess steam is exported to another facility.

Other than CO₂, methane is emitted in the next greatest quantity followed by non-methane hydrocarbons (NMHCs), NO_x, SO_x, CO, particulates, and benzene. Most of these air emissions are a result of natural gas production and distribution. In terms of resource consumption, as anticipated, natural gas is used at the highest rate, followed by coal, iron (ore plus scrap), limestone, and oil. There is also a considerable amount of water consumed primarily at the hydrogen plant. This is due to the steam requirements for reforming and shift conversion. The majority of the system waste is generated during natural gas production and distribution. Water emissions are small compared to the other emissions.

The energy balance of the system shows that for every 0.69 MJ of hydrogen produced, 1 MJ of fossil energy must be consumed. From both an environmental and economic standpoint, it is important to increase the energy efficiencies and ratios of any process. This in turn will lead to reduced resources, emissions, wastes, and energy consumption. A sensitivity analysis was performed on the following variables: materials of construction, natural gas losses, operating capacity factor, recycling versus landfilling of materials, natural gas boiler efficiency, hydrogen plant energy efficiency, and hydrogen plant steam balance (no credit for excess steam). Most of the variables examined had no noticeable effect on the results. Future work will involve comparing this study with hydrogen production via other routes such as biomass, wind, and photovoltaics.

Summary

The analyses conducted by NREL's process analysis task for the Hydrogen Program in 1999 served to refine our understanding of the economic feasibility of many research projects, as well as to quantify the environmental impacts of today's primary method of hydrogen production. The use of detailed Monte Carlo sensitivity analyses was demonstrated as a means of determining those parameters that can have the greatest impact on the potential for economic success. Of primary importance, these studies identified those areas of research in which improvements will result in the largest cost reductions. The comparison of various on-board hydrogen storage media to current gasoline storage allows the hydrogen community to make better decisions regarding which storage technology will best meet future transportation needs, as well as giving a consistent basis upon which the Program can assess each option with regard to meeting the Program storage goals. Finally, the life cycle assessment that was conducted on a steam methane reforming system sets the stage for a better understanding of the environmental benefits of hydrogen transportation systems. The net greenhouse gas emissions, energy balance, resource consumption, and other emissions were quantified, and will be compared to results of future LCAs on renewable hydrogen production systems. Because the full life cycle chain was included in the study, upstream processes that are responsible for significant environmental damage can be exposed.

Overall, process analysis at NREL helps the Hydrogen Program methodically assess the applied research portfolio, in order to focus on those projects that have the potential to significantly contribute to the

adoption of clean hydrogen systems. Results from the economic studies help researchers concentrate their efforts on those areas that have the greatest impact on cost, such that novel technologies can be commercialized more quickly. Hand-in-hand with cost analysis, LCA studies help the Program, and the hydrogen community as a whole, quantify the environmental status of various hydrogen technologies. Finally, process analysis helps streamline the transition to the hydrogen economy, balancing environmental requirements and economic constraints.

AN INVESTIGATION OF THE INTEGRATION OF HYDROGEN TECHNOLOGY INTO MARITIME APPLICATIONS

Richard W. Foster
DCH Technology, Inc.
Unit 6, Avenue Hopkins
Valencia, CA 91355

Abstract

The primary goal of the project was to identify the foundation and beginning steps of a systematically, vertically integrated, approach to the application of hydrogen technology, and precursor technologies, to the maritime transportation sector. The Maritime Hydrogen Technology Development Group (MHTDG), which is an industry working group of uniquely qualified industrial organizations, was formed to carry out the project analysis and future planning efforts. The MHTDG identified the vertically integrated system and the constituent technological and other infrastructure systems issues. The MHTDG members carried out technological and other analysis in their individual fields of expertise which was assembled into a final report. The primary objective in preparing this report was to provide a tool that will support taking the first steps towards developing a working relationship between two groups - those multidisciplinary workers in the new fuel and energy conversion technologies disciplines and those multidisciplinary workers that comprise the maritime transportation sector. A second objective was to provide a reasonable basis to support prudent management decision making by all the multidisciplinary groups with regard to the most appropriate actions that need to be taken next.

1. Project description

The use of hydrogen as the energy carrier in the maritime transportation sector is essentially unexplored as a system. Yet hydrogen, in combination with other enabling technologies, has the potential of offering significant emissions and energy consumption reductions in that transportation sector.

The major port and vessel systems impacted by the enabling technologies include hydrogen production, hydrogen storage, shipboard and on-shore; the prime propulsion system; auxiliary and emergency power, shipboard and on-shore; system controls and safety; as well as equipment installation; codes and standards; port operations; and public awareness, safety and protection. All of these aspects must be integrated in the processes

of design, construction and operation. Public safety, acceptance, and benefit as well as the interests of port authorities, liability issues, and boat builders needs must all be addressed and unifying interfaces identified and put in place if a transition to lower emissions generating and more energy efficient technologies are to find practical application in the maritime transportation sector.

The primary goal of the project was to identify the foundation and beginning steps of a systematically, vertically integrated, approach to the application of hydrogen technology, and precursor technologies, to the maritime transportation sector. To bring focus and direction to this untapped market, DCH Technology formed the Maritime Hydrogen Technology Development Group (MHTDG), which is an industry working group of uniquely qualified industrial organizations. The companies comprising the MHTDG participated on a significant cost sharing basis.

The project focused on identifying the critical technological and other related areas required to be addressed in order to begin the process of constructively and safely introducing hydrogen power to the maritime community.

Support of this project was provided by DOE's Office of Power Technologies under DOE Contract No. DE-FG01-99EE35102. The project specifically relates to the development of Maritime Applications within that Office's Hydrogen Program: System and Process Analysis and Information Dissemination.

2. Project objectives and rationale

The long term objective of the project is to reduce the energy consumption and emissions of the maritime transportation sector specifically through the use of hydrogen as an energy carrier and fuel cell and other related technologies as hydrogen energy conversion technologies.

This year's objectives were to start the process of exploring the path to reducing the energy consumption and emissions produced by the maritime transportation sector through the use of hydrogen. The principal product resulting from this effort is this report.

The rationale comprising our approach to this first phase of the project consisted of the following:

1. Assemble a multidisciplinary team, the Maritime Hydrogen Technology Development Group - the MHTDG - possessing the required knowledge, experience and skills in the constituent technologies.
2. Identify the technologies that would comprise a vertically integrated system.
3. Using the knowledge and experience of the MHTDG members identify the state of the art and identify and develop a plan of approach to implementing the nogoical next steps that could lead to the eventual implementation of an integrated maritime hydrogen system.
4. Identify and start to develop funding support for the implementation of that plan.

4. Major work areas and progress

The major work areas comprising the project work plan consisted of the following:

- #1 Establish the Maritime Hydrogen Technology Development Group (MHTDG).

Agreements were entered into between DCH Technology, Inc. and the following organizations in the technology areas indicated:

ABS Americas – Maritime regulatory requirements and related considerations
Art Anderson Associates – Marine engineering and architectural considerations, Vessel fuel cell conversion specification development
CryoFuel Systems, Inc. – Hydrogen infrastructure
Desert Research Institute – Fuel cell technology
Engineering Technical Associates – Environmental considerations and maritime fuel cell and alternative fuel state-of-the-art
Ergenics, Inc. - Hydride storage technology
Hydrogen Burner Technology, Inc. – Reformer technology
Rode & Associates, LLC – Risk planning
Longitude 122 West – Economic Analysis
Southwest Research Institute – Hydrogen piston engines
Teledyne Brown Engineering – Merchant Marine Academy Fuel Cell Laboratory Design Specification

- #2 MHTDG Tasks Definition - Develop specific tasks for each aspect to be addressed by the MHTDG. Each task will be the responsibility of a Working Group within the MHTDG. Working Groups will be multi-disciplinary and each group will be chosen from participating companies. The Working Groups will be managed by DCH.
- #3 MHTDG Interfacing - Develop clear interfaces between the Working Groups so each participant knows the requirements of the others. Interfaces and requirements of DoE, DoT, and DoD were included. The organizational structure of the MHTDG that resulted from this work is illustrated in figure 1.
- #4 MHTDG Architecture Definition - The MHTDG will develop their technologies and methodologies implementation requirements in a scaleable format. This task will include a design review with DoE, DoT, and DoD participation TBD by the COTR. The results of this work are presented in section 4.0 of this report.
- #5 Document the Project Findings – The Multidisciplinary Report
- #6 Start the development of Phase II support

5. The Multidisciplinary Report

The objective sought in the multidisciplinary report is to provide adequately detailed information of support prudent management decision making with regard to supporting Phase II.

The design, construction, operation and maintenance of any vessel, whether pleasure craft or supertanker, requires both broad and detailed knowledge in a wide range of technological disciplines – it is a multidisciplinary challenge. The approaches to carrying out the broad range of multidisciplinary activities, which are not unique to the maritime transportation sector, have evolved over decades into a body of knowledge. This body of knowledge includes acquired skills, process approaches, management methods and so forth. Specifications and standards, both government and industrial, comprise a critical component of that knowledge base.

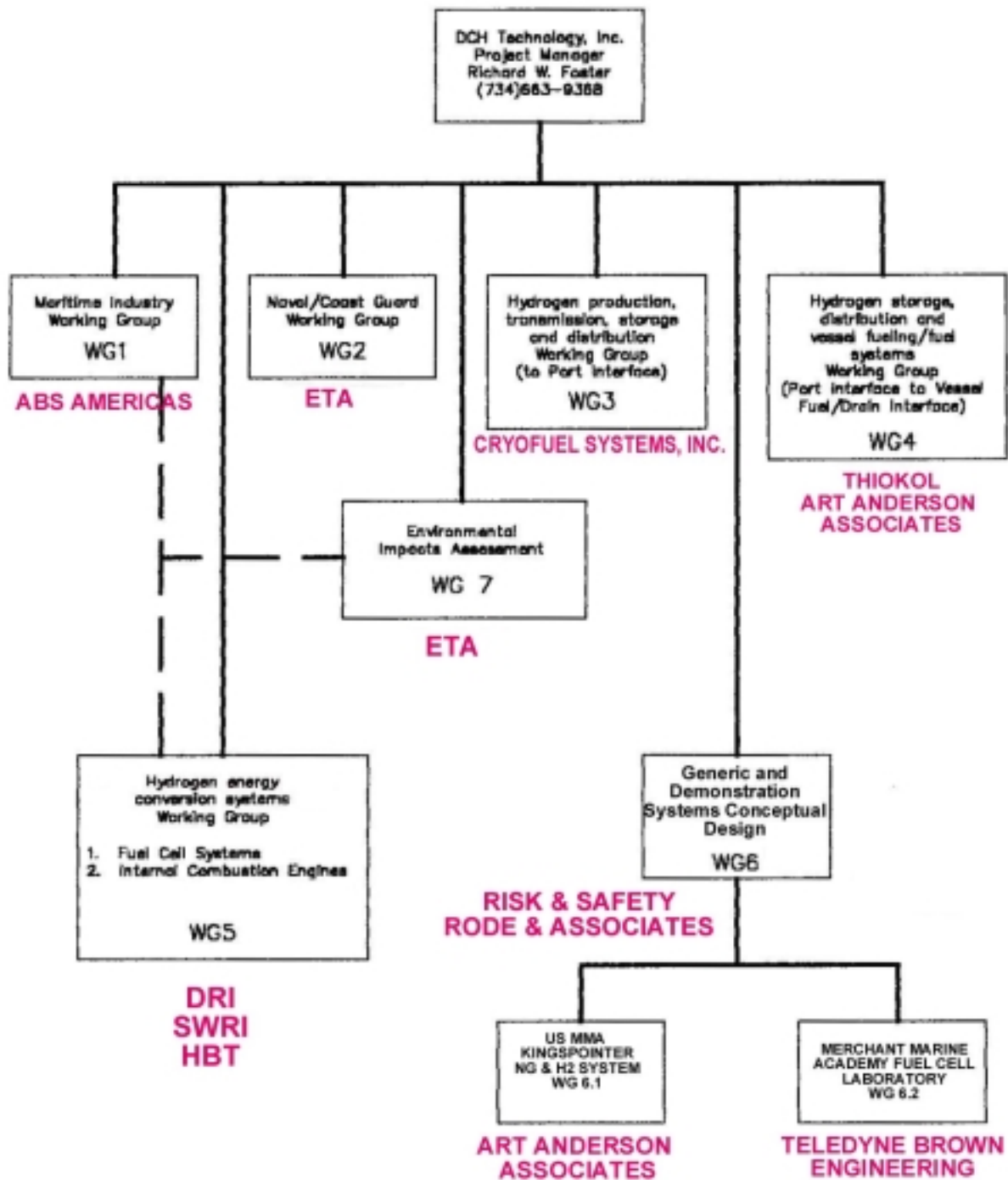


Figure 1 The Project organization chart with MHTDG members interfaces

The introduction of a very different set of fuels and propulsion technologies, the case here in terms of natural gas and hydrogen as fuels and fuel cell systems in the role of energy conversion systems for these new fuels, represents a radical departure from past

practices. Major parts of that knowledge base discussed in the preceding paragraphs do not exist but must be brought into beings. Doing this presents a significant challenge.

This report brings together, in as detailed a form as practical, a body of information describing the new fuel and energy conversions technologies that must be mastered if these new technologies are to find practical implementation in the maritime transportation sector.

Our primary objective in preparing this report is to provide a tool that will support taking the first steps towards developing a working relationship between two groups - those multidisciplinary workers in the new fuel and energy conversion technologies disciplines and those multidisciplinary workers that comprise the maritime transportation sector.

A second objective is to provide a reasonable basis to support prudent management decision making by all the multidisciplinary groups with regard to the most appropriate actions that need to be taken next.

Our approach to the development of the report was to make it as generic in its treatment of the various subjects as practical. In order to do so we avoided considering design specific approaches or implementations, except by way of example, also to the extent practical.

5.1 Technologies treatment

Figure 2 presents a flow chart that illustrates the fact that there are many alternatives in terms of the specific design approaches that may be taken to implementing low emissions, energy efficient marine main propulsion, auxiliary and emergency power systems. Discussion of these many design approaches was found to be impractical because of their number. Rather the MHTDG approached in terms of the major technologies that can provide the building blocks for specific design approaches.

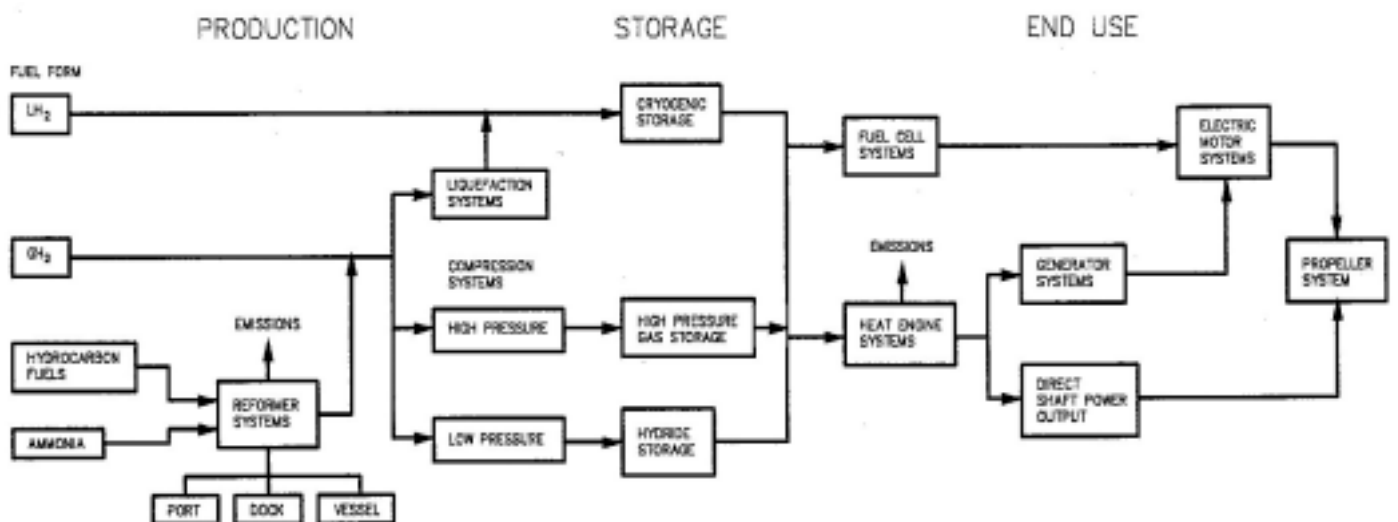


Figure 2 Breakdown of the constituent technologies considered in the MHTD project

5.2 The vessel types considered

One of the initial tasks undertaken by the MHTDG was the development of a listing of the vessel types and their ROM characteristics to be considered in the course of carrying out the project. The objective sought in doing this was to provide all MHTDG members with a common baseline set of vessels to be considered in the course of carrying out the tasks comprising the project work plan. The baseline list is presented in table 1.

Table 1 Generic Vessel Characteristics

| TYPE OF SHIP | tons | l, ft | BHP | V, kts |
|----------------------|-------|-------|-------|--------|
| Average tank model | 1 | 20 | -- | 4 |
| 6 m Sail boat | 4 | 23 | -- | 6 |
| Pleasure Craft | 5 | 30 | 150 | 15 |
| A Ferry | 30 | 55 | 300 | 14 |
| Small C.G. cutter | 200 | 85 | 500 | 14 |
| Average tug boat | 300 | 100 | 1000 | 10 |
| Coastal Motor Ship | 300 | 100 | 1000 | 10 |
| Average fishing boat | 300 | 100 | 600 | 10 |
| Coastal motorship | 750 | 155 | 400 | 11 |
| Tugboat | 800 | 200 | 2500 | 17 |
| Coast Guard cutter | 2000 | 300 | 5000 | 18 |
| Average destroyer | 3000 | 400 | 70000 | 36 |
| Average cargo ship | 9000 | 400 | 4000 | 14 |
| Old-type cruiser | 9000 | 650 | 80000 | 32 |
| Average tanker | 20000 | 500 | 5000 | 14 |
| Small cargo vessel | 20000 | 600 | 15000 | 20 |
| Modern tanker | 40000 | 600 | 20000 | 17 |

5.3 Multidisciplinary report structure

The outline of the multidisciplinary report consists of the following:

Table of Contents

- Title Page
- Report Objectives
- TOC
- 1. Overview of the Project Approach
- 2. The Global and U.S. Context – Energy Consumption and Environmental Considerations
- 3. Maritime Transportation Sector - Energy Consumption, Environmental Impacts, Current Fuel Cell Technology Development and other Related Efforts - ETA
- 4. Systems, Subsystems and Fuels Considered - DCH
- 5. The Hydrogen Energy System (HES) Concept - Cryofuel Systems, Inc

6. Systems and Technologies Assessments
 - 6.1 Port, dock and vessel fueling systems - AAA
 - 6.2 Hydrogen Fuel Storage and Reformers Technology
 - 6.2.1 Cryogenic storage tanks, design and manufacture - Thiokol
 - 6.2.2 Hydride Hydrogen Storage Systems – DCH/Ergenics
 - 6.2.3 Pressure Storage - Thiokol
 - 6.2.4 Reforming of alternative fuels for fuel cell systems - HBT
 - 6.3 Hydrogen Energy Conversion Technologies
 - 6.3.1 Fuel Cell Systems - DRI
 - 6.3.2 Turbines - DCH
 - 6.3.3 Piston Engines - SwRI
7. Vessel design and construction certification issues and Global and US Maritime industry requirements - ABS Americas
8. Risk Mitigation, Risk Management and Risk Management Planning Requirements - Rode & Associates, LLC
9. A General Level Overview of Financial/Cost Considerations – Latitude 122 West
10. The Development of New Technologies – an Overview
11. Conclusions and Recommendations
 - Appendices
 - Appendix 1 U.S. Merchant Marine Academy Fuel Cell Laboratory Requirements Specification
 - Appendix 2 Fuel Cell Vessel Preliminary Design Requirements Specification
 - Appendix 3 Vessel Fueling Infrastructure – Dock and Fuel Barge

6. Next steps

A major work product resulting from this effort was the joint development of a CRADA scope of work between MARAD and DCH Technology, Inc./MHTDG. The SOW embodies the summary conclusions of the MHTDG regarding the logical next steps to be carried out.

The tasks comprising this scope of work are listed below and represent the next steps that should be taken as determined by the findings of this project:

"Cooperative research and development activities between MARAD and the recipient may involve the following:

1. Determination of operational and logistic feasibility of utilizing alternative fuels, including hydrogen, aboard one or more specified marine vessels.
2. Determination of regulatory and safety feasibility of performing the above.
3. Determination of operational suitability of alternative fuel power plants such as fuel cells aboard one or more specified marine vessels, including regulatory and safety criteria.
4. Research and development of shipboard interface to above items, including power conditioning, control systems, sensing systems and ancillary systems.
5. Research and development of a marine fuel cell laboratory at the United States Merchant Marine Academy, including such items as hydrogen generation, hydrogen storage, fuel cell installation, safety systems, fuel cell controls, fuel cell power generation/conditioning, load controls, and transient load testing.
6. Design, installation and evaluation operation of actual shipboard alternative fuel and non-standard power plants.

7. Design, installation and operational testing of a hydrogen fuel cell powered vessel. The vessel may be provided by the Maritime Administration and may operate in the San Francisco Bay area.
8. Determination of other national and international partnership activities that could be formed in support of all the above."

7. Summary of accomplishments - Future plans

In summary:

1. The MHTDG has been established.
 2. The vertically integrated system has been defined.
 3. The state-of-the-art of the constituent systems and subsystems technologies has been established and problems and issues identified. The findings resulting from this work are presented in this report.
 4. The next logical steps have been identified.
 5. To the extent permitted by available resources, the MHTD project participants will work to identify and develop a source of funding support for a cooperative approach to the tasks specified in the MARAD CRADA.
5. To the extent permitted by the supporting resources that might be developed, our next year's goal will be to initiate the activities defined in the MARAD CRADA. Our objective will be to move the state of the art of the constituent technological and supporting infrastructure systems forward from that first demonstrated by the U.S. Navy over 2 decades ago.



Figure 3 USN gaseous hydrogen fueled turbine powered workboat – late 60's

ANALYSIS OF RESIDENTIAL FUEL CELL SYSTEMS & PNGV FUEL CELL VEHICLES

C. E. (Sandy) Thomas, Brian D. James
and Franklin D. Lomax, Jr.
Directed Technologies, Inc.
3601 Wilson Boulevard, Suite 650
Arlington, Virginia 22201
703-243-3383
Fax: 703-243-2724
www.DirectedTechnologies.com

Abstract

Directed Technologies, Inc. has completed two analysis projects for the hydrogen program office during the past year: an assessment of battery augmentation for residential fuel cell systems, and an analysis of the effects of applying PNGV (Partnership for a New Generation of Vehicles) body parameters to both fuel cell vehicles and to hybrid electric vehicles. We have also started the first activities in a three-year competitively bid grant to compare in detail hydrogen with methanol and gasoline as fuels for fuel cell vehicles.

The results of adding a battery to a residential fuel cell system were negligible. A storage battery provides the peak power to the home, permitting a much smaller and less expensive fuel cell system. However, the cost savings due to a smaller fuel cell system were nearly offset by the added costs of the battery system, resulting in very little change in our results from last year: in order to bring a 10% real, after-tax return on investment, a company would still have to charge a single family residence about 40 ¢/kWh, well above the average residential rate near 8 ¢/kWh.

In the transportation sector, using PNGV body parameters (drag coefficient, cross sectional area, rolling resistance, and weight) for passenger vehicles instead of current body parameters uniformly improved the performance of all vehicles in terms of increased fuel economy and decreased greenhouse gas emissions. This analysis shows that only a direct hydrogen FCV will meet the PNGV fuel economy goals of 80 mpgge on realistic driving cycles. Converting from current to PNGV body parameters also reduces the differential cost of a fuel cell vehicle compared to an internal combustion engine vehicle by \$450 – with conventional vehicle bodies, the fuel cell vehicle would cost about \$2,100 more, while a PNGV fuel cell vehicle would cost only \$1,650 more than a conventional car.

Executive Summary for PNGV Transportation Analysis

Directed Technologies, Inc. has previously compared the fuel economies, costs, and environmental impacts of various alternative fueled vehicles including three types of fuel cell vehicles (direct hydrogen, methanol and gasoline) and nine different types of hybrid electric vehicles (Thomas -1998a, 1998b, 1998c). All of these previous analyses used an AIV (aluminum intensive vehicle) Sable as the basic glider. The power source of the AIV Sable was varied, keeping the characteristics of the vehicle fixed. However, the Partnership for a New Generation of Vehicles (PNGV) is developing a new class of vehicle with the goal of a three times increase in fuel economy. We were therefore tasked to evaluate the same group of alternative power train systems with the proposed PNGV glider instead of the AIV Sable glider characteristics. The PNGV glider will have less weight, less aerodynamic drag and less rolling resistance than the AIV Sable, which itself is approximately 300 kg lighter than a conventional Sable or Taurus five-passenger vehicle.

This analysis has demonstrated that converting to a lighter and more aerodynamic vehicle body does not significantly alter the *relative* merits of the fuel cell and hybrid electric vehicles relative to conventional passenger vehicles. The fuel economies of all vehicles (including ICEVs) improves more or less uniformly by almost 30%, but the relative improvements in performance of the alternative fueled vehicles compared to a more conventional internal combustion engine vehicle (ICEV) remain nearly constant. For example, the fuel economy of a direct hydrogen FCV on the 1.25 times accelerated EPA combined 55/45 city/highway driving schedule¹ is about 2.19 times higher than the corresponding ICEV with the AIV Sable. This fuel economy advantage increases only slightly to 2.23 times higher when both vehicles use a PNGV glider.

From another perspective, the fuel economy of a direct hydrogen FCV improves by a factor of 1.29 (from 65.8 mpgge² with the AIV Sable up to 85.2 mpgge with the PNGV glider), while the conventional gasoline-powered ICEV improves by a factor of 1.27 (from 30.1 mpg to 38.2 mpg by converting to a PNGV glider). Both of these calculations assume no improvement in the efficiency of the power source -- the ICE and the fuel cell efficiencies are fixed -- only the vehicle glider characteristics change.

While the fractional change in fuel economy is only slightly better with the FCV compared to the ICEV, the absolute fuel economies illustrate that fuel cell technology is required to reach the 80 mpg fuel economy goal of the PNGV, as shown in Figure 1. Both the pure FCV that has no battery or other peak power augmentation device and the battery-augmented direct hydrogen

¹Directed Technologies, Inc. uses the U.S. Environmental Protection Agency (EPA) combined driving schedule (55% city and 45% highway) with each speed increased by a factor of 1.25 for all comparative analyses. This 1.25 times acceleration factor more closely resembles American driver habits as discussed below.

²Fuel economy is measured in miles per gallon of gasoline-equivalent (mpgge) on a lower heating value (LHV) basis. That is, the LHV energy content of hydrogen necessary to propel a 65.8 mpgge-FCV over 65.8 miles of the specified driving cycle would be equal to the lower heating value of one gallon of gasoline.

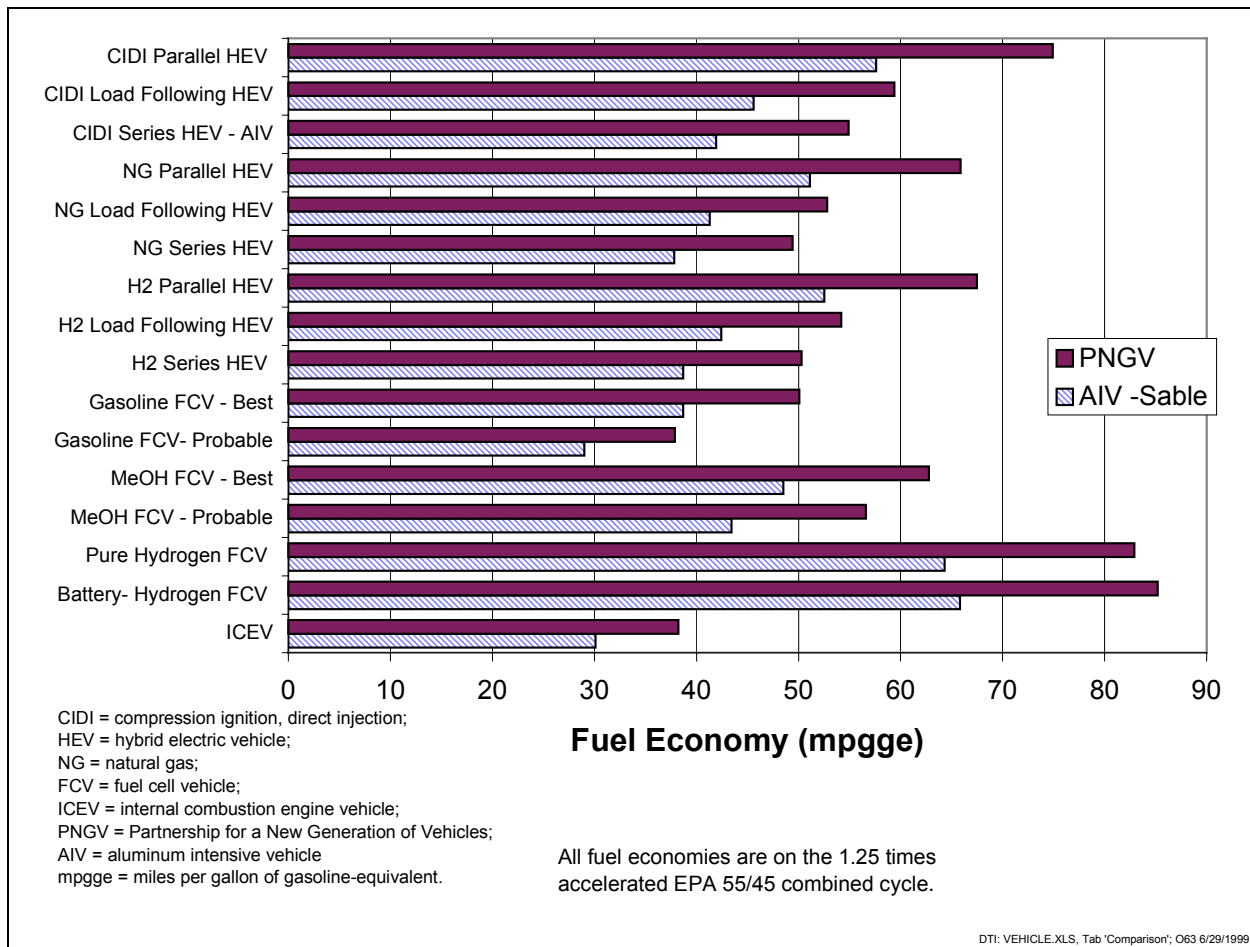


Figure 1. Estimated Fuel Economy for Various Fuel Cell and Hybrid Electric Vehicles on the 1.25 Times Accelerated EPA Combined Driving Cycle

FCV would achieve over 82 mpgge on the 1.25 times accelerated combined driving cycle. The diesel-powered compression ignition direct injection (CIDI) vehicle in the parallel hybrid mode would reach almost 75 mpgge, close to the PNGV goal. All series hybrid electric vehicles (in either the thermostat on/off mode or the load following mode) and all fuel cell vehicles powered by either gasoline and methanol in the probable cases would achieve less than 60 mpgge.

Both the hydrogen and the diesel parallel hybrid vehicles could achieve the 80 mpgge goal on the standard EPA 55/45 combined schedule without the 1.25 acceleration factor, as shown in Figure 2. However, this driving schedule does not reflect the speed and acceleration rate profiles of typical American drivers. These vehicles would meet the 80 mpgge goal on paper only. In any case, even with the unrealistic EPA combined cycle, the FCVs with onboard reformers would not meet the 80 mpgge goal, although the best-case methanol FCV would come very close at 79.8 mpgge. On this unrealistic driving cycle³, the direct hydrogen FCVs would achieve over 105 mpgge.

³ Although the EPA combined driving cycle is unrealistic, it is the standard often used to compare vehicle performance.

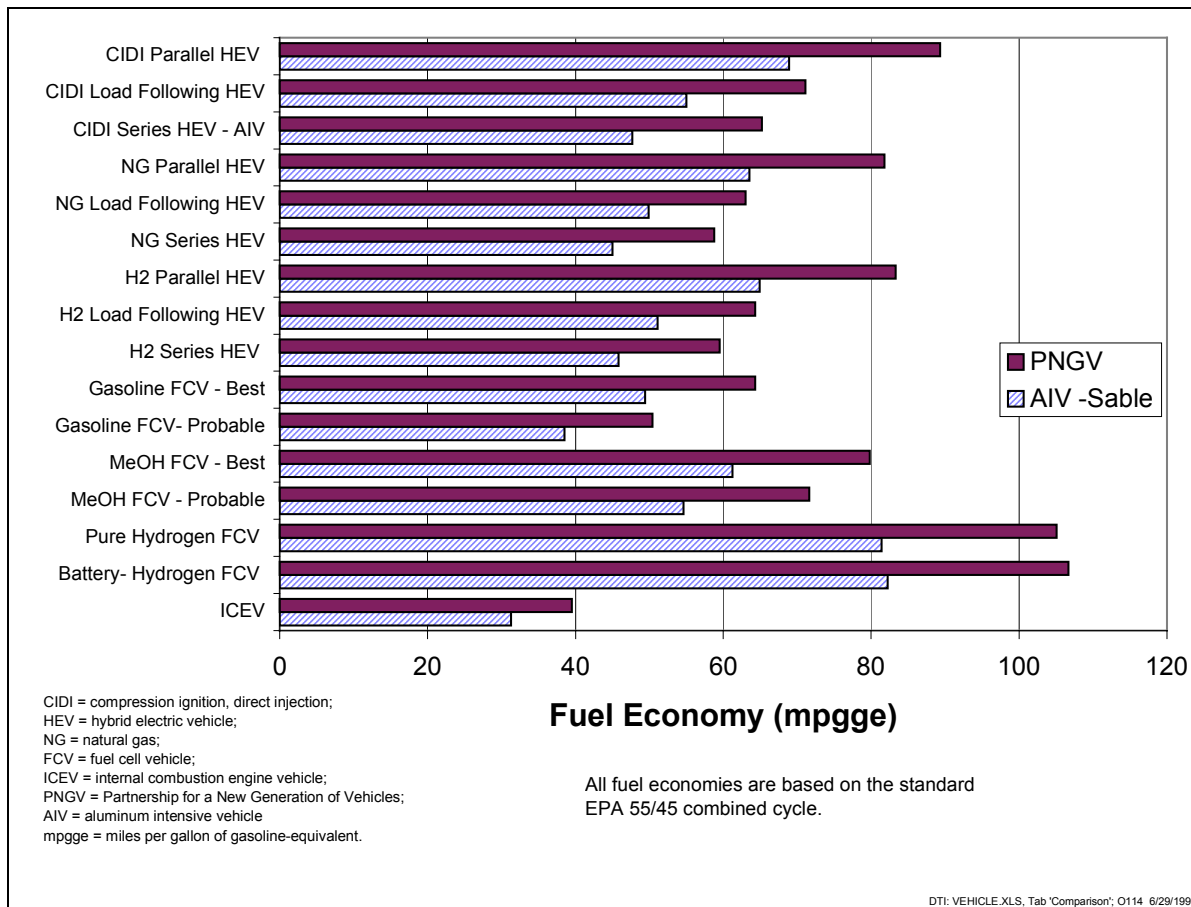


Figure 2. Estimated Fuel Economy for Various Fuel Cell and Hybrid Electric Vehicles on the Standard EPA Combined Driving Cycle

The environmental benefits of the alternative vehicles are generally proportional to fuel economy. Hence switching from the AIV Sable to the PNGV glider will also improve environmental benefits (both local emissions of criteria pollutants and greenhouse gas emissions) by the fuel economy factors -- an improvement of 1.29 for the FCV and an improvement of 1.27 for the ICEV. However, the diesel parallel hybrid vehicle has a net greenhouse gas advantage over the direct hydrogen FCV when the hydrogen is derived from natural gas by conventional steam methane reforming, as shown in Figure 3.

In addition, the natural gas parallel hybrid produces less greenhouse gas emissions than a hydrogen parallel hybrid, since more natural gas is consumed in making hydrogen than is used to directly fuel a hybrid vehicle. Thus there is no incentive from a climate change perspective in making a hydrogen hybrid vehicle -- storing natural gas directly on the vehicle not only reduces the volume of gas storage required, but also reduces net greenhouse gas emissions. The hydrogen hybrid vehicle would have an advantage in terms of local criteria pollutant emissions, as discussed in previous DTI reports (Thomas-1998a).

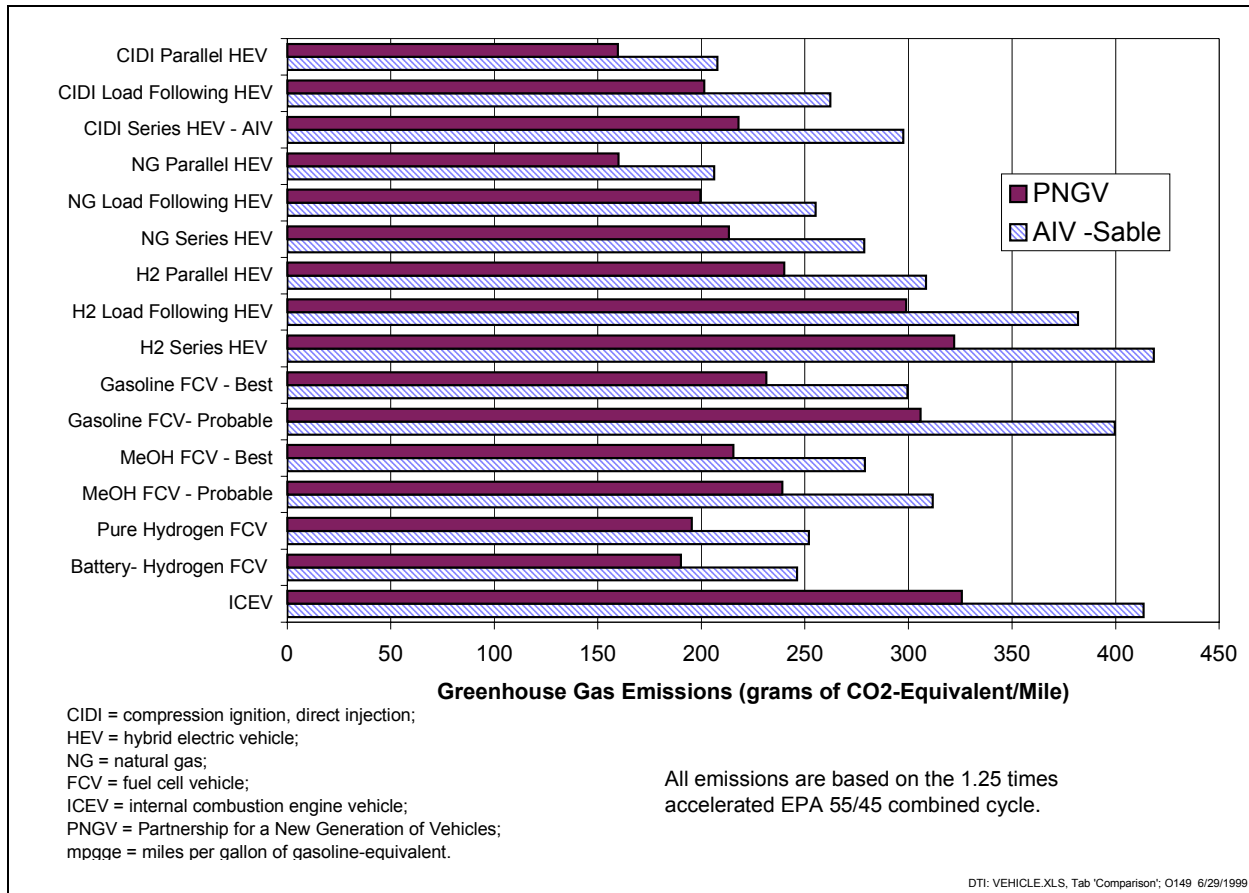


Figure 3. Estimated Greenhouse Gas Emissions from Alternative Vehicles

We conclude that switching from the AIV Sable glider to the PNGV glider for a five-passenger vehicle will improve fuel economy by about 30% and will decrease greenhouse gas and local emissions by about 23% for almost all vehicles. The relative advantage of a direct hydrogen fuel cell vehicle over the ICEV with the same vehicle glider will increase only one or two percent with the lighter, more aerodynamic bodies. Therefore most of the relative conclusions with respect to fuel cell vehicles compared to conventional vehicles and to hybrid electric vehicles from previous DTI reports are equally valid as vehicle gliders improve in the future. Only direct hydrogen fuel cell vehicles will achieve the PNGV goal of 80 mpgge fuel economy over realistic driving schedules, although parallel hybrid electric vehicles could achieve 80 mpgge fueled by hydrogen, natural gas or diesel fuel operating on the rather anemic EPA combined driving schedule.

Executive Summary for Battery Augmented Fuel Cell Systems

Directed Technologies, Inc. has previously estimated the cost of electricity from stationary proton exchange membrane (PEM) fuel cell systems, including the cogeneration of hydrogen from the natural gas fuel processor needed to run the stationary fuel cell system (Thomas - 1999). That analysis demonstrated that selling both hydrogen and electricity improved the economics of larger building fuel cell systems in the 50 kWe size range. In some circumstances, selling only electricity would not be competitive with current commercial electricity prices. But

producing and storing hydrogen during the off-peak hours when no electricity was needed for later sales to commercial users of hydrogen or to owners of direct hydrogen fuel cell vehicles would make the project economic -- electricity could be sold below the commercial price of electricity and the hydrogen could be sold to owners of fuel cell vehicles at a cost below the cost per mile of gasoline in a conventional vehicle. In effect the high value product (hydrogen for transportation) could be used to offset the cost of electricity for fuel cell systems larger than 50 kWe.

However, these favorable economics for larger stationary fuel cell systems do not hold for smaller residential systems, absent a fundamental reduction in small scale fuel cell or reformer cost. Using the detailed fuel cell cost analysis conducted by Directed Technologies, Inc., we concluded that even very large-scale mass production would not make stationary fuel cell systems competitive with current residential electricity rates. And yet several commercial ventures are attracting investment in the development of residential fuel cell systems. Most of these proposed ventures reportedly cut costs by using battery storage for peak power generation. That is, a typical residence in the United States might require an average power of only one kilowatt. But this home might require 3 to 5 kW of peak power during a hot August afternoon to run the air conditioner. Initially, providing that rare peak power by storing energy in batteries may cost less than building a fuel cell system to handle the peak load. We therefore added peak power battery augmentation to the stationary fuel cell systems analysis conducted previously.

The results of this analysis were all negative -- adding a peaking battery storage system would slightly increase the cost of electricity necessary to make the required return on investment. For a typical residence in California, for example, the fuel cell owner would have to charge 43.3 cents/kWh to make a 10% real, after-tax return on investment with a 4.3 peak kWe⁴ fuel cell system without battery, assuming that 10,000 such fuel cell systems were built. Adding the battery storage system and reducing the fuel cell power to 1.2 kWe would actually increase the required electricity price from 43.3 to 44.1 cents/kWh to make the 10% return on investment.

The actual capital costs for the battery-augmented system would be slightly lower than the pure fuel cell system for small production quantities, but nearly equal once production quantities reached the 10,000 unit level. We are projecting relatively high fixed costs for these small fuel cell systems -- reducing the peak power from 4.3 kWe to 1.2 kWe only reduces the initial capital costs from \$4,696 to \$4,019 for the fuel cell system, and from \$5,639 to \$5,184 for the steam methane reformer system. These cost reductions are barely adequate to cover the estimated cost of \$664 for a 6.7 kWh battery storage system, all at the 10,000 unit production volume. In addition, the battery system requires higher maintenance and has shorter lifetime (4 years assumed here compared to 10 years for the fuel cell system), producing a larger capital recovery factor for the battery storage system. Finally, extra natural gas is required for the battery system to cover the round-trip losses in storing energy in the battery. As a result of these factors, we conclude that the cost of electricity that must be charged to bring a 10% return on investment would be higher for the battery-augmented system even in the low (100 unit) production volume compared to a higher peak power pure fuel cell system.

⁴This fuel cell system would generate 4.33 kW of DC electricity, enough to supply 3.4 kW AC peak to the home in addition to providing the electricity to run the natural gas fuel processor.

Based on our analyses, we conclude that some combination of three factors must be exploited to make a fuel cell system for private residences economically viable:

- * Lower fuel cell or steam methane reformer mass production costs
- * Producing larger fuel cell systems to service 20 to 50 or more private residences
- * Serving individual utilities with higher than average electricity rates, or regions within a utility district with unusually high transmission and distribution costs, or within states like Alaska that have unusually high electricity rates and low natural gas prices.

It appears from our analysis that all three factors could be required to make fuel cells attractive for residential customers initially.

1.0 Introduction to the PNGV Transportation Analysis

In previous DTI vehicle simulations for the Hydrogen Program Office, we have fixed the vehicle glider, choosing the AIV Sable as a surrogate for advanced vehicles with respect to weight reduction. The AIV Sable is similar to a five-passenger vehicle weighing about 300 kg less than its conventional counterparts, the Ford Taurus and Mercury Sable. For each alternative fueled vehicle, we effectively stripped out the conventional power train and replaced it with either a fuel cell system and electric drive motor, or a hybrid electric drive system using an ICE to provide the main motive power. Some concern was expressed that as vehicle systems became more advanced, incorporating other features being developed by the PNGV partnership between government and the U.S. automakers, the previous conclusions based on the AIV Sable might not hold. We have therefore repeated all calculations of vehicle weight, fuel economy and emissions assuming the glider characteristics of a future PNGV-like vehicle.

1.1 Glider Characteristics

The PNGV program has set three major goals, the last of which is to increase fuel economy of passenger vehicles by “up to” a factor of three. This goal can be achieved by various combinations of higher efficiency power trains, reduced weight, reduced aerodynamic drag and reduced rolling resistance. Possible combinations include 45% thermal efficiency for the main power source such as a hydrogen fuel cell system, a 20 to 40% weight reduction, 20% lower drag and 20% lower rolling resistance. Table 1 illustrates our choice of vehicle glider parameters compared to the AIV-Sable parameters used previously. Although the 23.8% weight reduction is on the low side, the AIV Sable is already about 300 kg lighter than the conventional Sable. Thus the total weight reduction from today's mass produced vehicle is closer to 40%.

Table 1. Vehicle Glider Parameters for the AIV Sable and a PNGV-Like Vehicle

| | AIV Sable | PNGV | % Change |
|---|-----------|--------|----------|
| Drag Coefficient | 0.33 | 0.27 | 18.2 |
| Cross Sectional Area (m ²) | 2.127 | 2.08 | 2.2 |
| Rolling Resistance | 0.0092 | 0.0072 | 21.7 |
| Glider Weight ⁵ (kg) | 852 | 649 | 23.8 |
| Direct Hydrogen FCV Curb Weight (kg) [including battery peak power augmentation] | 1,155 | 896 | 22.4 |

⁵Glider as used here includes all vehicle components except the main power source (ICE or fuel cell system), fuel tank, fuel, exhaust system, transmission, electric motor, inverter & motor controller and peak power battery (if any).

1.2 Fuel Cell Electric Vehicles

We have analyzed three types of fuel cell vehicles (FCV): direct hydrogen FCVs, methanol FCVs and gasoline FCVs. The last two require an onboard fuel processor to convert the liquid fuel to hydrogen for the PEM fuel cell. Since no organization has yet built, tested and published performance results for a mature onboard fuel processor, we have assumed a "probable case" and a "best case" set of parameters for both processors. The parameters assumed for these two cases are summarized in Table 2. The fuel cell power capacity (on pure hydrogen) is increased by the factor shown in the first row to compensate for lower peak power operating on the gas reformat from the fuel processors. The methanol reformer reformat would have at best 80 to 85% hydrogen, and the gasoline reformer would have at best 35% to 40% hydrogen. These dilute hydrogen streams would then have to be exhausted from the anode cavity of the fuel cell. Otherwise the other gases in the reformat stream [CO_2 , N_2 (in the case of partial oxidation reformers), H_2O , CH_4 , etc.] would accumulate in the anode, smothering and shutting down the cells. As a result, some hydrogen must necessarily pass through the anode unreacted. This unused hydrogen can be burned to raise steam for the methanol reformer, but it might be difficult to utilize this heat in the case of an exothermic gasoline partial oxidation or autothermal reactor (ATR) system. For details on how these parameters were chosen, see Thomas-1998a.

Table 2. Fuel Processor Parameters for "Best Case" and "Probable Case"

| | Methanol Fuel Processor | | Gasoline Fuel Processor | |
|---|-------------------------|---------------|-------------------------|---------------|
| | Best Case | Probable Case | Best Case | Probable Case |
| Fuel Cell Size Increase w/r to H_2 Fuel Cell | 1.10 | 1.12 | 1.21 | 1.36 |
| Fuel Cell Efficiency Curve | LANL Theory | LANL Exper. | LANL Theory | LANL Exper. |
| Hydrogen Utilization | 90% | 83.3% | 90% | 83.3% |
| Fuel Processor Efficiency (LHV) | 84.5% | 80% | 75% | 70% |
| Anode Exhaust Gas Heat Recovery | 75% | 75% | 70% | 0 |
| Reformer Weight (kg) ⁶ | 46 | 60 | 55 | 100 |

The direct hydrogen FCV stores hydrogen at 34.5 MPa (5,000 psi) in carbon-fiber wrapped composite tanks. These tanks are extraordinarily strong, and have been shown to survive rear-end collisions at up to 50 mph without losing pressure. DTI has previously analyzed the weight, volume and cost various hydrogen storage systems, and has concluded that the 34.5 MPa compressed gas tanks are the best choice for passenger vehicle applications (James-1996, 1997b, 1999).

⁶This is the initial weight (before weight compounding) for a fuel processor to supply 40 kW peak power from a fuel cell system. Actual processor weights are increased in the program to provide the higher power to accelerate the slightly heavier vehicle.

1.3 Hybrid Electric Vehicles

We have also analyzed nine types of hybrid electric vehicles. Each of these vehicles uses a small internal combustion engine to provide steady-state power, combined with an electric motor or motors to provide traction to the wheels. In series operation, the ICE is connected to a generator which provides electrical power to charge a battery or to power the drive motor. All traction power comes from this motor. In a parallel hybrid, both the ICE and the electric motor are connected to the wheels through a transmission.

Two types of series HEVs were analyzed: a thermostat series hybrid where the ICE is turned on and off in response to battery state of charge, and a load-following series hybrid where the ICE power is varied over a limited range to track the vehicle power demands, with the battery providing extra power for acceleration and limited hill climbing. In addition, we analyzed one parallel hybrid vehicle configuration. The operating algorithms for both the load-following series hybrids and the parallel hybrids were devised by DTI. These algorithms were not vigorously optimized, and may not represent the highest possible fuel economy.

For each of the three HEVs (thermostat series, load-following series, and parallel), we also evaluated three different fuel options: hydrogen, natural gas and diesel fuel. We assumed that the ICE would be optimized for each fuel. We assumed a peak efficiency of 38% (on a lower heating value basis) for a natural gas ICE and 40% for a hydrogen ICE. In the case of diesel fuel, we assumed 43% peak efficiency for a compression ignition, direct injection engine such as those demonstrated in mass production by Volkswagen.

1.4 Vehicle Weight Estimates

We calculate the weight of each alternative vehicle based on a weight compounding formula derived earlier (See Appendix G of Thomas -1998a). The weights of all power train components are adjusted to provide equal vehicle performance, including equal acceleration. If extra weight is required for any function such as a fuel processor, for example, then the size (and weight) of other power train components must also be increased to accelerate the extra fuel processor weight. This added incremental weight in turn requires still further increases in other components in an iterative process. However, this iteration can be solved in closed form for both added power train weight components and for non- power train components. The amount of fuel stored on each vehicle is also adjusted to produce a range of 308 miles on the 1.25 times accelerated combined driving cycle, or about 380 miles for the FCV on the standard EPA combined driving cycle. As a result all vehicles considered in this report have identical performance in terms of range and acceleration.

The resulting vehicle test weights are summarized in Figure 4, along with the other vehicle characteristics. The test weight is equal to the vehicle curb weight plus 136 kg in all cases.

| Vehicle Characteristics | | | | | | | | | |
|---|-------------|-----------|------------------------|--------------|---------------------|------------------|-------------|------------------|--------------------|
| Vehicle Body | Fuel | Engine | Peak Engine Efficiency | Comment | Battery Peak Power? | Test Weight (kg) | Drag Coeff. | Cross Sect. Area | Rolling Resistance |
| AIV Sable | Gasoline | ICE | 29.6 | | No | 1304 | 0.33 | 2.127 | 0.0092 |
| AIV Sable | Hydrogen | Fuel Cell | | | Yes | 1291 | 0.33 | 2.127 | 0.0092 |
| AIV Sable | Hydrogen | Fuel Cell | | | No | 1283 | 0.33 | 2.127 | 0.0092 |
| AIV Sable | MeOH | Fuel Cell | | Probable | Yes | 1414 | 0.33 | 2.127 | 0.0092 |
| AIV Sable | MeOH | Fuel Cell | | Best | Yes | 1390 | 0.33 | 2.127 | 0.0092 |
| AIV Sable | Gasoline | Fuel Cell | | Probable | Yes | 1475 | 0.33 | 2.127 | 0.0092 |
| AIV Sable | Gasoline | Fuel Cell | | Best | Yes | 1387 | 0.33 | 2.127 | 0.0092 |
| PNGV | Gasoline | ICE | 29.6 | | No | 1042 | 0.27 | 2.08 | 0.0072 |
| PNGV | Hydrogen | Fuel Cell | | | Yes | 1032 | 0.27 | 2.08 | 0.0072 |
| PNGV | Hydrogen | Fuel Cell | | | No | 1023 | 0.27 | 2.08 | 0.0072 |
| PNGV | MeOH | Fuel Cell | | Probable | Yes | 1119 | 0.27 | 2.08 | 0.0072 |
| PNGV | MeOH | Fuel Cell | | Best | Yes | 1110 | 0.27 | 2.08 | 0.0072 |
| PNGV | Gasoline | Fuel Cell | | Probable | Yes | 1172 | 0.27 | 2.08 | 0.0072 |
| PNGV | Gasoline | Fuel Cell | | Best | Yes | 1099 | 0.27 | 2.08 | 0.0072 |
| Hybrid Electric Vehicles (HEV) -- Thermal Engine Plus Battery for Peak Power | | | | | | | | | |
| AIV Sable | Hydrogen | ICE | 40 | Series HEV | Yes | 1507 | 0.33 | 2.127 | 0.0092 |
| AIV Sable | Hydrogen | ICE | 40 | Load Follow | Yes | 1366 | 0.33 | 2.127 | 0.0092 |
| AIV Sable | Hydrogen | ICE | 40 | Parallel HEV | Yes | 1253 | 0.33 | 2.127 | 0.0092 |
| AIV Sable | Natural Gas | ICE | 38 | Series HEV | Yes | 1435 | 0.33 | 2.127 | 0.0092 |
| AIV Sable | Natural Gas | ICE | 38 | Load Follow | Yes | 1308 | 0.33 | 2.127 | 0.0092 |
| AIV Sable | Natural Gas | ICE | 38 | Parallel HEV | Yes | 1200 | 0.33 | 2.127 | 0.0092 |
| AIV Sable | Diesel | CIDI | 43 | Series HEV | Yes | 1472 | 0.33 | 2.127 | 0.0092 |
| AIV Sable | Diesel | CIDI | 43 | Load Follow | Yes | 1361 | 0.33 | 2.127 | 0.0092 |
| AIV Sable | Diesel | CIDI | 43 | Parallel HEV | Yes | 1245 | 0.33 | 2.127 | 0.0092 |
| PNGV | Hydrogen | ICE | 40 | Series HEV | Yes | 1229 | 0.27 | 2.08 | 0.0072 |
| PNGV | Hydrogen | ICE | 40 | Load Follow | Yes | 1117 | 0.27 | 2.08 | 0.0072 |
| PNGV | Hydrogen | ICE | 40 | Parallel HEV | Yes | 1016 | 0.27 | 2.08 | 0.0072 |
| PNGV | Natural Gas | ICE | 38 | Series HEV | Yes | 1158 | 0.27 | 2.08 | 0.0072 |
| PNGV | Natural Gas | ICE | 38 | Load Follow | Yes | 1057 | 0.27 | 2.08 | 0.0072 |
| PNGV | Natural Gas | ICE | 38 | Parallel HEV | Yes | 969 | 0.27 | 2.08 | 0.0072 |
| PNGV | Diesel | CIDI | 43 | Series HEV | Yes | 1185 | 0.27 | 2.08 | 0.0072 |
| PNGV | Diesel | CIDI | 43 | Load Follow | Yes | 1082 | 0.27 | 2.08 | 0.0072 |
| PNGV | Diesel | CIDI | 43 | Parallel HEV | Yes | 990 | 0.27 | 2.08 | 0.0072 |

Figure 4. Alternative Vehicle Characteristics

1.5 Fuel Economy and Drive Cycles

The fuel economy of a FCV depends much more on the drive cycle than that of a conventional vehicle. The ICE has variable efficiency that depends on both torque and engine speed. Efficiency peaks at moderate engine speed and output torque, and falls off significantly at low engine speed and low torque, and less so at higher speeds and torques. As a result, with more aggressive driving, the average fuel economy over a drive cycle does not always vary significantly with an ICEV. For example, at very low speeds, increasing speed may push the ICE closer to its high efficiency "sweet spot," thereby improving fuel economy over the low speed portion of the driving cycle, which helps to offset the drop in fuel economy associated with an increase in high speed driving. The efficiency of a fuel cell, however, declines monotonically above a very low power level. Hence more aggressive driving will always lead to lower fuel economy for the FCV. Therefore the relative advantage of the FCV fuel economy compared to the ICEV fuel economy will generally drop if both vehicles are driven more aggressively.

The most common drive schedule used to compare passenger vehicles in the United States is the EPA's federal urban driving schedule (FUDS), and the federal highway driving schedule (FHDS). Fuel economy is also estimated over a combination of these two cycles, typically 55% urban and 45% highway. However, these cycles are notoriously anemic. For example, the average highway speed in only 48.6 mph with a top speed of 60 mph, or far below typical American highway conditions. The average FUDS speed is 19.5 mph with a peak of 56.7 mph, which may be reasonable under some circumstances. However, the automobile companies have all developed their own proprietary customer driving schedules to test out their new cars. These schedules are all more aggressive than the EPA schedules. In addition, the EPA has generated a new drive cycle, called the US06 which is even more aggressive than some auto company drive cycles.

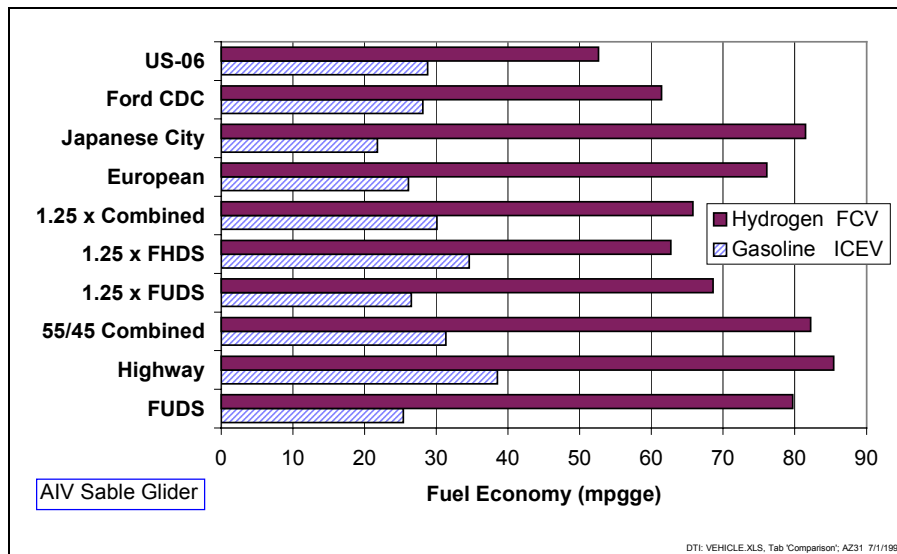


Figure 5. Fuel Economy for a Direct Hydrogen Fuel Cell Vehicle and a Conventional Gasoline Internal Combustion Engine Vehicle

The fuel economies predicted by the DTI simulation code are shown in Figure 5 for both a direct hydrogen FCV and a conventional ICEV, both based on the AIV-Sable glider. In addition to the EPA schedules with and without the 1.25 times speed multiplier, we show the fuel economies for the European and Japanese cycles, and the Ford Customer Driving Cycle. The ratios of the fuel economies for these driving cycles are shown in Figure 6 for both the AIV-Sable and for the PNGV glider. These driving cycles are displayed in more or less decreasing order of aggressiveness -- the US06 is the most aggressive cycle, while the Japanese City cycle is very anemic. The sluggish Japanese driving schedule provides over 3.5 times better fuel economy for the FCV compared to the ICEV, while the US06 produces only a 1.8 to one advantage. Note also that the 1.25 times accelerated combined cycle provides almost the same improvement factor, 2.2 to one, as the Ford Customer Driving Cycle, while the standard EPA combined cycle would predict a 2.6 to one advantage in fuel economy for the FCV over the ICEV. DTI has therefore chosen the 2.2 to one improvement factor in all of our comparisons as being more realistic for typical American drivers.

The effects of changing from the AIV-Sable glider to the PNGV glider are also shown in Figure 6. In all cases, the PNGV glider improves the relative performance of the FCV relative to the ICEV by about 2 to 3 percent. The actual fuel economies for both FCVs and for HEVs are shown in Figures 1 and 2 in the Executive Summary.

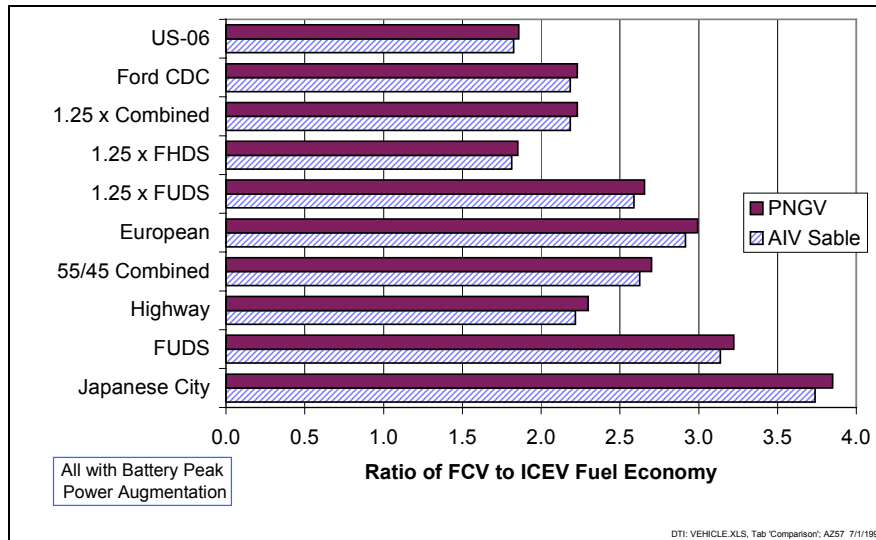


Figure 6. Ratio of FCV Fuel Economy to ICEV Fuel Economy

1.6 Mass Production Cost of Alternative Vehicles

DTI has previously estimated the cost of fuel cell vehicles for the Ford Motor Company and the U.S. Department of Energy (James-1997, Lomax-1997), using detailed, bottom-up cost analysis for material, process and assembly procedures assuming automotive scale production (500,000 units per year). We have also estimated costs for HEVs (Thomas-1998a, 1998b, 1998c) based on scaling from existing ICE and battery system costs, but have not applied detailed mass production cost estimation methodology to HEV components.

All previous cost estimates were based on the power trains necessary to propel the AIV-Sable glider. We have modified these estimates based on the PNGV glider, which requires less power and less fuel to meet our specifications of 380 miles range on the EPA combined cycle and acceleration of 0 to 60 mph in 10 seconds. While costs do not scale linearly with reduced power, they do decrease to some degree as peak power requirements decline for the lighter, more aerodynamic PNGV glider. In addition, more of the power train cost scales with power demand for fuel cell systems than for ICEs. Much of the cost of a six-cylinder engine is due to the engine block, pistons, rings, valves, etc. Increasing or decreasing the size of an engine over the limited range considered here does not change the number of components. The peak power of the fuel cell for a given current density and operating voltage depends linearly on the number of cells in the stack. Hence the total fuel cell system cost is more linearly dependent on peak power.

We have assumed a six-cylinder engine for the conventional passenger vehicles and a lower peak power four-cylinder engine for the hybrid electric vehicles. We assume a fixed cost dependent on the number of cylinders plus a variable cost dependent on the peak power required. The four

cylinder engine cost is given by:

$$C_4 = \$720 + 5.14 \times P \quad (1)$$

where P = the peak engine power. The cost of a six-cylinder engine is then:

$$C_6 = \$1080 + 5.14 \times P \quad (2)$$

For a 40-kW four-cylinder engine, the total cost would then be \$925 in mass production, with 78% of the cost fixed. For a 100-kW six-cylinder engine for the conventional car, the mass production cost would then be \$1,600, with 32% of the cost dependent on output power.

The total estimated cost for a PEM fuel cell system is given by:

$$C_{FC} = \$1,132 + P \times \left(3.27 + \left[\frac{3.46 + 29.66 \times L_p}{P_d} \right] \right) \quad (3)$$

where L_p = the total platinum catalyst loading (mg/cm^2), and
 P_d = the fuel cell power density (W/cm^2), assuming that platinum costs \$400/troy ounce (\$12.86/gram).

This cost includes the fuel cell stack itself, as well as all the auxiliary equipment such as humidification, air compressor, radiator, piping, and controls. Based on projected fuel cell performance of one W/cm^2 power density using $0.25 \text{ mg}/\text{cm}^2$ platinum catalyst loading (including both the anode and cathode), the fuel cell system cost becomes:

$$C_{FC} = \$1,132 + P \times 14.15 \quad (2)$$

An 80-kW fuel cell system for a pure FCV (no peak power augmentation) would then cost \$2264, with half the cost being power-dependent, versus only 32% for the six-cylinder ICE. For a FCV with peak power augmentation, both the fuel cell system and the battery scale down in size and cost for smaller PNGV power trains. As a result, the differential cost between a conventional ICE power train and the fuel cell power train diminishes for a PNGV power train with lower peak power demands as shown in Figure 7. The first two columns show the cost differential between the AIV Sable FC and the PNGV FC power train and the ICEV power train. The last column shows the difference between the AIV Sable and the PNGV incremental cost. Thus moving from the AIV Sable glider to the PNGV glider would reduce the power train

| | AIV Sable Delta Over ICEV | PNGV Delta Over ICEV | Delta |
|-------------------------|---------------------------------|-------------------------------|-------|
| Battery - Hydrogen FCV | \$2,302 | \$1,832 | \$470 |
| Pure Hydrogen FCV | \$2,102 | \$1,650 | \$452 |
| MeOH FCV - Probable | \$2,752 | \$2,308 | \$444 |
| MeOH FCV - Best | \$2,096 | \$1,734 | \$362 |
| Gasoline FCV - Probable | \$4,356 | \$3,699 | \$657 |
| Gasoline FCV - Best | \$2,717 | \$2,281 | \$436 |
| H2 Series HEV | \$3,851 | \$2,997 | \$854 |
| H2 Load Following HEV | \$2,879 | \$2,263 | \$616 |
| H2 Parallel HEV | \$1,827 | \$1,479 | \$348 |
| NG Series HEV | \$2,363 | \$1,866 | \$497 |
| NG Load Following HEV | \$1,563 | \$1,247 | \$316 |
| NG Parallel HEV | \$1,110 | \$702 | \$408 |
| CIDI Series HEV - AIV | \$2,647 | \$2,165 | \$482 |
| CIDI Load Following HEV | \$1,837 | \$1,532 | \$305 |
| CIDI Parallel HEV | \$1,067 | \$972 | \$95 |

DTI: VEHICLE.XLS, Tab 'Comparison'; D86 7/2/1999

Figure 7. Cost Differential Between Alternative Vehicle Power Train and Conventional ICE Power Train (Adjusted for weight compounding, except no glider cost increase is included for glider weight increase.)

differential by \$470 for the direct hydrogen FCV with battery peak power augmentation, and by \$452 for the pure FCV, etc. These data are also plotted in Figure 8.

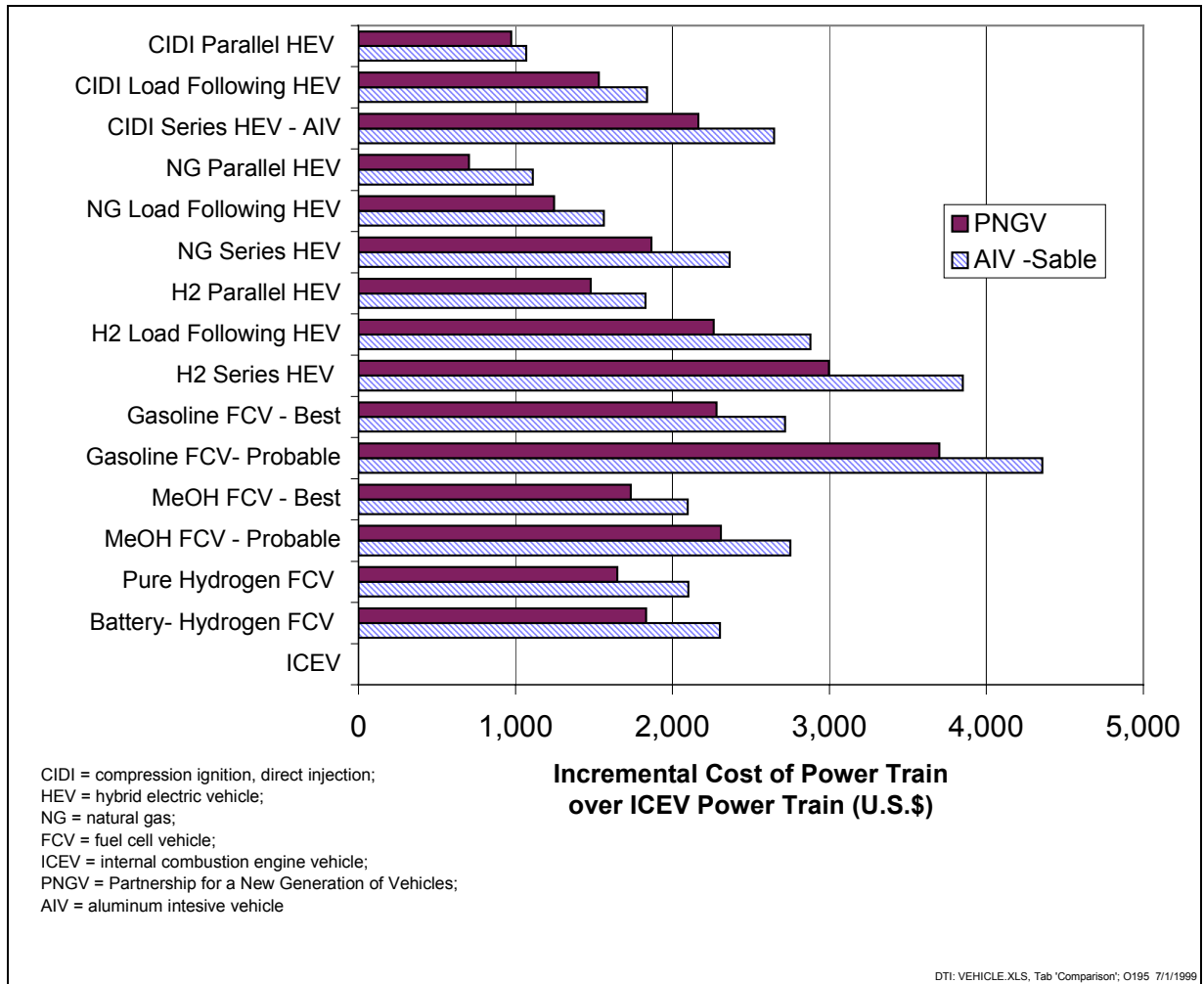


Figure 8. Incremental Cost of the Power Train for Alternative Vehicles Above the Cost of a Conventional ICE Power Train.

Component cost breakdowns are shown in Tables 3 and 4 for representative fuel cell vehicles assuming an AIV Sable glider (Table 3) and a PNGV glider (Table 4). Similar cost breakdowns are shown in Table 5 for the thermostat (on/off battery charging) series hybrid electric vehicle on the AIV Sable glider, and in Table 6 for the PNGV glider.

Table 3. Alternative Vehicle Component Cost Breakdown for Fuel Cell Vehicles with AIV Sable Glider

| | ICEV | | Hydrogen FCV | | Hydrogen FCV with Battery Power Augmentation | | Probable Methanol FCV with Battery | | Probable Gasoline FCV with Battery | |
|---------------------------|------------|-----------|--------------|-----------|--|-----------|------------------------------------|-----------|------------------------------------|-----------|
| Vehicle Weight (kg) | 1,304 | | 1,283 | | 1,291 | | 1,414 | | 1,475 | |
| | Power (kW) | Cost (\$) | Power (kW) | Cost (\$) | Power (kW) | Cost (\$) | Power (kW) | Cost (\$) | Power (kW) | Cost (\$) |
| Fuel Cell System | | | 74.1 | \$2,180 | 38 | \$1,670 | 45.1 | \$2,006 | 56.5 | \$2,410 |
| ICE System | 100 | \$1,600 | | | | | | | | |
| Transmission/Gear Box | | \$700 | | \$200 | | \$200 | | \$200 | | \$200 |
| Fuel Tank | | \$125 | | \$1,096 | | \$1,073 | | \$157 | | \$128 |
| Generator | | | | | | | | | | |
| Fuel Processor | | | | | | | 45.1 | \$950 | 56.5 | \$2,129 |
| Motor/Inverter/Controller | | | 81.5 | \$901 | 82.1 | \$906 | 88.1 | \$943 | 91.7 | \$966 |
| Battery | | | | | 40.3 | \$728 | 43.2 | \$771 | 45.0 | \$798 |
| Controller & misc. | | | | \$150 | | \$150 | | \$150 | | \$150 |
| Total | | \$2,425 | | \$4,527 | | \$4,727 | | \$5,177 | | \$6,781 |

Table 4. Alternative Vehicle Component Cost Breakdown for Fuel Cell Vehicles with PNGV Glider

| | ICEV | | Hydrogen FCV | | Hydrogen FCV with Battery Power Augmentation | | Probable Methanol FCV With Battery | | Probable Gasoline FCV with Battery | |
|---------------------------|-------------------|------------------|-------------------|------------------|--|------------------|------------------------------------|------------------|------------------------------------|------------------|
| Vehicle Weight (kg) | 1,042 | | 1,023 | | 1,032 | | 1,119 | | 1,172 | |
| | <i>Power (kW)</i> | <i>Cost (\$)</i> | <i>Power (kW)</i> | <i>Cost (\$)</i> | <i>Power (kW)</i> | <i>Cost (\$)</i> | <i>Power (kW)</i> | <i>Cost (\$)</i> | <i>Power (kW)</i> | <i>Cost (\$)</i> |
| Fuel Cell System | | | 59.1 | \$1,968 | 29.8 | \$1,554 | 35.7 | \$1,823 | 45.0 | \$2,149 |
| ICE System | 80 | \$1,491 | | | | | | | | |
| Transmission/Gear Box | | \$700 | | \$200 | | \$200 | | \$200 | | \$200 |
| Fuel Tank | | \$125 | | \$877 | | \$856 | | \$131 | | \$109 |
| Generator | | | | | | | | | | |
| Fuel Processor | | | | | | | 35.7 | \$856 | 45.0 | \$1,897 |
| Motor/Inverter/Controller | | | 65 | \$771 | 65.6 | \$776 | 71.1 | \$811 | 74.5 | \$832 |
| Battery | | | | | 32.8 | \$612 | 35.6 | \$653 | 37.3 | \$677 |
| Controller & misc. | | | | \$150 | | \$150 | | \$150 | | \$150 |
| Total | | \$2,316 | | \$3,966 | | \$4,148 | | \$4,624 | | \$6,014 |

Table 5. Alternative Vehicle Component Cost Breakdown for Thermostat Series Hybrid Electric Vehicles with AIV Sable Gliders
(ICEV and Pure Hydrogen FCV shown for reference)

| | ICEV | | Hydrogen FCV | | Natural Gas Thermostat HEV | | Hydrogen Thermostat HEV | | Diesel CIDI Thermostat HEV | |
|---------------------------|------------|-----------|--------------|-----------|----------------------------|-----------|-------------------------|-----------|----------------------------|-----------|
| Vehicle Weight (kg) | 1,304 | | 1,283 | | 1,435 | | 1,507 | | 1,472 | |
| | Power (kW) | Cost (\$) | Power (kW) | Cost (\$) | Power (kW) | Cost (\$) | Power (kW) | Cost (\$) | Power (kW) | Cost (\$) |
| Fuel Cell System | | | 74.1 | \$2,180 | | | | | | |
| ICE System | 100 | \$1,600 | | | 44.7 | \$950 | 46.5 | \$959 | 45.6 | \$1,432 |
| Transmission/Gear Box | | \$700 | | \$200 | | \$200 | | \$200 | | \$200 |
| Fuel Tank | | \$125 | | \$1,096 | | \$385 | | \$1,741 | | \$125 |
| Generator | | | | | 44.7 | \$612 | 46.5 | \$626 | 45.6 | \$619 |
| Fuel Processor | | | | | | | | | | |
| Motor/Inverter/Controller | | | 81.5 | \$901 | 90.8 | \$975 | 95.4 | \$1,011 | 93.2 | \$993 |
| Battery | | | | | 90.8 | \$1,517 | 95.4 | \$1,589 | 93.2 | \$1,554 |
| Controller & misc. | | | | \$150 | | \$150 | | \$150 | | \$150 |
| Total | | \$2,425 | | \$4,527 | | \$4,789 | | \$6,276 | | \$5,073 |

Table 6. Alternative Vehicle Component Cost Breakdown for Thermostat Series Hybrid Electric Vehicles with PNGV Glider
(ICEV and Pure Hydrogen FCV shown for reference)

| | ICEV | | Hydrogen FCV | | Natural Gas Thermostat HEV | | Hydrogen Thermostat HEV | | Diesel CIDI Thermostat HEV | |
|---------------------------|------------|-----------|--------------|-----------|----------------------------|-----------|-------------------------|-----------|----------------------------|-----------|
| Vehicle Weight (kg) | 1,042 | | 1,023 | | 1,158 | | 1,229 | | 1,185 | |
| | Power (kW) | Cost (\$) | Power (kW) | Cost (\$) | Power (kW) | Cost (\$) | Power (kW) | Cost (\$) | Power (kW) | Cost (\$) |
| Fuel Cell System | | | 59.1 | \$1,968 | | | | | | |
| ICE System | 80 | \$1,491 | | | 35 | \$900 | 36.4 | \$907 | 35.8 | \$1,356 |
| Transmission/Gear Box | | \$700 | | \$200 | | \$200 | | \$200 | | \$200 |
| Fuel Tank | | \$125 | | \$877 | | \$339 | | \$1,367 | | \$125 |
| Generator | | | | | 35 | \$535 | 36.4 | \$546 | 35.8 | \$542 |
| Fuel Processor | | | | | | | | | | |
| Motor/Inverter/Controller | | | 65 | \$771 | 72.3 | \$829 | 76.0 | \$858 | 74.5 | \$846 |
| Battery | | | | | 72.3 | \$1,229 | 76.0 | \$1,285 | 74.5 | \$1,262 |
| Controller & misc. | | | | \$150 | | \$150 | | \$150 | | \$150 |
| Total | | \$2,316 | | \$3,966 | | \$4,182 | | \$5,313 | | \$4,481 |

1.7 PNGV Transportation Conclusions

Based on this assessment, we conclude that converting from the AIV Sable glider assumed in previous studies to the PNGV type of glider would have minimum effect on the *relative merits* of fuel cell and hybrid electric vehicles compared to the conventional ICEV. However, the *absolute values* of fuel economy, emissions and cost would be superior for the PNGV vehicles. But the ICEV performance will improve almost as much as the fuel cell and hybrid vehicles with a lighter, more aerodynamic vehicle glider. Specifically, we conclude for the main figures-of-merit for these vehicles as follows:

Fuel Economy: In absolute terms the PNGV body parameters are essential to meet the PNGV goal of over 80 mpgge on realistic customer drive cycles. Only the direct hydrogen fuel cell vehicle can meet the 80 mpgge goal on the 1.25 times accelerated EPA 55/45 combined cycle, which more closely represents actual American driving habits. The direct hydrogen fuel economy improves from 65.8 mpgge on the 1.25 times accelerated combined cycle with the AIV Sable glider up to 85.2 mpgge with the PNGV glider. The next best vehicle in terms of fuel economy, the diesel CIDI engine in the parallel hybrid vehicle, increases from 57.6 mpgge to 74.9 mpg on the same drive cycle, close to the PNGV goal.

In relative terms, however, the PNGV glider improves the fuel economy of the FCV by about 29%, but the ICEV fuel economy also improves by 27% (from 30.1 to 38.2 mpg). So the net gain for the FCV relative to the ICEV is very small.

Greenhouse Gas Emissions: In absolute terms, greenhouse gases are reduced for each vehicle by their relative fuel economy improvements -- about 29% reduction for the FCV (from 246 grams of CO₂-equivalent per mile down to 190 g/mile). The HEVs also would have a 20% to 30% reduction in greenhouse gas emissions. The lowest emitters would be the natural gas parallel hybrids and the diesel CIDI parallel hybrids at 160 g/mile with the PNGV glider, down from 206 g/mile for the AIV Sable.

The relative improvements are marginal, however, since the ICEV greenhouse gas emissions would also be reduced by about 27%, from 414 g/mile of CO₂-equivalent with the AIV Sable glider down to 326 g/mile. Thus the direct hydrogen FCV would move from a net greenhouse gas advantage of 40.5% reductions compared to the ICEV for the AIV Sable, to a 41.7% reduction if both vehicles were based on the PNGV glider.

Local Air Pollution: The local emissions of criteria pollutants (VOCs, CO, NO_x) would also show a 27 to 30% reduction for all vehicles. The direct hydrogen FCV has no local emissions, but these vehicles could create emissions within the local urban airshed if, for example, the hydrogen were produced locally at small steam methane reformer appliances. In this case the FCV local emissions attributed to these reformers would also decrease by 29%.

Incremental Cost: In absolute terms, the PNGV body parameters would reduce the cost of the direct hydrogen FCV power train by about \$579, from an estimated mass production cost of \$4,727 down to \$4,148. Relative to the ICEV power train, the cost savings would be almost as great, since the ICE power train does not scale down as fast with reduced peak power demand as the fuel cell power train. The relative cost difference between the fuel cell power train and the ICEV power train would decrease by \$470, from \$2,302 cost differential for the AIV Sable down to \$1,832 for the PNGV glider.

In summary, converting from the AIV Sable to the PNGV glider is essential for the direct hydrogen fuel cell vehicle to meet the 80 mpgge fuel economy goal of the PNGV on realistic driving cycles. This improve glider would also reduce the cost differential of the power train relative to the ICEV by \$470, but otherwise has marginal (2 to 3%) impact on the relative performance of the fuel cell vehicle compared to either conventional ICEVs or to hybrid electric vehicles.

2.0 Introduction to Battery-Augmented Stationary Fuel Cell Systems

Stationary fuel cell systems can provide electricity at or near the end-user's facility, avoiding the cost of transmission and distribution that can account for up to half of the cost of delivered electrical power. For utilities faced with major investments to expand their transmission and distribution networks to portions of their service territory, placing fuel cell power generators on their customer's property could be a financially viable option. Other power generation sources such as gas turbines can provide local power, but efficiencies of gas turbines decline in smaller sizes, and fuel cells offer substantial advantage in terms of reduced air emissions and reduced noise.

Several companies are now reportedly developing stationary PEM fuel cell systems with fuel processors to convert natural gas, propane or methanol to hydrogen. These companies have stated that they can be competitive in the residential marketplace, offering the vision of homeowners generating their own electricity from natural gas, propane or methanol, independent of the electrical power grid. Some attributes of these residential fuel cell systems reported primarily in press releases are summarized in Table 7. It is not clear whether the quoted prices are goals or whether the companies involved have actually identified and thoroughly analyzed mass production costs for actual fuel cell system designs.

DTI has previously shown that stationary fuel cell systems are only head-to-head competitive in sizes above 50 kWe, as shown in Figure 9 based on average California electric utility and natural gas commercial rates, assuming that 10,000 systems are produced. The lower line in Figure 9 illustrates that selling only electricity from these systems would not be economic, generating a negative return on investment. Adding heat co-generation provides a positive return on investment for systems larger than 50-kWe, but the total system would only provide 10% real, after-tax return on investment if hydrogen were also produced during off-peak hours for use in fuel cell vehicles or other industrial hydrogen applications.

Table 7. Proposed Residential PEM Fuel Cell Systems

| Company | Parent Companies or Business Partners | Fuel | Projected FC System Costs |
|---|--|------------------------|---|
| Northwest Power Systems (Bend, Oregon) | DeNora PEM Fuel Cells (Italy), Methanex (Canada), Statoil (Norway) | Methanol | \$7,500 to \$10,000 ⁷ |
| Plug Power LLC (Lantham, N.Y.) / GE Fuel Cell Systems | Mechanical Technology, Inc (MTI), DTE Energy Company, GE Power Systems | Natural Gas | \$7,500 to \$10,000 (\$3,500 in mass production) (Wolk -1999) |
| American Power Corporation (Boston) | Analytic Power | Natural Gas or Propane | <\$5,000 (Wolk - 1999) |
| Avista Labs | Black & Veatch | | |
| H-Power Corp. (Bellville, N.J.) | | | |
| NuPower | | | |

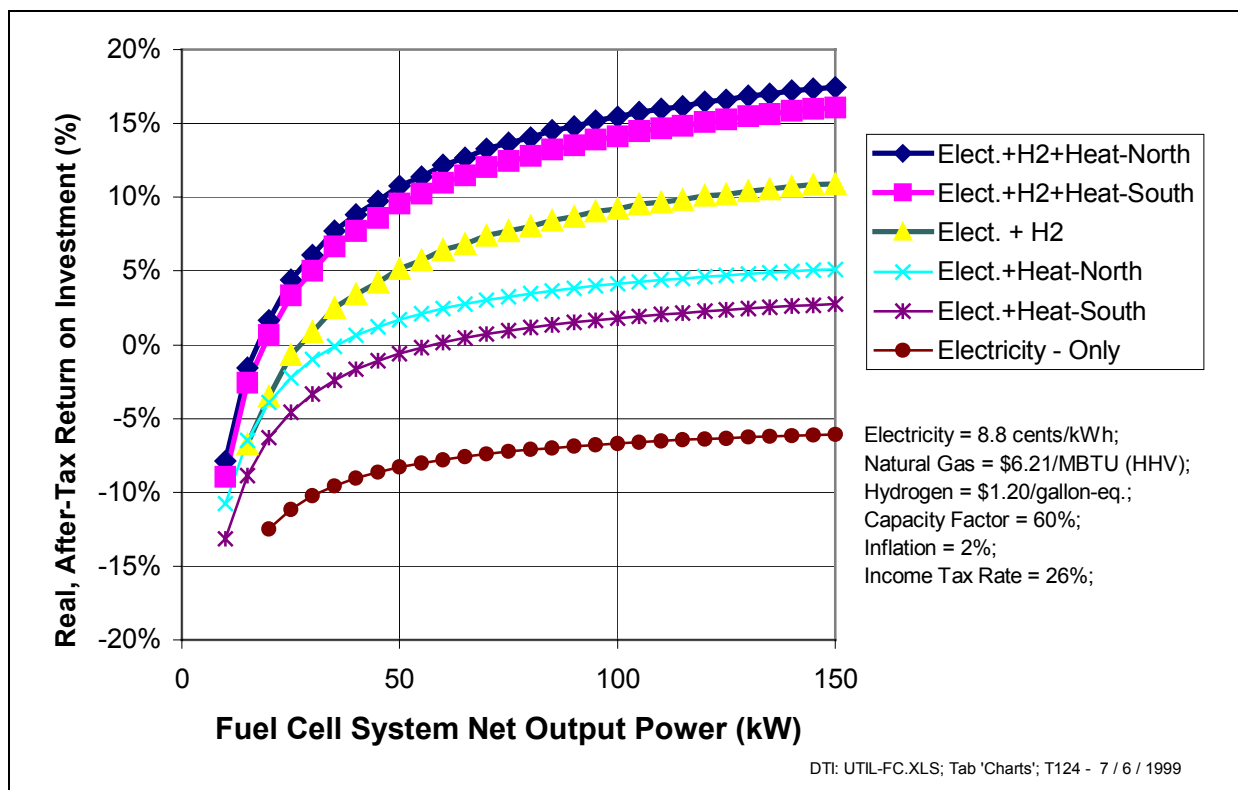


Figure 9. Return on Investment for a Commercial Fuel Cell System in California

⁷Cost based on Northwest Power Systems press release of February 17, 1998, stating that a 5-kW residential system would cost between \$1,500 to \$2,000/kW.

However, the typical residence in the United States uses only one kilowatt average power, with peak power levels near 3.4 kWe, including some surges to the 8 kW range, which would place the residential fuel cell system in the negative return region of Figure 9 even with hydrogen and heat co-generation. This poor result stems primarily from our analysis of fuel cell system costs in small sizes. Based on our evaluation, many of the fuel cell and fuel processor costs are fixed, independent of power output. As the systems become smaller, the cost per kilowatt increases as shown in Figure 10. A total system (including fuel processor and inverter/controller) that might cost under \$1,500/kWe for a 20 kWe fuel cell system would cost over \$5,000/kWe for a 2-kWe system. This pessimistic cost projection for residential systems might be due to our approach of scaling down from existing conceptual system designs. Other innovative fuel cell system designs for these very small systems might be more economic.

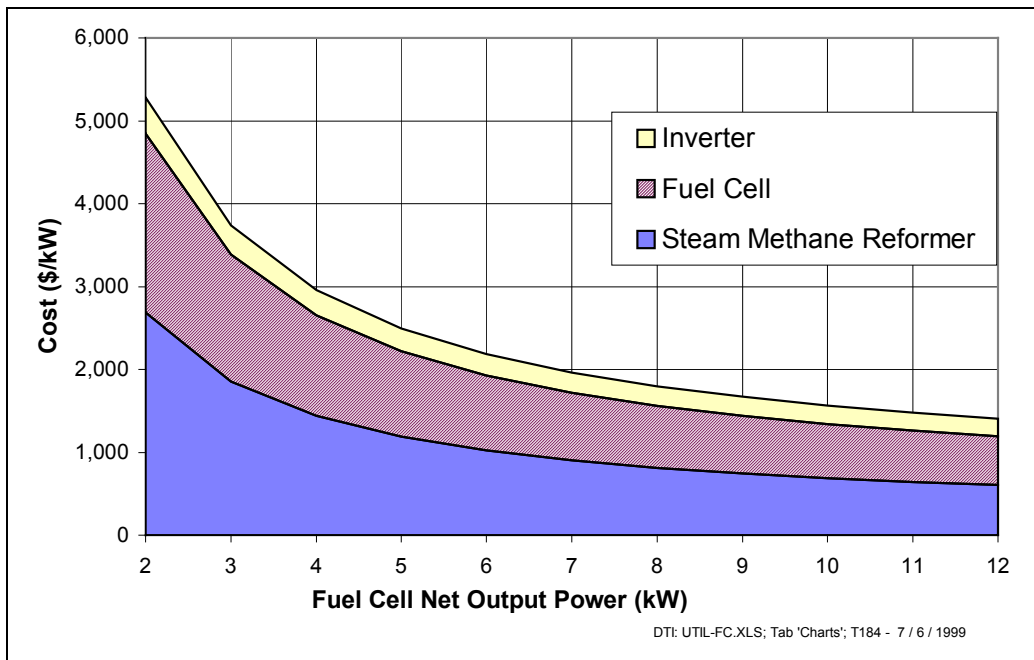


Figure 10. Estimated Capital Costs for a Residential Fuel Cell System (10,000 Production Level)

These previous estimates from DTI all assumed that the fuel cell provided the peak power requirements of the home or business. However, the capacity factor for residences is quite low, typically falling in the 25% range. The average power requirement is only one quarter of the peak power draw. Initially, when fuel cell systems cost is high, it might be beneficial to install lower power fuel cell systems in conjunction with a battery storage system to provide the rare peak power needed by the home. We have therefore added the battery storage option to our stationary fuel cell system model.

2.1 Fuel Cell System Description

The block diagram for the stationary fuel cell system is shown in Figure 11. The three main components (steam methane reformer, fuel cell system and inverter/controller) have been described in previous DTI reports (Thomas-1999). For this analysis, we have added deep discharge lead acid batteries to store electricity during the off-peak hours, along with the necessary charging, monitoring and control circuits. We assume here that the fuel cell and fuel processor both operate at a steady rate determined by the average annual power draw for the residence.⁸ For example, the average peak power for single family homes in the US is about 3.4 kWe, with a capacity factor of 27%, or an average power load of 0.92 kWe. We assume that the fuel cell system delivers a continuous load of 0.92 kWe of AC power to the home. When the demand is less than 0.92 kWe, then the excess is used to charge the battery bank. When the demand exceeds 0.92 kWe, then the battery supplies the peak power required. The exact load profile will vary from home to home, but we assume a very simple load profile here for costing purposes: we arbitrarily assume that the peak power of 3.4 kWe is required for two hours every day, and the load is reduced below the average of 0.92 during the other 22 hours to bring the average to 0.92 kWe. This choice requires a battery storage capacity of 6.7 kWh, which is close to the 6 kWh value projected by EPRI for a residential fuel cell system with peak power battery augmentation (EPRI-1995). The capital cost, operation and maintenance (O&M) costs, efficiencies and expected lifetimes of the various components are summarized in Table 8.

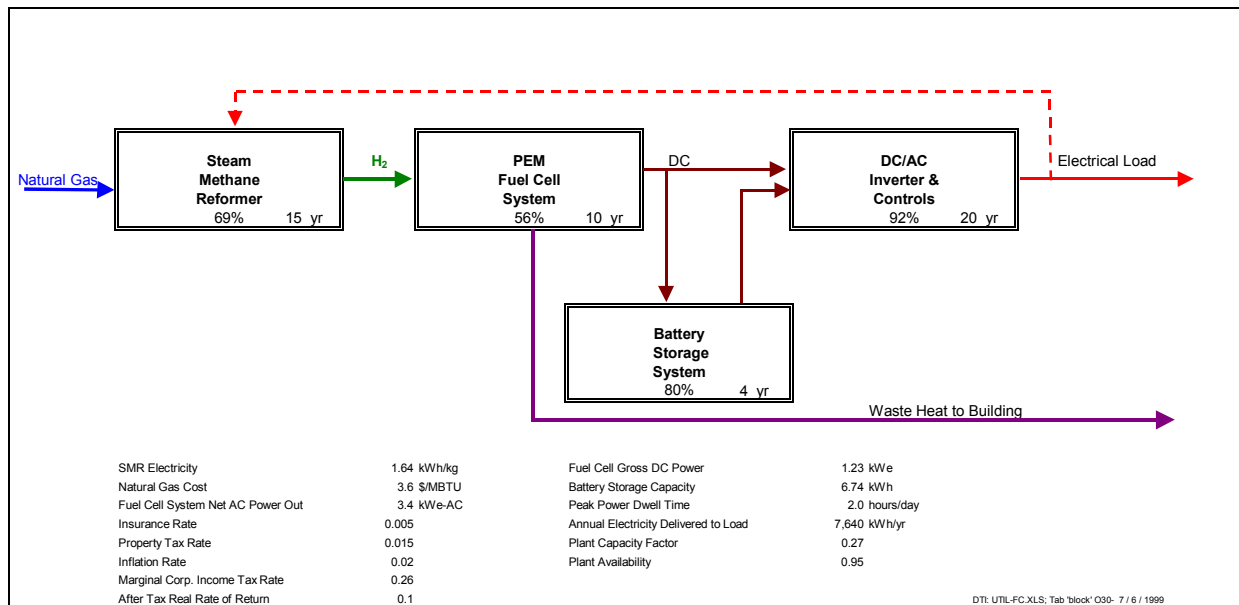


Figure 11. Block Diagram for a Stationary Fuel Cell System with Battery Storage

⁸In practice, the fuel cell system power output would be set to the average power load over the day, which would increase during the summer air conditioning season, and decrease in spring and fall. We assume constant annual output here for convenience.

Table 8. Assumed Component Parameters in DTI Cost Model

| | Steam Methane Reformer | Fuel Cell System | DC/AC Inverter & Controls | Battery System | Totals |
|-----------------------------------|------------------------|------------------|---------------------------|----------------|----------|
| Capital Cost -100 Qty | \$15,261 | \$5,570 | \$2,249 | \$759 | \$23,839 |
| Capital Cost - 10,000 Qty | \$5,184 | \$4,019 | \$1,117 | \$664 | \$10,984 |
| O&M Cost (% of Capital /year) | .035 | .03 | .01 | .02 | |
| Lifetime (years) | 15 | 10 | 20 | 4 | |
| Efficiency (LHV) | .686 | .56 | .92 | .8 | |
| After-Tax Capital Recovery Factor | 0.177 | 0.206 | 0.166 | 0.359 | |

2.2 Cost Projections for Residential Fuel Cell Systems

The estimated capital costs for a fuel cell system to supply a peak power of 3.4 kW_e AC to a private home is shown in Figure 12 for 100 production quantities and for 10,000 production quantities. Two cases are shown for each production level: the pure fuel cell system where the fuel cell has a 3.4 kW_e peak output power capacity, and a battery-augmented system where the fuel cell has a nominal 1.2 kW_e DC gross output power, and the battery supplies the peak power capability. The battery has an energy capacity of 6.7 kWh. The fuel cell supplies energy for both the house load (3.4 kW_e AC peak and 0.92 kW_e AC average load) and it supplies the AC electricity to run the steam methane reformer, which we estimate requires about 1.65 kWh of electricity per kg of hydrogen produced.

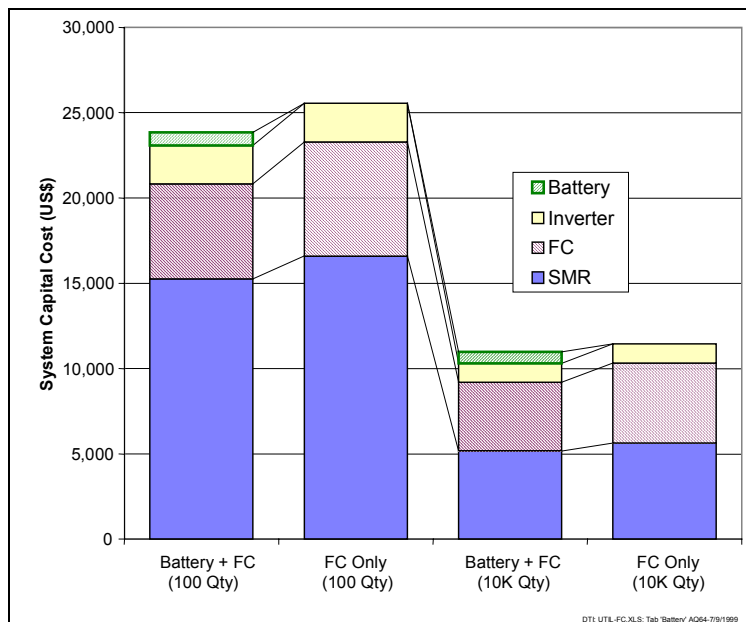


Figure 12. Capital Cost Estimates for a 3.4 kW_e Fuel Cell System with Battery Peak Power Augmentation

As shown in Figure 12, adding the battery at an assumed cost of \$100/kWh does reduce the total capital costs by about 7% for the 100-quantity production level, and by 4.2% for the 10,000 unit production level. These small reductions in capital cost have very little effect on the price of electricity necessary to provide the desired 10% real, after-tax return on capital, as shown in Figure 13. For the 100 quantity production level, the required price drops slightly with the battery system, from 86 to 83 ¢/kWh. At the 10,000 production level, the required price actually increases slightly, from 43.3 to 44 ¢/kWh. This increase is due to two factors: first the battery system has a very short lifetime (4 years assumed here), so the capital recovery rate is much larger for the battery than for the fuel cell system with an assumed life of 10 years. Second, the quantity of natural gas required increases slightly with the battery system, since the battery is in somewhat inefficient (80% round-trip efficiency assumed).

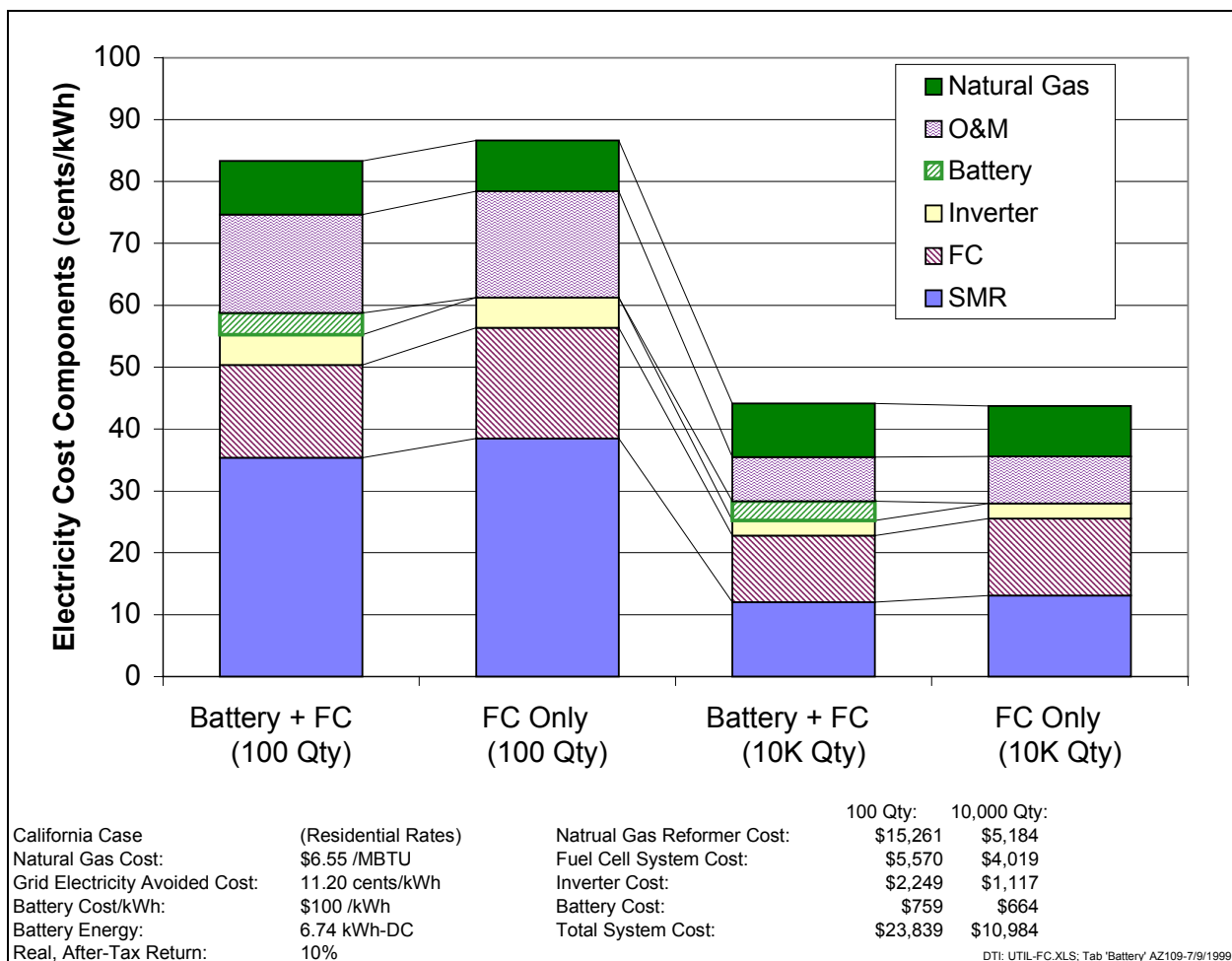


Figure 13. Electricity Price Required to Yield 10% Real, After-Tax Return on Investment for a Residential Fuel Cell System in California

In any case, the required electricity price in the range of 44 ¢/kWh is four times the average residential utility rate of 11.2 ¢/kWh in California. Adding the battery has negligible effect, and the system remains grossly uneconomic with the assumptions in the DTI cost model.

The situation changes very little in regions with more favorable electricity to natural gas prices such as Alaska. As shown in Figure 14, the lower natural gas costs (\$3.65/MBTU vs. \$6.55/MBTU in California) reduces the required electricity price by only 4 ¢/kWh. The required price of 40 ¢/kWh is still almost four times the average residential rate of 10.9 ¢/kWh in Alaska.

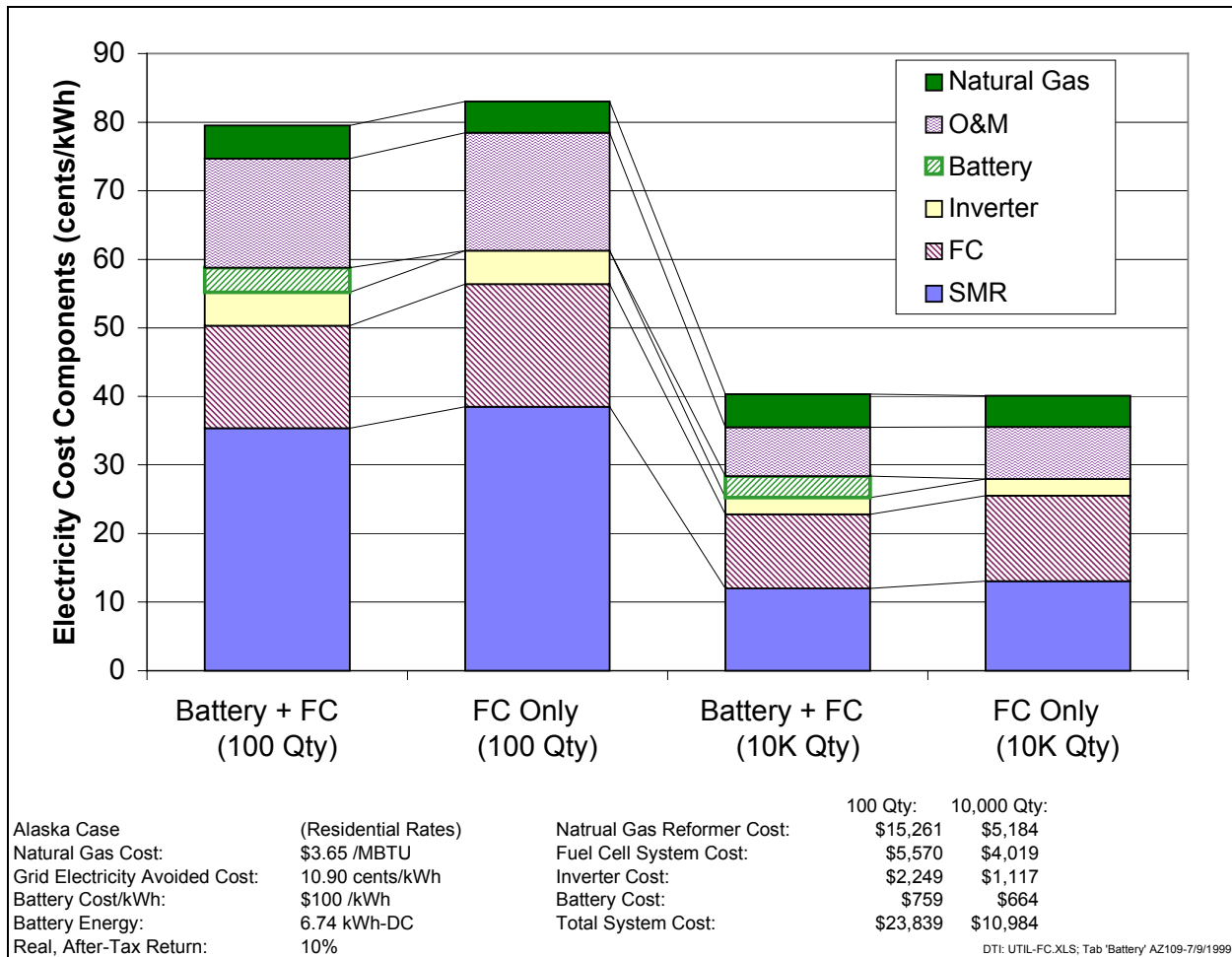


Figure 14. Electricity Price Required to Yield 10% Real, After-Tax Return on Investment for a Residential Fuel Cell System in Alaska

Finally, heat cogeneration has minor effect of the allowable electricity price. We estimate that the natural gas savings in California from using the low grade (80°C) heat from the PEM fuel cell would save at most \$90/year. This reduction in natural gas costs would translate into an electricity price lower by only 1.2 ¢/kWh.

2.3 Conclusions on Battery Augmentation

We conclude that adding batteries to a residential fuel cell system to reduce the peak power required from the fuel cell has negligible effect on the electricity price required to bring acceptable return on investment. For a typical single family residence with a one kilowatt average power draw and a 3.4 kWe peak power requirement, the fuel cell system owner would have to charge approximately 40 ¢/kWh to bring a 10% real, after-tax rate of return, which is almost four times the average residential utility rate in the United States. Hence we cannot rationalize a reasonable return on investment for a residential fuel cell system, with or without batteries, given our estimate of \$10,000 capital costs at the 10,000 unit production level.

Acknowledgments

We thank the Hydrogen Program Office of the U.S. Department of Energy for supporting these analyses, and for the technical guidance and direction provided by Dr. Sig Gronich. We also thank the Ford Motor Company for providing supporting related fuel cell vehicle analyses.

References

- EPRI (1995), *Market Opportunity Notice for Market-Derived Residential Fuel Cell Systems*, prepared by Polydyne, Inc. of San Mateo, California for the Electric Power Research Institute of Palo Alto, California, January 1995.
- James, Brian D. (1996), George N. Baum, Franklin D. Lomax, Jr., C.E. (Sandy) Thomas, and Ira F. Kuhn, Jr., *Comparison of Onboard Hydrogen Storage for Fuel Cell Vehicles*, Prepared for the Ford Motor Company by Directed Technologies, Inc., Arlington, Virginia, May 1996.
- James, Brian D. (1997a), Franklin D. Lomax, Jr., C. E. (Sandy) Thomas, and Whitney G. Colella (DTI), *PEM Fuel Cell Power System Cost Estimates: Sulfur-Free Gasoline Partial Oxidation and Compressed Direct Hydrogen*, October 1997.
- James, Brian D. (1997b), C. E. Thomas, George D. Baum, Franklin D. Lomax, Jr., and Ira F. Kuhn, Jr., "Making the Case for Direct Hydrogen Storage in Fuel Cell Vehicles, *Proceedings of the 8th Annual U.S. Hydrogen Meeting*, Alexandria, Virginia, March 11-13, 1997, p. 447
- James, Brian D. (1999), C. E. (Sandy) Thomas, and Franklin D. Lomax, Jr., "Onboard Compressed Hydrogen Storage, *Proceedings of the 9th Canadian Hydrogen Conference*, Vancouver, BC, p. 253-263 February 1999.

- Lomax, Franklin D. (1997), and Brian D. James (Directed Technologies, Inc.) and Robert P. Mooradian (Ford Motor Company), "PEM Fuel Cell Cost Minimization Using 'Design for Manufacture and Assembly' Techniques," *Proceedings of the 8th Annual U.S. Hydrogen Meeting*, Alexandria, Virginia, 11-13, 1997, p. 459.
- Thomas, C. E. (1998a), Brian D. James, Franklin D. Lomax, Jr., and Ira F. Kuhn, Jr., *Integrated Analysis of Hydrogen Passenger Vehicle Transportation Pathways*, prepared for the National Renewable Energy Laboratory under contract No. AXE-6-16685-01, March 1998.
- Thomas, C. E. (1998b), Brian D. James, Franklin D. Lomax, Jr., and Ira F. Kuhn, Jr., "Integrated Analysis of Hydrogen Passenger Vehicle Transportation Pathways," *Proceedings of the 1998 U.S. DOE Hydrogen Program Review*, Vol. 1, Alexandria, Virginia, April 28-30, 1998, pgs. 233-280.
- Thomas, C. E. (1998c), Brian D. James, Franklin D. Lomax, Jr., and Ira F. Kuhn, Jr., "Societal Impacts of Fuel Options for Fuel Cell Vehicles," *International Fall Fuels and Lubricants Meeting and Exposition*, San Francisco, California, 19-22 October, 1998, SAE Paper # 982496.
- Thomas, C. E. (1999), Jason P. Barbour, Brian D. James, and Franklin D. Lomax, Jr., "Analysis of Utility Hydrogen Systems & Hydrogen Airport Ground Support Equipment," *Proceedings of the 1999 U.S. Department of Energy Annual Hydrogen Program Review*, prepared for the National Renewable Energy Laboratory under contract No. ACG-8-18012-01, May 1999.
- Wolk, Ronald H. (1999), "Fuel Cells for Homes and Hospitals," *IEEE Spectrum*, May 1999, pg. 45.

ASSESSMENT OF HYDROGEN-FUELED PROTON EXCHANGE MEMBRANE FUEL CELLS FOR DISTRIBUTED GENERATION AND COGENERATION

Thomas G. Kreutz
Joan M. Ogden
Center for Energy and Environmental Studies
Princeton University
Princeton, NJ 08544

Abstract

Proton exchange membrane fuel cells (PEMFCs) are highly efficient power generators, achieving up to 50-60% conversion efficiency, even at sizes of a few kilowatts. PEMFCs have zero pollutant emissions when fueled directly with hydrogen, and near zero emissions when coupled to reformers. These attributes make them potentially attractive for a variety of applications including electric vehicles and distributed generation and cogeneration of heat and power in buildings. Over the past few years, there have been intense efforts worldwide to develop low-cost PEMFC systems. While the primary focus has been on vehicle applications, an equally important application may be combined heat and power generation in commercial and residential buildings.

In this progress report (covering the period July 1999-May 2000), we summarize results from ongoing technical and economic assessments of hydrogen-fueled proton exchange membrane fuel cell systems for distributed generation and cogeneration in residential markets. The objective of this research is to understand the prospects for hydrogen fueled PEMFC cogeneration technology for residential applications, and to identify the conditions under which hydrogen fueled PEM fuel cells might compete with other distributed generation options. Engineering and economic models of PEM fuel cell systems are developed for a variety of configurations. Using realistic load profiles for single and multi-family residential buildings, we size the system components and estimate the cost of producing electricity and cogenerated heat for a range of PEMFC costs, energy prices, and system sizes. The potential impact of distributed benefits will be addressed in future work under this contract. This work was carried out as part of the systems analysis activity of the US Department of Energy Hydrogen R&D Program under Contract No. DE-FG01-99EE35100.

Introduction

Motivation and Background

Proton exchange membrane fuel cells (PEMFCs) are highly efficient power generators, achieving up to 50-60% conversion efficiency, even at very small sizes (down to the household level – 1 to 5 kW). PEMFCs have zero pollutant emissions when fueled directly with hydrogen, and near zero emissions when coupled to reformers. These attributes make them potentially attractive for a variety of applications including electric vehicles and distributed generation and cogeneration of heat and power in buildings.

Over the past few years, there have been intense efforts worldwide to develop low-cost PEMFC systems. While the primary emphasis has been on vehicle applications, an equally important application may be combined heat and power generation in commercial and residential buildings.

Since the 1970s, there have been ongoing efforts to commercialize fuel cell cogeneration systems for use in buildings. Initially, these efforts focussed on phosphoric acid fuel cell (PAFC) technology. Phosphoric acid fuel cell (PAFC) systems run on reformed natural gas have been developed in the 200 kW size range for commercial building applications. These have shown good operational characteristics and reliability. However, the current capital cost of PAFC systems (\$3000/kW) is still too high for large penetration into building markets. Even at larger scale production PAFC system costs are projected to be \$1500/kW, and would face tough competition from natural gas fired engines or microturbines in the 50-500 kW size range.

Recently there has been considerable R&D aimed at commercializing PEMFC systems for cogeneration in buildings. PEM fuel cell cogeneration systems in the 200 kW size range are under development (a size appropriate for commercial or multifamily residential buildings), as well as smaller units (in the 5-10 kW size range), for use in individual houses.

There are several reasons why PEMFCs might become competitive for buildings applications before they appear in vehicles:

- 1) The cost barrier is lower for PEMFC cogeneration systems than for automotive applications. To compete with internal combustion engines in automobiles, PEMFCs must achieve stringent cost goals of perhaps \$50/kW. Recent studies indicate that significant cogeneration markets in commercial buildings could open for PEMFC stack costs of perhaps \$300-500/kW (corresponding to complete system costs of \$1000-1500/kW) [1]. Residential markets might open at stack costs of ~\$200/kW [2].

- 2) The technical challenges are in many respects less severe for stationary power generation than for vehicles. (Start-up behavior and transient operation is likely to be less of a problem for power generation than for vehicles which are characterized by rapidly varying loads; heat and water management issues should be much easier; weight and volume constraints are less stringent; peak power devices will not be needed; control systems should be simpler; robustness and resistance to mechanical shocks during driving will not be an issue.) In one respect, technical requirements are more demanding for cogeneration applications: a longer operating lifetime (50,000-100,000 hours) would be needed for a stationary power system as compared to perhaps 5000 hours for vehicles.

3) Infrastructure considerations might be easier for hydrogen fueled stationary power systems than for hydrogen vehicles. Hydrogen could be made as needed for PEMFC systems in buildings from widely available natural gas at the individual building or neighborhood level.

Scope of this Study

In this study we are carrying out a series of detailed technical and economic assessments aimed at understanding the prospects for hydrogen fueled PEM fuel cell cogeneration technology for residential applications. We concentrate on hydrogen derived from natural gas, a primary energy source which is widely available today, and is likely to give the lowest hydrogen cost in the near term.

We compare three types of PEM fuel cell cogeneration systems which could provide power and heat to residential users (see Figure 1).

- Case 1) a centralized "neighborhood" scale (200-1000 kW) natural gas reformer/PEM fuel cell system which distributes heat (via district heating) and electricity (via wire) to 40-200 residential users.
- Case 2) a centralized "neighborhood" scale natural gas reformer, which produces hydrogen or a hydrogen rich gas for distribution to users. Each house has a small hydrogen fueled (1 to 5 kWe) PEM fuel cell providing electricity and heat.
- Case 3) individual natural gas reformers coupled to small (1 to 5 kW) PEM fuel cells at each house.

For each case energy storage (in the form of hydrogen storage, hot water storage or electric batteries) could be used to meet time varying energy demands. Connections to the electric utility system could be made at the household or neighborhood level, allowing dispatch of power.

Building on earlier work by our group for the USDOE Office of Transportation Technologies CARAT program [5], we have developed engineering and economic models of hydrogen PEM fuel cell based cogeneration systems. The potential advantages and disadvantages of each configuration are investigated in terms of overall energy efficiency, performance, economics (capital cost, delivered cost of electricity and heat), and greenhouse gas emissions. PEMFC cogeneration systems are compared to other alternatives for production of residential heat and power.

Several tasks are underway:

- Task 1. Develop engineering models of various types of PEM fuel cell cogeneration systems capable of supplying residential heat and power at a household and neighborhood level. Model heat-integrated PEMFC cogeneration system using ASPEN-Plus software to simulate steady state performance.
- Task 2. Develop component sizing algorithms for various types of PEMFC cogeneration systems, based on the demand profile, energy prices, component performance and scale (single house vs. multi-family).
- Task 3. Investigate design trade-offs for various options: Reformer type (steam reformer vs. autothermal reformer); operating strategy (load following vs. non-load following);

cogeneration (hot water and/or space heating?); scale (single vs. multi-family); various types of loads; energy prices (natural gas, electricity); and utility connection strategies.

- Task 4. Discuss the costs and trade-offs involved in distributing different forms of energy to houses (case 1: electricity and heat, case 2: hydrogen or hydrogen-rich gas, case 3: natural gas).
- Task 5. Estimate the cost of electricity and heat from PEM fuel cells, as compared to alternatives.
- Task 6. Analyze and discuss the role of distributed benefits and emissions benefits in the economic competitiveness of fuel cells. Estimate the required component cost and performance goals for small scale PEMFC cogeneration systems to compete economically with alternatives, when distributed and emissions benefits are included. (This task is being performed in coordination with researchers at Distributed Utilities Associates.)

Tasks 1, 2, 3 and 5 are essentially completed and results will be given in this report, Tasks 4 and 6 will be completed in future work, and will be discussed in the final report for this contract.

Modeling the PEMFC Cogeneration System (Tasks 1, 2, 3 and 5)

System Design Options

The primary components of a residential PEMFC cogeneration system (as shown in Figure 2) are: 1) a fuel processor that converts natural gas into a hydrogen-rich fuel gas for the fuel cell, 2) a proton exchange membrane fuel cell (PEMFC) stack (and integrated air blower) that generates DC electricity from the hydrogen, 3) power conditioning electronics that convert the DC electricity into grid-quality AC power, 4) an optional battery subsystem to increase the peak power of the system, and 5) optional cogeneration for hot water production and/or space heating.

As shown in Figure 1, a variety of paths are possible for using natural gas derived hydrogen PEMFCs to supply power and heat to single-family or multi-family residences. In our results to date (which cover “case 3” above), we have assumed a connection to the electrical transmission grid so that the fuel cell power system is not required to provide *all* of the electrical load; rather, it generates a portion of the residential power demand while the grid provides “back-up” power when demand exceeds the fuel cell capacity. Cogeneration of hot water and space heating are considered as system options. The options of space and water heating from natural gas are included. Cases 1 and 2 will be explored in future work on this contract.

We assume that the system is owned by the consumer as a home (or neighborhood) “energy appliance” that generates electricity (and, optionally, heat). The consumer’s economic motivation for installing a fuel cell cogeneration system is to reduce overall energy costs relative to standard utility service. [In future work (Task 6), we plan to address the economics of distributed generation systems that are owned and potentially dispatched by the electric utility in order to capture various economic benefits associated with distributed power generation.]

A variety of options are examined that determine the system performance and economics. These include:

- Various reformer types (steam reforming vs. autothermal reformer).
- Various building sizes and types of energy load (single-family vs. multi-family dwelling vs. multiple single-family dwellings).
- Optional cogeneration of hot water or space heat.
- Various strategies for operating the fuel cell system. The power output can be: 1) varied during the day to meet the building electrical load (such a system is called a “load follower”), or 2) operated continuously at full load with the excess electricity sold back to the utility at reduced rates (“non-load follower”).
- Various utility interconnection scenarios (standard single meter, PURPA-type dual meters, monthly net metering, stand alone/grid-isolated system.)
- Various gas and electricity prices.
- Various assumptions about capital and O&M costs for the system.

We estimate the cost of electricity and the internal rate of return to the consumer for a variety of cases. We perform sensitivity analyses to identify the most important variables governing system performance and economics. The estimated cost of residential electric power from PEM fuel cells is compared to other electricity supply options, including grid power and microturbines.

System Component Models

PEMFC Stack

To model fuel cell (FC) stack performance, we use the measured performance (Fig. 3) of the IFC PC-29, a 50 kW atmospheric pressure, hydrogen-air, automotive PEMFC stack (with an integrated variable-speed blower) built by International Fuel Cells and delivered to the US Department of Energy in the fall of 1997 [3]. Our fuel cell model consists of an analytic formula used to fit the PC-29 performance data, with scaling variables included that allow us to model cogeneration systems of arbitrary size. We assume that the net fuel cell system efficiency curve as a function of power (see Fig. 3) is invariant with system scale. This allows us to model fuel cells over a range of sizes from about 1 to 100 kW.

Hydrogen utilization of 80% is assumed for PEMFCs run on reformat.

Fuel Processor

Hydrogen is produced from natural gas in a fuel processor at the neighborhood or household level. The fuel processor is a series of catalytic chemical reactors that convert natural gas into PEMFC-quality hydrogen gas. As shown in Fig. 2, the first stages of the fuel processor is a fuel reformer - either a steam methane reformer (SMR) or an autothermal reformer (ATR) - that converts natural gas into a synthesis gas that is rich in H₂ and CO. The syngas is then processed in high- and low-temperature water-gas shift reactors that convert the bulk of the CO to H₂ (down to ~0.5%vol). Finally, a preferential oxidation (PROX) unit is used remove CO (to less than ~100 ppmv) from the reformat in order to avoid poisoning the catalyst in the fuel cell anode. The fuel processor includes ancillary equipment such as a steam generator and numerous heat exchangers for heat integration.

Steady state heat and mass balances for integrated fuel processor/fuel cell systems were modeled using commercial (Aspen Plus) software [4]. The fuel processor energy efficiencies calculated in our model for steam methane reformers and autothermal reformers are shown in Table 1. Fuel processor models were adapted from those developed as part of earlier work for the DOE OTT CARAT program [5].

Table 1. Three definitions for the LHV energy efficiency of fuel processors; we use the third in this study

| Definition of η_{FP} | η_{FP} (SMR) | η_{FP} (ATR) |
|--|-------------------|-------------------|
| $\frac{LHV \text{ of } H_2 \text{ out}}{LHV \text{ of } NG \text{ in}}$ | 93.8% | 83.9% |
| $\frac{LHV \text{ of } H_2 \text{ out}}{LHV \text{ of } (NG + AE) \text{ in}}$ | 67.4% | 71.8% |
| $\frac{LHV \text{ of } H_2 \text{ consumed}}{LHV \text{ of } NG \text{ in}}$ | 75.0% | 67.1% |

The fuel processor efficiency is assumed to be independent of power and system size over a given turndown ratio (*TDR*), where *TDR* is defined as the ratio of the maximum to the minimum power. It is further assumed that the fuel cell cogeneration system runs continuously, *never* operating below its minimum power level. When the electricity demand falls below the minimum power level, the excess power is either stored, sold back to the grid, or lost. (One might envision a very low-power “stand-by mode” for use at night, in which the fuel processor (and stack) consumes just enough power to keep the catalysts warm. In the end, we chose not to include a standby mode in the model because we found that, in an optimally sized system with a reasonable turndown ratio (*TDR*=5), there is very little excess power to sell. As a result, the overall cost of electricity is quite insensitive to whether the excess power is sold or lost.)

Power Conditioning Electronics

Power conditioning (PC) electronics make up the third component of the system. If the stack contains enough individual fuel cells to generate a sufficiently high voltage (~350-600 V), a DC→DC voltage up-conversion is not necessary prior to DC→AC conversion with an inverter [6]. Because we investigate systems as small as a few kW, it is assumed that DC→DC up-conversion is required for *all* systems, regardless of scale. Both the DC→DC and DC→AC conversions are assumed to take place at a constant energy efficiency of 96% [6], for a total power conditioning efficiency, η_{PC} , of 92%.

Hot Water Cogeneration (Optional)

A hot water cogeneration system is included as an option (Fig. 4). [As discussed below, there is a good match (in both temperature and quantity) between the domestic hot water demand and the waste heat from the PEMFC stack, but, cogeneration for space heating does not appear to be economically viable and is not explored in this study.] To minimize both capital and installation/retrofit costs, the cogeneration system employs only liquid/liquid heat

exchangers (i.e. heat is not recovered from the stack but not from the cathode exhaust), and utilizes a pre-existing natural gas-fired hot water tank. The tank is assumed to have a 50 gal capacity, a HHV energy efficiency of 76%, and a HHV energy factor (i.e. including standby losses) of 70.1%. Aspen modeling of the heat recovery scheme in Fig. 4 indicates that ~68% of the waste heat from the stack can be captured as 60 C water for domestic hot water.

The cogeneration system is operated with a time varying load (determined by the building electricity demand profile), while continuously monitoring the extent to which water in the tank is fully heated. The available waste heat at any point in the fuel cell operating range was estimated with a simple linear fit to the PC-29 data shown in Fig. 3. Operationally, the tank is held between a minimum “set point” of 90% and a maximum of 100% by: 1) discarding any surplus hot water, and 2) firing the tank burner with natural gas when the tank falls below the set point. The 90% set point insures that adequate hot water is always available to the consumer, while leaving 10% of the full tank capacity for buffering the PEMFC stack from the domestic hot water demand.

Total Fuel Cell System Efficiency

The total fuel cell system efficiency [natural gas (LHV) to electricity] is the product of the stack net electrical efficiency (which varies with system output as shown in Figure 3) times the fuel processor efficiency (which is found from our ASPEN simulations to be 75.0% for a steam methane reformer) times the power conditioning efficiency, which is assumed to be 92%. Multiplying these factors together, we find a total system efficiency which varies with power output as shown in Figure 5. The maximum system electrical efficiency is about 36% which occurs at 20% part load.

Costs for Distributing Energy from Neighborhood Fuel Cell Systems

In cases 1 and 2 (Figure 1), electricity, heat or hydrogen-rich syngas are distributed to houses. Costs for distribution are being developed, and will be used in future work under this contract (Task 4).

Residential Electric Load Profiles

In order to model system performance, we obtained time-resolved electric load profiles for single- and multi-family residences from a series of studies on residential and commercial energy use by Lawrence Berkeley National Laboratory (LBNL) and the Gas Research Institute (GRI) conducted between 1988 and 1990 [7,8,9]. In those studies, the existing stock of U.S. residences was surveyed and broken down in to a small number of categories (from 8 to 16 different types in each of 16 separate U.S. climatic regions) that represent the dominant building practices between 1940 and 1990. Using DOE-2 software, prototypical model buildings were created for each category in each geographic region.

Space heating, cooling, and electric loads were generated on an hourly basis by subjecting each prototype to WYEC (Weather Year for Energy Calculations) weather tapes, which encapsulate average weather data (temperature, humidity, wind speed, solar insolation, etc.) throughout a “typical” year. In this study we focus primarily on the New York/New Jersey region because its energy prices are highly favorable for cogeneration systems (i.e. relatively high electricity prices and relatively low natural gas prices). Results presented here are calculated for the so-called “B1A” prototype, a thermally-improved, 2-story, wood frame house with a basement, built between 1950 and 1970. The NYBIA prototype represents the largest category of homes in the New York region and, as will be shown later, is a good

representative for all New York dwellings from the standpoint of the economics of PEMFC cogeneration.

Hourly energy demand, broken out as HVAC and non-HVAC electric, space heating, and hot water, are shown for a winter and a summer day in Figs. 6a and 6b. The difference in electric loads during summer and winter shown in the two figures is indicative of the characteristic “peakiness” of residential electric loads throughout the year. The peak hourly electric load for the whole year is 4.4 kW, while the average is only 1.0 kW. Depending on the connection scenario between the PEMFC system and the electric grid, the system economics can be quite sensitive to this peak-to-average load ratio, since the peak power governs the system size (i.e. maximum power output) - and therefore cost - while the average power controls the rate at which the system can generate revenue by producing power at a lower cost than it can be purchased from the public utility.

Figures 6a and 6b also illuminate the prospects for space heating and hot water cogeneration. In both figures the hot water demand is seen to be smaller than the electricity demand and also fairly well correlated (temporally) with it. Waste heat from the stack appears to be well matched with the hot water demand, both in terms of magnitude and temperature. These figures suggest that hot water cogeneration is a likely prospect, probably not requiring an unusually large storage tank to act as a buffer between supply and demand. In contrast, the space heating and electric loads are anti-correlated, with the space heating demand largest in winter when the average electric load is smallest, and vice versa.

The dim prospects for space heating cogeneration can be seen more clearly in Fig. 7 where the monthly average energy loads for the New York B1A prototype are plotted throughout the year. The peak demands for space heating and space cooling are out of phase by many months making thermal storage impractical. Furthermore, the space heating demand dwarfs the waste heat available from a PEMFC system, especially if the bulk of the heat (from the stack) is already used for hot water production. Finally, space heating cogeneration may require more expensive gas-liquid (or gas-gas) heat exchangers and more complex installation than hot water cogeneration. For these reasons, cogeneration for space heating does not seem (at first glance) to be economically viable, and was not examined further. [Because PEM fuel cells operate at relatively low temperatures (70-80 C), we also did not consider absorption air conditioning.]

In the LBNL-GRI studies, domestic hot water (DHW) demands for single-family residences were calculated on an hourly basis throughout the year. For cogeneration calculations, we modified their computer code to generate an hourly “composite” DHW load that includes both the energy for heating the water as well as “standby losses”, i.e. heat loss from the storage tank. The calculations are based upon the national average hot water consumption of 62.4 gal/day/person, 3 persons/household, a tank temperature 140 F (60 C), and in the base case (New York region), a well temperature of 52 F (11.1 C) and an average air temperature of 54.2 F (12.3 C).

System Economic Assumptions

In order to estimate the long-term potential economics of PEMFC cogeneration, we use cost estimates for PEM fuel cell cogeneration systems manufactured in high volume (e.g. hundreds of thousands of units per year—similar to the scale projected for manufacturing automotive fuel cell systems). As such, contingencies and design and engineering costs are deliberately excluded. The capital cost for each system component is assumed to be a linear function of its size (kW), with a cost-axis intercept that represents the minimum cost for manufacturing the system at *any* size.

Because cost and performance estimates for automotive components are more readily available than for stationary systems, we have chosen to construct the PEMFC cogeneration system studied here out of “automotive-grade” components whenever possible. Our “high volume” case uses automotive type component cost estimates, and assumes manufacturing levels of several hundred thousand units per year. We have compared these costs to those of a recent study by Directed Technologies, Inc. of costs for stationary PEMFC systems manufactured at lower volume (10,000 units per year) [10,11].

Perhaps the most significant difference between stationary and mobile fuel cell systems is their required lifetimes. While automotive equipment is generally designed to last for only ~5000 hours, the service life of residential furnaces and hot water heaters is typically 10 years or more, roughly 18 times as long. To model a stationary power system “built” of automotive components, we assume that various components are replaced or refurbished, as required during the 10 year life of the fuel cell system.

Assumed “high volume” mass produced capital costs for PEMFC cogeneration systems made from automotive type components are given in Table 2.

- The fuel cell is assumed to be an automotive stack whose membrane electrode assemblies (MEAs) and bipolar plates are replaced at 5-year intervals. Long time (>9000 hr) performance tests on a hydrogen-fuelled PEMFC stack at Mitsubishi Electric Corporation show a degradation rate of 4 mV per 1000 hr (at 250 mA/cm²), or 5.8% per year [12]. This implies a ~30% drop over 5 years, which would probably warrant MEA replacement at the end of that period. In this study, we assume that reformat-fueled fuel cells can be made to operate as well as hydrogen-fuelled systems (from the standpoint of degradation), and adopt a performance loss rate of 5.8%/yr, with complete MEA replacement every 5 years. For this system, whose lifetime is assumed to be 10 years, only one stack refurbishment is necessary, at the end of the 5th year.
- Detailed cost estimates for cost-optimized, high volume manufacturing of automotive fuel processors (gasoline-fueled ATR) [13] and PEMFC stacks [14] have been made by Directed Technologies Inc. (DTI) using a methodology known as Design For Manufacture and Assembly (DFMA) that has been formally adopted by the Ford Motor Company. The fuel processor costs used here (\$42/kWe at a scale of 50 kWe) are somewhat higher than those obtained in cost studies performed by Arthur D. Little on their 50 kWe catalytic partial oxidation/autothermal reformer (16-29 \$/kWe) [15,16]. In this study, we assume equal costs for the SMR and ATR systems.
- Price estimates for power electronics are from Trace Technologies and correspond to somewhat lower volumes (e.g. 10,000 units/yr at a size of 10 kW) [6].
- The added cost for hot water cogeneration (from stack cooling water) is assumed to be negligible; a pre-existing 50 gallon natural gas-fired hot water tank is presumed.
- Estimates for advanced lead-acid batteries are taken from a study of electric vehicle battery storage systems that was commissioned by the California Air Resources Board [17].

O&M costs include annual maintenance and replacement of MEAs and bipolar plates after year 5. The equipment is assumed to have no salvage value at the end of its lifetime. System availability is assumed to be 99.7%, based on a single day of down time per year for scheduled and unscheduled service. A real discount rate of 8% and a system lifetime of 10 years are assumed.

We use as our base case scenario New Jersey residential gas and electric prices, 6.07 \$/MMBtu HHV (2.07 ¢/kWh) and 12.65 ¢/kWh, respectively; the disparity between the two provides an exceptionally favorable economic climate for PEMFC cogeneration.

Table 2. Component costs and economic assumptions^a

| | |
|---|----------------------------|
| System Component Costs (high volume case): | |
| - Fuel processor (\$) | $320 + 36 P_{FC}^{max}$ |
| - FC stack, blower, & cooling (\$) | $1073 + 22 P_{FC}^{max}$ |
| - PC electronics (\$) | $840 + 97 P_{sys}^{max}$ |
| - HW cogeneration (\$, optional) | 0 |
| - Battery sub-system (\$/kWh, opt.) | 120 |
| System Capital Cost (\$) (no battery) | $2233 + 155 P_{sys}^{max}$ |
| O&M Costs (exclusive of fuel): | |
| - Annual service (\$/yr) | 100 |
| - Stack (1 refurb at end of 5th yr, \$) | $200 + 22 P_{FC}^{max}$ |
| PV of O&M costs above (\$) | $761 + 15 P_{FC}^{max}$ |
| Delivery and Installation (\$): | $500 + 4 P_{sys}^{max}$ |
| Total Installed Cost (no battery), $C_{PV}(P_{sys}^{max})$ (\$) | $3494 + 174 P_{sys}^{max}$ |
| Economic Assumptions (base case scenario): | |
| - Natural gas price, R_f (\$/MMBtu, HHV) | 6.07 |
| - Purchased electricity price, (¢/kWh) | 12.7 |
| - Price for electricity sold to grid, (¢/kWh) | 3.0 |
| - Availability, A (%) | 99.7 |
| - Discount rate, d (%/yr) | 8.0 |
| - System lifetime, Y (yr) | 10 |
| - Capital recovery factor, CRF (%/yr) | 14.9 |

In Table 2, the high volume, installed cost for the whole system (including the present value of all future maintenance, $C_{PV}(P_{sys}^{max})$), is \$3494+\$170/kW (for a system without batteries). DTI has recently formulated detailed system cost estimates for stationary PEMFC cogeneration systems manufactured in smaller volumes, from 100-10,000 units/yr. In order to investigate the relative importance of high volume manufacturing on overall system economics, we have included for comparison DTI's capital cost estimate for 10,000 units/yr: \$9656 + \$586/kW [10]. The significant increase in cost is due to smaller production runs as well as a system that is designed to have a significantly longer lifetime, for example, fuel cell MEAs that have more area, thicker membranes, and a higher catalyst loading. Note in both cases that, for relatively small systems (e.g. under 10-15 kW), the total installed cost is dominated by the constant term, i.e. only weakly dependent on system size.

In Fig. 8 we plot as a function of system size the total installed system cost (in both \$ and \$/kW), which includes overnight capital, delivery and installation, and the present value of system maintenance (including periodic replacements of the fuel cell MEAs). Reflecting our simple component cost models, the total cost rises linearly as a function of system size. The

cost *per kW* varies dramatically with power. Most importantly for single-family power systems, it rises sharply below 10-20 kW.

As a point of comparison with our cost model (indicated in Fig. 8 as a small box), the retail price of the 7 kW residential PEMFC cogeneration unit manufactured by Plug Power, LLC. is expected to be in the range of \$3000-5000 (430-714 \$/kW) [18]. (Not all of the 7 kW power is provided by the fuel cell; a portion of the power is provided by a less expensive battery sub-system [19].)

Economic Calculations: The SERC Method

Here we describe a novel method we have developed during earlier work for the DOE OTT CARAT program [5] -- called the ‘‘SERC’’ method -- for estimating the cost of electricity from a fuel cell cogeneration system. This method allows us to efficiently simulate many alternative configurations for cogeneration systems, to find the optimum (lowest cost) system.

Calculating the system performance and economics is traditionally carried out by simple time-domain (i.e. hour-by-hour) accounting, an effective technique, but one whose results are often unenlightening; in-depth analysis typically requires brute force finite difference sensitivity studies. For that reason, we have developed a novel alternative formalism called the ‘‘system economic response curve’’ (SERC) method which organizes the raw load data into a readily characterized load histogram (the ‘‘load energy distribution’’) that is entirely separate from the economic parameters of the PEMFC cogeneration system. The final electricity costs result from the interaction between these two components, which is both intuitively obvious and analytically simple. As a result, the method is extremely efficient with regard to computation, thereby facilitating multi-parameter system optimization. We begin the exposition of this method by looking first at the load.

Load Energy Distribution

A typical ‘‘load profile’’ consists of a time series of N consecutive values, $P_i(n)$ ($n=1,N$), that represent the load power averaged over the corresponding temporal widths, $\Delta t(n)$. The LBNL load profiles used in this study are hourly averaged values for one year (e.g. they have a constant time resolution of $\Delta t = 1$ hr, and span a single year, i.e. $N=8760$ hours/yr). As seen in Fig. 9, such a massive set of raw data is rather difficult to interpret, and is thus often transformed into a format that is more readily understood. For example, ordering the loads according to their size produces a so-called ‘‘load duration curve’’ (Fig. 10) which readily reveals the percentage of time is spent above (or below) any given power level.

In the SERC methodology, we transform the data into a ‘‘load energy distribution function’’, $L(P)$, which quantifies how much energy is demanded at any given power. This function is simply a power-weighted histogram obtained by ‘‘binning’’ the load data into discrete intervals of load power, ΔP , as follows:

$$L(P) \equiv \frac{P}{\Delta P} \sum_{n=1}^N \delta[P_i(n) - P; \Delta P] \Delta t(n) \quad , \quad (7)$$

where the pseudo-delta binning function is defined by

$$\delta[P_l(n) - P; \Delta P] \equiv \left\{ \begin{array}{l} 1 \text{ for } \left(P - \frac{\Delta P}{2}\right) \leq P_l(n) < \left(P + \frac{\Delta P}{2}\right) \\ 0 \text{ for } P_l(n) < \left(P - \frac{\Delta P}{2}\right), P_l(n) \geq \left(P + \frac{\Delta P}{2}\right) \end{array} \right\}. \quad (8)$$

The $1/\Delta P$ factor in Eq. (7) yields a “probability density” distribution function whose amplitude is independent of the “binning width”, ΔP . The function is further weighted by P to reflect our interest in the energy required at any given power rather than the time spent there. As such, $L(P)$ has units of kWh/kW, and integrating over all load power yields the total load energy, E_{load} (kWh):

$$E_{load} \equiv \int L(P) dP. \quad (9)$$

The load energy distribution function in Fig 11 is seen to be roughly bi-modal. The wide “spike” centered at ~ 1 kW (the yearly average power) is due primarily to non-HVAC “plug” loads. The broad hump from 1.5-4 kW is largely due to air conditioning (AC) electric loads that occur each day in the summer months. Note in the *yearly* load distributions shown below in Fig. 12, the AC hump is somewhat diminished relative to the plug load peak at 1 kW.

The System Economic Response Curve

The System Economic Response Curve (or “SERC”) is defined as the cost of electricity from a PEMFC system with capacity P_{max} (kW) when it is operated a constant output P , where $P > P_{max}/TDR$. As P is varied, the cost of electricity goes through a minimum value at about $P = P_{max}$. (At low values of P ($P < P_{max}$), the fuel cell capacity is not fully utilized, so that the capital cost contribution is large. At high values of P , ($P > P_{max}$), expensive electricity must be purchased from the grid, so that the SERC increases.

The SERC can be expressed mathematically in the fuel cell’s operating range ($P_{max}/TDR < P < P_{max}$) as:

$$SERC(P) = CRF C_{PV}(P_{max}) / (P \cdot 8760 \text{ h/y}) + R_f / \eta_{sys}(P) \times 0.00341 \text{ MBTU/kWh}$$

where:

SERC(P) = levelized cost of electricity (\$/kWh) from a PEMFC system with power capacity P_{max} , operated at constant power output P .

P = constant electrical power output of system kW

CRF = capital recovery factor = $1/[1-(1+d)^{-Y}]$

d = real discount rate

Y = system lifetime in years

$C_{PV}(P_{max})$ = present value of installed cost of system plus replacement of components (see Table 2)

A = availability of system

R_f = price of natural gas in \$/MBTU

$\eta_{sys}(P) = \eta_{FC}(P) \eta_{FP} \eta_{PC}$, where $\eta_{FC}(P)$ is taken from Figure 3.

When $P > P_{max}$, a term is added to reflect the cost of buying electricity from the grid. When $P < P_{max} / TDR$, electricity is sold back to the grid yielding a credit.

For different sized fuel cell systems, the SERC changes as shown in Figure 13. It is important to note that the SERC is independent of the building load.

Estimating the Cost of Electricity

The cost of electricity R for a PEMFC system meeting a particular load is found by multiplying the energy load profile $L(P)$ times the SERC and integrating over P .

$$R \equiv \frac{1}{E_{load}} \int SERC(P) L(P) dP.$$

This is formally equivalent to, but computationally much simpler than conducting the analysis by integrating over time, and gives an intuitive way to size the system for lowest cost for a particular load profile. The idea is to overlap the lowest cost part of the SERC with the peak/bulk of the load distribution to minimize the integral (and therefore the electricity cost).

We have used the SERC method to conduct sensitivity studies to find PEMFC system size that yields the minimum electricity cost to meet a particular load (or alternatively, gives the best internal rate of return for investing in a PEMFC system).

Sensitivity Studies

Sensitivity of Electricity Cost to System Size

We have used the SERC method to find optimized PEMFC systems designed to meet loads ranging in size from one household to 20 households. In Figure 14, the cost of electricity and the internal rate of return are plotted versus the number of single family homes served.

System scale is seen to have a tremendous impact upon the system economics. The strong dependence of electricity cost on system size is mostly due to the strong scale economies in the capital cost of PEMFC cogeneration systems (see Figure 7).

For example (Figure 14), without cogeneration, the electricity cost for a 2.6 kW system powering a single New Jersey residence is as high as 13.2 ¢/kWh, while a 22 kW system for 20 homes is less than 9.0 ¢/kWh. Over this same change of scale (from 1 to 20), the internal

rate of return rises from 3.6%/yr to 121%/yr! Despite the favorable economic climate - New Jersey has energy rates that are extremely conducive to residential power generation (natural gas: 6.1 \$/MMBtu HHV, electricity: 12.7 ¢/kWh) - the single-family system appears to be just barely viable from an economic standpoint. On the other hand, a 22 kW (half-automotive-scale) PEMFC system that powers multiple homes (or, more likely, a multi-family dwelling) shows great economic promise, with a simple payback times significantly less than a year.

The Effect of Cogeneration

The economics of hot water cogeneration was studied using a time domain analysis that monitors the flow of hot water in and out of the hot water tank. Surplus heat is discarded while deficit heat is generated by firing the tank's natural gas burner. The economic effect of hot water cogeneration is shown in Fig. 14 where optimized (i.e. minimum *IRR*) values of **R** and *IRR* - with and without cogeneration - are plotted as a function of system scale factor. Cogeneration is seen to add roughly 50% to the rate of return, and lowers the cost of electricity by ~1.5 ¢/kWh. It is clearly an attractive option where technically/economically feasible, for example, in a single family house or multi-family apartment building.

The Effect of Energy Prices

Energy prices have a strong impact on the economic viability of natural gas fired PEMFC systems. In our base case, we used New Jersey energy prices (which are favorable for natural gas fired cogeneration because of the high electricity cost and low natural gas cost). Plots of electricity cost and *IRR* are shown in Fig. 15 for average U.S. energy prices (natural gas: 6.6 \$/MMBtu HHV, electricity: 9.3 ¢/kWh) and for New Jersey prices. While the optimized electricity prices are roughly the same over the full range of scales, the rates of return are dramatically different between the two cases. The great disparity in *IRR* is due to the much higher cost of electricity in N.J. which allows the N.J. system to generate 'revenue' (by displacing purchased power) more rapidly and thus offset the cost of installed capital. At U.S. average gas and electricity prices, the system is not economically viable at *any* scale.

Given the high variability of energy prices throughout the U.S., we plot in Figs 16 and 17 the internal rate of return as a function of scale, electricity, and natural gas prices. These figures suggest that the PEMFC cogeneration system in a multiple single-family configuration (without cogeneration) will be viable in regions where: 1) at average U.S. gas prices (6.6 \$/MMBtu HHV), the electricity price exceeds 9-10 ¢/kWh, and 2) at average U.S. electricity prices (9.3 ¢/kWh), the gas price is below ~7 \$/MMBtu HHV.

The Effect of System Capital Cost

Capital costs plays a critical role in the economics of these systems. In Fig. 18 the optimized (i.e. minimum *IRR*) values of both **R** and *IRR* (without hot water cogeneration) are plotted as a function of system scale factor for both the high and low volume capital cost models. While the high volume model shows economic promise at almost all scales, the low volume system is economically unfeasible or marginal at all but the largest scale.

The Effect of Operational Strategy: Load Follower vs. Non-Load Follower

The SERCs plotted in Fig. 19 suggests that optimal economics are obtained with a system that is as large as possible yet have an operating range (i.e. P_{sys}^{max} / TDR to P_{sys}^{max}) that overlaps the bulk of the load distribution. This minimizes the amount of power that must be either bought from the utility (at a relatively high price) or produced and sold back to the grid at a loss. For example, in the optimized base case system (a load follower with a turndown ratio of 5), the great bulk of the load falls within the operating range from 2.44/5 kW to 2.44 kW. As the turndown ratio falls and the operating range shrinks (with the limit being a non-load follower, $TDR=1$), the optimized system size is found to “track” ever more closely the peak of the load distribution. This is because the cost of electricity is, in general, minimized when as much of the load as possible is generated by the PEMFC system. This is seen clearly in Fig. 19 where optimized SERC for both a load follower ($TDR=5$) and a non-load follower are plotted against the load distribution. Note that the non-load follower is optimally sized at 1.05 kW, almost the peak of the load distribution, and costs ~ 1.5 ¢/kWh more than the load follower to operate

PEMFCs versus Microturbines

Since the preceding results illustrate the economic attractiveness of large (e.g. multi-family) PEMFC cogeneration systems relative to single family units, it is appropriate to make a comparison with another emerging advanced technology for distributed electric power generation from natural gas: the microturbine. For this brief examination, we employ the published performance of the Capstone model 350 microturbine, which produces 27.4 kW of grid-quality AC power from natural gas delivered at 5 psig at a LHV energy conversion efficiency of 24.3% [20,21]. Part load performance is calculated using the work of Campanari [22]; a turndown ratio of 10 is assumed. The power-dependent LHV efficiency of the microturbine, $\eta_{mic}(P_{sys})$, can be expressed as a third order polynomial:

$$\eta_{mic}(P_{sys}) = 0.0608 + [0.548 + (-0.592 + 0.226 P_{sc}) P_{sc}] P_{sc} \quad (21)$$

where $P_{sc} \equiv P_{sys} / P_{sys}^{max}$ is the scaled part load power. Installed capital costs are derived from extremely uncertain cost projections from Capstone and Allied Signal: $\$7500+300$ \\$/kW [23].

Microturbine system economics are compared to PEMFCs in Fig. 20. It can be seen that, even with aggressive and highly uncertain cost projections for the microturbine, the economics are less promising than that of the PEMFC system.

Summary of Results

Results to Date

We have determined that the most favorable configuration for PEMFC cogeneration systems in residential buildings has the following characteristics :

- a load follower with a large (>5) turndown ratio,
- the fuel processor used a steam methane reformer,

- hot water cogeneration from PEMFC stack waste heat was economically attractive,

Scale is found to be crucially important for good economics. Our results indicate that, even with high volume (automotive-scale) cost assumptions and extremely favorable gas-to-electricity price ratios, PEMFC systems are likely to be only marginally attractive on the scale of a single-family residence. In contrast, multi-family units (above ~ 10 kW) appear to be economically extremely attractive, even when using less than optimal (e.g. national average) gas-to-electricity price ratios. Hence, in our initial economic modeling, there appears to be a potentially significant market for multi-family scale PEMFC cogeneration systems.

In typical residences, the domestic hot water demand is well correlated with the electric load, and also well matched - both in terms of magnitude and temperature - to the supply of waste heat from the fuel cell stack. Our preliminary analysis has shown that hot water cogeneration is an inexpensive option that lowers the cost of electricity by roughly 1.5 ¢/kWh. Cogeneration for space heating, on the other hand, does not appear to be economically viable.

Energy prices have a strong effect on the economic attractiveness of residential PEMFC cogeneration systems. At average US electricity and gas prices, the rates of return are economically unattractive. However, our calculations suggest that a PEMFC cogeneration system in a multiple single-family configuration (without cogeneration) will be viable in regions where: 1) at average U.S. gas prices (6.6 \$/MMBtu HHV), the electricity price exceeds 9-10 ¢/kWh, and 2) at average U.S. electricity prices (9.3 ¢/kWh), the gas price is below ~7 \$/MMBtu HHV.

Capital costs plays a critical role in the economics of residential PEMFC cogeneration systems. PEMFC systems must reach low mass produced costs to compete. Our high volume cost model shows economic promise at almost all system scales, the low volume system is economically unfeasible or marginal at all but the largest scale.

Comparing PEMFC systems to microturbines, we found a 32% increase in system efficiency (and therefore greenhouse gas benefit), lower criteria pollutant emissions, and potentially better economics. When compared with central station power systems, the overall efficiency was less favorable. Obtaining hot water and electric power from a PEMFC cogeneration system results in a 26% loss in energy efficiency compared with traditional hot water generation and electricity generation using modern natural gas-fired GTCC. It does offer the potential for reduced emissions of criteria pollutants, but precludes carbon sequestration.

The overall economic viability shows strong dependence on system size. A small (< 5 kW) single-family system unlikely. Multiple single-family system is potentially attractive (especially with hot water cogeneration). A system for multiple-family residence could be quite attractive in markets with high electric/gas price ratios (such as NY, NJ, CA).

We have developed an analytical methodology for calculating PEMFC system economics that greatly clarifies the key issue of system sizing as well as dramatically increasing computationally efficiency, thereby facilitating multi-parameter system optimization.

Work Plan To Complete This Study

Task 4. Discuss the costs and trade-offs involved in distributing different forms of energy to houses (case 1 electricity and heat.; case 2: hydrogen or hydrogen-rich gas, 3: natural gas

Task 6: Understanding the Role of Distributed Benefits

Our analysis thusfar has used a “consumer-driven” model where the decision to purchase a PEMFC power system is based on the expectation of long term savings, not unlike the decision to invest in a more efficient but more expensive appliance (such as a furnace, water heater, refrigerator, etc.). An important alternative model is a “utility-driven” strategy in which the public utility owns, locates, and operates these distributed power systems in order to offset the local load, thereby either avoiding (or delaying) having to upgrade the transmission system or, in sparsely populated areas, avoiding constructing a transmission grid altogether. In future work (Task 6) we will address how the newly deregulated energy market might accommodate (and be perturbed by) the introduction of PEMFC-based residential power systems. In some markets, such systems could forestall the electric utility from having to build additional generation and distribution capacity, thus perhaps qualifying for “credits” for distributed power generation.

Publications and Presentations

Past Results

Since 1986, researchers at Princeton University's Center for Energy and Environmental Studies have carried out technical and economic assessments of hydrogen energy systems. We have published numerous papers on: assessments of renewable hydrogen energy systems, use of hydrogen from natural gas as a transition strategy, studies of hydrogen infrastructure (including case studies of hydrogen refueling infrastructure in California and New York), studies of hydrogen as a fuel for fuel cell vehicles, and studies of the implications of CO₂ sequestration for hydrogen energy. Our approach is to assess the entire hydrogen energy system from production through end-use from several perspectives (fuel producer, consumer, society) considering technical performance, economics (e.g. capital cost, delivered hydrogen cost, cost of energy services), infrastructure, environmental and resource issues. The long term goal of our work is to illuminate possible pathways leading from present hydrogen markets and technologies toward wide scale use of hydrogen as an energy carrier, highlighting important technologies for RD&D. This work has been part of the systems analysis activity of the DOE Hydrogen Program since 1991.

Current Year Publications and Presentations

Over the past year (January 1999-May 2000), several papers based on our DOE sponsored work on hydrogen infrastructure and fuel cell system modeling have been published in peer reviewed journals. In addition, we have written several general review articles on hydrogen. These include:

J. Ogden, "Developing a Refueling Infrastructure for Hydrogen Vehicles: A Southern California Case Study," *International Journal of Hydrogen Energy*, vol. 24, pp. 709-730, 1999.

J. Ogden, M. Steinbugler and T. Kreutz, "A Comparison of Hydrogen, Methanol and Gasoline as Fuels for Fuel Cell Vehicles," *Journal of Power Sources*, vol. 79, pp. 143-168, 1999.

J. Ogden, 1999, "Prospects for Building a Hydrogen Energy Infrastructure," *Annual Review of Energy and the Environment*, Vol. 24, pp. 227-279.

J. Ogden, T. Kreutz and M. Steinbugler, "Fuels for Fuel Cell Vehicles," *Fuel Cells Bulletin*, Elsevier Advanced Technology, January 2000. p. 5-13.

We presented talks on our work on Hydrogen Energy Systems and CO₂ Sequestration at the 10th National Hydrogen Association Meeting (April 1999), and on our work on PEMFC systems for residential cogeneration at the 11th National Hydrogen Association meeting (March 2000).

J. Ogden, "Strategies for Developing Low-Emission Hydrogen Energy Systems: Implications of CO₂ Sequestration," *Proceedings of the 10th National Hydrogen Association Meeting*, Arlington, VA, April 7-9, 1999.

T. Kreutz and J. Ogden, "Assessment of PEM Fuel Cells for Residential Cogeneration Applications," *Proceedings of the 11th National Hydrogen Association Meeting*, Arlington, VA, February 29-March 2, 2000, pp. 303-324.

We have also given invited talks on hydrogen infrastructure to the LERDWG group (a group of energy R&D leaders at the National Laboratories) in November 1999, to the Energy Frontiers International meeting in January 2000 (to a group of oil and gas industry leaders in alternative fuels development) and at the IQPC Fuel Cells Infrastructure Meeting in December 1999 (to a group of energy and chemical industry engineers). In addition, we participated in the DOE/California Energy Commission, California Air Resources Board Workshop on Hydrogen Infrastructure (October 1999). I have been an invited speaker at the June 1999 Department of Transportation Meeting on the Spirit of Innovation in Transportation and the April 2000 American Physical Society Meeting, speaking on future roles for hydrogen and fuel cells in transportation.

Plans for Future Work (beyond this contract)

During the next year we propose to carry out technical and economic assessments of advanced fossil to hydrogen systems with co-production of electricity and CO₂ sequestration. The objective of the proposed work is to understand the implications of new process technologies for reducing the cost of fossil-derived hydrogen with CO₂ sequestration and co-production of electricity.

Acknowledgments

For useful conversations, the authors would like to thank Jeff Chen (Plug Power, LLC.), James Cross (Epyx), Pete Fonda-Bonardi, (Meruit, Inc.), Mark Haug (Trace Technologies), Joe Huang (Lawrence Berkeley National Laboratory), Joseph Iannucci (Distributed Utilities, Assoc.), Brian James (Directed Technologies, Inc.), Ryan Katofsky (Arthur D. Little), Lyle

Rawlings (FIRST, Inc.), Chris Larsen (North Carolina Solar Center), Colleen Mathis (Ballard Generation Systems), Al Meyer (International Fuel Cells), Jessica Reinkingh (Johnson Matthey), Richard Root Woods (Hydrogen Burner Technology), Nick Vanderborgh (Los Alamos National Laboratory), Sandy Thomas (Directed Technologies, Inc.) Brian Wells (Ballard Power Systems), and Robert Williams (Princeton University).

Figures

Figure 1. Possible configurations for PEM fuel cell cogeneration in buildings

Figure 2. System Configuration for Residential PEMFC Cogeneration System

Figure 3. Assumed efficiency curve for 50 kW PEMFC stack based on IFC PC-29

Figure 4. Schematic of Hot Water Cogeneration System

Figure 5. Total fuel cell system efficiency [$=\text{Electricity out}/\text{Natural Gas in (LHV)}$] for a 2.44 kW fuel cell system vs. electrical output power in kW. Also shown is the yearly load distribution for a single family house.

Figure 6a. Hourly-averaged loads for NY single-family residence during a typical summer day (July 1)

Figure 6b. Hourly-averaged loads for NY single-family residence during a typical winter day (January 1)

Figure 7. Monthly-averaged loads for the NYB1A single-family residence throughout a typical year.

Figure 8. Total installed system cost, $C_{PV}(P_{sys}^{max})$, as a function of size in kW

Figure 9. Hourly load data for the month of June.

Figure 10. Load duration curve for data in Figure 9.

Figure 11. Load Energy Distribution for a Single Family House for One Month

Figure 12. The System Economic Response Curve (SERC) for a 2.44 kW PEMFC system, shown with the yearly energy load distribution from a single family house.

Figure 13. System economic response curves (SERCs) for systems of various size, compared to the load.

Figure 14. Cost of Electricity and Internal rate of Return for PEMFC cogeneration systems, as function of system size. Cases with and without hot water cogeneration are shown.

Figure 15. Cost of electricity and internal rate of return as a function of scale for N.J. and U.S. energy prices.

Figure 16. Internal rate of return as a function of scale and electricity price (at U.S. average nat. gas price).

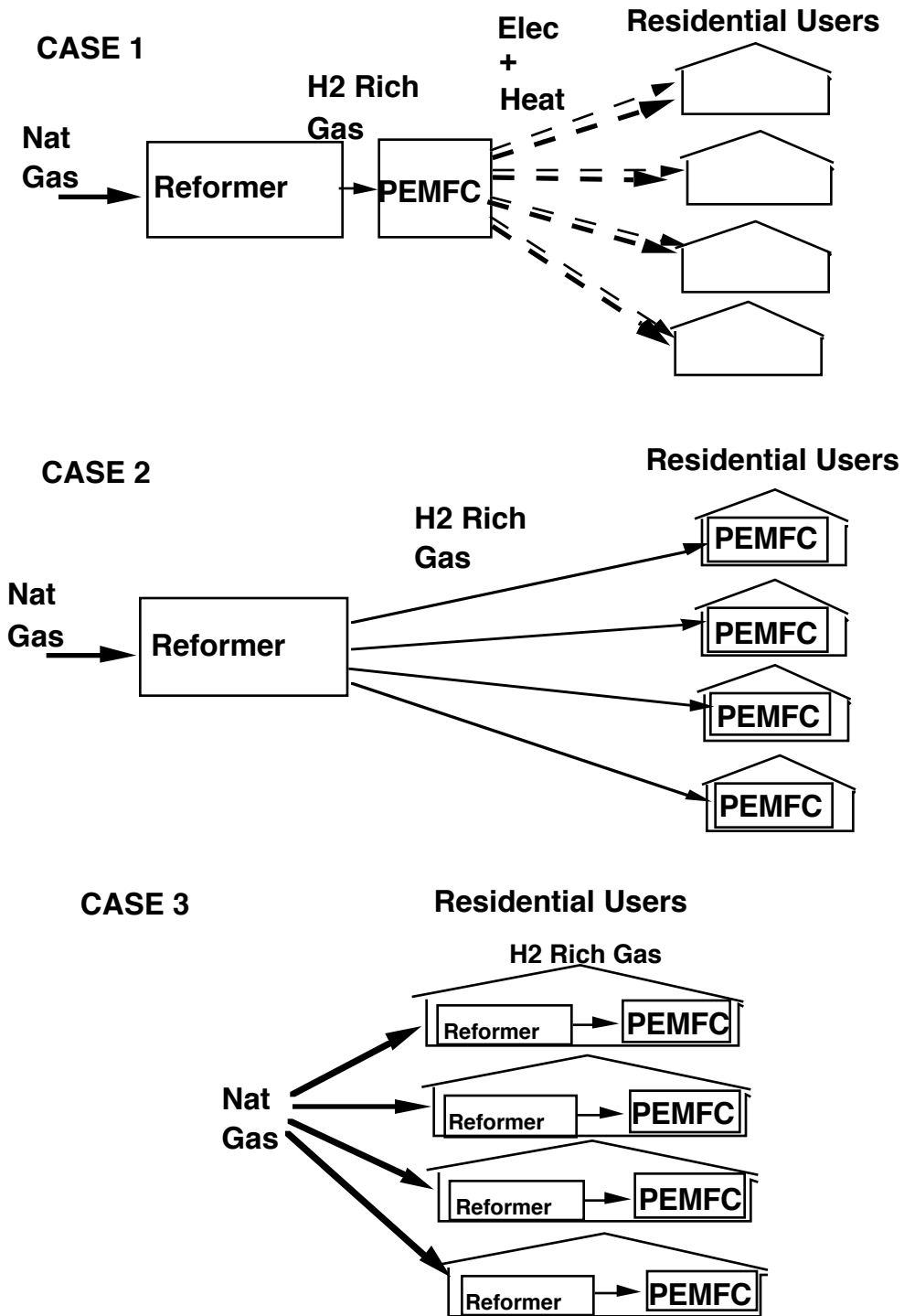
Figure 17. Internal rate of return as a function of scale and natural gas price (at U.S. average electricity price).

Figure 18. Electricity cost and rate of return as a function of scale, for high- and low-volume capital cost models.

Figure 19. SERCs for load followers ($TDR=5$) and non-load following systems, compared to the load.

Figure 20. Electricity cost and rate of return as a function of scale, for a PEMFC system vs. a microturbine.

FIGURE 1. CONFIGURATIONS FOR PEMFC COGENERATION FOR RESIDENTIAL USERS



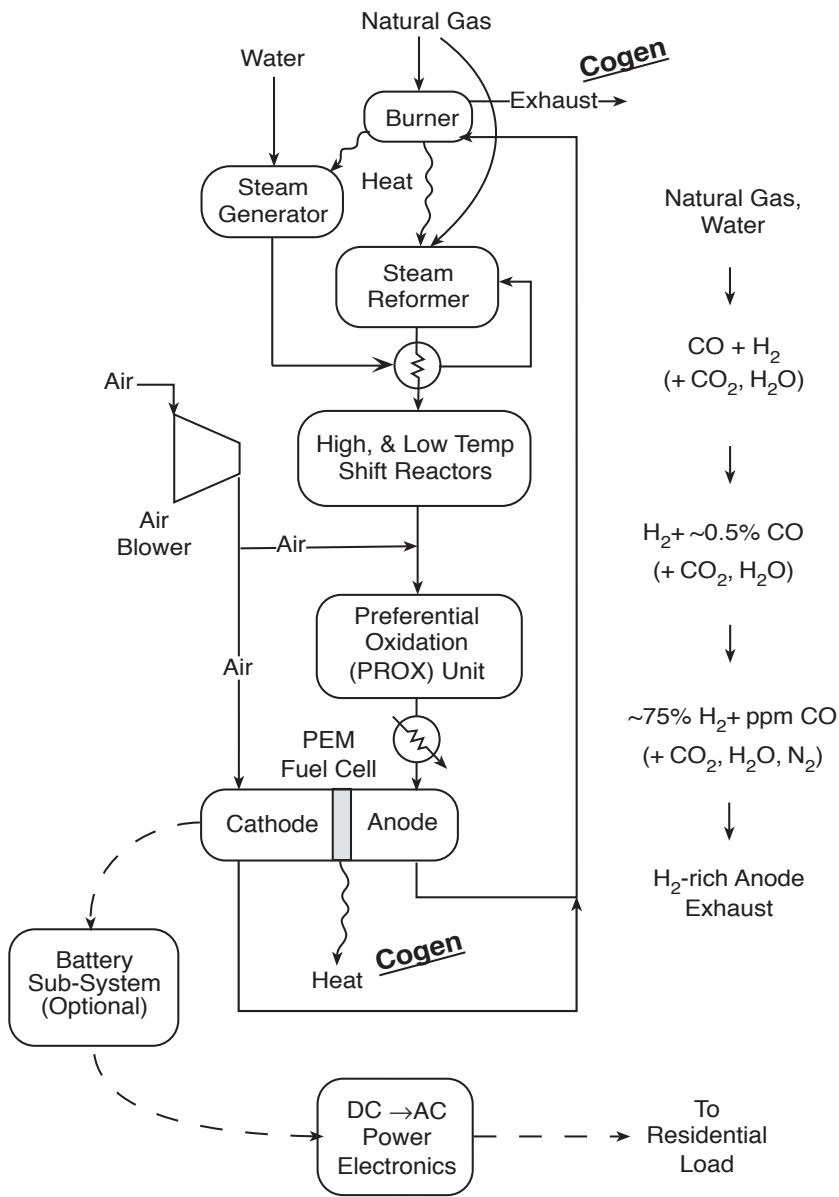


Figure 2. System Configuration for Residential PEMFC Cogeneration System

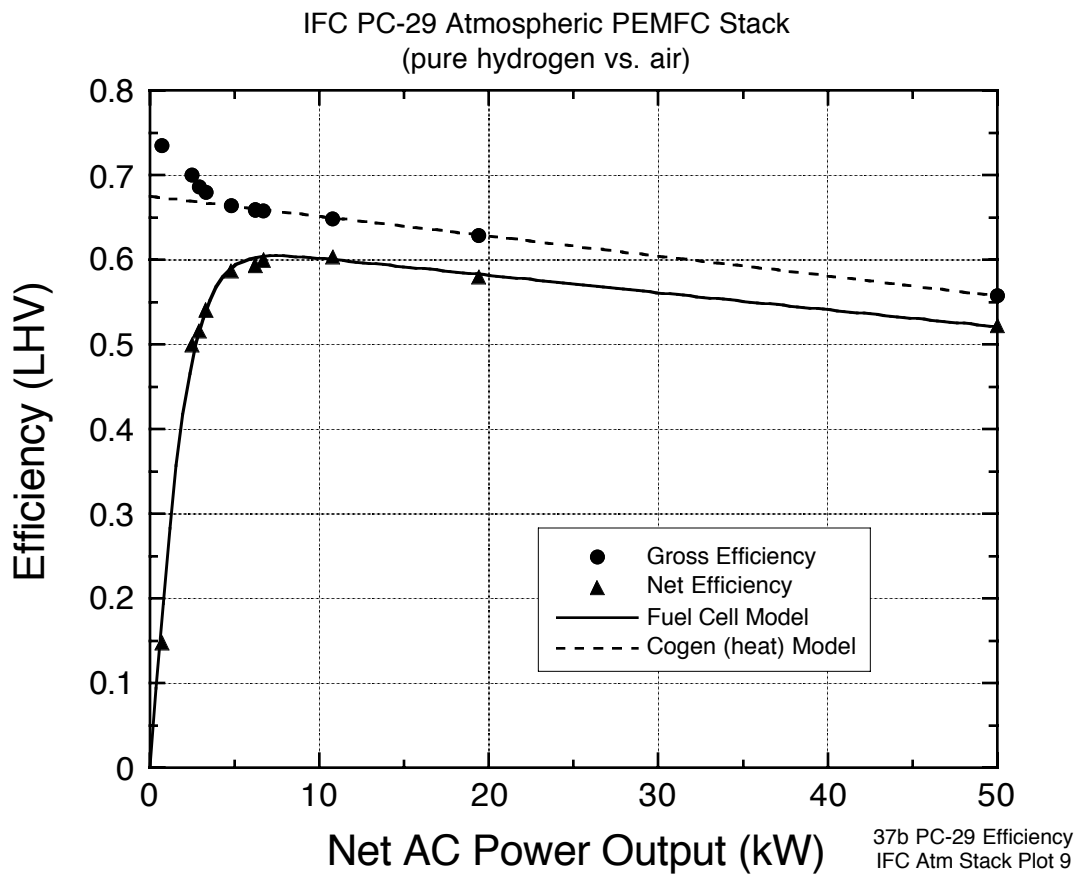


Figure 3. Assumed efficiency curve for 50 kW PEMFC stack based on IFC PC-29.

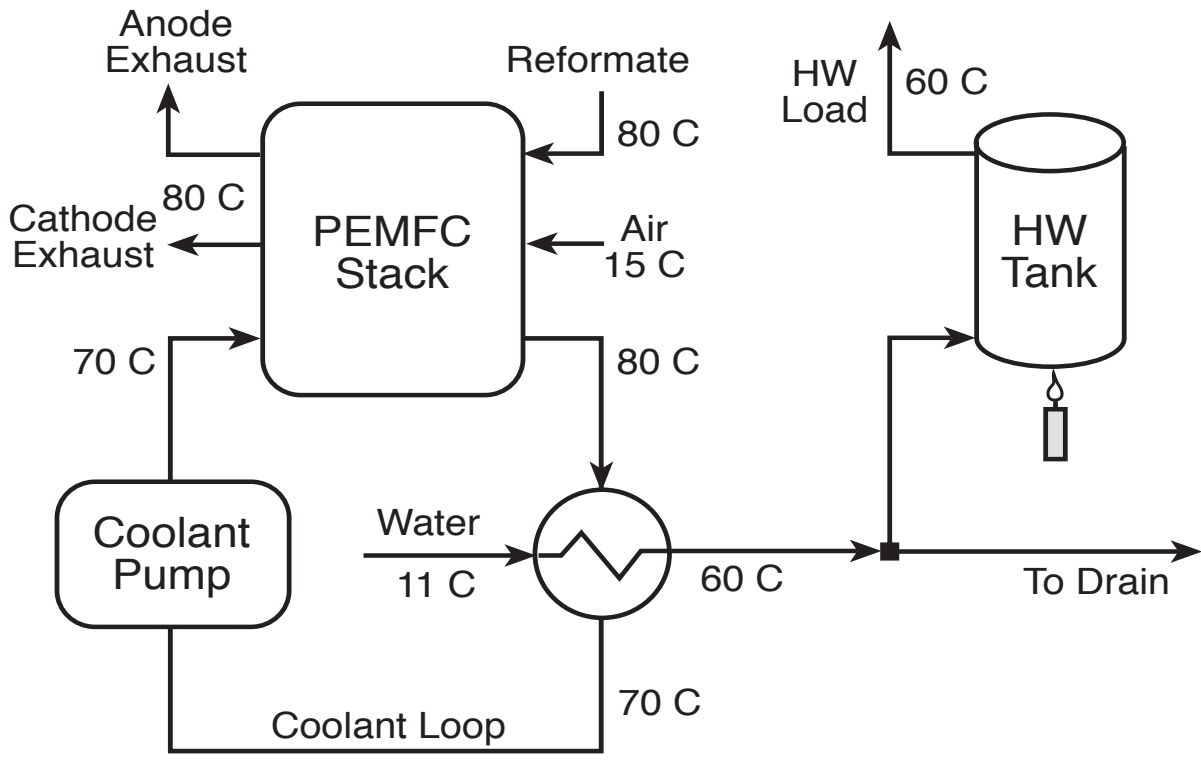


Figure 4. Schematic of Hot Water Cogeneration System.

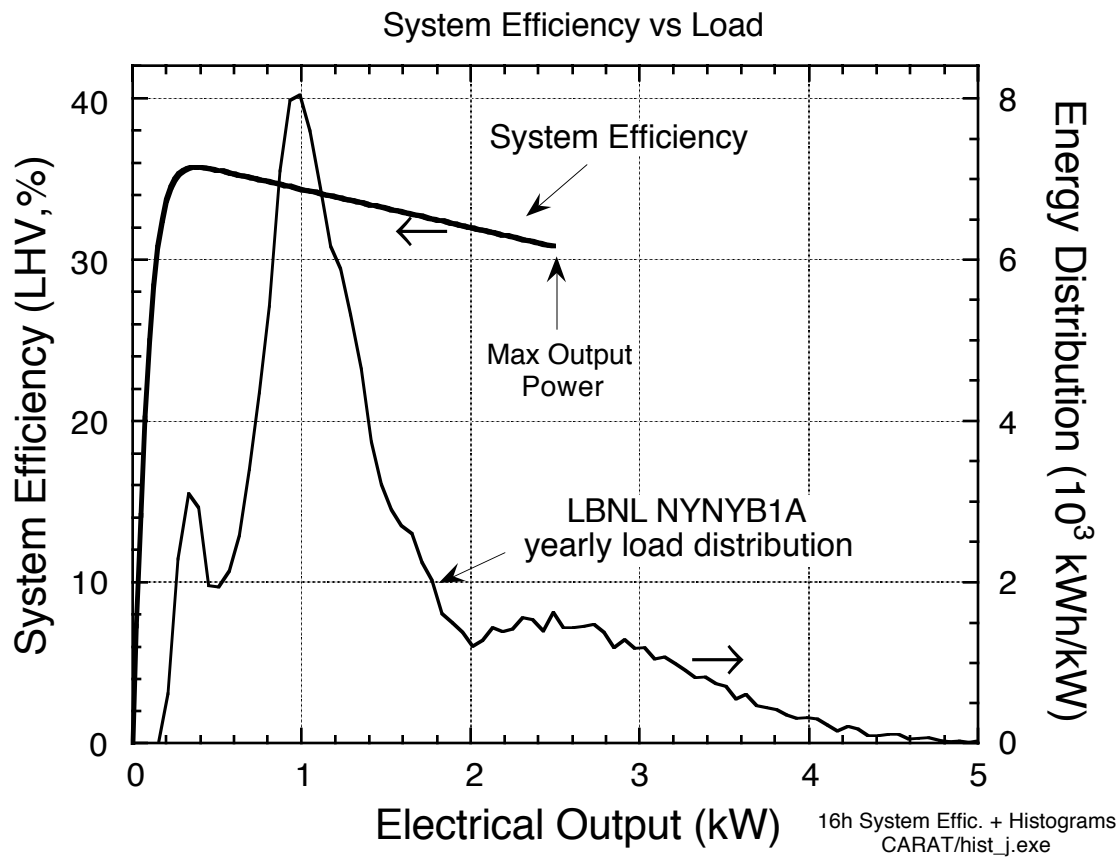


Figure 5. Total fuel cell system efficiency [=Electricity out/Natural Gas in (LHV)] for a 2.44 kW fuel cell system vs. electrical output power in kW. Also shown is the yearly load distribution for a single family house.

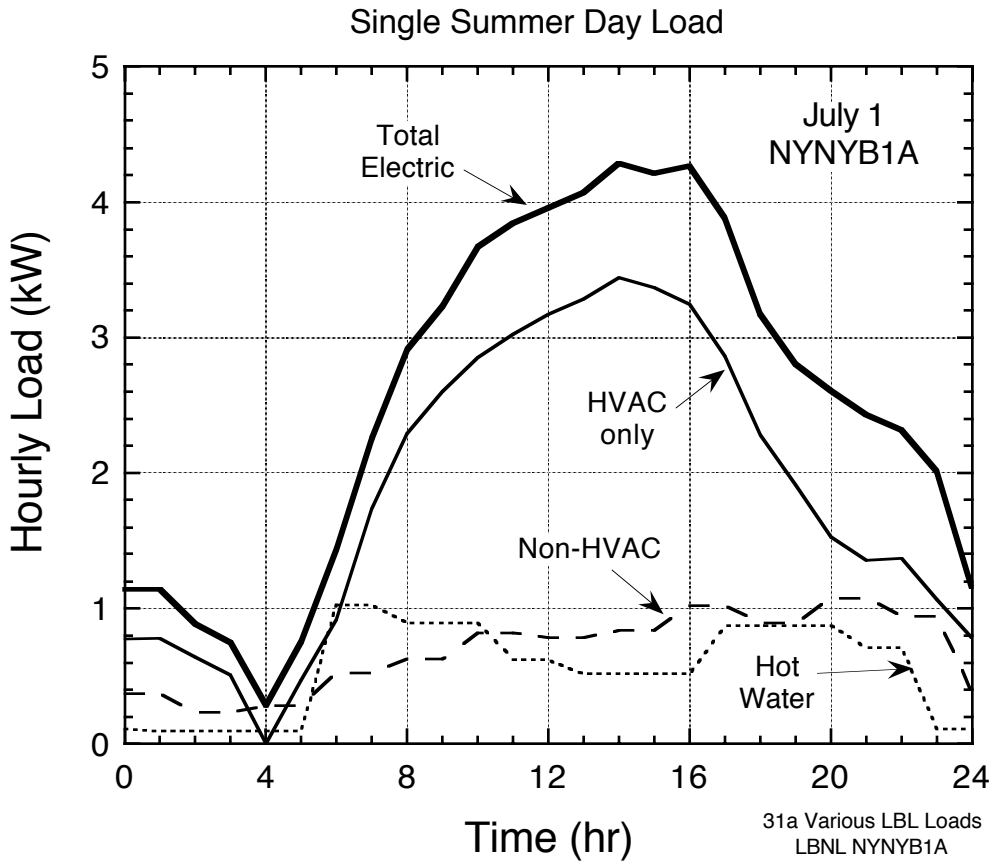


Figure 6a. Hourly-averaged loads for NY single-family residence during a typical summer day (July 1).

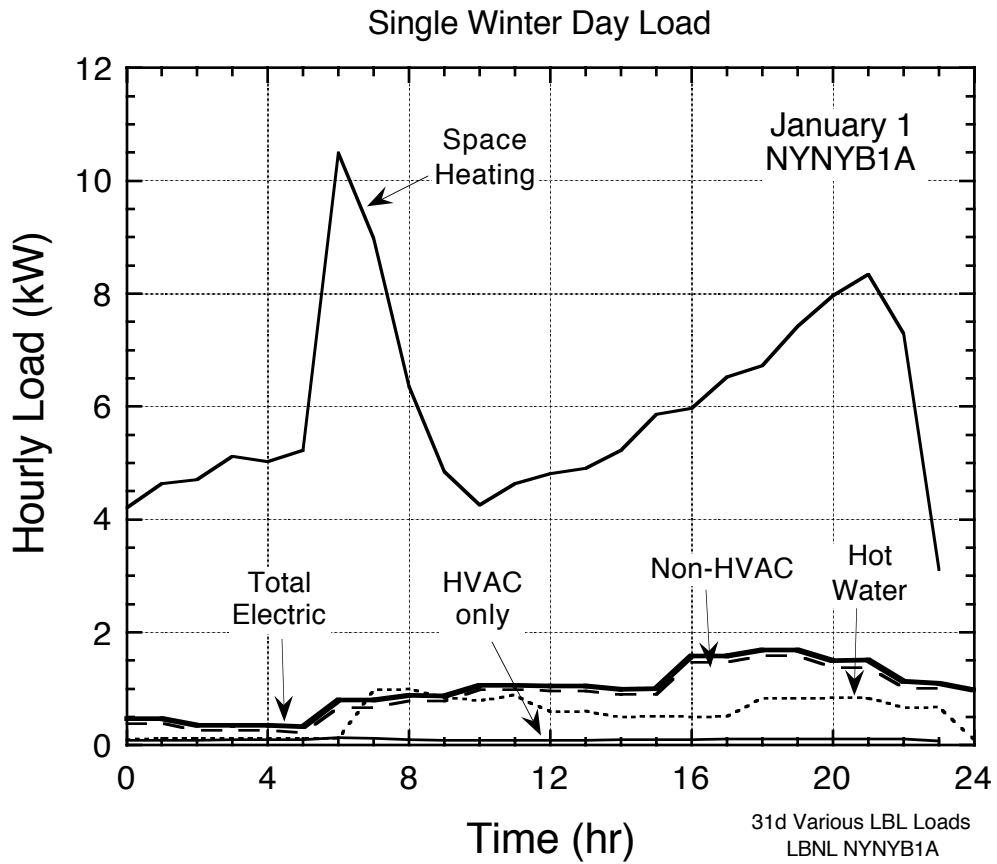


Figure 6b. Hourly-averaged loads for the NYB1A single-family residence during a typical winter day (January 1).

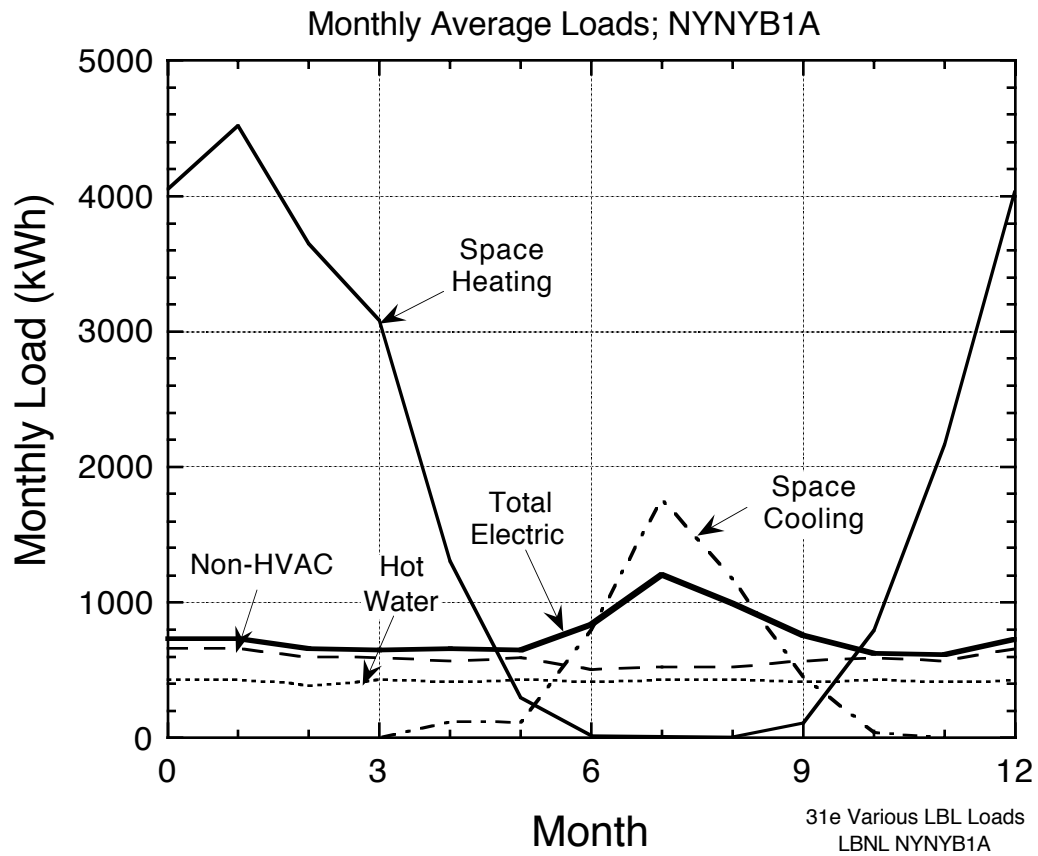


Figure 7. Monthly-averaged loads for the NYB1A single-family residence throughout a typical year.

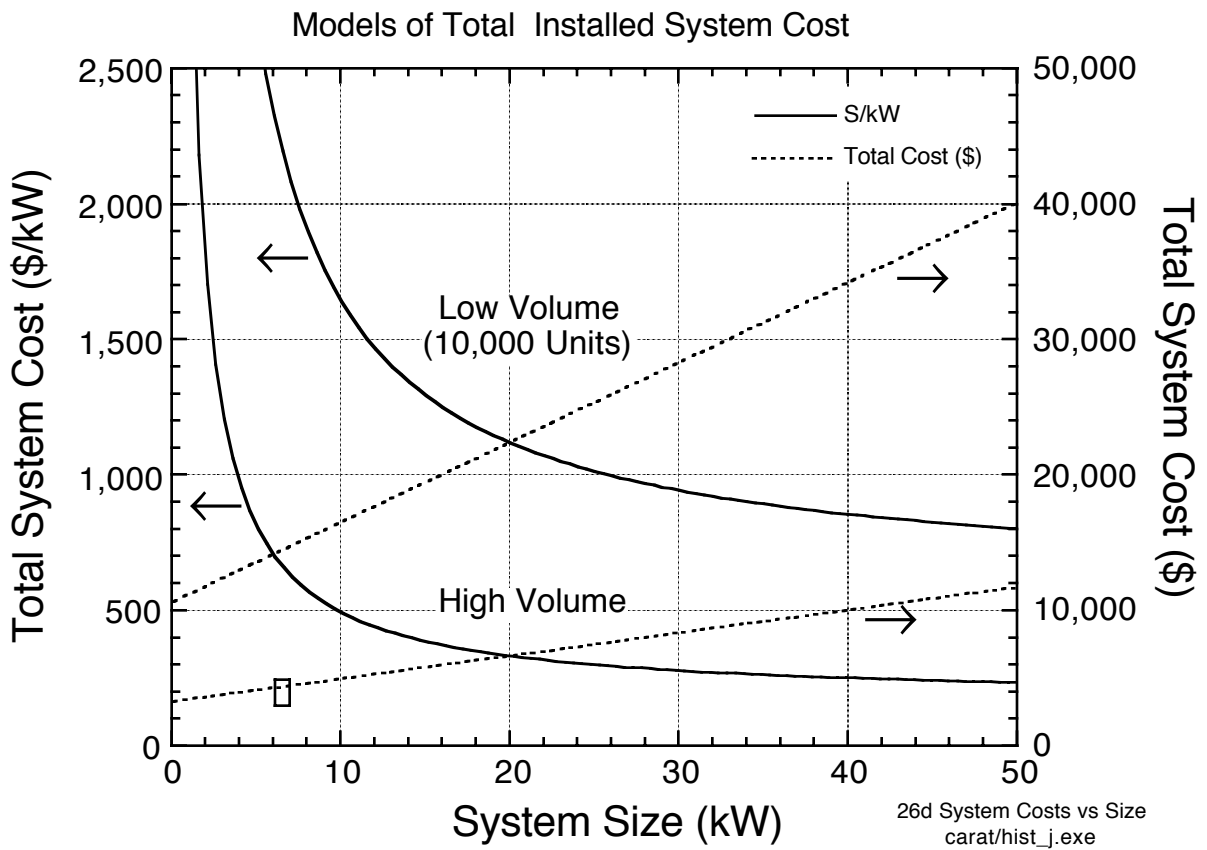


Figure 8. Total installed system cost, $C_{PV}(P_{sys}^{max})$, as a function of system size.

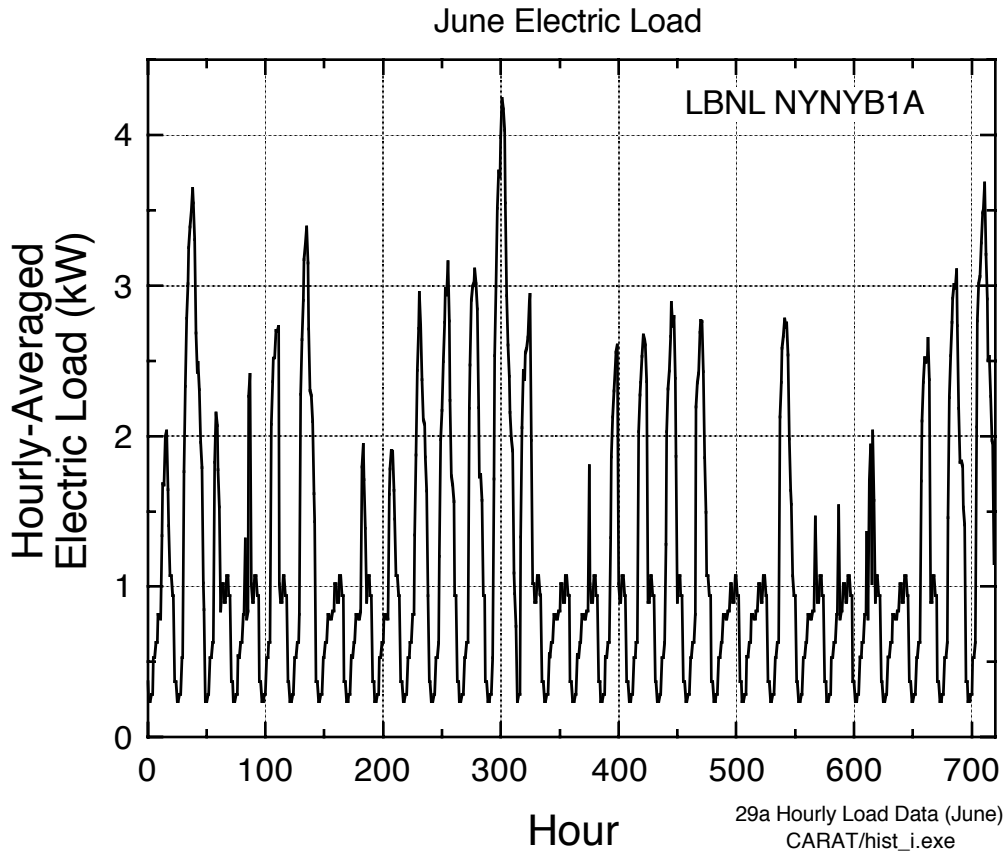


Figure 9. Hourly load data for the month of June.

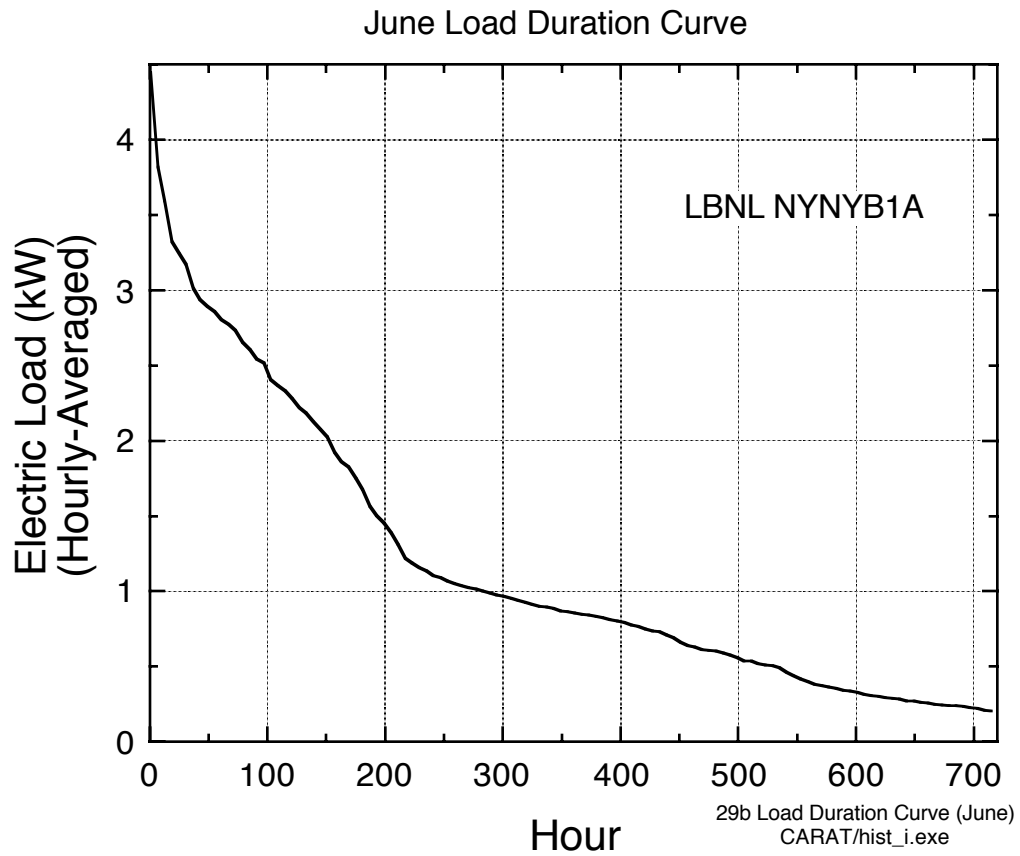


Figure 10. Load duration curve for data in Figure 9.

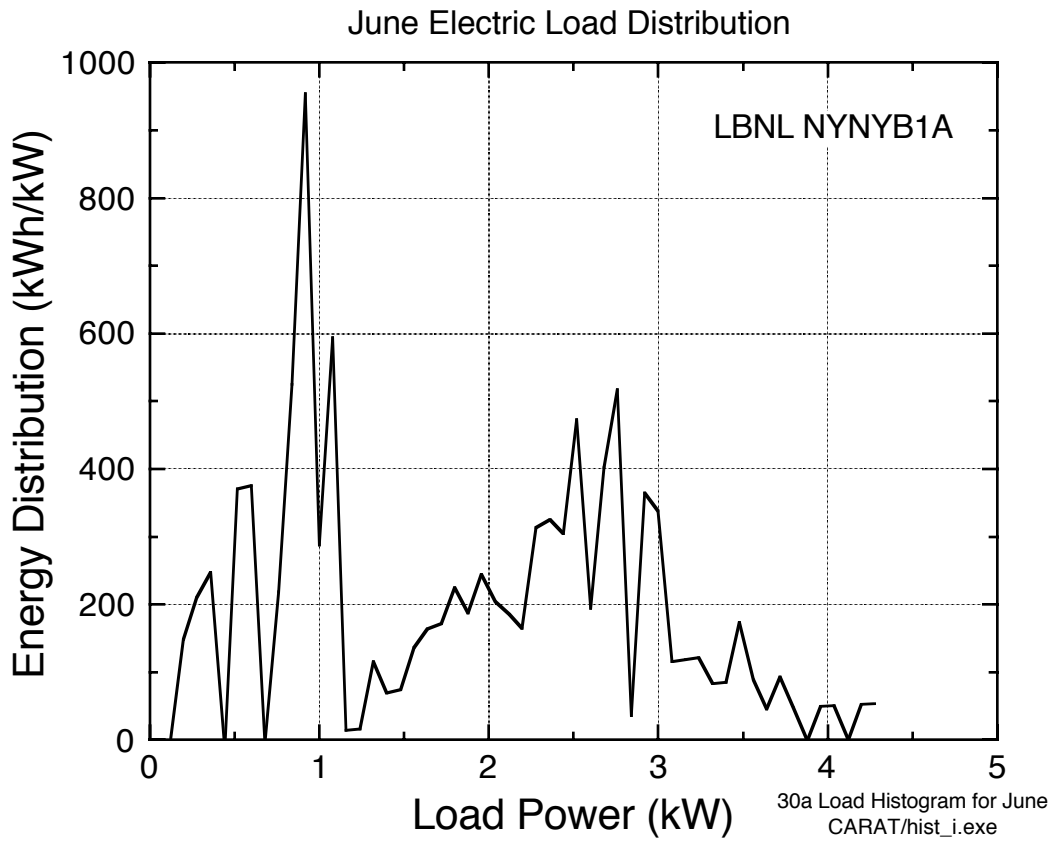


Figure 11. Load Energy Distribution for a Single Family House for One Month

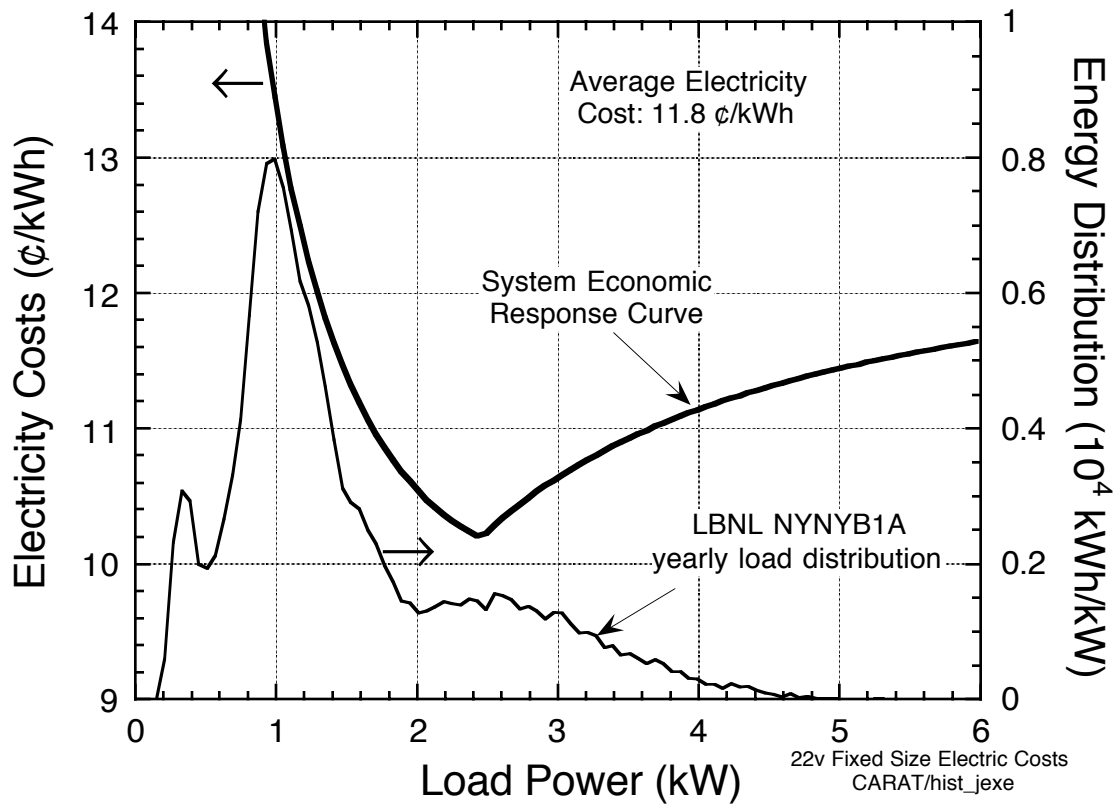


Figure 12. The System Economic Response Curve (SERC) for a 2.44 kW PEMFC system, shown with the yearly energy load distribution from a single family house.

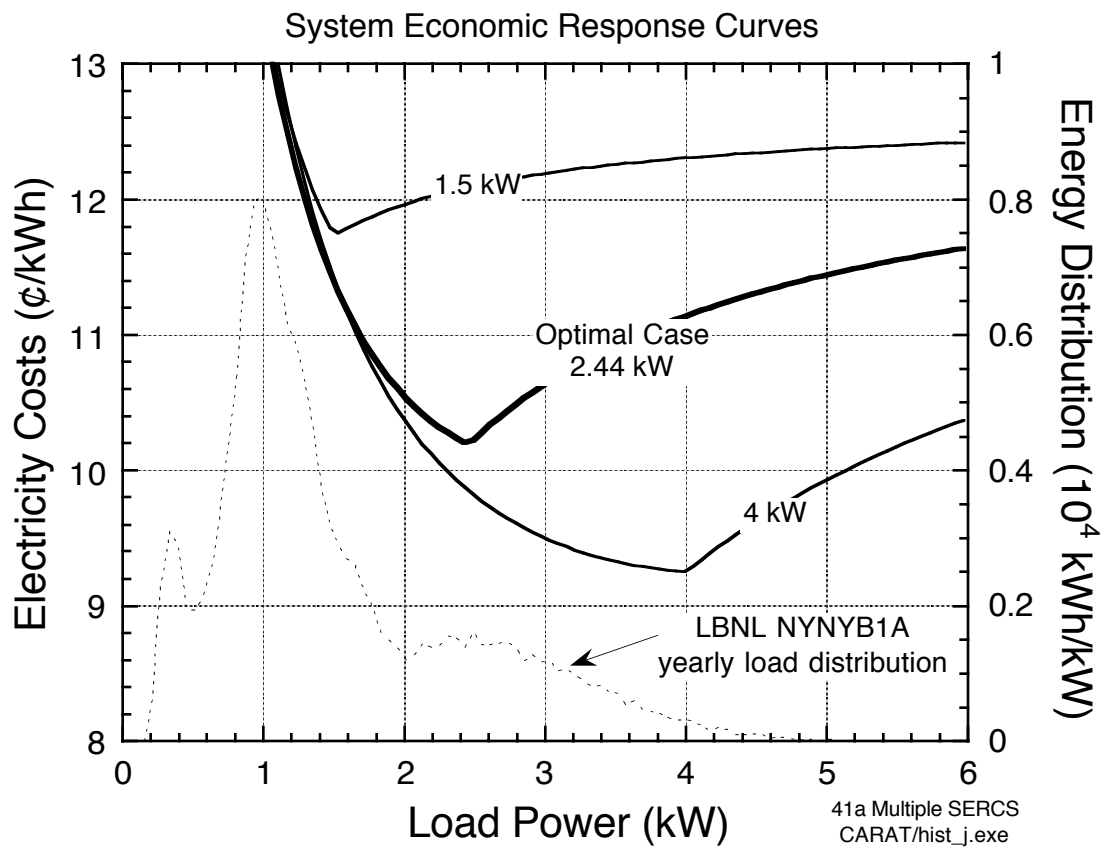


Figure 13. System economic response curves (SERCs) for systems of various size, compared to the load.

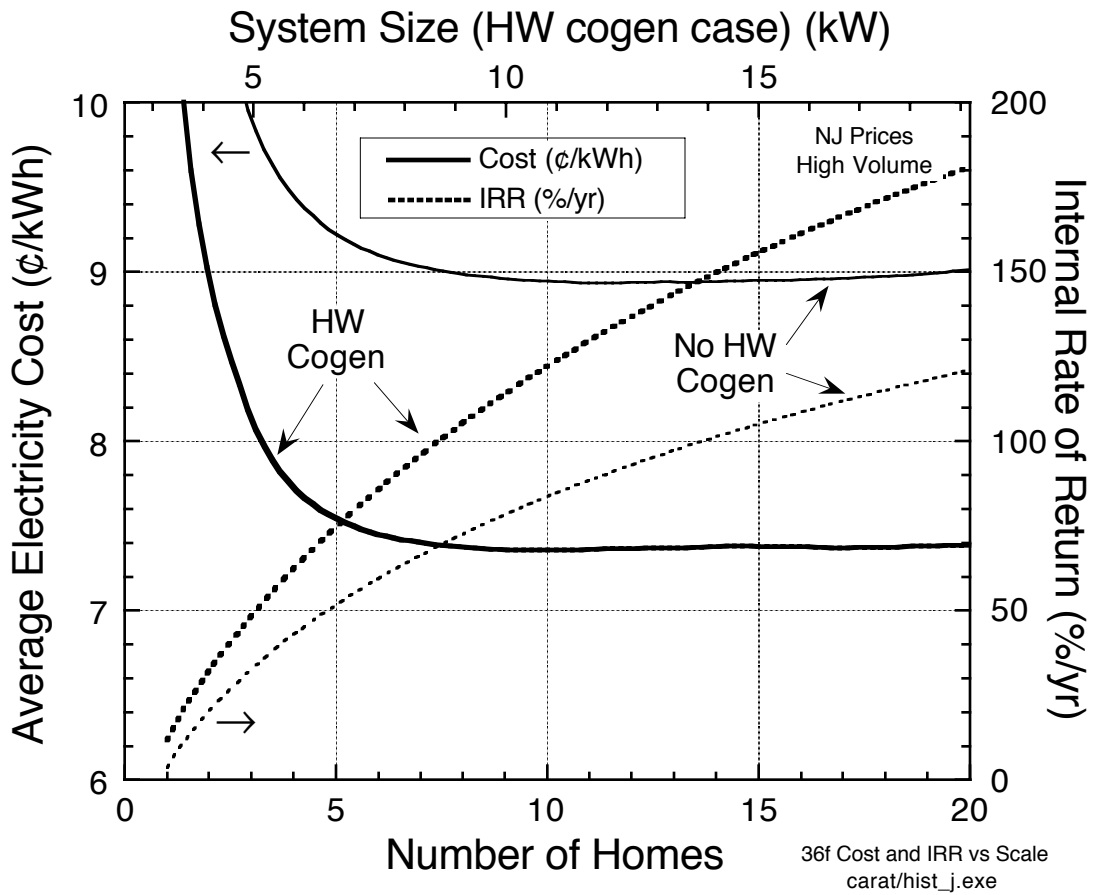


Figure 14. Cost of electricity and internal rate of return for PEMFC cogeneration systems, as function of system size. Cases with and without hot water cogeneration are shown.

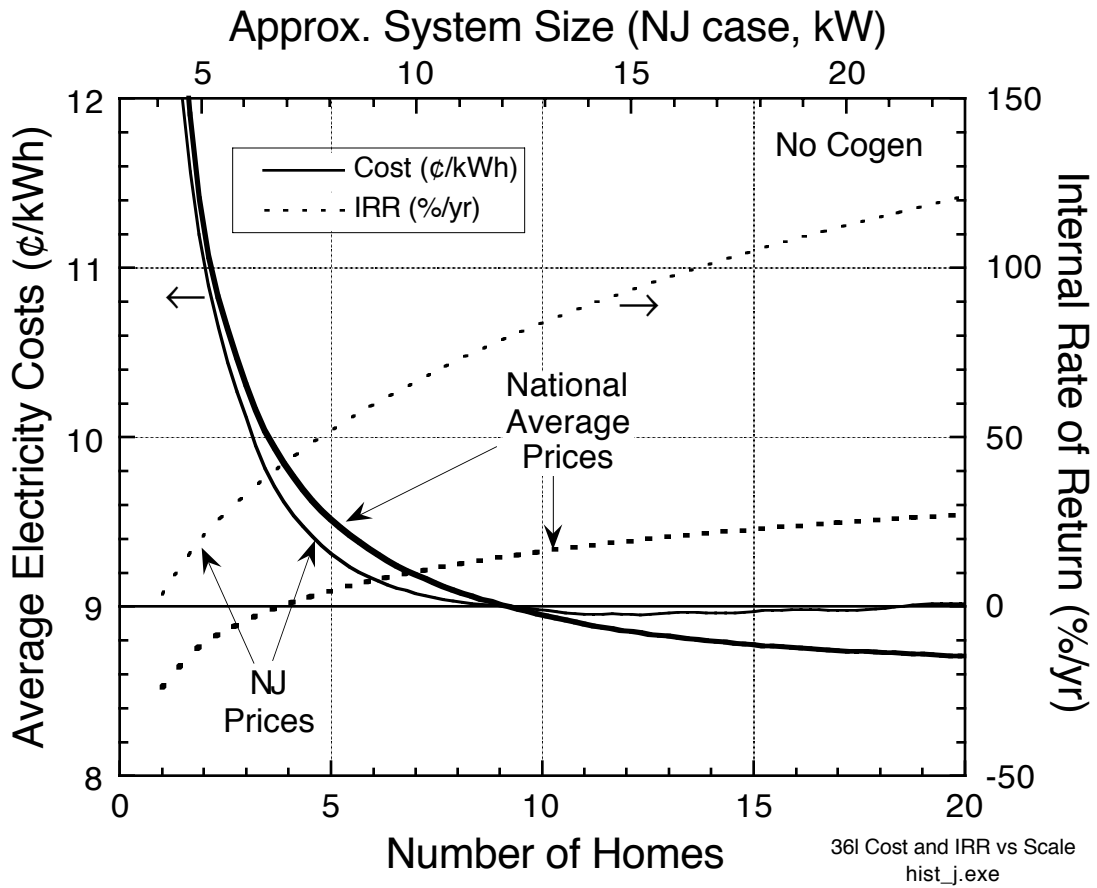


Figure 15. Cost of electricity and internal rate of return as a function of scale for N.J. and U.S. energy prices.

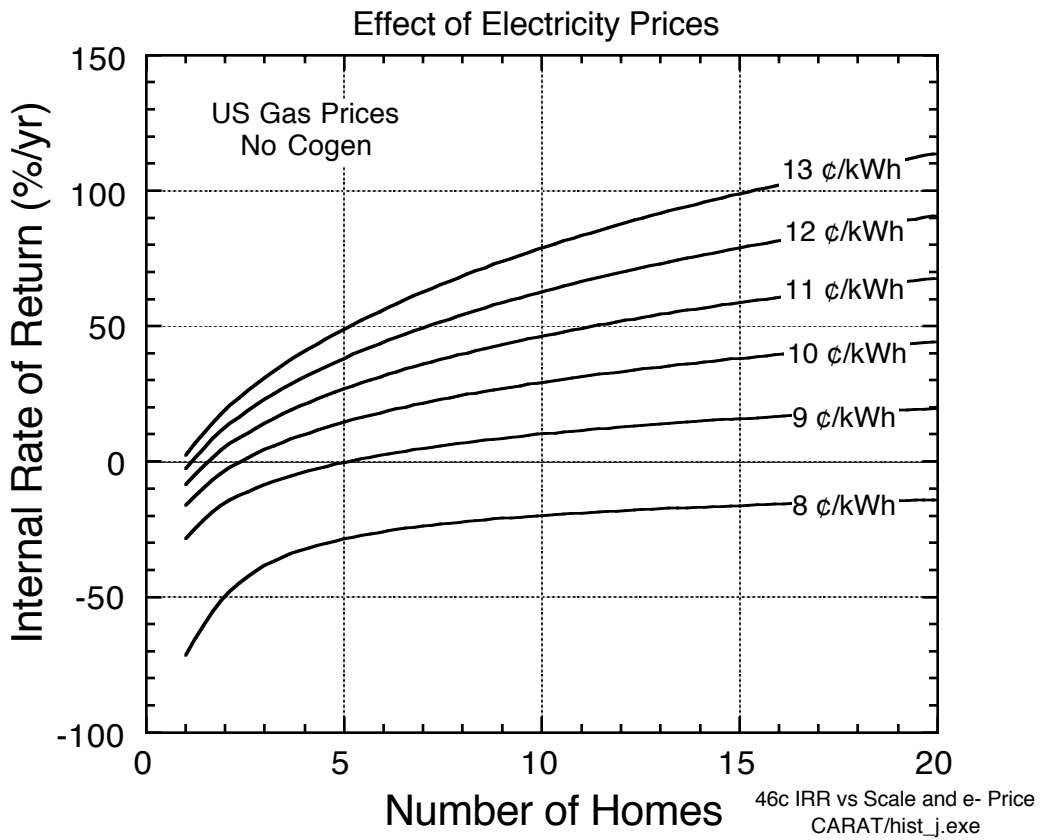


Figure 16. Internal rate of return as a function of scale and electricity price (at U.S. average nat. gas price).

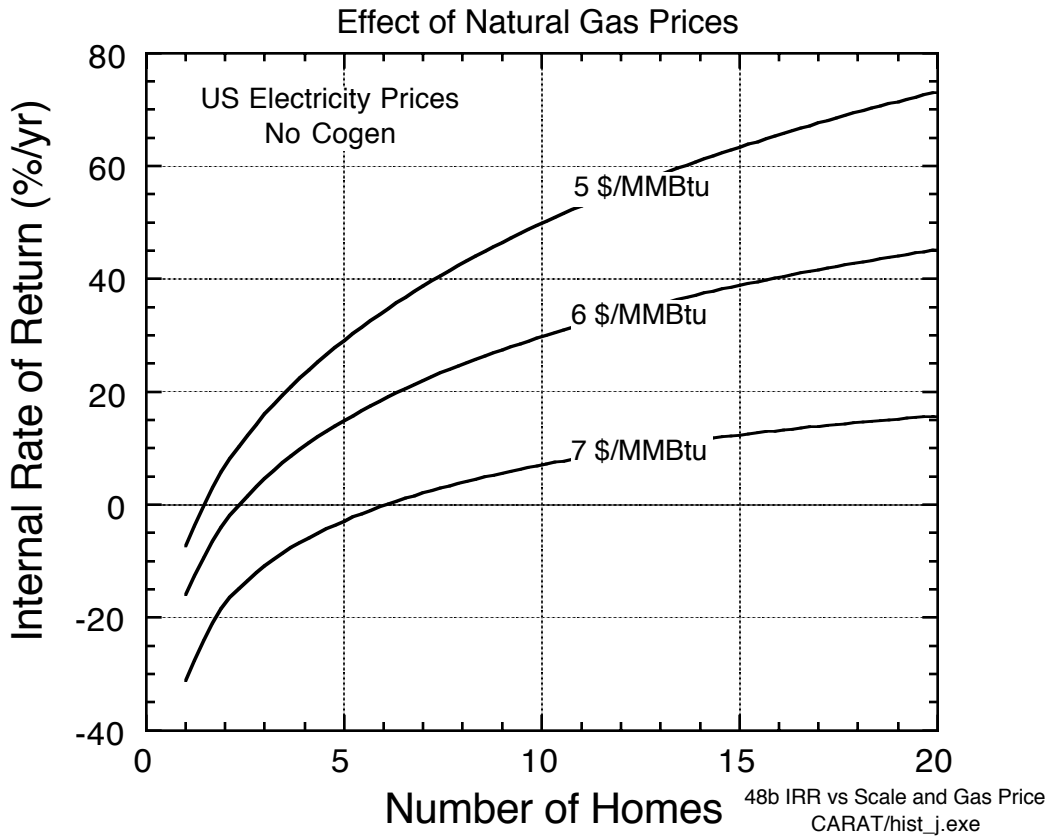


Figure 17. Internal rate of return as a function of scale and natural gas price (at U.S. average electricity price).

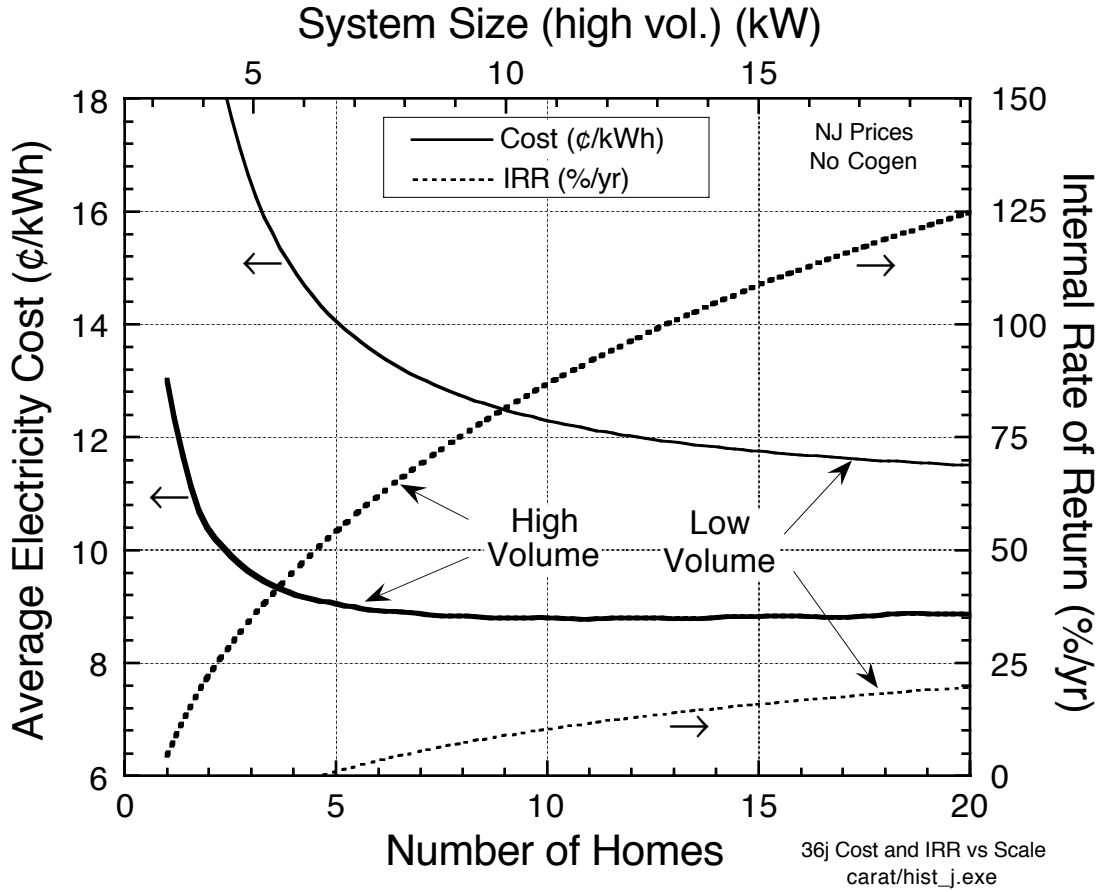


Figure 18. Electricity cost and rate of return as a function of scale, for high- and low-volume capital cost models.

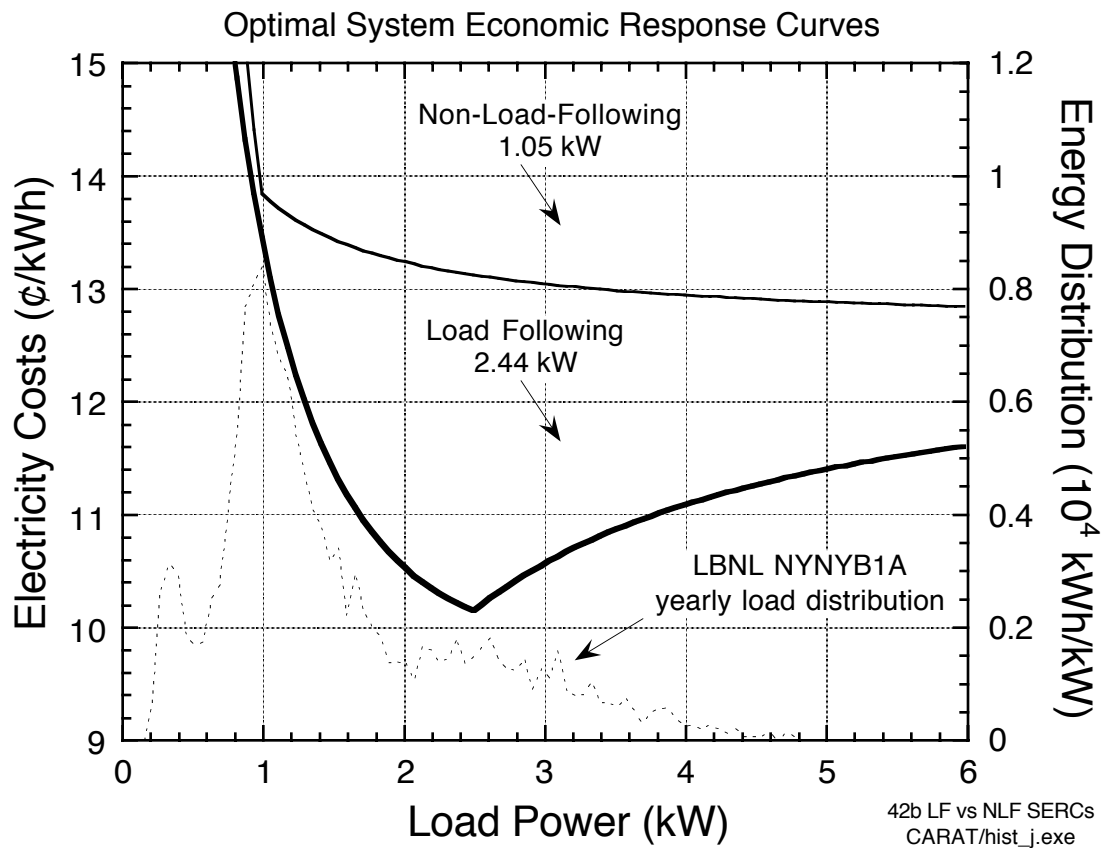


Figure 19. SERCs for load followers (TDR=5) and non-load following systems, compared to the load.

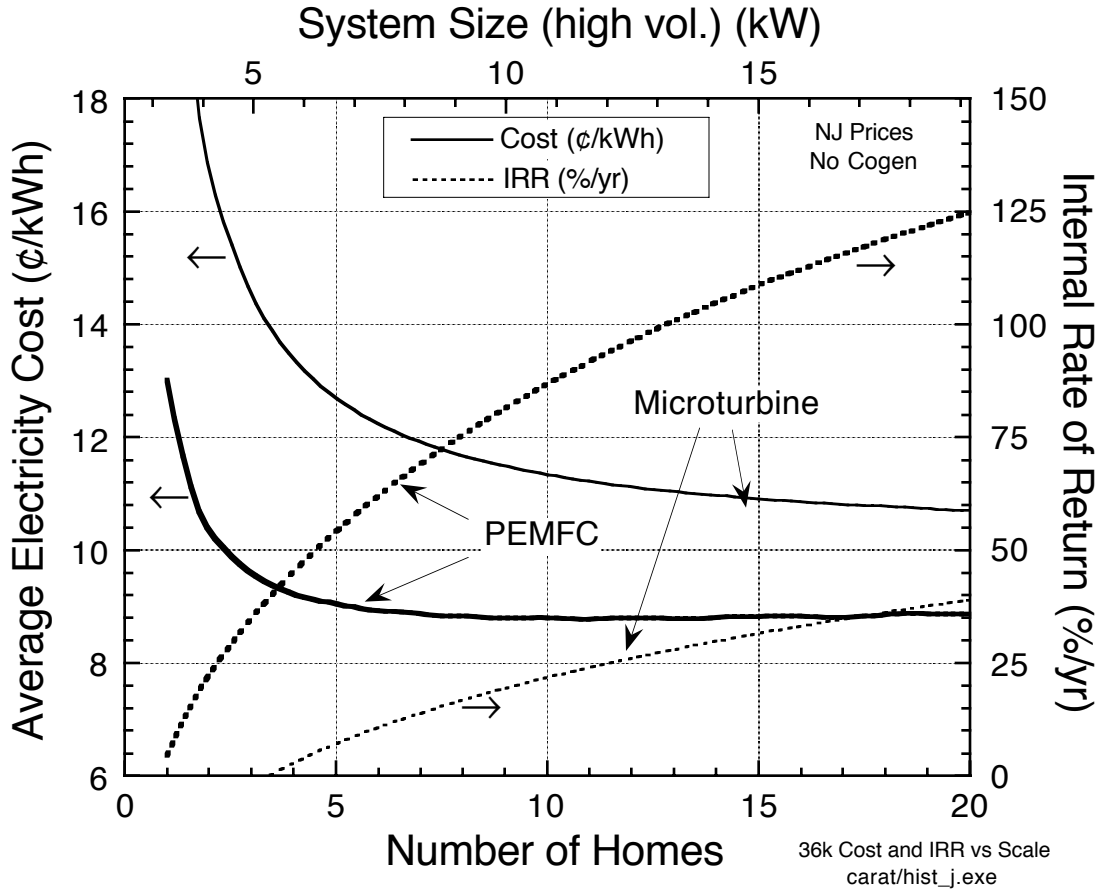


Figure 20. Electricity cost and rate of return as a function of scale, for a PEMFC system vs. a microturbine.

References

1. Arthur D. Little, "Fuel Cells for Building Cogeneration Applications - Cost/Performance Requirements and Markets", for the U.S. Department of Energy Office of Buildings Technologies by Arthur D. Little, Inc., Cambridge, MA, Reference No. 42526, January, 1995.
2. John O'Sullivan, Electric Power Research Institute, personal communication, January, 1998.
3. M. E. Gorman and T. F. Fuller, "50-Kilowatt Ambient Pressure Automotive PEM Fuel Cell and Direct Methanol Fuel Cell Development", Proceedings of the Annual Automotive Technology Development Customer's Coordination Meeting, DOE-OTT, Dearborn, MI, October 27-30, 1997, pp. 317.
4. Aspen Technology, Inc., Cambridge, MA 02141.
5. T. G. Kreutz and J. M. Ogden, "Development of an Efficient, Low Cost, Small Scale, Natural Gas Fuel Reformer for Residential-Scale Electric Power Generation", DOE Contract No. DE-FC02-98EE50534, Final Report, July, 2000.
6. Mark Haug, Trace Technologies Corp., personal communication, Sept. 3, 1999.
7. R. L. Ritschard, J. W. Hanford, and A. O. Sezgen, "Single-Family Heating and Cooling Requirements: Assumptions, Methods, and Summary Results", Gas Research Institute Report GRI-91/0236, Lawrence Berkeley Laboratory Report LBL-30377, March, 1992.
8. R. L. Ritschard and Y. J. Huang, "MultiFamily Heating and Cooling Requirements: Assumptions, Methods, and Summary Results", Gas Research Institute Report GRI-88/0239, November, 1989.
9. J. Huang, H. Akbari, L. Rainer, and R. Ritschard, "481 Prototypical Commercial Buildings for 20 Urban Market Areas", Gas Research Institute Report GRI-90/0326, Lawrence Berkeley Laboratory Report LBL-29798, April, 1991.
10. C. E. Thomas, J. P. Barbour, B. D. James, and F. D. Lomax, Jr., "Analysis of Utility Hydrogen Systems and Hydrogen Airport Ground Support Equipment", Proceedings of the U.S. DOE Annual Hydrogen Program Review, Golden, CO, May 6, 1999.
11. B. D. James, F. D. Lomax, Jr., and C. E. Thomas, "Manufacturing Cost of Stationary Polymer Electrolyte Membrane (PEM) Fuel Cell Systems", Report to the National Renewable Energy Laboratory, November, 1999.
12. K. Mitsuda, Y. Gonjo, H. Maeda, and H. Fukumoto, "Development of PEFC Technology at Mitsubishi Electric", Proceedings of the 1998 Fuel Cell Seminar, Palm Springs, CA, Nov. 16-19, 1998, pp. 541.
13. B. D. James, F. D. Lomax, Jr., C. E. Thomas, and W. G. Colella, "PEM Fuel Cell System Cost Estimates: Sulfur-Free Gasoline Partial Oxidation and Compressed Direct Hydrogen", October 17, 1997.
14. F. D. Lomax, Jr. B. D. James, G. N. Baum, and C. E. Thomas, "Detailed Manufacturing Cost Estimates for Polymer Electrolyte Membrane (PEM) Fuel Cells for Light Duty Vehicles", Report to the U.S. Department of Energy, August, 1998.
15. W. L. Mitchell, J. H. J. Thijssen, J. M. Bentley, and N. J. Marek, "Development of a Catalytic Partial Oxidation Ethanol Reformer for Fuel Cell Applications", SAE Paper No. 952761, The Society of Automotive Engineers, 1995.
16. W. P. Teagan, J. Bently, and B. Barnett, "Cost Reductions of Fuel Cells for Transportation Applications: Fuel Processing Options", *Journal of Power Sources*, **71**(1998) 80-85.
17. F. R. Kalhammer, A. Kozawa, C. B. Moyer, and B. B. Owens, "Performance and Availability of Batteries for Electric Vehicles: A Report of the Battery Technical Advisory Panel", California Air Resources Board, El Monte, CA, December 11, 1995.
18. Plug Power, LLC. press releases; see: <http://www.plugpower.com/news/>.

19. Jeffery Chen, Plug Power, LLC., personal communication, April, 1998.
20. Chris Broshart, Capstone Turbine Corporation, personal communication, July, 1999.
21. Capstone Turbine Corporation, <http://www.capstoneturbine.com/>.
22. S. Campanari, "Full Load and Part-Load Performance Prediction for Integrated SOFC and Microturbine Systems", Proceedings of the International Gas Turbine and Aerospace Congress and Exposition, Indianapolis, IN, June 7-10, 1999.
23. Glenn Murphy, Public Service Gas and Electric Company, personal communication, August, 1999.

INTEGRATED HYDROGEN FUEL INFRASTRUCTURE RESEARCH AND TECHNOLOGY DEVELOPMENT

**James Ohi, Barbara Farhar, Carol Hammel, Russel Hewett, and Paul Norton
National Renewable Energy Laboratory
1617 Cole Blvd.
Golden, CO 80401**

Abstract

The task seeks to establish an integrated hydrogen fuel infrastructure research and technology development effort. The long-term goal is to establish an initial hydrogen fueling infrastructure in several key locations, beginning with California, that will lead to development of a national infrastructure required to meet market demand by hydrogen-fueled vehicles. The task also seeks to establish integrated hydrogen safety codes and to establish a rationale for long-term hydrogen RD&D investments through scenario planning and analysis.

Introduction

The major objectives this year are to establish a comprehensive government industry approach to hydrogen infrastructure research and technology development. The rationale is to establish the framework and process for R&D and for government-industry guidance for this comprehensive approach. This approach includes preparation of an overall approach to infrastructure R&D (the Blueprint) and a government-industry team (the Core Team) to provide overall guidance. For codes and standards, a proposal was submitted to the Executive Committee of the International Code Council (ICC) to establish an ad hoc committee of code officials and hydrogen experts to consider establishing a comprehensive code for hydrogen safety under the ICC's model code format and process. The task also provides technical support to the DOE Hydrogen Technical Advisory Panel (HTAP), especially in the areas of scenario planning and fuel choice, to facilitate strategic guidance by the HTAP on RD&D priorities and interagency coordination at the federal and state levels.

Results

Hydrogen Infrastructure Activities

In October 1999, the U.S. Department of Energy (DOE), the California Air Resources Board (CARB), and the California Energy Commission (CEC) co-sponsored a workshop to answer the question: *What has to be done, beginning today, to implement a hydrogen fuel infrastructure so that when hydrogen vehicles become market-ready in 3-5 years, the infrastructure needed for on-board direct use of hydrogen will be available?*

The workshop did not specifically address the issue a fuel choice (direct hydrogen versus on-board reforming of a liquid fuel). Although the participants acknowledged that fuel choice is an open issue, the workshop focused on near-term direct hydrogen systems with on-board hydrogen storage. This near-term focus does not preclude longer-term concerns, such as climate change and the sustainable use of resources.

As a result of the workshop, the *Blueprint for Hydrogen Fuel Infrastructure Development* was formulated. The objective of the *Blueprint* is to outline a five-year action plan to develop a hydrogen fuel infrastructure needed by the 2003 - 2004 timeframe for both heavy-duty and light-duty vehicles. The *Blueprint* is based on a consensus among the workshop participants on the desirable attributes of a hydrogen fuel infrastructure, as well as on an estimate of the number, type, and uses of hydrogen vehicles anticipated in the 2000-2005 time. The *Blueprint* also explores how addressing near term requirements and barriers will facilitate establishment of a commercial-scale hydrogen fuel infrastructure.

Collaboration with DOE Office of Transportation Technologies (OTT), and Other Efforts

Subsequent to an initial *Blueprint* planning meeting held in February 2000, a second *Blueprint* meeting was held in May 2000. The primary purpose of this meeting was to develop better coordination and collaboration with the Gas Research Institute's Natural Gas Vehicle Infrastructure Industry Working Group (IWG), with the DOE Office of Transportation Technologies' (OTT) Fuels for Fuel Cells Plan, and with the California Fuel Cell Partnership. Due to the overlapping areas of interest, the *Blueprint* will focus considerable attention toward coordinating with these activities and others. Excellent opportunities exist to leverage skills and experience among all applicable programs.

Blueprint Roadmapping

The *Blueprint* is structured into four technical areas: Standardized Dispensing Station Design; Test and Certify Hydrogen Containers; Integrate Codes and Standards; and Safety RD&D for Public use of Hydrogen. In order to identify tasks within each technical area, and to develop associated action plans for their completion, a meeting will be held in August 2000 to roadmap the activities. Four sub-working groups will be established according to technical area, and include representation from hydrogen fueling companies and hands-on expertise from both the fueling station and advanced vehicle areas. Natural gas industry experience will also be represented by the natural gas IWG.

The products of the *Blueprint* roadmapping meeting will delineate activities that will be undertaken by industry, by government, and by collaborative efforts of government and industry. It will also aim at outlining a pre-competitive collaborative process for auto, energy, and government organizations to meet near term market needs for hydrogen fuel infrastructure. The *Blueprint* roadmap, when completed, will be available on the DOE Hydrogen Information Network web site.

Hydrogen Bus Data Acquisition Plan

Since 1993, NREL's Alternative Fuel Transit Bus Program has performed extensive data collection and fleet studies on alternative fuel buses around the country. The program, designed to evaluate early commercial products, has studied the reliability, fuel economy, repairs and maintenance, cost and emissions of buses operating on compressed natural gas, liquefied natural gas, methanol, ethanol, and biodiesel.

The data collection, analysis and reporting for this project cost approximately \$100k per site per year. An additional \$80k to \$200k per site was used for chassis dynamometer emissions testing. Although this level of effort is not appropriate for the hydrogen bus sites which are employing uncertified prototype technology in very low numbers, some lessons learned from the Alternative Fuel Transit Bus Program are appropriate for the hydrogen bus projects:

- It is critical to have control vehicles at the same site as the test vehicles for comparison.
- Consistency of data collection and analysis protocol between sites is important for comparing technologies.
- Sites must have high quality existing data systems to obtain reliable operational data.
- For emissions testing, data from several vehicles is necessary due to significant vehicle-to-vehicle variability.
- Lessons learned by sites implementing new technologies can be very helpful to other sites attempting to implement similar technology.

In addition to these fleet studies, NREL manages an On-Road Prototype Development Project aimed at moving alternative fuel engine technology from the laboratory to the road on the path to commercialization. This program places one to four vehicles with prototype engines into revenue service in existing fleets to reveal the weaknesses of the new technology and develop solutions that can be incorporated into the commercial version of the engine. These projects are executed in close cooperation with the engine manufacturer.

Since the California hydrogen bus projects fall somewhere between the existing NREL alternative fuel vehicle programs, the data and information collected on the hydrogen buses will be a hybrid of the types of information collected in the existing programs.

Three hydrogen bus development projects in California have been funded by FTA/DOE and the California Energy Commissions (CEC). The DOE has also provided support for hydrogen buses in Las Vegas, NV. An additional site will operate hydrogen buses as part of the California Fuel Cell Partnership. These sites are summarized in the table below.

| Site | Number of Fuel Cell Buses Planned | Number of H ₂ /Natural Gas Buses Planned | Number of Hydrogen Hybrid Buses Planned | Expected Date for First Bus |
|------------------------------|-----------------------------------|---|---|-----------------------------|
| SunLine Transit, Palm Desert | 1* | 2 | 0 | March 2000 |
| UC Davis, Sacramento | 2 | 3 | 0 | August 2000 |
| City of Chula Vista | 1 | 0 | 0 | 2003 |
| AC Transit, Oakland | 4* | 0 | 0 | 4Q 2001 |
| City of Las Vegas, NV | 0 | 4 | 1 | March 2001 |
| Totals | 8 | 9 | 1 | |

*The CA Fuel Cell Partnership plans to put five buses in service at SunLine Transit and AC Transit, the split between the sites may be different than shown here.

NREL applied its previous experience in evaluating alternative fuel transit bus fleets to design a draft Data Acquisition Plan for these hydrogen buses. Operational data on the hydrogen buses will be collected and analyzed to benchmark the state of development of the technologies and to identify areas in need of improvement. The questions to be answered by collecting operational data on the hydrogen buses are as follows:

1. Did the hydrogen buses meet the needs of the transit agencies?
2. What was the availability (or "up-time") of the prototype buses during the demonstration?
3. What problems were encountered with the prototype buses and what solutions were developed?
4. Were there any safety incidents? If so, what changes have been implemented to avoid similar incidents?
5. What is the fuel efficiency of the hydrogen buses?
6. What was the cost of the prototype buses?
7. What lessons were learned that would be of use to other transit agencies implementing hydrogen bus technology?

At each site, one or more diesel and/or CNG buses will be designated as control vehicles. The diesel or CNG buses that are as similar as possible to the program buses, and are dispatched on the same or similar service routes will be used. All data collected for the program buses will also be collected for the control buses.

Vehicle specifications of interest include:

- Vehicle use patterns
- Fuel economy
- Bus availability and reliability
- Capital and fuel costs
- Maintenance and repairs issues encountered
- Safety Incidents
- Emissions of hydrogen/natural gas buses

In addition to the data acquisition and analysis activity, a "Hydrogen Bus Information Exchange" website is also planned. The homepage for the Exchange will include publicly accessible background information on the projects as well as the results of the data acquisition effort as they become available. A password-protected area of this website will contain space for each of the bus sites and a threaded chatroom. Project members can post information they wish to share with other bus project participants but not with the public on their area of the protected site. In the chatroom section, project members can discuss issues that arise at the sites and learn from one another's experiences. These conversations can be archived and the experiences distilled into a written report that will be reviewed by the project members before being released on the public site and in hardcopy.

Codes and Standards

Incorporation of Hydrogen Technologies and Safe Engineering Practices into the National and International Safety Codes

One of the near-term objectives of the Hydrogen Program is to incorporate hydrogen safety into existing and proposed national/international building, fire and other applicable codes, in order to facilitate market acceptance and deployment of the hydrogen technologies. All interested parties (i.e., government, private industry and prospective users) would be best served if the International Code Council (ICC) faced the hydrogen issue directly and adopted a separate section specifically dealing with hydrogen fuel issues in either the International Building Code (IBC) or the International Fuel Gas Code (IFGC). In April 2000, the ICC Board of Directors approved the appointment of an Ad Hoc Committee to address the subject of hydrogen used as in fuel cells in vehicular or portable technology. The ICC concluded that the subject of stationary fuel cell power plants is already being well addressed in the International Codes. The ICC Board decided to establish a nine-member Ad Hoc Committee consisting of three code officials, three industry representatives and three design professionals. The Committee is scheduled to have its first meeting in late July 2000. NREL will participate as an *ex officio* member.

Generation of a Document for Building Code and Fire Safety Officials that Describes the Hydrogen Technologies and Safety Issues

One of the milestones in the FY2000 Hydrogen Program is generation of a "Draft Sourcebook for Building and Fire Code Officials." The objective of the draft is to be an abridged version of the "Sourcebook for Hydrogen Applications" that addresses the specific concerns of building and fire safety officials relating to the hydrogen technologies. The Program completed a draft report entitled "***The Hydrogen Primer for Building Codes and Fire Safety Codes Officials (Current and Emerging Uses of Hydrogen as an Energy Resource and Properties of Hydrogen Compared to Other Fuels)***." The draft, when finalized, is intended to be a professional-quality, visually-pleasing, non-technical report that familiarizes building code and fire safety officials with the following:

- Hydrogen as a fuel
- Current and emerging applications of hydrogen

- Properties of hydrogen (with respect to safety issues) compared to “conventional” fuels such as natural gas and propane
- Examples of successfully operating projects
- Status of standards and codes development
- Where to go to obtain detailed information.

NREL is using the review comments to generate a revised draft document. The revised draft will be disseminated to the ICC Hydrogen Ad Hoc Committee at its kickoff meeting in late July 2000.

HTAP Scenario Planning Committee Support

Thirty-three HTAP members and invited experts on scenario planning and hydrogen energy attended the Hydrogen Technical Advisory Panel (HTAP) Scenario Planning Workshop in Sacramento, California on October 21-22, 1999. The Workshop’s genesis was an HTAP recommendation in its Report to Congress. HTAP recommended that the Hydrogen Program host scenario development workshops to develop compelling visions and scenarios of a hydrogen energy future to advance the concept of hydrogen energy to senior DOE management, the Congress, and the public. The scenarios—which are tools to provide a context to explore planning for the DOE Hydrogen Program’s RD&D portfolio—are intended to help link HTAP’s overarching vision in the 21st Century with the portfolio by providing a rationale for the Program. The scenario planning approach was chosen over a more traditional strategic planning process because of the great numbers of uncertainties and variety of outcomes possible for the time frame to be examined.

The Workshop was structured so as to expose participants to selected existing future global scenarios to provide a thought-provoking context for developing focused scenarios by drawing out implications for energy in general and hydrogen in particular. The approach involved developing storylines that are compelling, plausible, and interesting to DOE and to key constituencies. Results can be used to explore the role that hydrogen energy can play in continuing and accentuating the positive trends evidence in the 21st Century.

As part of the discussion on *drivers*, participants pointed to the finite supply of fossil fuels, the potential for energy disruption, and tension between the developed and developing countries around such issues as growth, energy needs, and trade.

The *sociopolitical and economic trends* identified by participants included:

- The structure of population growth
- Economic output
- Energy consumption/energy demand
- Human attitudes and behavior
- Conflict between the “haves” and “have-nots” concerning energy
- Energy market developments
- Energy subsidies

The *environmental trends* identified by participants included:

- Changing environmental objectives and policies concerning emissions and hazardous wastes
- Improved data concerning environmental effects of energy alternatives, including climate change
- Economic valuation of clean environment
- Policies regarding greenhouse gases and climate change
- Policies regarding pollution credits and trading
- Hazardous energy-related events (such as oil spills or nuclear accidents)

The *technical trends* identified by participants included:

- The nature and rate of technological change
- Energy supply, including disruptions and limitations
- Fossil fuel supplies and extraction costs (including natural gas and petroleum)
- Improving technologies for fossil fuel production and consumption
- Improving hydrogen technologies
- Improving renewable technologies
- New technology inventions
- Carbon dioxide sequestration breakthroughs.

Emerging themes that participants identified included:

- A cataclysm results in breakdown of energy system
- Discontinuity leads to massive social breakdown and reduced population
- Investment results in massive technology efforts
- Social-political-technical solutions are found.
- A technological breakthrough in hydrogen technology occurs.

Markets affect the result through customer demand (market pull), regulation (policy push), manufacturer investments, and balancing business and environmental growth.

Participants discussed *how quickly change could occur*. It could be evolutionary, revolutionary, or discontinuous. Change could result from an epic event, a series of small crises, or market pull. Examples were given.

In summary, participants said the key driving forces that will determine the role of hydrogen in plausible energy futures are (1) the rate of hydrogen technology development and (2) the interplay between market forces and social concerns. The key uncertainties are (1) the nature and rate of hydrogen technology development, and (2) how social concerns about, for example, environmental quality and energy security, affect competitive market forces that determine fuel choice and commercial success of advanced technologies.

OPPORTUNITIES FOR HYDROGEN: AN ANALYSIS OF THE APPLICATION OF BIOMASS GASIFICATION TO FARMING OPERATIONS USING MICROTURBINES AND FUEL CELLS

Darren D. Schmidt and Jay R. Gunderson
Energy & Environmental Research Center
University of North Dakota
Grand Forks, ND 58203

Abstract

This paper examines the concept of using biomass gasification in conjunction with microturbines or fuel cells to generate electricity for on-farm installations. The biomass farm feedstock would be either switchgrass or wood. Various levels of hydrogen purity required relative to the prime mover are discussed. In general, individual on-farm electricity demand is relatively low (12 kW). Commercial stationary power generation fuel cells are currently available in the 200-kW size range, and many nonstationary power generation proton-exchange membrane fuel cells are being produced at lower power levels. Commercial microturbines are available as 30-kW units. Approximately 250 acres of land would be required to produce biomass in the form of switchgrass or willow for a 200-kW power plant. It is expected that higher-value crop production will most likely be the primary focus for U.S. farmers and that power production will remain a secondary interest. The primary factors holding back the interest in power production are low electric rates, high system capital costs, and operating costs. Gasification to fuel cells or microturbines could compete if capital costs approached < \$1000/kW and systems could be completely automated. The results of a study comparing the costs of gasifiers coupled to various fuel cells and a Flex-MicroturbineTM are presented. The capital cost of the systems studied ranged from \$1300 to \$4450/kW, with the Flex-MicroturbineTM and molten carbonate fuel cell systems having the lowest capital and operating costs.

Introduction

The U.S. Department of Energy's (DOE's) Hydrogen Program mission is to enhance and support the development of cost-competitive hydrogen technologies and systems that will reduce the environmental impacts of energy use and enable the penetration of renewable energy into the U.S. energy mix. To achieve this mission, the Hydrogen Program has four strategies, which include 1) expanding the use of hydrogen, 2) developing storage and generation technologies, 3) demonstrating hydrogen vehicles and fueling systems, and 4) lowering the cost of technologies that produce hydrogen directly from sunlight. The project described here was supported by DOE's Hydrogen Program to complete systems analysis for information dissemination and outreach.

Hydrogen is one of the most promising energy carriers for the future. It is an energy-efficient, low-polluting fuel. When hydrogen is used in a fuel cell to generate electricity or is combusted with air, the only products are water and a small amount of NO_x . Hydrogen is renewable and found in many compounds such as water, fossil fuels, and biomass. Hydrogen typically makes up about 6% by weight of dry biomass. Using biomass for energy results in lower emissions than using fossil fuels. Carbon dioxide is continuously recycled as biomass in the form of trees and other plants that use it to regenerate, and lower emissions of sulfur and NO_x can be expected when converting woody biomass in comparison to coal. To obtain hydrogen from biomass, pyrolysis or gasification must be applied, which typically produces a gas containing 20% hydrogen by volume, which can be further steam-reformed to make higher-purity streams for various fuel cells. The challenge is to overcome the economic barriers that current technology presents for converting biomass to hydrogen for use in clean, efficient energy conversion devices. The following analysis compares technologies, approaches, and costs for near-term small biomass gasification power technologies.

Design Criteria and Discussion

This analysis examines the concept of using biomass gasification in conjunction with microturbines or fuel cells to generate electricity for on-farm installations. The biomass farm feedstock would be either switchgrass or wood. The project decisions involve selecting size range, gasifiers, gas preparation equipment, and prime movers to analyze and compare. The purpose of the comparison is to identify challenges for technologies in this area.

The following are the basic drivers in the decision-making process:

- Resource availability
- On-farm energy use
- Technology status
- Cost

Information was collected to assess resource availability for small farming operations. It was assumed that dairy farms would most likely be the highest users of electricity, since refrigeration equipment is required to be operated around the clock for most of the year. Large dairy farms may house 2000 head of cattle, and small farms have lately trended toward about 500 milking head; however, the average is approximately 250 head. Resource availability is based on the number of cattle. Land ownership for dairy farms is typically an acreage 4 times the amount of cattle. The expected electrical use of a dairy farm is about 440 kWh/cow (University of Vermont Extension Service 1999). This equates to a 12.6-kW average annual load. According to Vogel and Masters (1998) the most productive switchgrass species can yield 12,500 lb/acre/year of product. Similar production rates have also been found for fast-growing willow species. A typical small biomass gasification power plant will consume 2 lb/hr/kW_e (Schmidt et al. 1998). Table 1 shows the various land area requirements of a dedicated biomass energy crop relative to total farm acreage and cattle population.

Table 1. Resource Availability for Energy Crop Power Production

| No. of Cows | Total Land Area (acres) | Annual Electricity Use (kWh) | Average Load (kW) | Land Required for Biomass Energy Crop (acres) |
|-------------|-------------------------|------------------------------|-------------------|---|
| 250 | 1000 | 110,000 | 12.6 | 17.6 |
| 500 | 2000 | 220,000 | 25.1 | 35.2 |
| 1000 | 4000 | 440,000 | 50.2 | 70.4 |
| 2000 | 8000 | 880,000 | 100.5 | 140.8 |

In general, individual on-farm electricity demand is relatively low (12 kW). Although the data in Table 1 suggest using very small power plants, commercial stationary power generation fuel cells are typically only available in the 200-kW size range. Proton-exchange membrane (PEM) fuel cells are being developed at smaller power levels for residential markets and the automotive industry, and may become good options; however, they require a higher level of gas purity. Commercial microturbines are available as 30-kW units. Given the status of current technology, the authors chose to compare all technologies at the 200-kW size. Some additional cases are also presented to show the potential of PEM technology in the smaller size ranges. In order to supply a 200-kW power plant, approximately 250 acres of land would be required.

Flex-Microturbine™

In the past, the primary technology focus for conversion of hydrogen to electricity has been the fuel cell. Fuel cells are promising, but currently expensive. They require extremely high-purity hydrogen, which is also expensive to produce. According to Prabhu et al. (1998), an innovative new approach is to use the Flex-Microturbine™ that will accept low-pressure fuel of significantly lower purity and concentration, would require much less capital, is closer to commercialization, and could stimulate hydrogen use in a shorter time frame than fuel cell technology. This investigation looks at whether the increased efficiency of fuel cells can offset the capital investment in the required gas-cleaning equipment.

Microturbines are already available commercially, with prices expected to drop sharply. They are currently designed to work on natural gas, not hydrogen. With key modifications, including a catalytic combustor, the microturbine could be converted into a Flex-Microturbine™, which is much more fuel flexible and capable of running on a whole range of hydrogen fuel gases with much lower purity than required by fuel cells. Figure 1 illustrates the Flex-Microturbine™ concept.

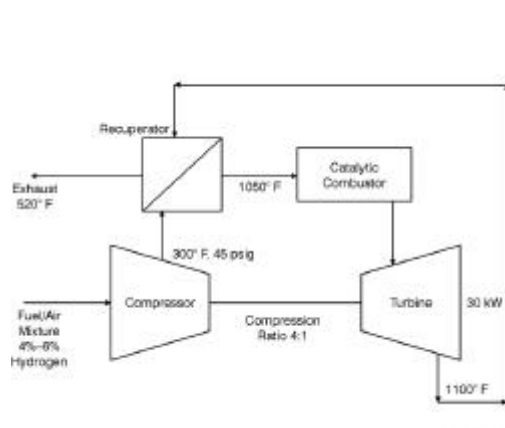


Figure 1 – Flex-Microturbine™

Fuel Cell Technology

Currently there are four basic types of fuel cells that can or have potential use with biomass gasification. They are characterized in terms of their electrolyte component and include PEMs, (also referred to as polymer electrolyte fuel cells), phosphoric acid fuel cells (PAFCs), molten carbonate fuel cells (MCFCs), and solid oxide fuel cells (SOFCs).

The PEM fuel cell electrolyte is a thin polymer. This semipermeable membrane allows protons to pass, but insulates the electrical contacts. The cell operates at a low temperature, approximately 80°C (175°F). A PEM fuel cell's output can vary quickly, making it well-suited for automobile applications and residential and commercial buildings. PEM technology is commercially available in the smaller size ranges, typically under 10 kW. Efficiency is 30%–35%. The costs of PEM fuel cells are expected to decrease sharply as applications occur in the automotive industry. Daimler Chrysler's NECAR fuel cell engine costs \$30,000 or approximately \$600/kW. Mass-produced automotive internal combustion engines typically sell for \$3000. Ballard is developing a 250-kW stationary unit currently in field trials. The capital cost target is \$1000–\$2000/kW.

PAFC technology is available commercially and being used in many applications, including buses and stationary power. Reliability averages over 96%. Electrical generation efficiency is typically 36%. Stationary units can be provided at 200 kW that operate on natural gas. A typical unit installation cost is \$850,000, and a \$1,000/kW federal rebate can be obtained. Costs are approaching \$2000/kW. The PAFC operates at 200°C (392°F), and uses a phosphoric acid electrolyte. ONSI corporation has sold over 200 units.

MCFCs technically offer the best potential to be coupled with large coal and biomass gasification processes. MCFCs can be built from stainless steel and less exotic materials than their SOFC counterpart. The cell can accept carbon monoxide and tolerate carbon dioxide. Carbon dioxide is used in the cathode reaction and obtained from the output of the anode reaction. The fuel cell operates at 650°C (1200°F), and offers the highest efficiency capability of all fuel cell types (45%–55%). MCFCs have been installed in several demonstration projects around the world, but are not commercially available products. Fuel Cell Energy is developing its Model 9000 fuel cell and demonstrating 250-kW stationary fuel cell stacks. A current MCFC would cost as high as \$8000/kW.

SOFCs also show good promise for high efficiencies. The cell operates at 1000°C (1800°F), and uses a solid yttria-stabilized zirconia electrolyte. This allows for the hard ceramic electrolyte to be formed in a tubular arrangement rather than a flat plate, which is difficult to seal at the ends. The SOFC is fuel-flexible, much like the MCFC, but will probably be geared toward large generation applications to be economically attractive because of the relative cost of the high-temperature materials. A lower-temperature 660°C (1220°F) SOFC is also under development. Siemens Westinghouse has demonstrated 100-kW stacks; however, costs remain high and proven operational time has been minimal.

All of the technologies mentioned above are essentially the same in several respects. They are all electrochemical devices that convert the chemical energy of reaction directly into electrical energy. They consist of an anode, cathode, and electrolyte. They continuously use fuel, primarily hydrogen, and air (oxygen) in a reverse electrolysis manner to produce electricity. These technologies differ in their electrochemical reactions, materials of construction, tolerance to contaminants, fuel flexibility, and operational characteristics. These characteristics, briefly described above, vary the application of the technologies and cost. Tables 2–4 below delineate the different characteristics of PEM, PAFC, MCFC, and SOFC technologies.

Table 2. Various Fuel Cell Technologies and Characteristics

| Fuel Cell Technology | Electrolyte | Anode | Cathode | Operating Temperature | Electrical Efficiency |
|----------------------|---|----------|------------------------------|-----------------------|-----------------------|
| PEM | Ion-exchange membrane, hydrated organic polymer | Platinum | Platinum | 175°F | 30%–35% |
| PAFC | Phosphoric acid | Platinum | Platinum | 392°F | 35% |
| MCFC | Molten Li/Na/K carbonate | Nickel | Nickel oxide | 1200°F | 45%–55% |
| SOFC | Yttria-doped zirconia | Nickel | Sr-doped lanthanum manganite | 1800°F | 45%–47% |

Table 3. Electrode Reactions for Various Fuel Cells

| Fuel Cell | Anode Reaction | | Cathode Reaction | |
|-----------|--|--|---|------------------|
| PEM | H ₂ | 2H ⁺ + 2e ⁻ | ½ O ₂ + 2H ⁺ + 2e ⁻ | H ₂ O |
| PAFC | H ₂ | 2H ⁺ + 2e ⁻ | ½ O ₂ + 2H ⁺ + 2e ⁻ | H ₂ O |
| MCFC | H ₂ + CO ₃ ²⁻ CO + CO ₃ ²⁻ | H ₂ O + CO ₂ + 2e ⁻ 2CO ₂ + 2e ⁻ | ½ O ₂ + CO ₂ + 2e ⁻ CO ₃ ²⁻ | |
| SOFC | H ₂ + O ²⁻ CO + O ²⁻ CH ₄ + 4O ²⁻ | H ₂ O + 2e ⁻ CO ₂ + 2e ⁻ 2 H ₂ O + CO ₂ + 8e ⁻ | ½ O ₂ + 2e ⁻ | O ²⁻ |

**Table 4. Contaminants and Poisons for Various Fuel Cells
(Hirschenhofer et al. 1998)**

| Gas Species | PEMFC | PAFC | MCFC | SOFC |
|--------------------------------------|-----------------------|---------------------|----------------------|----------------------|
| H ₂ | Fuel | Fuel | Fuel | Fuel |
| CO | Poison (>10ppm) | Poison (>0.5%) | Fuel | Fuel |
| CH ₄ | Diluent | Diluent | Diluent | Fuel |
| CO ₂ and H ₂ O | Diluent | Diluent | Diluent | Diluent |
| S as (H ₂ S and COS) | No studies to date | Poison (>50 ppm) | Poison (>0.5 ppm) | Poison (>1.0 ppm) |

Approach

Various methods were analyzed for producing power from biomass gasification. Four prime mover technologies were compared, including the Flex-MicroturbineTM, PEM fuel cell, PAFC, and MCFC. Two gasification technologies were also used in the analysis. Considering the various purity requirements, it appears that the Flex-MicroturbineTM, PAFC, and MCFC would couple well to a small downdraft gasifier. Downdraft gasifiers are relatively simple, low-cost, low-pressure devices, which produce relatively clean gas suitable for power generation. Figure 2 is a schematic of a downdraft gasifier system, and Table 5 compares gasification technologies and gas contaminant levels.

PEM fuel cells have the advantage of becoming the first mass-produced low-cost fuel cells in the marketplace, a good reason for considering this technology. In order to link a gasifier to PEM fuel cell technology, the fuel gas must be high-purity hydrogen. The Battelle indirectly heated biomass gasifier applies well to PEM technology. As compared to direct gasification, which produces a high-nitrogen-content gas stream, the indirect process enables production of a gas stream consisting primarily of carbon monoxide, hydrogen, methane, and carbon dioxide. This gas can be steam-reformed and catalyzed to produce a 62% hydrogen-rich gas. This gas is then run through a pressure swing absorption unit to separate the hydrogen.

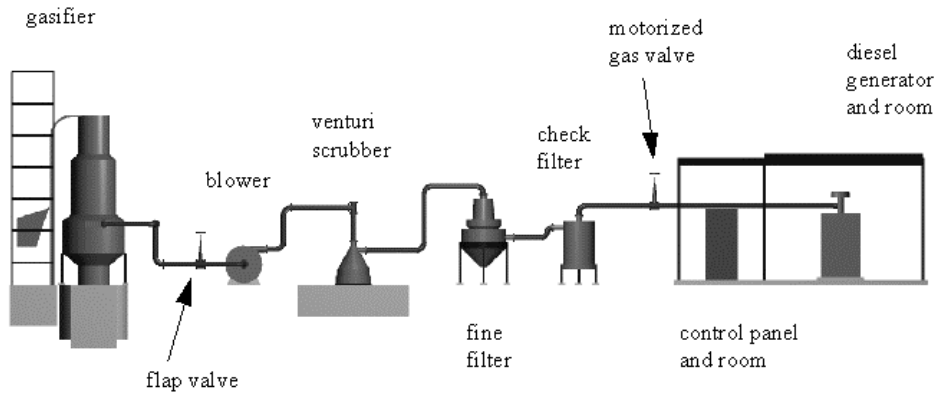


Figure 2 – Downdraft Gasification System

Table 5. Gasifier Contaminant Loadings

| Gasifier Type | Tar Production | Relative Particulate Loading |
|---------------|--------------------|------------------------------|
| Updraft | 50,000–200,000 ppm | Intermediate |
| Downdraft | 100–1000 ppm | Low |
| Fluidized Bed | 1000–50,000 ppm | High |

Analysis

Flex-Microturbine™

The Flex-Microturbine™ power system concept consists of the components shown in Figures 1 and 2. A small, simple downdraft gasification system is coupled to a microturbine that houses a small catalytic combustor (DeLaquil 1999). The catalytic combustor enables the microturbine to operate directly on low-Btu, low-pressure gas. An air–fuel mixture is induced through the compressor side of the turbine, then converted catalytically in the turbine and expanded through the power side of the turbine. This concept is currently being developed by Flex-Energy through DOE’s small modular biomass program. Capital and operating costs are compared in Tables 6 and 7, respectively.

Battelle Indirect Gasifier PEM Fuel Cell

Briefly described, the Battelle system gasifies biomass by injecting steam and recycling hot sand from a char combustion unit. The initial gas contains about 20% hydrogen. This gas is then scrubbed, pressurized, steam-reformed, shift-reacted, cooled, and purified in a pressure swing absorption unit. The steam used for gasification is created from process waste heat. The reformed gas contains 62% hydrogen and is purified for use in a PEM fuel cell. A complete description of the Battelle indirectly heated gasifier for producing hydrogen can be found in Mann (1995). This report gives process flow information, capital, and operating costs. Three systems, 1000-, 300-, and 30-tpd, are described in the report. The 30-tpd system is equivalent to a 750-kW gasifier fuel cell power system. Component cost curves were generated on the basis of the given data and used to estimate system costs below 30 tpd. The results are shown in Tables 6 and 7. PEM fuel cell costs are estimated at \$600/kW, which could be expected within the next 5 years.

Table 6. Capital Cost Comparison

| Capital Cost Comparison | Battelle PEMFC System | | | Flex-Microturbine | | MCFC | PAFC |
|---|-----------------------|------------|------------|-------------------|-----------|------------|------------|
| | 30 tpd | 8 tpd | 0.5 tpd | 5.4 tpd | 0.7 tpd | 2.8 tpd | 3.6 tpd |
| Plant size biomass feed rate | 30 tpd | 8 tpd | 0.5 tpd | 5.4 tpd | 0.7 tpd | 2.8 tpd | 3.6 tpd |
| Hydrogen production | 31,773 scfh | 8,473 scfh | 530 scfh | | | | |
| Power output | 754 kW | 201 kW | 13 kW | 210 kW | 27 kW | 200 kW | 200 kW |
| Gasification System Installed | \$ 655,964 | \$ 260,051 | \$ 37,340 | \$ 126,000 | \$ 16,200 | \$ 160,000 | \$ 200,000 |
| Gas Preparation & misc. Catalyst Module | \$ 804,567 | \$ 296,977 | \$ 46,596 | \$ 21,000 | \$ 2,700 | \$ 75,000 | \$ 233,000 |
| PSA system Installed | \$ 812,926 | \$ 216,784 | \$ 13,549 | | | | |
| PEMFC (projected \$600/kW) | \$ 452,400 | \$ 120,600 | \$ 7,800 | | | | |
| Microturbines @ \$600/kW | | | | \$ 126,000 | \$ 16,200 | | |
| MCFC & PAFC fuel cell @ \$2000/kW | | | | | | \$ 400,000 | \$ 400,000 |
| total | \$ 2,725,857 | \$ 894,412 | \$ 105,285 | \$ 273,000 | \$ 35,100 | \$ 635,000 | \$ 833,000 |
| Power system \$/kW Y2000 | \$ 3,615 | \$ 4,450 | \$ 8,099 | \$ 1,300 | \$ 1,300 | \$ 3,175 | \$ 4,165 |

Table 7. Operating Cost Comparison

| Operating Cost Comparison | Battelle PEMFC System | | | Flex-Microturbine | | MCFC | PAFC |
|------------------------------|-----------------------|-----------|-----------|-------------------|-----------|-----------|-----------|
| | 30 tpd | 8 tpd | 0.5 tpd | 5.4 tpd | 0.7 tpd | 2.8 tpd | 3.6 tpd |
| Plant size biomass feed rate | 30 tpd | 8 tpd | 0.5 tpd | 5.4 tpd | 0.7 tpd | 2.8 tpd | 3.6 tpd |
| PEM fuel cell output | 754 kW | 201 kW | 13 kW | 210 kW | 27 kW | 200 kW | 200 kW |
| Capacity Factor | 0.9 | 0.9 | 0.9 | 0.9 | 0.9 | 0.9 | 0.9 |
| Electricity @ \$0.05/kWh | \$ 165,279 | \$ 39,246 | \$ 2,471 | \$ 8,278 | \$ 1,064 | \$ 7,884 | \$ 7,884 |
| Water | \$ 3,250 | \$ 771 | \$ 49 | \$ 50 | \$ 10 | \$ 1,000 | \$ 2,000 |
| Sand @ \$7.00/ton | \$ 5,878 | \$ 1,394 | \$ 88 | | | | |
| Catalyst | | | | \$ 1,000 | \$ 1,000 | \$ 2,000 | \$ 2,500 |
| PSA operating cost | \$ 5,284 | \$ 1,255 | \$ 298 | | | | |
| Labor, operators | \$ 30,595 | \$ 30,595 | \$ 30,595 | \$ 30,595 | \$ 30,595 | \$ 30,595 | \$ 30,595 |
| Total Annual Cost | \$ 210,285 | \$ 73,261 | \$ 33,501 | \$ 39,923 | \$ 32,669 | \$ 41,479 | \$ 42,979 |

Downdraft Gasifier – Molten Carbonate Fuel Cell Process Options

The MCFC is technically well suited for use with gasification technology. The MCFC can use both carbon monoxide and hydrogen as a fuel, which typically comprises 35% to 40% of a syngas stream. Sulfur in the gas is the major contaminant that presents difficulty in utilizing a MCFC. Several systems were considered for preparing syngas from a downdraft gasifier. Although wood fuel typically contains very low sulfur levels, each system included sulfur removal, tar removal/conversion, and particulate removal. The downdraft gasifier does not favor tar production, as product gases generally contain between 100 and 1000 ppm tars. However, all tars must be removed or converted so that blinding of catalyst and particulate collection surfaces

is avoided. Particulates are expected to be present in the product gas as ash and char, with a size distribution from 1 μm to greater than 100 μm .

Hot-gas cleanup, cold sulfur removal, and activated carbon systems for preparing syngas produced by a downdraft gasifier for use in a molten carbonate fuel cell were considered. Hot-gas cleanup appeared to be the most attractive option on the basis of cost and operating conditions. Hot product gases exit the gasifier at approximately 1400+ F and pass through a fluid-bed tar cracker (with steam injection) to convert both tars and unreacted char contaminants to H_2 , CO , and light hydrocarbons. The refractory-lined fluid bed contains a zeolite catalyst that has been shown to provide excellent conversion of tars at high temperature as well as improved stability of the bed material relative to the degradation observed with dolomite catalysts (Milne et al. 1998, Timpe 1995). A cyclone is used to return catalyst material that is carried over with the gas stream. A portion of the CO stream will be converted in the tar cracker to H_2 and CO_2 . Design and operation are consistent for conversion of tars at the 1000-ppm level, and it is expected to be marginally effective in converting CO . The hot gases then pass through a heat exchanger to control gas temperature to approximately 1000 F prior to entering the hot-gas filter. The lower temperature allows condensation of all vapor-phase alkalis such as potassium that may be present in the gas stream following the tar cracker. The filter vessel uses a metallic tube sheet to support ceramic candle filters for removal of particulates. Cleaning is achieved by backpulsing. The clean product gas then passes through a packed bed of zinc-based sorbent to remove sulfur species. The bed operates at a temperature of approximately 1000 F. Beds of ZnO doped with either iron, copper, or titanium have proven highly effective for removal of sulfur species (Pineda et al. 2000, Jothimurugesan et al. 1995). These beds can be regenerated by high-temperature oxidation for reuse upon sulfur breakthrough. However, the effectiveness decreases after three to five regeneration cycles and may be subject to replacement on a regular basis. Certainly, lower sulfur contents of the primary fuel will extend the life of the sorbent. After passing through the sorbent bed, the clean gas passes through the heat exchanger preceding the hot-gas filter to reheat the gases to 1200 F before entering the molten carbonate fuel cell stack.

Two potential cold-gas cleaning strategies were considered; however, costs were 12% higher than the hot-gas cleanup option. The systems considered included low-temperature sulfur removal and activated carbon cleanup. The low-temperature sulfur removal system was similar to the above process using a fluid-bed tar cracker followed by venturi scrubbing and hydrodesulfurization. The activated carbon process takes advantage of char produced by the gasifier to use in the removal of tars and sulfur compounds. A venturi scrubber would be followed by two packed beds containing active carbon. The clean product gas would be reheated to 1200 F for feed to the MCFC. Additional heating could be achieved by combustion of gasifier char and spent carbon sorbent.

Gasifier–Phosphoric Acid Fuel Cell

The PAFC can use only hydrogen as a fuel and can tolerate CO at levels approaching 5000 ppm. The PAFC operates at a temperature of about 400 F. Product gas from the down-draft gasifier must be cleaned to remove particulate, tars, and sulfur compounds and requires the conversion of CO to H_2 and CO_2 by steam shift reaction.

The gas preparation approach considered here is similar to the MCFC hot-gas cleanup system described above. Removal of tars, particulate, and sulfur are accomplished by high-temperature catalytic cracking of tars, hot-gas filtration of particulates, and high-temperature sulfur reduction by zinc oxide/zinc titanate sorbents. The clean product gas is then reheated to 1400 °F by heat exchange with product gas supplemented with combustion of gasifier char and makeup natural gas. These hot gases are then moved through a nickel-based catalyst bed to convert any remaining CO. The product gases then pass through a heat recovery steam generator to produce steam for tar cracking and CO conversion, reducing the gas temperature to 400 °F for use in the PAFC.

Conclusion

The results of this study are provided in Tables 6 and 7. The primary capital and operating costs for each small gasification power system are shown for various plant sizes. The size chosen for direct comparison between systems is 200 kW. In the case of the Battelle PEM fuel cell system, 754- and 13-kW systems are shown. The 754-kW system represents the actual data provided by Mann (1995) and is adjusted to year 2000 dollars. The 13-kW system was extrapolated from cost curves and shows the cost for a system designed to match the typical load of a 1000-acre dairy farm. The costs show that for any small system (approximately 13 kW), complete automation is a must to realize any return on investment. In the case of the Flex-Microturbine™, a 27-kW system is shown because that is the size of a Capstone microturbine unit. Flex-microturbine systems would be modular in construction, therefore costs scale linearly. Only the most cost-effective MCFC and PAFC options are presented in the tables.

The Flex-Microturbine™ system appears to be the most cost-effective system when compared at 200 kW. This was the expected outcome of the study. However, the purpose for comparison is to show advanced small power system concepts for biomass gasification and to compare fuel cell systems in order to set cost goals and show where advances must be made in order for fuel cells to compete.

Comparing fuel cell systems overall, the MCFC system (\$3200/kW) appears to be more cost-effective than the PAFC system (\$4200/kW) or the Battelle PEM system (\$4450/kW). However, only PAFC and PEM are commercially available at this time. It should be noted that costs for both the MCFC and the PAFC are shown at \$2000/kW. MCFC cost targets are \$1200/kW, and current costs are between \$4000 and \$8000/kW. The most significant cost barrier for MCFC systems is the cost of the fuel cell. If fuel cell manufacturers can hit cost targets, further reductions will need to occur in the gas preparation area. PAFC suffers the same constraint, with additional gas preparation requirements. PEM is discussed below. The higher efficiency of the MCFC system, which means lower gas volumes and lower fuel requirements, provides for a more competitive cost scenario. Operation of each system is expected to require a single person working an 8-hour shift each day. Labor is the primary operational cost for each system, at approximately \$30,600 per year. Automation or applications in which operational costs are minimal are paramount for improving return on investment for small power systems.

Attempting to purify syngas for use in a PEM fuel cell is cost-prohibitive for this type of power system. Gasification system costs, gas preparation costs, and the pressure swing absorption

(PSA) system costs outweigh any gains in lowered fuel cell costs. However, for larger-scale power production (over 1 MWe), the costs improve. High-volume sources of biomass may be well suited for the installation and operation of a Battelle PEM fuel cell power system.

The Flex-Microturbine™ system represents an advanced power generation concept for small biomass gasification. Costs are relatively competitive with gasifier internal combustion engine systems. The primary cost factor is the microturbine, which is expected to decrease in the future. The costs provided in these tables were intended for comparison purposes. Fuel cost was not included. A final report to DOE is due September 30, 2000, and will include all references to cost figures.

References

DeLaquil, P. III, and F.S. Fische. 1999. "Installation, Operation, and Economics of Biomass Gasification System in Indonesia." In *Proceedings of the Fourth Biomass Conference of the Americas*, Vol 1. 1087–1092. Oxford, UK: Elsevier Science Ltd., Kidlington.

Hirschenhofer, J.H., D.B. Stauffer, R.R. Engleman, and M.G. Klett. 1998. *Fuel Cell Handbook, 4th Ed.*, DOE/FETC-99/1076 for Contract No. DE-AC21-94MC31166. Reading, PA: Parson Corporation.

Jothimurugesan, K., A.A. Adeyiga, and S.K. Gangwal. 1995. *Simultaneous Removal of H₂S and NH₃ in Coal Gasification Processes*, DOE report for Contract No. DE-FG22-93MT93005. Hampton, VA: Hampton University Department of Engineering.

Mann, M.K. 1995. *Technical and Economic Assessment of Producing Hydrogen by Reforming Syngas from the Battelle Indirectly Heated Biomass Gasifier*, NREL.

Milne, T.A., N. Abatzoglou, and R.J. Evans. 1998. *Biomass Gasifier "Tars": Their Nature, Formation, and Conversion*, NREL Technical Report TP-570-25357. Golden, CO: National Renewable Energy Laboratory.

Pineda, M., J.M. Palacios, L. Alonso, E. Garcia, and R. Moliner. 2000. "Performance of Zinc Oxide Based Sorbents for Hot Coal Gas Desulfurization in Multicycle Tests in a Fixed-Bed Reactor." *Fuel*, 79 (8): 885–896.

Prabhu E., V. Tiangco, et al. 1998. "Microturbines: New Hope for Electricity from Biomass?" In *Proceedings of the Bioenergy 98' Conference*.

Schmidt, D.D., C.R. Purvis, and J.G. Cleland. 1998. "Biomass Power Plant Demonstration at Camp Lejeune." In *Proceedings of the Bioenergy 98' Conference*.

Timpe, Ronald C. 1995. *Energy and Environmental Research Emphasizing Low-Rank Coal – Task 3.9 Catalytic Tar Cracking*. DOE Topical Report for Contract No. DE-FC21-93MC30097. Grand Forks, ND: University of North Dakota.

University of Vermont, The Extension Service. *The Dairy Farm Energy Book*.
http://www.inform.umd.edu/EdRed/Topic/AgrEnv/ndd/faciliti/THE_DAIRY_FARM_ENERGY_BOOK_PART_1_OF_3.html, accessed December 1999.

Vogel, K.P, and R.A. Masters. 1998. "Developing Switchgrass into a Biomass Fuel Crop for the Midwestern USA." In *Proceedings of Bioenergy '98 Conference*.

COMMERCIAL APPLICATIONS OF FUEL CELLS AT BILLINGS

Terry R. Galloway & Joseph Waidl
Intellergy Corp.
6801 Sherwick Drive
Berkeley, CA 94705-1744

Cheryl Heath
Center For Applied Economic Research
Montana State University, Billings, MT 59101

Lynn Ratcliff
Big Sky Economic Development Authority
222 North 32nd Street, Billings, MT 59101-1911

Abstract

This fuel cell project at Billings involves four components of programs: (1) Residential Housing, (2) Remote Rural Energy, (3) Commercial Facilities, and (4) Major Power Generation. As an umbrella to all of these programs the Center For Applied Economic Research – Montana State University, Billings provides current marketing and business economic background support as well as project economic payback analysis.

This paper will focus on the last two programs that are of special interest to DOE's Hydrogen Programs. Regarding Commercial Facilities, the program involves the implementation of a demonstration commercialization project in a local Billings hospital that involves steam-reforming of medical red-bag and other wastes to produce hydrogen-rich syngas that will drive a molten carbonate fuel cell that will provide production of electrical power, steam, and space heating. Regarding Major Power Generation: A Feasibility Study was recently completed that has shown that the repowering of the 163 MWe J. E. Corette coal power plant is economically attractive with a simple payback of 5 years when it takes advantage of high temperature fuel cells, particularly the Siemens/Westinghouse solid oxide fuel cells, to increase electrical generation efficiency. A Texaco gasifier can accept Conoco Refinery wastes and produce syngas (a mixture of hydrogen

and carbon monoxide) which is then converted into heavy paraffins that are returned to Conoco where they are converted to middle distillates and used as blending stock to improve the refinery output and produce low sulfur fuels. Hydrogen is produced from the syngas as an important product that is also sent to Conoco. The gasifier will also produce high quality steam to be augmented by steam from the fuel cell waste heat boilers to drive the Corette steam turbine-generator system.

Introduction

It has been said, “*the area that develops fuel cell technology will be the Silicon Valley of the 21st Century*” – certainly, the Billings, Montana region could fit the bill. Since this project has started, the amount of fuel cell business activity has increased tremendously at Billings. CTA Architects Engineers has directed their efforts toward the Commercial Facilities markets and has started design/planning work at Deaconess Medical Center, St. Vincent Hospital, Montana State University, and several businesses as well as an exciting project that plans an entirely new town in remote Montana that plans to be a model for energy efficiency and sustainability. These projects involve very large numbers of fuel cells, which will help reduce unit costs from the increased manufacturing level to approach the needed economy-of-scale commercial activity.

Power Generation needs in the area are supplied by a 1967 vintage, 33% efficient, 163 MWe, J. E. Corette coal power plant. The use of this plant has been less than desirable in the community because of its air emissions and use of out-of-state coal as feedstock. Our concept is to upgrade this coal plant to a first-of-its-kind coal plant of the future, where local coal can be fully utilized as an important energy and chemical resource without emissions of carbon dioxide (CO₂) and without the typical problems of NO_x, SO_x, VOCs, and other particulate emissions.

The plant upgrade conceptual design includes the use of several advanced technologies, most of which have been proven individually, but which have never been integrated into a single system. The Texaco gasifier would be located at the Corette site or an adjacent site where the coal feedstock, co-mixed with Conoco's petroleum coke, API separator bottoms, DAF float, and possibly other minor industrial/municipal waste, would be gasified to produce syngas and steam. Some of this syngas would be fed into a solid oxide fuel cell/turbo-electric generator system to produce electricity.

Royal Dutch Shell and Texaco are two well-known examples of organizations in the petroleum industry that have built, installed and operated full-scale gasification units as front ends to refineries and power plants. In addition, Intellergy has direct experience with steam-reforming waste products at Westinghouse's Oak Ridge, Tennessee commercial facility.

Two examples of fuel cells that can accept syngas are the Solid Oxide Fuel Cell and the Molten Carbonate Fuel Cell. Siemens/Westinghouse and others have made great progress with recent developments in Solid Oxide Fuel Cells (SOFCs) that can use syngas for this project.

The efficiency of the proposed plant would be around 68%, which would double the current plant's efficiency of 33%. This will allow the plant to produce the same electrical output of 163 MWe, while producing additional hydrogen for Conoco and syngas for fuel cells to produce more

electrical power and fully utilize the turbo-generator system capacity. Additional syngas is reacted over a Fischer-Tropsch catalyst to form higher hydrocarbons, such as heavy paraffins or waxes or other useful hydrocarbon products. These waxes, for example, form a feedstock to the Conoco gas-oil hydrotreater plant functioning as a moderate pressure hydrocracker where they are reacted to form low sulfur, high cetane diesel fuel, kerosene, and naphtha. Additional "Premium Power" would be supplied across the fence to Conoco that has higher quality specifications and high reliability (almost uninterruptible).

The production of some hydrocarbon products, like middle distillates, is necessary in order to utilize the feed carbon source so as to eliminate any carbon dioxide emission. With a mass feed rate to the plant of 2160 tons/day, the middle distillate production would be around 8,250-barrels/day while Corette's electrical power output would still be at 163 MWe.

Another parallel effort is to implement a demonstration commercialization project in a local Billings hospital that involves steam-reforming of medical red-bag and other wastes to produce hydrogen-rich syngas that will drive a molten carbonate fuel cell that will provide production of electrical power, steam, and space heating.

Discussion

The Center For Applied Economic Research – Montana State University has set the stage of the business environment with a resource inventory of electrical generation and distribution in Montana and Wyoming. It is important to understand how electricity is supplied to consumers in order to apply fuel cell technology efficiently and effectively in the future. A detailed market analysis and survey of the rural electric cooperatives in Montana and Northern Wyoming was prepared in the belief that they represent a large potential market for fuel cell technology in the Yellowstone Region.

The second part involves an economic analysis that first focuses on PEM fuel cell manufacturers. Although response to our mail survey by these manufacturers was nil, the information we obtained from follow-up telephone conversations was enlightening. While it is likely that the average cost of the initial PEM residential fuel cell systems will be around \$10,000 installed, this cost must decrease significantly in order to be cost effective for the consumer, to under \$4,000. Full commercialization is projected for 2003 to 2004, but this date could be pushed back as it has in the past. One of the major challenges that these PEM developers face is that there are not many companies that manufacturer parts and materials for PEM fuel cell systems. The developers often use in-house engineers to design parts for their test systems, and then go to the marketplace to find a vendor to manufacture the parts for production. This definitely presents an opportunity for the Billings region to manufacture parts for or to assemble PEM fuel cell systems. The obstacle we face is getting information from the PEM developers, as competition is fierce and they are hesitant to disclose too much information.

We studied related fuel cell organizations, and had the opportunity to visit two fuel cell research centers: The National Fuel Cell Research Center in Irvine, California and The Desert Research Institute in Reno, Nevada. These visits were very helpful and afforded us the opportunity to visit with the each center's director, who will be a good resource as this project continues.

We have provided some information on the net metering laws in Montana. The Montana legislature believes that it is in the best interest of the public to promote net metering because it encourages private investment in renewable energy resources, stimulates Montana's economy, and enhances the diversification of the energy resources in the State. However, the current PSC code would have to be modified slightly to allow an individual to actually sell their excess electricity rather than just receive a credit for it. Given the legislature's beliefs, one would think that this is possible, particularly with the many economic benefits that fuel cells could provide to the Yellowstone Region.

The Feasibility Study centers on Intellergy's concept for the re-powering of the Corette Power Plant in Billings. We are finalizing a detailed net present value and payback period analysis of the revenues and costs for this project. Both the NPV and payback period are encouraging.

We have compiled statistics on the 1,177 coal fired electrical generating units throughout the United States. Coal plants represent the largest generating capacity in the U.S., and have a median and average age of 25, and 24 years, respectively. Coal is an important national resource. With coal consumption by the electric power industry at 90% of the U.S. total coal production, coupled with the increasing energy demands of the nation, coal-fired utility plants will not disappear anytime soon.

In 1997, coal-fired units at electric utilities accounted for 72% of the country's carbon dioxide emissions, 80% of the country's nitrogen oxide emissions, and 86% of the country's sulfur dioxide emissions. Intellergy's concept for the Corette re-powering project in Montana provides a unique opportunity to upgrade a typical old coal plant to a new state-of-the-art coal plant where coal is utilized as an important energy resource without emissions of CO₂, and without the typical problems of NO_x and SO₂ emissions. The opportunity to package this concept and apply it to other coal-fired electric plants across the country is immense. We have quantified an estimated dollar value for each state if they reduce CO₂, NO_x and SO₂ emissions by just 50%, and the potential dollar benefits alone appear to be enough to pay for the technology/equipment in many instances. In the next phase of the project, we will begin to look at some individual coal-fired electrical generating plants around the country and prepare a cost-benefit analysis for re-powering these plants.

Currently, we are conducting two market studies – one of residential consumers and one of institutional consumers. The residential market study is a telephone survey of Yellowstone Valley Electric Cooperative customers, and we expect to have approximately 500 responses to analyze. The institutional survey is directed at hospitals of varying size throughout Montana, and we will contact as many of the 60+ hospitals as time allows. We can continue this study of hospital power requirements, as the Montana Society of Healthcare Engineering's quarterly meeting will be in Billings this September. This society's membership is made up of the facility service directors at Montana hospitals.

For Power Generation, we focus on the 1967 vintage, 33% efficient, 163 MWe Corette coal power plant. This petroleum coke/coal-steam-reforming/gasification project will require that the fuel cell type accept carbon monoxide and other light hydrocarbons in addition to the normal hydrogen. This requirement almost guarantees that the only two types to be considered are Solid Oxide Fuel Cells (SOFCs produced by Siemens Westinghouse Power Corp. (SWPC) [1-3] or Technology

Management, Inc.) or Molten Carbonate Fuel Cells (MCFC) [4]. We estimate that about 56 0.5 MWe AC fuel cells units can be powered at maximum by the 1379 tpd or 1900 lbs/min syngas generated from the coal feed stream, assuming around 85% coal to chemicals utilization and an electrochemical 68% fuel cell/turbo-generator efficiency [5-7]. This is 6.93 kW/scfm of H₂, which is much higher than the strictly electrochemical phosphoric acid fuel cell at 4 kW/scfm of H₂ (which cannot use CO in the syngas).

We envisage a four-phase program that begins with a single natural gas-fed 250 kWe fuel cell at atmospheric pressure that provides dc electrical power to an inverter and also a hot exhaust gas stream that can drive a waste heat boiler to raise up to 130 kWt (0.44 x10⁶ Btu/hr), 1005°F, 1950 psig steam for the Westinghouse steam turbine-generator system rated at 192MWe. The second phase would add additional natural gas-fed, commercially-priced SOFC fuel cells (maybe in 250 kW or 1 MW module increments or a combination) to total say 14 MWe and 7.2MWt of steam for the Corette turbine. The third phase would add say a single 1000 tpd Texaco gasifier to begin using more local coal plus petroleum coke from Conoco refinery next-door and supply syngas for the fuel cells and hydrogen for Conoco as well as high grade steam for Corette's steam turbine and possibly for Conoco. The fourth phase would add an additional gasifier around 1000 tpd to be co-fed with local coal and coke together with some community waste streams and supply syngas to a small plant supplying low-sulfur and high cetane middle distillates in addition to additional hydrogen and high grade steam to Conoco. This last fourth phase will expand the gasifier/fuel cell scale such that a full quantity of steam is supplied to the Corette steam turbine-generator system to produce full rated electrical output of 192 MWe of electrical power plus some additional 28 MWe from the fuel cells to increase the Corette plants output to around 220 MWe. Upon this full repowering of Corette, the old furnace/boiler can be retired. This newly configured plant would have substantial load-following capability. This four phase program, if fully implemented, could cover roughly ten years.

Delivery for the SOFC fuel cells to meet the project schedule involves a plan to reserve an early adopter position in the waiting list for fuel cell demonstrations in time frame from 2003 to 2004.

Process Configuration

The details of the integration of the fuel cells with the gasifier and the turbo-generator electric power producing system is shown in FIGURE 1. It is the combined cycle integration of the SOFC fuel cell with the Corette steam turbine train that raises the efficiency as a power plant to high values approaching 68%. The SOFC air feed is pressurized by one of the turbine-driven compressor (could be a separate blower) and then heated in the "Heat Recuperator" that recovers waste heat from the SOFC. This heated air is then expanded to generate power in the second turbine stage. And finally, a portion of the steam generated from gasifier together from steam generated in the SOFC are used to power the third stage. The purpose of the water condenser is to accept the SOFC gas outlet containing steam and CO₂, and separate the water to make steam for the steam turbine and to recycle the CO₂ for reuse in the gasifier. Although this water condenser is symbolically shown as a single simplified unit, there are heat exchangers as part of this unit to efficiently condense the water and reboil the separated water before it is passed to the gas-phase "Heat Recuperator" to elevate to the high temperature that feeds the steam turbine.

The low pressure steam discharge from the steam turbines that are an integral part of the fuel cell package can be provided to offsite users that are adjacent to the Corette Plant, such as the sugar plant and the Greenhouse business operations. This scheme will eliminate the need for large cooling towers with steam plume discharges. This is a significant cost savings and an environmental credit. We will need to insure that the heat demand of the sugar plant and greenhouses matches closely the low pressure steam discharge from the upgraded Corette Plant.

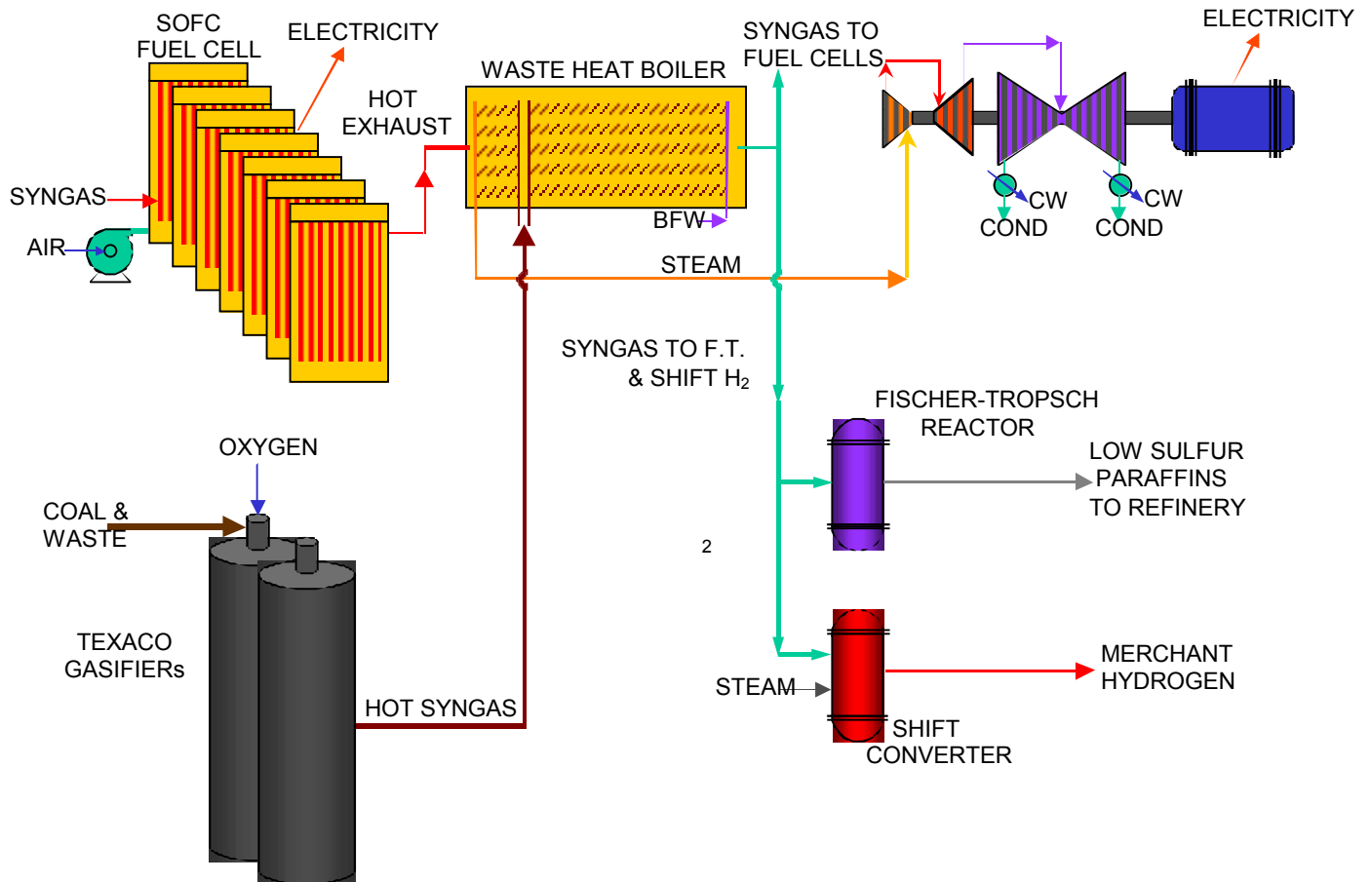


Figure 1: Integrated Gasification Fuel Cell Combined Cycle

The syngas can also be used for the production of speciality agricultural chemicals and solvents or other commodity chemicals at a significant profit. With a mass feed rate to the plant of 2160 tons/day of coke and coal, the hydrocarbon product production would be 346,000 gallons/day or 8,250 barrels per stream day (bpsd), which would be sold for additional income. And this approach of manufacturing carbon-based products which are never burned in their use lifecycle fully sequesters the carbon source so as to eliminate any carbon dioxide emission.

Current Year Progress:

A layout plan for Deaconess Hospital has been completed showing the locations and equipment sizes as well as the internal utility interconnections. The economic analysis is underway at this time.

The most labor-intense task for this year involved the completion of the Corette Power Plant Feasibility Report consisting of 22 chapters. The interfaces with the Corette Power Plant and Conoco Refinery have been identified and scoped for the exchange of critical process streams such as refinery delayed coke supply to the gasifier, hydrogen and paraffin co-product streams to the refinery, steam to Corette existing steam turbine and the utilization of waste heat. Also the recycle of any CO₂ streams back to the gasifier for conversion into useful chemical co-products.

Status of Economic and Systems Analysis:

The initial results of on-going economic analyses of the Corette Power Plant repowering with gasification and fuel cells shows that the simple payback period for around \$540 million in capital investments in plant and equipment is around 5 years. The critical aspects of this design leading to such encouraging economics is the fact that the plant not only produces 34% more electric power at a higher electrical generation efficiency, but it produces valuable chemical co-products such as hydrogen and low sulfur paraffins as well. Also being explored is the possibility of co-producing some valuable sulfur-containing agricultural products that can be sold for an attractive price. As mentioned earlier, greenhouse gas emissions are nearly eliminated through the chemical utilization of CO₂ and other gases to make the chemical co-products. If commercial CO₂ emissions trading becomes more active within the U.S., these reduced emissions can also represent an important income stream for this plant.

Conclusions

The Center For Applied Economic Research has set the stage of the business environment with a resource inventory of electrical generation and distribution in Montana and Wyoming. We are beginning to understand how electricity is supplied to consumers in the region and how they apply fuel cell technology efficiently and effectively in the future.

CTA Architects Engineers has identified and are pursuing Commercial Facilities markets and has started design/planning work at Deaconess Medical Center, St. Vincent Hospital, Montana State University, and several businesses as well as an exciting project that plans an entirely new town in remote Montana that plans to be a model for energy efficiency and sustainability.

The feasibility analysis has determined that the Corette plant repowering would be a cutting-edge, future-looking project that could gain the support and pride of both local communities and environmental groups alike that could be owned and operated by PPL Montana or a partnership with the gasifier supplier. It would be a model for future coal plants and would help coal to be considered one of the environmentally safe fuels for the future. The project makes full use of DOE's Vision 21 concepts and will demonstrate their commercialization. The project also has already started to stimulate the local economy by bringing in fuel cell activity and supporting technologies into the Billings area. There is planned the formation of the Center for Advanced Fuel Cell Technologies

that would provide the process system studies, operating data, construction costs, emissions performance, maintenance records, etc. to promote other similar projects around the world. These projects involve very large numbers of fuel cells, which will help reduce unit costs from the increased manufacturing level to approach the needed economy-of-scale commercial activity. This could mean additional jobs as well as additional business opportunities and improved tax base. It will also be a source of local pride as Montana becomes recognized as a leader in sustainable energy production without pollution.

Future Work

The Technical Advisory Team will critique the findings in the Feasibility Report and select the best combination of plant configurations, and then a design team will be assembled that will scope out the design effort to proceed to install the equipment and make plant changes as needed for the commercial demonstrations.

Objectives For Next Year: The following objectives are established as goals for next year:

- Continue economic analysis of the fuel cell business environment in the region
- Cost out the design effort for both the Deaconess &/or St. Vincent hospital design.
- Obtain Technical Advisory Team consensus on the optimal scope for process installations at Corette, at Conoco, at the Sulfur Plant, and possibly on an adjacent parcel of land.
- Assemble the design team to examine the plat locations for process units and piping runs.
- Cost out the design effort for four phases of Corette Plant conversion: (1) single SOFC low pressure fuel cell demonstration powered by natural gas, (2) a field of some significant number of natural gas-fed fuel cells, (3) a field of 56 fuel cells supplied by syngas from a 1000 tpd gasifier producing steam for the existing steam turbine, and (4) installation of a second 1000 tpd gasifier, plus Fischer-Tropsch reactor to produce paraffins, plus Shift Converter to produce high grade hydrogen for the refinery, and a sulfur process to market the sulfur.
- 5 Obtain funding to begin the design efforts for the two projects above.

Acknowledgements

Wish to thank Dan Gatch and Bob Hindley of PPL – Montana for the invaluable help with the details of the Corette Plant, as well as Dan Stevenson of CTA Architects Engineers, James Stevenson of Unifield Engineering, Prof. Dennis Clayson and Cheryl Heath of Montana State University - Billings, Center for Applied Economics Research, Darell Tunnicliff of Big Sky Economic Development Authority, and Mark Williams of DOE National Energy Technology Laboratory

References

1. Forbes, Christian A., "Preliminary Technical Description 250 kW SOFC CHP System," private communication, February 17, 2000.
2. Forbes, Christian A., "Demonstration...The Bridge to Commercialization for Siemens Westinghouse Tubular SOFC," private communication, Alan Casanova, December 29, 1999.
3. Siemens Westinghouse, "Solid Oxide Fuel Cells – The New Generation of Power," private communication, Alan Casanova, December 29, 1999.
4. C. M. Caruana, "Fuel Cells Poised to Provide Power," Chem. Eng. Progr., pp. 11-21, Sept. 1996

5. S. C. Singhal, "Advances in Tubular Solid Oxide Fuel Cell Technology," Proceedings of the 4th International Symposium on Solid Oxide Fuel Cells, Pennington, N.J. , Vol 95-1, 195-207 (1995)
6. W. L. Lundberg, "Solid Oxide Fuel Cell/GasTurbine Power Plant Cycles and Performance Estimates," Power-Gen International '96, Orlando, FL, Dec. 4-6, 1996
7. —, "100-Kilowatt Solid-Oxide Fuel Cell Tested," Chem. Eng. Progr., pg. 17, December 1997
8. U.S. Dept. of Energy, Office of Fossil Energy, National Energy Technology Laboratory (formerly FETC), "Integrated Gasification Combined Cycle," July 1999. [Recent brochure describing DOE's recommendations for the deployment of the new technology of Integrated Gasification Combined Cycle. Provides a very valuable introduction to this new energy field for the new professional not otherwise acquainted with the historical background and future direction and worldwide strategy.]

TECHNICAL ASSESSMENT AND ANALYSIS OF HYDROGEN R&D PROJECTS

**Edward G. Skolnik,
Energetics, Incorporated
501 School Street SW
Washington, DC 20024**

Abstract

Energetics performs independent site-visit-based assessments of projects associated with the DOE hydrogen program. A report on the results of these assessments is provided to the Peer Review Panel to augment the information that they obtain from the Principle Investigators prior to and during the Peer Review itself. In addition, a more general, abbreviated version of the site-visit reports are made available as information to the public.

During the period May 1999-April 2000, Energetics performed a total of five site visits on Hydrogen R&D projects. While the details of these visits as presented in writing to the Review Panel are competition-sensitive, this paper contains some more generic general comments about these site visits.

Energetics also completed an analysis of a process that was devised by PowerBall Technologies, LLC, which involves the use of plastic-encapsulated sodium hydride pellets as an on-board hydrogen storage system. The most recent work involved the analysis of a process modification to the recycling step as proposed by PowerBall. The modification dealt with the addition of oxygen to the recycling process in order to increase the exothermicity of the reaction.

Introduction

Part of the role that Energetics plays in the DOE Hydrogen Program is to provide independent technical assessments of ongoing hydrogen R&D projects. In addition, Energetics performs analyses on hydrogen-related processes and systems. During the period May 1999–April 2000, Energetics visited five laboratories in order to perform assessments on hydrogen production and storage R&D projects. This paper discusses these assessments. In addition, Energetics has analyzed an alternative regeneration scheme for a hydrolysis-based metal hydride storage system. This subject is discussed in the paper entitled “Analysis of the Sodium Hydride-based Hydrogen Storage System being developed by PowerBall Technologies, LLC” which follows the present report.

Technical Assessment of R&D Projects

Background/Approach

Over the past four years, Energetics has performed site visits at the laboratories of nineteen projects that have been part of the DOE Hydrogen Program. This work adds a new dimension to the review process: it provides the reviewers with in-depth information that they cannot get from once-a-year 20 minute presentations. It also provides for more continuity in the interfacing between the Program and the projects, helping to establish ongoing dialogs with the Principle Investigators (PI).

Once a project is chosen for technical assessment, a literature review is performed on the subject. This includes a review of the last two or three years of Annual Operating Plan submittals, monthly reports, the Annual Review paper, reviewers’ consensus comments from the past few years, publications in journals, and journal publications on the same or similar topics by other researchers. The PI is then contacted, and an on-site visit is arranged. A set of topic questions or discussion points is then drawn up and sent to the PI about two weeks prior to the visit. These questions form the basis for a major part of the discussion during the site visit.

During the site visit a tour is requested, preferably with a demonstration of the experimental process(es) as well as a presentation by the PI on the project and its current status. The visit then concludes with discussions based on the topic questions as well as on any other issues that may result from the tour, demonstration, and PI presentation. The on-site visit may last from a half-day to over a full day.

Following the site visit, two reports are written. The first is a detailed report that discusses the project and its strengths and weaknesses in a thorough manner. This report is provided to the Peer Review Team as part of their information package prior to the Peer Review Meeting. A copy is also provided to the Hydrogen Program Manager. The second report is a condensed narrative that discusses the technology but provides no critique. This second report is made available to the public.

Assessments Performed

Prior to May 1999 (the start date of this Annual Report), Energetics had performed a total of fourteen site-visit technical assessments of hydrogen R&D projects. These assessments are identified in Table 1. During the period of this current report (May 1999 – April 2000) a total of five additional technical assessments were completed. These are shown in Table 2.

Table 1. Technical Assessments Performed Prior to May 1999

| Project | Performing Laboratory | Date of Visit |
|---|--|---------------|
| Enzymatic Conversion: Biomass-Derived Glucose to Hydrogen | Oak Ridge National Laboratory | Feb. 1996 |
| Hydrogen from Catalytic Cracking of Natural Gas | Florida Solar Energy Center | Feb. 1996 |
| Hydrogen Manufacture by Plasma Reforming | Massachusetts Institute of Technology | April 1996 |
| Photovoltaic Hydrogen Production | U of Miami | May 1996 |
| Hydrogen Storage in Carbon Nanofibers | Northeastern U | Dec. 1996 |
| Carbon Nanotubes for Hydrogen Storage | National Renewable Energy Laboratory | June 1997 |
| Storage and Purification of Hydrogen Using Ni-coated Mg | Arthur D. Little, Inc. | June 1998 |
| Hydrogen Transmission and Storage with a Metal Hydride Organic Slurry | Thermo Power, Inc. | June 1998 |
| Thermal Management Technology for Hydrogen Storage | Oak Ridge National Laboratory & Materials and Environmental Research, Inc. | August 1998 |
| Improved Metal Hydride Technology | Energy Conversion Devices, Inc. | August 1998 |
| Hydride Development for Hydrogen Storage | Sandia National Laboratories (CA) | Sept. 1998 |
| Biomass to Hydrogen via Fast Pyrolysis and Catalytic Steam Reforming | National Renewable Energy Laboratory | Dec. 1998 |
| Hydrogen Separation Membrane Development | Savannah River Technology Center | March 1999 |
| Hydrogen Production by Photosynthetic Water Splitting | Oak Ridge National Laboratory | March 1999 |

Table 2. Technical Assessments Performed May 1999 – April 2000

| Project | Performing Laboratory | Date of Visit |
|---|--|----------------|
| Bioreactor Project | University of Hawaii | July 1999 |
| Insulated Pressure Vessels for Cryogenic Hydrogen Storage | Lawrence Livermore National Laboratory | September 1999 |
| PEM Fuel Cell Stacks for Power Generation | Los Alamos National Laboratory | January 2000 |
| Hydrogen from Biomass in Supercritical Water | University of Hawaii | March 2000 |
| Hydrogen Storage Tank Liners | Lawrence Livermore National Laboratory | March 2000 |

Results/Conclusions

The outcome of the individual technical assessments cannot be reported in this document due to the competition-sensitive nature of much of the results. However, several broad conclusions can be reported here:

- Projects in general appear technically sound.
- The majority of these five projects appeared to be going down the correct technical pathway.
- Good progress is being made in the areas of hydrogen storage tanks and fuel cells.
- Safe, inexpensive on-board storage is probably the single most important need if hydrogen is to be the fuel of choice for fuel cell vehicles. In the nearer term, at least, hydrogen will need to be stored as either a compressed gas or a liquid.
- Constant reminders that these are supposed to be **HYDROGEN** projects is still important. We have found over the years that for several reasons (multiple funding sources is one major one) some projects tend to lose their hydrogen focus. This can manifest itself as, for instance, research on alternative on-board fuel choices, extensive emphasis on byproducts of a hydrogen production system, or focus on basic research that does not improve hydrogen production efficiency.
- Too much “territorialism” exists.
- More tie-in of the PIs with other phases of the overall Program is needed. Surprisingly, we found that many PIs are not very well attuned to what is going on in other parts of the Program including research in other areas, overall Program technical direction, or the interaction of the Program with other areas of DOE.

Analysis of the

Sodium Hydride-based Hydrogen Storage System

being developed by

PowerBall Technologies, LLC

Prepared for

The US Department of Energy
Office of Power Technologies
Hydrogen Program

Prepared by

J. Philip DiPietro
and
Edward G. Skolnik,

Energetics, Incorporated

October 29, 1999

Analysis of the Sodium Hydride-Based Hydrogen Storage System being developed by PowerBall Technologies, LLC

We considered the viability of a system for storing hydrogen on-board a vehicle in the form of plastic-encapsulated sodium hydride (NaH) pellets. Hydrogen is produced when the pellets are cut and immersed in water. The exposed NaH surface reacts with water, releasing hydrogen and forming sodium hydroxide (NaOH) as a byproduct. Later, in an off-board activity, the hydroxide is recycled to hydride via a multi-step regeneration process that relies on methane as both a fuel and a reactant. This is a preliminary analysis that required the development of conceptual designs for several of the process steps and the need to make several assumptions in order to complete the overall systems analysis. The analysis was peer reviewed by several members of their hydrogen community, and their comments were taken into account in the preparation of this document.

Executive Summary

The reaction of sodium hydride with water to form hydrogen and sodium hydroxide can be utilized onboard a vehicle to deliver hydrogen to an onboard power system. PowerBall Technologies, LLC has developed a novel means of controlling the reaction: they encapsulate small amounts of sodium hydride in plastic balls. These balls are sliced open one at a time onboard the vehicle to deliver hydrogen as needed. We estimate a sodium hydride-based storage system can achieve a hydrogen storage density of 4.3 wt% and 47 kg/m³, including all ancillary equipment. PowerBall Technologies, LLC is also developing a novel method of manufacturing the sodium hydride material. Instead of the traditional electrochemical process, they propose to form sodium metal by reacting natural gas and sodium hydroxide. A preliminary assessment indicates the cost of hydrogen delivered to a vehicle is about \$5.3/kg (\$39.4/MMBtu) using the sodium hydride system being developed by PowerBall Technologies, LLC. The implementation of cost reduction steps, based primarily on an alternative source of NaOH, results in a decrease of the cost of hydrogen to about \$4.1/kg (\$30.5/MMBtu).

One large component of the cost of the process is the energy requirements, with the key factor being the cost of regenerating the sodium hydride from sodium hydroxide. The full life-cycle energy consumption of the base case sodium hydride process is 4.0 kWh of energy per kWh of hydrogen delivered to the vehicle compared to 2.2 and 1.7 for liquid hydrogen and compressed hydrogen gas, respectively.

A comparison of the cost of delivered hydrogen from the PowerBall process with compressed hydrogen and liquid hydrogen is \$5.3/kg for the base case PowerBall process, \$4.1/kg for the lower cost PowerBall option, \$ 1.4/kg for compressed hydrogen, and \$2.8/kg for liquid hydrogen. When one includes the estimated cost of the respective on-board systems, however, the numbers become somewhat closer. The onboard equipment for the PowerBall process is estimated at about \$0.46/ kg H₂ compared to the capital cost of a pressure vessel, \$750, which equals about \$0.88/kg of hydrogen stored over the life of a vehicle. The overall costs are then about \$5.76/kg for the base-case PowerBall system, \$4.56/kg for the lower cost PowerBall system, \$2.28/kg for compressed hydrogen, and \$3.30/kg for the liquid hydrogen system.

A comparison can also be made between the cost of hydrogen from the PowerBall system, and the cost of gasoline. Using the comparative values of 31.4 miles/gallon gasoline for a standard AIV (Aluminum Intensive Vehicle) Sable, and 82.3 miles per gallon-equivalent for a fuel cell vehicle¹, a hydrogen cost of \$5.30/kg is roughly equivalent to a gasoline cost of \$2.02 per gallon, not including taxes. (An on-board hydrogen fuel cell vehicle will be more fuel-efficient than a gasoline ICE vehicle). A hydrogen cost of \$4.10/kg is roughly equivalent to \$1.56 per gallon (untaxed).

Aside from the relatively low cost of the on-board PowerBall operating system, another “plus” is the fact that the encapsulated ball system is amenable to the initial situation of a small number of vehicles in a geographic area.

It should also be pointed out that the application of the PowerBall technology in the chemical industry represents an attractive option. The estimated plant gate manufacturing cost of sodium metal via PowerBall Industries’ thermochemical process could be as much as ten times less than the current commodity price for sodium produced via electrolysis. Also, the encapsulation concept could greatly lower the cost of transporting sodium and/or sodium hydride. PowerBall might consider pursuing applications for its technologies within the chemical industry in the near term, with a plan to expand into energy systems in the future.

Recently, PowerBall unveiled a modified recycling process. In this process, the syngas (CO + H₂) which is formed during the first step of the recycling process is in part combusted to produce heat to raise the reaction temperature, and in part reacted to produce more methane feedstock. As an addendum to this report, we have addressed this modification in the form of a very preliminary analysis.

PowerBall has indicated that the overall modified process is superior in that it produces more hydrogen per unit methane, and that the overall reaction is exothermic. Our preliminary analysis indicates that while

- *The amount of hydrogen produced per unit methane has indeed increased, and*
- *The overall reaction is exothermic.*

The following mitigating factors need to be considered as well:

- *The exothermicity of the overall reaction is in part due to the inclusion of a step (the hydriding of sodium) which is done separately, and from which the heat likely could not be used in the integrated process. Without this step, the overall reaction is endothermic.*
- *The benefit incurred by the decrease in the amount of methane feedstock needed is likely more than offset by the need for multiple separations, multiple reactors, and the added cost of oxygen to burn the syngas.*

¹ “Integrated Analysis of Hydrogen Passenger Vehicle Transportation Pathways”, C.E. Thomas et al, Directed Technologies, Inc., Report to the National Renewable Energy Laboratory, Subcontract AXE-6-16685, March 1998.

Background

The PEM fuel cell has potential to be the next-generation vehicle power system, but delivering pure hydrogen fuel to the PEM stack, either through onboard storage of neat hydrogen or the processing of fossil fuels on-board, remains a barrier on the basis of cost, weight, and/or volume. The two commercially available options for onboard storage of hydrogen, compressed gas or liquid, are energy-intensive and would require significant investment in distribution infrastructure.

The Department of Energy's Hydrogen Program seeks to improve the commercial viability of hydrogen-based energy systems, and the Program is funding R&D into advanced hydrogen storage technologies, including chemical hydrides and carbon absorbents. Another approach being explored by PowerBall Technologies, LLC is to react a metal hydride with water to produce hydrogen gas and the corresponding metal hydroxide. Potential reactants include sodium, sodium hydride, calcium, and lithium. PowerBall Technologies, LLC has focused its efforts on sodium hydride because, compared to the others, it offers adequate weight and volume density, fast kinetics, and a clear recycle loop as will be discussed below.

The sodium hydride / water reaction {1} is strongly exothermic and proceeds vigorously upon contact of the reactants. In order to control the reaction for use as an onboard hydrogen source, PowerBall Technologies, LLC proposes that the sodium hydride be encapsulated in plastic-coated pellets (nominally 1.5 inches in diameter with a coating of polyethylene 0.020 inches thick). The pellets are stored onboard a vehicle, sliced open one at a time, and contacted with water to produce hydrogen as needed.



The objective of this analysis is to characterize the sodium hydride-based hydrogen storage system and compare it to compressed gas and liquid hydrogen storage systems. The criteria for evaluation are:

1. Cost of hydrogen delivered to the vehicle
2. Weight and volume density of the onboard hydrogen storage system

Cost of Hydrogen Delivered to the Vehicle

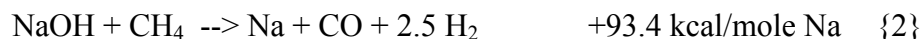
The cost and fuel efficiency of the sodium hydride system is determined by an assessment of the production and delivery of sodium hydride balls to the vehicle. Sodium hydride is available as a specialty chemical, however its cost is prohibitive for use as a hydrogen carrier. The conventional process for sodium hydride manufacture, electrolyzing sodium chloride and then sparging hydrogen gas through a bath of the molten sodium metal, is too expensive for use as a hydrogen carrier. We can estimate the cost of the NaCl electrolysis process by considering the cost of product sodium. DuPont's list price for sodium metal is \$3.3/kg for bulk shipments (36,000 kg or more, <http://www.dupont.com/sodium/price.mtml>). Assuming it costs 20 cents/kg to produce sodium hydride from sodium metal by the sparging process, the estimated cost of sodium hydride is \$3.5/kg. Based on reaction {1}, twelve kg of NaH are required to deliver 1 kg of hydrogen gas. Thus \$3.5/kg

of NaH converts to \$42/kg (\$300/MMBtu) of hydrogen delivered to the vehicle. Estimates of the cost of pressurized gas or liquid hydrogen delivered to a vehicle ranged from \$1.4-2.8/kg. Clearly, the conventional process is too expensive.

The high cost of sodium hydride from the conventional production pathway is due to high-energy consumption. According to DuPont, the electrolysis of sodium chloride consumes 9.7 kWh of electricity per kg of sodium, which, based on reaction {1}, works out to 3.4 kWh electricity per kWh hydrogen delivered to a vehicle. When one considers that most U.S. electricity generation is fossil-based with an efficiency of 30% to 60%, the full life-cycle energy consumption of the sodium hydride system is even higher.

To achieve lower cost, PowerBall Technologies, LLC is developing a process for manufacturing sodium hydride from sodium hydroxide. Figure 1 is a schematic of the vehicle fueling system, in which vehicles consume sodium hydride balls and generate sodium hydroxide solution. At refueling stations, the sodium hydroxide solution is drained from the vehicles and replaced with a fresh load of sodium hydride balls. The hydroxide is stored at the vehicle refueling station and transported to a central facility where it is used as feedstock in the manufacture of new sodium hydride balls. The balls are then shipped out to the refueling stations to replenish their inventories.

Figure 2 is a block diagram of the process being developed by PowerBall Technologies, LLC for converting sodium hydroxide to sodium hydride. The process flow is as follows: 30 wt% sodium hydroxide is charged to a first stage concentrator where roughly 80% of the water is boiled off. Effluent sodium hydroxide solution (70 wt%) is charged to a second stage concentrator where the remaining water is boiled off, leaving molten sodium hydroxide (melting point of sodium hydroxide is 318 C). The molten sodium hydroxide is mixed with methane and charged to the sodium reactor, which is a molten bath of sodium carbonate (Na₂CO₃). The sodium carbonate serves to disperse the reactants and raise their temperature to roughly 980C. The following overall reaction occurs



The reactant products are gases and escape from the top of the reactor. The reaction is strongly endothermic, and heat must be supplied to the reactor by circulating a portion of the sodium carbonate bath through a heater vessel. The sodium carbonate is heated by burning a fuel and injecting the combustion exhaust into the bottom of the bath. The exhaust gases bubble up through the molten sodium carbonate bath, transferring heat. The transfer of sodium carbonate between the reactor and heater vessels is driven by the density difference of the hot and cold material. The sodium reactor heater fuel is preheated with exhaust gas effluent, and it is assumed that a 500C inlet temperature is achieved.

The effluent from the sodium reactor, CO, H₂, and Na at 980C, is quenched with Dowtherm or mineral oil, condensing the sodium at 880C at atmospheric pressure. The quench fluid is cooled by an air cooler.

Forty percent of the hydrogen contained in the quench overhead stream is recovered via a membrane or pressure swing absorber. The hydrogen is then bubbled up through the molten sodium product

to produce sodium hydride. The carbon monoxide and hydrogen from the quench overheads (minus the hydrogen recovered for NaH production) is burned as fuel in the sodium reactor heater.

The concept is not entirely novel, as a United States patent was awarded to C. Netto of Germany in 1891 for the production of sodium from sodium hydroxide and carbon (patent number 460,985). In a patent filed in 1955 (patent number 2,930,689), McGriff moved the technology further. Among other ideas, he patented the concept of the sodium carbonate reactor.

Figure 2 contains a mass balance on the process based on 100 weight units of sodium hydroxide solution charged to the first stage concentrator (nominally kg/h). Also presented is the estimated duty of the heaters and coolers. The material balance is based on a process in which natural gas is used as both the carbon source for the sodium reactor and also to meet the process heating requirements.

Figure 3 shows a financial analysis of the NaH manufacturing process. We use a pro-forma cash flow model with capital, feedstock, and O&M costs as inputs. We then adjust the plant gate cost of sodium hydride to achieve an internal rate of return of 10% based on the after-tax cash flow.

The primary inputs into the financial analysis model are as follows:

PowerBall Technologies, LLC estimates it will cost \$1 million to build a pilot plant with a capacity of 45 kg/hr of sodium hydride production (unit cost \$22,000/kg/hr). Energetics has reviewed the cost estimate based on the results of the heat and material balance. The pilot plant makes enough sodium hydride per year to supply power balls to roughly 250 passenger vehicles. Our financial analysis is based on a commercial unit that produces 450 kg/hr of sodium hydride with a unit cost of \$10,000/kg/hr of NaH production capacity.

The O&M cost is estimated to be 6% of capital. This rather high estimate is based on the corrosive nature of the materials involved leading to frequent parts replacement, and the high labor cost associated with ensuring safe operation.

The natural gas consumption is 1.0 kg per kg of NaH production based on the material balance shown in Figure 2. The cost of natural gas is assumed to be \$.42 /MMBtu (\$.115 /kg, Annual Energy Outlook 1997 for industrial customers in the year 2000).

We estimate that the sodium hydride balls will need to be transported via truck an average of 50 miles from the sodium hydride production plant to the dispensing stations. Also, the sodium hydroxide will be transported from the dispensing stations back to the sodium hydride production facility. We estimate the cost of truck transportation to be 10 cents per kg of hydrogen delivered to the vehicle.

The base case analysis gives a sodium hydride plant gate cost of \$.44/kg which is substantially less than the cost derived from sodium chloride electrolysis of \$3.8/kg. An NaH cost of \$0.44 /kg translates to a delivered hydrogen cost of \$5.3/kg. Table 1 shows that the natural gas feedstock represents 27% of the total sodium hydride manufacturing cost. As we have shown, the full life-

cycle energy consumption of the base case sodium hydride process is high: 4.0 kWh of energy per kWh of hydrogen delivered to the vehicle (see addendum), compared to 2.2 and 1.7 for liquid hydrogen and compressed hydrogen gas, respectively. Notice that the truck transportation cost is a significant portion of the total cost.

| | cost \$/kg NaH | Percent of total cost |
|----------------------------|-------------------|-----------------------------|
| Natural gas (\$2.4/MMBtu) | 0.12 | 27% |
| O&M (6% of capital) | 0.08 | 17% |
| Capital recovery (10% IRR) | 0.15 | 33% |
| Truck transportation | 0.10 | 23% |
| Total | 0.44 | |

Methods for Further Reducing the Sodium Hydride Production Cost

Figure 4 shows an alternative system in which spent sodium hydroxide from the vehicles is sold as a chemical feedstock and the sodium hydride manufacturing process is fed spent sodium hydroxide solution from industry. This process is considered feasible because 1) the spent sodium hydroxide from the vehicles should be relatively pure, and 2) the NaH production process being developed by PowerBall Technologies, LLC should be relatively tolerant of impurities and able to accept low-value spent sodium hydroxide solution. The system in Figure 4 will generate additional revenue due to the price differential between the caustic solution sold as a commodity chemical and the spent caustic taken from industry. The market price for sodium hydroxide solution ranges from 20 to 100 cents per kg. The developers would need to identify a spent industrial caustic that did not coke up the sodium hydroxide drying process. Also significant cost would be incurred in additional storage systems and in handling, marketing, and distributing the sodium hydroxide product. We estimate the net profits from such a system could equal 10 cents per kg of NaH (\$1.20/kg of hydrogen).

Another method of reducing the natural gas cost would be to utilize by-product heat where possible. Table 2 shows the natural gas consumption broken out by its use in the process. Notice that the fuel credit from the syngas in stream 14 largely offsets the fuel required to provide the heat of reaction. By-product heat could be used instead of natural gas to concentrate the NaOH solution.

Another strategy for reducing costs is to substitute another hydrocarbon for natural gas. Because the natural gas charged to the sodium reactor is a carbon source for reaction {2}, the key criterion for displacing reactor feedstock is the cost per carbon atom. Table 3 shows the cost per carbon of several hydrocarbon feedstocks. No. 6 oil represents a 20% reduction compared to natural gas. Coal represents a 65% reduction in feedstock costs but would require increased capital for drying and solids handling equipment. Interestingly, diesel is more expensive per weight of carbon than natural gas.

| Stream number (from Figure 2) | Process use | Natural gas use | |
|-------------------------------------|---|----------------------------------|---------------------|
| | | (kg CH ₄ / kg NaH) | percent of total |
| 10 | Fuel for concentrating the NaOH solution | 0.32 | 21% |
| 11 | Reagent in the sodium reactor | 0.64 | 42% |
| 12 | Fuel to provide heat of reaction | 0.57 | 37% |
| | Subtotal | 1.53 | |
| 14 | Fuel credit from the by-product CO and H ₂ | -0.53 | -35% |
| Total | | 1.0 | |

| Hydrocarbon | Cost | |
|---|-----------|--------------|
| | \$/MMBtu* | \$/kg carbon |
| Natural gas | 2.42 | 0.154 |
| Diesel | 4.40 | 0.198 |
| No. 6 Oil | 2.55 | 0.114 |
| Coal | 1.48 | 0.050 |
| * Annual Energy Outlook 1997, Industrial users 2000 | | |

Alternately, if a less expensive source of natural gas can be found, this also would lower the overall process cost. Personnel from PowerBall Technologies, LLC, have stated that stranded natural gas assets can be obtained for as little as \$0.68/MMBtu, which is equivalent to \$.043/kg carbon. This would lower the cost of NaH production from \$0.44/kg NaH to \$0.36/kg NaH. However, while this may open up applications in some areas, it is unlikely that this cost of natural gas could be maintained on a large-scale basis.

Table 4 compares the cost of liquid and compressed gaseous hydrogen estimated by Air Products and Chemicals in a study conducted with Directed Technologies for Ford Motor Company. The table shows that even under the aggressive low-cost scenario the sodium hydride system is more than twice as expensive as compressed hydrogen gas from a gas-station-sized steam methane reformer.

| | Cost of delivered hydrogen \$/kg | Minimum number of vehicles served |
|---|----------------------------------|-----------------------------------|
| Liquid hydrogen | 2.8 | 400,000 |
| Compressed gaseous hydrogen from a gas-station-sized steam methane reformer (100 factory built units) | 1.4 | 1,000 per station, 100,000 total |
| Sodium hydride balls, base case | 5.3 | 2,500 |
| Sodium hydride balls, low cost case based on treatment of spent sodium hydroxide | 4.1 | 2,500 |

The results from Table 4 should not discount the sodium hydride option. The liquid hydrogen cost is for a relatively large system. Small quantities of merchant, liquid hydrogen can be much more expensive, in the \$5-7/kg range. With respect to gaseous hydrogen, in order to perform a comprehensive comparison, one must consider the cost of the onboard storage system. Table 5 shows the estimates for the cost of the onboard storage system for compressed gas, liquid hydrogen, and NaH systems. The sodium hydride system is inherently low-cost, and Table 5 shows that when levelized over the life of the vehicle, the cost of the onboard storage system per kg of hydrogen delivered to the power system is significant. This narrows the gap on the overall cost of using sodium hydride storage instead of compressed hydrogen: \$4.76/kg for the NaH-based process (including profit from sale of NaOH) and \$2.3/kg for compressed hydrogen. The cost for the liquid hydrogen system based on the same analysis is \$3.3/kg.

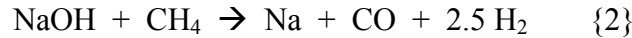
| | Unit cost \$/kg | Total cost \$ | Levelized cost \$/kg H2 * |
|-----------------|-----------------|---------------|---------------------------|
| Compressed gas | 190 | 760 | 0.88 |
| Liquid hydrogen | 100 | 400 | 0.46 |
| Sodium hydride | 100 | 400 | 0.46 |

*The capital recovery factor for the onboard hydrogen storage system equals 5.75 (based on an 8 year life and 8% interest rate). The levelized cost of the onboard storage system equals the annualized cost (initial cost / capital recovery factor) divided by the kg consumed by the vehicle per year. We assume a vehicle consumes 150 kg of hydrogen per year (80 miles per kg, 12,000 miles per year).

Energy Consumption in the Sodium Hydride-based Hydrogen Storage System

There are four sources of energy consumption associated with the sodium hydride system: 1) drying the sodium hydroxide, 2) raising the temperature of the system to 980C, 3) regenerating the hydride from the hydroxide, and 4) producing hydrogen from the hydride on-board. Table 6 below shows the various energy sinks in the sodium hydride-based hydrogen energy pathway.

By far the largest source of energy loss is in the conversion of sodium hydroxide to sodium hydride. Equation {2} below shows the primary conversion reaction.



The energy consumed by the conversion equals the heat value of the methane charge minus the heat value of the by-product carbon monoxide and hydrogen, plus the heat required to drive the reaction.

| | | | | | | |
|--|---|--------------------------------------|---|--|---|----------------------------------|
| Energy required to convert NaOH to NAH | = | Heat value of stoichiometric methane | - | Heat value of by-product CO and H ₂ | + | Heat of Reaction, 93.4 kcal/mole |
|--|---|--------------------------------------|---|--|---|----------------------------------|

One mole of methane is consumed per each mole of sodium hydroxide reacted. Based on the heat of combustion of the natural gas consumed, 191.8 unit of heat energy are consumed per mole of sodium hydroxide reacted.

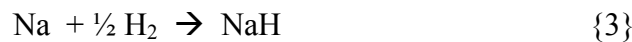
$$\frac{1 \text{ mole CH}_4}{1 \text{ mole Na}} * \frac{191.8 \text{ kcal}}{\text{mole CH}_4} = 191.8 \text{ kcal heat / kcal NaOH reacted}$$

The heating value of by-product hydrogen and carbon monoxide is calculated as follows:

$$\text{Hydrogen} \quad \frac{2 \text{ mole H}_2}{\text{mole NaOH}} * \frac{28,700 \text{ kcal}}{\text{kg H}_2} * \frac{0.002 \text{ kg H}_2}{\text{mole H}_2} = 114.8 \text{ kcal / mole NaOH}$$

$$\text{Carbon Monoxide} \quad \frac{1.0 \text{ mole H}_2}{\text{mole NaOH}} * \frac{2,415 \text{ kcal}}{\text{kg CO}} * \frac{0.028 \text{ kg CO}}{\text{mole CO}} = 67.6 \text{ kcal / mole NaOH}$$

Note that the amount of hydrogen is reduced from 2.5 moles to 2.0 moles to account for the hydrogen consumed in making NaH from Na:



| Process stage | Heat lost, Btu of thermal energy per Btu of hydrogen energy delivered to the vehicle | Notes |
|---|--|---|
| Drying the sodium hydroxide solution* | 0.44 | Assume a two stage drying process; the first stage takes the solution from 50% to 75%, and the second takes it from 75% to 100%. Assume the steam from the second stage is re-condensed in the first stage. |
| Raising the temperature of the reactants to 980C | 0.22 | Assume 50% of the duty is achieved via heat integration |
| Conversion of sodium hydroxide to sodium hydride | 2.81 | Assume by-product CO and H ₂ are burned for heat value in an 80% efficient burner. Heat consumption includes the heat value of the methane consumed. |
| Conversion of sodium hydride to hydrogen fuel onboard | 0.55 | Exothermic reaction with water produces heat onboard the vehicle, which is dissipated. |
| Total | 4.02 | |

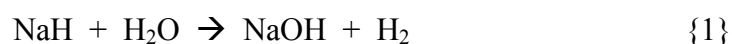
Note that for this analysis we have assumed a 50 wt % solution as opposed to 30 wt % in the base case analysis contained in the report. This reduces the amount of water that must be boiled off per unit of sodium by a factor of 2, although the impact on the overall energy consumption is small.

To calculate the net energy requirement from the reactor we assume that the hydrogen and CO burner is 80% efficient, and also that the transfer of heat into the reactor vessel is 80% efficient. The energy consumed is thus:

$$191.8 + 93.4 / 0.8 - 0.8 * (114.8 + 67.6) = 162.6 \text{ kcal/mole NaOH reacted}$$

For each mole of sodium hydroxide, one mole of hydrogen is provided to the vehicle power system. Each mole of Na is converted to NaH using a portion of the byproduct hydrogen as shown in reaction {3}. Since the heat from this exothermic reaction is non-recoverable, it is not included in this calculation.

Next, the 162.6 kcal/mole NaOH must be expressed in a hydrogen-equivalent manner. Each mole of NaH provides one mole of hydrogen to the vehicle power system upon reaction with water as shown in reaction {1}.



Based on a lower heating value of hydrogen of 57.8 kcal/mole, energy consumption is as follows.

$$\frac{162.6 \text{ kcal}}{\text{mole NaOH}} * \frac{1 \text{ mole NaOH}}{1 \text{ mole H}_2} * \frac{1 \text{ mole H}_2}{57.8 \text{ kcal}} = 2.81 \text{ kcal energy / kcal hydrogen}$$

The total energy consumed by the sodium hydride pathway, 4.02 kcal of energy per unit of hydrogen energy delivered, is high compared to liquid and pressurized gaseous storage (2.2 and 1.7 Btu energy per Btu of hydrogen delivered respectively). The estimate is credible when one considers that the overall steam methane reforming reaction as shown below produces four hydrogen molecules per methane molecule compared to only one hydrogen molecule per methane in the sodium hydride process.



Weight and volume density of the onboard hydrogen storage system

Weight density is defined as the kg of hydrogen fuel delivered to the on-board power system divided by the total weight of the hydrogen storage system, including ancillary equipment. Similarly, volume density is defined as the kg of hydrogen delivered to the vehicle per cubic meter of space that the hydrogen storage system takes up.

In order to develop a weight and volume density estimate, we characterized a sodium hydride-based hydrogen storage system designed to deliver 4.09 kg of hydrogen (a vehicle range requirement of 380 miles and a fuel efficiency of 93 miles per kg of hydrogen). Twelve kg of sodium hydride are required for each kg of hydrogen delivered to the PEM fuel cell, giving a total sodium hydride requirement of 49 kg.

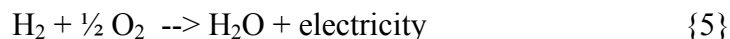
PowerBall claims that they are able to compact NaH to a density of 1.1 g/cc. Thus, a 1.5-inch diameter ball would hold 0.0319 kg of NaH; 1,540 balls would be required to hold a total of 49 kg of NaH. At the peak rate of hydrogen consumption by the PEM fuel cell, the ball slicer will be cutting NaH balls at the rate of fourteen per minute to maintain hydrogen supply.

The onboard hydrogen storage system is shown in Figure 5 and works as follows: As the PEM fuel cell is operated it draws hydrogen gas from the storage system. A ball-slicing device retrieves a plastic-coated sodium hydride ball from the inventory and slices it open so that the sodium hydride is contacted with the water, producing hydrogen gas. The rate of ball slicing is controlled to maintain the pressure in the tank between 120 and 150 psi.

The ball slicing device developed by PowerBall Technologies, LLC works as follows. A ball is corralled into a cartridge tube. The cartridge is then closed and a burst of high-pressure hydrogen gas accelerates the ball through a blade assembly and into a water reservoir where the sodium hydride reacts to form hydrogen gas. The high-pressure hydrogen gas is produced by a small intensifier that takes 120 psi hydrogen gas from the main containment vessel and divides it into a high-pressure stream (250 psi) and a low-pressure stream (30 psi). The high-pressure stream is used by the ball slicer, and the low-pressure stream is discharged to a small buffer tank that feeds the PEM

fuel cell. This is a somewhat complex system compared to an electric motor slicer, but it has the advantage that it does not represent a parasitic load and actually helps dissipate some of the thermal energy from the sodium hydride reaction.

Because the PEM fuel cell produces water as a by-product (the overall electrochemical reaction is shown below), it can supply the water required for the sodium hydride reaction, thus lowering the required weight of the system.



Inspection of reactions {1} and {5} indicates that the fuel cell could provide all the water required by the sodium hydride system. However, practical considerations require extra water: 1) some of the water produced in the PEM fuel cell escapes in the wet exit gas; 2) a water inventory is needed for start-up; and 3) it is possible that sodium hydroxide, being hygroscopic, may become associated with reactant water, making some of the water unavailable for reaction (this issue requires further investigation; it could increase the system water requirement and/or necessitate on-board dehydration and segregation of the sodium hydroxide product). Thus, we assume the initial water inventory equals 50% of the stoichiometric requirement.

Because the reaction {1} is strongly exothermic, the storage system will likely heat up during vehicle operation. We estimate the sodium hydride storage system will increase the onboard cooling duty by 100% and increase the weight of the radiator system by 75%.

The containment vessel will consist of a plastic liner for corrosion resistance and a stainless steel or carbon/glass fiber shell to provide strength. If stainless steel is used, the weight of the vessel could be 30 kg. We have lowered the estimate of the containment vessel to 20 kg assuming advanced materials are used.

Table 7 shows the weight and volume of the components of the sodium hydride hydrogen storage system. The sodium hydride balls are the primary component, representing 56% of the weight and 51% of the volume. This indicates that significant weight and cost reductions below the estimates presented are unlikely to be achieved in real systems.

Interestingly, the storage system gets heavier as hydrogen is consumed. This is because water from the PEM fuel cell that would otherwise be discharged from the vehicle is reacted with sodium hydride and the oxygen atom is captured in the sodium hydroxide product. Assuming that 10% of the water content remains with the depleted system, we estimate the weight of a fully depleted tank to be 113.6 kg. This is an equivalent weight density of 3.6%.

Figure 6 shows that the sodium hydride system weighs more than compressed hydrogen gas and liquid hydrogen, but is more compact. That trade-off is similar to the one presented by magnesium hydride systems. The primary performance difference between the magnesium hydride systems and the sodium hydride/water system is that the magnesium system's hydrogen release reaction is endothermic (it uses waste heat from the onboard power system and/or burns a portion of the hydrogen parasitically), whereas the sodium hydride system generates a large amount of heat when

it releases hydrogen. This means that the sodium hydride is simpler in that it does not have to be heat integrated with the on-board power system. On the other hand, because the heat generated onboard is lost, the sodium hydride system is inherently less energy-efficient.

| Table 7. Estimated size and weight of a Power Ball system designed to deliver 4.1 kg of hydrogen to a vehicle power system | | |
|---|------------------------|--------------------------|
| Component | Weight (kg) | Volume (m ³) |
| Sodium hydride balls | 49 | .0445 |
| Water | 18.4 | .0184 |
| Vapor space | Negligible | .0249 |
| Container | 20 | negligible |
| Incremental radiator requirement | 7 | negligible |
| Ball slicer | 3 | negligible |
| Total | 97.4 | 0.0879 |
| Weight density | 4.2% | |
| Volume density | 46.6 kg/m ³ | |

The density analysis above assumes that the reaction of the cut sodium hydride pellets and water will be essentially stoichiometric. In fact, in the absence of mixing, the reaction will become diffusion limited, and consequently less efficient on a kinetic basis. As a result, excess water will need to be used to increase the reaction rate. At a reasonable value of 1.5 times stoichiometric for the amount of water needed, the weight density of the system is reduced to 3.8 % (3.3% based on a depleted tank), and the volume density is about 42.2 kg/m³.

Other Concerns

Materials Concerns

Sodium hydride is regarded as an extremely reactive material and any system using it will come under close scrutiny for safety. Of concern is the potential for a chain reaction, in which the coating of one of the balls in the ball storage tank breaks for whatever reason (perhaps in a car crash) and reacts with water. The heat from this reaction then melts the coating of another balls and so on. A full safety analysis of the proposed on-board storage system is needed.

The density of NaH as claimed by PowerBall is 1.1 g/cc. This is the value we used above to calculate weight and volume system densities. Literature values for NaH, however, indicate that the density is actually 0.92 g/cc. With this lower density, the volume required for the PowerBalls would be about 16 % higher (including air space, 27% higher) than shown in Table 7.

Sodium hydroxide, though commonly used, is a caustic material and is hazardous. Siting of NaOH storage tanks in commercial areas where vehicle service stations are typically sited could cause resistance from local authorities. Also, onboard storage of sodium hydroxide solution will require Department of Transportation approval.

Above 30 wt%, aqueous solutions of sodium hydroxide freeze above 0 degrees Celsius. The NaH system must be designed to either avoid high concentration of sodium hydroxide to manage frozen reactant products.

Engineering/Processing Concerns

The storage system cost estimate may be low in that it does not include extensive coolant systems, buffer tanks, and interconnectivity. Nor is a method included for removal of the spent hydroxide liquid and refilling the tanks with water and PowerBalls. It has been hypothesized that the hydrogen-liberating reaction can be run stoichiometrically, leaving a dry hydroxide product, which would be easy to remove. Such a system would likely be difficult to control, especially due to the hygroscopic nature of NaOH.

The upcoming operation of the PowerBall Technologies, LLC pilot plant will be very instructive regarding the feasibility of sodium hydroxide-fed sodium hydride production. Anticipated issues include: corrosion of the submerged heater, coking in the sodium hydroxide dryer, temperature controls in the reactor, recovering heat from the sodium reactor heater, and recovering hydrogen from the reactor off-gas. A more detailed process cost estimate should be completed after the benefits of the pilot plant operation are available.

If the operating pressure of the onboard storage system were raised, it would be possible to power the PEM fuel cell air compressor via a hydrogen-fed expansion turbine. In addition to reducing the parasitic electric load of the air compressor, the expander would reduce the cooling requirements. This concept has been investigated for pressure vessel systems. It was largely abandoned because of cost and also because the pressure is gradually reducing as the tank is emptied. In the sodium hydride system, the pressure can be controlled over the full storage cycle by varying the rate of ball slicing. However, a high-pressure system would require a heavier containment tank. The trade-offs associated with this concept should be investigated in more detail.

Garnering additional revenues by supplying the sodium hydride production process with spent industrial caustic solution can substantially reduce the cost of sodium hydride. In many cases spent industrial caustic solutions fall under environmental regulations. Such regulations could affect handling requirements of the feedstock and the solids from the bottom of the sodium reactor and heater. Such regulations, if applicable, could diminish the economic incentives. A set of environmental case studies could be useful to assess the feasibility of this concept.

Environmental Concerns

Aside from the environmental concerns voiced above, dealing with the handling of NaOH, there is the question of CO₂ emissions. The regeneration reaction (reaction (2)) is powered by burning

methane, CO and hydrogen, resulting in the formation of CO₂. The amount of CO₂ produced is likely greater than current gasoline engines given the 4 to 1 energy requirement to deliver hydrogen. On the other hand, CO₂ production in the PowerBall case would be centralized, and therefore amenable to sequestration options. Overall CO₂ to the atmosphere would therefore likely be less. At any rate, if the PowerBall option is to be viable, greenhouse gas effects need to be given a closer look.

Conclusions

The base case cost of the sodium hydride system corresponds to a cost of hydrogen delivered to the vehicle power system of \$5.30/kg. A low-cost scenario reduces this cost to \$4.10/kg. The low-cost case is twice as expensive than costs predicted for compressed hydrogen gas systems. However, the fact that the sodium hydride system is amenable to geographically dispersed hydrogen vehicles, and that it promises a relatively low-cost on-board storage system, may make it attractive. Including the on-board equipment, the low-cost case of the PowerBall system is a little over \$1/kg more expensive than a comparable liquid hydrogen system, and a little over \$2/kg H₂ more expensive than a compressed hydrogen system. The safety features and ease of transportation of the encapsulated NaH pellets increases the attractiveness of the system, making it of interest at least to niche markets.

An onboard hydrogen storage system using plastic-coated balls of sodium hydride may achieve a hydrogen storage density of 4.3 wt% and 47 kg/m³ including all ancillary equipment. This is heavier, but more compact than compressed gas and liquid hydrogen systems.

Figure 1. Schematic Of The Sodium Hydride-based Hydrogen Storage And Delivery System

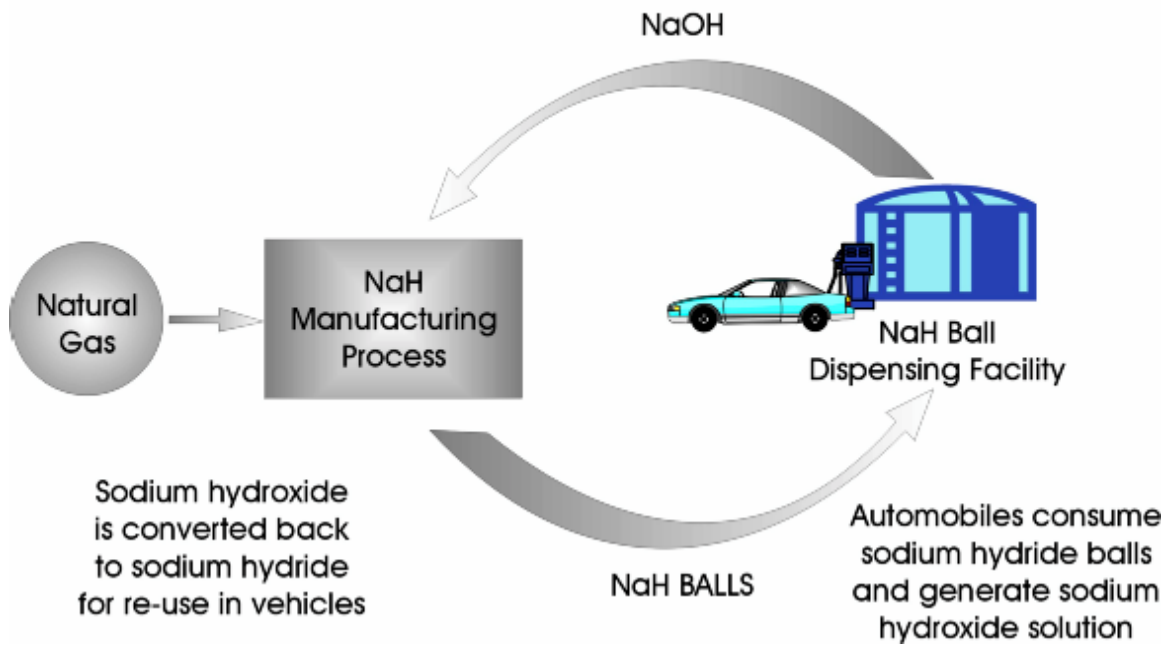
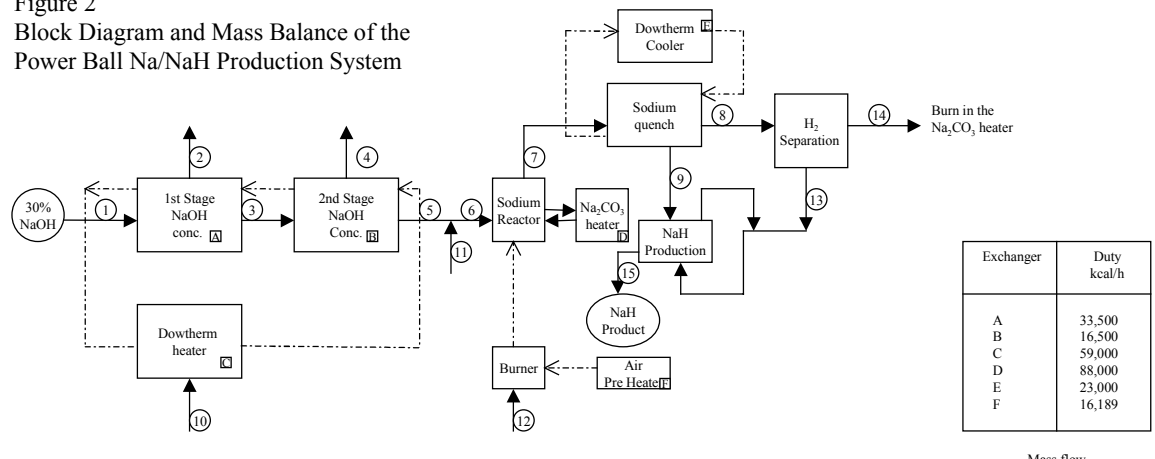


Figure 2
Block Diagram and Mass Balance of the
Power Ball Na/NaH Production System



| Exchanger | Duty kcal/h |
|-----------|-------------|
| A | 33,500 |
| B | 16,500 |
| C | 59,000 |
| D | 88,000 |
| E | 23,000 |
| F | 16,189 |

— Mass flow
- - - Heat flow

Flow Rates in kg/h

| | 1 | 2 | 3 | 4 | 5 | 6 | 7 | 8 | 9 | 10 | 11 | 12 | 13 | 14 | 15 |
|------------------|-----|-----|-----|-----|-----|-----|-------|-------|-------|-----|----|-----|-----|-------|-------|
| NaOH | 30 | | 30 | | 30 | 30 | | | | | | | | | |
| Na | | | | | | | 17.25 | | 17.25 | | | | | | |
| NaH | | | | | | | | | | | | | | | 18.75 |
| C | | | | | | | | | | | | | | | |
| CO | | | | | | | 21.0 | 21.0 | | | | | | 21.0 | |
| H ₂ O | 70 | 57 | 13 | 13 | | | | | | | | | | | |
| CH ₄ | | | | | | 12 | | | | 5.9 | 12 | 0.6 | | | |
| H ₂ | | | | | | | 3.75 | 3.75 | | | | | 1.5 | 2.25 | |
| Total | 100 | 57 | 43 | 13 | 30 | 42 | 42 | 24.75 | 17.25 | 4.9 | 12 | 0.6 | 1.5 | 23.25 | 18.75 |
| Temp °C | 20 | 120 | 120 | 320 | 320 | 320 | 980 | 500 | 500 | 20 | 20 | 20 | 300 | 300 | |

Figure 4. Potentially Higher Value System that also Provides Management of Spent Sodium Hydroxide Solution from Industry

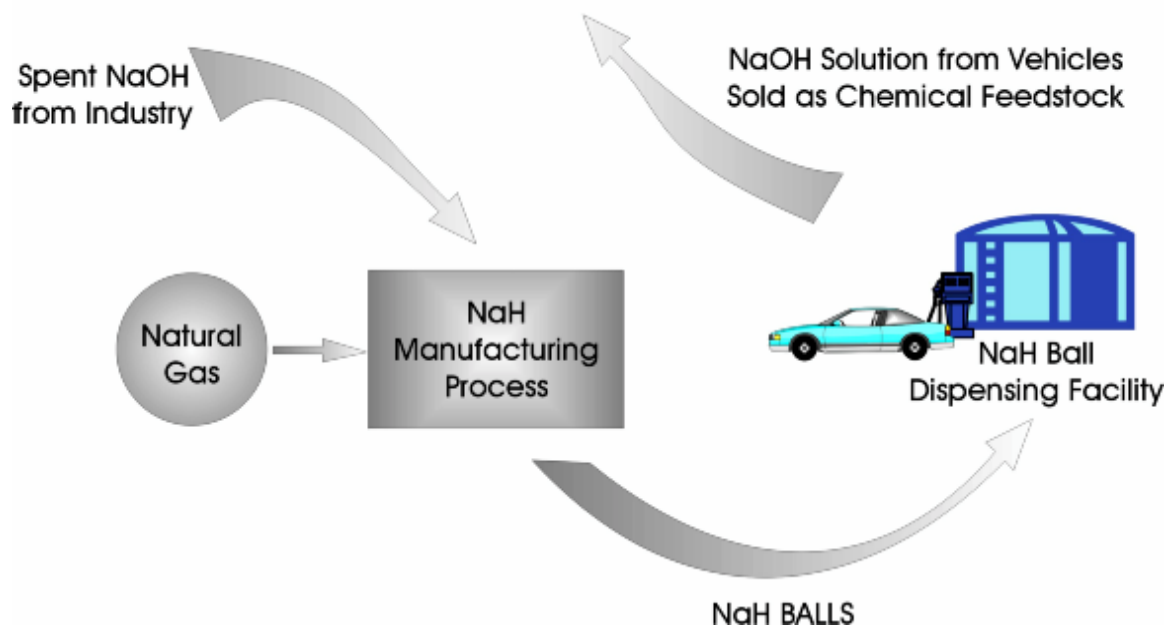


Figure 5. Schematic of a PEM Fuel Cell/Power Ball Hydrogen Storage On-board Power System

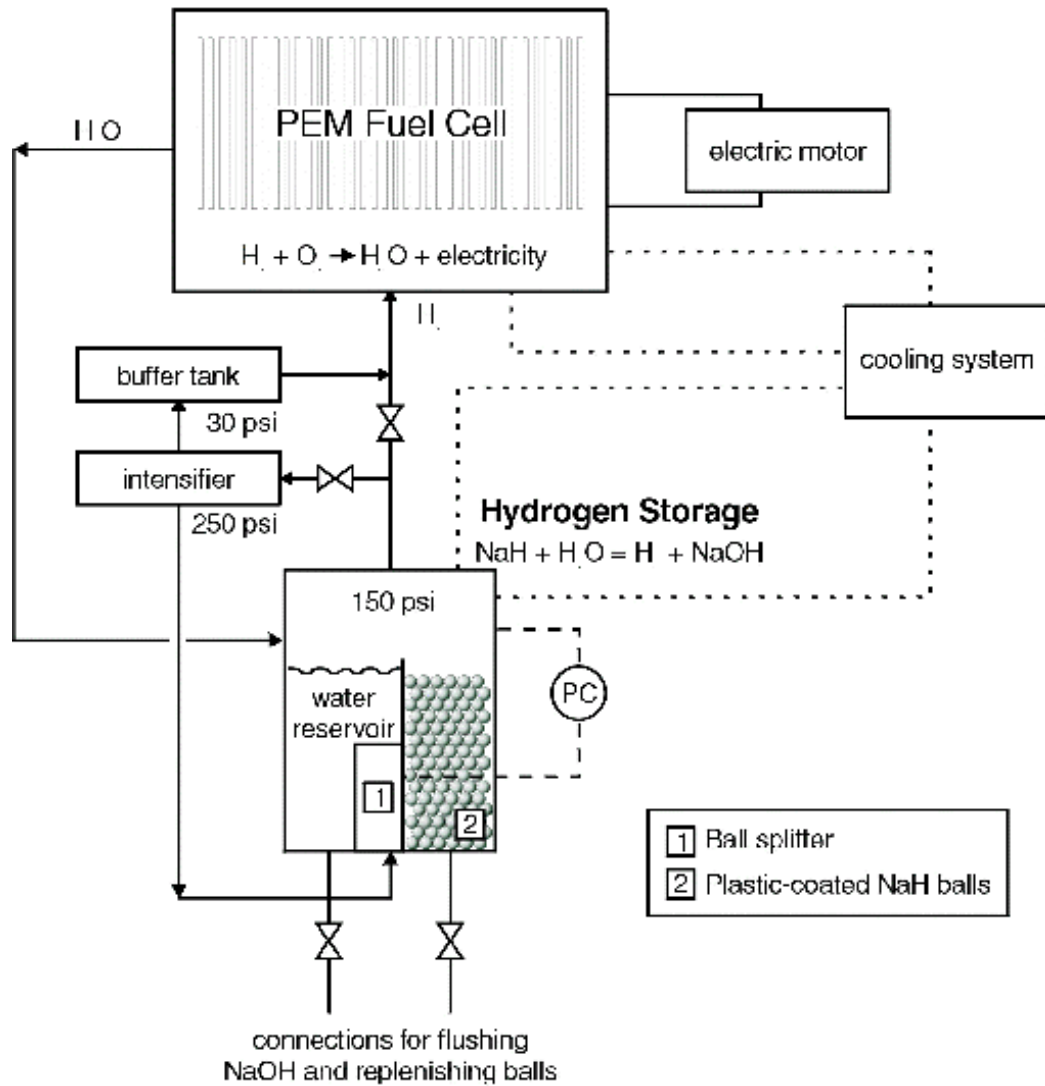
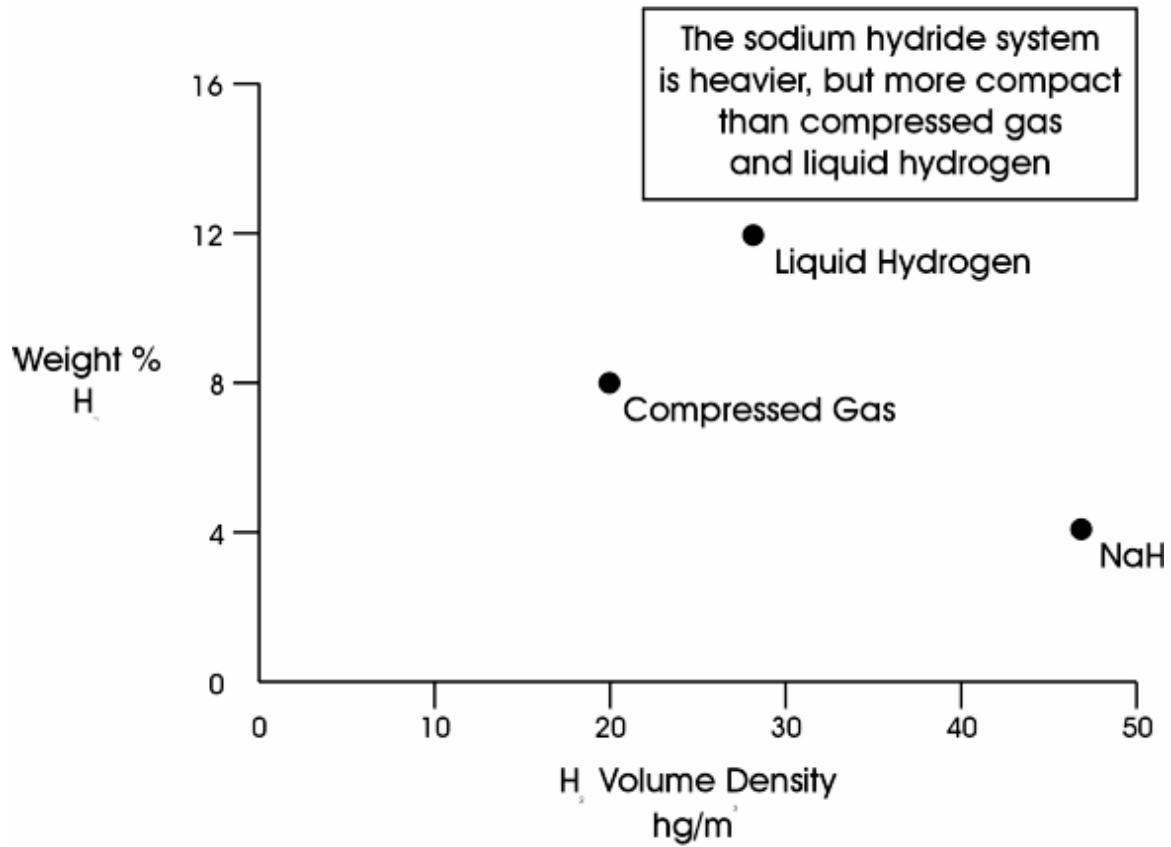


Figure 6. Hydrogen Storage Density*



* Based On Systems That Store 4.1 Kg Of Hydrogen

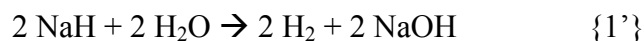
Addendum: Addressing A Change to the PowerBall Process

Note: To avoid confusion, we are continuing with the equation numbering scheme that was used in the main report.

PowerBall, Inc. has recently proposed a change to their overall schematic for producing and recycling their sodium hydride pellets. In their new scenario, they indicate that the overall reaction for the recycling process will be:



If this is combined with the on-board hydrogen-generation reaction:



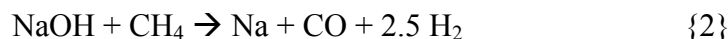
the result is:



So that in effect one mole of methane is being used to produce two moles of hydrogen.

PowerBall has indicated that a key factor in determining the viability of the recycling process that is being discussed here is the question of whether reaction {6} is exothermic. Reaction {6} is indeed exothermic, releasing 15.8 kcal/mole of methane.

However, some discussion is necessary as to the importance of this exothermicity. Reaction {6} is the result of a series of reactions and processes that involve the transfer of heat and mass, and thus any rational analysis must be based on a calculation that takes each of the individual component reactions into account. According to information supplied by PowerBall, the reaction would be carried out by first reacting methane with sodium hydroxide as in the previous scheme:



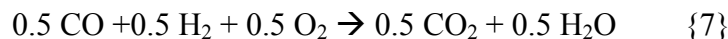
½ mole of hydrogen would still react with the sodium:



This leaves 2 moles of hydrogen and one mole of CO – a “syngas” mixture.

PowerBall then claims that about one half of the syngas can be combusted to provide the heat to run reaction {2}.

In order to provide the correct stoichiometry, we will use half of the CO, but only 0.5 mole of hydrogen:

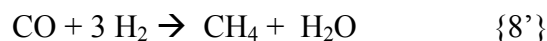
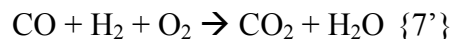
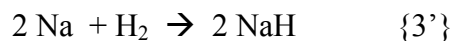


The remainder of the syngas, ½ mole of CO and 3/2 mole of hydrogen could then produce methane and water in the “reverse reforming” mode:



The methane product of reaction {8} can then be recycled to reaction {2}, etc. Thus, each subsequent recycling reclaims 1/2, 1/4, 1/8, 1/16, etc. moles of CH₄ for further reaction.

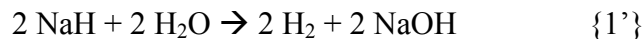
As the recycling continues, the theoretical limits to equations {2}, {3}, {7}, and {8} become:



which combine to produce:



Thus, stoichiometrically, it is true as PowerBall has contended, that one mole (16 grams) of methane will produce two moles (48 grams) of sodium hydride, which will in turn lead to the on-board production of two moles (4 grams) of hydrogen:

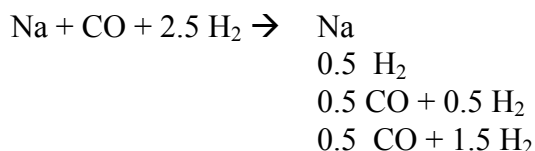


However, the overall exothermicity of equation {6} of -15.8 kcal, includes reaction {3'} as one of its components. This reaction occurs separately from the main recycling system, and its released heat cannot be used to aid in the recycle process. The reaction is exothermic by 28 kcal. Thus, the recycle process, which is composed of reactions {2}, {7'}, and {8'} combine as follows:



is actually endothermic by 12.2 kcal in total, or by 12.2/2 = 6.1 kcal/mole of NaOH reacted

Even more important is the fact that in order to follow the recycling process scheme as described by PowerBall, and shown here by reactions {2}, {3}, {7}, and {8}, the reaction {2} products must be followed by separation into 4 product streams:



with the first and second streams reacted to regenerate the sodium hydride by reaction {3}, the third stream reacted to liberate energy for recycling in the system by reaction {7}, and the fourth stream reacted to form methane by reaction {8}.

It should be further pointed out that yet another separation is then necessary – the methane produced in reaction {8} must be separated from the water before being reintroduced into reaction {2}.

Reaction {2} must be run a high temperature to produce the desired products. This is evident from Figure A, which shows the major species that occur in equilibrium between an equimolar mixture of liquid NaOH and CH₄. To form sodium, the reaction is best run at a temperature greater than 1200 K (927 C) and preferably closer to 1300 K (1027 C). In order to separate sodium from this mixture, the gases must be irreversibly quenched to a low temperature, thus freezing the high temperature mixture composition. The quenching of the products has some energy loss associated with it. In addition, although the conversion of sodium is high, it is not 100%, and thus there will be some loss of sodium in this process.

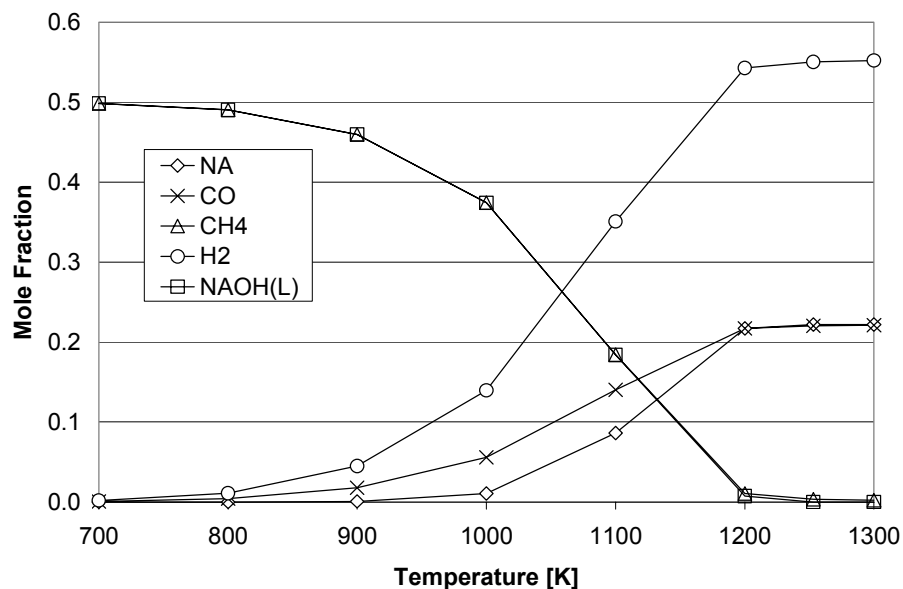


Figure A. Equilibrium composition of an equimolar mixture of methane and sodium hydroxide (CH₄ + NaOH_(L))

Another form of loss that will occur is the energy expenditure and less than unity conversion efficiency from each of the 5 separation processes described above.

We can now repeat the analysis for energy consumption that was presented in the main body of the report, modified based on the new set of equations:

We note that the energy consumed by the conversion now equals the heat value of the methane charge plus the heat required to drive the reaction. The heating value of the syngas is now incorporated into the equation (equation {9}). Note, however, that there is now more Na produced per unit methane.

One mole of methane is consumed for every two moles of sodium hydroxide reacted. Based on the heat of combustion of the natural gas consumed, 191.8 unit of heat energy are consumed for every two moles of sodium hydroxide reacted.

$$\frac{1 \text{ mole CH}_4}{2 \text{ mole Na}} \times \frac{191.8 \text{ kcal}}{\text{mole CH}_4} = 95.9 \text{ kcal heat / kcal NaOH reacted}$$

This is the heating value of stoichiometric methane, and is added to the heat of reaction {9}, 6.1 kcal/kcal NaOH reacted:

= 102.0 kcal/mole NaOH reacted. This is substantially lower than the energy requirement (162.6 kcal) for the original process.

On a hydrogen basis, as before, the energy requirement on a per hydrogen unit energy basis is calculated using the lower heating value of hydrogen:

$$\frac{102.0 \text{ kcal}}{\text{mole NaOH}} \times \frac{1 \text{ mole NaOH}}{1 \text{ mole H}_2} \times \frac{1 \text{ mole H}_2}{57.8 \text{ kcal}} = 1.76 \text{ kcal energy input / kcal hydrogen.}$$

We could also consider using the heat generated during the hydride production process,



-14 kcal/mole Na, as a drying source for NaOH. Recall that Table 6 showed the need of 0.44 energy units per energy unit of hydrogen produced to dry the hydroxide. Since each mole of Na eventually converts to one mole of hydrogen, the production of 57.8 kcal of hydrogen is preceded by the production of 14 kcal of heat during the hydriding step. Thus, there is a gain of $14/57.4 = 0.24$ energy units/ energy units of hydrogen produced due to the hydriding step. If we assume an 80% heat transfer, this is still 0.19 units. This reduces the need of fuel to $0.44 - 0.19 = 0.25$ units for this step.

In trying to look at the cost of the revised process, we must consider the fact that we have dropped the sodium carbonate heater and added what might be at first considered a more direct heating mechanism. However, due to the batch nature of the process, we are actually dealing with a different indirect heater – the walls of the reactor. We are also faced with the need either for a larger reactor to accommodate air as an oxygen supply, or to purchase reactant oxygen. Finally, we need a separate reactor to perform the reverse reforming reaction.

We can then modify Table 6 to incorporate these changes.

| Table 6'. Energy losses in the sodium hydride-based hydrogen energy pathway | | |
|---|--|---|
| Process stage | Heat lost, Btu of thermal energy per Btu of hydrogen energy delivered to the vehicle | Notes |
| Drying the sodium hydroxide solution* | 0.25 | Assume a two stage drying process; the first stage takes the solution from 50% to 75%, and the second takes it from 75% to 100%. Assume the steam from the second stage is re-condensed in the first stage. |
| Raising the temperature of the reactants to 980C | 0.22 | Assume 50% of the duty is achieved via heat integration |
| Conversion of sodium hydroxide to sodium hydride | 1.76 | Includes the heating value of the methane used |
| Conversion of sodium hydride to hydrogen fuel onboard | 0.55 | Exothermic reaction with water produces heat on-board the vehicle, which is dissipated. |
| Total | 2.78 | |
| Note that for this analysis we have assumed a 50 wt % solution as opposed to 30 wt % in the base case analysis contained in the report. This reduces the amount of water that must be boiled off per unit of sodium by a factor of 2, although the impact on the overall energy consumption is small. | | |

In addition, as already pointed out, the new process requires an increase in the number of separations necessary to provide reaction materials. In addition to the separation of sodium (already a factor in the original scheme) the separation of reaction {2} syngas components into three fractions would also be required. This would be manifested as 1) one-fifth of the H₂ for hydriding the sodium (as in the original system), 2) one-fifth of the H₂ and half of the CO to be combusted to provide heat, and 3) three-fifths of the H₂ and the other half of the CO to convert to methane. The separation of product methane from water represents yet another process. Membrane systems and pressure regulators could likely be set up to approximate this type of separation, but performing this inexpensively and efficiently represents a challenge to the project.

The improved utilization of methane as depicted by this revised process is offset by the additional expenses that are likely to be incurred by:

- The need for a separation process to provide the proper stoichiometry for the syngas combustion and the methane regenerating reactions,
- Either the need for a bigger reactor to accommodate air to oxidize the syngas, or the increased operating expenses that will be incurred to supply oxygen for the same process,
- The greater losses of efficiencies that come with more complex processes,
- The additional reactor needed to regenerate methane.

Disclaimers

This report was prepared as an account of work sponsored by an agency of the United States Government. Neither the United States Government, nor any agency thereof, nor any of their employees makes any warranty, express or implied, or assumes any legal liability or responsibility for the accuracy, completeness, or usefulness of any information, apparatus, product or process disclosed or represents that its use would not infringe privately owned rights. Reference herein to any specific commercial product, process, or service by trade name, trademark, manufacturer, or otherwise does not necessarily constitute or imply its endorsement, recommendation, or favoring by the United States Government or any agency thereof. The views and opinions of authors expressed herein do not necessarily state or reflect those of the United States Government, or any agency thereof.

This research report was prepared by Energetics, Incorporated as an account of work sponsored by the United States Department of Energy, Office of Energy Efficiency and Renewable Energy Under Cooperative Agreement Number DE-FC36-98GO10291. Because of the nature of the work performed, neither Energetics, Incorporated nor any of its employees makes any warranty, express or implied, or assumes any legal liability or responsibility for the accuracy, completeness, or usefulness of any information, apparatus, product, or process disclosed, or represents that its use would not infringe privately owned rights. Reference herein to any specific commercial product, process, or service by trade name, trademark, manufacturer, or otherwise does not necessarily constitute or imply its endorsement, recommendation, or favoring by Energetics, Incorporated.

NHA DOE COST SHARED ACTIVITIES

Robert L. Mauro and Karen I. Miller
National Hydrogen Association
1800 M Street NW, Suite 300
Washington, DC 20036-5802

Abstract

This paper describes the NHA tasks that have received cost share support from the U.S. Department of Energy Hydrogen Program for years 1999 or 2000. For the purpose of this review, we are including all activities for which the NHA normally receives DOE cost-share support, to include education and outreach tasks (including the new tasks being proposed for this year), our codes and standards work, and the annual meeting. This is in contrast to last year when we only presented our DOE cost-shared Codes and Standards tasks.

Introduction

We will begin by responding to the issue raised at the 1999 DOE Hydrogen Program Peer Review regarding an interest in more examples. We provided more examples this year, and in fact, the Proceedings from the Industry Perspective Workshop held at the end of October were handed out at the Peer Review. We held off on producing these Proceedings so that we could include the results of changes to the Hydrogen Commercialization Plan. The changes were adopted in March at the Annual Membership Meeting. You can add these to the list of publications for FY2000.

Since before the DOE had a hydrogen program, the NHA Mission has been to foster the development of hydrogen technologies and their use in commercial and industrial applications and to promote the role of hydrogen as a major energy carrier of the future

The basic long-term goals are determined by the greatest needs tempered by activities consistent with the role of the NHA as an association. Today these are:

- To Educate the public and policy makers on the benefits of hydrogen
- To Assist in the development of necessary hydrogen codes and standards
- And to Support the development of hydrogen infrastructure which in turn supports the deployment of hydrogen-related energy technologies

Discussion

There are three primary objectives to the tasks the NHA, in conjunction with DOE and other stakeholders, performs. The first is to facilitate timely information exchange between the hydrogen industry and DOE. The NHA strives to provide a forum for issues and present consensus positions to policy-makers, public and the rest of the energy community, as well as at international forums.

The Rationale for this is that the commercial deployment of hydrogen requires a partnership between industry and government. This can only be effective if the public and other potential stakeholders are educated to the promise of hydrogen.

Our second objective is to continue to work toward new hydrogen standards internationally and develop preliminary information prior to proposing new international standards and establish liaison with national and international organizations that are involved in developing hydrogen-related standards.

The rationale for this is simple: For hydrogen to be other than a curiosity, it requires standards to assure the public, financiers, and insurance companies that hydrogen products, equipment, and systems are safe.

Originally our role was to develop codes and standards for hydrogen systems where there were none. The NHA performed the preliminary work because hydrogen project proposals were questioned, and the standards did not yet exist. Now others are working on safety codes and standards and our role is evolving.

And finally, our third objective is to continue to update the Hydrogen Commercialization and Implementation Plans, Measure Progress toward Plan Goals and work to incorporate new hydrogen standards into demonstration and validation activities.

The Rationale for this is as follows: Measuring progress in reaching the commercialization goals will allow the hydrogen community to refocus its efforts on near term goals not yet achieved, while evaluating new standards on DOE field projects will allow for an early assessment of the effectiveness of the standard.

The tasks for which the BHA receives DOE support can be broken into three main areas: Education and Outreach, Codes and Standards, and Annual Meeting. I will go through the efforts we have been performing up to this point, and reserve discussion on the new items being proposed for the discussion on plans for next year.

Under Education and Outreach, the NHA carries out its information dissemination activities.

NHA Information Exchange:

Current year activities include our Quarterly Publication, the *NHA News*, Quarterly or bimonthly (based on available funding) Publication, *H2Digest*, a membership directory, the NHA web page, and a members-only website under development

Information Exchange within the Hydrogen Industry:

To provide a forum for issues, to present consensus hydrogen industry input domestically and furnish a collective U.S. hydrogen industry position at international meetings, attend key energy meeting, including hydrogen-specific and broader energy-related meetings and conferences. Current year activities include the Hydrogen brochure which the reviewers received I their advance publications package, participation in a number of meetings, including this one, participation in activities of the Hydrogen Technical Advisory Panel, and preparations to attend Energex 2000 in July.

Presentation of U.S. Hydrogen Positions and International Information Exchange at Safety, Codes and Standards Forums:

The NHA is tasked to present the U.S. hydrogen positions at international forums and participate in international meetings that are of benefit to the hydrogen community in the areas of hydrogen safety, codes and standards. In addition, the NHA will attend ISO/TC-197 work group meetings, plenary sessions, and other applicable international meetings. In addition to ISO, the NHA is now participating in a new IEC-TC-105 working group on fuel cell standards.

Industry Perspective:

The goal of this activity is to provide DOE and the hydrogen community with guidance on what institutional measures should be taken to insure the safe deployment of hydrogen technologies by government and industry funded projects. The NHA is in the process of revising the goals of the Hydrogen Commercialization Plan and make recommendations to changes for the Hydrogen Implementation Plan based on progress in achieving the goals contained therein. The Proceedings distributed to the review team today summarize our activities in this area over the past eight months.

Hydrogen Safety, Codes and Standards Outreach:

The NHA strives to coordinate efforts and provide information dissemination on domestic hydrogen codes and standards, which allow hydrogen energy systems to be sited and used in the United States in a manner similar to natural gas. The NHA continues its work on facilitating the development of recommended practices and codes and standards critical for the commercial use of hydrogen as an energy carrier. The NHA continues to coordinate codes and standards activities to avoid duplication of effort and enable hydrogen systems to be sited with industry groups and standards organizations such as International Standards Organization, Society of

Automotive Engineers, International Codes Council, IEEE, IEA, the U.S. Fuel Cell Council, Fuel Cell Propulsion Institute, National Fire Protection Association, and others.

Hydrogen Demonstration and Validation:

The NHA will continue efforts to review the codes and standards practices used in current hydrogen demonstrations and to validate the codes and standards being developed through the NHA, ISO and others. This effort includes the information dissemination and public outreach of hydrogen demonstration activities. This information dissemination and public outreach allows the public to become more familiar and comfortable with uses of hydrogen energy. The NHA has begun discussions with the California Fuel Cell Partnership, SunLine Transit, UCRiverside, Air Products, and others with plans to build hydrogen-refueling facilities. The NHA will work with these entities to provide draft standards for use in the refueling projects so that lessons learned can be utilized by the project managers, and real-world issues fed back into the codes and standards development process.

Codes and Standards Technical Tasks:

The Codes and Standards technical work includes consensus building within the hydrogen industry, other stakeholders, and a number of codes and standards development bodies. It involves the development of draft standards for hydrogen energy systems, and the validation of these draft standards through industry. Over the past few years, the NHA developed draft standards for compressed hydrogen tanks, vehicular refueling stations for gaseous hydrogen, and connectors for hydrogen refueling. These drafts were submitted and accepted by ISO-TC-197 as working items. The NHA continues to support these international activities through participation in the working groups and working with industry to validate the draft standards. In addition, last year the NHA began four new working groups. These groups will determine whether the required standards exist for hydrogen, whether other groups are developing the required standards, or whether the NHA should develop a draft standard in the following areas:

C&S for the Use of Electrolysers and Fuel Cells at Customer Sites, Including Homes.

Stuart Energy Systems, Teledyne Brown Engineering and other NHA members, as well as nonmember experts and stakeholders are looking into the creation of a draft standard.

C&S for Safe Self-Service Refueling of Vehicles with H₂.

Shell Hydrogen, BP Amoco, Air Products and Chemicals, Ford, and a number of other stakeholders are involved in this activity. The Society of Automotive Engineers is taking the lead on this, and works with the NHA on hydrogen safety issues.

Certification Program for Hydrogen Vehicle Fuel Systems.

Like the item above, the SAE has the lead on this, with support from NHA staff and members.

C&S for Maritime Unique Applications of Hydrogen.

This activity entails the identification of unique applications of hydrogen for maritime uses. The NHA has several members on the Maritime Hydrogen Technology Development Group, led by DCH Technology, which you heard about this morning. The purpose of this NHA Working Group is to interface with the MHTDG and others involved in fuel cells for maritime applications on Safety, Codes and Standards issues.

In addition to these groups, the working group on containers has begun to address the issues of codes and standards for hydrides. A report from each active group will be presented at the NHA Safety, Codes and Standards Workshops.

Annual Meeting:

The theme of this year's annual meeting was *The Universal Fuel*, universal meaning all-inclusive. The meeting addressed market issues through panels focused on hydrogen generation and why building a ground vehicle that uses hydrogen is necessary. It is clear from the discussions that storage and infrastructure remain issues to be overcome and demonstrated as well as the task of reducing fuel cell costs. The meeting addressed many of the activities necessary to successfully commercialize hydrogen including a panel on how best to publicize hydrogen demonstrations and developments through mainstream media. This meeting continues to enjoy support from DOE, NASA, and industry.

This is a listing of the NHA publications since the last Peer Review. Those publications prepared in FY2000 were provided in the review package.

- Quarterly Publication, NHA News: Vol. 3 Nos. 2 and 3 and Vol. 5 Nos. 1
- Quarterly Publication, H₂Digest: Vol. 11 Nos. 4 and 5 and Vol. 12 Nos. 1
- NHA Codes and Standards Workshop Proceedings 16-18 August, 1999
- NHA Implementation Plan Proceedings 26 October, 1999 (Draft)
- U.S. Annual Hydrogen Meeting Proceedings 7-9 April, 1999
- Creating a hydrogen-powered future 1 March, 2000
- 1st Quarterly Report Cooperative Agreement DE-FG03-99EE35108 10 November, 2000
- 2nd Quarterly Report Cooperative Agreement DE-FG03-99EE35108 24 February, 2000
- NREL Final Report "Development of Codes and Standards for the Safe Use of Hydrogen" 28 January, 2000

The *NHANews* issues are available on the NHA website at <www.HydrogenUS.com>.

The Codes and Standards Reports are generally sanitized to remove the contractual language, and are reformatted into a C&S Update report, which is also posted on the NHA website periodically.

If you are interested in additional copies of the hydrogen brochure “Creating a hydrogen-powered future”, which the NHA unveiled during the Annual Meeting in March, please contact the NHA at 202-223-5547.

Due to discontinuities in funding, the NHA has not presented at as many conferences as we had hoped. We did however meet the minimum requirement of three presentations. Staff presented at the *2nd Annual Lake Tahoe Fuel Cell Conference* in October, and made a presentation on the NHA Codes and standards activities as they relate to infrastructure development at the *F-Cells Infrastructure Conference* in Chicago in December. Both papers are included in published proceedings for those conferences. In addition, Bob Mauro was invited to make a presentation on hydrogen energy at the *Conference on the Future of Energy*, held by the Bureau of Intelligence and Research, U.S. Department of State, on 29 March, 2000.

In addition, Bob Mauro has been invited to participate in a number of HTAP workshops, which have also had reports published from those meetings.

And finally, the NHA is pleased to announce that we have developed a ‘members only’ section on our website, where we have posted an updated membership directory. We will also be posting NHA committee meeting minutes and copies of quarterly reports to help keep our members better informed between annual meetings. We also plan to make available copies of PowerPoint presentations made by the NHA for easy modification and use by the DOE, HTAP, and members.

Conclusions

The impact of the results of these efforts can be summarized as follows:

In Education and Outreach:

The new Hydrogen brochure was well received. There were many favorable comments when handed out at the 11th annual meeting.

Over 1,000 brochures were distributed to the general public at EarthDay 2000 in April.

The NHA News and H₂Digest keeps the hydrogen community and policy-makers informed of advances and activities in the hydrogen energy arena.

Working closely with HTAP, DOE, and other key stakeholders on the NHA Industry Perspective activities, including revisions to the Hydrogen Implementation Plan has efforts among these organizations, and throughout the hydrogen community dovetailing, which is helping to shape the direction of hydrogen activities.

In Codes and Standards:

Most standards efforts have resulted in proposals accepted by ISO to turn into standards (three standards are currently under development)

These standards will influence California Fuel Cell Partnership, Iceland, California and Nevada refueling station projects

In the Annual Meeting:

The Annual Meeting has greatly increased interest in hydrogen in Congress and among policy-makers. Participation and positive feedback regarding the meetings continues to grow.

Future Work

In addition to the ongoing work described already, the NHA hopes to build upon the liaisons already established to advance the efforts in the development of codes and standards to assure that hydrogen energy systems are safe and accepted by the public.

The NHA proposes coordinating with the national hydrogen associations of the Americas and Pacific Rim to form a Hydrogen Joint Working Group whose goals concern hydrogen economic interests of their respective countries. It is aimed at multinational cooperation and the exchange of information that each member organization can use for their own benefit. It may also have a role in helping countries, that request it, develop a national association around that country's energy needs.

In addition, the NHA hopes to begin an education initiative that supports and expands on the hydrogen curriculum development that Mary Rose Szoka is developing. The NHA would like to devise a series of modern hydrogen experiments that can be performed as part of a high school curriculum, and will make a contribution to the hydrogen activities carried out at the National Laboratories. The success of this effort would increase the visibility of hydrogen technologies on high school students current science curriculum allowing the students the opportunity to understand the role that hydrogen can play in their future. It would also speed the development and transfer of information and acceptance of hydrogen energy. This could begin with a pilot activity at one National Lab, a University and two or three high schools, with results made available on the Internet. The University could perform reviews and analysis, and maintain the Internet site and associated chat rooms. The project could grow based on popularity and funding. This work will be closely coordinated with existing efforts to avoid redundancy and ensure compatibility of the final products.

The NHA is also interested in expanding the hydrogen brochure to include notable success stories. This will include greater participation from the hydrogen community. If there are activities that you would like to see in the next revision, please let us know, and we will try to include them in the revision, funding permitting.

Our objectives for next year are to educate the public and policy makers on the benefits of hydrogen. Our planned activities support this objective.

We plan to conduct the 12th Annual U.S. Hydrogen Meeting with a theme surrounding hydrogen energy systems and success stories.

We plan to increase outreach to the public through wider distribution of new publications and enhancements to the NHA Web Site, as described earlier.

The NHA will continue to measure progress of the hydrogen community in achieving the interim goals of *the NHA Hydrogen Commercialization Plan* and the *DOE Hydrogen Program Plan*. This activity would involve polling the hydrogen community to determine where cost and performance targets are involved, and record the progress toward those targets. The information developed will be presented to the hydrogen community through a workshop and a report. It could serve as a mid-course correction in our efforts to achieve our goals or cause us to begin to modify those goals.

Through the Hydrogen Joint Working Group, we hope to develop regular meetings between hydrogen associations of various countries to share information, experiences and policy positions.

And as stated earlier, we are very interested in working with Mary Rose and the national labs to move hydrogen into the classrooms.

With regard to Safety Codes and Standards, we would like to continue the activities that are ongoing and advance the items in the new working groups toward a draft that can be submitted to ISO or other applicable code or standard body. We plan to continue and expand coordinated efforts with the automotive industry, fuel cell industry, hydrogen safety experts, electrical industry, and International Code Council to assure hydrogen systems may be sited, and acceptance of the new technologies.

We would like to work with the Compressed Gas Association and ANSI to take the first steps toward becoming the Technical Advisory Group in the U.S. for ISO TC 197. We also plan to begin activities on the newly formed IEC TC 105 on fuel cell standards.

Another objective is to support the development of a hydrogen infrastructure that supports the deployment of hydrogen-related energy technologies. Examples include increasing involvement in tracking demonstration projects that may provide success stories for hydrogen, and pave the way for a future hydrogen economy. These activities include the California Fuel Cell Partnership, the Iceland Energy Economy, Fuel Cell Mining Vehicles, Refueling station activities, and others.

And finally, we hope to support the development of a DOE hydrogen initiative, so that Hydrogen can begin to get the recognition it deserves from policy makers and the public.

EDUCATION OUTREACH

Mary-Rose Szoka-Valladares
M.R.S. Enterprises
P.O. Box 30452
Bethesda, MD 20814

Abstract

Recognizing the benefits of education, the Hydrogen Program conceived of an Outreach effort that would position hydrogen and hydrogen related technologies for current science study, formal and informal. Such study is intended to produce contemporary understanding and future adoption and use of hydrogen and related technologies.

The effort has produced high school and middle school versions of a curriculum (working title *Clean Corridor Curriculum*) and collateral video products. The curricula and collaterals are being branded as HOPE (Hydrogen Outreach Programming for Education) products.

M.R.S. intends to complement the core HOPE products with items such as Sentech's Mission H₂ CD ROM and Eco Soul's reversible fuel cell kit.

The effort has also produced live science shows that present Hydrogen Program content and programming to local secondary school audiences.

Development of the core curriculum and collateral products nears completion. Planning of marketing strategy for promotion and distribution has begun. Both Internet and traditional channels are contemplated for marketing.

There is every expectation that the products will be available in the marketplace over the coming year.

Long-Term Goals

The overarching long-term goal of this hydrogen outreach effort is to educate students and teachers about the properties and benefits of hydrogen, its technology applications and cross-cutting uses, as well as its potential as a fuel and energy carrier.

Consistent with the intent of the *Matsunaga Act* and the *Hydrogen Futures Act*, the specific goals of Hydrogen Instructional Programming (HIP) are:

- to increase awareness and preference for hydrogen energy uses and technologies
- to increase awareness and preference of renewable energy and energy efficiency technologies and practices

through development and dissemination of instructional materials (curricula, films, CD ROMs) and production of live science shows.

The instructional materials serve to accelerate adoption of hydrogen energy uses and technologies, building on increased awareness and preference for hydrogen energy uses and technologies, as well as renewable energy and energy efficiency technologies and practices. The dissemination strategy is intended to effectively distribute HIP products, resulting in deep penetration of our target markets, secondary school teachers and students. The production of live science shows is intended to complement development and dissemination of instructional materials and thereby reinforce the outreach effort.

Current Year's Objectives and Rationale

The demand for hydrogen education outreach is growing. This demand is spurred by Congress, industry and progress in hydrogen technology research and development. These activities press toward commercialization of hydrogen and hydrogen related products, notably fuel cell technology. The NHA has identified outreach as one of its top priorities and one of industry's greatest needs. Moreover, popular culture has discovered hydrogen. An increasing number of publications from *The Washington Post* to *Red Herring* are featuring hydrogen articles. The recent mini energy crisis offers another window of opportunity to introduce students and the greater public to hydrogen. Thus, this education outreach effort and its HIP products are very timely.

Important themes of this year's work are:

progress toward completion and assembly of curriculum and collateral film and video products;
enhancement of other outreach activities, notably live science shows;
a coordinated approach to promotion of these products and activities that includes preliminary formulation of a distribution strategy using mixed print and web-based solutions.

A final cross-cutting theme, greatly encouraged by the Hydrogen Program, involves cooperation and collaboration with other organizations.

Although no funding was available to allow M.R.S. to formally coordinate programmatic outreach efforts as stated in the Annual Operating Plan, great effort was made to cooperate informally with key players. They include: the NHA, Sentech, Inc., Drs. Jay Keller and George Thomas from Sandia Livermore National Laboratory, the Florida Solar Energy Center, Eco-Soul, the California Fuel Cell Partnership and the National Fuel Cell Research Center at the University of California Irvine.

Specific objectives of HIP, this year's work are:

- to reach teachers and education decision-makers through the field-testing and evaluation processes
- to reach students directly through modular curricula that educate students about hydrogen and hydrogen technologies while reflecting current science and technology pedagogy and practice, including national science standards
- to reach students directly through audio-visual support materials, video and video-clips, that educate students about hydrogen and hydrogen technologies while also providing informal education opportunities
- to position the DOE Hydrogen Program to successfully market and distribute the breakthrough curricula by ensuring the best possible curricula products

Current Year Tasks

Five discrete HIP tasks were funded by the Hydrogen Program. Two additional tasks, supported in part by the Hydrogen Program, proved sufficiently important to the long-term goals and current year objectives that other funding or M.R.S. cost-share resources were applied to their execution. These tasks are discussed below as Tasks 6 and other. A final task, listed in the Annual Operating Plan as (funding permitting) Task 5: Hydrogen Education Outreach Coordination, was not addressed because no resources were available from any source to create a comprehensive written plan for coordination of education outreach.

A brief description of each task appears below:

Task 1 Support for curriculum dissemination via field-testing and evaluation of the beta-version high school curriculum

Task 2 A workshop devoted to revision of the beta version of the high school curriculum per field testing and evaluation results followed by field-testing and evaluation of the 1.0 version high school curriculum preparatory to its formal launch in education markets.

Task 3 Modification of the high school curriculum to create a separate product that is appropriate for middle school populations, coupled with design of a framework for its field-test and evaluation.

Task 4 Creation of short videos (working title *Red Thunder* now called *The Pollution Solution*; working title the *Dr. Bob Show* and working title *Beakman's World: Beakman on Hydrogen*) as collateral products that complement the curricula, comprising part of the deluxe CCC teachers' kit. These products also contribute to the EERE and Hydrogen Program portfolio of information tools available for informal education and public outreach.

Task 5 Creation of a challenge project that will allow secondary schools to design and develop their own hydrogen technology demonstration

Task 6 (Not DOE funded) Production of live science shows, including the *DOE/NHA Secondary School Invitational* at the NHA annual Conference and the local middle school on-site production

Other Outreach and Promotion

(Not DOE funded) Conferences and Speaking engagements; general promotion; initial development of marketing strategy

Current Year Progress

Task 1 Support for curriculum dissemination via field-testing and evaluation of the beta version curriculum.

Initial field-testing of the beta version high school curriculum occurred during the spring of 1999 under previously funded work. Participating teachers were recruited from M.R.S. presentations and other curriculum promotion efforts. No monies were available to compensate teachers. Teachers "self-selected" to participate in the field test on the basis of interest in the subject and ability to integrate the curriculum into existing courses.

With HIP funding, a field test survey instrument was developed and administered to participating field test teachers. A Field Test Survey Report was developed from the survey. The Field Test Survey provided significant feedback about important curriculum issues. This feedback has guided the formal field test process for academic year 2000. Survey results were analyzed and findings were summarized as Lessons Learned. Key Lessons Learned include: the importance of requiring use of lessons from all modules; the need to provide a financial incentive for participation; the importance of field-test timing; and the need to provide teachers with a paper copy of the curriculum, even in cases where an electronic copy is also desired.

No monies were available to pursue active development of a reversible fuel cell. However, M.R.S. began to use the (loaned) Eco-Soul reversible fuel cell kit as well as the Eco-Soul Hydrogen Fueling Station (designed to complement the curriculum's final project by the same name) for demonstration purposes. Both M.R.S. and Eco-Soul undertook this joint activity on a cost-share basis without HIP funding. The M.R.S. interest in this collaboration is enhancement of the hydrogen education outreach effort through availability of a kit that shows the reversibility of fuel cell and electrolysis processes in a safe, portable device.

Task 2 ***After the initial field-testing, a workshop devoted to revision of the beta version curriculum, followed by field testing and evaluation produced high school version 1.0 preparatory to its formal launch in education markets.***

A workshop was held in late summer to revise the *Clean Corridor Curriculum* in accordance with the results of field test and evaluation. The original *Clean Corridor Curriculum* team worked on the revision to modify existing lessons and added some new lessons. Dr. Robert Reeves and Dr. Jay Keller reviewed the revised material.

To assure classroom safety, an independent safety review was also conducted. M.R.S. developed a three-category template to assess the safety of individual labs and demonstrations in the classroom. The three categories classify labs as follows:

- Category I) Low-no student safety risk;
- Category II) Student safety risk associated with this lab (student participation may be considered);
- Category III) Student safety risk (s) associated with this lab (student participation inappropriate).

The primary safety reviewer was Mr. Paul Mercier, a secondary school science teacher/former college science instructor from Arizona. (See the attached report). Dr. Robert Zalosh of Worcester Polytechnic Institute in Massachusetts provided a secondary safety review. The safety review was not anticipated or funded by DOE. The NHA graciously furnished a stipend for the principal reviewer for this activity. The secondary reviewer graciously declined a stipend.

An improved field test survey instrument was devised for the high school version 1.0. A new group of field test teachers was recruited from M.R.S. growing network of teachers. Now in a formal, nationwide field-test, the curriculum contains five major modules and a final project, plus a sixth module that features exercises related to the exciting Sentech CD ROM, *Mission H₂*.

Task 3 ***Modification of the existing curriculum to create a separate product that is appropriate for middle school populations, coupled with design of a framework for its field-test and evaluation.***

During the curriculum writing workshop substantial progress occurred on development of the middle school curriculum. The high school curriculum was modified and expanded to create a separate product that is appropriate for middle school populations. The middle school curriculum was structured in three modules: 1) Basics; 2) an event based module entitled “The Pollution Solution”; and 3) a unit constructed around *Renewable Power: Earth’s Clean Energy Destiny*. Additional work is needed before the draft will be ready for technical review.

A framework for an academic year 2000-2001 field test of the middle school beta version is substantially complete. It will be finalized on completion of the formal field-test for the high school curriculum. Recruiting for middle school field test participation has been brisk.

Task 4 *Creation of short videos that complement the curriculum, compromising part of the deluxe teachers' kit and contributing to the EERE and Hydrogen Program portfolio of informal education and public outreach information tools.*

Post-production work on the *Dr. Bob Show* editing continues in the DOE editing suite consistent with the Edit Decision List and storyboard. Narration was recorded; work on laying the sound track has begun. Although progress is good, S-1 projects have delayed completion of the video.

Production work on The *Pollution Solution* (working title *Red Thunder*), including fuel cell animation, was completed. The video has gone to the editing suite for post-production creation of the "off-line."

It was determined that *Beakman: Beakman on Hydrogen* will be able to proceed in accordance with Columbia Tri-Star's requests. The next phase will entail execution of necessary legal documents with Columbia Tri-Star, followed by contracts with the cast, crew and supporting science writers and advisors.

Task 5 *Creation of a challenge project that will allow secondary schools to design and develop their own hydrogen technology demonstration*

Challenge Project Grant applications will be distributed on completion of the formal field test. Field test participants will have priority for these awards. The awards are intended to allow secondary schools to design and develop their own hydrogen technology demonstrations. All grant recipients will be required to share their projects with the Hydrogen Education Outreach effort. This information will be available on the web site to be constructed as soon as funding is available. Amount of the awards is expected to range from \$50-\$250. Awards will be made in September 2000.

Task 6 *Other Progress (Not DOE funded)*

- *Production of live science shows, including the March 1 DOE/NHA Secondary School Invitational at the NHA annual Conference and the upcoming local middle school science show*

The *Secondary School Invitational (SSI)* was held in conjunction with the annual National Hydrogen Association on March 1. Over 100 students from the Nysmith School from Virginia and the Heights School from Maryland attended the full-day event. A live science show, formerly the *Dr. Bob Show*, featuring Jon Hurwitch and his crew from Sentech, Inc. was the highlight of the morning session. During the morning, Dr. Keller demonstrated *Red Thunder*, the remote control fuel cell vehicle, and students built a fuel cell model from everyday materials. Dr. Peter Lehman demonstrated the Schatz fuel cell at lunch. The afternoon consisted of rotations between the *Dr. Bob Laboratory*, the *Learning Center* (hydrogen and fuel cell exhibits for students) and the NHA trade show. The show closed with a career panel, *Career Opportunities of a Lifetime*. A press release announcing development of the *Clean Corridor Curriculum* was prepared for distribution by the NHA before and during the annual conference.

The other live science show is scheduled for May 23 at a local Washington area middle school.

Creation of curriculum safety review process for laboratories and demonstrations with support of NHA

As an adjunct to the technical review, laboratories and demonstrations were reviewed separately for classroom safety. From this exercise a 3 category safety review process evolved. The purpose of the safety review process is to determine whether a laboratory or demonstration is “safe” for classroom use. If a particular laboratory or demonstration is deemed to present no safety hazards for classroom use, it is accepted as is. If it is deemed to have safety hazards, either modifications are proposed to ensure its safe use in the classroom by students or a recommendation are made to use the laboratory as a teacher demonstration only. If use as a teacher demonstration is still deemed inappropriate for safety purposes, a recommendation can then be made either to remove the laboratory/demonstration or use it only as a “virtual” demonstration, on film or CD ROM.

Other Outreach and Promotion

- *National Science Teachers’ Association Annual Conference – Exhibition and Speaking*

M.R.S. exhibited at the National Science Teachers’ Association (NSTA) Annual Conference from April 6-9. This is the most important trade NSTA show, attracting upwards of 25,000 educators each year. The M.R.S. exhibition included: a curriculum workshop with a demonstration of *Red Thunder*, the remote control fuel cell car; use of the DOE funded Sentech exhibit *The Evolution of Energy*; the curricula; promotional material on the Sentech CD ROM *Mission H₂*; and demonstration of a reversible fuel cell by Eco-Soul. M.R.S developed special curriculum announcements for this important trade show.

Neither Sentech nor Eco-Soul had Hydrogen Program funding to support this event. However, in the spirit of collaboration intended to better position the Hydrogen Program’s products, M.R.S. invited Sentech (and Eco-Soul) to exhibit.

- *Biannual ChemEd Conference, Annual Maryland Association of Science Teachers’ (MAST) Conference, semi-annual MAST Road show, Harford County Teachers In-Service Training*

These speaking engagements afforded M.R.S. the opportunity to build awareness about our instructional materials in the education community. It also provided an opportunity to train teachers and recruit field test participation.

- *Published articles on hydrogen outreach education in NHA News*

The NHA published an article an M.R.S. Education Outreach article in the fall 1999 issue and another M.R.S. article on the *Secondary School Invitational* for its April publication. These

articles spread news of hydrogen education outreach activities throughout the hydrogen community.

- *2nd Annual Lake Tahoe Fuel Cell Conference and Canadian Fuel Cell Conference (not DOE funded)*

These opportunities permitted M.R.S. to expose the greater hydrogen energy community – a primary “affinity” marketing group -- to the existence of the curriculum and its collateral products. The Annual Lake Tahoe Fuel Cell Conference was held in the fall. The P.I. also spoke on the marketing of hydrogen education at the May Canadian Hydrogen Conference. No HIP funds were used in either effort. Rather, they were supported by M.R.S. cost-share.

Participated in Marketing Panel at 10th Annual Canadian Hydrogen Association Meeting

The M.R.S. presentation on the Marketing Panel was well received. The Canadians initiated discussions about possible use of the curricula and cooperation in that aspect of the Hydrogen Education Outreach effort.

- *Acquired domain rights to web addresses for use in promoting/distributing hydrogen outreach products (not DOE funded)*

M.R.S. purchased the rights to the following domain names: hydrogen education.org; hydrogen education.com; hyed.org and hyed.com. These were acquired in anticipation of construction of a web site for promotion and distribution of the curriculum and collateral products. The web site is a cornerstone of the promotion strategy for our products.

Initial development of marketing strategy

Thinking about distribution channels (web and print) for the curricula and collateral products is an ongoing process. The NSTA conference offered opportunities to explore general marketing approaches and specific distribution channels. Importantly, preliminary contacts were made with several potential publishers.

Product branding was key to initial development of a marketing strategy. After market research the name HOPE (Hydrogen Outreach Programming for Education) emerged as the best possible brand name for our hydrogen education outreach products. The curricula themselves will be renamed to reflect their science content and facilitate promotion and distribution.

As previously discussed, conference and speaking engagements offered important opportunities to build awareness about our instructional materials in the hydrogen and renewable energy communities. The community is viewed as a set of affinity groups, some of which are expected to become partners in the marketing effort. For instance, The Florida Solar Energy Center (FSEC) has made an offer to promote and distribute the instructional materials. Likewise, the National Fuel Cell Research at University of California Irvine has made a similar offer. The California Fuel Cell Partnership is expected to issue formal statements of support for the curriculum soon.

Impact of Current Results

Instructional materials

The high school version 1.0 of the *Clean Corridor Curriculum* is now available for field test and inspection. The field test of the beta version curriculum entailed 3,000 student contact hours with 300 students. Assuming a minimum of 50 teachers complete the 12 hour classroom requirement, the formal 2000 field test will entail a minimum of 9,000 contact hours with 1,500 students.

The technical review of the middle school curriculum should be complete by the beginning of FY 2001. The middle school field test framework anticipates 9,000 student contact hours in the 2000/2001 field test.

Films

The Pollution Solution and *Beakman's World: Beakman on Hydrogen* will be complete soon. They will be assembled with the middle school curriculum for field-testing and with the high school curriculum for distribution. On completion, *Dr. Bob* will be broadcast on cable TV.

Teacher contacts

This year's HIP activities included personal contact with 350+ teachers; the NSTA exhibit had an audience of 25,000 educators.

Live Science Show Student contact

This year's estimate for live science show contact is 400 middle school students

Publisher contacts

Preliminary meetings with over a dozen publishers

Mailing Lists

The contacts made at various shows and conferences will be used to develop customized, targeted mailing lists for use in marketing and promotion.

Objectives for next year:

Next year's objectives encompass three major themes: completion of product development, product dissemination and enhancement of live science shows. These objectives expand on current year objectives. Next year's specific objectives are, as follows:

- to complete product development of core curriculum products
- to perform field test and evaluation of the middle school curriculum in support of product development
- to participate in industry meetings and develop supporting communications that inform the education markets and greater hydrogen industry about our curricula and collateral products while encouraging their adoption and use

- to develop and implement a product distribution strategy, supported by a mixed-media promotion strategy that features internet use

Plans for next year

Plans for next year consists of tasks related the three objective areas: completion of product development in preparation for dissemination; create and begin execution of a marketing strategy for the HOPE products; and produce live science shows.

Task 1 Completion of product development in preparation for dissemination

- Revise high school curriculum using field test results, adding material on renewable energy
- Field-test middle school curriculum, subsequently revise as indicated
- Add value to the curricula while emphasizing safety through development of CD Rom of virtual experiments as well as acquisition and use of reversible fuel cell kit for classroom demonstration (funding permitting)
- Brand instructional materials as HOPE (Hydrogen Outreach Programming for Education) products

Task 2 Create and begin execution of a marketing strategy that addresses all relevant aspects of product, promotion, place and price

- Develop and implement strategy to market and distribute curricula and collateral products, including selection of a print publication channel
- Design a supporting public relations strategy that ensures state of the art internet-based promotion
- Hold industry meetings to promote awareness, preference and adoption of HOPE products among decision-makers and teachers in education markets, and key players in hydrogen and related industries, funding permitting

Task 3 Produce Live Science Shows

- Continue to produce the DOE/NHA *Secondary School Invitational* local middle school live science show in conjunction with Sentech and historical collaborators
- Create the *SuperSecondary* Science Show with professional talent, funding permitting

Acknowledgments

Technical Advisor

Dr. Robert Reeves

From Montgomery County Public Schools

Dr. Gerard Consuegra, Secondary Science Coordinator

Ms. Pat Hagan, Middle School Science Coordinator

From Frederick County Public Schools

Mr. Larkin Hohnke, Science Curriculum Specialist

Mr. Nusret Hissim, Science Department Chairperson Walkersville High School

Dr. George Seaton, II, Principal of Urbana High School

From Harford County Public Schools

Mr. Dennis L. Kirkwood, Supervisor of Science

From Sandia National Laboratory, Livermore, CA

Dr. Jay Keller

Dr. George Thomas

From the National Hydrogen Association

Mr. Robert Mauro

Ms. Karen Miller

Safety Review

Mr. Paul Mercier

Dr. Bob Zalosh

Clean Corridor Curriculum Team

Mr. George Smeller, Co-Team Leader

Ms. Laura Corbin, Editor and Technical Advisor

Mr. Jeff Charuhas

Mr. John Ekelund

Mr. Tom Leonard

Mr. Kendall Morton

Mr. Meredith Stevens

From Eco-Soul

Mr. Skip Staats

References

- American Association for the Advancement of Science. 1993. *Benchmarks for Science Literacy: Project 2061*, New York, New York. Oxford University Press.
- Cannon, James. *Harnessing Hydrogen. The Key to Sustainable Transportation*.
- Carol D. Perkins Vocational Education Act of 1984. Pub. L. 88-210 (1984). STAT 98-2435 (1984).
- Carol D. Perkins Vocational and Applied Technology Education Act Amendments of 1990. Pub. L. No. 202-392. Stat 104-753 (1990).
- The Clean Air Amendments of 1990. Pub. L. No. 101-549. STAT 104-2399 (1990).
- The Energy Policy Act of 1990. Pub. L. 102-486. Section 2026.
- Thomas, Sharon and Zalbowitz, Marcia. 2000. *Fuel Cells Green Power*. Los Alamos, New Mexico: Los Alamos National Laboratory.
- Hearkenen, Henry et al. *Chemistry in the Community*. Dubuque, Iowa. Kendall-Hunt Publishing Company.
- The Hydrogen Future Act of 1996. Pub. L. 104-271.
- International Technology Education Association. 1996. *Technology for All Americans: A Rationale and Structure for the Study of Technology*. Reston, Virginia. International Education Association.
- Kotler, Philip. *Marketing Management*. 1997. Upper Saddle River, NJ. Prentice Hall.
- Los Angeles Unified School District: Board of Education. 1997. *Draft Interim Guidelines for Instruction: Secondary School Curriculum: Science*. Los Angeles, California.
- The Matsunaga Hydrogen Research, Development and Demonstration Act of 1990. Pub. L. No. 101-566. Section 102.
- National Academy of Sciences. 1992. *Policy Implications of Greenhouse Warming: Mitigation, Adaptation, and the Science Base*. Washington, D.C. National Academy of Sciences.
- National Council for Teachers of Mathematics. 1997. *Mathematics: An Introduction to the NCTM Standards*. Reston, Virginia. National Council for Teachers of Mathematics.

National Council for Teachers of Mathematics, 1997. *Mathematics: Making a Living, Making a Life*. Reston, VA. National Council for Teachers of Mathematics.

National Research Council. 1996. *National Science Education Standards*. Washington, D.C. National Academy Press.

National Science Foundation. 1997. *ChemQuest: Chemistry for the Information Age: A Technology-Rich High School Chemistry Curriculum on CD ROM*. Washington, D.C. National Science Foundation.

MacKenzie, James J. 1994. *The Keys to the Car. Electric and Hydrogen Vehicles for the 21st Century*. The World Resources Institute.

M.R.S. Enterprises. *Clean Corridor Curriculum*. 1999. U.S. DOE Contract No. DE-FG01-EE35109.

Office of Technology Assessment. 1996. *Changing by Degrees: Steps to Reduce Greenhouse Gases* (OTA-0-482). Washington, D.C. Office of Technology Assessment.

President's Committee of Advisors on Science & Technology 1997. *Report to the President on the Use of Technology to Strengthen K-12 Education in the United States*. Washington D.C. President's Committee of Advisors on Science and Technology.

Ronkainen, M.R. and I.A. Czinkota. *International Marketing – Fifth Edition*. 1997. Orlando, FL. Harcourt Brace College Publishers.

Rocky Mountain Institute. *Green Development*. 1998. New York: John Wiley & Sons.

Sentech, Inc. 1997 *Mission H₂ CD ROM*. Bethesda, MD 20814.

Gordon, Deborah for Union of Concerned Scientists. 1991. *Steering a New Course*. Cambridge, MA. Union of Concerned Scientists.

U.S. Department of Energy. Office of Conservation and Renewable Energy. 1992. *Hydrogen Program Plan FY1993-FY1997*. Golden, CO. National Renewable Energy Laboratory.

U.S. Department of Energy. Office of Policy, Planning and Analysis. 1990. *The Potential of Renewable Energy: An Interlaboratory White Paper*, Golden, CO. Solar Energy Research Institute.

U.S. Department of Labor. 1991. *What Work Requires of Schools*. Washington, D.C. U.S. Government Printing Office.

**U.S. DOE Hydrogen Program
2000 Annual Review Meeting
May 11, 2000
San Ramon, California**

**Creating an Informed Public
through a Video on Hydrogen
Safety**

**presented by
Geoffrey Holland**

Hydrogen 2000, Inc. of Studio City, California, is a non-profit 501 (c) (3) corporation formed in 1994. It has brought together some of the best technical people together with the expertise of the media and communications industry as board members and advisors.

Hydrogen 2000, Inc. video projects have raised the level of awareness of hydrogen and fuel cell technologies to countless audiences.

Element One, a one-hour documentary about hydrogen energy

- **Broadcast** in six different languages and at least eleven countries.
- **Uplinked to satellite** in 1997 and 1999 for broadcast on PBS stations across North America.
- **Distributed** to schools, universities, and libraries across the country by The Video Project.
- **Premiered** at the 11th World Hydrogen Energy Conference in Stuttgart. **Invited Screening** at NASA headquarters, Congress, and NHA and CHA meetings.
- **Winner** of the 1998 EarthVision '98 Environmental Film and Video Competition, and Honorable Mention in the 45th Annual Columbus International Film & Video Festival in 1997

Renewable Power: Earth's Clean Energy Destiny, a 29-minute educational video on hydrogen and renewable energy

- **Distributed** to schools, universities, and libraries across the country by The Video Project.
- **Premiered** at the 9th Canadian Hydrogen Conference in Vancouver, B.C.
- WOSU, a PBS station in Ohio, is sponsoring the video for a national **PBS broadcast**.
- **Winner** of an Emmy Award, the National Educational Media Network's Gold Apple Award, CINE's Golden Eagle Award, and an honorable mention in 1999 EarthVision '99 Environmental Film and Video Competition.

Need for a Video on Hydrogen Safety

Lack of codes and standards for hydrogen energy systems and misconceptions about hydrogen safety has presented obstacles for those seeking to obtain necessary approvals from permitting officials and insurance companies.

Hydrogen: The Matter of Safety

Producer: William Hoagland

Director: Geoffrey Holland

Supervising Producer: Susan Leach

Written by:

Geoffrey Holland, Susan Leach, and William Hoagland

A 20-minute video to educate permitting officials, fire marshals, and insurance companies—as well as science and engineering students—about hydrogen as a clean, efficient alternative fuel that is not inherently more dangerous than other widely used fuels.

A companion brochure will summarize key points and list sources of further information.

Sponsors

The United States Department of Energy

Natural Resources Canada

**NEDO/The Engineering Advancement
Association of Japan**

Additional Support

**Air Products and Chemicals, Inc.
International Association of Hydrogen Energy
Praxair, Inc.**

Safety Video Review Process

Content Outline

- Reviewed by over 20 experts selected from among Hydrogen 2000 directors, technical advisors, safety experts, and sponsors.
- Also reviewed by representatives of the target audience:
 - S A fire marshal / hazmat instructor from Littleton, CO
 - S A risk manager / NFPA committee member for Alternative Fuels Vehicles at Marsh & McLennan, a large insurance broker.

Script

- Reviewed by the above who offered specific comments and suggestions, improving the quality of the project.

For information on obtaining the brochure and accompanying video, or to find out about other Hydrogen 2000 productions, contact:



**Hydrogen 2000, Inc.
11684 Ventura Blvd., Suite 5108
Studio City, California 91604 USA
818-980-0725
e-mail: h2000@earthlink.net**

**Boulder Office:
7253 Siena Way
Boulder, Colorado 80301 USA
303-530-1140
e-mail: hydrogen2000inc@aol.com**